Kinetics of Water-Rock Interaction

SUSAN L. BRANTLEY • JAMES D. KUBICKI • ART F. WHITE

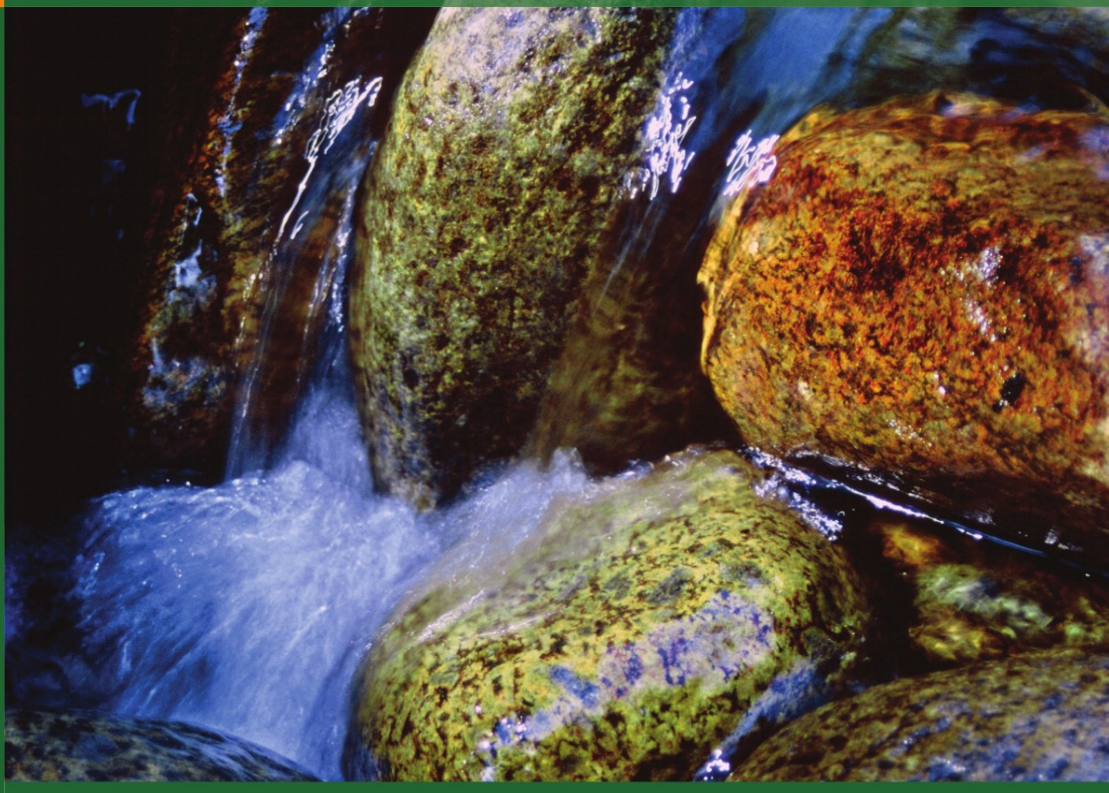

Springer

Kinetics of Water-Rock Interaction

Kinetics of Water-Rock Interaction

Edited by

Susan L. Brantley

James D. Kubicki

Art F. White

Springer

Editors:
Susan L. Brantley
The Pennsylvania State University
Earth and Environmental Systems Institute
2217 Earth-Engineering Science Building
University Park, PA 16802
USA
e-mail: brantley@essc.psu.edu

James D. Kubicki
The Pennsylvania State University
Department of Geosciences and the Earth and Environmental Systems Institute
335 Deike Building
University Park, PA 16802
USA
e-mail: kubicki@geosc.psu.edu

Art F. White
U.S. Geological Survey
MS 420, 345 Middlefield Rd.
Menlo Park, CA 94025
USA
e-mail: afwhite@usgs.gov

Cover photograph © Brady McTigue, courtesy of Brady McTigue Photography and Design.

ISBN 978-0-387-73562-7 e-ISBN 978-0-387-73563-1

Library of Congress Control Number: 2007937090

Cover illustration:

Printed on acid-free paper

9 8 7 6 5 4 3 2 1

springer.com

Preface

Systems at the surface of the Earth are continually responding to energy inputs derived ultimately from radiation from the Sun or from the radiogenic heat in the interior. These energy inputs drive plate movements and erosion, exposing metastable mineral phases at the Earth's surface. In addition, these energy fluxes are harvested and transformed by living organisms. As long as these processes persist, chemical disequilibrium at the Earth's surface will be perpetuated.

In addition, as human populations grow, the need to produce food, extract water, and extract energy resources increases. These processes continually contribute to chemical disequilibrium at the Earth surface. We therefore find it necessary to predict how the surface regolith will change in response to anthropogenic processes as well as long-term climatic and tectonic forcings. To address these questions, we must understand the rates at which reactions occur and the chemical feedbacks that relate these reactions across extreme temporal and spatial scales. Scientists and engineers who work on soil fertility, nuclear waste disposal, hydrocarbon production, and contaminant and CO_2 sequestration are among the many researchers who need to understand geochemical kinetics. Fundamental questions concerning the long-term geological, climatic and biological evolution of the planet also rely on geokinetic information.

In this book, we summarize approaches toward measuring and predicting the kinetics of water-rock interactions which contribute to the processes mentioned above. In our treatment, we transect multiple length and time scales to integrate molecular and macroscopic viewpoints of processes that shape our world. The treatment, as discussed below, begins at a chemical level with fundamental kinetic analysis and develops treatments for more geochemically complex systems. The focus of the book is low-temperature, but the treatments in the chapters lay the foundation for discussions of geochemical kinetics regardless of temperature and some high-temperature systems are treated in Ch. 12. An Appendix of data for mineral dissolution reaction rates is included that will be expanded online (see www.czen.org or chemxseer.ist.psu.edu).

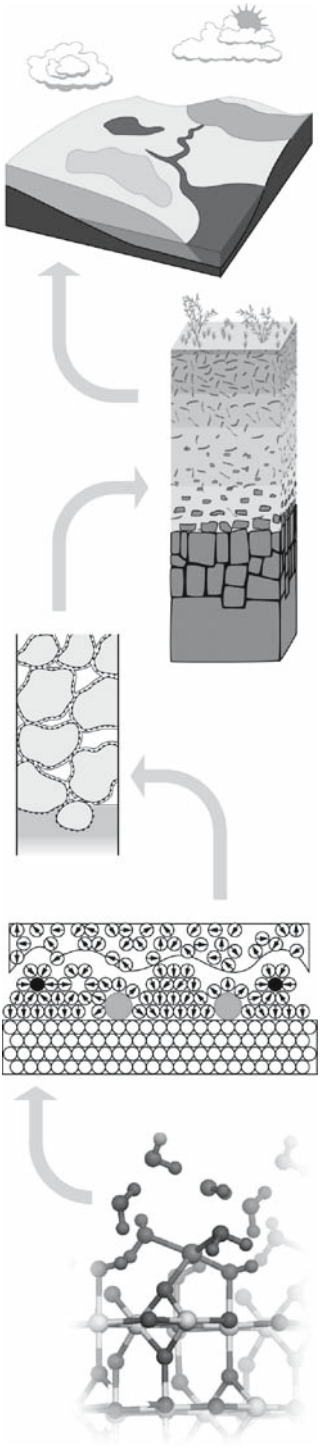

The first half of the book deals with basic issues of chemical kinetics. In Chapter 1, Brantley and Conrad address how geochemists define and measure reaction rates in the laboratory (Ch. 1, *Analysis of Rates of Geochemical Reactions*). In Chapter 2, Kubicki discusses transition state theory and how molecular orbital calculations can be used to understand or investigate geochemical reaction mechanisms (*Transition State Theory and Molecular Orbital Calculations Applied to Rates and Reaction Mechanisms in Geochemical Kinetics*). The next chapter discusses problems and approaches toward understanding how to investigate, analyze, and model the mineral surface (Chapter 3, *The Mineral-Water Interface*, by Lüttge and Arvidson). Important aspects of sorption-desorption reactions on mineral surfaces and the role of organic matter in soils are described in Chapter 4, written by Chorover and Brusseau (*Kinetics of Sorption-Desorption*). Approaches toward an integrated understanding of mineral dissolution and rigorous fitting of mineral dissolution data are discussed in Chapters 5 (Brantley, *Kinetics of Mineral Dissolution*) and 6 (Bandstra and Brantley, *Data Fitting Techniques with Applications to Mineral Dissolution Kinetics*). Importantly, Chapter 6 provides the mathematical background for fitting rate measurements that are compiled in the Appendix (Bandstra et al., *Compilation of Mineral Dissolution Rates*). The last chapter of this first half of the book reviews the models for assessing nucleation and growth of crystals. These models are necessary for evaluating the stable and metastable phases that form during mineral reaction (Benning and Waychunas, Chapter 7, *Nucleation, Growth, and Aggregation of Mineral Phases: Mechanisms and Kinetic Controls*).

In the last six chapters of the book, kinetic theory is applied to complex environmental systems. Roden introduces concepts of kinetic theory as applied to reductive ferric oxide dissolution mediated by microbes in Chapter 8 (*Microbiological Controls on Geochemical Kinetics 1: Fundamentals and Case Study on Microbial Fe(III) Oxide*

Reduction) and to microbiological metal sulfide oxidation in Chapter 9 (*Microbiological Controls on Geochemical Kinetics 2: Case Study on Microbial Oxidation of Metal Sulfide Minerals and Future Prospects*). Many of the ideas in the first nine chapters are utilized in discussions of chemical weathering in Chapter 10 by White (*Quantitative Approaches to Characterizing Natural Chemical Weathering Rates*). In this chapter, the problems associated with extrapolating kinetics from the laboratory to the field are also discussed. Modelling kinetics in environmental systems such as soils or aquifers requires understanding of both chemical kinetics and transport processes, and approaches to modeling such reactive transport problems are therefore discussed by Steefel in Chapter 11 (*Geochemical Kinetics and Transport*). In Chapter 12, Gaillardet explores the utility of isotopic techniques, including several new isotopic systems that are under development, to unravel complex environmental systems at both low and high temperature (*Isotope Geochemistry as a Tool for Deciphering Kinetics of Water-Rock Interaction*). Gaillardet also treats systems at both small and global scales. In the final chapter of the book, Lerman and Wu expand upon this treatment to discuss approaches toward modeling weathering and elemental cycling at the global scale (Chapter 13, *Kinetics of Global Geochemical Cycles*).

We hope the book will be useful for readers who are both experts and those peripherally involved in geochemical kinetics. We aimed the book at graduate students as well as professional earth and environmental scientists. From its inception, the book was to be used as a teaching tool for graduate students; however, as we compiled data and models since the last such compilation edited by SLB and AFW in 1995 (*Chemical Weathering Rates of Silicate Minerals*), we realized that our introductory text could also be used as a professional guidebook for geochemical kinetics. Harkening back to that earlier volume, perhaps it is fitting to quote (again) from James Hutton who wrote,

> *The ruins of an older world are visible in the present structure of our planet… The same forces are still destroying, by chemical decomposition or mechanical violence, even the hardest rocks and transporting the materials to the sea.*

or even to quote again from Al Hibbler in 1955,

> *Time goes by so slowly, but time can do so much.*

We hope this text will contribute at least in a small way to the collected wisdom of these and other authors interested in kinetics of the Earth.

S. L. Brantley, J. Kubicki
University Park, PA

A.F. White
Menlo Park, CA

Acknowledgements

Many of the authors of this book are associated with the *Center for Environmental Kinetics Analysis* at Penn State. Funding for this center from both the National Science Foundation (Environmental Molecular Sciences Institute Grant CHE-0431328) and from the U.S. Department of Energy, Biological and Environmental Research, was instrumental in most aspects of writing the book and compiling the data. Other specific sources of funding are acknowledged in each chapter. SLB and JK also acknowledge the students of the Penn State class, Geosciences 560 *Kinetics of Geochemical Systems*, who reviewed chapters in an earlier form. We furthermore acknowledge advice from Ken Howell (Springer), and help from Lee Carpenter, Debbie Lambert, and Sue Rockey (Penn State). Finally, Denise Kowalski (Penn State) is acknowledged for her infinite patience and attention to detail, along with her continual good humor in the face of the painstaking process of compiling this book.

Contents

List of Contributors

Rolf S. Arvidson
Rice University, Department of Earth Science MS-126, 6100 South Main Street, Houston TX 77005, e-mail: Rolf.S.Arvidson@rice.edu

Joel Z. Bandstra
The Pennsylvania State University, Center for Environmental Kinetics Analysis, 2217 Earth-Engineering Science Building, University Park, PA 16802, e-mail: jxb88@psu.edu

Liane G. Benning
University of Leeds, Earth and Biosphere Institute, School of Earth and Environment, Leeds LS2 9JT, UK, e-mail: liane@earth.leeds.ac.uk

Susan L. Brantley
The Pennsylvania State University, Earth and Environmental Systems Institute, 2217 Earth-Engineering Science Building, University Park, PA 16802, e-mail: brantley@essc.psu.edu

Mark L. Brusseau
University of Arizona, Department of Soil, Water and Environmental Science, Shantz 429, Building #38, Tucson, AZ 85721, e-mail: Brusseau@ag.arizona.edu

Heather L. Buss
The Pennsylvania State University, Department of Geosciences and the Earth and Environmental Systems Institute, 2217 Earth-Engineering Science Building, University Park, PA 16802, e-mail: hlbuss@usgs.gov

Richard Kramer Campen
The Pennsylvania State University, Department of Geosciences and the Center for Environmental Kinetics Analysis, 2217 Earth-Engineering Science Building, University Park, PA 16802, e-mail: k.campen@amolf.nl

Jon Chorover
University of Arizona, Department of Soil, Water and Environmental Science, Shantz 429, Building #38, Tucson, AZ 85721, e-mail: Chorover@cals.arizona.edu

Christine F. Conrad
The Pennsylvania State University, Center for Environmental Kinetics Analysis, 2217 Earth-Engineering Science Building, University Park, PA 16802, e-mail: cconrad@wegnet.com

Jérôme Gaillardet
Institut de Physique du Globe de Paris, Université Paris 7 – CNRS, 4 Place Jussieu, 75252 PARIS cedex 05, France, e-mail: gaillardet@ipgp.jussieu.fr

Elisabeth M. Hausrath
The Pennsylvania State University, Department of Geosciences and the Earth and Environmental Systems Institute, 2217 Earth-Engineering Science Building, University Park, PA 16802, e-mail: Elisabeth.M.Hausrath@nasa.gov

Je-Hun Jang
The Pennsylvania State University, Department of Civil and Environmental Engineering, 212 Sackett Building, University Park, PA 16802, e-mail: jehun@psu.edu

James D. Kubicki
The Pennsylvania State University, Department of Geosciences and the Earth and Environmental Systems Institute, 335 Deike Building, University Park, PA 16802, e-mail: kubicki@geosc.psu.edu

Abraham Lerman
Northwestern University, Department of Earth and Planetary Sciences, Locy Hall, 1850 Campus Drive, Evanston, IL 60208, e-mail: alerman@northwestern.edu

Laura J. Liermann
The Pennsylvania State University, Department of Geosciences, 503 Deike Building, University Park, PA 16802, e-mail: ljl8@psu.edu

Andreas Lüttge
Rice University, Department of Earth Science, Department of Chemistry, and Center for Biological and Environmental Nanotechnology, 6100 Main Street, Houston, TX 77005, e-mail: aluttge@rice.edu

Joel Moore
The Pennsylvania State University, Department of Geosciences and the Center for Environmental Kinetics Analysis, 2217 Earth-Engineering Science Building, University Park, PA 16802, e-mail: joelmoore@psu.edu

Alexis K. Navarre-Sitchler
The Pennsylvania State University, Department of Geosciences and the Center for Environmental Kinetics Analysis, 2217 Earth-Engineering Science Building, University Park, PA 16802, e-mail: anavarre@geosc.psu.edu

Eric E. Roden
University of Wisconsin, Department of Geology and Geophysics, 1215 W. Dayton Street, Madison, WI 53706, e-mail: eroden@geology.wisc.edu

Carl I. Steefel
Lawrence Berkeley National Laboratory, Earth Sciences Division, 1 Cyclotron Road, Mail Stop 90-1116, Berkeley CA 94720, USA, e-mail: CISteefel@lbl.gov

Glenn A. Waychunas
Lawrence Berkeley National Laboratory, Earth Sciences Division, MS 70-108B, One Cyclotron Road, Berkeley CA 94720, e-mail: GAWaychunas@lbl.gov

Art F. White
U.S. Geological Survey, MS 420, 345 Middlefield Rd, Menlo Park, CA 94025, e-mail: afwhite@usgs.gov

Lingling Wu
Northwestern University, Department of Earth and Planetary Sciences, 1850 Campus Drive, Evanston, Il 60208, e-mail: lingling@earth.northwestern.edu

Chapter 1
Analysis of Rates of Geochemical Reactions

Susan L. Brantley[1] and Christine F. Conrad[2]

1.1 Kinetics and Thermodynamics

Over the last several billion years, rocks formed at equilibrium within the mantle of the Earth have been exposed at the surface and have reacted to move towards a new equilibrium with the atmosphere and hydrosphere. At the same time that minerals, liquids, and gases react abiotically and progress toward chemical equilibrium at the Earth's surface, biological processes harvest solar energy and use it to store electrons in reservoirs which are vastly out of equilibrium with the Earth's other surface reservoirs. In addition to these processes, over the last several thousand years, humans have produced and disseminated non-equilibrated chemical phases into the Earth's pedosphere, hydrosphere, and atmosphere. To safeguard these mineral and fluid reservoirs so that they may continue to nurture ecosystems, we must understand the rates of chemical reactions as driven by tectonic, climatic, and anthropogenic forcings.

Chemists approach the understanding of the natural world by defining parts of the world as *systems* of study. The mechanically separable parts of the system—the crystalline and amorphous solids, liquids and gases—are known as phases. All the phases that are not inside the system are defined as the *environment* surrounding the system. By definition, a system at equilibrium will be characterized by phases with uniform composition that exist at uniform temperature and pressure. To be precise, equilibrium is defined as that state where the chemical potential of every component in every phase is equal throughout the system.

To chemically understand a system, the chemical species within the system must be identified and characterized: the minimum number of species needed to define a system at equilibrium comprises the set of *components* of that system. Likewise, the thermodynamic state of any system is completely defined by specifying the values

[1] The Pennsylvania State University, Center for Environmental Kinetics Analysis, Earth and Environmental Systems Institute, brantley@essc.psu.edu
[2] The Pennsylvania State University, Center for Environmental Kinetics Analysis, Earth and Environmental Systems Institute, cconrad@wegnet.com

of a critical number of properties. For example, the Gibbs phase rule states that the number of properties that must be defined to completely describe a system (the degrees of freedom, F) is dependent upon the number of phases, P, and components, C:

$$F = C - P + 2 \tag{1.1}$$

So, for example, to completely define the one-component one-phase pure H_2O system, we must only define the temperature, T, and pressure, P, of the system $(F = 2)$. If one adds sufficient NaCl as a second component so as to supersaturate this water with respect to halite and then isolates the system, the second law of thermodynamics states that the properties of this isolated system will evolve until the equilibrium state is reached. Indeed, the degrees of freedom of the final two-component, two-phase (NaCl-saturated water and solid NaCl) system must also equal two: in effect, the state of this system is defined solely by the temperature and pressure. Thermodynamics completely defines the final state of the system: however, thermodynamics cannot define the *rate* at which the system evolves.

The field of irreversible thermodynamics treats systems that are removed from equilibrium by modeling how the entropy of the system changes with time as equilibrium is approached (Prigogine, 1967). Irreversible thermodynamics defines the change in entropy of the system, dS, as the sum of the entropy supplied to the system by its surroundings, dS_e, and the entropy produced inside the system, dS_i. The second law of thermodynamics states $d_iS \geq 0$. For a reversible process, $dS_i = 0$, and for an irreversible process, this term is always positive, $dS_i > 0$. Furthermore, for a closed system at constant temperature and pressure, it can be shown that this term is related to the change in Gibbs free energy of the system, dG_{sys}:

$$T dS_i = -dG_{sys} \tag{1.2}$$

Therefore, for spontaneous reactions in closed systems at constant T and P, the entropy produced inside the system is related to the Gibbs free energy change of the system.

In the case of the system with one reaction, the differentiation of Eq. (1.2) over time and introduction of ξ, the extent of reaction (see Eq. (1.9)), results in the expression

$$T\frac{dS_i}{dt} = A\frac{d\xi}{dt}, \tag{1.3}$$

where the entropy production $\frac{d_iS}{dt} \geq 0$ and $A = -\Delta G_{reaction}$, the chemical affinity of the reaction. The chemical affinity, introduced by T. DeDonder, is the driving force of the reaction. For a reaction that occurs spontaneously as written (e.g., reactants on the left and products on the right of the reaction), A > 0 and $\Delta G_{reaction} < 0$. At equilibrium, the chemical affinity $(-\Delta G_{reaction})$ is equal to 0. The negative driving force of reaction can be shown to be equal to a simple expression for any reaction defined by an equilibrium constant K_{eq} and a reaction activity quotient, Q:

$$\Delta G_{reaction} = -A = RT \ln\left(\frac{Q}{K_{eq}}\right) \tag{1.4}$$

If the driving force of reaction is positive, the reaction should proceed spontaneously as written. For example, for the reaction of albite with water, the reaction and activity quotient can be written by inspection assuming that the activity of albite and H_2O can each be set equal to unity:

$$NaAlSi_3O_{8(s)} + 4H_2O_{(aq)} + 4H^+_{(aq)} \rightarrow Na^+_{(aq)} + Al^{3+}_{(aq)} + 3H_4SiO_{4(aq)}$$
$$Q = \frac{a_{Na^+} a_{Al^{3+}} a^3_{H_4SiO^0_4}}{a^4_{H^+}} \tag{1.5}$$

The value of log K_{eq} equals 4.70 at standard temperature and pressure (Drever, 1997). For a soil porewater in contact with albite where $Q < 10^{4.70}$, thermodynamics predicts that albite should dissolve spontaneously as $\Delta G_{reaction}$ is negative and the reaction should proceed as written. In contrast, if $Q > 10^{4.70}$, albite should precipitate. Of course, under ambient conditions, it is observed that precipitation of crystalline albite does not occur at a measurable rate; therefore, the kinetics of precipitation are extremely slow, even if albite is supersaturated.

Although thermodynamics does not allow the prediction of rates of chemical reactions, it does place a constraint on kinetics. In particular, at equilibrium, the rate of the forward reaction must equal the rate of the reverse reaction. This constraint, known as *microscopic reversibility*, is discussed further in Chap. 2. Microscopic reversibility leads to the conclusion that the equilibrium constant for a reaction that occurs as written must be equal to the ratio of the rate constants for the forward and reverse reactions (see Eq. (1.81)).

1.2 Rates of Reactions

1.2.1 Extent of Reaction

In kinetic experiments, the rates of change of reactant and product concentrations are measured. Consider the reaction,

$$A + 3B \rightarrow Z \tag{1.6}$$

which begins with a mixture of A and B without Z. We assume a system where no change in volume occurs as the reaction proceeds. At any time, t, the rate of consumption of A, r_A, is defined as the negative slope of the tangent to the plot of concentration of A, [A], versus time:

$$r_A = -\frac{d[A]}{dt} \tag{1.7}$$

The rate of formation of Z can be determined in the same manner:

$$r_Z = \frac{d[Z]}{dt} \tag{1.8}$$

For the reaction given in Eq. (1.6), $r_A = r_Z$. Note however, that the stoichiometry of the reaction requires that the negative of the rate of consumption of B must differ by a factor of 3 from the value of r_Z. Thus, if we define rates according to equations such as Eqs. (1.7) and (1.8), a given reaction may be characterized by different values for the rate at any given time.

A useful concept, the *extent of reaction,* was therefore introduced by T. de Donder in 1922 to correct for the stoichiometry of reaction. The extent of reaction is defined by the following,

$$\xi = \frac{n_i - n_i^0}{\nu_i}, \tag{1.9}$$

where n_i^0 is the initial number of moles of a reactant or product, n_i is the moles at time t, and ν_i is the stoichiometric coefficient for that species in the written reaction. The extent of reaction can only be determined unequivocally for reactions with time-independent stoichiometries where the stoichiometric equation for the reaction is specified.

1.2.2 Rate of Reaction

For a reaction in a system where reaction stoichiometry does not change with time, *rate of reaction* is defined as the derivative of the extent of reaction with time divided by the volume

$$r = \frac{1}{V}\frac{d\xi}{dt} \tag{1.10}$$

For an individual species, i, the time derivative is given by

$$\xi = \frac{1}{\nu_i}\frac{dn_i}{dt} \tag{1.11}$$

where ν_i is the stoichiometric coefficient for species i. The rate of reaction then becomes

$$r = \frac{1}{\nu_i V}\frac{dn_i}{dt} \tag{1.12}$$

Thus, for the reaction given in Eq. (1.6)

$$r = -\frac{1}{V}\frac{dn_A}{dt} = -\frac{1}{3V}\frac{dn_B}{dt} = \frac{1}{V}\frac{dn_Z}{dt} \tag{1.13}$$

If the volume does not change during the course of the reaction, the term dn_i/V in Eq. (1.12) may be replaced by the change in concentration yielding

$$r = -\frac{1}{\nu_A}\frac{d[A]}{dt} = -\frac{1}{\nu_B}\frac{d[B]}{dt} = \frac{1}{\nu_Z}\frac{d[Z]}{dt}. \tag{1.14}$$

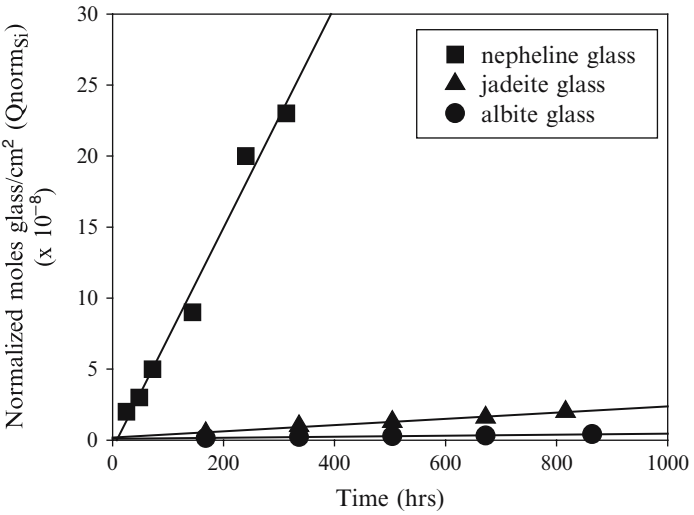

Fig. 1.1 Normalized moles of glass cm^{-2} released into solution as a function of time during dissolution of nepheline ($Na_6Al_6Si_6O_{24}$), jadeite ($Na_4Al_4Si_8O_{24}$), and albite ($Na_3Al_3Si_9O_{24}$) glass powder in batch experiments at pH 2 (Hamilton et al., 2001). $Qnorm_{Si}$ = number of moles of Si released into solution per cm^2 glass divided by the number of moles of Si in a mole of glass (based on a 24 oxygen formula unit). The slopes of these lines are the rates of dissolution of each glass.

The extent of reaction and stoichiometric coefficients has no meaning except in relation to the equation for the given reaction. Therefore, the reaction stoichiometry must be specified when referencing the rate of reaction.

For the reaction given in Eq. (1.6), the rate of reaction could be analyzed by measuring [A], [B], or [Z] versus time. Similarly, for mineral dissolution kinetics, it is common to measure multiple products of the reaction. For example, for albite dissolution, either Na, Al, or Si concentrations could be monitored versus time; however, it has become common to calculate silicate dissolution rates solely based on the rate of release of Si to solution. If albite dissolves stoichiometrically (Eqn. 1.5) then the release rate of Na (r_{Na}) or Al (r_{Al}) should be 1/3 the release rate of Si (r_{Si}). Even when the Si release is used to calculate the rate, the rate is often reported in units as $mol_{mineral}\ m^{-2}\ s^{-1}$. Note that the reported release rate of albite written in units of mol albite per unit area per unit time will differ depending upon whether the formula unit of albite is written as $Na_3Al_3Si_9O_{24}(r_{albite(24)})$ or as $NaAlSi_3O_8(r_{albite(8)})$:

$$r_{Si} = 3r_{Na} = 3r_{Al} = 3r_{albite(8)} = 9r_{albite(24)} \tag{1.15}$$

These ideas are demonstrated in Figs. 1.1 and 1.2. The first figure shows the rate of dissolution of three Na-Al-Si glasses as a function of time as determined by release of Si to solution. In this figure, the moles of Si released are normalized by the number of Si atoms per formula unit of glass (24 oxygen atoms per unit). The glass with the lowest Al/Si ratio (albite) dissolves the slowest. However, Fig. 1.2 demonstrates that Na and Al are preferentially released during initial albite glass

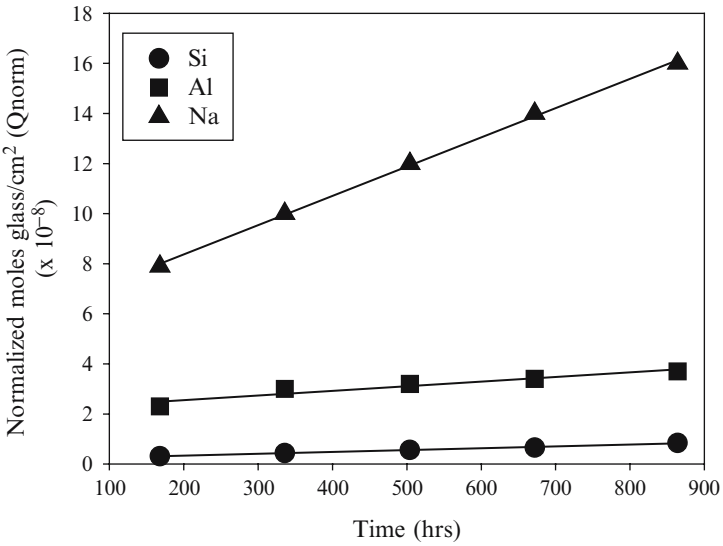

Fig. 1.2 Normalized moles of glass cm^{-2} released into solution as a function of time during dissolution of albite glass ($Na_3Al_3Si_9O_{24}$) at pH 2 in a batch experiment based on Si, Al, or Na concentrations (Hamilton et al., 2001). See Fig. 1.1 for definition of Qnorm. According to Eq. (1.15), the rate of release of Si should be three times faster than the release of Na and Al. The ratios of these release rates indicate non-stoichiometric dissolution in which a Si-rich layer is forming on the albite glass surface.

dissolution ($r_{Si} \neq 3r_{Na} \neq 3r_{Al}$) leaving behind a silica-rich leached layer (Hamilton et al., 2001).

1.3 Rate Equations

1.3.1 Rate Order and Rate Constant

Analysis of reaction rates is usually first attempted at a phenomenological level where the rates of reactions are measured as a function of solution, solid, and gas composition. At this phenomenological level, a *rate equation* or *rate law* is a mathematical expression that relates the change in concentration of a product or reactant versus time to the concentrations of species in a chemical reaction. For reactions among solutes, solids, and gas phases, concentrations may be denoted in a variety of units such as moles L^{-1} for aqueous or solid phase species, m^2 L^{-1} or sites L^{-1} for solid phase species, or partial pressures for gases.

For the reaction given in Eq. (1.6), the rate equation might be written as

$$r = k[A]^{\alpha}[B]^{\beta}[Z]^{\sigma} \tag{1.16}$$

where ideally, k, α, β, and σ are constants independent of concentration and time. Notice that rate laws are written in units of concentration rather than activities. In

contrast, in thermodynamic equations, activity coefficients are used to calculate activities from concentrations. However, in kinetics it is the spatial concentration (e.g., moles cm^{-3}) of the species that determines the rate of molecular collisions between or among reactants, and the rate of collision partially controls the rate of reaction (Lasaga, 1981).

The exponents α, β, and σ are known as the *partial orders of reaction* with respect to A, B, and Z and the sum of all of the partial orders is the *overall order* of reaction. For phenomenological treatments of reaction kinetics, these orders are empirical and need not be integral values. Note also that no simple relationship need exist between the stoichiometry of an equation and the order of the reaction. In fact, the kinetics of many geochemical systems are only treated with a phenomenological approach where equations such as Eq. (1.16) are treated simply as fitting equations. In general, this is also the level of analysis that is first utilized to understand a system.

An example of a first-order reaction that has been treated phenomenologically is the oxidation or pyrite and production of sulfuric acid. This reaction is largely responsible for decreased pH values in sulfide mine spoils. The rate of change in the concentration of $FeS_{2(s)}$ due to oxidation in pyrite-containing soils has been observed to be a function of the concentration of $FeS_{2(s)}$ in the soil, $[FeS_{2(s)}]$, and can be written as (Hossner and Doolittle, 2003)

$$r = -d[FeS_{2(s)}]/dt = k[FeS_{2(s)}] \tag{1.17}$$

A second-order reaction may refer to either the case where the rate of reaction is proportional to the second power of one species or, alternately, proportional to the product of the concentrations of two species each raised to the first power. An example of the first case can be seen in the rate of oxidation of dissolved As(III) in the presence of solid phase manganese dioxide, a process used to remove the toxic form of inorganic As(III) from drinking water. It has been determined that this reaction follows second-order kinetics (Driehaus et al., 1995):

$$r = -d[As(III)_{(aq)}]/dt = k[As(III)_{(aq)}]^2. \tag{1.18}$$

The second type of second-order kinetics is exhibited by the oxidation kinetics of ferrous minerals studied by Perez et al. (2005). Batch reactors were utilized to assess the ability of naturally occurring ferrous silicate minerals to act as an oxygen buffer in a nuclear fuel repository. The experimental oxidation data were fit by a second-order rate law of the form,

$$r = -d[O_{2(aq)}]/dt = k[O_{2(aq)}][Fe(II)_{(s)}] \tag{1.19}$$

where $[Fe(II)_{(s)}]$ refers to the concentration of ferrous sites on the surface of the mineral (sites m^{-2}).

Some reactions cannot be defined to have a reaction order. An example of such a reaction is an enzyme-catalyzed reaction that is described by the Michaelis-Menten equation (see Chap. 8). The rate law for a reaction of this type is given by

$$r = \frac{V_{\max}[A]}{K_m + [A]} \tag{1.20}$$

where V_{max} and K_m are constants and [A] is the concentration of the substrate reacting with the enzyme. The Michaelis-Menten rate equation is an example of a hyperbolic rate equation. Another rate law that is hyperbolic in form is derived if one assumes that the rate of a reaction is proportional to the surface site density of sorbed species on a solid where this sorbate concentration is modeled with a Langmuir adsorption isotherm. Regardless of the derivation of the rate equation, for a rate that can be modeled by a hyperbolic equation such as Eq. (1.20), no true rate order exists: for low [A], the rate is observed to be first order in A, while for high [A], the rate is observed to be zeroth order.

The constant k in a rate equation is called the *rate constant*. The units of the rate constant depend on the order of the reaction. A first-order reaction, such as Eq. (1.17) where the rate is described in units of mol L^{-1} s^{-1} is described by a rate constant with units of s^{-1}. The units for a second-order reaction rate constant (e.g., Eq. (1.19)) where the concentration terms are expressed in mol L^{-1} can be determined from

$$\frac{mol\ L^{-1}s^{-1}}{(mol\ L^{-1})^2} = mol^{-1}\ L\ s^{-1} \tag{1.21}$$

Whenever a value for a rate constant is cited, to interpret this rate constant the researcher must know both how the reaction rate and rate equation have been defined.

1.4 Reaction Mechanisms

1.4.1 Elementary Reactions

Many reactions take place in a series of steps and involve the formation of intermediate species. This set of steps is called the *mechanism*. Complex mechanisms can be broken down into a series of reactions—*elementary reactions*—that occur exactly as written. Elementary reactions are the building blocks of a complex reaction and cannot be broken down further into simpler reactions. In addition, elementary reactions have the desirable property that they exhibit the same rate regardless of the system: they can thus be extrapolated from one system to another at a given temperature and pressure.

The rate equation for an elementary reaction can be written for the reaction *a priori* because the reaction occurs exactly as written. Thus, the rate equations for the elementary reactions, $A \rightarrow B$, $2A \rightarrow B$, and $A + B \rightarrow C$, are written $r = k[A]$, $r = k[A]^2$, and $r = k[A][B]$, respectively. It is rare for more than two or at most three species to collide in the geometry conducive for reaction, and thus reaction orders for elementary reactions are seldom larger than 2, or at most, 3. The reaction order of an elementary reaction is also related to the *molecularity*—the number of reactant particles (e.g., atoms, molecules, or free radicals) involved in each individual chemical event. For example, the reaction $A \rightarrow Z$ involves only one molecule, *A*, and is therefore said to be *unimolecular*. The reaction $A + B \rightarrow Z$ involves two molecules and is said to be *bimolecular*.

Characteristically, a kineticist measures a reaction rate as a function of the concentration of reactants or products, and then proposes a rate equation such as Eq. (1.18) that describes the observations. In the next step of analysis, a rate mechanism that is consistent with the rate equation is proposed. For example, Icopini et al. (2005) measured the rate of disappearance of aqueous silica, $H_4SiO_{4(aq)}$, from solutions supersaturated with respect to amorphous silica and observed that the rate data was not well fit by first-, second-, or third-order rate laws, but was well fit by a fourth-order rate law of the form

$$r = -d[H_4SiO_{4(aq)}]/dt = k_4[H_4SiO_{4(aq)}]^4 \tag{1.22}$$

The high order of reaction observed in this work suggested that this rate equation described a complex reaction mechanism and not an elementary reaction. The authors thus derived a reaction mechanism that is consistent with a fourth-order rate law. They proposed the following elementary reactions to describe the mechanism for the polymerization of monomeric to tetrameric silica in aqueous solutions:

$$H_4SiO_{4(aq)} + H_4SiO_{4(aq)} \rightarrow H_6Si_2O_{7(aq)} + H_2O \tag{1.23}$$
$$H_6Si_2O_{7(aq)} + H_4SiO_{4(aq)} \rightarrow H_8Si_3O_{10(aq)} + H_2O \tag{1.24}$$
$$H_8Si_3O_{10(aq)} + H_4SiO_{4(aq)} \rightarrow H_8Si_4O_{12(aq)} + 2H_2O \tag{1.25}$$

According to their model, the polymerization of monomeric silica (H_4SiO_4) into tetrameric silica $(H_8Si_4O_{12})$ is hypothesized to occur via monomer addition (Eqs. (1.23)–(1.25)). In the final reaction (Eq. (1.25)) the extra water released is due to the formation of a cyclic compound. For this series, a *composite* or *overall reaction* can be written as the sum over the entire mechanism:

$$4H_4SiO_{4(aq)} \rightarrow H_8Si_4O_{12(aq)} + 4H_2O \tag{1.26}$$

If the reactions given in Eq. (1.23) (rate constant k_1) and Eq. (1.24) (k_2) are significantly faster than the reaction given in Eq. (1.25) (k_3), then these two reactions could achieve equilibrium (with equilibrium constants K_1 and K_2, respectively) while the third reaction could control the overall rate. Such a slow step that controls the rate is called the *rate-controlling* (or *–determining* or *–limiting*) step. If Eq. (1.25) is the rate-controlling step and it is an elementary reaction then the rate constant k_4 that describes the rate of reaction given in Eq. (1.26) and in Eq. (1.22) can be expressed as follows:

$$k_4 = k_3 f(y) \frac{K_1 K_2}{a_{H_2O}^2} \tag{1.27}$$

In this equation, $f(y)$ represents a term incorporating activity coefficients for the silica species, and a_{H2O} is the activity of water. Note that, because the overall rate equation is written in terms of concentration of species rather than activities of species, activity correction terms are incorporated into the rate constant k_4. It is common for rate constants for composite reactions to contain activity coefficients, equilibrium constants and rate constants for elementary reactions as shown by this example.

Another example of simplifying complex functions with a single rate constant is found in the discussion of calcite precipitation in Chap. 5.

It is common to hypothesize a mechanism such as Eqs. (1.23)–(1.25) and then to assume that the individual reactions are elementary reactions for which rate equations can be written *a priori*. Such an approach allows the kineticist to propose a hypothetical mechanism to test experimentally. If the data and rate equations derived from a mechanism agree, the mechanism can be said to be *consistent* with the kinetic evidence. If they do not agree, a new mechanism can be derived and tested. In general, without detailed spectroscopy to determine a mechanism, it is impossible to prove that a mechanism occurs as written, especially for geochemical reactions.

1.4.2 Heterogeneous Reactions

Reactions that occur in one phase are referred to as homogenous reactions, while reactions that occur at interfaces between phases are heterogeneous reactions. Modeling heterogeneous reactions such as water-rock reactions tends to be difficult in that a term must be included in the rate equation that describes the reacting species at the mineral interface (Chaps. 3 and 4). Often it is assumed that reactions occur at all sites on the mineral surface or at some constant fraction of the surface sites. For such a case, the concentration of reactant sites may be included in the rate equation as the total mineral-water interfacial area. Generally, to assess such an area, the mineral surface is measured by adsorption of an inert gas to the surface, and the *specific surface area* $\left(\mathrm{m}^2\ \mathrm{g}^{-1}\right)$ is determined from this sorbed gas using the Brunauer-Emmet-Taylor (BET) isotherm (Brantley and Mellott, 2000). However, since surface sites do not react identically, most reactions are proportional to the *reactive surface area* rather than the total surface area (Ch 3). For example, for biotite and other sheet silicates, edge sites dissolve faster than sites on the basal surface and often control the overall dissolution rate under acid conditions (Kalinowski and Schweda, 1996). In dissolution or precipitation reactions, a further complexity arises because the mineral surface area changes with time. To date, very few attempts have been made to incorporate the change in surface area with time into mineral dissolution/precipitation models.

1.4.3 Catalysis and Inhibition

Catalysts are substances that increase the rate of reaction but are not consumed during the course of the reaction. Therefore, they do not modify the standard Gibbs free energy change of the reaction nor do they appear in the equilibrium constant expression for the reaction. For example, a reaction containing a catalyst may be written as follows (after Laidler, 1987),

$$A + B + catalyst \rightarrow Y + Z + catalyst, \tag{1.28}$$

and the rate of the reaction proceeding from left to right, r_1, can be written as

$$r_1 = k_1[A][B][catalyst] \tag{1.29}$$

Accordingly, the rate of the reaction occurring from right to left, r_{-1}, can be written

$$r_{-1} = k_{-1}[Y][Z][catalyst] \tag{1.30}$$

Using the condition that $r_1 = r_{-1}$ at equilibrium, the catalyst concentration cancels out in the expression for the equilibrium constant, K, for the reaction

$$K = \frac{k_1}{k_{-1}} = \left(\frac{[Y][Z]}{[A][B]}\right)_{eq} \tag{1.31}$$

Catalysts can be classed as either *homogeneous* when only one phase is involved, or they can be *heterogeneous* where the reaction occurs at an interface between phases. Enzymes are examples of catalysts that can be either homogeneous or heterogeneous: some enzymes are soluble and catalyze soluble reactants homogeneously, but other enzymes are embedded in membranes that catalyze soluble reactants heterogeneously. In addition, enzymes can be produced intracellularly, thus capable only of catalysis of reactions inside the cell, or they can be secreted extracellularly, and can diffuse to environmental substrates. Some examples of important biogeochemical reactions catalyzed by enzymes are summarized in Chaps. 8 and 9. Many authors have also documented that mineral surfaces such as Mn oxides can act as catalysts for the reactions of organic molecules.

Autocatalysts are catalysts that are products of a reaction. Autocatalysts that build up in concentration in a solution cause the rate of a reaction to increase with time. An example in geochemistry of an autocatalyst is aqueous Fe(III) that forms during oxidation of pyrite, and which, once formed, acts as an oxidant for the continued oxidation of pyrite. The oxidation of pyrite is one of the main processes contributing to the acidification of lakes, streams and rivers by acid mine and acid rock drainage. The mechanism of the oxidation of pyrite is extremely complex and can vary according to species in solution, the nature of the intermediates, and the mechanism by which these intermediates produce the final product (Williamson and Rimstidt, 1994). The reaction for the oxidation of pyrite by ferric iron can be written as

$$FeS_2 + 14Fe^{3+} + 8H_2O \rightarrow 15Fe^{2+} + 2SO_4^{2-} + 16H^+ \tag{1.32}$$

The measured rate of oxidation of pyrite in the presence of dissolved oxygen increases with increasing concentration of Fe(III): thus, the ferric ion acts as an autocatalyst. Williamson and Rimstidt (1994) proposed the following rate law for pyrite oxidation in the presence of dissolved oxygen:

$$r = 10^{-6.07}\frac{m_{Fe^{3+}}^{0.93}}{m_{Fe^{2+}}^{0.40}} \tag{1.33}$$

where r is the rate of pyrite destruction in mol m^{-2} s^{-1} and m is the concentration of Fe^{3+} or Fe^{2+}.

Catalysts should not be confused with species that simply accelerate reactions: such species, known as *accelerators*, appear in the equilibrium constant expression. For example, many have observed that organic ligands accelerate the rate of dissolution of Fe-containing minerals (Kraemer, 2004). In a similar vein, *inhibitors* are species that reduce the rate of a reaction generally by affecting the ΔG of reaction. Inhibitors do not behave in the same manner as catalysts as they are often consumed during reaction. Inhibitors can sometimes decrease the rate of a heterogeneous reaction by physically blocking reactive sites. The degree of inhibition, ε_i, is defined as the rate of reaction without the inhibitor, r_0, minus the rate with the inhibitor, r, divided by r_0 (after Laidler, 1987):

$$\varepsilon_i = \frac{r_0 - r}{r_0} = 1 - \frac{r}{r_0} \tag{1.34}$$

Inhibition and catalysis or acceleration are often observed to be important in controlling the overall morphology and growth rate of crystals (Nagy, 1995). For example, Al-hydroxide crystallization rates have been shown to be slowed considerably by the presence of Si at concentrations as low as 2 mg L^{-1} (Hem et al., 1973). In contrast, the presence of aqueous Li^+ ions greatly accelerates the growth rate, suggesting that a Li-aluminate species acts to nucleate bayerite (Van Straten et al., 1985). Additionally, in weathering environments, organic components have been shown to accelerate the rates of formation of Al-hydroxides and kaolinite, promoting the formation of clays in organic-rich environments (Nagy, 1995 and references therein).

1.5 Analysis of Kinetic Results

The first step in analysis of geochemical kinetics is to measure the rates of change of reactants or products. The next step is generally to see how this rate varies as a function of the concentrations of species in solution, partial pressure of gases, or area of mineral surfaces in order to propose a rate equation. In general, two methods for determining rate equations are used: *the differential method* or the *method of integration*. The methods are described and exemplified below largely following the notation and methods of Laidler (1987).

1.5.1 Differential Method

The differential method is implemented by calculating the slope from a plot of concentrations of reactants or products versus time (e.g., Figs. 1.1 and 1.2). If these slopes are measured for experiments with different initial concentrations of reactants, then the logarithm of the rates of reaction can be plotted versus the logarithms of concentration to calculate the reaction order. For example, Hamilton et al. (2001) measured the dissolution rates of albite glass as a function of H^+ activity in solution

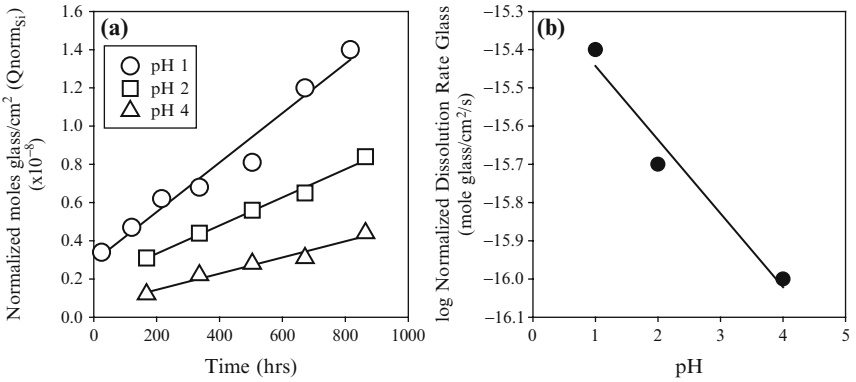

Fig. 1.3 Use of the differential method to determine the order of reaction with respect to H^+ for silica release from albite glass. (a) Rate of dissolution is determined under acidic pH conditions (pH = 1–4). Log rate is then plotted versus pH (b) to determine the order of reaction with respect to H^+ ($\approx$0.2, after Hamilton et al., 2001)

(pH 1–4). The dissolution rates were determined from the observed moles of Si released divided by the number of Si atoms per glass formula unit (on a 24 oxygen unit basis) as a function of time. To determine the order of reaction with respect to H^+, the logarithm of the dissolution rates were plotted against pH, and the order was found to be $\sim$0.2 (Fig. 1.3).

For a reaction that is dependent upon concentrations of more than one reactant, the experimentalist can measure the rate as a function of one reactant by varying that reactant concentration at the same time that all other concentrations are held in excess. By using this so-called *isolation method* for each reactant, the partial order with respect to each reactant can be determined. If one reactant is held at constant excess concentration and the rate is observed to vary as the first order of the concentration of a second reactant, such behavior is described as *pseudo-first order*.

1.5.2 Integral Method

In using this method, a researcher assumes that a reaction proceeds according to a particular rate equation and then derives the integrated rate expression for that assumed rate law. This assumption is then tested by using the measured observations of rate versus concentrations of reactants or products to calculate and plot integrated rate expressions. When the experimental data matches the characteristic plots, the data are said to be consistent with the corresponding rate equation. Below, we explicitly demonstrate examples of the method of integration applied to zero-order, first-order, second-order and n^{th}-order reactions (after Laidler, 1987). The results are tabulated in Table 1.1.

Table 1.1 Analytical solutions for integrated rate laws of *n*th order reactions (after Laidler, 1987)

Order	Stoichiometry	Differential form	Integrated form	Rate constant units
0	$A \rightarrow Z$	$\frac{dx}{dt} = k_A$	$k_A = \frac{x}{t}$	mol L^{-1} s^{-1}
1	$A \rightarrow Z$	$\frac{dx}{dt} = k(a_0 - x)$	$k_A = \frac{1}{t} \ln\left(\frac{a_0}{a_0 - x}\right)$	s^{-1}
2	$2A \rightarrow Z$, $A + B \rightarrow Z$	$\frac{dx}{dt} = k(a_0 - x)^2$	$k_A = \frac{1}{t}\left(\frac{x}{a_0(a_0 - x)}\right)$	L mol^{-1} s^{-1}
3	$A + 2B \rightarrow Z$	$\frac{dx}{dt} = k(a_0 - x) \times (a_0 - 2x)$	$k_A = \frac{1}{t}\left(\frac{1}{a_0 - b_0}\right) \ln\left[\frac{b_0(a_0 - x)}{a_0(b_0 - x)}\right]$	L mol^{-1} s^{-1}
n	$A \rightarrow Z$, $A + B + \cdots \rightarrow Z$	$\frac{dx}{dt} = k(a_0 - x)^n$	$k_A = \frac{1}{t(n-1)} \times \left[\frac{1}{(a_0 - x)^{n-1}} - \frac{1}{a_0^{n-1}}\right]$	L^{n-1} mol^{1-n} s^{-1}

For conditions of one reactant or reactants at equal initial concentrations (mol L^{-1}).

1.5.2.1 Zero-Order Reactions

A zero-order rate law for a reaction describes a rate that is independent of the concentration of reactants. These rate laws are uncommon because most reactions increase in rate as the collision frequency of reactants increases; thus, the rate increases with the concentration of reactants. Zeroth-order reaction kinetics are, however, observed for some complex reaction mechanisms. Consider a zero-order reaction of the form $A \rightarrow Z$ in a system where the starting concentration of Z is zero and A is a_0. The rate of the reaction expressed as the change of A with time is given by

$$r = \frac{dx}{dt} = k_A \tag{1.35}$$

where x represents the concentration of Z, or amount of A that has been consumed, at time t. Separating variables, integrating both sides of the equation, and applying the boundary condition that $x = 0$ when $t = 0$ yields the integrated rate law for a zero-order equation:

$$x = k_A t \tag{1.36}$$

Plotting the measured values of the product concentration versus time yields a straight line with slope equal to the apparent zero-order rate constant.

The data shown in Figs. 1.1–1.3 can be interpreted as zeroth-order kinetics for dissolution of albite, jadeite, and nepheline glasses. However, these are really pseudo-zeroth-order because rates of dissolution of these glasses vary with concentration of protons in solution (among other variables).

1.5.2.2 First-Order Reactions

A first-order elementary reaction must be a reaction such as the following,

$$A \rightarrow Z, \quad A \rightarrow 2Z, \quad A \rightarrow B + C, \tag{1.37}$$

although other more complex reactions can also show apparent first-order kinetics (Bandstra and Tratnyek, 2005). Following Laidler (1987), if the initial concentrations of A and Z can be defined as a_0 and zero respectively, then after time t the concentration of Z equals x and the concentration of A is $a_0 - x$. Thus, the rate of change in the concentration of Z can be written as

$$r = \frac{dx}{dt} = k_A(a_0 - x) \tag{1.38}$$

where k_A is the first order rate constant that relates to the consumption of A. Separation of variables yields

$$\frac{dx}{a_0 - x} = k_A dt \tag{1.39}$$

Integration of Eq. (1.39) yields

$$-\ln(a_0 - x) = k_A t - I \tag{1.40}$$

where I is the constant of integration. Evaluating I using the boundary condition that $x = 0$ when $t = 0$ yields a value for I $(= -\ln a_0)$, and Eq. (1.40) can be rewritten:

$$k_A t = \ln \frac{a_0}{a_0 - x} \tag{1.41}$$

Here the rate constant, k_A, has units of s^{-1}. This equation is also commonly written as

$$a_0 - x = a_0 e^{-k_A t} \tag{1.42}$$

For a reaction that is first order in A, a plot of $\ln[A]$ versus t is linear with slope $= -k_A$. Many geochemical systems are described with first-order kinetics: perhaps the best known examples of such kinetics known by all geologists are the decay of radioactive elements whose first-order kinetics are often described by their half-lives (see Sect. 1.6).

1.5.2.3 Second-Order Reactions

Second-order reactions can be treated in much the same way as first-order reactions (again, we follow the treatment of Laidler, 1987). However, with second-order elementary reactions, the rate of reaction may be proportional to the square of the concentration of one reactant (Eq. (1.43)) or to the product of two concentrations of two reactants (Eq. (1.44))

$$2A \rightarrow Z \tag{1.43}$$

$$A + B \rightarrow Z \tag{1.44}$$

If analysis of the second reaction were to be measured with the same value of starting concentration of A and B, the rate could be expressed as

$$r = \frac{dx}{dt} = k_A(a_0 - x)^2 \tag{1.45}$$

where x is the amount of A that has reacted in unit volume at time t and a_0 is again the initial concentration of A at $t = 0$. Again the variables are separated to yield

$$\frac{dx}{(a_0 - x)^2} = k_A dt \tag{1.46}$$

Integration of this equation leads to

$$\frac{1}{a_0 - x} = k_A t + I \tag{1.47}$$

Applying the boundary condition that $x = 0$ when $t = 0$ yields

$$I = \frac{1}{a_0} \tag{1.48}$$

Substituting this into Eq. (1.47) leads to the integrated form of the second-order rate law shown below

$$k_A t = \frac{x}{a_0(a_0 - x)} \tag{1.49}$$

Here, the rate constant has units of L mol^{-1} s^{-1}. Note that the variation of x with t is no longer exponential. A characteristic kinetic plot for a second-order reaction can be obtained by plotting $1/[A]$ versus time.

If the rate is proportional to the product of the concentrations of two different substances, and the concentrations are not initially equal, the procedure for integration follows a different approach (following notation and treatment of Laidler, 1987). For example, we assume a reaction stoichiometry described by $\nu_A \mathrm{A} + \nu_B \mathrm{B} \rightarrow \mathrm{Z}$, where ν_A and ν_B are the stoichiometric coefficients for A and B, respectively, and the initial concentrations are a_0 and b_0. The rate after x moles of A have reacted per unit volume is

$$r = \frac{dx}{dt} = k_A(a_0 - \nu_A x)(b_0 - \nu_B x) \tag{1.50}$$

For simplicity, we assume stoichiometric coefficients are unity. Therefore, integration of Eq. (1.50) and application of the boundary condition that $x = 0$ at $t = 0$ yields

$$\frac{1}{a_0 - b_0} \ln\left[\frac{b_0(a_0 - x)}{a_0(b_0 - x)}\right] = k_A t \tag{1.51}$$

Plotting the left hand side of this equation versus t yields a straight line for a second-order reaction whose slope is k_A.

1.5.2.4 nth-Order Reactions

Higher order reactions are uncommon due to the extremely low probability of simultaneous multiple body collisions. However, many rate laws incorporate multiple elementary reactions, resulting in a composite rate law with order >2 (see for example, the treatment of silica oligomerization in Sect. 1.4.1). While such treatments are largely phenomenological rather than molecular, the quantification of such a rate law followed by the proposal and testing of a hypothesized mechanism can lead to molecular insights. Furthermore, some phenomenological rate laws are successfully used to extrapolate kinetics.

To calculate the integrated rate law for an n^{th}-order rate, we consider a reaction of the n^{th}-order involving a single reactant A with an initial concentration a_0 (Laidler, 1987). As seen previously, the concentration of A remaining after time t is $a_0 - x$. Thus, following the previous examples, the rate of consumption of A is

$$r = \frac{dx}{dt} = k_A(a_0 - x)^n \tag{1.52}$$

Applying the boundary condition that $x = 0$ at $t = 0$ and assuming $n \neq 1$ leads to

$$k_A = \frac{1}{t(n-1)}\left[\frac{1}{(a_0 - x)^{n-1}} - \frac{1}{a_0^{n-1}}\right] \tag{1.53}$$

We can employ the integral method to calculate integrated expressions for *n*th order rate laws (Fig. 1.4) for the previous example of oligomerization of silica in aqueous solutions (Eq. (1.26)). For example, for the fourth-order rate law we derive

$$k_4 t = \left(\frac{1}{3}\right)\left[\left(\frac{1}{[H_4SiO_4]^3}\right) - \left(\frac{1}{[H_4SiO_4]_0^3}\right)\right] \tag{1.54}$$

where t is the elapsed time, $[H_4SiO_4]$ is the concentration of monomeric silica at time t, and $[H_4SiO_4]_0$ is the initial concentration of monomeric silica. The rate constant is defined as the slope of a linear fit of the right-hand side of Eq. (1.54) plotted versus time (Fig. 1.4c). The linear relationship in the 4$^{\text{th}}$-order plot (Fig. 1.4c) indicates that the rate of change of monomeric silica can be described by Eq. (1.53) with n = 4. We cannot say that we have *proven* the mechanism to be correct, however, but only that the proposed mechanism is *consistent* with the data.

1.6 Half Life

It is often difficult to compare the relative rates of reactions between two processes because of differences in units of rate constants and varying orders of reaction. A very useful approach for evaluating relative rates of reaction is to determine the half-life, or $t_{1/2}$, for each reaction of interest. The *half-life* is defined as the amount

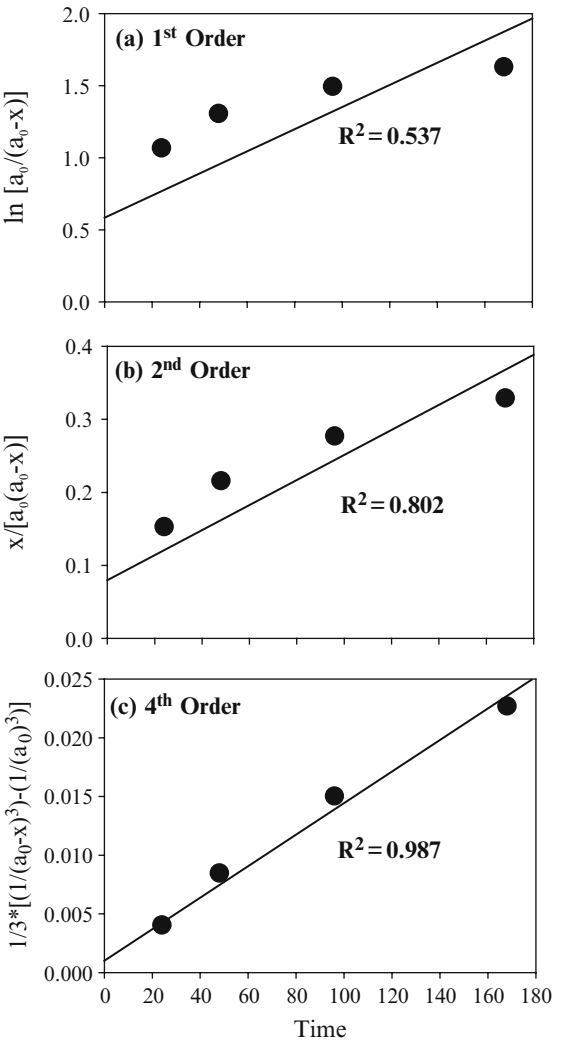

Fig. 1.4 Use of the integral method to determine the order of reaction of polymerization of monomeric to tetrameric silica (initial aqueous SiO_2 concentrations = 12.5 mmolal and an ionic strength of 0.24 M at pH 6). Notation of y-axes follows usage in Sect. 1.5.2. The non-linearity of the first- and second-order plots (frames (a) and (b), respectively) as compared to the fourth-order plot (frame (c)) indicates that a fourth-order model best fits the polymerization rate. The slope of the line in frame (c) is equal to the rate constant for the reaction (Eq. 1.54). See text for further explanation and citations for data.

of time it takes for the concentration of a reactant to reach a value that is half its initial concentration. For a first-order reaction, the half-life is calculated by setting x in Eq. (1.41) equal to $a_0/2$:

$$\ln\left(\frac{a_0}{a_0 - a_0/2}\right) = k_A t_{1/2} \tag{1.55}$$

Solving for the half-life, $t_{1/2}$, yields

$$t_{1/2} = \frac{\ln 2}{k_A} \tag{1.56}$$

Table 1.2 Half-life expressions for reactions of varying stoichiometries and orders (Laidler, 1987)

Single reacting substance A		**Reactants in their stoichiometric ratios; A + ⋯ → Z**	
Order	**Half-life $t_{1/2}$**	**Order**	**Half-life $t_{1/2}$**
0	$\frac{a_0}{2k_A}$	0	$\frac{a_0}{2k_A}$
1	$\frac{\ln 2}{k_A}$	$1(\upsilon_A = k_A[A])$	$\frac{\ln 2}{k_A}$
2	$\frac{1}{k_A a_0}$	$2(\upsilon_A = k_A[A][B])$	$\frac{1}{k_B a_0} = \frac{1}{k_A b_0}$
N	$\frac{2^{n-1}-1}{(n-1)k_A a_0^{n-1}}$	$\mathrm{n}(\upsilon_A = k_A[A][B][C])$	$\frac{2^{n-1}-1}{(n-1)k_A b_0 c_0}$

This half-life expression is used, for example, to describe the duration of time needed for a radioactive parent to decay to half of its initial concentration. Note that for a first-order reaction, the half-life is independent of the initial concentration. Half-lives describing rate of disappearance of a single reactant with a rate equation of higher order can be calculated in a similar manner as that shown above (i.e., by setting $x = a_0/2$ in the integrated rate equation and solving for $t_{1/2}$). Note that unlike first-order reactions, the half-lives of higher order reactions are inversely dependent on the initial concentration of a reactant (Table 1.2). Rate equations for more complex stoichiometries can also be manipulated to yield half-life expressions (Table 1.2). While reporting half-lives can have utility when comparing reaction rates of different order, measurement of half-lives can sometimes be used to estimate the reaction order if experiments are run with different initial concentrations of reactants (Laidler, 1987).

One of the most common uses for half-life calculations is to characterize the rates of processes or ages of rocks using radioactive decay rates. Radioisotopes spontaneously decay at a fixed rate proportional to the number of atoms present, N. This process can be expressed as a first-order reaction:

$$-\frac{dN}{dt} = \lambda N \tag{1.57}$$

where N is the number of atoms of the radionuclide and λ is the decay constant.

For the previous example of silica oligomerization in Fig. 1.4, the half-life can be defined as the time required for half of the initial monomeric silica to disappear from solution. The half lives can be calculated for solutions of varying ionic strengths and plotted versus pH (Fig. 1.5). The half-life of monomeric silica is many orders of magnitude larger in the lower ionic strength solution (0.01 M) as compared to the higher ionic strength solution (0.24 M), with the half-lives decreasing as pH increases especially in the low salt solutions. Thus, it can be discerned that the reaction rate for the oligomerization of silica is more rapid at near neutral pH and in solutions with higher ionic strengths (Icopini et al., 2005).

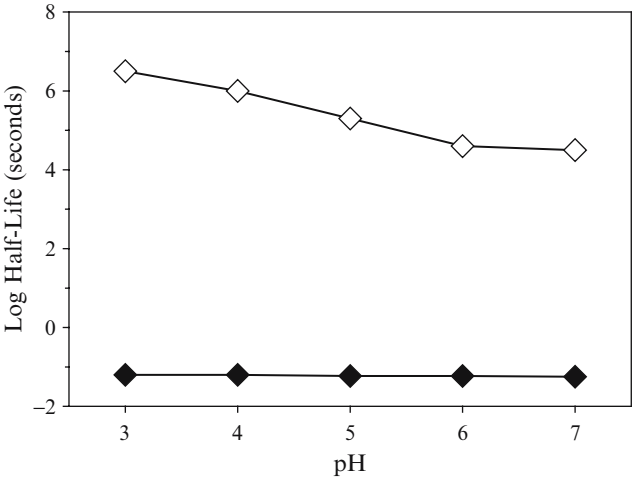

Fig. 1.5 Half-life of molybdate-reactive silica as a function of pH at high (0.24 M, closed symbols) and low (0.01 M; open symbols) ionic strength (IS) in solutions with initial aqueous silica concentration of 12.5 mmolal (Icopini et al., 2005). At high ionic strength, pH does not significantly affect the rate of silica polymerization but at low ionic strength, the pH effect is apparent. The short half-lives observed at near-neutral pH at high IS document faster reaction under these conditions.

1.7 Complex Reactions

1.7.1 Opposing Reactions

Both forward and reverse reactions may occur in the same experiment. For simplicity, we will consider the case where both the forward and reverse reactions are first-order and the reaction is of the form (after Laidler, 1987),

$$A \underset{k_{-1}}{\overset{k_1}{\rightleftharpoons}} Z \tag{1.58}$$

Experimentally, the starting concentration of A, which will be designated a_0, is known and the concentration of Z after time t, designated as x, can be measured. Therefore, the rate of change in concentration of Z can be written as

$$r = \frac{dx}{dt} = k_1(a_0 - x) - k_{-1}x \tag{1.59}$$

where k_1 is the rate constant for the forward reaction and k_{-1} is the rate constant for the opposing reaction. At equilibrium, we define the concentration of Z as x_e and note that, because the net rate is equal to zero at equilibrium, the following must be true:

$$k_1(a_0 - x_e) - k_{-1}x_e = 0 \tag{1.60}$$

Solving for k_{-1} in Eq. (1.60) and substituting into Eq. (1.59) yields

$$r = \frac{dx}{dt} = k_1(a_0 - x) - \left(\frac{k_1 a_0}{x_e} - \frac{k_1 x_e}{x_e}\right)x \tag{1.61}$$

Expanding Eq. (1.61) yields

$$r = k_1 a_0 - k_1 x - \frac{k_1 a_0 x}{x_e} + \frac{k_1 x_e x}{x_e} \tag{1.62}$$

This equation reduces to

$$r = k_1 a_0 - \frac{k_1 a_0 x}{x_e} \tag{1.63}$$

which can be further simplified to give the final form

$$r = \frac{dx}{dt} = \frac{k_1 a_0}{x_e}(x_e - x) \tag{1.64}$$

By applying the boundary condition that $x = 0$ at $t = 0$, we can integrate and derive a relationship between k_1 and x at various values of t:

$$k_1 t = \frac{x_e}{a_0} \ln\left(\frac{x_e}{x_e - x}\right) \tag{1.65}$$

Rearrangement of Eq. (1.65) yields

$$\frac{k_1 a_0}{x_e} = \frac{1}{t} \ln\left(\frac{x_e}{x_e - x}\right) \tag{1.66}$$

From Eq. (1.60) it can be seen that

$$\frac{k a_0}{x_e} = k_1 + k_{-1} \tag{1.67}$$

Substituting Eq. (1.67) into Eq. (1.66) yields

$$k_1 + k_{-1} = \frac{1}{t} \ln\left(\frac{x_e}{x_e - x}\right) \tag{1.68}$$

which is analogous to Eq. (1.41) with x_e replacing a_0 and $k_1 + k_{-1}$ replacing k_A. Note that when there is some initial concentration of Z present, the rate equation does not change.

Table 1.3 summarizes rate laws for more complex opposing reactions following the analysis and notation of Laidler (1987). For even more complex reaction mechanisms, the reader is referred to kinetic compilations (Capellos and Bielski 1972).

Table 1.3 Differential and integrated form of rate equations for some simple opposing reactions (Laidler, 1987)

	Rate equation	
Stoichiometric equation	**Differential form**	**Integrated form**
$A \rightleftharpoons Z$	$\frac{dx}{dt} = k(a_0 - x) - k_{-1}x$	$\frac{x_e}{a_0} \ln\left(\frac{x_e}{x_e - x}\right) = k_1 t$
$A \rightleftharpoons Z$	$\frac{dx}{dt} = k(a_0 - x) - k_{-1}(x + x_0)$	
$2A \rightleftharpoons Z$	$\frac{dx}{dt} = k(a_0 - x) - k_{-1}\frac{x}{2}$	
$A \rightleftharpoons 2Z$	$\frac{dx}{dt} = k\left(a_0 - \frac{x}{2}\right) - k_{-1}x$	
$A \rightleftharpoons Y + Z$	$\frac{dx}{dt} = k(a_0 - x) - k_{-1}x^2$	$\frac{x_e}{2a_0 - x_e} \ln\left(\frac{a_0 x_e + x(a_0 - x_e)}{a_0(x_e - x)}\right) = k_1 t$
$A + B \rightleftharpoons Z$	$\frac{dx}{dt} = k(a_0 - x)^2 - k_{-1}x$	$\frac{x_e}{a_0^2 - x_e^2} \ln\left(\frac{x_e(a_0^2 - x x_e)}{a_0^2(x_e - x)}\right) = k_1 t$
$A + B \rightleftharpoons Y + Z$	$\frac{dx}{dt} = k(a_0 - x)^2 - k_{-1}x^2$	$\frac{x_e}{2a_0(a_0 - x_e)} \ln\left(\frac{x(a_0 - 2x_e) + a_0 x_e}{a_0(x_e - x)}\right) = k_1 t$
$2A \rightleftharpoons Y + Z$	$\frac{dx}{dt} = k(a_0 - x)^2 - k_{-1}\left(\frac{x}{2}\right)^2$	

1.7.2 Sequential Reactions

Complex reactions often involve the formation and disappearance of intermediate species. These species can be atoms, free radicals or more complex molecules and are referred to as *reactive intermediates*.

For example, we have previously discussed the conversion of monomeric to tetrameric silica in Sect. 1.4.1. This, however, is only the initial step in a series of sequential reactions resulting in the precipitation of silica from supersaturated aqueous solutions. The full reaction can be written as

$$SiO_{2(mono)} \xrightarrow{k_1} SiO_{2(cn)} \xrightarrow{k_{fast}} SiO_{2(nano)} \xrightarrow{k_2} SiO_{2(ppt)} \tag{1.69}$$

where monomeric silica, $SiO_{2(mono)}$, condenses to form a cyclic tetramer which is hypothesized to be the critical nucleus, $SiO_{2(cn)}$ of this system (see Chap. 7 for further discussion of critical nucleus). Note that here we are using a different definition for k_1 and k_2 than we previously used for this example in Sect. 1.4.1. Once the critical nucleus is formed, it spontaneously converts to nanocolloidal silica, $SiO_{2(nano)}$, which in turn reacts to form the product, precipitated silica, $SiO_{2(ppt)}$. The rates of the first and last of these processes can be described by the rate constants k_1 (oligomerization) and k_2 (precipitation). The growth of the critical nucleus

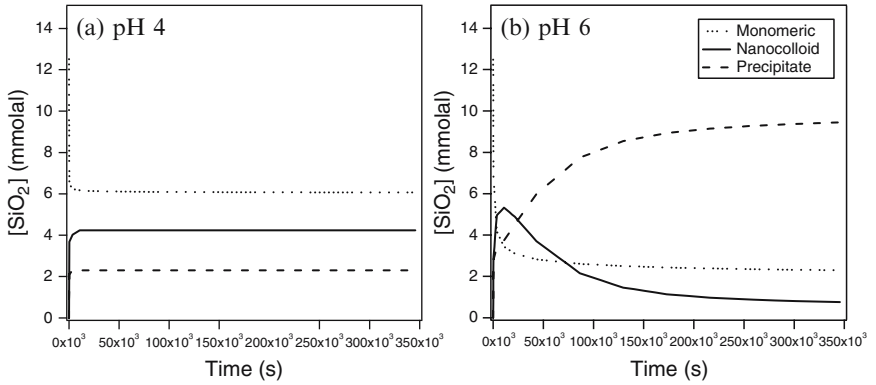

Fig. 1.6 Aqueous concentrations of monomeric (···), nanocolloidal (—) and precipitated (- - -) silica versus time as an illustration of the sequential reaction $A \xrightarrow{k_1} B \xrightarrow{k_2} Z$. Reactant A (monomeric silica) is consumed as B (nanocolloidal silica) is produced. However, the concentration of B is depleted by conversion to Z (precipitate). Lines indicate best fits (Conrad et al., 2007) to concentrations measured for experiments (Icopini et al., 2005) with initial silica concentrations of 12.5 mmolal and ionic strength 0.24 M at (**a**) pH 4 and (**b**) pH 6. At pH 4, $k_1 \gg k_2$ leading to the accumulation of nanocolloidal silica with little precipitate forming. At pH 6, $k_1 \ll k_2$ and the nanocolloidal fraction is rapidly converted to precipitated silica.

to nanocolloidal silica occurs quickly and is therefore assigned here the rate constant k_{fast} where k_{fast} is $\gg k_1, k_2$ (Icopini et al., 2005; Conrad et al., 2007).

This series of sequential reactions can be conceptually written as A $\rightarrow$ B′ $\rightarrow$ B $\rightarrow$ Z. However, because concentration of the reactive intermediate B′ (the critical nucleus) has not been measured, the overall reaction can be simplified even further as A $\rightarrow$ B $\rightarrow$ Z, where B is nanocolloidal silica and Z is the precipitate:

$$A \xrightarrow{k_1} B \xrightarrow{k_2} Z \tag{1.70}$$

For such reactions, the concentration of A decreases and Z increases with time (Fig. 1.6). The relative concentrations of A, C and Z depend on the relative magnitudes of k_1 and k_2.

As shown previously in Fig. 1.4, the disappearance of monomeric silica from solution is best fit by a fourth-order rate law (see discussion below). However, for simplicity we here treat the simpler case for A $\rightarrow$ B as a first-order rate law (following Laidler, 1987):

$$-\frac{d[A]}{dt} = k_1[A] \tag{1.71}$$

Integration of Eq. (1.71) and application of the boundary condition that $[A] = [A]_0$ at time $= 0$ yields

$$[A] = [A]_0 e^{-k_1 t} \tag{1.72}$$

The net rate of formation of B is expressed by the rate of reaction of species A minus the loss of B due to the conversion to species Z (also assumed here to be first-order):

$$\frac{d[B]}{dt} = k_1[A] - k_2[B] \tag{1.73}$$

Substituting Eq. (1.72) into Eq. (1.73) yields

$$\frac{d[B]}{dt} = k_1[A]_0 e^{-k_1 t} - k_2[B] \tag{1.74}$$

Integration of this expression can be shown to yield

$$[B] = [A]_0 \frac{k_1}{k_2 - k_1}\left(e^{-k_1 t} - e^{-k_2 t}\right) \tag{1.75}$$

The concentration of Z at any point in time can be determined by noting that

$$[A] + [B] + [Z] = [A]_0 \tag{1.76}$$

If one step in the overall reaction is much slower than the other steps, then the rate law can be considerably simplified. Two cases exist for the general reaction in Eq. (1.70): $k_1 \gg k_2$ (second reaction is rate-controlling) or $k_1 \ll k_2$ (first reaction is rate-controlling). In the first case, A is rapidly converted to B which then accumulates due to the slow conversion of B to Z. The rate at which product Z appears in solution is controlled by the rate of decrease in [B]. Because the rate at which Z is formed depends only on k_2, this is the rate-controlling step. In the second case, the conversion of A to B is very slow. As B forms, it is quickly transformed into Z and B does not accumulate. The rate constant for formation of B, k_1, is now rate-determining. In this case, the production of Z is determined by the rate of decrease in $[A]$. In either of these cases, treatment of the kinetics can be greatly simplified as the overall rate of production of Z depends only on the step with the smallest rate constant.

We return now to the homogeneous nucleation and precipitation of silica written as A → B → Z (Eq. (1.69)). The rate of silica oligomerization, k_1, and the rate of precipitation of silica, k_2, are both affected by pH (Icopini et al., 2005; Conrad et al., 2007). At low pH values, nanocolloidal silica rapidly forms, but does not convert readily to precipitated silica. In this case, $k_1 \gg k_2$ (Fig. 1.6a) and a measurable concentration of the nanocolloidal fraction remains in solution. At near-neutral pH values, monomeric silica reacts to form nanocolloidal silica, which is then rapidly converted to precipitated silica. Under these conditions, $k_1 \ll k_2$ and the concentration of the nanocolloidal fraction in solution decreases over time (Fig. 1.6b).

If the concentration of B builds up in solution and appears to remain constant in time, as seen in Fig. 1.6a, we refer to this as *steady state behavior*. Mathematically, [B] achieves a steady state (constant with respect to time) when $k_1 \gg k_2$ in Eq. (1.75). Steady state is defined as a non-equilibrium state in which the concentrations and the rates of the reactions are constant over some time interval. In contrast, equilibrium refers to a situation where the forward and reverse rates for all reactions are equal and opposite in sign. Note that a steady state condition can only be maintained

for a finite amount of time in a closed system but can be maintained indefinitely in a system open to a flux of mass or energy (Chap. 12).

In the discussion of silica polymerization and precipitation, we have only explicitly considered chemical reactions occurring at the interface. For any heterogeneous reaction, transport must also occur to bring reactants to the surface or to remove products from the surface. During heterogeneous reactions, therefore, both transport and interfacial reactions occur sequentially and can be discussed in relationship to equation 1.70 (see also Chap. 3). For a rapidly dissolving monocomponent mineral, for example, we can conceptualize these sequential reactions as $A_{(solid)} \rightarrow A_{(aq,interface)} \rightarrow A_{(aq,bulk)}$. Here, we recognize that the concentration of component A in solution released from the solid crystal varies with distance from the solid-fluid interface: we define $A_{(aq,interface)}$ as the solute at the mineral-water interface and $A_{(aq,bulk)}$ as the solute in bulk solution far from the interface. If transport away from the dissolving crystal is fast, then the concentration of the solute at the interface, $[A]_{(aq,interface)}$, is well below the equilibrium value. But if transport is slow, $[A]_{(aq,interface)}$ can increase until the equilibrium value (see also Chap. 3 Fig. 3.3 and Chap. 11). Stated differently, if the interfacial reaction is rate-limiting, the value of $[A]_{(aq,interface)}$ approaches $A_{(aq,bulk)}$, and if transport is rate-limiting, the value approaches the equilibrium value. Note that the activation energies (Sect. 1.8) of transport and interfacial reaction generally differ significantly (see Chap. 5) and thus measurement of the activation energy of a reaction is often used to delineate transport versus interfacial control.

1.7.3 Parallel Reactions

Multiple reactions within a given system can also occur in parallel: for example, the reactions $A \rightarrow B, A \rightarrow C$ and $A \rightarrow Z$ may all occur in *parallel* in one system but in *sequence* in another: $A \rightarrow B \rightarrow C \rightarrow Z$. In the parallel case, utilization of A is dictated by the competing rates of formation of B, C, and Z, and the fastest rate will control the rate of disappearance of A. For example, in the case of the anisotropic dissolution of biotite and other sheet silicates (Sect. 1.4.2), the dissolution of the edge and basal sites occur in parallel. Dissolution of edge sites occurs more quickly and therefore represents the rate-controlling step. In contrast, as discussed above, for the sequential case, the formation of Z often can be described by the rate of one *rate-controlling* step, but this step is generally the slowest step in the reaction sequence. Thus, for sequential reactions, the slow step controls the rate of formation of Z while in systems with parallel reactions, the fast step controls the rate.

1.7.4 Chain Reactions

Chain reactions consist of the multiple steps of chain initiation, propagation, and termination. A classic example of a chain reaction is the overall gas reaction

$H_2 + Br_2 \rightarrow 2HBr$ (Laidler and Meiser, 1995). The elementary reactions for this process are written as

$$Br + H_2 \rightarrow HBr + H \tag{1.77}$$

$$H + Br_2 \rightarrow HBr + Br \tag{1.78}$$

These two reactions together are said to form a chain, as the output of the second reaction is the input to the first reaction. Thus, the essential feature of a chain reaction is that there must be a closed sequence, or cycle, of reactions such that the intermediates (e.g., atoms, free radicals, or molecules) consumed in one step are regenerated in another. The reaction that begins the chain (Eq. (1.77)) is called the *initiation reaction* and subsequent reactions are termed *chain-propagation steps*. Atmospheric reactions involving free radicals commonly exemplify reactions of this type (Laidler and Meiser, 1995).

1.8 Temperature Dependence of Reaction Rates

To extrapolate reaction rates, the temperature dependence of the rate constant must be understood. The Arrhenius equation, proposed in 1889, is generally used to describe the temperature dependence of k:

$$k = A' \exp(-E/RT) \tag{1.79}$$

Here, A' is referred to as the *pre-exponential factor*, E is the *activation energy*, R is the gas constant and T is temperature in degrees Kelvin. These two new parameters are usually, but not always, observed to be independent of temperature. The slope of a plot of $\ln k$ versus $1/T$, such as the example in Fig. 1.7 for the dissolution of albite (Chen and Brantley, 1997), yields the activation energy.

In general, experimental activation energies for mineral-water reactions range from a few kcal/mol to larger than 100 kcal/mol. Arrhenius proposed that the activation energy is the minimum amount of energy required to initiate a reaction: the magnitude of this activation energy (also called the *Arrhenius energy*) is often interpreted with respect to the reaction mechanism. For example, activation energies for mineral dissolution that are as low as 5 kcal/mol have been interpreted to demonstrate reactions that are rate-limited by diffusion of reactants to the mineral or products away from the mineral. In contrast, activation energies of approximately 20 kcal/mol (e.g., Fig. 1.7) are generally diagnostic of bond-breakage during the rate-limiting step of reaction.

The activation energy for the forward reaction, E_F, can be conceptualized as the activation barrier that must be overcome to allow forward reaction. This is generally conceptualized as the energy required to transform the reactants to an activated state or complex that can then react to products (Chap. 2). Similarly, the activation energy of the reverse reaction, E_R, is the energy required to activate products to allow them to react in the reverse direction to form the original reactants. Such *activated*

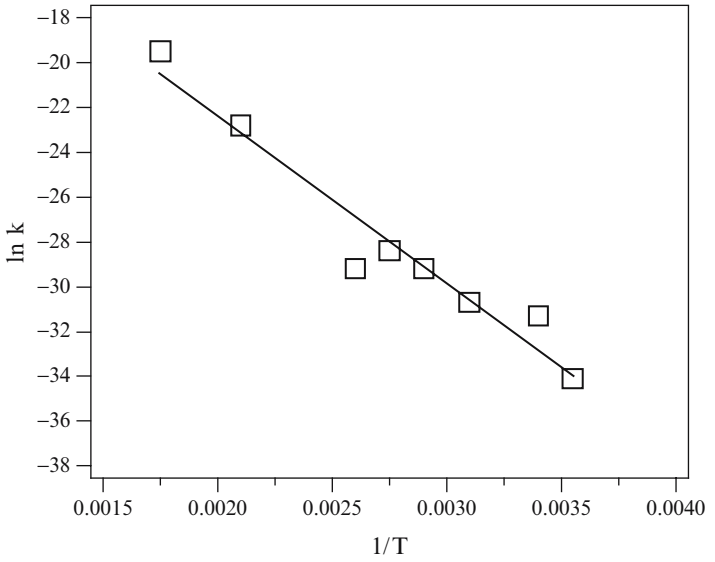

Fig. 1.7 Arrhenius plot showing natural logarithm of the rate of dissolution of albite versus 1/T (K). The activation energy of albite dissolution was estimated as 15.6 ± 0.8 kcal mol^{-1} based on this plot. Data sources summarized elsewhere (Chen and Brantley, 1997).

complex theory led to the development of *transition state theory* which is discussed in Chap. 2.

For an elementary reaction in which no volume change occurs, we can derive expressions that relate activation energies to the standard state Gibbs free energy of reaction, ΔG°, enthalpy of reaction, ΔH°, and entropy of reaction, ΔS°. We discuss the forward and reverse elementary reactions described by

$$A + B \rightleftarrows C + D \tag{1.80}$$

At equilibrium, the forward rate must equal the backward rate by *the principle of detailed balancing*. Assuming we are dealing with elementary reactions, we can write out the forward and reverse rates and equate them; furthermore, with rearrangement, we can show that the equilibrium constant, K_{eq}, for the reaction equals the ratio of forward and reverse rate constants (e.g. Skinner, 1974):

$$K_{eq} = \frac{[C][D]}{[A][B]} = \frac{k_f}{k_r} \tag{1.81}$$

In addition, noting the following thermodynamic expression

$$K_{eq} = \exp\left(\frac{-\Delta G^\circ}{RT}\right) = \exp\left(\frac{-(\Delta H^\circ - T\Delta S^\circ)}{RT}\right) = \exp\left(\frac{\Delta S^\circ}{R}\right)\exp\left(\frac{-\Delta H^\circ}{RT}\right) \tag{1.82}$$

we can derive an expression for the activation energy and pre-exponential factor

$$\frac{A'_F \exp(-E_F/RT)}{A'_R \exp(-E_R/RT)} = \exp\left(\frac{\Delta S^\circ}{R}\right)\exp\left(\frac{-\Delta H^\circ}{RT}\right) \tag{1.83}$$

where the subscript F or R refers to the value of A' or E for the forward or reverse rate respectively. This equation then yields the following two expressions

$$\frac{A'_F}{A'_R} = \exp\left(\frac{\Delta S^\circ}{R}\right) \tag{1.84}$$

$$E_F - E_R = \Delta H^\circ \tag{1.85}$$

These two expressions (Eqs. (1.84) and (1.85)) explicitly document how terms related to forward and reverse reaction *kinetics* (the activation energies and pre-exponential terms) are related to *thermodynamic* quantities.

Generally, an experimentalist measures the rate of a reaction as a function of temperature while holding all other variables constant, then determines the slope of a plot of $\ln k$ versus $1/T$ as shown in Fig. 1.7. If the reaction is an elementary reaction, then the slope reveals information about the activation barrier for that reaction. More likely for the reaction of a mineral in water is the case where the reaction represents a complex mechanism with multiple steps including transport and interfacial steps. For such a case, the temperature dependence determined in the Arrhenius plot will represent the sum of the true activation energy for the rate-limiting step and the ΔH of reaction for fast steps that attain equilibrium during the reaction. For example, the apparent activation energy of k_4 (see Eq. (1.27)) determined as described previously for the composite reaction given in Eq. (1.26) would equal the sum of the activation energy for rate-limiting step given in Eq. (1.25) plus the ΔH of the reaction given in Eq. (1.23) and ΔH of the reaction given in Eq. (1.24). The enthalpy term is derived from the van't Hoff equation which describes the temperature dependence of the equilibrium constant. If the activity coefficient term $(f(y))$ or activity of water showed a strong temperature dependence in Eq. (1.27), this contribution might also be seen in the apparent activation energy for k_4.

1.9 Chemical Reactors

Chemical reactors are reaction vessels that are used to measure the rates of chemical reactions as a function of time or species concentration (e.g., Chou and Wollast, 1985; Posey-Dowty et al., 1986; Rimstidt and Dove, 1986). Here, we use terminology largely derived from a textbook describing chemical reactor engineering (Hill, 1977).

The simplest type of reactor, an *ideal tank reactor,* is a perfectly stirred container whose contents are always homogeneous in concentration and temperature. Such reactors can be run in *batch* (no flow in or out) or *flow mode* (Fig. 1.8). In contrast to tank reactors, in *ideal tubular reactors,* fluid moves through a tube as plug-flow,

creating a continuous gradient in concentration of reactants and products. Tubular reactors may be packed with powder, in which case they are sometimes referred to as *packed bed reactors* (Fig. 1.10). Flow reactors can also be run as *recycle reactors* (Fig. 1.9), where the output solution is split so that one stream is sampled and another stream is pumped back into the reactor. Beyond these simple approaches, reactors can also be designed in more complex modes: for example, *semi-batch reactors* are used by kineticists who add reactants or remove products from a batch reactor during the reaction; *staged reactors* are used to isolate separate reactions in a series of ideal tank reactors hooked together in sequence.

In general, the interpretation of a reactor is completed by using a mass balance treatment for input and output as described for various types of reactors in the following sections.

1.9.1 Batch Reactors

Batch reactors, the simplest reactors for use, are agitated or stirred tanks which are set up with all reactants either closed or open to the atmosphere. Kineticists can use these reactors to follow the progress of reactions in which the chemistry changes with time due to the accumulation of reaction products. To interpret the behavior of a reaction occurring in a batch reactor, one must first know the stoichiometry of the reaction of interest: for example, let us assume we are using a batch reactor to monitor the reaction given in Eq. (1.6) ($A + 3B \rightarrow Z$). If the concentration of products (e.g., $[Z]$) can be monitored without sampling the reactor during the reaction progress, the rate can be calculated as $d[Z]/dt$ (see, for example, Fig. 1.1). If reaction progress for a mineral-water reaction cannot be monitored potentiometrically or spectroscopically, however, then aliquots of solution must be removed sequentially. Removal of aliquots of solution changes the volume in the reactor over time, which makes calculation of the reaction rate more complex. For example, to measure the rate of area-normalized release (r, mol $m^{-2}s^{-1}$) of element Z from a dissolving phase in a batch reactor that is sampled periodically, the rate can be calculated as follows:

$$r = \frac{1}{A_s m}\frac{dn_Z}{dt} \tag{1.86}$$

where n_Z = moles of element Z in solution, t = time in seconds, A = reactive surface area of the phase A in m^2 g^{-1}, and m = mass of phase A in grams. To calculate dn_Z/dt, the moles of Z at time point t, $n_{Z,t}$, can be determined by

$$n_{Z,t} = n_{Z,t-1} + ([Z]_t - [Z]_{t-1})V_{t-1} \tag{1.87}$$

where t = a sampling time point, t_{-1} = previous sampling time point, and V = the volume of medium in the flask in liters. Subscripts for n_Z or V refer to the sampling time point.

One analysis technique for estimating reaction rates from batch reactor experiments is the *initial rate method*. In the initial rate method, only data from a relatively short reaction interval in the beginning of the experiment is used. The time period is chosen such that the change in concentration of reactant A versus time can be fit to a linear first-order equation of the form

$$[A] = a_1 + b_1 t \tag{1.88}$$

where the derivative of this function is

$$r = \frac{d[A]}{dt} = b_1 \tag{1.89}$$

In this scheme, b_1 describes the apparent rate of disappearance of A at $t = 0$, and a_1 is the best fit initial concentration of A (Rimstidt and Newcomb, 1993). Long-term data from batch reactor experiments can be fit to non-linear functions of time. Complexities in fitting data are further discussed in Chap. 6.

Interpretation of batch reactors is complicated by the fact that the measured rate may change as a function of time as the solution chemistry changes in the reactor. For example, during a mineral dissolution experiment, pH may change during reaction progress unless the solution is well-buffered. To maintain constant pH, the experimentalist may also input acid or base as the pH changes, in effect running the reactor in semi-batch mode. Several researchers have discussed the problems of using batch reactors for reactions where rate changes with time (e.g., Oelkers et al., 2001).

1.9.2 Flow-Through Reactors

Stirred flow-through reactors allow maintenance of constant solution chemistry during reaction. In a continuously stirred tank reactor or CSTR (Hill, 1977), also known as a mixed flow reactor (Rimstidt and Dove, 1986), a mineral sample is placed in a tank of volume V through which fluid is continuously pumped at flow rate Q' (Figs. 1.8 and 1.9). Such a reactor is continuously stirred by a propeller or by agitation so that the concentration and temperature in the reactor is homogeneous under ideal conditions. If the reaction under study is a heterogeneous reaction with both solid and aqueous reactants, under ideal conditions the powdered solid reactant must be suspended in the fluid so that ideal mixing occurs. Mixed flow reactor experiments are generally the most difficult to construct but are the easiest to interpret because they provide a direct measurement of the reaction rate. Calculating the rate using a mixed flow reactor does not entail utilization of the differential method, thus avoiding complications that may arise during the process of differentiating concentration versus time (Rimstidt and Newcomb, 1993).

The rate of a heterogeneous reaction, r (mol $m^{-2}s^{-1}$), is assessed by comparing the inlet concentration ($[Z]_i$) to the outlet concentration ($[Z]_o$) of a component released from the reacting powder while a fluid is pumped through at rate Q'. Mass

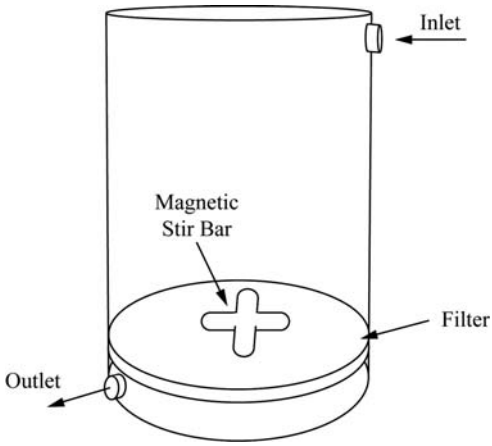

Fig. 1.8 Schematic drawing of a continuously stirred tank reactor (CSTR), also known as a mixed flow reactor. In mineral dissolution experiments, a mineral sample is placed in a tank of known volume and fluid is pumped at a controlled flow rate. The tank is continuously agitated so that the concentration and temperature in the reactor are homogeneous under ideal conditions.

balance requires that the flux of the component out of the reactor ($Q'[Z]_o$) must equal the flux into the reactor ($Q'[Z]_i$) plus the extent of reaction occurring in the reactor. Such a mass balance can then be solved for r:

$$r = \frac{Q'([Z]_0 - [Z]_i)}{A_s m}. \tag{1.90}$$

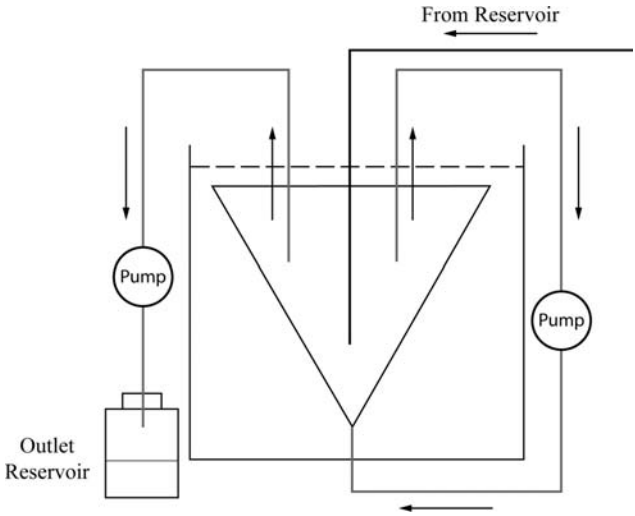

Fig. 1.9 Schematic diagram of a fluidized bed reactor. The direction of flow throughout the system is indicated by the arrows. Solution is pumped into and out of the reaction vessel at a known rate. Species in the vessel are continuously mixed by another circulating flow established by a second pump.

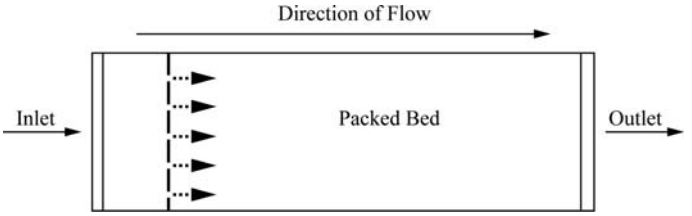

Fig. 1.10 Schematic diagram of a typical plug-flow reactor (PFR). Every packet of fluid is assumed to move through the packed bed of mineral grains with the same residence time as indicated schematically by arrows. These reactors are also sometimes referred to as packed bed reactors or column reactors (when run vertically).

The extent of reaction that occurs in the reactor can be controlled by controlling the flow rate and the *residence time* of the fluid in the reactor (residence time $= V/Q'$). The residence time for a heterogeneous reaction is also called the *contact time*.

Flow reactors are run until the outlet concentration reaches a constant value, the so-called steady-state value which yields the steady-state reaction rate. Reaction rates are reported as the observed rate with respect to solution chemistry as measured in the effluent. Thus, if inlet pH does not equal outlet pH, measured rate is reported with respect to the outlet pH. If final mass or final specific surface area differs significantly between the initial and final conditions, then this may also be measured and included in determining the rate.

One form of the CSTR, the fluidized bed reactor, utilizes two flows, one which is single pass, and a second recirculating flow which stirs the mineral powder (Fig. 1.9). The "stirring" flow is a very fast flow which keeps the mineral particles suspended in the reactor. The inlet and outlet concentrations measured in the single-pass flow are compared just as in a CSTR to analyze the chemical reaction rate (Chou and Wollast, 1985).

Plug-flow reactors (PFR) have often been used by geochemists to analyze water-rock reactions (Fig. 1.10). These tubular reactors more closely mimic natural systems; however, a PFR is often more complicated to model than a CSTR due to precipitation of product phases and due to non-ideality of flow through packed beds of particles (Chap. 12). In an ideal plug-flow reactor, every packet of fluid is assumed to move through a packed bed of mineral grains with the same residence time (Hill, 1977). For this reason, these reactors are also called *packed bed reactors*; when run vertically, they are often referred to as *column reactors*.

Assuming ideal axial flow with complete radial mixing in the PFR, the moles of reactant that enter a small volume element, dV, of the reactor during an increment of time $dt, Q'[Z]dt$, plus the extent of reaction that occurs during that time interval, $rdVdt$, must equal the moles of reactant exiting that volume over the same time interval, $Q'([Z]+d[Z])dt$. Assuming that the reaction occurs with no volume change and that the rate can be expressed as an n^{th}-order reaction,

$$r = k[Z]^n \tag{1.91}$$

we can derive the mass balance expression:

$$-\int_{[Z]_i}^{[Z]_o} \frac{d[Z]}{[Z]^n} = \frac{k}{Q'} \int_0^V dV \tag{1.92}$$

Integration shows that the outlet concentration is related to the inlet concentration by the following expression:

$$\frac{1}{1-n}\left[\frac{1}{[Z]_o^{n-1}} - \frac{1}{[Z]_i^{n-1}}\right] = \frac{kV}{Q'} \tag{1.93}$$

for $n \neq 1$ and, for $n = 1$,

$$[Z]_o = [Z]_i \exp\left(\frac{-kV}{Q'}\right) \tag{1.94}$$

Interpretation of plug-flow reactors is especially difficult due to the changing chemical affinity as a function of position in the reactor, and the possibility of precipitation of secondary phases (see Chap. 5). If the experimentalist does not know how the reaction rate varies with concentration, then interpretation of a plug-flow reactor is ambiguous (Taylor et al., 2000). Specifically, for such a case, the experimentalist must assume a rate equation and derive an expression to be integrated. In general, such an inverse modeling approach yields non-unique answers to the problem.

Interpretation of mineral dissolution rates using other chemical reactors can also be ambiguous. For example, dissolution experiments are usually interpreted with respect to interface- or transport-control, which may be a function of the stirring rate of the reactor. Whereas a packed bed reactor may easily become transport-controlled, a fluidized bed reactor suspends mineral particles and obviates against the maintenance of thick hydrodynamic boundary layers around mineral grains. However, fluidized reactors have been criticized for causing continuous abrasion and surface area changes during dissolution. On the other hand, mineral grains may not be thoroughly mixed with water in CSTRs, allowing the stagnation of fluid at the grain surface causing diffusion limitation. Often, experimentalists will run a reactor with different stirring rates to determine whether either transport of reactant to the surface or product away from the surface are controlling the reaction (Shiraki and Brantley, 1995).

Another problem with experiments to measure heterogeneous reactions of multicomponent phases in chemical reactors is that effluent concentrations are often observed to change with time over many thousands of hours (White and Brantley, 2003). For dissolution reactions, such non-steady state behavior may be related to chemical or physical changes in the surface over time. Chemical effects might include precipitation of secondary phases onto the surface, dissolution of impurities or exsolved phases embedded in the sample, or time-dependent, non-stoichiometric leaching of elements from the surface (Chap. 5). The physical topography of the mineral surface also changes during dissolution, which in turn affects the reactivity (Chap. 3).

1.10 Conclusions

Interpretation of geochemical kinetics has advanced significantly since the very earliest geochemical experiments (Rodgers and Rodgers, 1848). Scientists in the 1800s, like scientists today, wondered how to measure geochemical kinetics in the laboratory in order to scale those measurements to the field. In this chapter, we have summarized the basic approaches used to measure and analyze geochemical kinetics. Especially since the 1970s, the number of published studies of geochemical kinetics has grown significantly. Many of the approaches discussed in this chapter have been used to provide the databases (Chap. 6, Appendix) underlying modern reactive transport codes that are used in many applications ranging from fundamental geochemical science to environmental engineering (Chap. 11). Careful experimental and analytical work will always be needed to understand the complexities of geochemical kinetics.

Acknowledgements

SLB acknowledges V. Balashov and J. Bandstra and all the students of Penn State Geosciences 560 for editing advice. This chapter is based upon work supported by the Center for Environmental Kinetics Analysis funded by the National Science Foundation under Grant No. CHE-0431328 and the U.S. Department of Energy, Biological and Environmental Research (BER).

Glossary of Symbols

a_i	activity of species i in solution
a_0	concentration of reactant A at time $t = 0$
A	chemical affinity, or a species in a reaction
A'	pre-exponential factor in Arrhenius equation
A_s	surface area $(\mathrm{m}^2\ \mathrm{g}^{-1})$
C	number of components, or a species in a reaction
dS	entropy production of a process
E	activation energy
E_F	activation energy of the forward reaction
E_R	activation energy of the reverse reaction
F	degrees of freedom
$[i]$	concentration of species i
I	constant of integration
k	rate constant
k_n	forward rate constant
k_{-n}	reverse rate constant
K_{eq}, K_1, K_2	equilibrium constants
K_m	Michaelis-Menten constant
m	mass

n	order of reaction
n_i^0	initial number of moles of species i
n_i	number of moles of species i
N	number of radionuclide atoms
P	pressure
Q	reaction activity quotient
Q'	flow rate
r	rate of reaction
R	gas constant
t	time
$t_{1/2}$	half-life
T	temperature
V	volume
V_{max}	maximum velocity
x	concentration of product at time t
x_e	concentration of product at equilibrium
$[\mathrm{Z}]_\mathrm{i}$	inlet concentration of Z
$[\mathrm{Z}]_\mathrm{o}$	outlet concentration of Z
α	partial order of reaction with respect to reactant A
β	partial order of reaction with respect to reactant B
$\Delta G_{reaction}$	Gibbs free energy of reaction
ΔG°	standard Gibbs free energy
ΔH°	standard enthalpy of reaction
ΔS°	standard entropy of reaction
ε_i	degree of inhibition
λ	radioactive decay constant
ν_i	stoichiometric coefficient of species i
σ	partial order of reaction with respect to product Z
ξ	extent of reaction

References

Bandstra J. Z. and Tratnyek P. G. (2005) Central limit theorem for chemical kinetics in complex systems. *J. Math. Chem.* **37**(4), 409–422.

Brantley S. L. and Mellott N. (2000) Specific surface area and porosity of primary silicate minerals. *Am. Mineral.* **85**, 1767–1783.

Capellos C. and Bielski B. H. J. (1972) *Kinetic Systems*. Wiley-Interscience.

Chen Y. and Brantley S. L. (1997) Temperature- and pH-dependence of albite dissolution rate at acid pH. *Chem. Geol.* **135**, 275–292.

Chou L. and Wollast R. (1985) Steady-state kinetics and dissolution mechanisms of albite. *Am. J. Sci.* **285**, 963–993.

Conrad C. F., Icopini G. A., Yasahura H., Brantley S. L. and Heaney P. J. (2007) Modeling the Kinetics of Silica Nanocolloid Formation and Precipitation in Geologically Relevant Aqueous Solutions. *Geochimica et Cosmochimica Acta* **71**(3), 531–542.

Drever J. I. (1997) *The Geochemistry of Natural Waters: Surface and Groundwater Environments*. Prentice Hall, Englewood Cliffs, NJ.

Driehaus W., Seith R., and Jekel M. (1995) Oxidation of arsenate(III) with manganese oxides in water treatment. *Wat. Res.* **29**(1), 297–305.

Hamilton J. P., Brantley S. L., Pantano C. G., Criscenti L. J., and Kubicki J. D. (2001) Dissolution of nepheline, jadeite and albite glasses: Toward better models for aluminosilicate dissolution. *Geochim. Cosmochim. Acta* **65**(21), 3683–3702.

Hem J. D., Roberson C. E., Lind C. J., and Polzer W. L. (1973) Chemical interactions of aluminum with aqueous silica at 25C, pp. 57. US Geological Survey.

Hill C. G. (1977) *An Introduction to Chemical Engineering Kinetics and Reactor Design*. John Wiley & Sons, Inc., New York.

Hossner L. R. and Doolittle J. J. (2003) Iron sulfide oxidation as influenced by calcium carbonate application. *J. Environ. Qual.* **32**, 773–780.

Icopini G. A., Brantley S. L., and Heaney P. J. (2005) Kinetics of silica oligomerization and nanocolloid formation as a function of pH and ionic strength at 25° C. *Geochim. Cosmochim. Acta* **69**(2), 293–303.

Kalinowski B. E. and Schweda P. (1996) Kinetics of muscovite, phlogopite, and biotite dissolution and alteration at pH 1–4, room temperature. *Geochim. Cosmochim. Acta* **60**, 367–385.

Kraemer S. M. (2004) Iron oxide dissolution and solubility in the presence of siderophores. *Aquat. Sci.* **66**, 3–18.

Laidler K. J. (1987) *Chemical Kinetics*. Harper & Row, Publishers, Inc., New York.

Laidler K. J. and Meiser J. H. (1995) *Physical Chemistry*. Houghton Mifflin Company, Boston, MA.

Lasaga A. C. (1981) Rate laws of chemical reactions. In *Kinetics of Geochemical Processes*, Vol. 8 (ed. A. C. Lasaga and R. J. Kirkpatrick), pp. 1–68. Mineralogical Society of America.

Nagy K. L. (1995) Dissolution and precipitation kinetics of sheet silicates. In *Chemical Weathering Rates of Silicate Minerals*, Vol. 31 (ed. A. F. White and S. L. Brantley), pp. 173–225. Mineralogical Society of America.

Oelkers E. H., Schott J., and Devidal J.-L. (2001) On the interpretation of closed system mineral dissolution experiments: Comment on "mechanism of kaolinite dissolution at room temperature and pressure part II: Kinetic study" by Huertas et al. (1999). *Geochim. Cosmochim. Acta* **65**(23), 4429–4432.

Perez J. R., Banwart S. A., and Puigdomenech I. (2005) The kinetics of $O_{2(aq)}$ reduction by structural ferrous iron in naturally occurring ferrous silicate minerals. *App. Geochem.* **20**, 2003–2016.

Posey-Dowty J., Crerar D., Hellmann R., and Chang C. D. (1986) Kinetics of mineral-water reactions; theory, design and application of circulating hydrothermal equipment. *Am. Mineralog.* **71**, 85–94.

Prigogine I. (1967) *Introduction to Thermodynamics of Irreversible Processes*. John Wiley & Sons, Inc., New York.

Rimstidt J. D. and Newcomb W. D. (1993) Measurement and analysis of rate data: The rate of reaction of ferric iron with pyrite. *Geochim. Cosmochim. Acta* **57**, 1919–1934.

Rimstidt J. D. and Dove P. M. (1986) Mineral solution reaction rates in a mixed flow reactor: Wollastonite hydrolysis. *Geochim. Cosmochim. Acta* **50**(11), 2509–2516.

Rodgers W. B. and Rodgers R. E. (1848) On the decomposition and partial solution of minerals and rocks by pure water and water charged with carbonic acid. *Am. J. Sci.* **5**, 401–405.

Shiraki R. and Brantley S. L. (1995) Kinetics of near-equilibrium calcite precipitation at 100° C: An evaluation of elementary reaction-based and affinity-based rate laws. *Geochim. Cosmochim. Acta* **59**(8), 1457–1471.

Skinner G. B. (1974) *Introduction to Chemical Kinetics*. Academic Press.

Taylor A. S., Blum J. D., and Lasaga A. C. (2000) The dependence of labradorite dissolution and Sr isotope release rates on solution saturation state. *Geochim. Cosmochim. Acta* **64**(14), 2389–2400.

Van Straten H. A., Schoonen M. A. A., and De Bruyn P. L. (1985) Precipitation from supersaturated aluminate solutions III. Influence of alkali ions with special reference to Li^+. *J. Colloid Interface Sci.* **103**, 493–507.

White A. F. and Brantley S. L. (2003) The effect of time on the experimental and natural weathering rates of silicate minerals. *Chem. Geol.* **202**, 479–506.

Williamson M. A. and Rimstidt J. D. (1994) The kinetics and electrochemical rate-determining step of aqueous pyrite oxidation. *Geochim. Cosmochim. Acta* **58**(24), 5443–5454.

Chapter 2
Transition State Theory and Molecular Orbital Calculations Applied to Rates and Reaction Mechanisms in Geochemical Kinetics

James D. Kubicki

2.1 Introduction

2.1.1 Why are Mechanisms Important?

For much of the history of geochemistry, thermodynamics has dominated discussions on geological processes. Geologic time is so long that systems were generally thought to reach equilibrium, so only knowledge of the reactants and products were considered important. As an emphasis on lower temperature processes and environment geochemistry has increased, the need to understand reaction rates has become more obvious. As geochemists have become more aware of the role of kinetics, disequilibrium has been found to be common. Even in mantle rocks where high temperatures and long equilibration times are the norm, disequilibrium has been observed (Bell and Ihinger, 2000).

Most of geochemical kinetics has focused on determining the rates of chemical reactions. Will the reaction be rapid (i.e., reach equilibrium) or slow (i.e., result in metastable species)? As a result of these rate studies, geochemists have become interested in the pathways by which reactions occur. Several methods may be used to help determine reaction mechanisms. Experiments determining rate laws, activation energies, or isotope exchange kinetics provide insight into steps within the reaction mechanism. Spectroscopic studies can also elucidate the structure of steps along the reaction pathway and identify intermediate species, both of which provide clues to the reaction mechanism. The main emphasis of this chapter will be using computational chemistry techniques in order to map out reaction paths. It cannot be emphasized strongly enough, however, that this approach is most effective when used in concert with the other techniques listed here. The combined approach is

The Pennsylvania State University, Department of Geosciences and the Earth & Environmental Systems Institute, kubicki@geosc.psu.edu

necessary to test the results produced by whatever modeling technique is used; and, in practical terms, all that can be learned from experiment and spectroscopy will save time and effort in the attempt to model reaction pathways.

An equation found in the output of the Gaussian program (Frisch et al., 2004) suggests that this exercise may be quixotic –

$$\text{FACT}/\text{FICTION} = \text{RATE}/\text{MECHANISM}.$$

For anyone familiar with standardized tests, it is easy to see that prediction of reaction pathways is an area regarded with skepticism. Nonetheless, there are a number of reasons to engage upon this endeavor.

2.1.1.1 Can We Apply Laboratory Data to the Field?

One reason for understanding reaction mechanisms is that laboratory experiments are generally designed to mimic field situations, but approximations are often necessary in order to complete the experiments within the time span of a human lifetime (more specifically, the time span of a Ph.D. thesis). For an exception to this rule, see Suarez and Wood (1996) or White and Brantley (2003). Generally, the system is also simplified in order to control or eliminate variables to the greatest extent practical. Consequently, most reaction rates are conditional on the experimental setup. Extrapolating or applying conditional rates to the field is problematic if one is not sure that the same mechanisms occur in the field as in the laboratory. Experimentally determined rates can be used to infer mechanisms that lead to more detailed studies of reaction pathways, but the rate laws themselves do not provide a unique mechanism or prove the key step in a complex reaction (see Chap. 1). By determining the rate-determining species and the *activated or transition state complex*, one can have a clearer picture of which factors could influence the reaction rate in the field. An activated or transition state complex is defined as the transient state with the highest free energy along the minimum free energy pathway (i.e., the reaction coordinate or pathway) between the reactants and products. The difference in free energy between the reactants and this transition state complex is the key controlling factor in the overall rate of reaction.

2.1.1.2 Are Mechanisms Likely to Change with T or Other Factors?

A related issue is the effective temperature range of a given reaction mechanism. One example is the hydrous pyrolysis experiments intended to mimic formation of petroleum from kerogen. This process occurs over millions of years within the Earth at temperatures between 50 and 150° C, but laboratory experiments are usually

conducted at temperatures of 350° C (see Lewan and Ruble, 2002 for a good example of this type of study). The latter occurs in hours and the Arrhenius equation (see Chap. 1) is used to extrapolate to lower temperature conditions to predict rates, products, etc. If the reaction mechanism does not change over the 50–350° C temperature range, then this extrapolation may be warranted. Without any knowledge of the possible mechanisms at 50 or 350° C, testing whether the extrapolation is appropriate is difficult.

2.1.1.3 Can We Control Reactions in the Environment (e.g., Acid Mine Drainage)?

A third reason to understand reaction mechanisms is that environmental geochemistry has led us to a desire to control reactions rather than just be passive observers of these reactions. An important example is the problem of acid mine drainage. A great deal of work has been done to understand the mechanism of converting sulfides into sulfuric acid solutions from the point of view of understanding how rapidly a tailings pile will react. When one begins to think about remediation (prevention of the acid formation) of these tailings piles, determining details of the process and how they can be altered becomes a key issue. The work of Rosso & Becker and Schoonen & coworkers in this area (e.g., Becker et al., 2001; Elsetinow et al., 2003) are excellent examples of studies of reaction mechanisms for AMD applications.

2.1.2 Why are Reaction Mechanisms Hard to Determine?

As mentioned above, skepticism greets most attempts to determine reaction mechanisms. Mapping out all the elementary steps in a complex geochemical reaction is difficult for a number of reasons. Additionally, this area of interest and the techniques used are relatively new in geochemistry and not widely familiar to the general community. Finally, a number of studies in this area have been oversimplified. In spite of these barriers to studying reaction mechanisms, continued effort in this area is justified if only for the fact that the efforts force us to think more deeply about our experimental results and help guide future studies.

2.1.2.1 Transition States have no Stability in Time

There are a number of scientific reasons for taking a proposed reaction pathway with a pound of salt. First, the most important aspect of a reaction pathway is

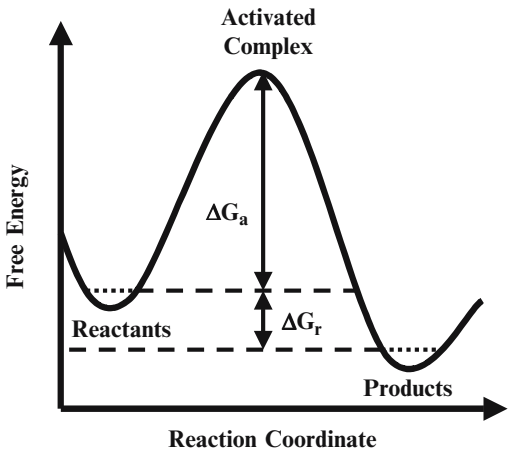

Fig. 2.1 Schematic of a general reaction barrier. Knowledge of the points where the derivative of G = 0 is required to predict reaction rates using transition state theory. The two minima are the reactants and products and are generally relatively easily determined. The maximum is known as the activated complex or transition state complex and generally cannot be determined to a great degree of certainty. Such diagrams represent a cross-section of the potential energy surface of the reaction which follows the minimum free (or potential) energy pathway between reactants and products

determining the transition state complex. By definition, this species has ***no*** stability in time and has no real finite concentration. Confusion has occurred in the literature between this theoretical species and reactive intermediates (i.e., species that are generated during the reaction but are quickly consumed such that they do not appear in the overall reaction stoichiometry) that can be detected (See Guevremont et al. (1998) for a good example of a study on reactive intermediates.). The reactive intermediates can provide clues as to the nature of the transition state complex, but the transition state complex is like a government surplus (i.e., vanishing as soon as it appears), so one can never be sure if the correct complex has been discovered. Figure 2.1 illustrates the precarious position of the transition state or "activated" complex. Positioned at the top of a saddle point (a free energy maximum along the trajectory of the reaction where all derivatives are positive except for one in the direction of the reaction), any atomic motion will result in this species becoming a reactant or product. Atoms are always moving, even at 0K, so the transition state complex is not temporally stable and measurable as a finite concentration. Recently, however, the development of femtosecond laser spectroscopy has allowed identification of species that can be realistically called transition state complexes (e.g., Gilijamse et al., 2005; Abramczyk et al., 2006). This does not imply that the transition state complex has any thermodynamic stability. The reason that complexes resembling a transition state complex can be observed is that there is a finite time where reactants crossover to products. With extremely rapid spectroscopic techniques, some properties of these configurations can be observed. Application of these techniques to geochemical kinetics would be an exciting area of future research.

2.1.2.2 Complex Geochemical Reactions can Occur in Many Elementary Steps

Common geochemical reactions of interest, such as dissolution of a mineral, will generally occur in a number of steps rather than as written stoichiometrically. For example, albite dissolution can be described thermodynamically by

$$NaAlSi_3O_8 + 4H_3O^+ \rightarrow Na^+ + Al^{3+} + 3H_4SiO_4,$$

but the probability of an albite formula unit reacting with 4 H_3O^+ molecules in one step is vanishingly small and would require the breakage of multiple bonds simultaneously. Instead, the reaction occurs in a number of elementary steps (see Chap. 1) such as ion exchange of H^+ for Na^+ followed by hydrolysis of individual Al-O-Si and Si-O-Si linkages. At a minimum, this would be 10 steps (Na^+/H^+exchange = 1, hydrolysis of 3 Al-O-Si linkages and 6 Si-O-Si linkages) to dissolve one formula unit of albite. Each step entails uncertainty, so the cumulative effect is to create a reaction pathway that cannot be considered exact or highly accurate. (See Criscenti et al. (2005a) for a hypothesized sequence of elementary steps for feldspar dissolution.)

2.1.2.3 Low Concentrations of Reacting Species in Many Geochemical Reactions

A third problem is that the concentrations of reactants, reactive intermediates, and products in geochemical reactions may be extremely low in the natural environment. Experiments may be forced to increase these concentrations by orders of magnitude in order to detect these species. This is especially true of spectroscopic studies that attempt to determine the structures of reacting species (e.g., Kubicki et al., 1999). Consequently, one may be forced to choose between missing out on important speciation information by using relevant concentrations and using high concentrations that may alter the reaction of interest.

2.1.2.4 Slow Geochemical Reactions

Many geochemical reactions can be slow as mentioned in the petroleum formation example above. Consequently, experiments may be impractical to conduct. Theory and simulation can only be tested against systems where the reactions occur more rapidly, but there will always be a degree of uncertainty as to the accuracy of the computational method for the system of interest.

This chapter will discuss a number of methods for studying potential reaction mechanisms and transition state complexes. The main focus will be on the use of

quantum mechanical calculations and transition state theory to examine proposed mechanisms. First, however, several experimental methods that provide important information on reaction mechanisms will be discussed because the theoretical modeling of reactions works best in tandem with experimental efforts to obtain as much data as possible on the details of the reaction kinetics.

2.2 Methods for Determining Mechanisms

2.2.1 Rate Laws

2.2.1.1 Well-Determined Rate Laws Provide Species Information on the Rate-Controlling Elementary Step

As discussed in Chap. 1, rate laws equate the overall rate of reaction to the concentrations of species participating in the reaction. Ideally, the rate law would reflect the elementary rate-controlling step of the reaction and the mechanism would be fairly clear from this determination alone. For example, a rate law such as $R = k[H]^2$ for the reaction $H + H \rightarrow H_2$ indicates that two H atoms collide to produce a H_2 molecule. (See McQuarrie and Simon (1997) for a more thorough discussion of the collision rate theory of reactions.) However, in complex geochemical reactions comprised of numerous elementary steps, the reactant and product concentrations may be a function of unknown and unmeasured species not represented in the rate law. For example, the rate of silica dissolution ($SiO_2 + 2H_2O \rightarrow H_4SiO_{4(aq)}$) may be represented by (Rimstidt and Barnes, 1980)—$\text{Rate} = (\partial a_{H4SiO4}/\partial t)_{P,T,M,\gamma} = (A/M)(\gamma_{H4SiO4})(k_+ a_{SiO2} a_{H2O}^2 - k_- a_{H4SiO4})$, but the actual species participating in this process are not clarified by this rate law even though the description of the kinetics is accurate.

2.2.1.2 Species Not Included in the Overall Reaction May Control Rates

To compound this problem, species may play a pivotal role in reactions that do not appear in the overall reaction. Catalysis reactions are of this type (see Xiao and Lasaga, 1994, 1996; Xu et al., 1996; Schoonen et al., 1998). A catalytic reaction is one where the catalyst is neither produced nor consumed but speeds the rate of reaction dramatically. If the role of the catalyst is not recognized in the reaction, then rate laws determined using the reactant and product species will not reflect the actual mechanism. The field of biogeochemistry is particularly influenced by this phenomenon because enzymes (DiChristina et al., 2005 and references therein) and mineral surfaces (Schoonen and Strongin, 2005 and references therein) catalyze reactions that would normally be much more sluggish.

The same is true when unrecognized intermediate species are critical to reaction rates. This is a common problem in heterogeneous kinetics (e.g., Grassian, 2001;

Goodman et al., 2001; Prince et al., 2002; Wang et al., 2003) where a species does not appear in the overall reaction, but the rates are too slow to be observed in the absence of this species.

2.2.2 Activation Energies—Estimate of Bond-Breaking Energy in Rate-Determining Steps

Experiments that measure rates over a range of temperature can be used to calculate activation energies as discussed in Chap. 1. Activation energies are useful for extrapolating rates into unexplored temperature ranges, and they provide clues to the nature of the rate-determining step of the reaction. Chemical processes have distinctive energy ranges associated with them; hence, determination of an activation energy suggests what is happening during the rate-determining step. For instance, covalent bonds have relatively high energies, so activation energies on the order of 100s of kJ/mol suggest covalent bond-breaking as the important step. On the other hand, diffusion of H_2O through minerals may require 10s of kJ/mol, so activation energies in this range are suggestive of diffusive transfer as the rate-controlling step. One must be cautious not to assume that a given energy indicates a unique bond-breaking mechanism.

2.2.3 Isotopic Exchange—Isotopic Tracers Can Identify Atom Types in a Reaction

Labeling certain reactants with enriched isotopic values can be valuable in recognizing important steps of the reaction mechanism. For instance, the oxidation/dissolution reaction on sulfide surface that drives the formation of acid mine drainage has been studied using ^{18}O in H_2O (Barnes et al., 1964; Taylor et al., 1984; Reedy et al., 1991; Usher et al., 2005). The observation that the SO_4^{2-} produced contains all ^{18}O is a clear indication that the O atoms in this species are derived from water rather than O_2 within the system. Richnow et al. (1994) have also used ^{18}O-labeled reactant to follow the incorporation of metabolic intermediates into natural organic matter (i.e., humic materials), which would be an extremely difficult task without labeling due to the complex nature of NOM. In addition, NMR kinetic studies using isotopically labeled species can be used to follow steps in aqueous exchange reactions (e.g., Yu et al., 2003; Lee and Stebbins, 2003).

2.2.4 Spectroscopy—Identification of Reactive Intermediates

As mentioned above, complex reactions consisting of numerous steps may result in the formation of reactive or metastable intermediate species. These species may be

amenable to identification via spectroscopic techniques and can help constrain important steps within the reaction pathway (i.e., the series of configurations and free energies generated as reactants transform into products). Recent work on mineral dissolution is illustrative of this approach.

Mineral and glass surfaces resulting from dissolution experiments (Hamilton et al. 2001) were analyzed using ^{1}H-^{27} Al Cross-Polarization Magic-Angle Spinning Nuclear Magnetic Resonance (CP MAS-NMR) spectroscopy (Tsomaia et al., 2002). This technique enhances the signal of surface Al atoms over those in the bulk because only Al atoms with connections to H atoms are observed. NMR spectra of bulk feldspar samples detected only tetrahedral Al, but an NMR peak due to octahedral Al species connected to OH or OH_2 groups on the surface of the glass was observed in CP MAS-NMR spectra. Subsequently, Criscenti et al. (2005a) suggested that formation of octahedral Al could be part of the dissolution reaction mechanism because hydrolysis of $^{[6]}$Al-O-Si linkages should require less energy than $^{[4]}$Al-O-Si linkages based on bond length/bond strength arguments. Calculated ^{27}Al NMR chemical shifts of $^{[6]}$Al linked to three silica tetrahedra were in good agreement with the measured values indicating that the coordination change could occur *in situ* on the mineral surface. Recent TEM work of Hellmann et al. (2003) has been interpreted to suggest that this tetrahedral to octahedral coordination change may occur in the near-surface solution and then re-precipitate rather *in situ* on the surface, but the coordination change remains an important part of the overall weathering mechanism under acidic conditions.

Dissolution of pyrite is a more complex reaction because it involves simultaneous oxidation of the surface atoms. Borda et al. (2003) and Usher et al. (2005) have studied this reaction using X-ray photoelectron spectroscopy (XPS) and attenuated total reflection Fourier-transform infrared (ATR-FTIR) spectroscopy and found the intermediate species as the reaction occurred. The species formed on the surface during the reaction were different from the reactants and products, so *in situ*, real-time characterization is necessary to make sense of the reaction mechanism. Cohn et al. (2006) have used spin-trapping methods to identify the production of OH radicals which are short-lived, highly reactive intermediates during pyrite oxidation and dissolution.

2.2.5 Molecular Modeling

The remainder of this chapter will focus on the application of transition state theory (TST) to reaction mechanisms via model reactions steps obtained through quantum mechanical calculations. This approach has been used for some time in geochemistry (Lasaga, 1981), but it has become increasingly useful recently with advances in computational power and software to treat solvation and long-range crystallographic effects (see Klamt and Schurrmann, 1993; Cancès et al., 1997; Stefanovich and Truong, 1997; Shoemaker et al., 1999; Paul et al., 2007).

Quantum mechanical calculations can be performed on isolated molecular clusters or on systems with periodic boundary conditions that mimic a bulk phase. At first, periodic models may seem more appropriate to study reaction mechanisms at the mineral-water interface, but, practical limitations have prevented this approach from being commonly employed in these mechanistic studies to date. The main difficulty is in computing the electron probability density for large surface cells where the reaction site is not affected by periodic images. Now that quantum mechanical calculations can be handled with 100's of atoms in the central cell, periodic quantum mechanical techniques are becoming more common in water-rock interaction mechanistic studies (Chizallet et al., 2006; Zhang et al., 2006).

2.2.5.1 Detailed Mapping of Reaction Pathway via Constrained Optimizations

One key advantage of the quantum mechanical modeling approach for studying reaction mechanisms is that the modeler has knowledge and control of the atoms within the system. The problem of activated complex instability is surmounted in this computational approach and each proposed elementary step can be followed in detail. Usually, this entails starting from reactants or products and moving a constrained atom along a postulated reaction path while allowing all other atoms in the model to relax according to the potential energy surface (PES) of the system (see Felipe et al., 2001 for a detailed description of this procedure). The PES is simply the potential energy (or internal energy) of the system as a function of atomic configuration. For example, a diatomic molecule will have a 1-dimensional PES as the potential energy rises as the interatomic distance decreases or increases from the minimum (i.e., equilibrium) value. More complex molecules and systems will have multi-dimensional PESs, but in general there will be one minimum potential energy that corresponds to a given configuration of atoms. (Note: the Gibbs free energy surface of the system controls the reaction, but as discussed below, it is convenient to break the G term into the H and S terms. The potential and internal energies are similar to the H term as long as the PV term is negligible and an adiabatic process is assumed. The S term is accounted for the by the pre-exponential factor in the Arrhenius equation $-\mathrm{k} = \mathrm{A}\exp(-\Delta \mathrm{E_a}/\mathrm{RT})$.)

A number of algorithms exist (e.g., linear and quadratic synchronous transit, (Halgren and Lipscomb, 1977); internal reaction coordinate (Schlegel, 1987); eigenvector following (Cerjan and Miller, 1981); synchronous transit quasi-Newton (Peng and Schlegel, 1994)) that potentially can predict reaction pathways, but with most geochemical reactions involving more than a few atoms, experimental data and chemical insight are usually more reliable in estimating an initial reaction step. The modeler-guided reaction pathways generated in this manner can then be checked using the algorithms listed above. The values of the activation energy (i.e., the energy difference between reactants and the transition state complex) or rate constants (see below for calculation of rate constants) predicted with this method can be compared to observed values in order to verify the computational method and the reaction pathway generated.

2.2.5.2 Comparison of Predicted Results to Experimental Observations

Comparisons between experiments and models are complicated by a number of factors. First, in the geochemical literature, experimental derivations of activation energies have been carried out using the relationship $\log(\text{Rate}) = -\Delta E_a/RT$ (W. H. Casey, *pers. comm.*) because the rate law was not determined. Thus, these conditional rates are used in place of the more appropriate rate constant relationship $\ln(k) = -\Delta E_a/RT$. For this reason, it is recommended to calculate the rate constant, k, as a function of temperature and then derive ΔE_a from the slope of the line of ln(k) versus (1/T) for both the experimental and model results (Felipe et al., 2005).

Second, complex geochemical reactions may occur in a series of elementary steps. If a number of these elementary steps have a significant activation energy barrier, it becomes difficult to compare the *apparent* activation energy (i.e., some combination of all the elementary activation energies) with the model activation energy of one rate-limiting elementary step. Ideally, one would model all the elementary reactions within a process, but time limitations have prevented this from being a practical approach for complicated reactions such as mineral dissolution. Even in these cases, however, the relative magnitude of the observed and modeled activation energies can help identify the rate-limiting step in the reaction. A feedback process between the experimental studies and modeling efforts results in a more detailed picture of the reaction mechanism than would have been obtainable with either approach alone.

2.3 Transition State Theory

2.3.1 Equilibrium Assumption

Figure 2.1 illustrates the concept of an energy barrier to reaction that can inhibit a thermodynamically favorable reaction from occurring. One of the main assumptions of transition state theory is that the reactants of the elementary reaction are in equilibrium with the transition state complex. (This derivation is based upon Cramer (2002) pp. 476–480.) This assumption is represented by the equation

$$k_1[A] = k_{TS}[A^{TS}] \tag{2.1}$$

where k_1 is the rate constant of the forward reaction, k_{TS} is the rate constant from the transition state complex back to reactants, and [A] & $[A^{TS}]$ are the concentrations of reactants and transition state complexes, respectively. If equilibrium is assumed between the products and transition state as well, with both forward and reverse reactions going through the same transition state complex, this is the assumption of *microscopic reversibility*. This condition leads to an important connection between thermodynamics and kinetics because $k_+/k_- = K_{eq}$ when microscopic reversibility

holds. (See Rimstidt and Barnes (1980) for a discussion of this concept applied to silica dissolution.)

With equilibrium assumed between reactants and transition state complexes, an equilibrium constant, $K_{TS} = [A^{TS}]/[A]$, theoretically exists that is related to the free energy change between reactants and transition state complexes. Using the thermodynamic relationships $G = U_0 + PV + k_B T \ln(Q)$ and $K = \exp(-\Delta G/RT)$

$$K_{TS} = \exp[-(G_{TS} - G_A)/k_B T] \tag{2.2a}$$

$$K_{TS} = \exp -[(U_{TS,0} + PV_{TS} - k_B T \ln(Q_{TS}) - (U_{A,0} + PV_A - k_B T \ln(Q_A))/k_B T. \tag{2.2b}$$

$U_{i,0}$ is the internal energy corrected for the zero-point vibrational energy, and Q_i is the vibrational partition function of a given species ($Q_i = Q_{vib} = \sum_{i=1}^{3N-6} \frac{1}{1-\exp(-h\omega/k_B T)}$). (Note: Do not confuse the partition function with the partition coefficient for predicting the concentration of species in different phases. See McQuarrie and Simon (1997) or a book on statistical mechanics for an explanation of partition functions. For gas-phase reactions, the translational and rotational partition functions also need to be included.) Extracting the $k_B T \ln(Q_{vib})$ terms from the exponential and making the assumption that the PV term is negligible gives

$$K_{TS} = (Q_{TS}/Q_A)\exp[-(U_{TS,0} - U_{A,0})/k_B T]. \tag{2.3}$$

(In general, neglecting the PV term for reactions at the surface of the Earth is a good assumption, but systems under pressure may have a considerable PV term related to the activation energy. In these cases, the PV term cannot be ignored and determination of the activation volume can be useful in deciphering a reaction mechanism as well (Kubicki and Lasaga, 1988).) Combining Eqs. (2.1) and (2.3) provides an expression for the forward rate constant

$$k_1 = k_{TS}[A^{TS}]/[A] = k_{TS}(Q_{TS}/Q_A)\exp[-(U_{TS,0} - U_{A,0})/k_B T]. \tag{2.4}$$

Computational chemistry techniques can provide estimates of the U_i and the Q_A terms. Consequently, the remaining terms to evaluate are k_{TS} and Q_{TS}. Non-linear molecules have $3N-6$ vibrational degrees of freedom (the "6" term represents the 3 translational +3 rotational degrees of freedom). However, the transition state complex is missing a degree of freedom – the vibration associated with crossing the energy barrier along the reaction pathway. Hence, Q_{TS} can be separated into a normal partition function for the $(3N-7)$ vibrational modes that have positive eigenvalues (frequencies) associated with them and imaginary (negative) frequency is associated with the reaction pathway

$$Q_{TS} = [1/(1 - \exp(-h\omega_{TS}/k_B T))Q'_{TS} \tag{2.5}$$

where Q'_{TS} is evaluated as a normal vibrational partition function except over $(3N-7)$ terms rather than $(3N-6)$. Using the first two terms of a power expansion of the exponential term in Eq. (2.5) gives $(1 - h\omega_{TS}/k_B T)$. Plugging this form

into Eq. (2.5) and re-arranging results in the expression

$$k_1 = (k_{TS}k_BT)/(h\omega_{TS})(Q'_{TS}/Q_A)\exp[-(U_{TS,0} - U_{A,0})/k_BT]. \quad (2.6)$$

The term ω_{TS} is the inverse time constant along the reaction coordinate, so $\omega_{TS} = k_{TS}$. These two terms cancel in Eq. (2.6) such that the simplified expression

$$k_1 = (k_BT/h)(Q'_{TS}/Q_A)\exp[-(U_{TS,0} - U_{A,0})/k_BT]. \quad (2.7)$$

remains. The partition functions and the exponential are dimensionless, and the units of (k_BT/h) are s^{-1}, which is appropriate for the rate constant. This term is called the *fundamental frequency* and limits the rate of reaction to approximately $10^{-13}\,s^{-1}$ – a reasonable value on the order of the time required for a molecular vibration.

A more general expression for k is

$$k_1 = (k_BT/h)\exp[-(\Delta G_{TS})/RT] = (k_BT/h)\exp[-(\Delta H_{TS})/RT]\exp[(\Delta S_{TS})/R] \quad (2.8)$$

where $\Delta G_{TS}, \Delta H_{TS}$, and ΔS_{TS} are the changes in Gibbs free energy, enthalpy and entropy between reactants and transition state complex at some standard state. The ΔH_{TS} term is related to the activation energy by $E_a = RT + \Delta H_{TS} + (P-1)\Delta V_{TS}$, and the ΔS_{TS} term is related to the pre-exponential factor, A, in the Arrhenius equation ($k = A\exp(-E_a/RT)$; see Chap. 1) by $A = (k_BT/h)\exp(\Delta S_{TS}/R]$ (Lasaga, 1997).

The "activation entropy" term, ΔS_{TS}, can also provide a clue as to the nature of the activated complex. ΔS_{TS} is generally negative because the activated complex often requires greater ordering than the reactants, but the magnitude of this term can suggest how much ordering will be required to create the activated complex. The greater the ordering required, the larger A will be and the slower the reaction. Empirical observations suggest that reactions with large ΔS_{TS} values will have smaller ΔH_{TS} values and vice versa. This correlation is termed the "compensation law" (Casey et al., 1993). One possible explanation of this observation is that reactions with both large ΔH_{TS} and ΔS_{TS} occur so slowly that they are not observed. However, chemical intuition suggests that a well-ordered activated complex would be likely to have a lower ΔH_{TS} because bonding interactions should be more favorable and vice versa.

Another implicit assumption in classical transition state theory is that the reactants and products follow the reaction pathway along the minimum energy path. This assumption is incorrect because atoms and molecules will be able to deviate from the minimum-energy path along the PES according to their kinetic energies. However, this assumption allows one to estimate a minimum rate for a reaction. The reaction can go faster if multiple crossings occur or if the reaction occurs via a lower energy barrier pathway. The minimum-energy path assumption will come closer to reality for a reaction with a PES containing a large ΔH_{TS} and narrow valley between reactants and products, but it will be a poor approximation for a PES with a low, broad connection between reactants and products. For a discussion of variational transition state theory (where this assumption is not made), see Cramer

(2002). Estimation of minimum rates is useful in geochemistry because one can determine whether or not kinetics will be important for a given process over a given time period or whether one can assume equilibrium.

A problem with the approach discussed above is that the actual reaction will follow the Gibbs free energy of the system (Eq. (2.8)), not the PES of the system. Hence, the rate constant and transition state complex determined based on potential energies or enthalpies alone will only serve as an approximation to the true rate constant and transition state complex unless the Gibbs free energy of the system is determined at each point along the reaction path. An excellent but computationally intensive method of calculating the free energy of activation is to use thermodynamic integration on directed quantum molecular dynamics simulations (e.g., Ciccotti et al., 2005).

Finally, TST assumes that the reactants must overcome the reaction energy barrier in order to reach the product configuration. However, due to quantum mechanical effects, this is not always the case as reactants may "tunnel" through the energy barrier (see Cramer (2002) for a more detailed discussion). Tunneling is generally significant in H^+ transfer reactions (Felipe et al., 2003) and less so for heavier elements.

2.3.2 Determining Reaction Pathways and Transition States

When studying a simple reaction (e.g., the reaction between two small gas-phase molecules) using quantum mechanical calculations, a scan of the PES is a desirable method to find a reaction pathway and transition state complex. A scan involves varying structural parameters (e.g., interatomic distances, bond angles, torsions, etc.) and calculating the potential energy for each configuration. No *a priori* assumptions are necessary, but the scan can be guided by experimental data or chemical insight as to possible reaction pathways. One would thus limit the number of structural parameters to those that are likely to control the reaction. Mapping a PES has the advantages of discovering novel pathways and determining the width of the reaction pathway discussed above. For example, an orthosilicic acid molecule reacting with a F^- ion –

$$Si(OH)_4 + F^- \rightarrow Si(OH)_3F + OH^- \tag{2.9}$$

can be modeled by calculating potential energies as a function of one Si-(OH) and the Si-F distance assuming that the attack of the F^- will drive one OH^- group away from the Si. Scanning the PES in this manner does not assume whether the reaction mechanism is associative (F^- bonds to Si first) or dissociative (one Si-OH bond breaks first).

The results of a PES scan using the semi-empirical method PM5 (Stewart, 2004), and the software CAChe Worksytem Pro (Fujitsu America, Inc.) are shown in Fig. 2.2. (PES scanning methods may be available in a number of computational chemistry packages, such as Gaussian 03 (Frisch et al., 2003). See Foresman and

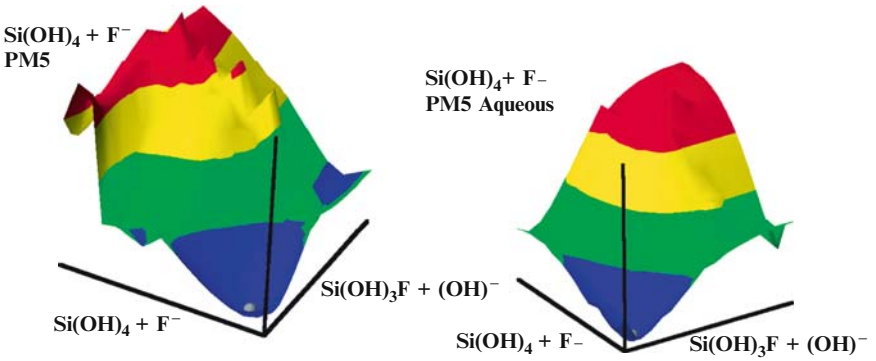

Fig. 2.2 Potential energy surface for the $Si(OH)_4 + F^- \rightarrow Si(OH)_3F + (OH)$-reaction calculated with the semi-empirical PM5 method using the program CAChe Worksystem Pro (Fujitsu, Inc.) in the (**a**) gas and (**b**) aqueous phases. Both suggest that the intermediate 5-coordinate species $Si(OH)_4F^-$ is more stable than the reactants and products. The results at this level of theory are probably not accurate but can serve as a basis for higher level calculations

Frisch (1996) for an explanation of how to implement PES scans in Gaussian programs. Note that using semi-empirical methods to determine the PES, transition state complex, and the activation energy of a reaction is not recommended because semi-empirical methods rely on parameters to describe bonding that were derived from equilibrium data. The choice of methods preferred for calculating reaction parameters is discussed in the next section, and the PM5 method was only used here for convenience in this example.)

Figure 2.2a and b represent the change in potential energy of the model $Si(OH)_4 + F^-$ gas-phase and aqueous systems, respectively, as the Si-(OH) and Si-F distances are varied between 1.5 and 3.0 Å (Fig. 2.3). Note that the PESs in Fig. 2.2a and b are different due to the effect of solvation as modeled with a dielectric continuum in this case. Most early studies modeling reaction mechanisms in geochemistry were conducted with the molecules isolated in a vacuum. Not only does this change the relative potential energies on the PES, but it can be responsible for predicting a completely different mechanism. Modeling reaction pathways with both explicit (i.e., inclusion of H_2O molecules) and implicit (i.e., continuum solvation) is recommended. This is especially important when H^+ transfer is involved because bonding the H^+ to a nearby H_2O molecule can make a dramatic difference in the activation energy barrier (Felipe et al., 2005).

Figure 2.3 illustrates how the approach of the F^- ion affects the structure and potential energy of the $Si(OH)_4$ molecule. Although the PM5 erroneously predicts that the 5-coordinate species $[SiF(OH)_4]^{1-}$ should be stable (Figs. 2.2 and 2.3a), the calculated changes are useful in showing how bonds respond to the nucleophilic attack of the highly electronegative F. For instance, in Fig. 2.3c, the three Si-(OH) groups bend away from the F^- as the fourth OH begins to leave the orthosilicic acid. This umbrella-like motion is suggestive of the inversion mechanism observed for NH_3.

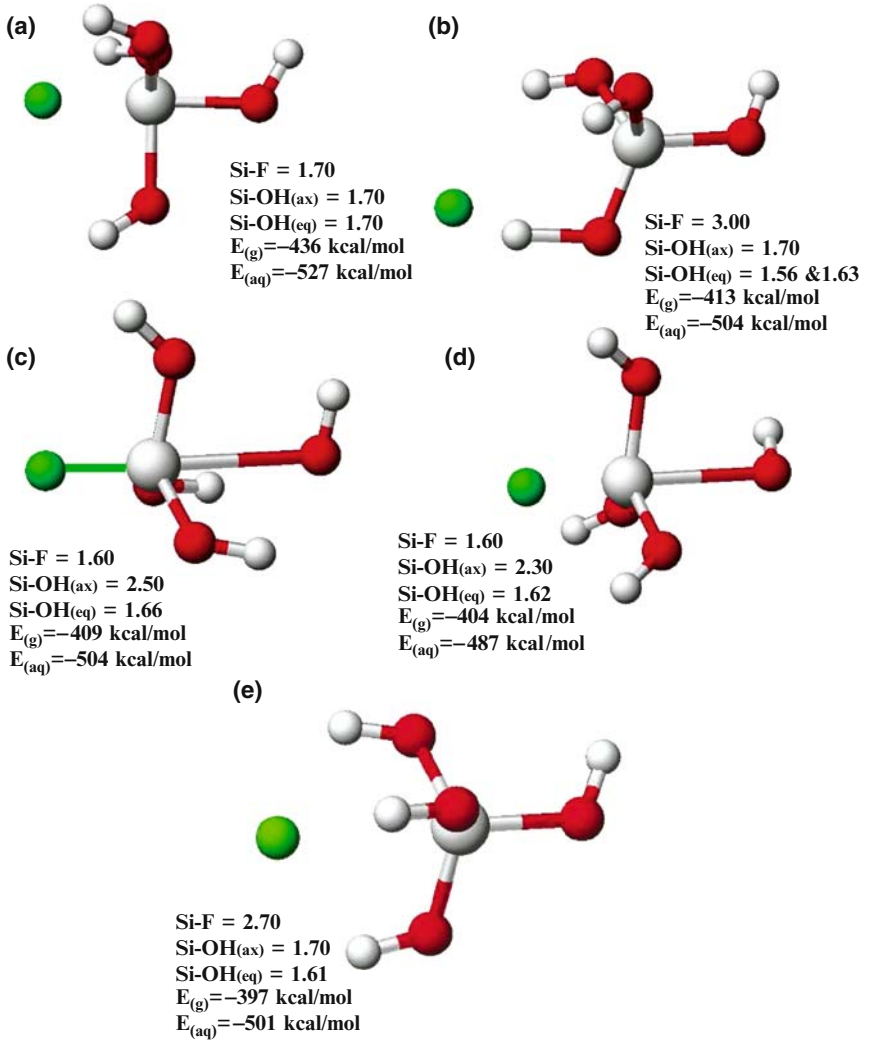

Fig. 2.3 Molecular configurations of various locations on the PES represented in Fig. 2. Relaxation of the remaining three Si-(OH) bonds occurs as the constrained Si—F and Si—(OH) distances vary. These constrained optimizations allow for investigation of a proposed reaction mechanism. If the calculated activation energies and rate constants determined by these calculations agree with observation, then one can say that the proposed mechanism is "consistent" with experiment. This does not prove that the model mechanism is the one and only mechanism.

For more complex geochemical reactions, PES scanning is not a practical option. There may be multiple elementary steps involved in the reaction and the number of structural parameters involved may be too great to vary in a PES scan. Consequently, the most common method employed to determine reaction pathways and transition state complexes has been the constrained optimization method (Felipe et al., 2001).

In constrained optimizations, a single structural parameter (e.g., interatomic distance, bond angle, torsion angle, etc.) is selected to be the reaction pathway. Preselecting the important structural parameter will bias the results compared to a PES scan; but, in many cases, the chosen parameter is relatively obvious in the context of the elementary reaction being modeled. If this is not the case, the modeler may be forced to examine several potential pathways and compare the activation energies predicted in each one. While one structural parameter is held constrained, all other atoms are allowed to relax to find the minimum energy structure given the one imposed constraint. Once this partially optimized structure is obtained, the constraint can be changed to model the next step along the reaction pathway.

Referring to the $Si(OH)_4 + F^- \rightarrow Si(OH)_3F + OH^-$ example above, one could optimize the $Si(OH)_4$ molecule by itself, then add the F^- at some distance where interaction would be minimal (e.g., $<$5 Å). The Si-F distance could then be decreased incrementally. The increments used can be larger (e.g., 0.5 Å) at long distances and then decreased (e.g., 0.1 Å) as the interaction between the reactants increases. In this step-by-step manner, a rough approximation of the reaction pathway and transition state complex can be mapped out (see examples below).

Once the highest potential energy point along the reaction pathway is found, a transition state optimization search can be conducted. This process is similar to a normal energy minimization in that a configuration where all the spatial derivatives of the potential energy should be equal to zero. The transition state complex should be located on a saddle point, however, where one of the second derivatives of the potential energy is negative and all others are positive. Once a guess for the transition state complex is obtained, a frequency calculation should be conducted to ensure that there is one and only one negative frequency. If this condition holds, then an intrinsic reaction coordinate (IRC) calculation should be conducted (Gonzalez and Schlegel, 1989 and 1990; Foresman and Frisch, 1996). IRC calculations trace the configurations of the transition state complex downhill toward reactants and products in a step-wise manner. If the IRC can successfully connect both reactants and products via the model transition state complex, then a reasonable approximation to the transition state complex has been determined. (Note that both the transition state optimization and IRC procedures rely on calculation of the force constants calculated for the initial transition state complex, so a frequency analysis of this initial guess is necessary before attempting to refine the structure of the transition state complex.)

2.3.3 Calculating Activation Energies and Rate Constants

Depending on the type of "activation energy" one plans to calculate, a few options exist for estimating this parameter. The simplest approach is to calculate the potential energies of the reactants, transition state complex, and products (if the back-reaction is of interest as well). This activation energy, ΔE_0, is the difference between the calculated potential energy of the activated complex and either

the reactants or products depending on whether the forward or reverse reaction is being considered. Calculating ΔE_0 in this manner can provide a reasonable estimate of the activation energy barrier for a given model elementary reaction. Such an estimate may suffice if one is attempting to predict whether a reaction is possible or if a specific mechanism is consistent with the experimentally determined activation energy. However, ΔE_0 is not likely to result in an accurate rate constant.

In cases where one is interested in estimating the rate constant, k, either the ΔH_{TS} or ΔG_{TS} should be calculated (see section above). The need for modeling one of these two thermodynamic parameters can be seen by rearranging the Arrhenius equation ($k = A\exp[-E_a/RT]$) to $E_a = \Delta H_{TS} + RT$ or $k = (k_B T/h)\exp[-(\Delta G_{TS})/RT]$ (Eq. 2.8); Cramer (2002)). To obtain ΔH_{TS}, the difference in enthalpies between the transition state complex and the reactants or products must be calculated. The enthalpy difference between species at 298K is (Foresman and Frisch, 1996)

$$\Delta H^{298} = \Delta E^{298} + \Delta(PV). \tag{2.9}$$

For a reaction, such as $A + B \rightarrow C$, the $\Delta(PV)$ work term is -RT in gas-phase reactions. In condensed phase reactions $\Delta(PV)$ is generally ignored unless the reaction occurs under high pressure. The term ΔE^{298} can be calculated from

$$\Delta E^{298} = \Delta E_e^0 + \Delta(\Delta E_e)^{298} + \Delta E_v^0 + \Delta(\Delta E_v)^{298} + \Delta E_r^{298} + \Delta E_t^{298} \tag{2.10}$$

where ΔE_e^0 = electronic energy difference at 0K, $\Delta(\Delta E_e)^{298}$ = difference between electronic energies at 0 and 298 K ≈ 0, ΔE_v^0 = difference in zero-point vibrational energies, $\Delta(\Delta E_v)^{298}$ = the thermal correction to zero-point vibrational energies at the temperature of interest, ΔE_r^{298} = rotational energy difference, and ΔE_t^{298} = translational energy difference $\approx$0 for condensed phase reactions (Foresman and Frisch, 1996). To determine all these parameters, frequency analyses of reactants, products, and transition state complex in a program such as Gaussian 03 (Frisch et al., 2003) will provide estimates of all the necessary values. The ΔE_e^0 term is the potential energy, and the remaining terms are included in the thermal correction to the enthalpy. The calculated zero-point vibrational energies may be scaled according to empirical factors determined for a given method and basis set (Wong, 1996; Scott and Radom, 1996). When more accurate results are desired, these scaling factors for the zero-point vibrational energies can be applied and the individual components in Eq. (2.10) combined manually to calculate ΔE^{298}.

In theory, for gas-phase reactions, ΔG can be readily calculated by evaluating the vibrational, rotational, and translational partition functions (Eqs. (2.2) and (2.3)). However, because the harmonic approximation is used to calculate the vibrational frequencies that go into calculating the vibrational partition function, significant errors can arise in the value of this model parameter (East and Radom, 1997). In addition, modeling reactions in condensed phases may be subject to errors due to hindered internal rotations being handled as low-frequency vibrations (Ayala and Schlegel, 1998). Furthermore, the ΔG term arising from a model calculation does not include the configurational entropy of the system. Considering these significant

problems, ΔG can be calculated from the statistical mechanical equations relating G and Q –

$$G = -k_B T \ln Q + PV, \tag{2.11}$$

but one must realize that this value is only an estimate and will not be highly accurate.

Many geochemical reactions of interest occur in the aqueous phase. A common methodology for treating solvation in quantum mechanical calculations is to embed the model solute in a dielectric continuum (Klamt and Schuurmann, 1993; Cancès et al., 1997). Because this method entails calculating the work done to open up a solute cavity within the solvent, the quantity determined in these self-consistent reaction field (SCRF) or polarized continuum calculations is the Gibbs free energy of the system (Keith and Frisch, 1994). Consequently, one may wish to correct gas-phase calculations for solvation effects by performing an SCRF calculation on the model, but all terms contributing to ΔG_{TS} should be included when this is done to ensure consistency.

If only the ΔH_{TS} parameter is calculated, then estimating the rate constant will require a secondary estimate of ΔS_{TS} in order to obtain the Arrhenius pre-exponential factor ($A = (k_B T/h)\exp(\Delta S_{TS}/R)$ from above). ΔS_{TS} can either be calculated from the partition function ($S = k_B \ln Q + k_B T(\partial \ln Q/\partial T)_{N,V}$) which has the problems mentioned above or one can estimate ΔS_{TS} from similar reactions where this quantity is known from experiment.

2.4 Quantum Mechanical Calculations

The discussion above assumes the ability to perform quantum mechanical calculations on the system of interest. A detailed description of these methods would require a book of its own (e.g., Cramer, 2002), but a brief introduction is useful here. A wide variety of quantum chemistry programs exists. Most are based on one of two theories: molecular orbital theory or density functional theory. The former has been used by chemists because it handles electron probability densities in terms of atomic orbitals. The latter has been traditionally used by solid-state physicists for treating periodic systems. (For more in-depth discussions of these techniques see Sherman (2001), Rosso (2001), and Stixrude (2001). The boundary between the methods is becoming blurred and the use of hybrid MO/DFT calculations is common. Because the majority of reaction pathway modeling studies in geochemistry have been conducted using the MO theory on relatively small molecular clusters, this chapter will focus on practical matters regarding application of MO theory to reaction mechanism modeling. The reader should be aware of the growing interest in applying periodic DFT calculations to mineral-water interface kinetics (Windus et al., 2003). This methodology should become more common in the future as increasing computational power makes this approach more practical.

In computational chemistry, there are two competing needs to be balanced: accuracy of results and speed of computation. Both of these parameters can vary widely

depending on the problem and the researcher. For example, some questions may revolve around two possible mechanisms for a given reaction. If the energy difference between the two pathways is huge (e.g., >100 kJ/mol), then a highly accurate calculation is not necessary and the study can be sped up significantly by choosing smaller (i.e., faster computation, less accurate) basis sets. If, on the other hand, you do nothing all day but eat coffee and drink donuts like me, then time is not an important factor to you; and calculations can run for a year or more. Some examples of this (not the laziness, just the long calculation time) can be found in Van Alsenoy et al. (1998), Hass et al. (2000), and Matsumoto et al. (2002). For quantum mechanical calculations, balancing these two concerns comes down to a selection of basis set, electron correlation method, and the size of the model system.

2.4.1 Choice of Basis Set

Basis sets can be divided into two basic components: the number of functions used to approximate the ground-state molecular orbitals and the number of extra functions represented beyond the ground-state configuration of the molecule. In general, the larger the number of both types included, the more accurate the resulting electron density. The first set can be represented by 3, 4 or 6 Gaussian functions in many common basis sets (e.g., Binkley et al., 1980; Gordon et al., 1982; Petersson et al., 1988). Furthermore, these functions can be sub-divided or split to allow for more flexibility in the valence electrons of the system. For example, a 6–311G basis set represents 6 Gaussian functions per atomic orbital with the valence electrons split into three sizes of contracted (linear combinations of Gaussian functions) functions for each orbital type (Foresman and Frisch, 1996).

The second set consists of diffuse functions (typically denoted by a "+" in Gaussian 03) and polarization functions. The former are *s*- and *p*-type functions that are used to describe low levels of electron density far from the nucleus of an atom. Inclusion of diffuse functions is important whenever the system of interest is expected to have a large electron cloud or strong H-bonding (e.g., anions). Polarization functions represent *p*-, *d*-, or *f*-orbitals that are not formally occupied in the ground state of the atom or molecule (e.g., the *d*-orbitals on Si). Although not formally occupied, polarization functions are extremely important for accurately describing bonding between atoms in many geochemical systems (e.g., Gibbs et al., 1987). The need for these types of functions increases when one begins to account for electron correlation effects (see below).

Because the choice of basis set will depend on the problem and the computational resources available, a "good" choice cannot be stated here unequivocally. The CPU and computational resources required generally increase as N^4 where N is the number of basis functions, so there are diminishing returns in accuracy as the expense of the calculation increases dramatically with larger basis sets. A general recommendation is to start with as small a basis set as possible (e.g., 3-21G(d) or 6-31G(d)) to generate structures for the system of interest. Test the model structures against

experiment wherever possible. Pick a simple model and perform an energy minimization with a larger basis set to check for convergence. Even if the smaller basis set does not provide a structure that is accurate enough for the problem at hand, the structure obtained is probably a better initial guess for the final state than can be obtained manually or by using default structural parameters. Consequently, one ends up saving time during the structure determination with the larger basis set because the initial guess is closer to the final endpoint.

Another critical point is that not all molecular properties will be calculated with the same accuracy with a given basis set. Three of particular interest here are structure, energy, and vibrational frequencies. Structure is generally the easiest property to obtain with reasonable accuracy (within 0.02 Å for bond lengths and a few degrees for bond angles). Hence, modelers commonly calculate structures with smaller basis sets and energies with larger basis sets. This type of calculation can be represented by B3LYP/6-311 + +G(d,p)//HF/3-21G(d,p) for example where an energy calculation with the larger basis set is performed on the structure determined with the smaller basis set.

Vibrational frequencies must be evaluated with the same basis set that the energy minimization was performed with. This is because the PES is basis set dependent and a potential energy minimum (all $d\Phi/dq = 0$ where Φ is the potential energy) configuration with one basis set is not a minimum with another basis set. Hence, when one is evaluating the zero-point energy corrections and vibrational partition functions discussed above, the accuracy of the vibrational frequencies will drive the choice of basis set rather than the accuracy of the molecular structure. A few papers with some examples of these rules will be discussed below. Some other references that examine this topic are Xiao and Lasaga (1996) and Sykes et al. (1997).

2.4.2 Choice of Electron Correlation

Many of the earlier papers using quantum mechanical methods in geochemistry relied upon Hartree-Fock calculations. Hartree-Fock calculations assume a single electron probability determinant (see any text on quantum mechanics). In this approximation, the probability density of a single electron is determined by the *average* density of all other electrons in the molecule. However, this self-consistent definition of the electron probability density neglects the fact that, when one electron is in a particular point in space, the other electrons are repulsed by its presence and tend to be farther away than the average probability density. This phenomenon is known as dynamical electron correlation. Another type of correlation arises when there are two orbitals that could be occupied as the highest occupied molecular orbital (HOMO). HF calculations use only a single determinant to describe the wave function, so one orbital will be chosen over the other, but the real molecule would have similar contributions from each orbital. This situation is known as non-dynamical correlation.

Many methods exist for treating electron correlation (Cramer, 2002), but two common schemes are Møller-Plesset (MP) perturbation theory (Møller and Plesset, 1934) and density functional theory (DFT; Hohenberg and Kohn, 1964; Kohn and Sham, 1965). The former is expensive in terms of computational demands such as memory and CPU usage. The latter requires only a minor amount of additional time over Hartree-Fock calculations.

MP calculations expand HF calculations by including contributions from excited state determinants. MP and HF are equivalent through the first-order perturbation (i.e., singly excited determinants only); hence, MP calculations are performed starting with doubly excited states (MP2) and progress to MP5 (single, double, triple, quadruple, and quintuple substitutions). MP2 typically does a reasonable job of estimating electron correlation energies, but it is not variational and may actually overestimate this term. Furthermore, MP2 calculations scale as N^5 (where N is the number of basis functions). MP3 generally does not offer much improvement over MP2; and MP4 calculations generally scale as N^7. Consequently, calculations performed on geochemical models are rarely carried out beyond the MP2 level (Xiao and Lasaga, 1996; Pelmenschikov et al., 1997). In some instances, energy calculations have been conducted with higher orders of perturbation and combined within the G2 (Curtiss et al., 1993) or W1 (Parthiban and Martin, 2001) schemes to obtain more accurate reaction energetics. Combination methods such as G2 and W1 use a variety of high-level calculations of increasing electron correlation and basis set size to estimate corrections to calculations done with non-infinite basis sets and incomplete configuration interaction. Such high level calculations are generally restricted to relatively small model systems (e.g., Kubicki et al. 1995).

DFT calculations rely on the theorem that the energy of a system can be described the electron density. One formulation of this theory (Kohn and Sham, 1965) results in a correction term, $E_{xc}[\rho]$ that accounts for the difference between the energy of an interacting and a non-interacting system of electrons. This *exchange-correlation* energy also includes the classical self-interaction energy and the difference in kinetic energy between the interacting and non-interacting systems. Although DFT is an exact theory, there is no guidance as to the functional form of the electron density; hence, approximate forms have been derived in an attempt to apply DFT. Because these derived functionals may attempt to account for kinetic energy differences, they may be fit using empirical parameters and are not strictly *ab initio*. Once these approximations are employed, DFT is no longer variational (i.e., the calculated energy may be lower than the actual energy).

Exchange-correlation functions are generally of two types—local density approximation (LDA) or generalized gradient approximation (GGA). The latter are generally preferred although LDA can give good results in some instances (Rosso and Rustad, 2001). A whole alphabet soup of methods exists for the acronyms of different exchange-correlation functions (see Cramer, 2002), so rather than confuse the reader, three commonly used methods are suggested here: the Becke 3-parameter exchange (B3; Becke, 1993), the Lee-Yang-Parr correlation functionals (LYP; Lee et al., 1988) and the PBE (Perdew et al. 1996). These functionals can be used with

the electron densities predicted in a HF calculation discussed above producing a hybrid MO/DFT calculation. The resulting method is more rapid than the MP methods mentioned above and provides an estimate of electron correlation energies that can be just as accurate. Note that HF methods also include an exchange term, so the actual energy for a molecule must be corrected for counting the exchange energy using both methods (Foresman and Frisch, 1996).

2.4.3 Choice of Model System

Building a realistic model system is probably the most important step and one of the most neglected in computational chemistry related to geochemical reactions. Not including the important components of a system will make even the most robust computation unrealistic. However, increasing the model system size can dramatically increase computational times, even when using low levels of theory, because the energy minimization step can require a dramatic increase in the number of steps to find a minimum. Consequently, one usually errs on the side of simplicity, and most of the earlier computational geochemistry studies were conducted on molecules in the gas-phase. Significant errors arise when comparing these calculations to aqueous species, minerals and glasses, but much was learned with this approach (e.g., Gibbs, 1982). Today, inclusion of solvation effects or treating a condensed phase within periodic boundary conditions is common, which provides a quantum leap in the realism of the model systems simulated.

As discussed above, there is no one method to determine the minimum model system that will adequately describe a geochemical reaction of interest. My recommendation is to use as much experimental information as possible to guide the selection of components in the model. Also, performing some test calculations to determine the effect of various components on the model results is helpful. Finally, checking the model results against as many experimental properties as possible will add reliability to the simulation. Reproducing one experimental parameter, such as a structure, is rarely enough to test the realism of a model system and the accuracy of its predictions.

2.5 Examples

2.5.1 O-isotope Exchange in $H_4SiO_{4(aq)}$

A recent example of the application of the MO-TST approach to isotope exchange kinetics can be found in Felipe et al. (2003). The exchange of O atoms in orthosilicic acid, $Si(OH)_4$, with H_2O molecules was followed to predict values of the fractionation factor and exchange rate. The former is an important parameter because one

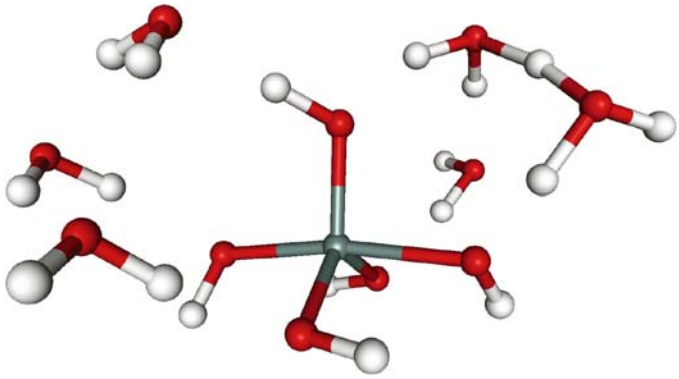

Fig. 2.4 Transition state for O-isotope exchange between $Si(OH)_4$ and H_2O as calculated in Felipe et al. (2003). The formation of the $Si(OH)_5$-intermediate and the H_3O+-H_2O dimer ($H_5O_2{}^+$) are significant and result from the inclusion of extra H_2O molecules solvating the central $Si(OH)_4$

must first be able to reproduce the equilibrium properties of reactants and products before venturing into the realm of reaction mechanisms. Although the predicted rate of exchange was rapid, consistent with the common assumption for this reaction in natural waters, this study developed a methodology that could be used in subsequent studies of isotopic exchange in aqueous systems. Other systems, such as $SO_4{}^{2-}$, $NO_3{}^-$, and $PO_4{}^{3-}$, could have slower, but finite O-exchange rates that could complicate the interpretation of ^{18}O isotopic studies of these anions in the environment.

A key to the success of the Felipe et al. (2003) study was the inclusion of multiple H_2O molecules in the model. Previously, a single H_2O molecule had been included to examine silica-H_2O interactions in the interest of computational efficiency. By performing simulations using 3 and 7 H_2O molecules reacting with $Si(OH)_4$, Felipe et al. (2003) were able to examine cooperative effects among the H_2O molecules that are critical to the H^+-transfer process. Model calculations that neglect this possibility will most likely be in error no matter what level of theory is used to calculate structures and energies.

Figure 2.4 illustrates the $Si(OH)_4 \bullet 7(H_2O)$ model system of Felipe et al. (2003). A B3LYP/6-31 + G(d,p) basis set was used to calculate structures and potential energies. In addition, solvation energies of the model were calculated within a dielectric continuum using the Integral Equation Formulism Polarized Continuum Model (IEFPCM; Cancès et al., 1997) because the 7 H_2O molecules do not account for solvation of the entire $Si(OH)_4$ (Fig. 2.4) and do not include long-range (dipole-dipole in this case) solvation effects. The reader should also note that other methods for calculating the structures and energies of test configurations within this study were also performed but not included in the publication. The use of varied methods should be common practice in order to estimate possible error within the model system.

Two main features of Fig. 2.4 are notable. First, the formation of the $^{[5]}Si$ complex was predicted as suggested in a number of earlier modeling studies of silica-water

interactions (Casey et al., 1990; Lasaga and Gibbs, 1990; Kubicki et al., 1993; Xiao and Lasaga, 1996). One difference is that instead of a $(OH)_4SiOH_2$ complex, a $[Si(OH)_5]^{1-}$ complex was predicted with a H^+ transfer occurring from the incoming H_2O molecule to a nearby H_2O to form an H_3O^+. In addition, this H_3O^+ forms a dimer with another H_2O molecule that facilitates the cooperative transfer of the proton to the leaving OH^- on the $[Si(OH)_5]^{1-}$ complex to result in the exchanged $Si(OH)_4$ molecule. Increasing the number of H_2O molecules included in such a model could increase the accuracy of the solvation effects, but it would also dramatically increase the computational time required. Seven H_2O molecules appears to be the minimum number required to capture this behavior for the $Si(OH)_4$-H_2O reaction which is the ideal situation in this type of study.

2.5.2 Ligand Exchange in Aqueous Solutions

Casey and coworkers have published numerous studies examining the exchange rates of O in the coordination spheres of dissolved metals and their relationship to mineral surface reactions. One excellent example where the experimental NMR spectroscopic data was complemented by molecular orbital calculations can be found in Phillips et al. (1998). In this study, the rates of O exchange between H_2O in the bulk and bonded to Al^{3+} were determined by using the T_2 relaxation constants measurable in NMR. Experimental results indicated that the rate of exchange could change by four orders of magnitude as the Al^{3+} species changed from $[Al(OH_2)_6]^{3+}$ to $[Al(OH_2)_5F]^{2+}$ to $[Al(OH_2)F_2]^+$ to $[Al(OH_2)_5(OH)]^{2+}$. One interpretation of this data is that formation of the Al-F and Al-(OH) bonds causes the remaining Al-(OH_2) bonds to lengthen and weaken. Thus, removing and H_2O to exchange with the bulk could have a lower activation energy barrier. Indeed, the derived activation enthalpies for this exchanged decreased significantly with the formation of Al-(OH) and Al-F bonds.

To test this explanation of the exchange mechanism, HF/6-31G(d) calculations were performed on the above complexes with and without an additional H_2O molecule of solvation. Model structures predicted that Al-(OH_2) bonds would lengthen significantly with the formation of Al-(OH) and Al-F bonds (e.g., from 1.934 Å in $[Al(OH_2)_6]^{3+}$ to 1.975 Å in $[Al(OH_2)_5F]^{2+}$). The calculated energies to remove an H_2O molecule from the Al^{3+} also decreased significantly in the species with Al-(OH) and Al-F bonds compared to $[Al(OH_2)_6]^{3+}$. The absolute agreement between experimental and model activation energies was not excellent in this case, but this difference was readily attributable to the neglect of long-range solvation effects and electron correlation. A similar approach was used by Hamilton et al. (2001) to rationalize the dissolution kinetics of feldspar glasses based on changes to the local cation environment on the surface.

2.5.3 Hydrolysis of Si-O-Si and Si-O-Al

A relatively common use of MO-TST in geochemistry has been to study the kinetics of silicate and aluminosilicate dissolution (Casey et al., 1990; Xiao and Lasaga, 1994, 1996; Kubicki et al., 1997; Pelmenschikov et al., 2000; Criscenti et al., 2005b). Mineral dissolution can be a complex process as discussed above and in Chap. 5, so modeling this reaction was probably not a great place to start testing MO-TST in hindsight. However, each study built upon the earlier ones and significant progress has been made in understanding the reaction mechanisms associated with this key geochemical reaction.

Casey et al. (1990) and Xiao and Lasaga (1994) used $H_3SiOSiH_3$ and $H_3SiOAlH_3$ models to represent the Si-O-Si or Si-O-Al linkages present on the surface of silica and feldspars. The H atoms are present to terminate the cluster such that the Si^{4+} and Al^{3+} cations are in tetrahedral coordination similar to the mineral environment. Hydrolysis of these linkages is thought to control weathering of these common Earth surface minerals, so model selection was focused on calculating this step in the most accurate method practical at the time.

Casey et al. (1990) used HF/6-31G(d) basis sets and Xiao and Lasaga (1994) used up to MP2/6-311G(d,p) basis sets, which illustrates the principle that more accurate calculations become more practical with time. Both studies were limited in the ability of the computers at that time to handle larger pieces of the mineral structure and solvation effects. However, through intelligent formulation of a hypothesis, both studies were able to produce useful results because they could address specific questions. The first study examined kinetic isotope effects (H/D substitution) during hydrolysis. Although the experiments and model calculations did not agree on the magnitude of kinetic isotope effects on the rate of hydrolysis, the model calculations did give insight into the nature of the H^+ transfer step and the activated complex of this important reaction. (An anonymous reviewer once commented that Casey et al. (1990) showed that MO calculations could not be used to model the silica hydrolysis reaction, but this overly pessimistic view is not warranted if one reads the Conclusions section of Casey et al., 1990.)

Xiao and Lasaga (1994, 1996) took the next logical step toward modeling silicate dissolution based on lessons learned in the Casey et al. (1990) paper. Investigating the hypothesis that H^+ or OH^- may catalyze hydrolysis, reaction pathways for both reactants attacking the Si-O-Si and Si-O-Al linkages were calculated. Model activation energies were obtained that were significantly lower than when H_2O was used as the hydrolyzing agent; hence, these studies pointed to the role that these minor species could play in silicate dissolution even when they were not part of the overall reaction (i.e., $SiO_2 + 2H_2O \rightarrow Si(OH)_4$; Rimstidt and Barnes, 1980).

Two more recent studies (Pelmenschikov et al., 2000, 2001; Criscenti et al., 2005, 2006) have used more extended clusters to model the Si-O-Si hydrolysis reaction. Again, a few years later, computer power has increased such that systems deemed "too large" by previous workers have become practical models for simulations.

In the extended cluster models of Pelmenschikov et al. (2000), many of the atoms were constrained to the positions present on the surface of β-cristobalite. The activation energy to hydrolyze a Si-O-Si linkage (calculated with both B3LYP and MP2 methods for electron correlation) with an H_2O molecule was calculated as a function of the polymerization state of the SiO_4 tetrahedron of interest. These authors concluded that the activation energy should increase as the polymerization state increased due to lattice constraints on the possible activated complex (see also Chap. 5). Such a conclusion is consistent with some experimental interpretations of mineral dissolution (e.g., Hiemstra and van Riemsdijk, 1990). The effect of re-polymerization or "self-healing" was investigated in Pelmenschikov et al. (2001). These authors concluded that for Si atoms on the surface with at least two Si-O-Si linkages remaining, the reaction $\text{Si-(OH)} + \text{Si(OH)} \rightarrow \text{Si-O-Si} + H_2O$ would be rapid and slow the overall rate of silica dissolution. Re-polymerization of broken Si-O-T linkages (where T is either Si or Al) could be important in the formation of a gel-like leach layer on the surface of alumino- and boro-silicates (Bunker et al., 1988; Casey et al., 1989; Hellmann, 1990).

Criscenti et al. (2005, 2006) modeled reaction pathways for hydrolyzing Si-O-Si and Si-O-Al using model clusters of a central Si or Al tetrahedron surrounded by three other Si tetrahedra. Such a model mimics the surface environment of a Si or Al atom to the third nearest neighbor. In addition, these studies used H_3O^+ as the agent of hydrolysis with solvent effects treated by the explicit method. Structures were optimized with HF/3–21G(d,p) and B3LYP/6-31G(d) basis sets, then energies along the reaction path were calculated using B3LYP/6-311 + G(d,p) basis sets. Note that energies were calculated with a larger basis set than the structures because structure determinations require numerous energy steps, so time was saved by using a smaller basis set. This approach is justifiable because accurate structures are generally more readily obtained with smaller basis sets (Foresman and Frisch, 1996). Accurate potential energies require larger basis sets, however, so combining the moderate and large basis set methods to obtain structures then energies is a common practice.

Full energy minimizations were performed which allows for calculation of the zero-point energy of reactants, products and transition states, but this assumes that relaxation is complete compared with the rigid surface model of Pelmenschikov et al. (2000). (Probably neither rigid or fully relaxed are accurate for a true mineral surface, but such model constructions allow the investigator to examine end-member cases and make limiting case predictions.) One advantage of using full relaxation is that it is possible to calculate the vibrational frequencies for the model to verify whether the structure is a stable configuration or an activated complex (i.e., one and only one negative frequency).

Criscenti et al. (2006) found that earlier hypotheses based on simpler model systems were correct. For example, the idea that H^+ transfer occurred before the hydrolysis step, and therefore that H/D isotope effects were not large in silica dissolution (Casey et al., 1990), was predicted in the multiple step hydrolysis reaction. In addition, a metastable 5-coordinate Si intermediate was also found in this case where the central Si was linked to three other Si tetrahedra, consistent with the prediction of Xiao and Lasaga (1994). An interesting new insight was the role that

nearby H_2O molecules play in the H^+ transfer reaction both to the bridging oxygen atom in the Si-O-Si linkage to form Si-(OH)-Si and back to a H_2O molecule to reform H_3O^+. These solvation effects can play a large role in the stability of various species (Sefcik and Goddard, 2001; Kubicki, 2001) and the calculated activation energy barriers and should not be overlooked.

The possibility of an Al coordination change from tetrahedral to octahedral was investigated in Criscenti et al. (2005). This step in the overall dissolution reaction had been suggested by Hellmann et al. (1990), and $^{[6]}$Al had been recently observed on the surface of feldspar glasses after reaction in acid by Tsomaia et al. (2002). The coordination change reaction was modeled in both the forward and reverse directions, with the reverse direction providing the lowest potential energy surface. The end result of this study was to conclude that the $^{[6]}$Al species is theoretically stable even when the Al is linked to three Si tetrahedra. This assumes the full relaxation allowed in the modeling actually occurs on the surface, but full relaxation may only occur if a hydrated gel-like leach layer is forming at the mineral-water interface. Further investigations of these reactions would be useful with a variety of constraints and polymerization states built into the model system.

2.6 Summary

Donkey to Shrek – "Are we there yet?" Shrek – "No, Donkey." Donkey – "Are we there yet?" Shrek – "Yes." Donkey – "Really!?" Shrek – "No, Donkey!" Or, more philosophically, it is not the destination that matters but the journey.

Although we may never be 100% certain of any reaction mechanism we hypothesize, the search for these mechanisms can teach us a lot about the geochemical reactions we are attempting to understand. If this search brings together field, experimental, analytical, and theoretical researchers to discuss a question of geochemical kinetics, the synthesis of information and development of techniques will push our understanding forward. The quest to determine reaction mechanisms will lead to suggestions of possible intermediate species and rate-controlling factors that would never be suspected by examination of overall stoichiometric reactions. These underlying factors may be important in geochemical kinetics of other reactions occurring in the system. They are certainly important in environmental chemistry where the effects of the environment on living organisms are being considered.

Acknowledgements

The author thanks Louise Criscenti and Susan Brantley for their valuable and constructive reviews of the manuscript. The author would also like to acknowledge Mihali Felipe and Kideok Kwon for discussing parts of the manuscript and the

Geosc 560 class at Penn State for commenting on all these chapters. This material is based upon work supported by the National Science Foundation under Grant No. CHE-0431328.

References

Abramczyk H., Brozek-Pluska B., Kurczewski K., Szymczyk I., Szymczyk I., Blaszczyk T., Scholl H., and Czajkowski, W. (2006) Femtosecond transient absorption, Raman, and electrochemistry studies of tetrasulfonated copper phthalocyanine in water solutions. *J. Phys. Chem. A* **110**: 8627–8636.

Ayala P. Y. and Schlegel H. B. (1998) Identification and treatment of internal rotation in normal mode vibrational analysis. *J. Chem. Phys.* **108**, 2314–2325.

Barnes I., Stuart W. T., and Fisher D. W. (1964) Field investigations of mine waters in the northern anthracite field. Pennsylvania. *U.S.G.S. Prof. Paper* **473-B**.

Becke A. D. (1993) Density-functional thermochemistry.3. The role of exact exchange. *J. Chem. Phys*. **98**, 5648–5652.

Becker U., Rosso K. M., and Hochella M. F. (2001) The proximity effect on semiconducting mineral surfaces: A new aspect of mineral surface reactivity and surface complexation theory? *Geochim. Cosmochim. Acta* **65**, 2641–2649.

Binkley J. S., Pople J. A., and Hehre W. J. (1980) Self-consistent molecular orbital methods. 21. Small split-valence basis sets for first-row elements. *J. Am. Chem. Soc.* **102**, 939–947.

Bell D. R. and Ihinger P. D. (2000) The isotopic composition of hydrogen in nominally anhydrous mantle minerals. *Geochim. Cosmochim. Acta* **64**, 2109–2118.

Borda M. J., Elsetinow A. R., Strongin D. R., and Schoonen M. A. A. (2003) A mechanism for the production of hydroxyl radical at surface defect sites on pyrite. *Geochim. Cosmochim. Acta* **67**, 935–939.

Bunker B. C., Tallant D. R., Headley T. J., Turner G. L., and Kirkpatrick R. J. (1988) The structure of leached sodium borosilicate glass. *Phys. Chem. Glasses* **29**, 106–120.

Cancès E., Mennucci B., and Tomasi J. (1997) A new integral equation formalism for the polarizable continuum model: Theoretical background and applications to isotropic and anisotropic dielectrics. *J. Chem. Phys*. **107**, 3032–3041.

Casey W. H., Westrich H. R., Massis T., Banfield J. F., and Arnold G. W.(1989) The surface of labradorite feldspar after acid-hydrolysis. *Chem. Geol.* **78** (3–4), 205–218.

Casey W. H., Lasaga A. C., and Gibbs G. V. (1990) Mechanisms of silica dissolution as inferred from the kinetic isotope effect. *Geochim. Cosmochim. Acta* **54**, 3369–3378.

Casey W. H., Hochella M. F., and Westrich H. R. (1993) The surface chemistry of manganiferous silicate minerals as inferred from experiments on tephroite (Mn_2SiO_4). *Geochim. Cosmochim. Acta* **57**, 785–793.

Cerjan C. J. and Miller W. H. (1981) On finding transition states. *J. Chem. Phys*. **75**, 2800–2807.

Chizallet C., Costentin G., Che M., Delbecq F., and Sautet, P. (2006) Revisiting acido-basicity of the MgO surface by periodic density functional theory calculations: Role of surface topology and ion coordination on water dissociation. *J. Phys. Chem. B* **110**: 15878–15886.

Ciccotti G., Kapral R., and Vanden-Eijnden E. (2005) Blue moon sampling, vectorial reaction coordinates, and unbiased constrained dynamics. *ChemPhysChem* **6**: 1809–1814.

Cohn C. A., Mueller S., Wimmer E., Leifer N., Greenbaum S., Strongin D.R., Schoonen M. A. A. (2006) Pyrite-induced hydroxyl radical formation and its effect on nucleic acids. *Geochem. Trans.* 7: Art. No. 3.

Cramer C. J. (2002) *Essentials of Computational Chemistry*. John Wiley & Sons Ltd., West Sussex, England, 542 pp.

Criscenti L. J., Brantley S. L., Mueller K.T., Tsomaia N., and Kubicki J. D. (2005) Theoretical and ^{27}Al CPMAS NMR investigation of aluminum coordination changes during aluminosilicate dissolution. *Geochim. Cosmochim. Acta*, **69**, 2205–2220.

Criscenti L. J., Kubicki J. D., and Brantley S. L. (2006) Silicate glass and mineral dissolution: Calculated reaction paths and activation energies for hydrolysis of a Q^3 Si by H_3O^+ using ab initio methods. *J. Phys. Chem. A*, 110, 198–206.

Curtiss L. A., Raghavachari K., and Pople J. A. (1993) Gaussian-2 theory using reduced Møller-Plesset orders. *J. Chem. Phys*. **98**, 1293–1298.

DiChristina T. J., Fredrickson J. K., and Zachara J. M. (2005) Enzymology of electron transport: Energy generation with geochemical consequences. In *Molecular Geomicrobiology*, J.F. Banfield, J. Cervini-Silva, and K.M. Nealson (eds), Mineralogical Society of America and Geochemical Society, Chantilly VA, pp. 27–52.

East A. L. L. and Radom L. (1997) Ab initio statistical thermodynamical models for the computation of third-law entropies. *J. Chem. Phys.* **106**, 6655–6674.

Elsetinow A. R., Borda M. J., Schoonen M. A. A., and Strongin D. R. (2003) Suppression of pyrite oxidation in acidic aqueous environments using lipids having two hydrophobic tails. *Adv. Environ. Res*. **7**, 969–974.

Felipe M., Xiao Y., and Kubicki J. D. (2001) Molecular orbital modeling and transition state theory in the geosciences. In Molecular Modeling Theory: Applications in the Geosciences, Reviews in Mineralogy and Geochemistry 42, R. T. Cygan and J. D. Kubicki (eds.) *Geochemical Society*. 485–531.

Felipe M. A., Kubicki J. D., and Rye D. M. (2003) Hydrogen isotope exchange kinetics between H_2O and H_4SiO_4 from ab initio calculations. *Geochim. Cosmochim. Acta* **67**, 1259–1276.

Felipe M. A., Kubicki J. D., and Freeman K. H. (2005) A mechanism for carbon isotope exchange between aqueous acetic acid and CO_2/HCO_3^-: An ab initio study. *Geochim. Cosmochim. Acta* in press.

Foresman J. B. and Frisch A. (1996) *Exploring Chemistry with Electronic Structure Methods Second Edition*; Gaussian, Inc.: Pittsburgh, 302 pp.

Frisch et al. (2004) Gaussian 03, Revision C.01, Wallingford CT.

Gibbs G. V. (1982) Molecules as models for bonding in silicates. *Am. Mineral*. **67**, 421–450.

Gibbs G. V., Finger L. W., and Boisen M. B. Jr. (1987) Molecular mimicry of the bond length-bond strength variations in oxide crystals. *Phys. Chem. Miner*. **14**, 327–331.

Gilijamse J. J., Lock A. J., and Bakker H. J. (2005) Dynamics of confined water molecules. *Proceedings of the National Academy of Sciences of the United States of America* **102**: 3202–3207.

Gonzalez C. and Schlegel H. B. (1989) An improved algorithm for reaction path following. *J. Phys. Chem*. **90**, 2154–2161.

Gonzalez C. and Schlegel H. B. (1990) Reaction-path following in mass-weighted internal coordinates. *J. Phys. Chem*. **94**, 5523–5527.

Goodman A. L., Bernard E. T., and Grassian V. H. (2001) Spectroscopic study of nitric acid and water adsorption on oxide particles: Enhanced nitric acid uptake kinetics in the presence of adsorbed water. *J. Phys. Chem. A* **105**(26), 6443–6457.

Gordon M. S., Binkley S., Pople J. A., Pietro W. J., and Hehre W. J. (1982) Self-consistent molecular-orbital methods. 22. Small split-valence basis sets for second-row elements. *J. Am. Chem. Soc*. **104**, 2797–2803.

Grassian V. H. (2001) Heterogeneous uptake and reaction of nitrogen oxides and volatile organic compounds on the surface of atmospheric particles including oxides, carbonates, soot and mineral dust: Implications for the chemical balance of the troposphere. *Int. Rev. Phys. Chem*. **20**, 467–548.

Guevremont J. M., Bebie J., Elsetinow A. R., Strongin D. R., and Schoonen M. A. A (1998) Reactivity of the (100) plane of pyrite in oxidizing gaseous and aqueous environments: Effects of surface imperfections. *Environ. Sci. Technol*. **32**, 3743–3748.

Halgren T. A. and Lipscomb W. N. (1977) The synchronous-transit method for determining reaction pathways and locating molecular transition states. *Chem. Phys. Lett*. **49**, 225–232.

Hamilton J. P., Brantley S. L., Pantano C. G., Criscenti L., and Kubicki J. D. (2001) Dissolution of nepheline, jadeite and albite glasses: Toward better models for aluminosilicate dissolution. *Geochim. Cosmochim. Acta* **65**, 3683–3702.

Hass K. C., Schneider W. F., Curioni A., and Andreoni W. (2000) First-principles molecular dynamics simulations of H_2O on alpha-Al_2O_3 (0001). *J. Phys. Chem. B* **104**, 5527–5540.

Hellmann R., Eggleston C. M., Hochella M. F., and Crerar D. A. (1990) The formation of leached layers on albite surfaces during dissolution under hydrothermal conditions. *Nature* **350**, 488–491.

Hellmann R., Penisson J. M., Hervig R. L., Thomassin J. H., and Abrioux M. F. (2003) An EFTEM/HRTEM high-resolution study of the near surface of labradorite feldspar altered at acid pH: Evidence for interfacial dissolution-reprecipitation. *Phys. Chem. Miner*. **30**, 192–197.

Hiemstra T. and van Riemsdijk W. H. (1990) Multiple activated complex dissolution of metal (hydr)oxides—A thermodynamic approach applied to quartz. *J. Colloid Interface Sci*. **136**, 132–150.

Hohenberg P. and Kohn W. (1964) Inhomogeneous electron gas. *Phys. Rev. B*. **136**, 864–871.

Keith T. A. and Frisch M. J. (1994) Inclusion of explicit solvent molecules in a self-consistent-reaction field model of solvation. Modeling the Hydrogen Bond. ACS Symposium Series 569, Washington DC, pp. 22–35.

Klamt A. and Schuurmann G. (1993) COSMO: A new approach to dielectric screening in solvents with explicit expressions for the screening energy and it gradient. *J. Chem. Soc. Perkin Trans*. **2**, 799–805.

Kohn W. and Sham L. J. (1965) Self-Consistent Equations Including Exchange and Correlation Effects. *Phys. Rev*. **140**(4A), A1133–A1138.

Kubicki J. D., Apitz S. E., and Blake G. A. (1997) Molecular orbital calculations for modeling acetate-aluminosilicate adsorption and dissolution reactions. *Geochim. Cosmochim. Acta* **61**, 1031–1046.

Kubicki J. D. and Lasaga A. C. (1988) Molecular dynamics simulations of SiO_2 melt and glass. Ionic and covalent models. *Am. Mineral.* **73**, 941–955.

Kubicki J. D., Xiao Y., and Lasaga A. C. (1993) Theoretical reaction pathways for the formation of $[Si(OH)_5]^{1-}$ and the deprotonation of orthosilicic acid in basic solution. *Geochim. Cosmochim. Acta*, **57**, 3847–3853.

Kubicki J. D., Blake G. A., and Apitz S. E. (1995) G2 theory calculations on $[H_3SiO_4]^-$, $[H_4SiO_4]$, $[H_3AlO_4]^{2-}$, $[H_4AlO_4]^-$, and $[H_5AlO_4]$: Basis set and electron correlation effects on molecular structures, atomic charges, infrared spectra, and potential energies. *Phys. Chem. Miner.* **22**, 481–488.

Kubicki J. D., Itoh M. J., Schroeter L. M., Nguyen B. N., and Apitz S. E. (1999) Attenuated total reflectance Fourier-transform infrared spectroscopy of carboxylic acids adsorbed onto mineral surfaces. *Geochim. Cosmochim. Acta* **63**, 2709–2725.

Kubicki J. D. (2001) Integral equation formalism polarized continuum model calculations of aqueous Al^{3+}, Fe^{3+} and Si^{4+}: Correlations of calculated aqueous-phase deprotonation energies with experimental $\ln(K_a)$ and pK_a values. *J. Phys. Chem. A* **105**, 8756–8762.

Lasaga A. C. (1981) Transition state theory. In: Lasaga A. C. and Kirkpatrick R. J. (ed) *Kinetics of Geochemical Processes. Rev* Mineral 8. Mineral Society of America, Washington DC, pp. 135–170.

Lasaga A. C. and Gibbs G. V. (1990) Ab-initio quantum mechanical calculations of water-rock interactions: Adsorption and hydrolysis reactions. *Am. J. Sci.* **290**, 263–295.

Lasaga A. C. (1997) *Kinetic Theory in the Earth Sciences*. Princeton University Press, Princeton, NJ, pp. 811.

Lee C., Yang W., and Parr R. G. (1988). Development of the Colle-Salvetti correlation-energy formula into a functional of the electron density. *Phys. Rev. B* **37**, 785–789.

Lee S. K. and Stebbins J. F. (2003) O atom sites in natural kaolinite and muscovite: O-17 MAS and 3QMAS NMR study. *Am. Mineral*. **88**, 493–500.

Lewan M.D. and Ruble T. E. (2002) Comparison of petroleum generation kinetics by isothermal hydrous and nonisothermal open-system pyrolysis. *Org. Geochem.* **33**, 1457–1475.

Matsumoto M., Saito S., and Ohmine I. (2002) Molecular dynamics simulation of the ice nucleation and growth process leading to water freezing. *Nature* **416**, 409–413.

McQuarrie D. A. and Simon J. D. (1997) Physical Chemistry—A Molecular Approach, *University Science Books*, Sausalito, CA, pp. 1360.

Møller C. and Plesset M. S. (1934) Note on an approximation treatment for many-electron systems. *Phys. Rev*. **46**, 618–622.

Parthiban S. and Martin J. M. L. (2001) Assessment of W1 and W2 theories for the computation of electron affinities, ionization potentials, heats of formation, and proton affinities. *J. Chem. Phys.* **114**, 6014–6029.

Paul K., Kubicki J. D., and Sparks D. L. (2007) Sulfate adsorption at the Fe-hydroxide-H_2O interface: Comparison of MO/DFT cluster and periodic DFT models. *Int. J. Soil Sci.* in press.

Pelmenschikov A. G., Morosi G., and Gamba A. (1997) Adsorption of water and methanol on silica hydroxyls: Ab initio energy and frequency calculations *J. Phys. Chem. A* **101** (6), 1178–1187.

Pelmenschikov A., Strandh H., Pettersson L. G. M., and Leszczynski J. (2000) Lattice resistance to hydrolysis of Si-O-Si bonds of silicate minerals: Ab initio calculations of a single water attack onto the (001) and (111) beta-cristobalite surfaces. *J. Phys. Chem. B* **104** (24), 5779–5783.

Pelmenschikov A., Leszczynski J., and Petterson L. G. M. (2001) Mechanism of dissolution of neutral silica surfaces: Including effect of self-healing. *J. Phys. Chem. A* **105**, 9528–8532.

Peng C. and Schlegel H. B. (1994) Combining synchronous transit and quasi-newton methods for finding transition states. *Israel J Chem*. **33**, 449–454.

Perdew, J. P., Burke, K., and Ernzerhof, M. (1996) Generalized gradient approximation made simple. *Phys. Rev. Lett.* **77**, 3865–3868.

Petersson G. A., Bennett A., Tensfeldt T. G., Al-Laham M. A., Shirley W. A., and Mantzaris J. (1988) A complete basis set model chemistry.1. The total energies of closed-shell atoms and hydrides of the 1^{st}-row elements. *J. Chem. Phys*. **89**, 2193–2218.

Phillips B. L., Tossell J. A., and Casey W. H. (1998) Experimental and theoretical treatment of elementary ligand exchange reactions in aluminum complexes. *Environ. Sci. Technol*. **32**, 2865–2870.

Prince A.P., Wade J. L., Grassian V. H., Kleiber P. D., and Young M. A. (2002) Heterogeneous reactions of soot aerosols with nitrogen dioxide and nitric acid: Atmospheric chamber and Knudsen cell studies. *Atmos. Environ*. **36**, 5729–5740.

Reedy B. J., Beattie J. K., and Lowson R. T. (1991) A vibrational spectroscopic O-18 tracer study of pyrite oxidation. *Geochim. Cosmochim. Acta* **55**, 1609–1614.

Richnow H. H., Seifert R., Hefter J., Kastner M., Mahro B., and Michaelis W. (1994) Metabolites of xenobiotica and mineral-oil constituents linked to macromolecular organic-matter in polluted environments. *Org. Geochem*. **22**, 671–681.

Rimstidt J. D. and Barnes H. L. (1980) The kinetics of silica-water reactions. *Geochim. Cosmochim. Acta* **44**, 1683–1699.

Rosso K. M. (2001) Structure and reactivity of semiconducting mineral surfaces: Convergence of molecular modeling and experiment. In Molecular Modeling Theory: Applications in the Geosciences, Reviews in Mineralogy and Geochemistry 42, R. T. Cygan and J. D. Kubicki (eds.) Geochemical Society, pp. 199–271.

Rosso K. M. and Rustad J. R. (2001) Structures and energies of AlOOH and FeOOH polymorphs from plane wave pseudopotential calculations. *Am. Mineralog.* **86**, 312–317.

Schlegel H. B. (1987) Optimization of equilibrium geometries and transition structures. *Adv. Chem. Phys*. **67**, 249–286.

Schoonen M. A. A., Xu Y., and Strongin D. R. (1998) An introduction to geocatalysis. *J. Geochem. Explor*. **62**, 201–215.

Schoonen M. A. A. and Strongin D. R. (2005) Catalysis of electron transfer reactions at mineral surfaces. In *Environmental Catalysis*, V. H. Grassian (ed), Taylor & Francis/CRC Press, Boca Raton, FL, pp. 37–60.

Sherman D. M. (2001) Quantum chemistry and classical simulations of metal complexes in aqueous solutions. In Molecular Modeling Theory: Applications in the Geosciences, Reviews in Mineralogy and Geochemistry **42**, R. T. Cygan and J. D. Kubicki (eds.) Geochemical Society, pp. 273–317.

Shoemaker J. R., Burggraf L. W., and Gordon M. S. (1999) SIMOMM: An integrated molecular orbital/molecular mechanics optimization scheme for surfaces. *J. Phys. Chem. A* **103**, 3245–3251.

Stefanovich E. V. and Truong T. N. (1997) A theoretical approach for modeling reactivity at solid-liquid interfaces. *J. Chem. Phys*. **106**, 7700–7705.

Stewart J. J. P. (2004) Comparison of the accuracy of semiempirical and some DFT methods for predicting heats of formation. *J. Mol. Model.* **10**, 6–12.

Stixrude L. (2001) First principles theory of mantle and core phases. In Molecular Modeling Theory: Applications in the Geosciences, Reviews in Mineralogy and Geochemistry 42, R. T. Cygan and J. D. Kubicki (eds.) *Geochemical Society*, pp. 319–343.

Stixrude L. and Peacor D. R. (2002) First-principles study of illite-smectite and implications for clay mineral systems. *Nature*, **420**, 165–168.

Suarez D.L. and Wood J.D. (1996) Short- and long-term weathering rates of a feldspar fraction isolated from an arid zone soil. *Chem. Geolog.* **132**, 143–150.

Sykes D., Kubicki J. D., and Farrar T. C. (1997) Molecular orbital calculation of ^{27}Al and ^{29}Si NMR parameters in Q^3 and Q^4 aluminosilicate molecules and implications for the interpretation of hydrous aluminosilicate glass NMR spectra. *J. Phys. Chem. A* **101**, 2715–2722.

Taylor B.E., Wheeler M.C., and Nordstrom D.K. (1984) Stable isotope geochemistry of acid mine drainage: Experimental oxidation of pyrite. *Geochim. Cosmochim. Acta* **48**, 2669–2678.

Tsomaia N., Brantley S. L., Hamilton J. P., Pantano C. G., and Mueller K. T. (2003) NMR evidence for formation of octahedral and tetrahedral Al and

repolymerization of the Si network during dissolution of aluminosilicate glass and crystal. *Am. Mineralog*. **88**, 54–67.

Usher C. R., Paul K. W., Narayansamy J., Kubicki J. D., Sparks D. L., Schoonen M. A. A., and Strongin D. R. (2005) Aspects of pyrite oxidation in an oxidizing gaseous environment: An in situ HATR-IR isotope study. *Environ. Sci. Technol.* **39** (19): 7576–7584.

Van Alsenoy C., Yu C. H., Peeters A., Martin J. M. L., and Schafer L. (1998) Ab initio geometry determinations of proteins. 1. Crambin. *J. Phys. Chem. A* **102**, 2246–2251.

Wang S. H., Ackermann R., Spicer C. W., Fast J. D., Schmeling M., and Stutz J. (2003) Atmospheric observations of enhanced NO_2-HONO conversion on mineral dust particles. *Geophys. Res. Lett. 30*: Art. no. **1595**.

White A. F. and Brantley S. L. (2003) The effect of time on the weathering of silicate minerals: Why do weathering rates differ in the laboratory and field? *Chem. Geolog.* **202**, 479–506.

Windus T. L., Bylaska E. J., Dupuis M., Hirata S., Pollack L., Smith D. M., Straatsma T. P., and Apra E. (2003) NWChem: New functionality. *Lecture Notes in Computer Science* 2660, 168–177.

Wong M. W. (1996) Vibrational frequency prediction using density functional theory. *Chem. Phys. Lett*. **256** (4–5), 391–399.

Xiao Y. T. and Lasaga A. C. (1994) Ab-initio quantum-mechanical studies of the kinetics and mechanisms of silicate dissolution – $H^+(H_3O^+)$ catalysis. *Geochim. Cosmochim. Acta* **58**, 5379–5400.

Xiao Y. T. and Lasaga A. C. (1996) Ab initio quantum mechanical studies of the kinetics and mechanisms of quartz dissolution: OH-catalysis. *Geochim. Cosmochim. Acta* **60**, 2283–2295.

Xu Y., Schoonen M. A. A., and Strongin D. R. (1996) Thiosulfate oxidation: Catalysis of synthetic sphalerite doped with transition metals. *Geochim. Cosmochim. Acta* **60**, 4701–4710.

Yu P., Lee A. P., Phillips B. L., and Casey W. H. (2003) Potentiometric and F-19 nuclear magnetic resonance spectroscopic study of fluoride substitution in the $GaAl_{12}$ polyoxocation: Implications for aluminum (hydr)oxide mineral surfaces. *Geochim. Cosmochim. Acta* **67**, 1065–1080.

Zhang Z., Fenter P., Kelly S. D., Catalano J. G., Bandura A. V., Kubicki J. D., Sofo J. O., Wesolowski D. J., Machesky M. L., Sturchio N. C., and Bedzyk M. J. (2006) Structure of hydrated Zn^{2+} at the rutile TiO_2 (110)-aqueous solution interface: Comparison of X-ray standing wave, X-ray absorption spectroscopy, and density functional theory results, *Geochim. Cosmochim. Acta* **70**, 4039–4056.

Chapter 3
The Mineral–Water Interface

A. Lüttge[1] and R. S. Arvidson[2]

3.1 Introduction: Definitions and Preliminary Concepts

3.1.1 Mineral–Water Interfaces are Everywhere

The typical satellite view of Earth's surface reveals ubiquitous contact between rocks and water (Fig. 3.1). Rocks are composed primarily of minerals, naturally crystallized materials having a periodic structure. The long-range structure of crystals, expressed internally as the periodic lattice, determines their fundamental physical and chemical properties. Water, in addition to supplying the basis for life on Earth, is also its critical solvent. It is the dominant medium through which rocks and minerals "communicate" during chemical precipitation and dissolution reactions. However, at room temperature the mobility of ions via diffusion to and from sites in the solid bulk crystal is extremely limited. Dissolution and precipitation reactions thus usually occur at the *mineral–water interface* (Fig. 3.2). This interface is the locus of exchange and interaction between the surface atoms of the solid and the overlying aqueous phase. In addition to water molecules, the fluid contains dissolved components: e.g., inorganic salts, hydrogen and hydroxyl ions, gases such as CO_2 and O_2, and organic molecules. These components interact with each other as well as with the mineral surface, yielding a complex distribution of species and functional groups (*moieties*) that characterize even compositionally "simple" solutions. This fluid–solid interaction alters both the surface layers of the crystal and the *boundary layer* of the fluid (Fig. 3.3). As used here, the term "boundary layer" applies to that fluid in direct contact with the mineral surface. Although the *bulk* fluid may be in turbulent motion (e.g., a stirred reactor), intermolecular attractive forces between the mineral surface and the fluid bring the fluid velocity to zero ("no-slip" condition). In classical theory, this constraint reduces advection and turbulent

[1] Rice University, Department of Earth Science, Department of Chemistry, and Center for Biological and Environmental Nanotechnology, aluttge@rice.edu
[2] Rice University, Department of Earth Science, Rolf.S.Arvidson@rice.edu

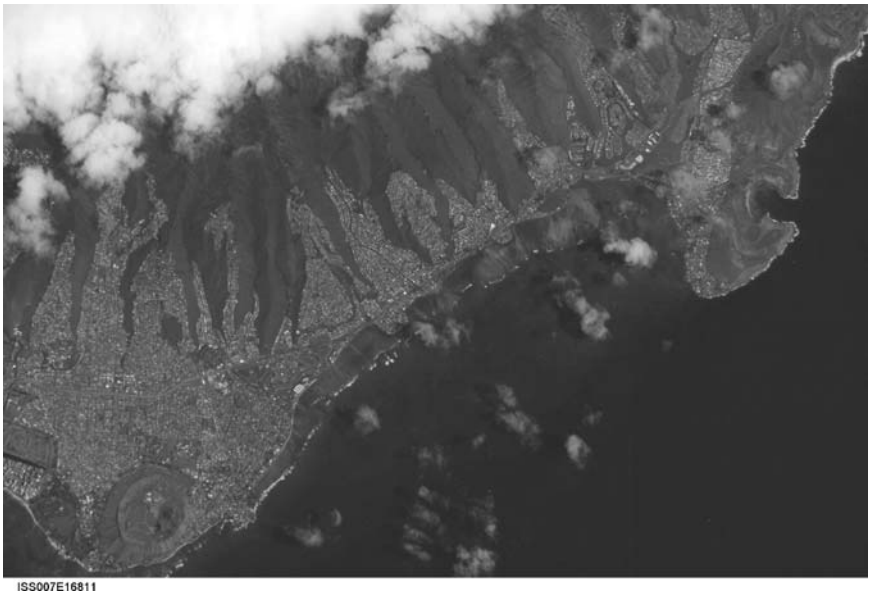

Fig. 3.1 Satellite image from 203 nautical miles elevation of the south shore of the island of Oahu, Hawaii (approximate location 21.5° N, 157.5° W), showing high relief from weathering of primary basalt terrain. Image courtesy of Earth Sciences and Image Analysis Laboratory, NASA Johnson Space Center, image reference Mission-Roll-Frame = ISS007-E-16811, http://eol.jsc.nasa.gov.

mixing within the boundary layer, whose thickness is a function of the flow characteristics prevailing in the overlying bulk fluid. The demands of reactive fluxes from precipitation or dissolution of the underlying mineral surface must be satisfied by the diffusive flux of components through the boundary layer. Much discussion is often devoted to the question of whether reactions are "controlled" by transport or surface reaction mechanisms (i.e., molecular detachment or attachment); because of the interplay between diffusion and reaction, the more pertinent question is whether the crystal surface is close to thermodynamic equilibrium with the fluid (see e.g., discussion in Lasaga, 1998). It is thus critical to recognize that at this interface neither the crystal nor the fluid is equivalent to its bulk counterpart. This central distinction is the subject of this chapter: the nature of the interfacial contact between a crystalline surface and an aqueous fluid, how this region of the crystal differs in terms of physical and chemical properties and behavior from its surroundings, how these differences are the basic engine for dynamic, scale-dependent interface processes, and how these atomic-scale processes express themselves as macroscopic phenomena.

Although the importance of the interface has long been recognized, its quantitative treatment has been limited both by (i) the availability of high-resolution analytical probes that yield information concerning the physical and chemical role of the crystal surface itself, and (ii) the integration of those data over relevant space and time scales. These constraints ultimately limit the application of information available at the molecular scale, derived both from direct observations and modeling of stochastic interface processes discussed in later sections, to longer term processes

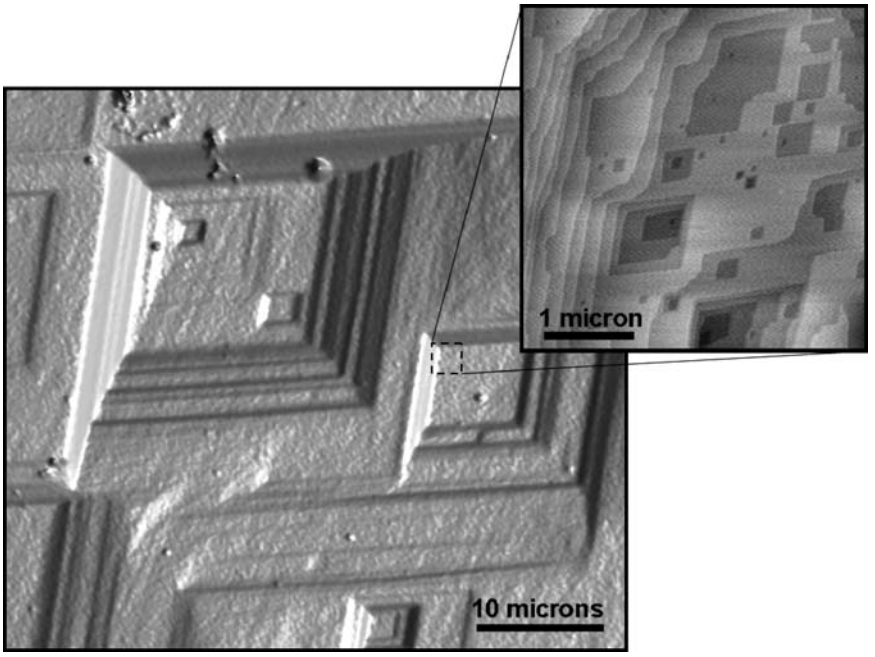

Fig. 3.2 Calcite crystal (104) cleavage surface topography, showing development of crystallographically controlled etch pits formed during dissolution. Digital image data were collected using different techniques: vertical scanning interferometery (VSI, lower left) and atomic force microscopy (AFM, upper right inset, note that field is rotated relative to VSI data). Image fields are $164 \times 128\,\mu m$ (VSI) and $5 \times 5\,\mu m$ (AFM). (Adapted from Vinson and Luttge (2005), reprinted with permission from *American Journal of Science*)

observed at the scale of the field environment. The understanding of the role of scale is at the center of some problems discussed in other chapters of this volume. In addition to "new" problems associated with developing technologies, these problems also include "old" classical ones that have resisted complete solution, as well as observations of "bulk" behavior that need to be reconciled in light of current knowledge. Examples include the potential environmental impact of nanocrystalline silica and carbonate phases, the relationship between grain size and chemical weathering, the understanding of how surface control of nascent mineralization in the ocean buffers seawater carbon chemistry and seawater-atmosphere CO_2 exchange, and the complex problem of how microbes directly and indirectly orchestrate exchange between particles and solution.

3.1.2 The Mineral–Water Interface: An Integrated Approach

Prior to the development of direct observational imaging technologies and surface probes, much of our understanding of the mineral interface was dependent on

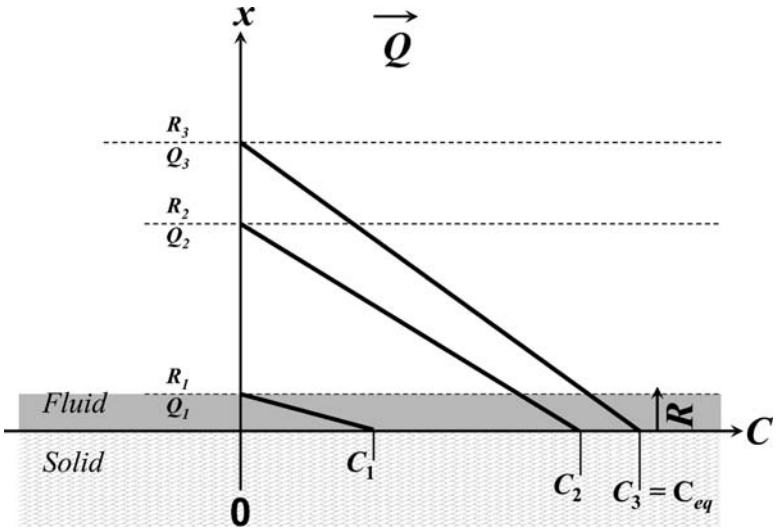

Fig. 3.3 Schematic fluid/mineral diffusional boundary layer. Boundary layer thickness is a function of the dissolved component and advection transport velocity in the overlying fluid. In the diagram, the mineral component is released at a given rate of dissolution (R_i), giving rise to a concentration at the interface (C_1); advective flux (i.e., stirring) of bulk fluid (Q_i) normal to the mineral surface maintains a boundary condition of zero concentration. Three *steady state* (i.e., $\partial C/\partial t = 0$) scenarios are depicted: (1) high undersaturation of a mineral with slow dissolution rate (R_1) is maintained by a high stirring rate (Q_1); (2) moderate undersaturation with intermediate dissolution (R_2) and stirring (Q_2) rate; a rapid dissolution rate (R_3) and weak stirring (Q_3) results in a thick boundary layer and an interface concentration essentially at equilibrium $(C_3 = C_{eq})$. Scenarios 1 and 2 would be termed surface-reaction limited; scenario 3 is transport limited

observations of solution chemistry in bulk experiments. The advent of sophisticated instruments has revolutionized our approach, permitting rigorous quantification of the chemistry and structure of crystal surfaces. Direct observations have focused attention on the solid surface itself, resulting in steady growth of new observations at a variety of space and time scales. The relationship of scale to physicochemical behavior is a fundamental one that we will revisit several times throughout our discussion. Its solution is our task for the future: an integrated approach that combines the complementary nature of analytical techniques to provide a comprehensive and consistent picture of the fluid–solid interface and its role in global scale geologic and environmental processes.

3.1.3 The Relationship of the Interface to the Bulk Solid

The surface of a crystal is fundamentally different from its bulk. Examples of these differences include "dangling" (unsatisfied) bonds, surface molecular relaxation, and chemical composition. In addition, the structure of the crystal surface is related

but not identical to the bulk crystal structure. Those differences create a strong driving force to reorganize and equilibrate the surface with the fluid. This overall process is accomplished by reactions such as hydration, adsorption of dissolved components and detachment of adatoms (see below).

The macroscopic morphology (form) of a crystal, that is the relationship of crystal surfaces to each other, reflects their environment of formation. If we cleave or fracture a crystal, the surface will reflect the crystal lattice and the conditions at which the surface was produced. For example, calcite or feldspars will develop *cleavage surfaces* while quartz crystals will fracture in an unpredictable and irregular shape. If a crystal grows or dissolves in a solution or melt, the surfaces will represent the prevailing thermodynamic and kinetic conditions of this process. For example, at this scale a crystal will develop so-called *growth faces*. This phenomenon is analogous to the development of *characteristic faces* during crystal dissolution. In contrast, during reorganization a crystal may develop so-called *equilibrium faces* distinct from those developed during growth or dissolution. For a crystal of a given volume with N potential face directions, with faces of total area A_i having characteristic surface work s_i (in units of $\mathrm{N} \times \mathrm{m}^{-1}$, or equivalently $\mathrm{J} \times \mathrm{m}^{-2}$), the total surface tension (Φ, in J) must be minimized at equilibrium, i.e.,

$$\Phi = \min\left(\sum_{i}^{N} s_i A_i\right) \tag{3.1}$$

These relationships have been recognized for a long time (e.g., Sunagawa, 1987). However, as we proceed in our investigations with the help of high-resolution instruments to microscopic and submicroscopic levels, we must consider the issue of scale and its relationship to those observations explicitly.

3.1.4 The Fundamental Importance of Scale

Figure 3.4 illustrates the great challenges that we face if we try to understand mineral–water interfaces and their implications for geologic and environmental processes. The figure shows the vast range both in time and length scales that connects atomic level processes and properties with their geologic scale counterparts. The main challenge is to understand quantitatively how phenomena observed at these vastly different scales relate to one another.

To further illustrate the complex nature of the problem we can recall the classical "coast-line problem" (Fig. 3.5). This classical example of fractal geometry reveals that the observed length of a coast-line depends on the scale at which the measurement is taken. The quantification of mineral surface area presents a similar but even more complex problem because of the multidimensional nature of spatial measurement, coupled with the fact that the "coastline" in this case is a dynamic entity (see also discussion in "reactive surface area section" below).

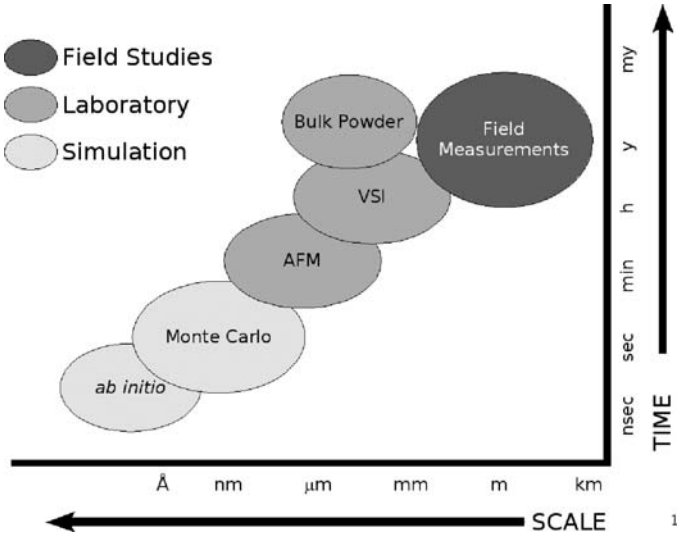

Fig. 3.4 Relationship of length and time scales and the characteristic mode of investigation

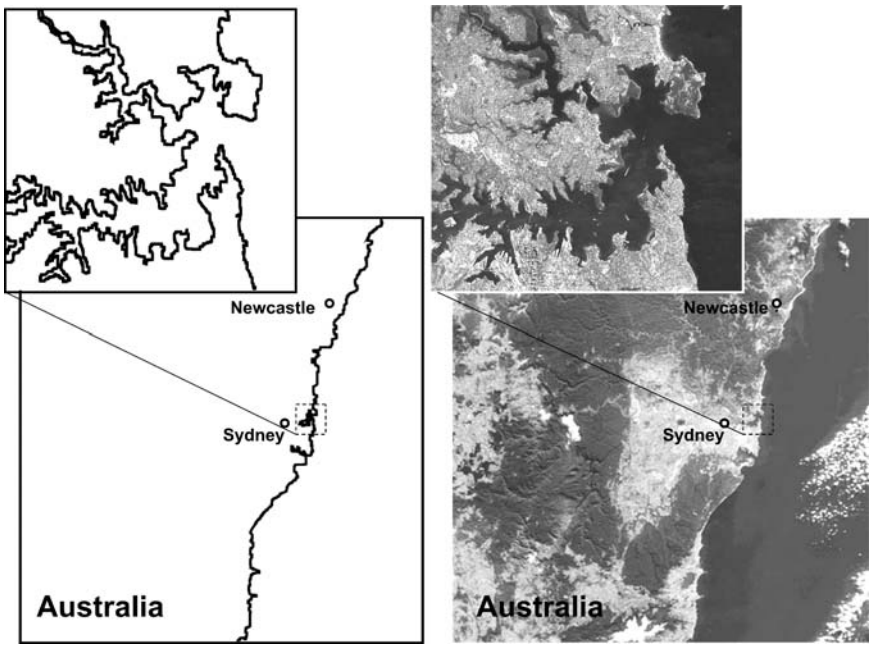

Fig. 3.5 Classical coastline problem, illustrated here by satellite imagery from different altitudes, showing dependence of the measured "length" (and obvious complexity) of the linear coastline on the scale at the measurement is taken. Top (inset), NASA/GSFC/METI/ERSDAC/JAROS, and US/Japan ASTER Science Team; Bottom taken from The Visible Earth, http://visibleearth.nasa.gov/

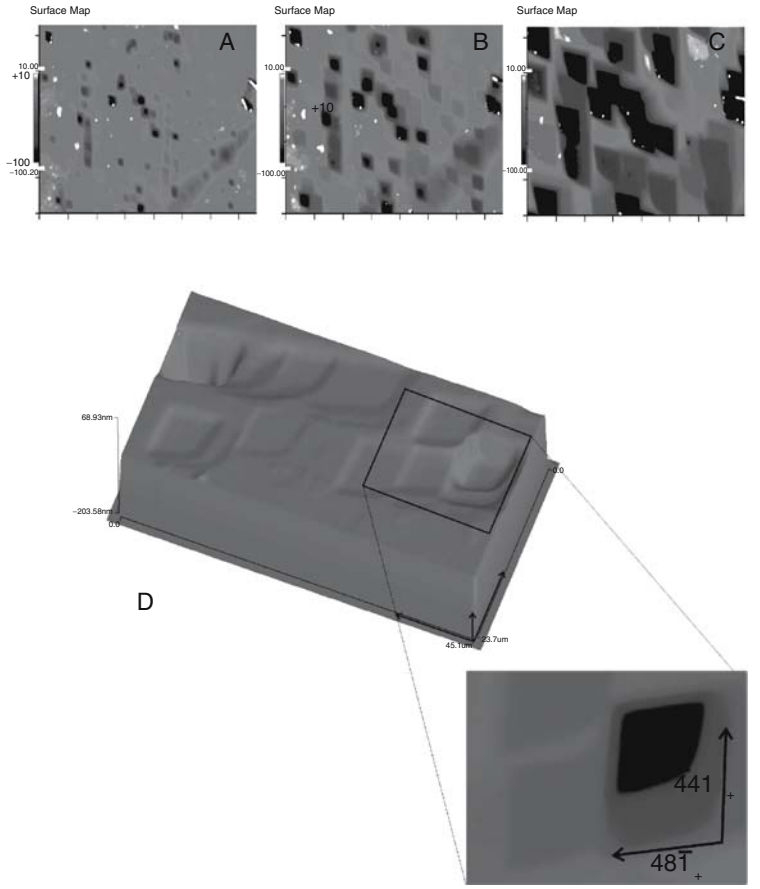

Fig. 3.6 Vertical scanning interferometer (VSI) surface height data of a calcite cleavage surface reacted in an undersaturated, carbonate-buffered solution. Time steps are shown at (**a**) 1, (**b**) 2, and (**c**) 4 h. Note expansion and ultimate coalescence of etch pits as reaction proceeds at a steady ready. (**d**) Detail of etch pits, showing variation of height (and thus step spacing). (Reprinted from Arvidson et al., 2003, Copyright (2003), with permission from Elsevier)

Figure 3.6 shows a typical calcite surface undergoing dissolution. This surface evolves from a state characterized by widely separated etch pits (Fig. 3.6a) that appear to have little effect on one another, to one in which pits have completely coalesced (Fig. 3.6c). The internal topography of the pits themselves (Fig. 3.6d) reflects local variation in terrace width (step spacing). Because this spacing is a product of step–step interactions, the velocity of a given step is dependent in a complex fashion on the proximity of neighboring steps. This condition in turn affects the contribution of "reactive" surface area to total surface area. Furthermore, we must also consider if such a system is capable of achieving a "steady-state" status, such that the overall dissolution rate, integrated over a sufficiently large surface area, converges on a constant value (see also Chap. 5). Dissolution experiments involving mineral powders and flow cells typically acquire a near-constant rate value; however, VSI (see below)

observations involving large single crystals tend to show a steady evolution in the distribution and organization of surface features and topography. The point here is that observations of crystal surfaces at ever-increasing resolution do not reveal simpler structures: even at very high resolution, the complexity of the surface itself and the dynamic interaction of surface topographic components underscore the need to understand their scale dependence in a rigorous, quantitative way.

Above we have illustrated the complexity of the scaling problem in a general way. In our further discussion we will try to introduce concepts and analytical tools that allow us to explore the fundamental nature of this problem in much greater detail. However, it is important to note that the data collected at the various scales are only the prerequisites; the main task is the integration of those results.

3.1.5 A Schematic View of the Surface Structure: The Importance of Defects and Dislocations

The study of mineral–water interface interactions bears close and obvious application to man-made materials as well, including synthetic crystals, glasses, ceramics, concrete, and metals. In this discussion we will focus completely on crystal surfaces. We define a crystal as a solid structure in which the building blocks, i.e., molecules or atoms, are ordered into 3-dimensional periodic lattice. We can understand crystallization as a process of *self-organization*, driven by a thermodynamic engine but controlled by kinetics (see also Chap. 7). This control exists regardless of whether the mobile phase is derived from a melt or from aqueous solution. Because the process is highly dynamic a large number of building blocks are involved, and natural systems always contain impurities, errors in construction are very likely to occur. The example of a unit mm^3 volume quartz crystal illustrates the complexity of the task. Such a relatively small crystal contains approximately 2.7×10^{19} Si- and O-atoms. These construction errors, lattice defects acquired during self-organization, are termed *dislocations*, and are invariably present in real crystals. We distinguish plane, line, and point defects (e.g., Fig. 3.7 for definitions; see also Klein, 2002). The distribution of dislocations in a given crystal depends strongly on the conditions that prevailed during the process of initial crystallization and growth. Minerals usually contain large numbers of different dislocations, with dislocation densities (having units of dislocation line length per unit volume) ranging from 10^4 to $10^{10}\,cm^{-2}$ (see e.g., Blum et al., 1990).

A significant amount of work has been performed to study and understand dislocations and their role in crystal growth and dissolution kinetics (e.g., Burton et al., 1951). Here, we will focus on the effect that dislocations have when they outcrop at the crystal surface. Some of these dislocations create a misfit and, therefore, a distortion of the crystal lattice (see also Lasaga, 1998 for a treatment of dislocations). An important type of line defect is the *screw dislocation*. Atomic force microscopy (AFM) studies often show a step at the surface that is created by such a dislocation (Figs. 3.8a and 3.9). In addition, the distortion of the crystal lattice creates a strain

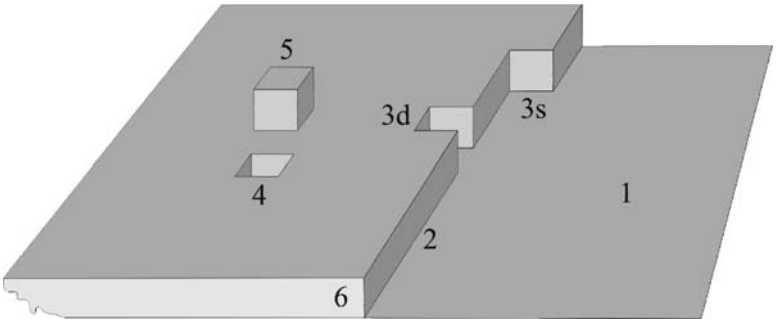

Fig. 3.7 Schematic representation of crystal surface, showing (1) atomically flat terrace, (2) step, (3) kink site ("3d" refers to "double", "3s" to "single" kink site), (4) hole or vacancy, (5) adatom, and (6) corner

field around the center of the dislocation. Therefore, such defects are important features in crystallization or dissolution processes. They are the centers for etch pits or growth spirals (Figs. 3.8b and 3.9). In the 1950s Burton, Cabrera, and Frank (BCF; Burton et al., 1951) recognized the importance of dislocations for crystal growth and dissolution and treated them specifically in their BCF theory. More recently, Lasaga and Lüttge (2001) have also presented a model of crystal dissolution that revolves around the role of dislocations (see discussion below).

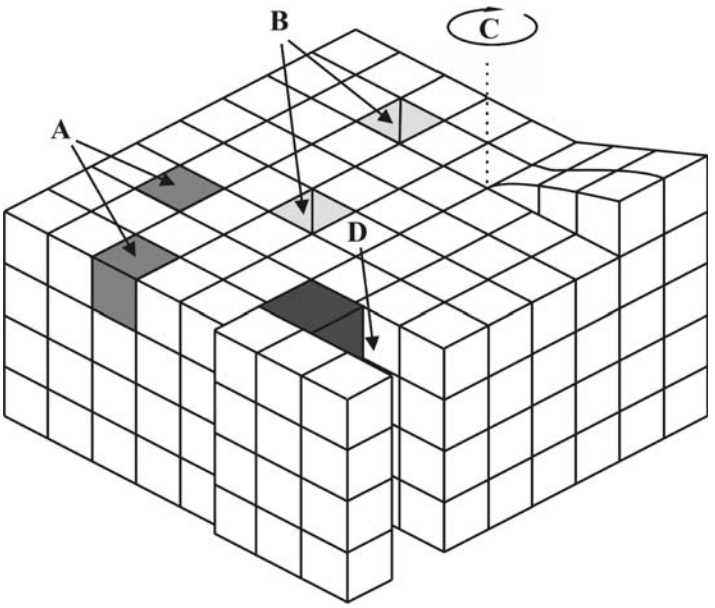

Fig. 3.8 Surface defect types, showing (**a**) impurity misfits, (**b**) point defects, (**c**) positive screw dislocation, and (**d**) line defects

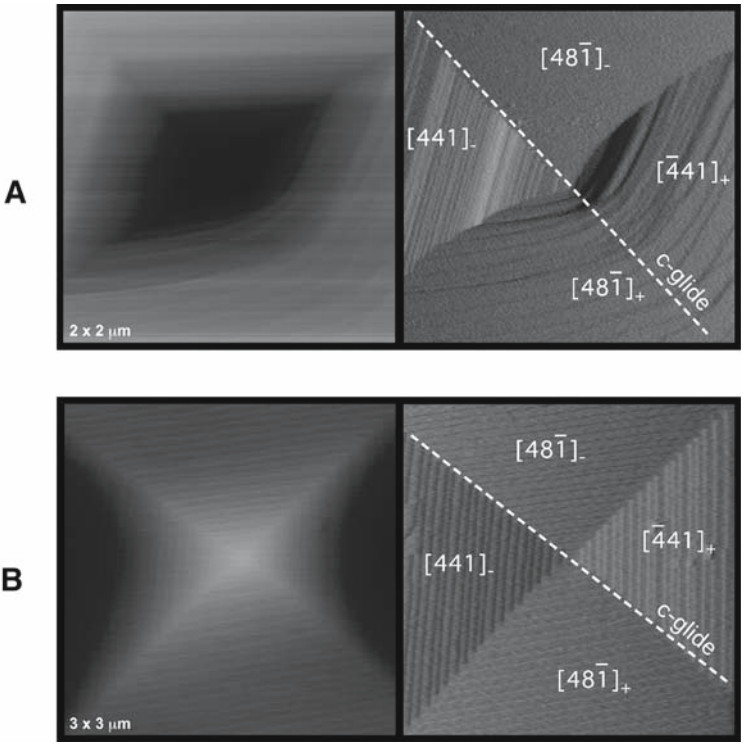

Fig. 3.9 AFM images of screw dislocations expressed on calcite (104). **a**: Dissolution spiral. **b**: Growth hillock. Indices refer to step directions on the surface, with $(+)$ and $(-)$ symbols denoting anisotropic inequivalence of steps. (Davis, Arvidson, and Luttge, unpublished data)

Dislocations are largely responsible for the specific reactivity of a given crystal surface. Dislocation-free surfaces will have a predictably smaller reactivity than surfaces with high dislocation densities. However, over long periods of time, large enough crystal surfaces will develop a steady state rate of dissolution that is not strongly dependent on their dislocation density (e.g., Blum et al., 1990). The observation that similar crystal surfaces often develop significantly different reactivity has caused large concern and has led to the concept of *reactive* surface area.

3.1.6 Introduction to the Processes of Adsorption, Dissolution, Nucleation, and Growth

Mineral–water interactions occur primarily at the external mineral surfaces (see discussion in Hochella and Banfield, 1995). These processes are typically "surface-controlled" at the temperatures and pressures at or near the Earth's surface. By "surface-controlled," we mean that the reaction rate is limited by the basic molecular

processes that finally lead – in the case of crystal dissolution – to the detachment of a molecule from the bulk crystal structure into the solution (see Lasaga, 1998). In contrast, reactions are called "transport-controlled" if the transport of molecules to and from the mineral surface into the bulk solution is rate limiting (e.g., Lasaga, 1998). The latter case is observed if the transport of molecules into the solution is slower than all the processes that lead to the formation of an adatom. An example for such a situation is no significant flow of the fluid across the mineral surface, i.e., stagnant fluid conditions often observed on internal surfaces (see below).

In all other cases, the reaction becomes surface-controlled. If this is the case, measured overall reaction rates are directly proportional to the surface area involved and thus must be normalized by a surface area term. Therefore, we will focus next on methods and problems of surface area quantification. Before we do that it makes sense to recall that adsorption, surface nucleation, dissolution, and crystal growth are all microscopic processes that occur at the mineral surface. Therefore, we will also focus on some techniques that allow us to observe these processes at different lengths and time scales.

3.2 Quantification: The Key to Understanding Mineral–Water Interface Processes

The mineral–water interface can be characterized both chemically and topographically, and a number of sophisticated analytical tools are available. In addition to analytical equipment, we can also employ powerful theoretical models and techniques, such as Monte Carlo and *ab initio* techniques to generate computer simulations of the mineral–water interface and the processes that are likely to change it. Before we introduce the different strategies and techniques in more detail, we will lay out a concept of the crystal surface and the various processes that can occur on it and alter it.

3.2.1 The Concept and Quantification of Surface Area

Mineral dissolution rate can be cast in a rate equation like

$$R = A \cdot k \cdot f(\Delta G), \tag{3.2}$$

where R is the overall dissolution rate of the reaction, k, is the rate constant, ΔG is the difference in Gibbs free energy between the solid and its dissolved molecules, and A is the surface area that participates in the dissolution process (see Chap. 5). Therefore, as long as the dissolution reaction is surface-controlled, we need to normalize bulk reaction rates by the surface area involved in the dissolution process to obtain the rate constant, k, in units of mol $m^{-2} s^{-1}$. An outstanding question that has received considerable attention in the literature is how to "correctly" quantify

the surface area involved in crystal–fluid interaction (e.g., Hochella and Banfield, 1995; MacInnis and Brantley, 1992, 1993; Gautier et al., 2001; Jeschke and Dreybrodt, 2002; Metz et al., 2004). Theoretically, there are three different possibilities that could be used by researchers: (1) *geometric*, (2) *total* or *BET* surface area, and (3) the so-called *reactive* surface area. Practically, however, only BET surface area is a robust measurement. In the following, we will briefly discuss these definitions and concepts of surface area. For a comparison and discussion of model results of geometric, total, and reactive surface area and the development of the differently defined surface area values during a dissolution process, see Lüttge (2005).

3.2.1.1 Geometric Surface Area

Geometric surface area is merely an abstraction or estimate that is usually calculated from the crystal dimensions and, therefore, requires an often simplified model of the mineral grain, e.g., a sphere (A), cube (B), or rhombohedron (C). We can then calculate the related geometric surface area: (A) $A_{\text{geo\_sphere}} = 4\pi r^2$; (B) $A_{\text{geo\_cube}} = 6a^2$;$A_{\text{geo\_rhomb}} = 2a^2 + 4ab$. At the same time it is obvious that geometric surface area does not consider any surface topography or roughness that might be present in the form of holes (e.g., etch pits or pores) and steps. If we assume an atomically flat crystal surface, we ignore such surface features that would of course add to the total surface area of the crystal or mineral powder (compare Figs. 3.10 and 3.11). Therefore, geometric surface area presents usually a minimum value and tends to underestimate the total surface area. To cure this problem, sometimes a "surface roughness factor" is introduced (e.g., Anbeek, 1992; see also below). If geometric surface area is calculated for a mineral powder, it also will depend on the way we compute the average grain diameter. In other words, the surface area will depend on the grain size distribution within the grain population or sample of interest.

3.2.1.2 Total Surface Area

Unlike geometric surface area, total surface area, A_{total}, accounts for the additional surface area that is created by surface roughness. Figure 3.10 illustrates that steps, hillocks, pits (these may also exist as microporosity), and cracks enlarge the actual surface area of a crystal significantly. As said above, this additional surface area can be accommodated through provision of a surface roughness term, λ, defined as (Helgeson et al., 1984))

$$\lambda = A_{total}/A_{geom}. \tag{3.3}$$

The additional area supplied by roughening may represent a large fraction of the total surface area, but can also vary significantly (e.g., Fig. 3.10). It is interesting to give some implications of pit size and pit density in a crystal surface a closer look. The surface area of a uniformly rough surface containing a large number of small pits or pores is not necessarily larger than that of a flat surface containing only one or two large pits (Fig. 3.11). Therefore, it is not always easy to *estimate* roughness

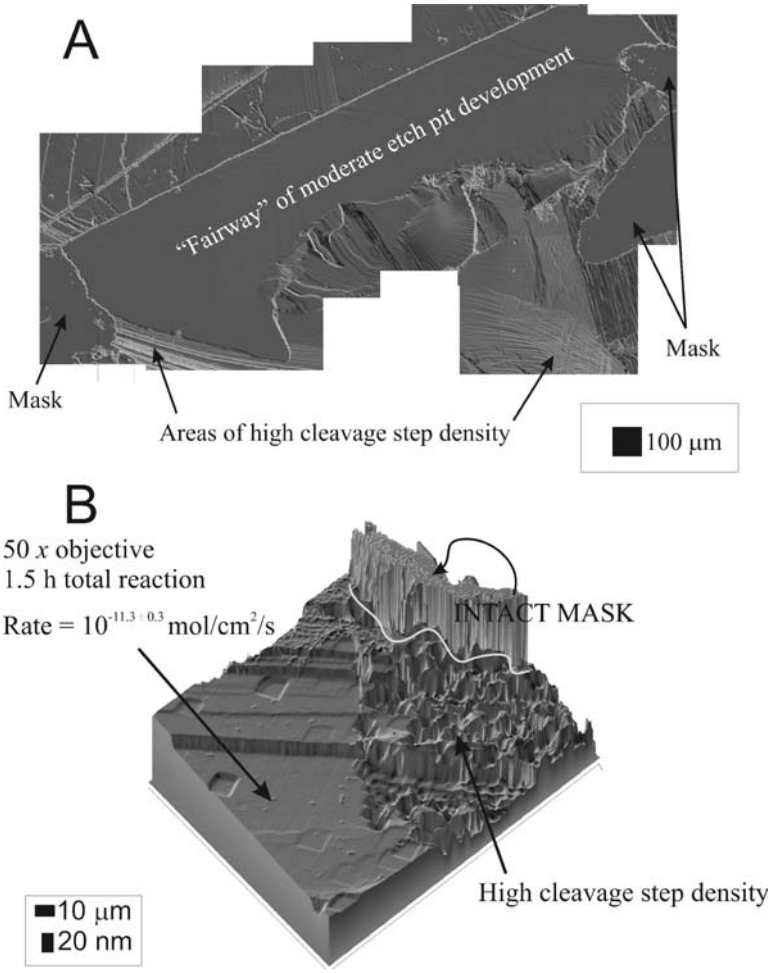

Fig. 3.10 Variation in surface area from VSI data, due to roughness (A, 10 × objective) and etch pits (B, 50 × objective), developed during dissolution of calcite (104) surfaces. (Arvidson and Luttge, unpublished data)

with sufficient precision. A common way of *measuring* total surface area is by gas adsorption. If we consult research papers and textbooks, we find that the term "total surface area" is often used synonymously with "BET" surface area.

3.2.1.3 BET Surface Area.

The acronym BET is created from the initial letters of three scientists, Brunauer, Edward, and Teller, who developed this elegant and efficient technique to quantify surface area in 1938 (Brunauer et al., 1938). Their apparatus measured the amount

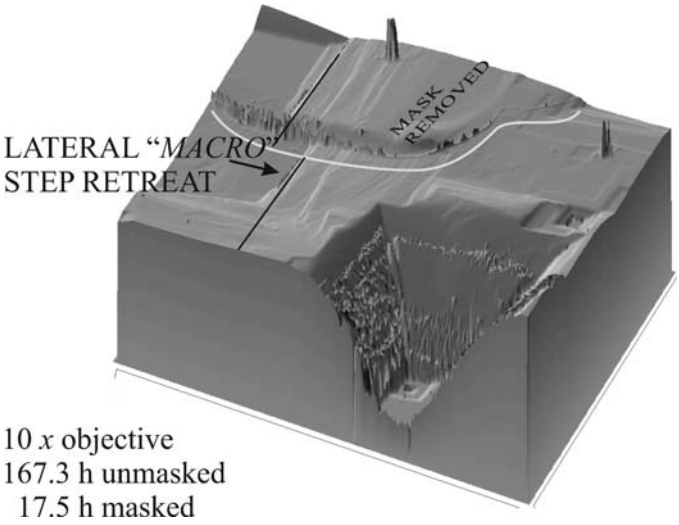

Fig. 3.11 Variation in scale of etch pit development in calcite after long term dissolution. Compare large pit at bottom with newly developing pit on shoulder. VSI, 10 × objective; compare scale with that in Fig. 3.10. (Arvidson and Luttge, unpublished data)

of an inert gas adsorbed on the sample surface under controlled conditions at a specific temperature (hence, an equilibrium adsorption *isotherm*). A key assumption is that the gas adsorbs in a monomolecular layer on the sample surface. In practice, BET techniques work well for a relatively large surface area, i.e., $1–1,000\,m^2/g$ (or larger). Smaller surface area values are difficult to measure with sufficient precision. However, measurements of specific surface area as low as $0.1\,m^2/g$ can be made by using krypton as the adsorbate gas. In addition, analysis of the isotherms at low partial saturation pressures can also reveal the distribution, size, and structure of nanometer-scale porosity (*micropores*) developed on the surface. The extent to which the BET surface area measurement reflects the total surface area is a function of both the gas used and the structure of the solid surface. These issues are discussed in detail in Brantley and Mellot (2000).

The chief merit of BET surface area measurements is that they represent a reliable and reproducible quantification of *total surface area* of a given mineral sample; however, these measurements are most probably not equivalent to other estimates of "surface area". Because of the need to normalize reactions with respect to surface area, these discrepancies are a key source of confusion and potential controversy. Their distinctions are discussed extensively below.

3.2.1.4 Specific Surface Area

Before we will discuss the concept of reactive surface area we introduce another term, often used in the literature: *specific* surface area. This term defines the (total) surface area of, e.g., a crystal or mineral powder divided by the mass of the sample

material. Note that the specific surface area of the same mineral or mineral powder, e.g., calcite can vary depending on the crystallographic form and the grain size of the sample material.

3.2.1.5 Reactive Surface Area

The introduction of *reactive* surface area by Helgeson et al. (1984), and later Hochella (1995) and Brantley and Chen (1995) has introduced a much more complex concept of surface area. This new concept has improved our thinking and has inspired an intensive discussion in the field of geochemical kinetics and mineral weathering. If we want to visualize what reactive surface area is, we can study Fig. 3.7 again, which was introduced earlier. Recall that it shows schematically five different energetic sites at a given crystal surface: (1) the bulk surface or terrace site with the maximum numbers of bonds and the minimum surface area, (2) the step position; (3) the kink site position, (4) the corner position, and (5) the adatom position with only one bond and the largest surface area. Any surface that is not atomically flat will have a density and distribution of these different sites across its surface, and the reactivity of each site varies. If a crystal surface is completely flat, its reactivity is defined by the site (1) molecules. In contrast, if a surface is rough and has high step density, it must be recognized that site (2) and site (3) molecules have a higher probability of reaction. The concept of reactive surface area (e.g., Hochella, 1995; Brantley and Mellot, 2000) recognized that certain areas of the crystal surface are significantly more reactive than others, but only considered features that were larger than the molecular sites above, e.g., steps or the outcrops of dislocations. However, it has become clear that the number and distribution of the molecular sites at a crystal surface will define its reactivity, a point that underscores the importance of scale in mineral reaction kinetics.

Many observations have indeed demonstrated that the highly reactive parts of the surface lead to the formation of etch pits, leading to increased surface normal retreat. The surface area between the etch pits is considered significantly less reactive. Therefore, there is usually agreement that reactive surface area is often significantly smaller than the total surface area. It has also been demonstrated that reactive surface area can change significantly over time. Unfortunately, this change can not be monitored easily in the laboratory.

The scenario of reactive surface area requires a modification because studies of crystal cleavage surfaces demonstrate that the entire crystal surface retreats during dissolution (for example, Lüttge et al., 1999, 2003). This retreat is not caused solely by the growth and coalescence of etch pits. Based on these observations Lasaga and Lüttge (2001, 2003) have suggested that etch pits are also the sources for so-called "dissolution stepwaves". These trains of steps travel across the surface and therefore are the main cause of surface-normal retreat and thus the overall dissolution rate. This model is now well supported by observations made by vertical scanning interferometry and AFM (Tang et al., 2001, 2003, 2004; Arvidson et al., 2003, 2004, 2006; Vinson and Lüttge, 2005). The stepwave model implies that the entire surface

is reactive. If we wish to quantify reactive surface area purely in geometric units, we can distinguish only between reactive or non-reactive surface area. However, the stepwave model is consistent with a (variable) degree of reactivity for all surface sites. Beside our common question "how large?", we also have to ask "how reactive?". We can answer these questions only if we add a second term that describes the reactivity of a given surface in addition to the geometric term that describes the size of the surface area undergoing the dissolution reaction. However, more work is needed and a detailed discussion of this topic is in preparation.

3.2.1.6 Internal Versus External Surface Area

Before we continue on, we have to make an important distinction between *internal* and *external* surface area (Hochella and Banfield, 1995). In their detailed contribution, Hochella and Banfield have given a very useful and thorough discussion of the topic including several definitions. Here, we can highlight only the main thoughts of this discussion. First, we follow the authors' preference for a working definition of external versus internal surface area based on the fluid interaction with the mineral grain. In this context, we can define as an external surface area the portion of the surface over which a fluid is free-flowing. Then, in contrast, we define as internal surface area the portion of a surface that is not in contact with the fluid (pores) or only in contact with the fluid under stagnant conditions. It is important to note, that the actual physical definition of external and internal surface area could be quite different. For example, if a mineral surface contains deep narrow channels, the surface area of the channels would count physically towards the external surface area. However, it might not contribute or only insignificantly contribute to a dissolution process. Therefore, from a dynamic fluid–solid interaction standpoint, it makes good sense to use our definition above. For further reading, we refer the reader to in-depth discussions available in White and Peterson (1990), Hochella and Banfield (1995), Brantley and Mellot (2000), and references therein.

3.3 Analytical Methods

3.3.1 Quantification of Surface Topography

3.3.1.1 Atomic Force Microscopy (AFM) and In Situ Measurement of Surface Dynamics

Over the past 10 years, atomic force microscopy (AFM) has emerged as a valuable technique for high-resolution imaging of mineral growth and dissolution. This is accomplished through the use of a stylus, or tip, to sense mineral-surface topography rather than the optical beam paths utilized by other microscopy techniques. As the extremely sharp tip is scanned across the sample surface by a piezoelectric scanner,

the topography of the surface causes the tip to deflect as the force between the tip and sample changes. These deflections are monitored by a laser beam that is focused at the end of the cantilever holding the tip. The x, y, and z displacements of the piezoelectric scanner that are required to maintain constant force between the surface and the tip are converted into a topographic map of the surface by a computer.

The power of this technique lies in its ability to track the motion of monomolecular steps *in situ*, as a function of solution composition in a flow-through environment. Ultimately it is the collective motion of steps on the surface that accounts for the macroscopic behavior observed in a given solution and it is at this scale that gaps in our understanding of the bulk system may be most directly addressed. The small length-scale of observation has the added advantage that changes in solution chemistry are immediately detectable at the surface, reducing measurement acquisition times and maximizing the precision by which solution chemistry can be controlled.

Geochemical investigations using AFM have generally focused on microtopographical features, such as growth hillocks or etch pits, generated by mineral-surfaces during growth or dissolution (see Fig. 3.9a,b). These features provide a collection of steps whose step velocity can be efficiently measured as a function of crystallographic orientation. The morphology and kinetics of development of these features has proven to be extremely sensitive to changes in solution chemistry and have been instrumental in achieving a mechanistic interpretation of growth and dissolution in the context of solution composition and impurity concentrations (Burton et al., 1951).

3.3.1.2 Interferometry Techniques

The use of interferometry techniques in earth science is a relatively new method. Therefore, we take here the opportunity to introduce this technique in more detail than the already largely established methods. Interferometry provides surface topography information over a wide range of length scales. Satellites for example use interferometry techniques to quantify the topography of the earth surface and its changes at the meter to kilometer scale. Since the pioneering work of Tsukamoto (1983, 1994), Onuma et al. (1989, 1990), Maiwa et al. (1990), Ohmoto et al. (1991), Vekilov et al. (1990), MacInnis and Brantley (1992, 1993), and later Lüttge et al. (1999), Li and Tsukamoto (2001) the technical progress allows us today to quantify surface topographies of minerals and other solids routinely. These much smaller surfaces can be quantified at the nanometer to centimeter scale by using Mirau or Michelson interferometric techniques (e.g., Lüttge, 2004a). Below, we focus on a special type of light interferometry that is increasingly used as a powerful research tool, i.e., vertical scanning Mirau interferometry.

Lüttge and coworkers (Lüttge et al., 1999, 2003; Lüttge, 2004a) introduced vertical scanning interferometry (VSI) and its application to mineral dissolution and growth. Schematic sketches, for example, of some of the principles of white light VSI can be studied in these publications. Thus, we can limit our discussion here to a

Fig. 3.12 Current generation vertical scanning interferometer. MicroXAM instrument, similar to that used to produce the VSI data within this paper (ADE-Phase Shift). This instruments utilizes Mirau optics, and was originally developed for purposes of quality control metrology in the semiconductor industry. Scanning interferometers permit high resolution, non-contact, rapid scanning-mode data acquisition of crystal surfaces, together with sophisticated data reduction and filtering routines (http://www.phase-shift.com/products/microxam.shtml)

brief summary. Figures 3.2, 3.6, and 3.9–3.11 show some typical examples of height maps produced with a Mirau vertical scanning interferometer. This instrument resembles a high-end optical microscope (Fig. 3.12). These instruments use reflective light as the analytical probe. The instrument achieves its high vertical resolution at the angstrom- to nanometer-scale by adding a piezoceramic for a z-scan of the sample. The lateral resolution, in contrast, depends on the resolution of the Mirau objective used. The field of view of an interferometer is generally larger than that of an AFM. As an example, a surface area of almost 1 mm^2 and up to 20 μm of surface relief can be quantified in less than 10 s.

With the help of a reference surface within the field of view VSI can precisely quantify both the absolute topography of a crystal surface and critical changes in this topography due to ongoing dissolution, corrosion, or growth processes. The measurements of surface-normal height changes can then be converted directly into dissolution or growth rates and averaged over the entire solid surface. This leads to a rate constant that is independent of any external measurement of the surface area, e.g., BET surface area (compare discussion above). Note, that the lateral resolution of the VSI system defines the "footprint" of a pixel (e.g., 500×500 nm), and that each height measurement, therefore, represents an average height across the pixel.

In this way, the interferometer quantifies surface topography in great detail (e.g., Figs. 3.2, 3.10, and 3.11). Time-lapse observations quantify the evolution of surface topography (Fig. 3.6). Recall, rates determined with VSI are based on

surface-normal velocities. An example is the change in height, h, of a given point (i, j) on the (hkl) crystal surface during the time interval from t_1 to t_2

$$\frac{\Delta h_{i,j}}{\Delta t} = \frac{h_{i,j2} - h_{i,j1}}{t_2 - t_1} \tag{3.4}$$

$$= v_{i,j(hkl)}, \tag{3.5}$$

where $v_{i,j(hkl)}$ is the velocity of dissolution or growth of every i, j coordinate at the (hkl) surface in units of $[\mathrm{m\ s^{-1}}]$. The rate constant, $k_{i,j}$, is then computed by dividing by the molar volume $(\overline{V})$ of the material dissolved or grown,

$$k_{i,j} = v_{(\mathrm{hkl})} \cdot \bar{V}^{-1}. \tag{3.6}$$

Rates computed in this way have units of flux $[\mathrm{mol\ m^{-2}\,s^{-1}}]$. Now, we sum all local rate constants, $k_{i,j,}$ and take the average,

$$k_{(hkl)} = \sum \frac{k_{i,j(hkl)}}{N_{i,j}}, \tag{3.7}$$

to obtain a rate constant $k_{(hkl)}$ for the entire surface. $N_{i,j}$ is the number of all pixels, ij, measured in a VSI scan. One scan provides typically up to 100,000 height data. From this treatment, we see that the rate constant is itself not a "true" constant but depends on the number and distribution of sites across the crystal surface. This approach leads directly into a statistical treatment of reaction rates on the crystal surface (e.g., Lüttge, 2004a).

3.3.1.3 Electron Microscopy (EM) Techniques

Scanning electron microscopy (SEM) is a robust microanalytical tool. It can provide images of the sample surface resolving surface features and microtopography significantly smaller than could otherwise be resolved by using a conventional light optical microscope. In addition, SEM can also provide valuable chemical information of the surface under investigation. However, all data, whether chemical or physical, are generated by the same principal technique. An electron source, i.e., a cathode, emits electrons which are accelerated and focused into a narrow electron beam by several electromagnets. This beam scans the sample surface while bombarding it with primary electrons. This bombardment of the sample surface causes interaction between the primary electrons and the sample. In this process, back-scattered electrons (BSE) and secondary electrons (SE) are generated and both can be used to render an image of the surface topography. The depth of investigation varies (on the order of a few microns) according to the beam energy and as a function of the element undergoing interaction with the beam. The results of the interaction are recorded by different detectors. During electron bombardment, x-rays are also emitted, whose spectra can be measured either according to their energy (EDS, energy dispersive spectroscopy) or wavelength (WDS, wavelength dispersive spectroscopy). The computer-controlled

EDS system provides a fast elemental analysis of the sample surface. The depth of information obtained by this method depends strongly on the power, i.e., the acceleration and the focus of the electron beam. For a variety of reasons (Goldstein et al., 1992), EDS generally produces rapid but semi-quantitative results, and greater accuracy can be achieved using WDS in an electron microprobe. WDS permits high elemental resolution and low detection limits, and also requires instrumental calibration against standards of known composition. Some SEM instruments can also be equipped with one or more WDS detectors.

In the general application, scanning electron microscopes are used to image the sample surface. The range of samples that can be investigated is enormous. In mineralogical and geochemical applications we can study mineral powders as well as singles crystals. However, it is important to note that in standard SEMs a high vacuum must be maintained for the electron beam and all non-conductive samples must be coated with a conductive coating (e.g., carbon, gold, or gold-palladium). The coating prevents the build up of electrons on the sample which would otherwise lead to surface charging. A recent technological breakthrough, i.e., the environmental SEM (ESEM) circumvents the necessity of the coating and the required high vacuum. The ESEM can function with little or no vacuum and without the need to sputter the sample surface with a conductive coating. This technique allows even the examination of liquids as well as delicate biological materials. For further reading we refer to Krinsley et al. (1998) and Goldstein et al. (2003).

3.3.2 Quantification of Surface Chemistry and Structure

3.3.2.1 X-Ray Photoelectron Spectroscopy (XPS)

XPS has been in widespread use for over 30 years, and has been reviewed in several excellent monographs (see e.g., Briggs and Seah, 1983; Hochella, 1988). XPS consists of measuring the kinetic (binding) energy of photoelectrons produced during interaction with an x-ray source. Because the mean free path of the emitted electrons is very small, electrons that escape the surface for detection originate from the uppermost few monolayers. In addition to elemental composition of the surface and near-surface layers, XPS is also sensitive to the chemical environment of these elements, including oxidation and (by inference) coordination state. Angle-resolved XPS (AR-XPS) provides a non-destructive means of analyzing compositional change with depth. In this approach (Fig. 3.13), x-ray excited photoelectrons and Auger electrons are selectively analyzed as a function of their take-off angle, θ. The main advantage of this technique lies in the capability of obtaining quantitative chemical determination of the species distribution with respect to depth via a non-destructive approach that avoids the use of an ion beam. In examples described below, AR-XPS has been successfully applied to characterize thin films as a function of depth (e.g., Biino et al., 1999; Boughriet et al., 2000). By varying the take-off angle θ it is possible to tune the escape depth (or inelastic mean free path)

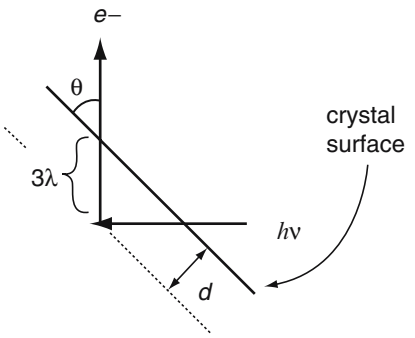

Fig. 3.13 Principle of angle-resolved XPS. Because the probability of electron escape decays as exp(-λ), where λ is the depth of origin, 3λ is typically taken as the limit of investigation ("information depth"), and thus $d = 3\lambda \sin \alpha$, where d is the analysis depth measured normal to the surface plane. The take-off angle, θ, lies between the sample plane and the analyzer axis

of the emitted photoelectrons and differentiate the chemical species and composition present at the surface and few monolayers below, as well as in the bulk sample. In addition, the thickness of the surface phase can be estimated by measuring the ratio of the relative intensities of one of the elements (e.g., Ca, C or O) at both high grazing and normal incidence angles (10° and 45°).

3.3.2.2 Secondary Ion Mass Spectrometry (SIMS)

Secondary Ion Mass Spectrometry is a highly sensitive surface technique for characterizing materials, and can be used as a complementary technique to XPS. The principle of the method is based on the mass analysis of secondary ions created through the interaction of a beam with the surface of a solid. The impinging ion beam, usually referred to as the primary ion beam, can be formed from inert ions (e.g., Ar^+), reactive ions (e.g., Li^+, Cs^+ or O^-) or molecular ions (e.g., Au clusters) and is generally accelerated to energies between 0.2 and 40 keV. Liquid Ga^+ beams are usually used for imaging and mapping the surface elemental distribution.

During the bombardment by ions or neutral particles, surface particles are sputtered and the primary impinging particles are implanted into the condensed phase. A small fraction of these sputtered atoms and molecules become further ionized at or above the sample surface. Charged ions are then extracted, their mass separated, and detected by one of a number of charged particle counting systems. SIMS techniques are also now in common use, and have been successfully used to measure the elemental composition of many important mineral phases, including silicates, oxides, and both abiotic and biogenic calcites (Jeffree et al., 1995; Vering et al., 2003; Denniston et al., 1997; Finch et al., 2001; Huang et al., 2001; Hoffmann and Stipp, 2001).

3.3.2.3 X-Ray (Grazing Incidence) Diffraction

Since the pioneering work in x-ray diffraction by crystalline materials by Friedrich et al. (1912), Ewald (1913), and Bragg (1912), this technique has been an established one for studying crystal structure. *Powder diffraction* methods are now used

routinely for tasks of phase identification, structure refinement, analysis of crystal strain, particle size distribution, and order-disorder relations. This work has been brought to an increasingly high level of sophistication with the availability of high intensity synchrotron beamlines coupled with state-of-the-art data reduction, analysis, profile fitting, and modeling capabilities. The expression of these basic relationships is the well-known formulation (Bragg's Law),

$$\nu\lambda = 2d\sin\theta, \tag{3.8}$$

which represents the diffraction condition resulting from incidence of source radiation having wavelength λ (ν in an integer) at a given angle θ. Diffraction results from the constructive interference of spherical waves scattered by planar sheets of atoms, that are in turn separated by a lattice unit (d) (see Fig. 3.14a). However, the diffraction condition acquires information from within the bulk crystal as well, thus increasing the depth of investigation well beyond the surface itself. If our aim is to selectively acquire information only from the uppermost atomic layers of the crystal, the incident beam geometry must be confined to a very shallow ("grazing") angle with the surface, typically 1° to 3°. By adjustment of a incident angle, depth penetration within the surface can be simultaneously limited to ~10–200 nm (the lower limit is composition dependent); the reduction in analytical volume in terms of depth, however, can be compensated by an increase in the path length of the beam through the sample, giving rise to an increase in signal intensity above background. During data acquisition, only the detector (2θ angle) is varied, thus maintaining a constant path length and sample volume. This geometry requires the use of a highly collimated incident beam and a detector slit assembly to create near parallel beam conditions. The results can be used to quantify the composition of overgrowths or alterations of the crystal surface with respect to the bulk crystal (Fig. 3.14b).

3.3.3 Integrated Quantitative Studies

As we have emphasized above, complex problems involving the mineral–water interface require a multi-dimensional approach, with various surface instruments employed to elucidate particular aspects of a given problem. An example of such a problem is the interaction and fate of uranyl species in contract with carbonate minerals. Boughriet et al. (2000) have explored the reactivity of UO_2^{2+} towards the surface of vaterite (orthorhombic $CaCO_3$), and the effect of this metal on the rate of transformation of this metastable phase to calcite. With the exception of AFM and VSI, their approach combined many of the techniques described above, with each devoted to quantification of either bulk (XRD, infrared (IR) spectroscopy, ICP-AES, thermogravimetric analysis) or surface (SEM, angle-resolved XPS, confocal laser Raman microscopy, BET) physical and chemistry properties. These data were used to (1) quantify the rate of transformation of vaterite → calcite, (2) to define a relationship between this transformation rate and the

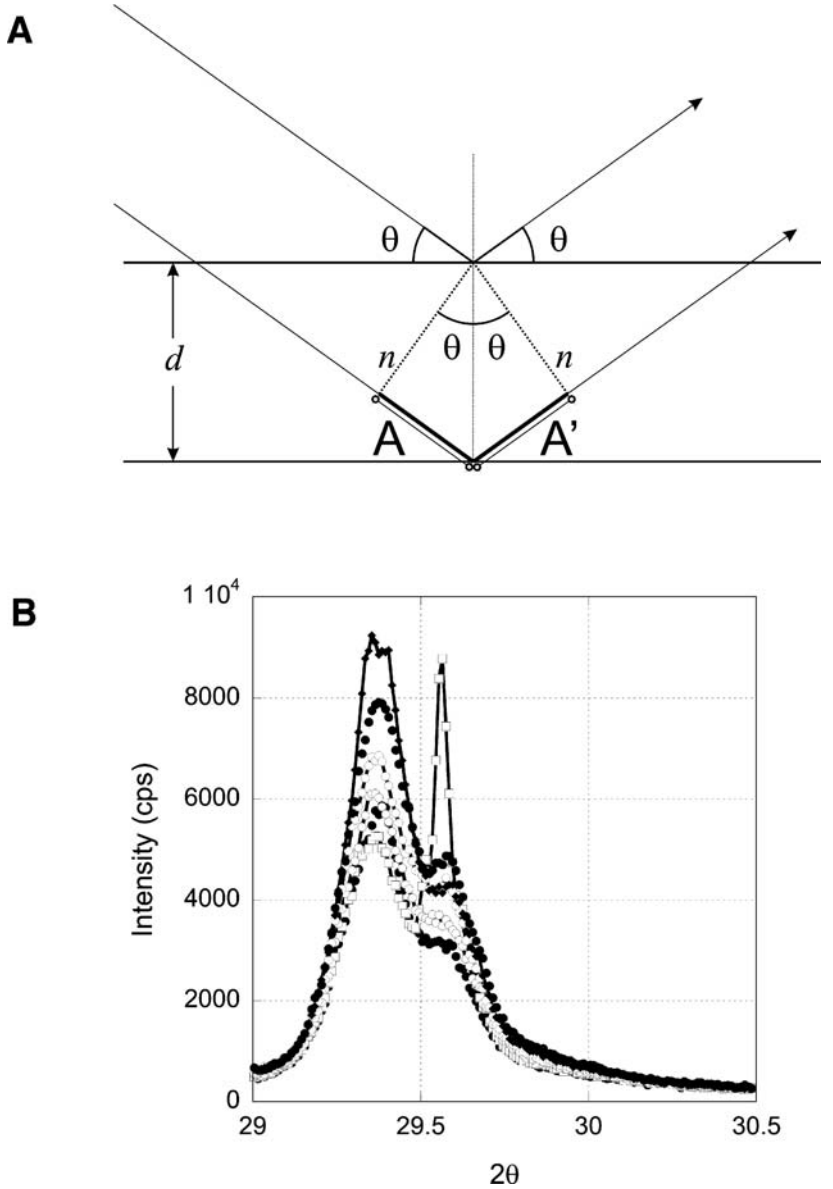

Fig. 3.14 X-ray diffraction. (**a**) Diffraction results when x-ray radiation interacts with the electron clouds of atoms that make up the crystal, shown here as parallel planes. Rayleigh scattering results in re-radiation; constructive interference produces an increase in intensity (Bragg peaks) only at specific angles (θ), for which the extra path length $A + A'$ is an integer (ν) multiple of the radiation's wavelength (λ). Wave normals are referred to by n, lattice spacing is given by d. This relationship is formalized as Bragg's law. (**b**) Application of shallow angle incidence diffraction in a single calcite crystal with Mg-rich overgrowth. Different curves correspond to variation in depth of investigation. (Arvidson and Luttge, unpublished data)

formation of $(OH, H_2O, UO_2, Ca)CO_3$ surface complexes, (3) to quantify changes in porosity that attend surface overgrowth development, and (4) to explore the variation in overgrowth chemistry as a function of depth. Boughriet et al. (2000) concluded that the lower computed solubility of this nascent phase relative to pure vaterite substrate stabilized the surface, and thus inhibited the transformation to calcite.

VSI and XPS have also been combined in a novel approach to study the role of phosphonic acid in the inhibition of calcium silicate and aluminate cement hydration (Lupu et al., 2005). VSI was used as a straightforward means of detecting changes in surface morphology and structure related to the development of Ca–phosphonate complexes. The observed pattern of surface structure reorganization (VSI) and attendant evolution in surface phase composition (XPS) could be explored over relatively long reaction times. The results clearly showed the relationship between the changes in the scale of the inhibition process and the surface area of the host substrate affected; a result unattainable from previous powder-based experiments.

3.4 Approaches to Modeling the Mineral–Water Interface

Above, we have presented a number of powerful analytical techniques that allow us to investigate and quantify the mineral surface, both chemically and physically. In this context, we have discussed the fact that our investigations need to be conducted at a variety of length and time scales to fully understand the complexity and implications of the crystal surface and the processes within the mineral–water interface (compare also Vekilov and Galkin, 2004). However, if we approach the atomic scale in this attempt, direct observations of surface topography and particularly the dynamic changes of topography due to adsorption/desorption and dissolution/growth processes become increasingly complicated or even infeasible.

In this situation, theoretical considerations and molecular modeling techniques, such as those introduced in Chapter 2, allow us often to extend our investigations to the molecular scale. Particularly the rapidly increasing computer power has allowed us to make substantial progress in this field over the last 25 years. Consequently, molecular modeling has developed into a powerful partner for our experimental and analytical efforts. Despite the constantly increasing computer power, we have to make some important decisions of which modeling technique to choose for our problem. Cygan and Kubicki (2001) have assembled a comprehensive overview of the more recent modeling work. Generally, we must decide at which level and at which size we seek to investigate our system. As a rule of thumb we can say that the larger the system the lower level theory we have to use. High level theoretical models using sophisticated quantum mechanical approaches are often limited to molecule clusters, only. Here, we focus briefly on two techniques, *ab initio* modeling, a high level theoretical method, and Monte Carlo simulations, a low-level technique that allows for the consideration of "large" systems. For example,

a system size of 100×100 barite unit cell layers can be explored conveniently with high-end PCs.

3.4.1 Ab Initio and Density Functional Theory Calculations: A Prerequisite for Monte Carlo Simulations

Ab initio means "from the beginning." We use this term because the *ab initio* method does not rely upon empirically- or experimentally-derived parameters (Cygan, 2001). Therefore, it is also often referred to as a *first* principles method (see also Chap. 2). From a practical standpoint, the method seeks numerical solutions to the Schrödinger equation

$$H\Psi = E\Psi \tag{3.9}$$

In this equation, H is the Hamiltonian differential operator, Ψ is the wave function, and E is the total energy of the system. For an in-depth discussion the reader is referred to, e.g., Hehre (1995, 2003), Hehre et al. (1986), Tossel and Vaughan (1992), and Cygan and Kubicki (2001), as well as Chap. 2 of this volume. Today, commercial software packages such as GAUSSIAN or SPARTAN are available to implement this approach, and provide a complete toolbox for many of our modeling problems.

We can apply *ab initio* modeling to mineral–surface reactions and make a significant contribution to our understanding of these processes. In particular, the modeling technique can provide detailed mechanisms at the molecular scale. This approach includes information on: type of bonding, reaction pathways, non-equilibrium configurations, and the energetics, i.e., electrostatic potentials. If sufficiently coupled with our proposed experimentation, this information can play an important role in eliminating hypotheses, focusing on new phenomena and systematizing available experimental data. Examples that show powerful applications to mineralogical and geochemical problems were published, e.g., by Lasaga and Gibbs (1990), Lasaga (1992), Xiao and Lasaga (1994, 1996), and Kubicki et al. (1996).

We can also use *ab initio* modeling to parameterize Monte Carlo simulations (see below). Xiao and Lüttge (2002) used *ab initio* calculations to investigate the detailed mechanism of plagioclase dissolution. The results, e.g., adsorption and bond-breaking energies were then used in Monte Carlo simulations of albite and anorthite dissolution kinetics (Zhang and Lüttge, 2003). Such a combined modeling approach allows us to study the reactivity of plagioclase surfaces (Fig. 3.15a) including the adsorption of H_2O, H^+, OH^- species due to pH variation, the protonation and deprotonation processes, and the formation of possible reaction intermediates. It also allows us to investigate the full reaction pathways of hydrolysis of surface Si–O–Si and Si–O–Al bonds including the relevant transition states (Fig. 3.15c). These results, once coupled with experimental VSI and AFM techniques, provide the ability to extract many kinetics properties such as changes in activation energy, kinetics isotope effects, catalytic effects, temperature effects, and the overall fundamental rate law.

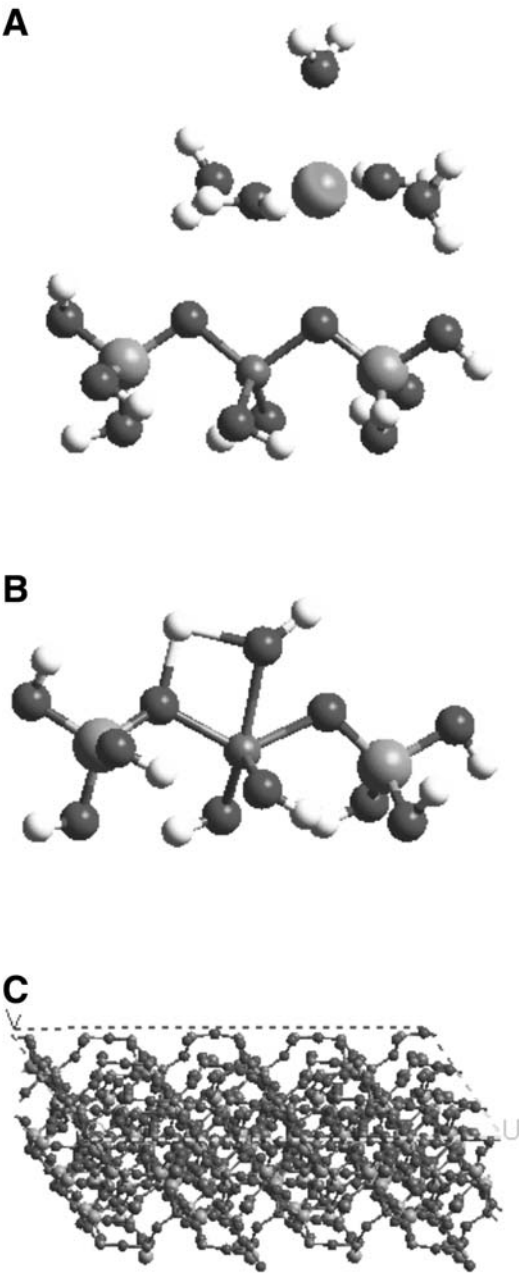

Fig. 3.15 **a**. Anorthite surface cleaved along [100]; **b**. molecular cluster representing prototype albite with an inner-sphere adsorbed Na^+ complex; **c**. optimized transition state structure of a water molecule hydrolyzing the key Si–O–Al–O–Si unit. Si, Al, and Ca are represented by intermediate greys, O by dark grey, H by white, and Na by light grey. (Xiao and Lüttge, 2002)

3.4.2 Monte Carlo Simulations of Surface Topography and Interface Processes

In addition to computer modeling techniques such as lattice dynamics (LD) and molecular dynamics (MD) (e.g., Parker et al., 2001), Monte Carlo simulation techniques allow us to explore the processes of crystal dissolution and growth at the atomic scale. For a comprehensive overview and in depth discussion of the approach that is also complementary to molecular dynamics (MD) calculations see Lasaga (1990, 1998). Earlier studies explored dissolution kinetics of mineral surfaces often in relatively crude molecular block models. Since then, the rapidly increasing speed of computers and the introduction of a new theoretical concept (Lasaga and Lüttge, 2001, 2003) for the dissolution of crystalline matter have provided the basis for further progress in crystal dissolution kinetics discussed below. Gilmer (1976, 1977, 1980) has used this technique successfully to study crystal growth. Lasaga and coworkers and later Wehrli applied Monte Carlo techniques to the study of crystal dissolution (Lasaga and Blum, 1986; Blum and Lasaga, 1987; Wehrli, 1989a,b).

By using Monte Carlo techniques we treat crystal dissolution or growth as a many-body problem and a stochastic process. Our method thus observes and counts random events generated by some probability distribution function. In the case of crystal–fluid interactions, we translate rates of microscopic processes, e.g., the bond-breaking/forming processes during dissolution or growth, into probabilities (e.g., Van der Eerden et al., 1978). The participation of the solution in the process can then be simulated by the probabilities of molecule arrival, i.e., the arrival rates. The reverse process is simulated by the probabilities of molecule (adatom) departure from the surface (departure rates). With this treatment, we can adjust the simulation for variations, e.g., in the saturation state of the solution or the pH. Next, we illustrate the case of an elementary reaction of bond-breaking and forming with an example taken from Lasaga and Lüttge (2004).

We assume that the total number of bonds between two A molecules (i.e., A–A bonds) on the dissolving surface is N_{AA}, and that the total number of broken A–A bonds on the same surface is ${N_{\mathrm{AA}}}^{\mathrm{broken}}$. If we assume steady state for these processes is achieved, we can write

$$\frac{N_{AA}^{broken}}{N_{AA}} = \frac{k_-}{k_+}, \tag{3.10}$$

where k_- and k_+ are the rate constants for the breaking and the formation of an A–A bond. If there are a few bonds broken at any one time, then $N_{\mathrm{AA}} \sim {N_{\mathrm{AA}}}^{\mathrm{tot}} \sim$ constant. As a result, the probability that any one given A–A bond is broken is given by

$$P_{AA} = \frac{k_-}{k_+}. \tag{3.11}$$

Here, we ignore all other complexities in the process. Now, the rate of dissolution of molecules with n bonds depends only on (i) the number of A molecules with n bonds on the surface, N_n^{A}, and (ii) on the probability that all n bonds are indeed

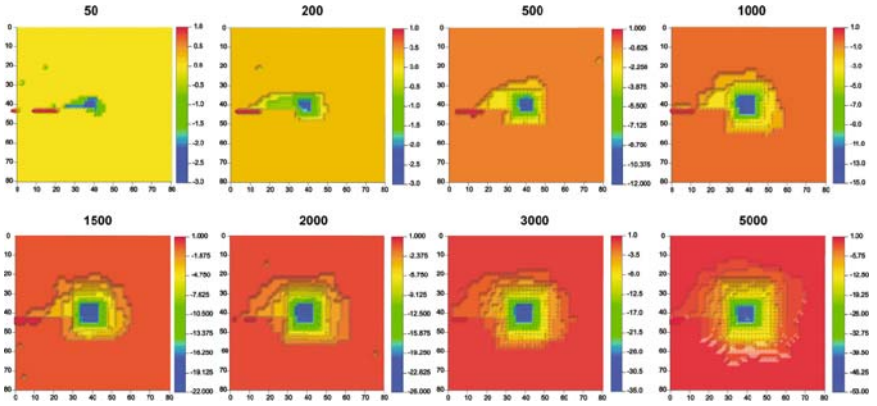

Fig. 3.16 Development of stepwaves from screw dislocation center seen in two component (AB) cubic block model in Monte Carlo simulation (see text for explanation). Stepwaves emanate following initial hollow core development. The number above each frame refers to the total number of dissolved atoms in the simulation. Scale: 80×80 units, color bar in atomic units. (Zhang and Luttge, unpublished data)

broken at the same time

$$Dissolution\ Rate = (P_{AA})^n N_n^A. \tag{3.12}$$

We rewrite this equation as

$$Rate = \left(\frac{k_-}{k_+}\right)^n N_n^A. \tag{3.13}$$

A more comprehensive approach may include additional complexities in the dissolution or growth process. Examples are the arrival of ligands and other units at the surface and also the surface diffusion of adatoms. Our example nicely illustrates the potential of this general approach. In the past, we have used Monte Carlo simulations successfully to analyze fundamental parameters and concepts such as activation energy, surface free energy, the solubility product, inhibition and catalysis, and the dependence on the saturation state of the solution (Lasaga and Lüttge, 2004; Lüttge, 2004a,b). The crystal-based reaction mechanism used in the simulation has lead to a unified explanation of many experimentally observed water-rock features. In addition, it has produced a series of unexpected but essential modifications of kinetic results that have not been completely understood before.

A recent development was the derivation of the so-called stepwave model (Lasaga and Lüttge, 2001, 2003) that presents a fundamental and quantitative concept for abiotic crystal dissolution kinetics. This model is different from other approaches in geochemical reaction kinetics that usually seek to identify a rate-limiting step or process, such as the formation of a precursor complex (compare Chap. 1,; see also, e.g., Oelkers, 2001). The Monte Carlo based approach in contrast does not require such strategic assumptions and it fully incorporates the three-dimensional crystal lattice and investigates its interactions with an aqueous solution. An example is shown in Fig. 3.16.

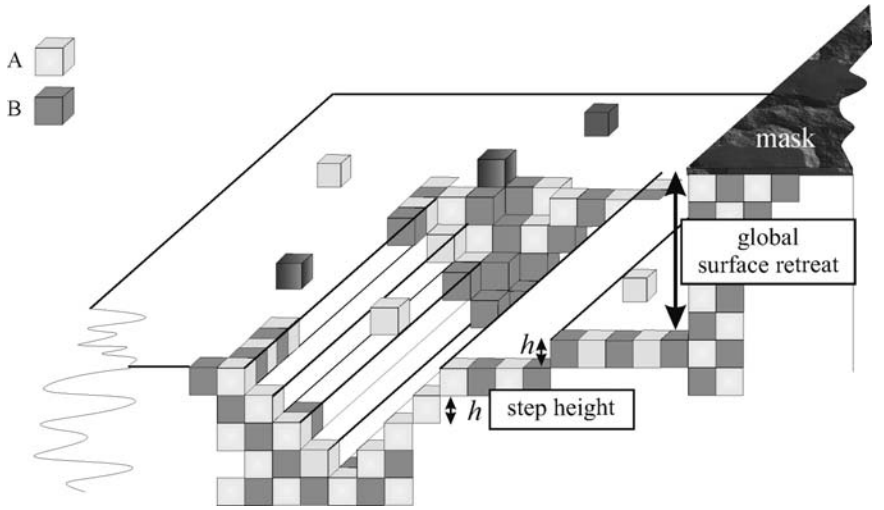

Fig. 3.17 Sketch of relationship between *stepwave* migration and cumulative, global surface retreat that develops as a result. (Adapted from Luttge et al. (2005), reprinted with permission from *American Journal of Science*)

A major result of the new model was the prediction of "stepwaves" that constantly emanate from the outskirts of etch pits and then travel across the entire crystal surface. The sketch in Fig. 3.17 shows that each stepwave will lower the crystal surface by a unit step height, *h*. Over time, this process causes the "global" or total surface-normal retreat that represents the overall dissolution rate, *R*, of the crystal at a given set of parameters. Recently, this reaction mechanism has been observed in dissolution experiments of several different minerals, e.g., calcite, barite, and plagioclase feldspar (compare Vinson and Lüttge, 2005; Arvidson et al., 2003, 2004, 2006). Additional support for the validity of the stepwave model comes from experimental observations and measurements as well as theoretical considerations by Tang and others, (Tang et al., 2001, 2003, 2004). These results demonstrate that an integrated approach that combines experimental and modeling techniques can be used as a powerful tool to improve our fundamental understanding of the water–mineral interface.

3.5 Summary and Outlook

In this brief paper we have tried to underscore the importance of understanding the nature of dynamic processes that characterize the interface environment through rigorous quantitative methods. These methods involve invasive and non-invasive probes that yield critical measures of surface area, topography, roughness, near-surface crystal chemistry and structure as it relates to the bulk crystal, and the distribution of adsorbed materials in various degrees of coordination and attachment.

However, it is also important to recognize that none of these technologies represent a stand-alone strategy, at least in terms of the solution of current and future generation problems. Problems involving the interaction of complex inorganic and organic materials with crystalline surfaces typically demand knowledge of property distributions in three dimensions; because of their inherently dynamic nature and the application to kinetic problems, measurements must also be acquired under real time, often *in situ*, conditions.

In addition, we should again emphasize that the primary problem is *not* a lack of sufficiently detailed observations in space or time. The primary challenge resides in the difficult of understanding how processes, observed on ever-finer scales of observation, integrate to yield phenomenological results of environmental significance. The solution to this problem will not come via any single "silver bullet", but through a combination of instrumental observations, field measurements, modeling and theoretical work that in particular focuses on scale dependence.

Acknowledgments

The authors wish to thank the editors for their support and patience. Special thanks to Y. Xiao (EXXONMOBIL), as well as M. D. Vinson, L. Zhang, and K. J. Davis (Rice University) for discussions and assistance with figures and references. We also acknowledge gratefully support for this work from the Office of Naval Research (ONR), the Department of Defence Multidisciplinary University Research Initiative (MURI) program, the Department of Energy (DE-FG07-01ER63295), the National Science Foundation (EAR-0125667), the Nanoscale Science and Engineering Initiative of the National Science Foundation under NSF Award Number EEC-0118007, EXXONMOBIL, Halliburton, VEECO-DI, ADE Phase Shift, and Molecular Instruments for the loan of a Pico Plus.

References

Anbeek C. (1992) Surface roughness of minerals and implications for dissolution studies. *Geochim. Cosmochim. Acta* **56**, 1461–1469.

Arvidson R. S., Collier M., Davis K. J., Vinson M. D., Amonette J. E., and Luttge A. (2006) Magnesium inhibition of calcite dissolution kinetics. *Geochim. Cosmochim. Acta* **70**, 583–594.

Arvidson R. S., Davis K. J., Collier M., Amonette J. E., and Lüttge A. (2004) Etch pit morphology and magnesium inhibition of calcite dissolution. In *Proceedings of the 11th International Symposium on Water-Rock Interaction WRI-11*, Saratoga Springs, New York (eds. R. B. Wanty and R. R. Seal). Balkema, New York, pp. 721–725.

Arvidson R. S., Ertan I. E., Amonette J. A., and Lüttge A. (2003) Variation in calcite dissolution rates: A fundamental problem? *Geochim. Cosmochim. Acta* **67**, 1623–1634.

Biino G. G., Mannella N., Kay A., Mun B., and Fadley C. S. (1999) Surface chemical characterization and surface diffraction effects of real margarite (001): An angle-resolved XPS investigation. *Am. Mineral.* **84**, 629–638.

Blum A. E., Lasaga A. C., and Yund R. A. (1990) The effect of dislocation density on the dissolution rate of quartz. *Geochim. Cosmochim. Acta* **54**, 283–297.

Blum A. E. and Lasaga A. C. (1987) Monte Carlo simulations of surface reaction rate laws. In *Aquatic Surface Chemistry; Chemical Processes at the Particle-Water Interface* (ed. W. Stumm). Wiley, New York, pp. 255–292.

Boughriet A., Gengembre L., Laureyns J., Recourt P., Langeline H. R., and Nacer A. (2000) Generation of uranyl/carbonate/hydroxide "coatings" at the vaterite surface. *Phys. Chem. Chem. Phys.* **2**, 1059–1068.

Bragg W. L. (1912) The diffraction of short electromagnetic waves by a crystal. *Proc. Cambridge Phil. Soc.* **17**, 43–57.

Brantley S. L. and Chen Y. (1995) Chemical weathering rates of pyroxenes and amphiboles. In *Chemical Weathering Rates of Silicate Minerals* (eds. A. F. White and S. L. Brantley). Reviews in Mineralogy, Vol. 31, Mineral Society of America, Washington, DC, pp. 119–172.

Brantley S. L. and Mellot N. P. (2000) Surface area and porosity of primary silicate minerals. *Am. Mineral.* **85**, 1767–1783.

Briggs D. and Seah M. P. (1983) *Practical Surface Analysis by Auger and X-Ray Photoelectron Spectroscopy*. Wiley, Chichester.

Brunauer S., Emmet P. H., and Teller E. (1938) Adsorption of gases in multimolecular layers. *J. Am. Chem. Soc*. **60**, 309–319.

Burton W. K., Cabrera N., and Frank F. C. (1951) The growth of crystals and the equilibrium structure of their surfaces. *Phil. Trans. Royal Soc. London A* (*Math. Phys. Sci.*) **243**, 299–358.

Cygan R. T. (2001) Molecular modeling in mineralogy and geochemistry. In *Molecular Modeling Theory: Applications in the Geosciences* (eds. R. T. Cygan and J. D. Kubicki). Reviews in Mineralogy and Geochemistry, Mineralogical Society of America, Washington, DC, pp. 1–35.

Cygan R. T. and Kubicki, J. D. (2001) (eds.), *Molecular Modeling Theory: Applications in the Geosciences.* Reviews in Mineralogy and Geochemistry, Vol. 42, Mineralogical Society of America, Washington, DC.

Denniston R. F., Shearer C. K., Layne G. D., and Vaniman D. T. (1997) SIMS analysis of minor and trace element distributions in fracture calcite from Yuccca Mountain, Nevada, USA. *Geochim. Cosmochim. Acta* **61**, 1803–1818.

Ewald P. P. (1913) Zur Theorie der Interferenzen der Röntgenstrahlen. *Phys. Z.* **14**, 465–472.

Finch A. A., Shaw P. A., Weedon G. P., and Holmgren K. (2001) Trace element variation in speleothem aragonite: Potential for palaeoenvironmental reconstruction. *Earth Planet. Sci. Lett.* **186**, 255–267.

Friedrich W., Knipping P., and von Laue M. (1912) Interferenz-Erscheinungen bei Rögenstrahlen, Sitzungsberichte der Königlich. *Bayerischen Akademie der Wissenschaften* 303–322.

Gautier J. -M., Oelkers E. H., and Schott J. (2001) Are quartz dissolution rates proportional to B.E.T. surface areas? *Geochim. Cosmochim. Acta* **65**, 1059–1070.

Gilmer G. H. (1976) Growth on imperfect crystal faces. I. Monte Carlo growth rates. *J. Cryst. Growth* **35**, 15–28.

Gilmer G. H. (1977) Computer simulations of crystal growth. *J. Cryst. Growth* **42**, 3–10.

Gilmer G. H. (1980) Computer models of crystal growth. *Science* **208**, 355–363.

Goldstein J. I., Newbury D. E., Echlin P., Joy D. C., Romig A. D., Jr., Lyman C. E., Fiori C., and Lifshin E. (1992) *Scanning Electron Microscopy and X-ray Microanalysis: A Text for Biologists, Material Scientists, and Geologists*, 2nd edition. Plenum Press, New York.

Goldstein J. I, Newbury D. E., Echlin P., Joy D. C., Lyman C. E., Lifshin E., Sawyer L., and Michael J. R. (2003) *Scanning Electron Microscopy and X-ray Microanalysis*, 3rd edition. Kluwer, New York.

Hehre W. J. (1995) *Practical Strategies for Electronic Structure Calculations*. Wavefunction, Irvine, CA.

Hehre W. J. (2003) *A Guide To Molecular Mechanics and Quantum Chemical Calculations*. Wavefunction, Irvine, CA.

Hehre W. J., Radom L., Schleyer P. V. R., and Pople J. A. (1986) *Ab Initio Molecular Orbital Theory*. Wiley, New York.

Helgeson H. C., Murphy W. M., and Aagard P. (1984) Thermodynamic and kinetic constraints on reaction rates among minerals and aqueous solutions II. Rate constants, effective surface area, and the hydrolysis of feldspar. *Geochim. Cosmochim. Acta* **48**, 2405–2432.

Hochella M. P., Jr. (1988) Auger electron and x-ray photoelectron spectroscopies. In *Spectroscopic Methods in Mineralogy and Geology* (ed. F. E. Hawthorne). Reviews in Mineralogy vol. 18. Mineralogical Society of America, Washington, DC, pp. 573–637.

Hochella M. F., Jr. (1995) Mineral surfaces: Characterization methods, and their chemical, physical, and reactive nature. In *Mineral Surfaces*, vol. 5 (eds. D. Vaughan and R. Pattrick). Chapman & Hall, London, pp. 17–60.

Hochella M. F., Jr. and Banfield J. F. (1995) Chemical weathering of silicates in nature: A microscopic perspective with theoretical considerations. In *Chemical Weathering Rates Of Silicate Minerals* (eds. A. F. White and S. L. Brantley). Reviews in Mineralogy vol. 31. Mineralogical Society of America, Washington, DC, pp. 353–406.

Hoffmann U. and Stipp, S. L. (2001) The behavior of Ni^{2+} on calcite surfaces. *Geochim. Cosmochim. Acta* **65**, 4131–4139.

Huang H. M., Fairchild I. J., Borsato A., Frisia S., Cassidy N. J., McDermott F., and Hawkesworth C. J. (2001) Seasonal variation in Sr, Mg and P in modern speleothems (Grotta di Ernesto, Italy). *Chem. Geol.* **175**, 429–448.

Jeffree, R. A., Markich S. L., Lefebvre R., Thellier M., and Ripoll C. (1995) Shell microlaminations in the freshwater bivalve Hyridella depressa (Lamarck) as an archival monitor of manganese water concentration: Experimental validation by depth profiling using secondary ion mass spectrometry (SIMS). *Experientia* **51**, 838–848.

Jeschke A. A. and Dreybrodt W. (2002) Dissolution rates of minerals and their relation to surface morphology. *Geochim. Cosmochim. Acta* **66**, 3055–3062.

Klein C. (2002) *Mineral Science*, 22nd edition. Wiley, New York.

Krinsley D. H., Pye K., Jr., Boggs S., and Tovey N. K. (1998) *Backscattered Scanning Electron Microscopy and Image Analysis of Sediments and Sedimentary Rocks.* Cambridge University Press, Cambridge.

Kubicki J. D., Blake G. A., and Apitz S. E. (1996) Ab initio calculations on Q^3Si^{4+} and Al^{3+} species: Implications for atomic structure of mineral surfaces. *Am. Mineral*. **81**, 789–799.

Lasaga A. C. (1990) Atomic treatment of mineral-water surface reactions. In *Mineral-Water Interface Geochemistry* (eds. M. F. Hochella, Jr. and A. F White). Reviews in Mineralogy vol. 23. Mineralogical Society of America, Washington DC, pp 17–85.

Lasaga A. C. (1992) Ab initio methods in mineral surface reactions. *Rev. Geophys*. **30**, 269–303.

Lasaga A. C. (1998) *Kinetic Theory and Applications in Earth Sciences.* Princeton Press, Princeton.

Lasaga A. C. and Blum A. E. (1986) Surface chemistry, etch pits and mineral-water reactions. *Geochim. Cosmochim. Acta* **50**, 2363–2379.

Lasaga A. C. and Gibbs G. V. (1990) Ab initio quantum mechanical calculations of water-rock interactions: Adsorption and hydrolysis reactions. *Am. J. Sci.* **290**, 263–295.

Lasaga A. C. and Lüttge A. (2001) Variation of crystal dissolution rate based on a dissolution stepwave model. *Science* **291**, 2400–2404.

Lasaga A. C. and Lüttge A. (2003) A model for crystal dissolution. *Eur. J. Min*. **15**, 603–615.

Lasaga A. C. and Lüttge A. (2004) A fundamental approach to mineral dissolution kinetics. *Am. Mineral*. **89**, 527–540.

Lüttge A., Zhang L., and Nealson K. H. (2005) Mineral surfaces and their implications for microbial attachment: Results from Monte Carlo simulations and direct surface observations. *Am. J. Sci*. **305**, 766–790.

Li C. and Tsukamoto K. (2001) The direct interference intensity phase analyzing technique for in situ Michelson interference and its application in studying of the fluctuation of crystal growth rates. *J. Cryst. Growth* **223**, 336–342.

Lupu C., Arvidson R. S., Luttge A., and Barron A. R. (2005) Phosphonate mediated surface reaction and reorganization: implications for the mechanism controlling cement hydration inhibition. *Chemical Communications* **2005**(18), 2354–2356.

Lüttge A., Bolton E. W., and Lasaga A. C. (1999) An interferometric study of the dissolution kinetics of anorthite: The role of reactive surface area. *Am. J. Sci.* **299**, 652–678.

Lüttge A. (2004a) Crystal dissolution kinetics studied by Vertical Scanning Interferometry (VSI) and Monte Carlo simulations: A brief review and outlook. In *Nanoscale Structure And Assembly at Solid-Fluid Interfaces. Vol. I. Interfacial Structures Versus Dynamics. Series on Nanoscience and Technologies* (eds. X.-Y. Liu and J. J. De Yoreo). Kluwer, New York, 700 pp.

Lüttge A. (2004b) Connecting the molecular- with the macro-scale: An integrated approach towards a quantitative understanding of crystal dissolution. In *Proceedings of the 11th International Symposium on Water-Rock Interaction WRI-11, Saratoga Springs, New York* (eds. R. B. Wanty and R. R. Seal). Balkema, New York, pp. 841–844.

Lüttge A. (2005) Etch pit coalescence, surface area, and overall mineral dissolution rates. *Am. Mineral.* **90**, 1776–1783.

Lüttge A., Winkler U., and Lasaga A. C. (2003) Dolomite dissolution kinetics studied with vertical scanning white light interferometry. *Geochim. Cosmochim. Acta* **67**, 1099–1116.

MacInnis I. N. and Brantley S. L. (1992) The role of dislocations and surface morphology in calcite dissolution. *Geochim. Cosmochim. Acta* **56**, 1113–1126.

MacInnis I. N. and Brantley S. L. (1993) Development of etch pit size distributions on dissolving minerals. *Chem. Geol.* **105**, 31–49.

Maiwa K., Tsukamoto K., and Sunagawa I. (1990) Activities of spiral growth hillocks on the (111) faces of barium nitrate crystals growing in an aqueous solution. *J. Cryst. Growth* **102**, 43–53.

Metz V. and Ganor J. (2001) Stirring effect on kaolinite dissolution rate. *Geochim. Cosmochim. Acta* **65**, 3475–3490.

Metz V., Raanan H., Pieper H., Bosbach D., and Ganor J. (2004) Towards the establishment of a reliable proxy for the reactive surface area of smectite. *Geochim. Cosmochim. Acta* **69**, 2581–2591.

Oelkers E. (2001) General kinetic description of multioxide silicate mineral and glass dissolution. *Geochim. Cosmochim. Acta* **65**, 3703–3720.

Ohmoto H., Hayashi K., Onuma K., Tsukamoto K., Kitakaze A., Nakano Y., and Yamamoto Y. (1991) Solubility and reaction kinetics of solution-solid reactions determined by in situ observations. *Nature* **351**, 634–636.

Onuma K., Tsukamoto K., and Sunagawa I. (1989) Measurements of surface supersaturations around a growing k-alum crystal in aqueous solution. *J. Cryst. Growth* **98**, 377–383.

Onuma K., Tsukamoto K., and Sunagawa I. (1990) Growth kinetics of K-Alum crystals in relation to the surface supersaturations. *J. Cryst. Growth* **100**, 125–132.

Parker S. C., de Leeuw N. H., and Redfern S. E. (1999) Atomistic simulation of oxide surfaces and their reactivity with water. *Faraday Disc.* **114**, 381–393.

Sunagawa I. (ed.) (1987) *Morphology of Crystals Part A, Materials Science of Minerals and Rocks*. Reidel, Dordrecht.

Tang R., Nancollas G. H., and Orme C. A. (2001) Mechanism of dissolution of sparingly soluble electrolytes. *J. Am. Chem. Soc.* **123**, 5437–5443.

Tang R., Orme C. A., and Nancollas G. H. (2003) A new understanding of demineralization: The dynamics of brushite dissolution: *J. Phys. Chem., Part B* **107**, 10653–10657.

Tang R., Orme C. A., and Nancollas G. H. (2004) Dissolution of crystallites: Surface energetic control and size effect. *Chem. Phys. Chem.* **5**, 688–696.

Tossel J. A. and Vaughan D. J. (1992) *Theoretical Geochemistry: Applications of Quantum Mechanics in the Earth and Mineral Sciences*. Oxford University Press, New York.

Tsukamoto K. (1983) In situ observation of mono-molecular growth steps on crystals growing in aqueous solution. *J. Cryst. Growth* **61**, 199–209.

Tsukamoto K. (1994) In situ observation of crystal growth from solution. *Faraday Disc*. **95**, 183–189.

Van der Eerden J. P., Bennema P., and Cheiepanova T. A. (1978) Survey of Monte Carlo simulations of crystal surfaces and crystal growth. *Progr. Crys. Growth Character* **1**, 219–251.

Vekilov P. G., Kuznetzov Y. G., and Chernov A. A. (1990) Dissolution morphology and kinetics of (101) ADP face: Mild etching of possible surface defects. *J. Cryst. Growth* **102**, 706–716.

Vekilov P. G. and Galkin O. (2004) Fundamental aspects of nucleation theory revealed in experiments with protein solid phases. In *Nanoscale Structure and Assembly at Solid-fluid Interfaces* (eds. X. Y. Lui and J. J. De Yoreo). Kluwer Press, New York, pp. 105–144.

Vering G., Crone C., Bijima J., and Arlinghaus H. F. (2003) TOF-SIMS characterization of planktonic foraminifera. *Appl. Surf. Sci*. **203**, 785–788.

Vinson M. D. and Lüttge A. (2005) Multiple length-scale kinetics: An integrated study of calcite dissolution rates and strontium inhibition. *Am. J. Sci*. **305**, 119–146.

Wehrli B. (1989a) Monte Carlo simulations of surface morphologies during mineral dissolution. *J. Colloid Interface Sci*. **132**, 230–242.

Wehrli B. (1989b) Surface structure and mineral dissolution kinetics: A Monte Carlo study. In *Proceedings of the 6th International Symposium on Water-Rock Interaction, Malvern, Rotterdam, The Netherlands* (ed. D. L. Miles). A. A. Balkema, Rotterdam, pp. 751–753.

White A. F. and Peterson M. L. (1990) Role of reactive surface area characterization in geochemical kinetic models. *Am. Chem. Soc. Symp. Ser*. **416**, 461–475.

Xiao Y. and Lasaga A. C. (1994) Ab initio quantum mechanical studies of the kinetics and mechanisms of silicate dissolution: H_3O^+ catalysis. *Geochim. Cosmochim. Acta*. **58**, 5379–5400.

Xiao Y. and Lasaga A. C. (1996) Ab initio quantum mechanical studies of the kinetics and mechanisms of quartz dissolution. OH^- catalysis. *Geochim. Cosmochim. Acta.* **60**, 2283–2295.

Xiao Y. and Lüttge A. (2002) Solvated ab initio and density functional theory (DFT) modeling of mineral-fluid surface reactions: Towards a fundamental understanding of aluminosilicate dissolution mechanisms. *Geological Society of America, Annual Meeting Abstracts with Programs* (abstr.).

Zhang L. and Lüttge A. (2003) Monte Carlo simulations of feldspar dissolution kinetics. *Eos Transactions American Geophysical Union* **84**(46), Fall Meeting Supplement, #V11D-0531 (abstr.).

Chapter 4
Kinetics of Sorption–Desorption

Jon Chorover[1] and Mark L. Brusseau[2]

4.1 Sorption–Desorption Reactions

The fate of nutrients, pollutants and other solutes in natural waters is coupled to their distribution between solid, aqueous and gas phases. The processes of phase distribution are many, including penetration and absorption into one of the phases, or accumulation at the interface between them. The term *sorption* is defined here as the full range of processes whereby matter is partitioned between the gas, aqueous and solid phases. In geochemical systems, this includes *adsorption* of matter at the surfaces of solid particles (minerals and organic matter) or at the air–water interface, and *absorption* into the solids during surface precipitation or solid phase diffusion. The complexity of natural geomedia (Fig. 4.1) implies that both broad classes of "sorption" reaction may occur simultaneously. As discussed in this chapter, recent research into the kinetics and mechanisms of sorption for inorganic and organic species indicates that both processes are indeed important. The relative predominance of a given reaction and sorbate–sorbent structure is a function of time scale, system loading and geochemical conditions.

4.1.1 Adsorption at the Solid–Liquid Interface

Adsorption refers to the accumulation of a substance at an interface between two phases, without the formation of a three-dimensional crystal structure. The inverse process, *desorption*, refers to the loss of matter from the interface, typically by diffusion into the bulk of one of the adjoining phases. Adsorption occurs at surfaces bounding the liquid–gas, solid–gas and solid–liquid interfaces. Among these,

[1] University of Arizona, Department of Soil, Water and Environmental Science, Chorover@cals.arizona.edu
[2] University of Arizona, Department of Soil, Water and Environmental Science, Brusseau@ag.arizona.edu

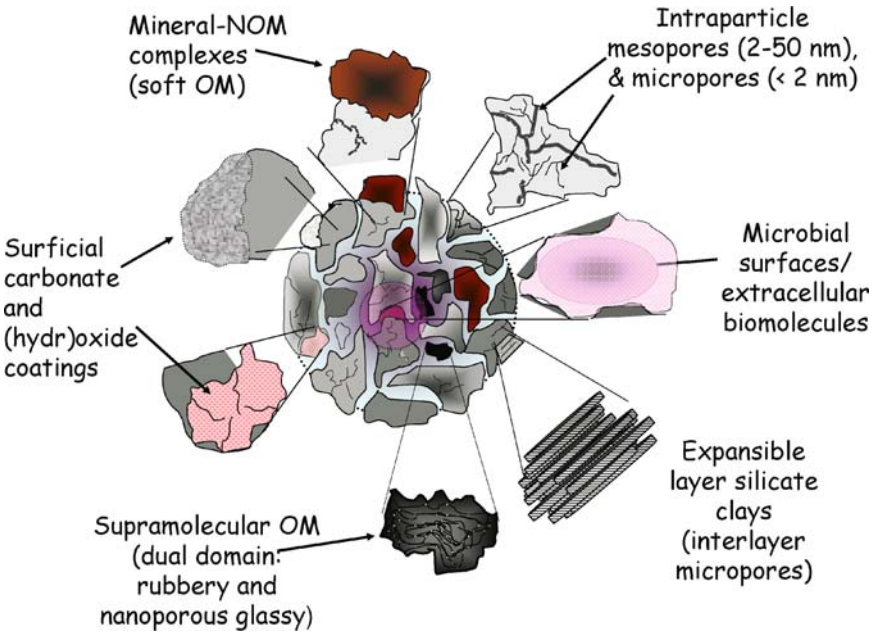

Fig. 4.1 Structural properties, surface coatings and porosity of geosorbents affecting transport-limited sorption kinetics

the solid–liquid interface – particularly the mineral–water interface discussed in Chap. 3, but also the organic–water interface at the surfaces of natural organic matter and microbial cells – exerts significant control over such diverse processes as mineral weathering kinetics (Chap. 5), nucleation and crystal growth (Chap. 7), natural organic matter (NOM) stabilization, and solute transport (Chap. 11). These extensive effects result from the fact that sorption–desorption reactions impact not only the concentrations of chemical reactants in the aqueous solution, but also the structure and reactivity of particle surfaces.

Matter that accumulates at the interface during the adsorption process is termed *adsorbate*, whereas the surface where it accumulates is called the *adsorbent*. The term *adsorptive* refers to any chemical species in the bulk solution that may potentially be adsorbed. In contrast, the terms *sorbate*, *sorbent* and *sorptive* apply in situations where the precise mechanism of solid–liquid transfer is not known and may include surface precipitation or solid state diffusion. Given the variation in adsorptive solutes, as well as in composition and charge of mineral surfaces (Chap. 3), mechanisms of adsorbate binding to mineral surfaces are highly variable.

4.1.2 Surface Excess is the Quantitative Measure of Adsorption

Adsorption of a substance (i) from aqueous solution is quantified conventionally by measuring the *surface excess* of the substance relative to that of the solvent itself

(Sposito, 2004). For aqueous systems, this measurement is typically performed by separating the wet slurry (comprising adsorbent, adsorptive species i, and interstitial solution) from the bulk supernatant solution and determining the surface excess of species i at time t ($\Gamma_{i,t}$) according to

$$\Gamma_{i,t} = n_{i,t} - \theta_w c_{i,t} \tag{4.1}$$

where n_i is the number of moles of substance i in the separated adsorbent slurry per unit mass of dry adsorbent, θ_w is the gravimetric water content of the slurry, and c_i is the molality of adsorptive i in the supernatant aqueous phase (equivalent to that of the interstitial solution). The subscript t refers to the potential time-dependency of the constituent measurements. For example, adsorption kinetics can be measured by the increase in Γ_i with time. Since n_i includes both adsorbed and aqueous phase moles of i in the wet sample slurry, the second term on the right side of Eq. (4.1) removes the mass contribution of i in interstitial water. In Eq. (4.1), the units for Γ_i are moles per kilogram of dry adsorbent, but surface excess can also be reported as moles per square meter of interfacial area if Γ_i is normalized to the specific surface area of the adsorbent (a_s) in square meters per kilogram of solid. Hence, surface excess is a measure of a species concentration at the particle–water interface relative to that in the bulk solution. Values of Γ_i are positive when attraction to the interface results in substance i being enriched there relative to bulk solution ($n_i > \theta_w c_i$). Conversely, Γ_i values are negative when a substance is repelled or excluded from the interface, resulting in its depletion there relative to bulk solution ($n_i < \theta_w c_i$).

In experiments conducted on adsorbent suspensions, surface excess is often calculated from the difference between initial ($t = 0$) and subsequent ($t > 0$) aqueous phase adsorptive concentration or molality:

$$\Gamma_{i,t} = (c_{i,0} - c_{i,t})\theta_w \tag{4.2}$$

where $c_{i,0}$ is the initial molality of adsorptive i and θ_w is now the gravimetric water content of the full aqueous suspension. Kinetic data on adsorption are often obtained on aqueous suspensions by measuring c_i on extracted (and filtered or centrifuged) aliquots as a function of reaction time, $t(c_{i,t})$ and calculating the time-dependent change in surface excess ($\Gamma_{i,t}$) from Eq. (4.2).

4.2 Rate Limiting Steps

In a sorption (or desorption) reaction, a solute becomes associated with (or displaced from) the solid phase. Sorption–desorption processes generally comprise multiple reactions or steps involving solid and aqueous phase components (Aharoni and Sparks, 1991). The steps include transport processes (displacement of adsorptives in the liquid phase and adsorbates at the interface) in addition to chemical reactions (formation or rupture of chemical bonds).

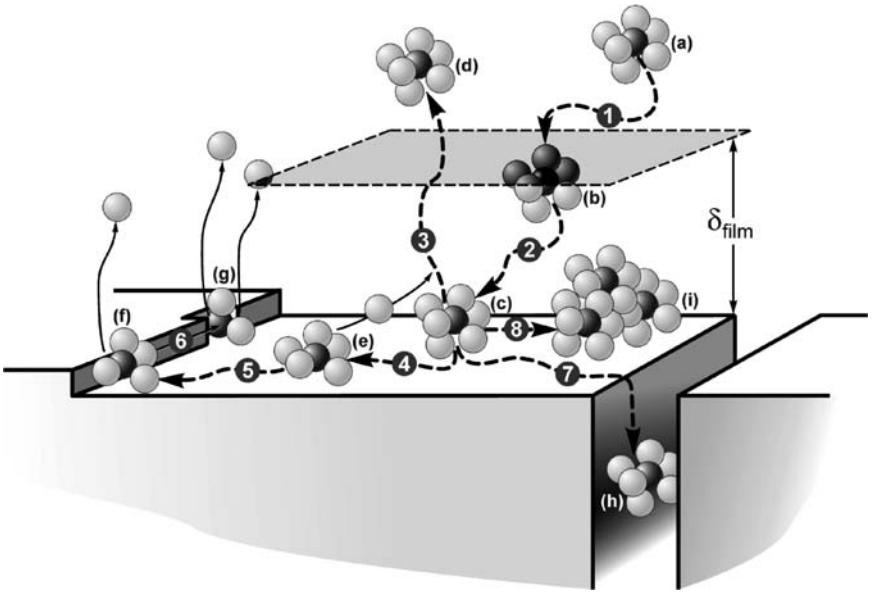

Fig. 4.2 Mechanisms of ion sorption at the mineral–water interface. The schematic represents an (**a**) hydrated metal ion (water molecules are represented by light colored spheres surrounding the dark colored metal ion) approaching the surface via (1) bulk and (2) film diffusion. Once at the surface, the hydrated ion may (**c**) form an outer sphere complex, (**d**) undergo desorption or (e) form an inner-sphere complex in association with loss of hydration water. Adsorbed ions may undergo (4, 5, 7, 8) surface diffusion to form stronger complexes at higher affinity (**f**) ledge or (**g**) kink sites, undergo (**h**) diffusion into intraparticle pores, and/or to (**i**) sites of surface polymerization

4.2.1 Transport Processes

In porous media, such as soils and sediments (Fig. 4.1), transport processes include advection and diffusion in the aqueous phase, migration across the solid–liquid interface, diffusion in liquid-filled micro- or meso-pores (intraparticle diffusion), surface diffusion, and solid-phase diffusion (Fig. 4.2). In the bulk aqueous phase, solute flux in the x direction (J_x) results from the combined effects of advection (due to fluid flow) and molecular diffusion. The flux may be modeled as the sum of these two processes:

$$J_{x,bulk} = -D\theta\left(\frac{\partial c_i}{\partial x}\right) + qc_i \tag{4.3}$$

where D is the aqueous phase solute diffusion coefficient, θ is soil-water content, and q is the Darcy velocity (specific discharge).

Adsorbent surfaces in aqueous systems are surrounded by a quiescent boundary layer film that is not subjected to the advective effects of the bulk aqueous phase (Fig. 4.2). The thickness of this layer (δ) is on the scale of nanometers $(10^{-9}\,\mathrm{m})$. It increases with adsorbent affinity for water (*surface hydrophilicity*) and it decreases

with the extent of mixing. Diffusive flux across the boundary layer is driven by the concentration gradient therein, which may be approximated by use of the stagnant film model for mass transfer:

$$J_{film} = D\left(\frac{c_{i,bulk} - c_{i,surface}}{\delta}\right) \tag{4.4a}$$

where the solute flux is driven by the difference in concentration of species i in the bulk solution, $c_{i,bulk}$, and at the surface, $c_{i,surface}$. The *rate of adsorption or desorption* by the film diffusion mechanism is then given by the product of adsorptive flux and the adsorbent surface area per unit volume of solution:

$$-\frac{\partial c_i}{\partial t} = D\, a_s c_s\left(\frac{c_{i,bulk} - c_{i,surface}}{\delta}\right) \tag{4.4b}$$

where a_s is the specific surface area of the adsorbent and c_s is the concentration of adsorbent in the aqueous suspension. Because the rate of adsorption via film diffusion is inversely proportional to film thickness, the degree to which film diffusion limits sorption kinetics may be assessed by varying δ through systematic changes in the mixing rate of particle suspensions; film thickness decreases with increased mixing rate.

Transport in small intraparticle pores is likewise governed by molecular diffusion because advection is typically insignificant given that the flow of fluid through such pores is generally minimal. In this case, the rate of adsorption–desorption is dominated by the first term on the right side of Eq. (4.3). Variable x is measured inward along an axis perpendicular to the adsorbent surface and D is the diffusion coefficient of adsorptive i within the adsorbent

$$\frac{\partial c_i}{\partial t} = Da_s c_s\left(\frac{\partial c_i}{dx}\right)_{pore} \tag{4.5}$$

Because intraparticle porosity is not impacted by fluid shear external to the particle, intraparticle diffusion is not normally affected by mixing rate. Poorly crystalline weathering products such as hydrous metal oxides exhibit significant internal porosity that can govern long term sorption kinetics. For example, Sr^{2+} sorption to microporous Al and Mn oxides is a two-step process: rapid and reversible adsorption to the external surface is completed within the first 24 h, whereas slow diffusion along the micropore walls of the oxides proceeds with surface diffusion coefficients ranging from 10^{-12} to $10^{-11}\,cm^2\,s^{-1}$ for up to 90 days and accounts for another 50% of the total sorbed amount at equilibrium (Trivedi and Axe, 1999).

As shown in Fig. 4.2, once an adsorptive species migrates via bulk (Step 1) and film (Step 2) diffusion to reside in close proximity to reactive moieties of the adsorbent, its subsequent fate may be controlled largely by chemical interactions including the formation (Step 4) and breaking (Step 3) of bonds with surface functional groups. However, transport processes may still contribute to overall kinetics via surface (Step 5) or bulk solid (Step 6) diffusion. Surface diffusion, which refers to the

lateral translocation of adsorbate via "jumps" between surface sites without desorption from the surface, can be driven by surficial concentration gradients. As such, the surface flux is modeled as

$$J_{x,surf} = -D_{surf}\left(\frac{\partial c_i}{dx}\right) \tag{4.6a}$$

where the surface diffusion coefficient, D_{surf}, is a function of the activation energy for adsorbate diffusion (E_D)

$$D_{surf} = D_0 \exp(-E_D/kT) \tag{4.6b}$$

The prefactor, D_0, is given by transition state theory (also see Chap. 2) as

$$D_0 = vl^2 \exp(S_D/k) \tag{4.6c}$$

v is the effective vibrational frequency, l is the jump length and S_D is the energy of activation (Tringides, 1997). In addition to being driven by surface concentration gradients, surface diffusion also results from migration to more favorable binding sites, including those associated with mineral defects including ledge, kink or step sites (Step 5 and 6, also see Chap. 3, and Lasaga, 1998) or locales of surface polymerization (Step 8), where the number and/or strength of adsorbate–adsorbent bonds can be maximized.

Bulk solid diffusion and *surface precipitation* are *sorption* processes that can eventually embed the sorbate in the bulk solid, effectively removing it from the solid–liquid interface. Bulk solid diffusion of inorganic sorbates may occur via transport into vacancies or defects in a mineral where they can substitute "isomorphically" into the crystal structure. Solid-phase incorporation of inorganic sorbate also occurs via surface precipitation and/or co-precipitation with solid phase dissolution products. Solid phase diffusion is not limited to inorganic sorbates. An example of bulk solid diffusion of an organic sorbate is the rate-limited uptake of a hydrophobic organic contaminant (HOC) into the internal, hydrophobic domains of aggregated NOM (Brusseau et al., 1991).

4.2.2 Surface Reactions

Adsorption–desorption reactions in aqueous geochemical systems may involve the full array of natural or anthropogenic solutes including inorganic major cations, anions, and neutral species, trace metals, polymeric species, and natural or xenobiotic organic molecules. In simplest form, the adsorption (desorption) chemical reaction is represented by Eq. (4.7), proceeding from left to right (right to left):

$$SFG(s) + i(aq) \leftrightarrow SFG - i(s) \tag{4.7}$$

where *SFG* is a surface functional group or reactive surface site, *i* is the adsorptive species in solution and *SFG-i* is the adsorbent–adsorbate surface product. The terms

Table 4.1 Reactive surface sites of high surface area geosorbents (Fig. 1)

Sorbent Type	*Reactive Sites*
Layer Silicates (*e.g., smectite, vermiculite, kaolinite*)	Siloxane ditrigonal cavity ($\equiv X^-$) Exchangeable metals ($\equiv XMe^+$) Edge surface hydroxyls ($\equiv SOH$)
Oxides and Hydroxides *(e.g., allophane, goethite, ferrihydrite, gibbsite)*	Surface hydroxyls ($\equiv SOH$)
Metal Carbonates *(e.g., calcite, dolomite)*	Surface hydroxyls ($\equiv MeOH^0$) Surface metal ($\equiv CO_3Me^+$) Surface carbonate ($\equiv MeHCO_3^0$)
Natural Organic Matter *(plant and microbial biomolecules and their degradation products, humic substances)*	Phenolic hydroxyls (*Ar-OH*) Carboxylic (*R-COOH*) Carbonyl ($R, R' - C = O$) Sulfhydryl (*R-SH*) Aromatic moieties (*Ar*) Aliphatic ($[\text{-}CH_2-]_n$) Aliphatic Hydroxyls (*R-OH*) Amide and Amino (*R-NH-R, R-NH*$_2$) Phosphoryl ($R\text{-}O\text{-}PO_2^- - O - R$)

(s) and (aq) refer to the solid phase and aqueous phase, respectively. It is critical to note that the term surface refers to any and all sorbent surfaces, internal as well as external to the bulk solid.

The composition of the reactive surface group varies with adsorbent structure and functional group content. Examples of *SFG* include the dissociable surface hydroxyl groups of Al, Fe, Si or Mn (hydr)oxides, siloxane sites of layer silicate clays, and the carboxyl, sulfhydryl, hydroxyl or hydrophobic (non-polar) moieties of NOM (Table 4.1). The adsorption–desorption reaction may be accompanied by proton, hydroxide, or other ion exchange, as well as metal hydrolysis, ligand protonation, etc. Thus, a more generalized form of the adsorption–desorption reaction of aqueous-phase species with a solid adsorbent may be written (Sposito, 1994):

$$\begin{aligned} &SFG^{Z_{SFG}}(s) + pM^{m+}(aq) + qL^{a-}(aq) + xH^+(aq) + yOH^-(aq) \\ &\quad \leftrightarrow SFG'M_p(OH)_yH_xL_q^{Z_{SR'Ads}}(s) + Q^{Z_Q}(aq) \end{aligned} \tag{4.8}$$

where m is the valence of an adsorptive metal M, $-a$ is the valence of an adsorptive ligand L, Z_{SFG} is the valence of a reactive surface site *SFG* comprising both a dissociable component Q of valence Z_Q, and an undissociable component SFG' of valence $Z_{SFG} - Z_Q$, and $Z_{SFG'Ads}$ is the valence of the adsorbent–adsorbate product (the sum of $Z_{SFG'}$ *and* Z_{Ads}, where Z_{Ads}, the valence of the adsorbate $M_p(OH)_yH_xL_q$, is given by $pm - qa + x - y$). The reaction in Eq. (4.8) may be represented by an

equilibrium constant for adsorption (K_{ads}):

$$K_{ads} = \frac{(SFG'M_p(OH)_yH_xL_q^{Z_{SR'Ads}})(Q^{Z_Q})}{(SFG^{Z_{SR}})(M^{m+})^p(H^+)^x(L^{a-})^q(OH^-)^y} \tag{4.9}$$

where the parentheses indicate species activities.

Some concrete examples of Eq. (4.9) include proton adsorption and desorption reactions on hydrous oxide surfaces

$$SOH(s) + H^+(aq) \leftrightarrow SOH_2^+(s) \tag{4.10a}$$

$$SOH(s) \leftrightarrow SO^-(s) + H^+(aq) \tag{4.10b}$$

surface complexation of transition metals

$$SOH(s) + Cu^{2+}(aq) \leftrightarrow SOCu^+(s) + H^+(aq) \tag{4.10c}$$

cation adsorption to carboxyl groups of solid phase NOM

$$SCOOH(s) + Ca^{2+}(aq) \leftrightarrow SCOOCa^+(s) + H^+(aq) \tag{4.10d}$$

and oxyanion adsorption at oxide surface hydroxyls via ligand exchange

$$SOH(s) + H_3AsO_4(aq) \leftrightarrow SHAsO_4^-(s) + H^+(aq) + H_2O(l) \tag{4.10e}$$

4.2.3 Transport and Surface Reaction Control of Sorption Kinetics

As outlined above, the macroscopic measurement of overall sorption–desorption kinetics includes both *physical* transport steps and *chemical* reaction (Aharoni and Sparks, 1991). Formulation of rate laws should reflect the relative importance of transport versus chemical reaction if one or the other process is rate limiting. The rate law for chemical-reaction-controlled adsorption (Eq. (4.7)) is given by:

$$-\frac{\partial c_i}{\partial t} = k_{ads}c_{i,surf}c_{SFG} - k_{des}c_{SFG-i} \tag{4.11}$$

where k_{ads} and k_{des} are the rate coefficients for the adsorption and desorption reactions, respectively, $c_{i,surf}$ is the concentration of species i at the adsorbent surface, and c_{SFG} and c_{SFG-i} are the concentrations of *SFG* and *SFG-i*, respectively. A steady state value for $c_{i,surf}$ implies that film diffusion supplies adsorptive i to the interface at a rate equal to its consumption in the chemical reaction, irrespective of which one is limiting the overall rate of adsorption:

$$Da_sc_s\left(\frac{c_{i,bulk} - c_{i,surface}}{\delta}\right) = k_{ads}c_{i,surf}c_{SFG} - k_{des}c_{SFG-i} \tag{4.12}$$

However, solving Eq. (4.12) for $c_{i,surf}$ shows that film diffusion is rate limiting when $k_{ads}c_{SFG} \gg Da_s c_s/\delta$, whereas surface reaction is rate limiting when the inverse is true (Sposito, 1994).

The relative significance of the various steps is dependent upon the properties and conditions of the specific system, as well as the time scales associated with the respective processes. For example, intraparticle diffusive mass transfer is often a significant factor for aggregated and macroporous soil materials, but is usually insignificant for sands. As noted above, solid-phase diffusion is a critical component of long-term sorption–desorption processes for particular systems.

4.3 Sorption Mechanisms and Kinetics for Inorganic Solutes

Intermolecular forces that contribute to sorption–desorption fall within a continuum from physical ("*physisorption*") to chemical ("*chemisorption*"), with a corresponding increase in the extent of sorbent–sorbate specificity. Physical mechanisms such as long-range electrostatic interaction are non-specific, and they are accompanied by relatively low adsorption enthalpy ($<40\,\mathrm{kJ\ mol^{-1}}$). Chemical mechanisms include short-range electrostatic forces and covalent bonding. They give rise to higher adsorption enthalpies ($>40\,\mathrm{kJ\ mol^{-1}}$) and typically involve greater bonding specificity.

4.3.1 Surface Complexes and the Diffuse Ion Swarm

The range in adsorbent–adsorbate specificity is reflected in the adsorption of cations and anions at the particle–water interface, which includes both *surface complexes* and the *diffuse ion swarm*. In analogy to aqueous solution complexes, those that occur at adsorbent surfaces may be either *outer-sphere* (OS, Fig. 4.3b) – in which case one or more water molecules are interposed between the adsorbate and the surface functional group of the adsorbent – or *inner-sphere* (IS, Fig. 4.3a) – in which case no water molecules are interposed. Figure 4.2c also shows an example of an OS complex, whereas loss of an intervening water ligand promotes the formation of an IS complex (Fig. 4.2e). In contrast, adsorption in the diffuse ion swarm (DIS) entails long-range, delocalized electrostatic interactions that neutralize the charged surface over some distance into the solution (Fig. 4.3b). Diffuse ion swarm adsorption is different from outer-sphere complexation because in the former case, individual ions undergo free diffusion into and out of the interfacial region without the immobilization over longer time scales that characterizes surface complexation. Adsorption of diffuse swarm ions is attractive (contributing to positive values of Γ_i) for ions of charge sign opposite to that of the surface, while ions of charge sign the same as the surface are subjected to repulsion (contributing to negative values of Γ_i).

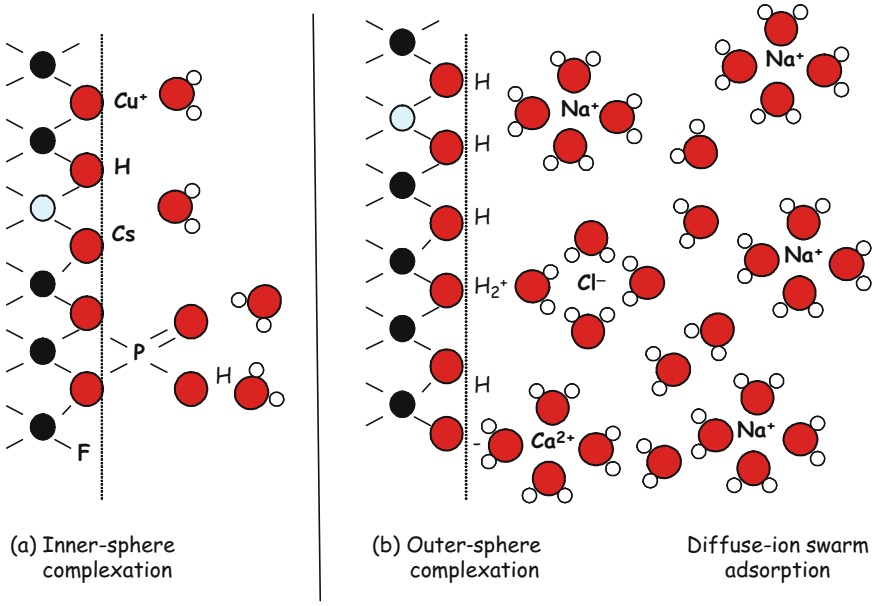

Fig. 4.3 Schematic illustration of inner-sphere (IS) and outer-sphere (OS) complex formation, and diffuse ion swarm adsorption at a hydroxylated surface

Because both DIS adsorption and OS complexation result from predominantly electrostatic interactions, these mechanisms are considered 'non-specific'. In contrast, IS complexation is termed 'specific adsorption' because it involves the contribution of both ionic and covalent bonding, and the latter requires some degree of electron orbital overlap between the adsorbate and surface functional groups of the adsorbent.

The distribution of ions into IS, OS and DIS environments results from a net balance between the system energy gained via enthalpy of ion dehydration and that which is released because of surface charge neutralization and bonding. Since our knowledge of the physical-chemical parameters governing hydrated ion behavior at interfaces (e.g., the dielectric constant of interfacial water) is incomplete, ion distributions can not yet be calculated unambiguously. Instead, such distributions are elucidated by coupling molecular-scale spectroscopies and modeling. For example, Zhang et al. (2004) found that inner-sphere complexation predominates for monovalent, bivalent and trivalent cation adsorption on the 110 surface of rutile (α-TiO_2), where negative charge is situated directly at the surface. Recent x-ray reflectivity studies have shown that ions of the same type may be adsorbed as inner-sphere, outer-sphere and diffuse swarm species. This method is capable of resolving, at the <1 Å scale, the spatial distribution of ions at a charged interface. X-ray reflectivity measurements of ion distribution at the 001 muscovite surface in contact with 0.01 M RbCl and 0.01 M $Sr(NO_3)_2$ solutions show distinct patterns for the two cations (Park et al., 2006). In RbCl solution, data indicate that a portion

of the muscovite surface charge is satisfied by Rb^+ adsorbed in IS coordination, with the remainder being attributed to ion adsorption in the diffuse ion swarm. In contrast, Sr^{2+} adsorption is distributed in a "dynamic equilibrium" between similar sized populations of IS and OS species that fully compensate for muscovite surface charge, with no Sr^{2+} adsorption attributed to the diffuse ion swarm (Park et al., 2006).

4.3.2 Surface Complexation Kinetics for Metal Cations

The type of surface complex (OS or IS) affects the rate and reversibility of sorption reactions. OS complexation is normally rapid and reversible, whereas IS bonding is slower and less reversible. Mechanisms and kinetics of *heterogeneous* OS and IS complex formation of metals at mineral surfaces are described in analogy to comparable *homogeneous* reactions in solution where formation of an OS electrostatic complex is followed by the rate-limiting loss of water from the inner-coordination sphere of the metal. This stepwise reaction is termed the *Eigen-Wilkins-Werner* mechanism (Morel and Hering, 1993). For example, reaction 4.10c, may, in fact, proceed through the coupled steps (where the water molecules hydrating the sorptive Cu^{2+} ion are shown explicitly):

$$SOH(s) + Cu(H_2O)_n^{2+}(aq) \underset{k_{-OS}}{\overset{k_{OS}}{\rightleftharpoons}} SO^- \cdots Cu(H_2O)_n^{2+}(s) + H^+(aq) \qquad (4.13a)$$

$$SO^- \cdots Cu(H_20)_n^{2+}(s) \xrightarrow{k_{IS}} SOCu(H_2O)_{n-1}^{+}(s) + H_2O(l) \qquad (4.13b)$$

The dotted line in Eq. (4.13a) represents the formation of an OS complex after ion exchange with H^+ (Wehrli et al., 1990). Formation of the OS complex (Eq. (4.13a)) is rapid relative to loss of interposed water and inner-sphere complexation (Eq. (4.13b)). Thus, equilibrium is assumed for the first step and k_{OS}/k_{-OS} is set equal to the outer-sphere complex formation constant, K_{OS} (see Chap. 1 for further description of kinetic modeling of consecutive reactions). The parameter k_{IS} in Eq. (4.13b) is the intrinsic inner-sphere complex formation rate constant at zero surface charge (Stumm, 1992). The overall rate of formation of the inner-sphere complex is then given by:

$$\frac{d[SOCu^+]}{dt} = K_{OS}k_{IS}[Cu^{2+}][SOH] \qquad (4.14)$$

Experimental data on Zn, Co, Ni and Cd sorption to hematite at pH 6.8 showed a rapid initial sorption ($t_{1/2} \sim 1$ min) followed by slower uptake for 1–5 days (Jeon et al., 2004). When these data were modeled as consecutive reactions according to Eqs. (4.13)–(4.14), they suggested that conversion from OS to IS complexes was indeed the rate-determining step. However, a time-dependent decrease in the extent of OS-complexed metal and also in K_{OS} was observed. The authors attributed this effect to an increase in positive surface charge because of cationic metal adsorption

(e.g., Eq. (4.13a)). The accumulation of positive surface charge inhibited further metal adsorption in OS complexes and thus contributed to a decreasing overall rate of metal uptake with time (Jeon et al., 2004). If K_{OS} varies with surface charge, then according to Eq. (4.14), adsorbent surface charge can be a critical determinant of ion adsorption kinetics. Model calculations indicate, for example, that kinetics of bivalent metal cation (M^{2+}) adsorption to the goethite (α-FeOOH) surface may be limited by film diffusion (Eq. (4.4)) of M^{2+} to a positively-charged surface (Polmeier and Lustfeld, 2004). That is, when the adsorbate and adsorptive are of like charge, film diffusion may be decelerated because of electrostatic repulsion.

For a constant value of K_{OS}, Eq. (4.14) implies that water ligand exchange is rate limiting. As shown in Fig. 4.4a, the rate constant for water ligand exchange in the inner-coordination sphere of hydrated bivalent and trivalent metal cations, as indicated by the reaction

$$M(H_2O)_n^{m+} + H_2O' \xrightarrow{k_{-w}} M(H_2O)_{n-1}H_2O'^{m+} + H_2O \tag{4.15}$$

is sensitively dependent on ionic potential (ion valence, Z, normalized to ionic radius, IR) (Morel and Hering, 1993; Sposito, 1994). Values of k_{-w} vary over 10 orders of magnitude for ionic potentials that range over less than one order of magnitude.

The term Z/r (ionic potential) is directly proportional to the strength of the cation-dipole (water) bond. Thus, stronger ion-dipole bonding leads to slower rates of water exchange. Given that loss of at least one water ligand is a prerequisite for inner-sphere surface coordination (e.g., see Step 4 in Fig. 4.2), it is not surprising that values of k_{IS} and k_{-w} are well correlated. Thus, known rates of water ligand exchange appear to provide a useful predictor for kinetics of IS surface complex formation (Fig. 4.4b). Though ions with low rates of water exchange (e.g., Al^{3+}) are expected to exhibit very slow kinetics of IS complex formation, it is important to note that values of k_{-w} increase by two or three log units with ion hydrolysis (Morel and Hering, 1993), which may be facilitated by interaction with the surface (Criscenti and Sverjensky, 2002). The value of k_{IS} is then expected to increase accordingly.

4.3.3 Cation Exchange on Layer Silicate Clays

The term "ion exchange" refers to an adsorption–desorption reaction of the type:

$$CaX_2(s) + 2K^+(aq) \leftrightarrow 2KX(s) + Ca^{2+}(aq) \tag{4.16}$$

where X^- represents one mole of adsorbent negative charge. Equation (4.16) is a *heterovalent* ion exchange reaction; one mole of an adsorbed *bivalent* cation (Ca^{2+}) is exchanged for two moles of adsorbed *monovalent* cation (K^+). By convention, ion exchange reactions typically refer to ions that are adsorbed into OS complexes or in the diffuse ion swarm (and hence are "exchangeable") and the relative rates of reaction are in the range of microseconds to hours. For such adsorption–desorption

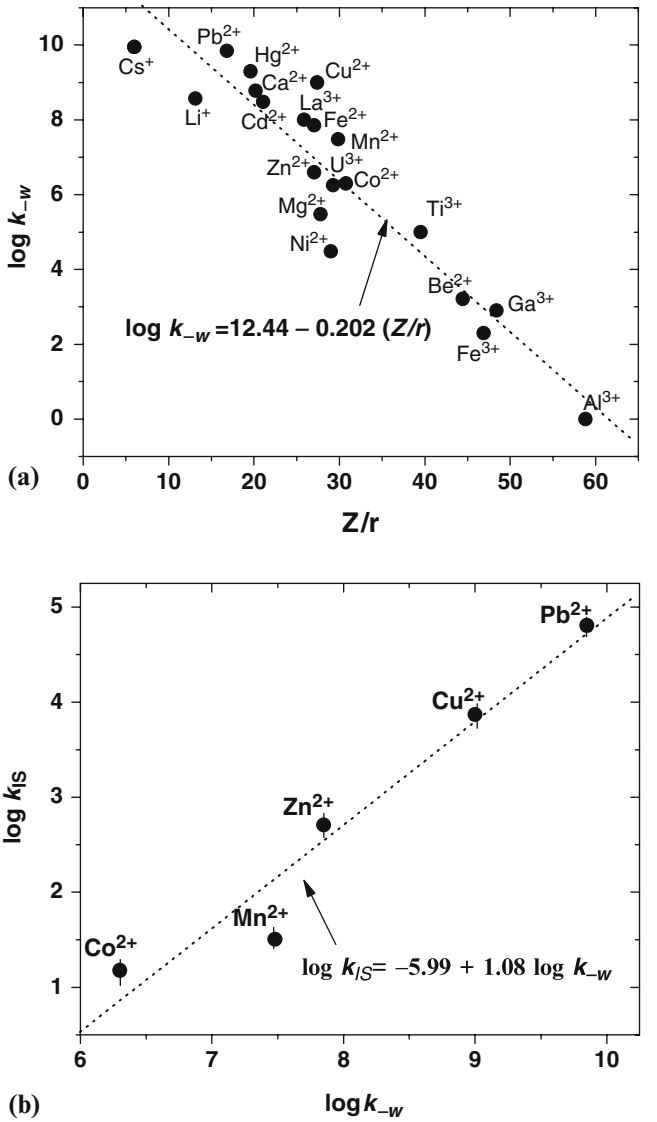

Fig. 4.4 *Top*: The rate constant for water ligand exchange of metal solvation complexes (k_{-w}) as a function of ionic potential (Z/r) of the metal (after Morel and Hering, 1993 with additional data from Casey, 2001). *Bottom:* Linear free energy relation between log k_{-w} and log k_{IS} for adsorption to γ-Al_2O_3 (data from Hachiya et al., 1984; after Wehrli et al., 1990). Units for k_{-w} and k_{IS} are s^{-1} and $mol^{-1}\,dm^3\,s^{-1}$, respectively

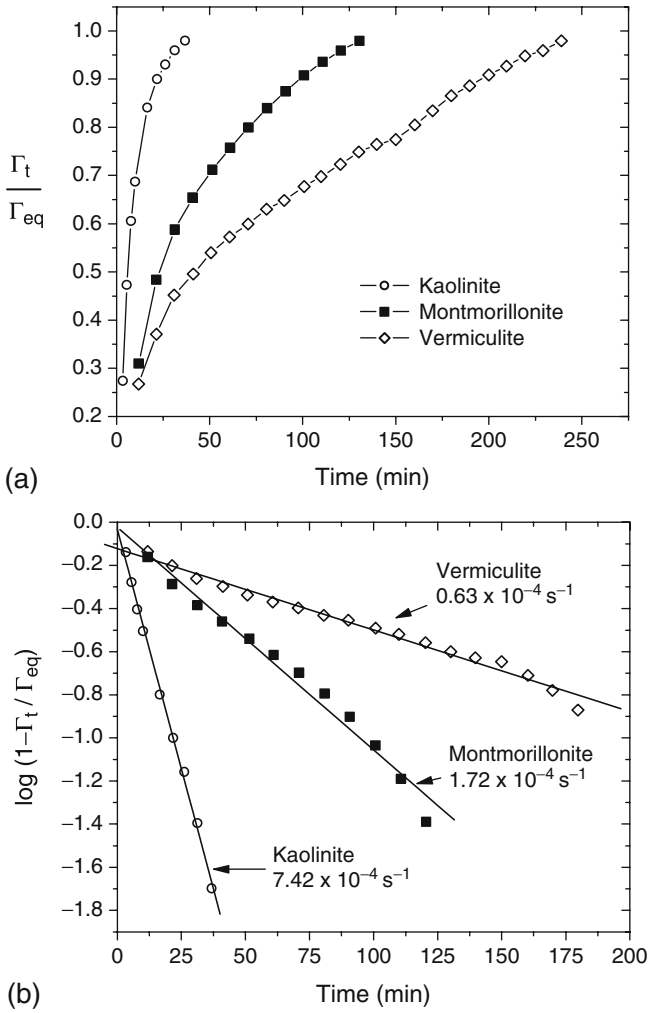

Fig. 4.5 (**a**) Kinetics of K^+ adsorption via ion exchange with Ca^{2+} on three layer silicate clays. (**b**) First order plots and rate constants. (Data from Sparks and Jardine, 1984)

reactions, mass transfer limitations are often significant. For Eq. (4.16) to take place in the forward direction, the following mass transfer and chemical reaction steps are required: (1) K^+ flux through the bulk solution to the proximity of the adsorbent, (2) diffusion of K^+ through the aqueous film surrounding the particle, (3) diffusion of K^+ along the surface or through pores of the adsorbent, (4) reaction involving exchange of K for Ca on the particle surface, (5) diffusion of Ca^{2+} along the surface or through pores of the adsorbent, (6) diffusion of Ca^{2+} through the film surrounding the particle and (7) Ca^{2+} flux through the bulk solution away from the adsorbent.

Kinetic plots for this reaction on three types of layer silicate clays (Fig. 4.5; Sparks and Jardine, 1984) indicate that the rate of the exchange reaction decreases

in the order kaolinite > montmorillonite > vermiculite. Apparent equilibrium ($\Gamma_t/\Gamma_{eq} \sim 1$ in Fig. 4.5a) is approached in 40, 120 and 250 min, respectively. Data for initial uptake to each of the clays are well fit to a first order rate law from which rate constants can be readily obtained (Fig. 4.5b). These adsorption rate differences are attributable to the structural properties of the three clays. As a result of strong interlayer hydrogen bonding, adsorption to kaolinite is limited to external basal surfaces and edge sites, so no interlayer diffusion is required. In montmorillonite, structural charge derives predominantly from isomorphic substitution in the octahedral sheet, which permits rapid diffusion of hydrated ions into an expansive interlayer. In contrast, expansion of the vermiculite interlayer is limited because charge resides in the tetrahedral sheet, in close proximity to the siloxane surface. The limited expansibility of the interlayer diminishes the rate of hydrated ion diffusion into the micro-porous interlayer of vermiculite particles, which limits the overall rate of adsorption kinetics. Despite the faster approach to equilibrium exchange on kaolinite, the values of K^+ surface excess at equilibrium (Γ_{eq}) are substantially higher for montmorillonite and vermiculite because of their higher cation exchange capacities (Sparks and Jardine, 1984). Since the basal spacings (interlayer pore sizes) of clay minerals are dependent on the composition of cations in the interlayer, the kinetics and reversibility (or hysteresis) of cation exchange exhibit strong dependence on system composition (Verberg and Baveye, 1994; Laird and Shang, 1997).

4.3.4 Surface Complexation Kinetics for Oxyanions

Metals and metalloids of high ionic potential (e.g., Cr^{VI}, P^{V}, Se^{IV}, Se^{VI}, As^{III}, As^{V}, Mo^{VI}, Tc^{VII}) occur as oxyanions in natural waters. Depending on surface chemistry and adsorptive speciation, oxyanions may be adsorbed to mineral surfaces via long-range electrostatic interaction (i.e., in the diffuse ion swarm), or via OS and IS surface complexation. Most silicate surfaces exhibit low affinity for oxyanions because of their negative surface charge that results from strongly acidic silanol groups and the prevalence of siloxane (bridging oxygen) sites that do not undergo significant protonation (Table 4.1). Furthermore, isomorphic substitution in layer silicates results in permanent negative charge at basal siloxane surfaces of clay minerals. Hence, values of anion surface excess (Γ), measured in accordance with Eq. (4.1), are often negative because of electrostatic repulsion. This phenomenon of *anion exclusion* is well documented for layer silicate clays that bear significant negative surface charge (Chang and Sposito, 1996) and it may lead to accelerated transport of oxyanion contaminants in silicaceous sediments (e.g., Kaplan and Serne, 1998).

In contrast, oxyanions often exhibit high affinity for metal (hydr)oxide surfaces, particularly those of Fe and Al, and also those of the poorly crystalline aluminosilicate, allophane, because they present positive surface charge at pH < 7–8. Proton adsorption to surface $\equiv$ FeOH and $\equiv$ AlOH groups in these solids (Eq. (4.10a)) promotes electrostatic adsorption of the hydrated anion at the surface and may also facilitate subsequent ligand-exchange to induce IS complex formation. Thus, anion

adsorption to protonated surface sites on (hydr)oxides, may be represented by:

$$SOH_2^+(s) + A^{a-}(aq) \leftrightarrow SOH_2^+ \cdots A^{a-}(s) \tag{4.17}$$

where the dotted line indicates formation of an OS complex. Inner-sphere complexation to surface metal centers (e.g., Fe or Al) occurs upon displacement of surface hydroxyl groups:

$$SOH_2^+(s) + A^{a-}(aq) \leftrightarrow SA^{1-a}(s) + H_2O(l) \tag{4.18}$$

where A is an oxyanion with valence $-a$. The precise mechanism of adsorption bears heavily on sorption–desorption kinetics, but its elucidation requires molecular-scale resolution. The formation of OS and IS complexes of carboxylic acids on mineral surfaces, for example, has been distinguished using infrared (IR) spectroscopy (e.g., Kubicki et al., 1999), whereas the coordinative environment of adsorbed inorganic oxyanions has been elucidated using IR and X-ray absorption spectroscopies (e.g., Suarez et al., 1998; Manceau et al., 2002).

Surface ligand-exchange reactions may be considered from the perspective of the stepwise Eigen-Wilkins-Werner mechanism in analogy to the discussion above for hydrated metal cations. In this case, the two steps involve the rapid formation of an OS complex of the oxyanion with a protonated surface hydroxyl group, followed by the rate-limiting exchange of that hydroxyl group with the oxyanion adsorbate. For example, the adsorption of chromate ($HCrO_4^-$) at the goethite (α-FeOOH) surface may be written as:

$$\equiv FeOH_2^+(s) + HCrO_4^-(aq) \leftrightarrow \equiv FeOH_2^+ \cdots HCrO_4^-(s) \tag{4.19a}$$

$$\equiv FeOH_2^+ \cdots HCrO_4^-(aq) \leftrightarrow \equiv FeOCrO_2OH(s) + H_2O(l) \tag{4.19b}$$

where the first step involves formation of an OS complex. In the second step, chromate exchanges for the protonated hydroxyl (i.e., H_2O) coordinated to the surface Fe metal center such that an oxygen atom of the chromate molecule binds directly to the Fe. The second "ligand-exchange" step is considered to be rate limiting (Yasunaga and Ikeda, 1986).

Relaxation methods have been employed to elucidate the rapid ($<10^{-2}$ s) kinetics of metal adsorption to mineral surfaces (Hachiya et al., 1984). The techniques involve a slight temperature or pressure perturbation of a system from equilibrium, followed by monitoring of its relaxation back to the equilibrium state (Bernasconi, 1976). Grossl et al. (1997) employed pressure-jump relaxation techniques, in which time-resolved changes in electrical conductivity are detected, to measure the rapid kinetics of chromate and arsenate adsorption to goethite. They observed a double relaxation event for both oxyanions. They attributed the first step to formation of a monodentate IS complex, and the second step to slower bidentate complex formation (Fig. 4.6).

Adsorption–desorption rates for oxyanions are also related quantitatively to adsorbent structure. Uptake and release rates are found to increase with increasing mineral crystallinity, whereas equilibrium surface excess values show the inverse trend (Suarez et al., 1998). These differences have been attributed to adsorbate

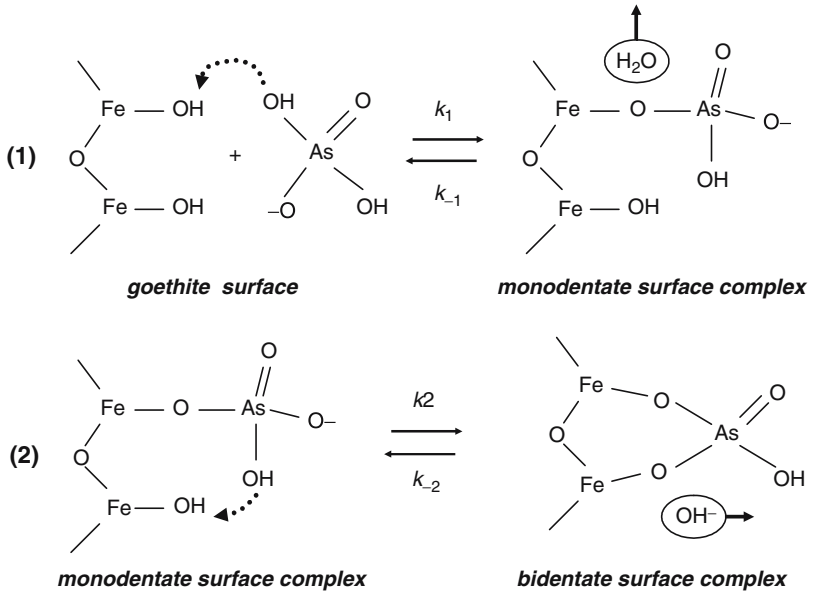

Fig. 4.6 The proposed reaction mechanism for arsenate and chromate adsorption at the goethite surface involves the initial formation of a monodentate surface complex, followed its evolution into a bidentate binuclear species (Grossl et al., 1997)

diffusion into the network of meso- and micro-pores leading to internal surface sites that permeate less crystalline solids (Torrent et al., 1992). Anion adsorption itself may alter adsorbent morphology by inducing particle aggregation and the creation of inter-particle porosity. For example, IS phosphate $\left(H_2PO_4^-\right)$ adsorption to positively-charged hematite $\left(\alpha\text{-}Fe_2O_3\right)$ or goethite (α-FeOOH) neutralizes the positive surface charge on the oxide surface in a manner similar to that for chromate (e.g., see Eq. (4.19b)). This decrease in surface charge diminishes inter-particle repulsion and enhances particle aggregation (Chorover et al., 1997). As a result, phosphate that is adsorbed initially on the *exterior* surfaces becomes buried (occluded) in the *interior* of growing aggregates, such that diffusion out of the aggregates inhibits its subsequent desorption rate (Anderson et al., 1985). Thus, sorbent structure may be altered by adsorption reactions themselves in ways that can then "feed back" to affect subsequent sorption–desorption kinetics.

4.3.5 Multinuclear Surface Complexes, Surface Polymers and Surface Precipitates

Adsorbate structure is dynamic and this impacts uptake or release kinetics. Depending on system composition, reaction time and surface coverage, adsorbate structure may evolve through water ligand exchange, surface diffusion and restructuring from isolated outer-sphere to inner-sphere surface complexes, and further to yield the

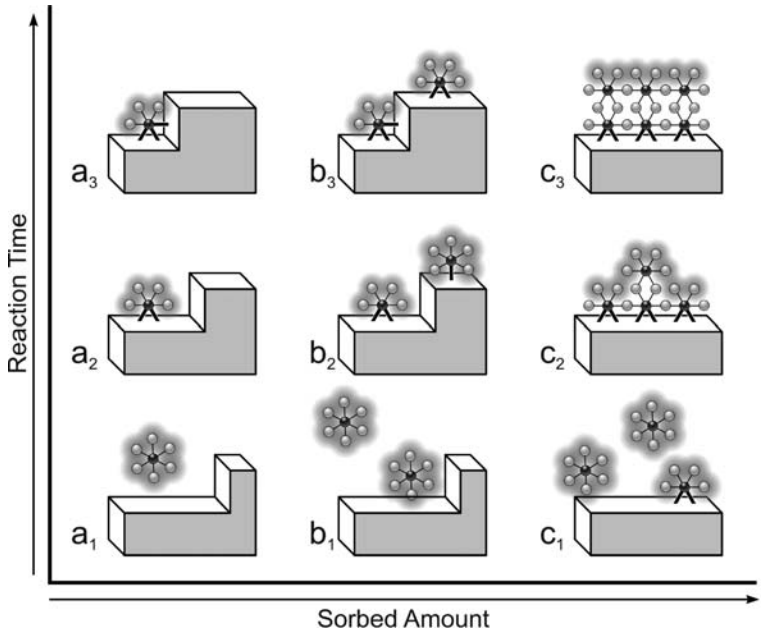

Fig. 4.7 Influence of surface loading and reaction time on sorbate structure. Transformation of OS to IS complexes is often observed at low surface loadings, whereas such mononuclear complexes give rise to multinuclear surface species, surface precipitates and surface coatings with increased loading and reaction time

formation of small groupings of adsorptive ions known as *multinuclear surface complexes* (Fig. 4.7). Further growth of multinuclear surface complexes may result in the formation of *surface polymers* and/or *surface precipitates*, with the latter being distinguished on the basis of its three-dimensional crystal structure (Charlet and Manceau, 1994). In Fig. 4.7, the formation of new bonds during IS complex formation or surface precipitation is denoted by thicker lines extending from the central metal cation toward coordinating oxygen atoms. These new bonds can involve direct metal coordination to oxygen atoms of the mineral surface as occurs in monodentate or bidentate IS complex formation (Fig. 4.7a_2–b_2) or bonding through bridging oxygens to other sorbate metal atoms during surface polymerization and precipitation (Fig. 4.7c_2–c_3). The tendency for such reactions to occur – where sorbate metals share bridging oxygen atoms with the mineral sorbent – is due, in part, to the similar oxygen coordination number for metals in solution and in mineral solids (Casey, 2001).

Solid phase uptake of inorganic sorptives occurs over a wide range of time frames from microseconds to years, even for the same sorbent–sorbate pair. Sorption by OS complex formation tends to be rapid and reversible, whereas IS complex formation is slower and may be irreversible. Indeed, metal sorption to layer silicate clays, hydrous oxides and humic substances is often characterized by a rapid initial uptake, followed by a slower, sustained reaction. Whereas the rapid phase is assumed to correspond to film diffusion and chemical reaction, the slower phase has been

variously attributed to surface or pore diffusion, uptake to sites of low reactivity, surface polymerization and co-precipitation (Figs. 4.2 and 4.7). The following two subsections provide examples of these effects.

4.3.5.1 Radionuclide Sequestration into Precipitating Solids

In real-world systems, sorption–desorption reactions co-occur with mineral transformation. This leads to complex interactions that may control the uptake of sorptive species from solution, and that can only be understood by using a multi-method approach. For example, sorption–desorption on clay minerals exerts strong control over the transport of ^{137}Cs and ^{90}Sr where high level radioactive waste (HLRW) has leaked from storage tanks into subsurface environments (Zachara et al., 2002). Some forms of liquid HLRW are quite alkaline pH (>12). When solutions of elevated pH percolate into mineral soils, the kinetics of silicate mineral dissolution can be increased significantly (see Chap. 5) and this has important implications for contaminant sorption. A recent study, depicted in Fig. 4.8, shows how macroscopic measurements can be combined with molecular spectroscopy to understand linkages between sorption–desorption kinetics and transformation reactions in geochemical systems (Chorover et al., 2003; Choi et al., 2006). In this case, time-dependent uptake of Cs^{+} and Sr^{2+} from a simulated HLRW solution occurs when the solution is contacted with kaolinite clay. Initial uptake of Sr is rapid, with nearly half being removed from solution in < 24 h, while a slower uptake process continues over days to months for both Sr and Cs (Fig. 4.8a). The slower uptake in Fig. 4.9a proceeds over a period that includes dissolution of Al and Si from kaolinite, followed by their re-precipitation into newly formed mineral phases (feldspathoids and zeolites) after 30 days of reaction (Fig. 4.8b). The kinetics of mineral transformation were assessed by monitoring the solid phase using ^{27}Al magic angle spinning nuclear magnetic resonance (MAS NMR) spectroscopy, which reports on the local coordination environment of Al^{3+}. Since each Al^{3+} atom is bonded to six oxygens in kaolinite (octahedral Al or Al^{VI}), the time-dependent emergence of a new NMR peak showing Al bonded to four oxygens (tetrahedral Al or Al^{IV}) provides a quantitative measure of mineral transformation rate. The changing ratio of feldspathoid Al^{IV} to total (kaolinite plus feldsphathoid) Al is shown in Fig. 4.8c. This mineral transformation is correlated not only with the slow uptake of Sr from solution, but also with a decrease in the tendency for Sr desorption from the reacted solid phase (Fig. 4.8c – note that the fraction of desorbable Sr decreases with time).

A molecular-scale explanation for these relations is obtained by examining the local coordination environment of the sorbed Sr atoms using extended X-ray absorption fine structure (EXAFS) spectroscopy. EXAFS spectroscopy provides information on coordination number of the X-ray absorbing atom, as well as bond distances to first and second shell nearest neighboring atoms. [For detailed discussions of EXAFS spectroscopy and related techniques applied to geochemical systems, see Charlet and Manceau (1993), Brown and Sturchio (2002), and Manceau et al. (2002)]. The left side of Fig. 4.8d shows background-normalized, k^3-weighted, Sr

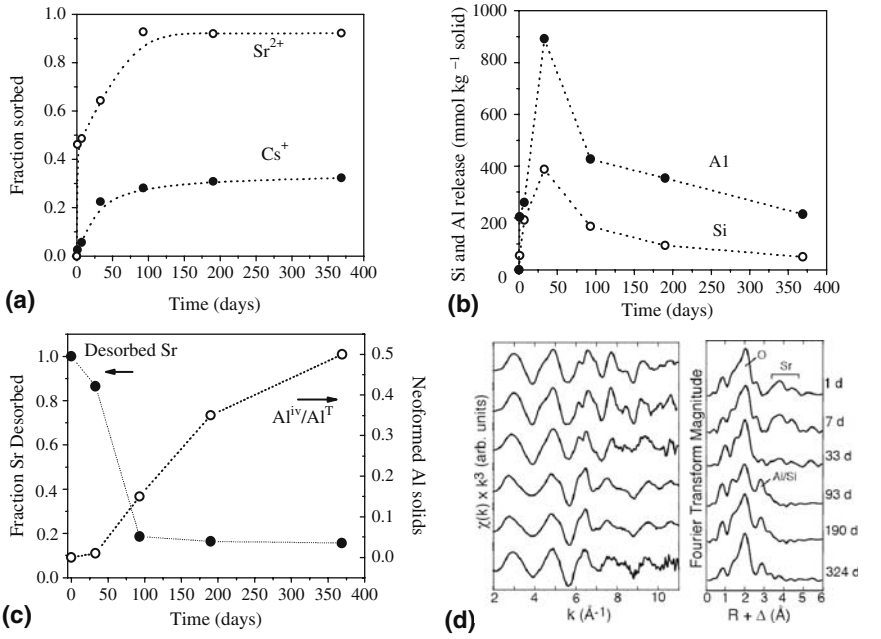

Fig. 4.8 Coupled kinetics of (**a**) contaminant (Cs^+ and Sr^{2+}) uptake and (**b**) mineral dissolution and precipitation (Al and Si solubility) kinetics for a simulated tank waste leachate reacted with kaolinite clay. (**c**) Resistance of sorbed Sr^{2+} to subsequent desorption is linked to the precipitation of feldspathoids and zeolites whose formation kinetics are measured by the accumulation of tetrahedrally coordinated Al (Al^{iv}) in the reacted solid phase. (**d**) Sr K-edge EXAFS spectra show the time-dependent change in sorbed Sr species. (From Chorover et al., 2003; Choi et al., 2006)

EXAFS spectra collected as a function of reaction time. The right side shows the corresponding Fourier transforms, where peak amplitudes correspond to coordination number and peak location gives inter-atomic distance. Detailed analyses of the EXAFS spectra depict the time-dependent change in bonding environment of Sr atoms in the solid phase. These data show that the contaminant occurs in weakly sorbed Sr-carbonate polymeric species at 1 and 7 d, with oxygen in the first shell and Sr in neighboring shells at distances to 4.9 Å. At times longer than 33 d, all spectra exhibit a first-shell O peak and second-neighbor peaks corresponding to Si or Al atoms at 3.43–3.46 Å. The emergence of Si or Al in the second shell signals the IS complexation and incorporation of Sr during growth of feldspathoid and zeolite sorbent products (Choi et al., 2006).

This example highlights the importance of long-term aging processes – including mineral transformation – that contribute to the changing nature of the sorbate bonding environment. As illustrated in Fig. 4.7a_1–a_3, crystal growth of a mineral adsorbent (represented by the leftward expansion of the top layer) can result in sequestration of sorbate molecules into forms that are increasingly resistant to desorption. At high adsorptive concentrations, polymerization of the sorbate molecules

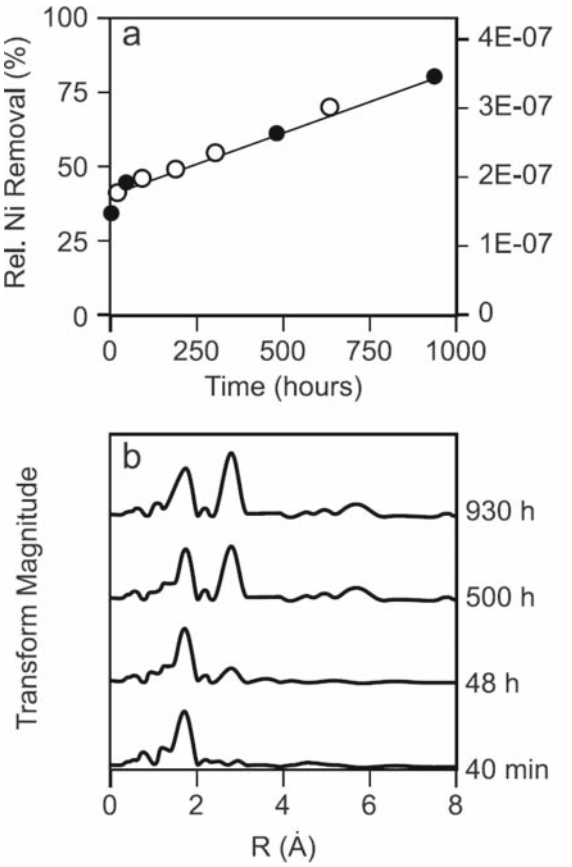

Fig. 4.9 Kinetics of Ni^{2+} sorption to montmorillonite showing (**a**) macroscopic measures of uptake and (**b**) Fourier transformed EXAFS spectra of sorbed Ni^{2+} speciation (Reprinted from Scheidegger et al., 1998, with permission from Elsevier)

themselves can result in crystal growth, likewise resulting in higher stability and diminished desorption (Fig. 4.7c_1–c_3).

4.3.5.2 Transition Metal Sorption to Smectite

A continuous evolution of adsorbate structure has also been observed with increasing time for transition metal ions reacted with layer silicate clays. In a study of Co and Zn adsorption to hectorite (a smectite), EXAFS results showed that adsorbate structure evolved from OS to IS coordination, suggesting that the metals sorbed initially as exchangeable OS complexes on external basal or interlayer sites, and then migrated to edge sites to form IS surface complexes (Schlegel et al., 1999; 2001a). Over longer reaction times, and in the presence of dissolved Si, nucleation

and epitaxial growth of a Zn layer silicate was observed on the smectite edges (Schlegel et al., 2001b). In contrast, Co was not found to form surface phyllosilicate precipitates, indicating the importance of adsorbate–adsorbent specificity for effective surface nucleation and crystal growth.

The coupling of kinetic and spectroscopic studies of Ni sorption to montmorillonite (a 2-to-1 layer silicate) reveal the formation of Ni/Al hydroxide surface precipitates at aqueous Ni concentrations well below the solubility product of $Ni(OH)_2(s)$ (Scheidegger et al., 1999). Sorption of Ni^{2+} to montmorillonite is fast initially (35% removal within 40 minutes), but the second stage is significantly slower, requiring approximately 40 days to achieve 80% removal (Fig. 4.9a). Fourier transforms of normalized, background subtracted and k^3-weighted EXAFS spectra show a peak at $R \sim 1.8$ Å, corresponding to oxygen atoms in the first coordination shell of Ni (Fig. 4.9b), which is expected for both inner- or outer-sphere complexes at clay mineral surfaces. However, a second nearest neighbor coordination shell corresponding to Ni at $R \sim 2.7$ Å is found to increase in intensity with increasing reaction time (Fig. 4.9b). Data analysis of the second coordination shell revealed that the number of second neighbor Ni atoms increased with increasing reaction time, whereas the number of second neighbor Al atoms was variable. These data indicate that whereas Ni initially forms a surface complex with the clay mineral, sorbate structure is converted over time because dissolution of clay-derived Al leads to incorporation of adsorbed Ni into neoformed mixed Ni/Al hydroxide polymers (Scheidegger et al., 1999). The rate of this transformation was found to correlate with the rate of Al dissolution from the sorbent clay.

Multinuclear structures (e.g., Fig. 4.2i) are particularly favored for adsorptive species that also have a tendency to form oligomers and polymers via hydrolysis in aqueous solution (e.g., transition metals). For a given metal, the rate and extent of this structural transformation depends on aqueous geochemical conditions (solution pH, ionic strength and composition). Recent studies using advanced analytical methods have shown that the sorption of heavy metals on clay and oxide surfaces results in the formation of multinuclear or polynuclear surface phases more frequently and more rapidly than previously thought. Polynuclear metal hydroxides of Pb, Co, Cu and Cr(III) on oxides and aluminosilicates have been identified using EXAFS. These surface phases have been observed at metal surface loadings far below a theoretical monolayer coverage and within a pH range well below that where the formation of metal hydroxide precipitates would be expected according to thermodynamic solubility product calculations. The process appears to be enhanced by labile sorbent surfaces that undergo dissolution and co-precipitation with sorbate in the time frame of the experiment (Schlegel et al., 2001a, b).

4.3.6 Effects of Residence Time on Desorption Kinetics

As indicated above, reaction of inorganic solutes at mineral surfaces is often characterized by initial rapid and subsequent slower uptake reflecting mass transfer

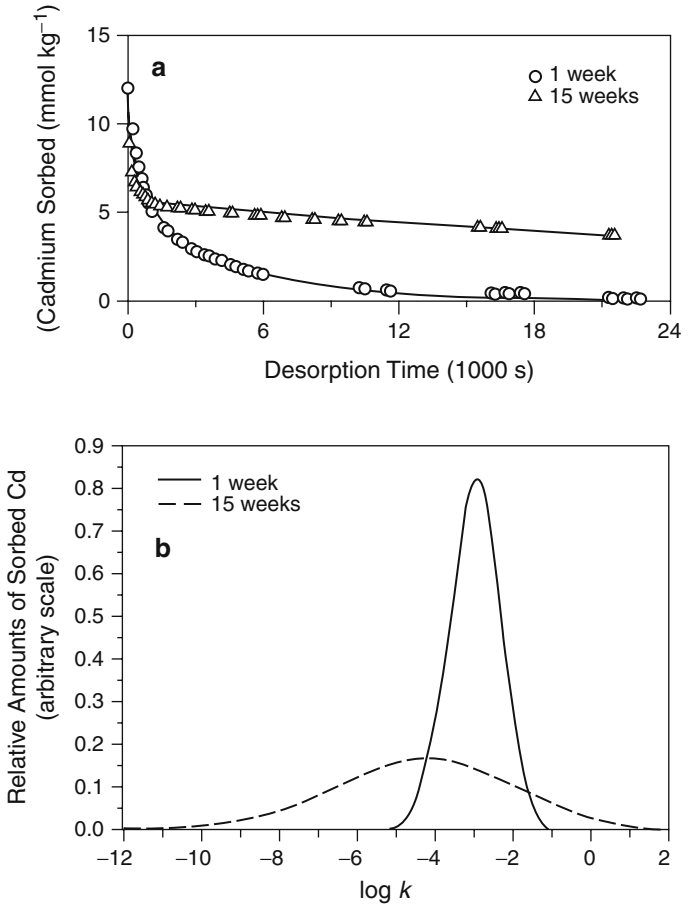

Fig. 4.10 Cadmium desorption kinetics as a function of contact time (1 or 15 weeks) in goethite (Backes et al., 1995): (**a**) Mass of Cd released from the reacted solid and (**b**) lognormal distribution of first order desorption rate constants for the reacted solids (Eq. (4.21)). (Backes et al., 1995, with permission)

limitations or an evolving sorbate structure. Therefore, it seems reasonable to expect that the length of time associated with sorptive uptake (referred to as "contact time", "aging time" or "residence time") should likewise influence subsequent *desorption* rate. This assertion is supported by several studies. Increasing the residence (i.e., sorbate–sorbent contact) time from 1 to 15 weeks substantially decreased the kinetics of Cd desorption from goethite (α-FeOOH) (Fig. 4.10a) (Backes et al., 1995). The data in Fig. 4.10a were fit to two different kinetic models. The first model assumes that desorption is controlled by two simultaneous first-order reactions with discrete rate constants, k_1 and k_2, representing rapid and slow desorption reactions, respectively. The adsorbed Cd at any time $(\Gamma_{Cd,t})$ is then given by:

$$\Gamma_{Cd,t} = \Gamma_{1,Cd_0} \exp(-k_1 t) + \Gamma_{2,Cd_0} \exp(-k_2 t) \tag{4.20}$$

where $\Gamma_{1,Cd0}$ and $\Gamma_{2,Cd0}$ are the sorbed masses, at time $t = 0$, of Cd associated with sites undergoing rapid and slow desorption, respectively. Fits to the data indicate that the proportion of initial sorbed Cd $(\Gamma_{Cd,0})$ in slowly desorbing (type 2) sites increased from 0.65 to 0.85 between 1 and 15 weeks of contact time, and log k_2 decreased from -3.63 to -4.73 over the same period. The second model assumes that metal ion bonding sites form a continuous lognormal distribution with respect to the first-order desorption rate constant, k (Rate et al., 1992):

$$\Gamma_{Cd,t} = \frac{\Gamma_{Cd,des}}{\sigma\sqrt{2\pi}} \int_{-4\sigma}^{4\sigma} exp\left[\frac{-1}{2}\left(\frac{\ln k - \mu}{\sigma}\right)^2\right] exp(-e^{\kappa}t) d\ln k \tag{4.21}$$

where $\Gamma_{Cd,des}$ is the total mass of Cd desorbed per unit mass of sorbent, μ is the mean of the normal distribution in $\ln k$, and σ is the corresponding standard deviation. The resulting distributions in log k (Fig. 4.10b) indicate a decrease in the mean value (from -3.06 to -4.24) and an increase the breadth of the distribution (σ increased from 0.65 to 2.37) with increasing contact time. That is, both data fitting approaches suggest an increase in the size and recalcitrance of the slowly desorbing pool accompanies an increase with contact time. The macroscopic kinetic data themselves do not indicate a distinct cause for this increase. One possible explanation is the time-dependent surface migration of Cd from sites of weaker bonding (e.g., Fig. 4.2c) to those with stronger bonding such as ledge or kink sites (Fig. 4.2f,g). Other possibilities include micropore diffusion into the adsorbent particle (Fig. 4.2h) or surface co-precipitation reactions (Figs. 4.2i and $4.7b_{1-3}$).

Some evidence for the latter mechanism, whereby metals are incorporated into the sorbent oxide structure via recrystallization, is provided by a study of Co, Cd and Pb sorption to hydrous ferric oxide (HFO) (Ainsworth et al., 1994). HFO $(Fe_5HO_8 \cdot 4H_2O)$ is a poorly crystalline and metastable form of Fe oxide that converts over time to more thermodynamically stable phases, such as goethite (α-FeOOH), lepidocrocite (γ-FeOOH) or hematite $(\alpha\text{-}Fe_2O_3)$. Sorption–desorption hysteresis (the difference in solid–liquid distribution of sorptive species during adsorption versus desorption runs) was found to increase with increasing contact time. Figure 4.11a shows sorption and desorption *edges* (sorbed mass versus pH for a constant total metal concentration in suspension) for Co reacted with HFO for 16 h, 2 weeks, 9 weeks and 16 weeks. The adsorption edge shows a sharp increase in adsorbed mass at pH 6.8, because a pH-dependent decrease in positive surface charge of HFO enhances cation uptake. The desorption edges are shifted to lower pH and higher sorbed mass with increased aging time, reflecting an increasing degree of sorption–desorption irreversibility or sorption *hysteresis*. The mass of metal *not* desorbed within the 16 h desorption period increased with increasing contact time for the ions of smaller radii Co^{2+} (0.072 nm) and Cd^{2+} (0.097 nm) but not for the larger Pb^{2+} (0.120 nm) ion (Fig. 4.11b), which led the authors to conclude that the smaller ions were substituting for Fe^{3+} (0.064 nm) during precipitation of goethite from HFO. Being too large to undergo isomorphic substitution with Fe, the Pb^{2+} cation was limited to surficial adsorption and it exhibited no hysteretic effect.

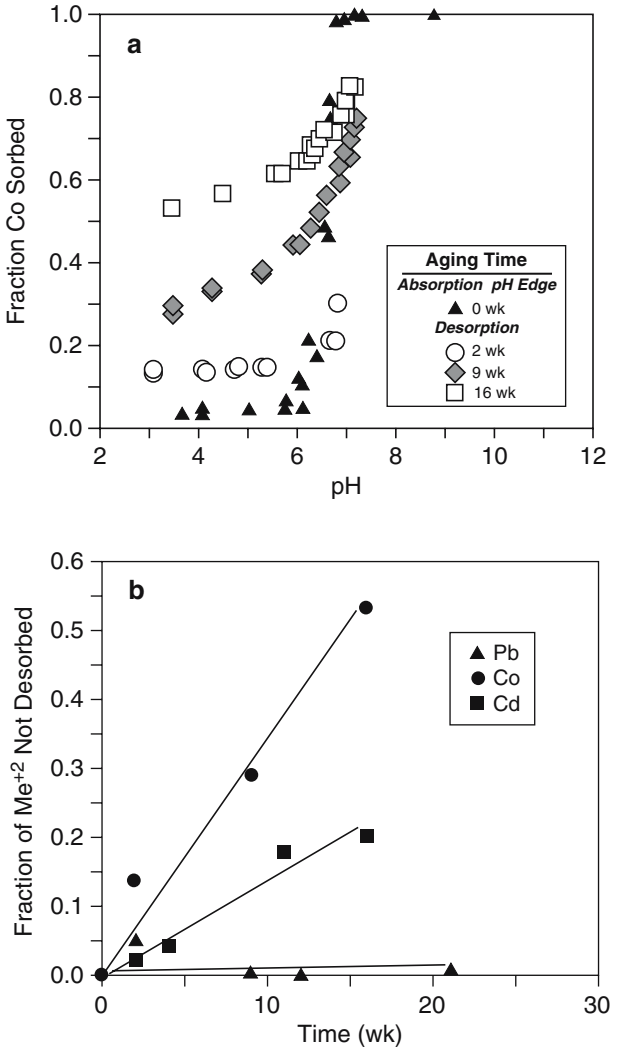

Fig. 4.11 Sorption–desorption data for transition metals on hydrous ferric oxide (ferrihydrite) showing the effects of contact time on (**a**) sorption–desorption edge of Co and (**b**) the mass of residual metal following desorption (Ainsworth et al. 1994, with permission)

4.4 Sorption Mechanisms and Kinetics for Organic Solutes

4.4.1 Polar Organic Compounds

A wide range of natural and anthropogenic organic solutes exhibit high solubility in aqueous solution because they possess polar and/or ionic functional groups that

are readily solvated by water molecules. Such compounds include simple low molar mass organic acids, surfactants, some polymeric biomolecules and soluble humic fractions. The sorption of these compounds to particle surfaces is controlled by chemical and physical mechanisms. As in the case of inorganic adsorptives, chemical mechanisms of adsorption (i.e., *chemisorption*) involve significant electron orbital overlap between the adsorbate and functional groups of the solid phase to form a bond that exhibits both covalent and ionic character. For example, the high affinity of hydrous Fe and Al oxides for polar organic compounds is attributed to the formation of IS complexes between weakly-acidic, oxygen-containing functional groups (e.g., carboxylate, phenolate, phosphate) and surface Fe or Al centers by a surface ligand exchange reaction. The reaction

$$SOH(s) + R - COOH(aq) \leftrightarrow SOOC - R(s) + H_2O(l) \tag{4.22}$$

shows the exchange of carboxylate for a surface OH group singly coordinated to the structural (e.g., Fe or Al) metal. The released OH^- (aq) combines with H^+ from carboxyl to form the product $H_2O(l)$.

Physical mechanisms of adsorption (i.e., *physisorption*) include the hydrophobic effect, electrostatic (e.g., OS) adsorption, van der Waals interaction, H-bonding and charge transfer complex formation, all of which tend to be weaker intermolecular attractive forces.

For example, OS adsorption may be mediated by a positively-charged amino group:

$$SOH(s) + R - NH_3^+(aq) \leftrightarrow SO^- \cdots {}^+H_3N - R(s) + H^+(aq) \tag{4.23}$$

Hence, low molar mass ionizable organic molecules participate in mineral surface reactions comparable to those observed for the inorganic oxyanions and cations.

In contrast, macromolecules, such as biopolymers and humic substances may become sorbed to mineral surfaces through multiple modes of attachment, including hydrophobic interaction, H-bonding, water or cation bridging and ligand exchange, even for a single molecule. In the case of large polymeric molecules, the number of points of attachment to a surface may increase following the initial adsorption event at a single site because of relaxation and surface conformational changes (Fleer et al., 1993). Thereafter, desorption becomes increasingly unfavorable since it requires the breaking of multiple bonds simultaneously followed by diffusion into bulk solution. This results in slower kinetics for desorption than for adsorption reactions (i.e., sorption–desorption hysteresis). For example, Zimmerman et al. (2004) observed large hysteresis effects for polypeptide adsorption–desorption at the surfaces of alumina and silica, whereas no significant difference between adsorption and desorption isotherms was observed for amino acid monomers. They also found that the hysteretic effect was enhanced in the presence of mineral "mesopores" that were similar in size to adsorptive species in solution (e.g., Fig. 4.2h).

Natural organic matter (NOM) in aqueous systems comprises a heterogeneous and polydisperse mixture of aggregated biomolecular fragments and degradation products with variable hydrophilicity and functional group composition (Sutton and

Sposito, 2005). Thus, adsorption of NOM to mineral surfaces exhibits some of the same characteristics as reported for adsorption of polymer mixtures, including adsorption–desorption hysteresis, and isotherm dependence on the ratio of adsorbent surface area to volume. Research on adsorption kinetics for non-ionic polymer mixtures has shown rapid initial uptake of low molecular weight (LMW) fractions followed by their subsequent displacement by high molecular weight (HMW) molecules (Fleer et al., 1993). The initial phase has been attributed to higher bulk and film diffusion coefficients (D in Eqs. (4.3) and (4.4) for the LMW molecules, which expedites their transport to the surface relative to the HMW fractions. The subsequent displacement of LMW molecules is consistent with more favorable energetics of adsorption of HMW molecules.

Dynamics of NOM adsorption at mineral surfaces are more complex than non-ionic polymers because the ionic species are subject to additional electrostatic and surface complexation interactions. As a result, changes in solution chemistry (e.g., pH, ionic strength and composition) can have a significant effect on adsorption–desorption processes. Adsorption of NOM to iron oxides (α-Fe_2O_3 and α-FeOOH) is characterized by a rapid initial step (completed in 2–15 min) followed by a slow uptake and restructuring of adsorbate, both of which show strong dependence on solution chemistry. For example, the initial adsorption rate for fulvic acid on goethite decreased from 1.39 to $0.12\,\mathrm{mg\,m^{-2}\,h^{-1}}$ as pH increased from 3.5 to 7.5, presumably because of increasing electrostatic repulsion between dissociated NOM molecules at the surface and in solution (Fig. 4.12a, Zhou et al., 2001). Slower adsorption–desorption of NOM continues after this initial uptake, involving conformational change of adsorbate and replacement of LMW adsorbate by HMW molecules in solution (Fig. 4.12b) (Avena and Koopal, 1999; Zhou et al., 2001).

4.4.2 Hydrophobic Organic Compounds (HOCs)

The sorption of sparingly soluble HOCs, many of which (e.g., polycyclic aromatic hydrocarbons, chlorinated solvents, hydrophobic pesticides, etc.) are important environmental pollutants, is driven primarily by the incompatibility between water and the organic compound, a phenomenon known as the "hydrophobic effect". In essence, this effect involves the expulsion of a low-polarity organic compound from the aqueous phase, and subsequent association with the sorbent phase. The hydrophobic effect derives from the fact that dissolution of HOCs in water requires breaking the hydrogen-bonded structure of liquid water to form "cavities" for the HOCs, and there are generally no favorable bonds formed between water molecules and non-polar organic molecules in return.

The surfaces of metal hydroxides tend to be hydrophilic because their hydroxylated (*SOH*) surface functional groups are quite polar and readily form coordinative bonds with water molecules and hydrated ions (Brown, 2001). Similarly, when layer silicate clays possess structural charge due to isomorphic substitution, they adsorb hydrated cations at siloxane sites to balance their negative surface charge (Sposito et al., 1999). Hence, at hydroxide and charged layer silicate surfaces, the adsorption of

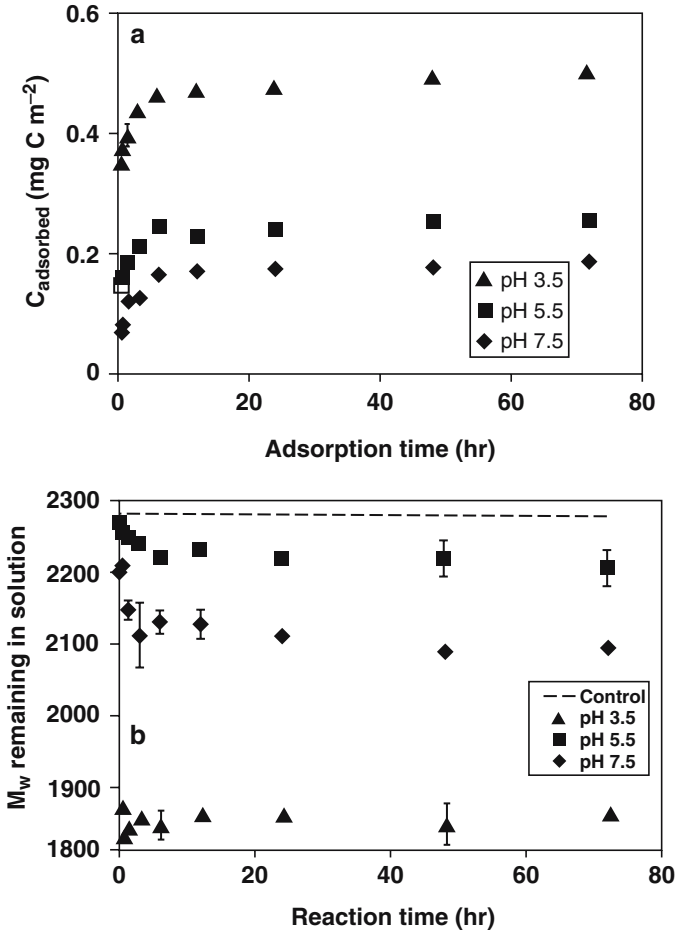

Fig. 4.12 (**a**) Time-dependent adsorption of NOM to the goethite surface at three different pH values. (**b**) Selective uptake of high molar mass constituents (mean initial molar mass is indicated by the dashed line). (Data from Zhou et al., 2001, with permission)

water or hydrated ions is more favorable energetically than is the adsorption of non-polar (hydrophobic) organic molecules. Conversely, sorbent organic matter (SOM), present both as mineral coatings and as discrete organic colloids (Fig. 4.1) plays a principal role in the sorptive uptake of HOCs. As a coating on mineral surfaces, SOM is thought to enhance the sorption affinity for HOCs by making the surface more hydrophobic, thus thereby enhancing the favorable overall energetics of sorption. Thus, although adsorption of HOCs to mineral surfaces can occur for example on the basal surfaces of low-charged layer silicates, particularly when the interlayer is not densely occupied by hydrated cations (e.g., Hundal et al., 2001), sorption of HOCs is predominated by interactions with SOM for most conditions and for most geomedia.

Many early phenomenological representations of HOC-SOM interactions were based on simple liquid–liquid partitioning concepts, wherein the SOM was treated as an organic liquid phase. Hence, for example, correlations based on octanol-water partition coefficients have been used to estimate sorption behavior (Karickhoff, 1981). Such correlations in many cases provide reasonable estimates of relative magnitudes of sorption. This is because liquid–liquid partitioning of HOCs is governed by the hydrophobic effect, as is the sorption of HOCs. However, the sorption/desorption of HOCs is often observed to be rate-limited, non-linear (with sorption decreasing with increasing sorptive concentration in solution), and competitive in multi-solute systems (e.g., Brusseau and Rao, 1989). These observations are not consistent with the simple liquid–liquid partitioning process. Currently, the uptake of HOCs by SOM is generally considered to be an *ab*sorption process, whereby organic molecules diffuse into the interior environment of SOM molecules and their aggregates, rather than remaining at the surface as in an *ad*sorption phenomenon (e.g., Brusseau et al., 1991; Brusseau, 1993; Pignatello, 2000). Thus, SOM does not behave as an impenetrable surface or as a simple organic liquid, but rather as a *random network polymer* phase that provides a three dimensional hydrophobic environment for organic molecules.

The sorption/desorption of HOCs by geomedia can be significantly rate limited, requiring days, weeks, or even months to attain equilibrium. For example, sorption of phenanthrene by a peat soil (93% organic matter) required more than 80 days to reach equilibrium (Fig. 4.13a). The degree of sorption/desorption rate limitations often correlates to the size of the organic solute and the quantity of SOM associated with the sorbent. Rate limitations associated with the sorption/desorption of HOCs are attributed to the permeation of the compounds within the three-dimensional matrix of the SOM, referred to as intraorganic matter diffusion. It is well established that diffusion of compounds within polymeric matrices is strongly influenced by the molecular morphology of the solute, as well as by the properties of the solvent and polymer. For example, application of quantitative-structure-activity relationship (QSAR) analysis to the rate-limited sorption/desorption behavior observed for 29 organic compounds with two soils showed that the sorption/desorption rate coefficient correlated well to the molecular connectivity index (Fig. 4.14), which is a measure of the topological size of molecules and their degree of branching (Brusseau, 1993).

Observations of rate-limited, nonlinear, and competitive sorption for HOCs have led to the development of the "dual-mode" sorption model, which presumes that SOM is comprised of "rubbery" and "glassy" phases (e.g., Huang et al., 1997; Zhao et al., 2001). Hydrated soft carbon components are considered to comprise the expanded "rubbery" domain, whereas condensed hard carbon components are considered to comprise the "glassy" domain. The rubbery domain is represented as a flexible polymeric domain, wherein organic compound sorption is linear and non-competitive (i.e., constituting *ab*sorption), and controlled by permeation interactions. The glassy domain comprises nanometer-scale pores in which retention – more akin to *ad*sorption – occurs via sorbate interaction with pore walls. Sorption to pores in the glassy SOM is thought to be responsible

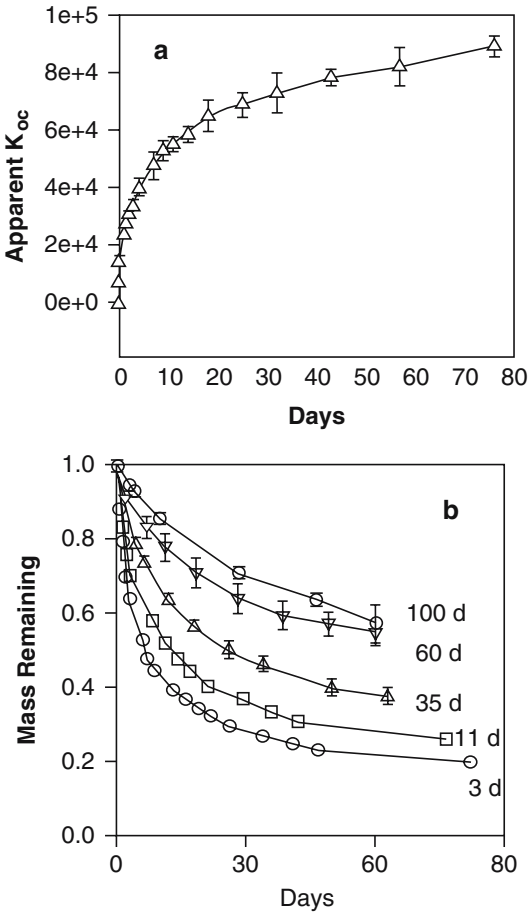

Fig. 4.13 Adsorption of hydrophobic organic compound to organic matter in a peat soil. (**a**) Time-dependent sorption of phenanthrene. (**b**) Desorption rate shows strong dependence on contact time and also exhibits strong hysteresis. (Data from Pignatello et al., 2000, with permission)

for the non-linear and competitive effects that are sometimes observed for HOC sorption.

A two-domain type isotherm can be used to represent dual-mode sorption behavior, such as the following equation that describes both linear and non-linear "Langmuir-type" sorption (Weber et al., 1992):

$$\Gamma_{HOC} = K_D c_{HOC} + \frac{Q^0 bc}{1 + bc} \tag{4.24}$$

where Γ_{HOC} is the sorbed mass of HOC, K_D is an affinity parameter incorporating the SOM-solution distribution coefficient for linear partitioning into the rubbery phase, c_{HOC} is the equilibrium solution phase concentration, and Q^0 and b are the Langmuir sorption capacity and affinity coefficients, respectively, of the pore filling

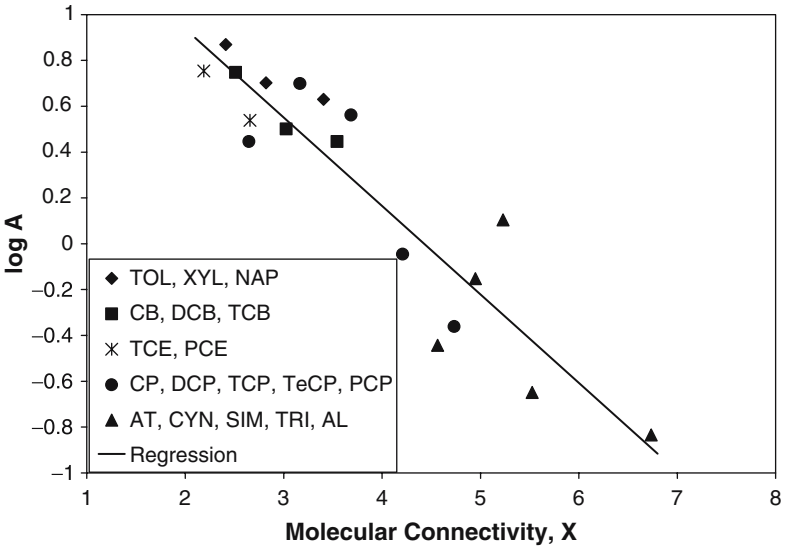

Fig. 4.14 Correlation between the diffusion-normalized mass-transfer coefficient A $[T^{-1}]$ and the first-order valence molecular connectivity index (X) for several HOCs. $A = a\,D/l^2$, where a is a shape factor for the diffusion domain, D is the solid-phase diffusion coefficient $[L\,T^{-2}]$, and l is the characteristic diffusion length [L]. The connectivity index (X), is calculated from the number of non-H bonds associated with each atom, using coefficients based on type of atom. TOL = toluene, XYL = p-xylene, NAP = naphthalene, CB = chlorobenzene, DCB = 1,3-dichlorobenzene, TCB = 1,2,4-trichlorobenzene, TCE = trichloroethene, PCE = tetrachloroethene, CP = chlorophenol, DCP = 2,4-dichlorophenol, TCP = 2,4,6-trichlorophenol, TeCP = 2,3,4,5-tetrachlorophenol, PCP = pentachlorophenol, AT = atrazine, CYN = cyanzine, SIM-simazine, TRI = trietazine, and AL = alachlor. (Reproduced from Brusseau, 1993)

domain. The first term on the right side of Eq. (4.24) describes the linear dissolution behavior, whereas the second term depicts site specific adsorption in the pores.

Another feature of HOC-SOM interaction is the observation of a *desorption resistant* fraction, indicative of sorption–desorption irreversibility or hysteresis. As illustrated in Fig. 4.13b, despite a short (3 day) contact time for sorption, a significant amount (20%) of phenanthrene still remains sorbed even after a much longer (85 day) desorption period. The formation of a desorption resistant pool has been attributed to a "pore deformation mechanism", in which sorbate bound into nanopores within the glassy phase becomes entrapped due to slow relaxation of the deformable SOM matrix (Lu and Pignatello, 2002; 2004). Indeed recent work suggests that "pre-conditioning" of the glassy phase with sorbate molecules leads to an expansion of sorbent nanopores, resulting in enhanced uptake of similar sorbate molecules once those that promote the "conditioning effect" have been removed. Thus, like the changes in inorganic sorbent–sorbate interactions that occur with time along the continuum from adsorption, surface polymerization and co-precipitation, sorbent organic matter exhibits time dependent changes in structure that influence its long-term interaction with sorbate molecules.

4.4.3 Vapor-Phase Processes

The preceding discussion has focused on water-saturated systems (wherein only solid and aqueous phases are present). Additional sorption processes may occur for volatile HOCs in unsaturated systems wherein a gas phase is present. One such process is often referred to as vapor adsorption. This issue is of particular interest for transport of volatile contaminants in the vadose zone, and for transport of contaminants sorbed to particles suspended in air, which can migrate great distances by atmospheric processes.

As noted above, mineral surfaces generally are of secondary importance for sorption of HOCs in water-saturated systems. Such is not the case for vapor sorption. Sorption of organic vapors occurs by adsorption to mineral surfaces, as well as by interactions with sorbent organic matter (e.g., Chiou and Shoup, 1985; Goss, 1992; Goss and Eisenreich, 1996).

Vapor adsorption is strongly influenced by the amount of water present at the surfaces of the porous-medium grains. For example, adsorption of vapor-phase HOCs by oven-dry soil has been observed to be orders-of-magnitude larger than sorption of the same HOCs in water-saturated soil. As water progressively coats the sorbent surfaces, the magnitude of HOC adsorption decreases greatly. This effect is related to the ability of water to "out compete" organic contaminants for adsorption at mineral surfaces. It does not take much water – the equivalent of approximately 4–8 layers of water molecules – to reduce the magnitude of sorption to that obtained for water saturated conditions. Given the relative humidities associated with most subsurface domains, it is unlikely that vapor-phase sorption will be of significance for field applications.

Adsorption of organic vapor at water surfaces in unsaturated systems, i.e., at the soil-gas/bulk–water interface, is another possible retention mechanism. Organic-vapor adsorption to thin water films and flat water surfaces is well documented in the physical chemistry literature (e.g., Karger et al., 1971). The potential significance of interfacial adsorption in contaminated vadose-zone systems has been demonstrated for several types of organic compounds (e.g., Hoff et al., 1993; Valsaraj, 1994; Costanza and Brusseau, 2000).

Vapor adsorption at the gas–water interface is an exothermic process and is, therefore, favorable enthalpically. Although there is a consequent decrease of entropy in the adsorbed phase relative to the free vapor phase, adsorption is typically a spontaneous process. The magnitude of accumulation at the air–water interface will be a function of the physicochemical properties of the compound (e.g., hydrophobicity, vapor pressure) and the extent of the air–water interface. Among non-polar organic compounds, those with lower saturated vapor pressures have the greatest tendency for air–water interfacial adsorption, as represented by higher adsorption coefficients. Although polar compounds may have greater intrinsic tendency to adsorb at the interface than non-polar compounds, the higher aqueous solubilities of polar compounds may limit the relative importance of interfacial adsorption to total retention. Experimental evidence indicates that vapor adsorption at the air–water interface may generally be considered as an instantaneous process (characteristic times

of seconds-minutes) relative to other retention and transport processes (Brusseau et al., 1997; Lorden et al., 1998).

The preceding discussion has focused on volatile organic compounds. However, it should be noted that accumulation at gas–water interfaces may also influence the retention and transport of colloids, such as clay particles and microbial cells. Thus, the retention of inorganic solutes may be indirectly influenced by air–water interfacial adsorption, through retention of colloids to which they are adsorbed.

4.5 Sorbent Heterogeneity

It is recognized that natural porous media are inherently heterogeneous, chemically as well as physically, and that this heterogeneity manifests at multiple scales. It is to be expected that this heterogeneity will influence the sorption/desorption process. For example, the magnitude and rate of sorption/desorption is likely to be influenced by: (1) the types of minerals present and their grain-scale distributions, (2) the quantity, type, and distribution of organic matter, (3) the morphology and composition of surface coatings, (4) the volume and topology of microporosity in particles and aggregates of particles, and (5) the composition and distribution of lithologic features.

Grain-scale heterogeneity is considered to result in the existence of multiple characteristic time scales of reaction or mass transfer. This behavior reflects the influence of heterogeneity-related factors such as multiple sorption sites of different reactivity, diffusion-controlled domains of differing path lengths and resistances, and the existence of multiple retention processes. It is also considered to be a cause of nonlinear sorption behavior.

Due to the heterogeneity of subsurface systems, it is logical to expect sorption/desorption properties (e.g., kinetic and equilibrium sorption parameters) to be spatially variable at the field scale. Several field-scale investigations have shown that this is indeed the case. Spatially variable sorption/desorption may cause nonideal transport behavior, depending on the form of the spatial variability. Consider, for example, a porous medium comprised of several layers, each with a different sorption affinity, but all with the same hydraulic conductivity. Solute is injected simultaneously into all layers. As transport proceeds, the solute fronts in each of the layers will move at different rates because of the variations in retardation. This differential-front advancement will lead to the observation of increased spreading at a depth-integrated sampling point down-gradient of the injection point. In real situations, spatial variations in both hydraulic conductivity and sorption would be expected. The existence and nature of correlations between the two properties would be important for such cases. The influence of spatially variable sorption properties on field-scale solute transport has been shown for two well-known field transport studies (Brusseau and Srivastava, 1997, 1999).

4.6 Modeling Sorption/Desorption Kinetics

The modeling of sorption/desorption processes is conducted at multiple scales, and for multiple purposes. Much of this modeling is associated with the analysis of data derived from bench-scale experiments. Another primary application is the incorporation of sorption/desorption into models used to simulate field-scale solute transport (see Chap. 10). A more recent application is molecular and pore-scale modeling of sorption/desorption. An ultimate goal in mathematical modeling is to incorporate fundamental mechanistic descriptions of molecular interactions directly into field-scale transport models. Although significant progress has been made recently along this front, this approach remains generally problematic. Thus, we continue to use local sample scale $(10^{-2}\,\mathrm{m})$ and macroscale (m) descriptions of sorption for bench and field scale applications. The discussion below is focused on this latter approach.

As noted in Sect. 4.2, sorption processes are rate limited by both transport (diffusion) and physical/chemical reactions. The latter are modeled using standard reaction kinetics equations (see Eq. (4.11)) that employ rate coefficients. For the transport-controlled processes, diffusive mass transfer can be represented with a diffusion equation based on Fick's law (e.g., Eq. (4.5)), or by employing a first-order mass transfer approximation. The first-order approximation takes the general form:

$$\partial C/\partial t = k_{mt}(C_{eq} - C) \tag{4.25}$$

where k_{mt} is the first-order mass transfer coefficient and C_{eq} is the concentration at equilibrium.

The conceptual basis and performance of these two approaches has been evaluated by many researchers. The diffusion-based approach is often considered superior due to its greater mechanistic accuracy. However, a major disadvantage associated with diffusion-based models is that detailed information is required for both the structure of the porous medium and the diffusion-controlled process. Without this information, a diffusion-based model loses its mechanistic basis and is generally no better than the first-order mass transfer approach. Given the nature of natural geologic media and the usual paucity of information on controlling mechanisms, it is unlikely that diffusion-based models can be accurately parameterized for many applications. Hence, the first-order model, which is not mechanism specific, is often used. The first-order model can be derived directly from the diffusion-based model for various configurations of the diffusion domain.

The simplest approach for characterizing rate-limited sorption/desorption is the "one-site" model. With this approach it is assumed that all sorption/desorption is rate-limited and governed by a single characteristic time scale (e.g., a single rate coefficient is employed). This approach is robust for only the simplest systems, such as those wherein sorption occurs by a single mechanism and involves a single-component sorbent (e.g., quartz). However, it is often used because of its mathematical expediency. The one-site model has been shown to be invalid for representing the sorption/desorption dynamics of many reactive contaminants (e.g., Brusseau and Rao, 1989).

As previously noted, the sorption/desorption of both inorganic and organic solutes often exhibit a biphasic behavior, with a short period of rapid sorption followed by a longer period of slower sorption. The *two-domain model* (also referred to as two-compartment or two-site) was developed in part to account for such behavior. With this model, sorption/desorption is assumed to be governed by two characteristic time scales (and thus two sets of rate coefficients), each representing a separate sorption domain (e.g., Eq. 4.20). Often, it is further assumed that the rate of sorption/desorption for one domain is so rapid that it can be considered instantaneous. The two-domain approach has been widely used to simulate the sorption/desorption of both organic and inorganic solutes in soils, sediments, and aquifer materials.

The two-domain model is an attempt to account for the fact that geomedia are typically heterogeneous and comprised of multiple components. As one might expect, the performance of the two-domain model deteriorates as the complexity of the system increases. Accordingly, the separation of the sorbent into two domains differing in characteristic reaction time may be extended to accommodate any number of domains, each with its associated set of rate coefficients (e.g., a "three-site" model). The limiting case for this approach would be a continuous distribution of domains or "sites" and associated rate coefficients (e.g., Eq. (4.21)). An early model based on this approach was presented by Villermaux (1974), wherein the site population was represented by a transfer-time distribution. Continuous-distribution models have seen increasing use over the past decade, and they appear to be a viable approach (providing good fit to data) for many systems (Fig. 4.15).

For many solutes, as discussed previously, the sorption/desorption process involves multiple mechanisms. Two basic approaches may be taken to model sorption/desorption in such cases. One is the "lumped" approach. In this approach, a single reaction or mass-transfer term is used to represent the contributions of all of the mechanisms influencing sorption. An example would be the application of the one-site model to describe sorption/desorption of a solute influenced by film diffusion, intraparticle diffusion, surface diffusion, and ion exchange. Models based on this approach are relatively simple to use. However, values for the lumped parameter (rate coefficient) contained in these models can usually be obtained only through calibration, and will be valid only for the specific set of conditions for which they were obtained. In addition, these lumped-parameter models can not provide process-specific information. The multiple-domain modeling methods described above can be employed in an attempt to improve the lumped-process approach. For example, the two different characteristic reaction times associated with the two-domain model may also be used to represent two different sorption mechanisms.

Another group of models are based on the use of mechanism-specific or "distributed" parameters. With this approach, each relevant sorption mechanism is represented separately and explicitly in the model. Representing each mechanism in this manner affords the possibility of determining parameter values by means other than calibration. It also provides the opportunity for obtaining process-level information about the system being simulated. An example of this type of model would be one that employs separate terms for film diffusion, intraparticle diffusion, surface diffusion, and ion exchange. A constraint to the use of these types of models is the difficulty involved in characterizing the system sufficiently to provide the

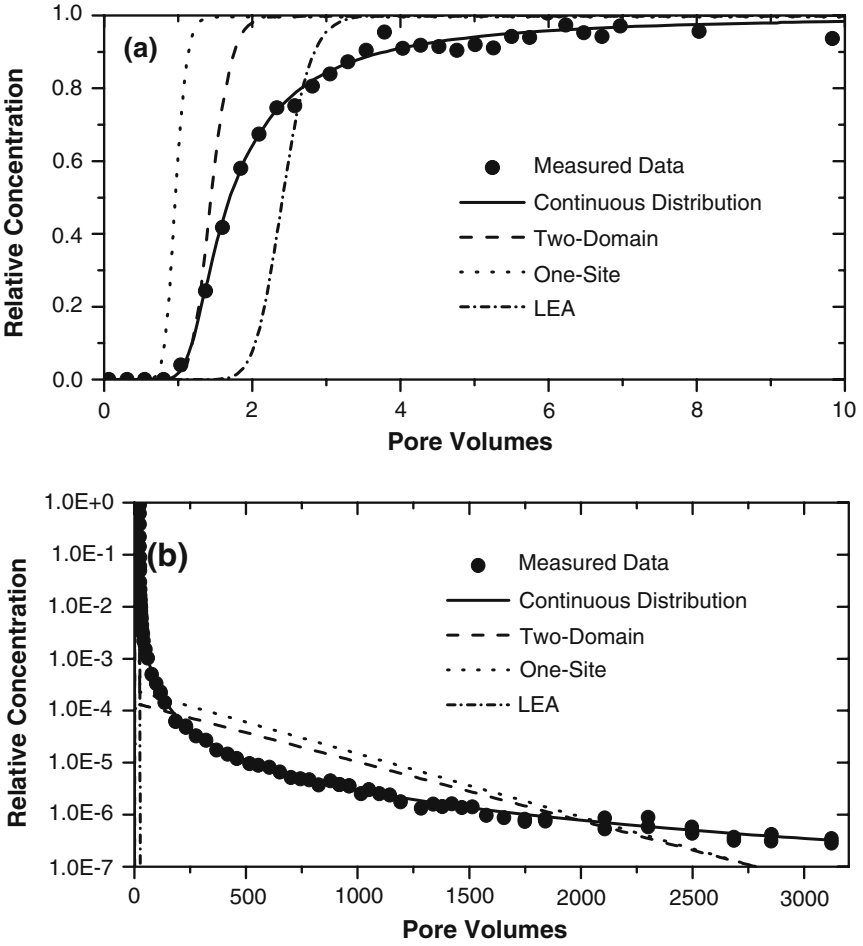

Fig. 4.15 Comparison of several sorption kinetics models for conformity to data for reactive column transport of a hydrophobic organic contaminant (trichloroethene) in natural porous media (**a**) Sorption-uptake breakthrough curve and (**b**) Desorption-release curve

requisite information. In recognition of such constraints, the application of this approach often focuses on the most significant rate-limiting mechanisms. For example, the rate-limited sorption/desorption of HOCs by geomedia is often controlled by intraparticle diffusion and intraorganic matter diffusion, whereas film diffusion and surface reactions are insignificant. A multi-process model was developed to simulate sorption/desorption and transport for such conditions (Brusseau et al., 1989).

A complicating factor in modeling sorption/desorption of solutes for geomedia is that sorbent heterogeneity and multiple sorption mechanisms are both typically involved. The most robust approach for this case would combine the use of multiple reaction terms, with continuous-distribution descriptions used for selected terms. Of course, the information requirements associated with this approach are significant.

References

Aharoni C. and Sparks D. L. (1991) Kinetics of soil chemical reactions: A theoretical treatment. In Sparks D. L. and Suarez D. L. (eds.), *Rates of Soil Chemical Processes.* SSSA Spec. Publ. No. 27, Soil Science Society of America, Madison, WI.

Ainsworth C. C., Pilon J. L., Gassman P. L., and Van Der Sluys W. G. (1994) Cobalt, cadmium and lead sorption to hydrous iron oxide: Residence time effect. *Soil Sci. Soc. Am. J.* **58**, 1615–1623.

Anderson M. A., Tejedor-Tejedor M. I., and Stanforth R. R. (1985) Influence of aggregation on the uptake kinetics of phosphate by goethite. *Environ. Sci. Technol.* **19**, 632–637.

Avena M. J. and Koopal L. K. (1999) Kinetics of humic acid adsorption at solid-water interfaces. *Environ. Sci. Technol.* **33**, 2739–2744.

Backes C. A., McLaren R. G., Rate A. W., and Swift R. S. (1995) Kinetics of cadmium and cobalt desorption from iron and manganese oxides. *Soil Sci. Soc. Am. J.* **59**, 778–785.

Bernasconi C. F. (1976) *Relaxation Kinetics*. Academic Press, New York.

Brown, G. E., Jr. (2001) How minerals react with water. *Science* **294**, 67–69.

Brown G. E., Jr. and Sturchio N. C. (2002) An overview of synchrotron radiation applications to low temperature geochemistry and environmental science. *Rev. Mineral. Geochem.* **49**, 1–115.

Brusseau M.L. (1993) Using QSAR to evaluate phenomenological models for sorption of organic compounds by soil. *Environ. Toxic. Chem.* **12**, 1835–1846.

Brusseau M. L. and Rao P. S. C. (1989) Sorption nonideality during organic contaminant transport in porous media. *CRC Crit. Rev. Environ. Control.* **19**, 33–99.

Brusseau M. L. and Srivastava R. (1997) Nonideal transport of reactive solutes in heterogeneous porous media: 2. Quantitative analysis of the borden natural-gradient field experiment. *J. Contam. Hydrol.* **28**, 115–155.

Brusseau M. L. and Srivastava R. (1999). Nonideal transport of reactive solutes in heterogeneous porous media: 4. Analysis of the Cape Cod Natural-Gradient Field Experiment. *Water Resour. Res.* **35**, 1113–1125.

Brusseau M. L., Jessup R. E., and Rao P. S. C. (1989) Modeling the transport of solutes influenced by multi-process nonequilibrium. *Water Resour. Res.* **25**, 1971–1988.

Brusseau M. L., Jessup R. E., and Rao P. S. C. (1991) Nonequilibrium sorption of organic chemicals: elucidation of rate-limiting processes. *Environ. Sci. Technol.* **25**, 134–142.

Brusseau M. L., Popovicova J., and Silva J. A. K. (1997) Characterizing gas-water-interfacial and bulk-water partitioning for gas-phase transport of organic contaminants in unsaturated porous media. *Environ. Sci. Technol.* **31**:1645–1649.

Casey W. H. (2001) A view of reactions at mineral surfaces from the aqueous phase. *Mineral. Mag.* **65**, 323–337.

Chang F. -R. and Sposito G. (1996) The electrical double layer of a disk-shaped clay mineral particle: effects of electrolyte properties and surface charge density. *J. Colloid Interface Sci.* **178**, 555–564.

Charlet L. and Manceau A. (1993) Structure, formation and reactivity of hydrous oxide particles: Insights from x-ray absorption spectroscopy. In Buffle J. and van Leeuwen H. P. (eds.) *Environmental Particles*, Vol. 2, Lewis Publishers, Boca Raton, pp. 117–164.

Chiou C. T. and Shoup T. D. (1985) Soil sorption of organic vapors and effects of humidity on sorptive mechanism and capacity. *Environ. Sci. Technol*. **19**, 1196–1200.

Choi S., O'Day P. A., Rivera N. A., Mueller K. T., Vairavamurthy M. A., Seraphin S., and Chorover J. (2006) Strontium speciation during reaction of kaolinite with simulated tank-waste leachate: bulk and microfocused EXAFS analysis. *Environ. Sci. Technol.* **40**, 2608–2614.

Chorover J., Choi S., Amistadi M. K., Karthikeyan K. G., Crosson G., and Mueller K. T. (2003) Linking cesium and strontium uptake to kaolinite weathering in simulated tank waste leachate. *Environ. Sci. Technol.* **37**, 2200–2208

Chorover J., Zhang J., Amistadi M. K., and Buffle J. (1997) Comparison of hematite coagulation by charge screening and phosphate adsorption: Differences in aggregate structure. *Clays Clay Miner.* **45**, 690–708.

Criscenti L. J. and Sverjensky D. A. (2002) A single-site model for divalent transition and heavy metal adsorption over a range of metal concentrations.*J. Colloid Interface Sci.* **253**, 329–352.

Fleer G. J., Cohen-Stuart M. A., Scheutjens J. M. H. M., Cosgrove T., and Vincent B. (1993) *Polymers at Interfaces*. Chapman & Hall, London.

Goss K. -U. (1992) Effects of temperature and relative humidity on the sorption of organic vapors on quartz sand. *Environ. Sci. Technol*. **26**, 2287–2294.

Goss K. -U. and Eisenreich S. J. (1996) Adsorption of VOCs from the gas phase to minerals and a mineral mixture. *Environ. Sci. Technol*. **30**, 2135–2142.

Grossl P. R., Eick M., Sparks D. L., Goldberg S., and Ainsworth C. C. (1997) Arsenate and chromate retention mechanisms on goethite. 2. Kinetic evaluation using a pressure-jump relaxation technique. *Environ. Sci. Technol.* **31**, 321–326.

Hachiya K., Sasaki M., Saruta Y., Mikami N., and Yasanuga T. (1984) Static and kinetic studies of adsorption-desorption of metal ions on the γ-Al_2O_3 surface. 2. Kinetic study by means of a pressure jump technique. *J. Phys. Chem.* **88**, 23–31.

Hoff J. T., Mackay D., Gillham R. W., and Shlu W. Y. (1993) Partitioning of organic chemicals at the air-water interface in environmental systems. *Environ. Sci. Technol.* **27**, 2174–2180.

Huang W., Young T., Schlautman M. A., Hu H., and Weber W. J., Jr. (1997) A distributed reactivity model for sorption by soils and sediments. 9. General isotherm non-linearity and applicability of the dual reactive domain model. *Environ. Sci. Technol.* **31**, 1703–1710.

Hundal L. S., Thompson M. L., Laird D. A., and Carmo A. M. (2001) Sorption of phenanthrene by reference smectites. *Environ. Sci. Technol.* **35**, 3456–3461.

Jeon B. -H., Dempsey B. A., Burgos W. D., Royer R. A., and Roden E. E. (2004) Modeling the sorption kinetics of divalent metal ions to hematite. *Wat. Res.* **38**, 2499–2504.

Kaplan D. I. and Serne R. J. (1998) Pertechnetate exclusion from sediments. *Radiochim. Acta* **81**, 117–124.

Karger B. L., Castells R. C., Sewell P. A., and Hartkopf A. (1971) Study of the adsorption of insoluble and sparingly soluble vapors at the gas-liquid interface of water by gas chromatography. *J. Phys. Chem.* **75**, 3870–3879.

Karickhoff S. W. (1981) Semi-empirical estimation of sorption of hydrophobic pollutants on natural sediments and soils. *Chemosphere* **10**, 833–846.

Kubicki J. D., Itoh M. J., Schroeter L. M., Nguyen B. N., and Apitz S. E. (1999) Attenuated total reflectance Fourier-transform infrared spectroscopy of carboxylic acids adsorbed onto mineral surfaces. *Geochim. Cosmochim. Acta*, **63**, 2709–2725.

Laird D. A., Shang C (1997) Relationship between cation exchange selectivity and crystalline swelling in expanding 2:1 phyllosilicates. *Clays Clay Miner.* **45**, 681–689.

Lasaga A. C. (1998) *Kinetic Theory in the Earth Sciences*. Princeton University Press, Princeton, NJ, 811 pp.

Lorden S. W., Chen W., and Lion L. W. (1998) Experiments and modeling of the transport of trichloroethene vapor in unsaturated aquifer material. *Environ. Sci. Technol*. **32**, 2009–2017.

Lu Y. and Pignatello J. J. (2002) Demonstration of the "conditioning effect" in soil organic matter in support of a pore deformation mechanism for sorption hysteresis. *Environ. Sci. Technol.* **36**, 4553–4561.

Lu Y. and Pignatello J. J. (2004) History-dependent sorption in humic acids and a lignite in the context of a polymer model for natural organic matter. *Environ. Sci. Technol.* **36**, 4553–4561.

Manceau A., Marcus M. A., and Tamura N. (2002) Quantitative speciation of heavy metals in soils and sediments by synchrotron x-ray techniques. In Fenter, P. A. et al. (ed.) *Applications of Synchrotron Radiation in Low Temperature Geochemistry and Environmental Science*, Vol. 49. Mineralogical Society of America, Washington, DC.

Morel F. M. M. and Hering J. G. (1993) *Principles and Applications of Aquatic Chemistry.* Wiley, New York.

Park C., Fenter P. A., Nagy K. L., and Sturchio N. C. (2006) Hydration and distribution of ions at the mica-water interface. *Phys. Rev. Lett.* **97**, 016101.

Pignatello J. J. (2000) The measurement and interpretation of sorption and desorption rates for organic compounds in soil media. *Adv. Agron*. **69**, 1–73.

Polmeier A. and Lustfeld H. (2004) Reaction rates of heavy metal ions at goethite: Relaxation experiments and modeling. *J. Colloid Interface Sci.* **269**, 131–142.

Rate A. W., McLaren R. G., and Swift R. S. (1992) Evaluation of a long-normal distribution first-order kinetic model for copper(II)-humic acid complex dissociation. *Environ. Sci. Technol.* **26**, 2477–2483.

Scheidegger A. M, Strawn D. G., Lamble G. M., and Sparks D. L. (1998) The kinetics of mixed Ni-Al hydroxide formation on clay and aluminum oxide minerals: a time-resolved XAFS study. *Geochim. Cosmochim. Acta* **63**, 2233–2245.

Schlegel M. L., Charlet L., and Manceau A. (1999) Sorption of metal ions on clay minerals – II. Mechanism of Co sorption on hectorite at high and low ionic strength and impact on the sorbent stability. *J. Coll. Interface Sci.* **220**, 392–405.

Schlegel M. L., Manceau A., Charlet L., and Hazemann J. L. (2001a) Adsorption mechanisms of Zn on hectorite as a function of time, pH, and ionic strength. *Am. J. Sci.* **301**, 798–830.

Schlegel M. L., Manceau A., Charlet L., Chateigner D., and Hazemann J. L. (2001b) Sorption of metal ions on clay minerals. III. Nucleation and epitaxial growth of Zn phyllosilicate on the edges of hectorite. *Geochim. Cosmochim. Acta* **65**, 4155–4170.

Sparks D. L. (1999) Kinetics and mechanisms of chemical reactions at the soil mineral/water interface. In Sparks D. L. (ed.) *Soil Physical Chemistry*, 2nd Edition. CRC Press, Boca Raton, FL, pp. 135–191.

Sparks D. L. and Jardine P. M. (1984) Comparison of kinetic equations to describe K-Ca exchange in pure and in mixed systems. *Soil Sci*. **138**, 115–122.

Sposito G. (1994) *Chemical Equilibria and Kinetics in Soils.* Oxford University Press, New York.

Sposito G., Skipper N. T., Sutton R., Park S. H., Soper A. K., Greathouse J. A. (1999) Surface geochemistry of the clay minerals. *Proc. Nat. Acad. Sci. USA* **96**, 3358–3364.

Sposito G. (2004) *The Surface Chemistry of Natural Particles.* Oxford University Press, New York.

Stumm W. (1992) *Chemistry of the Solid-Water Interface.* Wiley Interscience, New York.

Suarez D. L., Goldberg S., and Su C. (1998) Evaluation of oxyanion adsorption mechanisms on oxides using FTIR spectroscopy and electrophoretic mobility. In Sparks D. L. and Grundl T. J. (ed.) *Mineral-Water Interfacial Reactions*. ACS Symposium Series 715, American Chemical Society, Washington, DC, pp. 136–168.

Sutton R. and Sposito G. (2005) Molecular structure in soil humic substances: the new view. *Environ. Sci. Technol.* **39**, 9009–9015.

Torrent J., Schwertmann U., and Barron, V. (1992) Fast and slow phosphate sorption by goethite-rich natural materials. *Clays Clay Miner*. **40**, 14–21.

Tringides M. C. (1997) *Surface Diffusion: Atomistic and Collective Processes.* NATO ASI Series B-Physics, Vol. 360, Plenum Press, New York.

Trivedi P., Axe L. (1999) A comparison of strontium sorption to hydrous aluminum, iron, and manganese Oxides. *J. Colloid Interface Sci.* **218**, 554–563.

Valsaraj K. T. (1994) Hydrophobic compounds in the environment: adsorption equilibrium at the air-water interface. *Water Res*. **28**, 819–830.

Verberg K. and Baveye P. (1994) Hysteresis in the binary exchange of cations on 2/1 clay-minerals – A critical review. *Clays Clay Mineral.* **41**, 207–220.

Weber W. J., Jr., McGinley P. M., and Katz L. E. (1992) A distributed reactivity model for sorption by soils and sediments. 1. Conceptual basis and equilibrium assessments. *Environ. Sci. Technol.* **26**, 1955–1962.

Wehrli B., Ibric S., and Stumm W. (1990) Adsorption kinetics of vanadyl(IV) and chromium(III) to aluminum oxide: Evidence for a two-step mechanism. *Colloids Surf.* **51**, 77–88.

Yasunaga T. and Ikeda T. (1986) Adsorption-desorption kinetics at the oxide-solution interface studied by relaxation methods. Chapter 12. In Davis J. A. and Hayes K. F. (ed.) *Geochemical Processes at Mineral Surfaces*. American Chemical Society, Washington, DC.

Zachara J. M., Smith S. C., Liu C., McKinley J. P., Serne R. J., and Gassman P. L. (2002) Sorption of Cs^+ to micaceous subsurface sediments from the Hanford site, USA. *Geochim. Cosmochim. Acta* **66**, 193–211.

Zhang Z., Fenter P., Cheng L., Sturchio N. C., Bedzyk M. J., Pøedota M., Bandura A., Kubicki J., Lvov S. N., Cummings P. T., Chialvo A. A., Ridley M. K., Bénézeth P., Anovitz L., Palmer D. A., Machesky M. L., and Wesolowski D. J. (2004) Ion adsorption at the rutile-water interface: Linking molecular and macroscopic properties. *Langmuir* **20**, 4954–4969.

Zhao D., Pignatello J. J., White J. C., Braida W., and Ferrandino F. (2001) Dual-mode modeling of competitive and concentration-dependent sorption and desorption kinetics of polycyclic aromatic hydrocarbons in soils. *Wat. Resour. Res.* **37**, 2205–2212.

Zhou Q., Maurice P. A., and Cabaniss S. E. (2001) Size fractionation upon adsorption of fulvic acid on goethite: Equilibrium and kinetic studies. *Geochim. Cosmochim. Acta* **65**, 803–812.

Zimmerman A. R., Goyne K. W., Chorover J., Komarneni S., and Brantley S. L. (2004) Mineral mesopore effects on nitrogenous organic matter adsorption. *Org. Geochem.* **35**, 355–375.

Chapter 5
Kinetics of Mineral Dissolution

Susan L. Brantley

5.1 Introduction

5.1.1 Importance of Dissolution Reactions

The rates of mineral dissolution contribute to processes controlling soil fertility, porosity in aquifers and oil reservoirs, transport and sequestration of contaminants and CO_2, cycling of metals and formation of ore deposits, and many other geochemical characteristics and phenomena. For example, the weathering rates of Ca- and Mg-silicates influence the concentrations of CO_2 in the atmosphere over 10^5–10^6 y timescales, impacting the global carbon cycle. Mineral dissolution thus influences the chemical and physical nature of our landscape as well as the quality and quantity of potable water and fertile soil available to sustain ecosystems. The rates of mineral dissolution (Fig. 5.1) determine the lifetimes of minerals in soil environments. Especially since the 1970s, researchers have focused on measurement of mineral dissolution rates in order to promote quantitative prediction of the evolution of our environment (Stumm, 1997). In this chapter, we discuss many of the concepts and models used to predict mineral dissolution rates for oxide, carbonate, and silicate minerals.

5.1.2 Steady-State Dissolution

In general, for dissolution of a mineral $A_{\upsilon_A}B_{\upsilon_B}$ described by

$$A_{\upsilon_A}B_{\upsilon_{B(S)}} \rightarrow \nu_A A^{q_A}_{(aq)} + \nu_B B^{q_B}_{(aq)}, \tag{5.1}$$

Pennsylvania State University, Center for Environmental Kinetics Analysis, Earth and Environmental Systems Institute, brantley@essc.psu.edu

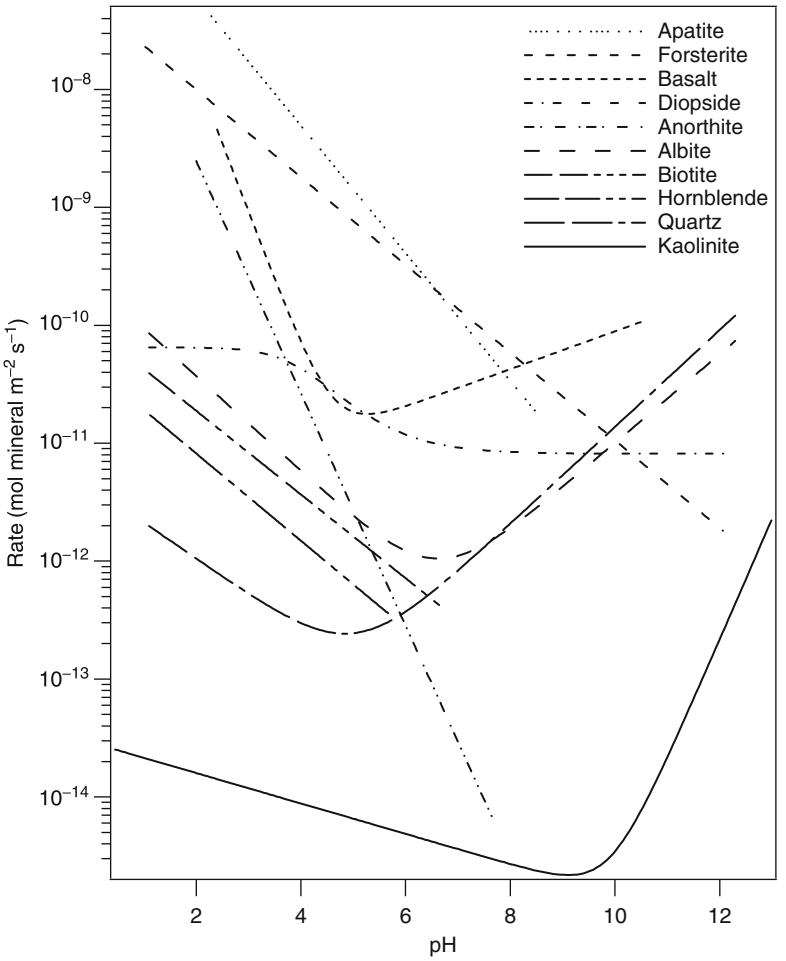

Fig. 5.1 Predicted dissolution rates as a function of pH derived from the fitting results described in Table 6.3 in Chap. 6 and data compiled in the Appendix. Basalt rates were calculated from a temperature dependent model assuming T = 298 K. Kaolinite rates were calculated using a rate constant from published data (Huertas et al., 1999) as described in Chap. 6.

the rate of reaction, r', is expressed (in mol mineral reacted per unit time per unit volume) as

$$r' = -\frac{d[A_{\upsilon_A} B_{\upsilon_B}]}{dt} = \frac{1}{\upsilon_A}\frac{d[A_{aq}]}{dt} = \frac{1}{\upsilon_B}\frac{d[B_{aq}]}{dt} \tag{5.2}$$

Here, $[i]$ refers to the concentration of species i, ν_i is the stoichiometric coefficient of the reaction, t is time, and q_i is the charge of the aqueous species. Here it is important to measure the total concentration of aqueous A and B, regardless of speciation, in order to determine the dissolution rate. For example, in analyzing the dissolution rate of gibbsite, the rate of release of all aqueous Al species must be

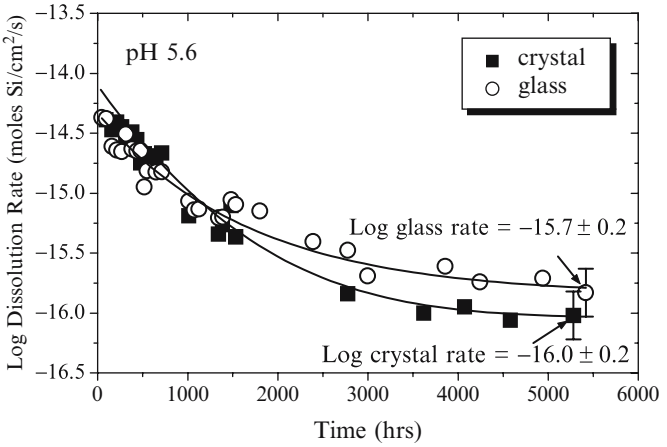

Fig. 5.2 Log dissolution rate (expressed as mol Si $cm^{-2} s^{-1}$) as a function of reaction time measured for albite crystal and glass in flow experiments (output pH = 5.6) at 25° C as previously reported (Hamilton et al., 2000). Rates, normalized using BET surface areas measured on powders at the start of the experiment, decrease to a steady state rate after about 4,000 h. For clarity, only every fifth data point is shown. (Reprinted from Hamilton et al. 2000. With permission from Elsevier).

summed. The most common way to measure mineral dissolution is to measure the rate of increase in concentration of solutes as a function of time as described by Eq. (5.2); however, analysis of the rate of surface retreat (Dove and Platt, 1996) or rate of disappearance of mass can also be measured (see Chap. 3). If the rate of dissolution of a phase is limited by the interfacial reaction, then the rate of a heterogeneous reaction such as that given by Eq. (5.1) has generally been observed to depend upon the total or reactive mineral surface area. Most mineral dissolution rates are therefore reported after normalization by the total mineral surface area as measured by geometric calculation or by the BET technique. Various approaches used to measure surface area-normalized dissolution rates are described in Chap. 1 and will not be further discussed here.

Rates of release of solutes from minerals in water are often used to estimate the dissolution rate using the *initial rate method* (Chap. 1). However, dissolution rates often decrease from the initial value if measured over long periods of dissolution duration (see for example Fig. 5.2). In addition, rates of dissolution of minerals pre-weathered under field conditions are generally observed to be slower than those measured on laboratory-ground samples (White and Brantley, 2003). In fact, area-normalized release rates, r, of components are often observed to vary with time according to the function, $r = kt^{-0.5}$, giving rise to the term *parabolic kinetics* (Luce et al., 1972; Paces, 1973). Parabolic kinetics measured for silicate dissolution have been attributed to the initial fast dissolution of fine particles or sites with high surface free energy (Holdren and Berner, 1979). Nonstoichiometric dissolution (see next section) may also cause the dissolution rate to vary with time. For example, jadeite glass ($NaAlSi_2O_6$, Fig. 5.3) dissolved at pH 2 develops an Al- and Na-depleted surface layer that is thousands of Angstroms thick (Hamilton et al.,

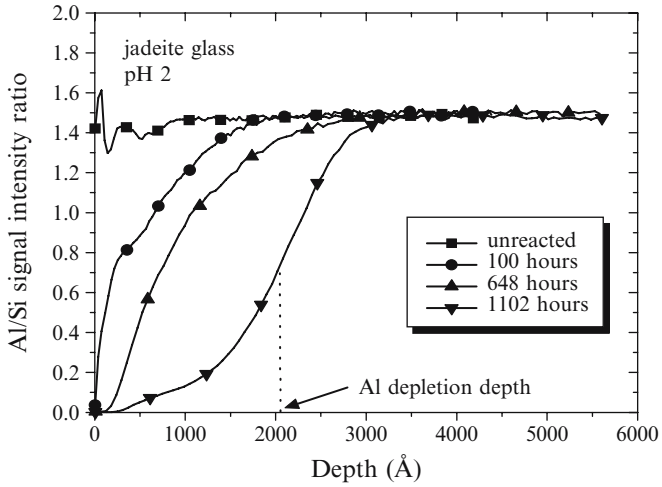

Fig. 5.3 Plots showing depth profiles of Al/Si ratios measured using secondary ion mass spectrometric (SIMS) analysis of jadeite glass plates reacted in static pH 2 solution at 25° C for varying durations of time (Hamilton et al., 2001). Depletion of Al at the surface was attributed to nonstoichiometric surface leaching and creation of an Al-depleted surface layer. For modeling purposes, the authors have also indicated a nominal depth to which Al is depleted. See also discussion of nonstoichiometric dissolution in Chap. 1. (Reprinted from Hamilton et al., 2001. With permission from Elsevier).

2001) The development of this layer is attributed to faster leaching of Na and Al as compared to Si: it can be shown that a parabolic release rate is predicted for diffusion of a component such as Na or Al across a thickening leached layer (Doremus, 1983).

Given these difficulties, geochemists generally measure the rate of dissolution of a mineral after many hours in order to determine the steady state rate. True steady state kinetics may not be attainable however since the mineral surface continues changing during dissolution (White and Brantley, 2003; Kohler et al., 2005). Steady-state dissolution, if it exists at all, would be expected to be characterized by a surface with a non-changing distribution of site energies and atoms. Figure 5.3 demonstrates that the dissolution rate of jadeite glass might not attain steady state until more than 1,100 h of dissolution. Nonstoichiometric dissolution is further discussed in the next section.

5.1.3 Stoichiometry of Dissolution

When a reaction rate is measured in a chemical reactor, the reaction is generally a composite reaction rather than an elementary reaction (Chap. 1). Reflecting the nature of these complex mechanisms, many silicates are observed to release elements

into solution at different rates. If the ratio of release rates does not equal the stoichiometry of the starting mineral, such dissolution is called *nonstoichiometric* or *incongruent dissolution*. Nonstoichiometric dissolution may be caused by dissolution of impurity phases or zones within the mineral, by precipitation of secondary minerals, or by preferential leaching of elements from the mineral surface (as inferred for jadeite in Fig. 5.3).

The preferential leaching of elements from a dissolving surface is driven by differences in site energies for cations in the mineral structure. For example, leaching of cations to depths of several thousand Å has been reported especially for the inosilicate minerals (pyroxenes and amphiboles) and glasses as shown in Fig. 5.3 (Casey and Cheney, 1993; Brantley and Chen, 1995; Hamilton et al., 2001). Cations in the M2 and M1 sites in pyroxenes and in the M4 sites in amphiboles are released preferentially due to differences in Madelung site energy (Schott and Berner, 1983, 1985; Brantley and Chen, 1995; Chen and Brantley, 1998).

For dissolving silicates, nonstoichiometric dissolution is especially pronounced at lower pH and can be detected using surface-sensitive spectroscopies such as X-ray photoelectron spectroscopy or secondary ion mass spectrometry (SIMS) (Chap. 3). Figure 5.3 shows how the Na/Si atomic ratio of the outer surface of albite crystal, measured by SIMS, changes during dissolution at pH 2 as a function of dissolution duration. In contrast, alteration layers on feldspars such as albite are generally relatively thin. Thicker alteration layers can develop at pH < 3 on plagioclase feldspars or on glasses of feldspar composition due to leaching of alkali, alkaline earth, and Al cations. Such layers can demonstrate the characteristics of amorphous silica when analyzed after dissolution (Casey et al., 1989; Hamilton et al., 2000, 2001).

The development of a leached layer on dissolving feldspar surfaces is influenced by the Al/Si ratio of the feldspar. Labradorite $(\mathrm{Al/Si} = 0.66\text{–}0.8)$ and bytownite $(\mathrm{Al/Si} = 0.8\text{–}0.9)$ crystals show much thicker altered layers when dissolved at low pH than albite $(\mathrm{Al/Si} < 0.4)$, oligoclase $(\mathrm{Al/Si} = 0.4\text{–}0.5)$ and andesine $(\mathrm{Al/Si} = 0.5\text{–}0.66)$ crystals (Muir et al., 1990; Stillings and Brantley, 1995). In contrast, dissolution of anorthite $(\mathrm{Al/Si} = 1.0)$ is almost stoichiometric at low pH (Amrhein and Suarez, 1992).

The mechanism underlying such observations has been investigated using many techniques (see Sect. 5.2.2.1). For example, *ab initio* calculations of the optimized geometries of dissolving surface clusters (Hamilton et al., 2001) have been calculated. As the Al/Si ratio is increased in the cluster, the average bond length of SiO bonds within AlOSi linkages increases from 1.58 to 1.60 to 1.62 Å, suggesting that hydrolysis of AlOSi bonds becomes easier. These theoretical results partially explain why the dissolution rates of plagioclase feldspar increases with the Al/Si ratio, and why preferential leaching of Al occurs more readily at high Al/Si ratio. Instead of formation by leaching, alteration layers on feldspars such as labradorite have also been attributed to solution-precipitation (see Sect. 5.2.2.1).

As discussed in Sect. 5.1.2, many silicates dissolve nonstoichiometrically at first but eventually show steady state dissolution that is stoichiometric. For minerals that never show stoichiometric dissolution, the determination of reaction rate depends upon which component released to solution is used in the rate equation. Due to

preferential release of cations such as Na, K, Ca, and Mg from silicates during dissolution, for example, dissolution rates are usually calculated from the observed Si release. Here, we report silicate dissolution rates based upon Si release, but we generally normalize by the stoichiometry of the mineral and report as mol mineral per unit (initial) surface area per unit time. It is important to note that dissolution rates reported on this basis depend upon both the formula unit and the monitored solute (Chap. 1).

5.2 Mechanisms of Dissolution

5.2.1 Interface Versus Transport Control

5.2.1.1 Carbonate Dissolution Mechanism

Dissolution rates of highly soluble and highly insoluble minerals tend to be relatively fast and slow, respectively. Dissolution of highly soluble minerals therefore have a greater likelihood of becoming transport-limited as compared to low-solubility minerals which are likely to be interface-limited. Experimentalists often test for transport control of dissolution of minerals by varying the agitation or recycle rate of the reactor (Rosso and Rimstidt, 2000). One mineral that has been investigated in the laboratory under both transport and interface limitation is calcite. The relative importance of interface versus transport control during calcite dissolution varies with pH (Plummer et al., 1978). Here we review the classic model of Plummer et al. but the reader is also referred to more recent surface complexation models for carbonate dissolution (Pokrovsky and Schott, 2000).

Plummer et al. suggested that the following reactions occur in parallel during carbonate dissolution under ambient conditions:

$$CaCO_{3(s)} + H^{+}_{(aq)} = Ca^{2+}_{(aq)} + HCO^{-}_{3(aq)} \tag{5.3}$$

$$CaCO_{3(s)} + H_2CO_{3(aq)} = Ca^{2+}_{(aq)} + 2HCO^{-}_{3(aq)} \tag{5.4}$$

$$CaCO_{3(s)} + H_2O_{(aq)} = Ca^{2+}_{(aq)} + HCO^{-}_{3(aq)} + OH^{-}_{(aq)} \tag{5.5}$$

Here, $H_2CO_3^*$ represents the sum of $H_2CO_{3(aq)}$ and $CO_{2(aq)}$. Rates of these reactions (r, mol cm^{-2} s^{-1}) were posited by Plummer et al. to be described by the following equations where k_1, k_2, and k_3 are rate constants and a_i refers to the activity of the relevant species:

$$r = k_1 a_{H^+} \tag{5.6a}$$

$$r = k_2 a_{H_2CO_3^*} \tag{5.6b}$$

$$r = k_3 a_{H_2O} \tag{5.6c}$$

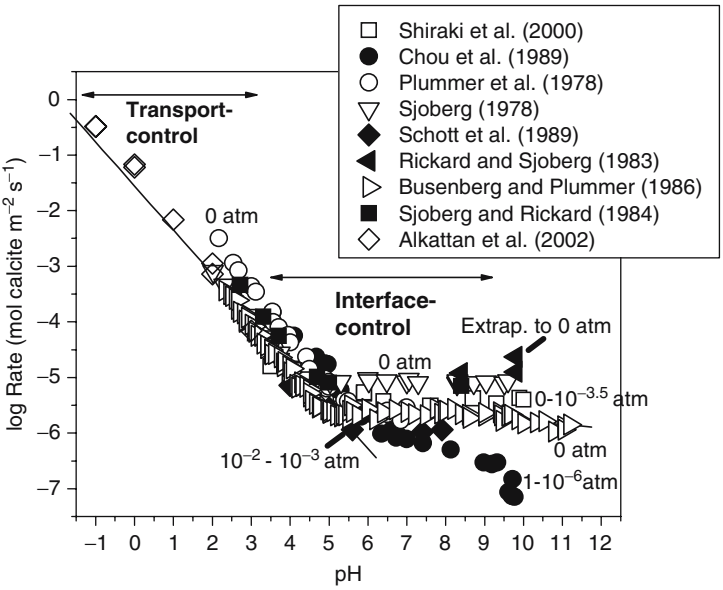

Fig. 5.4 Calcite dissolution rates measured at 298K and various CO_2 partial pressures. At low pH, rates are transport controlled and are not dependent upon CO_2 partial pressures, whereas at pH $>$ 3.5, dissolution becomes interface-controlled (see text). For pH $>$ 5.5, the precipitation reaction also contributes significantly to the overall rate (Plummer et al., 1978). All data from published values (Plummer et al., 1978; Sjoberg, 1978; Rickard and Sjoberg, 1983; Sjoberg and Rickard, 1984; Busenberg and Plummer, 1986; Chou et al., 1989; **?**; Shiraki et al., 2000; Alkattan et al., 2002). (Figure compiled by A. Zimmerman).

These reactions occur in parallel and the fastest reaction should therefore be rate-controlling (Chap. 1). However, at any pH, transport and interface reactions must occur consecutively, and for these steps, the slowest reaction must be rate-limiting. Two regions of dissolution were distinguished based on pH and P_{CO_2}: for pH $<$ 3.5, dissolution is controlled by transport while for pH $>$ 3.5 the interfacial reaction is slower than transport and the rate is interface-controlled (Fig. 5.4). Above pH 5.5, the precipitation reaction was also observed to be significant. Consistent with these observations, in the low-pH region where the reaction is dominated by Eq. (5.3), calcite dissolution is characterized by a very low activation energy consistent with transport control (see Sect. 5.4.1).

In region 1, where dissolution is fast enough that transport limits the rate, the concentration of dissolution products in the solution layer around the dissolving calcite (the boundary layer) approaches the equilibrium concentration (see Chaps. 1 and 3). In contrast, in region 2, where transport does not limit the rate, diffusion across the boundary layer is fast compared to the rate of the interface reaction and the concentration of solutes in the layer is equal to the bulk concentration (and this value is lower than the equilibrium value). Hence dissolution in the higher pH region is more dependent upon solution chemistry and P_{CO_2} (Fig. 5.4).

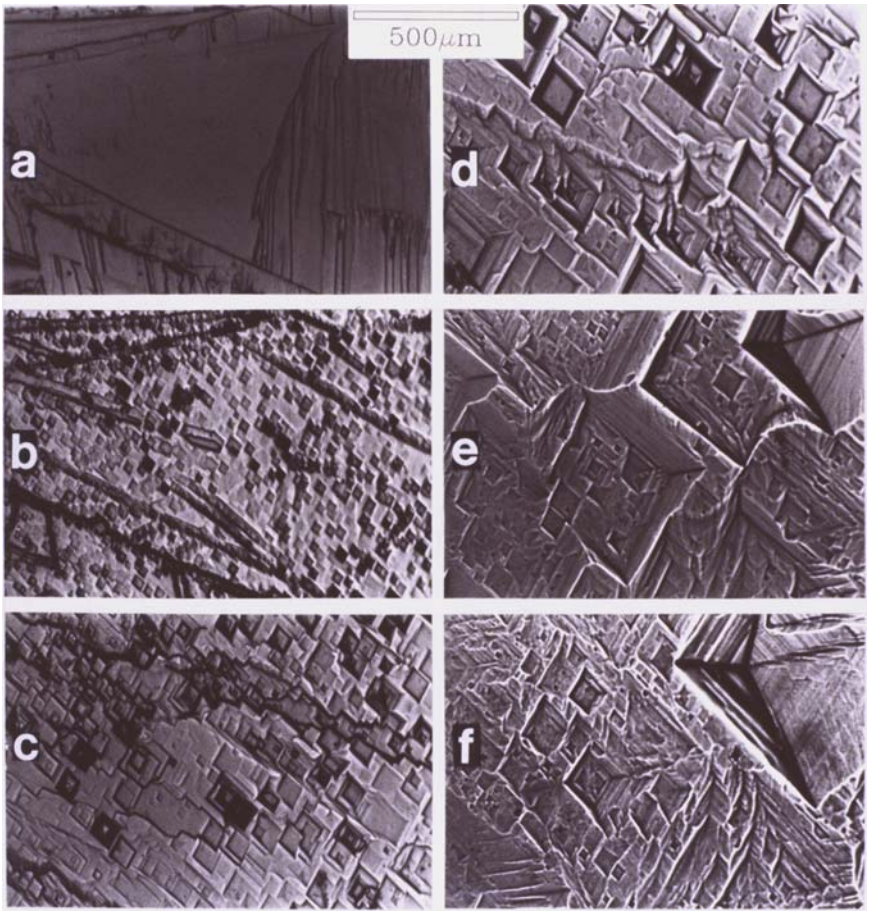

Fig. 5.5 Photomicrographs showing successive dissolution of the same area of a cleaved surface of unstrained calcite at 25° C after (**a**) 0, (**b**) 0.5, (**c**) 1.5, (**d**) 3, (**e**) 11, and (**f**) 17.5 h total dissolution time. Surface ledges imaged in (**a**) have almost completely disappeared in (**d**) due to step retreat and pitting. Examples of pits growing both horizontally (getting wider) and vertically (getting deeper) are prevalent on the surface. Many small pits nucleate and grow throughout the dissolution period until they are annihilated by intersection with other pits or by surface retreat: these pits deepen for awhile but eventually become flat-bottomed. In contrast, at least one large point-bottomed pit (upper right) grows deeper throughout the dissolution period. The large pit is inferred to be dissolving along a dislocation. These photographs are from run UC25-1 (MacInnis and Brantley, 1992). (Reprinted from MacInnis and Brantley, 1992. With permission from Elsevier).

5.2.1.2 Etch Pits

Transport or interface limitation during dissolution of minerals such as calcite can be inferred based upon the morphology of the dissolving surface of the mineral (e.g., Fig. 5.5); however, to understand this concept requires a better conceptual understanding of surface features related to dissolution (see also Chap. 3). In general,

dissolution can be conceptualized as the sum of i) the horizontal movement of atomic-scale steps defining incomplete surface layers (step retreat) and ii) removal of atoms by drilling into the mineral (2D or pit nucleation). For example, surface steps imaged in Fig. 5.5a represent many atomic steps that have bunched into visible macrosteps. Over the time evolution in this figure, these steps move by step retreat and disappear. The figure also shows many pits that nucleate, grow, and intersect. Etch pits generally nucleate at both perfect surface sites and at defect outcrops. Such defects can be 0-dimensional (point defects), 1-dimensional (line defects), or 2-dimensional (planar defects). Pits nucleated at 0-dimensional defects become flat-bottomed quickly because the defect is etched away, but new pits can nucleate homogeneously on the surface (Fig. 5.5). However, Fig. 5.5 also shows that pits that form at line defects continue to deepen along the dislocation line (MacInnis and Brantley, 1992). (Where dislocations jog or loop back to the surface, dislocation pits may terminate, but in general dislocation pits continue deepening as long as the dislocation line is present). The term *homogeneous nucleation* is used to describe nucleation of *vacancy islands*—pits at perfect surface (Dove et al., 2005) — and *dislocation etching* is used to describe formation of etch pits at line defects. The largest pit imaged on the calcite in Fig. 5.5f shows the pointed bottom that is characteristic of dislocation etching.

Regardless of the type of pit, when dissolution occurs near equilibrium, nucleation of pits is not energetically favored. Under these conditions, dissolution occurs as steps sweep across the crystal surface, but new steps can only nucleate at crystal edges. Surfaces become smoother rather than more pitted and edges become rounded. However, further from equilibrium, the large strain field around a dislocation can cause nucleation of an etch pit at a dislocation outcrop, so steps originate in parallel from both crystal edges and dislocation etch pits — the crystal therefore dissolves faster further from equilibrium. Even more removed from equilibrium, nucleation can occur due to the strain associated with impurities or point defects and eventually at the highest degree of undersaturation, homogeneous nucleation occurs everywhere. Steps nucleated at crystal edges, at dislocation etch pits, at impurity etch pits, at point defects, and at perfect surface thus dominate from small to large undersaturations respectively because i) the rates of reaction at these sites differs, and ii) the relative number of these sites varies. Of course, close to equilibrium, steps only form at edges, but as the undersaturation increases, step retreat occurs from all the sites in parallel.

Such conceptual models for dissolution were outgrowths of crystal growth theories known as Burton Cabrera Frank (or BCF) models (Burton et al., 1951; Cabrera et al., 1954; Cabrera and Levine, 1956). The BCF models quantify the values of the critical concentrations that define where pitting occurs at defects. For example, consider a pit that nucleates at a dislocation intersecting the surface of a crystal of composition A dissolving to $A_{(aq)}$. Assuming the pit consists of a cylindrical hole of radius ε and depth a, then the free energy of formation of this small pit is composed of volume, surface, and elastic strain energy terms respectively:

$$\Delta G_{dislocation} = \frac{\pi\varepsilon^2 aRT\ln([A]/[A_{eq}])}{V} + 2\pi\varepsilon a\gamma - \frac{a\tau b^2}{4\pi}\ln\left(\frac{\varepsilon}{\varepsilon_o}\right) \qquad (5.7)$$

Here, τ is an energy factor related to the dislocation, b is the Burger's vector describing the dislocation, ε_o is the dislocation core radius, V is molar volume, $[A_{eq}]$ is the equilibrium concentration of A in solution, and γ is the energy of the crystal-water interface. The cylindrical pit geometry is chosen for simplicity. This equation shows that opening of a pit on a crystal surface is a competition between the first and last terms which decrease the free energy (notice that $\ln[A]/[A_{eq}]$ is a negative value if the solution is undersaturated) and the second term which increases the free energy due to creation of surface area. Pit nucleation theory is thus similar to crystal nucleation theory (see Chap. 7).

Without a dislocation outcrop, the third term does not appear in Eq. (5.7) and an activation barrier therefore always slows down pit opening. Such pits only form at relatively high undersaturation because of this activation barrier. In contrast, it can be shown that there is no activation barrier to pit opening at a dislocation when $[A] < [A_{crit}]$, the critical aqueous concentration value (Brantley et al., 1986a; Blum and Lasaga, 1987). The critical concentration of $A_{(aq)}$, $[A_{crit}]$, can be calculated:

$$[A_{crit}] = [A_{eq}] \exp\left(\frac{-2\pi^2\gamma^2 V}{RT\tau b^2}\right) \tag{5.8}$$

Above this concentration, an activation barrier exists and etch pits do not spontaneously open up at dislocations with Burgers vector b.

The rate law and rate mechanism describing dissolution of a mineral therefore changes as a function of concentration: for $[A] \ll [A_{crit}]$, step retreat occurs from vacancy islands, impurities, dislocation etch pits, and crystal edges; for $[A] < [A_{crit}]$, step retreat occurs from dislocation etch pits and crystal edges; and for $[A_{crit}] < [A] < [A]_{eq}$, step retreat occurs only from crystal edges. Rate models such as those described in Sect. 5.5.2 attempt to describe how different surface sites dominate dissolution under different values of undersaturation, but this complexity is difficult to capture in one equation.

As mentioned at the beginning of this section, the distribution of etch pit size on the dissolving surface yields information about the dissolution (and deformation) history for calcite or other crystals (Schott et al., 1989a; MacInnis and Brantley, 1992, 1993). The observation of etch pits on a mineral surface indicates that the crystal experienced far-from-equilibrium dissolution. For example, the surface of the dissolved calcite crystal in Fig. 5.5 documents the characteristic features of a surface dissolved far enough from equilibrium where both homogeneous nucleation and dislocation pitting occurred in parallel. Such observations are characteristic of interface-controlled dissolution. In contrast, when a mineral such as calcite dissolves under transport control it becomes rounded because only the high-energy surface sites dissolve in the near-equilibrium conditions within the boundary layer (Berner, 1978). Furthermore, the effects of dislocations on rate suggest that dissolution rates should increase when defect densities on calcite increase above $10^7\,\mathrm{cm}^{-2}$: indeed, rate enhancements of 2–3 have been observed for highly strained as compared to unstrained calcite crystals (Schott et al., 1989a). Consistent with these observations,

pre-treatment of crystals by etching or roughening the surface causes a transient increase in the observed dissolution rate (MacInnis and Brantley, 1992; Beig and Luttge, 2006). Many of the geochemical implications of these phenomena were first discussed for calcite (see references above) and for silicates in the 1980s (Brantley et al., 1986a, b).

5.2.2 Silicate and Oxide Dissolution Mechanisms

5.2.2.1 Alteration of Silicate Surface

Transport-controlled dissolution can either refer to slow transport through the fluid boundary layer as discussed for carbonates in the previous section, or through an alteration layer on the mineral surface (e.g., Sect. 5.1.3). Such alteration layers grow on many dissolving silicates where the rate of Si release is less than release of other cations (e.g., Fig. 5.3). After long durations, the rate of diffusion of leaching cations through such a layer and the rate of release of Si to solution eventually becomes stoichiometric for many silicates (Schweda, 1990; Stillings and Brantley, 1995; Taylor et al., 2000b). For some silicates such as hornblende, however, even after long dissolution periods the alteration layer may never reach steady-state (Mogk and Locke, 1988).

The mechanism of formation of alteration layers on silicates has most commonly been attributed to simple leaching accompanied by surface condensation and reconstruction reactions (Brantley, 2004). For example, 6-coordinate Al, observed on the dissolving albite surface despite the fact that bulk albite only contains 4-coordinate Al, was attributed to reconstructive reactions occurring within a layer formed by leaching (Tsomaia et al., 2003). However in cases such as labradorite dissolved at low pH, the sharp interface between surface layer and bulk mineral may not be consistent with simple diffusion across a leached layer, but rather may document dissolution, reprecipitation, and reconstruction (Hellmann et al., 2003). According to this solution-precipitation hypothesis, reprecipitation reactions occur well below solubility limits for secondary phases. Regardless of whether dissolution is followed by precipitation, hydrolysis of bridging oxygens generally reduces the connectedness of network atoms (Fig. 5.7) from 4 (Q^4) to 3 (Q^3) to 2 (Q^2) to 1 (Q^1) before hydrolysis releases the atom to solution (Hellmann et al., 1990; Brantley and Stillings, 1997; Hamilton et al., 2001; Tsomaia et al., 2003). In this notation, tetrahedral sites, noted as Q^i sites, have 4, 3, 2, or 1 bridging oxygen ($= i$). The connectedness, or number of bridging oxygens around the tetrahedrally coordinated atom, increases with the relative polymerization of the silicate. A distribution of Q sites must characterize the layer regardless of whether the layer forms by solution-precipitation or by leaching. Interestingly, for some silicates, silica polymers may be released directly to solution before connectedness is reduced to 1 (Dietzel, 2000; Weissbart and Rimstidt, 2000).

5.2.2.2 Surface Complexation Models

Rates of oxide dissolution (Fig. 5.1) are generally observed to be affected by the proton concentration of the reacting solution and are often described by the following empirical equation:

$$r = k_H a_{H^+}^n + k_{OH} a_{OH^-}^m \tag{5.9}$$

where k_H and k_{OH} are the rate constants for proton- and hydroxyl-promoted dissolution respectively, a_i is the activity of species i in solution, and n and m are sometimes referred to as the partial orders of reaction. These partial orders vary as a function of mineral composition. Some authors include a third rate term in Eq. (5.9) describing dissolution as a function of the rate constant for reaction with H_2O, k_{H_2O}, at neutrally charged surface sites, $\equiv SiOH (= k_{H_2O}[\equiv SOH])$. While values of n vary for many minerals (Fig. 5.1), some researchers have suggested that m equals 0.3 for all aluminosilicates (Brady, 1991).

Stumm and coworkers (Furrer and Stumm, 1983, 1986; Stumm and Furrer, 1987; Wieland et al., 1988) first suggested that the pH effect can be explained by the fact that sorption of protons on an oxide surface polarizes the metal-oxygen bonds, weakening the bonding with the underlying lattice (see also Chap. 4). According to this model, if $[\equiv SOH_2^+]$, and $[\equiv SO^-]$ represent the concentration of positively and negatively charged surface complexes, respectively, then the dissolution rate, r, in solutions without reactive ligands can be predicted from these surface site concentrations (Fig. 5.6):

$$r = k_H [\equiv SOH_2^+]^{q_1} + = k_{OH} [\equiv SO^-]^{q_2} \tag{5.10}$$

where q_1 and q_2 are constants. Consistent with this model, the rate of dissolution of most oxides is slowest in solutions at the pH of the pristine point of zero charge (pH_{ppzc}) where the net concentration of charged sites equals zero (compare Fig. 5.1). These workers and others (Guy and Schott, 1989; Schott, 1990; Ludwig and Casey, 1996) suggested that q_1 corresponds to the number of protonation steps required to release a cation from the surface as the connectedness of this central metal is reduced to 0 (see for example Fig. 5.7). More simply, the value of q_1 represents the oxidation number of the metal: e.g., $q_1 = 2(\mathrm{BeO}), = 3(\delta - \mathrm{Al_2O_3}), = 3(\alpha - \mathrm{Fe_2O_3})$ and $= 4(\mathrm{SiO_2})$.

In general, application of this model to mixed oxides such as feldspar has been difficult. Proton sorption has been measured on feldspars and attributed to both Al and Si protonation for pH < 3 and to Al protonation between pH 3 and 7. Consistent with a value for q_1 equal to the oxidation number of the metal being protonated, a value of $q_1 = 3$ was reported for albite and a similar value reported for anorthite (Amrhein and Suarez, 1988; Schott, 1990). However, a value of $q_1 = 1$ was also reported for albite as exemplified in Fig. 5.6. Specifically, the logarithm of the surface charge of albite under acid conditions, $\log[\equiv SOH_2^+]$, was observed to be proportional to $\log a_{H^+}^{0.52}$ as shown in Fig. 5.6a (Blum and Lasaga, 1988; Blum and Lasaga, 1991). Because the rate of albite dissolution at low pH fit to Eq. (5.9) also

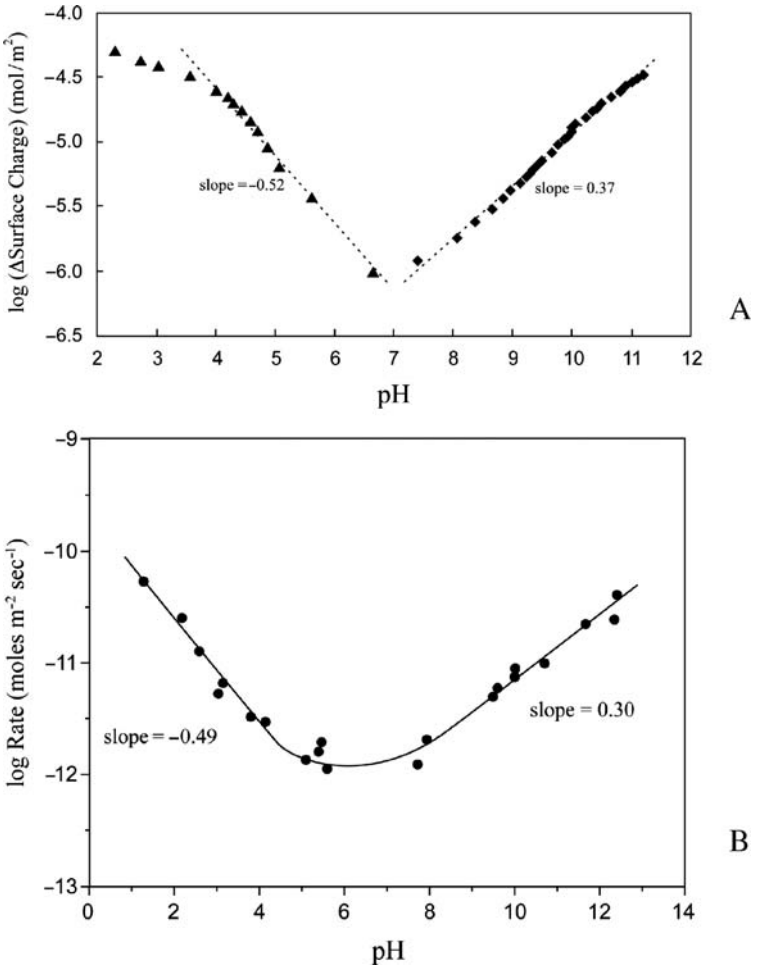

Fig. 5.6 (**a**) Logarithm of the change in surface charge (Δ Surface charge) as a function of pH during titration of an albite slurry (Blum and Lasaga, 1991). Δ Surface charge is interpreted as the concentration of protonated surface sites, $[\equiv SOH_2^+]$, for pH < 7 and deprotonated surface sites, $[\equiv SO^-]$, for pH > 7. (**b**) The logarithm of the dissolution rate of albite as measured previously (Chou and Wollast, 1985) and replotted by Blum and Lasaga. Blum and Lasaga argued that the similar slopes indicated in (**a**) and (**b**) were evidence suggesting that protonation of the surface was a precursor step to dissolution for subneutral pH while deprotonation of the surface was a precursor step for dissolution above neutral pH. They inferred that q_1 and q_2 were unity in Eq. (5.10). (Reprinted from Blum and Lasaga 1991. With permission from Elsevier).

yields $n = \sim 0.5$ (Fig. 5.6b), Blum and Lasaga proposed that $q_1 = 1$ for dissolution of albite at 25° C. These workers argued similarly that above pH 7 the increase in albite dissolution rate was due to the increase in density of deprotonated surface Al sites (compare Fig. 5.6a and 5.6b for pH > 7). Above pH 7, other researchers have attributed negative charge on feldspar surfaces to deprotonation of Si (Brady and Walther, 1992).

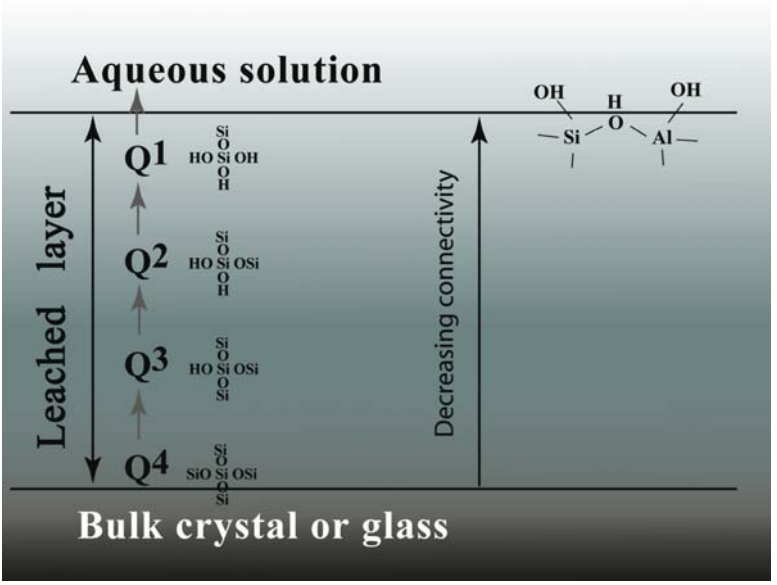

Fig. 5.7 For silicates, the number of bridging oxygens (the connectivity or connectedness) of Si atoms in the altered surface layer must decrease from 4 (tetrahedrally coordinated — Q^4 — sites) to 3 (Q^3 sites) to 2 (Q^2) to 1 (Q^1) to 0 in order to release Si into solution as shown. Although we are emphasizing here the distribution of these sites within an altered surface layer, Q^3, Q^2, and Q^1 sites when outcropping on the silicate surface could be conceptualized as perfect surface, step, and adatom sites respectively (see also Fig. 3.7). The number of protonation steps required to hydrolyze the central cation in an oxide as the cation is depolymerized has been related to the value of *n* in Eq. (5.9). Where Al replaces Si in the lattice, Al-O bonds may be attacked first by hydronium ions, and Al may be released to solution faster than Si, leaving behind a Si-rich altered layer (not shown). Back-reactions may also occur to build an altered surface layer and some authors interpret the altered surface layer as forming by dissolution-precipitation instead of leaching. (Figure courtesy of N. Tsomaia).

Despite the satisfyingly simple observations shown in Fig. 5.6, it is not generally possible to explain the value of q_1 in terms of an activated complex (Casey and Ludwig, 1996) and inconsistencies arise when comparing minerals treated differently (Schott, 1990). The proton-promoted surface complexation model appears inadequate to explain dissolution of mixed oxides such as feldspars where protonation and deprotonation reactions are difficult to measure and interpret (Brantley and Stillings, 1996, 1997). Furthermore, *ab initio* calculations do not show that protonation of either silanols or aluminols promotes dissolution. In fact, *ab initio* calculations document that protonation of terminal $\equiv$ SiOH and $\equiv$ AlOH groups strengthens rather than weakens the bonds connecting these groups to the underlying mineral (Kubicki et al., 1996). Nonetheless, equations such as Eqs. (5.9) and (5.10) are often used to provide a conceptual framework for predicting dissolution behavior and the lowest dissolution rates are often observed at the pH_{ppzc} of a mineral (see Fig. 5.1).

5.2.2.3 The Effect of Dissolved Cations and Anions

Recognizing that simple proton-promoted surface complexation models may be inadequate to describe the complex mechanism underlying mixed oxide dissolution, several research groups have proposed surface sorption or leaching models that incorporate the effects of cations other than protons (Oelkers et al., 1994; Hellmann, 1995; Oelkers and Schott, 1995; Brantley and Stillings, 1996, 1997; Pokrovsky and Schott, 2000). The model of Oelkers and Schott, which assumes that the dissolved concentration of cations other than protons must also be included in the rate model in order to predict dissolution, has been successfully applied to the widest range of minerals (Oelkers, 2001b).

For many pyroxenes, amphiboles, and feldspars, leaching of alkali, alkaline earth, or other cations leaves Si tetrahedra that are still connected to the lattice by bridging oxygens as shown in Fig. 5.7. For these minerals, the Oelkers and Schott model predicts that the dissolution rate varies with the activity of the leached cation in solution. In contrast, for other minerals, complete leaching of cations such as Ca and Al (anorthite) or Mg (forsterite) leaves Si tetrahedra that do not contain bridging oxygens (connectedness = 0). According to this model, minerals such as anorthite and forsterite therefore dissolve according to a proton-promoted mechanism and are not affected by the concentration of cations leached into solution.

A general kinetic rate equation for far-from-equilibrium dissolution of silicates containing cation M_i (Oelkers and Gislason, 2001) has been proposed assuming that a precursor species controls dissolution:

$$r = k \prod_{i=1, i\neq k}^{i} \left[\frac{K_i \left(\frac{a_{H^+}^{\nu_i}}{a_{M_i}^{\nu_i}} \right)^s}{\left(1 + K_i \left(\frac{a_{H^+}^{\nu_i}}{a_{M_i}^{\nu_i}} \right)^s \right)} \right] \tag{5.11}$$

Here k is the rate constant, and K_i is the equilibrium constant describing the exchange reaction between protons and the metal cation M_i at the surface that forms the precursor species. The parameters ν_i and s are stoichiometric coefficients for species appearing in the formation reaction for the precursor in the rate-limiting step. For this model, two endmember rate conditions may be considered. When the term $K_i(a_{H^+}^{\nu_i}/a_{M_i}^{\nu_i})^s$ is small, significant M_i remains in the surface layer, and the denominator becomes unity. This simplified rate equation predicts the rate will be affected by the dissolved concentration of M_i during dissolution: for example, this equation successfully described dissolution of basalt glass (25° C, pH 3), kaolinite (pH 2, 150° C), enstatite (70° C, pH 2), and muscovite (150° C, pH 2). In contrast, for forsterite (25° C, pH 2), and for anorthite (60° C, pH 2.5), $K_i a_{H^+}^{\nu_i}/a_{M_i}^{\nu_i})^s$ is large, and dissolution rates become independent of Mg^{2+} (forsterite) and Al^{3+} (anorthite). Consistent with this model, Fig. 5.8 (top) documents how dissolved Al concentrations have been observed to affect the dissolution rate of a mineral such as muscovite but not that of anorthite (bottom).

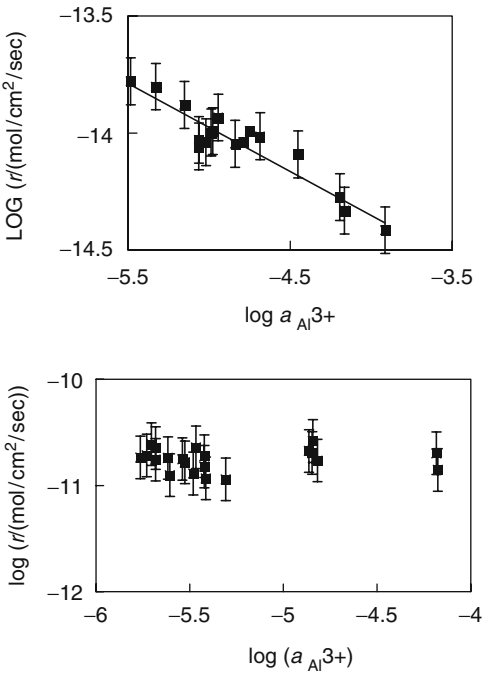

Fig. 5.8 Logarithm of the dissolution rate of muscovite (top) and anorthite (bottom) under acid conditions. As predicted theoretically (Oelkers, 2001b), no dependence on dissolved Al^{3+} is observed for anorthite, but a strong dependence is observed for muscovite. Oelkers argues that dissolution of muscovite is dependent upon the surface concentration of an Al-deficient surface species, but that anorthite dissolution is not dependent upon such a species (see Sect. 5.2.2.3). (Reprinted from Oelkers, 2001b. With permission from Elsevier).

The model yielding Eq. (5.11) provides a conceptual framework to predict the rate of mineral dissolution as a function of dissolved cation concentration when the cation is released to solution from the dissolving phase. The model is also consistent with the observation that addition of aqueous Al^{3+} as a background salt does not affect dissolution of forsterite but does inhibit dissolution of albite (Chen and Brantley, 1997; Chen and Brantley, 2000) and quartz (Dove, 1995). Other researchers have proposed similar models for the effect of background electrolytes by modeling cation sorption by Langmuir or competitive Langmuir isotherms. Such Langmuir models implicitly assume ideal sorption of ions onto identical surface sites without interaction of sorbate molecules with each other. These models yield rate equations that are not dissimilar from Eq. (5.11) in form.

For example, background electrolytes in solution generally decrease the rate of dissolution of feldspars (Sjoberg, 1989; Nesbitt et al., 1991; Stillings and Brantley, 1995). Feldspar dissolution in acidic solution far-from-equilibrium was therefore related to competitive adsorption of H^+ and other cations on the surface of feldspar (Stillings and Brantley, 1995):

$$r = k\left[\frac{K_H^{ads} a_{H^+}}{1 + K_H^{ads} a_{H^+} + \sum_i K_{M_i}^{ads} a_{M_i}}\right] \tag{5.12}$$

where k is the apparent rate constant, M_i refers to adsorbing cations, and K_H^{ads} and $K_{M_i}^{ads}$ refer to the equilibrium constants for adsorption of H^+ and M_i on reactive sites. Such a rate equation can be derived if one assumes that dissolution is a function of the sorbed proton density, and if this site density can be described by a competitive adsorption Langmuir model (Laidler, 1987).

In contrast to the feldspars, alkali or alkaline earth cations at low concentrations in solution increase the dissolution rate of quartz and amorphous silica by factors up to 100x in low and high temperature solutions. This effect has been attributed to cationic effects on the solvent at the mineral-water interface (Dove and Crerar, 1990; Bennett, 1991; Gratz and Bird, 1993; Dove, 1994, 1995; Dove and Nix, 1997; Icenhower and Dove, 2000). Recently, a model has been proposed to explain why salt solutions accelerate quartz dissolution but inhibit feldspar dissolution (Dove et al., 2005).

Although the effects of cationic solutes on mineral dissolution have been investigated intensively as described above, many fewer researchers have investigated the effects of inorganic anions. Anions that form binuclear surface complexes such as phosphate, borate, and arsenate inhibit oxide dissolution probably because they form bi- or multinuclear inner-sphere surface complexes. Stumm and coworkers have suggested that release or removal of such complexes is energetically unfavorable, inhibiting proton-or ligand-promoted dissolution (Biber et al., 1994; Stumm, 1997).

5.2.2.4 Effect of CO_2 on Dissolution

The increase in concentration of carbon dioxide in the atmosphere has led to many proposals to pump the gas into aquifers or through mineral media to promote mineral dissolution and precipitation reactions that can sequester the gas. The rates of mineral reaction as a function of CO_2 concentration are thus of current interest. For example, the dissolution of forsterite and precipitation of magnesite has been explored in the context of deep saline aquifer storage (Giammar et al., 2005). For this and several other studies, the effect of CO_2 on dissolution has been attributed not to a direct effect, but to the indirect effect on pH. The indirect effect of CO_2 on dissolution can be predicted using Eqs. (5.9)–(5.12). In contrast, some researchers have reported that adsorption of inorganic carbon species to surfaces can affect dissolution behavior for Fe oxides and Ca or Mg silicates (Wogelius and Walther, 1991; Bruno et al., 1992; Xie, 1994; Malmström and Banwart, 1997; Berg and Banwart, 2000; Pokrovsky and Schott, 2000; Golubev et al., 2005). However, even under alkaline conditions, silicate dissolution rates show only a negligible or at best weak dependence on P_{CO_2} when pH is held constant. For example, the release of Ca and Mg from diopside during dissolution decreased only slightly or not at all for $P_{CO_2} >$ atmospheric (Knauss et al., 1993) and the dissolution rates of augite and anorthite at pH 4 did not vary measurably as a function of P_{CO_2} (Brady and Carroll, 1994).

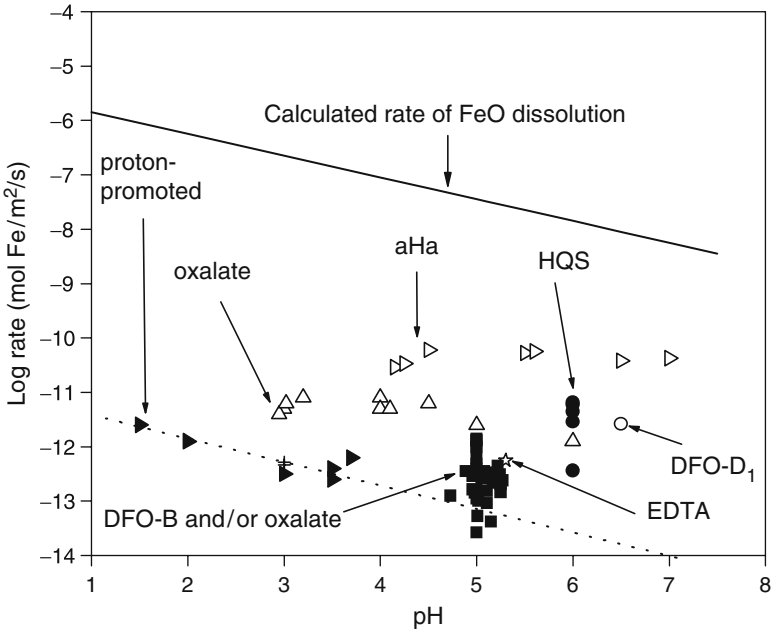
Calculated rate of FeO dissolution
proton-promoted
oxalate
aHa
HQS
DFO-D1
EDTA
DFO-B and/or oxalate
Log rate (mol Fe/m2/s)
pH

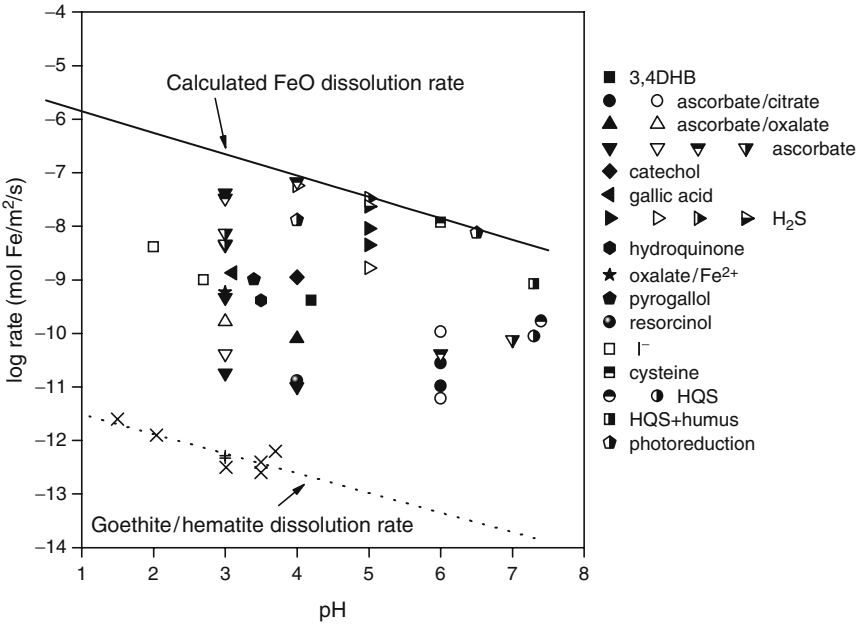
Calculated FeO dissolution rate
Goethite/hematite dissolution rate
log rate (mol Fe/m2/s)
pH
3,4DHB
ascorbate/citrate
ascorbate/oxalate
ascorbate
catechol
gallic acid
H2S
hydroquinone
oxalate/Fe2+
pyrogallol
resorcinol
I−
cysteine
HQS
HQS+humus
photoreduction

Dissolution rates of volcanic soils at low pH were similarly negligibly affected by variations in P_{CO_2} (Stephens and Hering, 2004).

5.2.2.5 Ligand-Promoted Dissolution

The effect of mM concentrations of organic anions on dissolution rates is less than a factor of ~10 for ortho- and inosilicates (Wogelius and Walther, 1991; Brantley and Chen, 1995) and less than a factor of ~15 for feldspars (Drever and Stillings, 1997). These effects are pH- and ligand-dependent (Wogelius and Walther, 1991; Welch and Ullman, 1996). When organic ligands are present in lower concentrations that are more similar to those observed in soil solutions, the effect of these ligands on dissolution rates of silicates are less than a factor of ~5 (van Hees et al., 2002). Perhaps because these effects are relatively small and are affected by both mineral and solution composition, reports of anionic effects have not always been consistent.

In contrast to silicates, the effects of organic ligands on Fe oxide dissolution are better understood. For example, goethite dissolution (Fig. 5.9a) is generally

Fig. 5.9 (**a**) Compilation of initial rates of proton- and ligand-promoted dissolution of Fe oxides from published sources summarized previously (Brantley et al., 2006). Proton-promoted dissolution of goethite (►) and hematite (+) are plotted as a function of pH for non-reductive conditions. The dotted line shows the equation, log (Rate) $= -10.98 - 0.43\,\mathrm{pH}$, and represents a linear fit to combined dissolution rates measured for goethite without ligands added and for goethite in the presence of 1 μM desferrioxamine B (DFO-B). Symbols marked HQS refer to goethite dissolution in the presence of 8-hydroxyquinoline-5-sulfonate with varying concentrations of Fe^{2+}. Oxalate-promoted goethite dissolution was measured under non-reductive conditions. aHa refers to goethite dissolution in acetohydroxamic acid. Goethite dissolution rates in the presence of oxalate ± desferrioxamine B (DFO-B) at varying concentrations are indicated as filled squares. Symbols marked DFO-D_1 represent goethite dissolution in the presence of 240 μM desferrioxamine D_1 and symbols marked EDTA represent goethite dissolution in 11.5 μM EDTA. The solid line is described in the caption for Fig. 5.9b. (**b**) Reductive dissolution rate data for Fe(III) (hydr)oxides. The dotted line is a linear fit (log (rate) $= -10.98 - 0.43 \cdot$ pH) for the non-reductive, proton-promoted dissolution rate of goethite and hematite (marked with × and +, respectively) as shown in Fig. 5.9a, and the solid line is the predicted dissolution rate of Fe(II)O. This rate was predicted based on the proportionality observed for divalent metal oxides (see for example Fig. 5.10a) between the log (dissolution rate) and the log (first-order rate constant, k_{solv}) for water exchange within the inner-coordination sphere of the hydrated metal ion (Casey et al., 1993a). These authors report dissolution rates for BeO, NiO, CoO, MnO, ZnO, and CaO that can be modeled as log (rate at pH2) $(\mathrm{mol\,m^{-2}\,s^{-1}}) = -17.20(\pm 0.69) + 1.68(\pm 0.11)\log k_{solv}$. Using $\log k_{solv}(\mathrm{s^{-1}}) = 6.5$ for Fe^{2+}, the dissolution rate of Fe(II)O at pH 2 was estimated to be $5.25 \times 10^{-7}\,\mathrm{mol\,m^{-2}\,s^{-1}}$. The slope of the log rate – pH line for FeO was set equal to −0.4 based upon the slope for goethite (−0.43, dotted line). Symbols represent the dissolving phase: solid (goethite), open (hematite), upper-half filled (ferrihydrite), lower-half filled (magnetite), right-half symbols (lepidocrocite). Data are plotted for 3,4 DHB (3,4-dihydroxybenzoic acid); ascorbate/citrate mixtures; ascorbate alone; catechol; cysteine; gallic acid; H_2S; hydroquinone; oxalate/Fe^{2+} mixtures; pyrogallol; resorcinol; I^-; cysteine; HQS (8-hydroxyquinoline-5-sulfonic acid); HQS + humus mixtures and under photoreductive conditions. Symbols represent initial rates of reductive dissolution of these minerals from data sources previously cited (Brantley et al., 2006). It is notable that all dissolution data is bracketted by the proton-promoted dissolution rates for Fe(III) and Fe(II) oxides.

unmeasurable at neutral pH in the presence of oxygen without complexing ligands (Kraemer, 2004). Indeed, enhancement of Fe oxide dissolution by micro-organisms (Banfield and Nealson, 1997) is often due to secretion of organic ligands. In particular, to extract Fe from the environment, many organisms secrete the low molecular weight chelating ligands known as siderophores (Hersman, 2000; Kalinowski et al., 2000b). Siderophores demonstrate high affinity for ferric iron. Experiments utilizing purified siderophores or siderophore analogues show enhanced Fe release during dissolution of goethite (Watteau and Berthelin, 1994; Holmen and Casey, 1996; Kraemer et al., 1999; Cocozza et al., 2002; Yoshida et al., 2002; Cheah et al., 2003), hematite (Hersman et al., 1995) and hornblende (Kalinowski et al., 2000a, b; Liermann et al., 2000). Such dissolution may leave signatures on the mineral surface. For example, X-ray photoelectron spectroscopic analysis of Fe-silicate surfaces after removal of adherent siderophore-secreting bacteria revealed that Fe was preferentially depleted in the outermost surface after several days of bacterial growth in Fe-depleted culture medium (Kalinowski et al., 2000a).

5.2.2.6 Mechanism of Ligand-Promoted Dissolution

Many researchers attribute the effect of ligands on dissolution to the ligand-promoted dissolution model. According to this simple model, the strength of the ligand-cation interaction at the mineral surface is thought to polarize and weaken the bond between the cation and mineral lattice (Furrer and Stumm, 1983). Assuming that the ligand-promoted dissolution occurs in parallel with proton-promoted dissolution, then the overall rate of dissolution is expected to be additive:

$$r = k_H[\equiv SOH_2^+]^{q_1} + k_{OH}[\equiv SO^-]^{q_2} + \sum_i k_{L_i}[\equiv SL_i]^{q_3} \tag{5.13}$$

Here L_i refers to a ligand, k_{L_i} refers to the rate constant for ligand-promoted dissolution, and $\equiv SL_i$ represents a metal-ligand surface complex. It may be possible to predict surface densities of some ligand-surface complexes based upon the observation that the equilibrium constant for sorption of ligands to a metal surface increases with the equilibrium constant for formation of the ligand-metal complex in solution (Sigg and Stumm, 1981). For example, both Fe oxides (Fig. 5.9a) and Al_2O_3 show variable rates of dissolution as a function of ligand identity in solution. At pH between 3 and 5, dissolution of Al_2O_3 has been observed to decrease in the presence of organic ligands at constant concentration in the order salicylate $>$ phthalate $>$ benzoate (Furrer and Stumm, 1983, 1986). Such trends can be used to predict dissolution behavior as a function of ligand chemistry and have been used to explain dissolution behavior of basalts and granites (Neaman et al., 2005, 2006).

Despite some predictive capability for this model, several lines of evidence suggest that the effect of ligands on mineral dissolution may be indirect rather than direct. For example, whereas some researchers have suggested that organic ligands such as oxalate can increase the solubility and rate of dissolution of quartz at 25° C

(Bennett et al., 1988; Bennett, 1991), other researchers have pointed out that neither evidence for oxalate complexation with aqueous Si nor adsorption of oxalate at the quartz surface have been observed or is theoretically predicted (Iler, 1979; Poulson et al., 1997; Pokrovski and Schott, 1998; Kubicki et al., 1999). For example, inner-sphere adsorption for acetic, citric, benzoic, salicylic, and phthalic acids at pH 3 and 6 on quartz and albite is not theoretically predicted, yet these ligands are observed to affect dissolution of these phases. Kubicki et al. have suggested that complexation of charge-balancing alkali or alkaline earth cations by organic ligands followed by proton attack of the mineral surface may explain organic-promoted dissolution of some silicates.

Other indirect mechanisms have also been invoked to describe the effect of organic ligands on aluminosilicate dissolution. Complexation of Al in solution could either decrease inhibition according to rate laws such as those discussed in Sect. 5.2.2.3 or change the driving force for dissolution as discussed in Sect. 5.5 (Drever and Stillings, 1997). As described in Sect. 5.2.2.3, the Oelkers and Schott model (Oelkers and Schott, 1998) attributes changes in feldspar dissolution rate in the presence of organic ligands to the effect of complexation reactions on free Al^{3+} concentrations and the effect of aqueous Al^{3+} on dissolution (see Eq. (5.11)). These workers also invoke an affinity effect during dissolution (see Eq. (5.36)). The change in affinity caused by the presence of a ligand has also been inferred to affect the dissolution rate of Fe phases (Kraemer and Hering, 1997).

Generally, enhanced mineral dissolution in the presence of siderophores has been attributed to adsorption of the siderophores at the mineral surface (Holmen et al., 1997; Kalinowski et al., 2000a). However, complex dissolution behavior occurs in the presence of multiple ligands, suggesting more complex mechanisms. For example, dissolution of goethite has been observed to double in the presence of the siderophore desferrioxamine B upon the addition of oxalate, and dissolution in the presence of oxalate is increased by an order of magnitude when the siderophore is added (Cheah et al., 2003). These workers inferred that the siderophore removed Fe(III) from the oxalate complex in solution and allowed the oxalate to react with the goethite repeatedly—enhancing the oxalate effect on dissolution.

The effects of naturally occurring high molecular weight organic acids may also not be well-predicted by equations such as Eq. (5.13): these organic molecules can both inhibit and accelerate mineral dissolution (Lundstrom and Ohman, 1990; Ochs et al., 1993). For example, adsorbed humic molecules inhibit dissolution at pH 4–4.5 and accelerate dissolution at pH 3 (Ochs et al., 1993). These observations have been attributed to the effects of protonation on complexation of the organic molecule at the mineral surface (Ochs, 1996). Extracellular polysaccharides can also either accelerate or inhibit dissolution of minerals (Welch and Ullman, 1999).

5.2.2.7 Mechanism for Redox-Sensitive Oxides

Dissolution of redox-sensitive minerals may be coupled with oxidation or reduction of cations, adding further complexity to the dissolution mechanism. For example,

oxidation of mineral sulfides generally enhances dissolution of these phases (Nordstrom, 1982, 2000). Such oxidative dissolution of sulfide minerals is of great environmental significance in generation of acid mine or rock drainage but will not be further discussed here.

Reduction of mineral surfaces can also enhance dissolution. For example, the reduction of surface Fe(III) to Fe(II) is thought to decrease the strength of the bond of Fe to the underlying lattice in oxide minerals (Suter et al., 1988, 1991), enhancing the dissolution rate. Such a model suggests that the upper limit for reductive dissolution of Fe(III) oxides should be the rate of dissolution of Fe(II) oxide. This idea is tested in Fig. 5.9b where reductive dissolution rates for Fe(III) oxide are plotted as a function of pH and ligand identity. The lines on the figure, representing the proton-promoted dissolution rate for Fe(III) oxide (lower line) and the theoretically predicted proton-promoted dissolution rate for Fe(II) oxide (upper line), successfully bracket the measured rates of reductive dissolution for the ferric oxides. The predicted rate for ferrous oxide dissolution was calculated based upon the observation that the rate constant for proton-promoted dissolution of divalent metal-oxides of a given structure measured at a given pH varies with the rate of exchange of water molecules around the metal cation in solution (Casey and Cheney, 1993). According to this idea (see Fig. 5.10a for the orthosilicate structure), the rate of dissolution of Fe(II) oxide at pH 2 is predicted to be 5.25×10^{-7} mol m^{-2} s^{-1} (Fig. 5.9b). The estimated line for dissolution of FeO was plotted assuming this value and a slope of -0.4. The rate-limiting step of reductive dissolution is inferred to be the release of the Fe(II)-L complex from the mineral surface.

The higher strength of Fe(III)-O bonds compared to Fe(II)-O bonds suggests that the rates of dissolution of Fe-containing oxide minerals should be slower under oxidative than reductive conditions (Casey and Cheney, 1993). Consistent with this, several workers have observed that the dissolution rates of the pyroxenes, hypersthene and bronzite decreased in the presence of oxygen (Schott and Berner, 1983, 1985). However, oxidation of Fe (II) to Fe (III) in hornblende and augite have been observed to increase dissolution rates (White and Yee, 1985; Zhang et al., 1990; Hoch et al., 1996). This increase in dissolution has been attributed to coupled reactions at the mineral surface and the oxidative effect of ferric iron released to solution during dissolution. During dissolution of ferrous silicates, release of charge-balancing cations occurs simultaneously with hydrolysis and protonation of the silicate structure or subsequent to oxidation (White and Yee, 1985; Kalinowski and Schweda, 1996; Perez et al., 2005). Fe^{3+} that is released to solution during dissolution can be reduced by ferrous ions in the mineral, regenerating the oxidized Fe surface layer. The rate of oxidation of ferrous surface sites on various minerals has been modeled as first order in concentration of surface ferrous sites and first order in dissolved oxygen concentration (see Eq. (5.19) in Chap. 1) (Wehrli, 1990; Perez et al., 2005). More research is needed to investigate the relative effects of oxidative versus reductive dissolution of redox-active silicates.

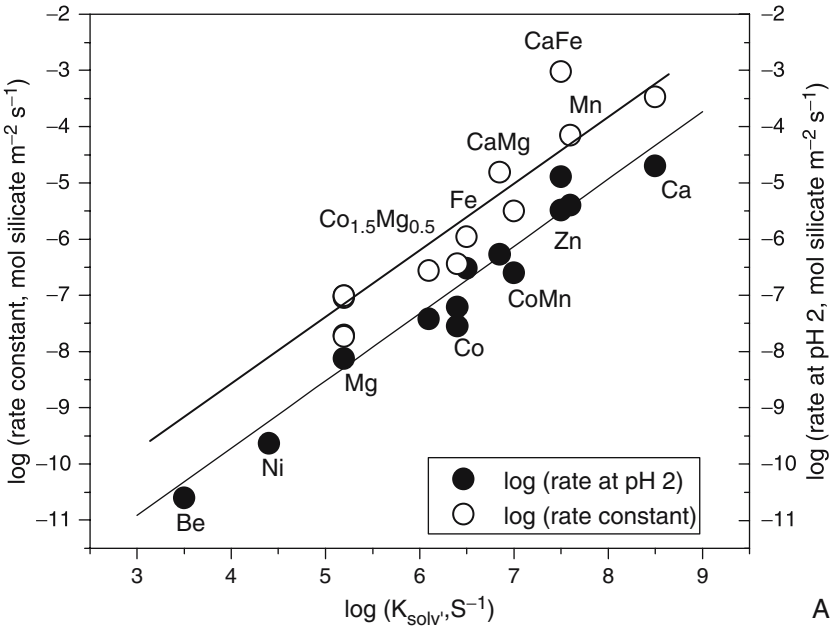

Fig. 5.10 (**a**) Correlation between log dissolution rates of orthosilicates of different composition measured at pH 2 (filled symbols) and the logarithm of the rate constants for exchange of water around the charge-balancing cations when the cation is hydrated in solution, k_{solv} (Westrich et al., 1993). Values of k_{solv} are derived from published sources (Hewkin and Prince, 1970). Westrich et al. identified this trend for the dissolution rates measured at pH 2; also plotted as open symbols are the values of the rate constants for the orthosilicate dissolution data fit to Eq. (5.9) (i.e., the intercept of a log dissolution rate – pH plot) (Kump et al., 2000). These trends are consistent with a model wherein the relative tendency for dissolution of orthosilicates can be predicted from the rate of exchange of waters in the hydration shell of the central metal. (Figure after Kump et al., 2000) (**b**) Plot of the logarithm of rate constants for dissolution of individual minerals plotted against the connectedness of the mineral (number of bridging oxygens per tetrahedral cation). Connectedness of 0 is an orthosilicate, 2 is a pyroxene, 2.5 is an amphibole, and 3 is a phyllosilicate. Dissolution rates decrease with increasing connectedness and as a function of the cations in the structure as shown. (Figure updated from original publication (Brantley, 2004)) (**c**) Estimates of the activation energy for k_H plotted versus connectedness for several minerals. Data sources are summarized in Table 5.5. The maximum and minimum estimates of the Ea are plotted for quartz and only the value estimated for anthophyllite using a temperature-dependent n is plotted (Table 5.5). Calculated estimates of activation energy are also included as indicated (Pelmenschikov et al., 2000; Pelmenschikov et al., 2001; Criscenti et al., 2006) (see text). Note that calculated and measured activation energies are only consistent for connectedness ≤ 2, suggesting that the precursor molecules in the rate-limiting steps of dissolution of all silicates may generally have a connectedness ≤ 2. Such a conclusion is consistent with step retreat or removal of adatoms as the precursor for silicate dissolution (see text). (Figure updated from original publication (Brantley, 2004)).

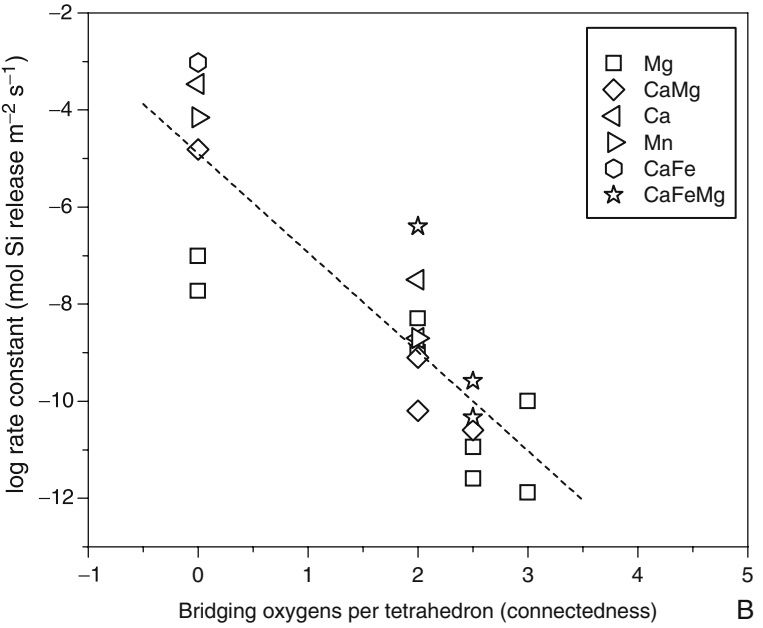

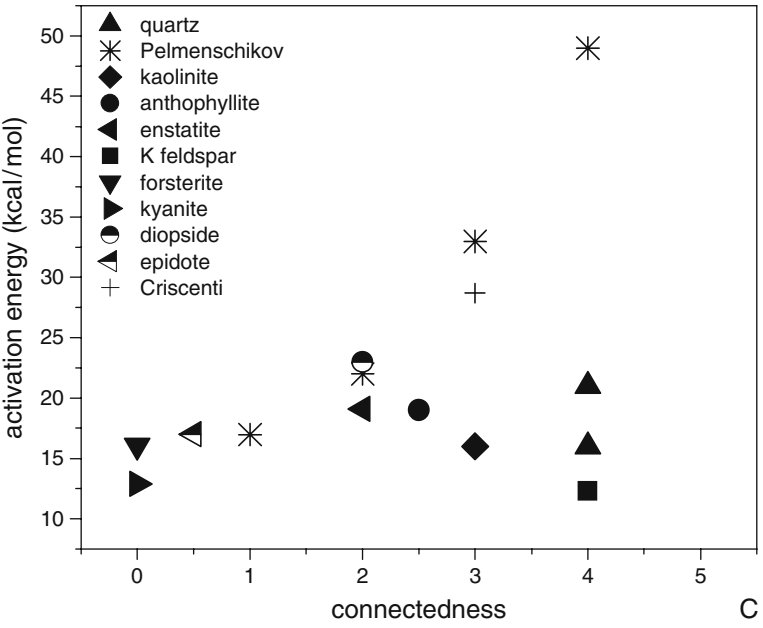

Fig. 5.10 (*Continued*)

5.3 Rate Constants as a Function of Mineral Composition

The database of rate constants for dissolution of primary silicate minerals (White and Brantley, 1995) has been updated in the Appendix of this book (Bandstra et al., 2007) and by other researchers (Palandri and Kharaka, 2004). In this chapter, we summarize empirical rate equations for silica and carbonate phases (Sects. 5.3.1 and 5.3.4) and for some silicates that were not discussed in the Appendix or Chap. 6 (Table 5.2). Readers interested in the dissolution kinetics of secondary silicates, oxides, and sulfides that are not treated extensively in this book are directed to other references and data compiled in Chap. 13 (Nordstrom, 1982; Sverjensky, 1992; Rimstidt and Newcomb, 1993; Rimstidt et al., 1994; Nagy, 1995).

Compilations of rate data show that rates of dissolution of silicates are generally found to be within ± 0.25 log units within one laboratory but may differ by up to ± 2 log units among laboratories. Some of these discrepancies are related to differences in laboratory technique, including duration of experiment (see Fig. 5.2), and others are related to differences in behavior of mineral specimens from different localities. In particular, short-duration dissolution experiments may yield rates that are highly dependent upon the preparation of samples for dissolution. Discrepancies among rate data make it difficult to fit compiled data (Chap. 6). In the future, general models to predict kinetic parameters (Sverjensky, 1992) should be used to discern which rate data are reliable and should lead to generalized rate equations. One such technique for comparing rate data is explained in Sect. 5.3.3.

5.3.1 Silica

Quartz dissolution has been investigated more thoroughly than any other silicate. Bandstra et al. (Chap. 6) present a fit of quartz dissolution data to Eq. (5.9) at 25° C which is plotted for comparison in Fig. 5.1. The rate of dissolution of quartz has also been expressed by a rate equation similar to Eq. (5.10) (Dove, 1994, 1995):

$$r = k_{SiOH}(T)\theta_{\equiv SiOH} + k_{SiO^-}(T)\theta_{\equiv SiO^-_{tot}} \tag{5.14}$$

where each rate constant describes the reaction at a given surface site as indicated, $\theta_{\equiv SiOH}$ is the fraction of total neutral surface sites, and $\theta_{\equiv SiO-}$ is the sum of the fractions of total sites existing as deprotonated surface hydroxyls and as sites with adsorbed Na^+ ($\equiv SiONa^+$). This equation successfully describes quartz dissolution from 25 to 300° C for pH 2–12 in variable ionic strength and Na concentrations to 0.5 m. The rate constants vary with temperature with an activation energy of 15.8 and 19.8 kcal mol^{-1} respectively (see Sect. 5.4.1). The rate of dissolution of quartz varies such that the minimum dissolution rate occurs at a pH $\approx$ pH_{ppzc}.

Net rates of dissolution for amorphous silica into solutions with and without NaCl have been described successfully using the following rate model (Icenhower

Table 5.1 Feldspar rate parameters at 25° C for $r = k_{\mathrm{H}}(a_{\mathrm{H}^+})^n + k_{\mathrm{H_2O}} + k_{\mathrm{OH}}(a_{\mathrm{OH}^-})^m$

	$Log\ k_H(E_a)$ $(mol\ m^{-2}s^{-1})$ $(kcal/mol)$	$Log\ k_{H_2O}(E_a)$ $(mol\ m^{-2}s^{-1})$ $(kcal/mol)$	$Log\ k_{OH}(E_a)$ $(mol\ m^{-2}s^{-1})$ $(kcal/mol)$	n	m	pH_{ppzc}[a]
K-feldspar[b]	−10.06(12.4)	−12.41(9.08)	−9.68(22.5)	0.500	0.823	6.1
Albite[c]	−9.62	—	−9.64	0.403	0.376	5.2
Albite[b]	−10.16(15.5)	−12.56(16.7)	−7.59(17.0)	0.457	0.572	5.2
Oligoclase[b]	−9.67(15.5)	−11.84(16.7)	—	0.457	—	
Andesine[b]	−8.88(12.8)	−11.47(13.7)	—	0.541	—	
Labradorite[b]	−7.87(10.1)	−10.91(10.8)	—	0.626	—	
Bytownite[c]	−5.85(7.00)	−9.82(7.53)	—	1.018	—	
Anorthite[b]	−6.64	—	—	0.985	—	5.6
Anorthite[c]	−3.50(3.97)	−9.12(4.25)	—	1.411	—	5.6

[a] Values of the pristine point of zero charge are calculated values (Sverjensky, 1994). Values of pH_{ppzc} for feldspars may be significantly lower than these quoted values, depending upon the model used for calculation (Parks, 1967) and upon the degree of proton-exchange of the surface.
[b] Published values (Palandri and Kharaka, 2004).
[c] Rate constants from Bandstra et al. (Chap. 6). See Appendix for data and fits.

and Dove, 2000):

$$r = k_+ \left(a_{SiO_{2(aq)}}\right) (a_{H2O})^2 (1 - \Omega) \tag{5.15}$$

Here, k_+ is the dissolution rate constant and $\Omega = \exp(\Delta G/RT)$ (see Sects. 5.5.1 and 5.5.2). This phase dissolves at a rate approximately ten times faster than quartz under comparable conditions.

5.3.2 Feldspar

As discussed earlier, feldspar dissolution has been described by empirical rate models using Eq. (5.9) (see Table 5.1), and fits for albite and anorthite dissolution to these equations are described in Bandstra et al. (Chap. 6). Where data is available, the dissolution rate of feldspars shows an increase at low and high pH, exhibiting a V shape (Fig. 5.1). The lowest dissolution rate is observed to be near-neutral for all feldspar compositions. As mentioned earlier, one explanation for these observations is that the low dissolution rate corresponds to the pH where the feldspar surface has zero charge (pH_{ppzc}), consistent with the proton-promoted surface complexation model. However, the value of the pH_{ppzc} for feldspar is not generally agreed upon (Parks, 1967; Sverjensky, 1994; Brantley and Stillings, 1996; Walther, 1996; Mukhopadhyay and Walther, 2001). Alternatively, the trough in dissolution for feldspars may be explained by the effect of free Al ions in solution and back-reactions at the mineral surface as described for the derivation of Eq. (5.11).

At pH 2–3 at ambient temperature, the log (rate) for dissolution of plagioclase feldspar increases linearly with increasing Ca (anorthite) content from An0 to An80 (Blum and Stillings, 1995). However, the rate of dissolution of An100 is significantly faster than the linear trend (Fleer, 1982; Chou and Wollast, 1985; Holdren and Speyer, 1987; Mast and Drever, 1987; Amrhein and Suarez, 1988; Sjoberg, 1989; Sverdrup, 1990; Casey et al., 1991; Amrhein and Suarez, 1992; Oxburgh et al., 1994; Stillings and Brantley, 1995). It has been pointed out that the values for log k_H and n in Eq. (5.9) vary systematically with the $Al/(Al + Si)$ ratio in the feldspar (Casey et al., 1991; Welch and Ullman, 1996). According to Blum and Stillings (using data from papers cited above), the value of n equals 0.5 from An0 to An70, but increases to about 0.75 at An76 and 1.0 at An100. Apparently, a threshold Al content exists such that dissolution behavior changes drastically (see Sects. 5.1.3 and 5.2.2.1).

5.3.3 Non-Framework Silicates

In Chap. 6, rate equations are summarized for the non-framework silicates biotite, diopside, forsteritic olivine, hornblende, and kaolinite. These equations were developed from fits to the published rate data in the Appendix. For other non-framework silicates, parameters are summarized in Table 5.2. Generally, only rates under acid conditions for longer durations are summarized in the table, and, where multiple researchers have published rates, only those rates are summarized that were measured under controlled conditions (usually flow reactors). Only a very few minerals have been measured in multiple laboratories to allow high confidence in prediction of the rate. It is often necessary therefore to predict rates for compositions that have never been investigated: as mentioned earlier, such rate predictions can also be used to interrogate rate data for errors.

For example, Fig. 5.10a documents that the dissolution rates of orthosilicates at pH 2 and 25° C (Casey and Westrich, 1992; Westrich et al., 1993) are correlated to the rate constants of exchange of water (k_{solv}) for the corresponding hydrated, divalent cations (see also Fig. 4.4). This correlation reflects the observation that the ease of hydrolysis of metals in silicate structures is correlated with the exchange of water in the hydration shell of the aqueous metal ions. Thus, the similarity of activated surface complexes for metal oxides and the corresponding aqueous complexes for these metals (Ludwig et al., 1995) allows predictions of rates of dissolution. Data and predictions from the literature (Blum and Lasaga, 1988; Wogelius and Walther, 1991; Casey and Westrich, 1992; Wogelius and Walther, 1992; Casey et al., 1993b; Westrich et al., 1993; Chen and Brantley, 2000; Pokrovsky and Schott, 2000; Rosso and Rimstidt, 2000) have been used previously to test a similar correlation between the rate constant of solvent exchange (k_{solv}) and the constant k_H for rate Eq. (5.9) for orthosilicate dissolution (Fig. 5.10a, plotted as open symbols). The correlation between k_H and k_{solv} was expressed (Brantley, 2004) as

$$log\ k_H = 1.22 log\ k_{solv} - 13.6(\pm 0.18) \tag{5.16}$$

Table 5.2 Summary of rates for selected silicates at subneutral pH based on Eq. (5.9)

Phase	log k_H	n	pH range	Data used	Formula
fayalite	−6.0	0.69		Wogelius and Walther, 1992	O_4
epidote	−10.7	0.26	2–4	Kalinowski et al., 1998	O_{12} (OH)
epidote	−10.6	0.34		Palandri and Kharaka, 2004	O_{12} (OH)
enstatite	−8.6	0.11	2–7	Ferruzzi, 1993	O_6
enstatite	−9.3	0.24	1–13	Oelkers and Gislason, 2001	O_6
enstatite	−9.0	0.60	<7	Palandri and Kharaka, 2004	O_6
bronzite [a]	−9.5	0.36	<5	Grandstaff, 1977; Schott and Berner, 1983	O_6
augite [a]	−6.7	0.85	<6	Siegel and Pfannkuch, 1984; Sverdrup, 1990	O_6
wollastonite[a]	−7.8	0.2	<7.2	Xie, 1994; Xie and Walther, 1994	O_6
wollastonite[a]	−11	0.27	>7	Xie, 1994; Xie and Walther, 1994	O_6
wollastonite[a]	−9	0	2–6	Weissbart and Rimstidt, 2000	O_6
Wollastonite	−5.37	0.4	not given	Palandri and Kharaka, 2004	
Rhodonite	−9	0.27	2.1–7.1	Banfield et al., 1995	O_6
spodumene[a]	−4.2	0.64	3–7	Sverdrup, 1990	O_6
jadeite[a]	−7	0.18	3–6	Sverdrup, 1990	O_6
Anthophyllite	−11.85	−0.05	2–5	Mast and Drever, 1987	$O_{22}(OH)$
anthophyllite[b]	−12.5	0.24	1–4	Chen and Brantley, 1998	$O_{22}(OH)$
Anthophyllite	−11.9	0.44	1–4	Chen and Brantley, 1998 (refit by Palandri and Kharaka, 2004)	$O_{22}(OH)$
tremolite[a]	−11.5	−0.11	1,6	Schott et al., 1981	$O_{22}(OH)$
glaucophane[a]	−6.1	0.64	3–7	Sverdrup, 1990	$O_{22}(OH)$
Muscovite	−11.8	0.14	1–4	Kalinowski and Schweda, 1996	$O_{20}(OH)_4$
Phlogopite	−10.5	0.40	1–4	Kalinowski and Schweda, 1996	$O_{20}(OH)_4$
chrysotile[a]	−10.0	0.24		Bales and Morgan, 1985	$O_5(OH)_4$
talc	−12.5	0		Lin and Clemency, 1981	$O_{10}(OH)_2$

All rates expressed as mol mineral $m^{-2}\,s^{-1}$, where formula units are given and where rates derive from Si release. Only non-framework silicate minerals not summarized in Bandstra et al. (Chap. 6) of this volume are included here. For biotite, diopside, forsterite, olivine, hornblende, and kaolinite, see Chap. 6 for rate fits and see the Appendix for compiled data.

[a] Indicates dissolution measured for less than 1000 h.

[b] indicates normalized by final, rather than initial, surface area.

Similar correlations have been investigated for inosilicates (Banfield et al., 1995). In general, values of k_H (inosilicate) are slower than k_H (orthosilicate), because the dissolution rate decreases with an increase in the connectedness (the average number of bridging oxygens around each Si atom, Fig. 5.10b). This trend in dissolution rate constant as a function of connectedness can be predicted from the ratio of non-tetrahedrally to tetrahedrally coordinated cations, X/Si, which varies with connectedness. X/Si equals 2 for orthosilicates, 1 for pyroxenes and pyroxenoids, 0.875 for amphiboles, 1.5 for chrysotile, and 0.75 for talc. The log rate constant (expressed in units of mol Si released $m^{-2}\ s^{-1}$) of dissolution decreases with X/Si:

$$k_{\mathrm{H}} = 10^{13.51\ \log(0.5\ \mathrm{X/Si})+1.22\log k_{\mathrm{solv}}-13.6}/v_{\mathrm{Si}} \tag{5.17}$$

Table 5.3 Values of k_{solv} and predicted dissolution rate constants for selected ortho-, ino-, and phyllosilicates using Eq. (17)

		logk_H[b] (mol silicate m^{-2}s^{-1})							
		Ortho-[c]		**single-chain[d]**		**double-chain[e]**		**Phyllo-silicates**	
M	**log k_{solv}[a] (s^{-1})**	pred-icted	meas-ured	pred-icted	meas-ured	pred-icted	meas-ured	pred-icted	meas-ured
Ca	8.5	−3.3	−3.5	−7.7	−7.8	−6.0			
Mn	7.6	−4.4	−4.2	−8.7	−9.0	−10.1			
Zn	7.5	−4.5		−8.9		−10.2			
Fe	6.5	−5.7	−6.0	−10.1		−11.4			
Co	6.4	−5.8	−6.4	−10.2		−11.5			
Mg	5.2	−7.2	−7.3	−11.6	−8.6	−13.0	−11.8	−9.2	−9.9[f]
	5.2				−9.3	−13.0	−12.2	−13.6	−12.5[g]
Ni	4.4	−8.2		−12.6		−14.0			
Be	3.5	−9.3		−13.6		−15.1			
CaMg	6.8	−5.3	−4.8	−9.6	−9.4	−11.0			
					−10.5				

Values listed are log rates of ortho- and inosilicate hypothetical end-members. Some end-members may not exist in nature. Rate constants for mixed composition silicates can be calculated as weighted averages of log rate constants of the end members. Rate equation is expressed: $k_H = 10^{13.51\log(0.5X/Si)+1.22\log ksolv-13.6}/\nu_{Si}$

[a] Data from literature compilation (Hewkin and Prince, 1970).

[b] Log rate constant at 25° C fit to Eq. 9 for "measured" or "predicted" from rate Eq. (17). See Table 5.2 for data sources for measured values of ino- and phyllosilicates.

[c] Orthosilicates of composition M_2SiO_4. Data from published rates (Casey and Westrich, 1992; Westrich et al., 1993) or from Chap. 6.

[d] Single-chain inosilicates of composition $M_2Si_2O_6$. Data summarized in Table 5.2 for measured rates (Ferruzzi, 1993; Knauss et al., 1993; Xie, 1994; Banfield et al., 1995; Chen and Brantley, 1998; Weissbart and Rimstidt, 2000; Oelkers and Schott, 2001). Multiple measured rates are summarized for some phases (see Table 5.2).

[e] Double-chain inosilicates of composition $M_7Si_8O_{22}(OH)_2$. Data for measured rates (Mast and Drever, 1987; Chen and Brantley, 1998). More than one measured rate is summarized for anthophyllite (see Table 5.2).

[f] Chrysotile of composition $Mg_3Si_2O_5(OH)_4$ (Bales and Morgan, 1985).

[g] Talc of composition $Mg_3Si_4O_{10}(OH)_2$. Rate was assumed to be constant with pH (Lin and Clemency, 1981; Nagy, 1995).

where k_H is the rate constant at 25° C for the rate model expressed in Eq. (5.9) (in mol silicate m^{-2} s^{-1}), and ν_{Si} is the number of Si in the mineral formula, e.g., $\nu_{Si} = 2$ for pyroxene and 8 for amphibole (Brantley, 2004).

This predictive equation estimates silicate dissolution accurately (Table 5.3) for many minerals but not all. Where discrepancies exist (e.g., Eq. (5.17) predicts that k_H (enstatite) $< k_H$ (diopside) but the data compiled in Table 5.3 shows the opposite), more experimental measurements are needed. Correlations such as those shown in Fig. 5.10a and 5.10b and others summarized in the literature (Sverjensky, 1992) should become increasingly useful to cull data for artifacts, to understand anomalous mineral dissolution behavior, or to predict dissolution behavior for minerals for which no data has been measured.

As discussed in Sect. 5.2.2.2, no well established theory is available to predict the pH dependence of dissolution rate as a function of structure or composition. The literature data for ortho-, soro-, ino- and phyllosilicate dissolution at 25° C bracket the value of n in Eq. (5.9) between 0 and 0.6 at 25° C (Table 5.4). Data in this table are derived from experiments of duration longer than a month except for forsterite and wollastonite. Some of the variability in n might be better explained if the dependence upon cation concentrations using Eq. (5.11) were taken into account (Oelkers, 2001b).

5.3.4 Carbonates

One composite rate equation can be used to describe the rates of calcite dissolution based upon the three reactions summarized in Sect. 5.2.1.1. Reactions given by Eqs. (5.3)–(5.5) are assumed to occur in parallel with the back-reaction, summing to r_{net}, the net rate of dissolution minus precipitation (Plummer et al., 1978):

$$r_{net} = k_1 a_{H^+} + k_2 a_{H_2CO_3^*} + k_3 a_{H_2O} - k_4 a_{Ca^{2+}} a_{HCO_3^-} \tag{5.18}$$

Here k_1, k_2, k_3 are rate constants for reactions given by Eqs. (5.3)–(5.5), and k_4 represents the rate constant for the precipitation of calcite. The values for these rate constants (mmol $cm^{-2} s^{-1}$) can be described as a function of temperature, T (K):

$$\log k_1 = 0.198 - 444/T \tag{5.19}$$

$$\log k_2 = 2.84 - 2177/T \tag{5.20}$$

$$\log k_3 = -1.10 - 1737/T \tag{5.21}$$

The rate constant for the precipitation reaction is described by

$$k_4 = \frac{K_2}{K_c}\left(k_1{}' + \frac{1}{a_{H^+_{(s)}}}\right)\left(k_2 a_{H_2CO^*_{3(s)}} + k_3 a_{H_2O}\right) \tag{5.22}$$

Here, K_2 is the equilibrium constant for dissociation of bicarbonate, K_c is the solubility product constant for calcite, k_1' is a modified rate constant for reaction given by Eq. (5.3), and the subscript (s) refers to concentrations in the surface adsorption layer. Importantly, as noted earlier, even under ambient conditions, calcite dissolution is fast and can become transport-controlled (Sect. 5.2.1). The low activation energy for reaction (5.3) is consistent with transport control for low pH dissolution. Eqs. (5.19) and (5.20) successfully describe dissolution over the temperature range 5–48° C, while Eq. (5.21) only describes dissolution from 25 to 48° C. At higher temperatures, different mechanisms may become important or the rate-limiting step may change. Such equations have been used by other workers to describe dolomite as well as calcite dissolution (Busenberg and Plummer, 1982; Chou et al., 1989).

Table 5.4 pH dependence for selected non-framework silicates as a function of temperature (pH < 7)

Phase	n	Run duration	Solution	Reference
Orthosilicates	0.5[a]			
forsterite	0.48 (25° C) 0.47 (35° C) 0.53 (45° C)	5000–25000 min	$HNO_3 + H_2O$	Rosso and Rimstidt, 2000
forsterite	0.49 (25° C) 0.70 (65° C)			Blum and Lasaga, 1988; Wogelius and Walther, 1991; Chen and Brantley, 2000
Sorosilicates	0.2[a]			
epidote	0.20 (90° C)			Rose, 1991
epidote	0.15 to 0.62 (25° C)	1000–4700 h	$H_2O \pm H_2SO_4 \pm HCl$	Kalinowski et al., 1998
Single chain silicates	0.2[a]			
enstatite	0.25	1500–2000 h	0.1 M buffer solutions	Ferruzzi, 1993
enstatite	0.24 (25° C) 0.24 (50° C) 0.23 (150° C)		0.0001 m Mg, 0.01 m ionic strength	Oelkers and Gislason, 2001
diopside[b]	0.2 (25, 70, 90° C)	40–60 days	buffer solutions pH 2–10	Knauss et al., 1993
diopside[c]	0.19 (25° C) 0.76 (90° C)	3400 h	HCl-H_2O	Chen and Brantley, 1998
wollastonite	0.24	80–220 h	$HCl \pm H_2O \pm KCl$	Xie, 1994; Xie and Walther, 1994
rhodonite/pyrox-manganite and synthetic rhodonite	0.27	2000–3500 h	buffer solutions	Banfield et al., 1995

Table 5.4 (*Continued*)

Phase	*n*	Run duration	Solution	Reference
Double chain silicates	0.2 (w/o Fe)[a] 0.4 (w/Fe)[a]			
anthophyllite[b]	0	1000–2000 h	$HCl + H_2O$	Mast and Drever, 1987
anthophyllite[c]	0.24 (25° C) 0.63 (90° C)	3400 h	$HCl + H_2O$	Chen and Brantley, 1998
hornblende	0.47 (25° C)			Frogner and Schweda, 1998
hornblende	0.4 (25° C)	1 year	$HCl\text{-}H_2O$	Givens and Brantley, unpub.
Phyllosilicates	0.14[a]			
muscovite	0.14 (25° C)	3000 h	$H_2SO_4 + HCl + H_2O$	Kalinowski and Schweda, 1996
muscovite	0.37 (70° C)		buffer solutions	Knauss and Wolery, 1989

[a] Suggested value for groups of silicates at 25° C.
[b] Indicates normalized by initial surface area.
[c] Indicates normalized by final surface area.

5.4 Temperature Dependence

5.4.1 Activation Energy

Extrapolation of the rate constant for dissolution to other temperatures, k_H(T), can be accomplished with the Arrhenius equation as described in Chap. 1:

$$k_H(T) = k_H(T_o)e^{-(Ea/RT)} \tag{5.23}$$

where $k_H(\mathrm{T_o})$ (mol mineral $\mathrm{m^{-2}\,s^{-1}}$) is the temperature-independent pre-exponential factor, $\mathrm{E_a}$ is the apparent activation energy, R is the gas constant, and T is absolute temperature.

Interestingly, the measured activation energies for silicate dissolution do not show a discernible pattern as a function of the connectedness of the mineral except perhaps for minerals of connectedness $\leq$2.5 (Fig. 5.10c). Given that dissolution of a silicate requires depolymerization of the Si from the lattice as depicted in Fig. 5.7, we might have expected more highly polymerized minerals to have higher activation energies than less polymerized minerals. For example, *ab initio* calculations suggest that the activation energy of hydrolysis of a Si-$\mathrm{O_{br}}$ bond (where the subscript refers to a bridging bond) decreases with decreasing connectedness of the Si atom. Such values are plotted in Fig. 5.10c (asterisks) for clusters that were assumed to experience no relaxation of the molecular geometry at the mineral surface as a function of lowered connectedness (see Chap. 2). These values decrease from 49 kcal $\mathrm{mol^{-1}}$ (connectedness of 4) to 33 (3) to 22 (2) to 17 (1) (Pelmenschikov et al., 2000., 2001). If the cluster is allowed to relax structurally, as it might if the Si atom were found at the mineral surface (see also Chap. 2), the calculated $\mathrm{E_a}$ decreases by several kcal/mol, as shown for a $\mathrm{Q^3}$ Si on Fig. 5.10c, but the calculated value is still much larger than the experimental values (Criscenti et al., 2006). Only the experimental values of $\mathrm{E_a}$ for minerals with connectedness $\leq$2 on Fig. 5.10c are roughly consistent with the calculated values for clusters of appropriate connectedness.

We infer from these observations that the connectedness of the Si atom in the precursor molecule for silicate dissolution is most likely $\leq$2 for all silicates regardless of connectedness (Fig. 5.10c). If $\mathrm{Q^3}$, $\mathrm{Q^2}$, and $\mathrm{Q^1}$ sites (where $\mathrm{Q^}i$ refers to tetrahedrally coordinated atoms surrounded by *i* bridging oxygens) are conceptualized as perfect surface, step, and adatom sites respectively (see also Fig. 3.7), then this conclusion suggests that the rate-limiting step of silicate dissolution is consistent with step retreat or removal of adatoms (hydrolysis of $\mathrm{Q^2}$ or $\mathrm{Q^1}$ sites respectively) rather than pit nucleation on perfect surface (see Sects. 5.2.1.2 and 5.5.2). For example, for biotite and other sheet silicates, edge sites rather than basal sites often control the overall dissolution rate under acid conditions (Kalinowski and Schweda, 1996). These conclusions are also consistent with the published prediction from the 1980s of an average activation energy for mineral oxide dissolution of 13 kcal $\mathrm{mol^{-1}}$ (Wood and Walther, 1983).

5.4.2 Solution Chemistry and Temperature Dependence

The activation energy describes how the rate constant changes with temperature for a given dissolution mechanism. If the rate-limiting step of dissolution changes with temperature, then the form of the rate equation, including the reaction order, might change as well as the rate constant. For example, as mentioned earlier, Eqs. (5.19)–(5.21) have been used to predict calcite dissolution successfully, suggesting that the rate-limiting mechanism is unchanged within the interval $25 < T < 48^{\circ}C$. Outside of this interval, however, it is impossible to know whether the rate equations are still valid. Commonly, as temperature is increased, a reaction may change from interface-limited at low temperature to transport-limited at high temperature because the activation energy of interface reactions is generally larger than the activation energy of transport (Fig. 5.11).

One complicating factor in predicting mineral dissolution rates versus temperature lies in the fact that, in addition to a temperature-dependent rate constant, the

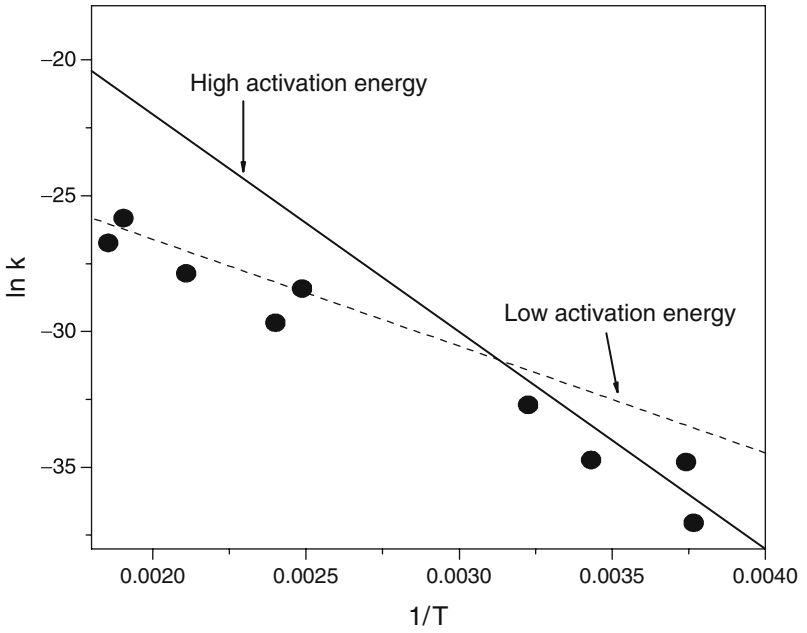

Fig. 5.11 Schematic Arrhenius plot demonstrating how the rate-limiting step generally changes with temperature. For a reaction mechanism with consecutive steps operating at low temperature (T), the step with the high activation energy (steeper slope on this plot) is typically rate-limiting (e.g., solid line), while at high T, the rate-limiting step often changes to the step with the lower activation energy (e.g., dashed line). For example, the activation energy of the mineral interface reaction ($\sim$15 kcal/mol) is often higher than the activation energy of diffusion ($\sim$5 kcal/mol): therefore, at low temperature, mineral dissolution is often interface-limited, but at high temperature, reactions are often transport-limited. Where the two rate constants are similar, the reaction exhibits mixed control.

orders of dissolution with respect to $H^+(n)$ and OH^- (m) are often temperature-dependent (Table 5.4). Given that the ΔH of sorption of protons onto surfaces is negative, an increase in temperature will result in an increase in n in Eq. (5.9) for pH < pH_{ppzc} (Brady and Walther, 1992; Casey and Sposito, 1992). However, both increased values of n (Carroll and Walther, 1990; Chen and Brantley, 1998) and insignificant changes in n have been observed as a function of temperature for various silicates (Casey and Cheney, 1993; Hellmann, 1994; Chen and Brantley, 1997, 2000; Rosso and Rimstidt, 2000). The variation of n in describing silicate dissolution has generally been neglected entirely or modeled as linearly dependent on temperature (Kump et al., 2000).

Where n varies with temperature, a pH-dependent (apparent) activation energy, E_a', has been reported by investigators who plot ln (*rate*) (instead of log (*rate constant*) versus 1/T and calculate the activation energy. This E_a' is valid only at the pH of measurement. A pH-independent value for E_a can be determined from a plot of ln (k_H) versus 1/T (Chen and Brantley, 1998). Where n is independent of temperature, $E_a' = E_a$. Arrhenius activation energies for mineral dissolution are theoretically predicted to be lowest at pH values near the pH_{ppzc} (Casey and Sposito, 1992; Casey and Cheney, 1993).

The temperature dependence of cation back-reactions must also be understood to predict dissolution rates (Fig. 5.8, top). For example, the inhibitory effect of aqueous Al on dissolution of albite could increase with increasing temperature due to the enhanced adsorption of cations onto surfaces with increasing temperature (Machesky, 1989; Chen and Brantley, 1997). In general, the effect of dissolved Al on the dissolution rate of aluminosilicates is not well understood as a function of temperature (Oelkers, 2001a).

5.5 Chemical Affinity

5.5.1 Linear Rate Laws

The driving force for reaction, ΔG, controls whether a mineral dissolves or precipitates under a given set of conditions. For example, as described in Chap. 1 for albite dissolution,

$$NaAlSi_3O_{8(s)} + 4H_2O_{(aq)} + 4H^+_{(aq)} \rightarrow Na^+_{(aq)} + Al^{3+}_{(aq)} + 3H_4SiO_{4(aq)} \qquad (5.24)$$

ΔG is defined as

$$\Delta G = RT\,ln(\Omega) \qquad (5.25)$$

where Ω is the ratio of the reaction activity quotient, $Q(= a_{Na^+} a_{Al^{3+}} a^3_{H_4SiO_4} / a^4_{H^+})$ and the equilibrium constant, K_{eq}, for the reaction at the specified temperature and pressure ($\Omega = Q/K_{eq}$). The chemical affinity of the reaction, defined as equal to -ΔG, equals 0 at equilibrium. Note that the sign of ΔG depends on which direction the chemical reaction is written (e.g. Eqn. 5.24). In this chapter we have strictly

Table 5.5 pH-independent E_a for dissolution of selected minerals far from equilibrium

Phase	E_a (kcal/mol)	Temperatures (°C)	Reference
Carbonates			
calcite	2	5–48	Eq. (11), Plummer et al., 1978
calcite	10	5–48	Eq. (12), Plummer et al., 1978
calcite	8	25–48	Eq. (13), Plummer et al., 1978
Orthosilicates			
tephroite	22	25–45	Casey et al., 1993
monticellite	17	25–45	Westrich et al., 1993
forsterite	16	25–65	Palandri and Kharaka, 2004
kyanite	13	108–194	Palandri and Kharaka, 2004
Sorosilicates			
Epidote	17	25–90	Palandri and Kharaka, 2004
Pyroxenes			
enstatite	12	28–168	Oelkers and Gislason, 2001, Ea measured at pH 2
enstatite	19	not given	Schott and Berner, 1985 (refit by Palandri and Kharaka, 2004)
diopside	23	25–90	Chen and Brantley, 1998 (fit with a temperature-dependent n)
diopside	23	not given	Palandri and Kharaka, 2004
Amphiboles			
anthophyllite	19	25–90	Chen and Brantley, 1998 (fit with a temperature-dependent n)
anthophyllite	12	25–90	Chen and Brantley, 1998 (refit with a temperature-independent n by Palandri and Kharaka (2004))
Phyllosilicates			
kaolinite	16		Palandri and Kharaka, 2004
montmorillonit	11		Palandri and Kharaka, 2004
Tectosilicates (see also Table 5.1)			
am. silica	18	25–250	Rimstidt and Barnes, 1980; Mazer and Walther, 1994; Icenhower and Dove, 2000
quartz[a]	16–18	25–300	Rimstidt and Barnes, 1980
quartz[a]	21	25–625	Tester et al., 1994
quartz[a]	19	100–300	Polster, 1994
quartz[a]	17	175–290	Dove, 1999

[a] Data only compiled for dissolution in distilled deionized water.

discussed rates measured far-from-equilibrium, except for the cases of amorphous silica (Eq. (5.15)) and calcite (Eq. (5.18)). Dissolution rates for both carbonates and silicates are described below as a function of chemical affinity.

Transition state theory (TST) is generally considered to be appropriate only for elementary reactions. However, if a complex mechanism is rate-limited by a single elementary reaction, then TST may be usefully applied to the overall reaction. In that regard, TST suggests that the forward rate minus the reverse rate, r_{net} (Lasaga, 1981; Aagaard and Helgeson, 1982; Lasaga, 1984), is linear with respect to ΔG near equilibrium according to the following equation with $n_1 = 1$:

$$r_{net} = -k_+ \Pi a_j^{m_j} \left(1 - \exp\left(\frac{n_1 \Delta G}{RT}\right)\right) \tag{5.26}$$

Here k_+ is the rate constant for the forward rate, a_j is the activity of species j in the rate-determining reaction, m_j and n_1 are constants, R is the gas constant, and T is the absolute temperature. The sign of r_{net} varies depending upon which direction the reaction is written. Explicitly, this rate expression with $n_1 = 1$ is derived for a reaction such as that given in Eq. (5.24) by i) writing the forward and reverse reactions, ii) assuming these are elementary reactions, iii) writing the rates of the forward and reverse reactions, and iv) calculating the net rate = forward – reverse rate. For a positive r_{net}, a reaction such as that given by Eq. (5.24) proceeds forward as written, and for a negative value, the reaction proceeds in reverse. In some treatments, the ΔG term is also divided by Temkin's average stoichiometric number, a constant that refers to the relative rate of destruction of the activated complex divided by the overall dissolution rate (Oelkers et al., 1994; Oelkers, 2001b). The reader is referred to several discussions in the literature of this equation with respect to transition state theory and irreversible kinetics (Alekseyev et al., 1997; Lasaga, 1995; Lichtner, 1998; Oelkers, 2001a; Hellmann and Tisserand, 2006).

Rate Eq. (5.26) with $n_1 = 1$ has been used successfully to predict net dissolution and precipitation of silica phases including quartz over a wide range in temperature and pressure (Rimstidt and Barnes, 1980; Dove, 1995). For example, Eq. (5.15) (Sect. 5.3.1) has been used for amorphous silica (note that $\Omega = \exp(\Delta G/RT)$). Rate expressions of this form with $n_1 = 0.5$ or 1 have also been used to describe calcite precipitation (Nancollas and Reddy, 1971; Reddy and Nancollas, 1971; Sjoberg, 1976; Kazmierczak et al., 1982; Rickard and Sjoberg, 1983; Sjoberg and Rickard, 1983; Shiraki and Brantley, 1995). A rate equation for dissolution that is linearly proportional to ΔG near equilibrium as described by Eq. (5.26) with $n_1 = 1$ is consistent with a mechanism rate-limited by sorption at the mineral surface (Nielsen, 1983; Shiraki and Brantley, 1995). Other mechanisms could also be consistent with such a rate law.

5.5.2 Non-Linear Rate Laws

Many minerals show dissolution and growth behavior that cannot be fit by equations such as Eq. (5.26) that are linear in ΔG near equilibrium (Fig. 5.12). For example,

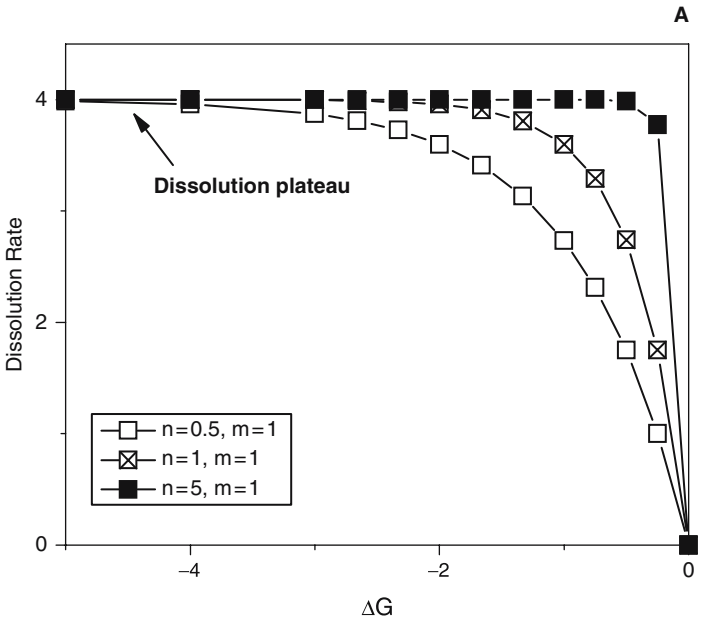

Fig. 5.12 (**A**) (**B**) Schematic diagrams depicting the dissolution rate of a phase as a function of ΔG (arbitrary units) based upon Eqs. (5.29) or (5.30). The legend indicates how the function changes with n_1 and m_1 (written on the figures as n or m for simplicity). Note that when $m_1 = 1$ as predicted by transition state theory (**A**), the predicted curves are not sigmoidal, but when m_1 does not equal 1 dissolution becomes a sigmoidal function of ΔG (**B**). Dissolution rates of many phases (e.g., albite shown in (**C**)) exhibit sigmoidal behavior. In (**C**), rate of albite dissolution was determined by averaging the release rate of Si, Al, and Na after correction for stoichiometry (Hellmann and Tisserand (2006)). A curve based on transition state theory (e.g., Eq. (5.26)) is shown by the dashed line while a sigmoidal curve that fits the data better is shown as the solid line. According to the authors, the sigmoidal curve is based upon a rate law such as Eq. (5.31), but a reasonable fit was also produced from an equation such as Eq. (5.29). As shown in (**a**) and (**b**), the sigmoidal behavior of the rate law increases as the exponent m_1 in rate law 29 increases. (Figure (**c**) reprinted from Hellmann and Tisserand 2006. With permission from Elsevier).

the following rate model that is nonlinear in ΔG describes calcite dissolution under some conditions (Morse, 1978):

$$r_{net} = k(1-\Omega)^{m_1} \tag{5.27}$$

Rewriting this equation using $\Omega = \exp(\Delta G/RT)$ yields:

$$r_{net} = \pm k\left(\left|1-\exp\left(\frac{\Delta G}{RT}\right)\right|\right)^{m_1} \tag{5.28}$$

For small ΔG, such a rate equation predicts that the net rate varies as ΔG^{m_1}. Nonlinear rate laws such as Eqs. (5.27) and (5.28) ($m_1 \neq 1$), often considered useful to describe reactions controlled by crystal defects (Lasaga and Kirkpatrick, 1981), have been used to model dissolution and growth of kaolinite (Nagy et al., 1990,

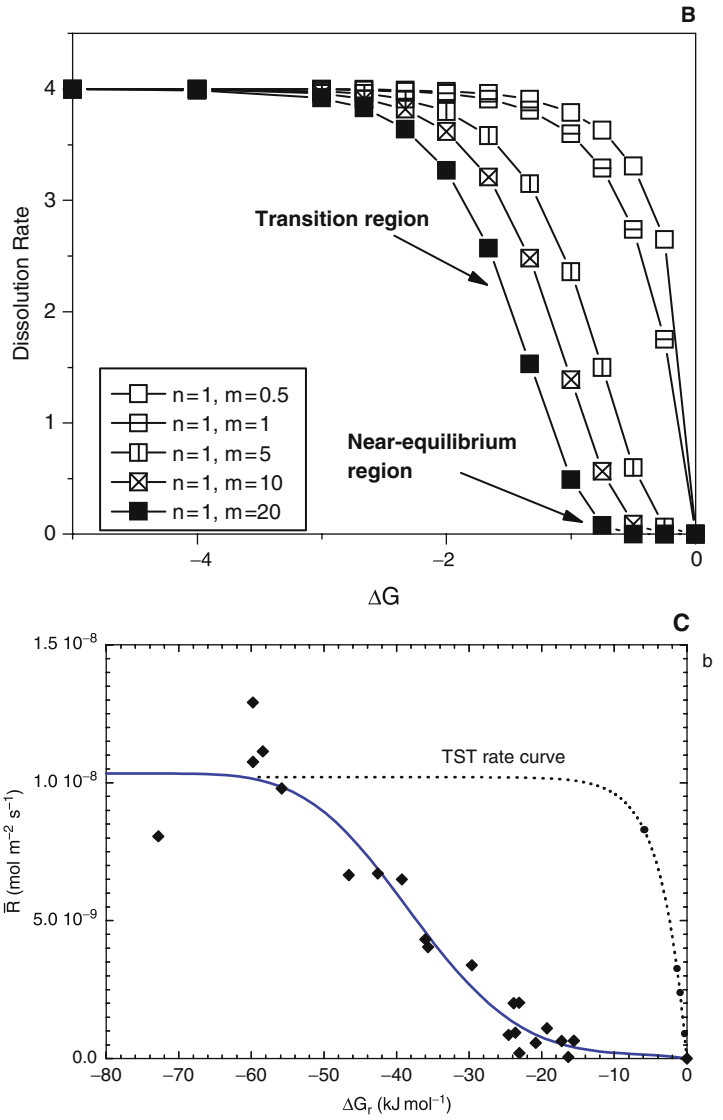

Fig. 5.12 (*Continued*)

1991), gibbsite (Nagy and Lasaga, 1992), quartz (Berger et al., 1994), and analcime (Murphy et al., 1992).

Many researchers have attempted to explain values of m_1 in terms of mechanisms of dissolution or precipitation. For example, spiral growth at screw dislocations is often well-described by rate Eq. (5.28) with $m_1 = 2$ (Burton et al., 1951; Blum and Lasaga, 1987; Teng et al., 2000). However, attribution of a mechanism on the basis of the value of this exponent is generally not defensible without further observations.

Rate equations that include two exponents n_1 and m_1 have been used to describe precipitation of calcite (Inskeep and Bloom, 1985):

$$r_{net} = k\left(\exp\left(\frac{n_1 \Delta G}{RT}\right) - 1\right)^{m_1} \tag{5.29}$$

Equation (5.29) is equivalent to

$$r_{net} = k\left(\Omega^{n_1} - 1\right)^{m_1} \tag{5.30}$$

As written, $r_{net} > 0$ refers to precipitation and $r_{net} < 0$ refers to dissolution. (Compare Figure 5.12 where r_{net} for dissolution is plotted as a positive value).

One of the first examples of the use of a form of Eq. (5.29) for silicate dissolution was the treatment of albite dissolved at 80° C near *pH* 8.8 (Burch et al., 1993):

$$r = k_5[1 - \exp\left(-\left(\frac{n_1\,|\Delta G|}{RT}\right)^{m_1}\right) + k_6[1 - \exp\left(-\left(\frac{|\Delta G|}{RT}\right)^{m_2}\right) \tag{5.31}$$

where k_5 and k_6 are rate constants, and n_1, m_1 and m_2 are fitting parameters. This equation contained two rate terms to describe two parallel reactions and was used because the rate of albite dissolution varies sigmoidally as a function of ΔG. Far from equilibrium, Burch et al. pointed out that the rate reaches a constant or "dissolution plateau". As the dissolution rate decreases to zero as the driving force decreases, an inflection point occurs in the rate-ΔG function. Similarly, it has been shown that albite dissolution at 150° C and pH 9.2 is well fit by an equation like Eq. (5.31) (Fig. 5.12c). Consistent with arguments described in Sect. 5.2.1.2, Burch et al. argued that the rate decreased sharply below the dissolution plateau when etch pits stopped nucleating at dislocation outcrops at the mineral surface: this occurs at the critical saturation index of etch pit nucleation at dislocations, Ω_{crit}, as described in Eq. (5.8). Closer to equilibrium, etch pits do not open even at dislocation outcrops (Brantley et al., 1986a, b; Blum and Lasaga, 1987; Lasaga and Luttge, 2001). For these smaller values of undersaturation ($\Omega_{\text{crit}} < \Omega < 1$), dissolution occurs by step retreat without nucleation of pits.

A sigmoidal function of dissolution versus ΔG was also observed for labradorite dissolved in column reactors with inlet pH ∼ 3 under ambient conditions (Taylor et al., 2000a). Similar to the work of Burch et al., far-from-equilibrium dissolution ($\Delta G < -42\,\text{kJ/mol}$) was attributed to defect-driven etch pit formation during labradorite dissolution. Using equations such as Eqs. (5.7) and (5.8), Taylor et al. calculated the critical value of ΔG for etch pit nucleation on labradorite, ΔG_{crit}, to lie between −26 and $-11\,\text{kJ/mol}$, roughly in agreement with the transition they observed between the dissolution plateau and the affinity-dependent region. Taylor et al. calculated the following expression for r_{net} as a function of ΔG in the column reactors using inverse modelling:

$$r = -k_{\min}\left\{0.76\left[1 - \exp\left(-1.3x10^{-17}\left(\frac{\Delta G}{RT}\right)^{14}\right)\right]\right.$$
$$\left. -0.24\left[1 - \exp\left(\frac{-0.35\,|\Delta G|}{RT}\right)\right]\right\} \tag{5.32}$$

where k_{min} is the far-from-equilibrium rate constant. The two terms in Eqs. (5.31) and (5.32) have been interpreted as describing the parallel reactions of etch pit-driven dissolution and non-pit related surface retreat of the mineral surface (see Chap. 3 and Sect. 5.2.1.2).

Although Burch et al. and Taylor et al. both used functions describing parallel reaction steps, rate Eq. (5.29) can also be used to describe sigmoidal rate behavior as shown in Fig. 5.12c (Hellmann and Tisserand, 2006). In contrast, the more simple linear equation given by Eq. (5.26) cannot predict the sigmoidal rate-ΔG behavior (Fig. 5.12a): for values of $m_1 = 1$, a plot of dissolution rate (plotted as a positive value) versus ΔG is everywhere concave down and shows no inflection point. As m_1 increases but n_1 remains constant in Eq. (5.29), however, the rate becomes a sigmoidal function of ΔG with both concave and convex regions (Fig. 5.12b). Both nonsigmoidal (Gautier et al., 1994; Oelkers et al., 1994; Devidal et al., 1997; Oelkers and Schott, 1999; Dove et al., 2005) and sigmoidal (Burch et al., 1993; Berger et al., 1994; Alekseyev et al., 1997; Taylor et al., 2000a) functions for rate versus ΔG have been observed for mineral reactions. As exemplified in Fig. 5.12c, some researchers have referred to these two types of behavior as either consistent with TST (nonsigmoidal) or not consistent with TST (sigmoidal).

Researchers point to various lines of evidence in explaining why sigmoidal and nonsigmoidal functionalities are observed. For example, samples of albite dissolved hydrothermally reveal that log (rate) versus ΔG is sigmoidal when measured on cleaved, untreated samples (Beig and Luttge, 2006). These workers observed very slow dissolution near equilibrium which they attributed to the lack of formation of dislocation etch pits. When crystals were pre-dissolved under conditions where etch pits formed and then were dissolved close to equilibrium, however, the observed rate of near-equilibrium dissolution was faster than observed for the untreated samples due to transient dissolution of the pre-existing etch pits. They further suggested that nonsigmoidal rate dependences described by other researchers could be attributed to the pre-etching of samples as experiments were started up far-from-equilibrium. As also described in Chap. 3, these researchers emphasize the importance of so-called *dissolution stepwaves* generated by etch pits and have proposed a generalized model to describe sigmoidal functions of rate versus ΔG (Lasaga and Luttge, 2001).

It is important to remember that all such rate laws, including Eqs. (5.26) and (5.28) represent complex reaction mechanisms for composite reactions. Since extrapolation of a rate from one system to another is only strictly guaranteed for an elementary reaction, the extrapolation of these rate models to new conditions is problematic (see Chap. 1). For example, both Eqs. (5.26) and (5.28) were unsuccessful in extrapolating calcite growth to conditions of undersaturation, and different versions of Eqs. (5.26) and (5.30) were needed for different conditions of solution chemistry (Shiraki and Brantley, 1995; Teng et al., 2000). The presence of low concentrations of aqueous ions was also observed to affect the mechanism of calcite growth and the value of exponents in these equations (Davis et al., 2000). Indeed, it is impossible to predict reaction rates of calcite over the full range of ΔG with one rate equation; rather, a family of such curves is needed to describe dissolution and precipitation as a function of the relevant variables such as pH, P_{CO_2}, total inorganic

carbon, and impurity concentration (Shiraki and Brantley, 1995). Use of equations like Eq. (5.18) that incorporate individual reaction steps may be more successful in extrapolating rates across conditions than equations such as Eq. (5.26) or Eq. (5.30) (Shiraki and Brantley, 1995).

Recently, models have been developed (Dove et al., 2005) that predict the rate of dissolution over a range of undersaturation by incorporating homogeneous, impurity pit, and dislocation pit nucleation (see Sect. 5.2.1.2). This work emphasizes that the surface normal retreat rate of a crystal, r_n, is affected by the step spacing, Γ, the step height, h, and the horizontal retreat rate of a moving step, v:

$$r_n = \frac{hv}{\Gamma} \tag{5.33}$$

The step density is controlled by the presence of pre-existing pits, or by the nucleation of dislocation etch pits, impurity etch pits, and vacancy islands. The step retreat rate can be calculated as a function of ω (the molecular volume), β (kinetic coefficient for the step), and the equilibrium constant K_{eq} to document that step retreat is a simple linear function of ΔG:

$$v = \omega\beta K_{eq}(\Omega - 1) \tag{5.34}$$

Thus near-equilibrium dissolution without pit nucleation can be discussed in the context of Eqs. (5.33)–(5.34). When 2D nucleation occurs (pitting), then the retreat rate of the crystal is a function of the step retreat rate and the pit nucleation rate J:

$$r_n = hv^{1/3}J^{2/3} \tag{5.35}$$

Equations such as (5.7) and (5.8) were used by Dove et al. with Eqs. (5.33)–(5.35) and expressions for the pit nucleation rates to derive rate dependencies for the different dissolution regimes. With this derivation, the nucleation rate is expected to show a complex dependence upon Ω, and when all the terms are summed, a rate versus ΔG function is derived that fits rate data for dissolution of quartz, kaolinite, and potassium feldspar (other researchers have also applied the model to diopside (Dixit and Carroll, 2007). Dove et al. also provided direct microscopic evidence to support the hypothesis that dissolution within the dissolution plateau is characterized by formation of all sorts of etch pits while the slower dissolution rates observed closer to equilibrium are characterized by a lack of dislocation etch pitting. The model allows prediction of the transition from homogeneous nucleation to defect-driven etching based on parameters such as the mineral-water interfacial energy and step energy and also provides some understanding for how salt affects dissolution of silicates. Such a model may be more successful in rate extrapolations than the generic rate Eq. (5.29) that is currently used in many reactive transport models. However, the model may also need more fit parameters to be useful.

5.5.2.1 Aluminum Inhibition and Affinity

As we have previously discussed, the presence of aqueous Al^{3+} has been observed to decelerate dissolution of aluminosilicates (Chou and Wollast, 1984, 1985; Gautier et al., 1994; Oelkers et al., 1994; Chen and Brantley, 1997). This effect has been ascribed to Al-inhibition (see Sect. 5.2.2.3), decreased chemical affinity, or both. For example, the decrease in dissolution rate of albite in the presence of dissolved aluminum was attributed to increasing adsorption of the trivalent cation with increasing temperature (Chen and Brantley, 1997). One way to distinguish affinity effects from inhibition effects are isotach plots: these plots of constant rate contoured on activity-activity diagrams have been used to determine the relative importance of ΔG and $a_{Al(aq)}$ during albite and K-feldspar dissolution respectively (Burch et al., 1993; Gautier et al., 1994).

Both the effect of aluminium inhibition and chemical affinity have been used in the cation exchange model for aluminosilicate dissolution described earlier with Eq. (5.11). Model Eq. (5.11) attributes the inhibitory effect of Al^{3+} on dissolution of some aluminosilicates to back-reactions occurring at specific precursor surface sites. However, the dissolution rates of certain aluminosilicates dissolving at low pH may be best modeled by modifying Eq. (5.11) to incorporate *both* aqueous aluminum activity and chemical affinity (Oelkers et al., 1994; Schott and Oelkers, 1995):

$$r_{net} = k_+ \left(\frac{\left(\frac{a_{H+}^{3s}}{a_{Al^{3+}}^{s}} \right) \prod_i a_{A_i}^{\upsilon_i}}{1 + K_{Al} \left(\frac{a_{H+}^{3s}}{a_{Al^{3+}}^{s}} \right) \prod_i a_{A_i}^{\upsilon_i}} \right) \left(1 - \exp\left(\frac{\Delta G}{\nu_{Si} RT} \right) \right) \tag{5.36}$$

Here, ν_{Si} signifies the stoichiometric number of moles of *Si* in one mole of dissolving aluminosilicate and other variables are defined earlier for Eq. (5.11). Such a model may be generalized for minerals that dissolve both nonstoichiometrically or stoichiometrically by extending the concept of chemical affinity to describe minerals whose surface chemistry differs from the bulk (Oelkers, 2001a).

5.6 Conclusion

Our understanding of mineral dissolution kinetics has advanced significantly over the last several decades. The relative rates of mineral weathering in the laboratory are established for many minerals and some minerals such as quartz and calcite have been thoroughly investigated. Many minerals have been fit to simple models of dissolution for behavior as a function of pH. More complex rate models have also been parameterized for some minerals to incorporate pH, dissolved species, surface chemistry, surface topography, and chemical affinity. At present however, different classes of rate models are available and no generalized rate equation can be used to model mineral dissolution over the full range of geochemical conditions.

As theoretical molecular geochemistry elucidates mechanisms of dissolution of minerals, experimental dissolution rates can be tested against results of new spectroscopies to synthesize rate data into more useful rate models.

Datasets for activation energies of mineral dissolution are not as well-constrained as rate data under ambient conditions largely because less data exists for high-temperature dissolution of minerals. However, activation energies of dissolution for silicates generally vary between 10 and 25 $\mathrm{kcal\,mol^{-1}}$. Lack of reproducibility in activation energies measured for a given mineral are presumed to be related to differences in mineral preparation or chemistry, solution chemistry, or experimental protocol. Effort is needed in both the prediction and measurement of such activation energies.

Quantitative extrapolation of laboratory rates to field systems remains difficult due to multiple contributing factors related to concepts discussed in this chapter. Intrinsic factors related to differences in mineral samples prepared in the laboratory or weathered in the field contribute to the laboratory-field discrepancy. Perhaps the most important intrinsic factor is the reactive surface area of dissolving mineral. As of yet, no general theory or measurement protocol for reactive surface area has been advanced. In addition, laboratory rates are generally measured far from equilibrium while natural weathering often occurs closer to equilibrium especially at natural mineral-water interfaces where fluid flow rates may be very low (White, Chap. 7). Dissolution of laboratory samples may therefore be rate-limited by the interface reaction while dissolution in field systems may be at least partially rate-limited by transport. Modeling that accurately incorporates both reaction and transport is necessary to elucidate the complexities of mineral reaction kinetics across these scales.

Acknowledgements

SLB acknowledges A. White for discussions, A. Zimmerman for Fig. 5.4, J. Bandstra for Fig. 5.1, J. Moore for help on Fig. 5.12, and all the students of Penn State Geosciences 560. This chapter is based upon work supported by the Center for Environmental Kinetics Analysis funded by the National Science Foundation under Grant No. CHE-0431328 and the U.S. Department of Energy, Biological and Environmental Research (BER).

5.7 Glossary of Symbols

a	depth of a pit on dissolving crystal surface
a_i	activity of species i in solution
b	Burgers vector

E_a	activation energy
E'_a	apparent activation energy measured at a given pH value
h	step height on a crystal surface
$H_2CO_3^*$	$CO_{2(aq)} + H_2CO_{3(aq)}$
$[i]$	concentration of species i
J	pit nucleation rate on a crystal surface
k	rate constant
k_H	rate constant for proton-promoted dissolution
k_{H2O}	rate constant for dissolution in neutral pH
k_{min}	rate constant measured far from equilibrium for Eq. (5.32)
k_{OH}	rate constant for hydroxyl-promoted dissolution
k_{L_i}	rate constant for ligand-promoted dissolution
k_{SiOH}	rate constant for reaction at $\equiv$ SiOH
k_{SiO-}	rate constant for reaction at $\equiv$ SiO^- and $\equiv$ SiONa
k_{solv}	rate constant for water exchange around a cation in solution
k_1, k_2, k_3, k_4	rate constants in the mechanism of dissolution/precipitation of calcite
k_5, k_6	rate constants in the albite dissolution rate Eq. (5.31)
k'_1	modified rate constant for reaction given by Eq. (5.3)
k_+	forward rate constant
K_H^{ads}	equilibrium constant for proton adsorption (Eq. (5.12))
$K_{M_i}^{ads}$	equilibrium constant for cation adsorption (Eq. (5.12))
K_2	dissociation constant for bicarbonate
K_c	solubility product constant for calcite
K_i	equilibrium constant for cation-proton exchange (Eq. (5.21))
K_{eq}	equilibrium constant
L_i	ligand i
m	order with respect to a reactant in Eq. (5.9)
m_1, m_2	constants used in rate Eqs. (5.26)–(5.32)
m_j	order with respect to species in Eq. (5.26)
M_i	cation
O_{br}	bridging oxygen
n	order with respect to a reactant in Eq. (5.9)
n_1	constant in rate Eqs. (5.26), (5.29), (5.30)
pH_{ppzc}	pH of pristine point of zero charge
q_1, q_2, q_3	order with respect to surface species in Eqs. (5.10), (5.13)
q_A, q_B	charge on a species
Q^i	a tetrahedrally coordinated atom surrounded by i bridging oxygens
r	surface-area normalized rate of reaction
r'	dissolution rate in units of mol L^{-1} t^{-1}
r_n	surface normal retreat rate of a crystal
r_{net}	net rate of reaction (forward rate – backward rate)
R	gas constant
s	stoichiometric coefficient for precursor species (Eq. (5.11))
$\equiv S$	metal cation at a surface site on a mineral
$\equiv SL_i$	surface metal-ligand complex
$\equiv SO^-$	deprotonated surface hydroxyl
$\equiv SOH$	surface hydroxyl species
$\equiv SOH_2^+$	protonated surface hydroxyl
$\equiv SiOAl \equiv$	bridging oxygen linkage between Si and Al cations

$\equiv SiOSi \equiv$	bridging oxygen linkage between two Si cations
$\equiv SiONa$	surface silanol with adsorbed Na ion
t	time
T	Temperature
T_o	reference temperature
v	horizontal retreat rate of a moving step on a crystal surface
V	molar volume
X	number of cations in non-tetrahedral sites in a mineral structure
X/Si	ratio of cations in nontetrahedral sites to cations in tetrahedral sites
β	kinetic coefficient for the step on a crystal surface
ΔG	Gibbs free energy of reaction
$\Delta G_{dislocation}$	Gibbs free energy of dissolution at a dislocation outcrop
ΔG_{crit}	critical Gibbs free energy for formation of dislocation etch pits
ε	radius of cylindrical etch pit
ε_o	dislocation core radius
γ	crystal-water interfacial energy
Γ	step spacing on a crystal surface
$\theta_{\equiv SiOH}$	fraction of the silica surface covered by silanol groups
$\theta_{\equiv SiO^-_{tot}}$	sum of the fractions of total sites existing as deprotonated surface hydroxyls and as sites with adsorbed Na^+ on a silica surface
τ	energy factor for a dislocation
ν_i	stoichiometric coefficient for species i
ν_{Si}	number of Si in mineral formula in Eq. (5.17)
ω	molecular volume
Ω	ratio of activity quotient to equilibrium constant for a reaction

References

Aagaard P. and Helgeson H. C. (1982) Thermodynamic and kinetic constraints on reaction rates among minerals and aqueous solutions I. Theoretical considerations. *American Journal of Science* **282**, 237–285.

Alekseyev V. A., Medvedeva L. S., and Prisyagina N. I. (1993) Rates of Na-K exchange between alkali feldspars in aqueous solutions. *Geochemistry International* **30**, 120–134.

Alekseyev V. A., Medvedeva L. S., Prisyagina N. I., Meshalkin S. S., and Balabin A. (1997) Change in the dissolution rates of alkali feldspars as a result of secondary mineral precipitation and approach to equilibrium. *Geochimica et Cosmochimica Acta* **59**, 19–31.

Alkattan M., Oelkers E. H., Dandurand J.-L., and Schott J. (2002) An experimental study of calcite dissolution rates at acidic conditions and 25° C in the presence of $NaPO_3$ and $MgCl_2$. *Chemical Geology* **190**, 291–302.

Amrhein C. and Suarez D. L. (1988) The use of a surface complexation model to describe the kinetics of ligand-promoted dissolution of anorthite. *Geochimica et Cosmochimica Acta* **52**, 2785–2793.

Amrhein C. and Suarez D. L. (1992) Some factors affecting the dissolution kinetics of anorthite at 25° C. *Geochimica et Cosmochimica Acta* **56**, 1815–1826.

Bales R. C. and Morgan J. J. (1985) Dissolution kinetics of chrysotile at pH 7 to 10. *Geochimica et Cosmochimica Acta* **49**(11), 2281–2288.

Banfield J. F., Ferruzzi C. G., Casey W. H., and Westrich H. R. (1995) HRTEM study comparing naturally and experimentally weathered pyroxenoids. *Geochimica et Cosmochimica Acta* **59**(1), 19–31.

Banfield J. F. and Nealson K. H. (1997) *Geomicrobiology: Interactions Between Microbes and Minerals*. Mineralogical Society of America.

Beig M. and Luttge A. (2006) Albite dissolution kinetics as a function of distance from equilibrium: Implications for natural feldspar weathering. *Geochimica et Cosmochimica Acta* **70**, 1402–1420.

Bennett P. C. (1991) Quartz dissolution in organic-rich aqueous systems. *Geochimica et Cosmochimica Acta* **55**, 1781–1797.

Bennett P. C., Melcer M. E., Siegel D. I., and Hassett J. P. (1988) The dissolution of quartz in dilute aqueous solutions of organic acids at 25° C. *Geochimica et Cosmochimica Acta* **52**, 1521–1530.

Berg A. and Banwart S. A. (2000) Carbon dioxide mediated dissolution of Ca-feldspar: Implications for silicate weathering. *Chemical Geology* **163**, 25–42.

Berger G., Cadore E., Schott J., and Dove P. M. (1994) Dissolution rate of quartz in lead and sodium electrolyte solutions between 25 and 300° C: Effect of the nature of surface complexes and reaction affinity. *Geochimica et Cosmochimica Acta* **58**, 541–551.

Berner R. A. (1978) Rate control of mineral dissolution under earth surface conditions. *American Journal of Science* **278**(9), 1235–1252.

Biber M. V., Afonso M. D., and Stumm W. (1994) The coordination chemistry of weathering 4. Inhibition of the dissolution of oxide minerals. *Geochimica et Cosmochimica Acta* **58**(9), 1999–2010.

Blum A. E. and Lasaga A. C. (1987) Monte Carlo simulations of surface reaction rate laws. In *Aquatic Surface Chemistry: Chemical Processes at the Particle-Water Interface* (ed. W. Stumm), pp. 255–291. John Wiley & Sons, Inc.

Blum A. E. and Lasaga A. C. (1988) Role of surface speciation in the low-temperature dissolution of minerals. *Nature* **331**, 431–433.

Blum A. E. and Lasaga A. C. (1991) The role of surface speciation in the dissolution of albite. *Geochimica et Cosmochimica Acta* **55**, 2193–2201.

Blum A. E. and Stillings L. L. (1995) Feldspar dissolution kinetics. In *Chemical Weathering Rates of Silicate Minerals*, Vol. 31 (ed. A. F. White and S. L. Brantley), pp. 291–351. Mineralogical Society of America.

Brady P. V. (1991) The effect of silicate weathering on global temperature and atmospheric CO_2. *Journal of Geophysical Research* **96B**, 18101–18106.

Brady P. V. and Carroll S. A. (1994) Direct effects of CO_2 and temperature on silicate weathering: Possible implications for climate control. *Geochimica et Cosmochimica Acta* **58**, 1853–1856.

Brady P. V. and Walther J. V. (1992) Surface chemistry and silicate dissolution at elevated temperatures. *American Journal of Science* **292**, 639–658.

Brantley S. L. (2004) Reaction kinetics of primary rock-forming minerals under ambient conditions. In *Surface and Ground Water, Weathering, and Soils*, Vol. 5 (ed. J. I. Drever), pp. 73–118. Elsevier.

Brantley S. L. and Chen Y. (1995) Chemical weathering rates of pyroxenes and amphiboles. In *Chemical Weathering Rates of Silicate Minerals*, Vol. 31 (ed. A. F. White and S. L. Brantley), pp. 119–172. Mineralogical Society of America.

Brantley S. L., Crane S. R., Crerar D., Hellmann R., and Stallard R. (1986a) Dissolution at dislocation etch pits in quartz. *Geochimica et Cosmochimica Acta* **50**, 2349–2361.

Brantley S. L., Crane S. R., Crerar D. A., Hellmann R., and Stallard R. (1986b) Dislocation etch pits in quartz. In *Geochemical Processes at Mineral Surfaces* (ed. J. A. Davis and K. F. Hayes), pp. 635–649. American Chemical Society.

Brantley S. L., Ruebush S., Jang J.-H., and Tien M. (2006) Analysis of (Bio) geochemical kinetics of Fe III oxides. In *Methods for Study of Microbe-Mineral Interactions*, Vol. 14 (ed. P. A. Maurice and L. A. Warren), pp. 79–116. Clay Mineral Society.

Brantley S. L. and Stillings L. L. (1996) Feldspar dissolution at 25° C and low pH. *American Journal of Science* **296**, 101–127.

Brantley S. L. and Stillings L. L. (1997) Reply to comment: Feldspar dissolution at 25° C and low pH. *American Journal of Science* **297**, 1021–1032.

Bruno J., Stumm W., Wersin P., and Brandberg F. (1992) On the influence of carbonate in mineral dissolution. I. The thermodynamics and kinetics of hematite dissolution in bicarbonate solutions at T = 25° C. *Geochimica et Cosmochimica Acta* **56**, 1139–1147.

Burch T. E., Nagy K. L., and Lasaga A. C. (1993) Free energy dependence of albite dissolution kinetics at 80° C and pH 8.8. *Chemical Geology* **105**, 137–162.

Burton W. K., Cabrera N., and Frank F. C. (1951) The growth of crystals and the equilibrium structure of their surfaces. *Philosophical Transactions of the Royal Society of London* **243**, 299–358.

Busenberg E. and Plummer L. N. (1982) The kinetics of dissolution of dolomite in CO2 - H2O systems at 1.5 to 65° C and 0 to 1 atm $^{p}CO_2$. *American Journal of Science* **282**, 45–78.

Busenberg E. and Plummer L. N. (1986) A comparative study of the dissolution and crystal growth kinetics of calcite and aragonite. In *Studies in Diagenesis* (ed. F. A. Mumpton), pp. 139–168. U.S. Geological Survey Bulletin.

Cabrera N. and Levine M. M. (1956) On the dislocation theory of evaporation of crystals. *Philosophical Magazine* **1**, 450–458.

Cabrera N., Levine M. M., and Plaskett J. S. (1954) Hollow dislocations and etch pits. *Physical Review* **96**, 1153.

Carroll S. A. and Walther J. V. (1990) Kaolinite dissolution at 25°, 60°, and 80° C. *American Journal of Science* **290**, 797–810.

Casey W. H., Banfield J. F., Westrich H. R., and McLaughlin L. (1993a) What do dissolution experiments tell us about natural weathering? *Chemical Geology* **105**(1–3), 1–15.

Casey W. H. and Cheney M. A. (1993) Bronsted reactions on oxide mineral surfaces and the temperature-dependence of their dissolution rates. *Aquatic Sciences* **55**, 304–313.

Casey W. H., Hochella Jr. M. F., and Westrich H. R. (1993b) The surface-chemistry of manganiferous silicate minerals as inferred from experiments on tephroite (Mn_2SiO_4). *Geochimica et Cosmochimica Acta* **57**(4), 785–793.

Casey W. H. and Ludwig C. (1996) The mechanism of dissolution of oxide minerals. *Nature* **381**, 506–509.

Casey W. H. and Sposito G. (1992) On the temperature dependence of mineral dissolution rates. *Geochimica et Cosmochimica Acta* **56**, 3825–3830.

Casey W. H. and Westrich H. R. (1992) Control of dissolution rates of orthosilicate minerals by divalent metal-oxygen bonds. *Nature* **355**, 157–159.

Casey W. H., Westrich H. R., Arnold G. W., and Banfield J. F. (1989) The surface chemistry of dissolving labradorite feldspar. *Geochimica et Cosmochimica Acta* **53**, 821–832.

Casey W. H., Westrich H. R., and Holdren G. R. (1991) Dissolution rates of plagioclase at pH = 2 and 3. *American Mineralogist* **76**, 211–217.

Cheah S.-F., Kraemer S. M., Cervini-Silva J., and Sposito G. (2003) Steady-state dissolution kinetics of goethite in the presence of desferrioxamine B and oxalate ligands: Implications for the microbial acquisition of iron. *Chemical Geology* **198**, 63–75.

Chen Y. and Brantley S. L. (1997) Temperature- and pH-dependence of albite dissolution rate at acid pH. *Chemical Geology* **135**, 275–292.

Chen Y. and Brantley S. L. (1998) Diopside and anthophyllite dissolution at 25° C and 90° C and acid pH. *Chemical Geology* **147**(3–4), 233–248.

Chen Y. and Brantley S. L. (2000) Dissolution of forsteritic olivine at 65° C and 2 < pH < 5. *Chemical Geology* **165**(3–4), 267–281.

Chou L., Garrels R. M., and Wollast R. (1989) Comparative study of the kinetics and mechanisms of dissolution of carbonate minerals. *Chemical Geology* **78**, 269–282.

Chou L. and Wollast R. (1984) Study of the weathering of albite at room temperature and pressure with a fluidized bed reactor. *Geochimica et Cosmochimica Acta* **48**, 2205–2217.

Chou L. and Wollast R. (1985) Steady-state kinetics and dissolution mechanisms of albite. *American Journal of Science* **285**, 963–993.

Cocozza C., Tsao C. C. G., Cheah S.-F., Kraemer S. M., Raymond K. N., Miano T. M., and Sposito G. (2002) Temperature dependence of goethite dissolution promoted by trihydroxamate siderophores. *Geochimica et Cosmochimica Acta* **66**, 431–438.

Criscenti L., Kubicki J., and Brantley S. L. (2006) Silicate glass and mineral dissolution: Calculated reaction paths and activation energies for hydrolysis of a Q^3 Si by H_3O^+ using *ab initio* methods. *Journal of Physical Chemistry* **110**, 198–206.

Davis K. J., Dove P. M., and De Yoreo J. J. (2000) The role of Mg^{2+} as an impurity in calcite growth. *Science* **290**, 1134–1137.

Devidal J. L., Schott J., and Dandurand J. L. (1997) An experimental study of kaolinite dissolution and precipitation kinetics as a function of chemical affinity and solution composition at 150° C, 40 bars, and pH 2, 6.8, and 7.8. *Geochimica et Cosmochimica Acta* **61**(24), 5165–5186.

Dietzel M. (2000) Dissolution of silicates and the stability of polysilicic acid. *Geochimica et Cosmochimica Acta* **64**(19), 3275–3281.

Dixit S. and Carroll S. A. (2007) Effect of solution saturation state and temperature on diopside dissolution. *Geochemical Transactions* **8**(3), in press.

Doremus R. H. (1983) Diffusion-controlled reaction of water with glass. *Journal of Non-Crystalline Solids* **55**, 143–147.

Dove P. M. (1994) The dissolution kinetics of quartz in sodium chloride solutions at 25° to 300° C. *American Journal of Science* **294**, 665–712.

Dove P. M. (1995) Kinetic and thermodynamic controls on silica reactivity in weathering environments. In *Chemical Weathering Rates of Silicate Minerals*, Vol. 31 (ed. A. F. White and S. L. Brantley), pp. 236–290. Mineralogical Society of America, Short Course.

Dove P. M. (1999) The dissolution kinetics of quartz in aqueous mixed cation solutions. *Geochimica et Cosmochimica Acta* **63**, 3715–3727.

Dove P. M. and Crerar D. A. (1990) Kinetics of quartz dissolution in electrolyte solutions using a hydrothermal mixed flow reactor. *Geochimica et Cosmochimica Acta* **54**, 955–969.

Dove P. M., Han N., and De Yoreo J. J. (2005) Mechanisms of classical crystal growth theory explain quartz and silicate dissolution behavior. *Proceedings of National Academy of Sciences* **102**(43), 15357–15362.

Dove P. M. and Nix C. J. (1997) The influence of the alkaline earth cations, magnesium, calcium, and barium on the dissolution kinetics of quartz. *Geochimica et Cosmochimica Acta* **61**, 3329–3340.

Dove P. M. and Platt F. M. (1996) Compatible real-time rates of mineral dissolution by Atomic Force Microscopy (AFM). *Chemical Geology* **127**, 331–338.

Drever J. I. and Stillings L. (1997) The role of organic acids in mineral weathering. *Colloids and Surfaces* **120**, 167–181.

Ferruzzi G. G. (1993) The character and rates of dissolution of pyroxenes and pyroxenoids. M.S., University of California, Davis.

Fleer V. N. (1982) The dissolution kinetics of anorthite ($CaAl_2Si_2O_8$) and synthetic strontium feldspar (Sr $Al_2Si_2O_8$) in aqueous solutions at temperatures below 100° C: Applications to the geological disposal of radioactive nuclear wastes. PhD, Pennsylvania State University.

Frogner P. and Schweda P. (1998) Hornblende dissolution kinetics at 25° C. *Chemical Geology* **151**(1–4), 169–179.

Furrer G. and Stumm W. (1983) The role of surface coordination in the dissolution of γ–Al_2O_3 in dilute acids. *Chimie* **37**.

Furrer G. and Stumm W. (1986) The coordination chemistry of weathering; I. Dissolution kinetics of δ-Al_2O_3 and BeO. *Geochimica et Cosmochimica Acta* **50**, 1847–1860.

Gautier J.-M., Oelkers E. H., and Schott J. (1994) Experimental study of K-feldspar dissolution rates as a function of chemical affinity at 150° C and pH 9. *Geochimica et Cosmochimica Acta* **58**(21), 4549–4560.

Giammar D. E., Bruant R. G. J., and Peters C. A. (2005) Forsterite dissolution and magnesite precipitation at conditions relevant for deep saline aquifer storage and sequestration of carbon dioxide. *Chemical Geology* **217**, 257–276.

Golubev S. V., Pokrovsky O. S., and Schott J. (2005) Experimental determination of the effect of dissolved CO_2 on the dissolution kinetics of Mg and Ca silicates at 25° C. *Chemical Geology* **217**, 227–238.

Grandstaff D. E. (1977) Some kinetics of bronzite orthopyroxene dissolution. *Geochimica et Cosmochimica Acta* **41**(8), 1097–1103.

Gratz A. J. and Bird P. (1993) Quartz dissolution: Negative crystal experiments and a rate law. *Geochimica et Cosmochimica Acta* **57**, 965–976.

Guy C. and Schott J. (1989) Multisite surface reaction versus transport control during the hydrolysis of a complex oxide. *Chemical Geology* **78**, 181–204.

Hamilton J. P., Brantley S. L., Pantano C. G., Criscenti L. J., and Kubicki J. D. (2001) Dissolution of nepheline, jadeite and albite glasses: Toward better models for aluminosilicate dissolution. *Geochimica et Cosmochimica Acta* **65**(21), 3683–3702.

Hamilton J. P., Pantano C. G., and Brantley S. L. (2000) Dissolution of albite glass and crystal. *Geochimica et Cosmochimica Acta* **64**, 2603–2615.

Hellmann R. (1994) The albite-water system: Part I. The kinetics of dissolution as a function of pH at 100, 200, and 300° C. *Geochimica et Cosmochimica Acta* **58**, 595–611.

Hellmann R. (1995) The albite-water system: Part II. The time-evolution of the stoichiometry of dissolution as a function of pH at 100, 200, and 300° C. *Geochimica et Cosmochimica Acta* **59**, 1669–1697.

Hellmann R., Eggleston C. M., Hochella M. F., and Crerar D. A. (1990) The formation of leached layers on albite surfaces during dissolution under hydrothermal conditions. *Geochimica et Cosmochimica Acta* **54**(5), 1267–1281.

Hellmann R., Penisson J.-M., Hervig R. L., Thomassin J.-H., and Abrioux M.-F. (2003) An EFTEM/HRTEM high-resolution study of the near surface of labradorite feldspar altered at acid pH: Evidence for interfacial dissolution-precipitation. *Physics and Chemistry of Minerals* **30**, 192–197.

Hellmann R. and Tisserand D. (2006) Dissolution kinetics as a function of the Gibbs free energy of reaction: An experimental study based on albite feldspar. *Geochimica et Cosmochimica Acta* **70**, 364–383.

Hersman L., Lloyd T., and Sposito G. (1995) Siderophore-promoted dissolution of hematite. *Geochimica et Cosmochimica Acta* **59**(16), 3327–3330.

Hersman L. E. (2000) The role of siderophores in iron oxide dissolution. In *Environmental Microbe-Metal Interactions* (ed. D. Lovley), pp. 145–157. ASM Press.

Hewkin D. J. and Prince R. H. (1970) The mechanism of octahedral complex formation by labile metal ions. *Coordination Chemistry Reviews* **5**, 45–73.

Hoch A. R., Reddy M. M., and Drever J. I. (1996) The effect of iron content and dissolved O_2 on dissolution fates of clinopyroxene at pH 5.8 and 25° C: Preliminary results. *Chemical Geology* **132**(1–4), 151–156.

Holdren G. R. and Berner R. A. (1979) Mechanism of feldspar weathering: I. Experimental studies. *Geochimica et Cosmochimica Acta* **43**(8), 1161–1172.

Holdren G. R. and Speyer P. M. (1987) Reaction rate-surface area relationships during the early stages of weathering. II. Data on eight additional feldspars. *Geochemica et Cosmochimica Acta* **51**, 2311–2318.

Holmen B. A. and Casey W. H. (1996) Hydroxymate ligands, surface chemistry, and the mechanism of ligand-promoted dissolution of goethite [α-FeOOH(s)]. *Geochimica et Cosmochimica Acta* **60**, 4403–4416.

Holmen B. A., Tejedor-Tejedor M. I., and Casey W. H. (1997) Hydroxamate complexes in solution and at the goethite-water interface: A cylindrical internal reflection Fourier transform infrared spectroscopy study. *Langmuir* **13**, 2197–2206.

Huertas F. J., Chou L., and Wollast R. (1999) Mechanism of kaolinite dissolution at room temperature and pressure Part II: Kinetic study. *Geochimica et Cosmochimica Acta* **63**, 3261–3275.

Icenhower J. and Dove P. M. (2000) The dissolution kinetics of amorphous silica into sodium chloride solutions: Effects of temperature and ionic strength. *Geochimica et Cosmochimica Acta* **64**, 4193–4203.

Iler R. K. (1979) *The Chemistry of Silica*. John Wiley and Sons, Inc.

Inskeep W. P. and Bloom P. R. (1985) An evaluation of rate equations for calcite precipitation kinetics at P_{CO2} less than 0.01 atm and pH greater than 8. *Geochimica et Cosmochimica Acta* **49**, 2165–2180.

Kalinowski B., Faith-Ell C., and Schweda P. (1998) Dissolution kinetics and alteration of epidote in acidic solutions at 25° C. *Chemical Geology* **151**, 181–197.

Kalinowski B. E., Liermann L. J., Brantley S. L., Barnes A., and Pantano C. G. (2000a) X-ray photoelectron evidence for bacteria-enhanced dissolution of hornblende. *Geochimica et Cosmochimica Acta* **64**(8), 1331–1343.

Kalinowski B. E., Liermann L. J., Givens S., and Brantley S. L. (2000b) Rates of bacteria-promoted solubilization of Fe from minerals: A review of problems and approaches. *Chemical Geology* **169**, 357–370.

Kalinowski B. E. and Schweda P. (1996) Kinetics of muscovite, phiogopite and biotite dissolution and alteration at pH 1–4, room temperature. *Geochimica et Cosmochimica Acta* **60**, 367–385.

Kazmierczak T. F., Tomson M. G., and Nancollas G. H. (1982) Crystal growth of calcium carbonate: A controlled composition kinetic study. *Journal of Physical Chemistry* **86**, 103–107.

Knauss K. G., Nguyen S. N., and Weed H. C. (1993) Diopside dissolution kinetics as a function of pH, CO_2, temperature, and time. *Geochimica et Cosmochimica Acta* **57**(2), 285–294.

Knauss K. G. and Wolery T. J. (1989) Muscovite dissolution kinetics as a function of pH and time at 70° C. *Geochimica et Cosmochimica Acta* **53**(7), 1493–1501.

Kohler S. J., Bosbach D., and Oelkers E. H. (2005) Do clay mineral dissolution rates reach steady state? *Geochimica et Cosmochimica Acta* **69**(8), 1997–2006.

Kraemer S. M. (2004) Iron oxide dissolution and solubility in the presence of siderophores. *Aquatic Science* **66**, 3–18.

Kraemer S. M., Cheah S.-F., Zapf R., Xu J., Raymond K. N., and Sposito G. (1999) Effect of hydroxamate siderophores on Fe release and Pb(II) adsorption by goethite. *Geochimica et Cosmochimica Acta* **63**, 3003–3008.

Kraemer S. M. and Hering J. G. (1997) Influence of solution saturation state on the kinetics of ligand-controlled dissolution of aluminum oxide. *Geochimica et Cosmochimica Acta* **61**, 2855–2866.

Kubicki J. D., Blake G. A., and S.E. A. (1996) *Ab initio* calculations on aluminosilicate Q^3 species: Implications for atomic structures of mineral surfaces and dissolution mechanisms of feldspars. *American Mineralogist* **81**, 789–799.

Kubicki J. D., Schroeter L. M., Itoh M. J., Nguyen B. N., and Apitz S. E. (1999) Attenuated total reflectance Fourier-transform infrared spectroscopy of carboxylic acids adsorbed onto mineral surfaces. *Geochimica et Cosmochimica Acta* **63**, 2709–2725.

Kump L. R., Brantley S. L., and Arthur M. A. (2000) Chemical weathering, atmospheric CO_2 and climate. *Annual Review of Earth and Planetary Sciences* **28**, 611–667.

Laidler K. J. (1987) *Chemical Kinetics*. Harper and Row.

Lasaga A. C. (1981) Transition state theory. In *Kinetics of Geochemical Processes*, Vol. 8 (ed. A. C. Lasaga and R. J. Kirkpatrick), pp. 135–169. Mineralogical Society of America.

Lasaga A. C. (1984) Chemical kinetics of water-rock interactions. *Journal of Geophysical Research* **89**, 4009–4025.

Lasaga A. C. (1995) Fundamental approaches in describing mineral dissolution and precipitation rates. In *Chemical Weathering Rates of Silicate Minerals*, Vol. 31 (ed. A. F. White and S. L. Brantley), pp. 23–81. Mineralogical Society of America.

Lasaga A. C., and Kirkpatrick, R. J. (1981) Kinetics of Geochemical Processes. *Reviews in Mineralogical Society of America* **3**(8), 1–408.

Lasaga A. C. and Luttge A. (2001) Variation of crystal dissolution rate based on a dissolution stepwise model. *Science* **291**, 2400–2404.

Lichtner P. C. (1998) Modeling reactive flow and transport in natural systems. *Proceedings of the Rome Seminar on Environmental Geochemistry*, 5–72.

Liermann L. J., Kalinowski B. E., Brantley S. L., and Ferry J. G. (2000) Role of bacterial siderophores in dissolution of hornblende. *Geochimica et Cosmochimica Acta* **64**(4), 587–602.

Lin C. L. and Clemency C. V. (1981) The dissolution kinetics of brucite, antigorite, talc, and phlogopite at room temperature and pressure. *American Mineralogist* **66**(7–8), 801–806.

Luce R. W., Bartlett R. W., and Parks G. A. (1972) Dissolution kinetics of magnesium silicates. *Geochimica et Cosmochimica Acta* **36**(1), 35–50.

Ludwig C. and Casey W. H. (1996) On the mechanisms of dissolution of bunsenite (NiO(s)) and other simple oxide minerals. *Journal of Colloid and Interface Science* **178**, 176–185.

Ludwig C., Casey W. H., and Rock P. A. (1995) Prediction of ligand-promoted dissolution rates from the reactivities of aqueous complexes. *Nature* **375**, 44–47.

Lundstrom U. and Ohman L.-O. (1990) Dissolution of feldspars in the presence of natural organic solutes. *Journal of Soil Science* **41**, 359–369.

Machesky M. L. (1989) Influence of temperature on ion adsorption by hydrous metal oxides. In *Chemical Modeling of Aqueous System II*, Vol. 416 (ed. D. C. Melchior and R. L. Bassett), pp. 282–292. American Chemical Society.

MacInnis I. N. and Brantley S. L. (1992) The role of dislocations and surface morphology in calcite dissolution. *Geochimica et Cosmochimica Acta* **56**(3), 1113–1126.

MacInnis I. N. and Brantley S. L. (1993) Development of etch pit size distributions (PSD) on dissolving minerals. *Chemical Geology* **105**(1–3), 31–49.

Malmström M. and Banwart S. (1997) Biotite dissolution at 25° C: The pH dependence of dissolution rate and stoichiometry. *Geochimica et Cosmochimica Acta* **61**(14), 2779–2799.

Mast M. A. and Drever J. I. (1987) The effect of oxalate on the dissolution rates of oligoclase and tremolite. *Geochimica et Cosmochimica Acta* **51**(9), 2559–2568.

Mazer J. J. and Walther J. V. (1994) Dissolution kinetics of silica glass as a function of pH between 40 and 85° C. *Journal of Non-Crystalline Solids* **170**(1), 32–45.

Mogk D. W. and Locke W. W. (1988) Application of auger electron spectroscopy (AES) to naturally weathered hornblende. *Geochimica et Cosmochimica Acta* **52**(10), 2537–2542.

Morse J. W. (1978) Dissolution kinetics on calcium carbonate in sea water VI. The near equilibrium dissolution kinetics of calcium carbonate-rich deep sea sediments. *American Journal of Science* **278**, 344–353.

Muir I. J., Bancroft M., Shotyk W., and Nesbitt H. W. (1990) A SIMS and XPS study of dissolving plagioclase. *Geochimica et Cosmochimica Acta* **54**, 2247–2256.

Mukhopadhyay B. and Walther J. V. (2001) Acid-base chemistry of albite surfaces in aqueous solutions at standard temperature and pressure. *Chemical Geology* **174**, 415–443.

Murphy W. M., Pabalan R. T., Prikryl J. D., and Goulet C. J. (1992) Dissolution rate and solubility of analcime at 25° C. *International Conference on Water-Rock Interaction* **7**, 107–110. Balkema Pub. (Park City, UT).

Nagy K. L. (1995) Dissolution and precipitation kinetics of sheet silicates. In *Chemical Weathering Rates of Silicate Minerals*, Vol. 31 (ed. A. F. White and S. L. Brantley), pp. 173–225. Mineralogical Society of America.

Nagy K. L., Blum A. E., and Lasaga A. C. (1991) Dissolution and precipitation kinetics of kaolinite at 80° C and pH 3: The dependence on solution saturation state. *Amer. J. Science* **291**(649–686).

Nagy K. L. and Lasaga A. C. (1992) Dissolution and precipitation kinetics of gibbsite at 80° C and pH 3: The dependence on solution saturation state. *Geochimica et Cosmochimica Acta* **56**, 3093–3111.

Nagy K. L., Steefel C. I., Blum A. E., and Lasaga A. C. (1990) Dissolution and precipitation kinetics of kaolinite: Initial results at 80° C with application to porosity

evolution in a sandstone. *American Association of Petroleum Geology Memoir* **49**, 85–101.

Nancollas G. H. and Reddy M. M. (1971) The crystallization of calcium carbonate II. Calcite growth mechanism. *Journal of Colloid Interface Science* **37**, 824–830.

Neaman A., Chorover J., and Brantley S. L. (2005) Implications of the evolution of organic acid moieties for basalt weathering over geologic time. *American Journal of Science* **305**, 147–185.

Neaman A., Chorover J., and Brantley S. L. (2006) Effects of organic ligands on granite dissolution in batch experiments at pH 6. *American Journal of Science* **306**, 1–23.

Nesbitt H. W., Macrae N. D., and Shotyk W. (1991) Congruent and incongruent dissolution of labradorite in dilute acidic salt solutions. *Journal of Geology* **99**, 429–442.

Nielsen A. (1983) Precipitates: Formation, coprecipitation, and aging. In *Treatise on Analytical Chemistry* (ed. I. M. Kolthoff and P. J. Elving), pp. 269–374. John Wiley & Sons, Inc.

Nordstrom D. K. (1982) Aqueous pyrite oxidation and the consequent formation of secondary iron minerals. In *Acid Sulfate Weathering*, Vol. 10 (ed. M. Kral), pp. 37–56. Soil Science Society of America.

Nordstrom D. K. (2000) Advances in the hydrogeochemistry and microbiology of acid mine waters. *International Geology Review* **42**(6), 499–515.

Ochs M. (1996) Influence of humified and non-humified natural organic compounds on mineral dissolution. *Chemical Geology* **132**, 119–124.

Ochs M., Brunner I., Stumm W., and Cosovic B. (1993) Effects of root exudates and humic substances on weathering kinetics. *Water Air and Soil Pollution* **68**(1–2), 213–229.

Oelkers E. H. (2001a) An experimental study of forsterite dissolution rates as a function of temperature and aqueous Mg and Si concentrations. *Chemical Geology* **175**(3–4), 485–494.

Oelkers E. H. (2001b) General kinetic description of multioxide silicate mineral and glass dissolution. *Geochimica et Cosmochimica Acta* **65**(21), 3703–3719.

Oelkers E. H. and Gislason S. R. (2001) The mechanism, rates and consequences of basaltic glass dissolution: I. An experimental study of the dissolution rates of basaltic glass as a function of aqueous Al, Si, and oxalic acid concentration at 25° C and pH = 3 and 11. *Geochimica et Cosmochimica Acta* **65**(21), 3671–3681.

Oelkers E. H. and Schott J. (1995) The dependence of silicate dissolution rates on their structure and composition. *Eighth International Symposium on Water-Rock Interaction, WRI-8*, 153–156.

Oelkers E. H. and Schott J. (1998) Does organic acid adsorption affect alkali-feldspar dissolution rates? *Chemical Geology* **151**(1–4), 235–245.

Oelkers E. H. and Schott J. (1999) Experimental study of kyanite dissolution rates as a function of chemical affinity and solution composition. *Geochimica et Cosmochimica Acta* **63**(6), 785–797.

Oelkers E. H. and Schott J. (2001) An experimental study of enstatite dissolution rates as a function of pH, temperature, and aqueous Mg and Si concentration, and

the mechanism of pyroxene/pyroxenoid dissolution. *Geochimica et Cosmochimica Acta* **65**(8), 1219–1231.

Oelkers E. H., Schott J., and Devidal J.-L. (1994) The effect of aluminum, pH, and chemical affinity on the rates of aluminosilicate dissolution reactions. *Geochimica et Cosmochimica Acta* **58**(9), 2011–2024.

Oxburgh R., Drever J. I., and Sun Y. (1994) Mechanism of plagioclase dissolution in acid solution at 25° C. *Geochimica et Cosmochimica Acta* **58**(2), 661–669.

Paces T. (1973) Steady-state kinetics and equilibrium between ground water and granitic rock. *Geochimica et Cosmochimica Acta* **37**(12), 2641–2663.

Palandri J. L. and Kharaka Y. (2004) A compilation of rate parameters of water-mineral interaction kinetics for application to geochemical modeling. In *U.S. Geological Survey Open File Report 2004–1068*, pp. 64. U.S. Department of the Interior.

Parks G. A. (1967) Aqueous surface chemistry of oxides and complex oxide minerals. In *Equilibrium Concepts in Natural Water Systems*, Vol. 67, pp. 121–160. American Chemical Society.

Pelmenschikov A., Leszczynski J., and Pettersson G. M. (2001) Mechanism of dissolution of neutral silica surfaces: Including effect of self-healing. *Journal of Physical Chemistry A* **105**, 9528–9532.

Pelmenschikov A., Strandh H., Pettersson L. G. M., and Leszczyynski J. (2000) *Journal of Physical Chemistry B* **104**, 5779.

Perez J. R., Banwart S., and Puigdomenech I. (2005) The kinetics of $O_{2(aq)}$ reduction by structural ferrous iron in naturally occurring ferrous silicate minerals. *Applied Geochemistry* **20**, 2003–2016.

Plummer L. N., Wigley T. M. L., and Parkhurst D. L. (1978) The kinetics of calcite dissolution in CO_2-water systems at 5 to 60° C and 0.0 to 1.0 atm CO_2. *American Journal of Science* **278**, 179–216.

Pokrovski G. S. and Schott J. (1998) Experimental study of the complexation of silicon and germanium with aqueous organic species: Implications for germanium and silicon transport and Ge/Si ratio in natural waters. *Geochimica et Cosmochimica Acta* **62**(21–22), 3413–3428.

Pokrovsky O. S. and Schott J. (2000) Kinetics and mechanism of forsterite dissolution at 25° C and pH from 1 to 12. *Geochimica et Cosmochimica Acta* **64**(19), 3313–3325.

Polster W. (1994) Hydrothermal precipitation and dissolution of silica Part I. Conditions in geothermal fields and sedimentary basins, Part 2. Experimental evaluation of kinetics. Ph.D., Pennsylvania State University.

Poulson S. R., Drever J. I., and Stillings L. L. (1997) Aqueous Si-oxalate complexing, oxalate adsorption onto quartz, and the effect of oxalate upon quartz dissolution rates. *Chemical Geology* **140**(1–2), 1–7.

Reddy M. M. and Nancollas G. H. (1971) The crystallization of calcium carbonate I. Isotopic exchange and kinetics. *Journal of Colloid Interface Science* **36**, 166–172.

Rickard D. and Sjoberg E. L. (1983) Mixed kinetic control of calcite dissolution rates. *American Journal of Science* **283**, 815–830.

Rimstidt J. D. and Barnes H. L. (1980) The kinetics of silica-water reactions. *Geochimica et Cosmochimica Acta* **44**(11), 1683–1700.

Rimstidt J. D., Chermak J. A., and Gagen P. M. (1994) Rates of reaction of galena, sphalerite, chalcopyrite, and arsenopyrite with Fe(III) in acidic solutions. In *Environmental Geochemistry of Sulfide Oxidation*, Vol. 550 (ed. C. N. Alpers and D. W. Blowes), pp. 2–13. American Chemical Society.

Rimstidt J. D. and Newcomb W. D. (1993) Measurement and analysis of rate data: The rate of reaction of ferric iron with pyrite. *Geochimica et Cosmochimica Acta* **57**(9), 1919–1934.

Rose N. M. (1991) Dissolution rates of prehnite, epidote, and albite. *Geochimica et Cosmochimica Acta* **55**(11), 3273–3286.

Rosso J. J. and Rimstidt J. D. (2000) A high resolution study of forsterite dissolution rates. *Geochimica et Cosmochimica Acta* **64**(5), 797–811.

Schott J. (1990) Modeling of the dissolution of strained and unstrained multiple oxides: The surface speciation approach. In *Aquatic Chemical Kinetics* (ed. W. Stumm), pp. 337–365. John Wiley & Sons, Inc.

Schott J. and Berner R. A. (1983) X-ray photoelectron studies of the mechanism of iron silicate dissolution during weathering. *Geochimica et Cosmochimica Acta* **47**, 2233–2240.

Schott J. and Berner R. A. (1985) Dissolution mechanisms of pyroxenes and olivines during weathering. In *The Chemistry of Weathering*, Vol. 149 (ed. J. I. Drever). D. Reidel.

Schott J., Berner R. A., and Sjoberg E. L. (1981) Mechanism of pyroxene and amphibole weathering: I. Experimental studies of iron-free minerals. *Geochimica et Cosmochimica Acta* **45**(11), 2123–2135.

Schott J., Brantley S. L., Crerar D., Guy C., Borcsik M., and Willaime C. (1989a) Dissolution kinetics of strained calcite. *Geochimica et Cosmochimica Acta* **53**(2), 373–382.

Schott J. and Oelkers E. H. (1995) Dissolution and crystallization rates of silicate minerals as a function of chemical affinity. *Pure and Applied Chemistry* **67**(6), 903–910.

Schweda P. (1990) Kinetics and mechanisms of alkali feldspar dissolution at low temperatures. Ph.D., Stockholm University.

Shiraki R. and Brantley S. L. (1995) Kinetics of near-equilibrium calcite precipitation at 100° C: An evaluation of elementary reaction-based and affinity-based rate laws. *Geochimica et Cosmochimica Acta* **59**(8), 1457–1471.

Shiraki R., Rock P. A., and Casey W. H. (2000) Dissolution of calcite in 0.1 M NaCl solution at room temperature: An atomic force microscope (AFM) study. *Aquatic Geochemistry* **6**, 87–108.

Siegel D. I. and Pfannkuch H. O. (1984) Silicate mineral dissolution at pH 4 and near standard temperature and pressure. *Geochimica et Cosmochimica Acta* **48**, 197–201.

Sigg L. and Stumm W. (1981) The interaction of anions and weak acids with the hydrous goethite (α-FeOOH) surface, *Colloids Surf* (2), 101–107.

Sjoberg E. L. (1976) A fundamental equation for calcite dissolution kinetics. *Geochimica et Cosmochimica Acta* **40**, 441–447.

Sjoberg E. L. (1978) Kinetics and mechanism of calcite dissolution in aqueous solutions at low temperatures. *Stockholm Contributions in Geology* **32**, 1–92.

Sjoberg E. L. and Rickard D. (1983) Calcite dissolution kinetics: Surface speciation and the origin of the variable pH dependence. *Chemical Geology* **42**, 119–136.

Sjoberg E. L. and Rickard D. (1984) Calcite dissolution kinetics: Surface speciation and the origin of the variable pH dependence. *Chemical Geology* **42**, 119–136.

Sjoberg L. (1989) Kinetics and non-stoichiometry of labradorite dissolution. *Sixth International Conference on Water-Rock Interaction* (ed. D. L. Miles), 639–642. Balkema Pub. (Malvern, UK).

Stephens J. C. and Hering J. G. (2004) Factors affecting the dissolution kinetics of volcanic ash soils: Dependencies on pH, CO_2, and oxalate. *Applied Geochemistry* **19**, 1217–1232.

Stillings L. L. and Brantley S. L. (1995) Feldspar dissolution at 25°C and pH 3: Reaction stoichiometry and the effect of cations. *Geochimica et Cosmochimica Acta* **59**(8), 1483–1496.

Stillings L. L., Drever, J.I., Brantley, S., Sun, Y., and Oxburgh, R. (1996) Rates of feldspar dissolution at pH 3–7 with 0–8 M oxalic acid. *Chemical Geology* **132**, 79–89.

Stumm W. (1997) Reactivity at the mineral-water interface: Dissolution and inhibition. *Colloids and Surfaces A: Physicochemical and Engineering Aspects* **120**, 143–166.

Stumm W. and Furrer G. (1987) The dissolution of oxides and aluminum silicates: Examples of surface-coordination-controlled kinetics. In *Aquatic Surface Chemistry: Chemical Processes at the Particle-Water Interface* (ed. W. Stumm), pp. 197–220. John Wiley & Sons, Inc.

Suter D., Banwart S., and Stumm W. (1991) Dissolution of hydrous iron(III) oxides by reductive mechanisms. *Langmuir* **7**(4), 809–813.

Suter D., Siffert C., Sulzberger B., and Stumm W. (1988) Catalytic dissolution of iron(III)(hydr)oxides by oxalic-acid in the presence of Fe(Ii). *Naturwissenschaften* **75**(11), 571–573.

Sverdrup H. U. (1990) *The Kinetics of Base Cation Release Due to Chemical Weathering*. Lund University Press.

Sverjensky D. A. (1992) Linear free energy relations for predicting dissolution rates of solids. *Nature* **358**(310–313).

Sverjensky D. A. (1994) Zero-point-of-charge prediction from crystal chemistry and solvation theory. *Geochimica et Cosmochimica Acta* **58**(14), 3123–3129.

Taylor A. S., Blum J. D., and Lasaga A. C. (2000a) The dependence of labradorite dissolution and Sr isotope release rates on solution saturation state. *Geochimica et Cosmochimica Acta* **64**(14), 2389–2400.

Taylor A. S., Blum J. D., Lasaga A. C., and MacInnis I. N. (2000b) Kinetics of dissolution and Sr release during biotite and phologopite weathering. *Geochimica et Cosmochimica Acta* **64**(7), 1191–1208.

Teng H. H., Dove P. M., and DeYoreo J. J. (2000) Kinetics of calcite growth: Surface processes and relationships to macroscopic rate laws. *Geochimica et Cosmochimica Acta* **64**, 2255–2266.

Tester J. W., Worley W. G., Robinson B. A., Grigsby C. O., and Feerer J. L. (1994) Correlating quartz dissolution kinetics in pure water from 25 to 625° C. *Geochimica et Cosmochimica Acta* **58**, 2407–2420.

Tsomaia N., Brantley S. L., Hamilton J. P., Pantano C. G., and Mueller K. T. (2003) NMR evidence for formation of octahedral and tetrahedral Al and repolymerization of the Si network during dissolution of aluminosilicate glass and crystal. *American Mineralogist* **88**, 54–67.

van Hees P. A. W., Lundstrom U. S., and Morth C.-M. (2002) Dissolution of microcline and labradorite in a forest O horizon extract: The effect of naturally occurring organic acids. *Chemical Geology* **189**, 199–211.

Walther J. V. (1996) Relation between rates of aluminosilicate mineral dissolution, pH, temperature, and surface charge. *American Journal of Science* **296**, 693–728.

Watteau F. and Berthelin J. (1994) Microbial dissolution of iron and aluminum from soil minerals: Efficiency and specificity of hydroxamate siderophores compared to aliphatic acids. *European Journal of Soil Biology* **30**(1), 1–9.

Wehrli B. (1990) Redox reactions of metal ions at mineral surfaces. In *Aquatic Chemical Kinetics: Reaction Rates of Processes in Natural Waters* (ed. W. Stumm), pp. 311–336. John Wiley & Sons, Inc.

Weissbart E. J. and Rimstidt J. D. (2000) Wollastonite: Incongruent dissolution and leached layer formation. *Geochimica et Cosmochimica Acta* **64**(23), 4007–4016.

Welch S. A. and Ullman W. J. (1996) Feldspar dissolution in acidic and organic solutions: Compositional and pH dependence of dissolution rate. *Geochimica et Cosmochimica Acta* **60**, 2939–2948.

Welch S. A. and Ullman W. J. (1999) The effect of microbial glucose metabolism on bytownite feldspar dissolution rates between 5 degrees and 35 degrees C. *Geochimica et Cosmochimica Acta* **63**, 3247–3259.

Westrich H. R., Cygan R. T., Casey W. H., Zemitis C., and Arbold G. W. (1993) The dissolution kinetics of mixed-cation orthosilicate minerals. *American Journal of Science* **293**(9), 869–893.

White A. F. and Brantley S. L. (1995) Chemical weathering rates of silicate minerals: An overview. In *Chemical Weathering Rates of Silicate Minerals*, Vol. 31 (ed. A. F. White and S. L. Brantley), pp. 1–22. Mineralogical Society of America.

White A. F. and Brantley S. L. (2003) The effect of time on the weathering of silicate minerals: Why do weathering rates differ in the laboratory and field? *Chemical Geology* **202**, 479–506.

White A. F. and Yee A. (1985) Aqueous oxidation-reduction kinetics associated with coupled electron-cation transfer from iron-containing silicates at 25° C. *Geochimica et Cosmochimica Acta* **49**, 1263–1275.

Wieland E., Wehrli B., and Stumm W. (1988) The coordination chemistry of weathering: III. A generalization in the dissolution rates of minerals. *Geochimica et Cosmochimica Acta* **52**(8), 1969–1981.

Wogelius R. A. and Walther J. V. (1991) Olivine dissolution at 25° C: Effects of pH, CO_2, and organic acids. *Geochimica et Cosmochimica Acta* **55**(4), 943–954.

Wogelius R. A. and Walther J. V. (1992) Olivine dissolution kinetics at near-surface conditions. *Chemical Geology* **97**(1–2), 101–112.

Wood B. J. and Walther J. V. (1983) Rates of hydrothermal reactions. *Science* **222**, 413–415.

Xie Z. (1994) Surface properties of silicates, their solubility and dissolution kinetics. Ph.D., Northwestern University.

Xie Z. and Walther J. V. (1994) Dissolution stoichiometry and adsorption of alkali and alkaline earth elements to the acid-reacted wollastonite surface at 25° C. *Geochimica et Cosmochimica Acta* **58**(12), 2587–2598.

Yoshida T., Hayashi K., and Ohmoto H. (2002) Dissolution of iron hydroxides by marine bacterial siderophore. *Chemical Geology* **184**(1–2), 1–9.

Zhang H., Bloom P. R., and Nater E. A. (1990) Morphology and chemistry of hornblende dissolution products in acid solutions. In *Soil Micromorphology: A Basic and Applied Science; Developments in Soil Science*, Vol. 19 (ed. L. A. Douglas), pp. 551–556. Elsevier.

Chapter 6
Data Fitting Techniques with Applications to Mineral Dissolution Kinetics

Joel Z. Bandstra[1] and Susan L. Brantley[2]

6.1 Introduction

A common problem in chemical kinetics is the development of a rate law that describes the dependence of the reaction rate on the surrounding conditions such as concentrations of reacting species or temperature of the reacting media (see Chap. 1). The most direct approach to solving this problem is to measure reaction rates under systematically varied conditions and then to perform mathematical analyses on these data to determine the form of the rate law and to generate estimates of any unknown constants, or parameters, that make up the proposed rate law. Other chapters in this book provide information both for designing kinetics experiments and for selecting appropriate rate laws for a variety of geochemical reactions. In this chapter we describe the mathematical analyses – known collectively as curve fitting or regression analysis – that can be used to select a rate equation that matches a given data set, to generate estimates for any unknown parameters in the rate equation (e.g., rate constants or reaction orders), and to quantify the uncertainty associated with the estimated values for the parameters. As we traverse this entirely quantitative process we will attempt to describe the underlying, qualitative process of looking at kinetic data: plots to make, features of these plots to examine, and conceptual sketches to draw.

In order to fit a curve to data one must first obtain the data. Over the past few decades, researchers have produced numerous high quality studies on the kinetics of mineral dissolution and the effects of experimental conditions such as pH, temperature, concentration of dissolved metal ions, mineral composition, etc. We have compiled this dissolution rate data for a number of rocks and minerals including apatite, basalt, biotite, hornblende, kaolinite, olivine, plagioclase, potassium feldspar, pyroxene, and quartz. We will use these data, which are available in Appendix I of

[1] The Pennsylvania State University, Center for Environmental Kinetics Analysis, jxb88@psu.edu
[2] The Pennsylvania State University, Center for Environmental Kinetics Analysis and Earth and Environmental Systems Institute, brantley@essc.psu.edu

this book, as the basis for examples of the techniques that we discuss. For convenience, our best-fit rate equation for each of these data sets is provided in table 6.3.

6.2 Rate Law Selection

The first step in fitting data is to select an equation that matches the data. For a finite data set, there are an infinite number of equations that will work. Of course, geochemical reasoning and compactness considerations can limit our options to a more manageable number. This, however, usually still leaves myriad possibilities with the precise selection of a fitting equation left to the intuition of the data analyst. The best way to solve this problem is to identify a number of key features contained in the data set and then to select a model that reproduces precisely these key features.

6.2.1 Identifying Key Features

Suppose that some number of experiments, N, are performed with some experimental condition, x_i (where $i = 1,\ldots,\mathrm{N}$), varied amongst them producing a data set, y_i. In the context of this chapter, the y_i could be the measured dissolution rate and the x_i could be the pH of the solution. Each of the measurements, y_i, can be broken into an (unknown) functional dependence on the condition, $f(x_i)$, and a random measurement error, ε_i:

$$y_i = f(x_i) + \varepsilon_i \tag{6.1}$$

The problem at hand, then, is to identify the form of the functional relationship, $f(x_i)$, between the x_i and y_i; that is, to identify the key features that $f(x_i)$ must possess. What are the key features of a function? Consider the Taylor expansion of $f(x_i)$ around a point x_j:

$$f(x_i) = f(x_j) + f'(x_j)(x_i - x_j) + f''(x_j)\frac{(x_i - x_j)^2}{2} + f'''(x_j)\frac{(x_i - x_j)^3}{3!} + \ldots \tag{6.2}$$

where the prime notation denotes differentiation with respect to x. Since higher order terms in a Taylor series become increasingly negligible, the most important feature of $f(x_i)$ is its value (the first term in Eq. (6.2)), the second most important is its slope (second term), the third most important is its concavity (third term), and so on. We are not, right now, concerned with the magnitude of $f(x_i)$, but rather its shape. The key features of $f(x_i)$ are, therefore, the sign and roots of the function and its derivatives.

The key features of a data set can be examined graphically. The first step is to plot the dependent variable (y_i) versus the independent variable (x_i). On a copy of

this graph, a curve should be sketched – by hand – through the data points. Note that since the measurements contain error, the sketched curve need not go through each point. It merely needs to pass near most of them. The zeroth-order features of the data (i.e., those pertaining to the zeroth derivative) can be ascertained by examining the sign of the sketched curve. If it is always positive then the fitting equation should take only positive values. If the sketched curve has a single root (as is often the case in, for example, electrochemical kinetics data) then the fitting equation should have a single root. The fitting equation should have sign and roots that match those of the sketched curve; otherwise the equation will not fit the data.

This graphing exercise can be continued by sketching first and second derivatives of the curve (sketching derivatives is covered in most introductory calculus textbooks such as Hughes-Hallett et al., 1994). If the data are everywhere increasing then the first derivative should be everywhere positive and the fitting equation should increase monotonically. If the data display an extremum or inflection point then the first or second derivative, respectively, should pass through zero and the fitting equation should behave accordingly. If the data display an asymptote then the fitting equation should contain an asymptote. If, on the other hand, the data are featureless (cf., the andesine and bytownite rate compilations in Appendix I), then the proper fitting equation is simply a constant (i.e., the average value of the y_i).

In chemical kinetics, appropriate fitting equations commonly take the form of an exponential or power–law (see Chap. 1). For this reason, when plotting data, it is often helpful to log-transform the axes of plotted data. If an exponential fitting equation – $f(x) = \exp(-k \cdot x)$ – is appropriate, log transforming the ordinate only (i.e., a semi-log plot) will generate a straight line. A straight line upon log transforming both the ordinate and the abscissa (i.e., a log–log plot) indicates a power–law relationship – $f(x) = k \cdot x^n$. Although the log-transform is the most common, other transformations may also prove useful. The inverse transform is often times used, for example, when analyzing the effects of temperature (cf., Fig. 7B and Chap. 1), and the Fourier transform is useful in analyzing periodicity in data. No transform, however, can replace the visual analysis of data, and therefore, even upon performing a transform one should proceed through the aforementioned graphing and sketching exercises on the transformed data.

Example sketches are shown in Fig. 6.1 and Fig. 6.2 where log-transformed reaction rates are plotted against pH for published measurements of, respectively, albite and diopside dissolution. It is usually easiest to make the derivative sketches directly below the plotted data. This format is helpful in ensuring accurate sketches and in identifying key features. Note, for example, the vertical dashed lines sketched at pH $\approx$ 6.5 in Fig. 6.1 and pH $\approx$ 4 in Fig. 6.2. These lines denote a minimum in Fig. 6.1 and an inflection point in Fig. 6.2. The line separates regions of positive and negative slope in Fig. 6.1 and regions of positive and negative concavity in Fig. 6.2. These features along with inferences about asymptotic behavior are listed in Tables 6.1 and 6.2. In Sect. 6.2.2 we will examine means for selecting a rate equation to match a list of key features.

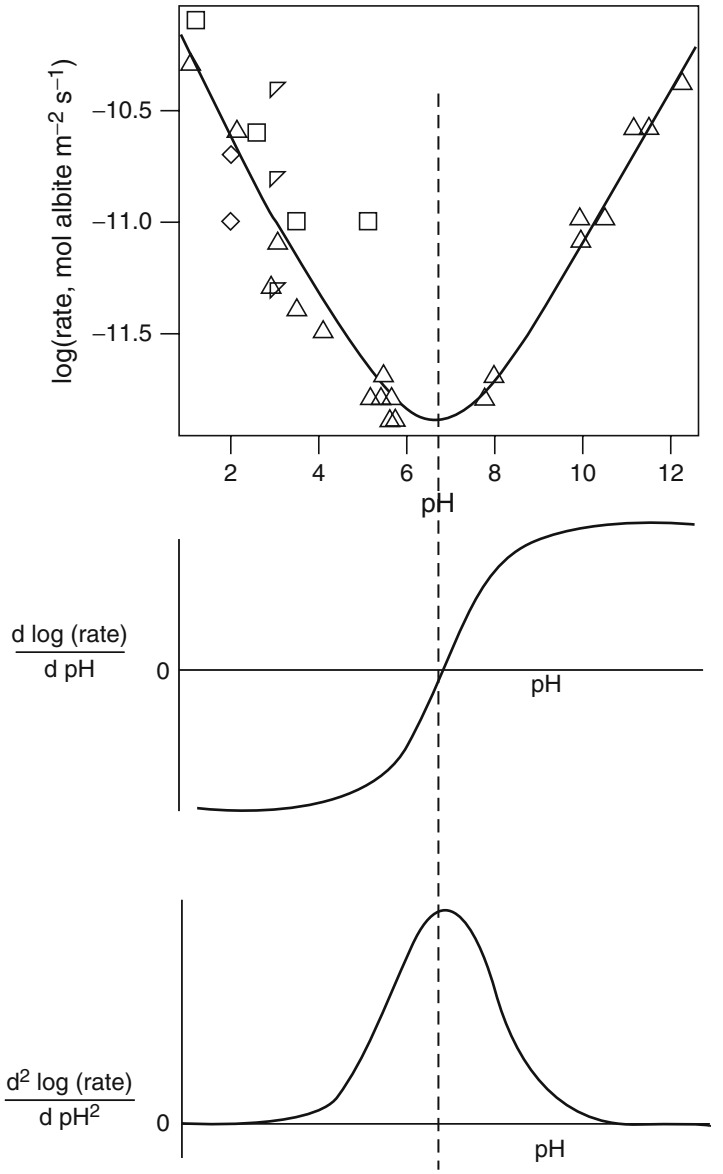

Fig. 6.1 Sketches of (**a**) zeroth, (**b**) first, and (**c**) second derivatives of log-transformed surface area-normalized albite dissolution rate data with respect to pH. □ Chou and Wollast (1984) △ Chou and Wollast (1985) ◇ Casey et al. (1991) ◸ Holdren and Speyer (1987). (See Appendix for data)

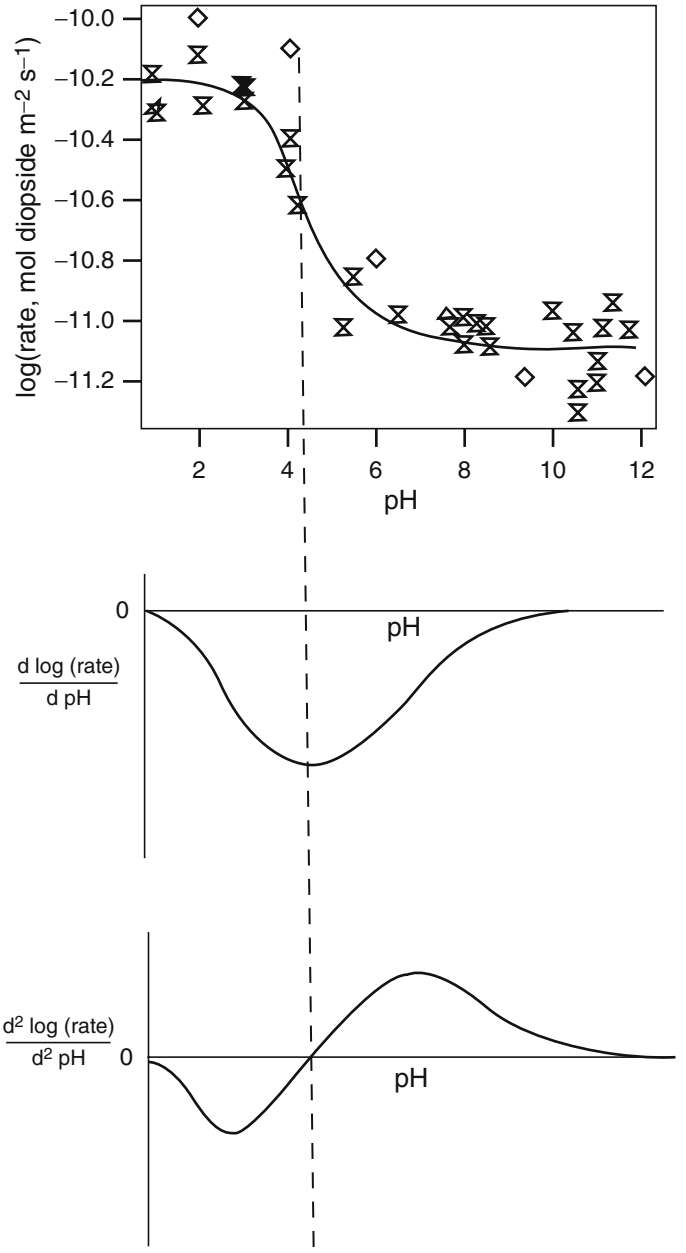

Fig. 6.2 Sketches of (**a**) zeroth, (**b**) first, and (**c**) second derivatives of log-transformed surface area-normalized diopside dissolution rate data with respect to pH. ⧖Golubev et al. (2005) ♢ Knauss et al. (1993) ◿ Eggleston et al. (1989). (See Appendix for data)

Table 6.1 Key features for albite dissolution rate data shown in Fig. 6.1

	<0	$=0$	>0
$\log(rate)$	$2 < \mathrm{pH} < 12$	Nowhere	Nowhere
$\frac{d\log(rate)}{d\mathrm{pH}}$	$2 < \mathrm{pH} < 6.5$	$\mathrm{pH} \approx 6.5$	$6.5 < \mathrm{pH} < 12$
$\frac{d^2\log(rate)}{d\mathrm{pH}^2}$	Nowhere	$\mathrm{pH} \to \pm\infty$	$2 < \mathrm{pH} < 12$

6.2.2 Modeling Key Features

A common approach to obtaining rate laws is direct derivation from a reaction mechanism assuming that the reacting molecules obey Markovian statistics (Gillespie, 2000; Ishida, 1966; McQuarrie, 1967) and, possibly, that some of the stages in the reaction rapidly achieve equilibrium (Zepp and Wolfe, 1987) or steady-state (Temkin, 1979). Rate laws of this type – which we will refer to as mechanistic rate laws – are derived for some simple reaction mechanisms in Chap. 1. In most cases, however, only partial information is known about the reaction mechanism and, therefore, mechanistic rate laws can not usually be derived with any sort of rigor. Fortunately, it is often effective to derive a rate law on the basis of the partial information that is known about a reaction mechanism and to then relax the molecularity constraint on the reaction orders by allowing non-integer values (Moore and Pearson, 1981). We will denote equations derived in this fashion, *contra mechanistic*, as empirical rate laws. In a surprising number of cases, very simple mechanistic rate laws are successful even when the underlying assumptions about the mechanism are clearly violated (Bandstra and Tratnyek, 2004; Bandstra and Tratnyek, 2005) indicating that such rate laws, too, are often empirical in nature. Before proceeding, a word of caution: the success of a mechanistic rate law is necessary but not sufficient grounds for concluding that the underlying mechanism is correct; likewise, the success of an empirical rate law does not prove correct any partial mechanistic information employed in its derivation.

Just as we identified key features (i.e., signs, roots, and asymptotes in the zeroth, first, and second derivatives) in rate data, we now turn to the identification of key

Table 6.2 Key features for diopside dissolution rate data shown in Fig. 6.2

	<0	$=0$	>0
$\log(rate)$	$2 < \mathrm{pH} < 12$	Nowhere	Nowhere
$\frac{d\log(rate)}{d\mathrm{pH}}$	$2 < \mathrm{pH} < 12$	$\mathrm{pH} \to \pm\infty$	Nowhere
$\frac{d^2\log(rate)}{d\mathrm{pH}^2}$	$2 < \mathrm{pH} < 4$	$\mathrm{pH} \approx 4$; $\mathrm{pH} \to \pm\infty$	$4 < \mathrm{pH} < 12$

Table 6.3 Fitting results for compiled mineral dissolution rates versus pH

Mineral (pH Range)	Source of Fitted Data	Rate Law	Fitted Parameters ±68.3% Confidence Intervals[a, b]
Albite (1.1–12.3)	Chou and Wollast (1984), Chou and Wollast (1985), Casey et al. (1991), Knauss and Wolery (1986), Rose (1991), Holdren and Speyer (1987), Stillings and Brantley (1995)	(4)	$k_{H^+} = 2.38 \times 10^{-10} \pm 9.82 \times 10^{-11}$(mol m^{-2} s^{-1}) $n_{H^+} = 0.403 \pm 0.0503$ $k_{OH^-} = 2.31 \times 10^{-10} \pm 1.46 \times 10^{-10}$(mol m^{-2} s^{-1}) $n_{OH^-} = 0.376 \pm 0.0721$
Anorthite (2.0–7.7)	Hodson (2003), Holdren and Speyer (1987), Casey et al. (1991), Amrhein and Suarez (1992)	(34)	$k_{H^+} = 2.31 \times 10^{-7} \pm 9.51 \times 10^{-8}$(mol m^{-2} s^{-1}) $n_{H^+} = 0.985 \pm 0.0391$
Apatite (2.2–8.5)	Guidry and Mackenzie (2003), Valsami-Jones et al. (1998), Welch et al. (2002)	(34)	$k_{H^+} = 7.22 \times 10^{-7} \pm 3.57 \times 10^{-7}$(mol m^{-2} s^{-1}) $n_{H^+} = 0.541 \pm 0.0408$
Basalt (2.4–10.6)	Gislason and Eugster (1987)	(52)	$E_a = 47500 \pm 2690$(J mol^{-1}) $\hat{k}_{H^+} = 588 \pm 558$(mol m^{-2} s^{-1}) $n_{H^+} = 1.16 \pm 0.107$ $\hat{k}_{OH^-} = 0.0822 \pm 0.079$(mol m^{-2} s^{-1}) $n_{OH^-} = 0.16 \pm 0.0309$
Biotite (1.1–6.7)	Kalinowski and Schweda (1996), Acker and Bricker (1992)	(34)	$k_{H^+} = 9.67 \times 10^{-11} \pm 2.97 \times 10^{-11}$(mol m^{-2} s^{-1}) $n_{H^+} = 0.355 \pm 0.03$
Diopside (1.0–12.1)	Eggleston et al. (1989), Knauss et al. (1993), Golubev et al. (2005)	(17)	$\hat{k}_{H^+} = 5.69 \times 10^{-11} \pm 6.71 \times 10^{-12}$(mol m^{-2} s^{-1}) $K = 6840 \pm 13000$ $n_{H^+} = 0.546 \pm 0.2$ $k_0 = 8.14 \times 10^{-12} \pm 5.78 \times 10^{-13}$(mol m^{-2} s^{-1})
Forsterite (1.0–12.1)	Pokrovsky and Schott (2000), Oelkers (2001), Rosso and Rimstidt (2000), Wogelius and Walther (1992), Brady and Walther (1989)	(34)	$k_{H^+} = 5.55 \times 10^{-8} \pm 6.63 \times 10^{-9}$(mol m^{-2} s^{-1}) $n_{H^+} = 0.372 \pm 0.0053$

Table 6.3 (*Continued*)

Mineral (pH Range)	Source of Fitted Data	Rate Law	Fitted Parameters ±68.3% Confidence Intervals[a, b]
Hornblende (1.1–5.7)	Givens and Brantley (unpublished), Zhang (1990), Zhang et al. (1996), Swoboda-Colberg and Drever (1993)	(34)	$k_{H^+} = 4.5 \times 10^{-11} \pm 7.83 \times 10^{-11}$ (mol m^{-2} s^{-1}) $n_{H^+} = 0.37 \pm 0.734$
Kaolinite 0.5–13.0)	[1]Carroll-Webb and Walther (1988), [2]Wieland and Stumm (1992), [3]Ganor et al. (1995), [4] Huertas et al. (1999), [5]Cama et al. (2002)	(4)	$k_{H^+} = \begin{cases} {}^1 4.23 \times 10^{-13} \pm 4.36 \times 10^{-14} \\ {}^2 1.58 \times 10^{-12} \pm 1.54 \times 10^{-13} \\ {}^3 1.13 \times 10^{-12} \pm 1.71 \times 10^{-13} \\ {}^4 5.76 \times 10^{-14} \pm 8.06 \times 10^{-15} \\ {}^5 5.61 \times 10^{-14} \pm 6.09 \times 10^{-15} \end{cases}$ (mol m^{-2} s^{-1}) $n_{H^+} = 0.129 \pm 0.00796$ $k_{OH^-} = 4.75 \times 10^{-11} \pm 1.75 \times 10^{-11}$ (mol m^{-2} s^{-1}) $n_{OH^-} = 1.02 \pm 0.0856$
Quartz (1.1–12.3)	Bennett et al. (1988), Wollast and Chou (1986), Brady and Walther (1990), Casey et al. (1990), Bennett (1991), House and Orr (1992), Berger et al. (1994), Tester et al. (1994)	(4)	$k_{H^+} = 4.34 \times 10^{-12} \pm 2.32 \times 10^{-12}$ (mol m^{-2} s^{-1}) $n_{H^+} = 0.309 \pm 0.0778$ $k_{OH^-} = 6.06 \times 10^{-10} \pm 2.33 \times 10^{-10}$ (mol m^{-2} s^{-1}) $n_{OH^-} = 0.411 \pm 0.0319$

[a] All fits by IRLS and confidence intervals by the bootstrap method except for kaolinite where confidence intervals were calculated from the covariance matrix.
[b] Rate constants are reported in terms of moles of mineral formula unit except for basalt where rate constants are reported in terms moles of Si. Number of oxygens per formula unit are as follows: albite, 8; anorthite, 8; apatite, 12; biotite, 20; diopside, 6; forsterite, 4; hornblende, 22; kaolinite, 5; quartz, 2.

features in a rate law, but with analysis instead of graphs. Consider the following empirical rate law given in Chap. 5:

$$r = k_{H^+} \cdot a_{H^+}^n + k_{OH^-} \cdot a_{OH^-}^m \tag{6.3}$$

where r is the surface area normalized rate, k_{H^+} and k_{OH^-} are, respectively, rate constants for proton- and hydroxide-promoted dissolution, a_{H^+} and a_{OH^-} are activities of the respective species, and n and m are reaction orders. A rate law that is similar to Eq. (6.3) but with $m = n = 1$ can be derived mechanistically by assuming that protons and hydroxide ions rapidly equilibrate with the mineral surface to form activated complexes that undergo dissolution with some (constant) probability per unit time.

Since we plotted $\log(r)$ versus pH data in Figs. 6.1 and 6.2, we will perform our analyses in this transformed space. Substituting $a_{H^+} = 10^{(-\mathrm{pH})}$ and $a_{OH^-} = 10^{(\mathrm{pH}-14)}$ into Eq. (6.3) gives rate as a function of pH.

$$r = k_{H^+} \cdot 10^{-n \cdot \mathrm{pH}} + k_{OH^-} \cdot 10^{m \cdot (\mathrm{pH}-14)} \tag{6.4}$$

Equation 4 is positive for any value of pH and, therefore, $\log(r)$ must take real values; negative real values if $r < 1$, which can always be achieved over a finite pH range with appropriate choice of rate constants. Thus, Eq. (6.3) can match the zeroth-order feature (i.e., that feature which derives from analysis of the zeroth derivative) of the albite dissolution rate data that $\log(r) < 0$ for $2 < \mathrm{pH} < 12$ (see Fig. 6.1, Table 6.1).

The first derivative of $\log(r)$ with respect to pH is given as follows:

$$\frac{d\log(r)}{d\mathrm{pH}} = \log(e)\,\frac{1}{r}\,\frac{dr}{d\mathrm{pH}} \tag{6.5}$$

Since r and $\log(e)$ are positive, $d\log(r)/d\mathrm{pH}$ must have the same sign and roots as dr/dpH. From Eq. (6.4):

$$\frac{dr}{d\mathrm{pH}} = \ln(10)\left(-n \cdot k_{H^+} \cdot 10^{-n \cdot \mathrm{pH}} + m \cdot k_{OH^-} \cdot 10^{m \cdot (\mathrm{pH}-14)}\right) \tag{6.6}$$

Setting the right hand side (rhs) of Eq. (6.6) to zero we find that $d\log(r)/d\mathrm{pH}$ has a root at $\mathrm{pH}_{\mathrm{crit}}$:

$$\mathrm{pH}_{\mathrm{crit}} = \frac{14m + \log\left(\frac{n \cdot k_{H^+}}{m \cdot k_{OH^-}}\right)}{m+n} \tag{6.7}$$

Taking the second derivative of Eq. (6.8) with respect to pH yields:

$$\frac{d^2 r}{d\mathrm{pH}^2} = (\ln(10))^2\left(n^2 \cdot k_{H^+} \cdot 10^{-n \cdot \mathrm{pH}} + m^2 \cdot k_{OH^-} \cdot 10^{m \cdot (\mathrm{pH}-14)}\right) \tag{6.8}$$

The rhs of Eq. (6.8) may take only positive values. Therefore, $dr/d\mathrm{pH}$ must increase monotonically as must $d\log(r)/d\mathrm{pH}$. Further, $d\log(r)/d\mathrm{pH} < 0$ for $\mathrm{pH} < \mathrm{pH}_{\mathrm{crit}}$

and $d\log(r)/d\mathrm{pH} > 0$ for $\mathrm{pH} > \mathrm{pH}_{\mathrm{crit}}$. Compare this pattern to the observed sign of $d\log(r)/d\mathrm{pH}$ shown in Fig. 6.1b where $\mathrm{pH}_{\mathrm{crit}} \approx 6.5$.

Substituting Eqs. (6.4) and (6.6) into Eq. (6.5) gives:

$$\frac{d\log(r)}{d\mathrm{pH}} = \frac{-n \cdot k_{H^+} \cdot 10^{-n \cdot \mathrm{pH}} + m \cdot k_{OH^-} \cdot 10^{m \cdot (\mathrm{pH}-14)}}{k_{H^+} \cdot 10^{-n \cdot \mathrm{pH}} + k_{OH^-} \cdot 10^{m \cdot (\mathrm{pH}-14)}} \tag{6.9}$$

We already know the signs and roots of Eq. (6.9) from the analysis above, but with the rate equation written in this form, we can easily identify asymptotic behavior at large and small values of pH. The limits of Eq. (6.9) as pH approaches $\pm\infty$ are

$$\lim_{pH \to \infty} \frac{d\log(r)}{d\mathrm{pH}} = \lim_{pH \to \infty} \frac{-n \cdot k_{H^+} 10^{-n \cdot \mathrm{pH} - m \cdot (\mathrm{pH}-14)} + m \cdot k_{OH^-}}{k_{H^+} 10^{-n \cdot \mathrm{pH} - m \cdot (\mathrm{pH}-14)} + k_{OH^-}} = m \tag{6.10}$$

$$\lim_{pH \to -\infty} \frac{d\log(r)}{d\mathrm{pH}} = \lim_{pH \to \infty} \frac{-n \cdot k_{H^+} + m \cdot k_{OH^-} \cdot 10^{m \cdot (\mathrm{pH}-14) + n \cdot \mathrm{pH}}}{k_{H^+} + k_{OH^-} \cdot 10^{m \cdot (\mathrm{pH}-14) + n \cdot \mathrm{pH}}} = -n \tag{6.11}$$

The slope of $\log(r)$ with respect to pH goes to a positive constant, m, at high pH and to a negative constant, $-n$, at low pH. This means that $\log(r)$ as given by Eq. (6.4) asymptotically approaches a straight line with positive slope at high pH and one with negative slope at low pH. In terms of Eq. (6.4), the second term of the *rhs* is dominant at high pH while the first term is dominant at low pH. Again comparing these first-order features of Eq. (6.4) to the albite data (Fig. 6.1, Table 6.1) indicates consistency between rate law and data. The second-order features, in this case, derive trivially from the above analysis and we may conclude that Eq. (6.4) is an appropriate rate law for fitting the albite dissolution rate data shown in Fig. 6.1.

In contrast to albite, the structure of the diopside data (Fig. 6.2, Table 6.2) is not consistent with the behavior of Eq. (6.4); $d\log(r)/d\mathrm{pH}$ is negative and appears to approach zero at high and low pH in Fig. 6.2b while the first derivative of Eq. (6.4) contains a root and approaches non-zero slopes. Further, $d^2\log(r)/d\mathrm{pH}^2$ contains a root in Fig. 6.2c while Eq. (6.4) possesses no inflection point. A different rate equation is needed for the diopside dissolution rate data shown in Fig. 6.2. From what source should we obtain this new rate equation?

While either of the mechanistic or empirical prescriptions discussed above could work, there is a third approach – one that also produces an empirical rate law – that we will employ in selecting an equation to match the key features of the diopside data. We previously detailed the ways that Eq. (6.4) is inconsistent with the diopside data, but in some respects the equation is consistent with these data. Most importantly, both the equation and the data have a region where $d\log(r)/d\mathrm{pH} < 0$. The first term on the *rhs*, $k_{H^+} \cdot 10^{-n \cdot \mathrm{pH}}$, imparts this behavior to Eq. (6.4) so it is reasonable to suppose that our rate equation for diopside should include something like this term. The second term on the *rhs*, $k_{OH^-} \cdot 10^{m \cdot (\mathrm{pH}-14)}$, imparts positive slope to Eq. (6.4) and we can, therefore, obtain a form that more closely resembles the diopside data by replacing this term with a constant (i.e., by setting $m = 0$):

$$r = k_{H^+} \cdot 10^{-n \cdot \mathrm{pH}} + k_0 \tag{6.12}$$

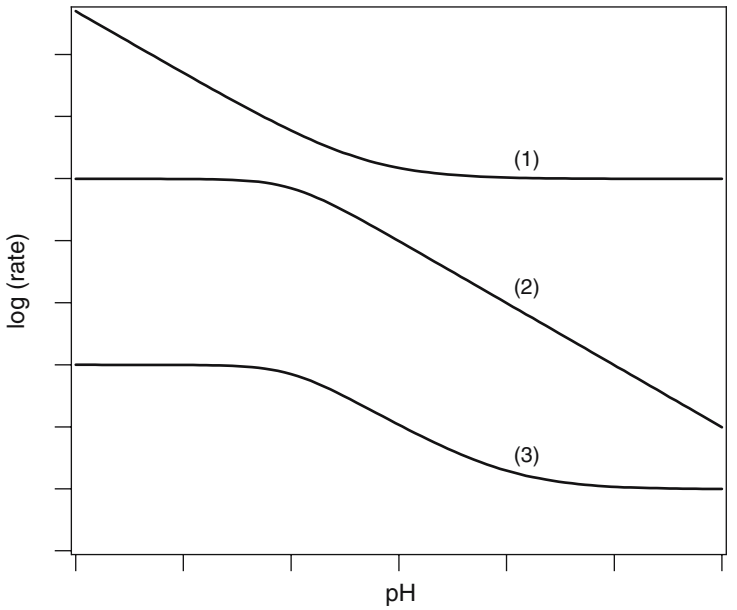

Fig. 6.3 Characteristic form of Eq. (6.12), expression (15), and Eq. (6.17) displayed as curves 1, 2, and 3, respectively

where k_0 is the rate constant for pH-independent dissolution. The characteristic shape of Eq. (6.12) is shown as curve (1) in Fig. 6.3.

Equation 12 has negative slope and an asymptote at high pH as do the data in Fig. 6.2, but Eq. (6.12) does not approach an asymptote at low pH. Since the low pH behavior of Eq. (6.12) is controlled by the first term on the *rhs*, we can impart correct behavior to the equation by modifying this term so that it approaches an asymptote. Note that an expression of the form:

$$k_{H^+} \cdot 10^{-n \cdot \mathrm{pH}} \cdot f(\mathrm{pH}) \tag{6.13}$$

will behave asymptotically at low pH if and only if $f(\mathrm{pH})$ behaves like $1/10^{-n \cdot \mathrm{pH}}$ as pH becomes small. One such function is

$$f(\mathrm{pH}) = \frac{1}{(\alpha \cdot 10^{-\mathrm{pH}} + \beta)^n} \tag{6.14}$$

where α and β are constants. With Eq. (6.14), expression Eq. (6.13) becomes

$$k_{H^+} \left(\frac{10^{-\mathrm{pH}}}{\alpha \cdot 10^{-\mathrm{pH}} + \beta} \right)^n \tag{6.15}$$

The behavior of this expression is shown by curve (2) in Fig. 6.3. Substituting expression (15) for the first term on the *rhs* of Eq. (6.12) gives the following rate law:

$$r = k_{H^+} \cdot \left(\frac{10^{-\mathrm{pH}}}{\alpha \cdot 10^{-\mathrm{pH}} + \beta} \right)^n + k_0 \tag{6.16}$$

The characteristic shape of Eq. (6.16) is shown as curve (3) in Fig. 6.3 and matches all the features of the diopside dissolution rate data in Fig. 6.2 and Table 6.2. Notice also that Eq. (6.16) can be written as

$$r = \hat{k}_{H^+} \cdot \left(\frac{K \cdot a_{H^+}}{K \cdot a_{H^+} + 1} \right)^n + k_0 \tag{6.17}$$

where $\hat{k}_{H^+} = k_{H^+}/\alpha^n$ and $K = \alpha/\beta$. The expression inside the parentheses in Eq. (6.17) is commonly applied to the kinetics of heterogeneous reactions where the reaction rate can become limited by the availability of adsorption sites on the reacting surface. Such expressions are typically derived on mechanistic grounds (cf., Hougen and Watson, 1943; Langmuir, 1918), but here we have achieved the same result on purely empirical grounds.

6.3 Parameter Estimation

Knowledge of the rate laws that match an experimental data set can be useful even without specific numerical values for the parameters in the rate law. For many purposes, however, it is desirable to estimate values of rate parameters from collected rate data. These parameters can be used for comparison of multiple experiments, even when those experiments are performed in different settings. Estimated kinetic parameters are also useful for making predictions and for examining lack of agreement between a rate law and experimental data. Parameter estimation usually involves some sort of data fitting (or regression) and error analysis usually involves statistics that are derived from the fitting. There are many techniques for affecting and analyzing a fit, each with a specific range of applicability. In the following, we describe the techniques that we have found useful in analyzing dissolution kinetics, but many of these techniques are useful for treating the kinetics of geochemical reactions in general.

6.3.1 Error Minimization

Suppose that we have N measurements of a dependent variable, y_i, at different values of an independent variable, x_i. In the cases discussed above, for example, the y_i are the mineral dissolution rates and the x_i are the values of pH. Further, suppose that the y_i are composed of some model (like a rate law) that describes the functional

dependence on the x_i and some measurement error, ε_i:

$$y_i = y(x_i;\Theta) + \varepsilon_i \tag{6.18}$$

where Θ denotes a vector of any adjustable parameters (rate constants, reaction orders, etc.) contained in the model. Assuming that we have already selected the form of $y(x_i;\Theta)$, the basic goal in fitting data is to adjust the parameters in Θ so that agreement between model and data is maximized. Stated another way, we seek values for Θ such that the ε_i are minimized in some conglomerate sense. This is commonly done by minimizing the sum of square errors (SSE), where the difference between the model and the measured datum (i.e., ε_i) is squared and these squared errors are summed:

$$\mathrm{SSE}(\Theta) = \sum_{i=1}^{N} (y_i - y(x_i;\Theta))^2 \tag{6.19}$$

This approach is known as ordinary least squares (OLS) and SSE(Θ) is referred to as the objective function. It is important to note that we have assumed that the measurements of independent variable, x_i, contain no error. This assumption is valid when the error in the dependent variable, y_i, is much greater than the error in the independent variable. When the assumption is invalid, the techniques described in this chapter can be used only as a first approximation.

There are objective functions other than SSE that are sometimes used in data fitting (e.g., the mean absolute deviation), but the sum of square errors and its extension, χ^2 (discussed below), are by far the most prevalent. This is because OLS (and weighted least squares) generates a maximum likelihood estimate of Θ when the measurement error on each y_i is normally distributed with zero mean. The likelihood is defined as the probability that the set of measurements arose from a particular set of parameter values. The likelihood may be written symbolically as $P(\{y_i\}|\Theta)$, where the notation $P(a|b)$ denotes the probability that "a" is true given that "b" is true. Since the $\{y_i\}$ are fixed, the likelihood is a function only of the parameters, Θ, and the goal is to find values for the parameters that produce maximum likelihood. Assuming that the measurement errors are independently and identically distributed (*iid*) according to density function $g(\varepsilon)$, the likelihood can be written as:

$$P(\{y_i\}|\Theta) = \prod_{i=1}^{N} g(\varepsilon_i) = \prod_{i=1}^{N} g(y_i - y(x_i;\Theta)) \tag{6.20}$$

When the ε_i are normally distributed with zero mean and σ variance – $\mathrm{N}(0,\sigma^2)$ – Eq. (6.20) becomes

$$P(\{y_i\}|\Theta) = \left(2\pi\sigma^2\right)^{-N/2} \prod_{i=1}^{N} \exp\left(-\frac{1}{2}\frac{(y_i - y(x_i;\Theta))^2}{\sigma^2}\right) \tag{6.21}$$

The product of exponentials of various arguments is equal to the exponential of the sum of the arguments, giving:

$$P(\{y_i\}|\Theta) = \left(2\pi\sigma^2\right)^{-N/2} \exp\left(-\frac{1}{2\sigma^2}\sum_{i=1}^{N} (y_i - y(x_i;\Theta))^2\right) \tag{6.22}$$

Notice that the argument of the exponential function in Eq. (6.22) is proportional to the negative sum of square errors. Therefore, the likelihood is maximized when Θ is chosen to minimize SSE.

When the measurement errors are not *iid* and $\mathrm{N}(0,\sigma^2)$, OLS does not generate a maximum likelihood estimate. Owing to the central limit theorem, however, error distributions comprised of a sum of many small random deviations are almost always normal. Furthermore, OLS produces a quasi-likelihood estimate for error distributions that are symmetric about the mean and not heavy-tailed (Seber and Wild, 2003).

The above maximum likelihood derivation is readily generalized to the case where the measurement errors, ε_i, are normally and independently distributed with zero mean, but not identically distributed. In this case, the maximum likelihood estimate is found by minimizing χ^2:

$$\chi^2(\Theta) = \sum_{i=1}^{N} \left(\frac{y_i - y(x_i;\Theta)}{\sigma_i} \right)^2 \tag{6.23}$$

where σ_i is the standard deviation on the i-th measurement. The σ_i in Eq. (6.23) act as weights on each datum and, therefore, minimizing χ^2 is known as weighted least squares (WLS). Note that when the σ_i are identical, minimizing χ^2 (Eq. (6.23)) is equivalent to minimizing SSE (Eq. (6.19)). Calculating χ^2 requires knowledge of the variance on each measurement which usually entails multiple measurements of the dependent variable (y) at each value of the independent variable (x). Given the number of additional measurements that this approach requires, it not advisable unless the σ_i are expected to be highly variable – even then, as we shall see in Sect. 6.3.5, employing a parametric model for the variance may make more efficient use of a given data set.

6.3.2 Linear Regression

Given some model, $y(x_i;\Theta)$, the task at hand is to find values of the parameter(s), Θ, so that $\chi^2(\Theta)$ is at a global minimum. Local minima of $\chi^2(\Theta)$ can be found setting the derivative(s) with respect to Θ equal to zero. Once we find all the possible local minima we take the global minimum to be the smallest of the local minima. Unfortunately, the equations generated from $\partial\chi^2(\Theta)/\partial\Theta = 0$ cannot be solved analytically for arbitrary $y(x_i;\Theta)$. When $y(x_i;\Theta)$ is linear, however, analytical solutions are readily available.

Let $y(x_i;\Theta)$ be a linear function with slope, m, and intercept, b:

$$y(x_i;\Theta) = m \cdot x_i + b \tag{6.24}$$

Note that $\Theta = (m,b)$ in this case. Substituting Eq. (6.24) into Eq. (6.23) gives:

$$\chi^2(\Theta) = \sum_{i=1}^{N} \left(\frac{y_i - m \cdot x_i - b}{\sigma_i} \right)^2 \tag{6.25}$$

The partial derivatives of $\chi^2(\Theta)$ with respect to m and b are

$$\frac{\partial \chi^2(\Theta)}{\partial m} = -2\sum_{i=1}^{N} \frac{x_i \cdot (y_i - m \cdot x_i - b)}{\sigma_i^2} \tag{6.26}$$

$$\frac{\partial \chi^2(\Theta)}{\partial b} = -2\sum_{i=1}^{N} \frac{y_i - m \cdot x_i - b}{\sigma_i^2} \tag{6.27}$$

Setting Eqs. (6.26) and (6.27) equal to zero and dividing by -2 gives two equations in two unknowns (m and b).

$$0 = \sum_{i=1}^{N} \frac{x_i \cdot y_i}{\sigma_i^2} - m \cdot \sum_{i=1}^{N} \frac{x_i^2}{\sigma_i^2} - b \cdot \sum_{i=1}^{N} \frac{x_i}{\sigma_i^2} = S_{xy} - m \cdot S_{xx} - b \cdot S_x \tag{6.28}$$

$$0 = \sum_{i=1}^{N} \frac{y_i}{\sigma_i^2} - m \cdot \sum_{i=1}^{N} \frac{x_i}{\sigma_i^2} - b \cdot \sum_{i=1}^{N} \frac{1}{\sigma_i^2} = S_y - m \cdot S_x - b \cdot S \tag{6.29}$$

On the *rhs* of Eqs. (6.28) and (6.29) we have employed the following definitions:

$$\begin{aligned} S = \sum_{i=1}^{N} \frac{1}{\sigma_i^2}; S_x = \sum_{i=1}^{N} \frac{x_i}{\sigma_i^2}; S_y = \sum_{i=1}^{N} \frac{y_i}{\sigma_i^2} \\ S_{xx} = \sum_{i=1}^{N} \frac{x_i^2}{\sigma_i^2}; S_{xy} = \sum_{i=1}^{N} \frac{x_i \cdot y_i}{\sigma_i^2} \end{aligned} \tag{6.30}$$

The system defined by Eqs. (6.28) and (6.29) admits a single solution which is given as follows:

$$m = \frac{S \cdot S_{xy} - S_x \cdot S_y}{S \cdot S_{xx} - (S_x)^2} \tag{6.31}$$

$$b = \frac{S_{xx} \cdot S_y - S_x \cdot S_{xy}}{S \cdot S_{xx} - (S_x)^2} \tag{6.32}$$

Since there is a single local minimum in $\chi^2(\Theta)$, Eqs. (6.31) and (6.32) define the global minimum and, therefore, the best linear fit of the data, (y_i, x_i), under the conditions on the error distribution discussed above. Notice that when the measurement errors are identically distributed $\sigma_i = \sigma$ and a σ^2 term can be factored out of both the numerators and denominators of Eqs. (6.31) and (6.32). In this case the slope and intercept of the best fit line are independent of the distribution on the measurement error. In Sects. 6.4 and 6.5 we will turn our attention to estimating goodness-of-fit and parameter uncertainty; there we will find, contrary to the above result, that the error distribution is critical even under identical distributions.

Figure 6.4 shows compiled biotite dissolution rates plotted as $\log(r)$ versus pH. The data appear to be linear, at least to a first approximation; hence we write the following:

$$y(pH_i; \Theta) = \log(k_{H^+}) - n \cdot \mathrm{pH}_i \tag{6.33}$$

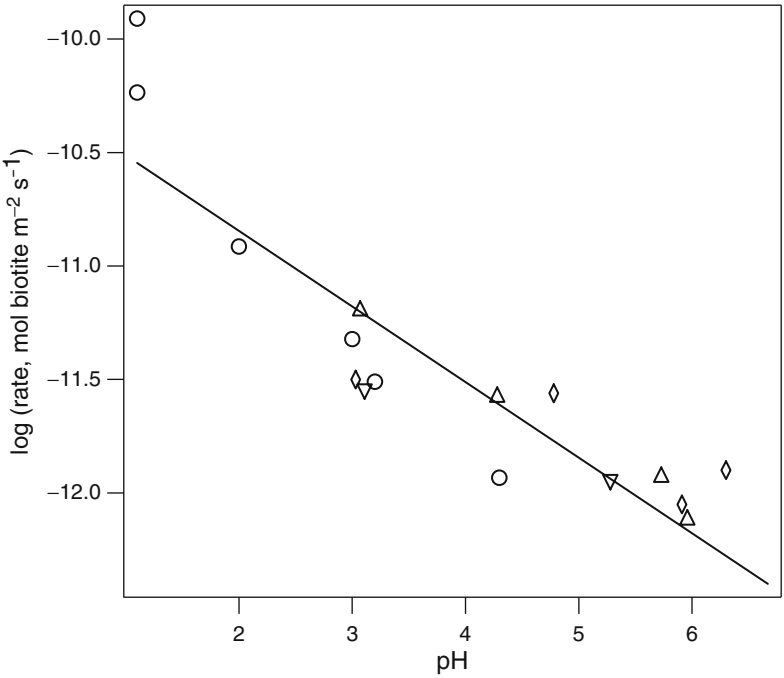

Fig. 6.4 Surface area-normalized biotite dissolution rates as a function of pH. ○ Kalinowski and Schweda (1996), ▽ Acker and Bricker (1992) ground <149 μm, □ Acker and Bricker (1992) ground 149–420 μm, ◇ Acker and Bricker (1992) broken 149–420 μm, △ Acker and Bricker (1992) ground >420 μm. Solid line represents the linear regression of log-transformed data. (See Appendix for data)

where the slope, $-n$, and the intercept, $\log(k_{H^+})$, are fitting parameters to be found according to Eqs. (6.31) and (6.32). The rate law implied by Eq. (6.33) is just the proton-promoted dissolution term from Eq. (6.3).

$$r(pH_i;\Theta) = k_{H^+} \cdot 10^{-n \cdot \mathrm{pH}_i} \tag{6.34}$$

The data given in Fig. 6.4 do not contain any information about the σ_i. We can proceed, however, by assuming that the measurement errors are *iid* (i.e., $\sigma_i = \sigma$, for all i). Applying Eqs. (6.31) and (6.32) to these data gives $-n = 0.333$ and $\log(k_{H^+}) = -10.2$; this is the best fit line to the log-transformed data under the assumptions discussed above. These assumptions – that the data are linear with respect to pH and that the error distributions are *iid* and $\mathrm{N}(0,\sigma^2)$ – still need to be checked. The basic tool for checking assumptions is the residual plot which is discussed in Sect. 6.4.

6.3.3 Non-Linear Fitting

In general, non-linear models do not permit closed form solutions for the minimization of χ^2. It is possible, however, to find parameter estimates numerically using

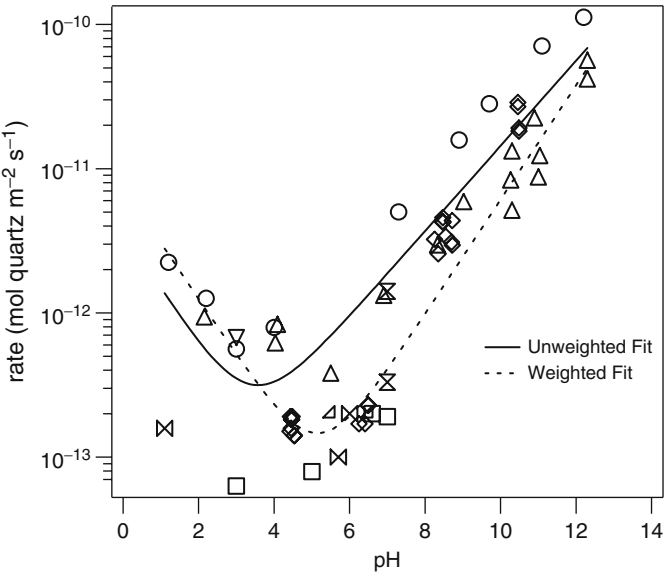

Fig. 6.5 Surface area-normalized quartz dissolution rates as a function of pH. ○ Wollast and Chou (1988), □ Bennett et al. (1988), △ Brady and Walther (1990), ⋈ Bennett (1991), ♢ House and Orr (1992), ◿ Berger et al. (1994), ▽ Casey et al. (1990), ⧖ Tester et al. (1994) column data. Solid and dashed lines represent non-linear ordinary and weighted least squares fits of Eq. (6.8), respectively. (See Appendix for data)

an iterative minimization routine (Dennis and Schnabel 1996; Draper and Smith, 1966). The details of iterative minimization are outside the scope of this chapter, but the basic idea is to (i) begin with an initial guess for Θ, (ii) evaluate $\chi^2(\Theta)$ in a small region around the initial guess, (iii) choose a new value of Θ that improves the value of χ^2 (i.e., makes it smaller), and (iv) repeat (*i-iii)* until χ^2 cannot be further improved. There is no assurance that a minimum found by a numerical routine is the global minimum and, therefore, caution should be exercised in the selection of initial guesses, perhaps even trying a variety of initial guesses to see if they converge to a common value.

Any good data analysis software package will include a selection of minimization routines and often times some that are specifically designed for χ^2 minimization. Some of the more common algorithms are the Gauss–Newton method (Hartley, 1961), the Levenberg–Marquardt method (Levenberg, 1944; Marquardt, 1963), and the full Newton-type methods (Dennis et al., 1981a,b). Of these, Levenberg–Marquardt is the most generally applicable method for curve fitting, though other methods may work well when Levenberg–Marquardt either fails to converge or requires too great a computational cost (e.g., when the number of adjustable parameters is very large). In the absence of a canned minimization routine, it is relatively straightforward to develop a serviceable code from scratch. The reference work "Numerical Recipes in C" (Press et al., 1992) provides a good basis from which to start such a project.

An example where non-linear fitting is needed is shown in Fig. 6.5 where compiled rate data are plotted versus pH for quartz dissolution in semi-log format. The

key features of these data are essentially the same as those for the albite dissolution data discussed above: two linear regions (on a semi-log plot) at high and low pH values and a minimum between the linear regions. We can therefore adopt the same rate law for these data as was suggested for the albite data – that is, Eq. (6.4). Substituting the rate law into Eq. (6.19) gives an expression for SSE:

$$SSE\left(\Theta\right) = \sum_{i=1}^{N} \left(r_i - k_{H^+} \cdot 10^{-n \cdot \mathrm{pH}} - k_{OH^-} \cdot 10^{m \cdot (\mathrm{pH}-14)} \right)^2 \tag{6.35}$$

where r_i are the measured dissolution rates (not log-transformed) and $\Theta = (k_{H^+}, n, k_{OH^-}, m)$. Parameter values that minimize Eq. (6.35) cannot be found analytically, so an iterative procedure is necessary. Before we can iterate, though, we need initial guesses for the parameters. A good way to generate initial guesses is to estimate the magnitudes and locations of key features. For the quartz data in Fig. 6.5, imagine that the data consist of two linear segments, one to the right of pH = 5 and the other to the left. The slope and pH = 0 intercept of the line to the left are good estimates of n and k_{H^+} while the slope and pH = 14 intercept of the line to the right give estimates of m and k_{OH^-}. Since the initial guesses do not need to be more precise than an order of magnitude, estimating the values graphically is usually sufficient. From Fig. 6.5 we obtained the following initial guesses:

$$\begin{aligned}
n^{guess} &= \frac{\log\left(r_{\mathrm{pH}\approx 2}\right) - \log\left(r_{\mathrm{pH}\approx 5}\right)}{2-5} \approx \frac{(-12)-(-13)}{2-5} = -\frac{1}{3} \\
k_{H^+}^{guess} &= r_{\mathrm{pH}\approx 0} \approx 2 \times 10^{-11} \\
m^{guess} &= \frac{\log\left(r_{\mathrm{pH}\approx 5}\right) - \log\left(r_{\mathrm{pH}\approx 12}\right)}{5-12} \approx \frac{(-13)-(-10)}{5-12} = -\frac{3}{7} \\
k_{OH^-}^{guess} &= r_{\mathrm{pH}\approx 14} \approx 1 \times 10^{-9}
\end{aligned} \tag{6.36}$$

Starting with these guesses and minimizing Eq. (6.35) with the Levenberg–Marquardt method generates the fitted curve shown in Fig. 6.5 as a solid line.

In subsequent sections we will discuss techniques for analyzing the success of a fit, but for now visual inspection will suffice. First, notice that the fit in Fig. 6.5 captures the key features of the data (two linear regions with a minimum between them). Second, notice that the model results replicate the scale of the data, generally falling within an order of magnitude of the measurements. Third, however, notice that the fitted model deviates from the data in a systematic fashion in the pH < 7 range, wherein the model overestimates the rates for $4 <$ pH < 7 and underestimates the rate for pH < 4. This type of systematic deviation can arise when the model does not fully capture the structure of the data. In this case, however, the deviation is due to the assumption – implicit in Eq. (6.19) – that the measurement error distributions (σ_i) are the same for each measurement.

As an alternative to the assumption of constant error, suppose that the σ_i are proportional to the measurements. That is, that the measurement error is constant

relative to the magnitude of the measurement.

$$\sigma_i = s \cdot y_i \tag{6.37}$$

where s is the (constant) percent error. Substituting Eq. (6.37) into the expression for χ^2, Eq. (6.23), gives

$$\chi^2(\Theta) = \frac{1}{s^2} \sum_{i=1}^{N} \left(\frac{y_i - y(x_i;\Theta)}{y_i} \right)^2 \tag{6.38}$$

Since s is a constant, parameter estimates can be found by minimizing $s^2 \cdot \chi^2(\Theta)$; this is equivalent to performing a weighted least squares (WLS) fit with weights equal to (or, proportional to) the measured values. The results of this approach to fitting the quartz dissolution data are shown in Fig. 6.5 as a dashed line. Compared to the OLS fit, the WLS approach does a better job of locating the minimum rate near pH $\approx$ 5. Notice, however, that when there are multiple rate measurements near a single pH, the WLS fit tends toward the smallest measurement. The reason for this is obvious from Eq. (6.38); since the weighting is inversely proportional to the magnitude of the measurement, the smaller measurements receive greater preference in terms of their contribution to χ^2. In Sect. 6.3.5 we will describe a better technique for handling data with relative error distributions – iteratively reweighted least squares fitting (IRLS). For now, just note that the assumptions that we make about the error structure are an important part of fitting data, nearly as important as selecting an appropriate fitting equation.

6.3.4 Linear Fitting of Log Transformed Data versus Non-linear Fitting

Because of the preponderance of exponential functions (e.g., the Arrhenius equation) and power laws (e.g., Eq. (6.34)) in chemical kinetics, logarithmically transformed rate data are often found to behave in a linear fashion. Historically, chemists have developed numerous graphical data analysis techniques based on such linear transformations. In these methods, transformed data are plotted and the slope and intercept are estimated directly from the graph. To obtain physically meaningful quantities, the slope and intercept must then be processed with an inverse transform. In recent decades, many chemists have adapted graphical techniques to the digital computer by performing linear regression on transformed data as a more precise means of generating estimates of the slope and intercept. This approach – as exemplified in our treatment of Fig. 6.4 above – takes advantage of the relative simplicity of linear fitting and maintains continuity with the older, graphical approach. Among the disadvantages of this approach is a lack of general applicability. Data such as those displayed in Fig. 6.5 where the log-transform produces multiple linear segments could not be handled with a single linear equation, even though linear behavior is evident.

An alternative approach is to fit a non-linear model to untransformed data.

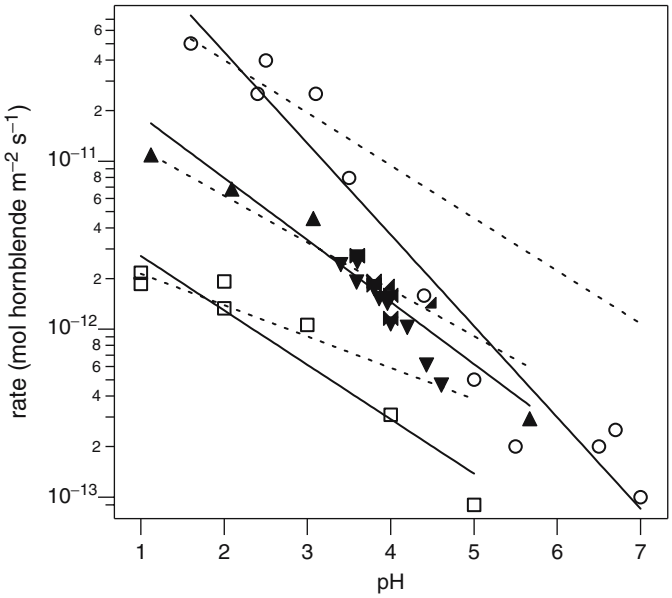

Fig. 6.6 Surface area-normalized hornblende dissolution rates as a function of pH. ○ Sverdrup (1990), ▲ Givens and Brantley (unpublished), ▼ Zhang (1990), ⋈ Zhang et al. (1996), ◢ Swoboda-Colberg and Drever (1993), □ Frogner and Schweda (1998). Solid lines represent linear fitting of log-transformed data and dashed lines represent non-linear fitting of untransformed data. Both fits were based on Eq. (6.6) and employed square error minimization. (See Appendix for data)

Non-linear fitting is fully general since any model can be employed; however, it is computationally more intensive since the minimum error cannot be found using linear algebra and care must be taken to ensure that a non-linear routine is converging to the global minimum. Additionally, non-linear fitting can produce markedly different results from the linear transformation approach. Reasons for this – chiefly, heterogeneity in the variance where the σ_i vary systematically – are discussed below. Many data analysis software packages support both linear and non-linear fitting and, therefore, both techniques should be readily accessible to those researching the kinetics of geochemical reactions.

In cases where both non-linear fitting and linear fitting of log-transformed data can be applied, the resulting parameter estimates may be significantly different. Figure 6.6 shows compiled rate data for hornblende dissolution as a function of pH. The data appear to be roughly linear on a semi-log plot so it is possible to fit Eq. (6.34) to the data by either linear or non-linear techniques. Since the (Frogner and Schweda, 1998) data appear to diverge from the remainder of the data, we have treated them separately. The remainder of the data was fit together with the (Cygan et al., 1989) data excluded due to unusual aspects of experimental protocol. Visually, the linear fits (solid lines) and the non-linear fits (dashed lines) produce very different results. In particular, the slopes (n) produced by non-linear fitting are systematically smaller than those produced by the linear approach.

To understand the reason for this discrepancy, consider the error structure that is implicit in the two approaches. In the non-linear fit, we assume that the measured rate is equal to the model fit plus (or minus) a random measurement error term, which, assuming the model given by Eq. (6.34) can be written as follows.

$$r_i = r(\mathrm{pH}_i;\Theta) + \varepsilon_i = k_{\mathrm{H}^+}\left(10^{-\mathrm{pH}_i}\right)^n + \varepsilon_i \tag{6.39}$$

In this context, the task of least squares fitting is to find the values of k_{H^+} and n that minimize the sum of square errors.

$$SSE = \sum_{i=1}^{N} \varepsilon_i^2 \tag{6.40}$$

As noted above, least squares fitting produce a maximum likelihood estimate if the measurement errors (ε_i) are independently and identically distributed in a normal fashion (with zero mean):

$$P(\varepsilon_i) = \frac{1}{\sigma\sqrt{2\pi}} e^{-\varepsilon_i^2/2\sigma^2} \tag{6.41}$$

When fitting a line to the log transformed data, we minimized the square error between the log of the measured values and the linear equation. The analogue to Eq. (6.39) for linear fitting is

$$log(r_i) = log(r(\mathrm{pH}_i;\Theta)) + \hat{\varepsilon}_i = log(k_{diss}) - n \cdot \mathrm{pH}_i + \hat{\varepsilon}_i \tag{6.42}$$

Linear fitting selects the values of $\log(k_{\mathrm{H}^+})$ and n that minimize the sum of square errors as defined by Eq. (6.42).

$$SSE = \sum_{i=1}^{N} \hat{\varepsilon}_i^2 \tag{6.43}$$

The implicit assumption in fitting log transformed data, then, is that the $\hat{\varepsilon}_i$, rather than the ε_i, are independently and identically distributed in a normal fashion (i.e., Eq. (6.41) with $\hat{\varepsilon}_i$ substituted for ε_i).

We may compare Eqs. (6.42) and (6.39) by inverting the logarithm in Eq. (6.42) giving:

$$r_i = k_{\mathrm{H}^+} 10^{-n \cdot \mathrm{pH}_i} 10^{\hat{\varepsilon}_i} \tag{6.44}$$

The error structure in Eq. (6.44) is multiplicative rather than additive as it was in Eq. (6.39). Linear fitting of log-transformed data, therefore, implicitly assumes that the measured data contain constant relative error (i.e., constant percent error), while non-linear least squares is based on the assumption of constant absolute error. This observation is borne out by the results in Fig. 6.6 where the non-linear fits appear to be dominated by a few high rate points while the log-transformed fits more closely match the magnitudes of the measured data throughout the pH range.

From the preceding discussion, we may conclude that linear fitting of log-transformed data is more robust than non-linear square error minimization when

constant relative errors can be assumed. There are, however, some problems with this approach. First, we typically expect the untransformed measurement error distribution to be symmetric (most commonly, a normal distribution). If this is the case, then the distribution for the log-transformed errors will be skewed towards smaller (i.e., negative) $\hat{\varepsilon}_i$, thus causing the log-transformed fit to tend toward an underestimate of the dissolution rate. Second, even under the unlikely assumption that the $\hat{\varepsilon}_i$ are normally distributed, a transformation bias arises when using the results of a log-transformed fit to predict absolute rate values such that the log-transformed fit provides an estimate of the median rate at each pH, rather than the expected value (Miller, 1984). This bias also causes the log-transformed fit to, on average, produce an underestimate of the dissolution rate.

6.3.5 Variance Heterogeneity

While each of the biases in log-transformed fitting can be corrected without abandoning the log-transform, in most cases it is better to adapt non-linear least squares to the case of constant relative error. This problem is an example of a more general class of problems wherein the variance (σ^2) in the measurement error is heterogeneous. The basis for fitting data with heterogeneous error (sometimes called heteroscedastic data) is the weighted least squares method discussed above (see Eq. (6.23)), where each measurement is weighted by its corresponding standard deviation. The most straightforward application of Eq. (6.23) is to calculate averages and standard deviations from a number of replicate experiments at each value of the independent variable (i.e., at each pH_i). In most cases where replicate experiments are performed, however, the sample size is too small (e.g., experiments only performed in triplicate) to accurately estimate σ_i. Therefore, most data will require methods that depend on estimates of the error distribution based on an assumed functional relationship between σ_i and the measured data, (y_i, x_i).

We have already considered two such functional relationships. In OLS fitting, where Eq. (6.19) is minimized, we assumed that $\sigma_i = \text{constant}$; that is, we assumed homoscedasticity. In Eq. (6.37), we assumed the functional relationship given in Eq. (6.36) which is a particular kind of heteroscedasticity. In both of these cases, we assumed an exact relationship between σ_i and r_i. That is, given our (assumed) model for the variance, we could calculate each σ_i once and for all from each r_i and then proceed with WLS fitting (this statement requires one minor modification: we really calculated the σ_i to within a constant of proportionality – e.g., s in Eq. (6.37) – that could be factored out of the summation; precise knowledge of this constant is not needed for parameter estimation, but will be needed when we calculate confidence intervals in Sect. 6.5).

When an exact relationship between σ_i and y_i is unknown, a parametric model can be used where the σ_i are functionally dependent on the observations and some set of parameters, Ω:

$$\sigma_i = f(y_i, x_i; \Omega) \tag{6.45}$$

The parameters in Ω must then be determined by the fitting procedure along with the parameters in the fitting equation, Θ. For example, we might be unsure if a particular data set is better described by constant absolute error or constant relative error. In this case we could assume that the σ_i obey a power law with respect to r_i.

$$\sigma_i = s \cdot r_i^{\tau} \tag{6.46}$$

where the constant, τ, will be $= 1$ for constant relative error and $= 0$ for constant absolute error. Parametric variance models, while broadly applicable, must be employed with significant care since model misspecification in the rate law can be compensated for in the variance model (or *vice versa*) making it difficult to determine if the model is appropriate for the given data (Huet et al., 2004).

Due to considerations associated with the likelihood function (see Sect. 6.3.1), fitting with weights that evolve over the course of the fit cannot be accomplished by substituting the variance model, into the expression for χ^2 given by Eq. (6.23). Instead, a routine known as iteratively reweighted least squares should be used. Consider the likelihood function (see Eqs. (6.20–6.22)) formed using Eq. (6.41) with Eq. (6.46) substituted for σ:

$$\begin{aligned} P(\{r_i\}|\Theta,\tau) &= \prod_{i=1}^{N} \frac{1}{s \cdot r_i^{\tau}\sqrt{2\pi}} \exp\left(-\frac{1}{2}\frac{(r_i - r(\mathrm{pH}_i;\Theta))^2}{(s \cdot r_i^{\tau})^2}\right) \\ &= \left(2\pi \cdot s^2\right)^{-N/2} \cdot \left(\prod_{i=1}^{N} \frac{1}{r_i^{\tau}}\right) \cdot \left(\prod_{i=1}^{N} \exp\left(-\frac{1}{2}\frac{(r_i - r(\mathrm{pH}_i;\Theta))^2}{(s \cdot r_i^{\tau})^2}\right)\right) \\ &= \left(2\pi \cdot s^2\right)^{-N/2} \cdot \left(\prod_{i=1}^{N} \frac{1}{r_i^{\tau}}\right) \cdot \exp\left(-\frac{1}{2} \cdot \sum_{i=1}^{N} \frac{(r_i - r(\mathrm{pH}_i;\Theta))^2}{(s \cdot r_i^{\tau})^2}\right) \end{aligned} \tag{6.47}$$

Note that the likelihood is here a function of both Θ and τ. Taking the natural logarithm of Eq. (6.47) gives:

$$\ln\left(P(\{r_i\}|\Theta,\tau)\right) = -N \cdot \ln\left(s \cdot \sqrt{2\pi}\right) - \tau \cdot \sum_{i=1}^{N} \ln(r_i) - \frac{1}{2} \cdot \sum_{i=1}^{N} \frac{(r_i - r(\mathrm{pH}_i;\Theta))^2}{(s \cdot r_i^{\tau})^2} \tag{6.48}$$

Observe that the last term on the *rhs* is essentially Eq. (6.46) substituted into the expression for χ^2. However, τ also appears in the second term and, therefore, finding the values of Θ and τ that minimize χ^2 will not maximize the likelihood function.

We could now abandon the WLS approach and instead seek to maximize Eq. (6.48). This approach, while perfectly valid, tends to produce function maximization problems of inordinate computational difficulty. Fortunately, for a very general class of heteroscedastic error distributions, χ^2 minimization can be adapted using a routine known as iteratively reweighted least squares (IRLS) (Green, 1984). In this method, we make an initial guess about the weights (e.g., that $\sigma_i = 1$ for all i), perform WLS with those (fixed) weights, and then calculate new weights on the basis of the fitting results. This procedure is iterated until the fitting results (and,

therefore, the weights) converge, to within some tolerance, from one iteration to the next. IRLS usually converges after just a few reweightings, but in certain cases it does not converge at all. When this happens, it may be possible to improve the convergence properties by performing the reweighting after a step or two in the WLS algorithm. Reweighing after convergence of WLS and after a fixed number of WLS steps are both justified under identical conditions (Charnes et al., 1976; Seber and Wild, 2003).

Recall the problem that we encountered when fitting the quartz data with a relative error model in Sect. 6.3.3: the weighting based on Eq. (6.37) over-emphasized the smaller members of a group of replicate or near replicate measurements. An alternative approach is to model σ_i as a function of the independent variable (e.g., pH_i) rather than the rate measurements themselves. Taking, again, the case of constant relative error as an example, we can formulate a variance model as:

$$\sigma_i = s \cdot r\left(\mathrm{pH}_i; \Theta\right) \tag{6.49}$$

Note that the σ_i are a function of the predicted rates (rather than the measured rates, as was the case in Eq. (6.37). Reiterating the above discussion, a maximum likelihood estimator of Θ cannot be found by substituting Eq. (6.49) into the expression for χ^2. Instead, after obtaining a WLS fit with some arbitrary initial guesses for the σ_i, we apply WLS recursively to the following expression:

$$\chi^2\left(\Theta^{k+1}\right) = \frac{1}{s^2}\sum_{i=1}^{N}\left(\frac{y_i - y\left(x_i; \Theta^{k+1}\right)}{y\left(x_i; \Theta^{k}\right)}\right)^2 \tag{6.50}$$

where Θ^k refers to the parameters generated in the k-th application of WLS and s can be ignored for fitting purposes since it is a constant.

The difference between using Eq. (6.37) for the error structure – weighting with measured data – and using Eq. (6.49) – weighting with model predictions – can be seen in Fig. 6.7 where Eq. (6.34) has been fit to forsterite dissolution rate data as a function of pH under both weighting schemes. The Eq. (6.37) weighted fit is systematically biased toward the lower range of measured rates, while the Eq. (6.49) weighted fit appears to be a more reasonable estimate of the average rate across the pH range. In this case, the two weighting schemes yield fairly similar fitting results, but in other cases (e.g., the quartz data in Fig. 6.5) significant disagreement is possible. Henceforth we will take IRLS fitting with relative error to refer to the application of Eq. (6.50) or its multivariate analogue.

6.3.6 Multiple Independent Variables

The fitting techniques described above all deal with the situation where a single dependent variable (e.g., rate) is a function of a single independent variable (e.g., pH). The kinetics of geochemical reactions and chemical kinetics in general are really

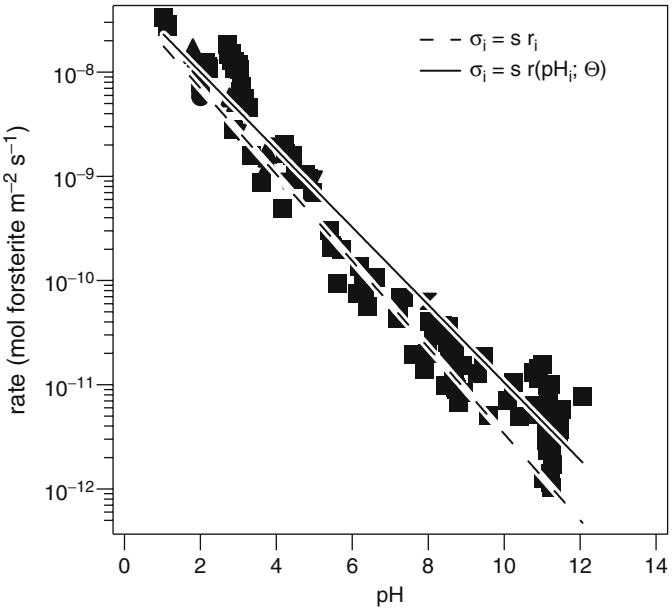

Fig. 6.7 Surface area-normalized forsterite dissolution rates as a function of pH. ■ Pokrovsky and Schott (2000), • Oelkers (2001), ▲ Rosso and Rimstidt (2000), ▼ Wogelius and Walther (1992), ⧗ Brady and Walther (1989). Data plotted as filled symbols were fit with weights proportional to r_i (dashed line) and using the IRLS technique assuming constant relative error. (See Appendix for data)

a function of a number of independent variables. In addition to pH, mineral dissolution rates depend on temperature, solute concentrations, mineral composition, surface roughness, and a host of other minor variables.

One approach to handling multiple dimensional rate data is to fit – using the mono-variate techniques described above – subsets of the data where all but one of the independent variables remain approximately constant. Figure 6.8a and b shows an example of such an analysis for basalt dissolution rate data collected at a variety of pH's and temperatures (Oelkers and Gislason, 2001). In Fig. 6.8a, we have fit the rate law given in Eq. (6.4) to three constant temperature subsets of the data, T = 280, 303, and 323 K assuming constant relative error and using the IRLS method. In Fig. 6.8b, we have fit Eq. (6.51) (the Arrhenius equation, see Chap. 1) to the subset of data measured at pH ≈ 5 using the same method:

$$r_i = A \exp\left(\frac{-E_a}{R \cdot \mathrm{T}_i}\right) \tag{6.51}$$

where r_i is the dissolution rate, T_i is the temperature (in K), R is the gas constant ($= 8.314\,\mathrm{J\,K^{-1}\,mol^{-1}}$), and A (the pre-exponential factor) and E_a (the activation energy) are treated as fitting parameters. Given that Eq. (6.4) describes the pH dependence of the data in Fig. 6.8 and Eq. (6.51) describes the temperature dependence,

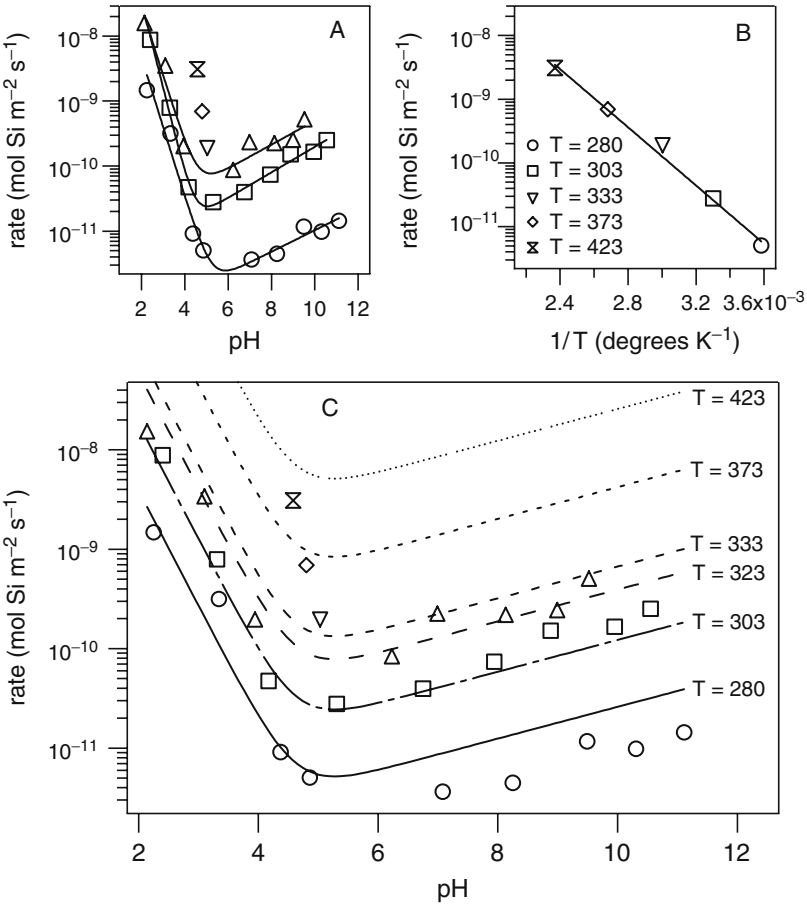

Fig. 6.8 Surface area-normalized basalt dissolution rate data from Oelkers and Gislason (2001) as a function of pH (**a** and **c**) and temperature (**b**). Mono-variate fits of Eqs. (6.8) and (6.22) are displayed in parts A and B; multi-variate fitting of Eq. (6.23) is displayed in part C. Values of temperature, T, in degrees Kelvin. (See Appendix for data)

we can formulate a multi-dimensional rate law from the product of the two equations.

$$r_i = \left(\hat{k}_{H^+} 10^{-n_{H^+} \cdot pH_i} + \hat{k}_{OH^-} 10^{n_{OH^-} \cdot (pH_i - 14)}\right) \exp\left(\frac{-E_a}{R \cdot T_i}\right) \tag{6.52}$$

where $\hat{k}_{H^+} = A \cdot k_{H^+}$ and $\hat{k}_{OH^-} = A \cdot k_{OH^-}$.

Since the multiple mono-variate approach generates multiple values for the fitting parameters, selecting values for the parameters in Eq. (6.52) on the basis of the fits in Figs. 6.8a and b presents a problem. We might try, for example, calculating average values of the parameters; however, this approach typically generates a poor fit to the data since it does not involve minimizing error. Furthermore, this

type of approach ignores information that is present in the data but cannot be fit using a mono-variate approach such as the temperature dependence information present in the pH > 10 measurements which contain too few points for fitting of Eq. (6.51).

These problems can be avoided by performing a multi-dimensional fit wherein a single kinetic model (which is a function of multiple independent variables) is fit to all the data simultaneously. This multi-variate fitting is based on the same error minimization concepts discussed for mono-variate fitting and algorithms for multi-variate fitting can be readily adapted from those for mono-variate fitting. The results of a multi-variate fit (assuming constant relative errors and using the IRLS method) of Eq. (6.52) are depicted in Fig. 6.8c. The authors of the source for the data in Fig. 6.8 argue for a rate model that includes, in addition to pH and temperature, the aqueous aluminum activity, $\{Al^{3+}\}$. The need for such a model is consistent with the systematic over-predictions at high and low temperatures, and, fitting such a tri-variate model represents another situation where multi-variate fitting is the appropriate technique.

6.3.7 Multiple Dependent Variables

In addition to rate laws that contain multiple independent variables, it is possible to find situations that require rate laws that contain multiple dependent variables. This could arise if, for example, the rate of a dissolution reaction is measured on the basis of multiple aqueous species and could also be important if a master variable such as pH responds dynamically to the chemistry of the system. As was the case with multiple independent variables, it is possible to treat multiple dependent variables separately, using mono-variate techniques, thereby, generating multiple estimates of rate parameters. While this approach is quite useful for identifying the form of appropriate rate laws, it is often desirable to fit all of the available data with a single set of fitting parameters. To do this we must modify the error metric so that it is calculated over all of the measurements. Using Eq. (6.23) for generalized least squares fitting as the template, this modified error metric can be written as:

$$\chi^2_{total} = \sum_{j=1}^{M} \chi^2_j = \sum_{j=1}^{M} \sum_{i=1}^{N_j} \left(\frac{r_i^j - r^j\left(\mathrm{pH}_i^j; \Theta\right)}{\sigma_i^j} \right)^2 \tag{6.53}$$

Where the index, j, is used to denote each of the M different dependent variables, χ^2_j denotes the weighted square error for the j-th dependent variable, χ^2_{total} denotes the total weighted square error (which is to be minimized), and the other variables follow the same notation as employed in Eq. (6.23). Algorithms for finding the Θ that minimizes Eq. (6.53) can be modified from those that minimize Eq. (6.23).

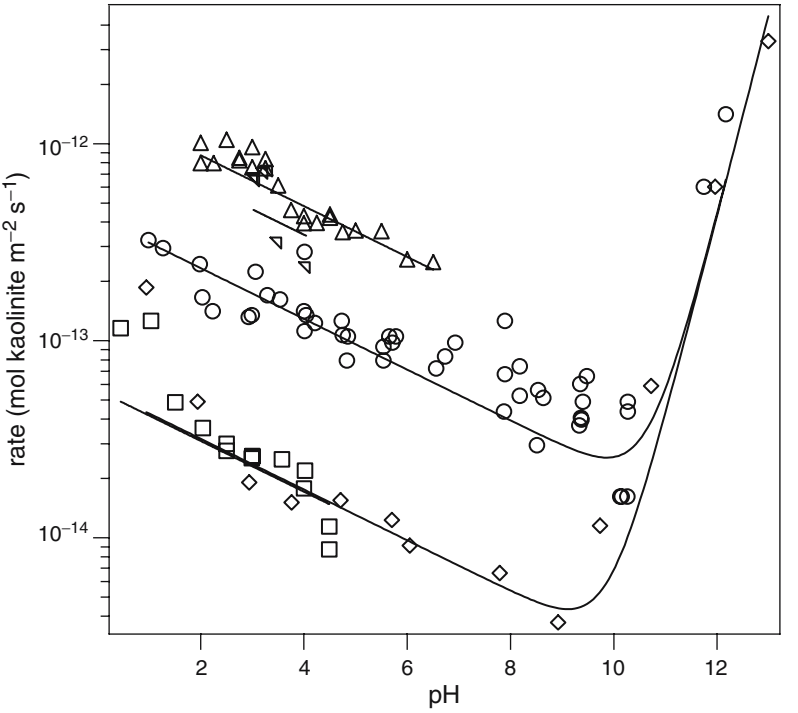

Fig. 6.9 Surface area-normalized kaolinite dissolution rate data as a function of pH and global fitting of Eq. (6.10) with k_{H^+} treated as a local parameter. 8 Wieland and Stumm (1992) ◥ Ganor et al. (1995) – Carroll-Webb and Walther (1988) M Huertas et al. (1999) ∀ Cama et al. (2002). (See Appendix for data)

6.3.8 Global Analysis

Data are sometimes encountered that cannot be lumped together and treated with a single model, but do share some common properties. This situation can arise when two different types of experiments are used to examine the same physical process as would be the case, for example, if electrochemical measurements and batch kinetics experiments are both performed to estimate the rate of a heterogeneous redox reaction. Alternatively, this can arise when data sets produced by similar methods are found to be discrepant in some, but not all of the key features. An example of the latter type is shown in Fig. 6.9 where dissolution rate data for kaolinite compiled from several papers display clear disagreement at low pH, but only in the sense that they are shifted vertically with respect to one another. Each of the data sets could be fit separately with Eq. (6.4). Given the nature of the discrepancy, however, it seems reasonable to suppose that the values of n_{H^+}, n_{OH^-}, and k_{OH^-} are shared amongst the data sets such that the discrepancy is confined to the value of k_{H^+}. This type of analysis – where some of the fitted parameters are shared amongst disparate data and/or models – is known as global analysis. Parameters that are

shared are known as global parameters and parameters that are unique to a given data set (such as k_{H^+}, in the kaolinite dissolution example) are known as local parameters. The results of a global analysis of the type described above are shown on Fig. 6.9.

6.4 Error Analysis

In the preceding sections we have discussed techniques for choosing rate equations, weights on data points, and values for model parameters. Naturally, we would like to know if our selections are correct and, where appropriate, to quantify the uncertainty associated with our choices. All of these matters can be addressed by means of analyzing the lack of fit, or error, between an optimized model and the data used in the optimization. We begin with techniques – both graphical and quantitative – for diagnosing the suitability of the model choice, we then turn to methods for reporting uncertainty in model parameters, and, finally, we conclude by applying these techniques to the problem of identifying discrepancies that may be embedded in a given data set.

6.4.1 Graphical Diagnostics

The best way to test goodness of fit is by visual comparison of model and data and the best plot for this purpose is that of dependent versus independent variables such as the rate versus pH plots discussed above. When examining these plots, first look at the features of the data that were to be captured by the model (e.g., slope and curvature, extrema and critical points). Do model and data possess the same key features? If so, do the estimated parameters correctly locate the key features of the model with respect to the key features of the data? The quartz dissolution data, for example, shown in Fig. 6.5 display a minimum near pH = 5 or 6, while the unweighted fit reaches its minimum at pH < 4. The model possesses the correct shape (i.e., correct key features) but miss-locates the minimum. As discussed above, this provides a clue about the heteroscedastic error structure in mineral dissolution rate data.

In addition to examining key features, it is also important to look at the distribution of the data points about the fitted curve. While this can be done directly from dependent versus independent variable plots, it is also advisable to make plots that specifically draw out the lack of fit. Recall that the measured rate is equal to the model plus an error:

$$y_i = y(x_i;\Theta) + \varepsilon_i \tag{6.54}$$

Equation (6.54) suggests two types of plots for directly examining lack of fit – $y(x_i;\Theta)$ versus y_i and ε_i versus x_i, y_i, or $y(x_i;\Theta)$. Plots involving ε_i are known

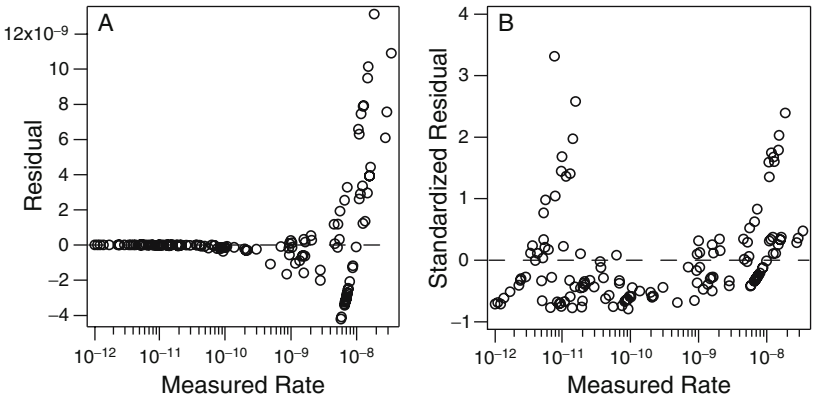

Fig. 6.10 Residuals (**a**) and standardized residuals (**b**) plotted versus the observed rate for IRLS fit of Eq. (6.8) to forsterite dissolution data using weights calculated according to Eq. (6.20)

as residual plots and in what follows we provide examples of both residual and predicted versus measured plots based on fits to the forsterite data discussed above.

In Sect. 6.3.3 we noted that the variance structure for mineral dissolution data is often heteroscedastic (i.e., measurement errors scale with the magnitude of the measurement). We justified this assessment by noting that heteroscedastic fitting techniques (such as linear regression of log-transformed data and IRLS) produce results that look better than those from homoscedastic techniques (such as un-weighted least squares) when plotted on top of the raw data – as is the case in Fig. 6.6. Residual plots provide an ideal means for examining the error structure in greater detail since they directly examine the ε_i. Recall that our two models for the error structure – additive and multiplicative as depicted in Eqs. (6.39) and (6.49), respectively – differ with respect to the dependence of the magnitude of the variance on the magnitude of the rate. A natural plot to make, therefore, is of ε_i versus the observed rate, r_i. A typical result of this type is shown in Fig. 6.10a where the residuals are derived from IRLS fitting of forsterite dissolution data (see Fig. 6.7 and Sect. 6.3.3 for fitting details). The residuals, in this case, show a strong dependence on dissolution rate since the residuals are more broadly scattered around zero at large r_i than at small r_i.

In the multiplicative error model, the errors are assumed to be proportional, in magnitude, to the dissolution rate. If this model holds, than the variability seen in Fig. 6.10a should be removed by normalizing the residuals by the dissolution rate. We could, of course, normalize by either the r_i or the expected value of $r_i(\mathrm{E}[r_i])$. In the case of IRLS, though it is immaterial to the validity of our eventual conclusion, we choose the latter. This gives the standardized residuals which are defined as:

$$\varepsilon_i^{std} = \frac{r_i - r\left(\mathrm{pH}_i;\Theta\right)}{\sigma_i} \tag{6.55}$$

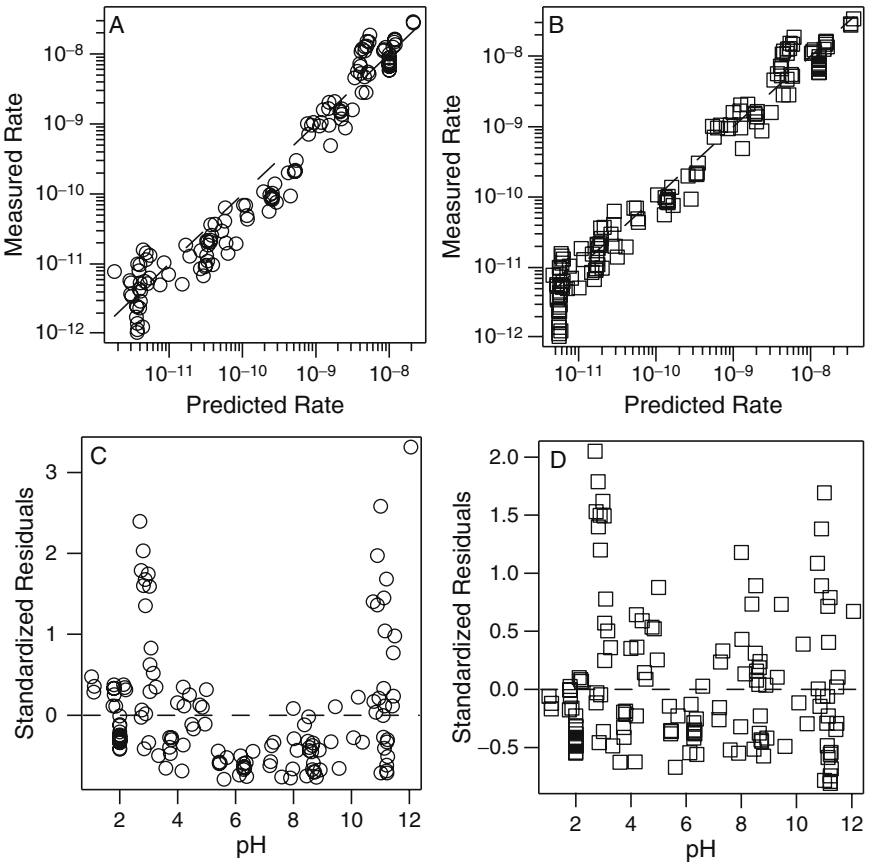

Fig. 6.11 Measured versus predicted (**a** and **b**) and standardized residual versus pH (**c** and **d**) plots for IRLS fitting of Eq. (6.10) (**a** and **c**) and a two-site acid catalysis model (**b** and **d**) to forsterite dissolution data using weights calculated according to Eq. (6.20)

Plotting the standardized residuals versus r_i for IRLS fitting of the forsterite data (Fig. 6.10b) demonstrates that standardization removes the pattern observed in the residuals, and, therefore, that the multiplicative error model is appropriate.

Although the strong dependency of the residuals on the rate is removed by standardization, Fig. 6.10b does contain a weaker pattern that could not be seen in Fig. 6.10a; the (standardized) residuals are almost all < 0 for $10^{-11} < r_i < 10^{-9}$. A careful examination of the raw data and the IRLS fit (Fig. 6.7) indicates that this residual pattern is due to the presence of curvature in the data that cannot be captured by the model. The curvature can also be viewed in Fig. 6.11a and c, which display measured versus predicted and standardized residuals versus pH, respectively, for the IRLS fit displayed in Fig. 6.7. Compare these plots to their counterparts for IRLS fitting of a two-site acid catalysis model ($r_i = k^a_{H^+} 10^{-n^a \cdot \mathrm{pH}_i} + k^b_{H^+} 10^{-n^b \cdot \mathrm{pH}_i}$) shown in Fig. 6.11b, d. The lack of a strong pattern in the latter two plots indicates that the more complicated model more accurately captures the features of the data.

6.4.2 Quantitative Diagnostics

A survey of the statistics literature will turn up numerous measures proposed for quantitatively evaluating the goodness-of-fit between a model and data (cf., Chen and Balakrishnan, 1995; Marin-Lof, 1974; Stewart et al., 1998). The sources of misfit, however, are diverse and no single measure can be considered complete. Furthermore, all such measures are inferior to the graphical diagnostics described above and, therefore, goodness-of-fit measures should be used in conjunction with – not a replacement for – graphical analyses. In the following discussion we examine two quantitative diagnostics: the coefficient of determination and the F-test for comparing values of χ^2. Since the usefulness of other measures is highly specific to each situation, the reader is encouraged to consult literature on the subject. Helpful sources include review papers (Legates and McCabe, 1999; Willmott et al., 1985) and textbooks (D'Agostino and Stephens, 1986; Huber-Carol et al., 2002).

The coefficient of determination (which is the square of the product-moment correlation coefficient, R, and, hence, denoted as R^2) is defined as:

$$R^2 = \frac{\sum_{i=1}^{N} \left(y_i - \langle y_i \rangle\right)\left(y\left(x_i;\Theta\right) - \langle y\left(x_i;\Theta\right)\rangle\right)}{\sqrt{\sum_{i=1}^{N} \left(y_i - \langle y_i \rangle\right)^2 \sum_{i=1}^{N} \left(y\left(x_i;\Theta\right) - \langle y\left(x_i;\Theta\right)\rangle\right)^2}} \tag{6.56}$$

where the angular brackets denote averaging. Note that when $y_i = y(x_i;\Theta), R^2 = 1$, and when $y_i = y(x_i;\Theta)$ diverges from y_i, R^2 tends toward zero. It is, therefore, common practice to calculate R^2 as a goodness-of-fit metric. Unfortunately, this practice is an entirely incorrect use of R^2 (Moore, 2001; Tiley, 1985). R^2 is generally insensitive to minor, but, systematic residuals and is generally over-sensitive to large, but, clearly random, measurement errors. The R^2's for the single and two site catalysis model fits to the forsterite data (= 0.864 and 0.866) are neither very good nor very different even though residual analyses indicate that both models are reasonable well-behaved and that the two-site model captures fine structure in the data that the single-site model cannot. R^2 should not, however, be ignored by geochemists since it is often necessary to distinguish variables that do not affect reaction rates from variables that do, and it is in this sense of comparing independent variables – rather than comparing models – that R^2 is appropriately deployed.

The best use of quantitative diagnostics is in comparing two competing models based on fits to the same data. The most obvious metric for this purpose is χ^2 itself. Simplistically stated, given a single data set with known measurement errors and two competing models, the model with the lower χ^2 is the better one. There are, however, several complicating issues. Since χ^2 is unbounded, we have no way of knowing, *a priori*, whether a certain difference in χ^2 is large or small. For this, we require a test for statistical significance and the appropriate test for χ^2 is the F-test (Martin, 1971). Additionally, since competing models may have different numbers of adjustable parameters, we will need to account for variable degrees of freedom

between values of χ^2. This can be accomplished by considering the reduced χ^2:

$$\chi^2_\upsilon = \frac{\chi^2}{\nu} \tag{6.57}$$

where the degrees of freedom, ν = number of measurements – number of parameters. Finally, when the measurement error estimates are model dependent (as with IRLS fitting), the weights used in calculating χ^2 will need to be adjusted so as not to bias the results toward one of the models. For the cases typical to geochemical kinetics, this can be accomplished by simple averaging. The tables needed for performing an F-test can be found in any standard handbook of mathematics.

6.5 Uncertainty Quantification

Experimental data contain error and, as such, the fitted parameters derived from data – and the rates predicted by a fitted curve – will also contain error. A critical last step in any fitting exercise, then, is to quantify these uncertainties. The basic entities that we will discuss are confidence intervals on the fitted parameters and confidence bands around the fitted curve. There are other ways to quantify uncertainty, such as confidence regions in the space of several parameters (Press et al., 1992) and prediction bands about the fitted curve (Brownlee, 1965). Confidence intervals and confidence bands, however, provide appropriate archetypes for these other entities.

Suppose that an experiment, which produces a data set (y_i, x_i), is repeated many times. Assuming that there is error in the y_i and no error in the x_i, this will produce an ensemble of data sets $(y_{i,j}, x_i)$, where the subscript j refers to the j-th repetition of the experiment. Now, suppose that we fit a model, $y = f(x_i, \Theta)$, to each member of the ensemble. Each fit will potentially produce different values for the parameters, Θ. In other words, there is a probability distribution on each parameter in Θ. The uncertainty associated with the parameters can be determined by examining the breadth of these probability distributions.

The standard way of quantifying the breadth of the probability distribution for a fitting parameter is the confidence interval. The confidence interval for a distribution is defined as a range of values that contains a certain percentage of the probability. Formally, the ρ-th confidence interval for a distribution, P(x), is any closed interval [a, b] such that:

$$\rho = 100 \cdot \int_a^b \mathrm{P}(x) \cdot dx \tag{6.58}$$

This definition leaves us with a couple of options. First, there are an infinite number of intervals that will satisfy Eq. (6.58). It is common to report only the interval that is symmetric about the expected value (i.e., the expected value $\pm$ half of the confidence interval). Second, any value of the percentage, ρ, between 0% and 100% is acceptable according to Eq. (6.58). It is common to use 68.3%, 95.4%, or 99.73%.

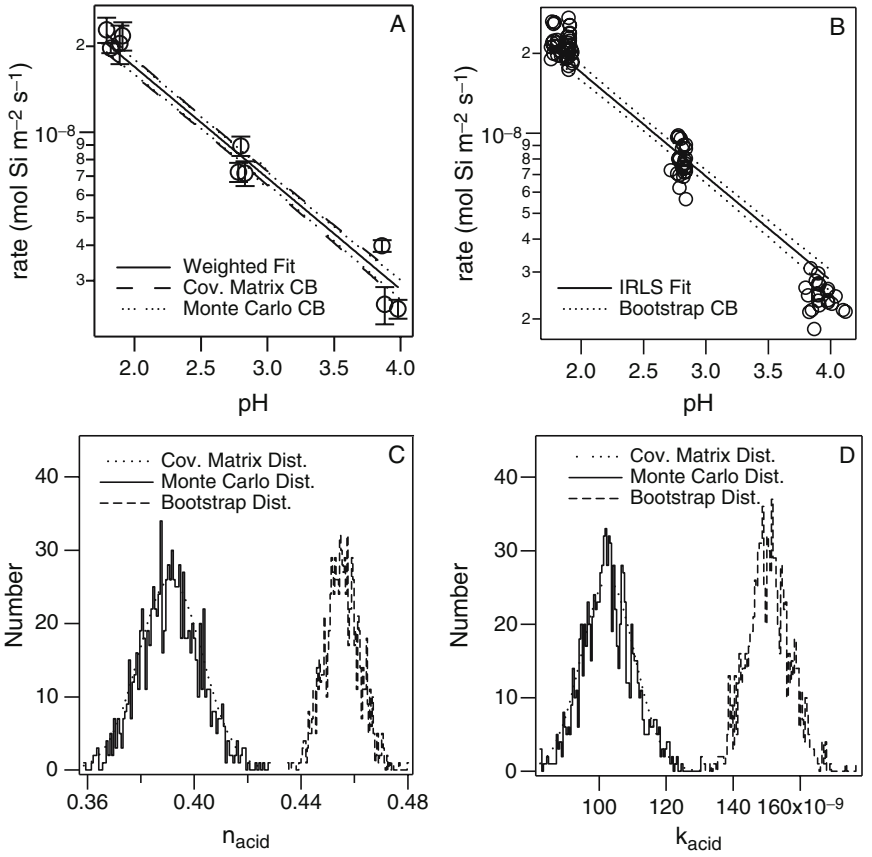

Fig. 6.12 Fitting and uncertainty analysis of olivine dissolution data from Rosso and Rimstidt (2000). Fitted curves and 95.4% confidence bands (denoted by CB) for (**a**) WLS fit of Eq. (6.8) to averaged data and (**b**) IRLS fit of Eq. (6.8) (weights calculated according to Eq. (6.20) raw data. Estimated distribution of fitting parameters, n_{H^+} (**c**) and k_{H^+} (**d**)

These choices are related to the predominance of normal distributions in much of statistics, but, they are usually reasonable for other distributions as well.

A confidence band is the region on the y versus x (e.g., rate versus pH) plot within which the fitted curve is expected to fall some percentage of the time were the experiment and fitting repeated many times. Examples of confidence bands can be seen in Fig. 6.12a, b for fits of Eq. (6.8) to olivine dissolution data (Rosso and Rimstidt, 2000). As with confidence intervals, it is the done thing, though other options may be more appropriate in specific instances, to employ symmetry about the fitted curve and percentages equal to 68.3, 95.4, or 99.73 when calculating confidence bands.

The preceding discussion might suggest that it is necessary to make many replicate measurements in order to quantify uncertainty. Fortunately, this is usually not the case. If we have a model that captures the trends in a data set (i.e., matches the

key features), then we can generate uncertainty estimates by analyzing the lack of fit between the model and the data (i.e., the residuals). In the following sections we describe several techniques for quantifying uncertainty even if there are no replicate measurements.

6.5.1 Composition of Errors

The variance of a function, f, whose argument is some set of independent random variables, y_i, can be composed from the variances, σ_i, on the y_i as follows:

$$\sigma_f^2 = \sum_{i=1}^{N} \sigma_i^2 \left(\frac{\partial f}{\partial y_i} \right)^2 \tag{6.59}$$

The estimated model parameters that we have been finding via χ^2 minimization are functions of the y_i. For example, had the measured rates of biotite dissolution been an order of magnitude larger than those shown in Fig. 6.1, the estimated values of $\log(k_{H^+})$ would have changed accordingly. In other words, each parameter in Θ is a function of the y_i. We can, therefore, use Eq. (6.59) to find the variance on any fitting parameter, θ_k, provided that we know $\partial\theta_k/\partial y_i$.

Consider the linear regression formulae given by Eqs. (6.31) and (6.32). Each of the "S" terms is a function of y_i, so it is straightforward to find the partial derivatives of m and b with respect to y_i.

$$\frac{\partial m}{\partial y_i} = \frac{S \cdot x_i - S_x}{\sigma_i^2 \cdot \left(S \cdot S_{xx} - (S_x)^2 \right)} \tag{6.60}$$

$$\frac{\partial b}{\partial y_i} = \frac{S_{xx} - S_x \cdot x_i}{\sigma_i^2 \cdot \left(S \cdot S_{xx} - (S_x)^2 \right)} \tag{6.61}$$

Substituting Eqs. (6.60) and (6.61) into Eq. (6.59) gives the variances for m and b:

$$\sigma_m^2 = \frac{S}{S \cdot S_{xx} - (S_x)^2} \tag{6.62}$$

$$\sigma_b^2 = \frac{S_{xx}}{S \cdot S_{xx} - (S_x)^2} \tag{6.63}$$

Confidence intervals on the fitted parameters m and b (denoted as δm and δb) can be calculated directly from the σ_m and σ_b: $\delta m = \sigma_m$, $2 \cdot \sigma_m$, and $3 \cdot \sigma_m$ at the 68.3%, 95.4%, and 99.73% levels, respectively. δb is found in the same manner.

Since Θ is a function of the y_i, it follows that $y(x_j;\Theta)$, for some fixed value of x_j, is also a function of the y_i. We can, therefore, calculate confidence bands from Eq. (6.59) provided that we can find the partial derivative: $\partial y(x_j;\Theta)/\partial y_i$. For linear

regression, $y(x_j;m,b) = m \cdot x_j + b$, and therefore the partial derivative is

$$\frac{\partial y(x_j;m,b)}{\partial y_i} = \frac{\partial m}{\partial y_i} \cdot x_j + \frac{\partial b}{\partial y_i} \tag{6.64}$$

Substituting Eq. (6.64) into Eq. (6.59) gives the variance on the model prediction at x_j:

$$\sigma^2_{y(x_j)} = \sigma^2_m \cdot x_j^2 + \frac{S_x^3}{\left(S \cdot S_{xx} - (S_x)^2\right)^2} \cdot x_j + \sigma_b^2 \tag{6.65}$$

Confidence bands at an arbitrary level can then be found according to the normal distribution with mean $= y(x_j;m,b)$. Note that while the model is linear, the confidence bands will be non-linear; they will curve away from the fitted line toward the ends of the range of x.

6.5.2 Approximations from the Covariance Matrix

The derivations shown in Sect. 6.5.1 dealt exclusively with linear regression. In the nonlinear case, the relevant partial derivatives with respect to y_i are generally not available (in closed form) and, therefore, application of Eq. (6.59) can be done only in an approximate sense. Nonlinear χ^2 minimization by a steepest decent method (e.g., Levenberg–Marquardt) involves the calculation of a curvature matrix $[\alpha]$:

$$\alpha_{k,l} = \sum_{i=1}^{N} \frac{1}{\sigma_i^2} \left[\frac{\partial y(x_i;\Theta)}{\partial \theta_k} \frac{\partial y(x_i;\Theta)}{\partial \theta_l} \right] \tag{6.66}$$

$[\alpha]$ is used to find the direction in which – and by how much – to move Θ during an iteration of the χ^2 minimization algorithm. Notice the similarity to Eq. (6.59). When second derivative terms can be neglected (i.e., when the fitting equation is linear in the fitting parameters), the covariance matrix for the fitting parameters is equal to the inverse of the curvature matrix.

$$Cov = \left[E\left[\left(\theta_k - \langle\theta_k\rangle\right)\left(\theta_l - \langle\theta_l\rangle\right)\right]\right] = \left[\alpha_{k,l}\right]^{-1} \tag{6.67}$$

If the errors on the fitted parameters and predicted rates are normally distributed, then confidence intervals can be calculated as:

$$\delta\theta_k = \pm\sqrt{\Delta\chi^2_{\nu=1}}\sqrt{Cov_{k,k}} \tag{6.68}$$

Where $\Delta\chi^2_{\nu=1}$ is the chi-square distribution with a single degree of freedom for the confidence level of interest (= 1, 4, or 9 for 68.3%, 95.4%, or 99.73%, respectively). Additionally, confidence bands can be calculated as:

$$\delta y(x) = t_\nu \sqrt{\left[\frac{\partial y(x,\Theta)}{\partial \Theta}\right]^T Cov \left[\frac{\partial y(x,\Theta)}{\partial \Theta}\right]} \tag{6.69}$$

where t_ν is the Student-t distribution for the confidence level of interest with ν (= number of measurements – number of parameters) degrees of freedom. Most scientific software support some form of non-linear curve fitting. The reported results typically include some form of error analysis derived from the equations described above. It is important, therefore, when considering such results, to remember the underlying assumptions of linearity and normality.

6.5.3 Monte Carlo Methods

Of the two assumptions made in estimating errors from the covariance matrix, the assumption of (near) linearity is often times more problematic than the assumption of normality. If the measurement error distribution is known, this difficulty can be surmounted by producing, and fitting, synthetic data sets until the distribution of the fitting parameters is sufficiently mapped out (usually between 100 and 1,000 simulations). This is known as the Monte Carlo method. The prescription is as follows: (*i*) fit the measured data using χ^2 minimization, (*ii*) create a synthetic data set by adding to the model prediction, at each value of the independent variable, a random number based on the known error distribution, (*iii*) fit the synthetic data, (*iv*) repeat steps (*ii–iv*) many times; 1,000, say, (*v*) calculate confidence intervals, bands, and other statistics from the resulting parameter distributions.

Since calculation of error estimates from the covariance matrix and by the Monte Carlo method have identical data requirements, it is possible to make direct comparison of these two methods. In a study of olivine dissolution (Rosso and Rimstidt, 2000), dissolution rates were measured at three pH values with a large (ca. 30) number of replicates. The averages of these replicate data are plotted in Fig. 6.12a along with error bars representing the calculated standard deviations. WLS fitting of Eq. (6.4) to these data using, for weights, the standard deviations gives $n_{H^+} = 0.391$ and $k_{H^+} = 1.03 \times 10^{-7}$ (mol Si m^{-2} s^{-1}) and the fitted curve is shown in Fig. 6.12a. Calculating 95.4% confidence intervals from the covariance matrix gives $n_{H^+} = 0.391 \pm 0.026$ and $k_{H^+} = 1.03 \times 10^{-7} \pm 1.8 \times 10^{-8}$ (mol Si m^{-2} s^{-1}), while the Monte Carlo method yields $n_{H^+} = 0.391 \pm 0.022$ and $k_{H^+} = 1.03 \times 10^{-7} \pm 1.5 \times 10^{-8}$ (mol Si m^{-2} s^{-1}). The confidence intervals generated by the two methods are nearly identical, indicating that the assumption of near linearity with respect to the parameters is quite good for this model/data pair. The histograms for n_{H^+} (Fig. 6.12c) and k_{H^+} (Fig. 6.12d) from the Monte Carlo calculation match the normal distribution calculated from the covariance matrix and the 95.4% confidence bands for the two methods fall on top of each other in Fig. 6.12a, further reinforcing equivalence of these methods. Unfortunately, this equivalence cannot be claimed in general since it is dependent both on the model and the data. As a rule of thumb, though, uncertainties from the covariance matrix are probably valid as an order of magnitude estimate. The Monte Carlo method should be used if more precise estimates are needed or if the distribution on the fitted parameters is in doubt.

6.5.4 Bootstrap Methods

The applicability of the Monte Carlo method is severely limited by the requirement that measurement error distributions be known. While it is not uncommon to find replicate data in studies of geochemical kinetics, the sample size is typically far to small to ensure accurate error estimates (NB: the number of replicate experiments required for any kind of reasonable precision is closer to thirty than it is to three). This difficulty, however, can be overcome by making use of information contained in the residuals for the fit via a procedure known as the bootstrap method. If a given model fit is good, then the residuals (or, when IRLS is required, the standardized residuals) will be randomly distributed around zero with constant variance (i.e., the errors will be independently and identically distributed). It is then possible to generate estimates of measurement errors by examining the distribution of the residuals in bulk. One could, for example, calculate the standard deviation of the residuals and then employ the formulae of Sect. 6.5.1. This, however, assumes normality in the residuals. Alternatively, one could select a more appropriate parametric distribution function (normal, log-normal, gamma, or whatever) by examining a histogram of the residuals and applying the Monte Carlo method.

The bootstrap avoids the need to make assumptions about the form of the error distribution by using the residuals themselves to generate synthetic data sets. The prescription for generating error estimates with the bootstrap is to (i) fit the original data and calculate residuals, (ii) create synthetic data by adding to the model prediction, at each value of the independent variable, a randomly selected residual, (iii) fit the synthetic data, (iv) repeat steps ii–iv many times, and (v) calculate confidence intervals, bands, and other statistics from the resulting parameter distributions. Note that the bootstrap method is essentially a Monte Carlo method with a normalized sum of delta functions at the observed residuals used for the error distribution function.

A primary advantage of the bootstrap method is that it can be used whenever a fit is performed; unlike the other methods, no additional data are required. For example, we can generate good uncertainty estimates for the olivine dissolution data mentioned above (Rosso and Rimstidt, 2000) without the need for averaging the replicates. Figure 6.12b shows the full (i.e., un-averaged) olivine data set and IRLS fitting of Eq. (6.4) with bootstrapping at the 95.4% level gives $n_{H^+} = 0.456 \pm 0.013$ and $k_{H^+} = 1.03 \times 10^{-7} \pm 1.8 \times 10^{-8}$ (mol Si m^{-2} s^{-1}). The fitted curve and the bootstrapped confidence band are shown in Fig. 6.12b. Comparing these fitted values and the parameter histograms (Fig. 6.12d) with those generated by the Monte Carlo and covariance matrix methods indicates that the uncertainty estimates generated by the bootstrap method are roughly equivalent to the uncertainties generated with the averaged data. The fitted parameters are, however, significantly different between the weighted and IRLS fits. This discrepancy could arise, in part, from the assumption in IRLS fitting that the measurement error is strictly relative; however, it is more likely due to ignoring the variability in the independent variable (pH) when fitting the average data. When significant measurement error is present in the independent variable – as is the case in the averaged data set considered here – more

advanced treatments are required (Seber and Wild, 2003). Given that the variability in pH for the un-averaged data is, likely, not random measurement error but rather caused by slight differences in experimental set-up, the preferred treatment for data of this type is fitting the full data (i.e., without averaging) and estimating uncertainty using the bootstrap method.

6.6 Commonly Encountered Problems

Every data fitting project is unique in some way. The techniques described in this chapter provide a starting point, but, they should be employed with the understanding that problems will inevitably be encountered. Problems can be inherent to a kinetic data set or they can arise as a result of type of fitting being attempted. Here we describe a few problems that are commonly encountered. This list is meant to encourage awareness rather than to offer complete solutions and, further, it is meant to be representative rather than comprehensive.

When examining large amounts of data, and especially data from multiple sources like the compiled dissolution data considered here, it is not uncommon to find discrepancies. The data may contain outliers – one, or a few measurements that are starkly different from the rest of the data. In other cases (cf., the kaolinite dissolution data in Fig. 6.9) data may contain several branches that are internally consistent but in clear disagreement with one another. When a datum is clearly outlying or branches clearly present, physical reasons for the discrepancy may be found in the protocols for the experiment(s) and separate treatments warranted. Often times, however, discrepancies are not entirely obvious and the treatment of potentially discrepant data involves the careful application of intuition, prudence, and trial-and-error in order to avoid undue prejudice in the data analysis.

Much of the discussion has heretofore revolved around the fact that measurements contain error. We have, however, idealized these errors to be random and much larger in the dependent variable than in the independent variable(s). As we have indicated above, more advanced fitting techniques are available for handling the error-in-regressor problem and if the data demand it, these techniques, though formidable, should not be ignored. The idealization of error as being random is, however, even more problematic. Measurement may contain systematic error wherein observed values are consistently larger (or smaller) than reality. Systematic error – or, bias – is a particular concern in the measurement of small reaction rates. The curvature in the forsterite dissolution data shown in Fig. 6.7 may be due to the existence of more than one reaction pathway (as mentioned above), but, this feature could also be due to bias in the data that becomes more prominent as the reaction rate becomes small. No statistical treatment can identify the source of bias and, as may be occurring with the forsterite dissolution data, statistical treatments could lead to over-analysis of biased data. As with discrepant data, intuition, prudence, and trial-and-error should be exercised.

Sometimes, data are internally problematic. More often, however, the treatment of data is misleading. The non-linear nature of the fitting techniques described above means that we can never be assured of a unique solution to a χ^2 minimization. Minimization algorithms sometimes converge to a local minimum when a much better fit could be achieved. When this occurs, it is usually apparent in the graphical diagnostics described in Sect. 6.4.1. Nevertheless, it is wise to try several initial guesses before accepting an apparent minimum as the best fit.

In contrast to the problem of false convergence, it is common to attempt a fit that does not converge. This problem is usually symptomatic of poor initial guesses. As a general rule, one should plot the fitting equation, together with the data to be fit, using the initial guesses before attempting the fit. If the initial guesses yield a curve that is too far from the data, the initial guesses should be modified so that convergence is more likely. Lack of convergence can also signify a problem internal to the minimization algorithm causing it to oscillate around the minimum or a problem with the fitting equation such as the existence of singularities for some values of the parameters. This latter problem can be addressed by constraining the parameters to avoid problematic values.

Convergence problems can also arise due to a poor choice of fitting equation. Two particular conditions warrant special mention: unidentifiability and ill-conditioning. Unidentifiability occurs when two or more sets of values for the parameters exist such that the same values for the fitting equation are returned at all values of the independent variable. For example, the fitting equation

$$f(\mathbf{x};\Theta) = \exp(-\beta\tau x_1) + \frac{\alpha}{\beta}(1-\exp(-\beta\tau x_1))x_2 \tag{6.70}$$

with $\Theta = (\alpha,\beta,\tau)$ possesses a lack of identifiability (Bird and Milliken, 1976), since $\Theta = (c\cdot\alpha, c\cdot\beta, \tau/\mathrm{c})$ gives the same value of $f(\mathbf{x};\Theta)$ for any non-zero c. In this case, the problem can be alleviated by reparameterization of the model using $a = \beta\cdot\tau$ and $b = \alpha/\beta$.

Ill-conditioning arises when the parameters cannot be uniquely distinguished at the measured points rather than over the entire range of the independent variable. For example, consider the Michalis–Menton equation, which describes the rate of many enzymatic reactions (as well as many surface mediated processes):

$$r(\mathrm{C};\Theta) = \frac{V_{\max}\mathrm{C}}{K_{1/2}+\mathrm{C}} \tag{6.71}$$

where r is the reaction rate, C is the concentration of the reacting species, and $\Theta = (V_{max}, K_{1/2})$. At small values of C, Eq. (6.71) collapses to:

$$r(\mathrm{C};\Theta) = \frac{V_{\max}}{K_{1/2}}\mathrm{C} \tag{6.72}$$

If rate measurements are made only at small values of C, the data will be ill-conditioned for application of the Michalis–Menton equation, since, as indicated

by Eq. (6.72), any values of V_{max} and $K_{1/2}$ that have a constant ratio will give equivalent values of χ^2 (Agrawal et al., 2002).

6.7 Conclusions

The most important tool for data analysis is the human brain. No formula or computer algorithm can replace visual analysis of data. In Sect. 6.2 we discussed a systematic method for looking at data based on the identification of key features. These key features – which are defined as the signs and roots of the zeroth, first, and second derivatives – provide a basis for examining the shape of a data set and for selecting rate laws that match the data. It is not always necessary to follow the detailed steps of sketching derivatives that we outlined in Sect. 6.2, but it is important to think about data in terms of sign, slope, and curvature.

The premise of curve fitting as discussed in Sect. 6.3 is that the dependent variable (e.g., rate) contains random measurement error while the independent variable (e.g., pH, temperature, etc.) contains no error. The proper fitting technique, therefore, hinges on the structure of the dependent variable error distribution. In Sects. 6.3.4 and 6.4.1, we examined two major classes of error: constant absolute error where the variance (σ) is the same for all measurements and constant relative error where the variance is proportional to the dependent variable (in both cases, we assumed the errors to be normally distributed though, as we noted, the techniques discussed will work well for most distributions that are symmetric about the mean). In general, we found that mineral dissolution rate data fall into the category of constant relative error (cf., Fig. 6.10). For this reason, ordinary least squares (OLS) fitting of log-transformed mineral dissolution rates is preferable to OLS fitting of the un-transformed data. However, we expect the log-transform to skew the error distribution and, therefore, weighted least squares (WLS) or iteratively reweighted least squares (IRLS) fitting of mineral dissolution rate data is preferable to OLS fitting of log-transformed data. As a rule of thumb, data that span several orders of magnitude and are generated by independent experiments are likely to exhibit heteroscedasticity while data that vary by less than a few orders of magnitude and are produced by a single experiment are likely to be homoscedastic.

Curve fitting is never complete without an analysis of the fitting results. It is absolutely necessary to plot the fitted curve on a graph along with the data before accepting the fit. It is also highly advisable to examine residual plots of the type described in Sect. 6.4.1. Quantitative goodness-of-fit diagnostics (discussed in Sect. 6.4.2) are generally superfluous and should be used mainly to support conclusions that can be seen visually through graphical diagnoses. Quantitative measures of uncertainty in the fitted parameters (i.e., confidence intervals), however, are necessary. All of the techniques discussed in Sect. 6.5 will produce confidence intervals that are accurate to an order of magnitude. For most purposes this is all that is required and, therefore, unless greater precision is required, the choice of method may be based primarily on convenience.

Acknowledgments

This material is based upon work supported by the National Science Foundation under Grant No. CHE-0431328.

References

Acker J. G. and Bricker O. P. (1992) The influence of pH on biotite dissolution and alteration kinetics at low temperature. *Geochimica et Cosmochimica Acta* **56**(8), 3073–3092.

Agrawal A., Ferguson W. J., Christ J. A., Bandstra J. Z., and Tratnyek P. G. (2002) Effects of carbonate species on the kinetics of dechlorination of 1,1,1-trichloroethane by zero-valent iron. *Environmental Science and Technology* **36**, 4326–4333.

Amrhein C. and Suarez D. (1992) Some factors affecting the dissolution kinetics of anorthite at 25° C. *Geochimica et Cosmochimica Acta* **56**, 1815–1826.

Bandstra J. Z. and Tratnyek P. G. (2004) Applicability of single-site rate equations for reactions on inhomogeneous surfaces. *Industrial and Engineering Chemistry Research* **43**(7), 1615–1622.

Bandstra J. Z. and Tratnyek P. G. (2005) Central limit theorem for chemical kinetics in complex systems. *Journal of Mathematical Chemistry* **37**(4), 409–422.

Bennett P. C. (1991) Quartz dissolution in organic-rich aqueous systems. *Geochimica et Cosmochimica Acta* **55**, 1781–1797.

Bennett P. C., Melcer M. E., Siegel D. I., and Hassett J. P. (1988) The dissolution of quartz in dilute aqueous-solutions of organic-acids at 25° C. *Geochimica et Cosmochimica Acta* **52**, 1521–1530.

Berger G., Cadore E., Schott J., and Dove P. M. (1994) Dissolution rate of quartz in lead and sodium electrolyte solutions between 25 and 300° C: effect of the nature of surface complexes and reaction affinity. *Geochimica et Cosmochimica Acta* **58**, 541–551.

Bird H. A. and Milliken G. A. (1976) Estimable functions in the nonlinear model. *Communications in Statistics: Theory and Methods* **6**, 999–1012.

Brady P. V. and Walther J. V. (1989) Controls on silicate dissolution rates in neutral and basic pH solutions at 25° C. *Geochimica et Cosmochimica Acta* **53**, 2823–2830.

Brady P. V. and Walther J. V. (1990) Kinetics of quartz dissolution at low temperature. *Chemical Geology* **82**, 253–264.

Brownlee K. A. (1965) *Statistical Theory and Methodology*. New York, John Wiley & Sons.

Busenberg E. and Clemency C. V. (1976) The dissolution kinetics of feldspars at 25° C and 1 atm CO_2 partial pressure. *Geochimica et Cosmochimica Acta* **40**, 41–49.

Cama J., Metz V., and Ganor J. (2002) The effect of pH and temperature on kaolinite dissolution rate under acidic conditions. *Geochimica et Cosmochimica Acta* **66**(22), 3913–3926.

Carroll-Webb S. A. and Walther J. V. (1988) A surface complexation model for the pH-dependence of corundum and kaolinite dissolution rates. *Geochimica et Cosmochimica Acta* **52**, 2609–2623.

Casey W. H., Lasaga A. C., and Gibbs G. V. (1990) Mechanisms of silica dissolution as inferred from the kinetic isotope effect. *Geochimica et Cosmochimica. Acta* **54**, 3369–3378.

Casey W. H., Westrich H. R., and Holdren G. R. (1991) Dissolution rates of plagioclase at pH = 2 and 3. *American Mineralogist* **76**, 211–217.

Charnes A., Frome E. L., and Yu P. L. (1976) The equivalence of generalized least squares and maximum likelihood estimates in the exponential family. *Journal of the American Statistical Association* **71**(353), 169–171.

Chen G. and Balakrishnan N. (1995) A general purpose approximate goodness-of-fit test. *Journal of Quality Technology* **27**(2), 154–161.

Chou L. and Wollast R. (1984) Study of the weathering of albite at room temperature and pressure with a fluidized bed reactor. *Geochimica et Cosmochimica Acta* **48**(11), 2205–2217.

Chou L. and Wollast R. (1985) Steady-state kinetics and dissolution mechanism of albite. *American Journal of Science* **285**, 963–993.

Cygan R. T., Casey W. H., Boslough M. B., Westrich H. R., Carr M. J., and Holdren G. R. (1989) Dissolution kinetics of experimentally shocked silicate minerals. *Chemical Geology* **78**, 229–244.

D'Agostino R. B. and Stephens M. A. (1986) *Goodness-of-Fit Techniques*. New York, Marcel Dekker.

Dennis J. E., Jr., Gay D. M., and Welsch R. E. (1981) An adaptive nonlinear least-squares algorithm. *ACM Transactions on Mathematical Software* **7**, 348–368.

Dennis J. E., Jr., Gay D. M., and Welsch R. E. (1981) Algorithm 573. NL2SQL-An adaptive nonlinear least-squares algorithm. *ACM Transactions on Mathematical Software* **7**, 369–383.

Dennis J. E., Jr. and Schnabel R. B. (1996) *Numerical Methods for Unconstrained Optimization and Nonlinear Equations*. New Jersey, Prentice-Hall.

Draper N. R. and Smith H. (1966) *Applied Regression Analysis*. New York, John Wiley & Sons.

Eggleston C. M., Hochella M. F., Jr., and Parks G. A. (1989) Sample preparation and aging effects on the dissolution rate and surface composition of diopside. *Geochimica et Cosmochimica Acta* **53**, 797–804.

Frogner P. and Schweda P. (1998) Hornblende dissolution kinetics at 25° C. *Chemical Geology* **151**, 169–179.

Ganor J., Mogollon J. L., and Lasaga A. C. (1995) The effect of pH on kaolinite dissolution rates and on activation energy. *Geochimica et Cosmochimica Acta* **59**(6), 1037–1052.

Gillespie D. T. (2000) The chemical Langevin equation. *Journal of Chemical Physics* **113**(1), 297–306.

Gislason S. R. and Eugster H. P. (1987) Meteoric water-basalt interactions. I: A laboratory study. *Geochimica et Cosmochimica Acta* **51**, 2827–2840.

Golubev S. V., Pokrovsky O. S., and Schott J. (2005) Experimental determination of the effect of dissolved CO_2 on te dissolution kinetics of Mg and Ca silicates at 25° C. *Chemical Geology* **217**, 227–238.

Green P. J. (1984) Iteratively reweighted least squares for maximum likelihood estimation, and some robust and resistant alternatives. *Journal of the Royal Statistical Society B* **46**(2), 149–192.

Guidry M. W. and Mackenzie F. T. (2003) Experimental study of igneous and sedimentary apatite dissolution – Control of pH, distance from equilibrium, and temperature on dissolution rates. *Geochimica et Cosmochimica Acta* **67**(16), 2949–2963.

Hartley H. O. (1961) The modified Gauss-Newton method for the fitting of nonlinear regression functions by least squares. *Technometrics* **3**, 269–280.

Hodson M. E. (2003). The influence of Fe-rich coatings on the dissolution of anorthite at pH 2.6. *Geochimica et Cosmochimica Acta* **67**(18), 3355–3363.

Holdren G. R. and Speyer P. M. (1987) Reaction-rate surface area relationships during the early states of weathering; II, Data on eight additional feldspars. *Geochimica et Cosmochimica Acta* **51**(9), 2311–2318.

Hougen O. A. and Watson K. M. (1943) Solid catalysts and reaction rates. *Industrial and Engineering Chemistry* **35**, 529.

House W. A. and Orr D. R. (1992) Investigation of the pH dependence of the kinetics of quartz dissolution at 25° C. *Journal of Chemical Society Faraday Transactions* **88**, 233–241.

Huber-Carol C., Balakrishnan N., Nikulin M. S., and Mesbah M. (2002) *Goodness-of-Fit Tests and Model Validity*. Boston, Birkhauser.

Huertas F. J., Chou L., and Wollast R. (1999) Mechanism of kaolinite at room temperature and pressure Part II: Kinetic study. *Geochimica et Cosmochimica Acta* **63**(19/20), 3261–3275.

Huet S., Bouvier A., Poursat M.-A., and Jolivet E. (2004) *Statistical Tools for Nonlinear Regression*. New York, Springer.

Hughes-Hallett D., Gleason A. M., Flath D. E., Gordon S. P., Lomen D. O., Lovelock D., McCallum W. G., Osgood B. G., Pasquale A., Tecosky-Feldman J., Thrash J. B., Thrash K. R., and Tucker T. W. (1994) *Calculus*. New York, John Wiley & Sons, Inc.

Ishida K. (1966) Stochastic approach to nonequilibrium thermodynamics of first-order chemical reactions. *Journal of Physical Chemistry* **70**(12), 3807–3811.

Kalinowski B. E. and Schweda P. (1996) Kinetics of muscovite, phlogopite, and biotite dissolution and alteration at pH 1–4, room temperature. *Geochimica et Cosmochimica Acta* **60**(3), 367–385.

Knauss K. G., Nguyen S. N., and Weed H. C. (1993) Diopside dissolution kinetics as a function of pH, CO_2, temperature, and time. *Geochimica et Cosmochimica Acta* **57**, 285–294.

Knauss K. G. and Wolery T. J. (1986) Dependence of albite dissolution kinetics on pH and time at 25° C and 70° C. *Geochimica et Cosmochimica Acta* **50**(11), 2481–2497.

Langmuir I. (1918) The adsorption of gases on plane surfaces of glass, mica, and platinum. *Journal of the American Chemical Society* **40**, 1361.

Legates D. R. and McCabe G. J. J. (1999) Evaluation of the use of "goodness-of-fit" measures in hydrologic and hydroclimatic model validation. *Water Resources Research* **35**(1), 233–241.

Levenberg K. (1944) A method for the solution of certain problems in least squares. *Quarterly of Applied Mathematics* **2**, 164–168.

Marin-Lof T. (1974) The notion of redundancy and its use as a quantitative measure of the discrepancy between a statistical hypothesis and a set of observation data. *Scandanavian Journal of Statistics* **1**, 3–18.

Marquardt D. (1963) An algorithm for least-squares estimation of nonlinear parameters. *SIAM Journal on Applied Mathematics* **11**, 431–441.

Martin B. R. (1971) *Statistics for Physicists*. London, Academic Press.

McQuarrie D. A. (1967) Stochastic approach to chemical kinetics. *Journal of Applied Probability* **4**, 413–478.

Miller D. C. (1984) Reducing transformation bias in curve fitting. *The American Statistician* **38**(2), 124–126.

Moore D. S. (2001) *Statistics: Concepts and Controversies*. New York, W. H. Freeman.

Moore J. W. and Pearson R. G. (1981) *Kinetics and Mechanism*. New York, John Wiley & Sons.

Oelkers E. H. (2001) An experimental study of forsterite dissolution rates as a function of temperature and aqueous Mg and Si concentrations. *Chemical Geology* **175**(3–4), 485–494.

Oelkers E. H. and Gislason S. R. (2001) The mechanism, rates and consequences of basaltic glass dissolution: I. An experimental study of the dissolution rates of basaltic glass as a function of aqueous Al, Si and oxalic acid concentration at 25° C and pH = 3 and 11. *Geochimica et Cosmochimica Acta* **65**(21), 3671–3681.

Pokrovsky O. S. and Schott J. (2000) Kinetics and mechanism of forsterite dissolution at 25° C and pH from 1 to 12. *Geochimica et Cosmochimica Acta* **64**(19), 3313–3325.

Press W. H., Teukolsky S. A., Vetterling W. T., and Flannery B. P. (1992) *Numerical Recipies in C*. Cambridge University Press.

Rose N. M. (1991) Dissolution rates of prehnite, epidote, and albite. *Geochimica et Cosmochimica Acta* **55**(11), 3273–3286.

Rosso J. J. and Rimstidt J. D. (2000) A high resolution study of forsterite dissolution rates. *Geochimica et Cosmochimica Acta* **64**(5), 797–811.

Schweeda P. (1989) Kinetics of alkali feldspar dissolution at low temperature. In *Proceedings of the Sixth International Symposium on Water/Rock Interaction* (ed. D. L. Miles), A. A. Balkema, Lisse, The Netherlands, pp. 609–612.

Seber G. A. F. and Wild C. J. (2003) *Nonlinear Regression*. New Jersey, John Wiley & Sons.

Stewart W. E., Shon Y., and Box G. E. P. (1998) Discrimination and goodness-of-fit of multiresponse mechanistic models. *AIChE Journal* **44**(6), 1404–1412.

Stillings L. L. and Brantley S. L. (1995) Feldspar Dissolution at 25° C and pH 3 – Reaction stoichiometry and the effect of cations. *Geochimica et Cosmochimica Acta* **59**(8), 1483–1496.

Sverdrup H. U. (1990) The kinetics of base cation release due to chemical weathering. Lund University Press, pp. 246.

Swoboda-Colberg N. G. and Drever J. I. (1993) Mineral dissolution rates in plot-scale field and laboratory experiments. *Chemical Geology* **105**, 51–69.

Temkin M. I. (1979) The kinetics of some industrial heterogeneous catalytic reactions. *Advances in Catalysis* **28**, 173.

Tester J. W., Worley W. G., Robinson B. A., Grigsby C. O., and Feerer J. L. (1994) Correlating quartz dissolution kinetics in pure water from 25° C to 625° C. *Geochimica et Cosmochimica Acta* **58**, 2407–2420.

Tiley P. F. (1985) The misuse of correlation coefficients. *Chemistry in Britain* **21**(2), 162–163.

Valsami-Jones E., Ragnarsdottir K. V., Putnis A., Bosbach D., Kemp A. J., and Cressey G. (1998) The dissolution of apatite in the presence of aqueous metal cations at pH 2–7. *Chemical Geology* **151**(1), 215–233.

van Hess P. A. W., Lundström U. S., and Mörth C.-M. (2002) Dissolution of microcline and labradorite in a forest O horizon extract: the effect of naturally occurring organic acids. *Chemical Geology* **189**, 199–211.

Welch S. A., Taunton A. E., and Banfield J. F. (2002) Effect of microorganisms and microbial metabolites on apatite dissolution. *Geomicrobiology Journal* **19**(3), 343–367.

Wieland W. and Stumm W. (1992) Dissolution kinetics of kaolinite in acidic aqueous solutions at 25° C. *Geochimica et Cosmochimica Acta* **56**, 3339–3355.

Willmott C. J., Ackleson S. G., Davis R. E., Reddema J. J., Klink K. M., Legates D. R., O'Donnell J., and Rowe C. M. (1985) Statistics for the evaluation and comparison of models. *Journal of Geophysical Research* **90**(C5), 8995–9005.

Wogelius R. A. and Walther J. V. (1992) Olivine dissolution kinetics at near-surface conditions. *Chemical Geology* **97**(1–2), 101–112.

Wollast R. and Chou L. (1986) Processes, rate, and proton consumption by silicate weathering. *Transactions of the 13th Congress of the International Society of Soil Science*, pp. 127–136.

Wollast R. and Chou L. (1988) Rate control of weathering of silicate minerals at room temperature and pressure. In *Physical and Chemical Weathering in Geochemical Cycles* (ed. A. Lerman and M. Maybeck). Amsterdam, Kluwer Academic, pp. 11–32.

Zepp R. G. and Wolfe N. L. (1987) Abiotic transformation of organic chemicals at the particle-water interface. In *Aquatic Surface Chemistry: Chemical Processes at the Particle-Water Interface* (ed. W. Stumm). New York, John Wiley & Sons, pp. 423–455.

Zhang H. (1990) Factors determining the rate and stoichiometry of hornblende dissolution. Ph.D. thesis, University of Minnesota.

Zhang H. and Bloom P. R. (1999) The pH dependence of hornblende dissolution. *Soil Science* **164**(9), 624–632.

Zhang H., Bloom P. R., Nater E. A., and Erich M. S. (1996) Rates and stoichiometry of hornblende dissolution over 115 days of laboratory weathering at pH 3.6–4.0 and 25° C in 0.01M lithium acetate. *Geochimica Cosmochimica Acta* **60**, 941–950.

Chapter 7
Nucleation, Growth, and Aggregation of Mineral Phases: Mechanisms and Kinetic Controls

Liane G. Benning[1] and Glenn A. Waychunas[2]

7.1 Introduction

The formation of any phase, whether natural or synthetic (Fig. 7.1), is usually a disequilibrium process that follows a series of steps until a thermodynamically stable state (equilibrium) is achieved. The first step in the process of creating a new solid phase from a supersaturated solution (either aqueous or solid) is called nucleation. A particle formed by the event of nucleation usually has a poorly ordered and often highly hydrated structure. This particle is metastable with respect to ordering into a well-defined phase, which can accompany growth of the particle. This process of initiation of a new phase is defined as a first order transition and can follow various pathways involving a host of mechanisms. One of these pathways occurs when individual nuclei coalesce into larger clusters, a process defined as aggregation, which itself can follow a series of different pathways. The new phase is thermodynamically defined when the growing nucleus or aggregate has distinct properties relative to its host matrix; for example, a well-defined crystal structure, composition and/or density. These processes depend on a plethora of chemical and physical parameters that control and strongly affect the formation of new nuclei, the growth of a new crystal, or the aggregation behavior of clusters, and it is these issues that will be the focus of this chapter. We will discuss the mechanisms and rates of each process as well as the methods of quantification or modeling from the point of view of existing theoretical understanding. Each step will be illustrated with natural examples or laboratory experimental quantifications. Complementary to the information in this chapter, a detailed analysis of the mechanisms and processes that govern dissolution of a phase are discussed in detail in Chap. 5 and more detailed information about molecular modeling approaches are outlined in Chap. 2.

[1] University of Leeds, Earth and Biosphere Institute, School of Earth and Environment, liane@see.leeds.ac.uk
[2] Lawrence Berkeley National Laboratory, Molecular Geochemistry and Nanogeoscience Group, Geochemistry Department, Earth Sciences Division, gawaychunas@lbl.gov

Fig. 7.1 Crystals formed in natural and laboratory settings; (**a**) ice crystals grown on a glass window (Benning unpublished image) and (**b**) hexagonal pyrrhotite platelets grown from an iron sulphide precursor at 200° C; the growth followed a solid state process (see also Hunger and Benning, 2007; image Benning, unpublished, the copyright for the colour image (b) in the online version of this chapter is copyrighted to Eric Condliffe, Leeds)

7.2 Nucleation

Nucleation is the process by which small clusters of a new phase are initiated. The stability of any phase is usually the realm of equilibrium thermodynamics because any phase that is stable under given pressure and temperature conditions at a minimum energy state for infinite time periods is considered at equilibrium. In contrast, here we concentrate on how deviations from equilibrium drive the formation of a new phase from nucleation at the atomic or molecular level all the way to achieving a stable state at some larger growth stage.

In any system, equilibrium is attained when the exchange of heat or mass between initial and end product is approaching zero. The degree to which the process in question departs from this equilibrium state corresponds to the driving force that initiates nucleation of a new phase. When a new phase is forming in solution, this driving force is related to the deviation from saturation state of the system or the difference in chemical potential between the solution and the newly formed phase. This can be expressed as:

$$\Delta\mu_{\mathrm{I}} = \mu_{\mathrm{I,n}} - \mu_{\mathrm{I,s}} \tag{7.1}$$

which describes the difference in chemical potential between $\mu_{\mathrm{I,n}}$ (the chemical potential of component I in the nucleating phase) and $\mu_{\mathrm{I,s}}$ (the chemical potential of component I in the nucleating solution). Nucleation occurs when the overall free energy is reduced because part of the system is transformed from a higher to a lower free energy state, and thus when $\Delta\mu_{\mathrm{I}} < 0$ nucleation and growth are favored. A general formula for the driving force is given by:

$$\Delta\mu(a,\mathrm{T}) = \mathrm{k}_B\mathrm{T}\ln[a/a_e(\mathrm{T})] = \mathrm{k}_B\mathrm{T}\ \ln\ \mathrm{S_R} \tag{7.2}$$

where k_B is the Boltzmann constant, T is the absolute temperature and $\mathrm{S_R}$ is the solute supersaturation ratio ($\mathrm{S_R} = a_{(e)}/a$, where $a_{(e)}$ is the activity at equilibrium and a the activity during nucleation and growth).

7.2.1 Classical Nucleation Theory (CNT)

There are two main conditions where nucleation processes can be evaluated: (a) under conditions where the host phase is nearly at equilibrium with the nuclei, and (b) under conditions where the host phase is very distant in stability from the nuclei. The former case is the basis for the Classical Nucleation Theory (CNT), which we will discuss first. CNT includes treatments of nucleation from a purely thermodynamic or statistical mechanics formalism, or via so-called kinetic theories. The latter are generally better equipped to handle dynamic phenomena, such as nucleation rates, and allow some problematic aspects of pure thermodynamics based CNT to be overcome. However, the pure thermodynamic formalisms are useful as both

a starting point for theory development and as a useful tool for gaining insight into these transformation processes.

Nucleation theory began with the work of Volmer and Weber (1925), Farkas (1927), and Becker and Doring (1935), all treating liquid droplet condensation from a saturated gas. Somewhat more generalized treatments were subsequently developed by Zeldovich (1943), Frenkel (1939, 1955), Turnbull and Fisher (1949), and Turnbull (1950, 1956). These workers largely considered *homogeneous* nucleation, i.e., initiation of the new phase within the bulk of the solution or matrix with the only energetic conditions being the host and nucleus volume free energy and the interfacial free energy between host and nucleus. Although homogeneous nucleation is rare in geochemical systems, it is a good starting point for the introduction of nucleation, growth parameters and theory. CNT makes the assumption that nuclei that are formed have the same properties as their analogous bulk phase. This allows the free energy of the nucleus to be estimated as a sum of the bulk and surface free energies depending only on volume and area, respectively, and not on radius, a concept known as the capillarity approximation. Though these assumptions are not accurate on the molecular level (Talanquer and Oxtoby, 1994; Oxtoby, 1992), because nano-sized particles often do not behave like bulk analogs, and their surface energy is dependent on the radius of curvature, nevertheless these assumptions allow for a reasonably accurate analysis.

7.2.1.1 Equilibrium Thermodynamic Analysis

Overall, the total free energy of nucleation, ΔG, can be viewed as the sum of the energy used up in forming a particle by condensation of atoms, $-\Delta G_P$, which is proportional to r^3, and the energy gained by creating the particles surface ΔG_S, which is proportional to r^2. Figure 7.2a shows the free energy versus radius for incipient nuclei. The total free energy of nucleation, ΔG, can thus be expressed as:

$$\Delta G = [4/3\pi r^3 \Delta g] + [4\pi r^2 \sigma], \tag{7.3}$$

where r is the nucleus radius, Δg is the free energy change per unit volume of nucleus, and σ is the free energy per unit area of the nucleus interface.

The free energy of the nucleus is less than that of the corresponding matrix, and thus Δg is negative. There is thus a crossover point where the free energy change added by creation of the nucleus begins to decrease, and this corresponds to the critical nucleus radius. For any growth beyond this point the free energy decreases and growth is progressively more favored. If the derivative $\partial(\Delta G)/\partial r = 0$ is evaluated for Eq. (7.3), we obtain the free energy for the homogeneous critical nucleus formation:

$$\Delta G_{homo} = 16\pi\sigma^3/3(\Delta g)^2 \tag{7.4a}$$

and the critical nucleus radius,

$$r_{homo} = -2\sigma/\Delta g \tag{7.4b}$$

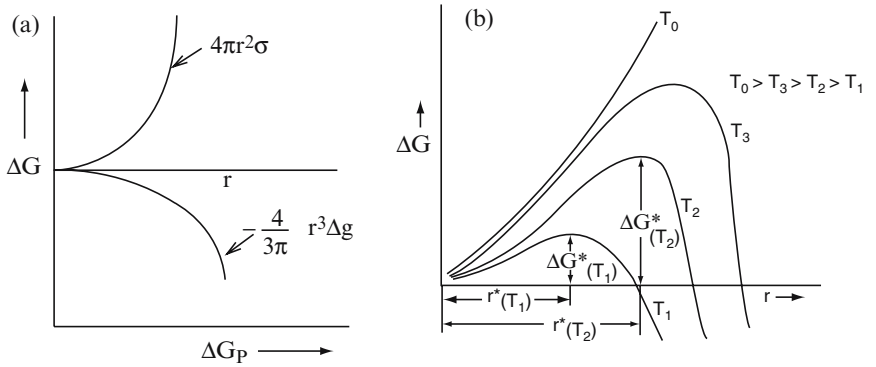

Fig. 7.2 Free energy of a cluster of atoms as a function of radius; (**a**) two main components of energy change in forming a cluster are defined: upper curve is surface free energy due to solid–liquid interfacial energy σ which increases with radius; lower curve is volume free energy that decreases with radius as the nucleation phase is more stable than the matrix and Δg is the difference in volume free energy between matrix and nucleus. (**b**) Sum of total free energy change at different temperatures as a function of radius. The "critical nucleus" free energy is ΔG^*. A larger nucleus is needed for stability at higher temperatures, or conversely nuclei formed at T_1 will cross into instability at T_2

Therefore, the critical energy of nucleation is governed by the magnitude of the free energy at the interface and the driving force. Usually, the smaller this critical energy the easier nucleation can occur. Figure 7.2b shows the effects of temperature on the critical nucleus size. As temperature increases there is less difference in the energy per unit volume of nucleus versus the matrix, thus the nuclei will have to grow larger in size before reaching stability. At some high temperature no nuclei of any size will be stable. This type of behavior can be looked upon as decreasing degrees of supersaturation as temperature increases.

The nucleation rate for such a CNT system can be determined by assuming that a single atom added to the subcritical size nucleus will result in a stable cluster. It is then possible to estimate the number of such subcritical nuclei by using Maxwell–Boltzmann statistics. Given a total number of atoms N_T, the number of critical nuclei can be expressed as:

$$N = N_T \exp(-\Delta G/k_B T) \tag{7.5}$$

Given that the largest subcritical nucleus is surrounded by *s* atoms in the matrix, and that the frequency of lattice vibrations (in a solid) or positional jumps (in a gas or liquid) is ν_j, then the frequency for which any of these can join the nucleus is:

$$\nu_j = s\nu_M \exp(-\Delta G_d/k_B T) \tag{7.6}$$

with G_d being the free energy of diffusion across the nucleus/matrix interface and ν_M the molar volume of the nucleus. This formulation allows one to include time in the nucleation equation, and hence the normalized homogeneous nucleation rate,

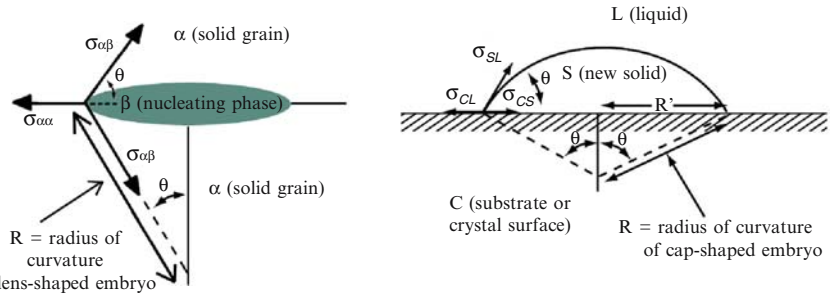

Fig. 7.3 Model geometries for idealized nucleation at grain boundaries (left), and at the solid–water interface (right). In the grain boundary case the nucleus (phase β) is lens-shaped and has all solid–solid interfaces, with the matrix being phase α. The contact angle, θ, is dictated by the surface energy $\sigma_{\alpha\beta}$. At the solid–water interface the nucleus (phase S) is a half-lens with different surface areas contacting the liquid (phase L) and solid (phase C) interfaces. In this case there are three different interface energies to consider, σ_{CL}, σ_{CS} and σ_{SL}

I_{homo}, can be deduced (Raghaven and Cohen, 1975):

$$I_{homo} = N_T s \nu_j \exp[-(\Delta G + \Delta G_d)/k_B T] \tag{7.7}$$

7.2.1.2 Heterogeneous Nucleation

In this volume, some aspects of the formation of new phases on mineral surfaces is discussed in Chap. 3. Nucleation on a surface, usually at defect sites and other regions where the energetics differ from the bulk matrix, is termed heterogeneous nucleation. For the homogeneous nucleation rate discussed above we can devise an analogous heterogeneous nucleation free energy diagram and nucleation rate. Figure 7.3 shows the situation for nucleation at a grain boundary (Clemm and Fisher, 1955), and nucleation on a mineral surface in contact with supersaturated aqueous solutions. These are two important cases for geochemical heterogeneous nucleation, with the former important for metamorphic systems, and the latter for aqueous systems. The key issue is that nucleus growth progressively removes boundary area at the interface of one grain with another. For nucleation from aqueous solution onto a surface, the analogous situation is removal of the surface-solution interface. Intuitively, nucleation in such cases is identical to homogeneous nucleation, except that it includes removal of an interface, and thus must lower the energy of the system more than a homogeneous nucleation event. Hence the energy barrier to nucleation must be reduced.

Heterogeneous nucleation may result in different spatial distributions depending on the shape of the solid–liquid interface. For a spherical or lens shaped interface, nucleation (and/or growth) will progress in three dimensions, while in the case of a disk shaped interface usually the height of the disc remains constant and two dimensional nucleation (and/or growth) takes place. In general it is considered that one-dimensional nucleation does not exist in the realm of heterogeneous nucleation.

However, in the literature 1D nucleation is often invoked when dealing with polymerization and it is described in terms of successive monomer addition. Below we discuss in more detail the case for heterogeneous nucleation on a planar surface and show how the nucleation rate can be derived based on geometrical and energetic considerations.

In Fig. 7.3, R is the radius of curvature of the spherical/lens shaped surfaces of the nucleus, θ is the included angle of the nucleus edge as controlled by surface tension, $\sigma_{\alpha\beta}$ is the matrix/nucleus interfacial energy, and $\sigma_{\alpha\alpha}$ is the grain boundary interfacial energy. The volume and surface area of a lens-shaped nucleus are thus:

$$V = 2\pi R^3(2 - 3\cos\theta + \cos^3\theta)/3 \tag{7.8a}$$

and

$$S = 4\pi R^2(1 - \cos\theta) \tag{7.8b}$$

respectively.

We note here that the total interfacial energy, $\sigma_{\alpha\alpha} = 2\sigma_{\alpha\beta}\ \cos\theta$, and thus the free energy change on nucleation can be derived:

$$\Delta G_{het} = (2/3\pi R^3\Delta g + 2\pi R^2\sigma_{\alpha\beta})(2 - 3\cos\theta + \cos^3\theta) \tag{7.9}$$

From these equations it is then an easy step towards deriving the free energy of critical nucleus formation:

$$\Delta G = 8\pi\sigma^3_{\alpha\beta}(2 - 3\cos\theta + \cos^3\theta)/3(\Delta g)^2 \tag{7.10}$$

In order to obtain the critical radius, *r*, we need to differentiate by R and thus obtain:

$$r = -2\sigma_{\alpha\beta}(\sin\theta)\Delta g \tag{7.11a}$$

and the critical free energy change:

$$\Delta G_{het} = \Delta G_{homo}(2 - 3\cos\theta + \cos^3\theta)/2 \tag{7.11b}$$

the latter obtained by substituting in the free energy for the homogeneous case. This shows that for small θ angles, and thus small interfacial energies, the heterogeneous free energy change is much smaller than the homogeneous case and the nucleating phase will "smear" out along the grain boundary. For $\theta = 90^\circ$, the energy changes are the same, and we obtain spherical nuclei with lowest surface area in both nucleation models.

For the aqueous interface model (Fig. 7.3, right), the same physical quantities can be substituted into the equations above with a slight variation. Here there are three kinds of interfaces, solid nucleus–liquid, substrate–liquid, and substrate–solid nucleus so the energy equations must include the interface area of the solid nucleus–substrate interface. We introduce slightly different designations here: R is the radius of the circle of substrate whereupon the new nucleus resides, and the interfacial energies for the three interfaces are σ_{SL}, σ_{CL} and σ_{CS}, respectively. We need the area under the nucleus, which is $\pi(R')^2$, and must also note that the nucleus has

half the volume and different surface area compared to the grain-boundary case. As $R' = R\sin\theta$, one can derive the analog of Eq. (7.9) as:

$$\Delta G_{aq-het} = \pi R^3/3(2-3\cos\theta+\cos^3\theta)\Delta g + 2\pi R^2(1-\cos\theta)\sigma_{SL} + \pi R^2\sin^2\theta\ \sigma_{CS} \tag{7.12}$$

and by setting $\partial(\Delta G)/\partial R = 0$ and evaluating as before, we get a critical nucleus:

$$r = -4(1-\cos\theta)\sigma_{SL} + 2\sin^2\theta\sigma_{CS/}(2-3\cos\theta+\cos^3\theta)\Delta g \tag{7.13}$$

This expression indicates the trade off between the various interfacial energies for aqueous solution nucleation. For example, in the case of strong hydrophobic interactions σ_{SL} may be significant and increase critical radii, so that precipitation is suppressed. For strong hydrophilic interactions, θ will tend to be small so that the critical radius approaches that for the grain boundary case.

Alternatively, for the grain-boundary nucleation case we can write the critical free energy change in terms of its volume, V, which turns out to be: $\Delta G_{het} = -(\Delta g)V/2$ (Raghavan and Cohen, 1975). This in turn is independent of the number of grain boundaries being absorbed (e.g., double or triple junctions). To obtain a nucleation rate for a heterogeneous nucleation process, it is subsequently necessary to take account of possible nucleation site densities. Note that in the case of homogeneous nucleation the site density was always 100% because nucleation position was unrestricted. Thus, the nucleation rate can be derived as:

$$I_{het} = \sum N_i\sigma_i\nu_j\exp[-(\Delta G_i + \Delta G_d)/k_B T] \tag{7.14}$$

where N_i is the nucleation site density with respect to the critical nucleation energy ΔG. When we compare the rate for heterogeneous nucleation with the nucleation rate for a homogeneous process (Eq. (7.7)) we observe that the pre-exponential term, $[N_i\sigma_i\nu_j]$ in Eq. (7.14) will be smaller than the equivalent term $[N_T s\nu_j]$ (see Eq. (7.7)), due to the appearance of the interfacial energy term. However, overall this will be offset by the much smaller nucleation barrier energy in a heterogeneous nucleation reaction.

As we have seen above, an equilibrium CNT model lets us derive conditions for formation of nuclei and rates of formation, despite its neglect of atomistic processes and variations, such as the shape, density, and crystallinity of such nuclei. CNT also neglects the fact that a small cluster will have more surface molecules than "bulk" molecules on a volume-normalized basis and thus the difference in surface energy has to be treated independently of the nucleus size. In addition to the failings in the homogeneous case, our development of equilibrium heterogeneous nucleation neglects important aspects of realistic surfaces, such as steps and terraces, dislocations, and other causes of surface strain, and variations in interface energy, some of which were previously discussed in Chap. 3. Examples of CNT that treat these issues can be found in metallurgical and semiconductor applications (Chernov, 1984; Tiller, 1991, 1992). Heterogeneous nucleation is affected by the periodicity of the nucleating phase and the substrate, and is generally enhanced by good registry such

as in near perfect epitaxial relationships, a matter of extreme importance in the nucleation and growth of semiconductor thin films (Venables et al., 1984), and a matter we return to below. However, in cases of greatly dissimilar substrates and nucleating phases (i.e., organic nuclei on ionic substrates) molecular dipole effects and growth anisotropy appear to outweigh lattice matching (Sarma et al., 1997).

7.2.2 Kinetic Nucleation Theory (KNT)

In order to use an equilibrium CNT model to explain precipitation kinetics, we would require good estimates of the interfacial energies, the density of nucleation sites, and the free energy of critical nucleus formation. While interfacial energies are relatively easy to obtain for bulk phases, this is problematic for small nuclei. Even more of a problem is estimation of the free energy of nucleus formation. The one area where modern technology presents a solution is for the density, and even the topology, of nucleation sites (especially relevant for heterogeneous nucleation). KNT provides a way around requiring good estimates of the free energy change on nucleation. An important aspect of the equilibrium CNT formulation is the absence of explicit treatment of backward reactions in determining the nucleation rate. Once formed, the critical nuclei are considered to be stable. However, the critical size nuclei can also dissolve back into the matrix or solution. Hence instead of only considering the rate at which nuclei form and reach stable sizes, a kinetic theory would include the rates of various nuclei dissolving. In the ideal conceptualization, by using KNT we can simply depend on interaction parameters for individual molecules to predict all of the necessary rate equation coefficients, and these parameters might ideally be estimated by the results of quantum mechanics calculations.

KNT originated from the consideration of a chain reaction of clusters of varying size. A general formulation for KNT is (Volmer, 1939; Toschev, 1973):

$$\frac{dc_i}{dt} = \sum_{k=1}^{M} D_{k->i} c_k - \sum_{k=1}^{M} D_{i->k} c_i, \tag{7.15}$$

where i = 1, 2, 3, …, M, and the first and second summations represent the formation and dissolution of clusters c_n, of various sizes n, respectively. The D_n operators represent the probability of an exchange occurring. This is a set of equations which is very bulky to handle, so we can simplify it by considering only "monomer" changes, i.e., clusters that change size by loss or gain of single elements (atoms or molecules). For example:

$$i-1 \underset{D_i^-}{\overset{D_{i-1}^+}{\rightleftharpoons}} i \underset{D_{i+1}^-}{\overset{D_i^+}{\rightleftharpoons}} i+1 \tag{7.16}$$

Thus combining with Eq. (7.15) this leads to the formulation:

$$\frac{dc_i}{dt} = \left(D_{i-1}^+ c_{i-1} + D_{i+1}^- c_{i+1}\right) - \left(D_i^+ c_i + D_i^- c_i\right), \tag{7.17}$$

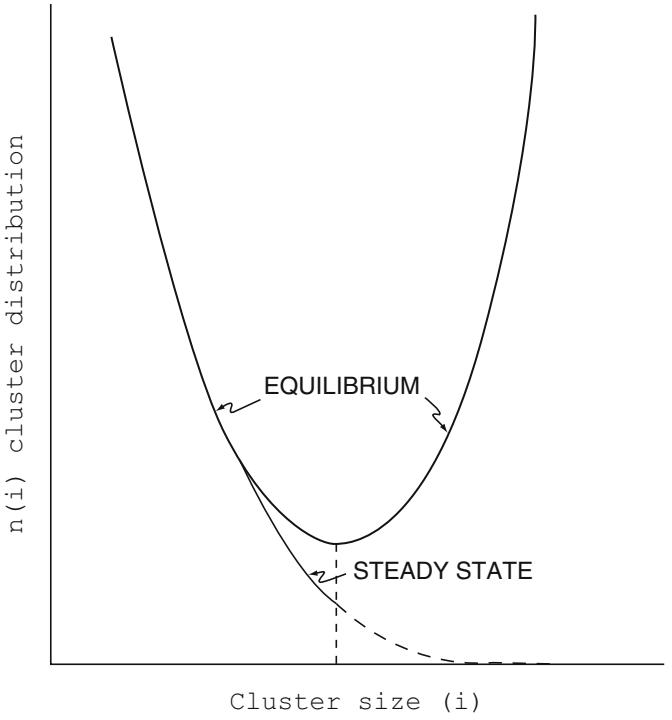

Fig. 7.4 Kinetic theory nucleation rate as a function of normalized cluster size. The critical nucleus is defined here as the cluster size where creation (birth) and dissolution (death) rates are equivalent and no explicit energy is considered. This calculated curve (after Toschev, 1973) is for water nuclei with $i^* = 64$ molecules at 300 K

where $i = 2, 3, \ldots, M-1$, with $c_i = 0$ when $M = i$, i.e., the largest clusters are continuously taken out of the system; $D_i^+ = A_i \beta_i$ and $D_i^- = A_i \alpha_i$, where A_i is the surface area of the i-sized cluster, and β_i and α_i are the numbers of atoms or molecules joining and leaving the cluster per unit time and surface area, respectively. It is useful to consider the ratio $D_i^+/D_i^- = \exp(\frac{\mu^* - \mu_i}{RT})$, where $\mu^* - \mu_i$ is the difference in chemical potential between the critical nucleus and a given cluster as derived by Volmer (1939). For spherical nuclei this can be shown to be equivalent to:

$$\frac{D_i^+}{D_i^-} = \exp\left\{ \frac{B}{i^{*1/3}} \left[1 - \left(\frac{i^*}{i} \right)^{1/3} \right] \right\} \tag{7.18}$$

where $B = \frac{2\sigma\nu}{RT} N_A^{1/3} (\frac{4\pi}{3\nu_M})^{1/3}$ with ν being the molar volume of the formed nucleus, N_A the Avogadro's number, and σ the nucleus surface free energy. A plot of this equation (Fig. 7.4) calculated for water droplets shows that subcritical clusters can

only reach the critical size by random fluctuations, rather than grow as might be intuited from equilibrium theory.

The flux of clusters through a given size is:

$$J_i = D_{i-1}^{+} c_{i-1} - D_i^{-} c_i. \tag{7.19}$$

Substituting Eq. (7.19) into Eq. (7.17) produces

$$\frac{dc_i}{dt} = J_i - J_{i+1}, \tag{7.20}$$

which represents the rate of flux through a given cluster size. In this terminology, the nucleation rate is equivalent to the flux J_i when the i values considered clusters at the critical cluster size. Two conditions are usually considered, the steady-state nucleation rate, i.e., the case where $\frac{dc_i}{dt} = 0$ (Becker and Doring, 1935) and there is continuous fixed flux of clusters through the various size regimes, and the equilibrium nucleation rate where there is no flux between cluster sizes.

7.2.2.1 Zeldovich-Frenkel Formulation

Zeldovich (1943) and Frenkel (1955) developed equations analogous to Eq. (7.17) and Eq. (7.20), but taking i as a continuous variable. Using the principle of detailed balance (i.e., all elementary reactions must have equal forward and reverse rates at equilibrium) with the relation $D^{+}(i)n(i) = D^{-}(i+1)n(i+1)$, where $n(i)$ is the equilibrium distribution function for all clusters i, the dissolution probabilities $D^{-}(i)$ can be eliminated from the equations. This produces a set of partial differential equations for cluster size evolution in time, and instantaneous fluxes:

$$\frac{dc_{(i,t)}}{dt} = \frac{\partial}{\partial_i}\left\{ D^{+}(i)n(i)\frac{\partial}{\partial_i}\left[\frac{c(i,t)}{n(i)}\right]\right\} \tag{7.21}$$

$$J(i,t) = -D^{+}(i)n(i)\frac{\partial}{\partial_i}\left[\frac{c(i,t)}{n(i)}\right] \tag{7.22}$$

At equilibrium the cluster sizes equal the equilibrium distribution function, $c(i) = n(i)$, and it can be shown that:

$$n(i) = N\exp\left(-\frac{\Delta G_i}{k_B T}\right), \tag{7.23}$$

where ΔG_i is the Gibbs free energy change associated with the i^{th} cluster formation, and N is the total number of clusters. For the steady state, one must integrate the partial differential equations over all values of i. The resulting approximate solutions for the total fluxes yields

$$\mathrm{J_o} = N\mathrm{D^{+}Z}\exp(-\Delta \mathrm{G^{*}}/\mathrm{k}_B\mathrm{T}), \tag{7.24}$$

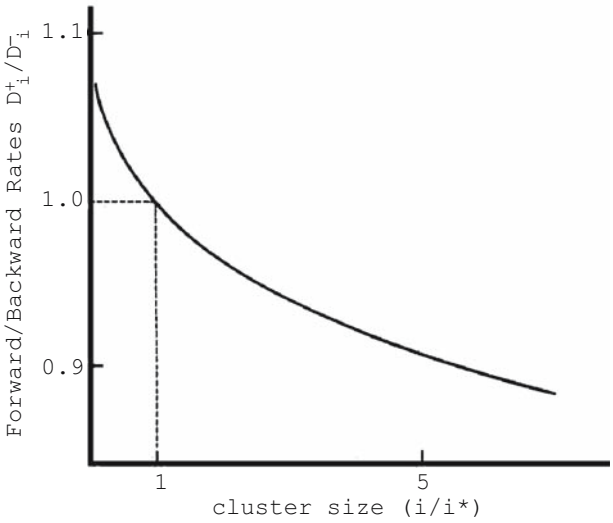

Fig. 7.5 Distribution of cluster sizes as calculated by kinetic theory for equilibrium and steady state conditions. In the equilibrium case critical nuclei are the lowest in abundance, while in the steady state case they have half the equilibrium abundance but larger clusters are still less abundant. (After Toschev, 1973)

where Z, the Zeldovich factor, is approximately $(\Delta G^*/2\pi k_B T)^{1/2}$ and is generally on the order of 0.05. This factor effectively corrects equilibrium classical nucleation rates for steady state situations. In this case the cluster distribution can be calculated from the flux via integral equations of the form $c(i)/n(i) = J_0 \int_i^M di/D^+(i)n(i)$ and the steady state and equilibrium cluster distributions are shown in Fig. 7.5. For the equilibrium case we note that the critical clusters have the lowest concentration, which is in keeping with the experimental problem of observing a critical nucleus. For the steady state the cluster size profile differs near the critical nucleus size, decreasing to half the equilibrium concentration at i^*, and declining for larger cluster sizes. For heterogeneous nucleation, the expressions derived for homogeneous nucleation are often used, with adjustments made for the difference in Gibbs free energy for nucleation. However, the literature consensus seems to be that detailed kinetic theories for heterogeneous nucleation are generally much less accurate than the corresponding homogeneous theory (Wu, 1997), and tests of heterogeneous theory using measured surface energies show poor agreement with experiment (Marasli and Hunt, 1998).

One other aspect of steady state nucleation is the concept of induction time, or time from the initial state until a steady state nucleation process has evolved. This is the period needed for the system to reorganize itself and adopt the steady state condition. A general expression for the induction time, τ, for homogeneous nucleation is:

$$\tau = 0.7b^3 \frac{RT\sigma^3 v_M^2 N_A}{\Delta\mu^4 D^+}, \tag{7.25}$$

where b is a geometrical coefficient equal to $6^{2/3}\pi^{1/3}$ for spherical nuclei, $\Delta\mu$ is the driving force for nucleation, and D^+ is the diffusion coefficient for transfer of atoms to the nucleus. For melts and solutions τ is proportional to the viscosity of the medium due to the D^{-1} dependence. In condensation from vapor, this time is sufficiently small as to be generally negligible, but such is not the case in liquids, glasses and solids. For example, for water condensation from vapor at 300 K $\tau = 3 \times 10^{-8}$ s, but for nucleation of wollastonite from $CaSiO_3$ glass at 1,060 K, τ is on the order of 10^4 s (Granasy et al., 1998). Hence, depending on the precise system being modeled, an assessment of the nucleation rate during the transient time may be crucial in understanding the experimentally measured nucleation rates. It is even possible that complete precipitation can occur before the steady state regime is reached, and hence nucleation rates can continuously change.

We have seen that a discrete cluster kinetic theory can be extended to a continuum partial differential equation formulation. An atomistic version is also possible, but with limitations on the size of clusters that it can consider. In our current vernacular, these treatments equate to molecular dynamics (MD) and kinetic Monte Carlo simulations (KMC). In the MD approach (see Chap. 2) the system is defined by the starting positions and interatomic potentials, with an energy flux related to absolute temperature driving the operations. In MD we can uncover the types of pathways that individual atoms make in producing nuclei whether adding to them or contributing to dissolution, and we can determine cluster statistics as a function of time. This information allows us to consider how and where clusters are formed, and how surfaces (for example) affect cluster formation and growth. Some simplification can be obtained by using transition state theory (TST) wherein we neglect molecular vibrations and just consider the specific diffusion events that characterize system reconfiguration. This is much less general, but much faster in execution computationally.

In the KMC simulation we take into account the spatial aspects of the system and the relevant stochastics, without calculations of complex interatomic interactions. The relevancy of the approach depends on including enough microscopic processes to yield meaningful results and significant time saving. But often this end requires much experimentation to determine what factors are of prime relevance (Ratsch and Venables, 2003). The current most intense use of these methods is in understanding and modeling thin film processes. In semiconductor (integrated circuit) processing, it is crucial to understand how new layers are nucleated and grown so as to limit defects, produce uniform layer thicknesses, and eliminate unfavorable grain boundaries due to the coalescence of two-dimensional islands (nuclei).

7.2.2.2 Density Functional Theory (DFT) Approach

Although DFT methods are frequently used for electronic structure calculations where the electron density of a system is treated (see Chap. 2), on a larger physical scale such as whole atoms or molecules they are important in modeling phase transformations that occur with a diffuse interface. Examples are growth of

compositional fluctuations in a solid solution (e.g., spinodal decomposition, Cahn and Hilliard (1958); Cahn (1962, 1966)), and diffuse nucleation in glasses (e.g., Granasy et al., 1998). For such cases the nature of the interface between matrix and nucleus is not defined, the systems are generally far from equilibrium, and classical methods cannot be applied.

In the DFT approach used in these cases one replaces the atomic or molecular nature of a system with chemical density variation over a continuous medium. One then formulates the free energy of this system as a functional containing local and nonlocal contributions. The approximate equation derived by Cahn and Hilliard (1958) for a cubic solid solution is:

$$F = \int_{\mathrm{v}} \left[f(c) + H(\nabla c)^2 \right] dx \tag{7.26}$$

where $f(c)$ is the local free energy per unit volume, and the second term is the gradient energy, H, that drives the transformation, with H being an approximation of the intramolecular potential, both being functions of the composition, c. Minimizing this integral equation yields the overall density fluctuations in the solution that are most stable. For solid solutions this approach predicts critical nuclei that have finite size and an infinitely sharp interface at equilibrium phase boundaries (e.g., crystal/melt) as in CNT, but have infinite size and a completely diffuse interface at the spinodal. This is in keeping with a process that is occurring far from equilibrium, and the usual form of spinodal decomposition is periodic compositional fluctuations, contrasting with random CNT-type nucleation (DeFontaine, 1975). The growth of these fluctuations is diffusion controlled, based on the local compositional gradients. Annealing of spinodal fluctuations eventually gives rise to coarsening and phase separation, and the appearance of exsolution structures in solid solutions (Yund et al., 1974; Zhu et al., 1999).

Talanquer and Oxtoby (1994) developed a DFT approach for heterogeneous nucleation of droplets with sharp interfaces and compared this with a CNT estimate of nucleation rate. They found that for conditions far from the equilibrium phase boundary, CNT failed drastically, again suggesting the need for a non-classical approach to nucleation at disequilibrium conditions.

7.2.2.3 A Statistical-Empirical Approach: Crystal Size Distribution (CSD) Analysis

From a practical standpoint, we can ask whether we have appropriate experimental information to use any of these theories to allow ab initio prediction of nucleation in geochemical systems. In order to describe nucleation rates over wide conditions for a specific system we would require, above all, good estimates of the interfacial energies, the density of nucleation sites, and the free energy of critical nucleus formation. This is extremely difficult to do (Kelton and Greer, 1988; Kirkpatrick, 1981), for geological systems, and thus nucleation models have been generally treated as empirical fits to the derived mathematical equation form and dimension. However, more

recently it has become possible to model interfacial energies and surface energies (i.e., for surfaces in vacuum) fairly accurately with quantum calculations (Henry, 2003; Bandura et al., 2004).

Regardless of whether we can ever expect to calculate all the parameters we need for the highest-level theoretical approaches, knowledge of the physical theory gives insight into the processes involved and ultimately such atomistic/cluster approaches ought to be applicable to any type of system.

Another approach that treats nucleation and growth kinetics in a statistical manner and allows kinetic parameters to be estimated without the need for accurate interface energies is crystal size distribution (CSD) analysis (Randolph and Larson, 1971). In this approach the distribution of observed crystallite sizes in a sample is measured from thin sections or other petrological/materials sampling to produce a population number density profile which is the numbers of crystals of a given size, $n(L_{CSD})$, divided by the size interval, L_{CSD}. Analysis of this profile is a useful statistical description of, e.g., an igneous crystallization system in a magma chamber, or of sedimentation structures, but can be greatly extended with mathematical analysis (Randolph and Larson, 1971; Marsh, 1988). The information in the $n(L_{CSD})$ versus L_{CSD} profile, as a snapshot of the system in time, is combined with "conservation" differential equations which tie together the change in integrated growth volume with the input and output flux of crystal volume when the system was operating. By using assumptions of various conditions in the system (e.g., flux of crystal mass in $=$ flux out, or growth independent of size, etc.), it is possible with such boundary conditions to evaluate the equations to yield estimates of nucleation and growth rates. Further, the moments of the crystal distribution can be evaluated to yield the most important sizes, masses or lengths of the crystal population, and these, in turn, can be used to extract estimates of nucleation density and other physical attributes (Cashman and Marsh, 1988). CSD analysis appears to be useful because certain reasonable but simplifying assumptions can be made in the analysis, and crystallites once formed appear to have constant growth rates.

7.3 Growth Processes

7.3.1 Classical Growth Theory

As CNT assumed monomer attachment to a growing critical nucleus, classical crystal growth theories assume atom-by-atom or molecule-by-molecule attachment to a growing surface. However the nature of these attachments is rooted in the precise description of the growth surface. Growth in the general case is often presented as an ideal type of epitaxial process, i.e., nucleation occurs with proper registry of new species to the existing atoms on a surface. Nucleation here is somewhat different than in the case of heterogeneous nucleation discussed previously, as the system is supercritical, layers rather than some finite cluster volume are being formed, and direct chemical binding of the new atoms occurs at the interface. Classical theory

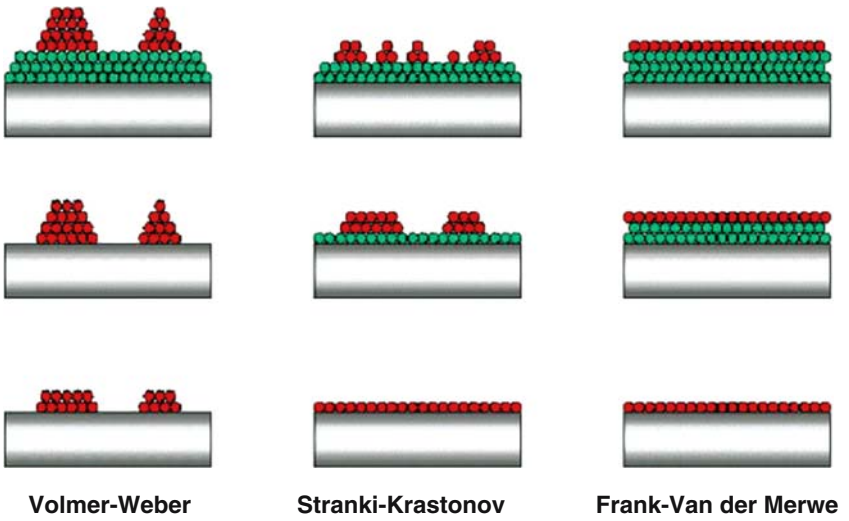

Fig. 7.6 Types of classical growth models. (**a**) Volmer-Weber type (island) growth where interface energy is relatively large. Hence discrete nuclei form and grow before a layer is completed by infilling. (**b**) Stranski–Krastanov type (layer + island) growth where interface energy is comparable to island interaction energy, and hence layer formation competes with nuclei formation. (**c**) Frank-van der Merwe (layer) growth. Here interface energy is relatively low and layers form readily from nearly any size nuclei

often begins with the assumption that growth is occurring under a supersaturated condition, so that the system is not close to equilibrium. Hence we start with that case.

The most common growth model is Frank-Van der Merwe growth, also known as "layer-by-layer" growth. In this model (Fig. 7.6) a layer of atoms is started and completed before another layer starts to grow. The model assumes that attachment of atoms to the edge of a growing layer is far more likely than attachment to the top of the layer, i.e., new nucleation, and hence the latter rarely occurs.

The simplest energetic interpretation is that the atom attaching to the growth layer edge makes two or more bonds while one connecting to the top surface makes only one, and hence reduces the interfacial energy by much more. In a kinetic interpretation the atom attached to the top of the surface will diffuse quickly until it encounters a new layer edge, and, now having two bonds, thereafter will have a much lower probability of moving back to the surface. Similarly, an atom bonded to the edge of the surface layer may diffuse along the edge until it can find additional bonding opportunities at "kink" sites (see also Figs. 7.7 and 7.8 in Chap. 3).

The direct opposite to this type of growth is the Volmer–Weber type (Fig. 7.6), where nucleation of islands is favored over extended growth at layer edges. This can occur if the new precipitating species have a tendency to cluster, i.e., the new atoms bond more strongly with one another than to the surface, or if diffusive processes slow layer growth until new surface nucleation far exceeds it (resulting

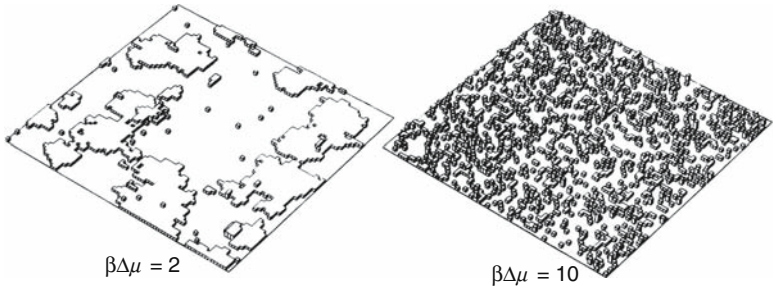

Fig. 7.7 Monte Carlo simulation of interface topology after 25% of a monolayer is deposited on a flat (001) crystal face at the same temperature but different values of the product of inverse energy ($\beta = 1/k_B T$), and difference in chemical potential from the equilibrium solid ($\Delta\mu$), which is equivalent to the driving force for growth. For a product of two layer formation is favored, but for ten, nucleation is favored over layer growth. (After Weeks and Gilmer, 1979)

in increased nuclei density). The net effect is that layers are filled in as islands are nucleated and merge. Finally there is a mixed alternative, known as Stranski–Krastonov growth, where growth is initiated as a layer-by-layer mode but shifts to an island mode.

Using these types of surface features in what is called the solid-on-solid (SOS) model, a kinetic equation can be generated that describes the rate of change in occupation of surface sites in any incomplete surface (growth) layer (Weeks and Gilmer, 1979):

$$\frac{dC_n(t)}{dT} = k^+[C_{n-1}(t) - C_n(t)] - k(n,t)[C_n(t) - C_{n+1}(t)] \tag{7.27}$$

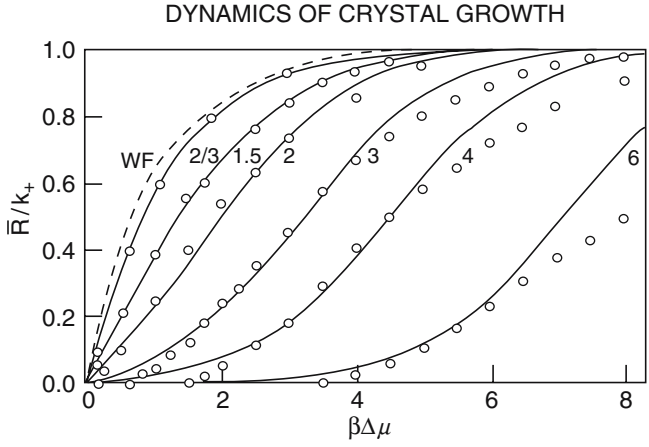

Fig. 7.8 Mean growth rates $\overline{R}$ normalized by the deposition rate k^+ for the 2-rate model (solid curves) compared to Monte Carlo simulations (circles) for a range of $\beta\Delta\mu$ values (After Weeks and Gilmer, 1979)

Here the $C_n(t)$ are the occupations of the nth layer parallel to the surface, k^+ is the deposition rate of atoms or molecules on the surface, and k^- is the effective evaporation or desorption rate:

$$k(n,t) = \nu_d \sum_{m=0}^{4} \exp(-m\beta\Phi)\, f_{n;m}(t), \tag{7.28}$$

where m is the number of adjacent layer neighbors, $f_{n;m}(t)$ is the fraction of surface atoms in layer n with m neighbors, ν_d is the desorption rate for an isolated surface atom, β is $1/k_B T$, and Φ is the chemical potential change on desorption. Equation (7.28) shows that the desorption rate is reduced as the number of atom neighbors increases, reflecting bonding with these atoms. With these expressions the growth rate, R_{SOS}, for the surface is now:

$$R_{SOS} = k^+ - \sum_{n=-\infty}^{\infty} k(n,t)\, f_{n;m}(t), \tag{7.29}$$

i.e., the difference between deposition processes and desorption processes, respectively, for all surface layers. Using Monte Carlo methods, Eq. (7.29) can be used to generate a model surface. For example, taking T constant and time interval t where 25% of a surface layer has formed, the atomic arrangement for two different values of $\beta\Delta\mu$ are shown in Fig. 7.7. For large $\beta\Delta\mu$, the desorption rate is low for isolated surface atoms and small islands saturate the surface, whereas for small $\beta\Delta\mu$ the desorption rate is high and only atoms associated with already nucleated layers persist. This approach is extremely basic, including no anisotropy in the surface (i.e., the system is rigorously cubic in symmetry), and making implicit assumptions about how atoms can diffuse (viz. only along layer surfaces). However it is not a poor assumption at high driving force, i.e., high supersaturations or low temperatures.

To improve the model we need to extend the applicability to cases near equilibrium at low driving force. One such theory is that of Weeks et al. (1976), called the "two-rate" model. In this model steady state growth is assumed, i.e., the surface condition at some time t is closely similar to that observed at a later time $t+\gamma$, where γ is the mean time required to deposit a monolayer of atoms. Hence each layer in the surface behaves essentially similarly with time, and a given upper layer looks like a buried one after the appropriate dwell period. For this model two rates for desorption are used, a fast one for layers that are less than half populated, and a slow one for layers that are more than half populated. This considers, in a very simple way, the effect of higher numbers of nearest neighbors on the desorption rate.

Rather than show the derivation of this model here, we just quote the resultant average growth rate:

$$\overline{R} = \frac{(k^+) - k_{eq}^2}{\bar{k} + k^+}, \tag{7.30}$$

where $\bar{k} = (k_{slow} + k_{fast})/2$, and $k_{eq} = (k_{slow} + k_{fast})^{1/2}$. By adding the mean probability, C, that a surface atom can find a neighboring occupied atomic site into this

expression, one obtains the growth rate:

$$\frac{\overline{R}}{k^+} = \frac{2\sinh(\beta\Delta\mu)}{\exp(\beta\Delta\mu)+\cosh(\varepsilon\beta\Phi)}, \tag{7.31}$$

where $\varepsilon = 2(1-2C)$. This is plotted (solid lines) for a range of $\beta\Delta\mu$ values in Fig. 7.8, and compared to the Wilson-Frenkel (WF) rate, which fixes the desorption rate to that of the bulk crystal phase at equilibrium. This theory agrees fairly well with MC simulations (circles) of growth rates at higher temperatures and high deposition rates for simple systems (Weeks et al., 1976). Another type of Monte Carlo growth simulation also agrees well with this type of kinetic approach (Jiang and Ebner, 1989).

7.3.1.1 Effects of Screw Dislocations on Growth

The models discussed above generally produce rather slower kinetics compared to what is commonly observed in natural systems. This is due in large part to the presence of growth defects in real systems that make it easier or unnecessary to nucleate a new growth layer. The most important case is that of screw dislocations, first described by Frank (1949) and Burton et al. (1951). Figure 7.9 shows the development of a spiral growth pattern about a screw dislocation.

MC calculations of growth rates from the SOS model on a perfect crystal and a spiral growth model are shown in Fig. 7.10. In the plot, $L/k_B\,T$ is a measure of atom-atom binding force, L, versus available energy, k_BT. For lower binding energies there is little difference between the two growth rates, but divergence is notable with increasing binding energy. One can see that at sufficiently low temperatures, layer-by layer growth is quenched relative to spiral growth. The effects of variation in the 2D nucleation of layers and evaporation rate have been considered explicitly by Weeks and Gilmer (1979). More details on this type of growth are available in Chap. 3.

7.3.1.2 Molecular Models

The models described so far do not consider the molecular basis of growth explicitly, and to practically consider the effects of impurity incorporation and the broader range of defects and surface processes a truly molecular model is required. Paquette and Reeder (1995) developed one such molecular model for impurity incorporation in calcite largely based on the concept of the periodic bond chain (PBC) model of Hartman and Perdok (1955). In this model crystal growth is favored by attachment of new species along the directions of the strongest PBCs. Hence analysis of the nature of the PBCs allows prediction of growth rates and habits. For impurity incorporation, the PBCs allow description of the kink sites where attachment of new species occurs, and it also identifies non-equivalent kink sites within the same growth layer (Fig. 7.11). Such inequivalent sites display different binding energies

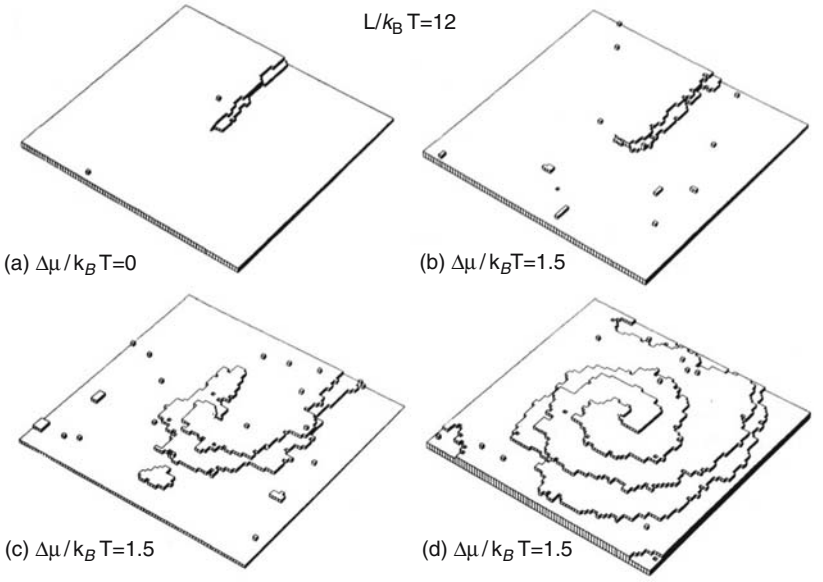

Fig. 7.9 Monte Carlo simulation of evolution of the double spiral type of layer growth produced by a screw dislocation. The temperature is parametrized by L/k_BT where L is the binding energy per atom in the lattice. (**a**) is the equilibrium state, and (**b**) through (**d**) show progressive evolution of growth with $\beta\Delta\mu = 1.5$ favoring layer growth. (After Weeks and Gilmer, 1979)

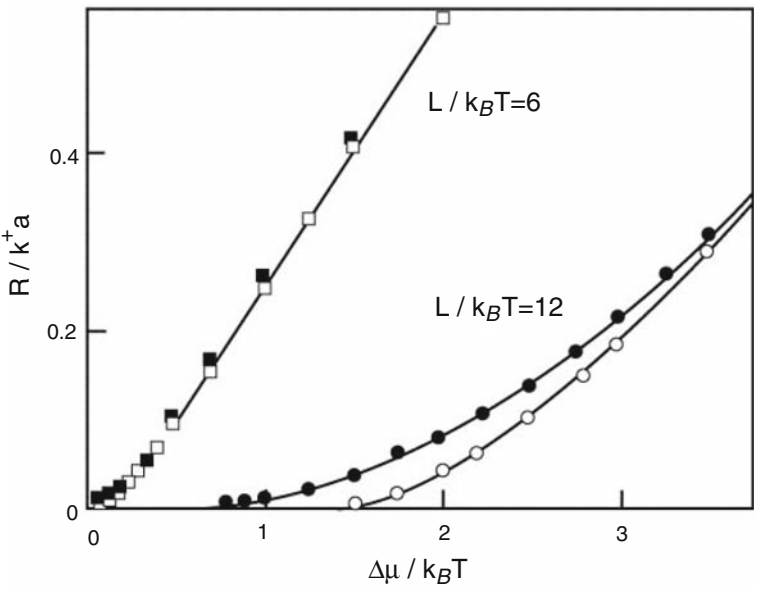

Fig. 7.10 Comparison of growth rates for perfect layer by layer (open symbols) versus spiral growth (solid symbols) for two parameterized temperatures. (After Weeks and Gilmer, 1979)

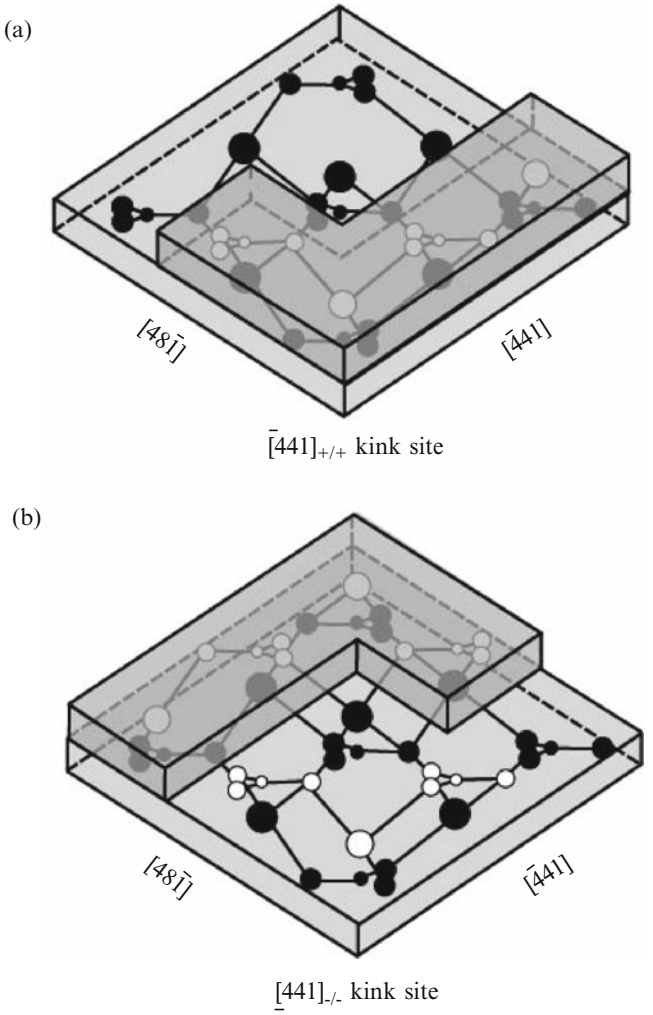

Fig. 7.11 Models of cation kink sites where divalent metals can be incorporated into growth steps on the calcite (10–14) surface. Open circles are atoms that reside in the upper slice, while solid atoms are in the lower slice. Divalent substituent atoms in the kink sites are depicted by arrows. In the $+/+$ kink site the divalent atom is coordinated by three oxygens of the same carbonate layer, whereas in the $-/-$ kink site the three O atoms reside in adjacent carbonate layers. Hence the geometry and effective size of the sites differ as "seen" by a possible substituting divalent atom. (After Paquette and Reeder, 1995)

for particular impurities, forcing these species to segregate in a particular manner, which in turn could be conducive to particular zonation effects.

A related model discussed by Pina et al. (1998) for the aqueous growth of barite considers the underlying atomic structure of the growth surface also with reference to PCBs, and the specific energetics of atomic attachment. AFM observations show that at high supersaturations nucleation on the barite (100) surface is initiated at

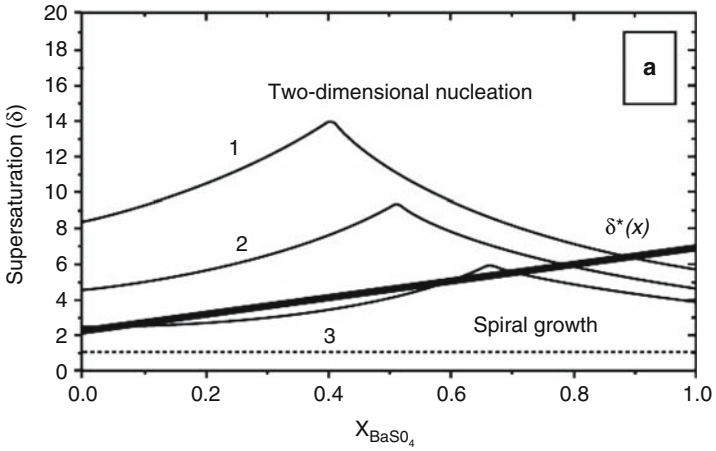

Fig. 7.12 Supersaturation trends for solid solutions $(Ba_x, Sr_{1-x})SO_4$ growing on barite (001) at three different solution compositions (see text). Each possible solid solution composition has a different supersaturation. Changeover from two-dimensional nucleation and layer growth to spiral growth occurs at the heavy line $(\delta^* x)$. (After Pina et al., 2004)

a screw dislocation, but does not proceed classically. Rather the growth spiral is extremely tight resulting in a hillock near the dislocation core with anisotropic lateral layer spreading. The disruption in the spiral mechanism is caused by the strong growth anisotropy, which is created by differing attachment energies for Ba and SO_4 units at particular positions on the growth layer. Effectively, growth dominates along a single direction having a specific polar orientation and hence lower symmetry than would be expected from any more classical growth model.

7.3.1.3 Solid Solutions

Crystal growth from solutions with mixed ions can produce markedly zoned crystals, but growth mechanisms and kinetics have been little treated. The main complication is that the degree of supersaturation of the solution phase, and thus the driving force for crystallization, is a function of the composition of the crystallizing solid phase. Pina et al. (2004) suggested a formulation for the supersaturation of barite-celestite solid solutions that illustrates the issues. Figure 7.12 shows a plot of supersaturation, δ, in this system as a function of barite fraction in the precipitated solid solution. The solution compositions are: (1) $[Ba] = 1\,\mu mol/L, [Sr] = [SO_4] = 3,000\,\mu mol/L$; (2) $[Ba] = 1\,\mu mol/L, [Sr] = [SO_4] = 2,000\,\mu mol/L$; (3) $[Ba] = 1\,\mu mol/L, [Sr] = [SO_4] = 1,100\,\mu mol/L$. The bold solid line is the observed delineation between two-dimensional layer nucleation and growth at higher supersaturations, and spiral growth about dislocation cores. As growth continues the solution changes composition and the solid solution composition having greatest supersaturation also varies, which can lead to a continuous change in the precipitate composition. A further consequence of these compositional dependences is that a

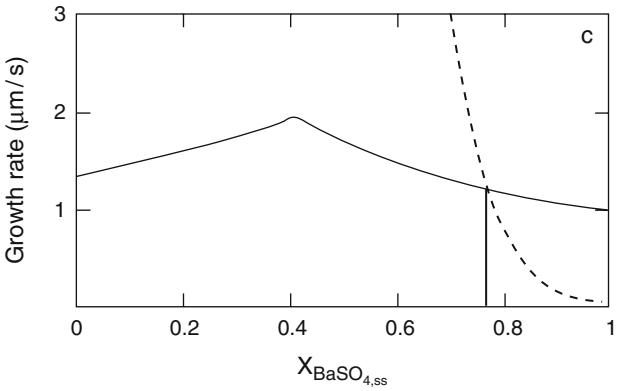

Fig. 7.13 Comparison of growth rates from solution #1 of Fig. 7.12 for different compositions of solid solution. Solid solutions of composition 0.766 barite or greater can only grow by the spiral growth mechanism. (After Pina et al., 2004)

change in growth mechanism can occur at a specific composition of the solid solution. Figure 7.13 shows the growth rates as a function of composition for one of the solutions (#1) shown in Fig. 7.12. Both growth rates calculated for layer growth (solid) and spiral growth (dashed) using classical rate formulations (Ohara and Reid, 1973) are shown. Layer growth is faster at compositions below 0.766% barite, but slower at higher barite fraction where spiral growth takes over.

7.3.1.4 Growth Kinetics as Measured by Volume Transformations

For certain types of systems, especially solid-state transformations in metals, semiconductors and metamorphic rocks, the use of layers (i.e., interface growth rates) is inconvenient. In these cases growth is often modeled by the rate of volume converted into a new phase. Such models are semi-empirical and consist mainly in the way in which certain types of grain growth will fill three-dimensional space as recrystallization or phase transformation proceeds. An example is the approach taken by Johnson and Mehl (1939), and Avrami (1941) for spherical grains and the impingement of transformed regions affecting the rate dependence. For empirical treatments, the volume fraction transformed, α_A, is given by:

$$\alpha_A = 1 - \exp[-(kt)^n], \tag{7.32}$$

where k is the first-order reaction rate constant, and n is the time exponent. Johnson and Mehl (1939) assume that the nucleation rate and the growth rate are independent of time and the amount of volume transformed, and that nucleation is random in position. This yields the formulation:

$$\alpha_A = 1 - \exp(-1/3\pi I U^3 t^4), \tag{7.33}$$

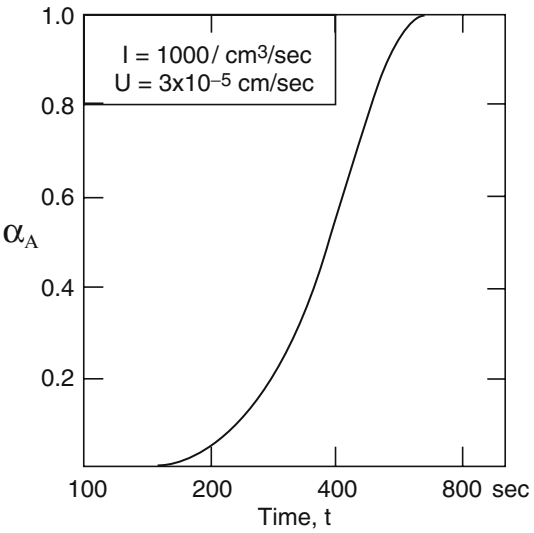

Fig. 7.14 Fraction of volume transformed in a material using the Johnson–Mehl empirical approach. The case shown assumes constant nucleation (I) and growth rates (U) and spherical particles, but other shapes of particles alter the exponent in the growth law and can be extracted from this type of analysis. The method is useful for describing transformation kinetics of various types, e.g., phase transformations, coarsening of grains, but does not include diffusion-controlled processes. (After Raghaven and Cohen, 1975)

with I being the nucleation rate and U the growth rate of individual grains, and α_A plots as a sigmoid with time (Fig. 7.14).

If we assume that nucleation is unlimited in position and speed, this reduces to the Avrami relation:

$$\alpha_A = 1 - \exp(-1/3\pi N_v U^3 t^3), \tag{7.34}$$

with N_v being the nucleation sites per unit volume. It is popular to use the exponent in the Avrami equation to determine the nature of the growing crystallites, whether plates, discs, rods and so forth (i.e., a smaller exponent leads progressively to plate then rod growth; for an example of such an approach see later in the example in IV: Aggregation processes; Sect. 7.4.4). However, it should be noted that this approach sometimes is of questionable validity unless only very small degrees of transformation occur (Price, 1965; Castro et al., 1999). Moreover, these kinds of empirical equations do not address nonisovolumetric changes during the transformations, and this in turn will lead to errors in their application if not considered.

7.3.1.5 Growth Morphologies

The near-equilibrium geometry of a growing crystal can be shown to be controlled by the relative interface energies of its bounding faces (Wulff, 1901; Herring, 1951). This is based on the assumptions that the overall surface energy of the crystal has to be a minimum but the surface must consist of flat facets. As impurities in the growth solution can change the interaction energies of surfaces, this model demonstrates why such impurities can lead to changes in crystal habit, i.e., the relative importance of the main set of surface facets. Kinetic factors can have large effects on this direct equilibrium picture. Impurity sorbants can interfere with addition of new

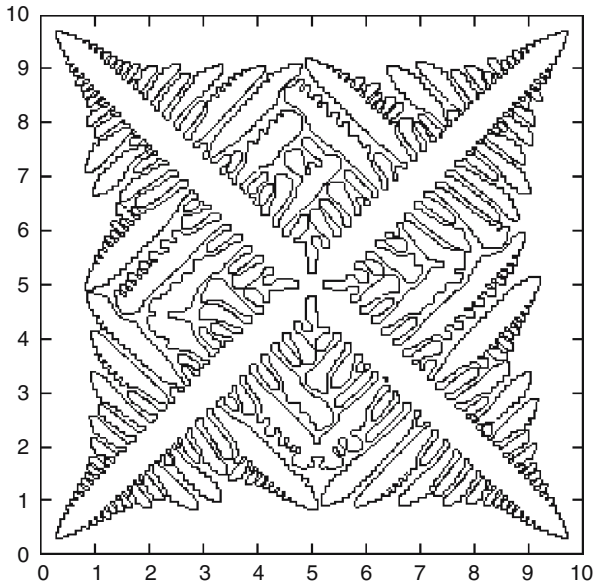

Fig. 7.15 Simulated dendritic crystallization pattern for a cubic alloy

species to a growth step, hence poisoning the growth (Van Enckevort et al., 1996; Kubota and Mullin, 1995). Impurities can also affect growth of secondary phases by influencing nucleation kinetics (Liu et al., 1997). In growth from a melt or aqueous solution the interface structure is also highly dependent on diffusion of species to the interface. For example, dendritic growth occurs when the tip of a growing crystallite exceeds the diffusion rate in the solution or melt. Growth is therefore retarded in certain directions until the diffusing species "catch up", resulting in a dendritic pattern (Fig. 7.15). Thermal effects relating to the dissipation of the heat of crystallization can also produce dendritic growth. Skeletal or "hopper" crystals result both from very rapid growth in particular directions, as may be assisted by screw dislocations, or from severe diffusion limitations.

7.3.2 (Nucleation and) Growth Far from Equilibrium

Growth characteristics may be markedly different at high supersaturation and driving force. We have already mentioned how dendritic growth can occur if a high driving force causes growth to exceed diffusion through a growth medium. This type of growth is actually an extreme case of diffusion-limited-colloid-aggregation (DLCA, see below) at the molecular level (Bunde and Havlin, 1991). But less obvious situations ensue from annealing of solid solutions well below the liquidus, creating the density fluctuations noted above in Cahn and Hilliard's (1958) pioneering work on spinodal decomposition and applied density functional theory. Several

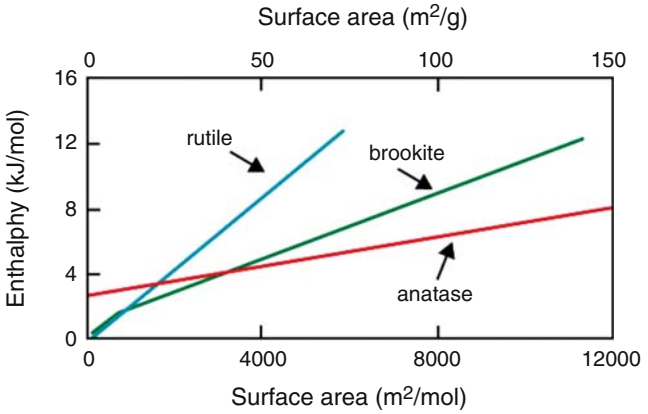

Fig. 7.16 Enthalpy of titania polymorphs as a function of surface area (After Navrotsky, 2004). The first nucleated phase is anatase which becomes unstable relative to brookite when it grows to a size of several nm. The rutile phase then becomes stable with particles on the order of 5 nm

other cases are important to consider: the growth of metastable phases and the Ostwald Step Rule, aggregation type growth processes, and other types of dissipative processes.

7.3.2.1 Metastable Phases and the Ostwald Step Rule

In all discussions above, we have considered that the nuclei that form during crystal growth are of the same phase (i.e., structure) as the equilibrium bulk phase. However, in reality the first crystallites that form may be limited kinetically to those that are most readily nucleated. This is most easily seen in polymorphic phase transformations where the initial nuclei are thought to be those with the lowest surface energies, despite their being absent on the equilibrium phase diagram at the (P, T, x) conditions of formation. The TiO_2 system affords an excellent example. In Fig. 7.16 (Ranade et al., 2002) the enthalpies of the TiO_2 polymorphs are shown as a function of specific surface area (i.e., inverse size regime). This suggests that the structure of the first formed nuclei would be that of anatase, which would become metastable with respect to the brookite structure at larger sizes, and then with respect to rutile at largest sizes. Fast growth would thus favor the creation and likely persistence of anatase, while slow growth would give time for transformations into the appropriate stable polymorphs.

Other systems where a metastable phase is first observed to form include disordered dolomite prior to ordered dolomite (Navrotsky, 1999), vaterite or aragonite prior to calcite, and a silica derivative prior to cordierite (Carpenter et al., 1983). Such observations support the Ostwald step rule, or the notion that the earliest formed phases may be the ones most easily nucleated rather than the most stable (Navrotsky, 2004). Interestingly, both kinetic and thermodynamic arguments support this “rule”. The kinetic analog of the surface energy argument is that structures

similar to their host matrix or solution may form faster than a markedly variant structure stable phase.

7.3.2.2 Oriented Aggregation as a Variation on Classical Growth Method

There have been both conjectures and observations that crystal growth on the nanoscale may occur not by the buildup of structures layer by layer, but by the aggregation of clusters that assemble with proper crystallographic orientations. This oriented aggregation (OA) would be decidedly nonclassical inasmuch as the free energy of cluster attachments, probability of attachment and geometric reorientations would need to be considered as a function of impingement trajectory. Hence this type of growth would be intermediate between aggregation "growth" (see section below) and classical approaches.

Direct evidence for OA has been acquired with TEM imaging of anatase (Penn and Banfield, 1999) and sphalerite (Huang et al., 2003) where small assemblies of oriented nano-scale crystallites are clearly observed. Nanogoethite particles on the 50 nm scale also appear to be formed from assembly of 5 nm particles under certain synthesis conditions (Waychunas et al., 2005). Such assemblies are difficult to explain by standard growth or coarsening mechanisms, yet detailed treatment of OA phenomena appear to be neglected in the literature. Changes in the kinetics of crystal growth that could occur due to OA might best be referenced to a kinetic nucleation model. Instead of nuclei growing to the critical size by addition of monomer units, they could reach this stage in a single step from the subcritical size via an OA mechanism. However further assembly may be limited by geometric conditions, e.g., at some small subcritical size any face of a growing unit might be attachable to a similar unit, but once some attachments are made the number of regular attachment surfaces would be decreased. This reasoning suggests that OA may be an important process in a particular size regime, and also that growth kinetics may vary markedly with size even with all other factors equal. OA may also turn out to be important only for supercritical nuclei, ostensibly because these would tend to be stable long enough for aggregation to occur while subcritical nuclei have a more fleeting lifetime.

7.3.2.3 Other Dissipative Processes

At conditions far from equilibrium a system may transform via quite complex stages including large exchanges of matter and energy with the surroundings, high entropy production, or unusual types of organization, possibly highly chaotic. Although it may be kinetically stable for some time period, i.e., in a *stationary* state, such systems can change suddenly and dramatically as they dissipate excess energy and gain entropy (see also Chap. 1). The concept of dissipative systems (DS), was originated by Prigogine (1961), and a large body of work describing biological, chemical and physical DS has followed his groundbreaking ideas (see, for example,

Nicolis and Progogine, 1977). In geochemical systems there are numerous examples of DS (see also Chap. 11), including oscillatory zonation in crystals, flow-driven reaction fronts, Liesegang banding, reaction-driven advection, and reactions featuring instability, feedback and bifurcation. Our only example above of such a system was that of spinodal decomposition treated by finite DFT methods, but aggregation processes, reactions that include an autocatalytic step (such as pyrite oxidation), and many types of biogeochemical precipitation processes may only be treatable as DS via non-equilibrium thermodynamic methodology (see, for example, Katchalsky and Curran, 1965; Trivedi et al., 2002). We mention this here as a reminder that natural growth processes in general are not close to equilibrium, and hence growth formulations that assume such can lead to misleading results.

7.4 Aggregation Processes

As we mentioned above, following nucleation, the newly formed particles can either grow to larger units and/or become more crystalline. Naturally, due to interparticle forces (both attractive and repulsive), the individual nuclei can grow by aggregation of smaller units. The aggregation of colloidal particles is prevalent in most natural environments and occurs in all physical, chemical and biological systems. Overall, aggregation is considered a non-equilibrium process that dominates when larger particles form from smaller ones and the structure of colloidal aggregates is believed to be scale invariant (Weitz et al., 1984) thus allowing for a new dimension to be introduced; the fractal dimension (see, for example, Mandelbrot, 1975 and below). This in turn, permits a more detailed study of aggregation processes via their physical relationships that link cluster structures to aggregation kinetics. In order to understand aggregation, first we need to remind ourselves of the various forces of attraction and repulsion between individual particles: covalent, electrostatic, dipole-charge and dipole, dipole as well as van der Waals and hydrophobic. A detailed description of these forces and their magnitude and range of action is outside the scope of this chapter but average values and examples can be found in Israelachvili (1992) and Waychunas (2001).

7.4.1 Aggregation Regimes: DLCA and RLCA

Similar to the theories that define the reactions during nucleation and growth, a whole series of theoretical and experimental approaches have been developed with the goal to quantify the mechanisms and kinetics of aggregation. Aggregation of monodispersed colloids will provide a specific cluster mass distribution (CMD) due to the fact that the aggregation pathway of the particles is random and this will result in different aggregate sizes. For charge stabilized colloids, usually the Derjaguin–Landau–Verwey–Overbeek (DLVO) model is invoked but the essential characteristics are applicable to all types of colloids. Overall the repulsive forces between

particles are dependent on the repulsive energy barrier between two particles that are approaching. When this barrier is still several k_BT (k_B = Boltzmann's constant and T = absolute temperature) the particles will be unable to stick to each other and thus they will repulse each other, despite the drive from the diffusion motion. Therefore, in such a system the particles will be stable and not aggregate. When this barrier is reduced aggregation can occur. When the energy barrier is smaller than k_BT and two particles collide, each collision will lead to the two particles sticking to each other (sticking probability = 1) and thus very rapid aggregation will occur. This process is subsequently only limited by the rate of the diffusion-induced collision efficiency and thus the resulting aggregation process is called diffusion-limited colloid aggregation (DLCA). DLCA is more rapid and every collision results in the formation of a new cluster with a relatively open structure. On the other hand if the energy barrier is equal or larger than k_BT, the number of collisions that will lead to sticking between particles is larger and the aggregation rate is limited by the probability of these collisions to overcome the repulsive barrier. This process can be expressed as a power law with:

$$P \sim \exp^{(-\mathrm{E}_b/k_B\mathrm{T})} \tag{7.35}$$

with P being the probability of collision and E_b, the energy barrier. Such a process is much slower and thus is governed by the speed of reaction and is termed reaction-limited colloid aggregation (RLCA). RLCA is slower and only a small fraction of all collisions leads to the formation of a new aggregate. In addition due to the lower sticking probability in a RLCA process relatively denser aggregates form.

In both cases once clusters are formed they continue to diffuse, collide and aggregate and thus both regimes are also examples of cluster-cluster aggregation. Noteworthy, is that once particles or clusters collide and stick, the aggregation is an irreversible process (Lin et al., 1990). Both regimes are characterized by a limited fractal dimensionalities (see below), specific shapes and CMD as well as kinetic rates. For many systems there will be an intermediate regime where the two models overlap but overall, the physical, chemical and mathematical concepts that support the two models are sufficiently well defined to describe the full range of kinetic processes linked to colloid aggregation (Lin et al., 1990).

Diffusion-limited aggregation was first mathematically described by Witten and Sander (1981) as a model in which a particle is added one at a time to a growing cluster. Such a single particle addition model invariably leads to a power law relationship between the number of individual particles and the dimensionality of the resulting cluster. In this case, diffusion is the movement of particles due to temperature fluctuations as seen in Brownian motion and this process can be simulated on a computer as a random walk. An aggregate is defined as a collection of particles that are connected together and the process is termed diffusion-limited when the aggregate increased in size by one particle at a time rather than by bunches (Witten and Sander, 1981). This is occurring because the density of particles is low and thus the particles do not come into contact with each other before reaching the aggregate. The forces between the particles can be either weak or strong. For particles that carry electrical charge (ions), these forces are typically much stronger and thus building

an aggregate is energetically favorable. It thus follows that overall, aggregates are the preferred state compared to individual ions or single particles.

In some cases when aggregates become well ordered, they form crystals. The ordering force is dependent on the shape and charge of the ions, and (almost) always for a distinct set of ions such a process leads to the same final shape (e.g., NaCl typically forms a cube). If no electrical charge exists, the forces are much weaker and thus, usually particles will stick to each other but at distinct opportunities they will separate and move around again. If this process does not lead to an ordering in the electrical field of the charged particles, the aggregates have no distinct shape and each aggregate that forms will be unique and thus such aggregates are very loose or poorly defined (e.g., Ferrihydrite).

A theoretical basis that takes into account diffusion, Brownian motion and aggregation and links them to the CMD was developed by Smoluchowski (1916) who derived a model for the time dependent changes (rates) in the CMD through a statistical approach. His approach takes into consideration the characterization of a reaction kernel (reaction core), $K_{i,j}$, and the aggregation rate of two particles/clusters of different masses. Aggregation modeling began with the development of three main computer simulation approaches: (a) the ballistic deposition model by Vold (1959, 1963), the ballistic cluster-cluster aggregation model by Sutherland (1967) and the surface growth model by Eden (1961). Due to the restricted capability of computer resources at the time these models were rather simple and used only a limited number of units (i.e., particles). In the last 10–15 years however, advances in our understanding of the physics and mathematics of aggregation, new experimental approaches that can deliver more accurate aggregation parameters and the increase in computer speed has allowed these models to be vastly refined and this has lead to the development of more complex concepts that include the fractal geometries (i.e., Mandelbrot, 1967, 1983; Witten and Sander, 1981; Meakin, 1983).

For most aggregation processes, the relationship between the number of clusters N, and the cluster mass, M, can be expressed as (see also Vicsek and Family, 1984):

$$N(M) = {M_n}^{-2}\psi(M/M_n) \tag{7.36}$$

where M_n is a function of the time elapsed since the initial aggregation process started and ψ is a time independent scaling factor that reflects the shape of the cluster mass distribution. The cluster-mass distribution can be expressed as a power law dependent expression with an exponential cutoff:

$$N(M) = \mathrm{A}M^{-\zeta}exp(-M/M_c) \tag{7.37}$$

where the value of ζ is a function of the kernel shape and A is dependent on the relationship between the total mass of particles and the number of primary colloidal particles. For RLCA, Ball et al. (1987) determined a theoretical scaling factor for each kernel and derived a value for ζ of 1.5. However, other theoretical studies suggested values for ζ of 2 (Meakin and Family, 1987).

A recent very elegant approach by Sandkühler et al. (2005) connected the numerical solution for CMD in the Smoluchowski equation (Smoluchowski, 1916) with

experimentally measured angle dependent hydrodynamic radii of the colloids (from dynamic light scattering) in order to model the link between DCLA and RCLA kinetics in colloidal dispersions. Sandkühler et al. (2005) showed that an aggregation rate that accurately described both DLCA and RLCA processes is a simple function that can be expressed as:

$$K_{\mathrm{i,j}} = \mathrm{K_B W^{-1}} B_{ij} P_{ij} \tag{7.38}$$

where $K_{\mathrm{i,j}}$ is the rate constant that determines the coalescing of particles of size i and j, B_{ij} expresses the size dependence of the diffusion coefficient for these particles and P_{ij} accounts for any matrix effects. Furthermore, $\mathrm{K_B}$ accounts for the diffusive Brownian motion of the particles and is equal to $8k_{\mathrm{B}}\mathrm{T}/3\eta$ (k_{B} = Boltzmann constant, T = absolute temperature; η = dynamic viscosity constant). The parameter W is a stability ratio that accounts for the interactions between the primary particles and is equal to the ratio between $\mathrm{K_B}$ and $\mathrm{K_{da}}$, which is the aggregation rate of particles that are partially destabilized during aggregation. This rate is usually smaller than $\mathrm{K_B}$. A fair approximation of W can be calculated from the DLVO theory but preferentially it should be determined directly from experimental data (i.e., scattering or spectroscopy).

For both aggregation regimes stringent analytical solutions have been formulated and additional details on the mathematical derivation of the aggregation equations as well as many examples based on computational and mixed experimental and theoretical cases can be found in Witten and Sander (1981), Ball et al. (1987), Barabasi and Stanley (1995), Everett (1988), Pfeifer and Obert (1989), Lin et al. (1990), Meakin (1998), and Sandkühler et al. (2005) and references therein.

7.4.2 Fractals

In the stochastic characterization of aggregation the fractal dimension is an indispensable but difficult to calculate/quantify concept. The word fractal is derived from the Latin "fractus" meaning "broken or uneven" and a fractal stands for "any of various extremely irregular curves or shapes for which any suitably chosen part is similar in shape to a given larger or smaller part when magnified or reduced to the same size" (Websters On-line Dictionary). Basically, a fractal is any pattern that reveals greater complexity as it is enlarged and is made of parts that are in some way similar to the whole (self-similarity principle, Mandelbrot, 1967; Nicolis and Prigogine, 1977; Whitesides and Grzybowski, 2002; Lehn, 2002)

Fractals were first described mathematically by Mandelbrot (1975, 1983) and a classical example of a Mandelbrot fractal shape is shown in Fig. 7.17a. Additional examples of fractals in nature are ammonite sutures, tree branches, coast lines rivers, sand dunes, ice crystals etc. (Fig. 7.17a–f, see also Fig. 7.1a).

The classical example used to describe fractals is the "coastline". If we want to know "how long a coastline is," a reasonable approach would be to go and measure the length of the coast with some kind of geometric device (i.e., a ruler). However, obviously, as you decrease the size of the measuring device, the length that you

Fig. 7.17 Examples of natural and mad-made fractals; (**a**) classical Mandelbrot fractal image (**b**) lightning fractal (**c**) fractal image of a tree canopy (**d**) fractal coast line, south coast of Norway; (cropped from image of Jacques Descloitres, MODIS Rapid Response Team, NASA/GSFC and Visible Earth; Image: Norway A2002306.1055.367.250m.jpg; source http://visibleearth.nasa.gov; see also Figure 5 in Chap. 3) (**e**) Fractals and Art: (Phoenix Galactic Ammonite; copyright Weed@wussu.com) (**f**) fractal image of ice crystals (reprinted with permission of Poul Jensen); Note: images a, b, and c, and f are all from clipart files derived from the copyright-free public domain

have to measure becomes greater. Yet, as you get closer and closer (better accuracy), the length of the coastline increases without limit, thus showing us its fractal nature. The "coastline" is the classical example of a self-similar fractal. Its length is a function of the size of the ruler and follows a power law (Mandelbrot, 1967). A two-dimensional DLCA aggregation model can serve as an example (Fig. 7.18) because it shows the same density gradient distribution at any length scale. The fractal theory was further developed in the last three decades in order to achieve a better characterization of different phenomena in physics, chemistry, biology, and medicine.

In order to quantify fractals we need to understand the notion of a fractal dimension. Classical geometry tells us that objects have integer dimensions: a point has no dimensions, a line has one dimension (only infinite length), a plane has two dimensions (length and width) and a cube or a sphere has three dimensions (length, width and height). However, due to the self-similarity concept, fractals have a fractional (or fractal) dimension, D_f, which usually lies between 1.4 and 3.

The fractal construct in Fig. 7.18b is a Vicsek fractal (Vicsek, 1992; Beelen et al., 1997), which is constructed by the endless addition of the same figure to the corner points of the original construct. This addition results in a threefold increase in the size of the construct, R_f.

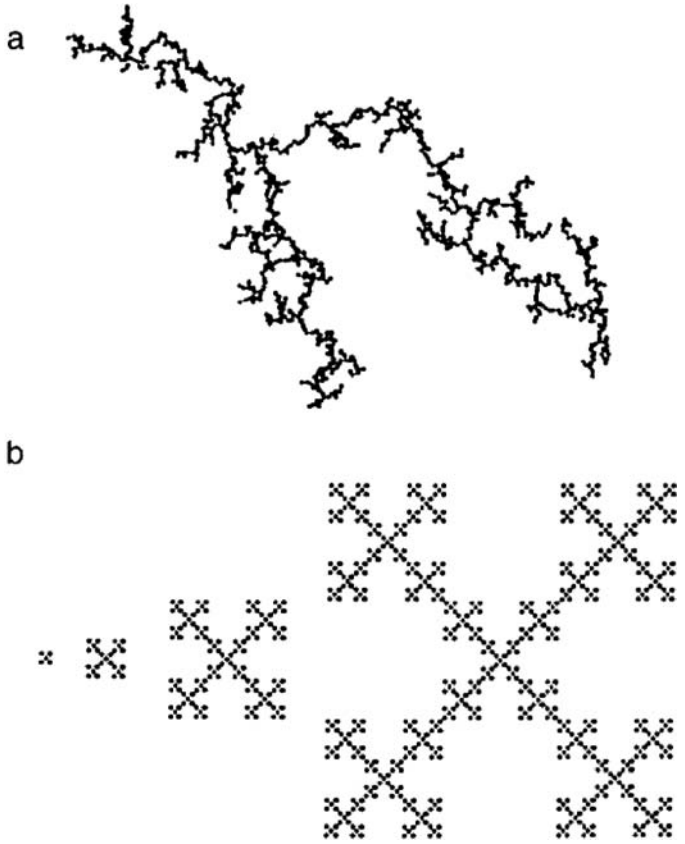

Fig. 7.18 (**a**) Fractal aggregate, constructed by computer-simulated diffusion-limited aggregation. Fractal dimension D = 1.44 (**b**) deterministic Vicsek fractal constructed of 1, 5, 25, and 125 basic units respectively. Fractal dimension D = −1.465. (Reprinted from *Journal of Colloid and Interface Science*, Volume 185, Beelen, T. P. M., Shi, W., Morrison, G. R., Van Garderen, H. F., Browne, M. T., Van Santen, R. A., Pantos, E., Scanning transmission x-ray microscopy; a new method for the investigation of aggregation in silica, pp. 217–227; Copyright (1997), with permission from Elsevier)

However, the number of points (or particles), N, in the fractal is increasing only fivefold (instead of the expected ninefold increase as Euclidian geometry would dictate) and this leads to a relationship between N and R_f that follows a power law $N \sim R_f^{D_f}$, and that links the two parameters via a logarithmic relationship with D_f being the fractal dimension that will be expressed as

$$D_f = \log N / \log R_f \tag{7.39}$$

In the example above we can than calculate D_f as $\log 5 / \log 3 = 1.465$ thus leading to a non-integer "fractal" dimension.

When we are looking at the aggregation of primary particles, we have to take into consideration that the produced fractal objects have fractal dimensions that are related to the number of primary particles. The only direct method to determine the fractal dimension is to analyze images obtained from high-resolution microscopy or from scattering experiments and these approaches will be explained briefly in a later section.

7.4.3 Ostwald Ripening

We have mentioned before briefly the Ostwald step rule. However, here we will slightly expand on the Ostwald ripening concepts. By IUPAC definition, Ostwald ripening is: "The growth of larger crystals from those of smaller size which have a higher solubility than the larger ones."

The history of the theory of Ostwald ripening goes back at least to Ostwald's observations in 1900 (Ostwald, 1900). The first analytical solution for this phenomenon, however, was presented in two papers by Lifshitz and Slyozov (1961) and Wagner (1961) and is thus often found in the literature as the LSW theory. Modern theories are often categorized by how they differ from LSW; yet more recently there have been a large number of papers extending and improving upon the work of LSW, including work by Voorhees and Glicksman (1984), Voorhees (1985), Tokuyama et al. (1986) and Yao et al. (1993, see also Fig. 7.19) with the latter being one of the best reviews on Ostwald ripening.

After small clusters/particles form initially in a system, they will slowly disappear except for a few that grow larger, at the expense of the small units. The smaller ones will act as "nutrients" for the bigger and possibly more ordered particles or crystals. As the larger units grow, the area around them is depleted of smaller units and this is the basis of the Ostwald rule. Thus Ostwald ripening involves a mass transfer from smaller particles to a lesser number of larger particles and this results in a net decrease in the number of particles in the system with the driving force for the process being the change in interfacial energy of the particles (Nielsen, 1964). At a given degree of supersaturation of the starting solution, δ, the critical radius of the resulting particles, r, can be expressed as a function of the molar volume, ν_M, the bulk solubility, S_{eq}, the density, ρ, and the concentration, a_c, and this represents the Gibbs-Kelvin equation (see also Steefel and Van Cappellen, 1990):

$$r = 2\rho\nu_M / R_U\, T \ln(c/S_{eq}) \tag{7.40}$$

Ostwald ripening is a spontaneous process that occurs because larger units are more energetically favored than smaller ones. While the formation of many small particles is kinetically favored, (i.e., they nucleate more easily) larger particles/clusters/crystals are thermodynamically more favored. Therefore, from a purely kinetic point of view to nucleate small particles is by far easier. This is specifically true as small

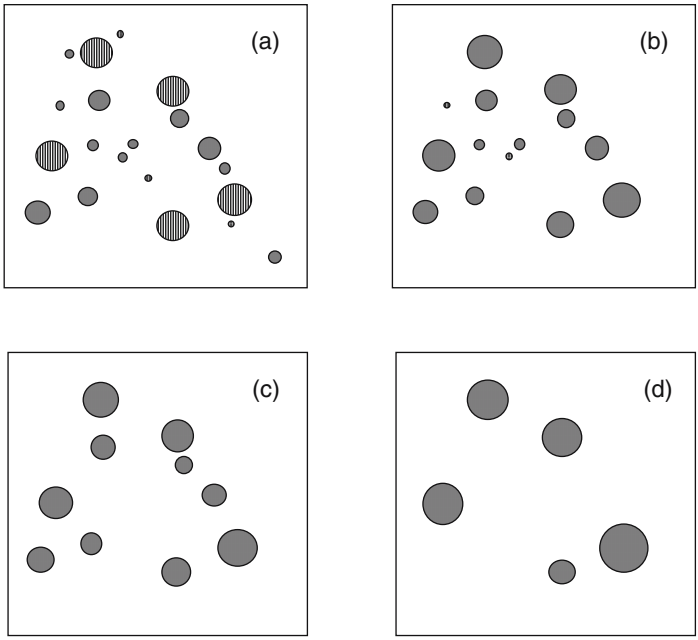

Fig. 7.19 Sketch showing an Ostwald-ripening phenomenon in two dimensions in a time evolution scenario (**a**–**d**). The total number of particles decreases and their average radius increases, but the volume fraction remains constant (Reprinted from *Physical Review B*, Volume 47, Yao, J. H, Elder, K. R., Guo, G., and Gran, M., Theory and simulation of Ostwald ripening, pp. 14110–14125; with permission from the American Physical Society)

particles have a larger surface area to volume ratio and the molecules on the surface of a poorly ordered small particle are energetically less stable than the molecules in the interior. Large particles/crystals have a much larger volume to surface area ratio and as such they represent a lower energy state. Thus, many small particles will attain a lower energy state if they will "transform" into large units.

However, in many systems Ostwald ripening is not occurring. If we want to understand why this happens we have to first think of the fact that the nucleation of a large number of small particles will affect the supersaturation of any solution. This in turn will prevent the formation of large particles or crystals. Basically if supersaturation is the controlling factor and the reactions are fast it is often the case that large particles/crystals never get a chance to appear and often the smaller ones just aggregate but do not grow. The process of Ostwald ripening is naturally linked to the "speed" or rate of nucleation and usually it governs the late stages of a first-order phase (trans-) formation. This phenomenon results from the elimination of regions of high curvature in favor of regions of low curvature, thereby decreasing the net interfacial energy through the elimination of surface area. Since this behavior results in an increase in the scale of the patterns formed in such systems, Ostwald ripening is often referred to simply as coarsening.

7.4.4 Example: Silica Aggregation

We finish this section of the chapter with an example illustrating the aggregation behaviour and fractal growth of silica colloids. An introduction to silica origometization and colloid formation kinetics has been introduced in Chap. 1 (Brantley and Conrad) while here the discussion will focus more on aspects of silica aggregation and fractal dimensions.

Soluble silica or monomeric orthosilicic acid (H_4SiO_4), is comprised of a silicon atom tetrahedrally coordinated to four hydroxyl groups and it remains stable in solution at 25° C as long as its concentration is below the equilibrium concentration for amorphous hydrated silica (at 25° C ∼ 100–125 ppm; Iler, 1979, 1980). In active subaerial geothermal systems where concentrations of dissolved silica can reach up to 1,000 ppm (i.e., highly supersaturated), once these solutions reach the surface autocatalytic polycondensation/polymerization of silica monomers will be induced.

The initial step of silica precipitation (oligomerization) is described in several elementary reactions in Chap. 1 (Eqs. (1.23)–(1.26)). Overall the first step in the process occurs via the condensation of two silicic acid molecules and the expulsion of water:

$$H_4SiO_4 + H_4SiO_4 \Leftrightarrow (HO)_3Si - O - Si(OH)_3 + H_2O \qquad (7.41)$$

Following the formation of Si-O-Si siloxane bonds, and of the first critical nuclei, the next step is growth at the expense of other monomers, dimers, etc. (i.e., Ostwald ripening) followed again by growth to form either large nanoparticles (several hundred nm up to 1 μm) or aggregation (e.g., Iler, 1979, 1980; Perry, 2003; Benning et al., 2004a, b and 2005; Icopini et al., 2005; see also Chap. 1 (Eq. (1.69) and associated discussion).

In most geothermal waters, nucleation will occur both in solution but also on any available surface (i.e., both homogeneous and heterogeneous processes). Thus the resulting amorphous silica phase will be highly variable from site to site. Microscopic observations of field-derived samples indicate that the first silica precipitates are made up of tens of nanometer-sized spheroids. These nuclei are bigger than the critical nucleus estimated for experimental silica precipitation studies (∼3 nm, Icopini et al., 2005; Tobler et al., 2006) and thus it is asserted that the observed particles in the field-derived samples represent already aggregates of smaller nuclei. However, it is asserted that once such initial nuclei have formed this will be followed by aggregation, growth or Ostwald ripening. Yet, due to the infinite resupply of aqueous monomeric silica in the geothermal solution, nucleation will be a continuous process. Many experimental studies – both with purely inorganic or mixed organic inorganic solutions – have shown that once silica nanoparticles formed in solution, their growth, ripening or aggregation behavior is strongly affected by pH, ionic strength, temperature (Iler, 1980; Rothbaum and Wilson, 1977; Makrides et al., 1980; Weres et al., 1981; Icopini et al., 2005, Tobler et al., 2006), surfactant type and concentration (e.g., Boukari et al., 1997; Green et al., 2003). Furthermore, the structure and complexity of the formed aggregates can be described by applying concepts of fractal geometry (Pfeifer and Obert, 1989; Lin et al., 1990) with

the condensation of primary monomers into nanoparticles or aggregates producing fractal objects with a fractal dimension D_f.

As mentioned above, this fractal dimension, D_f, is related to the number of primary particles (N) by a power law $N \sim {R_f}^{Df}$, where R_f is the radius of the aggregate spatial dimension which in turn is related to $N \sim {R_f}^3$ (see also Eq. (7.39)). We have also learned that two regimes (diffusion- and reaction-limited aggregation; DLCA and RLCA) can be defined. For silica in a DLCA case, the theoretical values of D_f have been confirmed experimentally (light and x-ray scattering methods) to be $D_f = 1.7–1.8$ (Martin et al., 1990; Lin et al., 1990). On the other hand, in a RLCA case, which is governed by slower condensation, the concentrations of the encountered reactant pairs will be maintained at equilibrium and a significant repulsive barrier will make the "sticking probability" upon particle-particle interaction to be less than 1. Numerous experimental investigations of reaction-limited silica aggregation processes have produced aggregates with $D_f = 2.1–2.2$ indicating that a more compact aggregate structure is formed under conditions of slow aggregation (Martin, 1987; Lin et al., 1990). In general, these fractal dimensions can be associated with a kinetic process, and low fractal dimensions are equated with rapid (diffusion-limited) aggregation and high fractal dimensions with slower (reaction-limited) aggregation.

Most experimental and modeling studies have quantified rates, fractal geometries and mechanisms from either purely inorganic or organic experiments. However, recently Benning et al. (2004b and 2005) derived aggregation rates and mechanisms from a mixed organic – inorganic system. They have studied the changes in infrared spectral features in silicification experiments in the presence of cyanobacterial cells and expressed the change in infrared signals as a function of concentration. The data was fitted using a modified Avrami approach (as described in a previous section and Eq. (7.32)) and, although from their experiments a fractal dimension for the forming silica aggregates can not be evaluated directly, it is possible to infer a fractal dimension from the value for the constant related to the aggregation mechanism, n (Eq. (7.32)). This can be achieved by comparing their values for n, to theoretical values derived by Hulbert (1969) and Gedde (1995). These authors have shown that for a DLCA process and for a particle of low but complex geometry (one or two-dimensional; e.g., fibre or sheath) the values for n vary between 0.5 and 2 with the highest values representing two-dimensional growth, while for a spherical (three-dimensional) macromolecule growing via DLCA, the n value will vary between 1.5 and 2.5. Alternatively, if the same three-dimensional spherical particle grows via a RLCA mechanism, values of 3–4 are expected for n. Based on these theoretical evaluations and using the values for (n) derived by Benning et al. (2004b) it can be concluded that the nucleation, growth and aggregation of silica nano-spheres on cynanobacterial surfaces occurs via a two stage process. Initially when silica polymerizes, a fast, diffusion-limited process dominates (n, values of 1.8 and 2.2). This is followed by a slower, reaction limited process (n of 3.4 and 3.8). The initial step starts with the polycondensation of silica monomers to form small three-dimensional particles and this is than followed by the aggregation of these nanoparticles via a three-dimensional, reaction-limited mechanism.

This aggregation process follows on from the first steps in the oligomerization reaction described in Chap. 1 (Eqs. (1.23)–(1.26)).

Lastly, we briefly compare the aggregation mechanisms derived from the cyanobacterial-silica system (Benning et al., 2004b and 2005) with aggregation in purely inorganic or ionic low molecular weight surfactant (e.g., via the Stöber process, e.g., Stöber et al., 1968). The Stöber process is used in many industrial processes to produce large quantities of highly monodispersed silica colloids that have a wide range of applications. Using an organic silica solution (TEOS, tetraethylorthosilicate) and a surfactant to induce the nucleation, results in a particle size that is relatively small (10's of Å to max. 10's of nm) and that has a narrow particle size distribution. However, in the TEOS case equilibrium is usually reached faster (1–1,000 sec) than in any inorganic process, In addition, in such reactions the process is purely diffusion-limited (Pontoni et al., 2002). At a first glance it seems that in both cases (inorganic and organic mediated silica formation) the observed mechanisms that control silica formation are similar. However, in the Stöber process the nucleation and aggregation of silica particles is dependent on a variety of parameters, including the hydration level of the starting organic silica solution (TEOS), the concentration and nature of the solvent (ethanol or methanol etc), the temperature and the salt or impurity concentrations. In addition, it is worth mentioning that in terms of size and fractal dimensions Martin (1987) showed that in the inorganic process when growth was induced from a 1% SiO_2 solution (using Å-size silica seeds) a slow aggregation to 30–700 nm large spherical particles occurred and the particle radius increased exponentially with time via diffusion-limited process, producing a fractal dimension $D_f = 2$. At lower silica concentrations (0.01–0.01 wt % SiO_2) – conditions that are more similar to natural geothermal environments – nano-spheres of about $10^2 - 10^3$ nm grew, but a switch from an initial diffusion- to a reaction-limited mechanisms with a fractal dimension $D_f = 1.7$ (Martin et al., 1990; Lin et al., 1990) was observed. Although, these fractal dimensions are lower, this latter process seems comparable to the aggregation reaction observed in the cyanobacterial silicification reactions (Benning et al., 2005).

7.5 Process Quantification: Direct versus Indirect Methods

The full quantification of the chemical and physical parameters governing nucleation, growth or aggregation reactions requires the use of several complementary approaches which may include simple batch or flow through reactors combined with detailed chemical analyses of the solutions or solid phases, or a combination of conventional or synchrotron-based scattering, diffraction or spectroscopy linked with high resolution microscopy. Some modeling, as well as experimental techniques regarding growth processes at surfaces, has been introduced in Chaps. 2 and 3 and thus below we introduce applications linked to processes occurring in solution. We will focus first on imaging techniques and then delve into x-ray scattering and absorption techniques and applications of these in earth sciences; the main driver for

this approach is that, as we will illustrate, this combination of techniques has been the most helpful in nucleation/growth/aggregation kinetic studies.

It is important to understand that many of the parameters needed for molecular models (i.e., cluster size, nucleation densities, nucleation or growth rates, critical nucleus size as well as cluster size distribution) cannot be quantified in any other way but by careful experimentation and thus the techniques described below are unique and crucial in providing molecular level base data that can than be applied to more and more complex molecular models (i.e., Chap. 2). Only the advances in the techniques described below have allowed the scientific community, in the last decade or so, to better understand and quantify molecular level reactions linked to the formation of particles in solution. For example, if we want to know what the nature of a heterogeneous nucleation site is, whether we really have true homogeneous nucleation, or what the link between aggregates formation and volume change is, etc., we cannot rely on molecular models alone but need the fundamental and ultimately better quantitative data that we can only reliably obtain from experiments. In addition, we will describe some aspects of the developments in *in situ* and *real-time* experimental approaches that allow us to follow and quantify the parameters that affect reactions as they occur (e.g., particles growing in solution at fast time scales etc.). This combination of approaches will ultimately help determine mechanisms of reactions and thus allow the selection of more useful models for predictive purposes for systems beyond those accessible to experimentation.

7.5.1 Imaging Techniques

In any study dealing with phase formation, in a first and very important step, the information gained from solution analyses and the imaging of end-product solid phases can give a good approximation of processes linked to the nucleation or growth reactions. A plethora of modern high-resolution imaging techniques based on non-contact mode principles can be used for the quantification of nucleation and growth on surfaces and some of these non-contact mode surface imaging techniques have been introduced in Chap. 3. However, many of these techniques are particularly adequate for processes and reactions on surface yet only in part useful when dealing with phases that grow free in a solution matrix.

Some of the key problems with imaging of phases forming in solution are related to the fact that in order to produce high-quality and high-resolution images, the samples often have to be dried or coated and subsequently submitted to high vacuum conditions, and thus it is not possible to truthfully determine their state *in situ*, i.e., in equilibrium with the solution in which they have formed. For several systems this is not a problem; for example, drying of ceramics or hard sphere ionic materials does not change upon dehydration or organic solvent evaporation. However, in systems where reactions are followed in aqueous solution drying and dehydration may induce changes in surface properties as well as aggregation. In addition, from such studies only modest amounts of accurate kinetic data can be gained because often only a few intermediates or end-products can be imaged. However, some novel

developments in this field are described below and they will show that high-resolution imaging is a most valued tool in the research field of nucleation and growth of phases because any studies involving phase formation are "blind" without the help of imaging techniques.

A technique that has been used in recent decades to image inorganic or biological specimens from experiments in solution is environmental scanning electron microscopy (E-SEM). This is a surface observation technique and samples will only partly be in equilibrium with the solution but, E-SEM requires no coating or high vacuum and thus imaging can be done with no sample treatment. However, again the limitations in resolution ($\sim$100 nm) and the need for high voltage and large beam size (usually $\sim$3–5 μm) for elemental analyses, usually prevents detailed elemental analyses of small newly formed particles using the E-SEM (i.e., Goldstein et al., 2003 and references therein).

High-resolution transmission electron microscopy (HR-TEM) is another imaging technique that has been extensively used in characterizing precipitated phases both in the chemical, earth, materials sciences or biological sciences (e.g., McLaren, 1991; Buseck, 1992; Hochella and Banfield, 1995; Banfield and Zhang, 2001; Fultz and Howe, 2002; Hayat, 2004). The main limitations of conventional TEM is the need for sample handling (depositing a liquid sample on a grid and drying, or embedding and microtoming), as well as beam damage from the high voltage used in imaging and the effects due to the high vacuum requirement.

The new generation of transmission electron microscopes, are based on field-emission gun electron source technology (both FEG–SEM, see Fig. 7.1b, and FEG–HR–TEM), and are usually equipped with energy dispersive spectrometers that are capable of both high-resolution imaging (e.g., by Z contrast imaging) as well as fine probe chemical analysis thus allowing elemental analysis and mapping of the formed phases. In addition, they usually have good capabilities to do high-resolution diffraction (selected area electron diffraction, SAED), spectral analyses (energy-filtered, EF-TEM, or electron energy loss spectroscopy, EELS) or even high angle annular dark field scanning TEM (HAADF-STEM) combined with energy dispersive spectrometry (EDX). All these techniques have been successfully applied to earth materials to characterize both the crystallographic and elemental composition as well as beam damage issues related to small particles (see for example: Buseck, 1992; Banfield and Zhang, 2001; Hochella, 2002a and b; Brydson, 2001; Utsunomiya and Ewing, 2003; Palenic et al., 2004, Pan et al., 2006).

The best SEM and TEM-based approaches for nucleation and growth imaging in an "as-*in-situ*-as-possible" mode are based on fast cryo-quench freezing of samples. These techniques, that will be described in brief below, have in part overcome some of the limitations related to *in situ* and realtime "capture" and imaging of precipitates at both high spatial- and spectral resolution because ultra-rapid cryo-freezing is extremely well suited for quenching samples of complex mixtures of fluids and solids (both inorganic and biological) that have a high water- (or solvent) content. Once flash-frozen, such samples can subsequently be imaged in cryo-mode, using special cryo-transfer stages and TEM systems that can run at -165°C. Both cryo-SEM and cryo-HR-TEM can be useful when phases need to be imaged during a

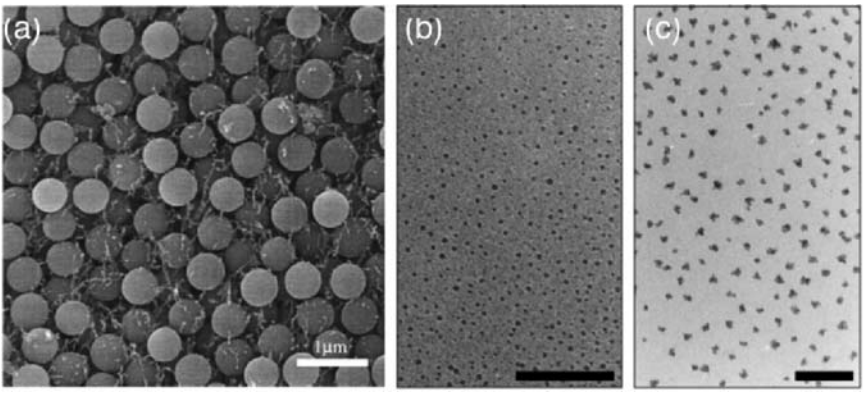

Fig. 7.20 (**a**) Cryo-SEM image of frozen stable silica suspension. Small filaments between particles are from the high concentration of surfactant used (Reprinted from *Journal of Non-Crystalline Solids*, Volume 248, Wyss, H. M., Huetter, M., Mueller, M., Meier, L. P., and Gauckler L. J., Quantification of microstructures in stable and gelated suspensions from Cryo-SEM, pp. 340–346; Copyright (2002), with permission from Elsevier) (**b**) and (**c**) cryo-TEM images of iron dispersions with increasing average particle radius; (**b**) radius $= 2.1 \pm 0.3$; (**c**) radius $= 6.9 \pm 1.0$. Scale bar in latter two images $= 100$ nm. (Reprinted from *Nature Materials*, Volume 2, Butter, K., Bomans, P. H. H., Frederik, P. M., Vroege, G. J., and Philipse, A. P., Direct observation of dipolar chains in iron ferrofluids by cryogenic electron microscopy, pp. 88–91; Copyright (2003), with permission from Macmillan)

process. Cryo-SEM techniques have extensively been used in earth science related research, specifically in freeze-fracture imaging of rock deformation processes by salt formation at grain boundaries (i.e., Mann et al., 1994; Samson and Walker, 2000; Schenk et al., 2006). However, cryo-SEM is naturally limited by resolution (Fig. 7.20a; Wyss et al., 2002) and thus not very suited for phases at the nanoscale.

Advances in cryo-TEM capabilities (both in terms of speed of quenching and high-resolution imaging) have made this a new tool that is extremely useful in following processes of nucleation and growth as a function of time and as *in situ* as possible. For example, envision a reaction where two aqueous solutions are mixed and new phases nucleate and grow in the mixture. If at specific time frames in the reaction a drop (usually $< 10\,\mu$l of a very dilute sample) of such a mixture is pipetted onto a TEM grid that is held in a vitrobot (see below) this will form a thin liquid film that is then immediately cryo-quench frozen (this can be achieved in less than 1 s) by plunging it into liquid propane or ethane. A vitrobot is basically a guillotine plunging device that can instantly vitrify a sample deposited on a TEM grid. After depositing the sample the vitrobot automatically blots the liquid on the grid with filter paper producing a sample that is thin in the middle and thicker at the edges of the holes. This grid is than plunged into the cryo-solution of choice and this way only vitreous ice is formed and this vitrification prevents phase separation and ice crystal growth. Propane or ethane is usually used for vitrification because of their high boiling points and high thermal conductivity (0.22 and 0.24 J/m s K). These solvents are much better than liquid nitrogen, which has a higher conductivity

(0.13 J/m s K) yet in some cases liquid nitrogen is also used if the sample may interfere with other cryo-preservation solutions (i.e., some other organics may dissolve in propane or ethane). However, when a warm object is plunged into liquid nitrogen for vitrification usually a thin boiling film and a thin insulating layer of nitrogen gas is produced (Leidenfrost phenomena), thus reducing drastically the cooling rate. For this reason propane and ethane are used as they allow for a faster and more reliable vitrification. Once the samples are vitrified they are transferred to a liquid nitrogen dewar for storage and than imaged at cryogenic temperatures (i.e., -165° C) using a TEM cryo-stage. This cryo-freezing process naturally also arrests any thermal or mechanical diffusion of the phase on the time scale of the vitrification thus allowing for quasi-real time *in situ* observations of nucleation and growth processes. A discussion of the advantages or disadvantages of the various cryo-preservation methods can be found in Fouchandour et al. (1999) and Frederik et al. (2002) and extensive literature on cryo-TEM imaging techniques can be found in Binks (1999). Here we mention two studies that were linked to earth based materials (silica and iron oxides) and that have used flash-freezing of the reacting solution and subsequent cryo-TEM imaging. These are (a) TEOS-based silica particles (Bailey and Macartney, 1992) and (b) surfactant-based magnetite iron oxide nanoparticles (Fig. 7.20b and 7.20c; Butter et al., 2003). However, many more studies are in progress and *in situ* and realtime high-resolution cryo-imaging will become more and more a vital tool in studies dealing with nucleation and growth of mineral phases from solution.

A vision for the future of in situ and realtime imaging and spectral/diffraction analyses of nucleation and growth processes in solution would be to combine cryo-quench freezing with a focused ion beam (FIB) sample handling system (e.g., Heaney et al., 2001) and high-resolution cryo-TEM imaging and spectral analyses to study freshly precipitated samples in various stages of the nucleation and growth process. Such a combination would tremendously improve our ability to follow nucleation and growth reactions as they occur and together with the techniques explained below we could than get a more quantitative and realistic understanding of these processes and of the mechanisms that control them.

7.5.2 SAXS/WAXS

7.5.2.1 General Introduction and Basic Concepts

The size, shape and crystallinity of "particles" are of fundamental interest for the understanding of microstructure of heterogeneous materials or complex inorganic or biological systems. Small-angle and Wide-angle x-ray scattering (SAXS/WAXS) are key techniques used in the study of inorganic and biological particles that exhibit poor structural ordering or nanosize properties. Overall, the larger the diffraction or scattering angle the smaller the length scale that can be probed, and thus WAXS is used to determine crystal structure on the atomic length scale while SAXS is used to explore structure on the nanoscale. Applications are as wide-ranging as alloys, melts, polymers, biological macromolecules, nanoparticulate or porous materials

(e.g., Glatter and Kratky, 1982; Singh et al., 1993; Svergun and Koch, 2003; Waychunas et al., 2005; Shaw et al., 2000 and references therein). SAXS and WAXS can be performed with different x-ray sources. Synchrotron radiation emitted by particle accelerators provides an added advantage over laboratory sources in that the emitter source has a high flux and brightness. For SAXS this is specifically important as it provides a capability of low divergence, thus allowing SAXS measurements to be collected at low angles. This in turn permits high quality data to be extracted for particle formation reactions and specifically the kinetics and mechanisms of processes can be followed *in situ* (i.e., in equilibrium with the reacting medium) and in realtime (with time resolutions down to milliseconds). SAXS has been extensively used in the last two decades for the study of biological macromolecules under near physiological conditions but not necessarily for kinetic studies (see for example review by Svergun and Koch, 2003). In inorganic systems, the combination of SAXS and WAXS is particularly important in systems where the structural changes, for example, linked to nucleation, growth or crystallization of particles respond to variations in external conditions (i.e., chemical or physical changes) and reactions need to be followed *in situ* (i.e., in solution or melt phase as solid state reactions) due to changes that occur in the pathways and progress of the reactions.

A simple and comprehensive textbook on SAXS/WAXS theory, data acquisition, processing and interpretation is sadly lacking. We refer the reader to several books or review papers that detail the basics of the SAXS/WAXS theory (e.g., Guinier, 1939; Guinier and Fournet, 1955; Glatter and Kratky, 1982; Glatter, 1992; Bras et al., 1993; Bras and Ryan, 1998). Only in the last decade have SAXS and WAXS been also applied to geological or environmental problems and a recent review applied to geomedia is discussed in Waychunas (2001) and Waychunas et al. (2001).

7.5.2.2 Basic Concepts

A schematic diagram, idealized scattering patterns and the relevant equations representing a dilute and non-dilute system are shown in Fig. 7.21. The simple way to describe scattering of x-rays is to think that scattering occurs due to the electron density contrasts at the samples. Overall, the x-ray scattering amplitude represents the Fourier transform of the electron density distribution in the matrix. The scattered intensity, $I(q)$, is measured in terms of the scattering vector, q, which in turn is a function of the scattering angle 2θ, and the radiation wavelength λ:

$$q = 4\pi \sin\theta/\lambda. \tag{7.42}$$

and at small angles and for homogenous particles the scattered intensity $I(q)$ can be expressed as:

$$I(q) = N/V\ V_p^2(\rho_p - \rho_o)^2 P(q)\ S(q) \tag{7.43}$$

where N represents the number of scatterers per volume of V of sample, V_p represents the volume of the individual scattering entity, ρ_p and ρ_o the density of the particle and density of the matrix, while $P(q)$ represents the form factor

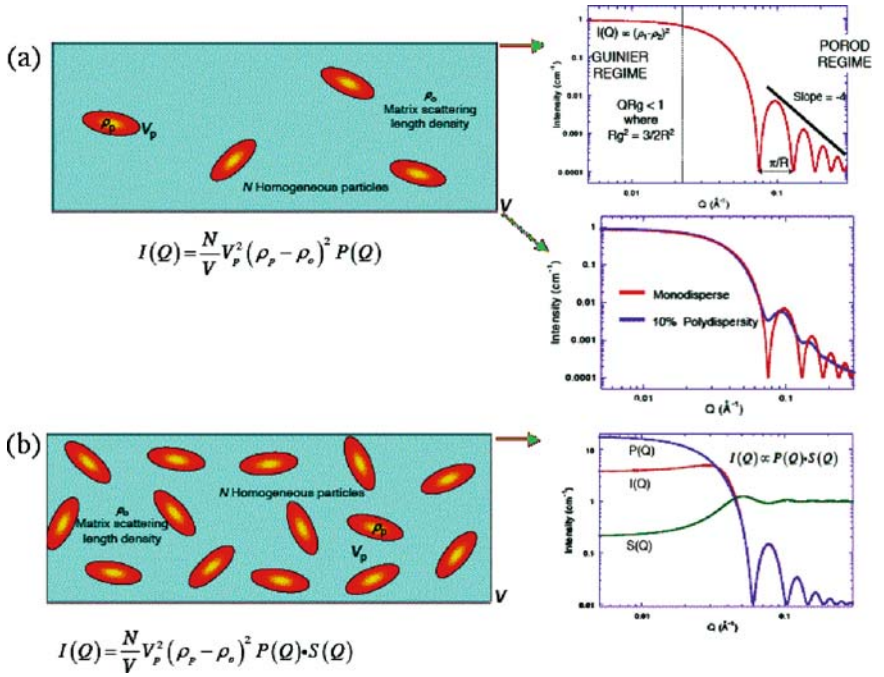

Fig. 7.21 Schematic diagram, relevant equation and corresponding scattering patterns for a dilute (**a**) and a concentrated (**b**) system; in (a) shown is also the effect of polydispersity in a dilute system. Details see text. (Modified and reprinted with permission of Jamie Shulz, ANSTO, Australia)

(containing information about shape, size and internal structure of the particles) and $S(q)$ represents the structure factor (containing information of the interactions between particles and their spatial arrangements). Both $P(q)$ and $S(q)$ are dimensionless parameters that are used in dilute systems $[P(q)]$ and non-dilute systems $[S(q)]$ for the evaluation of properties linked to the scatterers in the matrix (Fig. 7.21 and below).

In dilute systems there are no particle-particle interactions (Fig. 7.21a left panel) and thus the total scattering intensity is the sum of the individual particle scattering, and the structure factor, $S(q)$, does not play a role (see equation in Fig. 7.21a). As mentioned above, to a first approximation, the scattering curve is simply a Fourier transform of the scattering density, which is related to the number of electrons (for x-ray scattering) in a particular region of space, and thus to the structure that causes the scattering pattern. In a dilute system (Fig. 7.21a, right side) the scattering pattern contains information about the idealized radius of gyration, R_g, which represents the distance from the "centre of the scattering density". This R_g is not equal to the true radius, but it can be related to the true radius of the particle depending on the particle shape (e.g., for spheres $R_g^2 = 3/5\,r^2$; see Guinier, 1939 for other shapes). In a purely monodispersed systems, the best way to evaluate the particle size is from the minima in the scattering patterns (Fig. 7.21, right side). Although the Guinier approximation (7.44) does not strictly apply to monodisperse systems, one can also

get an estimate of the R_g from the slope of the scattering pattern in the lowest q region, $q \to 0$ (Guinier regime) via:

$$\ln I(q) = \ln I(0) - 4\pi^2/\lambda^2 R_g^2 (2\theta)^2 \tag{7.44}$$

Overall, the Guinier approximation can be viewed as "the poor-man's approximation" that can be applied to systems that have a certain degree of polydispersity or when the measured q range does not allow the evaluation of the minima in the spectra at higher q. The intensity at $q = 0, I(0)$, is also related to the volume fraction of the particles within the sample. Complementary to this, in the high q region (Porod regime) information about the interfaces present in the sample is contained and here the scattered intensity is expressed as (see for example Bras et al., 2005):

$$I(q) = K_1 + K_2/q^{\alpha} \tag{7.45}$$

where K_1 represents the thermal background and K_2 is the Porod constant which is linked to the dimension and surface roughness of the particle while the exponent α is linked to the slope of the scattering curve in the Porod region (Fig. 7.21a). Lastly, the decay in intensity of the scattering in the Porod region also contains information about the degree of polydispersity in the system (right side, middle panel Fig. 7.21; and Megens et al., 1997).

In a dilute monodispersed system (where $P(0) = 1, S(q) = 0$ and $P(q) \neq 1$), the form factor $P(q)$ basically represents the link between the reciprocal space of the measurement and the real space of the particle and can be expressed as:

$$P(q) = 4\pi \int_0^{\infty} p(r)(\sin(qr)/qr)\, dr \tag{7.46}$$

where $p(r)$ is the pair distribution function, or PDF. PDF analysis is a method of extracting structure-related information from SAXS and WAXS data and the evaluation takes into account both the Bragg (in non-dilute systems) as well as diffuse scattering (in dilute systems, related to short-range order effects). This sensitivity to the local structure has made the PDF analysis the tool of choice for structural studies of amorphous materials (e.g., Glatter, 1992; Bras and Ryan, 1998 and references therein). The scattering length distribution function $p(r)$, which is equal to the total scattering length of the atoms per unit volume of matrix are shown for various particle shapes in a Fig. 7.22a.

We can look at a PDF plot essentially as a histogram of all of the distances, d, within a particle and it can be calculated by an indirect Fourier transform of the full scattering pattern. From a PDF, the R_g can also be derived and this is usually more accurate than from the Guinier approximation mentioned above because it uses the entire scattering pattern, not only the lowest q angles. However, one needs to be careful as most solutions (with the exception of some biological samples) will indeed not contain 100% mondispserse particles. Overall a $p(r)$ versus intra particle length plot contains the same information as the scattering intensity $I(q)$, but the

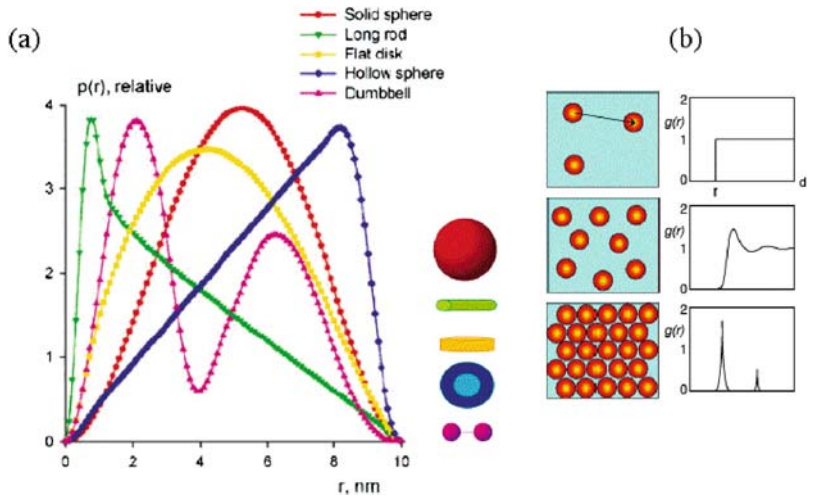

Fig. 7.22 (**a**) Idealized SAXS profiles of various geometrical bodies in dilute monodispersed systems, the corresponding p(r) and particle shapes as a function of particle radius (after Fig. 5, in Svergun and Koch (2003) Small-angle scattering studies of biological macromolecules in solution. Rep. Prog. Phys. 66: 1735–1782.) and (**b**) schematic diagrams of the pair correlation functions G(r) (see eq. 7.48) for a system at a series of increasing concentrations plotted in real space. (Modified and reprinted with permission of Jamie Shulz, ANSTO, Australia)

real space representation (i.e., the inverse Fourier transform) is more intuitive. A few possible curve shapes of $p(r)$ and the corresponding particle shapes are shown in Fig. 7.22a. For example, spherical particles display Gaussian-shaped $p(r)$ curves with a maximum at about the maximum radius (see curve for solid spheres), while elongated particles have skewed distributions with a maximum at small distances which can be related to the radius of the cross-section of the elongated particle (curve for long rod); lastly, particles consisting of well-separated subunits (curve for dumbbell) can display multiple maxima, the first one representing the intrasubunit distances, with the other maxima giving information about the separation between the subunits (dumbbell example).

If the system is polydispersed, the scattering curve can yield information about the average idealized particle radius, R_g (from the Guinier regime), and if the final shape of the particles in a system is known (via for example quantification with a different method, e.g., high resolution imaging see above) the R_g can be linked to the real space average particle radius and particle size distribution. However, because the scattering intensity correlates with the shape and the size of the forming particles the integral of $I(q)$ is defined as the invariant Q, which is sometimes also called "the Porod invariant" (although this is not a constant – see examples). Q basically represents the total scattering power law of the sample and it can be used to quantify the electron density contrast independent of particle shape or number and it is specifically useful in systems that are not monodispersed and that contain mixed particle shapes; where Q will change as a function of reaction time and changes in

particle properties (see examples below). For example for a two-phase system, Q can be expressed as:

$$Q = \int (I(q)q^2 dq = \phi(1-\phi)(\Delta\rho)^2 \tag{7.47}$$

where $\Delta\rho$ is the electron density difference, q the scattering vector and ϕ the fraction of one phase with a maximum predicted when ϕ is equal to 50%, thus allowing the proportions of the different shaped particles to be evaluated.

Finally, for non-dilute systems, where inter-particle effects play an important role (see examples below), the structure factor $[S(q)]$ is used for evaluation of the scattering parameters (Fig. 7.21b and 7.22b). The $S(q)$ is related to the real-space pair distribution or correlation function, $G(r)$, via the Fourier sine transform and it includes effects due to strain and disorder effects. It can be expressed as:

$$G(r) = 2/\pi \int_o^x q[S(q)-1]\sin(qr)\, dq \tag{7.48}$$

where $G(r)$ describes the "local" density of particles and the spatial arrangement defined by the direct as well as indirect interactions between particles (i.e., electrostatic interactions). As we mentioned above, in dilute systems $S(q)$ does not play a role as it is equal to one (no particle – particle interactions) while in non-dilute systems it differs from one and can sometimes be used to derive the PDF via the equation for $G(r)$. A simple schematic of the $G(r)$ as a function of the complexity of the system can be seen in Fig. 7.22b and specific examples are discussed below.

7.5.2.3 Examples of Nucleation and Growth SAXS/WAXS Analysis

As a first example we discuss the quantification of the reaction processes linked to the formation of CdS nanoparticles in dilute solutions based on data from *in situ* and real time synchrotron-based SAXS experiments (Meneau et al., 2003). The growth of CdS particles from solutions that were mixed just prior to commencement of the experiments ($t_o = 3$ min) is shown as a time-resolved 3D stacked plot in Fig. 7.23a. The gradual increase in intensity in the low q area and the three maxima observed after 6 h (Fig. 7.23b) indicating changes in the scattering intensity, $I(q)$, can be linked to the emergence of a form factor (i.e., a change in particle shape), showing a monodisperse product with no aggregation component. Furthermore, at t_o already particles with an R_g of 90 ± 9 Å are present indicating an almost instantaneous nucleation of the first particles (Fig. 7.23c). After about 45 min R_g reached a value of 133 ± 13 Å (vertical dashed line in Fig. 7.23c) and the observed change in slope of R_g (note different slope before and after vertical dashed line) indicate a change in the growth process. The observed change demonstrates a switch from an initial spherical particle (before $t_o + 40$ min) to a cylindrical particle (after $t_o + 40$ min). Finally, the relationships between R_g and the spherical and cylindrical radii (R_s and

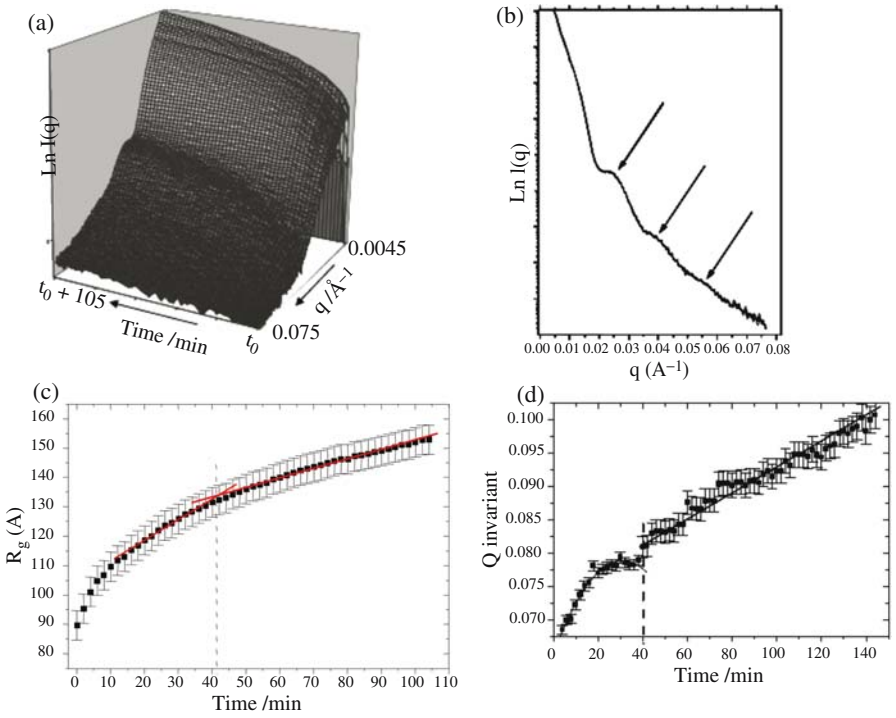

Fig. 7.23 (**a**) 3D plot of stacked *in situ* SAXS data for the formation of CdS nanoparticles (**b**) SAXS profile showing First, Second and third order maxima (arrows) suggesting highly monodispersed particles (**c**) Time resolved plot of the changes in the Guinier radius of gyration, R_g, for the CdS forming reaction; A change in slope at $\sim$40 min (vertical line) indicates a change in growth process (details see text); (**d**) Plot of invariant, Q versus time showing the change from spherical to cylindrical crystal growth (details see text). (After Maneau et al., 2003, Reprinted with permission from IUCr)

R_c) and the cylinder length, $L_c[R_g^2 = 3/5\,R_s^2$ and $R_g^2 = (R_c^2/2) + (L_c^2/12)]$, were used to determine the real dimensions of the particles. Modeling of the data showed that the R_g of the spherical particles was about 10 Å smaller that that evaluated from the Guinier regime (81 ± 16 Å versus 90 ± 9 Å), while the cylindrical particles had a final R_g of 271 ± 22 Å which was slightly bigger than the ones evaluated before from the Guinier plot. This difference was interpreted as a small contribution of polydispersity. The observed change in shape also makes sense when compared with DFT calculations (Hamad et al., 2002) and with the expected shape of the end CdS crystals (wurtzite, from standard XRD). Initially a spherical, poorly crystalline phase nucleates and grows and after $\sim$ 40 min the growth into standard wurtzite structure (cylindrical shape) occurs. The change from spherical to cylindrical growth is also supported by the Porod invariant, Q, which also indicates at $\sim$ 40 min a change in growth process (Fig. 7.23d).

Although Meneau et al. (2003) derived the change in R_g versus time (Fig. 7.23c), from the Guinier region; they could not evaluate the pair size distribution function.

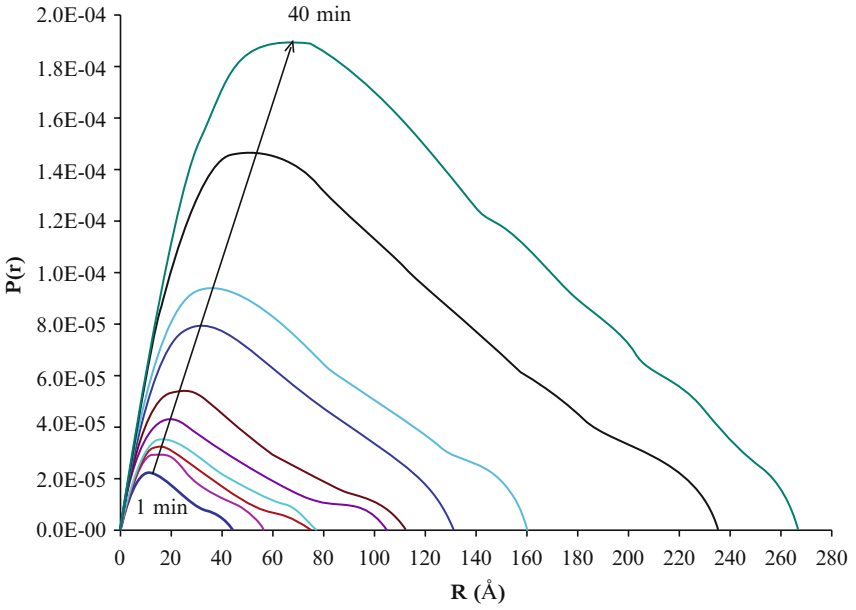

Fig. 7.24 Time resolved pair size distribution function plot for the formation of Cr-oxihydroxide colloids in aqueous suspensions determined from scattering patterns from 1 to 40 min (Shaw, Benning et al., unpublished data)

As mentioned above in a dilute system, where no interparticle intereactions exist (i.e., no structure factor effect), R_g values evaluated from the Guinier slope give only a rough approximation of the particle sizes. A more accurate way to derive R_g is to use the full scattering pattern and derive the PDF and this can be done by using a program like GNOM (Svergun, 1992).

In order to illustrate the usefulness of PDF in dilute solution SAXS, we use an example from an experiment that followed the formation of CrOOH colloids in alkaline solutions (Henderson, 2002; S. Shaw, personal communication). The PDF's extracted from the individual scattering patterns from a time resolved *in situ* solution SAXS experiment are plotted in Fig. 7.24. The fact that already in the first pattern (1 min) the PDF curve is skewed to the left indicates that the forming CrOOH particles are slightly elongated with an average particle radius of ~ 13 Å. With increasing time the overall shape of the PDF and thus the elongated shape of the particles does not change but the average radius increases and reaches ~ 80 Å at 40 min.

Using such PDF analyses it is subsequently also possible to confirm the real particle shape by using modeling approaches. This can be done for example by using the program DAMMIN (Svergun, 1999) that was developed for biological macromolecule shape determination from dilute SAXS data. The DAMMIN approach uses the PDF's from each pattern and calculates $I(q)$ by fitting experimental data and finding a dummy atom model – DAM-configuration corresponding to the minimal value of an energy function. This process is iterative and follows the minimization of the discrepancies between experimental data and DAM-evaluated scattering curves via

simulated annealing. The resulting DAMMIN shapes from each PDF can thus provide corroborating information on shapes at each step in the reaction. The combination of these approaches allows ultimately the evaluation of nucleation and growth reaction kinetics that are clearly linked to size and shape of particles in aqueous solution. A similar study by Davidson et al. (2005) followed the formation of schwertmannite in aqueous solution in a pure system and in the arsenic-contaminated system. Their PDF and DAMMIN evaluations showed that arsenate affects the shape of schwertmannite particles and it causes an increase in asymmetry of the $p(r)$, reflecting a more elongate particle in the presence of arsenate. These results fit well with the EXAFS analyses of Waychunas et al. (1995) who showed that arsenate does not get incorporated into the schwertmannite tunnel structure but that it binds via an inner sphere process to the surface of schwertmannite crystallites.

In the second example we discuss the work of Gilbert et al. (2004) who have used SAXS/WAXS analyses combined with XAS and molecular dynamics (MD) simulations to study the solid-state transformation in 3 nm ZnS nanoparticle properties during hydration (Fig. 7.25). They have observed a large increase in crystallinity and particle radius upon water addition and the analyses of their WAXS derived PDF showed a split and peak sharpening in the structure factor $S(q)$ [related to the PDF or $G(r)$ via Eq. (7.45) upon water addition]. This indicates a reduction in structural disorder within the original ZnS nanoparticles and the appearance of new peaks also supports an increase in crystallinity. Figure 7.25 also shows the good agreement between the modeled patterns (MD simulations) and the experimental data. From previous work of the same group (Zhang et al., 2003) it was known that the particles are fairly monodispersed and spherical in shape. However, the PDF was not fully Gaussian in shape and this may indicate that asymmetry in the bond length distribution could also have contributed to the observed increase in radius. When they compared the WAXS analyses with the XAS data however, the agreement was not so good although the WAXS and molecular dynamic modeling fitted better (see also examples below in the XAS section and Beale et al., 2006).

In the last example the high temperature nucleation, growth and crystallization (devitrification) of cordierite glass is discussed (Bras et al., 2005). Cordierite glass ceramics have many special characteristics (e.g., low thermal expansion, high chemical resistance), which makes them desirable as specialized materials for example in exhaust catalysts or tunable laser. Bras et al. (2005) followed the devitrification process via a combination of *in situ* SAXS, WAXS and *ex situ* EXAFS (see next section) measurements. Their time resolved SAXS and WAXS results (Fig. 7.26a and 7.26b) clearly show the increase in I(0) as a function of time with the associated formation of Bragg peaks in the WAXS for two phase (spinel – sp, and quartz, sq). For example, the combined SAXS and WAXS data from an experiments at 970° C (Fig. 7.26c) shows the changes in integrated peak intensity for the two main crystalline phases (Fig. 7.26c, panel (i)), the growth in R_g and I(0) with time (Fig. 7.26c, panel (ii)), the evolution of the Porod constants and slope (Fig. 7.26c, panel (iii)), and finally the development of the invariant, Q (Fig. 7.26c, panel (iv)). This clearly points towards the fact that the devitrification

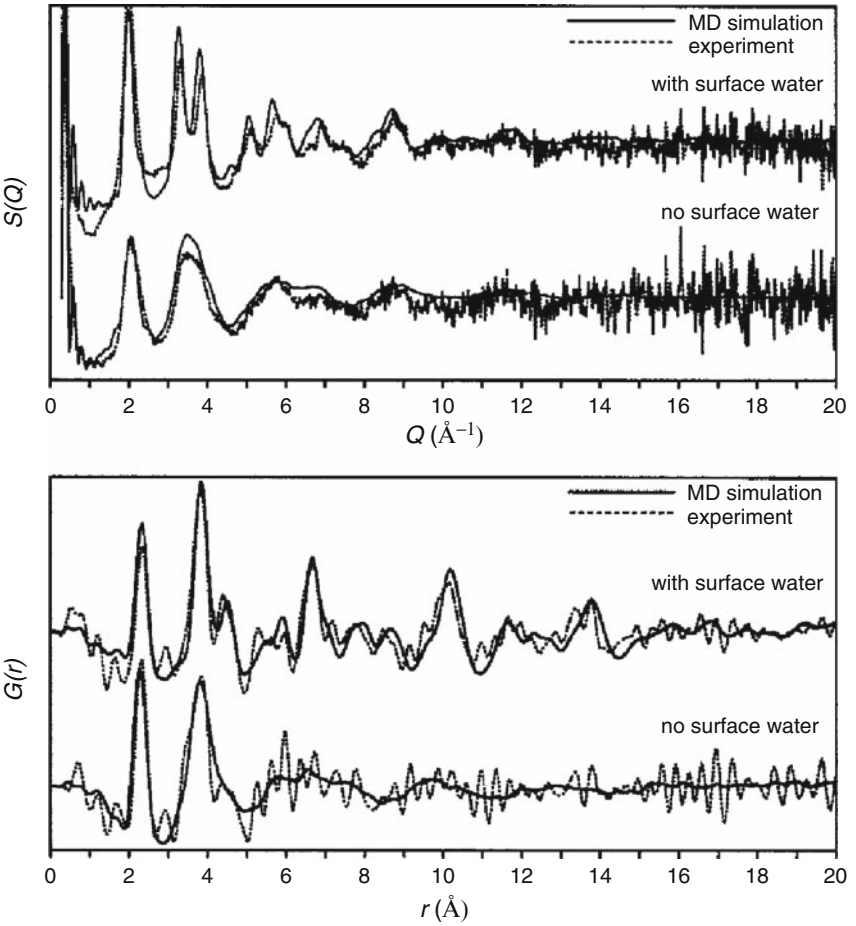

Fig. 7.25 WAXS PDF analyses for non-dilute solutions and structure factor S(q) effect relationships for ZnS particles (Reused from *Journal of Chemical Physics*, Volume 120, Gilbert, B., Huang, F., Zhang, H., Ren, Y., Haskel, D., Lang, J. C., Srajer, G., Jürgenssen, A., Waychunas, G., and Banfield, J. F., Analysis and simulation of a nanoparticle structures observed in a surface-driven transition, pp. 11785–11795; Copyright (2004), with permission from American Institute of Physics)

process produced monodispersed spherical crystallites of alumino-chromate spinel composition that grew from Cr nucleating sites. Interestingly the final spherical particle size reached $210 \pm 20\,\text{Å}(R_g = 180 \pm 20\,\text{Å})$, and the surface of the crystallites changed during the process from rough to smooth. In addition, the linear relationship between R_g^2 and time indicated clearly that the growth of the particles was governed by a diffusion-limited process that was solely dependent on the availability of Cr in the starting glass (Fig. 7.26d).

Lastly, from the EXAFS data they determined that the composition of the resulting spinel phase is directly correlated to the Cr content of the starting glass and

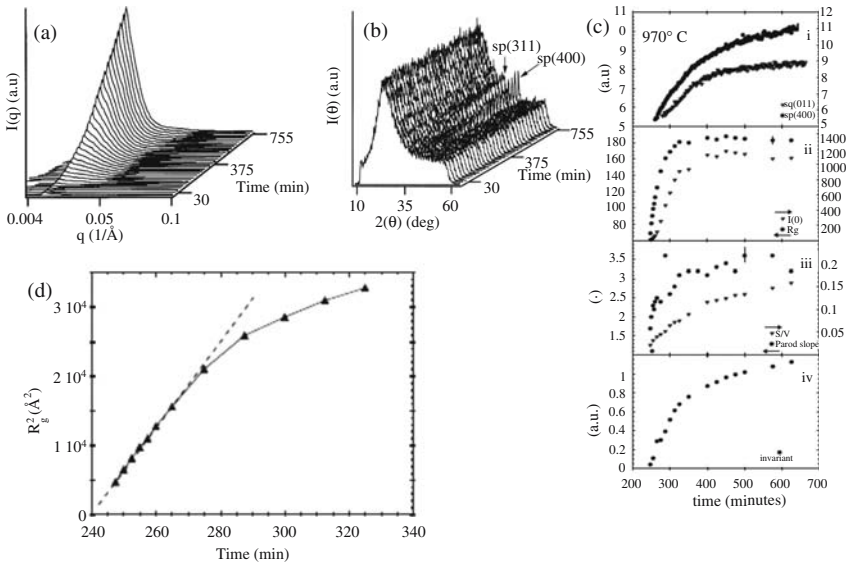

Fig. 7.26 Three-dimensional plots of the development of the scattering profiles in the SAXS (**a**) and WAXS (**b**) regions during isothermal crystallization of cordierite glasses at 920° C; (**c**) Parameters derived from the isothermal crystallization of cordierite glasses at 970° C; top panel (i) integrated peak intensity from representative peaks of spinel (sp) and quartz (sq); (ii) size development of R_g and I(0); (iii) evolution of the constants derived from the Porod equation; (iv) development of the invariant Q. (**d**) The development of R_g^2 versus time for the sample isothermally crystallized at 970 C. (Reprinted from *Journal of Non-Crystalline Solids*, Volume 135, Bras, W., Greaves, G.N., Oversluizen, M., Clark, S.M. and Eeckhaut G., The development of monodispersed aluminochromate spinel nanoparticles in doped cordierite glass, studied by in situ x-ray small and wide angle scattering, and chromium x-ray spectroscopy, pp. 2178–2193; Copyright (2005), with permission from Elsevier)

from the WAXS data they quantified the crystallization kinetics for the devitrification. This work also nicely exemplifies the power of combined SAXS/WAXS/and EXAFS analyses in order to elucidate the nanostructure, crystallinity and local structure of particle formation processes, examples of which are described more in detail below.

7.5.3 XAS

X-ray absorption spectroscopy [XAS = XANES (near absorption edge structure) + EXAFS (extended fine structure)] is a powerful tool for the extraction of short range structural and chemical information in almost any physical system (gases, liquids, solids, glasses). The main advantages or XAS are its element selectivity, i.e., spectra are collected from specific x-ray absorption edges holding information on only those species and their surroundings, and insensitivity to long range

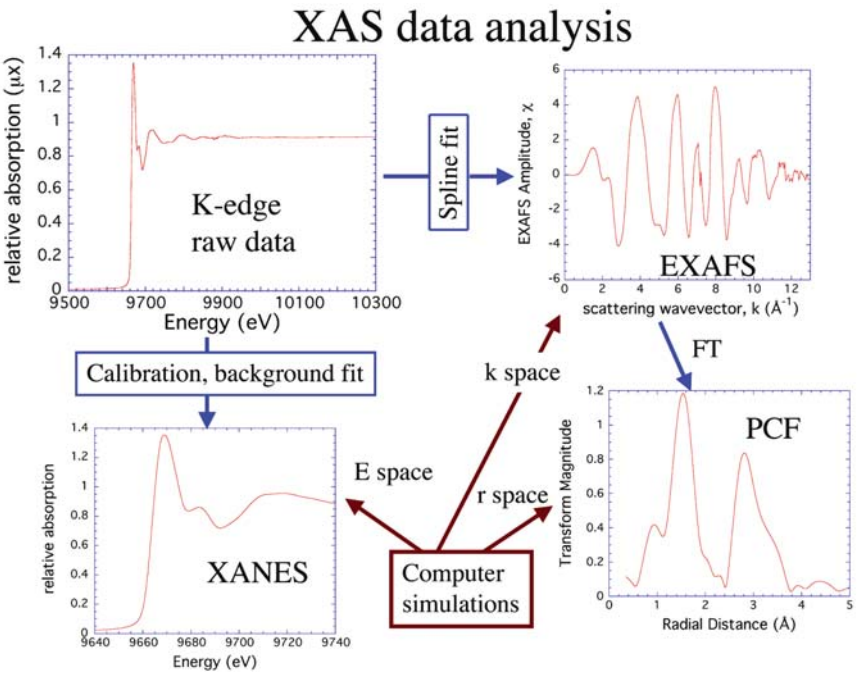

Fig. 7.27 XAS data and analysis scheme. Upper left: raw data with background subtracted to show the XANES (9660–9700 eV) and EXAFS (9700–10300 eV) regions at the Zn K-edge. Lower left: recalibrated XANES data ready for simulations by multiple scattering codes such as Feff. Upper right: extracted EXAFS region weighted by wavevector k^3. Ready for analysis by fitting of various shells of backscattering atoms about Zn absorber in k space. Lower right: Fourier transform of the EXAFS region showing the pair correlation function (PCF) which can be fitted by real-space analysis software. First peak is due to Zn–O shell and second peak to Zn–Zn and further Zn–O shells of neighbors. (After Waychunas, 2001)

order (and thus highly complementary to x-ray diffraction). Hence it is particularly useful for the study of complexation reactions from solution (Brown and Sturchio, 2002), the very beginnings of precipitation (Waychunas, 2001), and studies of localized reactive complexes in biochemical systems (Naqui et al., 1986; Kisker et al., 1997). It is also possible to employ XAS methods for extreme surface sensitivity by use of grazing-incidence synchrotron beams (Waychunas, 2002), for fast reaction processes using flow reactors (Grunwaldt et al., 2004), and at extreme conditions of pressure and temperature (Bassett et al., 2000; Badro et al., 1997).

7.5.3.1 Basic Concepts of EXAFS and XANES Analysis

Many thorough reviews of XAS analysis are available, e.g., Mottana, 2004; Galoisy, 2004; Brown et al., 1988; Stöhr, 1992, so here we limit our discussion to applications. Figure 7.27 shows a cartoon of EXAFS and XANES analyses schemes.

All elements have unique electron binding energies, so that their x-ray absorption edges occur at unique energies. Inner shell absorption involving K electrons give rise to K-edge spectra, while L-electrons give rise to L-edge spectra and so forth. EXAFS features, which occur in the x-ray spectrum above the absorption edge, arise because the x-ray energy is high enough to eject an electron from the atom as a photoelectric wave. This wave can then scatter off of adjacent atoms, with the waves returning to the absorbing atom creating interference and slightly modulating the absorption amplitude. This effect appears as an oscillating function in the edge from a few eV above the edge energy up to 1,500 eV above the edge. Each interatomic distance between the absorber atom and its neighbors produces a different frequency of these oscillations, and an amplitude depending on the number of scatterers and their atomic numbers. There is additionally a phase shift in the scattered waves, which is dependent on the atomic number of both absorber and backscatterer. Hence above the edge a complex oscillatory pattern is seen which records the first several shells of atoms about a particular absorber, i.e., the one whose edge is being investigated. For more distant shells of atoms the spacing becomes progressively closer and the individual frequencies tend to cancel one another out. Hence EXAFS analysis is mainly limited to the first few shells of atoms about an absorber. Analysis of the EXAFS is done by extracting the oscillations and taking a Fourier transform, thus generating a pair correlation function (PCF) with the absorbing atom as the center (origin). As this analysis can be done potentially for any element in a structure, one can extract independent structural information, even if the elements reside in the same nominal structural sites.

A related method, DAFS, or diffraction anomalous fine structure, can separate the EXAFS as a function of crystallographic site as well as by elemental identity (Pickering et al., 1993). For exacting analysis the EXAFS and PCF functions can be calculated and compared with the raw data or Fourier transform, respectively, or a least squares fitting procedure can be used. The output of this analysis is the number and distances of the first several shells of atoms and their disorder. By disorder we mean the damping of the EXAFS oscillations with increasing energy. The damping is caused by static disorder and vibrational disorder. Static disorder means that the shell of atoms has many interatomic distances, and thus contributes a range of frequencies to that shell's EXAFS. Vibrational disorder similarly contributes a range of interatomic distances with time. The more frequencies present in the EXAFS spectrum, especially within a given shell, the more the overall EXAFS will be damped out with increasing energy above the edge.

The XANES part of the XAS spectrum occurs both below and above the absorption edge, and is due to two processes. The lower energy "pre-edge" XANES are connected with excitation of electrons into bound states residing on the atom or on a localized molecular orbital. As these states are lower in energy than complete ejection of the electron from the atom, the features reside below the edge. Other XANES features occur on the edge and into the EXAFS region, and are due to multiple scattering effects, i.e., the ejected photoelectric wave makes at least two "bounces" off nearby atoms before returning to the absorber and creating interference. The interatomic paths for XANES are thus longer than those for single scattering, and

thus at higher frequencies. The resulting oscillations tend to damp out more quickly than the EXAFS, and as such are seen mainly near the absorption edge. XANES bound state transitions are very sensitive to the final state molecular orbital constitution, and thus can exhibit amplitude and energy changes indicative of valence, coordination and bonding changes. XANES analysis is often done empirically by comparison with model compounds. This is due to the complexity of accurately calculating the XANES spectra, compared to EXAFS calculations. However in recent years XANES calculations have improved (Waychunas, 2003) and many edges can be calculated, though direct fitting of spectra may still be a distant goal.

7.5.3.2 EXAFS Analysis of Nucleation and Precipitation

EXAFS is an excellent technique for the study of the initiation of nucleation and precipitation reactions, as it is in this regime that average short range structure about a given atom species in the sample may change the most. One recent illustrative study is that of Thoral et al. (2005) where solutions of Fe^{2+} and As^{3+} are oxidized and the precipitates examined by XAS. The precipitates change in character with time as oxidation proceeds, as shown in Figs. 7.28 and 7.29. Figure 7.28 shows the evolution of the EXAFS Fe K edge PCF for both the pure Fe^{2+} system and the mixed Fe^{2+}/As^{3+} system. In the pure Fe^{2+} system the PCF changes mainly due to the increase in the second shell coordination (and probable reduced disorder) as more aged precipitates are examined. The precipitates are presumably becoming larger and more ordered with time. In the mixed Fe^{2+}/As^{3+} system the initial state is very similar, but with time the second shell decreases in size. The analysis of this second shell requires several contributions, but in essence the attachment of $FeO_6 - AsO_3$

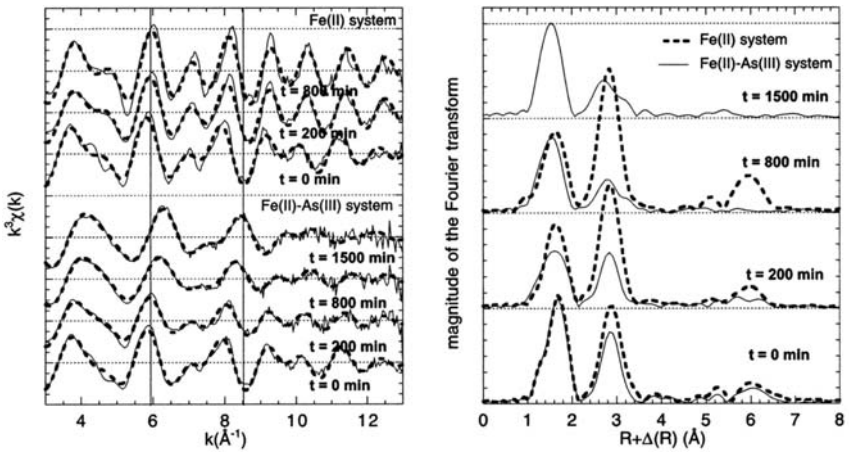

Fig. 7.28 Example of Fe K-edge EXAFS analysis of the oxidation of Fe^{2+} and Fe^{2+}–As^{3+} solutions as a function of time. Left: fitted EXAFS (dashed line-fit). Right: corresponding PCFs (dashed line-Fe^{2+} system). See text for further explanation. (After Thoral et al., 2005)

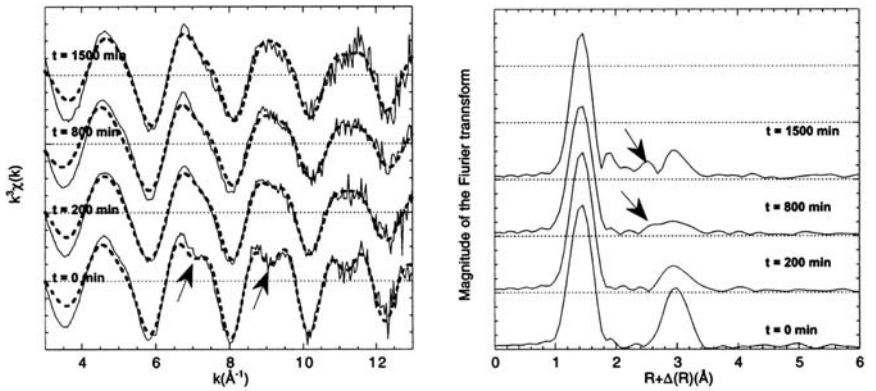

Fig. 7.29 The Fe^{2+}–As^{3+} system studied by EXAFS analysis on the As K-edge. Left: fitted EXAFS. The arrows indicate the higher frequency EXAFS oscillation due to Fe-As neighbors. Right: PCFs. Arrows indicate the appearance of a second As–Fe peak with continued oxidation due to formation of Fe^{3+}–As^{3+} neighbors. (After Thoral et al., 2005)

polyhedra must retard the development of the more organized Fe oxide. In Fig. 7.29 the analogous As K-edge EXAFS and PCFs are shown. Initially the arsenite attaches to small Fe oxide units yielding a well-defined $Fe^{2+} - As^{3+}$ second shell peak. With time this second shell broadens and splits into two contributions, the second being due to $Fe^{3+} - As^{3+}$ attachments. Hence several competing reactions are occurring. Although the authors do not go further to develop a quantitative model for the reaction kinetics, it is clear that such types of oxidative reactions can be characterized using XAS, while x-ray diffraction methods would have yielded little information due to the poor crystallinity of the precipitates.

A different example with catalytic materials is shown by the work of Ressler et al. (2002). In this study the reversible change of MoO_2 into MoO_3 was detailed by a fast XAS experiment (60 s resolution) where data could be collected on a continuously reacting solid sample. Figure 7.30 shows a plot of the time evolution of the XANES spectra over periods of oxidation, reduction and oxidation, as well as a plot of the phase proportions for another reaction series. If done at varied temperatures a series of oxidation reaction curves are produced (Fig. 7.31) which can be analyzed over their linear early regions with an Arrhenius plot to yield activation energies (Fig. 7.32) for the initial process. This is seen to clearly change at about 700 K to a much lower value, and it is suggested that the reaction changes from an oxygen-diffusion controlled reaction at lower temperatures into a nucleation and growth regime. Activation energies can also be derived from the longer duration somewhat non-linear parts of the oxidation curves, and indicate higher activation energies.

Another example is EXAFS analysis in the identification and characterization of phase transitions at high pressures. Badro et al. (1997) examined changes in the quartz-structure compound $\alpha - GaAsO_4$ at room temperature with pressures up to 30 Gpa. The crucial information derived from EXAFS analysis is the individual

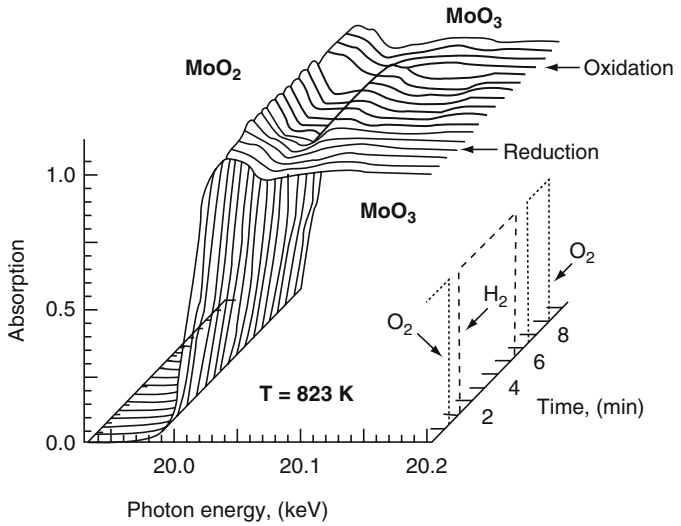

Fig. 7.30 Time-resolved Mo K-edge EXAFS measurements of redox changes in MoO_x catalysts over a programmed reaction series. From these data it is possible to extract the amount of new phase created as a function of time, as well as short range order and average valence. (After Ressler et al., 2002)

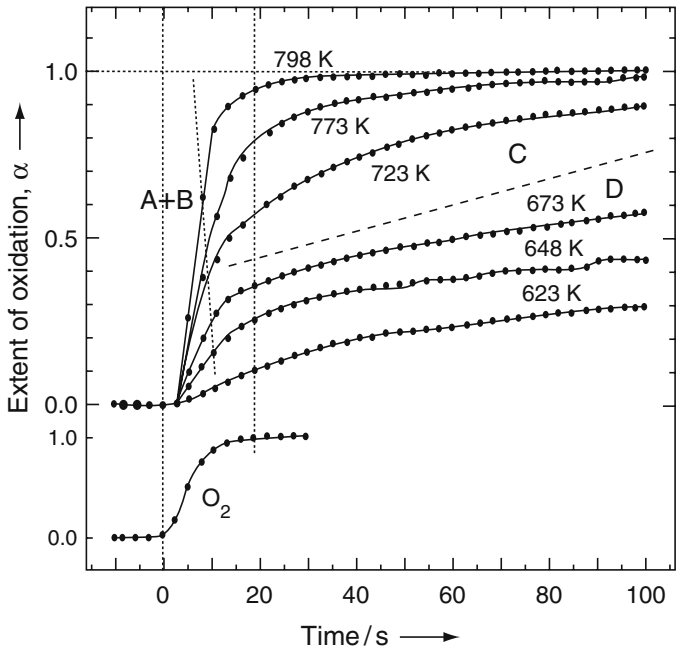

Fig. 7.31 Extracted oxidation change from MoO_2 to MoO_3 at varying temperature from data of the type shown in figure 31. In region A + B there is a linear increase with time, while region C shows an exponential dependence and region D a power-law dependence. (After Ressler et al., 2002)

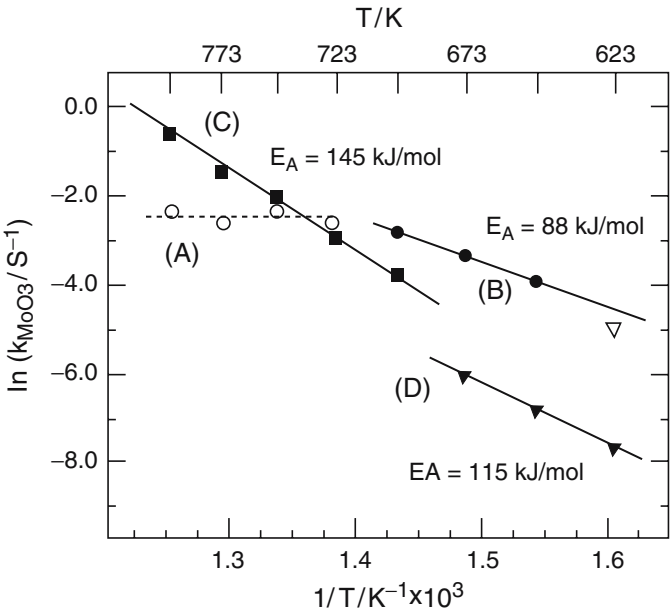

Fig. 7.32 Arrhenius plot for the data in the various regions of Fig. 7.32 plus that from two other temperatures (748 and 698 K) with corresponding activation energies. (After Ressler et al., 2002)

Ga–O and As–O interatomic distances, which decrease as pressure is increased and then increase dramatically as a coordination change occurs (Fig. 7.33). Interestingly, two separate transformation regimes are observed, the lower pressure one coinciding with all of the Ga changing from tetrahedral to octahedral coordination over the range 8–13 GPa, with the As partially converted to octahedral coordination. Above 13 GPa the As converts completely to sixfold coordination. These two regimes have consequences for the quench product. Samples quenched from the lower pressure regime return to the all tetrahedral coordination starting structure, but quenching from the higher pressure regime results in a partly or entirely amorphous material, i.e., the polyhedral deformations and rotations induce a glassy state which cannot readily recrystallize. XRD studies support these conclusions.

A final example is the EXAFS analysis of surface precipitates. The study of Waychunas et al. (1999) examined precipitates of Fe oxides formed on quartz single crystal substrates from acidic aqueous solution. The precipitates were nanosized, and of such a low density that most analysis methods would have not allowed characterization. However, by doing grazing-incidence EXAFS (GIXAFS), both the structure and the relationship to the quartz surface could be determined. A powerful advantage here is that a polarized experiment can be done (Fig. 7.34), where we can orient the sample with the electric vector of the synchrotron x-ray beam pointing either along the surface or normal to the surface. This effectively determines the "probe" direction of the EXAFS experiment, and identifies preferred

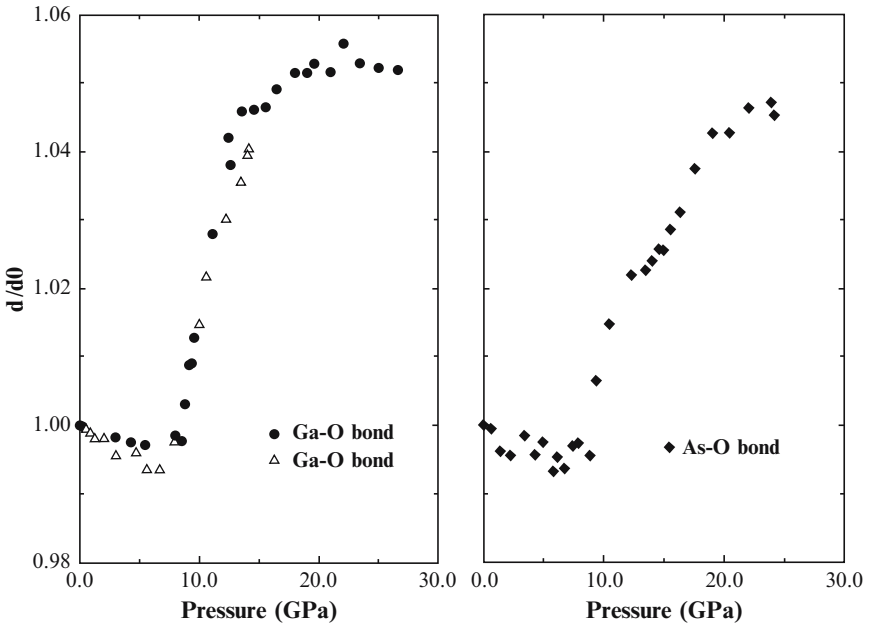

Fig. 7.33 Relative bond length changes derived from EXAFS analysis for Ga–O and As–O in berlinite as a function of increasing pressure at room temperature. A well-defined phase transformation is initiated at about 9 GPa with lengthening of the Ga–O bond due to coordination change from 4 to 6. The As–O bond length goes through a more complex transformation with a break at about 12.5 GPa at which point most of the Ga has changed coordination but the As is in both 4 and 6 coordination. Further pressure shifts all As to sixfold coordination at about 21 GPa. (After Badro et al., 1997)

orientation or epitaxial relationships should they be present. The Fe oxide precipitates in this case show very different PCFs depending on polarization direction. In particular, the short Fe–Fe distance characteristic of the shared $FeO_6 - FeO_6$ polyhedral faces along the c-axis in hematite are seen in the normal polarization PCF, but are missing from the in-plane PCF. This means that the precipitates are hematite-like rather than a FeOOH-type phase, and have their c-axes along the sample surface normal. Further analysis also revealed the precipitate minimum mean size of about 1 nm. Using this methodology it would be possible to observe nanoscale precipitation and aggregation processes at all types of mineral interfaces.

7.5.3.3 Complementarity of EXAFS, WAXS, and SAXS

EXAFS and wide-angle x-ray scattering (WAXS or "powder diffraction") are uniquely complementary as they yield short-range and long-range structure,

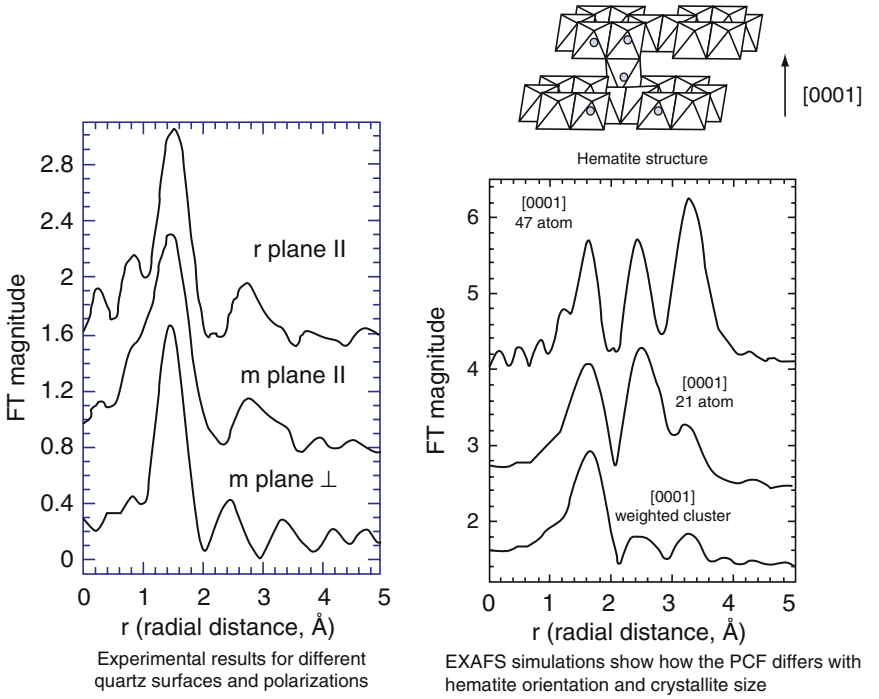

Fig. 7.34 Polarized (grazing-incidence) EXAFS analysis of hematite-like precipitates on quartz surfaces. The PCFs show very similar form when the electric vector (and thus EXAFS probe direction) is in the plane of the quartz whether it is the r- or m-plane surface. But the perpendicular electric vector orientation for the r-plane surface shows quite different structure. These differences are due to varied near neighbor Fe–Fe distances and numbers as a function of direction in hematite single crystals and suggest highly oriented nanocrystallites on the surface. The left side of the figure shows simulations of the r-plane perpendicular electric vector EXAFS for different cluster sizes with best agreement for roughly 1 nm diameters weighted for appropriate reduced Fe–Fe coordinations at the surface of the clusters. (After Waychunas, 2002)

respectively. Hence EXAFS can be used to characterize materials whose XRD pattern is poor, such as fine particles and nanoparticles, glasses, and even liquids or melts. On the other hand, WAXS measurements can yield quantitative measurement of the amount of product formed in a reaction as long as this phase is well crystallized. Use of both techniques together can then potentially allow characterization of reaction products from nucleation though crystal growth and coarsening. Small angle scattering (SAXS) yields no direct atomic structural information but can detect precipitate growth or aggregation and follow these processes quantitatively. Particularly in the case of aggregation, where the WAXS pattern may change negligibly, SAXS and EXAFS are highly complementary. A new technique, grazing-incidence SAXS (GISAXS) is now becoming available for the study of growth and aggregation processes and kinetics at surfaces and interfaces, and should be extremely useful for heterogeneous nucleation and surface-mitigated processes.

7.6 Synthesis and the Future

Many of the processes and molecular scale techniques described in this chapter complement the knowledge illustrated in several other chapters in this book that relate various theoretical concepts and models (e.g., Chap. 2) with kinetic rate laws (e.g., Chaps. 1 and 11) and mechanistic concepts describing both dissolution (e.g., Chap. 5) or precipitation pathways (Chap. 3), both at the macro as well as molecular scales. In this chapter, we have summarized the theoretical bases and introduced some specific experimental approaches and examples that underpin and explain our current knowledge of the processes and mechanisms that govern the nucleation, growth and aggregation of mineral phases in and from solution.

It is important to note the differences – and to distinguish – between nucleation and growth reactions that occur in solutions versus those that occur at surfaces or interfaces. However, regardless of the process, the quantification will always rely on the combination between rigurous experimental and molecular modeling approaches, and only this way will it further advance our knowledge in this field. We have shown that several direct and indirect methods can help acquire and quantify the critical parameters needed to model such processes. In certain cases we are now able to determine very accurately the size and shapes of critical nuclei, and thus derive energetic information of nucleation and growth; we can extract information about pair size distribution of nuclei in solutions or in the bulk aggregates; we can image these processes using high-resolution microscopic approaches and we are able to determine very accurately the bonding environment in dispersed or aggregated samples or on surfaces. Yet, despite all this, it is crucial to be aware of possible pitfalls as well as of the limitations of each of these approaches. We hope to have made it clear that only a complementary, multi-dimensional and intra-disciplinary approach can further our knowledge of the kinetics in such systems and that there is no single pathway that we can suggest to the reader to follow if they want to study such complex processes.

For example, with aqueous interfaces many techniques for characterizing the system are limited by the need to specially prepare or alter the sample and remove all moisture (TEM, SEM, STM), which can dramatically alter the system under study (although developments in cryo-imaging can help). Similarly, atomic force microscopy (AFM) cannot achieve the needed resolution under water in a reacting system (although it can provide unique data that are not achievable otherwise). Thus, such imaging techniques must always be complemented by atomic-scale spectroscopy, or simulations methods, if atomistic/molecular processes are to be considered.

In the last decade or so, more and more methods that can follow and quantify processes *in situ* and in a *time resolved* mode (and in the case of live materials also *in vivo*) have been tested and developed. Ultimately, only such well designed and painstakingly tested approaches will help us quantify reactions and mechanisms governing processes occurring from the atomistic all the way to the bulk scale and combine this with molecular modeling.

Despite all these advances, it is a bit disappointing that in most cases we cannot readily apply our most sophisticated theoretical models to the physical systems under study. This is due, on the one hand, to the inability to measure particular parameters for very small nuclei such as interaction energies at interfaces and surfaces, accurate densities and water contents, and molecular geometries, and on the other hand, to failures of elegant theory to model actual physical processes acceptably (suggesting more development is still required). However, we do expect that as computer cluster power increases and is more readily available, it will be possible to get better estimates for presently still unmeasureable parameters via *ab initio* simulations. We hope thus to gradually see a convergence between the more and more complex idealized theoretical models and the *in situ* and *realtime* derived quantitative data from experiments thus providing crucial parameters for a series of relevant applications.

Another consequence of faster and more accurate computer simulations is the ability to test theoretical models involving large numbers of atoms that approach the size of critical nuclei. This is especially important for cases where nuclei are unlikely ever to be observed due to their low number density and fleeting existence, and for systems involving mineral–water interfaces where water structure and the complexities of the electrical double layer (EDL) must also be considered. We thus look toward a future with more options for detailed theoretical development, better testing of theory applied to physical systems, and ultimately a much better description of the rate and rate dependences of precipitation and growth processes.

Acknowledgements

First and foremost the authors wish to thank the editors for their infinite patience with our continual delays as well as for supporting and encouraging us to finish this chapter. LGB acknowledges financial support for this work from the UK Natural Environmental Research Council (grant no: NER/A/S/2002/00761, and NE/C004566/1) and The Leverhulme Trust grant (Ref. #F/00122/F). GAW acknowledges support from the Department of Energy, Office of Biological and Environmental Research to LBNL, connected with the Center for Environmental Kinetics Analysis (an NSF-funded Environmental Molecular Sciences Institute at Pennsylvania State University). Comments from colleagues and students as well as two anonymous reviewers have tremendously helped shape this chapter.

Glossary of Symbols

a	chemical activity
a_c	concentration
A	function of total particle mass and number

A_i	surface area of an *i*-sized cluster
B_{ij}	size dependent diffusion coefficient for colloids
c	composition
c_i	number of clusters of size *i*
C	mean probability of adatom finding adjacent surface adatom
C_n	occupation of nth layer by adatoms
$D_{i->j}$	probability operator (exchange of i to j)
D^+, D^-	probability operators (growth, dissolution, respectively)
D_f	fractal dimension
$D(i)$	probability operator for cluster of size *i* (continuous distribution *i*)
E_b	energy barrier to colloid collision
f_c	local free energy per unit volume
$f_{n:m}$	fraction of surface atoms in layer n with m neighbors
F	free energy functional for Cahn-Hilliard equation
Δg	free energy change per unit volume of nucleus
G_d	free energy of diffusion across the nucleus matrix interface
$G(r)$	radial pair distribution function
ΔG	difference in free energy
ΔG^*	free energy change for critical nucleus formation
H	intramolecular interaction parameter for gradient energy in Cahn-Hilliard DFT
I	nucleation rate
$I(q)$	x-ray scattering intensity
$I(0)$	x-ray scattering intensity at $q = 0$
J_0	total cluster flux at steady state
J_i	flux of clusters growing through size *i*
k	first order rate constant
k^+, k^-	deposition, evaporation rates, respectively, for atom additions to growth surface
k_B	Boltzmann constant
K_B	function of diffusive Brownian motion
K_{da}	aggregation rate of particles partially destabilized during aggregation
K_1, K_2	thermal background and Porod constant related to scattering intensity $I(q)$
$K_{i,j}$	rate constant for coalescence or aggregation of particles *i* and *j*
L	atom-atom binding force
L_{CSD}	size interval for growing crystals in CSD analysis
L_c	cylinder length
m	number of adjacent layer nieghbors
M	total mass of clusters
n	time exponent related to mechanisms in Avrami equation
$n(i)$	equilibrium distribution function of all clusters in a system
$n(L_{CSD})$	number of growing crystals of a given size interval, L_{CSD}
N	number of critical nuclei or number of scatterers per volume of sample
N	total number of clusters or particles
N_A	Avogardo's number
N_T	total number of atoms in a system
N_i	site density for heterogeneous nucleation
N_V	nucleation sites/unit volume
$p(r)$	scattering length or pair distribution function
P	probability of a collision between colloids
$P(q)$	x-ray scattering form factor
P_{ij}	matrix effects related to aggregation rate $K_{i,j}$
q	x-ray scattering wave vector
Q	Integral of x-ray scattering intensity over q space; also termed Porod invariant
r	critical radius

R_U	universal gas constant
R	radius
R_{SOS}	growth rate for surface in SOS model
$\overline{R}$	mean growth rate
R_g	radius of gyration
R_s	radius of sphere
R_c	radius of cylinder
R_f	size of a fractal construct
s	number of atoms in matrix
S_R	solute supersaturation ratio
S_{eq}	bulk solubility
S	surface area
$S(q)$	x-ray scattering structure factor
t	time
T	absolute temperature
U	growth rate of individual grains in Avrami model
V	volume
V_p	volume of an individual scattering element
W	stability ratio for interactions between primary particles
Z	Zeldovich factor
α	factor related to slope of scattering profile in Porod region
α_A	volume fraction transformed in Avrami model
α_t	number of atoms of molecules leaving a cluster per unit time and surface area
β	thermal energy scaling factor, equal to $1/k_BT$
β_t	number of atoms of molecules joining a cluster per unit time and surface area
ε	reduced probability parameter in Week's adtom growth model $= 2(1-2C)$
η	dynamic viscosity constant
θ	x-ray scattering angle or angle between a nucleus edge and the underlying surface
λ	x-ray wavelength
μ	chemical potential
$\Delta\mu$	difference in chemical potential or driving force for nucleation
ν_M	molar volume of a nucleus
ν_d	desorption rate for an isolated surface atom
ν_j	frequency of diffusion jumps or lattice vibrations
ρ	density
ρ_π	density of a particle
ρ_o	density of the matrix
Δ_p	electron density difference
σ	free energy per unit area of surface
$\sigma_{\alpha,\beta}$	interfacial free energy (two phases)
$\sigma_{\alpha,\alpha}$	interfacial free energy (grain boundaries)
σ_{SL}	interfacial free energy (solid nucleus-liquid)
σ_{CL}	interfacial free energy (substrate-liquid)
σ_{CS}	interfacial free energy (substrate-solid nucleus)
τ	induction time
γ	the mean time required to deposit a monolayer of atoms
ζ	constant related to kernel shape in aggregation processes
δ	supersaturation
ϕ	fraction of one phase in the linked to the Porod invariant, Q
Φ	chemical potential change with atom desorption
χ	EXAFS function
ψ	time independent scaling factor

References

Avrami M. (1941) Kinetics of phase change III. *J. Chem. Phys.* **9**, 177–184.

Badro J., Gillet P., McMillan P. F., Polian A., and Itie J. -P. (1997) A combined XAS and XRD study of the high-pressure behavior of $GaAsO_4$ berlinite. *Europhys. Lett*. **40**, 533–538.

Bailey J. K. and Macartney M. L. (1992) Formation of colloidal silica particles from alkoxides. *Coll. Surf.* **63**(1–2), 151–161.

Ball R. C., Weitz D. A., Witten T. A., and Leyvraz F. (1987) Universal kinetics in reaction-limited aggregation. *Phys. Rev. Lett*. **58**, 274–277.

Bandura A. V., Sykes D., Shapovalov V., Truong T. N., and Kubicki J. D. (2004) Adsorption of water on the TiO_2 (rutile) [110] surface: A DFT study. *J. Phys. Chem. B* **108**, 7844–7853.

Banfield J. F. and Zhang H. (2001) Nanoparticles in the environment, In *Revs. in Miner. & Geochem.* **44**, 1–58. Mineralogical Society of America, Washington, DC.

Barabasi A. L. and Stanley H. E. (1995) *Fractal Concepts in Surface Growth*. Cambridge University Press, Cambridge.

Bassett W. A., Anderson A. J., Mayanovic R. A., and Chou I. M. (2000) Modified hydrothermal diamond anvil cells for XAFS analyses of elements with low energy absorption edges in aqueous solution at sub- and supercritical conditions. *Zeit. Krist.* **215**, 711–717.

Beale A. M., van der Eerden A. M. J., Jacques S. D. M., Leynaud O., O'Brien M. G., Meneau F., Nikitenko S., Bras W., and Weckhuysen, B. M. (2006) A combined SAXS/WAXS/XAFS setup capable of observing concurrent changes across the nano-to-micrometer size range in inorganic solid crystallization processes. *J. Am. Chem. Soc.* **128**, 12386–12387.

Becker R. and Doring W. (1935) Kinetische behandlung der keimbildung in übersättigten dampfen. *Ann. Phys*. **24**, 719–752 (in German).

Beelen T. P. M., Shi W., Morrison G. R., Van Garderen H. F., Browne M. T., Van Santen R. A., and Pantos E. (1997) Scanning transmission x-ray microscopy; a new method for the investigation of aggregation in silica. *J. Coll. Interface Sci.* **185**, 217–227.

Benning L. G., Phoenix V., Yee N., and Tobin M. J. (2004a) Molecular characterization of cyanobacterial cells (I): a synchrotron-based infrared study. *Geochim. Cosmochim. Acta* **68**, 743–757.

Benning L. G., Phoenix V. R., Yee N., and Konhauser K. O. (2004b) The dynamics of cyanobacterial silicification: an infrared micro-spectroscopic investigation. *Geochim. Cosmochim. Acta*. **68**, 729–741.

Benning L. G., Phoenix V., and Mountain B. W. (2005): Biosilicification: the role of cyanobacteria in silica sinter deposition. In Society of General Microbiology Symposium book *Micro-Organisms and Earth Systems – Advances in Geomicrobiology* (Eds. G. M. Gadd, K. T. Semple and H. M. Lappin-Scott), pp. 131–150.

Binks B. P. (Ed.) (1999) *Modern Characterization Methods of Surfactant Systems*. Surfactant Science Series, Vol. 83. Marcel Dekker, New York, Basel. 616 pp.

Boukari H., Lin J. S., and Harris M. T. (1997) Probing the dynamics of the silica nanostructure formation and growth by SAXS. *Chem. Mater.* **9**, 2376–2384.

Bras W., Derbyshire G. E., Ryan A. J., Mant G. R., Felton A., Lewis R. A., Hall C. J., and Greaves G. N. (1993) Simultaneous time resolved SAXS and WAXS experiments using synchrotron radiation. *Nucl. Instr. Methods Phys. Res. A* **326**, 587–591.

Bras W. and Ryan A. J. (1998) Sample environments and techniques combined with small angle x-ray scattering. *Adv. Coll. Interface Sci.* **75**, 1–43.

Bras W., Greaves G. N., Oversluizen M., Clark S. M., and Eeckhaut G. (2005) The development of monodispersed alumino-chromate spinel nanoparticles in doped cordierite glass, studied by in situ x-ray small and wide angle scattering, and chromium x-ray spectroscopy. *J. Non-Cryst. Solids* **351**, 2178–2193.

Brown G. E. and Sturchio N. C. (2002) An overview of synchrotron radiation applications to low temperature geochemistry and environmental science. *Rev. Mineral* **49**, 1–116.

Brown G. E., Calas G., Waychunas G. A., and Petiau J. (1988) X-Ray absorption spectroscopy: Applications in mineralogy and geochemistry. *Rev. Mineral*. **18**, 431–512.

Brydson R. (2001) *Electron energy loss spectroscopy*. Springer, New York, 160 pp.

Bunde A. and Havlin S. (1991) *Fractals and Disordered Systems.* Springer-Verlag, Berlin.

Burton W. K., Cabrera N., and Frank F. C. (1951) The growth of crystals and the equilibrium structure of their surfaces. *Phil. Trans. Royal Soc. London A* (*Math. Phys. Sci.*) **243**, 299–358.

Buseck P. R. (Ed.) (1992) *Minerals and Reactions at the Atomic Scale: Transmission Electron Microscopy*, Mineralogical Society of America, Washington, DC, 508 pp.

Butter K., Bomans P. H. H., Frederik P. M. Vroege G. J., and Philipse A. P. (2003) Direct observation of dipolar chains in iron ferrofluids by cryogenic electron microscopy. *Nat. Materials* **2**, 88–91.

Cahn J. W. and Hilliard J. E. (1958) Free energy of a non-uniform system. I. Interface free energy. *J. Chem. Phys*. **28**, 258–267.

Cahn J. W. (1962) Coherent fluctuations and nucleation in isotropic solids. *Acta Met*. **10**, 907–913.

Cahn J. W. (1966) The later stages of spinodal decomposition and the beginnings of particle coarsening. *Acta Met*. **14**, 1685–1692.

Carpenter M. A., Putnis A., Navrotsky A., and McConnell J. D. C. (1983) Enthalpy effects associated with Al, Si ordering in anhydrous Mg-cordierite. *Geochim. Cosmochim. Acta* **47**, 899–906.

Cashman K. V. and Marsh B. D. (1988) Crystal size distribution (CSD) in rocks and the kinetics and dynamics of crystallization II. Makaopuhi lava lake. *Contrib. Mineral Petrol* **99**, 292–305.

Castro M., Dominguez-Adame F., Sanchez A., and Rodriguez T. (1999) Model for crystallization kinetics: Deviations from Kolmogorov-Johnson-Mehl-Avrami kinetics. *Appl. Phys. Lett*. **75**, 2205–2207.

Chernov A. A. (1984) *Modern Crystallography III, Crystal Growth*. Springer, Berlin.

Clemm P. J. and Fisher J. C. (1955) The influence of grain boundaries on the nucleation of secondary phases. *Acta Met*. **3**,70–73.

Davidson L, Benning L. G., Shaw S., and Terrill N. J. (2005) The effect of arsenic on the nucleation and growth of schwertmannite: An in situ SAXS study. *Geochim. Cosmochim. Acta* **69/10S**, A773 (abstr).

DeFontaine D. (1975) Clustering effects in solid solutions. *Treatise on Solid State Chemistry*, Vol. 5 (Eds. N. B. Hannay), Plenum, New York, p. 129.

Eden M. (1961) In Proceedings of the *Fourth Berkeley Symposium on Mathematical Statistics and Probability*, Vol. IV (Ed. F. Neyman). University of California, Berkeley, p. 233.

Everett D. H. (1988) *Basic Principles of Colloid Science.* Royal Society of Chemistry Paperbacks, London.

Farkas L. (1927) Keimbildungsgeschwindigkeit in übersättigten Dämpfen. *Z. Physik. Chem.* **125**, 236–242. (in German).

Fauchadour D., Pouget T., Lechaire J.-P., Rouleau L., and Normand L. (1999) Evaluation of cryotechniques for TEM observation of sols – application to boehmite sols used in catalysts forming. *Oil Gas Sci. Technol. Rev. IFP* **54**(4), 513–524.

Frank F. C. (1949) The influence of dislocations on crystal growth. *Disc. Farad. Soc*. **5**, 48.

Frederik P. M., Bomans P. H. H., Laeven P. F. J., and Nijpels F. J. T. (2002) Device for preparing specimens for a cryoelectron microscope. Netherlands Industrial Property Office (RO/NL).

Frenkel J. (1939) A general theory of heterophase fluctuations and pretransition phenomena. *J. Chem. Phys.* **7**, 538–547.

Frenkel J. (1955) *Kinetic Theory of Liquids*. Dover, New York.

Fultz B. and Howe J. M. (2002) *Transmission Electron Microscopy and Diffractometry of Materials*, 2nd edition; Series: Advanced Texts in Physics, Springer.

Galoisy L. (2004) X-ray absorption spectroscopy in geosciences: information from the EXAFS region. In *Spectroscopic Methods in Mineralogy* (Eds. A. Beran and E. Libowitzky), Eötvös University Press, Budapest.

Gedde U. W. (1995) *Polymer Physics*. Kluwer Academic Publishers, Dordrecht, The Netherlands.

Gilbert B., Huang F., Zhang H., Ren Y., Haskel D., Lang J. C., Srajer G., Jürgenssen A., Waychunas G., and Banfield J. F. (2004) Analysis and simulation of a nanoparticle structures observed in a surface-driven transition. *J. Chem. Phys.* **120**, 11785–11795.

Glatter O. (1992) Small-angle scattering. In: *International Tables for Crystallography* (Ed. A. J. C. Wilson), Kluwer Academic Publishers, Dordrecht, The Netherlands, pp. 89–112.

Glatter O. and Kratky O. (1982) *Small Angle X-ray Scattering.* Academic Press, London.

Goldstein J., Newbury D. E., Joy D. C., Lyman C. E., Echlin P., Lifshin E., Sawyer L. C., and Michael J. R. (2003) *Scanning Electron Microscopy and X-ray Microanalysis*, 3rd edition. Kluwer Academic Plenum Publishers, New York, 586 pp.

Granasy L., Wang T., and James P. (1998) Kinetics of wollastonite nucleation in $CaO \cdot SiO_2$ glass. *J. Chem. Phys.* **108**, 7317–7326.

Green D. L., Lin J. S., Lam Y-F, Hu M. Z. -C., Schaefer D. W., and Harris M. T. (2003) Size, volume fraction, and nucleation of stober silica nanoparticles. *J. Coll. Interface Sci.* **266**, 346–358.

Grunwaldt J. D., Caravati M. Hannemann S. ,and Baiker A. (2004) X-ray absorption spectroscopy under reaction conditions: suitability of different reaction cells for combined catalyst characterization and time-resolved studies. *Phys. Chem. Chem. Phys.* **6**, 3037–3047.

Guinier A. (1939). La diffraction des rayons X aux tres petits angles: Application al'étude de phénomenes ultramicroscopiques. *Ann. Phys.* **12**, 161–237.

Guinier A and Fournet G. (1955) *Small-Angle Scattering of X-Rays*. Wiley, New York.

Hamad S. Cristol C., and Catlow R. A. (2002) Surface structures and crystal morphology of ZnS: Computational study. *J. Phys. Chem. B* **106**(42), 11002–11008.

Hartman P. and Perdok W. G. (1955) On the relations between structure and morphology of crystals. *Acta Cryst*. **8**, 49–52.

Hayat M. A. (2000) *Principles and Techniques of Electron Microscopy: Biological Applications*. Cambridge University Press, p. 543.

Heaney P. J., Vicenzi E. P., Gianuzzi L. P., and Livi K. J. T. (2001) Focused ion beam milling: a method of site-specific sample extraction for microanalysis of earth and planetary materials. *Am. Mineral.* **86**, 1094–1099.

Henderson C. M. B. (2002) Earth and environmental sciences synchrotron research in the UK: Ongoing work and future prospects. *Geochem. News* **110**, 14–17.

Henry M. (2003) First-principles derivation of vacuum surface energies from crystal structures. *Solid State Sci.* **5**, 1201–1205.

Herring C. (1951) Some theorems on the free energies of crystal surfaces. *Phys. Rev.* **82**, 87–93.

Hochella M. F. Jr. (2002a) Nanoscience and technology: the next revolution in the earth sciences. *Earth Planet. Sci. Lett.* **203**, 593–605.

Hochella M. F. Jr. (2002b) There's plenty of room at the bottom: nanoscience in geochemistry. *Geochim. Cosmochim. Acta* **66**, 735–743.

Hochella M. F., Jr. and Banfield J. F. (1995) Chemical weathering of silicates in nature: a microscopic perspective with theoretical considerations. In *Chemical Weathering Rates of Silicate Minerals* (Eds. A. F. White and S. L. Brantley). *Reviews in Mineralogy*, Vol. 31, Mineralogical Society of America, Washington DC, pp. 353–406.

Hof M., Hutterer R., and Fidler V. (Ed.) (2005) *Fluorescence Spectroscopy In Biology: Advanced Methods and Their Applications to Membranes, Proteins,*

DAN and cells. Springer Series on Fluorescence. Series Editor O. S. Wolfbeis, Springer, 305 pp.

Huang F., Zhang H., and Banfield J. F. (2003) Two-stage crystal growth kinetics observed during hydrothermal coarsening of nanocrystalline ZnS. *Nano Lett.* **3**, 373–378.

Hulbert S. F. (1969) Models for solid-state reactions in powder compacts: A review. *J Br. Ceramic Soc.* **6**, 11–20.

Icopini G. A., Brantley S. L., and Heaney P. J. (2005) Kinetics of silica oligomerization and nanocolloid formation as a function of pH and ionic strength at 25° C. *Geochim. Cosmochim. Acta* **69/2**, 293–303.

Iler R. K. (1979) *The Colloid Chemistry of Silica and Silicates*, Cornell University press, Ithaca, NY.

Iler R. K. (1980) Isolation and characterization of particle nuclei during the polymerization of silicic acid to colloidal silica. *J. Coll. Interface Sci* **71**, 138–148.

Israelachvili J. (1992) *Intermolecular and Surface Forces.* Academic Press, London.

Jiang Z. and Ebner C. (1989) Dynamical Monte Carlo study of crystal growth in a solid-on-solid model. *Phys. Rev. B* **40**, 4833–4837.

Johnson W. A. and Mehl R. F. (1939) Reaction kinetics in processes of nucleation and growth. *Trans. Amer. Inst. Min. Engrs*. **135**, 416–458.

Katchalsky A. and Curran P. F. (1965) *Nonequilibrium Thermodynamics in Biophysics.* Harvard University Press, Cambridge, MA, 248 pp.

Kelton K. F. and Greer A. L. (1988) Test of classical nucleation theory in glasses. *Phys. Rev*. B **38**, 10089–10092.

Kirkpatrick R. J. (1981) Kinetics of crystallization in igneous rocks. In *Kinetics of Geochemical Processes. Reviews in Mineralogy* (Eds. A. C. Lasaga, R. J. Kirkpatrick (eds), Mineralogical Society of America Vol. 8, pp. 321–398.

Kisker C., Schindelin H., and Rees D. C. (1997) Molybdenum-cofactor-containing enzymes: Structure and mechanism. *Ann. Rev. Biochem*. **66**, 233–267.

Kubota N. and Mullin J. W. (1995) A kinetic model for crystal growth from aqueous solution in the presence of impurity. *J. Cryst. Growth* **152**, 203–208.

Lehn J-M. (2002) Toward self-organization and complex matter. *Science* **295**, 2400–2403.

Lifshitz I. M. and Slyozov V. V. (1961) The kinetics of precipitation from supersaturated solid solutions. *J. Phys. Chem. Solids* **19**, 35–50 (translated by R. D.Lowde).

Lin M. Y., Lindsay H. M., Weitz D. A., Ball R. C., Klein R., and Meakin P. (1990) Universal reaction-limited colloid aggregation. *Phys Rev. A* **41/4**, 2005–2020.

Liu X. Y., Maiwa K., and Tsukamoto K. (1997) Heterogeneous two-dimensional nucleation and growth kinetics. *J. Chem. Phys*. **106**, 1870–1879.

Makrides A. C., Turner M., and Slaughter J. (1980) Condensation of silica from supersaturated silicic acid solutions. *J Coll Interf. Sci*. **73**, 345–367.

Mandelbrot B. B. (1967) How long is the coast of Britain? Statistical self-similarity and fractional dimension. *Science* **156**, 636–638.

Mandelbrot B. B. (1975) *Les Objets Fractals: Form, Hasard et Dimension*. Flamarion, Paris.

Mandelbrot B. B. (1983) *The Fractal Geometry of Nature*. W. H. Freeman and Co., New York, 495 pp.

Mann U., Neisel J. D., Burchard W. G., Heinen V., and Welte D. H. (1994) Fluid–rock interfaces as revealed by cryo-scanning electron microscopy. *First Break*, **12**, 131–36.

Marasli N. and Hunt J. D. (1998) The use of measured values of surface energies to test heterogeneous nucleation theory. *J. Cryst. Growth* **191**, 558–562.

Marsh B. D. (1988) Crystal size distribution (CSD) in rocks and the kinetics and dynamics of crystallization. I. theory. *Contrib. Mineral. Petrol* **99**, 277–229.

Martin J. E. (1987) Slow aggregation of colloidal silica. *Phys. Rev. A* **36/7**, 3415–3426.

Martin J. E., Wikcoxon J. P., Schaefer D., and Odinek J. (1990) Fast aggregation of colloidal silica. *Phys. Rev. A* **41/8**, 4379–4391.

McLaren A. C. (1991) *Transmission Electron Microscopy of Minerals and Rocks*. Cambridge University Press, p. 399.

Meakin P. (1998) *Fractals, Scaling and Growth Far from Equilibrium*. Cambridge University Press, Cambridge.

Meakin P. (1983) Formation of fractal clusters and networks by irreversible diffusion-limited aggregation. *Phys. Rev. Lett*. **51**, 1119–1122.

Meakin P. and Family F. (1987) Structure and dynamics of reaction-limited aggregation. *Phys. Rev.* A **36**, 5498–5501.

Megens M., van Kats C. M., Bösecke P., and Vos W. L. (1997) In situ characterization of colloidal spheres by synchrotron small-angle x-ray scattering. *Langmuir* **13**, 6120–6129.

Meneau. F., Cristol S., Sankar S., Dolbnya I. P, Bras W., Catlow C. R. A., Thomas J. M., and Greaves G. N. (2003) *In situ* study of the formation of CdS nanoparticles by small-angle x-ray scattering. *J. Appl. Cryst.* **36**, 718–721.

Mottana A. (2004) X-ray absorption spectroscopy in mineralogy: Theory and experiment in the XANES region. In *Spectroscopic Methods in Mineralogy* (Eds. A. Beran and E. Libowitzky), Eötvös University Press, Budapest.

Naqui A., Chance B., and Cadenas E. (1986) Reactive oxygen intermediates in biochemistry. *Ann. Rev. Biochem*. **55**, 137–166.

Navrotsky A. (2004) Energetic clues to pathways to biomineralization: Precursors, clusters, and nanoparticles. *Proc. Natl. Acad. Sci. USA* **101**, 12096–12101.

Navrotsky A. (1999) High temperature reaction calorimetry applied to metastable and nanophase materials. *J. Therm. Anal. Cal*. **57**, 653–658.

Nielsen A. E. (1064) *The Kinetics of Precipitation*, McMillan, New York, p. 151.

Nicolis G. and Prigogine I. (1977) *Self-organization in non-equilibrium systems: From dissipative structures to order through fluctuations*. Wiley & Sons, New York.

Ohara M. and Reid P. C. (1973) *Modelling Crystal Growth Rates from Solution*. Prentice Hall, Englewood Cliffs, NJ.

Ostwald W. (1900) Über die vermeintliche isomerie des roten und gelben quecksilberoxyds und die oberflächenspannung fester körper. *Zeitschrift fur Physikalische Chemie, Stochiometrie und Verwandschaftslehre*, **34**, 495–503. (in German).

Oxtoby D. W. (1992) Homogeneous nucleation: Theory and experiment. *J. Phys. Condensed Matter* **4**, 7627–7650.

Palenik C. S., Utsunomiya S., Reich M., Kesler S. E., Wang L.,and Ewing R. C. (2004) "Invisible" gold revealed: Direct imaging of gold nanoparticles in a Carlin-type deposit. *Am. Mineral*. **89**, 1359–1366.

Pan Y., Brown A., Brydson R., Warley A., Li A., and Powell J. (2006) Electron beam damage studies of synthetic 6-line ferrihydrite and ferritin molecule cores within a human liver biopsy. *Micron* **37**(5), 403–411.

Paquette J. and Reeder R. J. (1995) Relationship between surface structure, growth mechanism, and trace element incorporation in calcite. *Geochim. Cosmochim. Acta* **59**, 735–749.

Penn R. L. and Banfield J. F. (1999) Morphology development and crystal growth in nanocrystalline aggregates under hydrothermal conditions: Insights from titania. *Geochem. Cosmochim. Acta* **63**, 1549–1557.

Perry C. C. (2003) Silicification: the processes by which organisms capture and mineralize silica. In *Biomineralization* (Eds. P. M. Dove, J. J. De Yoreo and S. Weiner) *Reviews in Mineralogy and Geochemistry*, **54**, 291–327.

Pfeifer P. and Obert M. (1989) *The Fractal Approach to Heterogeneous Chemistry: Surfaces, Colloids, Polymers*. (Ed. D. Avnir) Wiley, New York.

Pickering I. J., Sansone M., Marsch J., and George G. N. (1993) Diffraction anomalous fine structure: a new technique for probing local atomic environment. *J. Am. Chem. Soc.* **115**, 6302–6311.

Pina C. M., Putnis A., and Astilleros J. M. (2004) The growth mechanisms of solid solutions crystallizing from aqueous solutions. *Chem. Geol*. **204**, 145–161.

Pina C. M., Becker U., Risthaus P., Bosbach D., and Putnis A. (1998) Molecular-scale mechanisms of crystal growth in barite. *Nature* **395**, 483–486.

Pontoni D., Narayanan T., and Rennie A. R. (2002) Time-resolved SAXS study of nucleation and growth of silica colloids. *Langmuir* **18**, 56–59.

Price F. P. (1965) Some comments on the "Avrami" equation. *J. Appl. Phys*. **36**, 3014–3016.

Prigogine I. (1961) *Introduction to the Thermodynamics of Irreversible Processes*. Interscience, New York.

Raghavan V. and Cohen M. (1975) Solid State Phase Transformations. In *Treatise on Solid State Chemistry*, *Vol. 5. Changes of State* (Ed. N. B. Hannay). Plenum Press, New York, pp. 67–128.

Ranade M. R., Navrotsky A., Zhang H. Z., Banfield J. F., Elder S. H., Zaban A., Borse P. H., Kulkarni S. K., Doran G. S., and Whitfield H. J. (2002) *Proc. Natl. Acad. Sci. USA* **99**(Suppl. 2), 6476–6481.

Randolph A. D. and Larsen M. A. (1971) *Theory of Particulate Processes*. Academic Press, New York, 251 pp.

Ratsch C. and Venables J. A. (2003) Nucleation theory and the early stages of thin film growth. *J. Vac. Soc. Technol.* A **21**, S96–S109.

Ressler T., Wienold J., Jentoft R. E., Neisius T., and Gunter M. M. (2002) Kinetics of solid-state reactions in heterogeneous catalysis from time-resolved x-ray absorption spectroscopy. *Topics Catalysis* **18**, 46–52.

Rothbaum H. P. and Wilson R. D. (1977) Effect of temperature and concentration on the rate of polymerisation of silica in geothermal waters. In: *Geochemistry 1977*. **218**, 37–43. New Zealand Department of Scientific and Industrial Research Bulletin.

Samson I. M. and Walker R. T. (2000) Cryogenic Raman spectroscopic studies in the system NaCl–CaCl2–H2O and implications for low-temperature phase behavior in aqueous fluid inclusions. *Can. Mineral.* **38**, 35–43.

Sandkühler P., Lattuada P., Wu H., Sefcik J., and Morbidelli M. (2005) Further insights into the universality of colloidal aggregation. *Adv. Coll. Interface Sci.* **113**, 65–83.

Sarma K. R., Shlichta P. J., Wilcox W. R., and Lefever R. A. (1997) Epitaxy versus oriented heterogeneous nucleation of organic crystals on ionic substrates. *J. Cryst. Growth* **174**, 487–494.

Shaw S., Henderson C. M. B., and Komanschek B. U. (2000) Dehydration/recrystallization mechanisms, energetics, and kinetics of hydrated calcium silicate minerals: an in situ TGA/DSC and synchrotron radiation SAXS/WAXS study. *Chem. Geol.* **167**, 141–159.

Schenk O., Urai J. L., and Piazolo S. (2006) Structure of grain boundaries in wet, synthetic polycrystalline, statically recrystallizing halite – evidence from cryo-SEM observations. *Geofluids* **6**(1), 93–104.

Singh M. A., Harkless C. R., Nagler S. E., Shannon R. F., and Ghosh S. S. (1993) Time-resolved small angle x-ray scattering study of ordering kinetics in diblock styrene-butadiene. *Phys. Rev. B* **47**(14), 8425–8435.

Smoluchowski M. V. (1916) Drei vortrage uber diffusion, brownsche bewegung und koagulation von kolloidteilchen. *Physik. Zeit*. **17**, 557–585. (in German).

Steefel C. I. and Van Cappellen P. (1990) A new kinetic approach to modeling water-rock interaction: The role of nucleation, precursors, and Ostwald ripening. *Geochimica et Cosmochimica Acta* **54**, 2657–2677.

Stöber W., Fink A., and Bohn E. (1968) Controlled growth of monodisperse. Silica spheres in the micron size range *J. Coll. Interface Sci.* **26**, 62.

Stöhr J. (1992) *NEXAFS Spectroscopy*. Springer-Verlag, Berlin.

Sutherland D. N. (1967) Theoretical model of floc structure. *J. Coll. Interface Sci*. **25**(3), 373–380.

Svergun D. I. (1992) Determination of the regularization parameter in indirect-transform methods using perceptual criteria. *J. Appl. Cryst.* **25**, 495–503.

Svergun D. I. (1999) Restoring low resolution structure of biological macromolecules from solution scattering using simulated annealing. *Biophys. J.* **76**, 2879–2886.

Svergun D. I and Koch M. H. J. (2003) Small-angle scattering studies of biological macromolecules in solution. *Rep. Prog. Phys.* **66**, 1735–1782.

Talanquer V. and Oxtoby D. W. (1994) Dynamical density functional theory of gas-liquid nucleation. *J. Chem. Phys*. **100**, 5190–5200.

Thoral S., Rose J., Garnier J. M., Van Geen A., Refait P., Traverse A., Fonda E., Nahon, D., and Bottero J. Y. (2005) XAS Study of iron and arsenic speciation during Fe(II) oxidation in the presence of As(III). *Environ. Sci. Technol*. **39**, 9478–9485.

Tiller W. A. (1991) T*he Science of Crystallization: Microscopic Interfacial Phenomena*. Cambridge University Press, New York.

Tiller W. A. (1992) *The Science of Crystallization: Macroscopic Phenomena and Defect Generation*. Cambridge University Press, New York.

Tobler D. J., Benning L. G., and Shaw S. (2006) Nucleation and growth of silica nanoparticles: An *in-situ* SAXS and DLS study. *Geochim. Cosmochim. Acta* 70/18: A652, (abstr).

Tokuyama M., Kawasaki K., and Yoshihisa E. (1986) Kinetic equations for Ostwald ripening. *Physica A*, **134**(2), 323–338.

Toschev S. (1973) Homogeneous Nucleation. In *Crystal Growth: An Introduction* (Ed. P. Hartman). Elsevier, Amsterdam, pp. 1–49.

Trivedi R., Liu S., and Williams S. (2002) Interface pattern formation in nonlinear dissipative systems. *Nat. Mater.* **1**, 157–159.

Turnbull D. (1950) Formation of crystal nuclei in liquid metals. *J. Appl. Phys*. **21**, 1022–1028.

Turnbull D. (1956) Phase changes. *Solid State Phys.* **3**, 224–306.

Turnbull D. and Fisher J. C. (1949) Rate of nucleation in condensed systems. *J. Chem. Phys.* **17**, 71–73.

Utsunomiya S. and Ewing R. C. (2003) Application of high-angle annular dark field scanning transmission electron microscopy, scanning transmission electron microscopy-energy dispersive x-ray spectrometry, and energy-filtered transmission electron microscopy to the characterization of nanoparticles in the environment. *Environ. Sci. Technol*. **37**, 786–791.

van Enckevort W. J. P., van der Berg A. C. J., Kreuwel K. B. G., Derksen A. J., and Couto M. S. (1996) Impurity blocking of growth steps: Experiments and theory. *J. Cryst. Growth* **166**, 156–161.

Venables J. A., Spiller G. D. T., and Hanbücken M. (1984) Nucleation and growth of thin films. *Rep. Prog. Phys*. **47**, 399–459.

Vicsek T. and Family F. (1984) Dynamic scaling for aggregation of clusters. *Phys. Rev. Lett.* **52**, 1669–1672.

Vicsek T. (1992) *Fractal Growth Phenomena*. World Scientific, Singapore.

Vold M. J. (1959) Sediment volume and structure in dispersions of anisometric particles. *J. Phys. Chem*. **63**, 1608–1612.

Vold M. J. (1963) Computer simulation of floc formation in a colloidal suspension. *J. Coll. Sci*. **8**(7), 684–695.

Volmer M. (1939) *Kinetik der Phasenbildung*. Steinkopf Verlag, Leipzig-Dresden (in German).

Volmer M. and Weber A. (1925) Keimbildung in übersättigten gebilden. *Z. Phys. Chem.* **119**, 277–301. (in German).

Voorhees P. W. and Glicksman M. E., (1984) Solution to the multiparticle diffusion problem with applications to Ostwald ripening. I.theory. *Acta Meta*. **32**(11), 2001–2011.

Voorhees P. W. (1985) The theory of Ostwald ripening. *J. Statist. Phys.* **38**(1–2), 231–252.

Wagner C. (1961) Theorie der Alterung von Niderschlagen durch Umlosen (Ostwald Reifung). *Zeitschrift fur Electrochemie* **65**, 581–591. (in German).

Waychunas G. A, Ning Xu, Fuller C. C., Davis J. A., and Bigham J. M., (1995) XAS study of AsO_4^{3-} and SeO_4^{2-} substituted schwertmannites. *Physica B* **208/209**, 481–483.

Waychunas G. A., Kim C. S., and Banfield J. F. (2005) Nanoparticulate iron oxide minerals in soils and sediments: unique properties and contaminant scavenging mechanisms. *J. Nanopart. Technol.* **7**, 409–433.

Waychunas G., Davis J., and Reitmeyer R. (1999) Grazing-incidence EXAFS study of Fe^{3+} sorption on single crystal quartz substrates. *J. Synchrotron Radiation* **6**, 615–617.

Waychunas G. A., Myneni S. C. B., Traina S. J., Bigham J. M., Fuller C. F., and Davis J. A., (2001) Reanalysis of the schwertmannite structure and the incorporation of SO_4-Groups: an IR, XAS, WAXS and simulation study. Conference-abstract: Eleventh annual V.M. Goldschmidt Conference.

Waychunas G. A. (2001) Structure, aggregation and characterization of nanoparticles. In Nanoparticles and the environment, Vol. 44 (Eds. J. F. Banfield and A. Navrotsky), pp. 105–166. *Reviews in Mineralogy and Geochemistry*, Mineralogical Society of America, Washington, DC.

Waychunas G. A. (2002) Grazing-incidence x-ray absorption and emission spectroscopy. In *Applications of Synchrotron radiation in Low-Temperature Geochemistry and Environmental Science*, Vol. 49 (Eds. P. A. Fenter, M. L. Rivers, N. C. Sturchio and S. R. Sutton), pp. 267–316. *Reviews in Mineralogy and Geochemistry*, Mineralogical Society of America, Washington, DC.

Waychunas G. A., Rehr J. J., Fuller C. C., and Davis J. A (2003) Surface complexation and precipitate geometry for aqueous Zn(II) sorption on ferrihydrite: II. XANES analysis and simulation. *Geochim. Cosmochim. Acta* **67**, 1031–1043.

Weeks J. D. and Gilmer G. H. (1979) Dynamics of crystal growth. *Adv. Chem. Phys.* **40**, 157–228.

Weeks J. D., Gilmer G. H., and Jackson K. A. (1976) Analytical theory of crystal growth. *J. Chem. Phys*. **65**, 712–720.

Weeks, E. R., Crocker, J. C., Levitt, A. C., Schofield, A., Weitz, D. A., (2000) Three-dimensional direct imaging of structural relaxation near the colloidal glass transition. *Science* **287**(5453), 627–631.

Weitz D. A., Huang J. S., Lin M. Y., and Sung J. (1984) Dynamics of diffusion-limited kinetic aggregation. *Phys. Rev. Lett*. **53/17**, 1657–1660.

Weres O., Yee A., and Tsao L. (1981) Kinetics of silica polymerization. *J. Coll. Interf. Sci*. **84**, 379–402.

Whitesides G. M. and Grzybowski B. (2002) Self-assembly at all scales. *Science* **295**, 2418–2421.

Witten T. A. Jr. and Sander L. M. (1981) Diffusion-limited aggregation, a kinetic critical phenomenon. *Phys. Rev. Lett*. **47**, 1400–1403.

Wu D. T. (1997) Nucleation theory. *Solid State Phys.* **50**, 37–187.

Wulff G. (1901) Zur frage der geschwindigkeit des wachstums und der auflösung der kristallflachen. *Zeitschrift für Kristallographie* **34**, 449–530. (in German).

Wyss H. M., Huetter M., Mueller M., Meier L. P., and Gauckler L. J., (2002) Quantification of microstructures in stable and gelated suspensions from Cryo-SEM. *J. Coll. Interface Sci.* **248**, 340–346.

Yao J. H, Elder K. R., Guo G., and Gran M. (1993) Theory and simulation of Ostwald ripening. *Phys. Rev. B* **47**, 14110–14125.

Yund R. A. J., McLaren A. C. J., and Hobbs B. E. J. (1974) Coarsening kinetics of the exsolution microstructure in alkali feldspar. *Contrib. Min. Pet*. **48**, 45–55.

Zeldovich J. B. (1943) On the theory of new phase formation: cavitation. Zhur. Eksper. Teor. Fiz. **12** (1942), pp. 525ff (in Russian); *Acta Physicochim. URSS*, **18** (1943), pp. 1–22 (in English).

Zhu J., Chen L.-Q., Shen J., and Tikare V. (1999) Coarsening kinetics from a variable-mobility Cahn-Hilliard equation: Application of a semi-implicit Fourier spectral method. *Phys. Rev. E* **60**, 3564–3572.

Zhang H., Gilbert B., Huang F., and Banfield J. F. (2003) Water-driven structure transformation in nanoparticles at room temperature. *Nature* **424**, 1025–1029.

Chapter 8
Microbiological Controls on Geochemical Kinetics 1: Fundamentals and Case Study on Microbial Fe(III) Oxide Reduction

Eric E. Roden

8.1 Introduction

The pervasive influence of microorganisms (abbreviated hereafter as "morgs"; see Table 8.1 for a list of abbreviations) on the geochemistry of low-temperature environments is well-recognized and has been the subject of voluminous experimental and observational research (Banfield and Nealson, 1997; Brezonik, 1994; Canfield et al., 2005; Chapelle, 2001; Ehrlich, 2002; Lovley, 2000b). Many of the foundational insights into the role of morgs as agents of geochemical reaction can be traced to basic discoveries in microbiology which took place in the 19th and early 20th centuries. Perhaps the most important contribution of all was Louis Pasteur's definitive demonstration that decomposition of OM does not proceed in the absence of living morgs (Pasteur, 1860). Though not made in the context of geochemistry, his decisive defeat of the theory of spontaneous generation was a key step toward recognizing the role of microbial life as a direct agent of chemical transformation in natural, medical, and industrial settings. A long series of discoveries followed in which the participation of morgs in various aspects of elemental cycling and mineral transformation was revealed, many in the context of soil and aquatic microbiology (Clarke, 1985; Ehrlich, 2002; Gorham, 1991). These early discoveries, together with developments in the fields of general microbiology and biochemistry (e.g., as embodied in Kluyver (1957)'s synthesis of unity and diversity in microbial metabolism) laid the groundwork for our current understanding of microbial metabolism based on principles of biochemical energetics (thermodynamics) and enzymatic reaction kinetics.

Interest in the participation of morgs in geochemical and geological phenomena has accelerated greatly in the past several years (Banfield et al., 2005a; Nealson et al., 2001; Newman and Banfield, 2002). This burgeoning interest in geomicrobiology has been sparked in part by the rapid increase in our knowledge of the diversity and ubiquity of morgs in all kinds of natural systems, including extremely

University of Wisconsin, Department of Geology and Geophysics, eroden@geology.wisc.edu

Table 8.1 List of abbreviations used in this chapter

Abbreviation	Meaning
AIO	Amorphous iron oxide
BM	Biomass
CE	Competitive exclusion
CIO	Crystalline iron oxide
DIR	Dissimilatory iron oxide reduction
DIRM(s)	Dissimilatory iron oxide-reducing microorganism(s)
DN	Denitrification
DOC	Dissolved organic carbon
DNM(s)	Denitrifying microorganism(s)
EA(s)	Electron acceptor(s)
ED(s)	Electron donor(s)
MG	Methanogenesis
MGM(s)	Methanogenic microorganism(s)
Morg(s)	Microorganism(s)
OC	Organic carbon
OM	Organic matter
PE	Partial equilibrium
POC	Particulate organic carbon
SA	Surface area
SR	Sulfate reduction
SRM(s)	Sulfate-reducing microorganism(s)
TEAP(s)	Terminal electron-accepting process(es)

hot, cold, dry, alkaline, and acidic environments. This revolution is being facilitated by the application of molecular genetic tools, as well as ongoing advances in culturing techniques (Banfield et al., 2005b; Barns and Nierzwicki-Bauer, 1997; Keller and Zengler, 2004; Madsen, 2005; Oremland et al., 2005). In addition, advances in analytical methodologies such as high-resolution transmission electron microscopy and various spectroscopic methods for characterizing are offering new insights into the mechanisms of microbe-mineral interactions (see Geesey et al. (2002) for a review). Much of the work to date in this area has focused on *qualitative* descriptions of phenomena, in particular on the mineralogical and/or biochemical mechanisms leading to the production or destruction of minerals. With several notable exceptions (e.g., in the area of OM diagenesis in aquatic environments), generally less attention has been paid to development of *quantitative* descriptions (i.e., kinetic models) of microbial contributions to geochemical processes in natural systems. This distinction reflects the difference between the fields of Geomicrobiology and Microbial Biogeochemistry (Ehrlich, 2002): whereas Geomicrobiology examines the role that morgs have played in the past and continue to play in fundamental geological processes such as rock weathering, soil and sediment formation, genesis and degradation of minerals, and in the genesis and degradation of fossil fuels, Microbial Biogeochemistry deals primarily with the kinetics of microbially influenced chemical reactions, often in the context of material (mineral) cycles with emphasis on mass transfer and energy flow. The latter subject is the primary focus of this and the companion chapter (Chap. 8.4.5.5).

The overall goals of the two chapters are to (1) summarize the role of microbial processes in water-rock interactions (e.g., oxidation-reduction and mineral dissolution-precipitation reactions); (2) present and illustrate by example the essential kinetic models that are typically used to describe microbial processes in the context of biogeochemical processes; and (3) discuss two detailed case studies that illustrate how microbial processes control the kinetics of environmentally significant geochemical processes, namely the dissimilatory reduction of iron oxide minerals, and the biological oxidation of metal sulfide minerals. Both of the latter processes represent unique coupled microbial-geochemical reaction systems that embody the essential features of microbially catalyzed water-rock interactions. Finally, a brief summary and overview of future prospects for advances in understanding coupled microbial-geochemical kinetics is presented.

Before proceeding, a brief clarification of the term "microorganism": with no exceptions, this term is used here to refer to prokaryotic organisms, which comprise two of the three domains of life, Bacteria and Archaea (Woese et al., 1990). Although microscopic eukaryotes are important in a wide variety of natural environments, we focus our attention here on prokaryotes because – as a result of their diverse metabolic potential (see next section) – they exert a much broader range of impacts on water-rock interactions than do eurkaryotic organisms.

8.2 Overview of the Role of Morgs in Water-Rock Interactions

8.2.1 Mechanisms and Definitions

There are three basic mechanisms whereby morgs participate in water-rock interactions: (1) enzymatic reactions linked to energy generation or other biochemical processes that lead directly to production or consumption of dissolved and/or solid-phase compounds; (2) non-enzymatic reactions in the bulk phase which are promoted by enzymatic production or consumption of dissolved and/or solid-phase species; (3) non-enzymatic reactions which are promoted via coordination of reactants by reactive cell surface ligands (e.g., cell surface adsorption or surface nucleation/precipitation reactions). Figure 8.1 provides a simple illustration of these three mechanisms in the context of dissimilatory (microbial) iron oxide reduction.

An important distinction here is that between "biologically induced mineralization" and "biologically controlled mineralization" (also sometime referred to as "organic matrix-mediated mineralization) (Lowenstam, 1981). The latter refers to formation of a mineral via cellular activities that direct the nucleation, growth, and morphology of a mineral *for a specific physiological or morphological purpose*, usually via an enzymatically coordinated process that is under genetic control. Classic examples include production of calcium carbonate shells or silicate tests by eurkaryotic organisms, and intracellular deposition of magnetite crystals by magnetotactic bacteria (Lowenstam and Weiner, 1989; Weiner

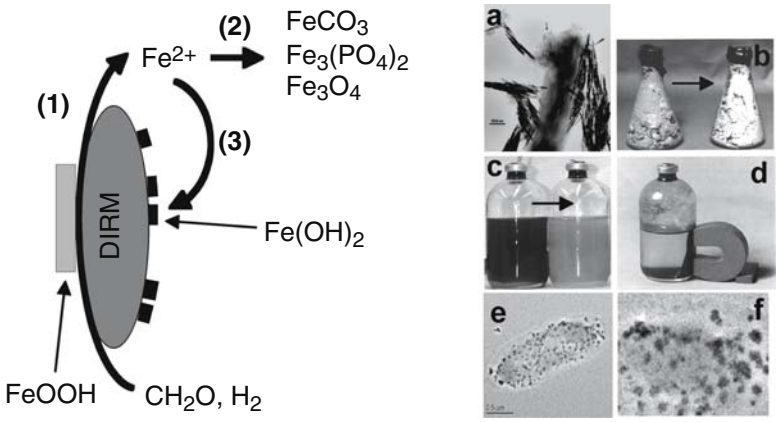

Fig. 8.1 Illustration of three basic mechanisms of microbial participation in water-rock interactions (as defined in section 8.2.1), in the context of dissimilatory Fe(III) oxide reduction. **Left**: Reaction mechanisms: (1) transfer (e.g. by outer membrane cytochromes or other redox-active appendages) of electrons from the surface of a DIRM to the surface of an insoluble Fe(III) oxide (see Case Study #1); (2) biologically-induced formation of Fe(II)-bearing mineral phases such as siderite ($FeCO_3$), vivianite ($Fe_3(PO_4)_2$), or magnetite (Fe_3O_4) through reaction of biogenic Fe(II) with aqueous species (CO_3^{2-}, PO_4^{3-}) or (in the case of magnetite) residual Fe(III) oxide surfaces; (3) surface precipitation of $Fe(OH)_2$ on DIRM cell surfaces, facilitated by accumulation of Fe^{2+} ions on negatively-charged functional groups on the cell surface. **Right**: Photoillustrations: (a) physical contact between a DIRM (*Shewanella algae*) and a synthetic Fe(III) oxide (goethite, α-FeOOH) (M. Urrutia, unpublished), a critical step in the direct transformation of the oxide surface via enzymatically-catalyzed electron transfer; (b) stripping of Fe(III) oxide coatings on subsurface sediments via dissimilatory microbial reductive dissolution in hydrocarbon-contaminated sediments (Lovley, 2000); (c) conversion of synthetic hydrous ferric oxide (HFO) to siderite ($FeCO_3$) during dissimilatory reduction by *Shewanella putrefaciens* (Roden et al., 2002); (d) conversion of HFO to magnetite (Fe_3O_4) during dissimilatory reduction by *Desulfuromonas acetoxidans* (Roden and Lovley, 1993); (e) and (f) TEM image of $Fe(OH)_2$ surface precipitates on *Shewanella putrefaciens* cells formed during dissimilatory reduction of ferric citrate (Y. Gorby, unpublished) (see also color insert)

and Dove, 2003). In contrast, biologically induced mineralization refers to reactions that occur *indirectly as a result of microbial metabolism*, but which do not serve a specific physiological purpose for the organism responsible for their formation (Bazylinski and Moskowitz, 1997; Frankel and Bazylinski, 2003). In biologically induced mineralization, the organisms generate or consume one or more substrates, which in turn results in the formation of extracellular minerals. The phases produced via biologically induced mineralization are typically (but not always) poorly crystallized, and have a broad range of particle size distribution and morphology – in contrast to those generated intracellularly via biologically controlled mineralization, which have a narrow size distribution and defined, consistent morphologies.

For example, the chains of magnetite formed by magnetotactic bacteria consist of stable, single-domain crystalline minerals with high structural perfection (Bazylinski and Frankel, 2000). Although the size and morphology of magnetite crystals

varies among different magnetotactic organisms, in all cases a given organism produces crystals with very narrow size range within a specialized membrane-bound prokaryotic organelle called a magnetosome (Bazylinski and Frankel, 2000). Recent studies indicate that bacterial magnetosomes are invaginations of the cell membrane flanked by cytoskeletal filaments composed of actin-like proteins analogous to those present in eukaryotic cells (Komeili et al., 2006), and that these and other proteins are likely to play a role in establishing the specific locus for production of the chains of magnetite crystals (Scheffel et al., 2006). Magnetotactic bacteria produce intracellular magnetite for a defined purpose, i.e., to align themselves vertically in the Earth's magnetic field in order to find and maintain a position of optimum dissolved O_2 concentration within redox gradients in the water column or sediments of aquatic systems (Bazylinski and Frankel, 2000).

In contrast to the magnetite produced by magnetotactic bacteria, the bulk quantities of extracellular magnetite produced by DIR (see Fig. 8.1d) result from the abiotic interaction of biogenic Fe(II) with ferrihydrite outside of the cell (Lovley et al., 1987). The magnetite so produced is poorly crystalline and irregular in shape, with a relatively broad size distribution, and with most particles being in the superparamagnetic size range (<35 nm) (Moskowitz et al., 1989; Sparks et al., 1990). Production of extracellular magnetite by DIR serves no known function for DIRMs; in fact, it actually limits DIR activity, because the magnetite is not readily reducible under the circumneutral pH conditions that are typical of DIR systems (Kostka and Nealson, 1995; Lovley and Phillips, 1986b; Lovley et al., 1987; Zachara et al., 2002).

This chapter deals solely with examples of biologically induced mineralization, and in particular on quantitative description of the physiological-biochemical processes that are directly responsible for mineral-water reactions (mechanism 1 above). The term "microbial mineral transformation" (Ehrlich, 1999) is recommended to refer collectively to mineral dissolution or precipitation reactions that involve microbial activity. This label is preferable to one that includes "mineralization", because for microbial physiologists and ecologists, as well as many geochemists, mineralization means conversion of OM to its inorganic constituents (Ehrlich, 1999).

8.2.2 Key Characteristics of Microorganisms

The significant quantitative role of morgs in water-rock interactions can be traced to fundamental aspects of biological metabolism and to the tremendous metabolic diversity and unique physical and chemical structure of morgs. Like all other living organisms, morgs utilize enzymes (proteins) to catalyze reactions associated with energy generation and cellular biosynthesis (Madigan et al., 2000). Although enzymes do not alter the overall thermodynamic favorability of a reaction, they lower the activation energy required for a reaction to proceed (see Fig. 2.1), thereby permitting reactions to occur under relatively low near-surface temperature and pressure conditions. For example, DIRMs produce redox-active proteins and localize them

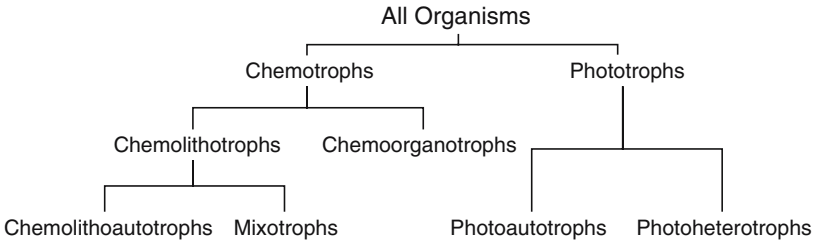

Fig. 8.2 Classification of microbial energy metabolism (Modified from Fig. 15.1 in Madigan et al. (2000), used with permission). Chemotrophs obtain energy from chemical compounds, whereas phototrophs use light as an energy source; chemolithotrophs use inorganic chemicals, whereas chemoorganotrophs use organic chemicals; chemolithoautotrophs and photoautotrophs fix CO_2 to synthesize cell biomass, whereas mixotrophs and photoheterotrophs incorporate pre-formed organic compounds into cell biomass

on the outer surface of the cell in order to transfer electrons from intracellular OC oxidation to Fe(III) oxide surfaces outside of the cell (see Fig. 8.11). In the absence of the whole suite of enzymes involved (intracellular and extracellular), there is no spontaneous reaction between Fe(III) oxides and OC. Similarly, Fe(II)-oxidizing morgs produce membrane-associated enzyme systems that catalyze the reaction between Fe(II) and O_2 at low pH (see Fig. 9.3), a reaction which is extremely slow in the absence of enzymatic catalysis (see Fig. 9.1).

An extraordinarily wide range of reactions – far more diverse than those known in the eukaryotic world – are facilitated by prokaryotic morgs, many of which are directly relevant to the subject of water-rock interactions. Often such reactions occur solely through enzymatic catalysis at near-surface temperature and pressure, although several important reactions (e.g., oxidation of reduced Fe and S species) may also proceed through abiotic reaction pathways. Figure 8.2 provides a simple classification of microbial energy metabolism that can be used as a basis for understanding the diverse manner in which morgs may participate in water-rock interactions. Table 8.2, in turn, provides a representative listing, organized in the context of Fig. 8.2, of the role of morgs as catalysts of geochemical processes relevant to the subject of water-rock interactions. Nealson and Stahl (1997) provide a brief but thorough description of virtually all of the metabolic processes listed in Table 8.2, as well as the organisms responsible for catalyzing them.

Another key feature of morgs is their small size, which has several fundamental implications for their ability to participate intensively in biogeochemical processes (Nealson and Stahl, 1997). Prokaryotic cells with a diameter on the order of 1 μm have surface area-to-volume ratio 10–1000 times higher than typical eukaryotic cells. As a result, morgs generally possess a relatively high metabolic rate per unit mass compared to larger organisms, which in turn enhances the effective connection (chemically and energetically) between cells and their local environment. A related implication of the small size of morgs is their potential to exhibit rapid rates of growth and population turnover. In a review of the ecological implications of body size, Peters (1983) calculates that the time required for morgs

Table 8.2 Survey of the role of microorganisms as catalysts of water-rock interactions, organized in relation to the classification of microbial energy metabolism in Fig. 8.2

Process type Chemotrophy	Process	Mechanisms of reaction	Representative organisms
Chemoorganotrophy	Oxidation of solid-phase organic matter	Enzymatic hydrolysis of polymeric OM and coupled fermentation-respiration of monomers	Wide range
	Reductive dissolution of Fe(III) and Mn(IV) oxides (circumneutral pH) coupled to organic acid & H_2 oxidation	Enzymatic (outer membrane redox-active cytochromes and/or pili) electron transfer to oxide surfaces	*Geobacter, Geothrix, Shewanella, Geoglobus*; some SRMs and MGMs; various thermophilic Archaea
	Production of magnetite, siderite, vivianite, and rhodocrocite	Reaction of biogenic Fe(II) or Mn(II) with residual oxide surfaces, carbonate, or phosphate	Same as above
	Production of U(IV), Tc(V), and other insoluble reduced metal/radionuclide phases	Enzymatic reduction of soluble oxidized metals and precipitation of insoluble reduced metals	Same as above
	Production of pyrite and other iron and metal-sulfide minerals	Enzymatic reduction of sulfate, excretion of dissolved sulfide, and reaction of dissolved sulfide with Fe(II) and/or Fe(III)	∂-Proteobacteria and others
Chemolithotrophy			
Chemolithoautotrophy	Oxidation of metal-sulfide minerals and S^0 (acidic pH) with O_2 or Fe^{3+}	Enzymatic oxidation of Fe(II) and S^0; electrochemical corrosion	*Acidithiobacillus, Leptospirillum, Ferroplasma, Sulfolobus/Acidanus*
	Aerobic and nitrate-dependent oxidation of FeS and S^0 (circumneutral pH)	Unknown	*Beggiatoa, Thiothrix*
	Disproportion of S^0, and $S_2O_3^{2-}$	Unknown	*Desulfocapsa*
	Oxidation of Fe(II) in FeS_2 and basalt glass	Unknown	α- and γ-Proteobacteria

(*cont.*)

Table 8.2 (*Continued*)

Process type Chemotrophy	Process	Mechanisms of reaction	Representative organisms
	Nitrate-dependent oxidation of aqueous Fe(II) & solid-phase Fe(II)	Unknown	*Geobacter, Ferroglobus, Thiobacillus denitrificans*, various β-Proteobacteria
Mixotrophy	Oxidative precipitation of Fe(III)/Mn(IV) oxides	Enzymatic Fe(II) (mechanism unknown) and Mn(II) (Cu-containing oxidases) oxidation	*Bacillus, Leptothrix, Gallionella*, ES1, TW2
	Aerobic and nitrate-dependent oxidation of FeS and S^0 (circumneutral pH)	Unknown	*Beggiatoa, Thiobacillus*
	Nitrate-dependent oxidation of aqueous Fe(II) & solid-phase Fe(II)	Unknown	*Geobacter, Ferroglobus, Thiobacillus denitrificans*, various β-Proteobacteria
Phototrophy			
	Production of calcium carbonate minerals	Photosynthesis-induced changes in alkalinity; coordination of ions on cell surfaces	Cyanobacteria and microeukaryotic algae
	Oxidative precipitation of Fe(III) oxides	Light-dependent enzymatic Fe(II) oxidation; mechanism unknown	Various anoxygenic photosynthetic β-Proteobacteria

to colonize an environment and reestablish an arbitrary biomass of $100\,mg\,m^{-2}$ is on the order of a few days, whereas for larger organisms such as insects the time scale is on the order of a year or at least a seasonal period. These calculations explain conceptually how morgs can quickly exploit resources in environmental systems and therefore have immediate major impacts on materials and energy processing in changing natural environments. Finally, the small size of morgs permits them to associate with local physical and chemical microenvironments. In many instances, high rates of chemical flux (including mineral transformations) take place at reaction fronts that are characterized by micrometer (or even nanometer) to millimeter-scale microenvironments (Revsbech and Jorgensen, 1986). Such microenvironments are colonized by morgs specifically adapted to take advantage of sources of energy or other environmental conditions available within the microenvironments. Indeed, in most instances, the metabolic activities of morgs often dictate the physical location and specific chemical conditions of the microenvironment, and in this sense the microbial-geochemical interactions can be viewed as a holistic system that defines its own internal parameters relative to external boundary conditions (Revsbech and Jorgensen, 1986). Visscher et al. (1998) provide a comprehensive example of such a system involved in the formation of modern marine stromatolites.

A final key feature of prokaryotic cells is the ability of the cell surface to serve as an interface for sorption and concentration of metal cations in dilute environmental solutions. The long-standing attribution of this property to the presence of deprotonated carboxylate and phosphate groups on the bacterial outer membrane (Beveridge, 1989) was recently confirmed for both gram positive and gram negative organisms by infrared spectroscopy (Jiang et al., 2004). Thus there is an apparent universality of functional group chemistry on prokaryotic cell surfaces (i.e., carboxyl, phosphoryl, and hydroxyl sites, with pKa values of 4.8, 6.9, and 9.4, respectively; (Fein et al., 1997)), which validates the use of standard surface complexation models (see Chap. 4) for simulation of cation adsorption processes (Borrok and Fein, 2004; Fein et al., 2001; Yee and Fein, 2001). The key implication of this phenomenon for water-rock interactions is that once metal ions have interacted with electronegative sites on the outer membrane, they nucleate the formation of a wide range of fine-grained minerals (e.g., oxide/hydroxide, carbonate, sulfate/sulfide, silicate, and phosphate) by incorporating common anions from their surroundings (Schultze-Lam et al., 1996). This process in turn promotes further metal sorption and precipitation, and thus generally accelerates the kinetics of mineral precipitation in environments where prokaryotic cells are abundant. Two different modes of action can be distinguished in this context (Southam, 2000): *passive* microbially induced mineral formation refers to simple binding of cations and recruitment of solution anions, resulting in surface nucleation and mineral growth (essentially mechanism 3 above); *active* microbially induced mineral formation occurs via direct redox transformation of surface-associated metal ions (e.g., enzymatic electron transfer to or from a mineral surface), or by the production of metabolic endproducts that form minerals on cell surfaces (a combination of mechanisms 1 and 3 above).

8.3 Kinetic Models in Microbial Geochemistry

8.3.1 Introduction

The literature on kinetic analysis and modeling of geochemical processes is vast and has been systematically reviewed several times over the past few decades (Berner, 1980; Boudreau, 1997; Brezonik, 1994; Lasaga and Kirkpatrick, 1981; Lasaga, 1998; Lerman, 1979; Schnoor, 1996; Stumm, 1990). The purpose of this section is to explain how standard kinetic rate laws can be applied to microbially catalyzed reactions. The subject is approached from a macroscopic point of view, in which rates of microbial metabolism are related to observed (or estimated) properties such as reactant concentration, microbial biomass, and the thermodynamic favorability (i.e., the ΔG) of the reaction.

Virtually all biogeochemical reactions (as well as many abiotic geochemical reactions; see Chap. 2) are the net result of numerous elementary reactions. For example, the reduction of Fe(III) oxides coupled to oxidation of OM in sediments

$$CH_2O + 4Fe(OH)_3 + 7H^+ \rightarrow HCO_3^- + 4Fe^{2+} + 10H_2O \tag{8.1}$$

is the net result of a complex series of enzymatic reactions, carried out by multiple groups of morgs, during which polymeric organic carbon (OC) undergoes hydrolysis and fermentation to generate the organic acids (e.g., acetate) and H_2 that are the substrates for dissimilatory iron-reducing morgs (DIRMs) (Lovley, 1991). The metabolism of individual energy substrates such as acetate and H_2 coupled to DIR by DIRMs

$$CH_3COO^- + 8Fe(OH)_3 + 15H^+ \rightarrow 2HCO_3^- + 8Fe^{2+} + 20H_2O \tag{8.2}$$

$$H_2 + 2Fe(OH)_3 + 4H^+ \rightarrow 2Fe^{2+} + 6H_2O \tag{8.3}$$

are also complex processes that involve several different enzyme systems both inside and outside of the cell membrane (Gorby et al., 2006; Lovley et al., 2004; Methe, 2003; Reguera et al., 2005). Even in cases where the rate-limiting step in a microbial reaction can be traced to a specific enzymatic process (e.g., uptake of an organic substrate or a soluble electron acceptor across the cell membrane, or an intracellular enzymatic reaction), that biochemical process is never the result of a single elementary reaction, but rather a multistep process involving one or more enzymes. Thus, for our purposes kinetic expressions for rates of microbial reaction are by definition macroscopic descriptions of overall reactions. Fortunately, in many cases, it is possible to use elementary rate expressions to describe the dependence of an overall multistep reaction on the concentration of one or a few reactions that control the rate of the overall reaction.

8.3.2 Zero-Order Kinetics

A zero-order reaction is one whose rate is (apparently) not dependent on the concentration of the reactant of interest (see Chap. 1). Although such a reaction would appear to violate the principle of mass action, the violation is only an apparent one. Zero-order kinetics are common in homogeneous chemical reactions in which the concentration of a catalyst controls the rate of reaction, and in reactions at surfaces where a physical constraint such as surface area limits the reaction rate (Brezonik, 1994). A zero-order rate law may also describe biogeochemical reactions in which the reactant concentration(s) are above saturation, or to describe reaction rates in experiments where the period of observation is sufficiently short so as to avoid curvature in a plot of reactant concentration versus time.

A classic example of the latter situation comes from Martens and Berner's (1974) experiments on microbial sulfate reduction (SR) in marine sediments. Rates of microbial SR in marine sediments are independent of sulfate concentration down to sulfate concentrations of ca. 3 mM (Boudreau and Westrich, 1984; Roden and Tuttle, 1993), tenfold lower than the concentration of sulfate in seawater (28 mM). As a result, Martens and Berner (1974) observed a linear decrease in sulfate concentration during their salt marsh sediment incubation experiment (Fig. 8.3a), in which the rate of SR was limited by the abundance and reactivity of OM rather than sulfate concentration down to sulfate concentrations of $\leq$ca. 1 mM.

Another good example of a zero-order rate process in a geomicrobiological reaction system comes from studies of the kinetics of microbial (enzymatic) reduction of synthetic Fe(III) oxides with differing SAs (Roden, 2003a, 2006). Although the long-term kinetics of DIR can be well-described as a first-order process dependent on the abundance of microbially reducible surface sites (discussed in detail in Case Study #1), rates of reduction are generally constant during the first few days of incubation, such that initial, zero-order rates of reaction can be extracted from linear plots of Fe(II) versus time (e.g., Fig. 8.3b).

8.3.3 First-Order Kinetics

Several major classes of geomicrobiological processes (e.g., oxidation of dissolved and solid-phase OM, oxidation and reduction of insoluble mineral phases) can be well-described by first-order kinetics, in which the reaction rate is directly proportional to the concentration of the reactant (see Chap. 1). The first-order dependence of bulk DIR and FeS_2 oxidation rates on the abundance of mineral SA is examined in detail in Case Studies 1 and 2, respectively. We focus here on oxidation of sediment OC as premier example of first-order reaction kinetics in microbial geochemistry. The development provides a segue into descriptions of the use of mixed

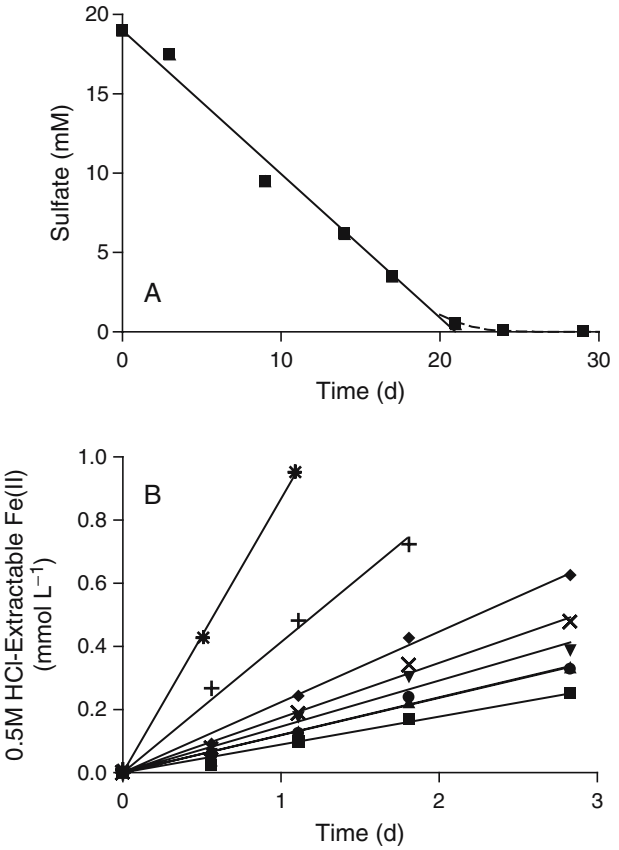

Fig. 8.3 Two examples of zero-order rate processes: (A) Consumption of sulfate during laboratory incubation of organic-rich saltmarsh sediments (data from Martens and Berner (1974), used with permission); (B) Production of Fe(II) during reduction of different synthetic Fe(III) oxides by *S. putrefaciens* (data not shown in Roden (2003)). Solid lines show the results of linear least-squares regression analysis of the concentration vs. time data. The zero-order rate of sulfate consumption in panel A is 0.91 mM d^{-1}; the zero-order rates of Fe(II) production in panel B range from ca. 0.09 for crystalline hematite (squares) to 0.9 mmol L^{-1} d^{-1} for poorly crystalline hydrous ferric oxide (asterisks). The dashed line in panel A illustrates the influence of sulfate limitation on sulfate consumption at very low (< 1 mM) sulfate concentration

first-order/Monod kinetics to describe consumption of soluble EAs during OM oxidation (see Sect. 8.3.4).

Berner (1964) proposed the use of a first-order rate model to depict decay of POC in order to explain the observed depth distribution of sulfate in marine sediment porewater (see Berner (1980) for review). This early work led to a generation of kinetic models in which first-order decay of POC is the primary driving force for a wide range of sediment diagenetic processes (Berner, 1977; Boudreau, 1996; Dhakar and Burdige, 1996; Klump and Martens, 1989; Soetaert et al., 1996; VanCappellen et al., 1993; VanCappellen and Wang, 1996). Although multiple fractions of POC, with differing intrinsic reactivities (see Boudreau (1991) for review),

must typically be invoked to properly describe the overall kinetics of degradation, introduction of the basic first-order rate model for POC metabolism was crucial in that it provided an adequate tool for quantifying the impact of OM degradation on sediment geochemistry (VanCappellen and Gaillard, 1996). Such impacts include a wide variety of mineral dissolution and precipitation reactions (Berner, 1981) that strongly influence both present day biogeochemical dynamics as well as long-term geochemical cycles on earth, e.g., the role of FeS_2 burial in planetary redox balance (Berner, 1982, 1989).

The basic assumption underlying application of the first-order rate model to POC metabolism is that hydrolysis of solid-phase OM by attached morgs is the rate-limiting step in the overall degradation process. Thus, POC oxidation can be viewed as a surface-controlled process analogous to microbial mineral transformations such as Fe(III) oxide reduction and FeS_2 oxidation. Westrich and Berner (1984) provided two pieces of direct experimental evidence in support of this model. First, loss of POC mass during aerobic oxidation of coastal phytoplankton could be well-described by a so-called "two-G" rate model (where "G" is the generic symbol used to represent POC), in which G_1 represents the most labile fraction of POC, and G_2 represents a less-labile (but still metabolizable on a time scale of years) fraction (Fig. 8.4a). Second, Westrich and Berner (1984) demonstrated that addition of increasing amounts of either fresh or partially degraded phytoplankton POC to organic-poor coastal marine sediment lead to a linear increase in the rate of OM oxidation coupled to microbial SR (Fig. 8.4b). The latter experiments were performed using short-term incubation experiments (after a 10-day preincubation period following POC addition) with ^{35}S-labeled sulfate, which (after analyzing data on the accumulation of ^{35}S-labeled sulfide using a zero-order rate model) yielded instantaneous rates of OM metabolism for each level of POC addition. These results provided conclusive support for the first-order rate model for POC decay first proposed by Berner 20 years earlier (Berner, 1964). Subsequent studies of marine sediment OM metabolism have also supported this approach (e.g., (Burdige, 1991; Klump and Martens, 1987; Roden and Tuttle, 1996)), as well as studies in freshwater sediments in which Fe(III) oxide reduction and methanogenesis (MG) were the predominant pathways for OM oxidation (Roden and Wetzel, 2002).

8.3.4 Hyperbolic Kinetics: Enzyme Activity and Microbial Growth/Metabolism

The basic rate expressions that describe the kinetics of enzyme activity and microbial metabolism are referred to as "Michaelis-Menton" and "Monod" kinetics, respectively, in honor of the scientists who first introduced them (Michaelis and Menten, 1913; Monod, 1942, 1949). The term "hyperbolic kinetics" is often used in reference to these rate laws, since a plot of rate against reactant concentration takes the form of a rectangular hyperbola through the origin. Table 8.3 provides derivations of the hyperbolic rate law applied to enzyme and microbial metabolic activity.

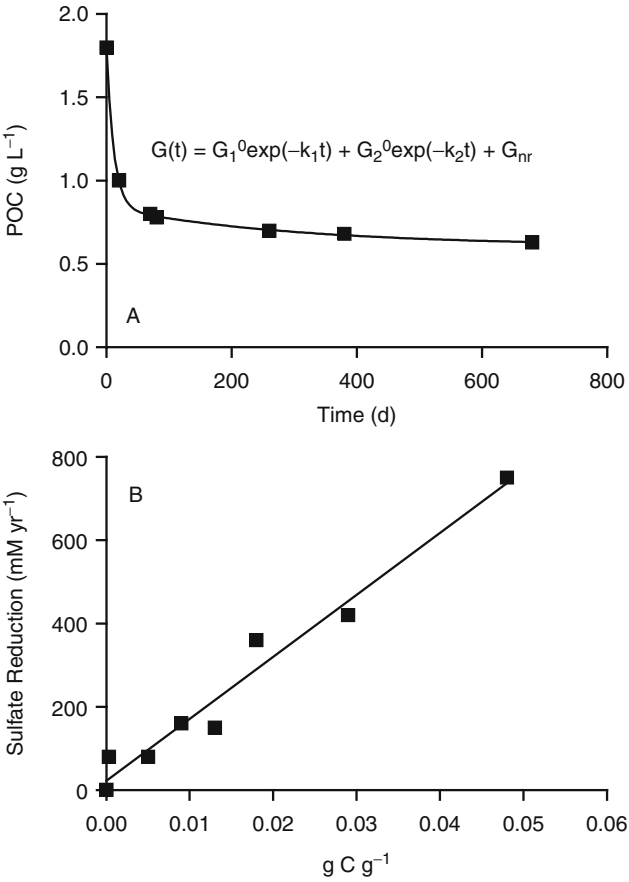

Fig. 8.4 Microbial oxidation of POC as an example of first-order reaction kinetics: (A) Time-dependent decay of coastal marine phytoplankton POC decay under aerobic conditions. The data (symbols) were fit (line) to the integrated form of a "two-G" first-order decay model (see section 8.3.3). (B) Decay of labile phytoplankton POC coupled to microbial sulfate reduction (SR) in organic-poor sediment from Long Island Sound. After a 10-day preincubation period, rates of SR were directly proportional (line shows results of linear least-squares regression analysis) to the amount of labile POC added. Data in both panels are from Westrich and Berner (1984), used with permission

Hyperbolic rate expressions find broad use in microbiology, engineering, and environmental science. Because of the importance of these rate laws, their history is briefly reviewed prior to examining examples of their applications in geomicrobiology.

The Michaelis-Menton (1913) equation was derived to describe the activity of the invertase enzyme (which splits sucrose into glucose and fructose) in terms of the law of mass action, based on the formation of an enzyme-substrate complex and its subsequent conversion to reaction products. In contrast, the Monod (1942, 1949) equation was originally used as a strictly empirical tool to describe the influence of

Table 8.3A Derivation of classical Michaelis-Menton enzyme kinetics

Overall reaction:

$$S \xrightarrow{E} P \tag{1}$$

where:

S = substrate
P = product
E = enzyme (catalyst)

Reaction mechanism:

$$E + S \underset{k_{-1}}{\overset{k_1}{\Leftrightarrow}} ES \overset{k_2}{\Rightarrow} P + E \tag{2}$$

where:

ES = enzyme-substrate complex

Rate of P accumulation:

$$\frac{d[P]}{dt} = k_2[ES] \tag{3}$$

Assume $d[ES]/dt = 0$ and solve for [E]:

$$[E] = \frac{k_{-1} + k_2}{k_1[S]}[ES] \tag{4}$$

Assuming total amount of E (E_T) is constant:

$$[E]_T = [E] + [ES] \tag{5}$$

Substitute for [E] in (4) and solve for [ES]:

$$[ES] = \frac{[S][E]_T}{(k_{-1} + k_2)/k_1 + [S]} \tag{6}$$

Substitute for [ES] in (3) (7)

$$\frac{d[P]}{dt} = V_{max}\frac{[S]}{K_m + [S]} \tag{8}$$

where:

$$V_{max} = k_2[E]_T \tag{9}$$

$$K_m = \frac{k_{-1} + k_2}{k_1} \tag{10}$$

Table 8.3B Derivation of general Monod rate law for microbial metabolism

Overall reaction:

$$S \xrightarrow{B} P \tag{1}$$

where:

S = substrate
P = product
B = cell biomass (catalyst)

Reaction mechanism:

$$B + S \underset{k_{-1}}{\overset{k_1}{\Leftrightarrow}} BS \overset{k_2}{\Rightarrow} P + B \tag{2}$$

where:

BS = cell-substrate complex

Rate of P accumulation:

$$\frac{d[P]}{dt} = k_2[BS] \tag{3}$$

Assume $d[BS]/dt = 0$ and solve for [B]:

$$[B] = \frac{k_{-1} + k_2}{k_1[S]}[BS] \tag{4}$$

Assuming total biomass of cells (B_T) is constant:

$$[B]_T = [B] + [BS] \tag{5}$$

Substitute for [B] in (4) and solve for [BS]:

$$[BS] = \frac{[S][B]_T}{(k_{-1} + k_2)/k_1 + [S]} \tag{6}$$

Substitute for [BS] in (3) (7)

$$\frac{d[P]}{dt} = V_{max}\frac{[S]}{K_s + [S]} \tag{8}$$

where:

$$V_{max} = k_2[B]_T \tag{9}$$

$$K_s = \frac{k_{-1} + k_2}{k_1} \tag{10}$$

limiting substrate concentration on the specific growth rate (e.g., in units of d^{-1}) of morgs during exponential growth (Koch, 1998). Subsequent work by Monod and colleagues (Rickenberg et al., 1956) adapted the basic framework of the Michaelis-Menton equation to describe the kinetics of lactose uptake across the bacterial cell membrane in terms of a substrate-enzyme (permease) complex. Both of these applications of the Monod equation can be recovered from the general derivation given in Table 8.3B. To account for substrate uptake across the cell membrane, S can be assumed to represent substrate on the outside of the cell, and P substrate on the inside of the cell. To account for microbial growth kinetics, B is substituted for P such that the reaction mechanism leads to production of an additional unit of cell biomass as a function of substrate concentration. This leads to the following rate expression:

$$\frac{d[B]}{dt} = k_2[B]_T \frac{[S]}{K_s + [S]} \tag{8.4}$$

Dividing both sides by the total biomass at time t, $[B]_T$, yields

$$\frac{d[B]/dt}{[B]_T} = k_2 \frac{[S]}{K_s + [S]} \tag{8.5}$$

in which the left hand term represents the instantaneous rate of biomass production relative to the current total biomass (i.e., the specific growth rate), and in which k_2 can be identified as the maximum specific growth rate at very high substrate concentration. The specific and maximum specific growth rates are typically referred to by the symbols μ and μ_{max}, which leads to the following classical expression for Monod growth kinetics (Koch, 1998):

$$\mu = \mu_{max} \frac{[S]}{K_s + [S]} \tag{8.6}$$

The Michaelis-Menton and Monod equations can be generalized to the following rate expression for use in describing biogeochemical process rates

$$R = R_{max} \frac{[S]}{K_m + [S]} \tag{8.7}$$

where R is the rate of substrate metabolism (e.g., in units of mol $L^{-1}\,d^{-1}$), R_{max} is the maximum rate of metabolism (at saturating substrate concentration), [S] is the substrate concentration (e.g. in units of mol L^{-1}) and K_m is the half-saturating substrate concentration at which $R = 0.5R_{max}$. Formal association of Eq. (8.7) with the Michaelis-Menton or Monod equation would require the assumption that the biogeochemical process of interest is limited by the activity of a specific enzyme or substrate uptake system with fixed bulk abundance in the reaction medium. In practice such an assumption is unnecessary, since a wide variety of more complicated enzyme-catalyzed reactions (i.e., processes that involve multiple enzymatic steps) obey the general form of Eq. (8.7). Thus, Eq. (8.7) provides a robust expression

for representing the overall rate of substrate consumption in a complex microbial process, even when detailed information on the reaction pathway(s) involved is not available (VanCappellen and Gaillard, 1996). In situations where morg biomass is included in the overall rate law (i.e., in biomass-dependent models), Eq. (8.7) becomes

$$R = R_{max} \frac{[S]}{K_m + [S]} [B] \tag{8.8}$$

where [B] represents biomass (e.g., in units of g L^{-1}), and the parameter R_{max} now has units of mol g $biomass^{-1}$ d^{-1}. The corresponding rate expression for biomass growth is

$$\frac{d[B]}{dt} = YR_{max} \frac{[S]}{K_m + [S]} [B] - k_d[B] \tag{8.9}$$

where Y is the growth yield in units of g biomass produced per mol substrate metabolized, and k_d is a first-order endogenous cell decay constant (Rittmann and McCarty, 2001), e.g., in units of d^{-1}.

Hyperbolic rate laws analogous to Eqs. (8.7)–(8.9) have been used to describe a wide variety of biogeochemical processes in natural systems, most notably the consumption of natural and contaminant DOC, soluble inorganic electron donors such as Fe^{2+} and HS^-, and soluble EAs such as O_2, NO_3^-, and SO_4^{2-}. Figure 8.5 shows an example of the kinetics of microbial SR in oligohaline (salinity < 2 ppt, $SO_4^{2-} < 2$ mM) and mesohaline (salinity 10–20 ppt, SO_4^{2-} 7–15 mM) estuarine sediments. The results illustrate an important principle in microbial geochemistry, namely that environmental conditions can lead to adaptation of the kinetic properties of the resident microbial populations to local conditions. In this case, long-term differences in sulfate availability between low-salinity and high-salinity estuarine environments has led to the development of SRM populations with different K_s values for sulfate uptake.

Multiplicative hyperbolic equations have been adopted to describe rate limitations imposed by more than one limiting substrate. A good example is the so-called "dual Monod" equation (Bader, 1982):

$$R = R_{max} \frac{[S_1]}{K_{m,S1} + [S_1]} \frac{[S_2]}{K_{m,S2} + [S_2]} \tag{8.10}$$

where the rate of reaction is limited by two different substrates (S_1 and S_2). This formulation is commonly used to describe rates of natural or contaminant DOC oxidation coupled to the reduction of a specific EA (e.g., Lovley (1986), Molz (1986), Bae and Rittmann (1995)), where S_1 and S_2 would correspond to DOC and EA, respectively (see further discussion below). In addition, Eq. (8.10) provides a mechanistic basis for use of a second-order rate law to model secondary redox reactions between EAs and reduced end-products of primary redox reactions associated with organic matter decay (VanCappellen and Wang, 1996) (some of which are known only to proceed via biological catalysis, e.g., oxidation of Mn(II) and CH_4 by O_2), since Eq. (8.10) reduces to a second-order equation when $S_1 \ll K_{m,S1}$ and $S_2 \ll K_{m,S2}$.

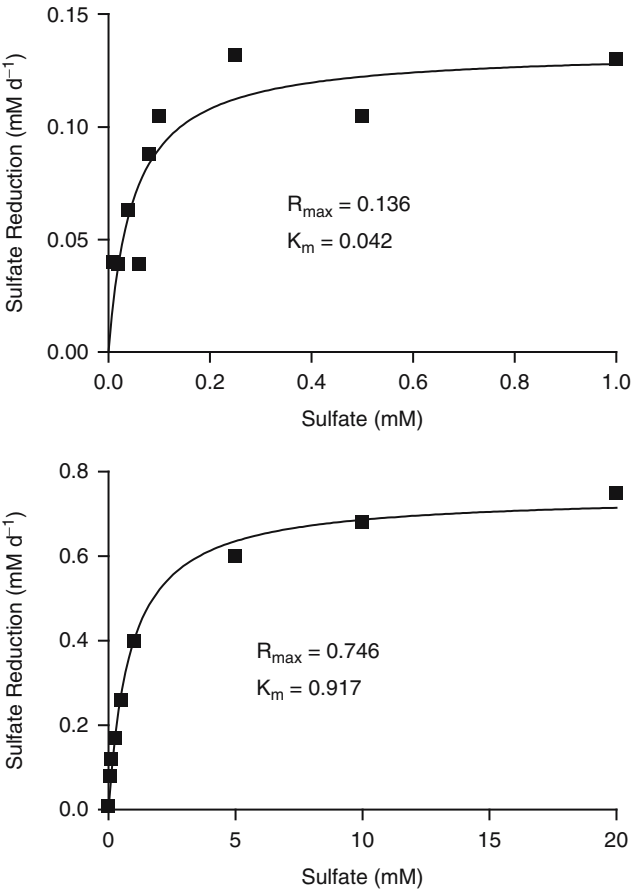

Fig. 8.5 Kinetics of microbial sulfate reduction in oligohaline (salinity < 2 ppt, $SO_4^{2-} < 2$ mM) (A) and mesohaline (salinity = 10–15 ppt, SO_4^{2-} = 7–15 mM) (B) Chesapeake Bay sediments. Note that the K_m value for sulfate uptake by SRMs in the low-salinity sediments is ca. 20-fold lower than that for SRMs in the mid-salinity sediments. Data are from Roden and Tuttle (1993), used with permission

An important variant on the dual Monod approach to model rates of POC decay with different EAs is the following mixed first-order/hyperbolic rate scheme:

$$R = k_1[POC]\frac{[EA]}{K_m + [EA]} \tag{8.11}$$

where k_1 is a first-order decay constant for POC and [POC] is the bulk reactive POC concentration. Boudreau (1992) provides a mechanistic derivation of Eq. (8.11) based on the formation of a transient complex (similar to the enzyme-substrate complex in the Michaelis-Menton framework) between the EA and a reactive POC surface site.

Some sediment biogeochemical modeling studies have adopted a modified version of Eq. (8.11) to model EA limitation and competition among different TEAPs in redox stratified environments such as aquatic sediments and groundwater aquifers (Boudreau and Westrich, 1984; Gaillard and Rabouille, 1992; Hunter et al., 1998; VanCappellen and Wang, 1995, 1996; Wang and VanCappellen, 1996). In this "modified Monod" approach (which is identical in form to the empirical model devised by Blackman (1905)), the hyperbolic rate term is simplified by assuming that the rate of reaction is independent of the EA concentration above a certain limiting concentration, and directly proportional to it below that concentration:

$$R = R_{max} \text{ where } [EA] \geq [EA]_{lim} \tag{8.12}$$

$$R = R_{max} \frac{[EA]}{[EA]_{lim}} \text{ where } [EA] < [EA]_{lim} \tag{8.13}$$

This approach offers a convenient way to model the temporal-spatial sequencing of different TEAPs (VanCappellen and Wang, 1995, 1996): when the concentration of a more energetically favorable EA exceeds the limiting concentration for that EA, the rate of EA consumption is independent of EA concentration, and all other less energetically favorable TEAPs are suppressed. When the concentration of the EA falls below the limiting concentration, the rate of EA consumption is proportional to EA concentration, and less favorable TEAPs become active. This scheme allows for a smooth transition in space and/or time from one predominant TEAP to another. It should be noted that the limiting concentration for a given EA is a semi-empirical parameter that accounts collectively for the influence of kinetic limitations on EA consumption, inhibition of enzyme systems by higher redox potential electron acceptors, and the influence of competition for energy substrates (discussed further below) on the spatial/temporal segregation of different TEAPs (VanCappellen and Wang, 1996). Table 8.4 provides a summary of this computational scheme applied to the typical sequence of TEAPs found in aquatic sediments and groundwater aquifers, and Fig. 8.6a,b shows an application of this approach to modeling[1] the temporal sequence of TEAPs in a slurry experiment with anoxic freshwater wetland sediment.

An attractive aspect of the modified Monod approach for modeling competing microbial respiratory reactions is that it alleviates the need for terms to depict inhibition of TEAPs by more energetically favorable EAs. Although a wide variety of equations are available to describe inhibition of metabolic pathways (cf. Humphrey (1972), Rawn (1983)), the "noncompetitive" inhibition approach is most commonly used to depict inhibition of a given TEAP by a more favorable EA (VanCappellen et al., 1993; Widdowson et al., 1988). For example, inhibition by NO_3^- of Fe(III)

[1] All model simulations presented in this and the companion chapter involved the solution of one or more ordinary differential equations, which was achieved using either the Runga-Kutta or Burlisch-Stoer ODE solver algorithms in Press et al. (1992) *Numerical Recipes in FORTRAN*. Cambridge University Press.. The simulations were implemented in Microsoft Visual Basic for Applications associated with Microsoft Excel, and are available as stand-alone Excel files from the author.

Table 8.4 Computational scheme for the "modified Monod" rate law applied to temporal-spatial sequencing of major TEAPs in sediments

If $[O_2] > [O_2]_{lim}$ Then
$R_{O2} = R_{max}$
$R_{NO3} = R_{Mn(IV)} = R_{Fe(III)} = R_{SO4} = R_{CH4} = 0$

Otherwise
$R_{O2} = R_{max} \times [O_2]/[O_2]_{lim}$
If $[NO_3^-] > [NO_3^-]_{lim}$ Then
$R_{NO3} = (R_{max} - R_{O2})$
$R_{Mn(IV)} = R_{Fe(III)} = R_{SO4} = R_{CH4} = 0$

Otherwise
$R_{NO3} = (R_{max} - R_{O2}) \times [NO_3^-]/[NO_3^-]_{lim}$
If $[Mn(IV)] > [Mn(IV)]_{lim}$ Then
$R_{Mn(IV)} = (R_{max} - R_{O2} - R_{NO3})$
$R_{Fe(III)} = R_{SO4} = R_{CH4} = 0$

Otherwise
$R_{Mn(IV)} = (R_{max} - R_{O2} - R_{NO3}) \times [Mn(IV)]/[Mn(IV)]_{lim}$
If $[Fe(III)] > [Fe(III)]_{lim}$ Then
$R_{Fe(III)} = (R_{max} - R_{O2} - R_{NO3} - R_{Mn(IV)})$
$R_{SO4} = R_{CH4} = 0$

Otherwise
$R_{Fe(III)} = (R_{max} - R_{O2} - R_{NO3} - R_{Mn(IV)}) \times [Fe(III)]/[Fe(III)]_{lim}$
If $[SO_4^{2-}] > [SO_4^{2-}]_{lim}$ Then
$R_{SO4} = (R_{max} - R_{O2} - R_{NO3} - R_{Mn(IV)} - R_{Fe(III)})$
$R_{CH4} = 0$

Otherwise
$R_{SO4} = (R_{max} - R_{O2} - R_{NO3} - R_{Mn(IV)} - R_{Fe(III)}) \times [SO_4^{2-}]/[SO_4^{2-}]_{lim}$
$R_{CH4} = (R_{max} - R_{O2} - R_{NO3} - R_{Mn(IV)} - R_{Fe(III)} - R_{SO4})$

Adapted from Van Cappellen and Wang (1995; 1996).
R_{max} represents the maximum collective rate of all TEAPs, e.g. as limited by the first-order rate of POC hydrolysis (see section 8.3.3). R_{O2}, R_{NO3}, $R_{Mn(IV)}$, $R_{Fe(III)}$, R_{SO4}, and R_{CH4} refer to rates of OC oxidation coupled to O_2 reduction (aerobic respiration), NO_3^- reduction (e.g. to N_2 or NH_4^+) , Mn(IV) oxide reduction, Fe(III) oxide reduction, SO_4^{2-} reduction, and methanogenesis, respectively. The subscript "lim" refers to the limiting concentration for a given EA.

reduction coupled to first-order decay of sediment POC is expressed as follows:

$$R_{Fe(III)} = k_1 [POC] \frac{[Fe(III)]}{K_{m,Fe(III)} + [Fe(III)]} \frac{K_{I,NO3}}{K_{I,NO3} + [NO_3^-]} \tag{8.14}$$

where $K_{m,Fe(III)}$ is the standard half-saturating concentration of Fe(III) as an electron acceptor for OC oxidation, and $K_{I,NO3}$ is the noncompetitive inhibition constant for NO_3^-. Note here that the inhibition constant corresponds to the concentration of the inhibitor at which the rate of reaction is one-half of what it would be in the absence of the inhibitor; thus, when $[NO_3^-] = K_{I,NO3}$, the rate of Fe(III) reduction $(R_{Fe(III)})$ is equal to one-half of it would be in the total absence of NO_3^-. When

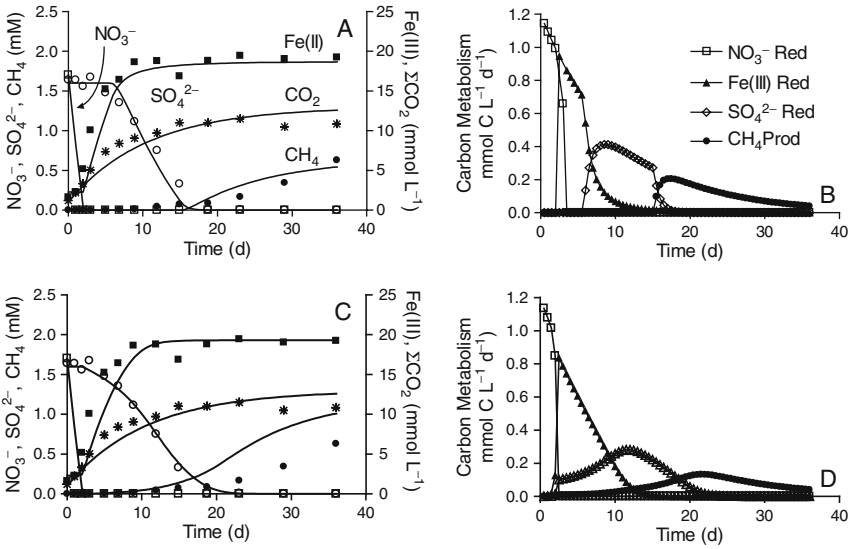

Fig. 8.6 Simulation of TEAPs in a slurry (batch reactor) of anoxic freshwater wetland sediment using the modified Monod (A,B) and standard Monod with inhibition (C,D) approaches (see section 3.3 for details). The slurry was amended with 1 wt % of POC (heat-killed Baker's yeast), and OM decay was modeled according to first-order rate law using a first-order decay constant of 0.1 d^{-1} (derived from data in Fig. 8.10C). Concentrations of NO_3^-, SO_4^{2-}, 0.5M HCl-extractable amorphous Fe(III) and Fe(II), total CO_2 ($\Sigma CO_2 = CO_2(g)$ + total dissolved inorganic carbon), and CH_4 were measured over time using standard methods (Roden and Wetzel, 1996). Limiting electron acceptor concentrations of 0.01, 2, and 0.1 mmol L^{-1} were assumed for NO_3^-, Fe(III) oxide surface sites, and SO_4^{2-} in the modified Monod simulation; these same values were used for the half-saturation and inhibition constants in the standard Monod simulations (see text for details). The concentration of Fe(III) oxide surface sites was computed assuming an initial SA of 600 m^2 g^{-1} (Dzombak and Morel, 1990), together with a standard mineral site density of 3.84 μmol sites m^{-2}; the SA of the oxide mineral was assumed to change over time according to a standard dissolution function for uniform spherical particles (Postma, 1993; see Eq. (9.21) in Chapter 9)

more than one inhibitor is present, the combined effect of all inhibitors is described by the product of multiple terms analogous to the last term in Eq. (8.14). To illustrate this approach, the sediment slurry data in Fig. 8.6a were simulated using a standard Monod scheme based on Eq. (8.11) (summarized in Table 8.5), with inhibition functions for NO_3^-, Fe(III), and SO_4^{2-}. As a first approximation, the inhibition constants for NO_3^-, Fe(III), and SO_4^{2-} were set equal to the half-saturation constants for these EAs (VanCappellen and Gaillard, 1996). The simulation including the inhibition functions produced results similar to those from the modified Monod model (Fig. 8.6c,d).

Use of the modified Monod approach, or the standard Monod equation together with noncompetitive inhibition functions, provides a convenient way to model the effects of competition between different microbial respiratory groups without having to include microbial biomass in the reaction network. However, there are established approaches to model microbial competition and associated populations dynamics, and their use is an often overlooked aspect of biogeochemical

Table 8.5 Computational scheme for the standard Monod rate law with noncompetitive inhibition applied to temporal-spatial sequencing of major terminal electron acceptor processes (TEAPs) coupled to first-order POC decay in sediments

$$R_{O2} = k_1[POC]\frac{[O_2]}{K_{m,O2} + [O_2]}$$

$$R_{NO3} = k_1[POC]\frac{[NO_3^-]}{K_{m,NO3} + [NO_3^-]}\frac{K_{I,O2}}{K_{I,O2} + [O_2]}$$

$$R_{Mn(IV)} = k_1[POC]\frac{[Mn(IV)]}{K_{m,Mn(IV)} + [Mn(IV)]}\frac{K_{I,NO3}}{K_{I,NO3} + [NO_3^-]}\frac{K_{I,O2}}{K_{I,O2} + [O_2]}$$

$$R_{Fe(III)} = k_1[POC]\frac{[Fe(III)]}{K_{m,Fe(III)} + [Fe(III)]}\frac{K_{I,Mn(IV)}}{K_{I,Mn(IV)} + [Mn(IV)]}\frac{K_{I,NO3}}{K_{I,NO3} + [NO_3^-]}\frac{K_{I,O2}}{K_{I,O2} + [O_2]}$$

$$R_{SO4} = k_1[POC]\frac{[SO_4^{2-}]}{K_{m,SO4} + [SO_4^{2-}]}\frac{K_{I,Fe(III)}}{K_{I,Fe(III)} + [Fe(III)]}\frac{K_{I,Mn(IV)}}{K_{I,Mn(IV)} + [Mn(IV)]}\frac{K_{I,NO3}}{K_{I,NO3} + [NO_3^-]} \times \frac{K_{I,O2}}{K_{I,O2} + [O_2]}$$

$$R_{SO4} = k_1[POC]\frac{K_{I,SO4}}{K_{I,SO4} + [SO_4^{2-}]}\frac{K_{I,Fe(III)}}{K_{I,Fe(III)} + [Fe(III)]}\frac{K_{I,Mn(IV)}}{K_{I,Mn(IV)} + [Mn(IV)]}\frac{K_{I,NO3}}{K_{I,NO3} + [NO_3^-]} \times \frac{K_{I,O2}}{K_{I,O2} + [O_2]}$$

Adapted from Van Cappellen and Gaillard (1996).
The K_m terms refer to half-saturating EA concentrations in the generalized hyperbolic rate expression (see Eq. 8.7). The K_I values refer to noncompetitive inhibition constants that depict inhibition of a given TEAP by one or more favorable EAs.

reaction modeling (Rittmann and VanBriesen, 1996). From a mechanistic standpoint, it makes sense that a kinetic model that includes microbial reactions should include the morgs themselves together with the factors that determine their abundance and metabolic rates (Rittmann and VanBriesen, 1996); otherwise rates of energy metabolism and associated geochemical processes (e.g., mineral dissolution and precipitation) are functionally disconnected from the temporal/spatial evolution of the microbial communities responsible for those processes. Since the next wave of microbial reaction models is likely to include multiple groups of interacting populations with different physiological properties (Rittmann and McCarty (2001); see Watson et al. (2003), Wirtz (2003), and Maurer and Rittmann (2004) for recent examples), we examine the basic framework for depicting competition and population dynamics in some detail below, using sediment TEAPs as an example. In this case, the kinetic expressions depict utilization of dissolved monomeric substrates such as acetate or H_2, which are in fact the major substrates for TEAPs in anaerobic sediments (Christensen, 1984; Lovley and Klug, 1982; Lovley and Phillips, 1989; Sorensen et al., 1981). This kinetic analysis sets the stage for subsequent consideration of thermodynamic effects on microbial metabolism. **Moreover, it demonstrates the important general principle that the physiological properties**

of different groups of morgs can directly control the relative rates of competing geochemical processes.

8.3.5 Microbial Population Dynamics and Competition

To illustrate the microbial population dynamics approach, the sediment slurry data from Fig. 8.6 was simulated using the model described in Table 8.6, in which POC was assumed to undergo first-order hydrolytic/fermentative decay, liberating acetate as an energy source for the metabolism and growth of anaerobic respiratory morgs. This structure is based on Lovley and Klug's (1986) model of the competition between SR and MG in freshwater lake sediments. Numerous studies have shown that acetate is the main carbon and energy substrate for respiration in anaerobic sediments (Christensen, 1984; Lovley and Klug, 1982; Lovley and Phillips, 1989; Sorensen et al., 1981), which justifies the use of acetate as the sole ED for the microbial population-based simulation of TEAPs in sediments. Parameter values were chosen from data available in the literature and research in the author's laboratory. Yield coefficients for the different morg groups were estimated using the energy balance approach described in Rittmann and McCarty (2001), which provides a theoretically sound and practical alternative in situations where detailed information on growth yield for different types of physiological reactions are not available. The approach involves comparison of the amount of energy required to convert a carbon source to cellular carbon (assuming pyruvate is the central carbon intermediate) with the amount of energy liberated from energy-generating reactions, taking into account the efficiency of cellular energy transfer. The free energies for acetate oxidation coupled to DN, DIR, SR, and MG were estimated (see ΔG values listed in Table 8.6A) using reactant and product ΔG_f values from Stumm and Morgan (1990), assuming dissolved acetate, NO_3^-, SO_4^{2-}, HCO_3^-, Fe(II), HS^-, and CH_4 concentrations of 100 μM, 1 mM, 2 mM, 5 mM, 1 mM, 20 μM, and 1 μM, respectively. All these values are reasonable for the conditions present in the slurry experiment. Pyruvate was assumed to be the main cellular carbon intermediate, and NH_4^+ was assumed to be available in excess for incorporation into cell biomass. The estimated yield coefficients for SRMs and MGMs (see Parameter Values in Table 8.6D) agreed within ca. 30% of the values for these microbial groups used in the model of Lovley and Klug (1986).

The only parameters adjusted to fit the slurry incubation data were the initial population densities of the DNMs, DIRMs, SRMs, and MGMs. Using initial biomass values equivalent to 0.02–1.0 g L^{-1}, the model reproduced the observed biogeochemical data (Fig. 8.7a) as well as (to a first approximation) the results of the biomass-independent modified and standard Monod models shown in Fig. 8.6. In other words, the microbial population dynamics approach accounted for the temporal sequence of TEAPs without the need for semi-empirical "limiting concentration" or "inhibition constant" parameters. Although accurate depiction of the myriad of microbial competitive interactions in natural systems (e.g., in

Table 8.6 Description of microbial population-based model used to depict competition between TEAPs for acetate (CH_3COO^-) in the sediment slurry experiment (see Fig. 8.7)

A. Stoichiometric Equations

(1) $CH_3COO^- + 1.6NO_3^- + 0.6H^+ \rightarrow 2HCO_3^- + 0.8N_2 + 0.8H_2O$ [a] $\Delta G = -798\,kJ/mol\,CH_3COO^-$

(2) $CH_3COO^- + 8Fe(OH)_3 + 15H^+ \rightarrow 2HCO_3^- + 8Fe^{2+} + 20H_2O$ [b] $\Delta G = -171\,kJ/mol\,CH_3COO^-$

(3) $CH_3COO^- + SO_4^{2-} \rightarrow 2HCO_3^- + HS^-$ [c] $\Delta G = -62.4\,kJ/mol\,CH_3COO^-$

(4) $CH_3COO^- + H_2O \rightarrow HCO_3^- + CH_4$ [d] $\Delta G = -39.1\,kJ/mol\,CH_3COO^-$

[a] assuming $\{CH_3COO^-\} = 1 \times 10^{-4}\,M$, $\{NO_3^-\} = 1 \times 10^{-3}\,M$, $\{HCO_3^-\} = 5 \times 10^{-3}\,M$, and $\{N_2\} = 1 \times 10^{-3}\,M$

[b] assuming $\{CH_3COO^-\} = 1 \times 10^{-4}\,M$, $\{Fe(III)\} = 1\,M$, $\{HCO_3^-\} = 5 \times 10^{-3}\,M$, and $\{Fe^{2+}\} = 1 \times 10^{-3}\,M$

[c] assuming $\{CH_3COO^-\} = 1 \times 10^{-4}\,M$, $\{SO_4^{2-}\} = 2 \times 10^{-3}\,M$, $\{HCO_3^-\} = 5 \times 10^{-3}\,M$, and $\{HS^-\} = 2 \times 10^{-5}\,M$

[d] assuming $\{CH_3COO^-\} = 1 \times 10^{-4}\,M$, $\{HCO_3^-\} = 5 \times 10^{-3}\,M$, and $\{CH_4\} = 1 \times 10^{-6}\,M$

B. Metabolic Rate Expressions

(1) $R_{POC} = k_1[POC]$

(2) $$R_{CH3COO,DNM} = R_{max,CH3COO,DNM}\frac{[CH_3COO^-]}{K_{m,CH3COO,DNM} + [CH_3COO^-]}\frac{[NO_3^-]}{K_{m,NO3} + [NO_3^-]}[DNM]$$

(4) $$R_{CH3COO,DIRM} = R_{max,CH3COO,DIRM}\frac{[CH_3COO^-]}{K_{m,CH3COO,DIRM} + [CH_3COO^-]}\frac{[Fe(III)]}{K_{m,Fe(III)} + [Fe(III)]}[DIRM]$$

(5) $$R_{CH3COO,SRM} = R_{max,CH3COO,SRM}\frac{[CH_3COO^-]}{K_{m,CH3COO,SRM} + [CH_3COO^-]}\frac{[SO_4^{2-}]}{K_{m,SO4} + [SO_4^{2-}]}[SRM]$$

(6) $$R_{CH3COO,MGM} = R_{max,CH3COO,MGM}\frac{[CH_3COO^-]}{K_{m,CH3COO,MGM} + [CH_3COO^-]}[MGM]$$

(*cont.*)

Table 8.6 (*Continued*)

C. Conservation Equations

(1) $$\frac{d[POC]}{dt} = -k_1[POC]$$

(2) $$\frac{d[CH_3COO^-]}{dt} = 0.5k_1[POC] - R_{CH3COO,DNM} - R_{CH3COO,DIRM} - R_{CH3COO,SRM} - R_{CH3COO,MGM}$$

(3) $$\frac{d[NO_3^-]}{dt} = -R_{CH3COO,DNM}\,\alpha_{NO3/CH3COO}$$

(4) $$\frac{d[Fe(III)]}{dt} = -R_{CH3COO,DIRM}\,\alpha_{Fe(III)/CH3COO}$$

(5) $$\frac{d[Fe(II)]}{dt} = R_{CH3COO,DIRM}\,\alpha_{Fe(III)/CH3COO}$$

(6) $$\frac{d[SO_4^{2-}]}{dt} = -R_{CH3COO,SRM}\,\alpha_{SO4/CH3COO}$$

(7) $$\frac{d[CH_4]}{dt} = -R_{CH3COO,MGM}\,\alpha_{CH4/CH3COO}$$

(8) $$\frac{d[DNM]}{dt} = Y_{DNM}R_{CH3COO,DNM} - k_d[DNM]$$

(9) $$\frac{d[DIRM]}{dt} = Y_{DIRM}R_{CH3COO,DIRM} - k_d[DIRM]$$

(10) $$\frac{d[SRM]}{dt} = Y_{SRM}R_{CH3COO,SRM} - k_d[SRM]$$

(11) $$\frac{d[MGM]}{dt} = Y_{MGM}R_{CH3COO,MGM} - k_d[MGM]$$

D. Parameter Values

Parameter	Value	Units	Source
$[POC]_0$	20.8	mmol L^{-1}	Experimental data
$[NO_3^-]_0$	0.97	mM	Experimental data
$[Fe(III)]_0$	20.8	mmol L^{-1}	Experimental data
$[SO_4^{2-}]_0$	2.0	mM	Experimental data
$[CH_4]_0$	0.0	mmol L^{-1}	Experimental data
$[DNM]_0$	0.1	g L^{-1}	Trial and error to achieve fit to slurry data
$[DIRM]_0$	0.1	g L^{-1}	Trial and error to achieve fit to slurry data
$[SRM]_0$	0.1	g L^{-1}	Trial and error to achieve fit to slurry data
$[MGM]_0$	0.02	g L^{-1}	Trial and error to achieve fit to slurry data
k_1	0.04	d^{-1}	Roden & Wetzel (2002)
k_d	0.01	d^{-1}	Lovley & Klug (1986)
Rmax,CH3COO, DNM	188	mmol CH_3COO^- g^{-1} d^{-1}	Rittmann & McCarty (2001)
Rmax,CH3COO, DIRM	121	mmol CH_3COO^- g^{-1} d^{-1}	Roden, unpublished data for *G. metallireducens*
Rmax,CH3COO, SRM	9.9	mmol CH_3COO^- g^{-1} d^{-1}	Lovley & Klug (1986)
Rmax,CH3COO, MGM	15.7	mmol CH_3COO^- g^{-1} d^{-1}	Lovley & Klug (1986)
K_m,CH3COO, DNM	0.001	mM	Arbitrarily set equal to $K_{m,CH3COO,DIRM}$
K_m,CH3COO, DIRM	0.001	mM	Roden & Wetzel (2003)
K_m,CH3COO, SRM	0.003	mM	Lovley & Klug (1986)
K_m,CH3COO, MGM	0.05	mM	Lovley & Klug (1986)
Y_{DNM}	0.0203	g cells/mmol CH_3COO^-	Energetics approach of Rittmann & McCarty (2001) (see section 3.3)
Y_{DIRM}	0.0123	g cells/mmol CH_3COO^-	Energetics approach of Rittmann & McCarty (2001) (see section 3.3)
Y_{SRM}	0.00484	g cells/mmol CH_3COO^-	Energetics approach of Rittmann & McCarty (2001) (see section 3.3)
Y_{MGM}	0.00286	g cells/mmol CH_3COO^-	Energetics approach of Rittmann & McCarty (2001) (see section 3.3)
K_m,NO3	0.01	mM	Simulation in Fig. 8.6B
K_m,Fe(III)	2.0	mmol surface sites L^{-1}	Simulation in Fig. 8.6B
K_m,SO4	0.068	mM	Lovley & Klug (1986)
$\alpha_{NO3/CH3COO}$	1.6	mmol NO_3^-/mmol CH_3COO^-	Stoichiometric equation (1)
$\alpha_{Fe(III)/CH3COO}$	8.0	mmol Fe(III)/mmol CH_3COO^-	Stoichiometric equation (2)
$\alpha_{SO4/CH3COO}$	1.0	mmol SO_4^{2-}/mmol CH_3COO^-	Stoichiometric equation (3)
$\alpha_{CH4/CH3COO}$	1.0	mmol CH_4/mmol CH_3COO^-	Stoichiometric equation (4)

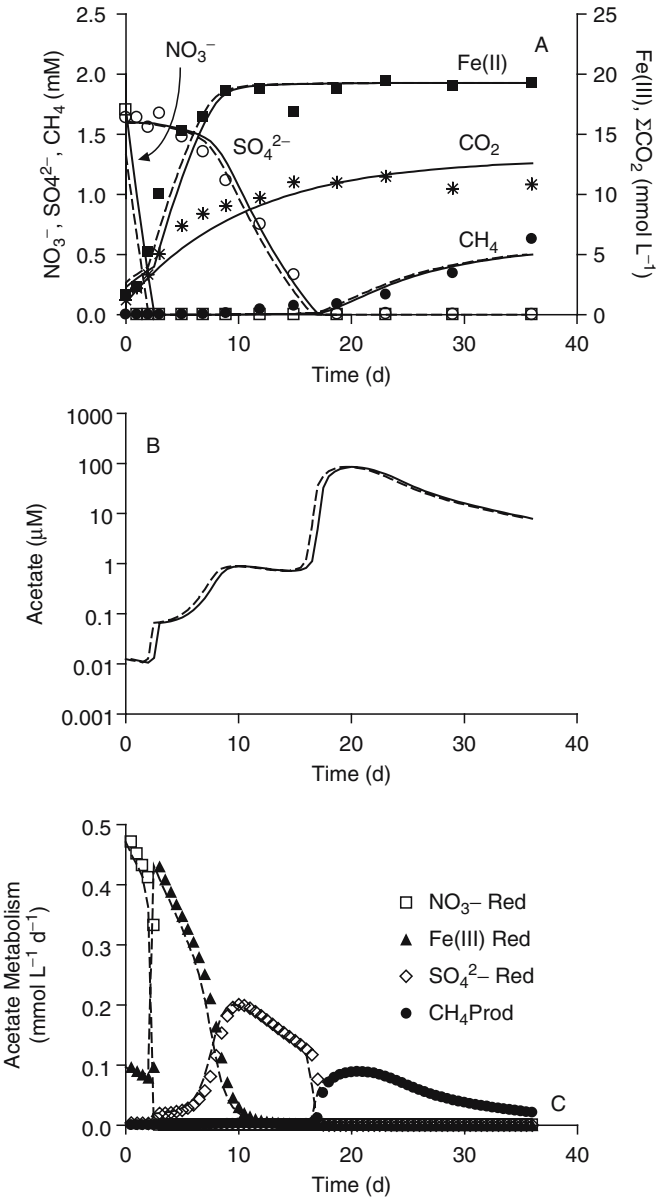

Fig. 8.7 Microbial population-based simulation of TEAPs in the same slurry of anoxic freshwater wetland sediment depicted in Fig. 8.6. See section 8.3.5 and Table 8.6 for model description. Solid and dashed lines show results of simulations with and without, respectively, a thermodynamic control term based on the free energy of acetate oxidation for each TEAP (see section 8.3.6). Symbols in panel C show results of simulation without thermodynamic control term; dashed lines show simulation with thermodynamic control term

situations where the same group of morgs can utilize more than one EA) will likely require the development of more complicated models that include inhibition effects (such as the repression of denitrification by O_2 (Tiedje, 1988), the inhibition of DIR by NO_3^- (Sorensen, 1982; Weber et al., 2006), and the inhibition of acetoclastic MG by Fe(III) (Bond and Lovley, 2002; vanBodegom et al., 2004)) the results of this simple simulation provide important insight into how microbial competition, as dictated by morg physiological parameters, can govern reaction dynamics in a biogeochemical system.

Predicted acetate concentrations displayed a step-wise increase (Fig. 8.7b) as the more favorable EAs were depleted (Fig. 8.7a) and different TEAP reactions became dominant (Fig. 8.7c). This pattern can be explained on the basis of the physiological properties of the different acetate-utilizing microbial groups. A key parameter governing the outcome of competitive interactions among different microbial populations is the ratio of the maximum rate of substrate uptake to the half-saturation constant for uptake ($R_{max,CH3COO}/K_{m,CH3COO}$ in the present context). This ratio is often referred to as the "clearance rate", since it has units of inverse time. Populations with higher clearance rates dominate substrate uptake under limiting substrate conditions (as in the case of the sediment slurry experiment), because they are able to maintain substrate concentrations at values much lower than the K_m values for less competitive populations. Clearance rates for the DNM, DIRM, SRM, and MGM groups in our model were 750,000, 121,000, 3300, and 314, respectively. The upshot of this wide range of clearance rates is that the mean acetate concentration during the initial nitrate-reducing phase of the simulation, ca. 0.015 μM, was 100–1000 times lower than the $K_{m,CH3COO}$ values for the DIRM, SRM, and MGM populations (Fig. 8.7b). Likewise, the mean acetate concentration during the Fe(III)-reducing phase of the simulation (ca. 0.06 μM) was 10–100 times lower than the $K_{m,CH3COO}$ for the SRMs and MGMs; and the mean acetate concentration during the sulfate-reducing phase (ca. 1.3 μM) was 10 times lower than the $K_{m,CH3COO}$ for the MGMs.

The importance of considering microbial population dynamics in kinetic analyses of geomicrobiological processes becomes even more apparent in situations where the reaction system approaches steady-state over long time periods. Although this did not occur in the slurry experiment discussed above, there are many examples of steady-state or near steady-state biogeochemical reaction systems in nature, notably aquatic sediments undergoing steady-state chemical diagenesis (VanCappellen and Gaillard, 1996), and ancient, deeply buried groundwater aquifers which display stable redox zonation over very long time scales (Chapelle and Lovley, 1992). Long-term microbial redox zonation translates into long-term patterns of geochemical flux that can have a profound impact on the mobility of trace and contaminant compounds in natural systems (see Davis et al. (2004) for an interesting discussion of this topic). Hence it is worthwhile to examine how microbial population dynamics can affect the steady-state configuration of a biogeochemical reaction system, once again using the sediment TEAP system as a means of illustration.

The basic mass balance equation for microbial biomass in the sediment TEAP system (Eqs. (8) to (11) in Table 8.6C) can be manipulated to show that, at steady-state (i.e., when the rates of change in biomass and other substrate

concentration are equal to zero), the dissolved acetate concentration is solely a function of the physiological parameters R_{max}, K_m, Y, and k_d (Lovley, 1988); see also Lovley and Chapelle (1998)):

$$[CH_3COO^-]_{ss} = \frac{K_{m,CH3COO,i} \times C}{1 - C} \tag{8.15}$$

where

$$C = \frac{k_{d,i}\,(K_{m,EA,i} + [EA_i])}{R_{max,CH3COO,i} \times Y_i \times [EA_i]}, \tag{8.16}$$

the subscript i denotes a given TEAP pathway. It is easy to show that the following condition must be met in order for the rate of change of biomass (BM) to be greater than zero at any given point in time:

$$Y_i R_{CH3COO,i} = k_{d,i}[BM_i] \tag{8.17}$$

The key insight here is that if the physiological properties of one group of morgs (as modified by the abundance of their EA) allows them to maintain the concentration of an energy substrate (e.g., acetate) at a value where the left hand side of Eq. (8.17) is less than the value of the right hand side for a second group of organisms (i.e., where $Y_2 R_{CH3COO,2} < k_{d,2}[BM_2]$, where the subscript 2 indicates the second group of organisms), then the population of the second group of organisms will undergo decline, whereas the biomass of first group of organisms will increase. The net effect of this interaction is that the physiologically more competitive groups will always dominate over less competitive groups – until, that is, their supply of EA acceptor becomes limiting, at which time the next most efficient group of organisms will become dominant. In situations where sufficient abundance of a given EA is maintained (e.g., through mass transport in sedimentary environments), all other less competitive groups will be completely excluded over long time scales.

To illustrate this concept, the microbial population-based TEAP model was modified to simulate situations in which either nitrate reduction, Fe(III) reduction, SR, or MG became the dominant TEAP at steady-state. This was easily achieved by keeping the concentrations of all EAs (as well as the labile POC) fixed over time, and running the model for a long enough period of time (e.g., 10 years) to achieve steady-state. With the nitrate concentration fixed at a constant value of 1 mM, the system became completely dominated by DNMs; with nitrate set to zero and Fe(III) fixed at 20 mmol L^{-1}, the system became dominated by DIRMs; with nitrate and Fe(III) set to zero and sulfate fixed at 2 mM, the system became dominated by SRMs; and finally with nitrate, Fe(III) and sulfate all set to zero the system was dominated by MGMs. The predicted acetate concentrations for the different TEAP conditions evolved to steady-state values that were very similar to the critical concentration at which $dB/dt \approx 0$, i.e., the $[CH_3COO^-]_{ss}$ concentrations dictated by Eqs. (8.15) and (8.16) for a given TEAP. The long-term presence of more thermodynamically efficient EAs led to steady-state acetate concentrations lower than the critical values for acetate metabolism by organisms using less favorable EAs, which

in turn led to extinction of these less competitive populations. This result illustrates the general principle that biological populations tend to draw the concentration of a limiting substrate down to the lowest possible level (as defined by their physiological capacities and other environmental tolerances) so as to maximize their ability to compete with other groups of organisms (Blackman, 1905).

8.3.6 Kinetic Versus Thermodynamic Control of Microbial Reaction Rates

An important consideration in interpreting the kinetics of microbially driven geochemical reactions is the relative influence of kinetic versus thermodynamic effects on the rate and extent of reaction. A key feature of the rate laws discussed above is that they represent irreversible reactions that ignore the potential impact of thermodynamic driving force on reaction rate. Many metabolic reactions proceed at conditions close to thermodynamic equilibrium (Crabtree and Nicholson, 1988). This phenomenon has important implications for understanding the rates and spatial-temporal distribution of geomicrobiological processes such as oxidation of natural and contaminant organics via different TEAP pathways (Curtis, 2003). The basic issue is whether irreversible kinetic models based on morg physiological properties can universally explain spatial-temporal patterns of microbial metabolism, or whether models that consider thermodynamic driving force are required.

In a lucid review of this question, Banwart and Thornton (2003) refer to the irreversible kinetic/physiological approach (i.e., the one employed above to simulate the results of the sediment slurry experiment) as the "competitive exclusion" (CE) approach, whereas approaches that include thermodynamic considerations are referred to as the "partial equilibrium" (PE) approach. The term PE was coined by Postma and Jakobsen (1996), based on the idea that the overall irreversible reaction between OM and EAs could be subdivided into two basic steps: (1) a slow, overall rate limiting hydrolysis/fermentation step (e.g., one that could be depicted as a zero or a first-order reaction), and (2) a fast, electron-accepting step that approaches thermodynamic equilibrium. In the PE approach, the concentration of an energy substrate (e.g., acetate or H_2) is used together with other geochemical information to calculate the available free energy (ΔG) for one or more TEAPs. If the ΔG for a given TEAP is more positive than the minimum amount of energy required for conservation of energy via ATP biosynthesis (on the order of $-20\,\mathrm{kJ/rxn}$; Schink (1997)), then this TEAP cannot proceed under ambient conditions. TEAPs for which the ΔG is sufficiently negative can potentially coexist, subject to constraints posed by competitive effects as described in the previous section. A major motivation for development of the PE approach was the apparent coexistence (in space and time) of TEAPs in both pristine (Jakobsen and Postma, 1999) and organic-contaminated (Jakobsen et al., 1998; Vroblesky et al., 1997) aquifer environments, which would not occur if competitive exclusion effects were strictly enforced.

The sediment slurry TEAP simulations discussed above can be used to gain insight into potential thermodynamic versus kinetic controls on microbial metabolism under idealized conditions. The acetate concentrations predicted in the steady-state microbial population-based simulations were used to estimate ΔG values for the four different TEAP reactions, using the same reactant and product concentrations employed to compute ΔG values for the purpose of estimating yield coefficients (see Table 8.6A). The results suggest that acetate scavenging by DNMs and DIRMs could in principle have led to conditions under which MG would not have been thermodynamically feasible, assuming a minimum energy requirement of $-20\,\mathrm{kJ/rxn}$. In all other cases, however, the computed ΔG values for competing TEAP reactions were more negative $-20\,\mathrm{kJ/rxn}$, even though competitive exclusion took place. This result suggests a simple explanation for the failure of the CE model to explain the distribution of TEAPs in certain shallow aquifer environments, namely that resident microbial populations may not have been able to achieve long-term steady-state conditions in the face of spatial-temporal heterogeneity in environmental conditions, most importantly the abundance of EDs and EAs.

Although the forgoing analysis suggests that competitive exclusion provides a robust explanation for segregation of microbial redox processes (at least under steady-state conditions), there are some situations in which consideration of thermodynamic driving force must be invoked to explain reaction dynamics. A clear example of this can be identified in the oxidation of H_2 via different groups of respiratory morgs. Laboratory experiments have shown that anaerobic morgs have a threshold level for H_2 scavenging that is related to the redox potential of the EA used (Cord-Ruwisch et al., 1988; Lovley, 1985). The threshold concentration represents the lowest dissolved H_2 concentration that can support H_2-driven respiration by a given group of organisms; as H_2 concentrations approach the threshold value, rates of H_2 uptake approach zero. As a result of this phenomenon, dissolved H_2 concentrations in sediments dominated by different TEAPs (Lovley and Goodwin, 1988) may reflect thermodynamic rather than competitive control of substrate metabolism (Ho and Cord-Ruwisch, 1996; Hoehler et al., 1998). Another well-known example of this phenomenon comes from anaerobic digestion of domestic and industrial organic waste, in which accumulation of end-products such as acetate and H_2 can limit the overall rate of OM digestion (Ho and Cord-Ruwisch, 1996). An analogous example in the context of microbial geochemistry can be identified in the influence of Fe(II) on enzymatic reductive dissolution of Fe(III) oxides. Although (as discussed in detail in Case Study #1) thermodynamic driving force does not appear to strongly influence initial rates of electron transfer from DIRM to Fe(III) oxide surfaces, it can clearly play an important role in governing the long-term extent of oxide reduction. Moreover, from the practical point of view of kinetic modeling, a thermodynamic "control switch" of some sort is required to simulate the observed cessation of oxide reduction activity after only partial reduction in closed reaction systems. To set the stage for this analysis, the basic framework for including thermodynamic control of microbial metabolic activity is presented below.

The basis of all kinetic rate versus thermodynamic driving force considerations is the idea that the reaction system is a reversible one (in contrast to the irreversible

rate laws discussed previously). This basic feature is common to all derivations of thermodynamic control terms, including ones based on transition state theory that are common in chemistry and earth science (Laidler, 1987; Lasaga, 1998), and ones based on the laws of mass action used in enzyme kinetics (Haldane, 1930; Roels, 1983). Jin and Bethke (2002) recently provided a mechanistic derivation to explain coupled kinetic and thermodynamic controls on electron transport during microbial respiration, as well as several applications of the resulting new rate law to microbial metabolism in geochemical systems (Jin and Bethke, 2003, 2005). The authors produced the following compact expression:

$$R = R_{max}\, F_D\, F_A\, F_T \tag{8.18}$$

where F_D and F_A are hyperbolic rate terms that account for the influence (kinetic) of electron donor and electron acceptor concentration on respiration rate, and F_T is a thermodynamic driving force term which takes the form

$$F_T = 1 - \exp\left(\frac{f}{\chi RT}\right) \tag{8.19}$$

in which f is the thermodynamic driving force, R is the ideal gas constant, T is temperature in degrees Kelvin, and χ is the average stoichiometric number, which corresponds to the number of times a rate-determining step occurs during an overall reaction. For respiratory reactions involving proton translocation across the cell membrane, the value of χ can be constrained by the number of protons translocated per rate-limiting electron transfer step. However, the general form of Eq. (8.19) can be applied to other processes in which there is no mechanistic basis for assigning a value to χ. In this case, and for our purposes below, χ can be arbitrarily assigned a value of 1.0. The usual way to express thermodynamic driving force is the ΔG value. In the case of biologically catalyzed reactions that involve energy conservation, a modification is required to take into account the minimum amount of free energy required to synthesize ATP. In some situations, the amount of energy required to transport a substrate across a biological membrane can also strongly influence the minimum free energy required for a microbial reaction to proceed (Jackson and McInerney, 2002). Liu et al. (2001a) assigned the term ΔG_{min} to this minimum energy requirement, and expressed f as

$$f = (\Delta G - \Delta G_{min}) \tag{8.20}$$

so that F_T becomes (assuming $\chi = 1$)

$$F_T = 1 - \exp\left(\frac{\Delta G - \Delta G_{min}}{RT}\right) \tag{8.21}$$

A value of ca. $-20\,\text{kJ mol}^{-1}$ is typically assumed to be the smallest quantum of metabolically convertible energy for prokaryotic cells, which corresponds to the energy required to synthesize one-third of a mol of ATP during transport of one ion (e.g., a proton) across the cytoplasmic membrane (Schink, 1997).

To illustrate the use of Eq. (8.21), the microbial population-based simulation of the sediment slurry experiment was re-run including a F_T term (along with the usual F_D and F_A Monod terms for acetate and the different external EAs, respectively) applied to each of the TEAP reactions with a common ΔG_{min} value of $-20\,kJ/mol$ acetate. The ΔG values for each TEAP were computed dynamically during the simulation using the predicted concentrations of reactants and products. The simulated reactant/product concentrations and metabolic rates (Fig. 8.7, dashed lines) were not much different from those produced by the model lacking the thermodynamic control term. This result reinforces the general conclusion that microbial competition is likely to play the dominant role in governing the distribution of TEAPs and associated geochemical processes in sedimentary environments.

8.4 Case Study #1 – Microbial Fe(III) Oxide Reduction

8.4.1 Introduction

Dissimilatory microbial reduction of Fe(III) oxides has broad range of influences on the aqueous/solid-phase geochemistry and behavior of natural and contaminant compounds in modern circumneutral, nonsulfidogenic subsurface sedimentary environments. In addition, there is compelling evidence for the role of DIRMs in the formation of mineral phases (e.g., magnetite and siderite) on the ancient Earth (Walker, 1984, 1987), as well as for their potential role in the early evolution of microbial respiration (Lovley, 2004; Vargas et al., 1998). It is therefore not surprising that Fe(III) oxide reduction and its associated geochemical effects has emerged as a major focal point for sediment biogeochemical research. There is ongoing interest in the factors controlling the rate and long-term extent (i.e., the kinetics) of enzymatic DIR. The rate and extent of DIR are governed by complex surface-chemical and physiological interactions which are still only partially understood. In this case study information on factors that govern the kinetics of DIR is presented and analyzed. Studies with natural wetland sediments as well as pure culture experiments with synthetic and natural Fe(III) oxides are discussed.

8.4.2 Mechanisms of Enzymatic Fe(III) Oxide Reduction

Enzymatic DIR involves transfer of electrons from organic substrates or H_2 to insoluble Fe(III) oxides through the enzymatic activity of DIRMs under anoxic conditions in soil and sedimentary environments. Although certain morgs can transfer small quantities of reducing equivalents to Fe(III) during fermentative growth, the vast majority of DIR activity in nature is linked to oxidation of organic carbon or H_2 coupled to respiration with Fe(III) (see Lovley (1987, 1991) for review). Certain

organics (reducing acids and thiols) can abiotically reduce Fe(III) oxides (Stone and Morgan, 1987), however abiotic reduction by such compounds is likely to be only a minor process compared to DIRM respiration (Lovley and Phillips, 1991). Moreover, a wide variety of organic carbon compounds can be readily oxidized in the presence of DIRM, but do not react spontaneously with Fe(III) oxides under abiotic conditions (Arnold et al., 1988; Lovley and Phillips, 1991; Munch and Ottow, 1980, 1983; Ottow, 1968, 1971; Ottow and Glathe, 1971). Likewise, the mere presence of a low system redox potential (e.g., as a result of microbial consumption of oxidants such as oxygen and nitrate, or production of fermentation intermediates) does not lead to spontaneous Fe(III) oxide reduction (Lovley and Phillips, 1991; Munch and Ottow, 1983). Thus classical models that treat Fe(III) oxide reduction as a freely reversible process dependent on system redox potential (Hem, 1972; Ponnamperuma, 1972; Starkey and Halvorson, 1927; Zehnder and Stumm, 1988), while providing a convenient framework for conceptualizing Fe geochemistry, do not accurately represent reality (Lovley, 1991). In fact, low redox potentials are the *result* of DIR rather than the cause of Fe(III) oxide reduction, since the redox potential of non-sulfidogenic environments is typically controlled by the Fe(II)-Fe(III) redox couple (Stumm and Morgan, 1996). Reaction with hydrogen sulfide produced by dissimilatory SRMs is the only significant abiotic pathway for abiotic Fe(III) oxide reduction in low-temperature sedimentary environments. This is a quantitatively significant process in shallow coastal marine sediments, and there is strong competition between enzymatic and abiotic Fe(III) reduction in such environments (Canfield and DesMarais, 1993; Canfield et al., 1993; Kostka et al., 1999, 2002; Thamdrup et al., 1994, 2000). In contrast, DIR is the dominant mechanism for Fe(III) reduction in low-S freshwater systems (Thamdrup, 2000)

There are three basic mechanisms whereby enzymatic DIR can take place (Nevin and Lovley, 2002), which are summarized in Fig. 8.8a: (1) direct electron transfer from the DIRM cell surface to the Fe(III) oxide surface; (2) dissolution of Fe(III) oxides by organic chelators followed by reduction of chelated Fe(III) at the surface of or within the DIRM; and (3) indirect electron transfer to the oxide surface via electron shuttling compounds (e.g., quinone-bearing humic substances), which are reduced at the surface of or within the DIRM cell and subsequently react with the oxide surface. The discussion and analysis below focuses implicitly on mechanism 1. While there are undoubtedly situations in nature where mechanisms 2 and 3 are operative (e.g., organic-rich sediments, and biofilm environments where chelators and/or electron shuttling compounds produced by DIRMs may accumulate and thereby promote oxide reduction (Hernandez and Newman, 2001; Hernandez et al., 2004; Lies et al., 2005; Nevin and Lovley, 2002), metal chelators and electron shuttling compounds are likely to be relatively scarce in most natural environments. As a result, direct electron transfer is likely to be the default means by which DIRMs "earn a living" in nature. The energetic cost of producing endogenous chelators or electron-shuttling compounds (as opposed to exogenous compounds already present in the environment) is undoubtedly very high, resulting in a relatively low growth yield per unit energy substrate metabolized for organisms that utilize such compounds to reduce Fe(III) oxides. Organisms that require such compounds

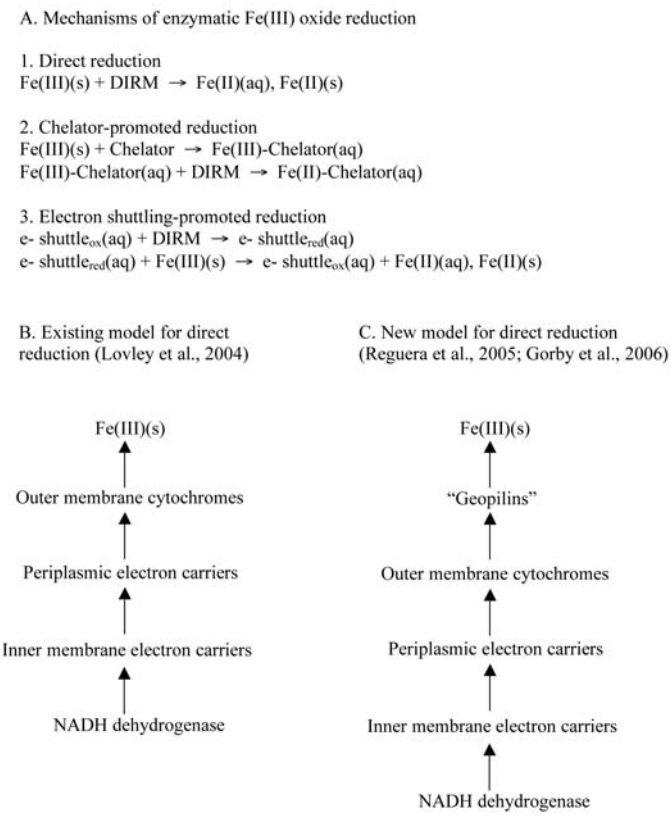

Fig. 8.8 Mechanisms and biochemical models of enzymatic DIR. See section 8.4.2 for details

would therefore not be expected to compete effectively with DIRMs that transfer electrons directly to Fe(III) oxide surfaces in situations where exogenous chelators or electron shuttles are scarce (Lovley et al., 2004).

Although the exact molecular mechanism(s) for direct electron transfer from DIRMs to Fe(III) oxides surfaces is not known, there has been rapid progress in the last few years in our understanding of how this process can take place. A system of inner membrane-, periplasmic-, and outer membrane-associated cytochromes and other electron carriers is known to participate in the transfer of electrons from the cytoplasm (e.g., from NADH) to the cell surface (DiChristina et al., 2005; Lovley, 2000a, 2002; Lovley et al., 2004; Richardson, 2000; Ruebush et al., 2006a, 2006b). Until recently, *c*-type cytochromes embedded in the outer face of the outer membrane were thought to be solely responsible for electron transfer to Fe(III) oxides in direct association with the DIRM cell surface (see Fig. 8.8b). However, two very recent studies have demonstrated that pili attached to the outer membrane of DIRMs such as *Geobacter sulfurreducens* (Reguera et al., 2005) and *Shewanella oneidensis* (Gorby et al., 2006), which were previously thought to be involved

in attachment to Fe(III) oxide surfaces (Childers et al., 2002), are electrically conductive. Pili are extracellular appendages that are present in a wide variety of morgs. It is possible that pili produced by DIRMs (referred to by Reguera et al. (2005) as "geopilins") serve as microbial "nanowires" (ca. 5 nm in diameter and up to 20 μm in length) that form the final electrical connection between the cell and the surface of the Fe(III) oxides (Fig. 8.8c). The pili are anchored in the periplasm and outer membrane of the DIRM cell, and may thus be able to accept electrons from the various electron carriers (e.g., *c*-type cytochromes) that are known (from biochemical and genetic studies) to be involved in Fe(III) oxide reduction, thereby completing the circuit between these electron carriers and the Fe(III) oxide. Such appendages extend the capacity for electron transfer well beyond the outer surface of the DIRM cell, which is likely to be important in natural soils and sediments where Fe(III) oxides typically exist as coatings on various mineral and organic phases. Current knowledge thus provides a plausible mechanism whereby direct electron transfer from DIRMs to Fe(III) oxides may take place.

8.4.3 Fe(III) Oxide Mineralogy and Microbial Reducibility

Prior to discussing the kinetics of enzymatic DIR, it is necessary to briefly consider the physical and thermodynamic properties of different Fe(III) oxides in soils and sediment, as these have a fundamental influence on the susceptibility of Fe(III) oxides to enzymatic reduction, and on the nature of the Fe(II)-bearing end-products of oxide reduction. Fe(III) oxides occur in nature as a spectrum of phases ranging from completely (or near completely) amorphous minerals such as ferrihydrite, to minerals such as goethite and hematite with well-defined crystal structures (Cornell and Schwertmann, 1996). For a particular Fe(III) oxide phase, a range of crystallinity can exist which is correlated with the particle size, SA, and solubility of the mineral. With regard to microbial Fe(III) oxide reduction it is possible to draw a fundamental distinction between amorphous (or poorly crystalline) and crystalline Fe(III) oxides. The pioneering studies of Lovley and colleagues (Lovley and Phillips, 1986a, 1987) showed that amorphous Fe(III) oxides, operationally defined by their solubility in 0.25 M NH_2OH-HCl/0.25 M HCl (Chao and Zhou, 1983) or dilute HCl (0.5 or 1.0 M) (Roden and Lovley, 1993; Wallmann et al., 1993), in both riverine and hydrocarbon-contaminated aquifer sediments were subject to essentially complete microbial reduction to a combination of dissolved and solid-phase Fe(II) compounds. In contrast, both synthetic and natural crystalline Fe(III) oxides, which are poorly dissolved in NH_2OH-HCl or dilute HCl, were found to undergo much lower degrees of reduction, and to be preserved in highly reducing (methanogenic) sediments (Lovley and Phillips, 1987; Phillips et al., 1993). Subsequent studies of microbial Fe(III) oxide reduction in a variety of surface and subsurface sediments have verified the potential for near complete reduction of amorphous Fe(III) oxides, and for the preservation of substantial quantities of crystalline Fe(III) oxides (Albrechtsen et al., 1995; Amirbahman et al.,

1998; Cozzarelli et al., 1999, 2000; Roden and Wetzel, 1996; Roden and Edmonds, 1997; Tuccillo et al., 1999; Wallmann et al., 1993).

Although phase transformations induced during enzymatic reduction may in some situations limit the long-term reducibility of amorphous Fe(III) oxides (see Hansel et al. (2003) for analysis and review), the results of studies to date lead collectively to the view that, because of their relatively high degree of reducibility, amorphous Fe(III) oxides are the dominant forms of solid-phase Fe(III) subject to microbial reduction in sedimentary environments (Lovley, 1991, 1993, 2000a). While this is very likely to be the case when substantial quantities of amorphous Fe(III) oxides are present, in sediments where crystalline Fe(III) oxides are more abundant than amorphous phases, crystalline Fe(III) bioreduction may contribute substantially to Fe(II) generation and attendant effects on aqueous/solid-phase geochemical conditions.

8.4.4 Kinetics of Amorphous Fe(III) Oxide Reduction in Sediments

Analysis of the kinetics of microbial Fe(III) reduction in sediments presents a unique problem relative to other TEAPs (e.g., oxygen, nitrate, and sulfate reduction), because the process involves the interaction of bacterial cell surfaces with particulate oxide phases which are not transported into the cell (Ghiorse, 1988; Lovley, 1987). For the sake of simplicity, the TEAP models developed in Sect. 8.3 treated Fe(III) oxide reduction kinetics using a Monod-style rate term (dependent on bulk Fe(III) oxide surface site concentration) analogous to that used for soluble TEAPs. However, there are two important reasons why such a rate formulation is not appropriate for describing Fe(III) oxide reduction kinetics: (1) the Monod equation was designed to depict saturation of intracellular reaction rates (or substrate uptake) with respect to a *soluble* substrate; and (2) empirical evidence suggests a robust first-order linear relationship between reduction rate and Fe(III) oxide concentration.

8.4.4.1 Empirical Evidence for First-Order Rate Law

Roden and Wetzel (2002) reported on the kinetics of amorphous Fe(III) oxide (abbreviated hereafter as AIO) reduction in sediments from a freshwater wetland in northcentral Alabama, USA. Concentrations of AIO decreased exponentially over time to a nonzero asymptote during anaerobic incubation of oxidized sediment slurries (Fig. 8.9a) and homogenized surface sediments (Fig. 8.9b). Similar patterns of AIO depletion were observed during anaerobic incubation of slurries containing different proportions of oxidized and reduced sediment and homogenized sediments from various depth intervals in the upper 3 cm of wetland sediment cores. The Fe(III) versus time data from these experiments were normalized to the initial AIO concentration $(\mathrm{Fe(III)}_0)$ in order to permit nonlinear regression analysis of pooled

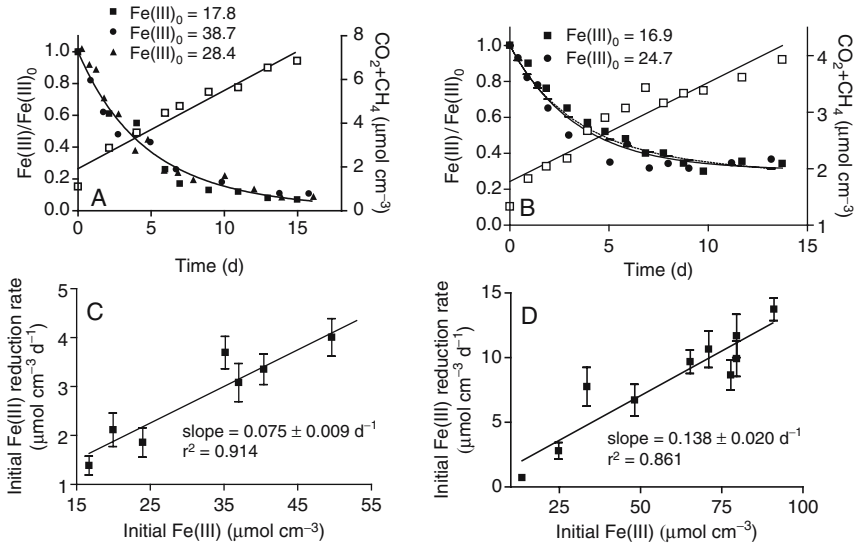

Fig. 8.9 Panels A and B: Fe(III) reduction during anaerobic incubation of (A) oxidized wetland sediment slurries and (B) wetland surface sediments. Symbol legends indicate initial Fe(III) oxide concentrations in μmol cm^{-3}. Solid lines are nonlinear least-squares regression fits of pooled data to Eq. (8.22). Open symbols show ΣCO_2+CH_4 production during anaerobic incubation; the lines are a linear least-squares regression fits. Panels C and D: Initial Fe(III) reduction rate vs. initial Fe(III) oxide concentration in slurries (C) and surface sediments (D) containing different initial amounts of AIO. Initial rates were computed from the first derivative of the nonlinear regression fits to Eq. (8.22), evaluated at t = 0. The different symbols show averages of triplicate bottles for two separate experiments. Error bars were computed from the standard error of the k_{red} and ($Fe(III)_0$ − $Fe(III)_{nr}$) regression parameters via error propagation (Bevington and Robinson, 1992). The line is a linear least-squares regression fit; the error term for the slope is the standard error of the regression parameter. All data are from Roden and Wetzel (2002), used with permission

data from experiments with different starting Fe(III) concentrations. The data were fit by nonlinear least-squares regression analysis to the following equation:

$$\frac{Fe(III)_{(t)}}{Fe(III)_0} = \frac{(Fe(III)_0 - Fe(III)_{nr})}{Fe(III)_0} \exp(-k_{red}t) + \frac{Fe(III)_{nr}}{Fe(III)_0} \qquad (8.22)$$

where $Fe(III)_{(t)}$ is the AIO concentration at time t, $Fe(III)_0$ is the initial AIO concentration, $Fe(III)_{nr}$ is the nonreactive AIO concentration, and k_{red} is a first-order rate constant. The nonreactive (i.e., nonmicrobially reducible) Fe(III) oxide probably represents moderately crystalline Fe(III) oxides (e.g., nanocrystalline goethite; Vanderzee et al. (2003)) which were subject to dissolution by 0.5 M HCl but not readily susceptible to microbial reduction on the time scale of our experiments. Equation (8.22) is an integrated form of the first-order rate expression

$$\frac{dFe(III)_{(t)}}{dt} = -k_{red}\left(Fe(III)_{(t)} - Fe(III)_{nr}\right) = -k_{red}Fe(III)_{reac} \qquad (8.23)$$

which is analogous to the equation used by Westrich and Berner (1984) for kinetic analysis of POC decomposition. The close adherence of the AIO reduction time course data to Eq. (8.22) provides explicit evidence that rates of microbial AIO reduction in the wetland sediment are first-order with respect to AIO concentration.

Further support for a first-order relationship between AIO reduction rate and concentration comes from experiments which demonstrated that initial rates of AIO reduction (computed from the first derivative of nonlinear regression fits of Fe(III) versus time data to Eq. (8.22), evaluated $t = 0$) were directly (linearly) correlated with starting AIO concentrations in sediment slurries (Fig. 8.9c) and surface sediments (Fig. 8.9d). Studies in marine sediments have also demonstrated direct correlations between Fe(II) production rate and AIO abundance (Hines et al., 1997; Thamdrup, 2000).

8.4.4.2 Theoretical Basis for First-Order Rate Model

None of the Fe(III) reduction rate versus concentration data discussed above provided obvious evidence of saturation behavior at high AIO abundance. Although rates of Fe(III) reduction at the highest AIO concentrations were often not statistically different from one another, the general trend of the rate versus concentration data was clearly linear rather than hyperbolic. The observed first-order kinetics of AIO reduction can be rationalized in terms of the principles of chemical (abiotic) mineral transformation discussed in Chap. 5. Chemical dissolution of metal oxide and silicate minerals is commonly described by the following generalized rate law (Hering and Stumm, 1990; Stumm and Sulzberger, 1992):

$$R_{surf}(t) = -k \times C_{surf}(t) \tag{8.24}$$

where $R_{surf}(t)$ is the SA-normalized dissolution rate (e.g., in $\mu mol\ m^{-2}\ d^{-1}$) at time t, k is a rate constant (d^{-1}), and $C_{surf}(t)$ is the concentration of surface species $(\mu mol\ m^{-2})$ involved in the dissolution reaction present at time t. Here surface species refers to an oxide surface site coordinated with H^+, OH^-, or organic ligands which polarize, weaken, and ultimately break the metal-oxygen bonds in the lattice of the oxide surface (Stumm and Sulzberger, 1992). This formulation assumes that reactions at the Fe(III) oxide surface are surface-controlled, i.e., that reactions at the surface are slow in comparison with other reaction steps, such as association of the ligand with the mineral surface to produce a surface species (Stumm and Morgan, 1996). A well-known example of abiotic mineral dissolution is the reductive dissolution of crystalline hematite $(\alpha\text{-}Fe_2O_3)$ by ascorbic acid (Sulzberger et al., 1989; Suter et al., 1991). The R_{surf} for this reaction is dependent on the concentration of ascorbate adsorbed to the oxide surface, which in turn is related to the concentration of ascorbic acid in solution according a Langmuir adsorption isotherm (Hering and Stumm, 1990).

A conceptual analogy can be drawn between abiotic Fe(III) oxide reductive dissolution by surface bound chemical reductants and enzymatic AIO reduction by DIRM. Because Fe(III) oxides are not taken up into the cell, microbial Fe(III)

oxide reduction is a surface-controlled reaction between DIRM cells and particulate Fe(III) oxides. As such, SA-specific rates of Fe(III) oxide reduction must be controlled by the abundance of cellular Fe(III) reduction moieties in contact with oxide surface sites. In other words, the abundance of active cellular reduction moieties will determine the rate constant for SA-specific enzymatic Fe(III) oxide reduction. The magnitude of this rate constant will be a complex function of the rate at which electron donors for Fe(III) oxide reduction are liberated through particulate OM hydrolysis and fermentation, the abundance of DIRM cells, and the relative susceptibility of oxide surface sites to reduction. The abundance of DIRM, in turn, will be dynamically controlled by the rate of electron donor supply, the abundance of reducible Fe(III) oxide surface sites, and the growth and death rates of the DIRM cells.

Given some specified rate constant for electron transfer to particulate Fe(III) oxide surfaces, the relationship between SA-specific and bulk volumetric mineral transformation rate can be defined as follows:

$$R_{bulk}(t) = R_{surf}(t) \times \psi_s(t) \times SA(t) = -k \times C_{surf}(t) \times \psi_s(t) \times SA(t) \tag{8.25}$$

where $R_{bulk}(t)$ is the bulk volumetric reaction rate $(\mu mol\ cm^{-3}\ d^{-1})$ at time t, $\psi_s(t)$ is the concentration of solids per unit volume $(g\ cm^{-3})$ at time t, and SA(t) is the specific SA of the mineral $(m^2\ g^{-1})$ at time t. The bulk molar concentration of mineral is defined by

$$C_{bulk}(t) = \psi_s(t)/MW \tag{8.26}$$

where MW is the molecular weight of the mineral $(g\ \mu mol^{-1})$. Substituting this expression into Eq. (8.25) yields the following expression for volumetric mineral reaction rate:

$$R_{bulk}(t) = dC_{bulk}(t)/dt = -kC_{surf}(t) \times SA(t) \times MW \times C_{bulk}(t) \tag{8.27}$$

The term $kC_{surf}(t) \times SA(t) \times MW$ in Eq. (8.27) can be identified as an effective rate constant, $k'(t)$:

$$k'(t) = kC_{surf}(t) \times SA(t) \times MW \tag{8.28}$$

If we assume that $C_{surf}(t)$ and SA(t) remain constant over time, i.e., that reactive surface sites are efficiently regenerated and that mineral morphology and surface site density remain constant during reaction, Eq. (8.27) reduces to a simple first-order rate expression:

$$R_{bulk} = dC_{bulk}/dt = -k'C_{bulk} \tag{8.29}$$

which when integrated yields an exponential decay equation which is identical in form to the first-order rate law for microbial Fe(III) oxide reduction depicted by Eq. (8.22):

$$C_{bulk}(t) = C_{0,bulk} \exp(-k't) \tag{8.30}$$

Equations (8.25)–(8.30) show that bulk-phase concentrations of an oxide mineral can decrease exponentially over time as a result of enzymatic (or abiotic) reduction, while surface-controlled reactions at the mineral-water interface are in steady-state with respect to SA-specific reaction rate. Because rates of electron donor supply through organic carbon mineralization, as indicated by $\Sigma CO_2 + CH_4$ production, were essentially constant during Fe(III) oxide reduction in our experiments (Fig. 8.9a,b, open symbols), effective rate constants for SA-specific enzymatic reduction were apparently approximately constant over time. Hence, a direct analogy can be drawn between the exponential decline in bulk AIO concentration observed in the microbial reduction experiments and the evolution of bulk-phase mineral concentration predicted by Eq. (8.30).

8.4.4.3 Influence of Labile OM Abundance on Fe(III) Reduction Kinetics

Thamdrup (2000) emphasized that the abundance and decomposition rate of labile OM is expected to exert a major influence on the kinetics of AIO reduction in sediments. Roden and Wetzel (2002) explicitly evaluated the relationship between labile OC and Fe(III) oxide reduction kinetics by adding different amounts of heat-killed Baker's yeast to AIO rich wetland sediment slurries, and monitoring rates of OC mineralization and Fe(III) consumption over time (see Fig. 8.10). The results demonstrated a direct correlation between the Fe(III) reduction rate constant, as well as the initial Fe(III) reduction rate, and the abundance (Fig. 8.10c) and mineralization rate (Fig. 8.10d) of labile OC, i.e., rates of AIO reduction were directly controlled by bulk OC abundance and decomposition rate. These findings are analogous to the demonstration by Westrich and Berner (1984) of a linear correlation between SR rate and reactive OC concentration in marine sediments (Fig. 8.4b).

It is possible to interpret the results of the OM addition experiment in relation to the SA-controlled framework for microbial Fe(III) oxide reduction discussed above. The correlation between k_{red} and OC mineralization can be attributed to a progressive increase in the SA-specific rate constant for AIO reduction (k in Eq. (8.24)) with increasing OC mineralization rate. These SA-specific rate constants translate into increased effective rate constants for bulk Fe(III) depletion according to Eq. (8.28), which are equivalent to the k_{red} parameters obtained from curve-fits of the Fe(III) time course data.

8.4.4.4 Relationship Between DIRM Abundance and Fe(III) Reduction Kinetics

The assumption of a time-invariant SA-specific Fe(III) oxide reduction rate constant (k value) ignores the potential influence of changes in DIRM population density on rates of enzymatic electron transfer. This is tantamount to assuming that DIRM populations respond instantaneously to changes in the rate of electron donor supply, i.e., as dictated by rates of OC hydrolysis and fermentation. This assumption

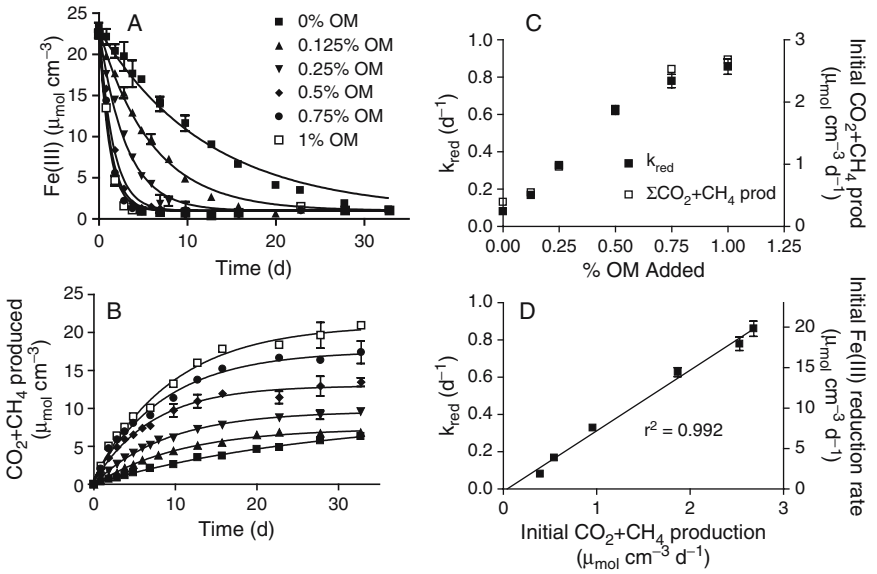

Fig. 8.10 Panels A and B: Fe(III) reduction (A) and organic carbon mineralization (B) during anaerobic incubation of oxidized wetland sediment slurries amended with different amounts (in % dry weight) of labile OM. Solid lines in panel A are nonlinear least-squares regression fits of pooled data to Eq. (8.22). Solid lines in panel B show nonlinear least-squares regression fits of the data to an equation of the form $C(t) = C_{max}[1 - \exp(-at)]$, where C(t) represents the amount of ΣCO_2+CH_4 produced at time t, C_{max} represents the maximum (asymptotic) amount of ΣCO_2+CH_4 produced during the incubation period, and *a* represents a first-order rate constant. Panels C and D: First-order Fe(III) reduction rate constants (k_{red}) and initial ΣCO_2+CH_4 production rates for oxidized wetland sediment slurries amended with different amounts of labile OM, and Fe(III) reduction rate constants and initial Fe(III) reduction rates versus initial ΣCO_2+CH_4 production. All data are from Roden and Wetzel (2002), used with permission

is probably defensible for modeling long-term Fe(III) oxide reduction kinetics in sediments (Roden and Wetzel, 2002). However, as discussed in Sect. 8.3.5, proper mechanistic models of competitive interactions among different TEAPs should include the biomass of different functional respiratory populations. This points out the need for a framework for depicting biomass-dependent Fe(III) oxide reduction kinetics.

DIRM pure culture experiments with synthetic Fe(III) oxides have shown that rates of Fe(III) oxide reduction are a hyperbolic function of DIRM cell density (Roden and Zachara, 1996; Roden, 2003a, 2006) (see following section). This relationship is analogous to that between mineral dissolution and ligand concentration in abiotic systems (Hering and Stumm, 1990), which makes sense given that redox-active components on DIRM cell surfaces can be viewed as the "ligands" responsible for enzymatic Fe(III) oxide reduction. Controlled experiments with Fe(III) oxide-rich wetland sediment clearly demonstrate this analogy (Fig. 8.11a,b). The results can be used to assemble a kinetic expression for biomass- and SA-dependent Fe(III) oxide reduction in the wetland sediment. To facilitate this, the biological reduction data in Fig. 8.11b were re-expressed in terms of a SA-specific rate

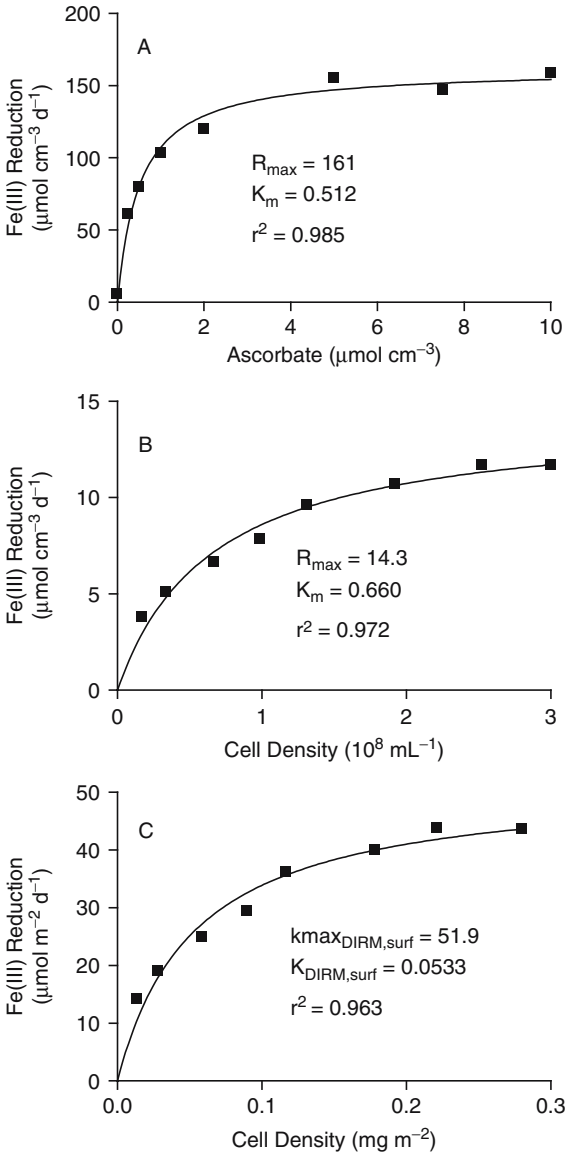

Fig. 8.11 Rates of abiotic (A) and biotic (B) wetland sediment AIO reduction as a function of ligand (ascorbate or DIRM) concentration (E. Roden, unpublished). The abiotic reduction experiments were conducted with a suspension of ca. 1 mmol Fe(III) L^{-1} in 10 mM ascorbate at pH 2. The biotic reduction experiments were conducted with a suspension of ca. 5 mmol Fe(III) L^{-1} in 30 mM $NaHCO_3$ at pH 6.8, inoculated with different quantities of washed acetate/Fe(III) citrate-grown *G. metallireducens* cells. An average cell mass of 4×10^{-10} mg cell^{-1} (E. Roden, unpublished) was used to convert cell numbers to dry weight cell density. The solid lines show nonlinear least-squares regression fits of the data to the equation for a rectangular hyperbola (see Eq. (8.7)). SA-normalized rates and cell densities shown in panel C were computed using an assumed AIO SA of 600 m^2 g^{-1} (see section 8.4.4.4 for details)

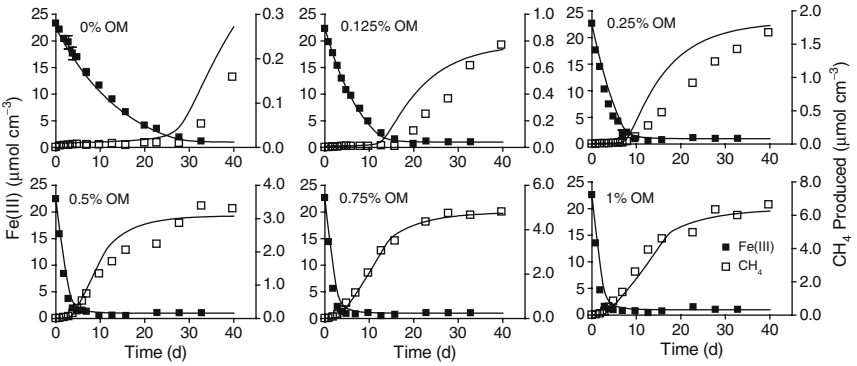

Fig. 8.12 Simulation of Fe(III) oxide reduction and methanogenesis in wetland sediment slurries amended with different amounts (0-1% dry weight) of labile OM (data from the same experiments shown Fig. 8.11). The model was based on competition for acetate as in the simulations shown in Fig. 8.7, but employed a SA-dependent rate law for DIRM metabolism (Eqs. (8.31–8.32)) rather than the standard Monod equation used in other simulations. See section 8.4.4.4 for details

constant versus SA-normalized DIRM cell density (Fig. 8.11c). This relationship leads to the following expression for the biomass-dependent reduction rate constant $k_{DIRM,surf}$

$$k_{DIRM,surf} = k\,max_{DIRM,surf}\frac{[DIRM]_{surf}}{K_{DIRM,surf} + [DIRM]_{surf}} \tag{8.31}$$

where $kmax_{DIRM,surf}$ and $k_{DIRM,surf}$ have units of $\mu mol\ m^{-2}\,d^{-1}$, and $[DIRM]_{surf}$ and $K_{DIRM,surf}$ have units of mg cells m^{-2}. The bulk rate of Fe(III) oxide reduction is then computed from the expression

$$R_{Fe(III),bulk}(t) = k_{DIRM,surf} \times \psi_s(t) \times SA(t) \tag{8.32}$$

where $\psi_s(t)$ and SA(t) are defined in Eq. (8.25).

A standard (and time-invariant) SA value of $600\,m^2\,g^{-1}$ for AIO (Dzombak and Morel, 1990) was used to compute the values for $kmax_{DIRM,surf}$ and $K_{DIRM,surf}$ shown in Fig. 8.11c from the bulk reaction rate and cell density data in Fig. 8.11b. Equations (8.31) and (8.32), together with an expression such as

$$d[DIRM]/dt = YR_{Fe(III),bulk} - k_d[DIRM] \tag{8.33}$$

for DIRM growth (where Y is the yield coefficient and k_d the cell decay coefficient), provide a means for computing rates Fe(III) oxide in a manner consistent with the known relationship between DIRM cell density and oxide reduction kinetics. Figure 8.12 illustrates the application of this approach to simulation of the Fe(III) reduction and CH_4 production data from the OM addition experiment shown in Fig. 8.10. DIRMs and MGMs were assumed to compete for acetate as the primary energy source for respiration as in previous simulations (Fig. 8.7). The rate of acetate production from POM hydrolysis and fermentation was computed from

curve-fits to the $\Sigma CO_2 + CH_4$ production data shown in Fig. 8.10b. The rate law for Fe(III) oxide reduction (Eq. (8.32)) was modified to account for dependence on acetate concentration using a standard Monod function and the same K_m value ($1\,\mu M$) used in previous simulations. The rate equations for MGM metabolism and growth were the same as in previous simulations. Assuming an initial DIRM and MGM cell density of $0.02\,mg\,cm^{-3}$, the model generally reproduced the timing and magnitude of the switch between Fe(III) reduction and methanogenesis in the sediment slurries (Fig. 8.12). Inclusion of a thermodynamic control term (Eq. (8.21)) had little influence on the predicted pattern of TEAPs. Although other rate formulations (e.g., biomass-independent Modified Monod and mixed first-order/Monod models, and a standard biomass-dependent Monod model) were also able to reproduce the experimental results with comparable accuracy, the biomass- and SA-dependent rate law summarized in Eq. (8.32) is mechanistically the most realistic way to describe the reaction system.

A final word regarding actual determination of DIRM cell densities in natural sediments: Roden and Wetzel (2002) employed a most probable number (MPN) enumeration procedure (with synthetic growth medium) to estimate changes in DIRM population size in response to addition of different amounts of labile OM. The results indicated that although DIRM abundance increased ca. 10-fold in OM-amended sediments compared to unamended slurries, there was no correlation between DIRM abundance and OM addition above 0.25% OM. This is perhaps not surprising in light of the relatively small changes in DIRM biomass (< 2.5-fold) predicted in the biomass-dependent model simulations. It is well known that MPN procedures employing synthetic growth media typically underestimate the abundance of anaerobic respiratory morgs such as SRMs by one or more orders of magnitude in both marine (Gibson et al., 1987; Jorgensen, 1978; Ramsing et al., 1996; Vester and Invorsen, 1998) and freshwater (Bak and Pfenning, 1991) environments, which complicates quantitative analysis of DIRM abundance under changing biogeochemical conditions. Thus, it is not possible to accurately verify the changes in DIRM abundance predicted in the biomass-dependent model simulations. Refinement of MPN procedures for enumeration of DIRM (e.g., through use of natural media (Vester and Invorsen, 1998) and/or application of molecular genetic techniques for nonculture-based estimation of DIRM abundance (e.g., MPN-PCR (Anderson et al., 1998; Rooney-Varga et al., 1999; Snoeyenbos-West et al., 2000), or real-time PCR (Stults et al., 2001)) will be required definitively to link variations in DIRM biomass to the kinetics of Fe(III) oxide reduction in sediments.

8.4.5 Pure Culture Studies of Fe(III) Oxide Reduction Kinetics

Although AIO is the most bioavailable and in many cases the dominant form of Fe(III) oxide reduced in sedimentary environments (Lovley, 2000a), in many situations crystalline Fe(III) oxides (CIOs) may be much more abundant than AIO (Roden and Urrutia, 2002). Because of their relatively high abundance, enzymatic

reduction of CIOs may contribute significantly to the long-term potential for Fe(II) generation and associated impacts on the aqueous/solid-phase geochemistry of subsurface environments, even if only a minor fraction of the crystalline Fe(III) oxide content is subject to microbial reduction. In addition, slow reduction of crystalline Fe(III) could play a major role in altering Fe geochemistry over geological time scales in nonsulfidogenic subsurface environments (Lovley et al., 1990; Lovley, 1992).

The studies discussed in this section explored how the surface chemical (e.g., specific SA) and thermodynamic properties (e.g., oxide reduction potential) of various Fe(III) oxides influence the rate and extent of microbial versus chemical Fe(III) oxide reduction. The results lead to a general quantitative model of enzymatic Fe(III) oxide reduction at circumneutral pH that can be compared and contrasted with models of abiotic mineral dissolution and enzymatic reduction of soluble metals and other aqueous EAs.

8.4.5.1 Initial Rates of Enzymatic Versus Abiotic Reduction

Initial rates of enzymatic Fe(III) oxide reduction were examined for a wide range of synthetic oxide phases using *S. putrefaciens* and *G. sulfurreducens* as model DIRMs (Roden, 2003a, 2006). Transmission electron microscope images of four representative oxide phases in the presence of a related DIRM (*Shewanella algae*) are shown in Fig. 8.13. The results showed that initial bulk rates of microbial Fe(III) oxide reduction were directly controlled by oxide SA (Fig. 8.14a). However, initial SA-normalized reduction rates (Fig. 8.14b) were independent of oxide SA, as well as oxide reduction potential (E_h^0, as inferred from long-term abiotic reduction experiments; see Fig. 8.14 legend). These results contrast with SA-normalized rates of abiotic Fe(III) oxide reduction by ascorbate and AH_2DS, which were significantly correlated with oxide SA and E_h^0 (Fig. 8.14c).

More than 65% of total dilute (0.5 M) HCl-soluble Fe(II) produced in the biological reduction experiments accumulated as $Fe^{2+}_{(aq)}$. Hence, enzymatic Fe(III) oxide reduction was mainly a reductive dissolution process in these experiments, e.g., as opposed to the Fe(II) mineralization processes that typically dominate AIO reduction systems (Zachara et al., 2002). If Fe(II) detachment from the oxide surface during enzymatic reduction was affected by the thermodynamic properties of the oxide and thus controlled the bulk reduction rate, we would have expected to see a significant correlation between initial surface-area normalized reductive dissolution rate and oxide E_h^0 – as was clearly the case for reductive dissolution by ascorbate and AH_2DS. Since this was not the observed, we conclude that the mechanism and/or the rate-limiting step during enzymatic Fe(III) oxide reduction is fundamentally different than that for abiotic reductive dissolution. The simplest explanation is that the rate of electron transfer, rather than Fe(II) detachment, is the rate limiting step during enzymatic reduction, and that rates of enzymatic electron transfer are not strongly affected by oxide thermodynamic properties. **This phenomenon**

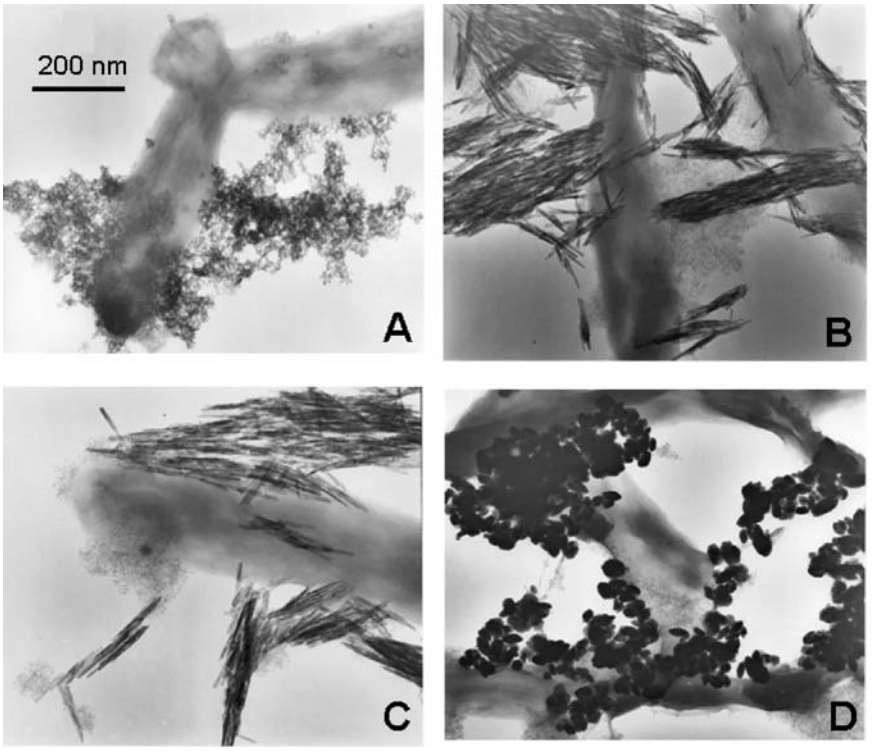

Fig. 8.13 Transmission electron microscope images of synthetic Fe(III) oxide phases in the presence of *S. algae* cells (M. Urrutia, unpublished). A: Hydrous ferric oxide (SA = 600 $m^2\ g^{-1}$); B: Goethite (SA = 96 $m^2\ g^{-1}$); C: Goethite (SA = 55 $m^2\ g^{-1}$); D: Hematite (SA = 18 $m^2\ g^{-1}$)

provides a clear example of a fundamental difference in the kinetic controls on an enzymatic versus an abiotic mineral-water reaction.

Ongoing studies with well-characterized DIRMs such as *Shewanella* and *Geobacter* have provided evidence that low redox potential, outer membrane-associated *c*-type cytochromes and/or electrically conductive pili are involved in electron transfer from DIRMs to Fe(III) oxides (see Sect. 8.4.2). In addition, a atomic force microscopy study by Lower et al. (2001) demonstrated apparent molecular "recognition" of Fe(III) oxide surface sites by a putative ca. 150 kDa outer membrane protein of the dissimilatory DIRM *Shewanella oneidensis* (formerly *S. putrefaciens* strain MR-1), a close relative of the organism used in this study. Together these findings suggest the possibility that the similarity of SA normalized electron transfer rates across a broad range of oxide minerals results from the fact that DIRMs "recognize" different Fe(III) oxide surfaces more-or-less equally, independent of the underlying crystal structure, such that initial rates of electron transfer subsequent to recognition are not strongly dependent on crystal structure. This suggestion is consistent with an argument presented by Fischer (Fischer, 1988) to account for the relatively minor influence of oxide solubility on rates of synthetic

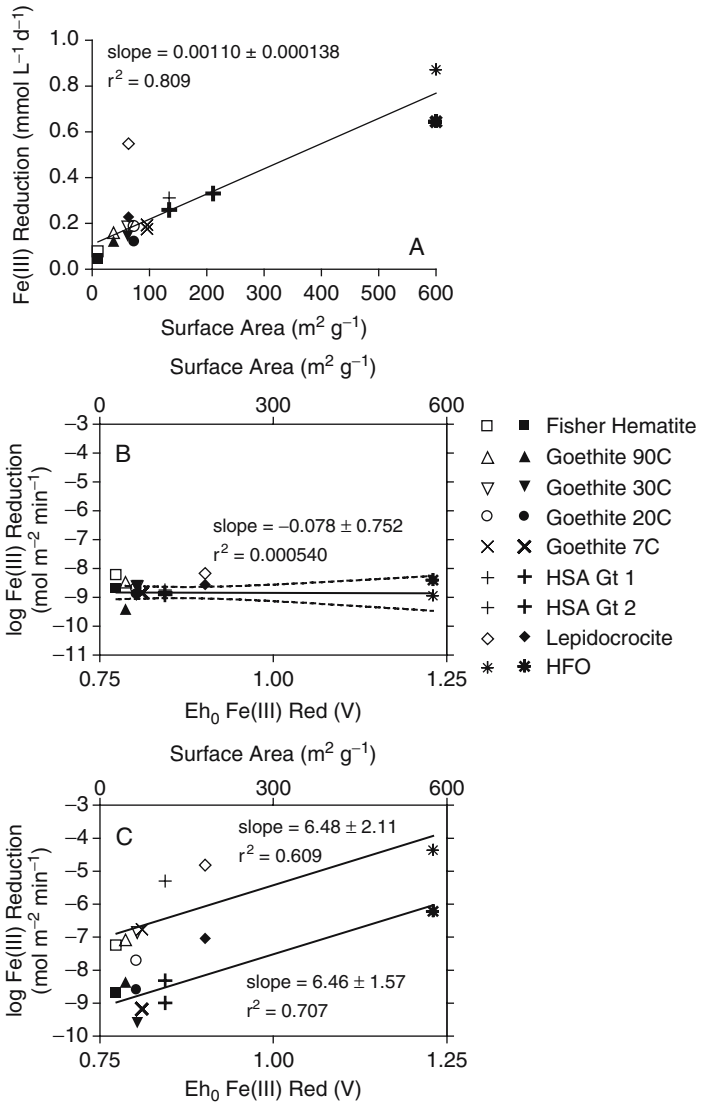

Fig. 8.14 Initial (2–3 day incubation) rates of bacterial (A,B) and abiotic (C) reduction of synthetic Fe(III) oxides as a function of oxide surface area and standard reduction potential (E_h^0). E_h^0 values for the different oxides were estimated from the final (after reduction ceased) dissolved Fe(II) concentration and pH values achieved in the AH_2DS reduction experiments, together with the E_h^0 of the AQDS/AH_2DS couple (+0.23V; (Clark, 1960)). Different symbols correspond to different Fe(III) oxide phases as indicated in the legend. Filled and thick-lined symbols refer to biological reduction by *S. putrefaciens* or abiotic reduction by ascorbate; open and thin-lined symbols refer to biological reduction by *G. sulfurreducens* or abiotic reduction by AH_2DS. Starting Fe(III) concentrations in the biotic and abiotic reduction experiments were 10 mmol L^{-1} and 5 mmol L^{-1}, respectively. *S. putrefaciens* and ascorbate reduction data are reproduced with permission from Roden (2003). *G. sulfurreducens* data are reproduced with permission from Roden (2006)

Fe(III) oxide reduction by *Corynebacteria* at pH 7. Fischer reasoned that if the redox potential of the microbial cells (i.e., their outer membrane redox-active components) is sufficiently negative for reduction of well-crystallized oxide phases like hematite or goethite, each contact (or "recognition") of a redox-active DIRM cell surface component with an oxide particle will trigger reduction of a Fe(III) surface site. Therefore the amount of Fe(II) produced during each contact event will not increase markedly with increasing oxide solubility. This conclusion is supported by the results of a literature survey of enzymatic versus abiotic (ascorbate-catalyzed) SA-specific rates of synthetic Fe(III) oxide reduction (Roden, 2003a). The survey revealed that initial ascorbate catalyzed reduction rates vary by more than three orders of magnitude, with rates for highly ordered minerals such as goethite and hematite being far lower than those for ferrihydrite and lepidocrocite. In contrast, initial microbial reduction rates are much more uniform, with rates for 2-line ferrihydrite actually being the lowest due to the effect of particle aggregation during dehydration. No statistically significant difference was detected between SA normalized initial enzymatic rates of AIO, goethite, hematite, and lepidocrocite reduction.

8.4.5.2 Influence of DIRM Cell Density and Association with Oxide Particles on Reduction Kinetics

As described above for wetland sediment AIO reduction (Fig. 8.11b,c), SA-normalized rates of enzymatic oxide reduction are directly influenced by the density of DIRM cells, and by inference the abundance of their redox active surface components. This phenomenon can be traced to the requirement for contact between DIRM and Fe(III) oxide surfaces in order for electron transfer to take place in the absence of soluble chelators or electron-shuttling compounds (see Sect. 8.4.2). It is relevant to note here that Fe(III) oxide particles are generally much smaller than the DIRM cells. Hence, "contact" between DIRMs and oxide surfaces corresponds to binding of Fe(III) oxides by DIRM cells (discussed in detail in Glasauer et al. (2001)). Figure 8.15 summarizes the results of DIRM cell loading experiments conducted with *S. putrefaciens* or *G. sulfurreducens* and a variety of synthetic Fe(III) oxide phases with excess H_2 as an energy source. Although the data show considerable scatter, they suggest a maximum SA-specific reduction rate on the order of 6 μmol $m^{-2}\,d^{-1}$, and a half-saturating SA-normalized cell density of ca. 1 mg cells m^{-2} (Fig. 8.15a). Initial rates of oxide reduction correlated directly with the abundance of DIRMs associated with Fe(III) oxide surfaces (Fig. 8.15b), which in turn could be related to free (non-oxide-associated) cell density according to a Langmuir isotherm (Fig. 8.15c). Previous work by Das and Caccavo (2000, 2001), as well as a recent study by Bonneville et al. (2006), revealed qualitatively similar results for the association of Fe(III) oxides with DIRM cell surfaces, and the relationship between oxide-adhered DIRM cell density and Fe(III) reduction rate. The association of DIRMs with Fe(III) oxides is probably driven by hydrophobic rather than electrostatic forces, since both DIRM cells and Fe(III) oxides bear a net negative charge at pH (Caccavo et al., 1997; Das and Caccavo, 2000, 2001). Cell surface

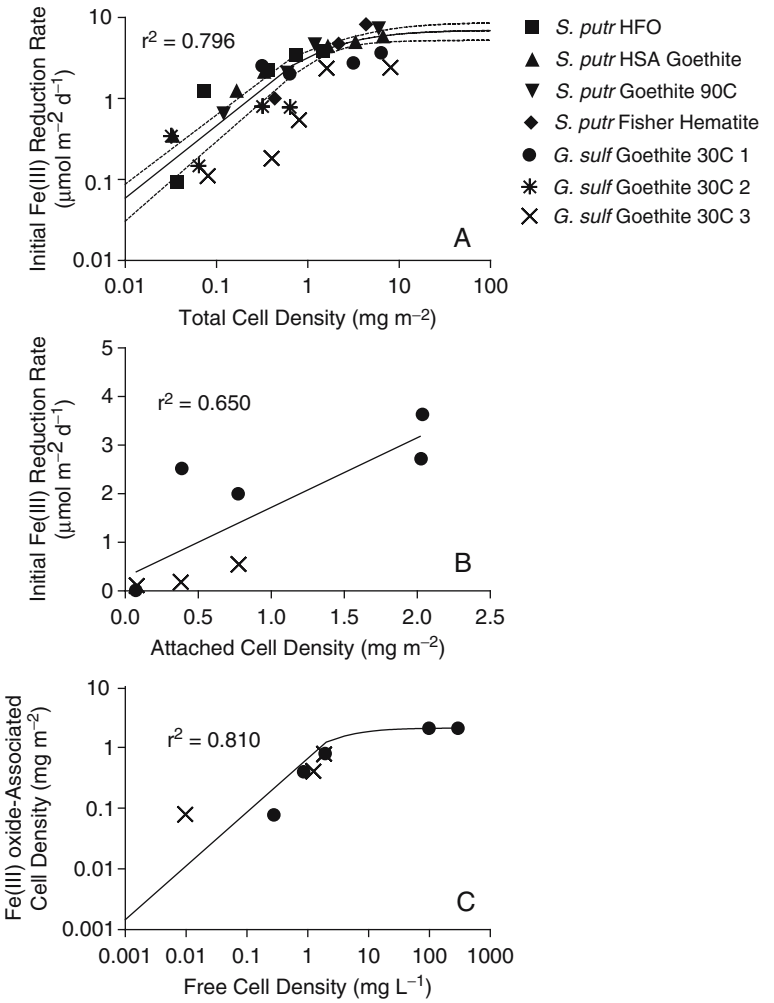

Fig. 8.15 Initial SA-normalized rates of enzymatic Fe(III) oxide reduction as a function of total (A) or attached (B) DIRM cell density, and relationship between oxide-associated and free cell density (C). *S. putrefaciens* and *G. sulfurreducens* data in (A) are reproduced with permission from data not shown in Roden (2003) and Roden (2006), respectively. Data in (B) and (C) are unpublished data of E. Roden. The concentration of surface sites was calculated based on oxide loading (10 mmol $L^{-1} \approx 0.89$ g L^{-1}), the measured mineral SA areas, and an assumed mineral surface site density of 3.84×10^{-6} mol sites m^{-2} (Davis and Kent, 1990). The abundance of attached cells was determined by direct cell counting as described in Caccavo et al. (1997). The non-linear regression fit in panel A is defined by Eq. 1 in Table 8.7; best-fit values for $kmax_{DIRM,surf}$ and $K_{DIRM,surf}$ are 6.98 μmol m^{-2} d^{-1} and 1.18 mg cells m^{-2}, respectively. Solid line in panel B shows results of a linear least-squares regression. Solid line in panel C shows nonlinear least-squares regression fit of the data to a Langmuir isotherm

proteins and/or flagella are likely to be involved in the binding of Fe(III) oxides by DIRM cells (Caccavo, 1999; Caccavo and Das, 2002). Current evidence suggests that the latter components are required for the irreversible adhesion of Fe(III) oxides to DIRM cells (Caccavo and Das, 2002) that has been observed in several studies (Bonneville et al., 2006; Caccavo, 1999; Caccavo et al., 1996; Glasauer et al., 2001). However, irreversible adhesion is not required for enzymatic reduction to take place (Caccavo et al., 1997; Caccavo and Das, 2002; Grantham et al., 1997), and detachment and transport of DIRM cells clearly takes place in hydrologically open reaction systems (Roden and Urrutia, 1999; Roden et al., 2000). The physiochemical mechanisms and controls on DIRM-Fe(III) oxide association are still not well-understood, and represent an important area of future research (Caccavo and Das, 2002).

Although the above relationships are logically consistent, uncertainties exist with respect to the quantitative relationship between DIRM abundance, DIRM-Fe(III) oxide association, and oxide reduction rate. An example of such uncertainty is evidenced by Fe(III) oxide loading experiments conducted with *G. sulfurreducens* and *S. putrefaciens*. Initial reduction rates were determined in the presence of 5–200 mmol L^{-1} of synthetic goethite (ca. 55 $m^2 g^{-1}$) and 1×10^8 cells mL^{-1} of washed DIRM cells under non-growth conditions (Fig. 8.16). A linear correlation was observed between Fe(III) oxide loading and initial reduction rate, analogous to the first-order kinetics documented in wetland surface sediment (Fig. 8.9c,d), and similar to the results of several previous pure cultures studies of synthetic Fe(III) oxide reduction kinetics (Liu et al., 2001a; Roden and Zachara, 1996; Roden and Urrutia, 1999). In contrast, rates predicted using the relationship between SA-normalized reduction rate and DIRM cell density shown in Fig. 8.15a (and defined by Eqs. (8.31–8.32)) were invariant and considerably lower than observed values above 50 mmol Fe(III) L^{-1}; i.e., the saturation behavior predicted by the rate equation was clearly not observed (Fig. 8.16). The cell-oxide binding isotherm shown in Fig. 8.15c predicts that all the DIRM cells present in these experiments should have been associated with Fe(III) oxides. Thus, it appears that the attached DIRM cells were somehow able (at least initially) to transfer electrons to Fe(III) oxides at SA-normalized rates considerably higher than those predicted by the data shown in Fig. 8.15a. Although the basis for this phenomenon is unclear, it is possible that aggregation of cells and oxides at high particle loading (visibly obvious in these experiments) facilitated contact between cell surface redox-active components and oxide surface sites – an effect that is obviously not taken into account in the rate law depicted in Eqs. (8.31–8.32).

8.4.5.3 Controls on Long-Term Reduction Kinetics

A common pattern of Fe(II) accumulation was observed during long-term (3-week incubation) reduction of the various synthetic Fe(III) oxides by *G. sulfurreducens* with H_2 as the ED (Fig. 8.17a). After an initial period of rapid Fe(II) accumulation, rates of reduction decreased and Fe(II) levels approached an asymptote.

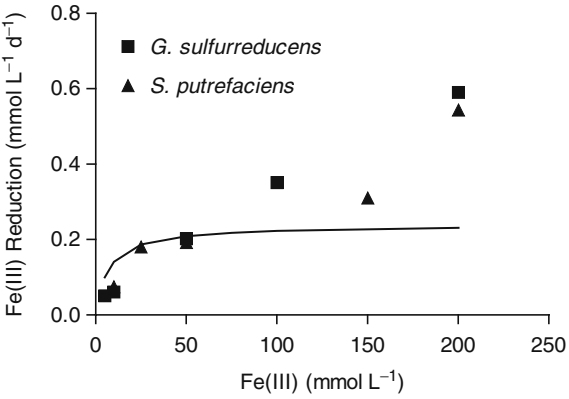

Fig. 8.16 Relationship between initial Fe(III) oxide reduction rate and bulk Fe(III) oxide loading in the presence of 1×10^8 cells mL^{-1} of *G. sulfurreducens* or *S. putrefaciens* cells (data from Roden (2006), used with permission). The solid lines shows rates predicted based on the relationship between SA-normalized reduction rate and DIRM cell density shown in Fig. 8.15A

Similar patterns have been observed in many previous microbial reduction experiments with synthetic and natural Fe(III) oxide phases (see Roden and Urrutia (2002) for review). Solution pH was correlated with $Fe^{2+}{}_{(aq)}$ accumulation during synthetic Fe(III) oxide reduction (Fig. 8.17b), as expected from the stoichiometry of Fe(III) oxide reduction coupled to H_2 oxidation:

$$H_2 + 2FeOOH + 4H^+ \rightarrow 2Fe^{2+} + 4H_2O$$

Measured pH values and $Fe^{2+}{}_{(aq)}$ concentrations were used, together with the estimated $E_h{}^0$ values for the different Fe(III) oxides, to compute the free energy of Fe(III) oxide reduction (ΔG values) for the different synthetic phases during the course of the long-term reduction experiments (Fig. 8.17c). The results indicate that the cessation of oxide reduction activity cannot be attributed to free energy constraints posed by dissolved Fe(II) ($Fe^{2+}{}_{(aq)}$) accumulation and pH increase, because reduction rates approached zero at ΔG values substantially lower than the theoretical minimum of ca. $-20\,kJ\,mol^{-1}$ required for energy conservation during biological energy metabolism (Schink, 1997). Similar conclusions were reached in a recent study of synthetic Fe(III) oxide reduction coupled to acetate oxidation by *G. metallireducens* (Dominik and Kaupenjohann, 2004), a result supported by an experiment examining reduction of synthetic goethite ($55\,m^2\,g^{-1}$) by *G. sulfurreducens* with acetate as the electron donor (asterisks in Fig. 8.17c; estimated ΔG data were converted to $kJ/2e^-$ to allow direct comparison with H_2 oxidation metabolism). The solid line in Fig. 8.17c corresponds to a thermodynamic control function which accounts for the influence of thermodynamic driving force on reaction rate, modified to account for the minimum free requirement for biological energy conservation as described in Liu et al. (2001a) (see Eq. (8.21) in Sect. 8.3.6). The experimental data clearly do not correspond to this function, in contrast to results obtained in studies of abiotic ligand-promoted dissolution of δ-Al_2O_3 and goethite (Kraemer and Hering, 1997).

Both the total amount of Fe(II) generated and the amount of Fe(II) associated with oxide surfaces (referred to as "sorbed Fe(II)") at the end of the reduction experiments correlated directly with the measured (BET) SA of the mineral phases (Fig. 8.18). These results suggest that accumulation of Fe(II) on oxide surfaces was

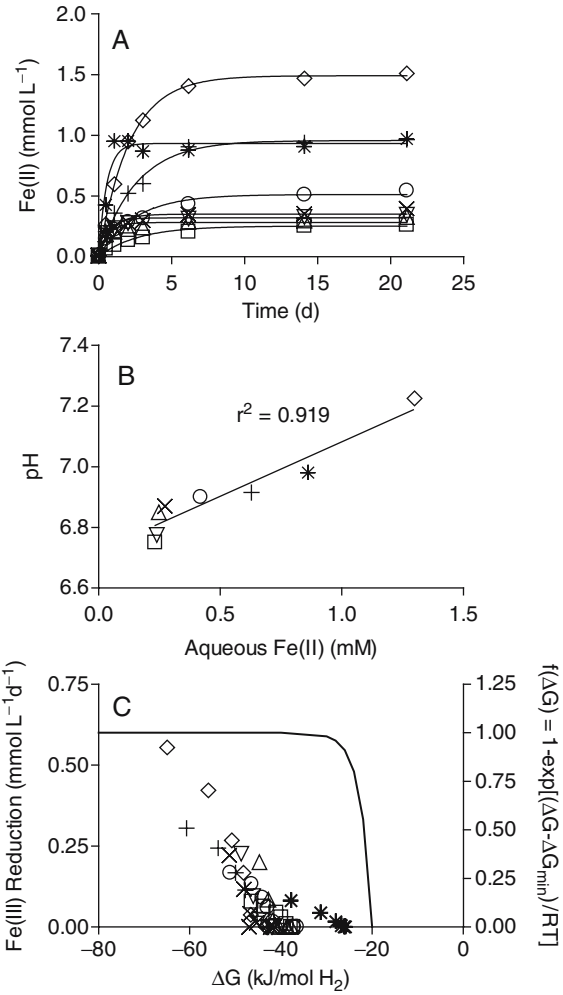

Fig. 8.17 Panels A and B: Total (0.5M HCl extraction) Fe(II) production (A) and relationship between pH and aqueous Fe(II) accumulation (B) during reduction of synthetic Fe(III) oxides by *G. sulfurreducens* with H_2 as the electron donor (data from Roden (2006)). Symbols as in Fig. 8.14, except thick asterisks, which show results of an experiment with acetate as the electron donor . Lines in panel A show nonlinear regression fits of the data to an equation of the form $C(t) = C_{max}[1 - \exp(-at)]$, where C(t) represents the amount of Fe(II) produced at time t, C_{max} represents the maximum (asymptotic) amount of Fe(II) produced during the incubation period, and *a* represents a first-order rate constant. Line in panel B shows result of a linear least-squares regression analysis. Panel C: Rate of Fe(III) reduction as a function of the estimated free energy of reaction during the Fe(III) reduction experiments. Fe(III) reduction rates were computed from derivatives of the nonlinear curve-fits shown in panel A. The solid line shows the relationship between reaction rate and energetics predicted by Eq. (8.21)

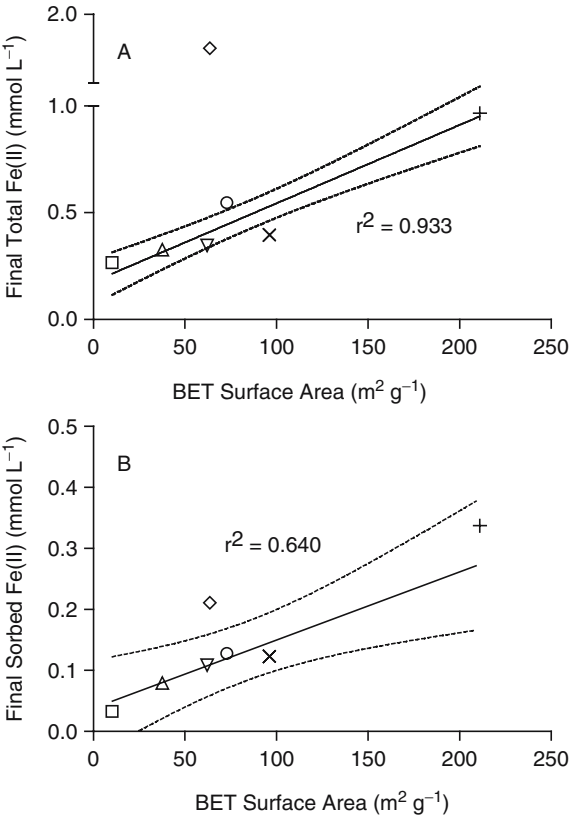

Fig. 8.18 Correlation between oxide mineral SA and (A) the final concentration of total HCl-extractable Fe(II) or (B) surface-associated ("sorbed") Fe(II) during long-term *G. sulfurreducens* experiments. Symbols as in Fig. 8.1.4. Data for the HFO reduction system are omitted, since the mineral was transformed to goethite during partial reductive dissolution (Hansel et al., 2004). Lines show linear least-squares regression fits of the data; data for lepidocrocite (diamond) were omitted from the regression analysis shown in panel A

responsible for cessation of oxide reduction activity, with higher surface area CIOs supporting production of greater amounts of Fe(II) by virtue of their higher Fe(II) binding capacity per unit mass. This conclusion is consistent with many previous studies of CIO reduction at circumneutral pH, and has been attributed to kinetic and/or thermodynamic impacts of surface-associated Fe(II) on enzymatic electron transfer, including impacts of Fe(II) sorption/surface precipitation on FeRB cell surfaces (Roden and Urrutia, 2002). Recent Mössbauer studies (Williams and Scherer, 2004) as well as experiments on the behavior of Fe isotopes during DIR (Crosby et al., 2005; Icopini et al., 2004) verify previous speculations (Coughlin and Stone, 1995; Roden and Urrutia, 2002) that electron (and Fe atom) exchange takes place between $Fe^{2+}_{(aq)}$ and CIO surfaces. These studies indicate that Fe(II) atoms accumulate within the surface of the CIO crystal lattice during DIR, the net effect of which is to render the bulk oxide progressively more resistant to enzymatic reduction.

8.4.5.4 General Conceptual Model and Rate Law for Microbial Fe(III) Oxide Reduction

The experimental findings summarized above point to a conceptual model of microbial Fe(III) oxide reduction kinetics in which oxide SA exerts primary control on both the initial rate and the long-term extent of reduction. The explicit SA control of the initial rate and long-term extent of oxide reduction leads to a general rate law for oxide reduction as a function of electron acceptor and DIRM abundance that differs fundamentally from that for reduction of chelated Fe(III) and other soluble metal species. Table 8.7 provides a summary of rate laws that are appropriate for use in modeling solid-phase as compared to dissolved metal (and other soluble electron acceptor) reduction. Equation (1) in Table 8.7 states that the bulk Fe(III) oxide reduction rate is a linear function of "free", microbially reducible oxide surface abundance (discussed further below) at fixed DIRM cell density. DIRM cell density in turn defines the Fe(III) reduction rate constant (e.g., in units of $\mu mol\ m^{-2}\ d^{-1}$) according to a hyperbolic function (Fig. 8.15a). The observed relationships between DIRM cell density and oxide reduction rate are analogous to the well-recognized dependence of abiotic reductive dissolution rate on total and surface-associated ligand concentration (Hering and Stumm, 1990), and are the opposite of those for reduction of soluble metals and other electron acceptors. As illustrated for Fe(III)-citrate in Fig. 8.19, rates of soluble EA reduction are a hyperbolic function of EA concentration, and a linear function of DIRM cell density (Eq. (8.3) in Table 8.7). Similar patterns hold for reduction of various soluble metals such as U(VI), Co(III), Cr(VI), and Tc(VI) (Liu et al., 2001b, 2002; Roden, 2005; Roden and Scheibe, 2005; Truex et al., 1997).

A key issue in the quantitative interpretation and modeling of CIO reduction is how to conceptualize controls on the long-term extent of oxide reduction. Several studies have shown that it is possible to model the long-term extent of CIO reduction by assuming that oxide surface sites occupied by surface-bound (sorbed and/or surface-precipitated) Fe(II) are no longer available for microbial reduction (Burgos et al., 2002, 2003; Hacherl et al., 2003; Liu et al., 2001a; Roden and Urrutia, 1999). In this approach, mass-action relationships between surface-associated and $Fe^{2+}_{(aq)}$, together with bulk oxide SA loading, control the availability of microbially reducible Fe(III) oxide SA. This strategy and its limitations is illustrated below using data on synthetic Fe(III) oxide reduction by *G. sulfurreducens*.

The partitioning of biogenic Fe(II) between the aqueous phase an oxide/DIRM surfaces during the reduction experiments (Fig. 8.20) was generally consistent with previous studies of Fe(II) sorption to synthetic goethite at similar pH and ionic strength (Liu et al., 2001a; Urrutia et al., 1998), with maximum sorption densities of 2–4 $\mu mol\ Fe(II)\ m^{-2}$. Nonlinear-fitting of the data to a Langmuir isotherm (Eq. (8.2) in Table 8.7) yielded a best-fit maximum sorption density value of $3.67\ \mu mol\ m^{-2}$, which is close to the "universal" mineral surface site density of $3.84\ \mu mol\ m^{-2}$ recommended by Davis and Kent (1990) for use in surface complexation modeling. Although DIRM cells possess a mass-normalized Fe(II) sorption capacity comparable to that of $55\ m^2\ g^{-1}$ synthetic goethite (Liu et al., 2001b; Urrutia et al.,

Table 8.7 Rate laws for microbial reduction of solid-phase and aqueous Fe(III)

A. Solid-Phase

$$R_{Fe(III)} = k\,max_{DIRM,surf}\frac{[DIRM]_{surf}}{K_{DIRM,surf}+[DIRM]_{surf}}[Fe(III)_{fsa}] \quad (1)$$

where:

$R_{Fe(III)}$ = bulk volumetric rate of Fe(III) oxide reduction (e.g. mmol/L/d)
$k\,max_{DIRM,surf}$ = Maximum SA-normalized reduction rate constant (e.g. $\mu mol/m^2$ free oxide surface/d) at very high SA-normalized DIRM density (see Fig. 8.15A)
$[DIRM]_{surf}$ = SA-normalized DIRM cell density (e.g. mg cells/m^2 free oxide SA) (see Fig. 8.15A)
$K_{DIRM,surf}$ = Half-saturation constant for relationship between DIRM cell density and oxide reduction rate constant (e.g. mg cells/m^2 free oxide SA) (see Fig. 8.15A)
$[Fe(III)_{fsa}]$ = bulk volumetric abundance of "free" (i.e. microbially-reducible) Fe(III) oxide surface (e.g. m^2/L) = $[Fe(III)_{tsa}]$–$[Fe(II)_{sa}]$, where $[Fe(III)_{tsa}]$ is total bulk volumetric oxide SA (m^2/L), and $[Fe(II)_{sa}]$ is the bulk volumetric area of surface-associated Fe(II) (m^2/L), e.g. as computed from a sorption isotherm such as (see Fig. 8.20):

$$[Fe(II)_{sa}] = [Fe(II)_{sa}]_{max}\frac{[Fe(II)_{aq}]}{K_{ads}+[Fe(II)_{aq}]} \quad (2)$$

B. Aqueous

$$R_{Fe(III)} = \alpha_{DIRM}[DIRM]_{bulk}\frac{[Fe(III)_{aq}]}{K_{Fe(III)}+[Fe(III)_{aq}]} \quad (3)$$

where:

$R_{Fe(III)}$ = bulk volumetric rate of Fe(III) oxide reduction (e.g. mmol/L/d)
α_{DIRM} = proportionality constant for relationship between bulk DIRM cell density and soluble Fe(III) reduction rate in the presence of excess soluble Fe(III) (e.g. mmol/cell/d) (see Fig. 8.19B)
$[DIRM]_{bulk}$ = bulk DIRM cell density (e.g. cells/L)
$[Fe(III)_{aq}]$ = Concentration of aqueous Fe(III) (e.g. mmol/L)
$K_{Fe(III)}$ = Half-saturation constant for relationship between $Fe(III)_{aq}$ concentration and reduction rate (e.g. mmol/L) (see Fig. 8.19A)

1998), the mass of cells (ca. 40 mg L^{-1}) was much lower than that of Fe(III) oxides (890 mg L^{-1}) in these experiments, such that the cells contributed only negligibly to Fe(II) sorption capacity. The sorption isotherm shown in Fig. 8.20 was used in conjunction with the relationship between SA-normalized reduction rate and DIRM cell density (Eq. (8.1) in Table 8.7) to simulate the time course data shown in Fig. 8.17a. The bulk concentration of microbially reducible Fe(III) oxide surface (e.g., in $m^2\ L^{-1}$) was computed dynamically during as the simulation (using

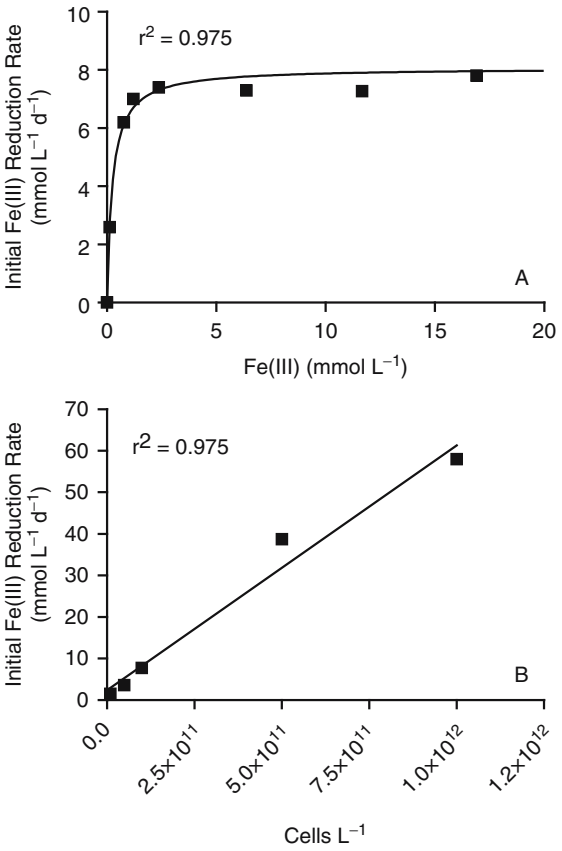

Fig. 8.19 Kinetics of Fe(III)-citrate reduction by *G. sulfurreducens* (data from Roden, (2006), used with permission). Solid lines in panels A and B show results of nonlinear and linear least-squares regression fits to the following expressions, respectively: $R_{Fe(III)} = [Fe(III)_{aq}]/(K_{Fe(III)} + [Fe(III)_{aq}]$; and $R_{Fe(III)} = \alpha_{DIRM}\ [DIRM]_{bulk}$ (see Table 7B). Best-fit values for $K_{Fe(III)}$ and α_{DIRM} are 0.25 mmol L^{-1} and 5.9×10^{-11} mmol $cell^{-1}$ d^{-1}, respectively

the MICROQL algorithm (Westall, 1986) as described in Roden (2004)) from the difference between total oxide SA and Fe(II) SA coverage predicted by the Fe(II) sorption isotherm (note that for these and other calculations below, the pH- and ionic strength-dependent speciation of $Fe^{2+}{}_{(aq)}$ between Fe^{2+} and $FeOH^{+}$ was computed in parallel with Fe(II) sorption using the MICROQL algorithm).

The results illustrate a fundamental problem with this approach, which is that cessation of oxide reduction does not take place because some quantity of free surface sites remains available until all the oxide is consumed (data not shown). It is possible to account for the cessation of oxide reduction in an "ad hoc" manner by fixing the oxide SA at a pre-chosen value and subtracting the Fe(II) surface coverage computed at each time step until no surface is left available (Roden and Urrutia, 1999). However, this approach suffers from obvious theoretical limitations in that the mechanistic link between available SA and the sorption

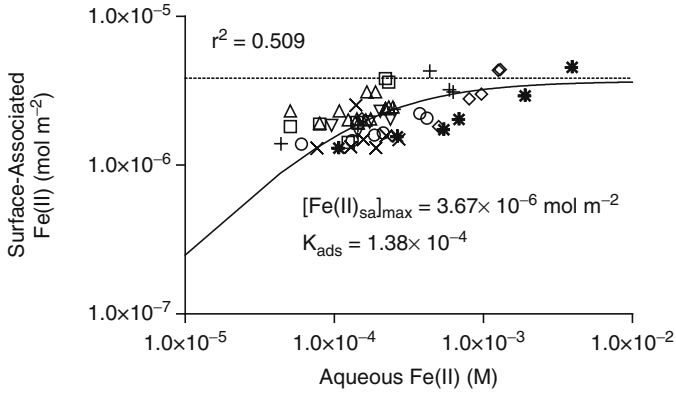

Fig. 8.20 Aqueous/solid-phase partitioning of Fe(II) during long-term synthetic Fe(II) oxide reduction experiments with *G. sulfurreducens* (data from experiments shown in Figs. 8.17 and 8.18; symbols as in Fig. 8.15). Asterisks show data for sorption of Fe(II) to synthetic goethite (55 $m^2\ g^{-1}$) from Urrutia et al. (1998). Solid line shows nonlinear regression fit of the data to a Langmuir isotherm (Eq. 2 in Table 8.7). Dashed line indicates the "universal" mineral surface site density of 3.84 μmol m^{-2} recommended by Davis and Kent (1990) for use in surface complexation modeling

isotherm is broken. Some investigators have assumed that precipitation of siderite on oxide surface leads to blockage of available SA and thereby contributes to the cessation of oxide reduction (Hacherl et al., 2003; Liu et al., 2001a). While the latter approach may be defensible in situations where dissolved inorganic carbon (DIC) is abundant, it does not apply to the reactions systems considered here, which contained very little DIC and therefore were not likely to involve siderite precipitation.

Liu et al. (Liu et al., 2001a) introduced the concept of a mixed kinetic/thermodynamic approach for simulation of long-term Fe(III) oxide reduction kinetics, which is equivalent to combining Eq. (8.21) with Eqs. (8.31–8.32). In this approach the value of the thermodynamic control term (F_T) is computed based on the measured (or estimated) concentrations of reactants and products, and an assumed ΔG_f value for the oxide phase undergoing reduction. For the purposes of simulating the oxide reduction data in Fig. 8.21, the oxide ΔG_f can be treated as an adjustable, empirical parameter (referred to hereafter as ΔG_f^*) whose value defines the point at which F_T (and thus the rate of oxide reduction) approaches zero. Using this approach together with the expressions for enzymatic oxide reduction kinetics and Fe(II) sorption (Eqs. (8.1) and (8.2) in Table 8.7), it was possible to reproduce the observed reduction of various synthetic Fe(III) oxides by *G. sulfurreducens* (Fig. 8.21). It is important to note that the ΔG_f^* values listed in Fig. 8.25 are not the same as the ΔG_f values that correspond (vis-à-vis the Nernst equation) to the E_h^0 values for the different oxide phases indicated in Fig. 8.18. Although it is not appropriate to assign a formal meaning to the ΔG_f^* values, they could be interpreted as values that account (albeit indirectly) for the effect of sorbed Fe(II) accumulation on the thermodynamic favorability of enzymatic electron transfer. The fact that it was possible to simulate reduction of all four goethite phases (i.e., those formed

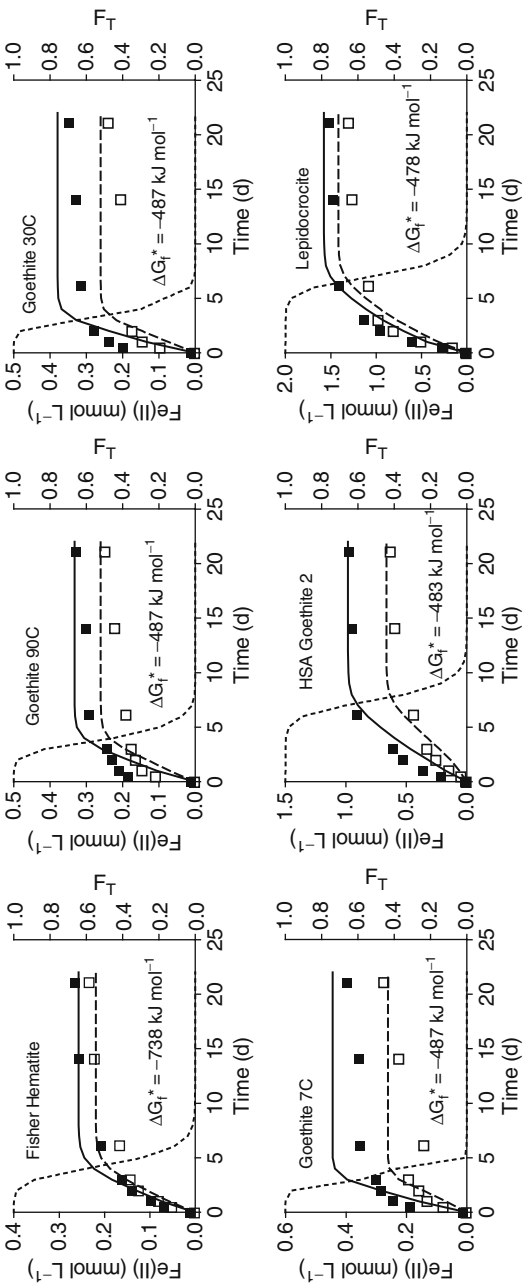

Fig. 8.21 Simulation of synthetic Fe(III) oxide reduction coupled to H_2 oxidation by *G. sulfurreducens* (data from Fig. 8.17) using a combination of Eqs. (8.21) and (8.31–8.32) together with the Fe(II) sorption isotherm shown in Fig. 8.20 to compute (dynamically during the simulation) the abundance of free, microbially-reducible oxide surface as described in Table 8.7A. The free energy of formation for the oxide phase undergoing reduction was treated as an adjustable parameter (ΔG_f^*) in order to obtain a reasonable fit (by eye) to the observed data. Filled symbols and solid lines refer to total Fe(II); open symbols and dashed lines refer to aqueous Fe(II). Dotted line shows the value of the thermodynamic control function (F_T in Eq. (8.21))

by Fe^{3+} precipitation at either 7, 20, 30, or 90° C) with the same ΔG_f^* value of $-487\,kJ\,mol^{-1}$ suggests that these oxides respond (relative to enzymatic reduction) in a common way to the accumulation of surface-associated Fe(II).

In order to evaluate the robustness of the above approach, data from the goethite loading experiment with *G. sulfurreducens* described in Fig. 8.16 (and associated text) were simulated using a ΔG_f^* value of $-487\,kJ\,mol^{-1}$. The results illustrate an important limitation of the kinetic framework, which reflects an impact of the geochemical environment on DIRM cell viability that is not included in the framework. Although the data for the lowest levels of goethite loading (5 and 10 mmol Fe(III) L^{-1}) were reproduced reasonably well, the simulations over-predicted the extent of reduction 2–3 fold at higher levels of loading (Fig. 8.22). These results can be tentatively attributed to the inhibitory influence that Fe(II) sorption onto DIRM cell surfaces has on enzymatic reduction activity, particularly under non-growth conditions (Roden and Urrutia, 2002; Urrutia et al., 1998). Increased production of Fe(II) at higher levels of goethite loading probably led to coating of DIRM surfaces with sorbed and/or surface-precipitated Fe(II) (see Fig. 8.1e,f), thereby inhibiting Fe(III) reduction. If this explanation is correct, then it follows that the ΔG_f^* values listed in Fig. 8.21 account (in a lumped manner) for the influence of Fe(II) binding by both oxide *and* DIRM surfaces on long-term oxide reduction. Further studies of the relative influence of these two phenomena will be required to formulate and parameterize a more accurate kinetic model for controls on the long-term extent of CIO reduction.

8.4.5.5 Implications and Application to Natural Soils and Sediments

Virtually all experimental work to date on microbial synthetic Fe(III) oxide reduction indicates that oxide mineral heterogeneity in natural soils and sediments is likely to affect initial reduction kinetics (e.g., during the early stages of anaerobic metabolism following the onset of anoxic conditions) mainly via an influence on reactive surface site density. This assertion is supported by experiments with a mixed culture of wetland sediment morgs and a range of synthetic Fe(III) oxides, which showed that DIRMs could outcompete MGMs for acetate with equal effectiveness when the different oxides are present at comparable SA loadings – despite major differences in computed ΔG values for acetate oxidation coupled to DIR (Roden, 2003b). An immediate implication of these findings is that the SA of different oxides phases present in a natural soil or sediment will exert primary control on initial rates of enzymatic reduction, e.g., in situations where DIR contributes to the oxidation of natural or contaminant organic compounds.

During the later stages of DIR in permanently reduced sediments, accumulation of aqueous and (more importantly) surface-bound Fe(II) is expected to exert a dominant control on apparent Fe(III) oxide reactivity toward enzymatic reduction, particularly in situations where removal of Fe(II) end-products is slow compared to the kinetics of reduction (Roden and Urrutia, 1999, 2002). As discussed above, there is a general relationship between oxide SA and long-term extent of oxide

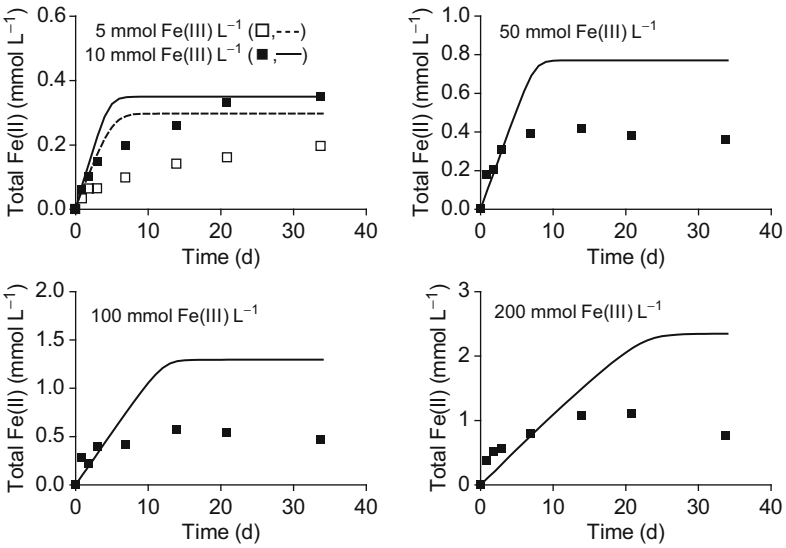

Fig. 8.22 Simulation of the results of the synthetic goethite loading experiment with *G. sulfurreducens* described in Fig. 8.16 (and associated text) using the same expressions and parameter values used in Fig. 8.21

reduction in closed reaction systems (see Fig. 8.18), which results from the function of oxide surfaces as a repository for sorbed and/or surface-precipitated biogenic Fe(II). Although the existence of this relationship implies a connection between extent of microbial reduction and oxide thermodynamic properties, evidence suggests that this connection is not directly related to thermodynamic properties such as E_h^0 or ΔG_f, but rather results mainly from the correlation between these properties and oxide SA. Consequently, inferences regarding the ability of DIR to compete with other TEAPs in soils and sediments should be based on estimates of bulk reactive (i.e., microbially accessible) surface site density – rather than the thermodynamic properties of the oxide(s) identified as the dominant phase(s) in a particular soil or sediment.

In order to formally evaluate changes in the apparent reactivity of Fe(III) oxides during long-term enzymatic versus abiotic reduction, data from long-term experiments on reduction of three different natural CIOs by *S. putrefaciens* versus ascorbate (Roden, 2004) were interpreted in relation to a standard generalized rate law for mineral dissolution (Larsen and Postma, 2001; Postma, 1993):

$$J(t)/m_0 = k'(m/m_0)^{\gamma} \tag{8.34}$$

where J(t) is the rate of dissolution and/or reduction at time t, m_0 is the initial mass (or molar concentration) of oxide, k' is a rate constant, m/m_0 is the unreduced (or undissolved) mineral fraction, and γ is a parameter that accounts for changes in reactivity over time that may arise as a result of (i) heterogeneity in the reactivity

of the initial population of minerals undergoing dissolution, and/or (ii) changes in reactivity of the dissolving mineral phase over time. Equation (8.34) corresponds to a power rate law, which reduces to a first-order rate law when $\gamma \approx 1$.

The Fe(III) oxide pool in each of the materials was dominated $(\geq 97\%)$ by crystalline phases, as indicated by the ratio of hydroxylamine HCl- to total citrate/dithionite-extractable Fe. The natural Fe(III) oxide assemblages demonstrated significant changes in reactivity during long-term abiotic reductive dissolution (Fig. 8.23a), as indicated by γ values in excess of 1 for curve-fits of the data to the generalized rate law (Larsen and Postma, 2001; Postma, 1993). Much larger changes in reactivity were estimated for the microbial reduction experiments (Fig. 8.23b, solid symbols). However, when the analysis was restricted to the long-term "microbially reducible" fraction of the Fe(III) oxide content of the natural solids (Fig. 8.23b, open symbols), the data could be well-approximated with γ values of ca. 1, i.e., by a first-order rate law. Note here that the "microbially reducible" fraction refers simply to that fraction of total Fe(III) that was subject to reduction, directly analogous to $\mathrm{Fe(III)}_{\mathrm{reac}}$ in Eq. (8.23).

Kinetic and thermodynamic considerations indicated that neither the abundance of electron donor (lactate) nor the accumulation of aqueous end-products of oxide reduction (Fe(II), acetate, dissolved inorganic carbon) are likely to have posed significant limitations on the long-term kinetics of oxide reduction. Rather, accumulation of biogenic Fe(II) on residual oxide surfaces appeared to play a dominant role in governing the long-term kinetics of natural CIO, as described for synthetic Fe(III) oxide reduction above. Exploratory numerical simulations of SA-controlled DIR (based on a constrained model for synthetic goethite reduction) indicate that this phenomenon can account for the pseudo-first order kinetics of reduction of the operationally defined "microbially reducible" fraction of the sediment Fe(III) oxide pool (see Roden (2004) for more a more detailed explanation).

To illustrate how the above-developed reaction framework for the kinetics of DIR can be applied to a natural soil or sediment, data on the reduction of shallow subsurface Atlantic coastal plain sediment (designated as material AP in Fig. 8.23) by *S. putrefaciens* (under growth conditions with lactate as an energy source) was simulated using an approach that incorporates Fe(II) partitioning onto mineral surfaces, analogous to that used to model synthetic Fe(III) oxide reduction shown in Figs. 8.21 and 8.22. Two important additions to the approach were to (i) include DIRM growth using a yield coefficient (ca. 1 mg of cells per mmol Fe(III) reduced) estimated using the energy balance approach of Rittmann and McCarty (2001); and (ii) include an auxiliary solid-phase capable of sorbing biogenic Fe(II). Inclusion of such a phase is required because the total amount of solid-associated Fe(II) produced during Fe(III) reduction, when normalized to the residual (after reduction ceased) Fe(III) content of the sediment, was at least 10-fold higher (ca. 0.4 mol Fe(II) mol $\mathrm{Fe(III)}^{-1}$) than that observed for synthetic Fe(III) oxide reduction (ca. 0.003–0.04 mol Fe(II) mol $\mathrm{Fe(III)}^{-1}$); in other words, the Fe(III) oxides present in the sediment cannot account for the majority of the solid-associated Fe(II) that accumulated during enzymatic reduction. In addition, previous experimental studies have shown that the presence of mineral phases (e.g., aluminum oxide and layered

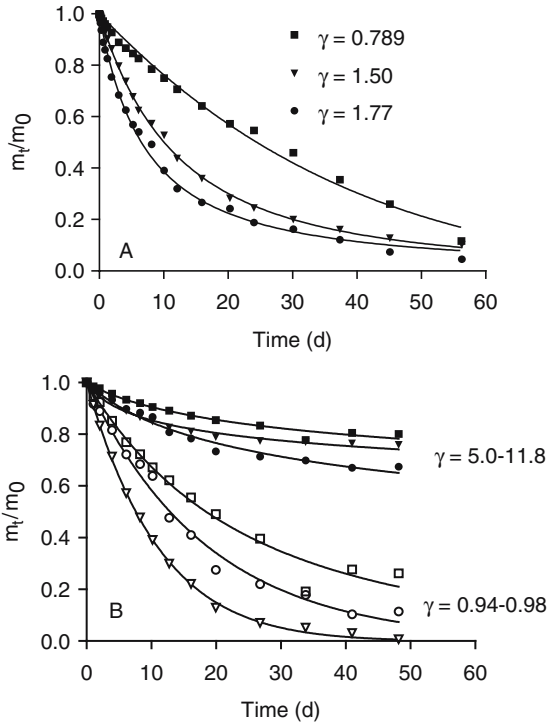

Fig. 8.23 Kinetic analysis of ascorbate (A) and microbial (*S. putrefaciens*) (B) reduction of three different Fe(III) oxide-bearing subsurface materials. All data are from anaerobic batch reactor experiments reported in Roden (2004), used with permission. Squares, triangles, and circles represent the HC, CP, and AP materials described in detail in Roden (2004). Ascorbate reduction experiments were conducted with shaken (well-mixed) particle suspensions containing 1 mmol Fe(III) L^{-1} in 10 mM ascorbic acid, pH 2. Microbial reduction experiments were conducted with static (unmixed) suspensions containing 12 mmol Fe(III) L^{-1} in Pipes (10 mM, pH 6.8) buffer with excess lactate (10 mM) as the electron donor. Open symbols in panel B refer to reduction of the "microbially-available" fraction of the oxide pool (equivalent to $Fe(III)_{reac}$ in Eq. (8.23)). The terms m_0 and m_t refer to the mass (concentration) of Fe(III) oxide present at the start of the experiment and at time t, respectively. Solid lines show nonlinear regression fits of the data to the integrated form of the generalized mineral dissolution rate law (Eq. (8.34)). γ values refer to the results of the nonlinear curve fits

silicates) capable of binding Fe(II) can dramatically extend the degree of CIO reduction by serving as a sink for biogenic Fe(II) that would otherwise down-regulate Fe(III) oxide reduction by the mechanisms discussed above (Urrutia et al., 1999). Thus, inclusion of the auxiliary solid-phase is important for accurate simulation of both aqueous/solid-phase Fe(II) partitioning as well as Fe(III) oxide reduction kinetics.

In order to minimize the number of adjustable parameters in the sediment Fe(III) oxide reduction model, the following values were chosen a priori based on available information: (1) the mass of the auxiliary Fe(II) sorbing phase was set equal to the total mass of solids per unit volume in the reaction system $(142\,g\,L^{-1})$, to which the

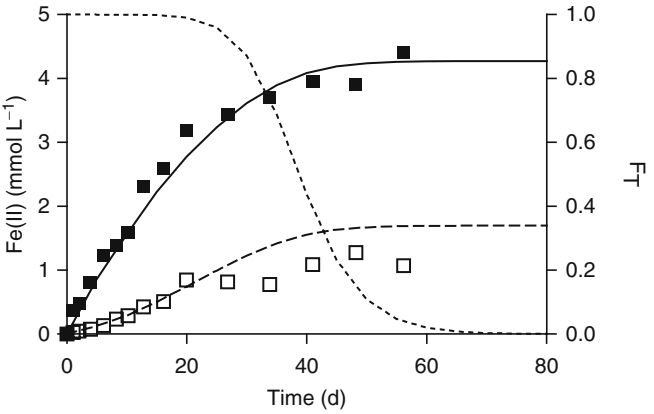

Fig. 8.24 Simulation of Fe(III) oxide reduction in shallow subsurface Atlantic coastal plain sediment (material AP depicted in Fig. 8.23) using the approach demonstrated in Fig. 8.21, modified to include DIRM growth and the presence of an auxiliary Fe(II)-sorbing solid-phase (see section 8.4.5.5 for details). Solid symbols and lines show total Fe(II) data and simulation; open symbols and dashed line show aqueous Fe(II) data and simulation. Dotted line shows the value of the thermodynamic control function (F_T in Eq. (8.21))

mass of Fe(III) oxide contributed less than 1% (ca. 9 mg/g); (2) the SA of the auxiliary phase was set equal to the measured (BET) SA of the sediment ($5.6\,m^2\,g^{-1}$); (3) the surface site density of the auxiliary phase was set equal to the universal site density of $3.84\,\mu mol\,m^{-2}$ recommended by Davis and Kent (1990); (4) the Fe(III) oxide pool in the sediment was assumed to be dominated by goethite, in accordance with previous detailed characterization of similar materials (Penn et al., 2001); (5) the initial bulk Fe(III) oxide abundance in the reaction system (ca. 12 mmol Fe(III) L^{-1}) was computed from the total citrate/dithionite-extractable Fe(III) content of the sediment (ca. $100\,\mu mol\,g^{-1}$) and the total solid mass loading; (6) the ΔG_f^* value (see Sect. 8.4.5.4) for the sediment Fe(III) oxide pool was set equal to $-485\,kJ\,mol^{-1}$, which is the mean of the ΔG_f^* values estimated for the synthetic goethite reduction systems depicted in Fig. 8.21; (7) the maximum SA-normalized sorption capacity and binding constant for Fe(II) sorption by Fe(III) oxides were set equal to the best-fit values for the synthetic phases shown in Fig. 8.20; and (8) the $kmax_{biomass,surf}$ and $K_{DIRM,surf}$ values for enzymatic Fe(III) reduction (see Table 8.7) were set equal to the best-fit values for the synthetic oxide phases shown in Fig. 8.15.

With the above parameter values fixed, only two additional parameters needed to be defined to run the model: (1) the average SA for the sediment Fe(III) oxide pool; and (2) the binding constant (log K_{ads} value) for Fe(II) sorption by the auxiliary phase. Systematic testing showed that only a limited combination of values for these two parameters could reproduce the observed total and $Fe^{2+}_{(aq)}$ versus time data (SA values of 100–150 $m^2\,g^{-1}$ and log K_{ads} values of -3.5 to -3.7), all of which are reasonable for soil/sediment mineral phases. The results of a simulation using an SA value of 120 and a log K_{ads} value of -3.5 are shown in Fig. 8.24. The results of

this exercise, together with the analysis of wetland sediment Fe(III) oxide reduction kinetics, suggest that it is possible to use mechanistic, reaction-based models (which incorporate a wide array of microbial and geochemical phenomena) to describe the kinetics of DIR in natural sediments.

Acknowledgements

The research from my laboratory discussed in this chapter was supported by grants from the U.S. Department of Energy (DE-FG07–96ER62321 and DE-FG04-ER63915) and the U.S. National Science Foundation (DEB-9407233 and EAR-0525510). Financial and logistical support for the preparation of this and the companion chapter was provided by the Department of Geology and Geophysics at the University of Wisconsin, and the University of Wisconsin-Madison Libraries. The intellectual effort that went into this work is dedicated to the memory of Dr. Robert G. Wetzel, who was for decades (prior to his death in 2005) a leading proponent of the importance of microbially mediated elemental cycling in natural systems.

References

Albrechtsen H. J., Heron G., and Christensen T. H. (1995) Limiting factors for microbial Fe(III)-reduction in a landfill leachate polluted aquifer (Vejen, Denmark). *FEMS Microbiol. Ecol.* **16**, 233–247.

Amirbahman A., Schonenberger R., Johnson C. A., and Sigg L. (1998) Aqueous- and solid-phase biogeochemistry of a calcareous aquifer system downgradient from a municipal solid waste landfill (Winterthur, Switzerland). *Environ. Sci. Technol.* **32**, 1933–1940.

Anderson R. T., Rooney-Varga J. N., Gaw C. V., and Lovley D. R. (1998) Anaerobic benzene oxidation in the Fe(III) reduction zone of petroleum-contaminated aquifers. *Environ. Sci. Technol.* **32**, 1222–1229.

Arnold R. G., DiChristina T. J., and Hoffman M. R. (1988) Reductive dissolution of Fe(III) oxides by *Pseudomonas* sp. 200. *Biotechnol. Bioengin.* **32**, 1081–1096.

Bader F. B. (1982) Kinetics of double-substrate limited growth. In *Microbial Population Dynamics* (ed. M. J. Bazin), pp. 1–32. CRC Press, Boca Raton, FL.

Bae W. and Rittmann B. E. (1995) A structured model of dual-limitation kinetics. *Biotechnol. Bioengin.* **49**, 683–689.

Bak F. and Pfenning N. (1991) Sulfate-reducing bacteria in littoral sediment of Lake Konstanz. *FEMS Microbiol. Ecol.* **85**, 43–52.

Banfield J. F. and Nealson K. H. (1997) Geomicrobiology: Interactions Between Microbes and Minerals, Vol. 35. Mineralogical Society of America.

Banfield J. F., Cervini-Silva J., and Nealson K. H. (2005a) *Molecular Geomicrobiology*, Vol. 59. Mineralogical Society of America.

Banfield J. F., Tyson G. W., Allen E. A., and Whitaker R. J. (2005b) The search for a molecular-level understanding of processes that underpin Earth's biogeochemical cycles. In *Molecular Geomicrobiology*, Vol. 59 (ed. J. F. Banfield, J. Cervini-Silva, and K. H. Nealson), pp. 1–7. Mineralogical Society of America.

Banwart S. A. and Thornton S. F. (2003) The geochemistry and hydrology of groundwater bioremediation by natural attenuation. In *Bioremediation: A Critical Review* (ed. I. M. Head, I. Singleton, and Milner), pp. 93–138. Horizon Scientific, Norfolk, UK.

Barns S. M. and Nierzwicki-Bauer S. (1997) Microbial diversity in modern subsurface, ocean, surface environments. In *Geomicrobiology: Interactions Between Microbes and Minerals*, Vol. 35 (ed. J. F. Banfield and K. H. Nealson), pp. 35–79. Mineralogical Society of America.

Bazylinski D. A. and Moskowitz B. M. (1997) Microbial biomineralization of magnetic iron minerals: Microbiology, magnetism, and environmental significance. In *Geomicrobiology: Interactions Between Microbes and Minerals*, Vol. 35 (ed. J. F. Banfield and K. H. Nealson), pp. 181–223. Mineralogical Society of America.

Bazylinski D. A. and Frankel R. B. (2000) Biologically controlled mineralization of magnetic iron minerals by magnetotactic bacteria. In *Environmental Microbe-Metal Interactions* (ed. D. R. Lovley). ASM Press, Washington, DC.

Berner R. A. (1964) An idealized model of dissolved sulfate in recent sediments. *Geochim. Cosmochim. Acta* **28**, 1497–1503.

Berner R. A. (1977) Stoichiometric models for nutrient regeneration in anoxic sediments. *Limnol. Oceanogr.* **22**, 781–786.

Berner R. A. (1980) *Early Diagenesis: A Theoretical Approach*. Princeton University Press, Princeton, NJ.

Berner R. A. (1981) Authigenic mineral formation resulting from organic matter decomposition in modern sediments. *Fortschr. Mineral.* **59**, 117–135.

Berner R. A. (1982) Burial of organic carbon and pyrite sulfur in the modern ocean: Its geochemical and environmental significance. *Am. J. Sci.* **282**, 451–473.

Berner R. A. (1989) Biogeochemical cycles of carbon and sulfur and their effect on atmospheric oxygen over phanerozoic time. *Global Planet. Change* **75**, 97–122.

Beveridge T. J. (1989) Role of cellular design in bacterial metal accumulation and mineralization. *Annu. Rev. Microbiol.* **43**, 147–171.

Bevington P. R. and Robinson D. K. (1992) *Data Reduction and Error Analysis for the Physical Sciences*. McGraw Hill, New York.

Blackman F. F. (1905) Optima and limiting factors. *Ann. Botany* **19**, 281–295.

Bond D. R. and Lovley D. R. (2002) Reduction of Fe(III) by methanogens in the presence and absence of extracellular quinones. *Environ. Microbiol.* **4**, 115–124.

Bonneville S., Behrends T., VanCappellen P., Hyacinthe C., and Roling W. F. M. (2006) Reduction of Fe(III) colloids by *Shewanella putrefaciens*: A kinetic model. *Geochim. Cosmochim. Acta* **70**, 5842–5854.

Borrok D. and Fein J. B. (2004) Distribution of protons and Cd between bacterial surfaces and dissolved humic substances determined through chemical equilibrium modeling. *Geochim. Cosmochim. Acta* **68**, 3043–3052.

Boudreau B. P. and Westrich J. T. (1984) The dependence of bacterial sulfate reduction on sulfate concentration in marine sediments. *Geochim. Cosmochim. Acta* **48**, 2503–2516.

Boudreau B. P. and Ruddick B. R. (1991) On a reactive continuum representation of organic matter diagenesis. *Am. J. Sci.* **291**, 507–538.

Boudreau B. P. (1992) A kinetic model for microbic organic-matter decomposition in marine sediments. *FEMS Microb. Ecol.* **102**, 1–14.

Boudreau B. P. (1996) A numerical-method-of-lines code for carbon and nutrient diagenesis in aquatic sediments. *Comput. Geosci.* **22**, 479–496.

Boudreau B. P. (1997) *Diagenetic Models and Their Implementation*. Springer, Berlin.

Brezonik P. L. (1994) *Chemical Kinetics and Process Dynamics in Aquatic Systems*. Lewis Publishers, Boca Raton, FL.

Burdige D. J. (1991) The kinetics of organic matter mineralization in anoxic marine sediment. *J. Mar. Res.* **49**, 727–761.

Burgos W. D., Royer R. A., Fang Y., Yeh G. T., Fisher A. S., Jeon B. H., and Dempsey B. A. (2002) Theoretical and experimental considerations related to reaction-based modeling: A case study using iron(III) oxide bioreduction. *Geomicrobiol. J.* **19**, 253–292.

Burgos W. D., Fang Y., Royer R. A., Yeh G. T., Stone J. T., Jeon B. H., and Dempsey B. A. (2003) Reaction-based modeling of quinone-mediated bacterial iron(III) reduction. *Geochim. Cosmochim. Acta* **67**, 2735–2748.

Caccavo F., Schamberger P. C., Keiding K., and Nielsen P. H. (1997) Role of hydrophobicity in adhesion of the dissimilatory Fe(III)-reducing bacterium *Shewanella alga* to amorphous Fe(III) oxide. *Appl. Environ. Microbiol.* **63**, 3837–3843.

Caccavo F. (1999) Protein-mediated adhesion of the dissimilatory Fe(III)-reducing bacterium *Shewanella alga* BrY to hydrous ferric oxide. *Appl. Environ. Microbiol.* **65**, 5017–5022.

Caccavo F. and Das A. (2002) Adhesion of dissimilatory Fe(III)-reducing bacteria to Fe(III) minerals. *Geomicrobiol. J.* **19**, 161–177.

Caccavo F., Jr, Frolund B., Van Ommen Kloeke F., and Nielsen P. (1996) Deflocculation of activated sludge by the dissimilatory Fe(III)-reducing bacterium *Shewanella alga* BrY. *Appl. Environ. Microbiol.* **62**, 1487–1490.

Canfield D. E. and DesMarais D. J. (1993) Biogeochemical cycles of carbon, sulfur, and free oxygen in a microbial mat. *Geochim. Cosmochim. Acta* **57**, 3971–3984.

Canfield D. E., Jorgensen B. B., Fossing H., Glud R., Gundersen J., Ramsing N. B., Thamdrup B., Hansen J. W., Neilsen L. P., and Hall P. O. J. (1993) Pathways of organic carbon oxidation in three continental margin sediments. *Mar. Geol.* **113**, 27–40.

Canfield D. E., Thamdrup B., and Kristensen E. (2005) *Aquatic Geomicrobiology*. Elsevier.

Chao T. T. and Zhou L. (1983) Extraction techniques for selective dissolution of amorphous iron oxides from soils and sediments. *Soil Sci. Soc. Am. J.* **47**, 225–232.

Chapelle F. H. and Lovley D. R. (1992) Competitive exclusion of sulfate reduction by Fe(III)-reducing bacteria: A mechanism for producing discrete zones of high-iron ground water. *Ground Water* **30**, 29–36.

Chapelle F. H. (2001) *Ground-water Microbiology and Geochemistry*. John Wiley & Sons, New York.

Childers S. E., Ciufo S., and Lovley D. R. (2002) Geobacter metallilreducens accesses insoluble Fe(III) oxide by chemotaxis. *Nature* **416**, 767–769.

Christensen D. (1984) Determination of substrates oxidized by sulfate reduction in intact cores of marine sediments. *Limnol. Oceanogr.* **29**, 189–192.

Clark W. M. (1960) *Oxidation-Reduction Potentials of Organic Systems*. The Williams and Wilkins Company, Baltimore, MD.

Clarke P. H. (1985) The scientific study of bacteria, 1780–1980. In *Bacteria in Nature*, Vol. 1 (ed. E. R. Leadbetter and J. S. Poindexter), pp. 1–37. Plenum Press, New York.

Cord-Ruwisch R., Seitz H. J., and Conrad R. (1988) The capacity of hydrogenotrophic anaerobic bacteria to compete for traces of hydrogen depends on the redox potential of the terminal electron acceptor. *Arch. Microbiol.* **149**, 350–357.

Cornell R. M. and Schwertmann U. (1996) *The Iron Oxides*. VCH Verlagsgesellschaft mbH/VCH Publishers, Inc.

Coughlin B. R. and Stone A. T. (1995) Nonreversible adsorption of divalent metal ions (Mn-II, Co-II, Ni-II, Cu-II and Pb-II) onto goethite: Effects of acidification, Fe-II addition, and picolinic acid addition. *Environ. Sci. Technol.* **29**, 2445–2455.

Cozzarelli I. M., Herman J. S., Baedecker M. J., and Fischer J. M. (1999) Geochemical heterogeneity of a gasoline-contaminated aquifer. *J. Contam. Hydrol.* **40**, 261–284.

Cozzarelli I. M., Suflita J. M., Ulrich G. A., Harris S. H., Scholl M. A., Schlottmann J. L., and Christenson S. (2000) Geochemical and microbiological methods for evaluating anaerobic processes in an aquifer contaminated by landfill leachate. *Environ. Sci. Technol.* **34**, 4025–4033.

Crabtree B. and Nicholson B. (1988) Thermodyamics and metabolism. In *Biochemical Thermodynamics* (ed. M. Jones), pp. 347–395. Elsevier, Amsterdam.

Crosby H. A., Johnson C. M., Roden E. E., and Beard B. L. (2005) Fe(II)-Fe(III) electron/atom exchange as a mechanism for Fe isotope fractionation during dissimilatory iron oxide reduction. *Environ. Sci. Technol* **39**, 6698–6704.

Curtis G. P. (2003) Comparison of approaches for simulating reactive solute transport involving organic degradation reactions by multiple terminal electron acceptors. *Comput. Geosci.* **29**, 319–329.

Das A. and Caccavo F. (2000) Dissimiliatory Fe(III) oxide reduction by *Shewanella alga* BrY requires adhesion. *Curr. Microbiol.* **40**, 344–347.

Das A. and Caccavo F. (2001) Adhesion of the dissimilatory Fe(III)-reducing bacterium *Shewanella alga* BrY to crystalline Fe(III) oxides. *Curr. Microbiol.* **42**, 151–154.

Davis J. A. and Kent D. B. (1990) Surface complexation modeling in aqueous geochemistry. In *Mineral-water interface geochemistry* (ed. M. F. Hochella and A. F. White), pp. 177–260. Mineralogical Society of America.

Davis J. A., Yabusaki S. B., Steefel C. I., Zachara J. M., Curtis G. P., Redden G. D., Criscenti L. J., and Honeyman B. D. (2004) Assessing conceptual models for subsurface reactive transport of inorganic contaminants. *EOS* **85**, 449–455.

Dhakar S. P. and Burdige D. J. (1996) A coupled, non-linear, steady state model for early diagenetic processes In pelagic sediments. *AMJ* **296**, 296–330.

DiChristina T. J., Fredrickson J. K., and Zachara J. M. (2005) Enzymology of electron transport: Energy generation with geochemical consequences. In *Molecular Geomicrobiology*, Vol. 59 (ed. J. F. Banfield, J. Cervini-Silva, and K. H. Nealson), pp. 27–52. Mineralogical Society of America.

Dominik P. and Kaupenjohann M. (2004) Reduction of Fe(III) (Hydr)oxides with known thermodynamic stability by *Geobacter metallireducens*. *Geomicrobiol. J.* **21**, 287–295.

Dzombak D. A. and Morel F. M. M. (1990) *Surface Complexation Modeling: Hydrous Ferric Oxide*. John Wiley & Sons, New York.

Ehrlich H. L. (1999) Microbes as geologic agents: Their role in mineral formation. *Geomicrobiol. J.* **16**, 135–153.

Ehrlich H. L. (2002) *Geomicrobiology*. Marcel Dekker, New York.

Fein J. B., Daughney C. J., Yee N., and Davis T. A. (1997) A chemical equilibrium model for metal adsorption onto bacterial surfaces. *Geochim. Cosmochim. Acta* **61**, 3319–3328.

Fein J. B., Martin A. M., and Wightman P. G. (2001) Metal adsorption onto bacterial surfaces: Development of a predictive approach. *Geochim. Cosmochim. Acta* **65**, 4267–4273.

Fischer W. R. (1988) Microbiological reactions of iron in soils. In *Iron in soils and clay minerals* (ed. J. W. Stucki, B. A. Goodman, and U. Schwertmann), pp. 715–748. D. Reidel Publishing Co., Dordrecht.

Frankel R. B. and Bazylinski D. A. (2003) Biologically induced mineralization by bacteria. In *Biomineralization*, Vol. 55 (ed. P. M. Dove, J. J. DeYoreo, and S. Weiner), pp. 95–114. Mineralogical Society of America.

Gaillard J. F. and Rabouille C. (1992) Using Monod kinetics in geochemical models of organic carbon mineralization in deep-sea surficial sediments. In *Deep-Sea Food Chains and the Global Carbon Cycle* (ed. G. T. Rowe and V. Pariente), pp. 309–324. Kluwer Academic Publishing, Dordrecht.

Geesey G. G., Neal A. L., Suci P. A., and Peyton B. M. (2002) A review of spectroscopic methods for characterizing microbial transformation of minerals. *J. Microbiol. Meth.* **51**, 125–139.

Ghiorse W. C. (1988) Microbial reduction of manganese and iron. In *Biology of Anaerobic Microorganisms* (ed. A. J. B. Zehnder), pp. 305–331. John Wiley & Sons.

Gibson G. R., Parkes R. J., and Herbert R. A. (1987) Evaluation of viable counting procedures for the enumeration of sulfate-reducing bacteria in estuarine sediments. *J. Microbiol. Meth.* **7**, 201–210.

Glasauer S., Langley S., and Beveridge T. J. (2001) Sorption of Fe (hydr)oxides to the surface of *Shewanella putrefaciens*: Cell-bound fine-grained minerals are not always formed de novo. *Appl. Environ. Microbiol.* **67**, 5544–5550.

Gorby Y. A., Yanina S., McLean J. S., Rosso K. M., Moyles D., Dohnalkova A., Chang I. S., Kim B. H., Kim K. S., Culley D. E., Reed S. B., Romine M. F., Saffarini D. A., Hill E. A., Shi L., Elias D. A., Kennedy D. W., Pinchuk G., Watanabe K., Ishii S., Logan B., Nealson K. H., and Fredrickson J. K. (2006) Electrically conductive bacterial nanowires produced by *Shewanella oneidensis* MR-1 and other microorganisms. *Proc. Nat. Acad. Sci. USA* **103**, 11358–11363.

Gorham E. (1991) Biogeochemistry: Its origins and development. *Biogeochemistry* **13**, 199–239.

Grantham M. C., Dove P. M., and DiChristina T. J. (1997) Microbially catalyzed dissolution of iron and aluminum oxyhydroxide mineral surface coatings. *Geochim. Cosmochim. Acta* **61**, 4467–4477.

Hacherl E. L., Kosson D. S., and Cowan R. M. (2003) A kinetic model for bacterial Fe(III) oxide reduction in batch cultures. *Water Resour. Res.* **39**, Art. No. 1098.

Haldane J. B. S. (1930) *Enzymes*. Longman Green and Co., London.

Hansel C. M., Benner S. G., Neiss J., Dohnalkova A., Kukkadapu R. K., and Fendorf S. (2003) Secondary mineralization pathways induced by dissimilatory iron reduction of ferrihydrite under advective flow. *Geochim. Cosmochim. Acta* **67**, 2977–2992.

Hansel C. M., Benner S. G., Nico P., and Fendorf S. (2004) Structural constraints of ferric (hydr)oxides on dissimilatory iron reduction and the fate of Fe(II). *Geochim. Cosmochim. Acta* **68**, 3217–3229.

Hem J. D. (1972) Chemical factors that influence the availability of iron and manganese in aqueous systems. *Geol. Soc. Am. Bull.* **83**, 443–450.

Hering J. G. and Stumm W. (1990) Oxidative and reductive dissolution of minerals. In *Mineral-water interface geochemistry*, Vol. 23 (ed. M. F. Hochella and A. F. White), pp. 427–464. Mineralogical Society of America.

Hernandez M. E. and Newman D. K. (2001) Extracellular electron transfer. *CMLS Cell Mol Life Sci* **58**, 1562–1571.

Hernandez M. E., Kappler A., and Newman D. K. (2004) Phenazines and other redox active antibiotics promote microbial mineral reduction. *Appl. Environ. Microbiol.* **70**, 921–928.

Hines M. E., Faganeli J., and Planinc R. (1997) Sedimentary anaerobic microbial biogeochemistry in the Gulf of Trieste, northern Adriatic Sea: Influences of bottom water oxygen depletion. *Biogeochemistry* **39**, 65–86.

Ho C. Y. and Cord-Ruwisch R. (1996) A practical kinetic model that considers end-product inhibition in anaerobic digestion processes by including the equilibrium constant. *Biotechnol. Bioengin.* **51**, 597–604.

Hoehler T. M., Alperin M. J., Albert D. B., and Martens C. S. (1998) Thermodynamic control on hydrogen concentrations in anoxic sediments. *Geochim. Cosmochim. Acta* **62**, 1745–1756.

Humphrey A. E. (1972) The kinetics of biosystems: A review. In *Chemical Reactor Engineering*, Vol. 109 (ed. R. F. Gould), pp. 630–650. American Chemical Society.

Hunter K. S., Wang Y., and VanCappellen P. (1998) Kinetic modeling of microbially-driven redox chemistry of subsurface environments: Coupling transport, microbial metabolism and geochemistry. *J. Hydrol.* **209**, 53–80.

Icopini G. A., Anbar A. D., Ruebush S. S., Tien M., and Brantley S. L. (2004) Iron isotope fractionation during microbial reduction of iron: The importance of adsorption. *Geology* **32**, 205–208.

Jackson B. E. and McInerney M. J. (2002) Anaerobic microbial metabolism can proceed close to thermodynamic limits. *Nature* **415**, 454–456.

Jakobsen R., Albrechtsen H. J., Rasmussen M., Bay H., Bjerg P., and Christensen T. H. (1998) H_2 concentrations in a landfill leachate plume (Grindsted, Denmark): *In situ* energetics of terminal electron acceptor processes. *Environ. Sci. Technol.* **32**, 2142–2148.

Jakobsen R. and Postma D. (1999) Redox zoning, rates of sulfate reduction and interactions with Fe-reduction and methanogenesis in a shallow sandy aquifer, Romo, Denmark. *Geochim. Cosmochim. Acta* **63**, 137–151.

Jiang W., Saxena A., Song B., Ward B. B., Beveridge T. J., and Myneni S. C. B. (2004) Elucidation of functional groups on gram-positive and gram-negative bacterial surfaces using infrared spectroscopy. *Langmuir* **20**, 11433–11442.

Jin Q. and Bethke C. M. (2002) Kinetics of electron transfer through the respiratory chain. *Biophys. J.* **83**, 1797–1808.

Jin Q. and Bethke C. M. (2003) A new rate law describing microbial respiration. *Appl. Environ. Microbiol.* **69**, 2340–2348.

Jin Q. and Bethke C. M. (2005) Predicting the rate of microbial respiration in geochemical environments. *Geochim. Cosmochim. Acta* **69**, 1133–1143.

Jorgensen B. B. (1978) A comparison of methods for the quantification of bacterial sulfate reduction in coastal marine sediments I. Measurement with radiotracer techniques. *Geomicrobiol. J.* **1**, 11–28.

Keller M. and Zengler K. (2004) Tapping into microbial diversity. *Nat. Rev. Micro.* **2**, 141–150.

Klump J. V. and Martens C. S. (1987) Biogeochemical cycling in an organic-rich coastal marine basin 5. Sedimentary nitrogen and phosphorus budgets based upon kinetic models, mass balances, and the stoichiometry of nutrient regeneration. *Geochim. Cosmochim. Acta* **51**, 1161–1173.

Klump J. V. and Martens C. S. (1989) The seasonality of nutrient regeneration in an organic-rich coastal sediment: Kinetic modeling of changing pore-water nutrient and sulfate distributions. *Limnol. Oceanogr.* **34**, 559–577.

Kluyver A. J. (1957) Unity and diversity in the metabolism of micro-organisms. In *A.J. Kluyver: His Life and Work* (ed. A. F. Kamp, J. W. M. LaRiviere, and W. Verhoeven), pp. 186–210. North-Holland, Amsterdam.

Koch A. L. (1998) The Monod model and its alternatives. In *Mathematical Modeling in Microbial Ecology* (ed. A. L. Koch, J. A. Robinson, and G. A. Milliken). Chapman & Hall, London.

Komeili A., Li Z., Newman D. K., and Jensen G. J. (2006) Magnetosomes are cell membrane invaginations organized by the actin-likeprotein MamK. *Science* **311**, 242–245.

Kostka J. E. and Nealson K. H. (1995) Dissolution and reduction of magnetite by bacteria. *Environ. Sci. Technol.* **29**, 2535–2540.

Kostka J. E., Thamdrup B., Glud R. N., and Canfield D. E. (1999) Rates and pathways of carbon oxidation in permanently cold arctic sediments. *Mar. Ecol. Prog. Ser.* **180**, 7–21.

Kostka J. E., Roychoudhury A., and VanCappellen P. (2002) Rates and controls of anaerobic microbial respiration across spatial and temporal gradients in saltmarsh sediments. *Biogeochemistry* **60**, 49–76.

Kraemer S. M. and Hering J. G. (1997) Influence of solution saturation state on the kinetics of ligand-controlled dissolution of oxide phases. *Geochim. Cosmochim. Acta* **61**, 2855–2866.

Laidler K. J. (1987) *Chemical Kinetics*. Harper & Row, New York.

Larsen O. and Postma D. (2001) Kinetics of reductive bulk dissolution of lepidocrocite, ferrihydrite, and goethite. *Geochim. Cosmochim. Acta* **65**, 1367–1379.

Lasaga A. C. and Kirkpatrick R. J. (1981) Kinetics of Geochemical Processes. In *Reviews in Mineralogy and Geochemistry*, Vol. 8 (ed. P. H. Ribbe), pp. 398. Mineralogical Society of America.

Lasaga A. C. (1998) *Kinetic Theory in the Earth Sciences*. Princeton University Press, Princeton, NJ.

Lerman A. (1979) *Geochemical Processes – Water and Sediment Environments*. John Wiley & Sons, New York.

Lies D. P., Hernandez M. E., Kappler A., Mielke R. E., Gralnick J. A., and Newman D. K. (2005) *Shewanella oneidensis* MR-1 uses overlapping pathways for iron reduction at a distance and by direct contact under conditions relevant for biofilms. *Appl. Environ. Microbiol.* **71**, 4414–4426.

Liu C., Kota S., Zachara J. M., Fredrickson J. K., and Brinkman C. (2001a) Kinetic analysis of the bacterial reduction of goethite. *Environ. Sci. Technol.* **35**, 2482–2490.

Liu C., Zachara J. M., Gorby Y. A., Szecsody J. E., and Brown C. F. (2001b) Microbial reduction of Fe(III) and sorption/precipitation of Fe(II) on *Shewanella putrefaciens* strain CN32. *Environ. Sci. Technol.* **35**, 1385–1393.

Liu C., Gorby Y. A., Zachara J. M., Fredrickson J. K., and Brown C. F. (2002) Reduction kinetics of Fe(III), Co(III), U(VI), Cr(VI), Tc(VII) in cultures of dissimilatory metal reducing bacteria. *Biotechnol. Bioengin.* **80**, 637–649.

Lovley D. R. and Klug M. J. (1982) Intermediary metabolism of organic matter in the sediments of a eutrophic lake. *Appl. Environ. Microbiol.* **43**, 552–560.

Lovley D. R. (1985) Minimum threshold for hydrogen metabolism in methanogenic bacteria. *Appl. Environ. Microbiol.* **49**, 1530–1531.

Lovley D. R. and Klug M. J. (1986) Model for the distribution of sulfate reduction and methanogenesis in freshwater sediments. *Geochim. Cosmochim. Acta* **50**, 11–18.

Lovley D. R. and Phillips E. J. P. (1986a) Availability of ferric iron for microbial reduction in bottom sediments of the freshwater tidal Potomac River. *Appl. Environ. Microbiol.* **52**, 751–757.

Lovley D. R. and Phillips E. J. P. (1986b) Organic matter mineralization with reduction of ferric iron in anaerobic sediments. *Appl. Environ. Microbiol.* **51**, 683–689.

Lovley D. R. (1987) Organic matter mineralization with the reduction of ferric iron: A review. *Geomicrobiol. J.* **5**, 375–399.

Lovley D. R. and Phillips E. J. P. (1987) Rapid assay for microbially reducible ferric iron in aquatic sediments. *Appl. Environ. Microbiol.* **53**, 1536–1540.

Lovley D. R., Stolz J. F., Nord G. L., and Phillips E. J. P. (1987) Anaerobic production of magnetite by a dissimilatory iron-reducing microorganism. *Nature* **330**, 252–254.

Lovley D. R. and Goodwin S. (1988) Hydrogen concentrations as an indicator or the predominant terminal electron-accepting reactions in aquatic sediments. *Geochim. Cosmochim. Acta* **52**, 2993–3003.

Lovley D. R. and Phillips E. J. P. (1989) Requirement for a microbial consortium to completely oxidize glucose in Fe(III)-reducing sediments. *Appl. Environ. Microbiol.* **55**, 3234–3236.

Lovley D. R., Chapelle F. H., and Philips E. J. P. (1990) Fe(III)-reducing bacteria in deeply buried sediments of the Atlantic coastal plain. *Geology* **18**, 954–957.

Lovley D. R. (1991) Dissimilatory Fe(III) and Mn(IV) reduction. *Microbiol. Rev.* **55**, 259–287.

Lovley D. R. and Phillips E. J. P. (1991) Enzymatic versus nonenzymatic mechanisms for Fe(III) reduction in aquatic sediments. *Environ. Sci. Technol.* **25**, 1062–1067.

Lovley D. R. (1992) Microbial oxidation of organic matter coupled to the reduction of Fe(III) and Mn(IV) oxides. In *Biomineralization processes of iron and manganese*, Vol. 21 (ed. H. C. W. Skinner and R. W. Fitzpatrick), pp. 101–114. Catena Verlag.

Lovley D. R. (1993) Dissimilatory metal reduction. *Annu. Rev. Microbiol.* **47**, 263–290.

Lovley D. R. and Chapelle F. H. (1998) A modeling approach to elucidating the distribution and rates of microbially catalyzed redox reactions in anoxic groundwater. In *Mathematical Modeling in Microbial Ecology* (ed. A. L. Koch, J. A. Robinson, and G. A. Milliken), pp. 196–209. Chapman & Hall, London.

Lovley D. R. (2000a) Fe(III) and Mn(IV) reduction. In *Environmental Metal-Microbe Interactions* (ed. D. R. Lovley), pp. 3–30. ASM Press.

Lovley D. R. (2000b) Environmental Metal-Microbe Interactions, pp. 395. ASM Press.

Lovley D. R. (2002) Fe(III)- and Mn(IV)-reducing prokaryotes. In *The Prokaryotes* (ed. S. F. M. Dworkin, E. Rosenberg, K.H Schleifer, E. Stackebrandt), pp. [www

document]. URL http://et.springer-ny.com:8080/prokPUB/index.htm. Springer-Verlag, Berlin.

Lovley D. R. (2004) Potential role of dissimilatory iron reduction in the early evolution of microbial respiration. In *Origins, Evolution and Biodiversity of Microbial Life* (ed. J. Seckbach), pp. 301–313. Kluwer, Dordrecht.

Lovley D. R., Holmes D. E., and Nevin K. P. (2004) Dissimilatory Fe(III) and Mn(IV) Reduction. *Adv. Microbiol. Physiol.* **49**, 219–286.

Lowenstam H. A. (1981) Minerals formed by organisms. *Science* **211**, 1126–1131.

Lowenstam H. A. and Weiner S. (1989) *On Biomineralization*. Oxford University Press.

Lower S. K., Hochella M. F., and Beveridge T. J. (2001) Bacterial recognition of mineral surfaces: Nanoscale interactions between *Shewanella* and α-FeOOH. *Science* **292**, 1360–1363.

Madigan M. T., Martinko J. M., and Parker J. (2000) *Brock Biology of Microorganisms*. Prentice–Hall, Englewood Cliffs, NJ.

Madsen E. L. (2005) Identifying microorganisms responsible for ecologically significant biogeochemcial processes. *Nat. Rev. Microbiol.* **3**, 439–446.

Martens C. S. and Berner R. A. (1974) Methane production in the interstitial waters of sulfate depleted marine sediments. *Science* **185**, 1167–1169.

Maurer M. and Rittmann B. E. (2004) Formulation of the CBC-model for modelling the contaminants and footprints in natural attenuation of BTEX. *Biodegradation* **15**, 419–434.

Methe B. A., Nelson K. E., Eisen J. A., Paulsen I. T., Nelson W., Heidelberg J. F., Wu D., Wu M., Ward N., Beanan M. J., Dodson R. J., Madupu R., Brinkac L. M., Daugherty S. C., DeBoy R. T., Durkin A. S., Gwinn M., Kolonay J. F., Sullivan S. A., Haft D. H., Selengut J., Davidsen T. M., Zafar N., White O., Tran B., Romero C., Forberger H. A., Weidman J., Khouri H., Feldblyum T. V., Utterback T. R., Van Aken S. E., Lovley D. R., and Fraser C. M. (2003) Genome of *Geobacter sulfurreducens*: Metal reduction in subsurface environments. *Science* **302**, 1967–1969.

Michaelis L. and Menten M. M. (1913) Die Kinetik der Invertingwirkung (The kinetics of invertase activity). *Biochem. Z.* **49**, 333–369.

Molz F. J., Widdowson M. A., and Benefield L. D. (1986) Simulation of microbial growth dynamics coupled to nutrient and oxygen transport in porous media. *Water Resour. Res.* **22**, 1207–1216.

Monod J. (1942) *Recherches sur las croissance des culture bacteriennes (Research on the growth of bacterial cultures)*. Hermann et Cie.

Monod J. (1949) The growth of bacterial cultures. *Annu. Rev. Microbiol.* **3**, 371–394.

Moskowitz B. M., Frankel R. B., Bazylinski D. A., Jannasch H. W., and Lovley D. R. (1989) A comparison of magnetite particles produced anaerobically by magnetotactic and dissimilatory iron-reducing bacteria. *Geophys. Res. Lett.* **16**, 665–668.

Munch J. C. and Ottow J. C. G. (1980) Preferential reduction of amorphous to crystalline iron oxides by bacterial activity. *Soil Sci.* **129**, 15–21.

Munch J. C. and Ottow J. C. G. (1983) Reductive transformation mechanism of ferric oxides in hydromorphic soils. *Ecol. Bull.* **35**, 383–394.

Nealson K. H. and Stahl D. A. (1997) Microorganisms and biogeochemical cycles: What can we learn from layered microbial communities? In *Geomicrobiology: Interactions Between Microbes and Minerals*, Vol. 35 (ed. J. F. Banfield and K. H. Nealson), pp. 5–34. Mineralogical Society of America.

Nealson K. H., Ghiorse W. A., and Strauss E. (2001) Geobiology: Exploring the interface between the biosphere and the geosphere (A Report from the American Academy of Microbiology). American Academy of Microbiology, Washington, DC. (Available at: http://www.asm.org/Academy/index.asp?bid = 2132.)

Nevin K. P. and Lovley D. R. (2002) Mechanisms of Fe(III) oxide reduction in sedimentary environments. *Geomicrobiol. J.* **19**, 141–159.

Newman D. K. and Banfield J. F. (2002) Geomicrobiology: How molecular-scale interactions underpin biogeochemical systems. *Science* **296**, 1071–1077.

Oremland R. S., Capone D. G., Stolz J. F., and Fuhrman J. (2005) Whither or wither geomicrobiology in the era of 'community metagenomics'. *Nat. Rev. Microbiol.* **3**, 572–578.

Ottow J. C. G. (1968) Evaluation of iron-reducing bacteria in soil and the physiological mechanism of iron reduction in Aerobacter aerogenes. *Z. Alig. Mikrobiol* **8**, 441–443.

Ottow J. C. G. (1971) Iron reduction and gley formation by nitrogen-fixing *Clostridia*. *Oecologia* **6**, 164–175.

Ottow J. C. G. and Glathe H. (1971) Isolation and identification of iron-reducing bacteria from gley soils. *Soil Biol. Biochem.* **3**, 43–55.

Pasteur L. (1860) Experiences relatives aux generations spontanees. *Compt. Rend. Acad. Sci* **50**, 303–675.

Penn R. L., Zhu C., Xu H., and Veblen D. R. (2001) Iron oxide coatings on sand grains from the Atlantic coastal plain: High-resolution transmission electron microscopy characterization. *Geology* **29**, 843–846.

Peters R. H. (1983) *The Ecological Implications of Body Size*. Cambridge University Press.

Phillips E. J. P., Lovley D. R., and Roden E. E. (1993) Composition of non-microbially reducible Fe(III) in aquatic sediments. *Appl. Environ. Microbiol.* **59**, 2727–2729.

Ponnamperuma F. N. (1972) The chemistry of submerged soils. *Adv. Agron.* **24**, 29–96.

Postma D. (1993) The reactivity of iron oxides in sediments: A kinetic approach. *Geochim. Cosmochim. Acta* **57**, 5027–5034.

Postma D. and Jakobsen R. (1996) Redox zonation: Equilibrium constraints on the Fe(III)/S04-reduction interface. *Geochim. Cosmochim. Acta* **60**, 3169–3175.

Press W. H., Teukolsky S. A., Vetterling W. T., and Flannery B. P. (1992) *Numerical Recipes in FORTRAN*. Cambridge University Press.

Ramsing N. R., Fossing H., Ferdelman T. G., Andersen F., and Thamdrup B. (1996) Distribution of bacterial populations in a stratified fjord (Mariager Fjord,

Denmark) quantified by in situ hybridization and related to chemical gradients in the water column. *Appl. Environ. Microbiol.* **62**, 1391–1404.

Rawn J. D. (1983) *Biochemistry*. Harper and Row, New York.

Reguera G., McCarthy K. D., Mehta T., Nicoll J. S., Tuominen M. T., and Lovley D. R. (2005) Extracellular electron transfer via microbial nanowires. *Nature* **435**, 1098–1101.

Revsbech N. P. and Jorgensen B. B. (1986) Microelectrodes: Their use in microbial ecology. In *Advanced Microbial Ecology*, Vol. 9 (ed. K. C. Marshall), pp. 293–352. Plenum Press, New York.

Richardson D. J. (2000) Bacterial respiration: A flexible process for a changing environment. *Microbiology* **146**, 551–571.

Rickenberg H. V., Cohen G. N., Buttin G., and Monod J. (1956) La galactoside permease d'*Escherichia coli*. *Ann. Inst. Pasteur* **91**, 829–857.

Rittmann B. E. and VanBriesen J. M. (1996) Microbiological processes in reactive transport modeling. In *Reactive Transport in Porous Media*, Vol. 34 (ed. P. C. Lichtner, C. I. Steefel, and E. H. Oelkers), pp. 311–334. The Mineralogical Society of America.

Rittmann B. E. and McCarty P. L. (2001) *Environmental Biotechnology*. McGraw-Hill, New York.

Roden E. E. and Lovley D. R. (1993a) Evaluation of ^{55}Fe as a tracer of Fe(III) reduction in aquatic sediments. *Geomicrobiol. J.* **11**, 49–56.

Roden E. E. and Lovley D. R. (1993b) Dissimilatory Fe(III) reduction by the marine microorganism *Desulfuromonas acetoxidans*. *Appl. Environ. Microbiol.* **59**, 734–742.

Roden E. E. and Tuttle J. H. (1993) Inorganic sulfur turnover in oligohaline estuarine sediments. *Biogeochemistry* **22**, 81–105.

Roden E. E. and Tuttle J. H. (1996) Carbon cycling in mesohaline Chesapeake Bay sediments 2: Kinetics of particulate and dissolved organic carbon turnover. *J. Mar. Sci.* **54**, 343–383.

Roden E. E. and Wetzel R. G. (1996) Organic carbon oxidation and suppression of methane production by microbial Fe(III) oxide reduction in vegetated and unvegetated freshwater wetland sediments. *Limnol. Oceanogr.* **41**, 1733–1748.

Roden E. E. and Zachara J. M. (1996) Microbial reduction of crystalline iron(III) oxides: Influence of oxide surface area and potential for cell growth. *Environ. Sci. Technol.* **30**, 1618–1628.

Roden E. E. and Edmonds J. W. (1997) Phosphate mobilization in iron-rich anaerobic sediments: Microbial Fe(III) oxide reduction versus iron-sulfide formation. *Arch. Hydrobiol.* **139**, 347–378.

Roden E. E. and Urrutia M. M. (1999) Ferrous iron removal promotes microbial reduction of crystalline iron(III) oxides. *Environ. Sci. Technol.* **33**, 1847–1853.

Roden E. E., Urrutia M. M., and Mann C. J. (2000) Bacterial reductive dissolution of crystalline Fe(III) oxide in continuous-flow column reactors. *Appl. Environ. Microbiol.* **66**, 1062–1065.

Roden E. E., Leonardo M. R., and Ferris F. G. (2002) Immobilization of strontium during iron biomineralization coupled to dissimilatory hydrous ferric oxide reduction. *Geochim. Cosmochim. Acta* **66**, 2823–2839.

Roden E. E. and Urrutia M. M. (2002) Influence of biogenic Fe(II) on bacterial reduction of crystalline Fe(III) oxides. *Geomicrobiol. J.* **19**, 209–251.

Roden E. E. and Wetzel R. G. (2002) Kinetics of microbial Fe(III) oxide reduction in freshwater wetland sediments. *Limnol. Oceanogr.* **47**, 198–211.

Roden E. E. (2003a) Fe(III) oxide reactivity toward biological versus chemical reduction. *Environ. Sci. Technol.* **37**, 1319–1324.

Roden E. E. (2003b) Diversion of electron flow from methanogenesis to crystalline Fe(III) oxide reduction in acetate-limited cultures of wetland sediment microorganisms. *Appl. Environ. Microbiol.* **69**, 5702–5706.

Roden E. E. and Wetzel R. G. (2003) Competition between Fe(III)-reducing and methanogenic bacteria for acetate in iron-rich freshwater sediments. *Microb. Ecol.* **45**, 252–258.

Roden E. E. (2004) Analysis of long-term bacterial versus chemical Fe(III) oxide reduction kinetics. *Geochim. Cosmochim. Acta* **68**, 3205–3216.

Roden E. E. (2005) Unpublished data.

Roden E. E. and Scheibe T. D. (2005) Conceptual and numerical model of uranium(VI) reductive immobilization in fractured subsurface sediments. *Chemosphere* **59**, 617–628.

Roden E. E. (2006) Geochemical and microbiological controls on dissimilatory iron reduction. *C.R. Geosci.* **338**, 456–467.

Roels J. A. (1983) *Energetics and Kinetics in Biotechnology*. Elsevier Biomedical Press, Amsterdam.

Rooney-Varga J. N., Anderson R. T., Fraga J. L., Ringelberg D., and Lovley D. R. (1999) Microbial communities associated with anaerobic benzene degradation in a petroleum-contaminated aquifer. *Appl. Environ. Microbiol.* **65**, 3056–3063.

Ruebush S. S., Brantley S. L., and Tien M. (2006a) Reduction of soluble and insoluble iron forms by membrane fractions of *Shewanella oneidensis* grown under aerobic and anaerobic conditions. *Appl. Environ. Microbiol.* **72**, 2925–2935.

Ruebush S. S., Icopini G. A., Brantley S. L., and Tien M. (2006b) In vitro reduction kinetics of mineral oxides by membrane fractions of *Shewanella oneidensis* MR-1. *Geochim. Cosmochim. Acta* **70**, 56–70.

Scheffel A., Gruska M., Faive D., Linaroudisn A., Graumann P. L., Plitzko J. M., and Schuler D. (2006) An acidic protein aligns magnetosomes along a filamentous structure in magnetotactic bacteria. *Nature*.

Schink B. (1997) Energetics of syntrophic cooperation in methanogenic degradation. *Microbiol. Mol. Biol. Rev.* **61**, 262–280.

Schnoor J. L. (1996) *Environmental Modeling*. Wiley Interscience, New York.

Schultze-Lam S., Fortin D., Davis B. S., and Beveridge T. J. (1996) Mineralization of bacterial surfaces. *Chem. Geol.* **132**, 171–181.

Snoeyenbos-West O. L., Nevin K. P., Anderson R. T., and Lovley D. R. (2000) Enrichment of *Geobacter* species in response to stimulation of Fe(III) reduction in sandy aquifer sediments. *Microb. Ecol.* **39**, 153–167.

Soetaert K., Herman P. M. J., and Middelburg J. J. (1996) A model of early diagenetic processes from the shelf to abyssal depths. *Geochim. Cosmochim. Acta* **60**, 1019–1040.

Sorensen J., Christensen D., and Jorgensen B. B. (1981) Volatile fatty acids and hydrogen as substrates for sulfate-reducing bacteria in anaerobic marine sediment. *Appl. Environ. Microbiol.* **42**, 5–11.

Sorensen J. (1982) Reduction of ferric iron in anaerobic, marine sediment and interaction with reduction of nitrate and sulfate. *Appl. Environ. Microbiol.* **43**, 319–324.

Southam G. (2000) Bacterial surface-mediated mineral formation. In *Environmental Metal-Microbe Interactions* (ed. D. R. Lovley), pp. 257–276. ASM Press, Washington.

Sparks N. H. C., Mann S., Bazylinskio D. A., Lovley D. R., Jannasch H. W., and Frankel R. B. (1990) Structure and morphology of magnetite anaerobically-produced by a marine magnetotactic bacterium and a dissimilatory iron-reducing bacterium. *Earth Planet. Sci. Lett.* **98**, 14–22.

Starkey R. L. and Halvorson H. O. (1927) Studies on the transformations of iron in nature. II. Concerning the importance of microorganisms in the solution and precipitation of iron. *Soil Sci.* **24**, 381–402.

Stone A. T. and Morgan J. J. (1987) Reductive dissolution of metal oxides. In *Aquatic Surface Chemistry* (ed. W. Stumm), pp. 221–254. John Wiley & Sons, New York.

Stults J. R., Snoeyenbos-West O., Methe B., Lovley D. R., and Chandler D. P. (2001) Application of the 5′ fluorogenic exonuclease assay (TaqMan) for quantitative ribosomal DNA and rRNA analysis in sediments. *Appl. Environ. Microbiol.* **67**, 2781–2789.

Stumm W. (1990) Aquatic Chemical Kinetics: Reaction Rates of Processes in Natural Waters, pp. 545. Wiley-Interscience, New York.

Stumm W. and Sulzberger B. (1992) The cycling of iron in natural environments: Considerations based on laboratory studies of heterogeneous redox processes. *Geochim. Cosmochim. Acta* **56**, 3233–3257.

Stumm W. and Morgan J. J. (1996) *Aquatic Chemistry*. John Wiley & Sons, New York.

Sulzberger B., Suter D., Siffert C., Banwart S., and Stumm W. (1989) Dissolution of Fe(III) (hydr)oxides in natural waters; Laboratory assessment on the kinetics controlled by surface coordination. *Mar. Chem.* **28**, 127–144.

Suter D., Banwart S., and Stumm W. (1991) Dissolution of hydrous iron(III) oxides by reductive mechanisms. *Langmuir* **7**, 809–813.

Thamdrup B., Fossing H., and Jorgensen B. B. (1994) Manganese, iron, and sulfur cycling in a coastal marine sediment, Aarhus Bay, Denmark. *Geochim. Cosmochim. Acta* **58**, 5115–5129.

Thamdrup B. (2000) Bacterial manganese and iron reduction in aquatic sediments. *Adv. Microb. Ecol.* **16**, 41–84.

Tiedje J. M. (1988) Ecology of denitrification and dissimilatory nitrate reduction to ammonium. In *Biology of Anaerobic Microorganisms* (ed. A. J. B. Zehnder). John Wiley & Sons, New York.

Truex M. J., Peyton B. M., Valentine N. B., and Gorby Y. A. (1997) Kinetics of U(VI) reduction by a dissimilatory Fe(III)-reducing bacterium under non-growth conditions. *Biotech. Bioengin.* **55**, 490–496.

Tuccillo M. E., Cozzarelli I. M., and Herman J. S. (1999) Iron reduction in the sediments of a hydrocarbon-contaminated aquifer. *Appl. Geochem.* **14**, 655–667.

Urrutia M. M., Roden E. E., Fredrickson J. K., and Zachara J. M. (1998) Microbial and geochemical controls on synthetic Fe(III) oxide reduction by *Shewanella alga* strain BrY. *Geomicrobiol. J.* **15**, 269–291.

Urrutia M. M., Roden E. E., and Zachara J. M. (1999) Influence of aqueous and solid-phase Fe(II) complexants on microbial reduction of crystalline Fe(III) oxides. *Environ. Sci. Technol.* **33**, 4022–4028.

vanBodegom P. M., Scholten J. C. M., and Stams A. J. M. (2004) Direct inhibition of methanogenesis by ferric iron. *FEMS Microb. Ecol.* **49**, 261–268.

VanCappellen P., Gaillard J., and Rabouille C. (1993) Biogeochemical transformations in sediments: Kinetic models of early diagenesis. *NATO ASI Series* **1 4**, 401–445.

VanCappellen P. and Wang Y. (1995) Metal cycling in surface sediments: Modeling the interplay of transport and reaction. In *Metal Contaminated Aquatic Sediments* (ed. H. E. Allen), pp. 21–64. Ann Arbor Press, Chelsea, MI.

VanCappellen P. and Gaillard J. F. (1996) Biogeochemical dynamics in aquatic sediments. In *Reactive Transport in Porous Media*, Vol. 34 (ed. P. C. Lichtner, C. I. Steefel, and E. H. Oelkers), pp. 335–376. The Mineralogical Society of America.

VanCappellen P. and Wang Y. (1996) Cycling of iron and manganese in surface sediments: A general theory for the coupled transport and reaction of carbon, oxygen, nitrogen, sulfur, iron, and manganese. *Am. J. Sci.* **296**, 197–243.

Vanderzee C., Roberts D. R., Rancourt D. G., and Slomp C. P. (2003) Nanogoethite is the dominant reactive oxyhydroxide phase in lake and marine sediments. *Geology* **31**, 993–996.

Vargas M., Kashefi K., Blunt-Harris E. L., and Lovley D. R. (1998) Microbiological evidence for Fe(III) reduction on early Earth. *Nature* **395**.

Vester F. and Invorsen K. (1998) Improved most-probable-number method to detect sulfate-reducing bacteria with natural media and a radiotracer. *Appl. Environ. Microbiol.* **64**, 1700–1707.

Visscher P. T., Reid R. P., Bebout B. M., Hoeft S. E., MacIntyre I. G., and Thompson J. A. (1998) Formation of lithified micritic laminae in modern marine stromatolites (Bahamas): The role of sulfur cycling. *Am. Min.* **83**, 1482–1493.

Vroblesky D. A., Bradley P. M., and Chapelle F. H. (1997) Lack of correlation between organic acid concentrations and predominant electron-accepting processes in a contaminated aquifer. *Environ. Sci. Technol.* **31**, 1416–1418.

Walker J. C. G. (1984) Suboxic diagenesis in banded iron formations. *Nature* **309**, 340–342.

Walker J. C. G. (1987) Was the archaean biosphere upside down? *Nature* **329**, 710–712.

Wallmann K., Hennies K., Konig I., Petersen W., and Knauth H. D. (1993) New procedure for determining reactive Fe(III) and Fe(II) minerals in sediments. *Limnol. Oceanogr.* **38**, 1803–1812.

Wang Y. and VanCappellen P. (1996) A multicomponent reactive transport model of early diagenesis: Application to redox cycling in coastal marine sediments. *Geochim. Cosmochim. Acta* **60**, 2993–3014.

Watson I. A., Oswald S. E., Mayer R. U., Wu Y., and Banwart S. A. (2003) Modeling kinetic processes controlling hydrogen and acetate concentrations in an aquifer-derived microcosm. *Environ. Sci. Technol.* **37**, 3910–3919.

Weber K. A., Churchill P. F., Urrutia M. M., Kukkadapu R. K., and Roden E. E. (2006) Anaerobic redox cycling of iron by wetland sediment microorganisms. *Environ. Microbiol.* **8**, 100–113.

Weiner S. and Dove P. M. (2003) An overview of biomineralization processes and the problem of the vital effect. In *Biomineralization*, Vol. 54 (ed. P. M. Dove, J. J. DeYoreo, and S. Weiner), pp. 1–29. Mineralogical Society of America.

Westall J. C. (1986) MICROQL I. A chemical equilibrium program in BASIC. Report 86–02, Department of Chemistry, Oregon State University, Corvalis, OR.

Westrich J. T. and Berner R. A. (1984) The role of sedimentary organic matter in bacterial sulfate reduction: The G model tested. *Limnol. Oceanogr.* **29**, 236–249.

Widdowson M. A., Molz F. J., and Benefield L. D. (1988) A numerical transport model of oxygen- and nitrate-based respiration linked to substrate and nutrient availability in porous media. *Water Resour. Res.* **24**, 1553–1565.

Williams A. G. B. and Scherer M. M. (2004) Spectroscopic evidence for Fe(II)-Fe(III) electron transfer at the iron oxide-water interface. *Environ. Sci. Technol.* **38**, 4782–4790.

Wirtz K. A. (2003) Control of biogeochemical cycling by mobility and metabolic strategies of microbes in sediments: An integrated model study. *FEMS Microb. Ecol.* **46**, 295–306.

Woese C. R., Kandler O., and Wheelis M. L. (1990) Toward a natural system of organisms: Proposal for the domains Archaea, Bacteria, and Eucarya. *Proc. Nat. Acad. Sci. USA* **87**, 4576–4579.

Yee N. and Fein J. (2001) Cd adsorption onto bacterial surfaces: A universal adsorption edge? *Geochim. Cosmochim. Acta* **65**, 2037–2042.

Zachara J. M., Kukkadapu R. K., Fredrickson J. K., Gorby Y. A., and Smith S. C. (2002) Biomineralization of poorly crystalline Fe(III) oxides by dissimilatory metal reducing bacteria (DMRB). *Geomicrobiol. J.* **19**, 179–207.

Zehnder A. J. B. and Stumm W. (1988) Geochemistry and biogeochemistry of anaerobic habitats. In *Biology of Anaerobic Microorganisms* (ed. A. J. B. Zehnder), pp. 1–38. John Wiley & Sons, New York.

Chapter 9
Microbiological Controls on Geochemical Kinetics 2: Case Study on Microbial Oxidation of Metal Sulfide Minerals and Future Prospects

Eric E. Roden

9.1 Case Study #2 – Microbial Oxidation of Metal Sulfide Minerals

9.1.1 Introduction

Sulfide minerals are components of magmatic, igneous, and sedimentary rocks, as well as hydrothermal deposits (ore bodies). They are exploited economically as sources of sulfuric acid and metals, such as Co, Cu, Au, Ni, and Zn that are present either as discrete sulfide phases (e.g., CuS, Cu_2S, NiS, ZnS) or coprecipitates with major iron-sulfide phases such as FeS_2 (e.g., chalcopyrite, $CuFeS_2$). However, in many situations, sulfide minerals (in particular FeS_2, the most abundant sulfide phase in most mineral deposits) are waste ("gangue") phases associated with mining and metallurgical operations. Exposure of these phases to atmospheric O_2 during and after such operations causes acid mine/acid rock drainage (referred to hereafter simply as acid mine drainage or AMD; see Table 9.1 for a list of abbreviations), an environmental problem of major environmental concern (Evangelou and Zhang, 1995). A vast amount of research has been conducted on the mechanisms and controls on sulfide mineral oxidation for the purposes of (i) understanding and predicting environmental risk associated with AMD; (ii) understanding sulfur and metal cycling associated with natural sulfide mineral weathering; and (iii) optimizing commercial recovery of metals from low-grade ores and wastes. Microorganisms play a pivotal role in sulfide mineral oxidation, and this phenomenon represents another premier example of how microbial activity exerts fundamental control on water–rock interaction phenomena.

In this case study, the basic chemistry of metal sulfide minerals is reviewed, and the role of microbial processes in sulfide mineral oxidation is summarized in the

University of Wisconsin, Department of Geology and Geophysics, eroden@geology.wisc.edu

Table 9.1 List of abbreviations used in this chapter

Abbreviation	Meaning
AMD	Acid mine drainage
DIR	Dissimilatory iron oxide reduction
DIRM(s)	Dissimilatory iron oxide-reducing microorganism(s)
EA(s)	Electron acceptor(s)
EPS	Extracellular polysaccharide
FeOM(s)	Fe(II)-oxidizing microorganism(s)
Morg(s)	Microorganism(s)
SA	Surface area
SOM(s)	Sulfur-oxidizing microorganism(s)

context of recent experimental and analytical information. A kinetic model of coupled aqueous and solid-phase geochemical reactions is then developed to illustrate the role of microbial processes in FeS_2 oxidation, including a diffusion-reaction model of processes occurring at the mineral–water interface.

9.1.2 Influence of Sulfide Mineral Electronic Configuration on Dissolution/Oxidation Pathway

Differences in the electronic configuration of different metal sulfide phases have a fundamental influence on the pathway of and reactivity of such phases toward oxidative dissolution (Crundwell, 1988; Tributsch and Bennett, 1981a). These differences are briefly summarized here in order to set the stage for later detailed considerations of FeS_2 oxidation kinetics. Metal sulfides whose valance bands are derived from both metal and sulfide orbitals (e.g., CdS, CoS, CuS, FeS, NiS, PbS, ZnS) are generally acid-soluble (i.e., they are subject to proton-promoted dissolution). The initial end-product of acid dissolution of these minerals is the divalent metal ion and H_2S. In the presence of O_2 and $Fe^{3+}_{(aq)}$, H_2S is converted rapidly to element sulfur (S^0) via polysulfide intermediates (Stuedel, 1996). Because of the ability of $Fe^{3+}_{(aq)}$ to disrupt metal sulfide bonds more effectively than protons (Tributsch and Bennett, 1981a, b), acid-soluble sulfides may be converted directly to S^0 in the presence of $Fe^{3+}_{(aq)}$ via an overall reaction such as

$$MeS + 2Fe^{3+} \rightarrow Me^{2+} + S^0 + 2Fe^{2+} \tag{9.1}$$

where Me represents the metal in the sulfide mineral. The Fe^{2+} and S^0 formed by this reaction are energy substrates for lithotrophic acidophilic morgs (Eqs. (9.7)–(9.9) below). Even in the absence of Fe, sulfur-oxidizing organisms such as *A. ferrooxidans* can oxidize acid-soluble metal sulfides by virtue of their ability to generate protons during S^0 oxidation (Sakaguchi et al., 1976; Torma and Sakaguchi, 1978; Tributsch and Bennett, 1981a). The leaching rate of such phases is correlated

with their solubility products (Torma and Sakaguchi, 1978; Tributsch and Bennett, 1981b).

In contrast to the monosulfide minerals discussed above, the valence bands of metal disulfide phases, such as FeS_2, MoS_2, and WS_2 are derived only from their metal orbitals, and thus do not contribute to the chemical bond between the metal and sulfur moieties of the crystal (Crundwell, 1988; Schippers and Sand, 1999; Tributsch and Bennett, 1981a). As a result, these metal sulfides are not acid-soluble, and are therefore dissolved only via oxidation, e.g., by O_2 or (more importantly) $Fe^{3+}_{(aq)}$. FeS_2 is a semiconductor, and its oxidation can be treated as an electrochemical process composed of anodic and cathodic reactions that are linked through electron transfer processes within the mineral surface structure (Rimstidt and Vaughan, 2003; Williamson and Rimstidt, 1994). The relevant overall anodic and cathodic reactions are as follows:

$$\text{Anodic}: FeS_2 + 8H_2O \rightarrow Fe^{2+} + 2SO_4^{2-} + 16H^+ + 14e^- \quad (9.2)$$

$$\text{Cathodic}: 14e^- + 3.5O_2 + 14H^+ \rightarrow 7H_2O \quad (9.3)$$

$$14Fe^{3+} + 14e^- \rightarrow 14Fe^{2+} \quad (9.4)$$

which yield the following overall coupled reactions:

$$FeS_2 + 3.5O_2 + H_2O \rightarrow Fe^{2+} + 2SO_4^{2-} + 2H^+ \quad (9.5)$$

$$FeS_2 + 14Fe^{3+} + 8H_2O \rightarrow 15Fe^{2+} + 2SO_4^{2-} + 16H^+ \quad (9.6)$$

Surface-area normalized rates of FeS_2 oxidation by Fe^{3+} (assuming $[Fe^{3+}] = [Fe^{2+}] = [O_2] = 0.2\,\text{mM}$) are ca. 2 orders of magnitude higher than those for oxidation by O_2 at pH 2 (Williamson and Rimstidt, 1994), and thus Fe^{3+} is the dominant oxidant for FeS_2 in Fe^{3+}-rich solutions. Although the details of the reaction mechanism of FeS_2 oxidation are beyond the scope of this chapter (see Rimstidt and Vaughn (2003) for an up-to-date review), two key features are relevant in terms of microbial catalysis. First, both O_2 and $Fe^{3+}_{(aq)}$ are capable of nearly stoichiometric oxidation of FeS_2 to Fe^{2+} and $SO_4{}^{2-}$ at sub-neutral pH (Boon and Heijnen, 1998a; Holmes and Crundwell, 2000; McKibben and Barnes, 1986; Moses et al., 1987; Nicholson et al., 1988; Schippers and Sand, 1999; Williamson and Rimstidt, 1994). The fact that $Fe^{3+}_{(aq)}$ can function as an effective oxidant means that enzymatic oxidation of $Fe^{2+}_{(aq)}$ at low pH can alone sustain FeS_2 oxidation (this is the "indirect" oxidation mechanism discussed in more detail below), and explains why organisms such as *Leptospirillum ferrooxidans*, which is a very effective Fe(II) oxidizer but cannot metabolize reduced S, is able to oxidize FeS_2 (Sand et al., 1992). Second, $S_2O_3{}^{2-}$ is a key transient intermediate in the FeS_2 oxidation process, which reacts rapidly with $Fe^{2+}_{(aq)}$ to form tetrathionite that subsequently decomposes (e.g., through polysulfide intermediates) to S^0, sulfate, and traces of tri- and pentathionite (see Schippers et al. (1996) and references therein). This sequence of reactions accounts for the commonly observed (e.g., through wet-chemical analysis, electron microscopy, or Raman spectroscopy) accumulation of small but significant quantities of polysulfides and/or S^0 during abiotic

and microbially catalyzed FeS_2 oxidation (Edwards et al., 2001a; McGuire et al., 2001a; Rojas-Chapana et al., 1995; Schippers et al., 1996; Schippers and Sand, 1999). This accumulation of S^0 is significant in that it provides an ecological niche for acidophilic morgs that are capable of sulfur oxidation, and in turn provides the basis for the "cooperative leaching" model for FeS_2 oxidation discussed below.

9.1.3 Microbial Participation in Sulfide Mineral Oxidation

Microorganisms participate in metal sulfide oxidation in several ways (Nordstrom and Southam, 1997). First, they oxidize Fe^{2+} ions released during mineral dissolution, which regenerates $Fe^{3+}{}_{(aq)}$ that can catalyze further mineral oxidative dissolution:

$$Fe^{2+}{}_{(aq)} + 0.25O_2 + H^+ \rightarrow Fe^{3+}{}_{(aq)} + 0.5H_2O \tag{9.7}$$

Second, they oxidize reduced sulfur compounds (e.g., S^0) generated as side products during sulfide mineral dissolution with either O_2 or $Fe^{3+}{}_{(aq)}$ as an EA:

$$S^0 + 1.5O_2 + H_2O \rightarrow SO_4^{2-} + 2H^+ \tag{9.8}$$

$$S^0 + 6Fe^{3+} + 4H_2O \rightarrow SO_4^{2-} + 6Fe^{2+} + 8H^+ \tag{9.9}$$

A wide range of acidophilic autotrophic and heterotrophic morgs (both bacteria and archeae) are capable of catalyzing reactions (Eqs. 9.7–9.9). Blake and Johnson (2000), Ehrlich (2002), and Rawlings (2002) provide overviews of the phylogenetic and physiological characteristics and diversity of such organisms. The well-known acidophile *Acidithiobacillus ferrooxidans* (formerly known as *Thiobacillus ferrooxidans*; Kelly and Wood (2000)) is an example of a lithoautotrophic morg that is capable of catalyzing all 3 of the reactions listed above. The key point is that the enzymatic activity catalyzes reactions that are strongly kinetically hindered under conditions typical of metal sulfide-oxidizing environments. Most importantly, the rate of Fe(II) oxidation by O_2 is very slow at pH values below 4 (Singer and Stumm, 1972) and potential rates of microbially catalyzed oxidation are many orders of magnitude higher (Fig. 9.1). Thus, enzymatic catalysis of Fe(II) oxidation is a critical step in Fe-mediated electron and proton transfer during metal sulfide oxidation (Eqs. (9.1), (9.6), and (9.9)). Quantitative calculations based on cell-specific rates of Fe(II) oxidation suggest that microbial catalysis is responsible for ca. 75% of total AMD release from the Richmond Mine at Iron Mountain, CA (Edwards et al., 2001a).

In addition to the crucial role of morgs in Fe(II) oxidation at low pH, microbial oxidation of reduced S compounds contributes to production of acidity, which helps to maintain the stability of both Fe(II) (as an energy source) and Fe(III) (as a chemical oxidant) in solution (note that oxidation of $Fe^{2+}_{(aq)}$ consumes acidity;

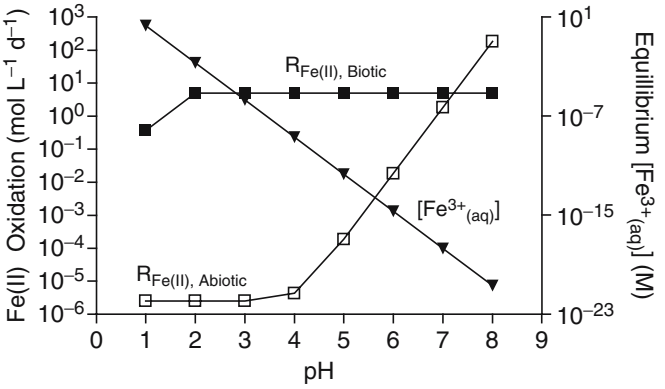

Fig. 9.1 Rates of abiotic and biotic $Fe^{2+}_{(aq)}$ oxidation as a function of solution pH. Abiotic rates were computed according to equation 12 in the text, assuming P_{O2} = 0.159 atm (equivalent to 2 $\times$ 10^{-4} M dissolved O_2) and $[Fe^{2+}_{(aq)}] = 10^{-2}$M. Biotic rates were computed according to equation 2 in Table 2 using kinetic parameters for *A. ferrooxidans* from Boon et al. (1998). Equilibrium $[Fe^{3+}_{(aq)}]$ values were computed as a function of pH assuming a log K value of 3.3 for Fe(III) oxyhydroxide

see Eq. (9.7)). Edwards et al. (2000a; 2001a) argued that microbial oxidation of S^0 formed on FeS_2 surfaces is ultimately the rate-limiting step in the generation of acidity during FeS_2 oxidation. By analogy, Schippers and Sand (1999) point out the possibility that formation of AMD could be reduced if S^0 oxidation could be retarded. It is important in this regard that the electrochemical properties of metal sulfides may change with the accumulation of S^0 on the mineral surface. Retardation of ZnS and $CuFeS_2$ dissolution through formation of S^0 layers on the mineral surface in the absence of SOMs has been reported for relatively low-redox potential (Fe(II)-rich) reaction systems (Bevilaqua et al., 2002; Fowler and Crundwell, 1999). In addition, several studies have suggested that formation of an S^0 layer might retard further oxidation by blocking access of oxidants to the mineral surface (Curutchet et al., 1996; Dopson and Lindstrom, 1999; Garcia et al., 1995a, b). However, comparable rates of sulfide mineral oxidation have been reported for reaction systems with very different amounts of S^0 accumulation, e.g., in cultures of Fe(II) (only)-oxidizing versus S (only)-oxidizing organisms (McGuire et al., 2001a; Schippers et al., 1996), and in abiotic systems versus Fe(II) and/or S oxidizing cultures (McGuire et al., 2001a; Schippers et al., 1996). McGuire et al. (2001a) suggested two possible explanations for the minimal impact of S^0 on sulfide mineral oxidation, namely that (i) S^0 may accumulate in patches rather than as a continuous layer (as suggested by scanning electron (McGuire et al., 2001a) and Raman imaging microscopy (McGuire et al., 2001b), and that the patches may not necessarily form on the step edges and defects that are likely to be most susceptible to dissolution; or (ii) the S^0 layer may spread more-or-less uniformly over the mineral surface, but remain sufficiently porous so that reactants and products can diffuse through it.

The processes discussed above represent *indirect* mechanisms whereby morgs participate in metal sulfide oxidation mainly through the regeneration of $Fe^{3+}_{(aq)}$ and

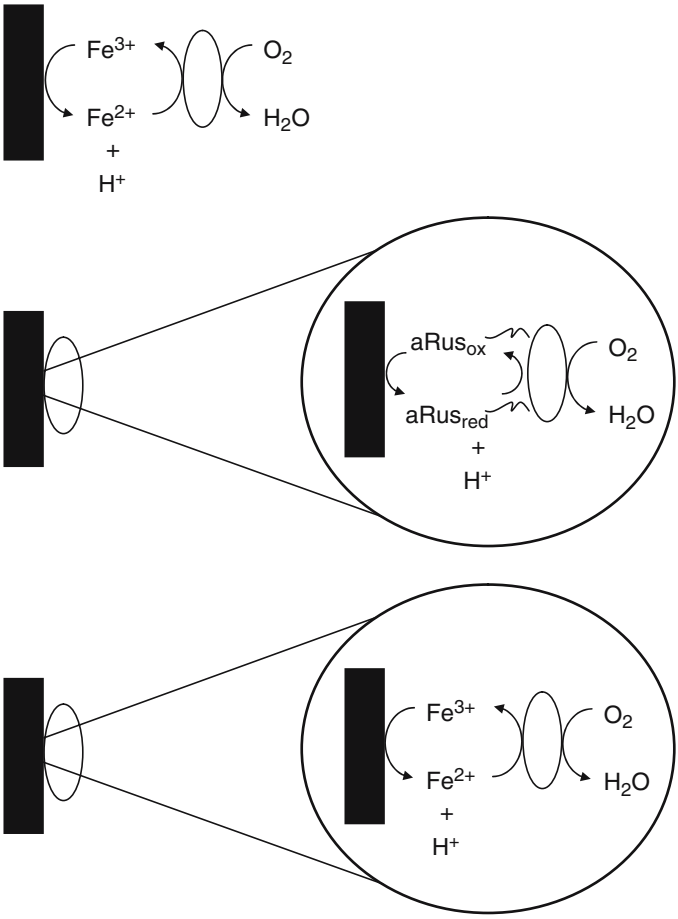

Fig. 9.2 Conceptual models of FeS_2 (rectangles) oxidation by acidophilic Fe(II)-oxidizing morgs (ovals) via (A) an indirect mechanism in which organisms oxidize Fe^{2+} in solution and Fe^{3+} ions dissolve the mineral; (B) a direct, enzymatically-mediated (e.g. via aporusticyanin (aRus); see section 1.3.1) mechanism that does not require Fe^{3+}; or (C) by an indirect contact mechanism in which attached organisms oxidize Fe(II) within a layer of cells and EPS, and Fe^{3+} ions within the layer dissolve the mineral. Diagram is based on conceptual models discussed in Fowler et al. (2001), Sand et al. (2001), and Tributsch (2001)

the production of acidity (illustrated conceptually in Fig. 9.2a). The possibility also exists for morgs to participate more directly in the oxidation of sulfide minerals, e.g., through electron transfer from the sulfide mineral to a redox-active protein at the cell surface, or through production of an extracellular compound (e.g., cysteine; see below) that destabilizes the mineral surface. This idea was originally proposed by Silverman and Ehrlich (1964) to account for the common observation that rates of FeS_2 dissolution are generally much more rapid in the presence of acidophilic organisms such as *A. ferrooxidans* compared to abiotic controls, and that such organisms have a propensity to attach to metal sulfide surfaces. The question of whether

or not organisms such as *A. ferrooxidans* participate directly in metal sulfide oxidation is a long-standing controversy and is still a matter of debate. To date there exists only circumstantial evidence in favor of a direct oxidation mechanism. However, the prevailing model for indirect oxidation presented below includes the participation of attached morgs that carry out lithotrophic metabolism in close proximity to the mineral surface.

9.1.3.1 Direct versus Indirect Oxidation and Cell Attachment

Ehrlich (2002) presents a compelling argument in favor of direct oxidation in the context of the mineral covellite (CuS), in which sulfide is the only oxidizable constituent. CuS is highly insoluble $(\log K_{sp} \approx -44)$, such that equilibrium concentration of dissolved sulfide at pH 2 is on the order of 10^{-13} M. This concentration is many orders of magnitude lower than the K_m value for the sulfide oxidation by *A. ferrooxidans* (ca. 10^{-5} M; (Pronk et al., 1990)). Thus, the mere dissociation of CuS into Cu^{2+} and H_2S cannot provide sufficient substrate for sustained enzymatic metabolism, i.e., the amount of H_2S released by CuS dissolution alone could never satisfy the energy requirements for lithoautotrophic growth. Nevertheless, *A. ferrooxidans* can grow at the expense of CuS oxidation at pH 2 in the absence of Fe, as revealed by measurements of O_2 consumption and Cu^{2+} and $SO_4{}^{2-}$ production (Rickard and Vanselow, 1978). In contrast, the neutrophilic SOM *Thiobacillus thioparus* was found to promote covellite oxidation only after significant autooxidation of the mineral to $CuSO_4$ and S^0 (Rickard and Vanselow, 1978). These results suggested that *A. ferrooxidans* can directly attack the CuS surface, probably resulting in the production of S^0 that serves as a substrate for further energy metabolism:

$$\mathrm{CuS} + 0.5\mathrm{O_2} + 2\mathrm{H^+} + \text{bacteria} \rightarrow \mathrm{Cu^{2+}} + \mathrm{S^0} + \mathrm{H_2O} \tag{9.10}$$

$$\mathrm{S^0} + 1.5\mathrm{O_2} + \mathrm{H_2O} + \text{bacteria} \rightarrow \mathrm{SO_4^{2-}} + 2\mathrm{H^+} \tag{9.11}$$

Pogliani and colleagues later verified the ability of *A. ferrooxidans* to oxidize CuS, and showed that (i) direct contact between the organism and the mineral surface is required for oxidation in the absence of Fe (Pogliani et al., 1990), and (ii) EPS plays a key role in attachment of cells to the mineral surface (Pogliani and Donati, 1999). In related research, *A. thiooxidans*, which can oxidize S^0 but not Fe(II), was shown to be able to oxidize CuS at rates comparable to *A. ferrooxidans* only if $Fe^{3+}_{(aq)}$ was added to the medium to catalyze chemical oxidation of CuS to provide S^0 for enzymatic metabolism (Curutchet et al., 1995; Donati et al., 1996; Pogliani and Donati, 2000). Together these findings indicate that *A. ferrooxidans*, in contrast to *T. thioparus* and *A. thiooxidans*, has the ability to disrupt the CuS surface.

How can this happen, and does it require involvement of cellular components? Although a definitive answer is not available, recent studies by Tributsch and colleagues (summarized in Rojas-Chapana and Tributsch (2001)) have suggested that *A. ferrooxidans* may utilize –SH groups on the amino acid cysteine (e.g., contained

within a capsule surrounding the cell) to disrupt the FeS_2 surface through formation of Fe-cysteine and cysteine-pyrite surface complexes, leading eventually to production of S^0 and transfer of Fe(II) to the cell. This concept is supported by the transient release of S^0 colloids that takes place during FeS_2 oxidation by *A. ferrooxidans* (Rojas-Chapana et al., 1995), and by the ability of cysteine to accelerate FeS_2 bioleaching (Rojas-Chapana and Tributsch, 2000). While this proposed mechanism is speculative and has yet to be verified, if correct it would provide a possible means whereby *A. ferrooxidans* could disrupt the CuS surface, assuming that cell surface cysteine–SH groups can interact with CuS in a manner analogous to their proposed interaction with FeS_2.

Another circumstantial line of evidence for a direct oxidation mechanism is the recent finding that a compound called aporusticyanin plays a specific role in the adhesion of *A. ferrooxidans* to FeS_2 surfaces (Blake et al., 2001). Aporusticyanin is the copper-free form of rusticyanin, an acid-stable Cu-protein that is produced in large quantities during growth of *A. ferrooxidans* on Fe(II), and that is thought to be a component of the electron transport chain from Fe(II) to O_2 (see Blake and Johnson (2000) for review). Blake and colleagues (2001) observed that purified aporusticyanin (produced recombinantly in *E. coli*) and intact *A. ferrooxidans* cells showed identical patterns of adhesion to a variety of iron-sulfide minerals (FeS_2, FeS, $Fe_{1-x}S$, $CuFeS_2$, and $FeAsS_2$). Addition of exogenous rusticyanin suppressed adhesion of intact *A. ferrooxidans* cells to FeS_2. Interestingly, the presence of high concentrations of Fe(II) had a dramatic effect on the force required to dissociate washed, Fe(II)-grown cells from FeS_2, as determined by laser optical trapping: 96 out of 100 cells could be dissociated at the maximum power of the laser, compared to only 8 out of 100 in the absence of added Fe(II). These results were interpreted in terms of a model in which aporusticyanin located on the surface of the bacterial cell acts as a mineral receptor for the initial adhesion of *A. ferrooxidans* to FeS_2, and in which binding is accomplished (at least in part) by coordination of the unoccupied copper ligands with a Fe atom at the exposed edge of the pyrite crystal lattice. Blake speculates that binding of one or more coordination ligands in aporusticyanin to edge-exposed Fe atoms could lead to destabilization of the mineral surface (see Blake et al. (2001) for details), resulting in release of Fe(II) to solution and transfer of electrons to sulfur atoms that are subsequently oxidized as part of the sulfur metabolism of the cell (Fig. 9.2b). This argument is consistent with recent gene expression studies which showed that genes for both Fe and S oxidation are upregulated during growth on FeS_2 (Ramirez et al., 2004). Such coupled processes would clearly constitute a direct oxidation mechanism. An alternative way in which aporusticyanin could directly catalyze FeS_2 oxidation would be to facilitate charge (i.e., electron) transfer from FeS_2 to cellular EAs by an inner-sphere mechanism. This speculation is consistent with previous studies showing that bridge complexes formed by adsorbing –O–, –CN–, or –CO– groups to interfacial Fe atoms in FeS_2 greatly accelerate the transfer of photogenerated charge carriers between FeS_2 and $Fe^{3+}_{(aq)}$ (Shubert and Tributsch, 1990). A logical candidate for the initial EA would be the c-type cytochrome Cyc2, which was recently shown to be located in the outer membrane of *A. ferrooxidans*

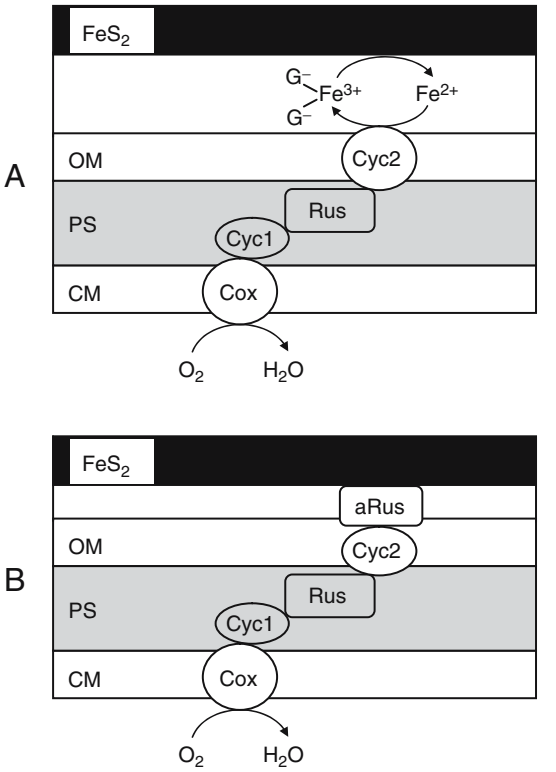

Fig. 9.3 (A) Model for electron transport during FeS_2 oxidation by *A. ferrooxidans* from Rohwerder et al. (2003) (used with permission) in which the initial step involves indirect mineral dissolution by Fe^{3+} ions coordinated by glucuronic acid moieties within a surrounding layer of EPS. (B) Modified model in which the initial step involves direct electron transfer from FeS_2 to aporusticyanin and subsequent transfer to Cyc2 via an inner-sphere mechanism (Blake et al., 2001). Abbreviations: OM = outer membrane; PS = periplasmic space; CM = cell membrane; G^- = glucuronic acid; Rus = rusticyanin; aRus = aporusticyanin; Cyc1 = *c*-type cytochrome #1; Cyc2 = *c*-type cytochrome #2; Cox = aa_3-type cytochrome oxidase

(Yarzabal et al., 2002a, b). Rohwerder et al. (2003) provide a useful summary of current knowledge of the biochemistry of Fe(II) oxidation in *A. ferrooxidans*, and their model is reproduced in Fig. 9.3 along with a modified version that takes into account the possible role of aporusticyanin in electron transfer from FeS_2 to Cyc2.

The direct oxidation mechanism(s) described above might be expected to be most active during the early stages of mineral oxidation, when the concentration of soluble Fe as an agent for mineral-to-cell electron transfer is relatively low. Later in the oxidation process, higher concentrations of $Fe^{2+}_{(aq)}$ would be expected (based on the results presented in Blake et al. (Blake et al., 2001) as well as Ohmura et al. (1993)) to inhibit cell attachment, and the ensuing production of high concentrations of $Fe^{3+}_{(aq)}$ would promote rapid chemical oxidation, thereby obviating the need for the cells to attach to the mineral surface (see below). The accumulation of relatively large numbers of unattached versus attached cells during the latter stages of FeS_2 oxidation by *A. ferrooxidans* in closed systems is well-known (e.g., Edwards et al., 1998; Espejo and Ruiz, 1987; Mustin et al., 1992a; Norris et al., 1988; Rodriguez et al., 2003). However, there is no evidence that attachment of *A. ferrooxidans* to FeS_2 is inhibited by $Fe^{3+}_{(aq)}$ (Blake et al., 2001; Ohmura et al., 1993), and there is ample evidence to suggest that

A. ferrooxidans forms distinct biofilms on FeS_2 surfaces in the presence of high concentrations of $Fe^{3+}_{(aq)}$ (Crundwell, 1996) and that (as discussed in more detail below) the presence of attached cells accelerates FeS_2 dissolution by altering aqueous geochemical conditions at the mineral surface (Fowler et al., 1999; Holmes et al., 1999).

9.1.3.2 Cell Attachment and Colonization of Sulfide Mineral Surfaces

Attachment of acidophilic FeOMs to FeS_2 and other metal sulfide mineral surfaces is well-known (see Crundwell (1997) for reviews), and subsequent surface colonization can (at least in some cases) lead to specific surface features that provide compelling evidence for localized enzymatic activity that may or may not reflect direct enzymatic oxidation. Recent studies of FeS_2 colonization by *A. ferrooxidans* at neutral pH demonstrated that the cells form a distinct biofilm that become encrusted in Fe(III) oxyhydroxides, leading ultimately to the formation of mineralized microcolonies (Mielke et al., 2003; Pace et al., 2005). The microcolonies produce an expanding acidification front at the mineral surface which leads to the formation of distinct corrosion pits of size and shape similar to that of the bacteria (Mielke et al., 2003). Although it is still unknown whether the Fe(II) oxidation that takes place in the vicinity of the microcolonies occurs via direct or an indirect mechanism, the fact that removal of Fe(III) oxyhydroxides by oxalate did not dislodge bacteria within the pits (Mielke et al., 2003) is consistent with the operation of a specific cell-mineral adhesion mechanism such as that postulated by Blake et al. (2001). This assertion is consistent with studies of *A. ferrooxidans* attachment to metal sulfides that suggest the involvement of biochemical interactions rather than purely physical (e.g., electrostatic or hydrophobic) interactions (Crundwell, 1997; Devasia et al., 1993; Ohmura et al., 1993).

A number of studies have demonstrated that the presence of attached acidophilic FeOM is associated with local, crystallographically controlled dissolution (Bennet and Tributsch, 1978; Edwards et al., 1998, 1999; Konishi et al., 1990). Cell attachment is clearly specific to the sulfide mineral, as revealed by the demonstration by Edwards et al. (1998) of the conspicuous absence of organisms on a silicate inclusion within a cubic FeS_2 crystal (see Fig. 9.4a,b). Cells preferentially attach to scratches, pits, grooves, and steps, which are presumably sites of high surface energy and thus locally elevated rates of dissolution. Interestingly, where cells attach distant from surface scratches, cell orientation occurs in nonrandom directions. Alignment occurs parallel to the <100> and <110> crystallographic direction, and the edges of dissolution pits associated with the cells are also parallel to the <100> and <110> plane orientations. Fig. 9.4c provides a summary of FeS_2 surface attachment details (Edwards et al., 1999). Oriented cell attachment (pyrite, marcasite and arsenopyrite) has also been demonstrated for the SOM *Acidithiobacillus caldus*, and has been interpreted as a chemotactic response to localized zones of S^0 enrichment associated with mineral dissolution along the <100> and <110> surfaces (Edwards et al., 2000a).

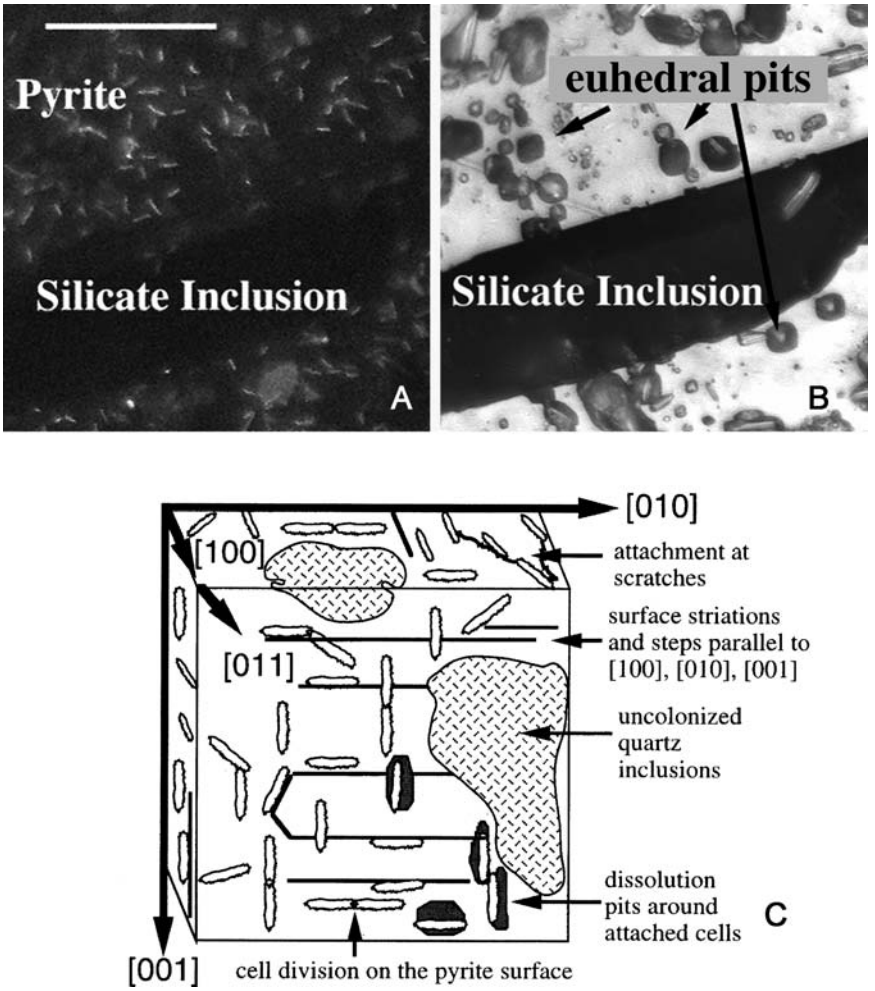

Fig. 9.4 Upper left (A): UV fluorescence image of DAPI-stained acidophilic Fe(II)-oxidizing morgs from Iron Mountain, CA adhering to a polished pyrite crystal; morgs appear as light, rod-shaped objects; scale bar is 25 μm, and applies to both left and right images. Upper right (B): reflected plane light image corresponding to image on left; note that organisms did not adhere to silicate inclusions exposed by polishing. Both images are slightly modified from Fig. 5 in Edwards et al. (1998), used with permission. Lower (C): conceptual diagram of the attachment of Fe(II)-oxidizing morgs to a pyrite cube; the <100>, <010>, and <001> crystallographic directions are parallel to the cube edges; the <110>, <101>, and <011> directions are diagonal to the cube edges. Slightly modified from Fig. 5 in Edwards et al. (1999), used with permission

Despite the existence of distinct patterns of FeOM attachment to metal sulfide surfaces, detailed SEM studies with *A. ferrooxidans* and the Fe(II)-oxidizing archaeon *Ferroplasma acidarmanus* (Edwards et al., 2000b), in comparison to abiotic dissolution by $Fe^{3+}{}_{(aq)}$, led Edwards et al. (2001b) to conclude that FeS_2 dissolution involves the formation of discrete (and in many cases bacteria cell-sized) euhedral

dissolution pits (see Fig. 9.4b) regardless of whether or not morgs are involved in the process. In addition, neither *A. ferrooxidans* nor *F. acidarmanus* cells were observed within dissolution pits on FeS_2 surfaces. These findings are consistent with many previous SEM studies of FeS_2 oxidation by *A. ferrooxidans* (Bennet and Tributsch, 1978; Fernandez et al., 1995; Fowler et al., 2001; Mustin et al., 1992b, c; Rodrieguez and Tributsch, 1988). Only in the case of *F. acidarmanus* reacting with arsenopyrite were cells observed within cell-sized and -shaped pits. This result was attributed to an increased reactivity of arsenopyrite relative to FeS_2, such that dissolution rates at the cell surface were faster than those on the bulk surface, which would allow for the persistence of cell-associated pitting. In all other cases, bulk surface dissolution rates were presumably at least as fast as any cell-associated pitting, such that preferential dissolution in the vicinity of the cells (if in fact it took place) could not be discerned by SEM. It is important to note, however, that FeOM such as *A. ferrooxidans* are likely (because of differences in adhesion energy) to preferentially associate with the edges of corrosion pits (Edwards and Rutenberg, 2001), which in some cases can lead to corrosion morphologies (e.g., in the <100> and <110> plane orientation) that are distinct from those formed under abiotic conditions, (Ndlovu and Monhemius, 2005).

In contrast to the results obtained with *A. ferrooxidans* and *F. acidarmanus*, a recent study of low-pH FeS_2 leaching by *L. ferrooxidans* provided clear evidence of localized pitting associated with attached cells (Rojas-Chapana and Tributsch, 2004). As surface colonization progressed, electro-dense nanoparticles of FeS_2 were found to accumulate in a layer of EPS surrounding the bacteria. Patterns of surface corrosion during abiotic dissolution by $Fe^{3+}_{(aq)}$ did not reveal the same localized pitting observed in the presence of cells, and no release of FeS_2 nanoparticles was observed. Rojas-Chapana and Tributsch (2004) suggested that the cells accumulate high concentrations of Fe^{3+} ions within the surrounding layer of EPS, which induces localized disruption of the FeS_2 surface, leading to release of FeS_2 nanofragments. An analogy was drawn between the observed patterns of cell-localized corrosion and the process of electrochemical machining in which a needle cathode is used to induce local anodic dissolution (Ting et al., 2000). The idea that acidophilic FeOM accumulate $Fe^{3+}_{(aq)}$ within a layer of EPS in order to promote FeS_2 dissolution had been suggested previously as a mechanism whereby *A. ferrooxidans* and *L. ferrooxidans* could carry out surface-associated FeS_2 dissolution (Gehrke et al. (1995, 1998); Sand et al. (1995); see Sand et al. (2001) and Kinzler et al. (2003) for reviews). The presence of high concentrations of $Fe^{3+}_{(aq)}$ within an EPS capsule is also thought to promote adhesion to the FeS_2 surface (Arredondo et al., 1994; Sand et al., 1995), since FeS_2 surfaces are negatively charged even at low pH (Blake et al., 1994). Glucuronic acid residues, which are abundant within the EPS (Gehrke et al., 1998) and have been shown previously to be involved in microbial metal binding (Urrutia, 1997), are logical candidates for Fe^{3+}-binding ligands in EPS (Fig. 9.3a). *L. ferrooxidans* is likely to be more effective with this strategy compared to *A. ferrooxidans*, since it is able to remain active at much higher concentrations of $Fe^{3+}_{(aq)}$ (Norris et al., 1988), which would presumably allow it to carry out localized FeS_2 dissolution at a rate in excess of bulk dissolution. This line of

reasoning is consistent with the greater propensity of *L. ferrooxidans* to grow attached to FeS_2 surfaces as compared to *A. ferrooxidans* (Norris et al., 1988). This capacity in turn provides a mechanistic explanation for the tendency for *Leptospirilli* to dominate over *Acidithiobacilli* in most commercial bioleaching (Rawlings et al., 1999) and certain AMD environments (Schrenk et al., 1998), a phenomenon which is analyzed quantitatively below.

9.1.3.3 An Integrated Model for Microbial Sulfide Mineral Oxidation

Because nonferrous metal sulfides are always accompanied by FeS_2 in ore deposits, dissolved Fe is generally abundant in low-pH sulfide mineral oxidation systems (Ehrlich, 2002). This basic reality, together with the fact that $Fe^{3+}_{(aq)}$ is a potent oxidant for virtually all metal sulfide phases (RuS_2 being the only exception; Tributsch (2001)), means that direct oxidation, if it occurs at all, must always take place in conjunction with indirect oxidation by $Fe^{3+}_{(aq)}$. In addition, it is clear from the preceding discussion that any model for microbial metal sulfide oxidation must take into account the fact that acidophilic FeOM attach to sulfide mineral surfaces. In the absence definitive evidence for a direct mineral-to-cell oxidation mechanism, the prevailing model for microbial sulfide mineral oxidation is one that combines bulk-phase Fe(II) oxidation with a so-called "contact leaching" (Tributsch, 2001) or "indirect contact" mechanism (Fowler et al., 2001), in which the mineral surface is progressively dissolved through Fe redox cycling (Fig. 9.2c) and/or sulfhydrl group-mediated surface disruption within a layer of attached cells. Tributsch (2001) and Rawlings (2002) refer to this combined process as "cooperative leaching" in which suspended bacteria feed on species released to solution in conjunction with contact-mediated dissolution. Such species include (in addition to $Fe^{2+}_{(aq)}$) small but significant quantities of S^0 colloids and dissolved polythionites. The recent findings of Rojas-Chapana and Tributsch (2004) suggest the possibility that nanoparticulate FeS_2 may also be released to the bulk phase during FeS_2 oxidation. The cooperative leaching model predicts that consortia of FeOM and SOM should be more efficient than either FeOM-only or SOM-only oxidizing systems, a prediction that has been verified on numerous occasions (Dopson and Lindstrom, 1999; Falco et al., 2003; McGuire et al., 2001a; Okibe and Johnson, 2004; Sand et al., 1992).

In addition to the obvious potential for enhanced metal sulfide oxidation in the combined presence of FeOM and SOM, several studies have indicated that the presence of heterotrophic and/or mixotrophic morgs (see Fig. 8.2 in companion chapter for review of these metabolic types) can accelerate FeS_2 oxidation in mixed culture with autotrophic FeOMs and SOMs (Clark and Norris, 1996; Dopson and Lindstrom, 1999; Hallmann et al., 1992; Okibe and Johnson, 2004). Hallmann et al. (1992) speculated that the presence of the heterotrophic organism *Acidiphilium* sp. degraded EPS produced by *L. ferrooxidans*, thereby freeing-up fresh FeS_2 surface for attachment and degradation by other *L. ferrooxidans* cells. It is also possible

that degradation of EPS and other cellular debris by heterotrophic or mixotrophic organisms helps to regenerate CO_2 that can be reassimilated by the autotrophic microflora (Okibe and Johnson, 2004; Sand et al., 1995). This phenomenon could be quite significant given that CO_2 abundance often limits sulfide mineral oxidation in systems with high solid-to-liquid ratios (Boon and Heijnen, 1998b). Regardless of the exact mechanism(s), heterotrophic and mixotrophic organisms are abundant in both bioleaching (Johnson and Roberto, 1997) and AMD (Baker and Banfield, 2003; Edwards et al., 1999; Johnson, 1998; Peccia et al., 2000) environments, and thus it is appears that the biogeochemical functioning of these systems involves synergistic interactions among Fe-, S-, and C-metabolizing organisms (Baker and Banfield, 2003; Druschel et al., 2004).

9.1.3.4 Experimental Evidence for the "Indirect Contact" Mechanism

Crundwell and colleagues have carried out a series of elegant experiments on the influence of *A. ferrooxidans* on the kinetics of FeS_2 and other metal sulfide mineral dissolution in a constant redox potential apparatus (Fowler and Crundwell, 1998; Fowler et al., 1999; Holmes et al., 1999). This device allows concentrations of Fe(II) and Fe(III) in solution to remain constant during short-term (tens of minutes to a few days) experiments in both the presence and absence of bacteria, and therefore could be used to gain insight into the impact of bacteria on dissolution kinetics independent of their influence on $Fe^{2+}_{(aq)}$ and $Fe^{3+}_{(aq)}$ abundance. Using this device, it was shown that *A. ferrooxidans* (10^8 cells mL^{-1}) accelerated FeS_2 ($0.097\,m^2 mL^{-1}$) dissolution by ca. 25% relative to abiotic systems across a range of pH (1.3 to 1.7) and $Fe^{3+}_{(aq)}$ concentrations (18 to 358 mM) at a fixed $Fe^{2-}_{(aq)}$ concentration of 18 mM (Fowler et al., 1999). These studies were crucial in that they provided a definitive answer to the long-standing question of whether or not morgs can accelerate the dissolution of FeS_2 relative to equivalent abiotic reaction systems. Parallel studies with pyrite electrodes demonstrated that the mixed potential (which corresponds to the net electrochemical potential that arises from simultaneous anodic and cathodic reactions at the mineral surface) of the electrode decreased as microcolonies and biofilms formed on its surface over a 14-day period (Holmes et al., 1999). In contrast, the mixed potential of chemically dissolved FeS_2 remained constant over time. The results were interpreted in terms of an established electrochemical model of FeS_2 dissolution based on the Butler-Volmer equation (see Holmes et al. (1999) and Holmes and Crundwell (2000) for details). The analysis indicated that the decrease in mixed potential and increase in FeS_2 dissolution rate in the presence of *A. ferrooxidans* could be explained by an increase in pH at the mineral surface, which accelerates the rate of mineral dissolution (see next section). Such an increase in interfacial pH was attributed to H^+ consumption associated with localized Fe(II) oxidation (see Eq. (9.7)) within the biofilm on the mineral surface. This interpretation reinforces, albeit indirectly, the idea that $Fe^{3+}_{(aq)}$ concentrations are likely to be locally elevated within biofilms of FeOM on sulfide mineral surfaces (Sand et al. (1995; 2001); see Sect. 9.1.3.2 above): although $Fe^{3+}_{(aq)}$ concentrations were rigorously maintained at

a constant level in the well-mixed constant redox apparatus, in nature one would expect local increases in $Fe^{3+}_{(aq)}$ abundance to accompany Fe(II) oxidation activity at the mineral surface. Numerical simulations of diffusive transport and reaction at the mineral–water interface are employed below to illustrate this concept. Crundwell and colleagues conclude that the mechanism of microbial acceleration of FeS_2 oxidation is essentially an indirect one, i.e., that the acceleration is driven by locally elevated rates of $Fe^{2+}_{(aq)}$ oxidation in the vicinity of the mineral surface—as opposed to direct biochemically mediated mineral dissolution. An important piece of evidence supporting this conclusion was the prior observation (using confocal laser microscopy) by Crundwell (1996) that a layer of Fe(III) hydroxide forms on the FeS_2 surface during bacterial (*A. ferrooxidans*) biofilm formation, and that the organisms become concentrated on the solution side of the hydroxide. Based on these data, Crundwell (1997) concluded that bacteria did not require direct attachment to the unreacted FeS_2 surface in order to promote its oxidation, but rather they did so by catalyzing redox cycling of Fe within the biofilm (see Fig. 9.2c). This model is complementary to the model developed by Sand and colleagues (1995, 2001) in which Fe cycling takes place within the EPS layers of individual bacteria as opposed to within the biofilm as a whole.

The interpretation that microbially mediated FeS_2 dissolution proceeds via an indirect contact mechanism is consistent with detailed studies by Boon and colleagues of Fe(II) oxidation and FeS_2 dissolution in batch and continuous cultures (Boon et al., 1995, 1998; Hansford, 1997), which showed that FeS_2 dissolution rates could be accurately reproduced by a "two subprocess model" in which chemical FeS_2 leaching by $Fe^{3+}_{(aq)}$ (Eq. (9.6)) is linked at pseudo steady-state to microbial Fe(II) oxidation (Eq. (9.7)). Although the models developed by Boon and colleagues to explain their experimental data did not take into account the impact of microbial surface colonization on FeS_2 dissolution, it is important to keep in mind that the influence of such colonization on rates of mineral dissolution is modest (only ca. 25% under optimal conditions), and thus it is not surprising that the simplified models of bulk-phase Fe(II) oxidation and chemical FeS_2 leaching were able to reproduce the experimental data accurately.

9.1.4 Kinetics of Coupled Aqueous and Solid-Phase Oxidation Reactions

In this section, the kinetics of key aqueous and solid-phase reactions associated with metal sulfide mineral dissolution and oxidation are described using FeS_2 as a model sulfide mineral phase. The resulting framework is then used to illustrate by numerical simulation several key aspects of the role of morgs in this process, including the competition between *A. ferrooxidans* and *L. ferrooxidans* as an example of the interaction between microbial physiology and aqueous geochemistry. A key assumption in the simulations is that Fe(II) oxidation takes place solely in the aqueous phase, i.e., there is no explicit inclusion of the process of attachment or

the activity of attached FeOM. However, a transport-reaction model was developed (see Sect. 9.1.4.7) to explore how the passive accumulation of cells at the FeS_2 surface (due to lack of cell transport within a defined boundary layer) could influence dissolution kinetics.

9.1.4.1 Kinetics of Chemical and Biological Oxidation of $Fe^{2+}_{(aq)}$

Figure 9.1 illustrates the contrasting kinetics of chemical (abiotic) versus biological Fe(II) oxidation as a function of solution pH. The kinetics of chemical $Fe^{2+}_{(aq)}$ oxidation by O_2 was studied by (among others) Singer and Stumm (1972), and the results have been interpreted quantitatively in terms of a second-order rate law in which the rate constant is dependent on hydroxyl ion activity (Parkhurst and Appelo, 1999):

$$R = (10^{-8.54} + 10^{12.12} \times \{OH^-\}^2) \times P_{O2} \times [Fe^{2+}{}_{(aq)}] \tag{9.12}$$

where $\{OH^-\}$ is the activity of hydroxyl ions ($\log\{OH^-\} = 14 - pH$), P_{O2} is the partial pressure of O_2 in equilibrium with the aqueous phase (set equal to 0.159 atm, equivalent to 2×10^{-4} M dissolved O_2), and $[Fe^{2+}_{(aq)}]$ is the molar concentration of $Fe^{2+}_{(aq)}$ (set equal to 10^{-2} M). This expression was included in all model calculations, i.e., abiotic Fe(II) oxidation was allowed to take place in all the simulations. However, calculated rates of abiotic Fe(II) oxidation were always several orders of magnitude lower than those calculated for microbial oxidation as described below.

The kinetics of microbial Fe(II) oxidation at low pH have been studied extensively, and are reviewed succinctly in Hansford (1997). Table 9.2 provides a summary of the rate expressions that are typically used to simulate this process. The consensus model employs a Monod expression for dependence of the (biomass-specific) oxidation rate on $Fe^{2+}_{(aq)}$ concentration, together with a competitive inhibition term to account for the inhibitory influence of $Fe^{3+}_{(aq)}$. This formulation corresponds to the following general rate law (Rawn, 1983):

$$R = \frac{R_{max}}{1 + \frac{K_m}{[S]} + \frac{K_m}{K_I}\frac{[I]}{[S]}} \tag{9.13}$$

where [I] is the concentration of the inhibitor, K_I is the inhibition constant, and K_m and [S] are the usual terms in the Monod equation. The competitive inhibition term is used under the assumption that $Fe^{3+}_{(aq)}$ can bind with the enzyme responsible for the initial step in Fe(II) oxidation and thereby render some fraction of the enzyme pool inactive (Jones and Kelly, 1983; Kelly and Jones, 1978). The overall set of reactions that result in the rate expression are as follows:

$$E + Fe^{2+} \leftrightarrow E - Fe^{2+} \tag{9.14}$$

$$E - Fe^{2+} \rightarrow Fe^{3+} + e^- + E \tag{9.15}$$

$$E + Fe^{3+} \leftrightarrow E - Fe^{3+} \tag{9.16}$$

Table 9.2 Rate expressions for microbial Fe(II) oxidation and cell growth

A. Fe(II) oxidation:

$$R_{\mathrm{Fe(II)}} = \left(\frac{R_{\mathrm{max,Fe(II)}}}{1 + \dfrac{K_{\mathrm{m,Fe(II)}}}{[\mathrm{Fe}^{2+}]} + \dfrac{K_{\mathrm{m,Fe(II)}}}{K_{\mathrm{I,Fe(III)}}} \dfrac{[\mathrm{Fe}^{3+}]}{[\mathrm{Fe}^{2+}]}} \right) \times F_{\mathrm{T}} \times [\mathrm{B}] \tag{1}$$

where:

$R_{\mathrm{Fe(II)}}$ = rate of Fe(II) oxidation
$R_{\mathrm{max,Fe(II)}}$ = maximum biomass-specific rate of Fe(II) oxidation
$K_{\mathrm{m,Fe(II)}}$ = half-saturation constant for Fe(II) utilization
$K_{\mathrm{I,Fe(III)}}$ = constant for competitive inhibition of Fe(II) oxidation by Fe^{3+}

$$F_{\mathrm{T}} = 1 - \exp\left(\frac{\Delta G - \Delta G_{\mathrm{min}}}{RT} \right) \tag{2}$$

[B] = biomass (mol cell-C L^{-1})

B. Bacterial growth:

$R_{\mathrm{BM}} = \mathrm{Y} R_{\mathrm{Fe(II)}} - \mathrm{m}_{\mathrm{Fe(II)}} \mathrm{Y}_{\mathrm{Fe(II)}} [\mathrm{B}]$

where:

$\mathrm{Y}_{\mathrm{Fe(II)}}$ = yield coefficient for growth on Fe(II)
$\mathrm{m}_{\mathrm{Fe(II)}}$ = maintenance coefficient for growth on Fe(II)

C. Parameter values:

Parameter	Units	*A. ferrooxidans*	*L. ferrooxidans*
$R_{\mathrm{max,Fe(II)}}$	mol Fe(II) mol cell-C^{-1} hr^{-1}	8.8	6.8
$K_{\mathrm{m,Fe(II)}}$	mol L^{-1}	0.0002	0.0002
$K_{\mathrm{I,Fe(III)}}$	mol L^{-1}	0.0031	0.0428
ΔG_{min}	kJ mol^{-1}	−20	−10
m	mol Fe(II) mol cell-C^{-1} hr^{-1}	0.25	0.45
Y	mol cell-C mol Fe(II)$^{-1}$	0.0114	0.0099

where E represents the enzyme. The net effect of the inhibitor is to increase the apparent value of $K_{\mathrm{m}} (K_{\mathrm{m,app}})$ according to the equation

$$K_{\mathrm{m,app}} = K_{\mathrm{m}} \left(1 + \frac{[\mathrm{I}]}{K_{\mathrm{I}}} \right) \tag{9.17}$$

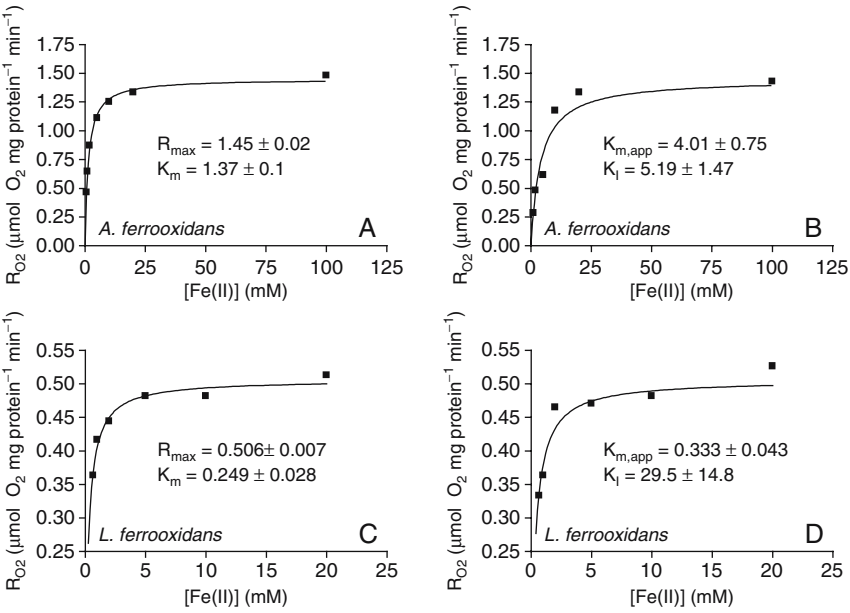

Fig. 9.5 Short-term (zero order) rates of O_2 uptake coupled to Fe(II) oxidation by *A. ferrooxidans* and *L. ferrooxidans* in the absence (panels A and C) and presence (panels B and D) of 10 mM $Fe^{3+}_{(aq)}$ (data reproduced from batch experiments depicted in Fig. 2 of Norris et al. (1988), with permission). Lines represent nonlinear least-squares regression fits of the data to the basic Monod rate law (equation 7 in the companion chapter) for the Fe^{3+} free systems, or to the Monod rate law with competitive inhibition (equation 13 in text, where Fe^{3+} corresponds to the competitive inhibitor I, and Fe^{2+} corresponds to the substrate S) for the Fe^{3+} amended systems (see also Table 2A). The R_{max} and K_m values for the Fe^{3+} free systems were used as fixed parameters for the regression analysis of the Fe^{3+} amended systems. $K_{m,app}$ values were calculated from according to equation 17 in the text

Competitive inhibition has no influence on R_{max}, in contrast to noncompetitive inhibition (see Eq. (9.14) and Table 8.5), which reduces the value of R_{max} but has no influence on the apparent K_m.

The influence of $Fe^{3+}_{(aq)}$ on $Fe^{2+}_{(aq)}$ oxidation kinetics can be illustrated using data from Norris et al. (1988), in which short-term (zero order) rates of O_2 uptake by *A. ferrooxidans* and *L. ferrooxidans* were measured as a function of $Fe^{2+}_{(aq)}$ concentration in the presence and absence of 10 mM $Fe^{3+}_{(aq)}$. The results (Fig. 9.5) illustrate the general principle that competitive inhibition increases the apparent K_m value for the reaction. The implications of the different R_{max}, K_m, and K_I values for *A. ferrooxidans* and *L. ferrooxidans* are discussed below. It should be noted that a simplified form of the coupled Monod-competitive inhibition is often used to model microbial Fe(II) oxidation kinetics in which the term $K_{m,Fe(II)}/[Fe^{2+}_{(aq)}]$ ($K_m/[S]$ in Eq. (9.13)) is omitted because the value of K_m is small and difficult to determine independently of $K_{m,Fe(II)}/K_{I,Fe(III)}$ (Boon et al., 1998b). This approach is *not* adopted here because we wish to examine the influence of both $Fe^{2+}_{(aq)}$ (as an energy substrate) and $Fe^{3+}_{(aq)}$

(as an inhibitor) abundance on oxidation kinetics by *A. ferrooxidans* versus *L. ferrooxidans*.

An additional phenomenon that must be accounted for in the rate law for microbial Fe(II) oxidation is the existence of a threshold $Fe^{2+}_{(aq)}$ concentration below which Fe(II) oxidation ceases (Braddock et al., 1984). Threshold $Fe^{2+}_{(aq)}$ values of 0.2–0.5 mM and ca. 0.005 mM have been reported for *A. ferrooxidans* and *L. ferrooxidans*, respectively (Boon et al., 1998b; Braddock et al., 1984; vanScherpenzeel et al., 1998). The Monod expression can be modified empirically to account for such thresholds by replacing $[Fe^{2+}_{(aq)}]$ with the quantity $[Fe^{2+}_{(aq)}] - [Fe^{2+}_{(aq)}]_{thresh}$, where $[Fe^{2+}_{(aq)}]_{thresh}$ is the threshold $Fe^{2+}_{(aq)}$ concentration (Boon et al., 1998b). However, it is very likely that the thresholds are the result of thermodynamic constraints (see Sect. 1.4.3), and thus inclusion of a thermodynamic control term (e.g., Eq. (8.21)) in the rate equation for Fe(II) oxidation is mechanistically the most appropriate way to account for the threshold (Meruane et al., 2002). For the reaction systems studied by Boon et al. (1998b) and vanScherpenzeel et al. (1998), which utilized a total dissolved Fe concentration of 210 mM and pH values of 1.5–1.6, the observed threshold $Fe^{2+}_{(aq)}$ concentrations correspond to ΔG_{min} values of ca. -20 and -10 kJ mol^{-1} for *A. ferrooxidans* and *L. ferrooxidans*, respectively (assuming a fixed dissolved O_2 concentration of 0.2 mM). Although the estimated ΔG_{min} value for *L. ferrooxidans* is lower than the generally accepted value of -20 kJ mol^{-1} (Schink, 1997), recent studies suggest that alteration of internal ADP/ATP ratios and/or variation in the number of protons translocated across the cell membrane during ATP synthesis could lead to ΔG_{min} value substantially lower than the standard value of -20 kJ mol^{-1} (which assumes an ADP/ATP ratio of 0.1, an internal total inorganic P concentration of 10 mM, and that three protons are translocated during ATP synthesis) (Jackson and McInerney, 2002). In addition, the electron transfer machinery of *L. ferrooxidans* differs significantly from that of *A. ferrooxidans* (Blake and Johnson, 2000), and this may have an important influence on the minimum amount of energy required for these different FeOMs to oxidize Fe(II) (Rohwerder et al., 2003).

Coupled Fe(II) oxidation and microbial growth is treated using a standard framework (Table 9.2) that includes a maintenance coefficient for consumption of the energy substrate (in this case Fe(II)) for endogenous respiration (Rittmann and McCarty, 2001). This approach differs from that used in Chap. 8 to model acetate metabolism, in which consumption of energy substrate for maintenance was embedded in the biomass-dependent uptake rate constant, and the impact of endogenous respiration was accounted for by the generalized cell death/decay term (k_d). In practice the two approaches yield very similar results; the maintenance energy approach is adopted here because it has been used routinely to model Fe(II) oxidation by *A. ferrooxidans* (Boon et al., 1995; 1998a, b) and *L. ferrooxidans* (vanScherpenzeel et al., 1998). The R_{max}, K_m, K_I, m, and Y values for *A. ferrooxidans* and *L. ferrooxidans* listed in Table 9.2 are the mean values summarized in Norris et al. (1988) and Hansford (1997). The R_{max} values correspond to ca. 3×10^{-7} μmol Fe cell^{-1} day^{-1} (assuming a standard mean prokaryotic cell carbon

Table 9.3 Equilibrium speciation system for the Fe(II) oxidation/FeS_2 dissolution simulations. All log K values were obtained from the MINEQL+ (Schecher and McAvoy, 1998) database

Components	**Fe^{2+}**	**Fe^{3+}**	**SO_4^{2-}**	**H^+**	**$CO_2(g)^*$**	**log K**
Species:						
$H_2CO_{3(aq)}$	0	0	0	0	1	16.68
HCO_3^-	0	0	0	−1	1	10.33
CO_3	0	0	0	−2	1	0.00
Fe^{2+}	1	0	0	0	0	0
$FeOH^+$	1	0	0	−1	0	−9.5
$FeHCO_3^+$	1	0	0	1	1	12.33
$FeCO_3(aq)$	1	0	0	0	1	5.5
$Fe(CO_3)_2^{2-}$	1	0	0	0	2	7.1
$FeSO_4(aq)$	1	0	1	0	0	2.25
Fe^{3+}	0	1	0	0	0	0
$FeOH^{2+}$	0	1	0	−1	0	−2.19
$Fe(OH)_2^+$	0	1	0	−2	0	−5.67
$Fe_2(OH)_2^{4+}$	0	2	0	−2	0	−2.95
$Fe(OH)_3(aq)$	0	1	0	−3	0	−13.6
$Fe(OH)_4^-$	0	1	0	−4	0	−21.6
$Fe_3(OH)_4^{5+}$	0	3	0	−4	0	−6.3
$FeSO_4^+$	0	1	1	0	0	3.92
$Fe(SO_4)_2^-$	0	1	2	0	0	5.42
SO_4^{2-}	0	0	1	0	0	0
HSO_4^-	0	0	1	1	0	1.99
OH^-	0	0	0	−1	0	−14
H^+	0	0	0	1	0	0

* pCO_2 was fixed at the atmospheric value ($10^{-3.5}$ atm).

content of 2×10^{-14} gC cell^{-1}; (Hoff, 1993)), which is very similar to the value of ca. 4×10^{-7} μmol Fe cell^{-1} day^{-1} reported for enrichment cultures of FeOM from Iron Mountain, CA (Edwards et al., 1998). The experimentally determined yield coefficients listed in Table 9.2 (ca. 0.01 mol cell-C per mol Fe(II) oxidized) are similar to theoretical values obtained using the energy balance approach of Rittmann and McCarty (2001), assuming a 40% efficiency of energy transfer during FeOM metabolism. The ΔG_{min} values arrived at above (−20 and −10 kJ mol^{-1}) are used for the two organisms. Evaluation of the thermodynamic control term (F_T) in the kinetic equations for Fe(II) oxidation required calculation of the speciation of $Fe^{2+}{}_{(aq)}$ and $Fe^{3+}{}_{(aq)}$, together with the solution pH. This was achieved using the MICROQL algorithm (Westall, 1986); the equilibrium speciation system for the calculations is shown in Table 9.3.

9.1.4.2 FeS_2 Dissolution Kinetics

Research conducted by Rimstidt and colleagues (Rimstidt and Vaughan, 2003; Williamson and Rimstidt, 1994) has provided rate equations for SA-specific FeS_2 dissolution that can be used to estimate FeS_2 dissolution rates as a function of solution composition, assuming an indirect, *abiotic* mechanism of dissolution in all cases. Because all the simulations assumed that dissolved O_2 was present at near-saturation levels (0.2 mM, compared to 0.26 mM at saturation at 25° C), the expressions presented by Williamson and Rimstidt (1994) for systems with dissolved O_2 present were employed:

$$R_{\mathrm{FeS_2-O_2,surf}} = k_{\mathrm{FeS_2-O_2}} \frac{[\mathrm{O_2}]^{0.50}}{[\mathrm{H^+}]^{0.11}} \tag{9.18}$$

$$R_{\mathrm{FeS_2-Fe^{3+},surf}} = k_{\mathrm{FeS_2-Fe(III)}} \frac{[\mathrm{Fe^{3+}}]^{0.93}}{[\mathrm{Fe^{2+}}]^{0.40}} \tag{9.19}$$

where the terms $k_{\mathrm{FeS2-O2}}$ and $k_{\mathrm{FeS2-Fe(III)}}$ are rate constants. The stoichiometric equations to which Eqs. (9.18) and (9.19) apply are those depicted in Eqs. (9.5) and (9.6) above, and thus the units of $R_{\mathrm{FeS2-O2,surf}}$ and $R_{\mathrm{FeS2-Fe3+,surf}}$ are mol Fe(II) released $\mathrm{m^{-2}s^{-1}}$. The rate law for abiotic, $\mathrm{Fe^{3+}_{(aq)}}$-catalyzed oxidation differs from the electrochemical rate law derived in the work of Crundwell and colleagues (Fowler et al., 1999, 2001; Holmes et al., 1999; Holmes and Crundwell, 2000) which has the basic form

$$R_{\mathrm{FeS_2-Fe^{3+},surf}} = k_{\mathrm{FeS_2}}[\mathrm{H^+}]^{-0.5} \frac{k_{\mathrm{Fe^{3+}}}[\mathrm{Fe^{3+}}]}{k_{\mathrm{FeS_2}}[\mathrm{H^+}]^{0.50} + k_{\mathrm{Fe^{2+}}}[\mathrm{Fe^{2+}}]} \tag{9.20}$$

Williamson and Rimstidt (1994) found that the presence of dissolved O_2 accelerates FeS_2 oxidation rates at high $\mathrm{Fe^{3+}_{(aq)}}/\mathrm{Fe^{2+}_{(aq)}}$ ratios, but decreases rates when $\mathrm{Fe^{3+}_{(aq)}}/\mathrm{Fe^{2+}_{(aq)}}$ is low, with the result that there is no statistically significant dependence of the dissolution rate constant on H^+. Since the simulations presented here assumed that O_2 was present at 0.2 mM, Eq. (9.19) was used to calculate rates of FeS_2 dissolution.

Bulk FeS_2 dissolution was modeled under the assumption that the mineral particles dissolve as ideal spheres, which is equivalent to assuming a γ value of 2/3 during mineral dissolution defined in Eq. (8.34) in Chap. 8. The specific SA of the pyrite particles thus changed (increased) with progressive dissolution according to the equation

$$\mathrm{SA}_{(t)} = \mathrm{SA}_0 \times [\mathrm{FeS_2}]_0/[\mathrm{FeS_2}]_{(t)} \times ([\mathrm{FeS_2}]_{(t)}/[\mathrm{FeS_2}]_0)^{2/3} \tag{9.21}$$

where SA_0 is the initial specific surface area $(\mathrm{m^2 g^{-1}})$, and $[\mathrm{FeS_2}]_{(t)}$ and $[\mathrm{FeS_2}]_0$ are the bulk FeS_2 concentrations $(\mathrm{mol\,L^{-1}})$ at time t and time zero, respectively. The combination of Eqs. (9.18), (9.19), and (9.21) accurately reproduced the long-term (4–7 days) kinetics of abiotic FeS_2 dissolution reported in Schippers et al. (1996).

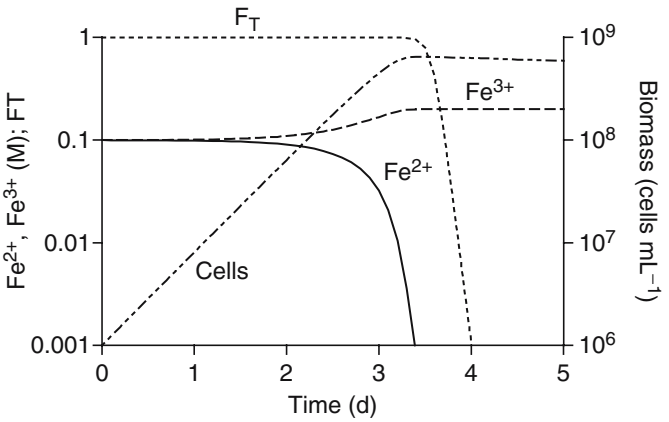

Fig. 9.6 Simulation illustrating the relative importance of kinetic vs. thermodynamic controls on microbial Fe(II) oxidation. A hypothetical batch reaction system was simulated using the kinetic framework and parameter values for *A. ferrooxidans* given in Table 2. Initial Fe^{2+}, Fe^{3+}, and biomass concentrations were 0.1M, 0.1M, and 10^8 cells mL^{-1}, respectively. F_T corresponds to the thermodynamic control function defined by equation 21 in the companion chapter

9.1.4.3 Simulation #1: Kinetic versus Thermodynamic Control on Microbial Fe(II) Oxidation

A simulation using the equations for biological Fe(II) oxidation (by *A. ferrooxidans*) was conducted to assess the extent to which kinetic versus thermodynamic controls would be expected to govern rates of oxidation in a typical reaction system with initial $Fe^{2+}_{(aq)}$ and $Fe^{3+}_{(aq)}$ concentrations of 100 mM, and initial FeOM cell density of ca. 10^6 cells mL^{-1}, and a (fixed) pH of 2 (Fig. 9.6). The results indicate that thermodynamic limitations became critical $(F_T < 0.1)$ only after $> 99\%$ of the Fe(II) had been oxidized and $Fe^{3+}_{(aq)}/Fe^{2+}_{(aq)}$ ratios increased to a value greater than 4,500. Kinetics is therefore likely to play the major role in controlling FeOM metabolism in typical bioleaching and AMD environments.

9.1.4.4 Simulation #2: Influence of Microbial Fe(II) Oxidation on FeS_2 Dissolution

The fundamental influence of microbial Fe(II) oxidation on FeS_2 dissolution is illustrated by a simulation designed to mimic the biotic (enrichment culture from Iron Mountain, CA) versus abiotic oxidation experiments ($320\,mm^2 FeS_2$ surface area in pH 0.7 Fe-free medium) shown in Fig. 9.10a of Edwards et al. (1998). The Fe(II) oxidation parameters for *L. ferrooxidans* (Table 9.2) were used for this simulation, since *L. ferrooxidans* constituted an important component (10%–40%) of the enrichment culture, and since *A. ferrooxidans* was not present in it. The maximum biomass-specific Fe(II) oxidation rate constant $(R_{\max,Fe(II)})$ and maintenance coefficient $(m_{Fe(II)})$ for *L. ferrooxidans* at 30° C (vanScherpenzeel et al.,

1998) were scaled to the temperature used in Edwards et al. (1998) (42° C) using the Q_{10} model (with an average Q_{10} value of 2) for enzymatic reactions (Rawn, 1983). The Q_{10} value corresponds to the ratio of reaction rates (or rate constants) at temperatures 10° C apart; rates are calculated from the following expression:

$$R_{(T)} = R_0 \exp\left(\frac{\ln(Q_{10})}{10} T\right) \tag{9.22}$$

where $R_{(T)}$ is the rate (or rate constant) at temperature T, and R_0 is the rate (or rate constant) at 0° C. The R_0 values for $R_{\max,\mathrm{Fe(II)}}$ and $m_{\mathrm{Fe(II)}}$ were computed from the $R_{(30^\circ\mathrm{C})}$ values by substituting them into Eq. (9.22) and solving for R_0. The rate constants in the FeS_2 dissolution rate laws (Eqs. (9.18) and (9.19)) at 25° C were also scaled for increased temperature, in this case using the Arrhenius equation (see Chap. 1) and an E_a value of 64.5 kJ mol^{-1} for FeS_2 dissolution (Lu et al., 2005). The reference value for the FeS_2 dissolution rate constants ($k_{\mathrm{FeS2-O2}}$ and $k_{\mathrm{FeS2-Fe(III)}}$) at 25° C was set equal to the value of $10^{-7.0}$ determined from simulation of the data from Hansford and Chapman (1992) as described below.

The results of the simulation matched the experimental data in Fig. 10A of Edwards et al. (1998) fairly well, with a few hundred μM total Fe released to solution in the abiotic system which included only slow abiotic $Fe^{2+}_{(aq)}$ oxidation according to Eq. (9.12), compared to $>8,000$ μM in the biotic system which included the enzymatic Fe^{2+} oxidation system described in Table 9.2 (Fig. 9.7a). As observed in the experiment, virtually all of the Fe solubilized in the abiotic system was $Fe^{2+}_{(aq)}$, in contrast to the biotic systems in which $Fe^{3+}_{(aq)}$ totally dominated. Rates of FeS_2 oxidation by $Fe^{3+}_{(aq)}$ were strictly controlled by rates of aqueous-phase Fe(II) oxidation (after an initial burst of FeS_2 oxidation driven by the initial 100 μM $Fe^{3+}_{(aq)}$ present in the reaction system), and ca. 4 orders of magnitude higher in the biotic versus abiotic systems (Fig. 9.7b).

9.1.4.5 Simulation #3: Kinetics of FeS_2 Dissolution Coupled to Microbial Fe(II) Oxidation

Because FeS_2 oxidation involves electron transfer reactions at the mineral surface, particle size, surface area, and solids concentration are expected to exert a fundamental influence on rates of microbially driven FeS_2 oxidative dissolution. There have been many investigations of these phenomena—many more than in the case of Fe(III) oxide reduction (see Hansford and Drossou (1988) for a review of the older literature). Of the various datasets available, that of Hansford and Chapman (1992) on oxidation of different gold-bearing FeS_2 size fractions by *A. ferrooxidans* is one that is amendable to numerical modeling in the context of particle size and surface area effects. The authors conducted batch leaching experiments with FeS_2 particles with diameters of <38 μm, 38–53 μm, or 53–75 μm; the mean surface areas of the different size fractions were 0.0488, 0.0268, and 0.0196 $m^2\,g^{-1}$, respectively. Bulk particle loading was adjusted to provide approximately equal surface area loading

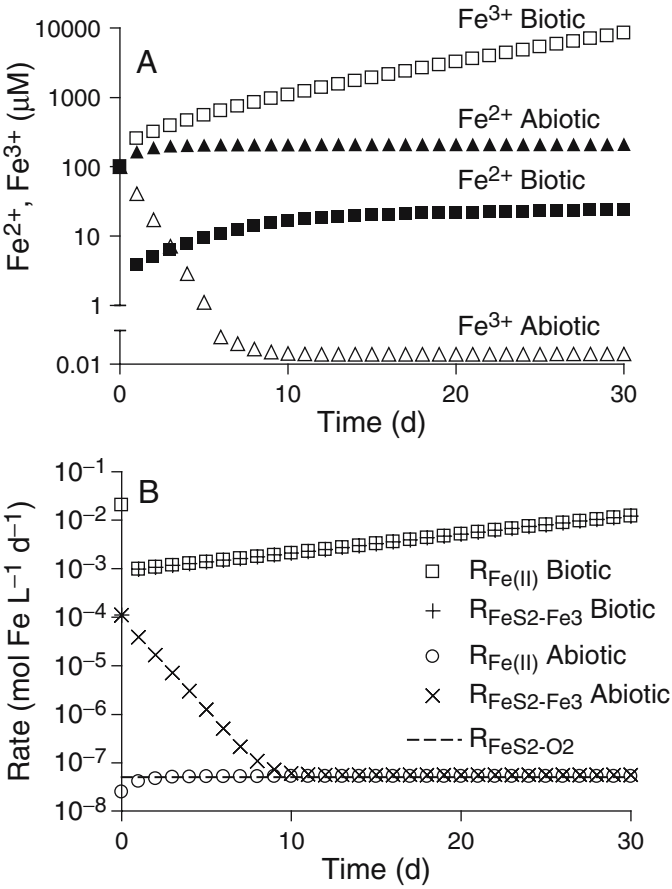

Fig. 9.7 Simulation of the biotic vs. abiotic FeS_2 oxidation systems depicted in Fig. 10A of Edwards et al. (1998). Abiotic Fe(II) oxidation was simulated using equation 12 in the text. Biotic Fe(II) oxidation was simulated using the kinetic framework and parameter values for *L. ferrooxidans* given in Table 2. Chemical (abiotic) FeS_2 oxidation was simulated using equations 18 and 19. Rates of biotic and abiotic reaction were scaled to a temperature of 42 °C as described in section 1.4.4

of ca. $2.7\,m^2\,L^{-1}$. The solids were suspended in low-Fe ($<1\,g\,L^{-1}$) medium and inoculated with ca. 10^8 cells mL^{-1} of *A. ferrooxidans*. The oxidation rate during the linear portion of dissolution curves correlated directly with particle surface area and inversely with particle diameter (Fig. 9.8a). Simulations of coupled microbial Fe(II) oxidation and chemical FeS_2 dissolution accurately reproduced the experimental data (Fig. 9.8b), with two caveats: (1) the effective rate constant for $Fe^{3+}_{(aq)}$-catalyzed FeS_2 oxidation was reduced by an order of magnitude (to $10^{-7.0}$) relative to the best-fit value listed in Williamson and Rimstidt (1994) ($10^{-6.07}$); (2) the fraction of total FeS_2 subject to oxidation was set at a value of 0.94 for the $<38\,\mu m$ fraction and a value of 0.66 for the 38–53 and 53–75 μm size fractions. The adjusted

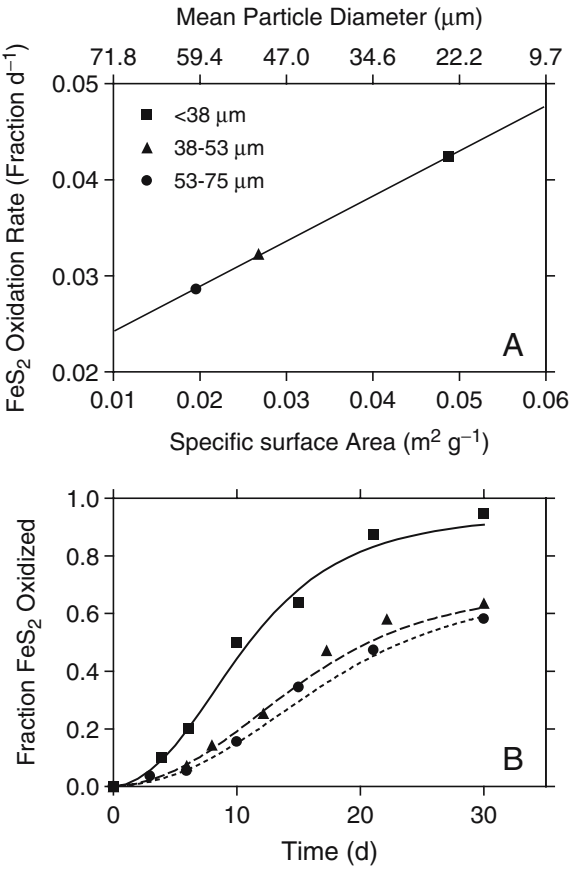

Fig. 9.8 Oxidation of different FeS_2 particle size fractions by *A. ferrooxidans* (Hansford and Chapman (1992); data reproduced with permission). Panel A: fractional rate of oxidation during the linear portion of the dissolution curves shown in panel B. Panel B: Time course of FeS_2 oxidation; solid lines show results of simulation of coupled microbial Fe(II) oxidation (Table 2) and chemical (abiotic) FeS_2 oxidation (equations 18 and 19 in text)

rate constant is easily rationalized, as there is considerable variability in surface area-specific rates of FeS_2 dissolution under fixed aqueous geochemical conditions (Williamson and Rimstidt, 1994). Differences of the fraction of FeS_2 subject to oxidation can be explained by the fact that FeS_2 dissolution occurs via formation of pores rather than by uniform particle shrinkage (e.g., Mustin et al. (1992a), Hansford and Drossou (1988)), and that different mineral preparations could almost certainly produce different pore structures with different reactivity toward long-term dissolution. The important point is that the overall process of FeS_2 dissolution coupled to microbial Fe(II) oxidation can be interpreted macroscopically as a SA-controlled process akin to many other mineral dissolution processes.

This basic reality is further illustrated by the batch *L. ferrooxidans* FeS_2 oxidation experiments of Boon et al. (1995), in which increasing amounts of mineral

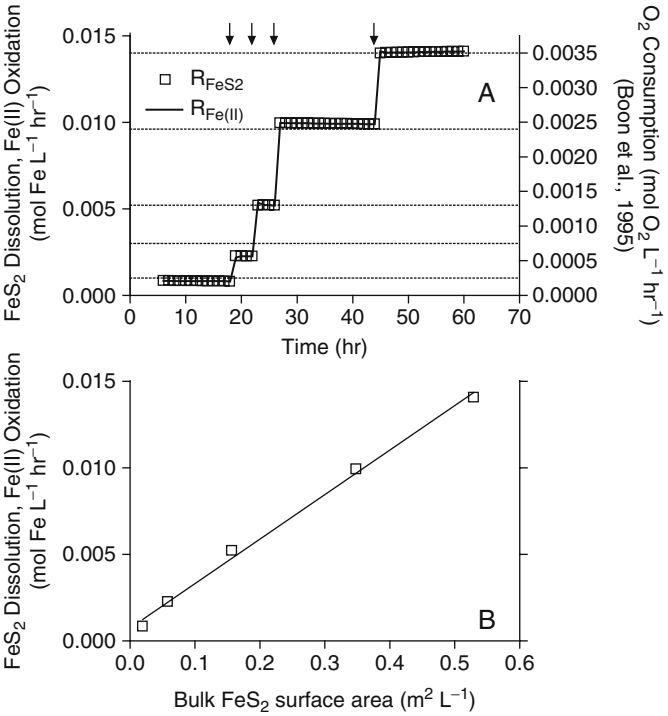

Fig. 9.9 Modeling of the batch FeS_2 oxidation experiments (*L. ferrooxidans*) of Boon et al. (1995) with staged FeS_2 addition (arrows indicate time of FeS_2 addition). Panel A: Rates of chemical FeS_2 dissolution ($k_{FeS2-Fe(III)}$ of $10^{-7.32}$) and microbial Fe(II) oxidation. Dashed lines correspond to measured rates of O_2 consumption shown on the right-hand y-axis. Panel B: Mean rates of FeS_2 dissolution and Fe(II) oxidation as a function of bulk FeS_2 surface area

were added to a reactor containing $10\,g\,L^{-1}$ of $Fe^{3+}_{(aq)}$ at pH 1.6 over a ca. 3-day period, and in which rates of Fe(II) oxidation were measured by monitoring O_2 consumption in the reactor. Modeling of this experiment with a $k_{FeS2-Fe3+(aq)}$ value of $10^{-7.32}$ accurately reproduced the measured O_2 consumption rates (Fig. 9.9a), and illustrates how rates of coupled Fe(II) oxidation andFeS_2 dissolution were directly proportional to the FeS_2 surface loading (Fig. 9.9b).

9.1.4.6 Simulation #4: Competition between A. ferrooxidans and L. ferrooxidans

Although *A. ferrooxidans* has historically been considered to be a dominant component of microbial communities in mesophilic ($\leq 40^{\circ}C$) AMD environments and commercial bioleaching systems (Nordstrom and Southam, 1997; Rawlings, 2002), it is now widely recognized that *A. ferrooxidans* in not favored in extremely acidic AMD (Druschel et al., 2004; Schrenk et al., 1998)

or in continuous bioleaching reactors where $Fe^{3+}_{(aq)}$ is much more abundant than $Fe^{2+}_{(aq)}$ (Rawlings et al., 1999). *L. ferrooxidans* and related *Leptospirilli* are dominant organisms in such environments (Bond et al., 2000a, b; Coram and Rawlings, 2002; DeWulf-Durand et al., 1997; Schrenk et al., 1998; Vasquez and Espejo, 1997). However, *A. ferrooxidans* may be a dominant organism in higher pH, lower temperature AMD environments (e.g., in tunnels outside of the ore body within the Richmond Mine at Iron Mountain; Schrenk et al. (1998)); and in dump and heap leaching environments with restricted O_2 input, where the $Fe^{3+}_{(aq)}/Fe^{2+}_{(aq)}$ is relatively low (Pizarro et al., 1996).

Apart from basic physiological limitations posed by differences in pH and temperature tolerance, the predominance of *Leptospririllum* over *Acidithiobacillus* in many situations has been attributed to the ability of *Leptospirillum* to function at relatively high $Fe^{3+}_{(aq)}/Fe^{2+}_{(aq)}$ ratios (Rawlings et al., 1999), as illustrated by the kinetic data from Norris et al. (1988) shown in Fig. 9.5, and by the results of the mixed culture competition experiments presented in the same paper (which showed that *L. ferrooxidans* accounted for 92% of microbial biomass after 200 h of continuous cultivation). Conversely, the tendency for *A. ferrooxidans* to predominate over *L. ferrooxidans* and other chemolithotrophs in more Fe(II)-rich environments, including typical ferrous sulfate-containing enrichment/enumeration culture media, can be attributed to the rapid growth rate of *A. ferrooxidans* compared to other FeOM. The ability of *L. ferrooxidans* to oxidize $Fe^{2+}_{(aq)}$ at higher $Fe^{3+}_{(aq)}/Fe^{2+}_{(aq)}$ ratios (i.e., at higher redox potentials) compared to *A. ferrooxidans* is likely related to differences in the respiratory chain components of these two organisms (Rohwerder et al., 2003). *L. ferrooxidans* produces an acid-stable periplasmic and/or outer membrane cytochrome (cyt_{579}) with a E^0_h of ca. +670 mV (Blake et al., 1993; Hart et al., 1991) that is currently thought to be the initial EA for Fe(II) oxidation (see Fig. S5 in Ram et al. (2005)). In contrast, the outer membrane cytochrome Cyc2 which is thought to be the initial EA for Fe(II) oxidation by *A. ferrooxidans* has a E^0_h of ca. +560 mV (Yarzabal et al., 2002b).

Two different simulations were conducted to illustrate competitive interactions between *A. ferrooxidans* and *L. ferrooxidans* in the context of FeS_2 oxidation. The simulations assumed a hydrologically open reaction system with a fluid residence of time of 1 day. A time-invariant bulk FeS_2 concentration of 0.5 mol L^{-1} (equivalent to ca. 5 wt % FeS_2 in a sediment with 50% porosity) was assumed, which at a specific surface area of ca. 0.01 $m^2\,g^{-1}$ (corresponding to a mean particle size of ca. 60 μm) corresponds to surface loading of ca. 6 $m^2\,L^{-1}$. Initial $Fe^{3+}_{(aq)}$ and $Fe^{2+}_{(aq)}$ concentrations were set at 10 mM, and initial *A. ferrooxidans* and *L. ferrooxidans* cell densities at 10^6 cells mL^{-1}. The potential for precipitation of AIO was included in the simulations in order to assess how loss of $Fe^{3+}_{(aq)}$ from solution via Fe(III) oxide precipitation could alter the $Fe^{3+}_{(aq)}/Fe^{2+}_{(aq)}$ ratio and thereby influence competition between these two organisms. Precipitation of Fe(III) oxides is a common process in AMD environments (Bigman et al., 1990), particularly where the rocks undergoing weathering are less enriched in FeS_2, and/or or where the H^+ buffering capacity is relatively high, such that extremely acidic pH values do not occur. AIO $(Fe(OH)_3)$ precipitation was modeled using a standard transition state theory rate law in which

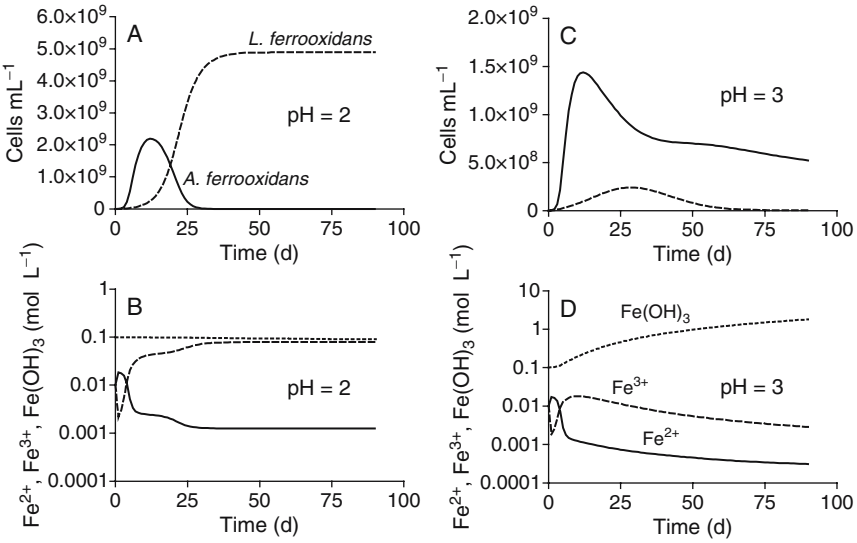

Fig. 9.10 Simulation of coupled FeS_2 dissolution and aqueous-phase Fe(II) oxidation by *A. ferrooxidans* and *L. ferrooxidans* in a hypothetical flow-through reaction system at pH 2 (no AIO precipitation) vs. pH 3 (AIO precipitation). The reaction system was assumed to have a hydraulic residence time of 1 day, a fixed bulk FeS_2 concentration of 0.5 mol L^{-1}, an initial bulk HFO concentration of 0.1 mol L^{-1}, and initial *A. ferrooxidans* and *L. ferrooxidans* cell densities of 10^6 cells mL^{-1}. The $k_{FeS2-O2}$ and $k_{FeS2-Fe3+}$ values were set equal to the best-fit values listed in Williamson and Rimstidt (1994) ($10^{-8.19}$ and $10^{-6.07}$, respectively)

the rate of precipitation is dependent on the available mineral surface area together with the degree of supersaturation (Eq. (29) in Steefel and Lasaga (1994)):

$$R_{\mathrm{Fe(OH)_3}} = k_{\mathrm{precip,Fe(OH)_3}} A_{\mathrm{Fe(OH)_3}} \left(\frac{\{\mathrm{H^+}\}^3 \{\mathrm{Fe^{3+}}\}}{K_{\mathrm{sp,Fe(OH)_3}}} - 1 \right) \tag{9.23}$$

where $R_{\mathrm{Fe(OH)3}}$ is the rate of AIO precipitation $(\mathrm{mol\,L^{-1}\,s^{-1}})$; $k_{\mathrm{precip,Fe(OH)3}}$ is the precipitation rate constant $(\mathrm{mol\,m^{-2}\,s^{-1}})$; $A_{\mathrm{Fe(OH)3}}$ is the bulk available mineral surface area $(\mathrm{m^2\,L^{-1}})$, which was calculated from the bulk AIO concentration (set initially to 0.1 mol L^{-1}) at each time step assuming a molecular weight of 89 g mol^{-1} and an assumed specific SA of 600 $m^2\,g^{-1}$ (Dzombak and Morel, 1990); and $K_{\mathrm{sp,Fe(OH)3}}$ is the solubility product for AIO. The AIO solubility product $(10^{3.3})$ and precipitation rate constant $(k = 5.0 \times 10^{-10}\,\mathrm{mol\,m^{-2}\,s^{-1}})$ were optimized to fit the data of Grundl and Delwiche (1993).

In the first simulation, pH was fixed at a value of 2, at which AIO precipitation was not favorable, and relatively high concentrations of $Fe^{3+}{}_{(aq)}$ accumulated (Fig. 9.10a,b). *L. ferrooxidans* prevailed under these conditions, although *A. ferrooxidans* dominated during the early stages of the simulation as a result of its

higher biomass-specific Fe(II) oxidation rate and lower maintenance coefficient (Table 9.2C). *A. ferrooxidans* dominated throughout the second simulation at pH 3 (Fig. 9.10c,d), in which AIO precipitation maintained $Fe^{3+}_{(aq)}/Fe^{2+}_{(aq)}$ ratios below 10 (compared to values in excess of 50 at pH 2).

It is of interest to interpret the simulation results in relation to the framework first suggested by Hansford (1997), in which rates of microbial Fe(II) oxidation and FeS_2 dissolution are plotted as a function of an imposed system redox potential (E_h) and total aqueous Fe concentration, together with and $Fe^{3+}_{(aq)}$ and $Fe^{2+}_{(aq)}$ concentrations calculated using the Nernst equation. The point of intersection of the FeS_2 dissolution and the upper (higher) Fe(II) oxidation curve represents the pseudo-steady-state rate of Fe(II) turnover and associated E_h at the end of the 90-day simulations. For the pH 2 simulation, the dissolution curve intersects the Fe(II) oxidation curve of *L. ferrooxidans* at a higher rate of Fe(II) turnover compared to *A. ferrooxidans* (Fig. 9.11a), and therefore *L. ferrooxidans* is the dominant species; the reverse is true for the pH 3 simulation (Fig. 9.11b), in which overall rates of Fe(II) turnover are ca. tenfold lower because of the lower abundance of $Fe^{3+}_{(aq)}$ as an oxidant for FeS_2. These results provide a clear illustration of how the interplay between microbial ecophysiology and aqueous geochemistry can control overall rates of water–rock interaction.

9.1.4.7 Simulation #5: Influence of FeOM Attachment on FeS_2 Dissolution Kinetics

As discussed in Sect. 9.1.3, local decrease in H^+ and/or elevation of $Fe^{3+}_{(aq)}$ at the mineral–water interface during Fe(II) oxidation by attached FeOM could have an important influence on bulk mineral dissolution kinetics. In order to quantitatively explore this concept, the microbial Fe(II) oxidation/FeS_2 dissolution system described above was incorporated into a one-dimensional transport-reaction model (in Visual Fortran) which accounted for diffusion of solutes and random (diffusion-like) transport of FeOM cells within a 1 cm-thick layer of fluid overlying $1\,cm^2$ of FeS_2 surface. The primary dependent variables in the model included the five components in the equilibrium speciation system ($Fe^{2+}, Fe^{3+}, {SO_4}^{2-}, H^+, CO_2$; see Table 9.3) together with FeOM biomass. Multicomponent solute transport was simulated by allowing the components to diffuse according to a weighted-average diffusion coefficient based on the relative abundance of the different species that include that component (listed in Table 9.3). Diffusion coefficients for ion pairs were estimated by multiplying the ratio of the molecular weight of the ion pair to that of the free ion times the diffusion coefficient for the free ion. This approach provides (C.I. Steefel, personal communication) a practical way to account for charge effects in multicomponent diffusion (see Chap. 11 by Steefel in this volume). Free ion diffusion coefficients (25° C, infinite dilution) were obtained from the DIFCOEF subroutine in Boudreau (1997). Diffusive transport was modeled using central differences on an uneven grid (100 node points) using the approach of Pearson

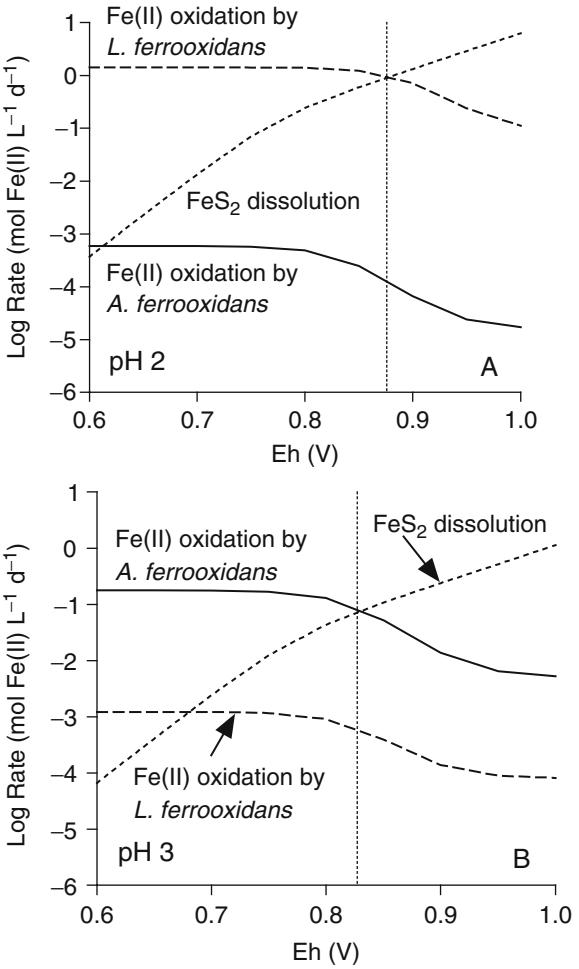

Fig. 9.11 Rates of microbial Fe(II) oxidation and chemical (abiotic) FeS_2 dissolution vs. imposed system redox potential (E_h) with fixed total aqueous Fe concentration, based on the development presented in Hansford (1997). The total dissolved Fe concentrations present at the end of the two 90-d simulations shown in Fig. 10 were used to compute concentrations of $Fe^{3+}_{(aq)}$ and $Fe^{2+}_{(aq)}$ across a range of imposed E_h values using the Nernst equation. The resulting $Fe^{2+}_{(aq)}$ and $Fe^{3+}_{(aq)}$ concentrations were used to compute rates of microbial Fe(II) oxidation (for both *A. ferrooxidans* and *L. ferrooxidans*) according to the equation 1 in Table 2, and of abiotic FeS_2 dissolution according to equations 18 and 19 in the text. Dashed vertical lines indicate the calculated system E_h at the end of the 90-day simulations. The point of intersection of the FeS_2 dissolution curves, the upper (higher) Fe(II) oxidation curves, and the vertical dashed lines represents the pseudo-steady-state rates of Fe(II) turnover at the end of the two 90-day simulations shown in Fig. 10

(Pearson, 1968) as explained on pp. 326–227 in Boudreau (1997). Grid node points were concentrated near the mineral–water interface in order to accurately simulate transport where reaction rates were maximal; the grid spacing increased smoothly from 1.3 μm at the mineral surface to 180 μm at 1 cm from the surface.

Zero-gradient (Neumann) boundary conditions were assumed at the upper and lower boundaries such that there was no flux of solutes into or out of the $1\,cm^3$ reaction system. Initial $Fe^{2+}_{(aq)}$ and $Fe^{3+}_{(aq)}$ concentrations were set equal to 1 mM throughout the system.

FeS_2 dissolution was assumed to take place in the uppermost grid layer (top 1.3 μm) according to Eqs. (9.18) and (9.19) and the computed $Fe^{3+}_{(aq)}$ and $Fe^{2+}_{(aq)}$ concentrations within that layer. The available FeS_2 surface area was fixed at $1\,cm^2$ throughout the 3-day simulation period. Chemical and biological Fe(II) oxidation (together with FeOM cell growth) in each layer were modeled as described for the reactor systems discussed above. In order to assess the potential significance of FeOM surface association on FeS_2 dissolution, simulations were conducted with or without random, diffusion-like cell transport within a 50 μm-thick boundary layer above the mineral surface. The coefficient for random cell transport was arbitrarily set to a value of $1\,cm^2\ day^{-1}$, which is comparable to the coefficient for diffusion of the heavier ions such as $Fe^{2+}(0.610\,cm^2\ day^{-1})$ and $SO_4^{2-}(0.923\,cm^2\,day^{-1})$. The thickness of the boundary layer in which cells could "attach" was based on the observation by Crundwell (1996) that colonization of FeS_2 by *A. ferrooxidans* results in the formation of clusters of cells and EPS that are between 30 and 50 μm thick. Diffusive transport of solutes took place across the entire spatial domain in all cases, as did diffusive cell transport above the boundary layer. In the absence of cell transport, all cells remained within the layer in which they were produced. Although more mechanistic models of FeOM attachment to and surface colonization of FeS_2 have been developed (Chandraprabha et al., 2003; Crundwell, 1994), this approach provides a default way of accounting for the fundamental tendency of motile cells to proliferate within sharp geochemical gradients where their energy sources are locally concentrated (Koch, 1991).

The transport-reaction (mass conservation) equations for each of the six primary variables were solved using the numerical method of lines (Schiesser, 1991), implemented with the stiff ODE solver VODE (Brown et al., 1989) as described in Boudreau (1997). The equilibrium speciation routine operated within the numerical transport-reaction integration procedure, so that the results correspond effectively (within prescribed relative and absolute error tolerances, which were set at 10^{-3} and 10^{-9}, respectively) to those of a fully coupled (implicit) solution to a mixed kinetic-equilibrium speciation reactive transport problem (Steefel and MacQuarrie, 1996). Six simulations were conducted across a range of initial pH values of 1.5–2.0 in order to assess the impact of system pH on Fe turnover.

The results of the simulations showed that accumulation of cell biomass in the vicinity of the FeS_2 surface (referred to hereafter as "attachment", with the caveat that attachment was not explicitly simulated) had a modest but distinct impact on the distribution of solutes at the mineral–water interface: after a 3-day colonization period, concentrations of $Fe^{3+}_{(aq)}$ were higher within the upper few hundred μm compared to the no-attachment systems, whereas $Fe^{2+}_{(aq)}$ concentrations were lower (Fig. 9.12a). pH values were nearly uniform (Fig. 9.12b), and slightly lower for the system with attachment, presumably because of the higher rate of FeS_2 surface dissolution (see Fig. 9.13a). As expected, attachment had a dramatic impact

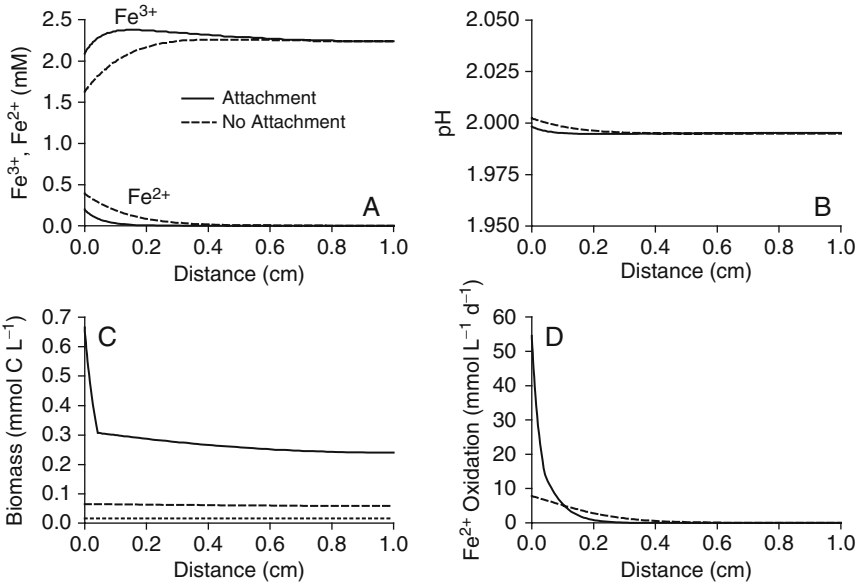

Fig. 9.12 Results of transport-reaction simulation of microbial Fe(II) oxidation, FeS_2 surface dissolution, diffusive solute transport, and random (diffusion-like) FeOM transport within a 1-cm layer overlying 1 cm^2 of FeS_2 surface. The terms "attachment" and "no attachment" refer to simulations in which random cell transport was absent or present within a 50 μm-thick boundary layer overlying the FeS_2 surface. Results shown are from the end of 3-day simulations, starting with an initial uniform FeOM (assumed to be *A. ferrooxidans*) cell density of 6.0×10^8 cells mL^{-1} (indicated by the dotted line in panel C), dissolved Fe^{2+} and Fe^{3+} concentrations of 1 mM, and a pH of 2.0

on the distribution of FeOM biomass and Fe(II) oxidation rate, which increased sharply within the 50 μm boundary layer above the FeS_2 surface (Fig. 9.12c,d).

Results virtually identical to those for the pH 2 system shown in Fig. 9.12 were obtained in simulations with initial pH values of 1.5–1.9. The total quantity of Fe released to solution over the 3-day simulation period in the attachment versus no-attachment systems indicates that attachment enhanced FeS_2 dissolution by ca. 25% under all of the pH conditions (Fig. 9.13b, solid symbols). Interestingly, there was no significant influence of pH on total Fe release. The latter results contrast with those obtained in the constant redox potential experiments of Crundwell and colleagues (Fowler and Crundwell, 1998; Fowler et al., 1999; Holmes et al., 1999; Holmes and Crundwell, 2000), which showed a positive correlation between system pH and FeS_2 dissolution rate. One might expect that this disagreement can be traced to the rate law used to simulate $Fe^{3+}{}_{(aq)}$-catalyzed FeS_2 dissolution (Eq. (9.4)), which is independent of pH (Fig. 9.13a, solid symbols). To evaluate this issue, the simulations were re-run using the rate law for FeS_2 dissolution in the absence of O_2 given in Williamson and Rimstidt (1994), which is dependent on pH:

$$R_{FeS_2-Fe^{3+},surf} = k_{FeS_2-Fe^{3+}} \frac{[Fe^{3+}]^{0.30}}{[Fe^{2+}]^{0.47}[H^+]^{0.32}} \tag{9.24}$$

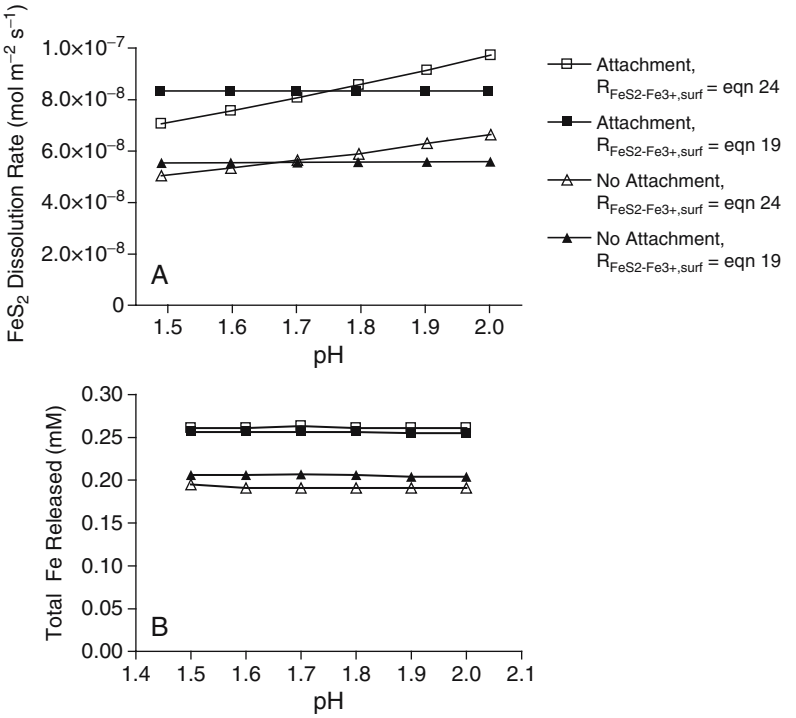

Fig. 9.13 Rates of FeS_2 surface dissolution (A) and total amount of Fe released (B) at the end of the 3-d transport-reaction simulations with and without FeOM "attachment" at different pH values and with different rate laws for Fe^{3+}-catalyzed FeS_2 dissolution

Although this change caused the surface area-specific FeS_2 dissolution rate to vary with pH (Fig. 9.13a, open symbols), the total quantity of Fe released and the influence of attachment on Fe release were only slightly altered and did not change with pH (Fig. 9.13b, open symbols). These results clearly indicate that the primary mechanism by which attachment accelerated FeS_2 dissolution was through elevation of $Fe^{3+}_{(aq)}$ concentration at the mineral–water interface (Fig. 9.12a).

In summary, the results of this modeling exercise demonstrate a positive feedback between FeOM attachment and FeS_2 dissolution that is consistent with available experimental data. The modest (ca. 25%) acceleration of FeS_2 dissolution associated with cell attachment agrees well with the results of Crundwell and colleagues on the influence of attached FeOM (*A. ferrooxidans*) on FeS_2 dissolution in redox potentiostats, although the mechanism of acceleration is different. The no-attachment simulations are analogous to the abiotic potentiostats in that they maintained $Fe^{3+}_{(aq)}$ and $Fe^{2+}_{(aq)}$ at concentrations close to those present in the attachment systems, such that the influence of attachment on FeS_2 dissolution could be clearly discerned.

9.2 Summary and Prospects

9.2.1 Near-Term Advances in Modeling Coupled Microbial-Geochemical Reaction Systems

The discussion and analyses presented in this and the preceding chapter focused on development of macroscopic kinetic expressions of microbially catalyzed geochemical reactions. Such expressions provide a simple (relatively) but powerful way to quantitatively connect microbial metabolism and population dynamics to geochemical flux in virtually any reaction system. Reaction frameworks developed to analyze experimental, laboratory-scale systems can be incorporated into standard numerical transport-reaction codes in order to address the complex interactions between hydrology, geochemistry, and microbiology that govern in situ reactive transport (Yeh et al., 2001). Although there is a considerable history of including microbial processes in reactive transport models (see Hunter et al. (1998) for a review), incorporation of mixed kinetic-thermodynamic reaction networks together with multispecies population dynamics into such models is in its infancy. Apart from (now fading) limitations posed by computing power, development of such models has been hindered by a paucity of experimental information required to assemble reaction networks for coupled microbial-geochemical processes, as well as by the need for reliable numerical strategies and software for representing such systems.

Within the past few years, several groups have introduced modeling frameworks that are capable of handling the full spectrum of aqueous/solid-phase geochemistry and microbial population dynamics (Aguilera et al., 2005; Fang et al., 2003; Islam and Singhal, 2002; Jin and Bethke, 2003; Krautle and Knabner, 2005; Maurer and Rittmann, 2004; Mayer et al., 2002; Phanikumar and McGuire, 2004; Regnier et al., 2002; Roden et al., 2005; Wirtz, 2003; Yeh et al., 1998), and these models have been applied to a limited number of laboratory- (Roden et al., 2005; Thullner et al., 2005; Watson et al., 2003) and field-scale (Scheibe et al., 2006; Thullner et al., 2005; Watson et al., 2005) systems. The application of multispecies modeling to geochemical systems is bound to increase rapidly in the coming years, and will in due course catch-up with the sophisticated multispecies models that exist for activated sludge, anaerobic digestion, and various biofilm processes (Rittmann and McCarty, 2001).

A key ingredient to near-term advances in our understanding (both qualitative and quantitative) of microbially catalyzed geochemical processes will be to identify the morgs responsible for the reactions and to quantify their biomass and activity. Although radioisotopic and stable isotopic tracer techniques (often used in conjunction with numerical modeling) for determining bulk biogeochemical processes rates are available and steadily advancing, the ability to identify and quantify morgs responsible for biogeochemical processes is an important new frontier (see Madsen (2005) for review and examples). Culture-independent molecular biological techniques based on the analysis of ribosomal rRNA genes (phylogenetic markers) and functional genes (genes that code for the enzyme(s) responsible for the process of interest) and their products (ribosomal RNA, functional gene mRNA transcripts,

and translated proteins), when combined with classical geomicrobiological techniques (e.g., bulk process measurements and cultivation-based methods for identification/quantification of functional microbial groups), are playing a crucial role in the exploration of this frontier (Oremland et al. (2005); see Fig. 9.14a). The systematic quantification of processes and interactions that takes place during kinetic model development provides an important way to synthesize the information derived from these molecular tools (Rittmann and McCarty, 2001).

9.2.2 The Genomics Revolution

We are now in the era of metagenomics (see Fig. 9.14b), in which information on entire (or partial) microbial genomes retrieved from multiple pure cultures as well as environmental samples can be used to gain deeper insight into the organisms and metabolic pathways responsible for biogeochemical processes (Banfield et al., 2005; Croal et al., 2004; DeLong, 2004; Handelsman, 2004; Macalady and Banfield, 2003). There are three basic ways in which genomic information can contribute to our understanding of the kinetics of microbially catalyzed geochemical reactions. First, genome-facilitated studies of microbial physiology and metabolism can be used to identify the key gene(s) that are responsible for catalyzing the reaction(s) of interest, which in turn can be used to develop tools to detect and quantify the presence of the morg(s) carrying out that reaction (illustrated in Fig. 9.14a). Recent relevant examples include identification of the genes for (i) outer membrane cytochromes involved in DIR (Chin et al., 2004); (ii) periplasm/membrane-associated cytochromes involved in acidophilic Fe(II) oxidation (Ram et al., 2005; Tyson et al., 2004); and (iii) reductase enzymes responsible for dissimilatory reduction of As(V) to As(III) (Malasarn et al., 2004). An interesting related example of this approach is the recent discovery that DIRMs from the family *Geobacteraceae* possess a unique, eukaryotic-like citrate synthase gene that can be used to assess the activity of *Geobacteraceae* in subsurface environments (Holmes et al., 2005). Similarly, tools for detecting genes for N_2 fixation by *Geobacteraceae* have been developed to assess the role of nitrogen limitation in subsurface Fe(III) oxide reduction activity (Holmes et al., 2004). These genome-enabled techniques will soon be essential components of the biogeochemist's toolbox (Oremland et al., 2005).

A second important way in which genomics has the potential to inform the study of microbial-geochemical kinetics is through development of whole genome-scale metabolic network reconstructions of individual prokaryotic cells. Such network reconstructions can be used together with using linear optimization to simulate the metabolism of microbial cells as a function of various internal constraints and external boundary conditions (Price et al., 2004). Table 9.4 and Fig. 9.15 provide a brief introduction to metabolic network modeling. The level of mechanistic detail included in a metabolic network model (e.g., explicit kinetic constraints on key reaction steps) is open-ended and can increase incrementally as new information is acquired (Edwards et al., 2002). Such models have thus far been applied mainly to model morgs such as *Escherichia coli* and *Saccharomyces cerevisiae*, and pathogens

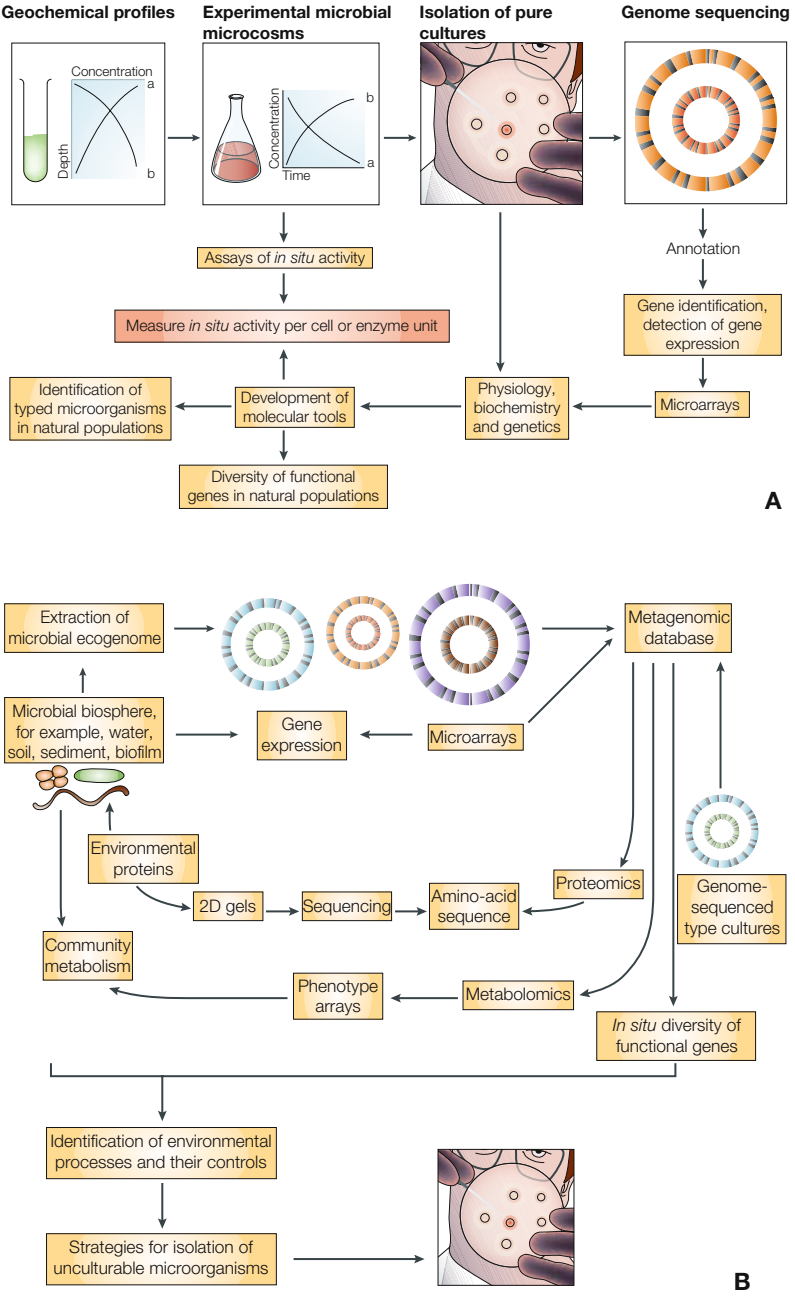

Fig. 9.14 Illustration of (A) merging of classical geomicrobiological techniques with modern molecular biological methods, and (B) the metagenomic approach to geomicrobiological investigation. Both diagrams are from Oremland et al. (2005), used with permission (see also color insert)

Table 9.4 Overview of microbial metabolic network modeling and identification of potential linkages to biogeochemical reaction modeling

As in the case of the macroscopic reaction modeling approaches described in this chapter, the fundamental principle underlying whole-cell metabolic network modeling is conservation of mass. A stoichiometric flux balance equation is written for each metabolite in the reaction network, which yields a set of mass balance equations that interconnect the various metabolites (Schilling et al., 1999). These mass balance equations can be expressed by the following compact matrix expression:

$$\frac{d\mathbf{X}}{dt} = \mathbf{S} \cdot \mathbf{v} - \mathbf{b} \tag{1}$$

where **X** is vector of metabolite concentrations, **S** is a matrix containing the stoichiometric coefficients of all the reactions in the network, **v** is a vector of fluxes through each node in the metabolic network, and **b** is a vector of net metabolite transfer into our out of the network (Schilling et al., 1999). This expression is identical in form to that used to describe conservation of mass in coupled transport-reaction systems (Steefel and VanCappellen, 1998). Figure 9.15 shows a simple example of a metabolic network consisting of three reactions (modified from Fig. 2 in Edwards et al. (2002), used with permission). A steady-state assumption is typically made in which production of metabolites is balanced by their consumption, which results a system of linear equations

$$\mathbf{S} \cdot \mathbf{v}' = 0 \tag{2}$$

where $\mathbf{v}'$ is a vector that contains both the original **v** and **b** vectors (Varma and Palsson, 1994b). Since there are always more fluxes than there are metabolites in the system (by virtue of the flux terms in the **b** vector), this system of equations is undetermined and must therefore formulated as a linear programming problem. Equation (2) is solved by linear optimization to determine flux distributions that minimize or maximize a particular objective function, a process referred to as "flux balance analysis" (FBA). FBA can be used to identify particular behaviors within the allowable solution space, such as behaviors that produce the highest possible growth rate, or maximal production of a particular metabolite, under various types of constraints (Covert and Palsson, 2002; Edwards et al., 2002; Price et al., 2004). It can also be used to predict the metabolic activity of cells over time (Covert and Palsson, 2002; Varma and Palsson, 1994a), under the assumption that timescales associated with internal cellular processes are much shorter than those associated with the morg's environment. The latter idea is key to the potential application of FBA to biogeochemical reaction modeling: in principle it should be possible to solve Eq. (9.2) (i.e. to optimize a given objective function under appropriate constraints) at each time step in dynamic a simulation along with the equations that depict macroscopic chemical fluxes. Numerically speaking, this task would be analogous to use of multidimensional Newton–Raphson (Press et al., 1992) to solve the systems of nonlinear equations that describe equilibrium speciation and kinetic reactions in a typical (bio)geochemical reaction model (Steefel and VanCappellen, 1998). As genome-scale metabolic models are developed for different types of morgs involved in biogeochemical processes, it should be possible to develop coupled macroscopic biogeochemical/metabolic network models for multiple interacting species. Pramanik et al. (1999) provide an example of the application of a simplified (not based on genomic reconstruction) metabolic network model to a mixed culture of organisms involved in enhanced biological phosphorous removal.

such as *Haemophilus influenzae* and *Helicobacter pylori*. However, a genome-scale metabolic network model has been developed for *G. sulfurreducens* (Price et al., 2004), and the model has already provided important insight into regulation of metal reduction activity in this and related *Geobacteraceae* (Mahadevan et al., 2006). The potential exists for combining genome-scale metabolic network models with biogeochemical reactive transport models such as those discussed in this chapter

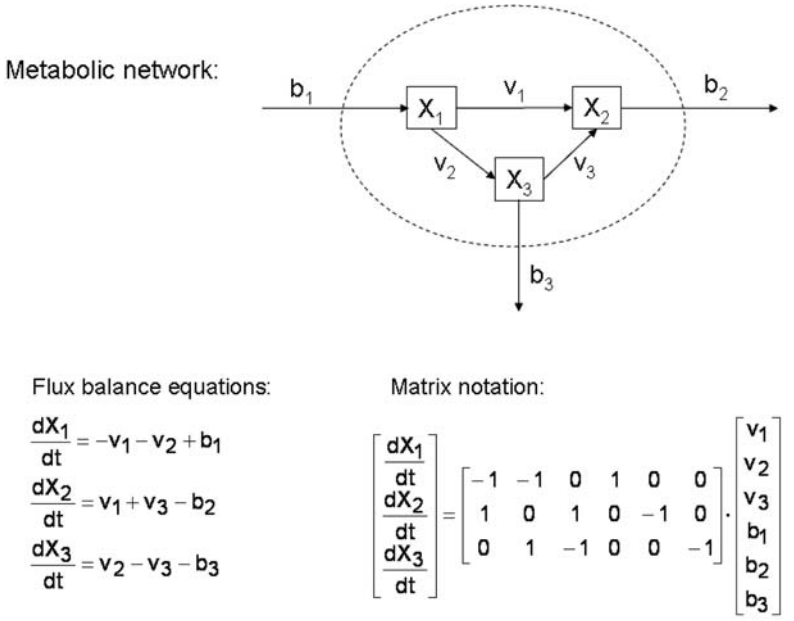

Fig. 9.15 Structure and mass balance equations for a hypothetical metabolic network consisting of three reactions. X_1, X_2, and X_3 correspond to metabolite reservoirs; v_1, v_2, and v_3 correspond to internal metabolite fluxes (conversion rates); and b_1, b_2, and b_3 correspond to external fluxes (uptake and secretion rates). Modified from Fig. 2 in Edwards et al. (2002), used with permission

(see Table 9.4), which could revolutionize prediction of the response of key functional groups of organisms to environmental perturbations and gradients (Lovley, 2003).

Finally, information on the genomic composition of entire microbial communities could further the quantitative description of biogeochemical processes in several ways (see Fig. 9.14b). In addition to providing information required to develop tools to track the abundance and activity of key populations within the community (including genome-enabled strategies for isolation of previously unculturable organisms; see Tyson et al. (2005) and Tyson and Banfield (2005) for an example and a review), community metagenomics can reveal the presence or absence of genes for certain metabolic functions within different populations, which in turn could point to important ecological relationships among those populations. Moreover, reconstruction of the genomes of key components of the microbial community could be used to assemble and constrain coupled biogeochemical reaction/metabolic network models that include multiple populations. Together these pieces of information will eventually lead to a quantitative understanding of the metabolic functions of the microbial community at a molecular level, and along the way provide insight into the pathways of genetic exchange (e.g., homologous recombination, lateral gene transfer) that are now recognized to be key to the development of microbial

populations, and ultimately to the structure and function of communities of interacting morgs (Tyson et al., 2004; Whitaker and Banfield, 2005).

Acknowledgments

The review and analysis of sulfide mineral oxidation mechanisms and kinetics discussed in this chapter was supported in part by salary funds from the U.S. Department of Energy (DE-FG04-ER63915) and the U.S. National Science Foundation (EAR-0525510). Other financial and logistical support for the preparation of this and the companion chapter was provided by the Department of Geology and Geophysics at the University of Wisconsin, and the University of Wisconsin-Madison Libraries. I wish to acknowledge the influence that the published works of Jill Banfield, Derek Lovley, Bruce Rittmann, Ronald Oremland, and Bernhard Palsson had on my way of thinking about the future directions in biogeochemical modeling discussed in the last section of this chapter.

References

Aguilera D. R., Jourabchi P., Spiteri C., and Regnier P. (2005) A knowledge-based reactive transport approach for the simulation of biogeochemical dynamics in Earth systems. *Geochem. Geophys. Geosys.* **6**, Art. No. Q07012 JUL 27 2005.

Arredondo R., Garcia A., and Jerez C. A. (1994) Partial removal of lipopolysaccharide from *Thiobacillus ferrooxidans* affects it adhesion to solids. *Appl. Environ. Microbiol.* **60**, 2846–2851.

Baker B. J. and Banfield J. F. (2003) Microbial communities in acid mine drainage. *FEMS Microb. Ecol.* **44**, 139–152.

Banfield J. F., Tyson G. W., Allen E. A., and Whitaker R. J. (2005) The search for a molecular-level understanding of processes that underpin Earth's biogeochemical cycles. In *Molecular Geomicrobiology*, Vol. 59 (eds. J. F. Banfield, J. Cervini-Silva, and K. H. Nealson), pp. 1–7. Mineralogical Society of America, Washington DC.

Bennet J. C. and Tributsch H. (1978) Bacterial leaching patterns on pyrite crystal surface. *J. Bacteriol.* **134**, 310–326.

Bevilaqua D., Leite A. L. L. C., Garcia O., and Tuovinen O. H. (2002) Oxidation of chalcopyrite by *Acidithiobacillus ferrooxidans* and *Acidithiobacillus thiooxidans* in shake flasks. *Process. Biochem.* **38**, 587–592.

Bigman J. M., Schwertmann U., Carlson L., and Murad E. (1990) A poorly crystallized oxyhydroxysulfate of iron formed by bacterial oxidation of Fe(II) in acid mine waters. *Geochim. Cosmochim. Acta* **54**, 2743–2758.

Blake R. and Johnson D. B. (2000) Phylogenetic and biochemical diversity among acidophilic bacteria that respire on iron. In *Environmental metal-microbe interactions* (ed. D. R. Lovley), pp. 53–78. ASM Press, Washington DC.

Blake R. C., Sasaki K., and Ohmura N. (2001) Does aporusticyanin mediate the adhesion of *Thiobacillus ferrooxidans* to pyrite? *Hydrometallurgy* **59**, 357–372.

Blake R. C., Shute E. A., and Howard G. T. (1994) Solubilization of minerals by bacteria: Electrophoretic mobility of *Thiobacillus ferrooxidans* in the presence of iron, pyrite, and sulfur. *Appl. Environ. Microbiol.* **60**, 3349–3357.

Blake R. C., Shute E. A., Greenwood M. M., Spencer G. H., and Ingledew W. J. (1993) Enzymes of aerobic respiration on iron. *FEMS Microbiol. Rev.* **11**, 9–18.

Bond P. L., Druschel G. K., and Banfield J. F. (2000a) Comparison of acid mine drainage microbial communities in physically and geochemically distinct ecosystems. *Appl. Environ. Microbiol.* **66**, 4962–4971.

Bond P. L., Smriga S. P., and Banfield J. F. (2000b) Phylogeny of microorganisms populating a thick, subaerial, predominantly lithotrophic biofilm at an extreme acid mine drainage site. *Appl. Environ. Microbiol.* **66**, 3842–3849.

Boon M. and Heijnen J. J. (1998a) Chemical oxidation kinetics of pyrite in bioleaching processes. *Hydrometallurgy* **48**, 27–41.

Boon M. and Heijnen J. J. (1998b) Gas-liquid mass transfer phenomena in bio-oxidation experiments of sulphide minerals: A critical review of literature data. *Hydrometallurgy* **48**, 187–204.

Boon M., Brasser H. J., Hansford G. S., and Heijnen J. J. (1999) Comparison of the oxidation kinetics of different pyrites in the presence of *Thiobacillus ferrooxidans* or *Leptospirillum ferrooxidans*. *Hydrometallurgy* **53**, 57–72.

Boon M., Hansford G. S., and Heijnen J. J. (1995) The role of bacterial ferrous iron oxidation in the bio-oxidation of pyrite. In *Biohydrometallurgical Processing, Volume 1* (eds. T. Vargas, C. A. Jerez, J. V. Wiertz, and H. Toledo), pp. 153–163. University of Chile, Santiago, Chile.

Boon M., Meeder T. A., Thone C., Ras C., and Heijnen J. J. (1998a) The ferrous iron oxidation kinetics of *Thiobacillus ferrooxidans* in continuous cultures. *Appl. Microbiol. Biotechnol.* **51**, 820–826.

Boon M., Ras C., and Heijnen J. J. (1998b) The ferrous iron oxidation kinetics of *Thiobacillus ferrooxidans* in batch cultures. *Appl. Microbiol. Biotechnol.* **51**, 813–819.

Boudreau B. P. (1997) *Diagenetic Models and Their Implementation*. Springer, Berlin.

Braddock J. F., Luong H. V., and Brown E. J. (1984) Growth kinetics of *Thiobacillus ferrooxidans* isolated from arsenic mine drainage. *Appl. Environ. Microbiol.* **48**, 48–55.

Brown P. N., Byrne G. D., and Hindmarsh A. C. (1989) VODE: A variable-coefficient ODE solver. *SIAM J. Sci. Stat. Comput.* **10**, 1038–1051.

Chandraprabha M. N., Modak J. M., Natarajan K. A., and Raichur A. M. (2003) Modeling and analysis of biooxidation of gold bearing pyrite-arsenopyrite concentrates by *Thiobacillus ferrooxidans*. *Biotechnol. Prog.* **19**, 1244–1254.

Chin K.-J., Esteve-Nunez A., Leang C., and Lovley D. R. (2004) Direct correlation between rates of anaerobic respiration and levels of mRNA for key respiratory genes in *Geobacter sulfurreducens*. *Appl. Environ. Microbiol.* **70**, 5183–5189.

Clark D. A. and Norris P. R. (1996) *Acidimicrobium ferrooxidans* gen. nov. sp. nov. mixed-culture ferrous iron oxidation with *Sulfobacillus* species. *Microbiology* **142**, 785–790.

Coram N. J. and Rawlings D. E. (2002) Molecular relationships between two groups of the genus *Leptospirillum* and the finding that *Leptospirillum ferriphilum* sp. nov. dominates South African commercial biooxidation tanks that operate at 40° C. *Appl. Environ. Microbiol.* **68**, 838–845.

Covert M. W. and Palsson B. O. (2002) Transcriptional regulation in constraints-based metabolic models of *Escherichia coli*. *J. Biol. Chem.* **277**, 28058–28064.

Croal L. R., Gralnick J. A., Malasarn D., and Newman D. K. (2004) The genetics of geochemistry. *Annu. Rev. Genet.* **38**, 175–202.

Crundwell F. (1996) The formation of biofilms of iron-oxidizing bacteria on pyrite. *Miner. Engin.* **9**, 1081–1089.

Crundwell F. K. (1988) The influence of the electronic structure of solids on the anodic dissolution and leaching of semiconducting sulphide minerals. *Hydrometallurgy* **21**.

Crundwell F. K. (1994) Mathematical modeling of batch and continuous bacterial leaching. *Chem. Eng. Biochem. Eng. J.* **54**, 207–220.

Crundwell F. K. (1997) Physical chemistry of bacterial leaching. In *Biomining* (ed. D. E. Rawlings), pp. 177–200. Springer-Verlag, Berlin Heidelberg, Germany.

Curutchet G., Pogliani C., and Donati E. (1995) Indirect bioleaching of covellite by *Thiobacillus thiooxidans* with an oxidant agent. *Biotechnol. Lett.* **17**, 1251–1256.

Curutchet G., Tedesco P., and Donati E. (1996) Combined degradation of covellite by *Thiobacillus ferroxidans* and *Thiobacillus thiooxidans*. *Biotechnol. Lett.* **18**, 1471–1476.

DeLong E. F. (2004) Microbial population genomics and ecology: The road ahead. *Environ. Microbiol.* **6**, 875–878.

Devasia P., Natarajan K. A., Sathyanarayana D. N., and Rao G. R. (1993) Surface chemistry of *Thiobacillus ferrooxidans* relevant to adhesion on mineral surfaces. *Appl. Environ. Microbiol.* **59**, 4051–4055.

DeWulf-Durand P., Bryant L. J., and Sly L. I. (1997) PCR-mediated detection of acidophilic, bioleaching-associated bacteria. *Appl. Environ. Microbiol.* **62**, 2944–2948.

Donati E., Curutchet G., Pogliani C., and Tedesco P. (1996) Bioleaching of covellite using pure and mixed cultures of *Thiobacillus ferrooxidans* and *Thiobacillus thiooxidans*. *Proc. Biochem.* **31**, 129–134.

Dopson M. and Lindstrom E. B. (1999) Potential role of *Thiobacillus caldus* in arsenopyrite bioleaching. *Appl. Environ. Microbiol.*

Druschel G. K., Baker B. J., Gihring T. M., and Banfield J. F. (2004) Acid mine drainage biogeochemistry at Iron Mountain, California. *Geochemical Transactions* **5**, 13–32.

Dzombak D. A. and Morel F. M. M. (1990) *Surface Complexation Modeling: Hydrous Ferric Oxide*. John Wiley & Sons, NY.

Edwards J. S., Covert M., and Palsson B. (2002) Metabolic modelling of microbes: The flux-balance approach. *Environ. Microbiol.* **4**, 133–140.

Edwards K. J. and Rutenberg A. D. (2001) Microbial response to surface microtopography: The role of metabolism in localized mineral dissolution. *Chem. Geol.* **180**, 19–32.

Edwards K. J., Bond P. L., and Banfield J. F. (2000a) Characteristics of attachment and growth of *Thiobacillus caldus* on sulphide minerals: A chemotactic response to sulphur minerals? *Environ. Microbiol.* **2**, 324–332.

Edwards K. J., Bond P. L., Druschel G. K., McGuire M. M., Hamers R. J., and Banfield J. F. (2001a) Geochemical and biological aspects of sulfide mineral dissolution: Lessons from Iron Mountain, California. *Chem. Geol.* **169**, 383–397.

Edwards K. J., Bond P. L., Gihring T. M., and Banfield J. F. (2000b) An archaeal iron-oxidizing extreme acidophile important in acid mine drainage. *Science* **287**, 1701–1876.

Edwards K. J., Goebel B. M., Rogers T. M., Schrenk M. O., Gihring T. M., Cardona M. M., Hu B., McGuire M. M., Hamers R. J., Pace N. R., and Banfield J. F. (1999) Geomicrobiology of pyrite (FeS_2) dissolution: Case study at Iron Mountain, California. *Geomicrobiol. J.* **16**, 155–179.

Edwards K. J., Hu B., Hamers R. J., and Banfield J. F. (2001b) A new look at microbial leaching patterns on sulfide minerals. *FEMS Microbial Ecology* **34**, 197–206.

Edwards K. J., Schrenk M. O., Hamers R. J., and Banfield J. F. (1998) Microbial oxidation of pyrite: Experiments using microorganisms from an extreme acid environment. *Am. Min.* **83**, 1444–1453.

Ehrlich H. L. (2002) *Geomicrobiology*. Marcel Dekker, NY.

Espejo R. and Ruiz P. (1987) Growth of free and attached *Thiobacillus ferrooxidans* in ore suspension. *Biotechnol. Bioengin.* **30**, 586–592.

Evangelou V. P. and Zhang Y. L. (1995) A review: Pyrite oxidation mechanisms and acid mine drainage prevention. *Crit Rev Environ Sci Technol* **25**, 141–199.

Falco L., Pogliani C., Curutchet G., and Donati E. (2003) A comparison of bioleaching of covellite using pure cultures of *Acidithiobacillus ferrooxidans* and *Acidithiobacillus thiooxidans* or a mixed culture of *Leptospirillum ferrooxidans* and *Acidithiobacillus thiooxidans*. *Hydrometallurgy* **71**, 31–36.

Fang Y., Yeh G. T., and Burgos W. D. (2003) A general paradigm to model reaction-based biogeochemical processes in batch systems. *Wat. Resour. Res.* **39**, 1083–1108.

Fernandez M. G. M., Mustin C., Dedonato P., Barres O., Marion P., and Berthelin J. (1995) Occurrences at mineral bacteria interface during oxidation of arsenopyrite by *Thiobacillus Ferrooxidans. Biotechnology and Bioengineering* **46**, 13–21.

Fowler T. A. and Crundwell F. K. (1998) Leaching of zinc sulfide by *Thiobacillus ferrooxidans*: Experiments with a controlled redox potential indicate no direct bacterial mechanism. *Appl. Environ. Microbiol.* **64**, 3570–3575.

Fowler T. A. and Crundwell F. K. (1999) Leaching of zinc sulfide by *Thiobacillus ferrooxidans*: Bacterial oxidation of the sulfur product layer increases the rate

of zinc sulfide dissolution at high concentrations of ferrous iron. *Appl. Environ. Microbiol.* **65**, 5285–5292.

Fowler T. A., Holmes P. R., and Crundwell F. K. (1999) Mechanism of pyrite dissolution in the presence of *Thiobacillus ferrooxidans*. *Appl. Environ. Microbiol.* **65**, 2987–2993.

Fowler T. A., Holmes P. R., and Crundwell F. K. (2001) On the kinetics and mechanism of the dissolution of pyrite in the presence of *Thiobacillus ferooxidans*. *Hydrometallurgy* **59**, 257–270.

Garcia O., Bigham J. M., and Tuovinen O. H. (1995a) Oxidation of galena by *Thiobacillus ferrooxidans* and *Thiobacillus thiooxidans*. *Canadian J. Microbiology* **41**, 508–514.

Garcia O., Bigham J. M., and Tuovinen O. H. (1995b) Sphalerite oxidation by *Thiobacillus ferrooxidans* and *Thiobacillus thiooxidans*. *Can. J. Microbiol.* **41**, 578–584.

Gehrke T., Hallmann R., and Sand W. (1995) Importance of exopolymers from *Thiobacillus ferrooxidans* and *Leptospirillum ferrooxidans* for bioleaching. In *Biohydrometallurgical Processing, Volume 1* (eds. T. Vargas, C. A. Jerez, J. V. Wiertz, and H. Toledo), pp. 1–11. University of Chile, Santiago, Chile.

Gehrke T., Telegdi J., Thierry D., and Sand W. (1998) Importance of extracellular polymeric substances from *Thiobacillus ferrooxidans* for bioleaching. *Appl. Environ. Microbiol.* **64**, 2743–2747.

Grundl T. and Delwiche J. (1993) Kinetics of ferric oxyhydroxide precipitation. *J. Contam. Hydrol* **14**, 71–97.

Hallmann R., Friedrich A., Koops H. P., Pommereningroser A., Rohde K., Zenneck C., and Sand W. (1992) Physiological-characteristics of *Thiobacillus ferrooxidans* and *Leptospirillum ferrooxidans* and physicochemical factors influence microbial metal leaching. *Geomicrobiol. J.* **10**, 193–206.

Handelsman J. (2004) Metagenomics: Application of genomics to uncultured microorganisms. *Microbiol. Mol. Biol. Rev.* **68**, 669–685.

Hansford G. S. (1997) Recent developments in modeling the kinetics of bioleaching. In *Biomining* (ed. D. E. Rawlings), pp. 153–175. Springer-Verlag, Heidelberg NY.

Hansford G. S. and Chapman J. T. (1992) Batch and continuous biooxidation kinetics of a refractory gold-bearing pyrite concentrate. *Miner. Eng.* **6**, 597–612.

Hansford G. S. and Drossou M. (1988) A propogating-pore model for the batch bioleach kinetics of refractor gold-bearing pyrite. In *Biohydrometallurgy: Proceedings of the 1987 International Symposium* (eds. P. R. Norris and D. P. Kelly), pp. 345–358. Kew: Science and Technology Letters.

Hart A., Murrell J. C., Poole R. K., and Norris P. R. (1991) An acid-stable cytochrome in iIron-oxidizing *Leptospirillum ferrooxidans*. *FEMS Microbiol. Lett.* **81**, 89–94.

Hoff K. A. (1993) Total and specific bacterial counts by simultaneous staining with DAPI and fluorochrome-labeled antibodies. In *Handbook of Methods in Aquatic Microbial Ecology* (eds. P. F. Kemp, B. F. Sherr, and E. B. Cole). Lewis Publishers, Boca Raton, FL.

Holmes D. E., Nevin K. P., and Lovley D. R. (2004) In situ expression of *nifD* in Geobacteraceae in subsurface sediments. *Appl. Environ. Microbiol.* **70**, 7251–7259.

Holmes D. E., Nevin K. P., O'Neil R. A., Ward J. E., Adams L. A., Woodard T. L., Vrionis H. A., and Lovley D. R. (2005) Potential for quantifying expression of the Geobacteraceae citrate synthase gene to assess the activity of Geobacteraceae in the subsurface and on current-harvesting electrodes. *Appl. Environ. Microbiol.* **71**, 6870–6877.

Holmes P. R. and Crundwell F. K. (2000) The kinetics of the oxidation of pyrite by ferric ions and dissolved oxygen: An electrochemical study. *Geochim. Cosmochim. Acta* **64**, 263–274.

Holmes P. R., Fowler T. A., and Crundwell F. K. (1999) The mechanism of bacterial action in the leaching of pyrite by *Thiobacillus ferrooxidans*: An electrochemical study. *J. Electrochem. Soc.* **146**, 2906–2912.

Hunter K. S., Wang Y., and VanCappellen P. (1998) Kinetic modeling of microbially -driven redox chemistry of subsurface environments: Coupling transport, microbial metabolism and geochemistry. *J. Hydrol.* **209**, 53–80.

Islam J. and Singhal N. (2002) A one-dimensional reactive multi-component landfill leachate transport model. *Environ. Model. Softw.* **17**, 531–543.

Jackson B. E. and McInerney M. J. (2002) Anaerobic microbial metabolism can proceed close to thermodynamic limits. *Nature* **415**, 454–456.

Jin Q. and Bethke C. M. (2003) A new rate law describing microbial respiration. *Appl. Environ. Microbiol.* **69**, 2340–2348.

Johnson D. B. (1998) Biodiversity and ecology of acidophilic microorganisms. *FEMS Microbiol. Ecol.* **27**, 307–317.

Johnson D. B. and Roberto F. R. (1997) Heterotrophic acidophiles and their roles in the bioleaching of sulfide minerals. In *Biomining* (ed. D. E. Rawlings), pp. 259–279. Springer-Verlag, Heidelberg, NY.

Jones C. A. and Kelly D. P. (1983) Growth of *Thiobacillus ferroxidans* on ferrous iron in chemostat culture: Influence of product and substrate inhibition. *J. Chem. Technol. Biotechnol.* **33B**, 241–261.

Kelly D. P. and Jones C. A. (1978) Factors affecting metabolism and ferrous iron oxidation in suspensions and batch cultures of *Thiobacillus ferroxidans*: Relevance to ferric iron leach solution regeneration. In *Metallurgical applications of bacterial leaching and related microbiological phenomena* (eds. L. E. Murr, A. E. Torma, and J. A. Brierley), pp. 19–44. Academic Press, San Diego, CA.

Kelly D. P. and Wood A. P. (2000) Re-classification of some species of *Thiobacillus* to the newly designated genera *Acidthiobacillus* gen. novl, *Halothiobacillus* gen. nov., and *Thermithiobacillus* gen. nov. *Int. J. Syst. Evol. Microbiol.* **50**, 511–516.

Kinzler K., Gehrke T., Telegdi J., and Sand W. (2003) Bioleaching—a result of interfacial processes caused by extracellular polymeric substances (EPS). *Hydrometallurgy* **71**, 83–88.

Koch A. L. (1991) Diffusion: The crucial process in many aspects of the biology of bacteria. *Adv. Microb. Ecol.* 11: 37–70.

Konishi Y., Asai S., and Sakai H. K. (1990) Bacterial dissolution of pyrite by *Thiobacillus ferrooxidans*. *Bioprocess Eng.* **5**, 5–17.

Krautle S. and Knabner P. (2005) A new numerical reduction scheme for fully coupled multicomponent transport-reaction problems in porous media. *Wat. Resour. Res.* **41**, Art. No. W09414 SEP 20 2005.

Lovley D. R. (2003) Cleaning up with genomics: Applying molecular biology to bioremediation. *Nat. Rev. Micro.* **1**, 35–44.

Lu L., Wang R. C., Xue J. Y., Chen F. R., and Chen J. (2005) Dependence of reaction rate of pyrite oxidation on temperature, pH and oxidant concentration. *Science in China Series D-Earth Sci.* **48**, 1690–1697.

Macalady J. and Banfield J. F. (2003) Molecular geomicrobiology: Genes and geochemical cycling. *Earth Planet. Sci. Lett.* **209**, 1–17.

Madsen E. L. (2005) Identifying microorganisms responsible for ecologically significant biogeochemcial processes. *Nat. Rev. Microbiol.* **3**, 439–446.

Mahadevan R., Bond D. R., Butler J. E., Esteve-Núñez A., Coppi M. V., Palsson B. O., Schilling C. H., and Lovley D. R. (2006) Characterization of metabolism in the Fe(III)-reducing organism *Geobacter sulfurreducens* by constraint-based modeling. *Appl. Environ. Microbiol.* **72**, 1558–1568.

Malasarn D., Saltikov C. W., Campbell K. M., Santini J. M., Hering J. G., and Newman D. K. (2004) *arrA* is a reliable marker for As(V) respiration. *Science* **306**, 455.

Maurer M. and Rittmann B. E. (2004) Modeling intrinsic bioremediation for interpret observable biogeochemical footprints of BTEX biodegradation: The need for fermentation and abiotic chemical processes. *Biodegradation* **15**, 405–417.

Mayer K. U., Frind E. O., and Blowes D. W. (2002) Multicomponent reactive transport modeling in variably saturated porous media using a generalized formulation for kinetically controlled reactions. *Wat. Resour. Res.* **38**, Art. No. 1174 SEP 2002.

McGuire M. M., Edwards K. J., Banfield J. F., and Hamers R. J. (2001a) Kinetics, surface chemistry, and structural evolution of microbially mediated sulfide mineral dissolution. *Geochim. Cosmochim. Acta* **65**, 1243–1258.

McGuire M. M., Jallad K. N., Ben-Amotz D., and Hamers R. J. (2001b) Chemical mapping of elemental sulfur on pyrite and arsenopyrite surfaces using near-infrared Raman imaging microscopy. *Appl. Surf. Sci.* **178**, 105–115.

McKibben M. A. and Barnes H. L. (1986) Oxidation of pyrite in low temperature acidic solutions: Rate laws and surface textures. *Geochim. Cosmochim. Acta* **50**, 1509–1520.

Meruane G., Salhe C., Wiertz J., and Vargas T. (2002) Novel electrochemical-enzymatic model which quantifies the effect of the solution Eh on the kinetics of ferrous iron oxidation with *Acidithiobacillus ferrooxidans*. *Biotechnol. Bioeng.* **80**, 280–288.

Mielke R. E., Pace D. L., Porter T., and Southam G. (2003) A critical stage in the formation of acid mine drainage: Colonization of pyrite by *Acidithiobacillus ferrooxidans* under pH-neutral conditions. *Geobiology* **1**, 81–90.

Moses C. O., Nordstrom D. K., Herman J. S., and Mills A. L. (1987) Aqueous pyrite oxidation by dissolved oxygen and by ferric iron. *Geo. et Cos Acta* **51**, 1561–1571.

Mustin C., Berthelin J., Marion P., and deDonato P. (1992a) Corrosion and electrochemical oxidation of a pyrite by *Thiobacillus ferrooxidans*. *Appl. Environ. Microbiol.* **58**, 1175–1182.

Mustin C., DeDonato P., and Berthelin J. (1992b) Quantification of the intragranular porosity formed in bioleaching of pyrite by *Thiobacillus ferrooxidans*. *Biotechnol. Bioeng.* **39**, 1121–1127.

Mustin C., Dedonato P., and Berthelin J. (1992c) Quantification of the intragranular porosity formed in bioleaching of pyrite by *Thiobacillus-Ferrooxidans*. *Biotechnol. Bioeng.* **39**, 1121–1127.

Ndlovu S. and Monhemius A. J. (2005) The influence of crystal orientation on the bacterial dissolution of pyrite. *Hydrometallurgy* **78**, 187–197.

Nicholson R. V., Gillham R. W., and Rearson E. J. (1988) Pyrite oxidation in carbonate-buffered solution: I. Experimental kinetics. *Geochim. Cosmochim. Acta* **52**, 1077–1085.

Nordstrom D. K. and Southam G. (1997) Geomicrobiology of sulfide mineral oxidation. In *Geomicrobiology: Interactions between Microbes and Minerals*, Vol. 35 (eds. J. F. Banfield and K. Nealson), pp. 361–382. Mineralogical Society of America, Washington DC.

Norris P. R., Barr D. W., and Hinson D. (1988) Iron and mineral oxidation by acidophilic bacteria: Affinities for iron and attachment to pyrite. In *Biohydrometallurgy: Proceedings of the 1987 International Symposium* (eds. P. R. Norris and D. P. Kelly), pp. 43–59. Kew: Science and Technology Letters.

Ohmura N., Kitamura K., and Saiki H. (1993) Selective adhesion of *Thiobacillus ferrooxidans* to pyrite. *Appl. Environ. Microbiol.* **59**, 4044–4050.

Okibe N. and Johnson D. B. (2004) Biooxidation of pyrite by defined mixed cultures of moderately thermophilic acidophiles in pH-controlled bioreactors: Significance of microbial interactions. *Biotechnol. Bioeng.* **87**, 574–583.

Oremland R. S., Capone D. G., Stolz J. F., and Fuhrman J. (2005) Whither or wither geomicrobiology in the era of 'community metagenomics'. *Nat. Rev. Micro.* **3**, 572–578.

Pace D. L., Mielke R. E., Southam G., and Porter T. L. (2005) Scanning force microscopy studies of the colonization and growth of *A. ferrooxidans* on the surface of pyrite minerals. *Scanning* **27**, 136–140.

Parkhurst D. A. and Appelo C. A. (1999) User's guide to PHREEQC (Version 2). Water-Resources Investigation Report 99–4259.

Pearson C. E. (1968) On a differential equation of boundary layer type'. *J. Math. Phys.* **47**, 134–154.

Peccia J., Marchand E. A., Silverstein J., and Hernandez M. (2000) Development and application of small-subunit rRNA probes for assessment of selected *Thiobacillus* species and members of the genus *Acidiphilium*. *Appl. Environ. Microbiol.* **66**, 3065–3072.

Phanikumar M. S. and McGuire J. T. (2004) A 3D partial-equilibrium model to simulate coupled hydrogeological, microbiological, and geochemical processes in subsurface systems. *Geophys. Res. Lett.* **31**, Art. No. L11503 JUN 15 2004.

Pizarro J., Jedlicki E., Orellana O., romero J., and Espejo R. T. (1996) Bacterial populations in samples of bioleached copper ore as revealed by analysis of DNA obtained before and after cultivation. *Appl. Environ. Microbiol.* **62**, 1323–1328.

Pogliani C. and Donati E. (1999) The role of exopolymers in the bioleaching of a non-ferrous metal sulphide. *J. Indust. Microbiol. Biotechnol.* **22**, 88–92.

Pogliani C. and Donati E. (2000) Enhancement of copper dissolution from a sulfide ore by using *Thiobacillus thiooxidans*. *Geomicrobiol. J.* **17**, 35–42.

Pogliani C., Curutchet G., Donati E., and Tedesco P. H. (1990) A need for direct contact with particle surfaces in the bacterial oxidation of covellite in the absence of a chemical lixiviant. *Biotechnol. Lett.* **12**, 515–518.

Pramanik J., Trelstad P. L., Schuler A. J., Jenkins D., and Keasling J. D. (1999) Development and validation of a flux-based stoichiometric model for enhanced biological phosphorus removal metabolism. *Wat. Res.* **33**, 462–476.

Press W. H., Teukolsky S. A., Vetterling W. T., and Flannery B. P. (1992) *Numerical Recipes in FORTRAN*. Cambridge University Press, Cambridge.

Price N. D., Reed J. L., and Palsson B. O. (2004) Genome-scale models of microbial cells: Evaluating the consequences of constraints. *Nat. Rev. Micro.* **2**, 886–897.

Pronk J. T., Meulenberg R., Hazeu W., Bos P., and Kuenen J. G. (1990) Oxidation of reduced inorganic sulfur compounds by acidophilic thiobacilli. *FEMS Microbiol. Rev.* **75**, 293–306.

Ram R. J., VerBerkmoes N. C., Thelen M. P., Tyson G. W., Baker B. J., Blake R. C., Shah M., Hettich R. L., and Banfield J. F. (2005) Community proteomics of a natural microbial biofilm. *Science* **308**, 1915–1920.

Ramirez P., Guiliani N., Valenzuela L., Beard S., and Jerez C. A. (2004) Differential protein expression during growth of *Acidithiobacillus ferrooxidans* on ferrous iron, sulfur compounds, or metal sulfides. *Appl. Environ. Microbiol.* **70**, 4491–4498.

Rawlings D. E. (2002) Heavy metal mining using microbes. *Annu. Rev. Microbiol.* **56**, 65–91.

Rawlings D. E., Tributsch H., and Hansford G. S. (1999) Reasons why '*Leptospirillum*'-like species rather than *Thiobacillus ferrooxidans* are the dominant iron-oxidizing bacteria in many commercial processes for the biooxidation of pyrite and related ores. *Microbiology* **145**, 5–13.

Rawn J. D. (1983) *Biochemistry*. Harper and Row, NY.

Regnier P., O'Kane J. P., Steefel C. I., and Vanderborght P. (2002) Modeling complex multi-component reactive-transport systems: Towards a simulation environment based on the concept of a Knowledge Base. *Appl. Math. Model.* **26**, 913–927.

Rickard P. A. D. and Vanselow D. G. (1978) Investigations into the kinetics and stoichiometry of bacterial oxidation of covellite (CuS) using a polarographic oxygen probe. *Can. J. Microbiol.* **24**, 998–1003.

Rimstidt J. D. and Vaughan D. J. (2003) Pyrite oxidation: A state-of-the-art assessment of the reaction mechanism. *Geochim. Cosmochim. Acta* **67**, 873–880.

Rittmann B. E. and McCarty P. L. (2001) *Environmental Biotechnology*. McGraw-Hill, NY.

Roden E. E., Fang Y., Scheibe T. D., Brooks S. C., and Burgos W. D. (2005) TEAPREVU: A numerical simulation model of Terminal Electron-Accepting Processes in a Representative Elementary Volume of Uranium-contaminated subsurface sediment. *Available at: http://www.geology.wisc.edu/∼eroden/Reports& OtherDocuments.html*.

Rodrieguez L. M. and Tributsch H. (1988) Morphology of bacterial leaching patterns by *Thiobacillus ferrooxidans* on synthetic pyrite. *Arch. Microbiol* **149**, 401–405.

Rodriguez Y., Ballester A., Blazquez M. L., Gonzalez F., and Munoz J. A. (2003) Study of bacterial attachment during the bioleaching of pyrite, chalcopyrite, and sphalerite. *Geomicrobiol. J.* **20**, 131–141.

Rohwerder T., Gehrke T., Kinzler K., and Sand W. (2003) Bioleaching review part A: Progress in bioleaching: Fundamentals and mechanisms of bacterial metal sulfide oxidation. *Arch. Microbiol. Biotechnol.* **63**, 239–248.

Rojas-Chapana J. A. and Tributsch H. (2004) Interfacial activity and leaching patterns of *Leptospirillum ferrooxidans* on pyrite. *FEMS Microbiol. Ecol.* **47**, 19–29.

Rojas-Chapana J. and Tributsch H. (2000) Bio-leaching of pyrite accelerated by cysteine. *Process Biochem.* **35**, 815–824.

Rojas-Chapana J. and Tributsch H. (2001) Biochemistry of sulfur extraction in biocorrosion of pyrite by *Thiobacillus ferrooxidans*. *Hydrometallurgy* **59**, 291–300.

Rojas-Chapana J., Giersig M., and Tributsch H. (1995) Sulfur colloids as temporary energy reservoirs for *Thiobacillus ferrooxidans* during pyrite oxidation. *Arch. Microbiol.* **163**, 256–352.

Sakaguchi H., Torma A. E., and Silver M. (1976) Microbiological oxidation of synthetic chalcocite and covellite by *Thiobacillus ferroxidans*. *Appl. Environ. Microbiol.* **31**, 7–10.

Sand W., Gehrke T., Hallmann R., and Schippers A. (1995) Sulfur chemistry, biofilm, and the (in)direct attack mechanism—a critical evaluation of bacterial leaching. *Appl. Environ. Microbiol.* **43**, 961–966.

Sand W., Gehrke T., Jozsa P. G., and Schippers A. (2001) (Bio)chemistry of bacterial leaching—direct vs. indirect bioleaching. *Hydrometallurgy* **59**, 159–175.

Sand W., Rohde K., Sobotke B., and Zenneck G. (1992) Evaluation of *Leptospirillum ferrooxidans* for leaching. *Appl. Environ. Microbiol.* **58**, 85–92.

Schecher W. D. and McAvoy D. C. (1998) *MINEQL + A chemical equilibrium modeling system. Version 4.0 for Winders User's Manual*. Environmental Research Software.

Scheibe T. D., Fang Y., Murray C. J., Roden E. E., Chen J., Chien Y. J., Brooks S. C., and Hubbard S. S. (2006) Transport and biogeochemical reaction of metals in a physically and chemically heterogeneous aquifer. *Geosphere* **2**, 220–235.

Schiesser W. E. (1991) *The Numerical Method of Lines*. Academic Press, San Diego, CA.

Schilling C. H., Edwards J. S., and Palsson B. O. (1999) Toward metabolic phenomics: Analysis of genomic data using flux balances. *Biotechnol. Prog.* **15**, 288–295.

Schink B. (1997) Energetics of syntrophic cooperation in methanogenic degradation. *Microbiol. Mol. Biol. Rev.* **61**, 262–280.

Schippers A. and Sand W. (1999) Bacterial leaching of metal sulfides proceeds by two indirect mechanisms via thiosulfate or via polysulfides and sulfur. *Appl. Environ. Microbiol.* **65**, 319–321.

Schippers A., Jozsa P. G., and Sand W. (1996) Sulfur chemistry in bacterial leaching of pyrite. *Appl. Environ. Microbiol.* **62**, 3424–3431.

Schrenk M. O., Edwards K. J., Goodman R. M., Hamers R. J., and Banfield J. F. (1998) Distribution of *Thiobacillus ferrooxidans* and *Leptospirillum ferrooxidans*: Implications for generation of acid mine drainage. *Science* **279**, 1519–1522.

Shubert B. and Tributsch H. (1990) Photoinduced electron transfer by coordination chemical pathways across pyrite/electrolyte interfaces. *Inorg. Chem.* **29**, 5041–5046.

Silverman M. P. and Ehrlich H. L. (1964) Microbial formation and degradation of minerals. *Adv. Appl. Microbiol.* **6**, 153–206.

Singer P. C. and Stumm W. (1972) Acid mine drainage—the rate limiting step. *Science* **167**, 1121–1123.

Steefel C. I. and Lasaga A. C. (1994) A coupled model for transport of multiple chemical species and kinetic precipitation/dissolution reactions with application to reactive flow in single phase hydrothermal systems. *Am. J. Sci.* **294**, 529–592.

Steefel C. I. and MacQuarrie K. T. B. (1996) Approaches to modeling of reactive transport in porous media. In *Reactive transport in porous media*, Vol. 34 (eds. P. C. Lichtner, C. I. Steefel, and E. H. Oelkers), pp. 83–129. Mineralogical Society of America, Washington DC.

Steefel C. I. and VanCappellen P. (1998) Reactive transport modeling of natural systems. *J. Hydrol.* **209**, 1–7.

Stuedel R. (1996) Mechanism for the formation of elemental sulfur from aqueous sulfide in chemical and microbiological desulfurization processes. *Ind. Eng. Chem. Res.* **35**, 1417–1423.

Thullner M., Van Cappellen P., and Regnier P. (2005) Modeling the impact of microbial activity on redox dynamics in porous media. *Geochim. Cosmochim. Acta* **69**, 5005–5019.

Ting Y. P., Senthil-Kumar A., Rahman M., and Chia B. K. (2000) Innovative use of *Thiobacillus ferrooxidans* for biological machining of metals. *Acta Biotechnol.* **20**, 87–96.

Torma A. E. and Sakaguchi H. (1978) Relation between the solubility product and the rate of metal sulfide oxidation by *Thiobacillus ferroxidans*. *J. Ferment. Technol.* **56**, 173–178.

Tributsch H. (2001) Direct versus indirect bioleaching. *Hydrometallurgy* **59**, 177–185.

Tributsch H. and Bennett J. C. (1981a) Semiconductor-electrochemical aspects of bacterial leaching. I. Oxidation of metal sulphides with large energy gaps. *J. Chem. Technol. Biotechnol.* **32**, 565–577.

Tributsch H. and Bennett J. C. (1981b) Semiconductor-electrochemical aspects of bacterial leaching. II. Survey of rate-controlling sulphide properties. *J. Chem. Technol. Biotechnol.* **32**, 627–635.

Tyson G. W. and Banfield J. F. (2005) Cultivating the uncultivated: A community genomics perspective. *Trends Microbiol.* **13**, 411–415.

Tyson G. W., Chapman J., Hugenholtz P., Allen E. E., Ram R. J., Richardson P. M., Solovyev V. V., Rubin E. M., Rokhsar D. S., and Banfield J. F. (2004) Community structure and metabolism through reconstruction of microbial genomes from the environment. *Nature* **428**, 37–43.

Tyson G. W., Lo I., Baker B. J., Allen E. E., Hugenholtz P., and Banfield J. F. (2005) Genome-directed isolation of the key nitrogen fixer *Leptospirillum ferrodiazotrophum* sp nov from an acidophilic microbial community. *Appl. Environ. Microbiol.* **71**, 6319–6324.

Urrutia M. M. (1997) General bacterial sorption processes. In *Biosorbents for Metal Ions* (eds. J. D. A. Wase and C. Forster), pp. 39–66. Taylor & Francis, London, UK.

vanScherpenzeel D. A., Boon M., Ras C., Hansford G. S., and Heijnen J. J. (1998) Kinetics of ferrous iron oxidation by *Leptospirillum* bacteria in continuous culture. *Biotechnol. Prog.* **14**, 425–433.

Varma A. and Palsson B. O. (1994a) Stoichiometric flux balance models quantitatively predict growth and metabolic by-product secretion in wild-type *Escherichia coli* W3110. *Appl. Environ. Microbiol.* **60**, 3724–3731.

Varma A. and Palsson B. O. (1994b) Metabolic flux balancing: Basic concepts, scientific and practical use. *Bio-Technology* **12**, 994–998.

Vasquez M. and Espejo R. T. (1997) Chemolithotrophic bacteria in copper ores leached at high sulfuric acid concentration. *Appl. Environ. Microbiol* **63**, 332–334.

Watson I. A., Oswald S. E., Banwart S. A., Crouch R. S., and Thornton S. F. (2005) Modeling the dynamics of fermentation and respiratory processes in a groundwater plume of phenolic contaminants interpreted from laboratory- to field-scale. *Environ. Sci. Technol.* **39**, 8829–8839.

Watson I. A., Oswald S. E., Mayer R. U., Wu Y., and Banwart S. A. (2003) Modeling kinetic processes controlling hydrogen and acetate concentrations in an aquifer-derived microcosm. *Environ. Sci. Technol.* **37**, 3910–3919.

Westall J. C. (1986) MICROQL I. A chemical equilibrium program in BASIC. Report 86–02, Department of Chemistry, Oregon State University, Corvallis, OR.

Whitaker R. J. and Banfield J. F. (2005) Population dynamics through the lens of extreme environments. In *Molecular Geomicrobiology*, Vol. 59 (eds. J. F. Banfield, J. Cervini-Silva, and K. H. Nealson), pp. 259–277. Mineralogical Society of America, Washington DC.

Williamson M. A. and Rimstidt J. D. (1994) The kinetics and electrochemical rate-determining step of aqueous pyrite oxidation. *Geochim. Cosmochim. Acta* **58**, 5443–5454.

Wirtz K. A. (2003) Control of biogeochemical cycling by mobility and metabolic strategies of microbes in sediments: An integrated model study. *FEMS Microbiol. Ecol.* **46**, 295–306.

Yarzabal A., Brasseur G., and Bonnefoy V. (2002a) Cytochromes *c* of *Acidithiobacillus ferrooxidans*. *FEMS Microbiol. Lett.* **209**, 189–195.

Yarzabal A., Brasseur G., Ratouchniak J., Lund K., Lemesle-Meunier D., DeMoss J. A., and Bonnefoy V. (2002b) The high-molecular-weight cytochrome *c* Cyc2 of of *Acidithiobacillus ferrooxidans* is an outer membrane protein. *FEMS Microbiol. Lett.* **209**, 189–195.

Yeh G. T., Iskra G., Zachara J. M., and Szecsody J. E. (1998) Development and verification of a mixed chemical kinetic and equilibrium model. *Adv. Environ. Res.* **2**, 24–56.

Yeh G. T., Burgos W. D., and Zachara J. M. (2001) Modeling and measuring biogeochemical reactions: System consistency, data needs, and rate formulations. *Adv. Environ. Res.* **5**, 219–237.

Chapter 10
Quantitative Approaches to Characterizing Natural Chemical Weathering Rates

Art F. White

10.1 Introduction

Silicate minerals, constituting more than 90% of the rocks exposed at the earth's surface, are commonly formed under temperature and pressure conditions that make them inherently unstable in surficial environments. Undoubtedly, the most significant aspect of chemical weathering resulting from this instability is the formation of soils which makes life possible on the surface of the earth. Many soil macronutrients in this "critical zone" are directly related to the rate at which primary minerals weather (Huntington, 1995; Chadwick et al., 2003). Chemical weathering also creates economically significant ore deposits, such as those for Al and U (Samma, 1986; Misra, 2000), as well as potentially releasing high concentrations of toxic trace elements such as Se and As (Frankenberger and Benson, 1994). Silicate weathering is a significant buffer to acidification caused by atmospheric deposition (Driscoll et al., 1989) and from land use practices (Farley and Werritty, 1989). Atmospheric CO_2 levels have been primarily controlled by the balance between silicate weathering and the rate of volcanic inputs from the Earth's interior, a relationship which may explain long-term climate stability (Ruddiman, 1997)

These issues require quantifying natural chemical weathering rates, the topic of the present discussion. Mass balance approaches describing changes in solid state and solute compositions in weathered regoliths will be emphasized. Additional discussions on fundamental mechanisms controlling weathering reactions and the development of advanced computation approaches are described elsewhere in this volume. Chemical weathering is commonly dependent on a complex relationship between geochemistry, hydrology, biology, and physical erosion and is therefore site specific. As such, mass balance techniques for a number of field examples will be discussed.

U.S. Geological Survey, Menlo Park, afwhite@usgs.gov

10.2 Scales of Chemical Weathering

A typical weathering reaction is the dissolution of primary albite feldspar to form secondary kaolinite

$$2NaAlSi_3O_8 + 2H^+ + H_2O \rightarrow Al_2Si_2O_5(OH)_4 + 2Na^+ + 4SiO_2 \qquad (10.1)$$

This reaction also consumes hydrogen ions and water and produces solute Na and SiO_2. While the form of Eq. (10.1) is simple, the quantification of this reaction in the natural environment is difficult due to the extremely large spatial and temporal scales over which it occurs. While theoretical and experimental studies of weathering reactions commonly consider atomic to micro-scales, emphasizing chemical bonds, surface complexation and distributions of reactive sites (see other chapters in this volume, including Chaps. 2 and 3), most natural weathering studies characterize macro-environments, ranging from individual soil profiles to large river basins (for a discussion of global scale weathering processes, see Chap. 13, this volume).

The time scale over which natural weathering is measured is also very large. Some studies focus on changes in the chemical composition of soils and regoliths that have occurred over geologic time; while other studies describe weathering in terms of solute fluxes in soils and small catchments involving time scales of weeks to years. An example of this scaling is demonstrated in the solid-state and pore water Na distributions with depth in a regolith developed on a marine terrace near Santa Cruz, California (Fig. 10.1). Mineralogical analyses of the regolith indicate that significant Na is contained only in plagioclase (White et al., 2007). Therefore, the increases in both solid and solute Na with depth correlate closely with the relative weathering intensity of plagioclase (Eq. (10.1)).

While the spatial scales of weathering in Fig. 10.1 are identical, i.e., the thickness of the regolith, the time scales of weathering are very different. The solid Na weathering profile reflects the integrated effects of plagioclase weathering since the deposition of the original beach sand, which based on cosmogenic isotopes, was about 194 kyrs ago (Perg et al., 2001). The distributions of solute Na represent the effects of weathering on a contemporary basis, i.e, the amount of time the pore water has been in contact with plagioclase during flow through the soil. Based on hydrologic considerations, this is estimated to be about 2 decades (White et al., 2007).

10.3 Weathering Calculations that Consider the Solid State

Characterizing the element and mineral distributions in soils and weathered rock has been a major endeavor in soil science and geology. Therefore, many approaches have evolved reflecting increasingly sophisticated analytical techniques (see the discussion of isotopes, Chap. 12) and an enhanced understanding of the complex

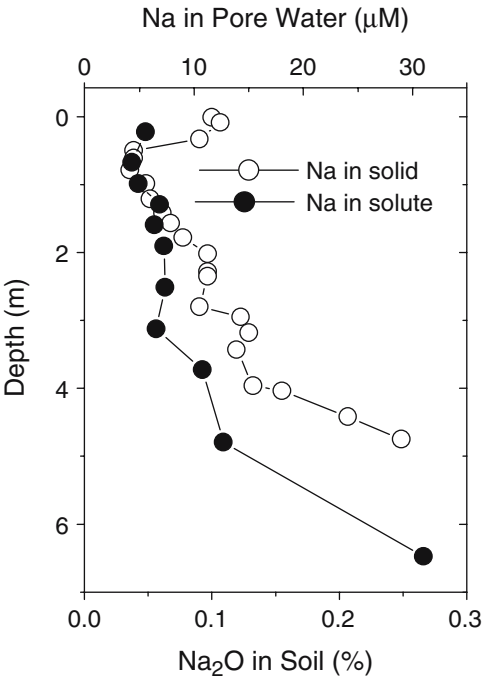

Fig. 10.1 Distributions of Na in the regolith (soil) and pore waters of a 157 kyr old marine terrace, Santa Cruz, California, USA. (Data from White et al., 2007)

processes that influence weathering (Chap. 1). This section will review the most commonly employed solid-state approaches used to characterize natural weathering. Parameters used in these calculations are listed in Table 10.1.

10.3.1 Weathering Indexes

Elemental ratios have long been used to characterize weathering intensities in soils and regoliths (Merrill, 1906; Jenny, 1941). They commonly involve major element oxides and are used to characterize soil fertility, the formation and cycling of siliciclastic sediments, the impact of climate on bedrock weathering and as indicators of soil physical and engineering properties (Delvaux et al., 1989; Nesbitt et al., 1996; Duzgoren-Aydin et al., 2002; Price and Velbel, 2003).

Such ratios most commonly compare the concentration of one or more mobile elements $C_{j,w}$ against one or more immobile elements $C_{i,w}$. The general form of such a relationship is termed the weathering index I_w where

$$I_w = \sum_{0}^{n_1} C_{j,w} \Big/ \sum_{0}^{n_2} C_{i,w} \tag{10.2}$$

Duzgoren-Aydin et al. (2002) and Price and Velbel (2003) performed intercomparisons of up to 30 chemical weathering indexes. Table 10.2 lists a subset

Table 10.1 Selective parameters used in discussion

Symbol	Definition	Units
IAP	Ionic activity product	dimensionless
$\mathbf{C_{i,p}}$	Conc. of inert component in protolith	moles kg^{-1}
$\mathbf{C_{i,w}}$	Conc. of inert component in regolith	moles kg^{-1}
$\mathbf{C_{j,p}}$	Conc. of mobile component in protolith	moles kg^{-1}
$\mathbf{C_{j,w}}$	Conc. of mobile component in regolith	moles kg^{-1}
$\mathbf{c_{j,w}}$	elemental concentration in solute	moles L^{-1}
$\mathbf{\Delta c_{j,w}}$	Change in solute concentration due to weathering	moles L^{-1}
D	Total denudation rate	kg m^{-2} s^{-1}
d	Grain diameter	mm
E	Physical denudation rate	kg m^{-2} s^{-1}
$\mathbf{E_a}$	Apparent activation energy	kJ
∇ **H**	Hydraulic gradient	m m^{-1}
$\mathbf{k_j}$	Intrinsic reaction rate constant	moles m^{-2} s^{1}
$\mathbf{K_s}$	Mineral thermodynamic saturation constant	kJ $mole^{-1}$
$\mathbf{I_w}$	Weathering index	moles kg^{-1}
$\mathbf{K_m}$	Hydraulic conductivity	m s^{-1}
$\mathbf{\Delta M_j}$	Mass change of component j due to solid-state weathering	moles m^{-3}
$\mathbf{\Delta M_m}$	Mass change in reactive mineral	moles m^{-3}
$\mathbf{\Delta m_j}$	Mass change of component in water	moles m^{-3}
P	Precipitation	mm
$\mathbf{p_r}$	Porosity	%
$\mathbf{Q_{j,w}}$	Solid-state weathering flux of component j	moles m^{-2} s^{-1}
$\mathbf{q_{j,bio}}$	Flux of component j related to biologic cycling	moles m^{-2} s^{-1}
$\mathbf{q_{j,exch}}$	Flux of component j related to exchange disequilibrium	moles m^{-2} s^{-1}
$\mathbf{q_h}$	Flux density of water	m s^{-1}
$\mathbf{q_{j,w}}$	Flux of solute j produced from weathering	moles m^{-2} s^{-1}
$\mathbf{q_j}$	Flux of solute j	moles m^{-2} s^{-1}
$\mathbf{q_{j,precip}}$	Flux of component j related to precipitation	moles m^{-2} s^{-1}
$\mathbf{R_m}$	Mineral reaction rate	moles m^{-2} s^{-1}
S	Surface area of regolith	m^2
$\mathbf{S_{Bet}}$	BET measured specific mineral surface area	m^2 g^{-1}
$\mathbf{S_m}$	Specific mineral surface area	m^2 g^{-1}
$\mathbf{S_{geo}}$	Geometric measurement of specific mineral surface area	m^2 g^{-1}
T	Temperature	°K
$\mathbf{t_{geo}}$	Time scale associated with solid state weathering (geologic)	year
$\mathbf{t_{comp}}$	Time scale associated with solute weathering (contemporary)	year
$\mathbf{V_r}$	Regolith volume	m^3
$\mathbf{v_s}$	Solute volume	L
W	Weathering denudation rate	m $year^{-1}$
$\beta_{\mathbf{j,m}}$	Stoichiometric coefficient for elemental distribution j in mineral m	mole $mole^{-1}$
ε_i	Strain factor	dimensionless
λ	Surface roughness	dimensionless
$\rho_{\mathbf{p}}$	Protolith specific density	g cm^{-3}
$\rho_{\mathbf{w}}$	Regolith specific density	g cm^{-3}
$\rho_{\mathbf{m}}$	Mineral density	g cm^{-3}
τ_j	Mass transfer coefficient	dimensionless
ω	Solid state weathering velocity	m s^{-1}
Ω	Saturation index	dimensionless

Table 10.2 Definitions of selected weathering indexes (after Duzgocren-Aydin et al., 2002)

Group	Index	Formula	Fresh value	Weathered value	Reference
I	JE	$SiO_2/(Al_2O_3 + Fe_2O_3 + TiO_2)$	>10	0	Jenny (1941)
	RU	$SiO_2/(Al_2O_3)$	>5	0	Ruxton (1968)
II	CIA	$(100)[Al_2O_3/(Al_2O_3 + CaO + Na_2O + K_2O)]$	<50	100	Nesbitt and Young (1982)
	CIW	$(100)[Al_2O_3/(Al_2O_3 + CaO + Na_2O)]$	<50	100	Harnois (1988)
	PIA	$(100)[Al_2O_3\text{-}K_2O/(Al_2O_3 + CaO + Na_2O\text{-}K_2O)]$	<50	100	Fedo et al., 1995
III	WIP	$(100)[(2^*Na_2O)/0.35) + (MgO/0.9) + (2K_2O/0.25) + (CaO/0.7)]$	>50	0	Parker (1970)

of commonly used weathering indexes cited in these studies. Group I treats silica as a mobile oxide ratioed against one or more major element oxides that are considered immobile, i.e., Al_2O_3, Fe_2O_3 and/or TiO_2. Group II indexes ratio Al_2O_3 against the major base cations and, finally, the Group III indexes consider only the abundances of the mobile element oxides with numerical factors assigned to each cation based on its ionic field strength, a measure of weathering susceptibility (Parker, 1970).

The usefulness and limitations of these weathering indexes (Table 10.2) are now examined in actual weathering profiles. Two major rock types are considered; basalt, which dominates oceanic crust and granite, the dominant igneous rock underlying the continents.

10.3.2 Case Study: Basalt Weathering Indexes

The weathering indexes in Table 10.2 are used to evaluate basalt weathering in a regolith developed on the Hawi flow on the island of Hawaii based on oxide data in Table 10.3 (Chadwick et al., 2003). These indexes, along with regolith bulk density p_w, which is an independent parameter describing mass loss, are plotted as functions of regolith depth in Fig. 10.2a–c. The RU and WIP indexes decrease while the CIA, CIW and PIA increase with decreasing depth (see ranges for fresh versus weathered regoliths in Table 10.2).

These trends, along with decreases in bulk density, produce a consistent picture of more intense chemical weathering at progressively shallower depths in the basalt profile. This agreement supports a major assumption of the Group I and II indexes that Al_2O_3, the most abundant element next to SiO_2, is relatively immobile during weathering. Table 10.3 shows Al_2O_3 actually increasing with decreasing depth in the basalt profile due the significant loss of other more mobile elements. The Group III indexes directly reflect the extent of base cation loss independent of Al_2O_3 concentrations. One concludes, based on this example, that all the indexes listed in Table 10.2 are applicable to describing basalt weathering.

Table 10.3 Selected oxide compositions and densities used for indexes

Soil Horizon	Depth m	Density g cm^{-3}	Wt%							
			SiO_2	Al_2O_3	Fe_2O_2	MgO	CaO	Na_2O	K_2O	TiO_2
Regolith on Hawi basalt flow (after Chadwick et al., 2003).										
A	0.10	0.80	31.3	24.5	nd	1.68	1.59	0.61	0.50	nd
Bw1	0.37	1.03	27.6	29.5	nd	0.95	0.20	0.27	0.60	nd
Bw2	0.65	0.94	26.5	31.6	nd	1.74	0.40	0.53	0.34	nd
2Bw3	1.00	0.94	41.6	23.1	nd	1.63	1.88	3.81	1.82	nd
2Cr1	1.09	0.99	50.2	19.9	nd	1.32	2.86	5.98	2.35	nd
2Cr2	1.38	1.62	51.6	19.0	nd	1.42	3.70	6.40	2.25	nd
2Cr3	1.75	1.73	51.9	18.1	nd	1.68	4.44	5.98	2.16	nd
Fresh Lava	nd	nd	49.4	16.8	nd	3.74	5.91	5.21	1.77	nd
Regolith on Granite at Davis Run (after Pavich, 1986)										
Soil	0.60	1.54	67.0	16.5	4.60	0.50	0.08	0.30	1.90	1.10
	1.50	1.69	73.4	14.3	4.46	0.49	0.07	0.30	1.70	0.79
	4.30	1.61	78.3	13.3	2.16	0.47	0.20	0.15	1.60	0.33
	6.70	1.51	70.9	17.3	2.06	0.49	0.03	0.07	2.50	0.34
Saprolite	11.00	1.69	72.6	16.0	2.12	0.47	0.02	0.06	3.20	0.33
	15.00	2.00	79.3	12.7	1.50	0.37	0.36	0.84	2.60	0.26
	20.00	2.37	75.6	14.7	1.74	0.39	1.80	2.70	2.90	0.24
Weathered Granite	21.00	2.52	74.7	15.2	1.86	0.40	2.20	2.80	3.20	0.25
Fresh Granite	22.00	2.69	74.4	13.5	1.63	0.37	2.20	2.70	3.00	0.23

10.3.3 Case Study: Granite Weathering Indexes

The oxide compositions for a weathered regolith developed on the Occoquan Granite in Virginia, USA are also in Table 10.3 (Pavich, 1986). As indicated by Fig. 10.2d–f, bulk densities decrease with decreasing depth, which, as in the case for basalt, denotes the effects of increased weathering. However, there is significant disagreement between the various weathering indexes listed in Table 10.2. Class I indexes, which treat SiO_2 as a mobile element, exhibit essentially random scatter with depth in the granite regolith (Fig. 10.2d). Much of the SiO_2 contained in the Occoquan Granite is present as weathering-resistant quartz which is absent in the Hawaiian basalt. As indicated in Table 10.3, both SiO_2 and Al_2O_3 concentrations are essentially constant with depth in the granite regolith.

The Group II and III indexes (except for PIA) exhibit the same general weathering trends as does the bulk density data (Fig. 10.2d–f). The CIA and CIW indexes are the lowest in the deepest part of the profile (60–75), denoting relatively fresh granite and increase to higher values at shallower depths (85–100), indicating a highly weathered regolith. The principal difference in the CIA and CIW indexes is that the former treats K strictly as a mobile component whereas the latter does not. Plagioclase, containing Ca and Na, weathers out of the profile more rapidly than does microcline and biotite, which both contain K. The role of K in weathering indexes is discussed in detail by Fedo et al. (1995). Although based on a significantly different approach (use of ionic field strength), the WIP index produces a similar trend as the CIA and CIW indexes (Fig. 10.2).

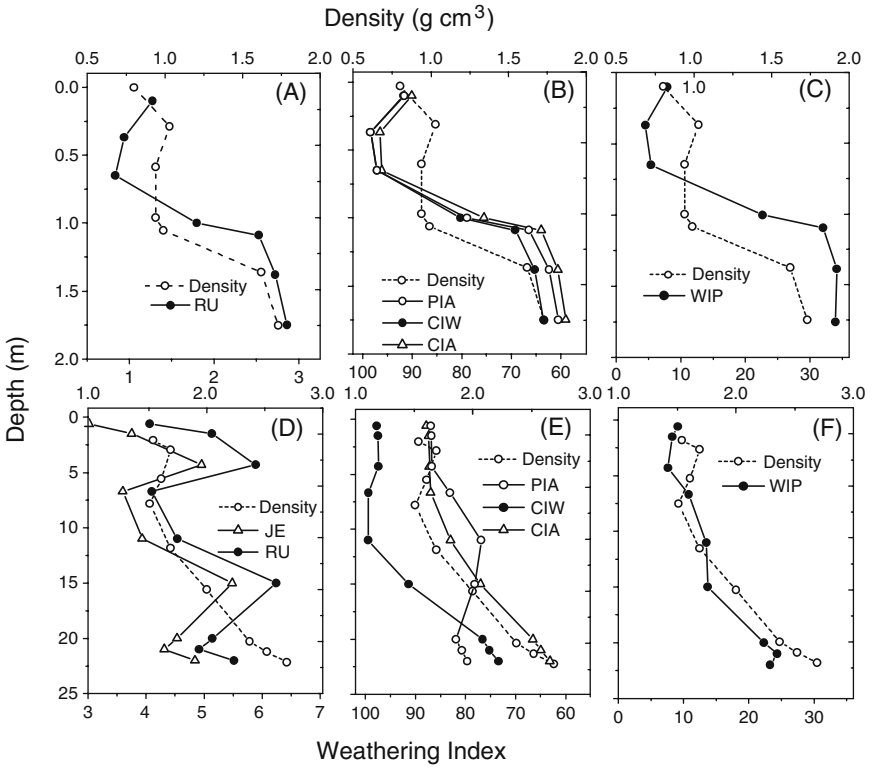

Fig. 10.2 Weathering indexes for the Hawi basalt flow, Hawaii (**a–c**) and for the granitic Davis Run regolith, Virginia, USA (**d–f**). Designations refer to specific indexes tabulated in Table 10.2 and based on oxide compositions listed in Table 10.3. Solid lines are corresponding bulk densities.

The best correlation between all the weathering indexes occurs when the protolith is composed exclusively of readily weatherable minerals such as in basalt. The greater differences in the weatherability of various minerals in rocks, such as granite, the greater will be the difference in various weathering indexes. The usefulness of specific indexes is also dependent on weathering intensity. The Group I indexes are ineffective in characterizing granitic saprolite weathering due to the stability of quartz. However, in more intensively weathered granitic profiles, such as laterites, SiO_2 in quartz is mobile and the Group I indexes are more effective indicators of weathering (Beauvais, 1999).

In deep regoliths, Al_2O_3 released from primary silicates is immobile, being precipitated in secondary minerals, principally clays. However, in relatively shallow soils, such as spodsols, with acidic conditions and/or with high organic contents, significant Al_2O_3 is mobilized (Driscoll et al., 1985). Similarly, Fe_2O_3 is considered an immobile component in some indexes (JE, Table 10.2) due to the retention of Fe in secondary phases. However, under reducing weathering conditions, ferric iron is converted to ferrous iron and becomes much more mobile (Price and Velbel, 2003).

In addition to the major elements discussed above, other weathering indexes incorporate trace elements, such as lanthanides (rare earths) and isotopes, including Nd and Sr (Brown et al., 2003). In sediment studies involving large rivers draining areas representative of average continental crust, Gaillardet et al. (1999) used weathering indexes defined by pairs of elements which have similar characteristics relative to the degree of differentiation between the upper crust and primitive mantle abundances but which exhibit significant mobilities in the weathering environment. An example of such a weathering index is

$$I_w = \left[\frac{Sm}{Na}\right]_{sed} \Big/ \left[\frac{Sm}{Na}\right]_{crust} \tag{10.3}$$

Gaillardet et al. (1999) showed that this weathering index for sediments in the world's rivers was always greater than unity ($I_w = 1 - 25$), indicating that Na is always depleted relative to the continental crust.

10.3.4 Solid Mass Transfers

While weathering indexes are useful in characterizing relative weathering intensities, they do not define the amount of a specific component mobilized during weathering, a prerequisite to calculating weathering rates. Mass losses require comparing the concentration of a weatherable component j in a soil or regolith $C_{j,w}$ against it's corresponding concentration in the rock or protolith $C_{j,p}$. This component can consist of an element, isotope or mineral. The concentration of $C_{j,w}$ reflects not only its own mass changes but also relative changes due to gains and losses of other components in the regolith, as well as external factors such as compaction or dilation of the soil or regolith. The most common method for overcoming such effects is to compare the ratio of the mobile component j to the ratio of an additional component i, which is chemically inert during weathering (Merrill, 1906; Barth, 1961).

Brimhall et al. (1991) defined the concentration ratio of a weatherable component in the regolith and protolith based on the relationship

$$\frac{C_{j,w}}{C_{j,p}} = \frac{\rho_p}{\rho_w} \frac{1}{(\varepsilon_i + 1)} (1 + \tau_j) \tag{10.4}$$

in which the change in the mobile element concentration ratio $C_{j,w}/C_{j,p}$, resulting from weathering, is dependent on three parameters: (1) the ratio of the bulk densities of the parent and weathered material, ρ_p/ρ_w, (2) the volume change resulting from soil compaction or extension described by the strain factor $1/\varepsilon_i + 1)$ where $\varepsilon_i = V_w/V_p - 1$ and (3) the mass transport coefficient τ_j. The strain and volume changes describe closed system contributions which occur without mobilization of the component under consideration (i.e., C_j). The term τ_j describes the mobility of component j within a unit volume of regolith.

The volumetric strain or volume change is calculated from the ratios of densities and concentrations of the inert element *i* in regolith and protolith (Eq. (10.4)).

$$\varepsilon_i = \frac{\rho_p C_{i,p}}{\rho_w C_{i,w}} - 1 \tag{10.5}$$

Positive values of ε_j indicate regolith expansion and negative values indicate regolith collapse. A value of $\varepsilon_j \approx 0$ is indicative of isovolumetric weathering.

The mass transfer τ_j in Eq. (10.4) is such that (Brimhall et al., 1991)

$$\tau_j = \frac{C_{j,w}}{C_{j,p}} \frac{C_{i,p}}{C_{i,w}} - 1 \tag{10.6}$$

When $\tau_j = 0$, no mobilization of the weatherable component j has occurred. When $\tau_j = -1$, complete mobilization has occurred. An external addition of component j has occurred if $\tau_j > 0$

The total mass of a component lost or added to the weathered profile $\Delta M_{j,}$ is obtained by integrating the mass transfer coefficient τ_j over the regolith thickness z (Chadwick et al., 1990; White et al., 1996)

$$\Delta M_j = \left(\rho_p \frac{C_{j,p}}{m_j^o} 10^4 \right) \int_0^z -(\tau_j) dz \tag{10.7}$$

where m_j^o is the atomic weight of element j. Mass losses are commonly normalized with respect to unit regolith surface area.

Calculations of strain ε_i (Eq. (10.5)), mass transfer τ_j (Eq. (10.6)) and mass change ΔM_j (Eq. (10.7)) require that at least one component in the regolith (C_i) remains inert or immobile during chemical weathering. Commonly assumed conservative elements include Zr (Riebe et al., 2003), Ti (Johnsson et al., 1993) and rare earth elements such as Nb (Brimhall and Dietrich, 1991). However, there is considerable disagreement in the literature as to the relative mobilities of these elements under differing weathering conditions (Gardner, 1980; Hodson, 2002). As proposed by White (1995), probably the best approach to establishing conservation is to compare the relative mobility of a suite of refractory elements for a specific weathering environment.

The composition of the parent material or protolith, $C_{j,p}$ is also required in calculating the above weathering parameters (Eqs. (10.4–10.7)). This composition is generally easy to determine for regoliths developed *in situ* on relatively homogenous bedrock. Determinations of parent concentrations are more difficult for heterogeneous protoliths such as some sediments. One approach is to equate the parent material to similar recent unweathered sediments, assuming that the depositional environment has not changed significantly. An example is the weathering of beach sands in marine soil chronosequences (Chadwick et al., 1990). The second approach utilizes the common observation that weathering intensity decreases with depth in a regolith (see weathering indexes in Fig. 10.2). Samples acquired at sufficient depths

may therefore reflect the unweathered protolith composition (see example of White et al., 2007).

Mass transfer calculations based on Eqs. (10.4–10.7) will now be illustrated for *in situ* formation of saprolite on granite.

10.3.5 Case Study: Element Mobilities During Granite Weathering

The regolith developed on the Panola Granite located in central Georgia USA has been described extensively (Hooper et al., 1990; White et al., 2001; 2002). The regolith consists of a dense unstructured kaolinitic soil, overlying a porous saprolite, resting on partially weathered granodiorite bedrock. Saprolites, common in many subtropical to tropical weathering environments, are clay-rich regoliths that retain the original bedrock texture. The chemical compositions and bulk densities of the Panola regolith are presented in Table 10.4. The protolith is represented as the deepest sample in the profile (fresh granite). The volumetric strains shown in Fig. 10.3a are calculated from Eq. (10.5) using Zr, Ti, and Nb as conservative components. Strain values center close to $\varepsilon_i \approx 0$ for the different inert elements, indicating that weathering is iso-volumetric in the saprolite and underlying bedrock. In contrast, the shallowest soils (<0.5 m) have undergone volume increases or dilation due to bioturbation and the introduction of organic matter ($\varepsilon_i > 0$).

Table 10.4 Selected oxide compositions and densities of the ridge top regolith in the Panola watershed (data from White et al., 2001)

Depth[1]	SiO_2	Al_2O_3	Fe_2O_3	MgO	CaO	Na_2O	K_2O	TiO_2	P_2O_5	MnO	Zr[2]	Nb[2]	Density[3]
0.10	81.1	8.8	2.74	0.21	0.14	0.44	3.05	1.91	0.04	0.093	1525	26	2.34
0.20	50.8	24.2	7.45	0.53	0.09	0.10	2.75	1.12	0.16	0.040	476	25	2.34
0.61	59.3	19.6	6.32	0.87	0.01	0.14	4.44	1.19	0.12	0.050	688	27	1.83
1.19	68.9	14.1	5.42	0.67	0.01	0.14	4.15	1.11	0.10	0.040	724	23	1.83
1.82	61.3	17.8	4.93	1.02	0.17	0.81	5.13	1.13	0.41	0.070	840	23	1.81
2.28	66.4	15.9	4.48	1.06	0.79	2.11	5.17	0.94	0.32	0.060	686	21	1.83
2.74	64.7	15.8	4.51	1.01	0.68	1.63	5.28	1.02	0.63	0.050	656	26	2.25
2.99	64.7	17.3	5.26	0.81	0.01	0.07	3.47	1.24	0.21	0.060	829	28	1.97
4.36	62.6	21.2	4.22	0.67	0.01	0.06	2.66	0.90	0.12	0.050	672	21	2.00
4.79	60.9	18.7	4.95	1.10	0.08	0.47	5.48	1.08	0.31	0.060	725	23	2.50
6.69	65.5	15.4	5.39	1.27	0.06	0.42	5.86	1.16	0.19	0.070	758	23	2.50
7.30	65.3	14.6	5.83	1.35	0.08	0.54	5.87	1.22	0.22	0.080	817	25	2.50
7.75	66.2	14.9	5.57	1.28	0.13	0.60	5.63	1.19	0.36	0.080	762	25	2.50
8.66	64.9	15.6	4.68	1.09	0.96	2.36	5.01	1.02	0.39	0.060	680	21	2.50
9.27	65.2	15.2	4.78	1.11	1.33	2.51	4.90	1.05	0.39	0.050	675	20	2.50
9.88	65.4	15.2	4.69	1.11	1.39	2.17	4.83	1.02	0.40	0.050	673	24	2.50
10.18	66.6	15.0	4.38	0.99	1.50	2.88	4.66	0.94	0.36	0.060	632	17	2.50
10.49	68.8	14.9	4.29	0.93	1.88	3.31	4.55	0.87	0.35	0.050	632	23	2.50
10.94	66.5	14.8	4.86	1.13	2.09	3.20	4.53	1.00	0.39	0.060	676	18	2.50
11.55	66.5	14.7	4.340	1.01	2.41	3.16	4.75	0.90	0.39	0.060	642	18	2.50

[1] Depth in m; [2] ppm; [3] density estimated below 4.79 m, g cm^{-3}.

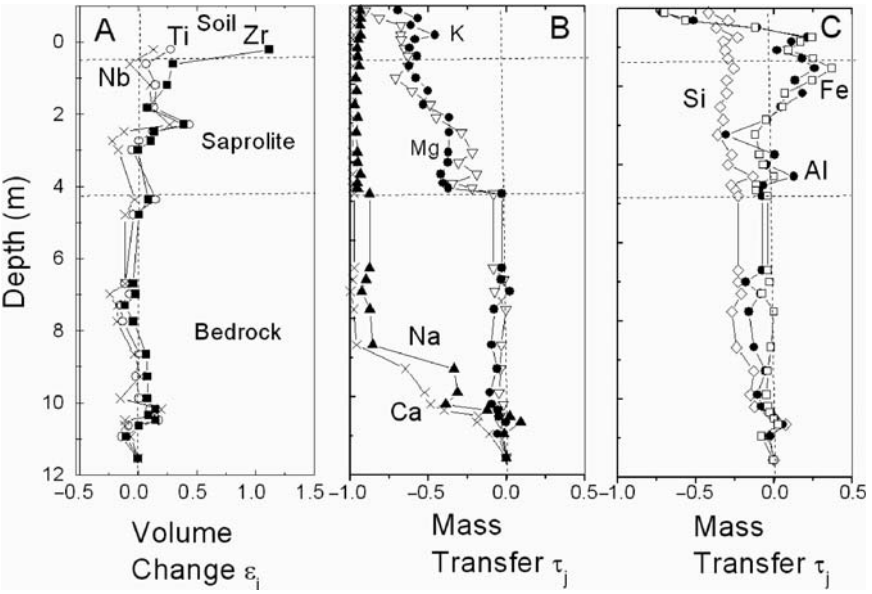

Fig. 10.3 Volume changes (strain) and elemental mobilities (mass transfers) within the Panola regolith, Georgia, USA. (**a**). Compaction and dilation are denoted by values of $\varepsilon_i < 0$ and $\varepsilon_i > 0$ respectively (Eq. (10.5)). A value of $\varepsilon_i = 0$ denotes isovolumetric weathering. (**b** and **c**) Element mobilities with regolith depth (Eq. (10.6)). A value $\tau_j = 0$ denotes no elemental loss and a value of $\tau_j = -1$ denotes complete elemental loss. (After White et al., 2001)

Mass transfer coefficients calculated for the Panola profile are plotted in Fig. 10.3b, c using Ti as the immobile component *i* and the reported fresh bedrock composition as the value for $C_{j,p}$ (White et al., 2001). These results show that values for τ_j (Eq. (10.6)) cluster near zero below about 10 m indicating no elemental mobility in deep bedrock. However, with decreasing depth in the shallower bedrock (10–6 m), τ_{Ca} and τ_{Na} approach a value of -1, indicating that both Ca and Na are almost completely mobilized by weathering. Weathering in this environment is highly selective because other base cations are not depleted at the same depths, i.e., τ_K and $\tau_{Mg} \approx 0$.

K and Mg are mobilized in the overlying saprolite (4.5–1.0 m). Fe and Al are strongly depleted in the upper soil and enriched in the lower soil horizons (τ_{Fe} and τ_{Si} approach $+0.4$) which is indicative of downward Fe and Al mobilization and subsequent re-precipitation in an argillic horizon at the soil–saprolite interface (White et al., 2002). These results demonstrate the usefulness of mass transfer coefficients in characterizing different weathering regimes that commonly exist within a single regolith.

The elemental mobilities shown in Fig. 10.3 correspond to the weathered regolith mineralogy which was calculated by White et al. (2002), using a spreadsheet approach originally developed by Garrels and Mackenzie (1967) This calculation sequentially distributed elements into residual phases based on mineral stoichimetries. The mass of plagioclase was first calculated using the plagioclase stoichimetries and

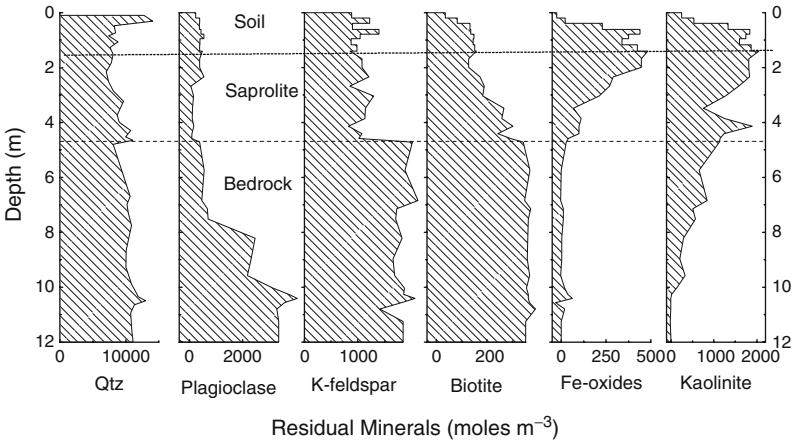

Fig. 10.4 Residual mineral distributions with depth in the Panola regolith, Georgia, USA. (After White et al. 2001)

Na concentrations. Next, all of the Mg was partitioned into a mica phase. The remaining steps sequentially distributed the K into the K-feldspar phase, the Al into the kaolinite phase, the Fe into Fe-oxide and the final residual Si into quartz.

The resulting residual mineral distributions (Fig. 10.4) closely mimic elemental losses described by the mass transfer coefficients (Fig. 10.3). The decrease in plagioclase in the upper bedrock correlates with losses of Na and Ca. The losses of K-feldspar and mica at and above the saprolite–bedrock interface correspond to losses of Mg and K. Finally, the precipitation and translocation of clay and Fe-oxides at the saprolite/soil interface correlates with positive increases in Al and Fe. The relatively low mobility of SiO_2 in the regolith is explained by the conservative nature of quartz (see previous discussion of weathering indexes for granites in Sect. 10.3.3), plus the retention of Si in secondary kaolinite.

The total elemental loss (ΔM_j) from the different weathering environments in the Panola regolith, i.e., bedrock, saprolite and soil was determined by integrating τ_j over their respective thicknesses (Eq. (10.7)). The highlighted data in Table 10.5 indicate that Ca and Na are strongly mobilized during bedrock weathering.

Table 10.5 Elemental mobility (kmoles.m^3) and total % loss in the Panola regolith. Negetative values indicate element increases. Highlighted data emphasize losses from from respective weathering environments (data from White et al., 2001)

	Bedrock	**Saprolite**	**Soil**	**Total**	**% loss**
Ca	**4550**	40	−10	9590	77
Na	**8190**	670	−90	19870	67
Si	**15030**	5520	−160	50350	16
K	−33	**3360**	10	5160	18
Mg	−229	**630**	−20	1170	16
Fe	−550	−130	**540**	−800	−5
Al	1520	−2030	**1780**	−150	0

Subsequently, most of the Mg and K are lost during the conversion of weathered bedrock to saprolite and finally Fe and Al are mobilized during the conversion of saprolite to soil. Although only elemental mobilities have been considered in the Panola example, Eqs. (10.4–10.7) are also applicable to other components, such as isotopes and mineral phases.

10.4 Weathering Calculations that Consider Solute Distributions

The alternate approach to characterizing chemical weathering is based on solute distributions (Fig. 10.1). Weathering inputs to soil pore water, groundwater and surface water occur over much shorter time spans than for solid state changes and describe present day or contemporary weathering processes.

10.4.1 Solute Fluxes

Water is the medium in which weathering reactants and products are transported to and from the minerals undergoing reaction. As discussed elsewhere in this volume (Chaps. 3 and 5), this transfer process has important ramifications for the mechanisms controlling silicate weathering reactions. In the present context, the solute mass loss or gain Δm_j (moles) is defined as

$$\Delta m_j = \Delta c_j v_s \tag{10.8}$$

where Δc_j (moles m^{-3}) is the change in solute component in a volume of water v_s. The solute flux q_j(m s^{-1}) is the product of the change in the solute concentration and the flux of water q_h. Both units are normalized with respect to time and a given cross section of regolith or aquifer and are sometimes referred to as flux densities

$$q_j = \Delta c_j \cdot q_h \tag{10.9}$$

The fluid flux q_h, is commonly defined by Darcy's law as the product of the hydraulic conductivity K_m(m s^{-1}) and the hydraulic gradient ∇H(m m^{-1}) (Hillel, 1982).

$$q_h = -K_m \nabla H \tag{10.10}$$

The weathering, flux $q_{j,w,}$ is commonly only a fraction of the total solute flux q_j such that (Paces, 1986)

$$q_{j,w} = q_j - q_{j,precip} \pm q_{j,bio} \pm q_{j,exch} \tag{10.11}$$

where $q_{j,precip}$ is the solute input from precipitation and $q_{j.bio}$ and $q_{j,exch}$ are inputs and/or outputs from biological processes such as nutrient cycling in vegetation and exchange processes between water and mineral surfaces (Velbel, 1996). Commonly

net biologic and exchange processes are assumed to be in equilibrium, therefore

$$q_{j,w} = q_j - q_{j,precip} \tag{10.12}$$

However, a number of scenarios can be considered that produce net positive or negative of fluxes for $q_{j.bio}$ and $q_{j,exch}$ (Velbel, 1986). Examples include forest aggradation or degradation or changes in exchangeable base cations resulting from acid precipitation, Anthropogenic inputs can also occur from pollution and application of fertilizers (Paces, 1986).

10.4.2 Mineral Contributions to Solute Fluxes

Once the solute weathering flux $q_{j,w}$ has been defined (Eq. (10.11)), an additional issue commonly arises as to what minerals contribute to these solute outputs. Changes in solute concentrations $\Delta c_{j,w}$, due to weathering of individual minerals m, is defined by the relationship (Velbel, 1986)

$$\Delta c_{j,w} = \sum_{m=1}^{\phi} \Delta M_m \beta_{j,m} \quad j = 1 \ldots n \tag{10.13}$$

where ϕ and n are, respectively, the total number of minerals and solute phases considered, ΔM_m is the mass of a specific mineral reacted (positive for dissolution and negative for precipitation) and $\beta_{j,m}$ is the stoichiometric factor describing the distribution of element j in mineral m. Eq. (10.13) defines a matrix of linear equations with the dimensions of ϕ times n.

Several approaches are used to partition solute compositions between different reactive mineral phases. The simplest approach, originally used by Garrels and Mackenzie (1967), is to sequentially solve Eq. (10.13) using an array of linear equations assuming that specific elements are uniquely constrained by individual mineral phases (see Panola example; Sect. 10.3.5). The original spreadsheet approach has been subsequently refined as an EXCEL program by Bowser and Jones (2002) with the significant restriction that the number of plausible mineral phases included in the model must equal the total number of solute species, i.e., the matrix defined by Eq. (10.13) is uniquely defined. In spite of this limitation, the spreadsheet approach has proven to be very useful in understanding the role of variable mineralogy and rock type on solute weathering reactions.

The second approach in partitioning solute compositions into minerals is to consider all possible sets of weathering reactions regardless of the number of species and phases considered. Such calculations are most commonly performed using computer codes such as NETPATH (Plummer et al., 1991). In most cases, the number of possible reactants remains greater than the number of linear equations describing these reactions (Eq. (10.13)) and no unique solution is possible. The program searches for sets of reactive phases that exactly account for the difference in chemical composition between the initial and final solutes. The result is commonly a

set of solutions describing different proportions of mineral phases that characterize these changes. As pointed out by Plummer et al. (1991), the number of realistic reactions can be significantly reduced using petrographic, x-ray and other data which characterize the actual weathering processes.

The third approach to characterizing solute contributions from weathering is to statistically optimize the matrix of possible mineral reactions by using an inverse methods (Allegre et al., 1983; Steefle, 2007; this volume). This method has been used extensively in determining weathering inputs to river solutes (Dupre et al., 1996; Gaillardet et al., 1999). The matrix inversion technique consists of finding the best values for a set of model equations. No formal distinction is made between the known solute compositions and the unknown proportion of mineral reactants. Each parameter is initially estimated and a calculated value is produced. In the case of solute inputs, the errors are small, corresponding to sampling and analytical uncertainties. In the case of the reactants the errors are large, corresponding to a range of possible mineral contributions. The efficiency of the inversion calculation is evaluated by comparing the size of the resultant error. If the latter is less than the former, then a gain of precision has occurred in the calculation. The program propagates the error, reaching an optimum set of values for the mineral reactions considered.

10.4.3 Solute Weathering Fluxes in Soils

Vertical infiltration of pore water through a soil profile, accompanied by weathering of reactive silicate minerals, is conceptually simple. However, the paucity of studies that quantify soil weathering based on pore water fluxes reflects a number of practical difficulties (Sverdrup and Warfvinge, 1995). Most pore water infiltration occurs as unsaturated flow, which requires extraction using *in situ* suction water samplers or laboratory centrifugation. Fluid fluxes occurring under unsaturated flow conditions are also often difficult to determine because both the hydraulic gradient and the conductivity (Eq. (10.10)) are strongly dependent on moisture content (Stonestrom et al., 1998).

In addition, relatively shallow soils and regoliths are subjected to perturbations including evapotranspiration and cycling as mineral nutrients by plants. The magnitude and complexity of these fluxes make estimating the weathering flux difficult (Eq. (10.11)). In spite of such issues, quantifying weathering rates in soils, based on solute characteristics, is an area for fruitful investigation, in part due to its importance in many ecosystem processes.

10.4.4 Case Study: Solute Weathering Fluxes in a Tropical Soil

One site in which regolith weathering has been intensely studied is the tropical Rio Icacos watershed in the Luquillo Mountains of Puerto Rico (White et al., 1998;

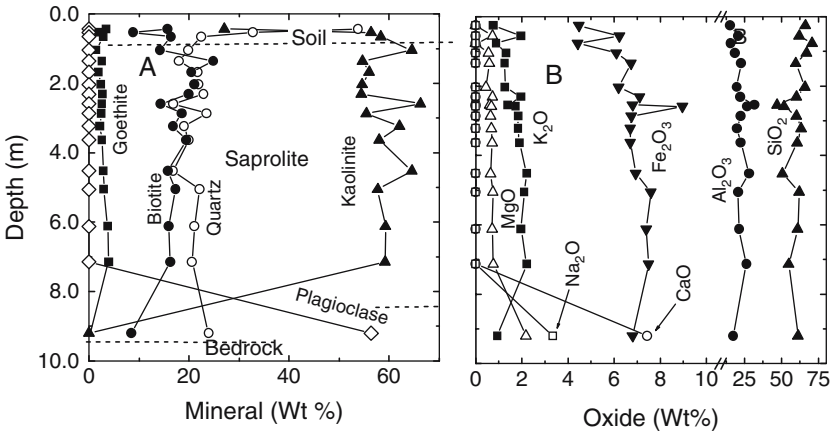

Fig. 10.5 (**a**) Mineral and (**b**) oxide abundances in the Rio Icacos regolith, Puerto Rico. (After White et al., 1998)

Murphy et al., 1998; Schulz and White, 1999; Kurtz et al., 2002; Turner et al., 2003; Riebe et al., 2003). The regolith comprises a clay-rich soil (<1 m), underlain by a saprolite up to 15 m deep, developed on quartz diorite. The nearly complete losses of Na and Ca occur in the soil and saprolite due to the weathering of plagioclase at the bedrock interface (Fig. 10.5). In contrast, slower weathering of biotite and quartz predominate in the overlying thick saprolite, producing only slight concentration changes in solid state Mg, K and Si. Fine-grained kaolinite is produced by plagioclase weathering at the bedrock interface as well as by pseudomorphic replacement of altered biotite in the saprolite. Mineral stoichimetries and abundances at selective depths are presented in Table 10.6.

Table 10.6 Mineral stoichiometries and abundances (wt %) in the soil, saprolite and bedrock in the Rio lcacos regolith (after Murphy, 1998)

Mineral	Formula	Soil 0.17 m	Saprolite 0.76 m	Saprolite 2.87 m	Saprolite 7.13 m	Quartz Diorite
Quartz	SiO_2	53.7	21.9	23.5	20.6	24.9
Plagioclase	$Na_{0.60}\ Ca_{0.40}\ Al_{1.36}\ Si_{2.63}\ O_8$	0.0	0.0	0.0	0.0	56.4
K-feldspar	$Na_{0.09}\ K_{0.91}\ AlSi_3O_8$	0.0	0.0	0.0	0.0	1.8
Biotite (rock)	$K_{0.85}(Al_{0.10}Ti_{0.20}Fe^{2+}{}_{1.30}Fe^{3+}{}_{0.05}Mg_{1.25})(Si_{2.8}Al_{1.2})O_{10}(OH)_2$	NA	NA	NA	NA	9.5
Biotite (regolith):	$K_{0.65}(Al_{0.10}Ti_{0.15}Fe^{2+}{}_{0.35}Fe^{3+}{}_{0.15}Mg_{0.55})(Si_{3.2}Al_{0.8})O_{10}(OH)_2$	15.7	21.1	18.6	16.2	NA
Homblende	$(Na_{0.34}, K_{0.05})(Ca_{1.71}Mg_{2.84}Fe_{2.06}Al_{0.89}[Al_{1.00}Si_{6.68}]O_{22}(OH)_2$	0.0	0.0	0.0	0.0	6.3
Kaolinite*	$(K_{0.01}Fe_{0.07}Mg_{0.04})(Si_{2.21}Al_{1.69})O_5(OH)_4$	27.1	57.0	57.9	63.2	0.0
Goethite	FeO(OH)	3.4	2.4	2.5	3.9	1.9

*High Si/Al ratios probably reflect qtz contamination.

Table 10.7 Average chemical compositions in the Rio Icacos watershed (data from White et al., 1998*)

	Rain		Pore Water (m)					Rio
	Open	**Thru**	**0.92**	**1.23**	**3.62**	**6.75**	**8.52**	**Icacos[1]**
pH	5.6	5.2	4.9	4.0	4.58	5.11	5.1	6.8
Na	59.2	119	204	90.2	128	174	156	222
K	1.4	12.3	6.0	5.2	8.8	23.9	39.1	13.0
Ca	3.8	6.8	12.1	12.7	9.8	12.6	27.0	83.0
Mg	6.8	13.2	24.4	18.9	28.8	32.9	59.3	49.0
Li	0.0	0.0	5.7	2.3	9.70	4.10	4.3	nd
Mn	0.0	0.0	1.4	0.2	1.31	1.57	3.6	nd
Fe	0.0	0.0	0.2	0.0	0.20	1.60	0.3	nd
Al	0.0	0.0	3.4	9.0	5.56	2.31	15.6	nd
Si	0.0	0.0	61.1	60.7	104	200	216	305
Sr	1.9	0.0	0.1	0.3	0.02	0.09	0.1	nd
Alk	0.0	0.0	16.4	12.3	17.2	21.2	67.6	347
Cl	64.9	163	246	128	208	148	171	176
NO_3	0.0	0.0	6.2	0.0	10.2	14.1	18.9	50.0
SO_4	6.9	15.4	11.0	12.4	7.88	7.02	7.65	23.5

*Units are in μM except as noted; [1] measured at gauge.

Selected average pore water compositions, based on samples collected from suction water samplers at selected regolith depths are tabulated in Table 10.7. Also included are average open and through fall precipitation and surface water compositions in the Rio Icacos stream. Vertical variations in solute Cl, Na, Ca, K, Mg and SiO_2 are shown in Fig. 10.6. Shallow soil pore waters $(<1\,\text{m})$ exhibit significant variability due to the dynamic effects of evapotranspiration and nutrient cycling through shallow plant roots. At greater depths (1–9 m), linear increases in solute K and Mg occur due to weathering of biotite in the saprolite (Fig. 10.5). Increased Si concentrations are contributed both from biotite and quartz weathering (Murphy et al., 1998; Schulz and White, 1999). No consistent increases in Na and Ca occur because plagioclase is weathered out at the underlying bedrock/saprolite interface (Fig. 10.5a). Cl exhibits no significant variations at depth because it is not contained in any weatherable mineral phase.

Mineral weathering in the Rio Icacos regolith was modeled by White et al. (1998) as a step-wise process that sequentially defines the solute reservoirs, the compositions of the input and output solutions and the relevant mineral weathering reactions (Fig. 10.7). The regolith reservoirs are (1) the shallow saprolite $(<1\,\text{m})$, which integrates chemical inputs from open-fall precipitation and through-fall precipitation recharged from the forest canopy and weathering in the soil, (2) the deep saprolite which integrates chemical inputs between the shallow saprolite to the bedrock interface (1 to 9 m), and (3) surface flow in the stream which reflects a mixture of shallow and deep saprolite pore waters that have been modified by weathering at the saprolite–bedrock interface.

A total fluid mass (1 kg) is conserved in the calculations and is apportioned during mixing and evapotranspiration based on the solute Cl concentrations (Fig. 10.7, arrows). Results indicate that 0.36 kg of open-fall and 0.64 kg of through-fall

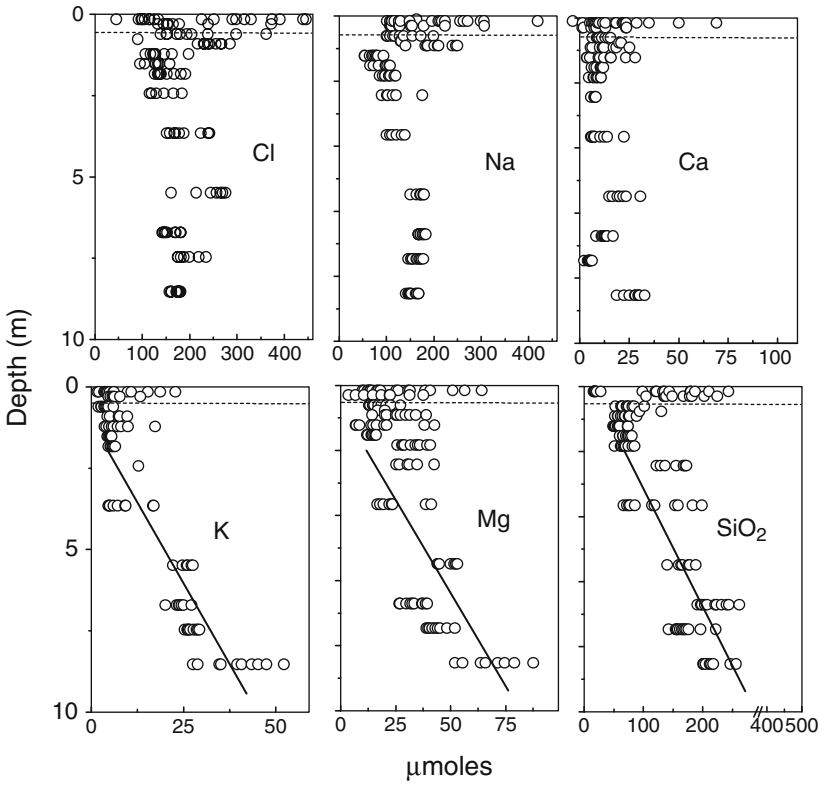

Fig. 10.6 Pore water concentrations as functions of depth at the Rio Icacos regolith, Puerto Rico. Dashed horizontal line is the depth of the soil/saprolite interface. Diagonal solid lines correspond to linear regression fits through the pore water K, Mg and Si data as functions of depth in the saprolites. (After White et al., 1998)

produce the observed solute Cl in the shallow saprolite. The evapotranspiration loss in the overlying soil was incorporated into the two precipitation terms. The subsequent increase in Cl in the deeper saprolite reflects an additional loss of 0.22 kg of water to evapotranspiration. Average surface water compositions are composed of about 60% shallow saprolite (0.47 kg) and 40% deep saprolite (0.31 kg) water. No additional evaporation is assumed to occur as inputs to the surface water.

The sequence of linear equations describing the mineral solute inputs is solved using the NETPATH computer program (Plummer et al., 1991). The calculations are constrained by the number of elements and minerals considered (n and m in Eq. (10.13)) and the changes in the mass of water due to mixing and evaporation. Reactions involving primary and secondary minerals in the soil and saprolite are described by two sets of elemental constraints, K–Ca–Fe–Si–Al–Cl and Mg–Ca–Fe–Si–Al–Cl (Fig. 10.7, boxes A–B). Each set contains four of the five elements that comprise the dominant mineral phases in the regolith, i.e., biotite, quartz, kaolinite and goethite (Fig. 10.5). Incorporation of additional constraints into a single mass

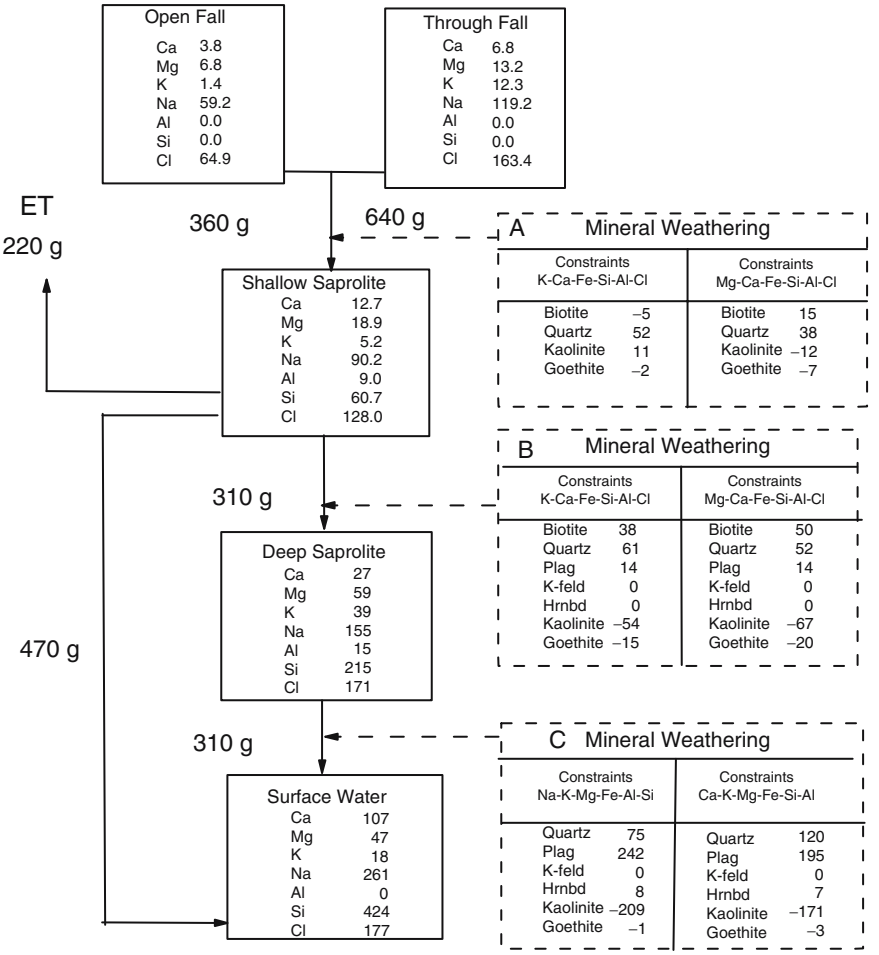

Fig. 10.7 Schematic describing mineral and fluid fluxes in the Rio Icacos regolith. Solid arrows are water transfers (solute fluxes, Eq. (10.11)) due to infiltration, mixing and evapotranspiration (calculations assume that 1 kg of water is conserved). Dashed arrows are mineral inputs (Eq. (10.13)). Solid boxes are solute concentrations (μmoles kg^{-1} H_2O) and dashed boxes are masses of minerals reacted (uM) under different model constraints in NETPATH (Plummer et al., 1991) ($[-] =$ dissolution and $[+] =$ precipitation). (After White et al., 1998)

balance calculation was not possible because solutions to Eq. (10.13) became overdetermined.

Calculations of weathering inputs at $<$1 m produced contradictory results using the separate K–Ca–Fe–Si–Al–Cl and Mg–Ca–Fe–Si–Al–Cl constraints (Fig. 10.7, dashed box A). This is due principally to the large uptake of K in the biologic reservoir which is not considered in the calculations. In contrast, both the K–Ca–Fe–Si–Al–Cl and Mg–Ca–Fe–Si–Al–Cl constraints produce consistent changes in solute compositions between the top (1 m) and bottom (9 m) of the saprolite (Fig. 10.7,

Table 10.8 Estimated fluid fluxes $q_h (m\,s^{-1})$ and fluid residence times in pore water and groundwater at Rio Icacos

Rate q_h	Time (yr)	Method	Reference
5.510^{-6}	0.049	Experimental K_{sat}	White et al., 1988
4.010^{-6}	0.067	Pump test in saturated saprolite	McDowell et al., 1992
1.310^{-7}	2.07	Precipitation	McDowell and Asbury, 1994
1.110^{-7}	2.45	Annual stream discharge	McDowell and Asbury, 1994
6.310^{-8}	4.28	LiBr tracer test	Turner et al. 2003
3.410^{-8}	7.93	Experimental K_{unsat}	White et al., 1988
2.110^{-8}	12.83	Base stream discharge	McDowell and Asbury, 1994

dashed box B). The dissolution of 38 μmoles of biotite produces the K increase while 50 μmoles of biotite produces the Mg increase. The significant increases in solute Si (Fig. 10.7) result from both biotite and quartz (61 and 52 μmoles) dissolution. Equal but small amounts of plagioclase (14 μmoles) are dissolved under both constraints (the only source of solute Ca in the saprolite is plagioclase). All the Al produced by biotite and plagioclase dissolution is incorporated into kaolinite (54 and 67 μmoles) and all the Fe is incorporated into goethite (15 and 20 μmoles) which is in agreement with very low concentrations of these species in the saprolite pore waters

Stream compositions in the Rio Icacos watershed represent a mixture of shallow and deep pore waters (Fig. 10.7). Stream water is also characterized by significant increases in Ca, Na and Si, reflecting dissolution of plagioclase at the bedrock interface. Two sets of weathering constraints, Ca–K–Mg–Fe–Al–Si and Na–K–Mg–Fe–Al–Si (Fig. 10.7, box C) each contain two of the three elements (Ca, Na and Si) most dependent on plagioclase dissolution. The Na–K–Mg–Fe–Si–Al constraints predict that 242 μmoles of plagioclase dissolve while the Ca–K–Mg–Fe–Al–Si constraints predicted that 195 μmoles dissolve into the stream

Solute fluxes associated with present day weathering of the Rio Icacos regolith (Eq. (10.9)) are calculated as the product of the solute concentration $\Delta c_{j,w}$ (moles m^{-3}) which are described in Fig. 10.6 and the flux density of water q_h which was estimated by an array of techniques in Rio Icacos watershed (Table 10.8). In the analysis of Stonestrom et al. (1998), the average experimental K_{sat} measured in cores at average field saturation was considered the best estimate of the regolith flux density $q_h = 3.4 \times 10^{-8}\,m\,s^{-1}$. This value is between measurements based on the Br tracer test $(6.3 \times 10^{-8}\,m\,s^{-1})$ and base flow of the Rio Icacos $(2.1 \times 10^{-8}\,m\,s^{-1})$. The corresponding solute fluxes q_j for major solutes are then calculated for the regolith (Eq. (10.11)) and shown in Table 10.9. These values are compared to stream fluxes previously calculated by McDowell and Asbury (1994).

10.4.5 Solute Weathering Fluxes in Groundwater Systems

The discussion up to this point has considered solute weathering fluxes during simple vertical pore water infiltration through a regolith. In contrast, calculating

Table 10.9 Weathering fluxes in the Rio lcacos wateshed. Units are moles $m^{-2} s^{-1}$ (data from White et al., 1998)

	Pore water flux, q_j; White et al., 1998	Stream flux, q_j; McDowell & Asbury, 1994	Regolith flux, Q_j; White et al., 1998	Regolith flux, Q_j; Riebe et al., 2003
Si	1.38E-08	2.56E-08	1.74E-08	1.56E-08
Na	4.34E-09	3.45E-09	1.90E-09	1.45E-09
K	1.10E-09	1.04E-09	8.21E-10	3.01E-10
Ca	3.25E-09	6.72E-09	2.70E-09	3.17E-09
Mg	2.13E-09	3.64E-09	1.01E-09	1.45E-09

weathering fluxes in groundwater systems is often closely tied to a more detailed understanding of flow paths often considered in two or three dimensional hydrologic models (for a more detailed discussion of coupling of weathering and fluid flow see Chap. 11). The physical isolation of groundwater aquifers, compared to soils, is advantageous for characterizing weathering rates because short-term biologic and climatic perturbations are often diminished. Furthermore, modeling saturated flow is simpler than unsaturated flow common to soil systems. However, the characterizations of mineral distributions, aquifer heterogeneities and mineral surface areas are more difficult because of greater physical inaccessibility.

10.4.6 Case Study: Spring Discharge

One of the earliest and simplest characterizations of groundwater weathering was based on spring discharge from granitic rocks of the Sierra Nevada Mountains of California (Garrels and Mackenzie, 1967). Changes in solute concentrations due to weathering ($\Delta c_{j,w}$ in Eq. (10.8)) were assumed to be the differences between the discharge compositions and atmospheric inputs from precipitation (Eq. (10.12)). The fluid flux was the measured spring discharge. The authors, after partitioning the various solutes between mineral phases contained in the plutonic rocks, found that plagioclase was the dominant reactive mineral followed by biotite and K-feldspar. A similar spring discharge approach was later used by Katz (1989) to characterize groundwater weathering of interbedded metabasalts and sedimentary rocks in the Catoctin watershed in Maryland, USA which was dominated by calcite and followed by albite, actinolite and chlorite

With the advent of new techniques for age dating groundwater, including chlorinated fluorocarbons (CFC), ^{3}H and ^{3}He (Plummer et al., 1996), fluid residence times can be assigned to spring discharge. Rademacher et al. (2001) used this approach to calculate weathering fluxes in springs issuing from granodiorite rocks in the Sagehen basin in the Sierra Nevada Mountains of California. The NETPATH computer code (Plummer et al., 1994) partitioned solutes between different minerals. These masses were then divided by the groundwater ages of each spring to produce mineral weathering fluxes normalized to the specific volume of water (moles L^{-1} $year^{-1}$). Flux data for plagioclase and hornblende for springs of different recharge age are

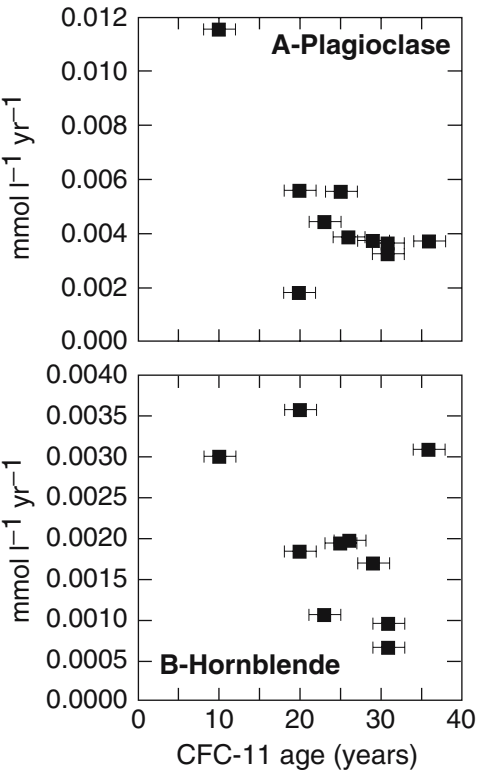

Fig. 10.8 Weathering fluxes ($q_{j,w}$ in Eq. (10.13)) for (**a**) plagioclase and (**b**) hornblende as functions of residence times of spring discharge, Sage Hen watershed, California, USA (Rademacher et al., 2001)

plotted in Fig. 10.8. Results indicate that groundwaters are young and that much of the weathering occurs during the initial stages of recharge though the soil zone (Rademacher et al., 2001).

10.4.7 Weathering along Groundwater Flow Paths

A more rigorous and intrusive approach to characterizing groundwater weathering is based on changes in solute concentrations along a specified flow path, commonly measured in an array of wells. In some cases, the groundwater flow path can be estimated by lithologic or topographic constraints. A simple case of groundwater weathering in the Panola watershed (also see Sect. 10.3.5) is described by Burns et al. (2003), who sampled a series of shallow wells along the riparian zone alluvium of the Panola stream. In general, solute compositions increased along this flow path and with increasing well depth. Based on CFC and $^3H/^3He$ ratios, estimated groundwater ages varied from 0.5 to 1.2 years in the upper reaches of the watershed to 28 years at the downstream gauge. As shown in Fig. 10.9, strong positive correlations were found between the apparent age and solute SiO_2, Na

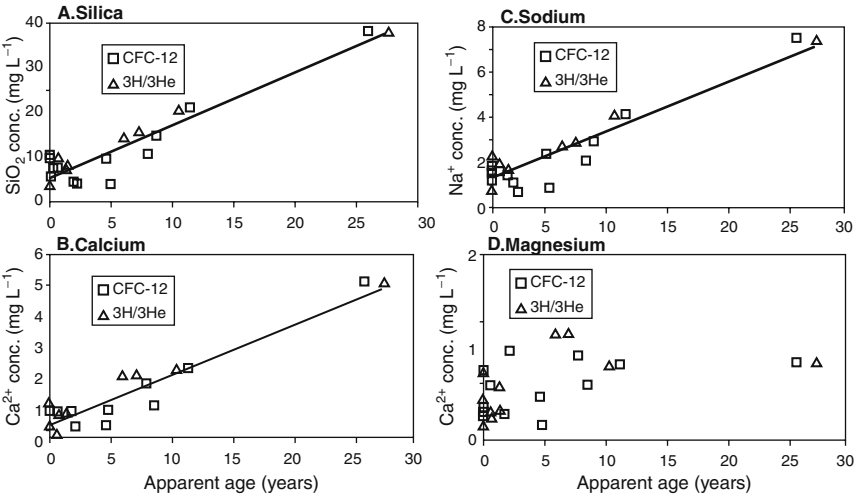

Fig. 10.9 Concentrations of Si, Ca, Na and Mg in groundwater in the riparian zone along Panola Creek, Georgia, USA plotted as a function of groundwater age as calculated from CFC-12 and $^3H/^3He$ (Burns et al., 2003)

and Ca concentrations. Burns et al. (2003) used the NETPATH model (Plummer et al., 1991) to calculated probable mineral reactions. Dividing the mass of minerals reacted based on the different weathering scenarios by the groundwater residence times produced average mineral weathering fluxes listed in Table 10.10. Plagioclase weathering fluxes at Panola are comparable to those calculated for the Sage Hen watershed (Fig. 10.8) but the hornblende weathering at Panola is significantly less.

Table 10.10 Average weathering fluxes based on mass balance calculations of the evolution of groundwater in the riparian aquifer in the Panola watershed, Georgia, USA. (Data after Burns et al., 2003)

Mineral Phase	Number of Models that Include Phase	Median Mineral Weathering Rate, in μmol L^{-1} yr^{-1}	Range in Mineral Weathering Rate, in μmol L^{-1} yr^{-1}
Scenario 1 – Upstream Wells to Well 150	Total Models = 8		
Plagioclase (total)	8	6.4	6.3–7.2
Biotite	5	0.40	0.18–0.47
K-Feldspar	5	0.29	0.20–0.42
Homblende	4	0.55	0.27–0.84
Calcite	3	0.82	0.56–0.83
Scenario 2 – Upstream Wells to 300-Series Wells	Total Models = 4		
Plagioclase (total)	4	3.7	3.7
Biotite	4	0.60	0.58–0.60
Homblende	4	2.3	2.3
K-Feldspar	1	0.015	0.015

Rates based on 26 years for scenario 1 and 6.5 years for scenario 2.

Quantifying chemical weathering in groundwater commonly requires a more detailed understanding of groundwater flow paths than was required in the Panola case. An example of the Trout Lake aquifer is presented below.

10.4.8 Case Study: Weathering in an Unconfined Aquifer

The groundwater in clastic-dominated sediments of the Trout Lake area of Northern Wisconsin (Fig. 10.10) has been the subject of a number of chemical weathering studies (Kenoyer and Bowser, 1992a,b; Bullen et al., 1996; Bowser and Jones, 2002; Walker et al., 2003). The lithology of the area consists of thick ($\sim$50 m) glacio-fluvial sediments derived from a suite of granitic to gabbroic intrusive rocks, metavolcanics and metasedimentary rocks from the Canadian Shield. These sediments overlay relatively impervious, crystalline Precambrian bedrock. Average mineralogical analyses and abundances are presented in Table 10.11.

Most weathering studies in the area have focused on groundwater data from a network of wells on a 120 m wide isthmus of land that separates Crystal Lake which is upgradient from Big Muskellunge Lake (Fig. 10.10a). Groundwater compositions, listed in Table 10.12, reflect a mixture of seepage recharged from Crystal Lake and infiltration through the upland area between the two lakes. Water levels and *in situ* slug tests in the wells defined the groundwater gradients and estimated flow paths plotted in Fig. 10.10b. Note that the flow lines are perpendicular to the potential gradients. The oxygen isotopic contrasts between the two sources of groundwater allowed for determination mixing ratios (Fig. 10.10c). Groundwater velocities were determined from a groundwater flow model and checked using tracer tests. Clear deflections of velocity contours occur across a low permeability silt layer (Fig. 10.10b, c).

The chemical evolution of groundwater due to chemical weathering along specific flow paths was modeled by Kenoyer and Bowser (1992a and b), Kim (2002) and Bowser and Jones (2002). One specific flow path, shown in Fig. 10.10b and c, approximately intersects the monitoring wells, K87, K70, K71 and K5. Changes in groundwater composition between these wells as a function of residence time are shown in Fig. 10.11. In general, the solute concentrations increase down the flow path, with most rapid changes occurring across the silt interbed. This concentration–time plot is similar to that previously shown in Fig. 10.9 for the Panola groundwater (Burns et al., 2003). However, at Panola, the flow was constrained by the physical geometry of the groundwater basin, whereas at Trout Lake, the flow path plotted in Fig. 10.11 is actually one of many flow paths in the aquifer and is defined by potentiometric gradients and hydraulic conductivities.

Kenoyer and Bowser (1992a) used the forward modeling code PHREEQE (Parkhurst and Plummer, 1993) to calculate mineral weathering inputs along the flow paths across the isthmus site. Based on more detailed mineral analyses and hydrology (Kim, 2002; Bowser and Jones, 2002) revised the calculations, based on more detailed mineralogy listed in Table 10.11, with results shown in Table 10.13.

Table 10.11 Mineral properties and stoichimetries in the Trout Lake aquifer (Kim, 2002)

Mineral type	Density (g/cm^3)	Shape factor	Modal %	Surface area %[a]	Weight %[b]	$S'_i(m^2/g)$[c]	Chemical composition
Quartz	2.65	1	75–85	48–85	75–87	0.27–0.76	SiO_2
K-feldspar	2.55	1	6.8–14.5	5.2–14.5	6.7–14.2	0.038–0.125	$(K_{0.91}Na_{0.08}Ca_{0.01})(Al_{1.03}Si_{2.96})O_8$
Plagioclase	2.63	1	2.8–3.3	2.0–3.3	2.8–3.4	0.011–0.029	$(Na_{0.77}Ca_{0.17}K_{0.02})(Al_{1.19}Si_{2.82})O_8$
Amphibole	3.20	1–5	0.8–1.6	0.8–5.3	1.0–2.0	0.004–0047	$Ca_{1.35}Na_{0.35}K_{0.12}(Mg_{2.33}Fe_{2.14}Al_{0.65})$ $(Si_{6.94}Al_{1.06})O_{22}(OH)_2$
Pyroxene	3.30	1–5	0.2–1.4	0.2–4.7	0.2–1.8	0.001–0.041	Opx: $(Mg_{1.08}Fe_{0.71}Ca_{0.17}Al_{0.03}Ti_{0.01})$ $(Si_{1.99}Al_{0.01})O_6$ Opx: $(Mg_{0.78}Ca_{0.74}Fe_{0.40}Na_{0.02}Al_{0.06}Ti_{0.02})$ $(Si_{1.96}Al_{0.04})O_6$
Epidote	3.40	1–3	0.4–1.4	0.4–2.8	0.5–1.9	0.002–0.025	$Ca_{0.0}Al_{2.2}Fe_{0.8}Si_3O_{12}(OH)$
Chlorite	2.90	1–10	0.7–1.4	0.7–9.5	0.7–1.6	0.004–0.084	$(Fe_{2.38}Mg_{2.09}Al_{1.43}Ti_{0.01}Ca_{0.01}K_{0.01})$ $(Si_{2.73}Al_{1.27})O_10(OH)_8$
Biotite	3.10	1–10	0.0–0.2	0.0–1.2	0.0–0.2	0–0.011	$K_{1.96}Na_{0.01}(Fe_{2.84}Mg_{2.48}Al_{0.51})$ $Al_{2.18}Si_{5.82}O_{20}(OH)_4$
Pumpellyite	3.20	1–3	0.0–0.2	0.0–0.4	0.0–0.2	0–0.004	$(Ca_{3.94}Na_{0.03}K_{0.01})(Mg_{0.61}Fe_{0.39})$ $(Al_{4.57}Fe_{0.50}Ti_{0.01})$–$Si_{6.10}O_{23}(OH)_3$
Staurolite	3.75	1	0.0–0.2	0.0–0.2	0.0–0.3	0–0.002	$(Fe_{1.58}Mg_{0.35})(Al_{8.93}Ti_{0.07})O_6(SiO_4)_{3.84}$ $(O_{1.57}(OH)_{0.43})$
Weathered and Opaques	2.7	1–10	2.0–2.5	2.0–16.5	2.1–2.6	0.011–0.145	

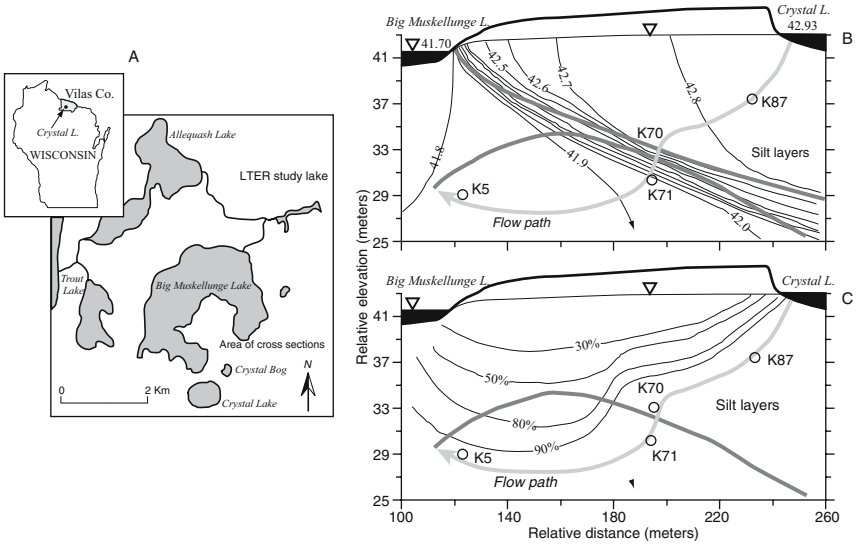

Fig. 10.10 Weathering in groundwaters in the isthmus between Crystal Lake and Big Muskellunge Lake, Wisconsin. (**a**) Location map. (**b**) Hydraulic head contours (m). Also shown are two silt layers with lower hydraulic conductivities and the modeled flow water flow path. (**c**) Contours of the percentage of lake water recharge to groundwater based on $\delta^{18}O$ contents. (After Bowser and Jones, 2002)

Most of the weathering occurs across the silt-dominated portion of the aquifer between Wells K70 and K71, presumably due to greater surface reactivity associated with smaller grain sizes. Results indicate that hornblende dominates the weathering process. The rate of plagioclase weathering between the up-gradient wells is comparable to that previously reported for the Panola and Sagehen studies (Figs. 10.8 and 10.9). Along the lower portion of the flow path, the rate of plagioclase weathering decreased, a phenomena attributed by Kenoyer and Bowser (1992b) to the approach of thermodynamic saturation of plagioclase. Other examples of chemical weathering in aquifers are addressed in studies by Keating and Bahr (1998), Brantley et al. (2001) and Zhu (2005).

10.4.9 Weathering Fluxes in Surface Waters

Weathering processes associated with surface waters are most often considered on the catchment and river basin scale. In such systems, actual weathering between surface water and the stream bed is negligible. Rather, the surface water solutes reflect the integration of weathering and other processes associated with the hyporheic zone surrounding the steam, hillslope discharge and groundwater inputs.

The determination of the solute fluxes in stream and rivers is conceptually straight-forward although often labor- and equipment-intensive. Solute

Table 10.12 Solute compositions sampled from selected wells in the Trout Lake aquifer. Units in mg/L. (Data from Kim, 2002)

Sampling	Site	pH	Alkalinity	DIC	CI	SO_4	Ca	Mg	Na	K	Fe	Silica
	m	**6.03**	**18.3**	**0.6**	**0.47**	**3.4**	**1.16**	**0.27**	**0.34**	**0.37**	**0.00**	**19**
Crystal	**σ**	**0.261**	**7.95**	–	**0.055**	**0.290**	**0.100**	**0.017**	**0.030**	**0.044**	–	–
Lake	**CV**	**0.04**	**0.43**	–	**0.12**	**0.09**	**0.09**	**0.06**	**0.09**	**0.12**	–	–
K1		5.73	300	17.6	0.74	4.28	4.10	0.73	0.84	0.38	2.29	744
K2		7.36	437	6.5	0.37	3.56	5.18	1.97	1.56	0.52	0.00	4821
K5		7.73	636	8.6	0.44	3.27	7.83	3.20	1.44	0.47	0.26	8140
K6		6.12	506	14.8	1.09	5.37	4.03	1.75	1.56	1.96	10.50	5643
K66		6.31	711	19.4	0.86	1.59	4.86	1.25	1.78	3.10	22.05	3389
K67		5.83	196	10.2	0.78	5.23	2.47	0.77	1.28	0.65	2.55	4807
K68		5.79	121	8.7	0.65	5.65	3.24	0.81	1.39	0.83	0.04	3862
K69		5.79	105	6.9	0.62	4.94	2.63	0.63	1.05	0.59	0.00	3813
K70		6.27	158	4.7	0.51	3.55	2.67	0.85	1.11	0.51	0.12	3862
K71		8.26	494	6.6	0.50	3.67	6.15	2.57	1.46	0.53	0.04	5834
K73		5.67	230	12.8	0.77	13.72	5.19	1.66	1.68	1.62	3.89	4373
K74		5.79	269	11.6	0.68	8.23	3.28	1.41	1.42	1.03	3.21	4639
K75		5.88	279	10.3	0.51	6.22	2.88	0.81	1.46	0.53	4.43	4773
K76		6.29	292	6.9	0.85	3.63	3.35	1.42	1.77	1.00	4.90	6652
K77		7.52	567	7.9	0.58	3.24	7.07	2.76	1.51	0.60	0.07	5560
K78		5.82	164	5.1	1.14	6.86	2.81	1.15	1.31	1.75	6.08	5163
K79		5.81	122	7.0	1.26	10.35	2.91	1.15	1.76	0.74	0.84	6123
K80		6.33	431	9.9	1.02	8.70	3.24	1.99	2.06	0.56	6.52	6924
K81		6.74	403	7.7	0.69	4.85	5.16	2.30	1.84	0.57	3.44	7063
K82		7.13	628	9.3	1.53	3.65	7.58	3.33	1.71	0.56	1.91	9464
K84		6.25	390	11.3	0.54	4.41	1.79	0.47	3.40	0.60	8.91	887
K85		5.37	56	8.1	0.49	5.79	2.06	0.60	0.76	0.55	0.07	685
K86		5.83	69	3.9	0.52	3.62	1.84	0.33	0.56	0.55	0.50	905
K87		5.85	69	3.9	0.54	3.61	1.79	0.35	0.53	0.50	0.56	868
K88		5.94	63	3.6	0.52	3.87	1.55	0.42	0.79	0.47	0.58	1759
K89		6.09	130	4.7	0.50	3.33	2.33	0.96	0.79	0.71	0.35	2614

compositions and fluid fluxes are most commonly determined at a gauged stream position. Fluid flow, expressed in terms of stage, is constantly measured, and water samples are periodically taken. Since a strong inverse correlation commonly exists between stage and solute concentration, a number of approaches were developed to produce a continual estimate of discharge-weighted solute compositions (Likens et al., 1977; Zeman and Slaymaker, 1978). Integrating both the discharge and solute concentrations over a given time interval, commonly on an annual basis, and dividing this output by the geographical area of the watershed produces a solute flux q_j (Eq. (10.11)) which is commonly expressed as moles ha^{-1} $year^{-1}$.

Determining the weathering component of the total stream or river solute fluxes is a much more difficult process. Such calculations require subtracting out other sources of solutes (Eq. (10.11)). Such inputs are often reflected in spatially and temporally separated inputs as demonstrated for discharge from the Panola watershed (Hooper et al., 1990). For example, solute Si and Mg concentrations are explained as a mixture of 3 end-member sources (Fig. 10.12) a groundwater component from fractured granite, a hill slope component representing waters from deeper soils and

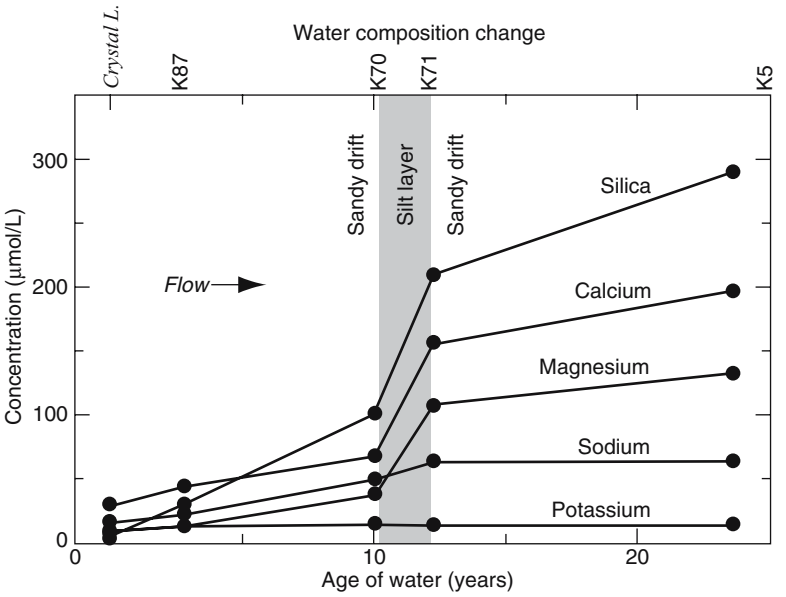

Fig. 10.11 Change in groundwater compositions along flow paths shown in Fig. 10.10**b** and **c** (after Bowser and Jones, 2002)

saprolites and an organic component consisting of near-surface runoff in the shallow soils. To further complicate the interpretation of the solute fluxes, the relative proportions of these components vary seasonally. Hillslope waters dominate during the wet season (January to May), groundwater dominates at low flow during seasonally dry period (June to December) and the organic component is present only during intense storm events. The determination of such end-member components of stream discharge is commonly done using statistical approaches (Hooper et al., 1990).

Table 10.13 Summary of mineral contributions to groundwater measured between pairs of wells along a flow path in the Trout Lake aquifer shown in Fig. 10.11 (units in μmoles. data from Bowser and Jones (2002)

	Wells pairs		
	K87− >K70	**K70− >K71**	**K71− >K5**
Plagioclase	31.57	18.96	0.00
K-feldspar	0.23	0.51	−1.47
Hornblende	13.32	105.60	44.54
Chlorite	3.37	20.66	0.10
CO2-gas	89.08	335.91	141.30
Goethite	−28.47	−154.74	−37.98
Smectite_ss	8.89	−90.31	−10.53
Kaolinite	−36.93	−24.59	−13.78
Halite	0.00	0.00	0.00
Pyrite	−0.35	0.63	−2.06

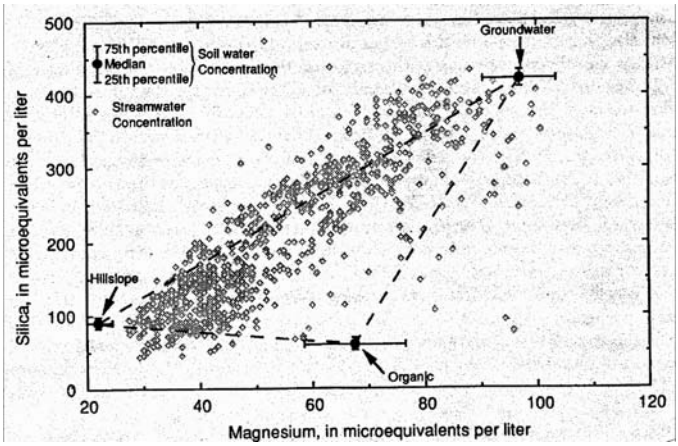

Fig. 10.12 Dissolved Si and Mg in stream discharge from the Panola catchment, Georgia, USA. Dashed lines encompass the hillslope, groundwater and shallow soil (organic) inputs. (After Hooper et al., 1990)

The above example serves as a cautionary note to the complexities involved in interpreting solute discharge fluxes and calculating weathering rates, even in intensely studied small-scale watersheds. However, significant advances have been made with hydrograph separation techniques (Trudgill, 1995), making the intercomparison of watershed solute fluxes an effective tools for establishing the impact of rock type, precipitation, temperature and other parameters on chemical weathering rates (Dethier, 1986; Bluth and Kump, 1994; White et al., 1999; Oliva et al., 2003). As the scale and heterogeneity of weathering increases, as in the case of large river systems, the ability to define components contributing to the overall solute fluxes becomes more difficult. In addition, only a very small subset of large rivers is not impacted by anthropogenic effects including dams and pollution.

10.4.10 Case Study: Weathering Inputs from a Small Stream

A number of detailed hydrochemical studies have been conducted on watersheds draining the Catoctin Mountains of Maryland, USA (Katz et al., 1985; Rice and Bricker, 1995; O'Brien et al., 1997; Rice and Hornberger, 1998). One of the more intensely studied of these watersheds is the Hauver Branch, which is underlain by metabasalts in the Blue Ridge province of the Appalachian Mountains. The principal mineralogy of the bedrock is chlorite, epidote, albite and actinolite with secondary quartz and calcite (Table 10.14). Soils thicknesses vary from 0 to 50 cm in depth.

Although precipitation is fairly evenly distributed throughout the year, stream stage exhibits strong seasonal fluctuations that correlated closely with groundwater elevation in the watershed. Groundwater levels declined rapidly in May as the trees foliate and evapotranspiration becomes a significant factor in water discharge.

Table 10.14 Mineralogy and mineral abundance (wt %) in the Catoctin Formation underlying Hauver Branch watershed, Maryland, USA. (Data from O'Brien et al., 1997)

Amphibole:	$(Ca_{1.701}Na_{0.552}K_{0.157})Mg_{2.202}Mn_{0.044}Fe_{2.801}$ $Ti_{0.174}Al_{0.908}Si_{7.02}Cl_{0.06}H_{1.711}F_{0.229}O_{24}$	2.4
Albite	$Na_{0.936}Ca_{0.023}K_{0.013}Mg_{0.004}Fe_{0.007}Mn_{0.002}$ $Al_{1.053}Si_{2.955}O_8$	36.9
Biotite:	$K_{1.871}(Na_{0.022}Ca_{0.014}Mg_{0.515}Fe_{4.347}Ti_{0.217}Mn_{0.048}$ $Al_{0.532})Al_{2.466}Si_{5.534}O_{20}(OH)_4$	tr
Calcite	$CaCO_3$	1.6
Chlorite:	$Mg_{2.017}Fe_{2.225}Mn_{0.048}Al_{1.332}Na_{0.004}Ca_{0.032}$ $K_{0.197}Al_{0.903}Si_{3.097}O_{10}(OH)_8$	20.6
Clinopyroxen:	$(Ca_{0.787}Na_{0.02}K_{0.001}Mg_{0.881}Fe_{0.257}Ti_{0.022}$ $Mn_{0.007}Al_{0.036})Al_{0.083}Si_{1.917}O_6$	1.1
Epidote	$(Ca_{1.994}K_{0.006}Ba_{0.002})Mg_{0.055}Fe_{1.089}$ $Mn_{0.032}Ti_{0.007}Al_{2.034}Si_{3.128}O_{12}(OH)$	23.9
Garnet:	$K_{0.002}Ca_{1.304}Mg_{0.048}Fe_{1.295}Mn_{0.341}$ $Fe_{0.099}Al_{1.901}Si_{3.024}O_{12}$	tr
K-spar	$KAlSi_3O_8$	tr
Kaolinite	$Al_2Si_2O_5(OH)_4$	
Mag/Haem	Fe_3O_4, Fe_2O_3	4.6
Plagioclase:	$Na_{0.441}Ca_{0.525}K_{0.018}Mg_{0.01}Fe_{0.031}Ti_{0.005}$ $Al_{1.46}Si_{2.502}O_8$	tr
Quartz	SiO_2	1.5

Discharge increases in the fall when the vegetation becomes dormant. Solute concentrations also exhibited seasonal differences. In general, Ca, Mg Si and alkalinity concentrations increased at the onset of the non-growing season (Fig. 10.13). In contrast, the concentrations of Na, K and Cl concentrations showed much less variability.

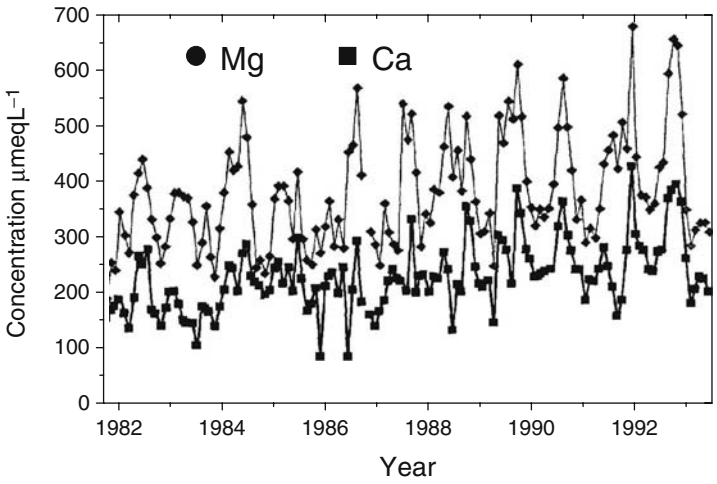

Fig. 10.13 Long-term solute discharge records for Ca and Mg in discharge from the Catoctin Mountain watershed, Maryland, USA. (From Rice and Bricker, 1995)

Table 10.15 Mean weighted solute concentrations and fluxes calculated for Hauver Branch stream for discharge between 1982 and 1992 based on NETPATH calculations using mineral data contained in Table 10.14

Mineral	mmol l^{-1}	mol ha^{-1} yr^{-1}
Biotite	0.0427	486
Calcite	0.01268	144
Chlorite	0.05537	630
Clinopyroxen	0.24522	2791
CO_2 gas	−0.04123	−469
Kaolinite		
K-spar	0.04515	514
Albite	−0.02765	−315
SiO_2		
Evap. fac	2.2	

(After O'Brien et al., 1997).

Annual solute mass balances were calculated for the Hauver Branch for all the years of available record by the period-weighted method (Katz et al., 1985; O'Brien et al., 1997). Watershed inputs were calculated by multiplying the concentration of the sample representing the period by the corresponding precipitation volume. Watershed outputs were calculated by multiplying the concentration of the stream sample by runoff volume for a given period. The differences between these inputs and outputs were divided by the watershed surface area to produce annual solute fluxes

Mineral weathering inputs to the Hauver Branch catchment were first calculated by Katz et al. (1985) based on the idealized mineral stoichimetries. The system was cast in terms of 5 unknown quantities, the amount of albite, actinolite, chlorite and calcite weathered and the amount of H_2CO_3 consumed. Results indicated that albite and calcite were the dominant reactive phases, although calcite is only a trace component in the metabasalts.

A second mineral mass balance calculation was performed by O'Brien et al. (1997) using average solute input/output values based on a much longer monitoring record (1983–1992) and using additional mineral compositions based on microprobe analyses (Table 10.14). The calculations using NETPATH (Plummer et al., 1991) produced results comparable to Katz et al. (1985) in that calcite dissolution and the weathering of albite and chlorite to form kaolinite were the dominant reactions (Table 10.15). The differences in the relative proportions of minerals in the two approaches are related to the specific compositions of amphibole and chlorite (O'Brien et al., 1997).

10.4.11 Case Study: Weathering Contributions in a Large River

Chemical weathering inputs for the Congo river have been characterized in studies by Negrel et al. (1993), Dupre et al. (1996) and Gaillardet et al. (1999).

Table 10.16 Solute compositions associated with major tributaries of the Congo River (after Negrel et al., 1993)

	Ca	Na	Mg	Sr	Rb	$^{87}Sr/^{86}Sr$	HCO_3	Cl	SO_4
Oubangui	65	63	41	0.17	0.031	0.719682	235	22	13
Lobaye	48	23	38	0.13	0.023	0.715395		9	9
Zaire	68	135	98	0.28	0.045	0.717924	375	47	29
Loikouaia	40	13	39	0.09	0.040	0.716216		16	8
Allma	38	34	37	0.11	0.045	0.716277		18	12
Kasai	44	53	38	0.12	0.032	0.723044	155	26	13
Sangha	63	34	31	0.15	0.042	0.716346	130	18	10

(mmoles L^{-1} except as noted).

The Congo basin occupies the center of the African continent and comprises the second largest river system in the world after the Amazon ($3.7 \times 10^6\,km^2$). In terms of scale, the Congo watershed is approximately a million times larger than the Hauver Branch watershed considered in the previous section. The Congo basin is underlain by a range of rock types consisting of crystalline and sedimentary silicate rocks (90%) with lesser amounts of limestones and dolomites (10%). Evaporates, including halite and gypsum, although not exposed at the surface, are identified from subsurface information. Selected major element and $^{87}Sr/^{86}Sr$ analyses for major tributaries of the Congo River are listed in Table 10.16 (Negrel et al., 1993).

Due to the lithologic heterogeneity, a principal goal of the studies of Negrel et al. (1993) and Gaillardet et al. (1995) was to determine the relative fractions (X) to which weathering of silicates, carbonates and evaporates contributed to solute compositions of the Congo River. This approach is contrasted to most studies of smaller lithologically homogeneous catchments in which the goal is to define the weathering contributions of specific mineral phases.

In the analysis of Negrel et al. (1993), the various solute contributions are characterized by elemental and isotopic ratios rather than by concentrations to decrease the effects of variability due to river stage, mixing and other processes. In the calculations, Na was used as the reference. The model equations were set up as follows:

For Cl in precipitation

$$\left(\frac{Cl}{Na}\right)_{riv} = X(Na)_{precip}\left(\frac{Cl}{Na}\right)_{precip} + X(Na)_{evap}\left(\frac{Cl}{Na}\right)_{evap} \tag{10.14}$$

For major cations (Z = Ca, Mg and Sr)

$$\left(\frac{Z}{Na}\right)_{riv} = X(Na)_{precip}\left(\frac{Z}{Na}\right)_{precip} + X(Na)_{sil}\left(\frac{Z}{Na}\right)_{sil} + X(Na)_{evap}\left(\frac{Z}{Na}\right)_{evap} X(Na)_{carb}\left(\frac{Z}{Na}\right)_{carb} \tag{10.15}$$

and for Sr isotopes

$$\frac{^{87}Sr}{^{86}Sr}\left(\frac{Sr}{Na}\right)_{riv} = \frac{^{87}Sr}{^{86}Sr}X(Na)_{precip}\left(\frac{Sr}{Na}\right)_{precip} + \frac{^{87}Sr}{^{86}Sr}X(Na)_{sil}\left(\frac{Sr}{Na}\right)_{sil} + \frac{^{87}Sr}{^{86}Sr}X(Na)_{evap}\left(\frac{Sr}{Na}\right)_{evap} + \frac{^{87}Sr}{^{86}Sr}X(Na)_{carb}\left(\frac{Sr}{Na}\right)_{carb} \quad (10.16)$$

A final closure equation describes the conservation of mass:

$$X(Na)_{riv} + X(Na)_{evap} + X(Na)_{carb} + X(Na)_{sil} = 1 \quad (10.17)$$

The next step in computing the percentages of each rock type contributing to solute input was to determine the best estimates of the end member compositions. Precipitation compositions were determined by direct measurement. Solute compositions derived from the different rock types, i.e., carbonates, evaporites and silicates were determined by extrapolating mixing curves to end member compositions. These values were substituted into the mass balance relationships (Eqs. (10.14–10.17)) and solved using the inversion method previously described (see Sect. 4.2) and the best non-linear weighted fit was obtained. The relative proportions of the various sources to the dissolved load of the tributaries of the Congo River showed that most of the dissolved Na and Sr originate from silicate weathering while most of the Ca and Mg are derived from carbonate weathering.

Chemical weathering studies in the Congo basin were further extended to characterize the contributions of major and trace elements in both the dissolved and suspended loads (Gaillardet et al., 1995). In these calculations, the inversion approach used the original six equations describing the soluble phases (Eqs. (10.14–10.17)) with an additional 15 equations describing the distribution of major and traces insoluble elements concentrated in the suspended load. The contributions of the different rock types to chemical weathering, in addition to the physical weathering of sediments, are shown in Fig. 10.14.

10.5 Comparison of Contemporary and Long Term Chemical Weathering Fluxes

Weathering fluxes calculated from the solid and solute techniques discussed in the preceding sections occur over very different time scales. The solid-state flux $Q_{j,w}$ is defined as

$$Q_{j,w} = \frac{\Delta M_j}{S\Delta t_{geo}} \quad (10.18)$$

and involves dividing large solid-state mass changes in soils ΔM_j (kg or mole) by large time spans associated with their formation Δt_{geo} (thousands to millions of years). This ratio, in turn, is normalized to the regolith surface S_A commonly defined as a unit of land surface (m^2 or ha)

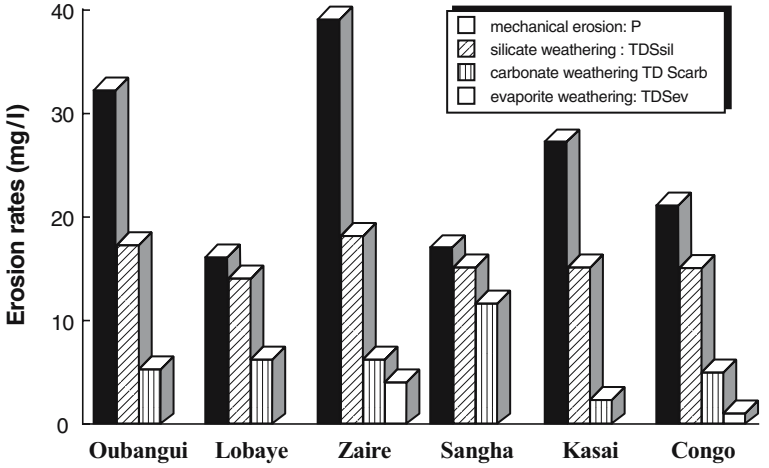

Fig. 10.14 Chemical and mechanical fluxes in rivers over different drainage areas of the Congo basin. (After Gaillardet et al., 1995)

In contrast, solute weathering fluxes, $q_{j,w}$ reflect small solute mass changes Δm_j (mg L^{-1} or μmoles) ratioed against the residence time of water t_{solute} which is commonly in the order of days to years,

$$q_{j,w} = \frac{\Delta m_j}{S\Delta t_{solute}} \tag{10.19}$$

In spite of large scale differences, the geologic and contemporary fluxes should be equal under constant weathering conditions, i.e.

$$Q_{j,w} = q_{j,w} = \frac{\Delta M_j}{S\Delta t_{geo}} = \frac{\Delta m_j}{S\Delta t_{solute}} \tag{10.20}$$

Considerable debate exists in the literature as to whether the two types weathering fluxes, defined in Eq. (10.20), are similar in natural systems. Some workers conclude that present day base cation fluxes measured in North America and Northern European watersheds may be significantly faster than long-term past weathering rates due to the impacts of acidic precipitation (April et al., 1986; Kirkwood and Nesbitt, 1991; Land et al., 1999). Cleaves (1993) found watershed solute fluxes in the Piedmont of the eastern USA to be 2–5 times faster than for long term past periglacial fluxes represented by long-term saprolite weathering and attributed these weathering differences to past periods of lower precipitation, colder temperatures and lower soil gas CO_2. In contrast, Pavich (1986) concluded long-term weathering rates of saprolites in the Virginia Piedmont are comparable to current-day weathering rates based on stream solute fluxes. Rates of saprolite formation are also found to be similar to current weathering rates in the Panola and Rio Icacos watersheds described previously (Sects. 10.3.5 and 10.4.4 and Table 10.9).

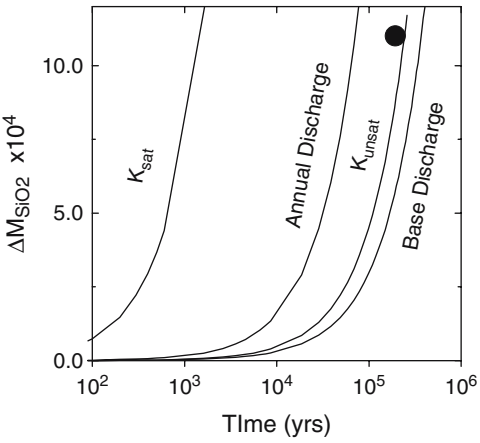

Fig. 10.15 Comparison of short and long term Si weathering for the Rio Icacos regolith. Solid symbol corresponds to solid-state regolith mass loss $\Delta M_{Si,w}$ (Eq. (10.7)) Lines correspond to weathering trajectories describing the extrapolation of contemporary solute fluxes (Table 10.9)

The extent of agreement between contemporary and long-term weathering is strongly dependent on accurately estimating parameters involved in the respective calculations. Weathering trajectories, produced by extrapolating mass changes associated with solute fluxes (Eq. (10.8)) to the time scale associated with observed solid state changes in the regolith (Eq. (10.7)) is one approach for graphically comparing the magnitude of these variables (White et al., 1998; Stonestrom et al., 1998).

For the Rio Icacos regolith, significantly different weathering trajectories are produced by differing estimates of the hydrologic flux (Table 10.8). Experimental conductivities measured in saturated soil cores (K_{sat}) produce large solute fluxes that greatly overestimate ΔM_{SiO2} (trajectory is to the far left in Fig. 10.15). In contrast, conductivities in soil cores at unsaturated field conditions $(K_{unsat,})$ are much slower (Table 10.8) and result in a trajectory that nearly intersects the SiO_2 mass loss produced by long time weathering. This trajectory is similar to that generated by base discharge in the Rio Iacos stream. White et al. (1998) concluded that present day solute weathering fluxes are capable of producing the long-term weathering observed in the Rio Icacos regolith.

10.6 Mineral Weathering Rates

The elemental and mineral fluxes described in the preceding sections do not explicitly consider the mass and/or surface area of the reactive phases. For example, weathering fluxes characterized by stream solute discharge are normalized to catchment area but commonly do not consider the distribution of weatherable minerals with depth in the regolith. In some studies, mineral contents are defined on a volume basis (see the Panola case study in Sect. 10.3.5) but grain size distributions are not considered. Silt-size grains, compared to sand-size grains, are expected to weather faster, an effect implied in the flow path calculations for the Trout Lake aquifer (see case study in Sect. 10.4.8).

Mineral weathering is optimally characterized by a mineral speicifc weathering rate R_m (moles m^{-2} s^{-1}). R_m is analogous to weathering fluxes define in Eq. (10.20) with the difference that the rate is defined as the mass transport across the mineral surface area rather than across a unit of land surface or aquifer cross section. R_m is mechanistically defined as (Maher et al., 2006; Chap. 1, this volume).

$$R_m = k_r \cdot \beta_j \cdot f(\Delta G_{excess}) \tag{10.21}$$

where k_r is the kinetic rate constant (mole m^{-2} s^{-1}). External or extrinsic controls commonly considered are the inhibitory or catalytic effects of dissolved species β_j (Oelkers, 2001) and ΔG_{excess} which defines the excess free energy as the solution approaches thermodynamic saturation with respect to the dissolving mineral (Lasaga, 1984, and Chap. 2).

In studies of natural weathering systems, the evaluation of individual intrinsic and extrinsic controls is difficult and the mineral weathering rate is most commonly empirically defined as the mass of mineral reacted per unit time and mineral surface area S_m

$$R_m = \frac{\Delta M_j}{t_{geo} S_m} = \frac{\Delta m_j}{t_{solute} S_m} \tag{10.22}$$

Mineral weathering rates are characterized either in terms of geologic or contemporary time intervals t_{geo} and t_{comp} in a fashion analogous to that of weathering fluxes (Eq. (10.20)).

10.6.1 Weathering Gradients

An alternative approach to calculating weathering rates considers the spatial distributions of residual minerals in the weathering profile and thus looks at the details of weathering which exist beyond the simple input-output mass balances implied in Eq. (10.22). Under such conditions (White et al., 2002, 2007).

$$R_m = \frac{\omega}{b_s S_m} = \frac{v}{b_p S_m} \tag{10.23}$$

The respective weathering gradients in a regolith profile, b_s and b_p(m^4 $mole^{-1}$), are shown by the schematic in Fig. 10.16, be are defined by solid and solute mass changes, i.e., ΔM_j and Δm_j (Eq. (10.22)) with depth z. Respective examples of solid and solute weathering gradients are evident for plagioclase weathering in the Panola regolith (Fig. 10.3b) and solute K and Mg gradients produced by biotite weathering in the Rio Icacos regolith (Fig. 10.6). The solid state velocity ω is the rate at which the weathering front propagates through the regolith and the solute weathering velocity v is the rate of solute transport or fluid flux (m s^{-1}).

Eq. (10.23) defines the shape of a weathering profile in a regolith in Fig. 10.16. For constant conditions, the mineral gradient is linear. For a given weathering velocity, faster mineral weathering rates R_m produce shallower weathering gradients

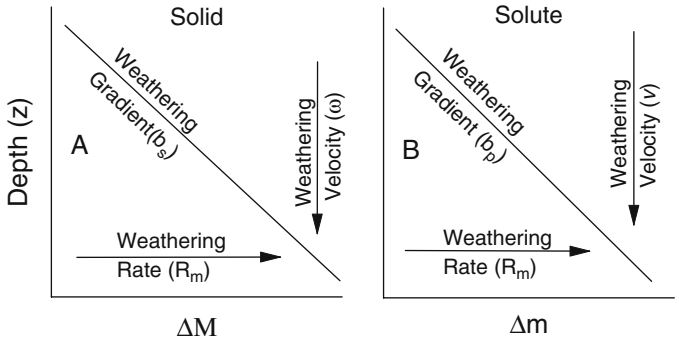

Fig. 10.16 Schematic showing parameters defining a weathering profile (Eq. (10.23)). (**a**) Change in solid state and (**b**) solute compositions with depth. R_m is the mineral weathering rate. The weathering gradients b_s and b_p describe slope of the linear solid and solute gradients and ω and υ describe the solid and solute weathering velocities. (After White, 2002)

b_s and b_p, i.e., more rapid concentration changes with depth. In contrast, a slower weathering rate produces steeper gradients. Alternately, for a constant rate of mineral weathering, increases or decreases in the weathering velocities ω and v will decrease or increase the slopes of the respective weathering gradients b_s and b_p.

10.6.2 Mineral Surface Areas

Normalizing mineral changes against surface area is required for calculating mineral weathering rates (Eqs. (10.21–10.23)). On a fundamental level, weathering is proportional to the reactive surface area defined as the density of reactive sites on a silicate surface at which hydrolysis reactions occur (see Chaps. 2 and 3). Natural weathering studies, however, generally equate reactive site densities with the physical surface area of the weathering mineral. An additional caveat is that the mineral surface must be in physical contact with the reactive fluid phase. Thus, the wetted surface area in a partially saturated soil may be considerably less than the total physical surface area of exposed mineral grains. The specific mineral surface area S_m area is generally considered constant over short time intervals associated of solute transport (t_{solute} in Eq. (10.22)), while over geologic scale time (t_{geo}), surface areas vary with changes mineral surface morphology.

Commonly, the mineral substrate is removed and disaggregated in the laboratory before surface areas are measured. Limited attempts have been made to characterize surface areas of fracture surfaces and in pore spaces in drill cores (Paces, 1986; Gislason and Eugster, 1987; Kieffer, 1999).The scale of the measurement technique operationally defines the specific surface area of a mineral. The geometric surface area S_{geo} of a mineral grain is (Brantley et al., 1999).

$$S_{geo} = \frac{a'}{\rho_m r} \tag{10.24}$$

where ρ_m is the density, r is the length and a' is the geometric parameter relating area to volume ($a' = 6$ for a cube and 3 for a sphere) Eq. (10.24) predicts that for a constant mass of a mineral (ΔM and Δm, Eq. (10.22)), the geometric surface area increases as the size of the individual particles decreases.

Surface area determinations using Brunauer, Emmett and Teller gas sorption isotherms (BET) is the alternate approach commonly used to measure the surface areas of geologic materials (Brantley et al., 1999). For a perfectly smooth surface, without internal porosity, geometric and BET surface area measurements would be similar. However, because BET measurements define surface areas on an atomic scale, they include surface etching and pitting produced by weathering. For a natural mineral surface, the BET-defined area is almost always greater than the equivalent geometric area. Conversely, weathering rates normalized in terms of geometric surface areas are almost always faster than rates based on BET surface areas (Eqs. (10.21–10.23)).

Surface roughness λ is the ratio of the geometric (S_{geo}) to the BET (S_{BET}) surface areas (Helgeson, 1971; White and Peterson, 1990). For non-ideal surfaces of geometric spheres, the roughness can be related directly to the particle diameter d and the mineral density ρ_m such that

$$\lambda = \frac{S_{BET}}{S_{geo}} = \frac{\rho_m d S_{BET}}{6} \tag{10.25}$$

Whether geometric and BET measurements are best estimate of the physical surface is a subject of significant debate, focused around what portion of the total physical surface area is actually exposed to weathering reactions. Surfaces exposed in dead-end pore spaces are not reactive if the water is essentially immobile and therefore thermodynamically saturated. (Drever and Clow, 1995). This criterion also eliminates primarily mineral surfaces which are coated with impermeable secondary mineral phases or mineral-organic aggregates (Tisdall, 1982). The extent to which such coatings constitute physical barriers to solute transport is debatable. Additional surface-sensitive techniques, including atomic force microscopy and the interferometry (Maurice et al., 1996; Luttge and Lasaga, 1999; Chap. 3, this volume), employ measurement scales intermediate between atomic and macro-surface characterization and have proven useful in characterizing physical surface areas of minerals.

10.6.3 Case Study: Weathering in a Soil Chronosequence

A number of studies have characterized the Merced chronosequence, which consists of a series of soils developed on terraces along rivers draining the Sierra Nevada Mountains of California (Harden, 1987; Bullen et al., 1987; Brenner et al., 2001). The age range of soils in the chronosequence (3–3,000 kyrs) permits a description of how surface area and associated mineral weathering rates evolved with time (White et al., 1996).

The BET surface areas of the bulk Merced soils is attributed mostly to secondary clay, principally kaolinite, which increases from 20 to 72 wt% from the youngest to the oldest soils (Fig. 10.17a). Primary silicates, whose surfaces comprise a small portion of the total soil surface area, also increase with age. The surface area of individual aluminosilicates (50–150 μm diameter) shows comparable increases, with plagioclase increasing from 0.3 to 1.5 $m^2\ g^{-1}$ (17B). K-feldspar and hornblende generally exhibit smaller increases in surface area over the same period. Quartz surface areas remain similar in all the soils (0.1–0.2 $m^2\ g^{-1}$), suggesting significant resistance to chemical weathering Fig. 10.17b.

The corresponding surface roughness of minerals also increase with soil age (Fig. 10.17c). This is attributed to increased external pitting and the creation of significant internal porosity in which pores enlarged and coalesced, forming very open internal structures.

White et al. (1996) calculated mineral weathering rates R_m (Eq. (10.22)) based on changes in mineral abundances, grain sizes, and surface areas with soil age. A forward dissolution approach was employed in which a unit mass of starting mineral was proportioned into grain size fractions assuming uniform grains with a radius equal to the geometric mean of that interval. The initial population of grain sizes was based on the reconstructed grain-size distributions. Dissolution of each grain size of several silicate minerals was sequentially calculated from the age of initial deposition to the present and the weathering rate of the different minerals calculated. The model was run with and without consideration of surface roughness λ (Eq. (10.25)).

The final fits of the model rates to the measured residual mineral fractions in different age soil horizons age are shown in Fig. 10.18. Fits are based on both the geometric and variable surface roughness assumptions. Although both approaches produce internally consistent results, significant differences exist in the magnitude of the calculated rates. The geometric model produces dissolution rates that are 10^2–10^3 orders of magnitude faster than the variable-roughness model. The magnitude of this difference is to a first approximation proportional to the difference between the measured BET surface areas and the geometrically-estimated surface areas (Fig. 10.18). Due to increasing roughness (Fig. 10.17), the BET normalized calculations also show significant decreases in weathering rates over the age span of the Merced chronosequence.

10.6.4 Comparing Mineral Weathering Rates

Tabulations of reported rates are used to compare the weathering of a specific mineral in different environments, to compare relative weathering of different minerals and to compare natural to experimental weathering (Schnoor, 1990; White and Blum, 1995; White and Brantley, 2003; Oliva et al., 2003). Natural weathering rates for several rock-forming minerals are reproduced in Table 10.17 from a review by White and Brantley (2003) with additional newer data.

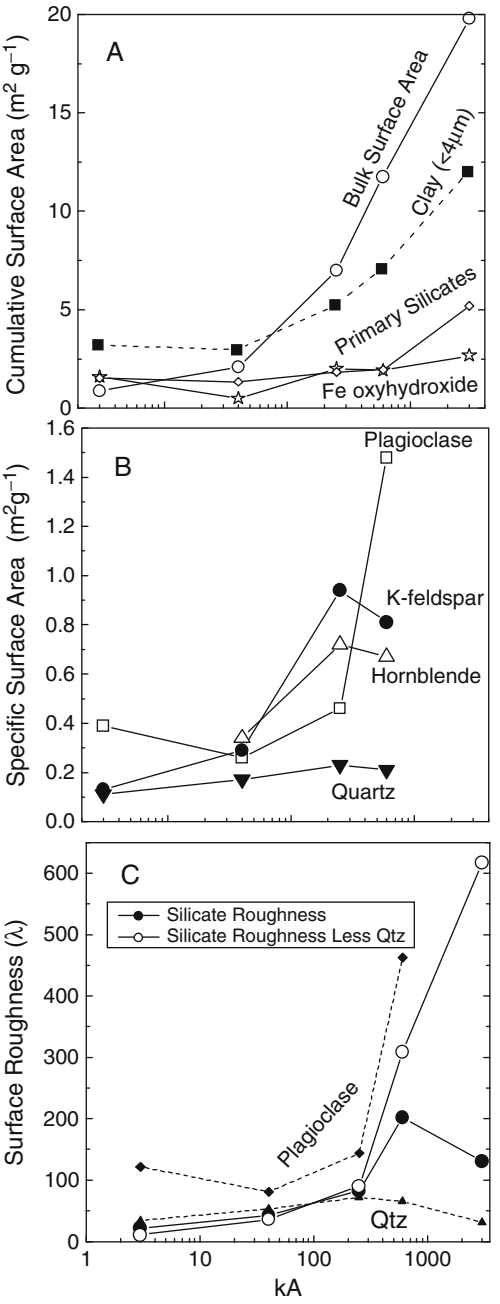

Fig. 10.17 Surface area parameters in the Merced chronosequence plotted as functions of soil age. (**a**) Surface areas of bulk soil components. (**b**) Surface areas of primary mineral phases (0.5–1 mm size fraction). (**c**) Surface roughness of minerals (Eq. (10.23)). (After White et al., 1996)

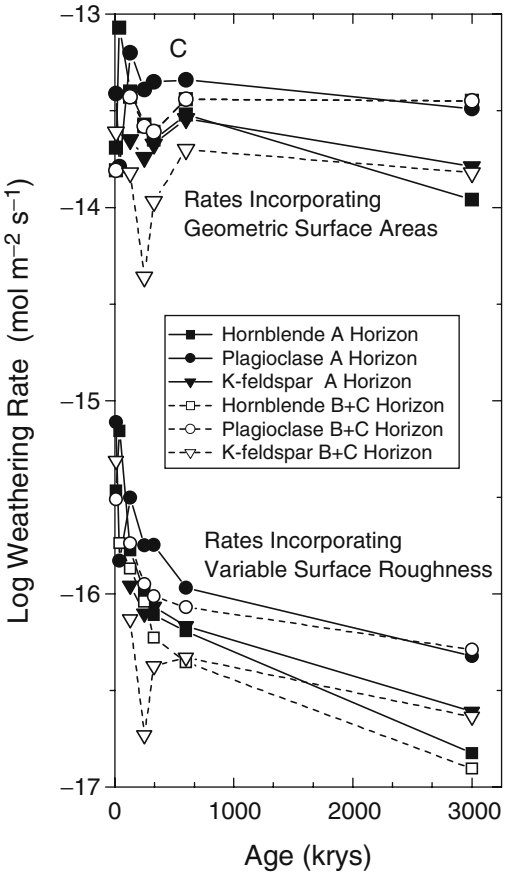

Fig. 10.18 Dissolution rates for specific minerals as a function of age in the Merced chronosequence. Rates incorporate either geometric surface areas or variable roughness for grain size distributions. (After White et al., 1996)

Much of the difference in reported natural rates of silicate weathering is directly attributed to differences in mineral surface area measurements. Studies reporting lower rates usually utilized BET measured surface areas while studies reporting faster rates utilized geometric surface areas (Table 10.17). One approach for overcoming this discrepancy is to normalize the weathering rates by a time dependent surface roughness factor λ which converts geometric-based rates to their BET equivalent (White and Brantley, 2003). While this approach does not resolve the issue of which measurement is most representative of reactive surface area, it does cast all rates in the same form which permits direct comparisons

A plot of the K-feldspar and plagioclase rate data in Fig. 10.19 indicates that short term experimental rates, summarized by White and Brantley (2003), are several orders of magnitude faster than the long-term natural rates (Fig. 10.19). This discrepancy has long been recognized in the literature (Schnoor, 1990; Sverdrup and Warfvinge, 1995). In addition, a consistent trend exists between progressively older natural weathering environments and slower weathering rates. The faster natural rates plotted in Fig. 10.19 are typically for watersheds glaciated in the last 15 kyrs whereas the slowest rates are for older regoliths and aquifer weathering

Table 10.17 Weathering rates of some common silicates. Age corresponds to the approximate duration of weathering. Included are the methods and measurements of surface area, the average paricle sizes and calculated surface roughnesses. Data in paratheses are normalized BET rates based on method of White and Brantley (2003)

Weathering Environment	Rate (moles $m^{-2} s^{-1}$)	Log Yrs	Surface Measurement	Surface Area (m2 g-1)	Grain Size (um)	Roughness (λ)	Reference
Plagioclase							
Black Mesa, Az, USA	−16.5	>7.0	BET	0.69	100	30	Zhu, 2005
Davis Run saprolite, VA, USA	−16.4	5.93	BET	1.0*	nd	nd	White et al., 2001
China Hat Soil, Merced CA, USA	−16.3	6.48	BET	1.5*	500	331	White et al., 1996
Turlock Lake Soil, Merced, CA, USA	−16.0	5.78	BET	1.48	730	477	White et al., 1996
Modesto Soil, Merced, CA, USA	−15.8	4.00	BET	0.26	320	37	White et al., 1996
Riverbank Soil, Merced, CA, USA	−15.7	5.40	BET	0.46	650*	132	White et al., 1996
Panola bedrock, GA, USA	−15.7	5.70	BET	1.0*	500	221	White et al., 2001
Santa Cruz chronosequence	−15.0	5.42	BET	1.90	190	160	White et al. 2007
Modesto Soil, Merced, CA, USA	−15.1	4.00	BET	0.26	320	37	White et al. 1996
Filson Ck. Watershed, MN, USA[3]	−14.7(−15.3)	4.00	GEO	0.50*	63–125	21	Siegel and Pfannkuch, 1984
Bear Brook Watershed, ME, USA	−14.5 (15.2)	4.00	GEO	0.50*	63–125	15	Schnoor, 1990
Crystal Lake Aquifer, WI, USA	−13.7(15.3)	4.00	GEO	0.12[a]	1–100	2	Kenoyer & Bowser, 1992b
Bear Brook watershed soil, ME, USA	−13.3(−15.2)	4.00	GEO	0.020	1–4000	1	Swoboda-Colberg and Drever, 1992
Gardsjon watershed soil, Sweden	−13.1	4.00	BET	1.53	na	nd	Sverdrup and Warfvinge, 1995
Loch Vale Nano-Catchment, CO, USA	−12.8	4.00	BET	0.21[d]	53–208	9	Clow and Drever, 1996
Coweeta Watershed, NC, USA	−12.5(−14.9)	5.50	GEO	0.003	1000	1	Velbel, 1985
Trnavka River watershed, Czech.	−12.1(−14.0)	4.00	GEO	0.057	nd	1	Paces, 1986
Plastic Lake, Ontario, Canada	−11.8(−13.7)	4.00	GEO	0.030	100	1	Kirkwood and Nesbitt, 1991
K-feldspar							
Black Mesa, Az, USA	−18.5	>7.0	BET	0.69	100	30	Zhu, 2005
Davis Run Saprolite, VA, USA	−16.8	5.93	BET	1.0*	nd	nd	White et al. 2001
China Hat Soil, Merced CA, USA	−16.6	6.48	BET	0.81*	500	179	White et al., 1996
Riverbank Soil, Merced, CA, USA	−16.4	5.52	BET	0.94*	650	270	White et al., 1996
Turlock Lake Soil, Merced, CA, USA	−16.3	5.78	BET	0.81	730	261	White et al., 1996
Upper Modesto Soil, Merced, CA, USA	−15.3	4.00	BET	0.26	170	20	White et al., 1996

Adams County IL	−14.7(−16.6)	4.10	GEO	0.02	53–100	1	Brantley et al 1993
Loch Vale Nano-Catchment, CO, USA	−13.8	4.00	BET	na	na	nd	Clow and Drever, 1996
Bear Brook watershed soil, ME, USA	−13.3(−15.2)	4.00	GEO	0.020	1–4000	1	Swoboda-Colberg and Drever, 1992
Gardsjon watershed soil, Sweden	−13.3	4.08	BET	1.53	nd	nd	Sverdrup and Warfvinge, 1995
Surface exposures of Shap Granite	−12.9(−14.8)	3.70	GEO[a]	nd	na	1	Lee et al., 1998
Plastic Lake, Ontario, Canada	−11.8(−13.6)	4.00	GEO	0.03	100	1	Kirkwood and Nesbitt, 1991
Hornblende							
China Hat Soil, Merced CA, USA	−17.0	6.48	BET	0.67*	500	179	White et al., 1996
Turlock Lake Soil, Merced, CA, USA	−16.4	5.78	BET	0.67	730	261	White et al., 1996
Riverbank Soil, Merced, CA, USA	−16.0	5.40	BET	0.72	650*	250	White et al., 1996
Riverbank Soil, Merced, CA, USA	−15.9	5.11	BET	0.72*	650*	250	White et al., 1996
Lower Modesto Soil, Merced, CA, USA	−15.7	4.60	BET	0.34	320	58	White et al., 1996
Bear Brook, ME	−14.5(−16.4)	4.00	GEO	0.020	1–4000	1	Swoboda-Colberg and Drever, 1992
Adams County IL	−14.1(−16.0)	4.10	GEO	0.02	53–100	1	Brantley et al 1993
Lake Gardsjon	−13.6	4.00	BET	1.53	na	nd	Sverdrup and Warfvinge, 1995
Plastic Lake, Ontario, Canada	−12.3(−14.2)	4.00	GEO	0.03	100	1	Kirkwood and Nesbitt, 1991
Biotite							
Panola, GA USA	−16.5	5.70	BET	5	100–500	775	White, 2002
Crystal Lake Aquifer, WI, USA	−15.5(−17.4)	4.00	GEO	12	1–100	1	Kenoyer and Bowser, 1992
Rio Icacos, PR	−15.4	5.48	BET	8.1[a]	200–1200	2900	White et al., 2002
Rio Icacos, PR	−15.4	5.48	BET	8.1	200–1200	2900	Murphy et al. 1998
Loch Vale Nano-Catchment, CO, USA	−14.1	4.00	BET	3.2	na	nd	Clow and Drever, 1996
Bear Brook, MA USA	−14.0(−15.9)	4.00	GEO	0.0800	1–4000	1	Swoboda-Colberg & Drever (1993)
Coweeta, NC USA	−12.9(−14.8)	5.48	GEO[b]	0.006	1	1	Velbel (1985)

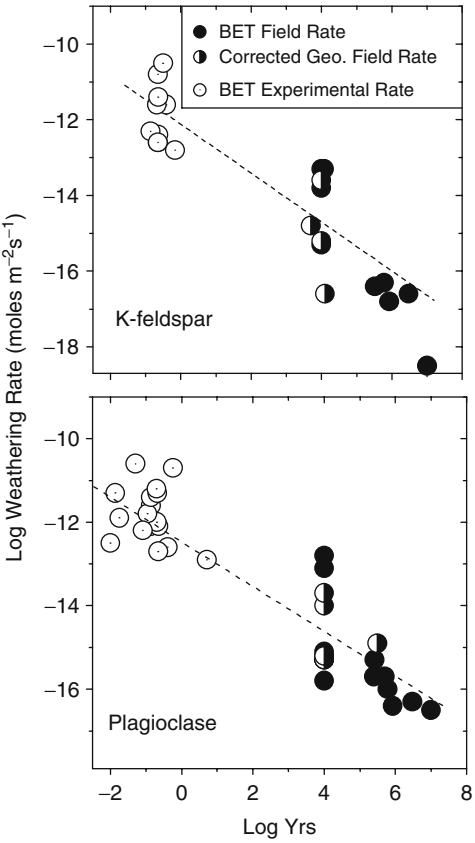

Fig. 10.19 Relationship between weathering rates and weathering duration for K-feldspar and plagioclase. Natural rates are tabulated in Table 10.18. Reported geometric surface areas are normalized to BET surface areas using the method described in White and Brantley (2003). Experimental rates are also from the review of White and Brantley

environments in excess of a million years old. Comparable age trends where also observed for BET-normalized rates in the Merced chronosequence (Fig. 10.18).

10.7 Factors Controlling Rates of Chemical Weathering

Controls on natural weathering are categorized as either intrinsic or extrinsic to the silicate minerals undergoing reaction (White and Brantley, 2003). Intrinsic features are physical and chemical properties of the mineral while extrinsic features are environmental conditions external to the silicate phase that impact the chemical weathering rate such as solute compositions and hydrologic and biologic interactions.

10.7.1 Intrinsic Effects

Bulk chemical and structural prosperities are the most obvious and easily described intrinsic characteristics of weatherable minerals. Based on early weathering studies,

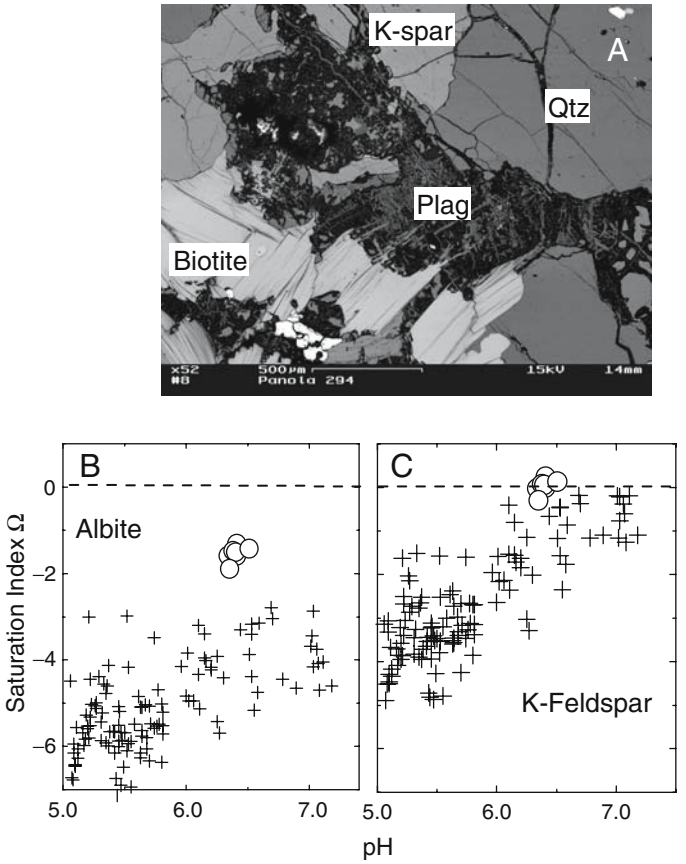

Fig. 10.20 Primary silicate weathering in the Panola regolith. (**a**) Back-scatter SEM micrograph of weathered granite at a depth 7.5 m. The center grain is a plagioclase phenocryst almost completely replaced by kaolinite (dark region). Minor residual plagioclase remains on outside rim. The adjacent K-feldspar grain is essentially pristine. Saturation states of soil pore water (x) and groundwater (o) relative to (**b**) plagioclase (albite) and (**c**) K-feldspar (after White et al., 2001)

Goldlich (1938) observed that the mineral weathering sequence in common igneous rocks was, in general, the reverse of Bowen's reaction series that ranked minerals in the order of the crystallization sequence in magma. Amphiboles and pyroxenes weather faster than feldspars which, in turn, weather faster than quartz. The weathering rates are dependent on the strengths of coordinated metal ions within the mineral structure relative to the strength of the metal–ligand bond. Casey and Westrich (1992) showed for that for simple compositional series, such as olivines, the dissolution rate decreased with the increase in the metal valence state. Evidence also indicates that the relative weathering rates of multi-oxides such as feldspars approximate the relative dissolution rates of the single oxide components (Oelkers, 2001).

In addition to bulk chemical characteristics, minerals also contain compositional heterogeneities on the scale of individual mineral grains. Such heterogeneities are responsible for the commonly observed preferential weathering of the calcic cores of plagioclase (Clayton, 1986) and for microtextures which often produce spectacular natural weathering features in alkali feldspars (Lee et al., 1998). With time, selective weathering will diminish these features, leading to a decrease in the overall weathering rate. On an even finer scale, silicate minerals contain structural defects and dislocations which represent sites of anomalously high surface energies. With continued weathering, the densities of structural defects may also diminish as etch pits form, thus producing a decrease in the overall weathering rate (Brantley et al., 1986; Blum and Lasaga, 1987).

Mineral surfaces are commonly compositionally different than the bulk mineral phase and also possess both macroscopic and microscopic heterogeneities. Leached layers have been documented on feldspars weathered in spodsols (Nugent et al., 1998) and on naturally weathered hornblende (Mogk and Locke, 1988). The progressive occlusion of the reactive mineral substrate by secondary clays and Fe- and Al oxides and the adsorption of organic compounds are proposed mechanisms that decrease chemical weathering rates with time by producing slower diffusion-limited transport (Banfield and Barker, 1994; Nugent et al., 1998).

10.7.2 Extrinsic Effects

10.7.2.1 Solution compositions

Chemical weathering is ultimately dependent on the concentration of reactants which complex with and detach the oxygen-bonded metal species in the silicate structure (See reviews in the volume; Chaps. 2 and 5). As documented by numerous experimental studies, the principal species involved in this reaction are hydrogen ions, although other complexing agents such as organic acids can participate in this process (see Chap. 5). In contrast, some solute species, including Al and Na, inhibit experimental dissolution by interfering with and competing with the ligand exchange processes (Oelkers and Schott, 1995; Stillings et al., 1996).

The direct effect of aqueous species on natural weathering is often more difficult to demonstrate. For example, a summary of experimental findings indicates that feldspar weathering rates decrease almost 4 orders of magnitude over a pH range of 2–6 (Blum and Stillings, 1995). However, when this effect is investigated for natural systems, the evidence is ambiguous. Over a 25 year period, the pH of solute discharge from Hubbard Brook has increased from pH 4.1–4.4 due to a gradual recovery from acid deposition (Driscoll et al., 1989). However, solute Si concentrations, a good indicator of silicate weathering, have remained essentially unchanged during the time. Although these results do not disprove that the hydrogen ion activities accelerate weathering, as demonstrated experimentally, they do serve to show that other processes sometimes overwhelm expected results for natural systems.

10.7.2.2 Role of Thermodynamic Saturation

The thermodynamic saturation state of a mineral relative to the aqueous solution is a primary extrinsic control on chemical weathering (Chap. 5). The saturation index Ω is defined for a weathering reaction as the ratio of the solute ionic activity product IAP to the mineral solubility or stability constant K_s

$$\Omega = \frac{IAP}{K_s} \tag{10.26}$$

Transition state theory (TST) (see Chap. 2) predicts that the net rate of a weathering reaction (Eq. (10.1)) is the sum of both forward and backward reactions (Lasaga, 1984). If $\log \Omega < 0$, the mineral is undersaturated, the forward dissolution reaction dominates over the precipitation reaction and the mineral will weather. At $\log \Omega = 0$, the forward and backward reactions are equal and the mineral is stable in the weathering environment. A corollary to the TST approach is that as solutions approach saturation, commonly defined by the reaction affinity, the rate of the weathering reaction decreases, i.e., the rate of the backward reaction approaches that of the forward reaction.

Although the relationship between weathering rates and reaction affinities has been validated for experimental weathering studies (Nagy et al., 1991; Burch et al., 1993; Taylor et al., 2000), a comparable effect has not been conclusively demonstrated for natural weathering. However saturation control is often cited as a cause for differences in natural weathering rates. For example, the observation that the rate of plagioclase weathering for the Trout Lake aquifer approaches zero at the distal end of the flow (Fig. 10.11) is explained by thermodynamic saturation (Bowser and Jones, 2002). At thermodynamic saturation, mineral weathering becomes transport-limited and dependent on the amount of water that is transported through the system rather than on the kinetic rate of the reaction. This scenario is investigated in the following study.

10.7.2.3 Case Study: Saturation and Hydrologic Controls on Panola Feldspar Weathering

Plagioclase behaves very different than K-feldspar in the Panola weathering environment (see Sect. 10.3.5). While plagioclase is almost completely removed at depth in the granite, K-feldspar remains stable up to the overlying bedrock–saprolite interface (Fig. 10.4). This contrast in feldspar weathering is evident in electron backscatter images (EBS) which show the complete replacement of plagioclase to kaolinite (dark gray areas) in the Panola bedrock while adjacent K-feldspar grains are essentially pristine (Fig. 10.20a).

The relative weatherability of minerals in the natural environment commonly differs from that predicted by experimental dissolution. For example, in a review of experimental feldspar dissolution studies, Blum and Stillings (1995) concluded that, under neutral to acidic pH conditions, the rates of sodic plagioclase and K-feldspar

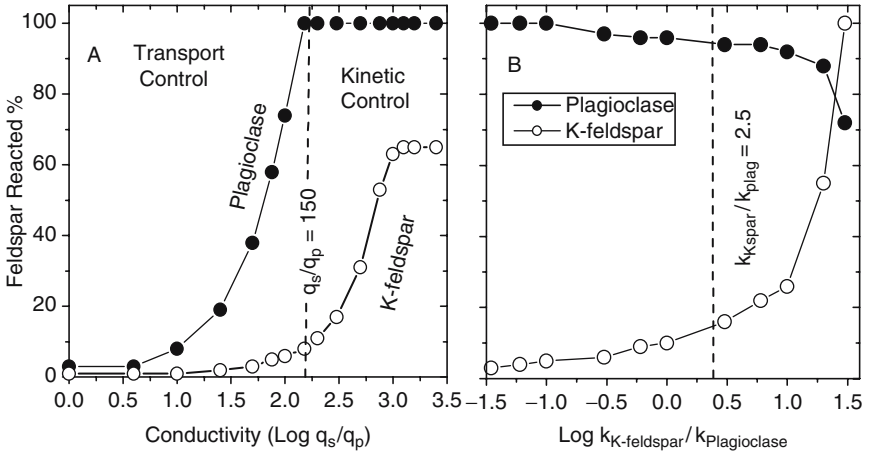

Fig. 10.21 The percent of plagioclase and K-feldspar reacted as a function of the ratios of (**a**) secondary to primary fluid fluxes (q_s/q_p) and (**b**) kinetic rate constants ($k_{Keldspar}$ and $k_{plagioclase}$ in the Panola Granite. The vertical dashed line in (**a**) is the respective conductivity ratios at which plagioclase is completely weathered and the K-feldspar weathering has not yet commenced. This condition is evident in the thin section in Fig. 10.21A. The vertical dashed line in (**b**) is the estimated ratio of rate constants based on far from equilibrium experimental dissolution studies. (after White et al., 2001)

were essentially the same. However, K-feldspar commonly is much more resistant to weathering than is plagioclase during natural weathering (Nesbitt et al., 1997; also Fig. 10.20a).

The very different behavior of plagioclase and K-feldspar in Panola bedrock implies feldspar weathering is saturation limited. This conclusion is supported by data presented in Fig. 10.20b, c in which Ω_{albite} and $\Omega_{K\text{-}spar}$ values (Eq. (10.26)) are plotted versus pH for pore waters extracted from the saprolites by suction water samplers and for deeper groundwaters sampled from wells in the Panola bedrock (White et al., 2001). The groundwaters are 1–2 orders of magnitude undersaturated with respect albite but are essentially saturated with respect to K-feldspar, thus explaining the relative reactivity of the two feldspars in the bedrock. In contrast, in the overlying saprolite, pore waters become thermodynamically undersaturated with K feldspar, thus increasing its reactivity as shown in Fig. 10.4

White et al. (2001) developed a simple forward spreadsheet model that explained the plagioclase and K-feldspar distributions in Fig. 10.20a. The principal parameters controlling the rate of feldspar weathering were assumed to be the respective feldspar rate constants k_{albite} and k_{Kspar}, the thermodynamic solubilities K_{albite} and K_{Kspar} and the change in fluid flow rates q_s/q_p. Changes in this last ratio were produced by secondary porosity generated by the masses of minerals reacted. Weathering rates were shown to be very sensitive to the hydrologic regime that controls fluid volumes, and, therefore, thermodynamic saturation. This is demonstrated in Fig. 10.21a where the proportions of plagioclase and K-feldspar in the weathered Panola bedrock are plotted as functions of q_s/q_p.

During the initial stages of weathering, the water flux is similar to that of the fresh granite ($\log q_s/q_p \approx 0$) and both plagioclase (albite) and K-feldspar reactions are strongly suppressed by thermodynamic saturation and controlled by the slow rates by which fluids can be transported into the regolith. As small amounts of feldspar dissolve, secondary permeability increases, allowing for the exponential increase in plagioclase reaction. At a ratio of about $\log q_s/q_p = 2.4$, the fluid flow rate become fast enough that the pore water no longer becomes thermodynamically saturated. Beyond this ratio, rate of plagioclase reaction is dependent on the kinetic rate constant k_r and independent of further increases in fluid flow.

Within the same range in q_s/q_p, K-feldspar reactivity remains strongly suppressed due to greater thermodynamic saturation (Fig. 10.20c). K-feldspar is approximately 400 times less soluble than albite. Pore water saturation is produced both by small amounts of K-feldspar dissolution and significant SiO_2 contributed from the more soluble plagioclase. With increases in q_s/q_p, the rate of transport-controlled K-feldspar dissolution gradually increases and reaches kinetically controlled weathering at a flow rate ratio of $\log q_s/q_p = 3.1$. At this point, the ratio of reacted plagioclase and K-feldspar becomes constant and equal to the ratio of their kinetic rate constants. The vertical line in Fig. 10.21a, corresponding to a flux ratio of $\log q_s/q_p = 2.4$, reproduces the condition shown in the SEM microphotograph in 20A in which all of the plagioclase is essentially dissolved while K-feldspar remains inert.

In contrast to fluid fluxes, the relative mineral losses were not particularly sensitive to the intrinsic rate constants describing K-feldspar and plagioclase dissolution (Eq. (10.21)). As shown in Fig. 10.21b, the K-feldspar rate must be more than 10 times greater than for plagioclase, i.e., $k_{Ksapr}/k_{plag} > 10$, for significant amounts of K-feldspar to weather in the presence of plagioclase in low permeability granitic bedrock. Such rapid K-feldspar rates are not in accord with experimental studies conducted far from equilibrium (vertical dashed line in Fig. 10.21b). The above results imply that natural weathering is often transport limited and controlled by mineral solubilites rather than kinetically controlled by rate constants.

10.7.2.4 Weathering Profiles in the Santa Cruz Marine Terraces

Weathering of plagioclase in beach sand was identified as the principal control on both the solute and solid-state Na distributions in the Santa Cruz Marine terrace chronosequence in California (Fig. 10.1 and White et al., 2007). High concentrations of plagioclase at depths >8 m are indicative of this protolith concentration (Fig. 10.22). In contrast, essentially all of the plagioclase is weathered out at shallow depths (<3 m). Over intermediate depths, residual plagioclase exhibits an approximate linear increase, the slope of which defines the solid state weathering gradient b_s (Eq. (10.23) and Fig. 10.16). The total mass loss of plagioclase reacted along this gradient (ΔM_j, Eq. (10.22)) is equal to the initial plagioclase content ($M_{total} = 2.35$ kmoles from White et al., 2007). Dividing ΔM_{total} by the depth

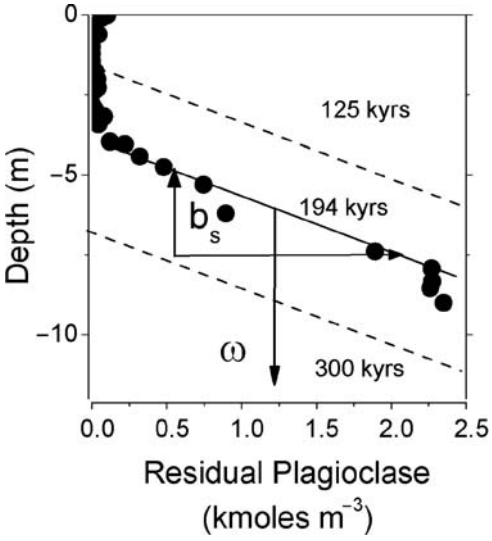

Fig. 10.22 Plagioclase weathering profile in a 194 kyr old soil developed on a marine terrace deposit, Santa Cruz, California. Solid points are measured residual mineral concentrations and solid dashed line is the fitted profile based on Eq. (10.28). The weathering gradient is defined by b_s and the weathering velocity by ω. Dashed lines correspond to the projected position of the profiles at past and future soil ages

interval over which this loss occurs ($z = 5\,m$, Fig. 10.22) results in a weathering gradient b_s of $2.1\,m^4$ moles^{-1} (White et al., 2007).

The mineral weathering rate is directly proportional to the weathering velocity (Eq. (10.23)). For Santa Cruz, cosmogenic ^{10}Be data indicate that very little erosion has occurred on the relatively flat terrace surfaces (Perg et al., 2001). Under such conditions, the profile progressively thickens as weathering progresses deeper into the beach sand protolith at a constant rate defined by ω (Fig. 10.22).

The pore waters in the Santa Cruz terraces, like that of the Panola regolith (see Sect. 10.7.2.3), are close to thermodynamic saturation with respect to plagioclase (White et al., 2007). Under such transport-limited conditions, the velocity at which the weathering profile moves downward in the regolith is proportional to the mass of plagioclase that is solubilized in a thermodynamically-saturated volume of fluid m_{sol}(moles m^{-3}) and inversely proportional to the total amount of plagioclase present in the protolith M_{total}(moles m^{-3}). In general, $M_{total} \gg m_{sol}$ and the weathering profile propagates in downward under transport-limited conditions such that

$$\omega = q_h \cdot \left[\frac{m_{sol}}{M_{total}}\right] \tag{10.27}$$

The weathering velocity, based on the calculated solubility of plagioclase and the estimated fluid flux is $\omega = 3.1 \times 10^{-5}\,m\,year^{-1}$ (White et al., 2007). Under constant fluid fluxes, the position of the weathering profile can also be established at different times during the weathering history of the terrace deposit (Fig. 10.22).

At such conditions, the weathering velocity of every point on the weathering profile moves downward at the same rate. Combining Eqs. (10.23) and (10.27) produces the result

$$R_m = \frac{1}{S}\left[\frac{q_s}{b_s}\right] \cdot \left[\frac{m_{sol}}{M_{total}}\right] \tag{10.28}$$

Table 10.18 Average compositions of the Rio Icacos regolith (Ribbe et al, 2003). Units as wt% except as noted

	Soil	Saptolite	Bedrock
Na	0.13	0.15	1.26
Mg	0.37	72	1.46
Al	3.6	6.4	4.6
Si	36	29.1	28.9
P	0.011	0.018	0.026
K	0.13	0.27	0.45
Ca	0.41	0.46	4.62
Ti	0.33	0.42	0.3
Mn	0.05	0.14	0.12
Fe	2.36	3.4	2.3
Rb[1]	8	33.8	26.9
Sr[1]	19	17.1	255
Y[1]	8.1	13.9	21
Zr[1]	236	124	90

[1]concentration in ppm.

After including estimates of surface area, a weathering rate of $R_m = 1 \times 10^{-16}$ moles m^{-2} s^{-1} was calculated for Santa Cruz plagioclase weathering. This value is similar with other natural plagioclase weathering rates for regoliths of comparable age (Table 10.17 and Fig. 10.19).

Eq. 10.28 produces is a first order linear approximation of a weathering gradient which assumes steady state conditions (Fig. 10.22). When examined in greater detail, weathering profiles commonly exhibit sigmoid shapes, with asymptotic increases in the weathering gradient at low and high residual concentrations (Fig. 10.22). These characteristics contain information on additional processes affecting weathering, including changes in mineral surface area and roughness (Eq. (10.25)), hydrologic conductivity (Eq. (10.10)) and the role of excess free energies as pore waters approach thermodynamic saturation (Eq. (10.21)). The description of such non-linearity in weathering profiles requires more elaborate computational methods than Eq. (10.28) (Maher et al., 2004; White et al., 2007 and Chap. 11).

10.7.3 Influences of Climate

The term *weathering* implies that chemical weathering is influenced by climate. This relationship is important from the standpoint of comparing silicate weathering rates under different current climate conditions, understanding the potential long-term feedback between weathering and climate variations during the Earth's history and to addressing issues related to mineral nutrient availability in soils undergoing human-forced climate change.

A number of solute fluxes studies comparing weathering rates in soils and smaller scale upland watersheds of similar rock type find a significant climate effects

described in terms of temperature and precipitation variability (Velbel, 1993; White and Blum, 1995; Desert et al., 2001; Oliva et al., 2003). However, studies of other environments have found minimal or no climate effect suggesting that topography and physical denudation are the principal controls on weathering (Riebe et al., 2001; Von Blanckenburg, 2006).

The validity of such comparisons depends on the ability to isolate the effects of climate from other variables influencing weathering including lithology, geomorphology, and vegetation. This explains, for example, why solute concentrations and fluxes originating from large scale river systems most often fail to detect a climate signature (Edmond et al., 1995; Huh et al., 1998). Other weathering parameters often scale with climate, making the isolation of individual variables difficult. Physical erosion generally increases with precipitation, exposing fresher mineral surfaces and increasing weathering rates. Likewise, higher rainfall may produce greater plant productivity, increased soil CO_2 and higher dissolved organic acids, all of which tend to accelerate weathering.

A definitive study would involve a weathering environment that has undergone consistent sustained climate change. However the long-term data required for such a study are not available and surrogate weathering studies comparing spatially separated climatic regimes will continue to be used. The two aspects of climate, temperature and precipitation, are most often considered in weathering studies.

10.7.3.1 Temperature

The effect of temperature on weathering is the easiest climate parameter to predict on a fundamental basis. The rates of most chemical reactions, including silicate hydrolysis (Eq. (10.1)),

$$\frac{R}{R_o} = \exp\left[\frac{E_a}{R'}\left(\frac{1}{T_o} - \frac{1}{T}\right)\right] \tag{10.29}$$

increase exponentially with temperature according to the Arrhenius expression.

This relationship is represented as the ratio of reaction rates at different temperatures T and $T_o(K)$ (Brady and Carroll, 1994). The experimental activation energies E_a(kJ mole^{-1}K^{-1}) of common silicate minerals vary between 50 and 75 kJ mole^{-1} (Casey and Westrich, 1992; Brady, 1991; White et al., 1999a). Eq. (10.29) predicts that reaction rates should increase by about an order of magnitude between 0° C and 25° C, the temperature range for most natural weathering.

Determining the temperature effect on natural weathering requires an understanding of the spatial variable. Watersheds commonly have a significant range in elevation that impacts temperatures. In addition, measurements commonly reflect air temperatures which do not consider thermal gradients in the regolith. In many climates, significant seasonal temperature variations occur, including seasonal freezing of the ground.

A number of studies find correlations between annual mean temperatures of watersheds and chemical weathering based on stream discharge (Velbel, 1993; Dorn

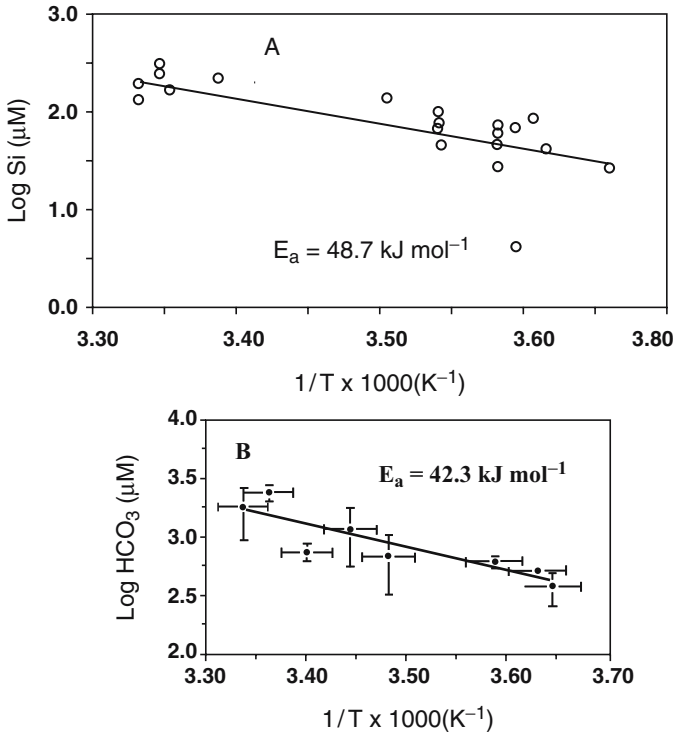

Fig. 10.23 Arrhenius relationships between mean annual temperature and mean annual solute concentrations from global distributions of watersheds. (**a**) SiO_2 discharge from granitic watersheds with runoff >1000 mm year^{-1} (Oliva et al., 2003). (**b**) Bicarbonate discharge from watersheds underlain by basalt (Dessert et al., 2001)

and Brady, 1995; White and Blum, 1995; Louvat and Allegre, 1998). Examples are shown in Fig. 10.23 for mean annual solute SiO_2 and bicarbonate concentrations for compilations of watersheds underlain by granite and basalt (Olivia et al., 2003; Desert et al., 2001). Both sets of data are plotted as log concentration against the reciprocal of absolute mean annual temperature (K). In this form, the slopes of the linear least squares fits are equal to the apparent average activation energies for basalt and granite ($E_a = 42$ and 49 kJ/mole respectively).

10.7.3.2 Precipitation

While precipitation is a primary climate parameter, the amount of water impacting weathering environments are more commonly reported as runoff or discharge measured directly in streams. A number of studies have observed a linear correlation between runoff and solute fluxes (Dunne, 1978; Dethier, 1986; Stewart et al., 2001). Gaillardet et al. (1999) concluded that the runoff was the major control based on the

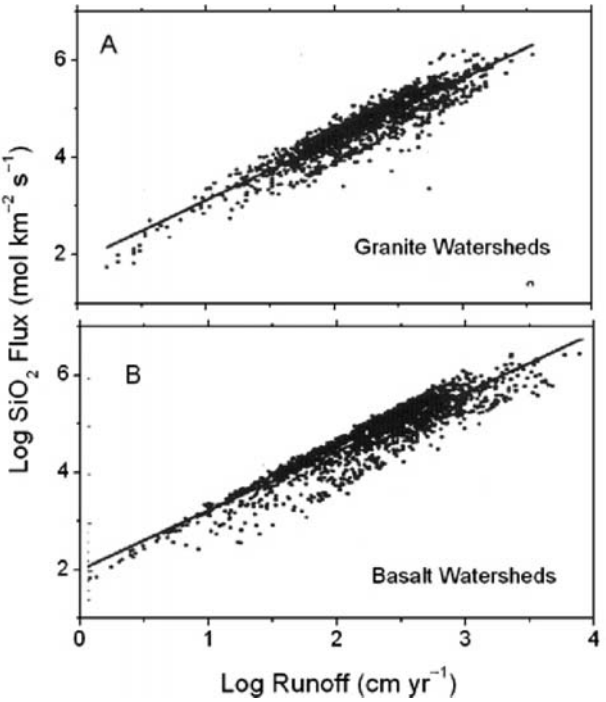

Fig. 10.24 Relationship between Si fluxes and runoff from watersheds draining (**a**) granitic and (**b**) basaltic watersheds (after Bluth and Kump, 1994). Respects slopes of the data are slope = 0.85 and 0.80

magnitude of the silicate component in 60 largest rivers in the world, based on the methods described in Sect. 10.4.11.

The relationship between the Si fluxes and runoff from a large set of basalt and granitic watersheds in the USA are shown in Fig. 10.24 (Bluth and Kump, 1994). The flux/runoff relationship is commonly linear with slopes less than unity, indicating that high runoff accelerates weathering. As pointed out by Drever and Clow (1995), greater precipitation increases the wetted surface areas of minerals, thereby promoting increased weathering. In addition, increased water flow increases the rates at which reactants, such as dissolved CO_2 and organic acids, are flushed through the system. A precipitation influence is also expected based on the strong correlation between fluid flow and transport-limited weathering in most natural environments (Fig. 10.21a).

Several workers (Brady, 1991; White and Blum, 1995; Desert et al., 2001) have proposed a coupled climate relationship of the form

$$Q = (aP)\exp\left[-\frac{E_a}{R}\left(\frac{1}{T}-\frac{1}{T_0}\right)\right] \tag{10.30}$$

Solute fluxes were proportional to a product of a linear precipitation function *(aP)* and the exponential temperature function. Equation (10.30) was fitted to data for

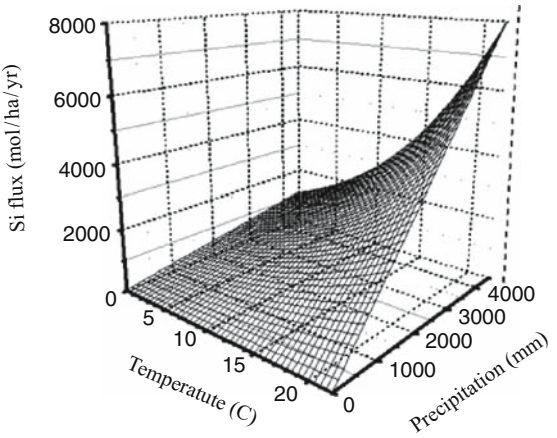

Fig. 10.25 Three-dimensional surface representing the optimized fit of watershed Si fluxes to Eq. (10.30) as functions of precipitation and temperature (after White and Blum, 1995)

well-characterized upland catchments underlain by granitoid rocks by White and Blum (1995). A 3-dimensional plot generated for Si fluxes is shown in Fig. 10.25. The net climate effect was to accelerate weathering rates in watersheds with both high temperatures and precipitation and to decrease weathering fluxes in watersheds with low temperature and precipitation. This conclusion is in agreement with Meyback (1994) who has shown that maximum concentrations of dissolved species from chemical weathering occur in rivers draining humid mountainous terrains and that minimum fluxes occur in arid and cold environments.

10.7.4 Chemical Weathering Under Physically Eroding Conditions

Chemical weathering, as calculated either as solute or solid state fluxes, is often converted in geomorphic studies to a chemical denudation or chemical erosion rate. Although chemical denudation is commonly reported in units equivalent to landscape lower W (mm year^{-1}), this relationship is valid only if the regolith density remains constant. For example, in the case of isovolumetric weathering (see Sect. 10.3.5) no landscape lower by chemical weathering occurs at all.

Chemical weathering at the earth's surface occurs concurrently with physical erosion or denudation E (mm year^{-1}). This erosion is most often measured in terms of sediment transport as done for the Congo River (Fig. 10.14, Sect. 10.4.11). However physical denudation is increasingly addressed using cosmogenic isotopes (Heimsath et al., 2000; von Blanckenburg, 2006). The total denudation rate D is defined as the sum of the chemical and physical denudation rates

$$\mathrm{D} = \mathrm{E} + \mathrm{W} \tag{10.31}$$

Typically, in watersheds with high topographic relief, physical erosion dominates over chemical denudation ($\mathrm{E} > \mathrm{W}$ in Eq. (10.31)). For example, for the Ganges

river, which drains portions of the Himalayan Range, chemical denudation comprises only about 10% of the load. Such conditions are weathering-limited in that the most reactive mineral are involved in weathering (Kirby, 1972; Stallard and Edmond, 1983). Examples include the dissolution of trace amounts of calcite in plutonic rocks which produce excess solute Ca and alkalinity (Mast et al., 1990; White et al., 1999b; 2005) and the rapid oxidation of ferrous-containing biotite and the release of interlayer K (Blum and Erel, 1997). These reactions dominate where large amounts of fresh rock are continually exposed by physical denudation such as in recently glaciated watersheds (Anderson et al., 1997).

Transport-controlled conditions ($W > E$ in Eq. (10.31)), in contrast, occur in deep regoliths where the amount of fresh rock available to weathering is limited and all minerals ultimately contribute solutes in proportions to their abundances in the bedrock. Such conditions are common in low relief landscapes such as the Zaire River, where chemical denudation accounts for 45% of the total load (Berner and Berner, 1996). Given enough time, a dynamic equilibrium may be reached between the chemical and physical weathering rates (Stallard, 1995). Under such a conveyor belt scenario ($W = E$), the regolith depth will remain constant as additional rock is chemically weathered at depth and soils are physically removed at the surface.

An example of the relationship between chemical and physical erosion is now discussed for the Rio Icacos watershed (see previous discussion of weathering at Rio Icacos in Sect. 10.4.4).

10.7.5 Case Study: Steady State Denudation in a Tropical Soil

Riebe et al. (2003) employed a steady weathering model to characterize chemical and physical denudation associated with steady state weathering of the Rio Icacos regolith ($W = E$). In such a situation, conservation of regolith mass requires that

$$D\,C_{j,p} = E\,C_{j,w} + Q_{j,w} \tag{10.32}$$

where the denudation rate of a mobile component j is equal to the sum of that produced by physical erosion and the chemical weathering flux. This assumes that the regolith is maintained at a constant thickness and therefore does not act as a reservoir or sink for component j.

In the case of a conservative component C_i that is not mobilized during weathering

$$D\,C_{i,p} = E\,C_{i,w} \tag{10.33}$$

Substituting Eq. (10.33) into Eq. (10.31) results in the relationship

$$W = D\left(1 - \frac{C_{i,w}}{C_{i,p}}\right) \tag{10.34}$$

where the chemical erosion is expressed as a fraction of the total denudation The chemical flux for individual weatherable species is defined by substituting

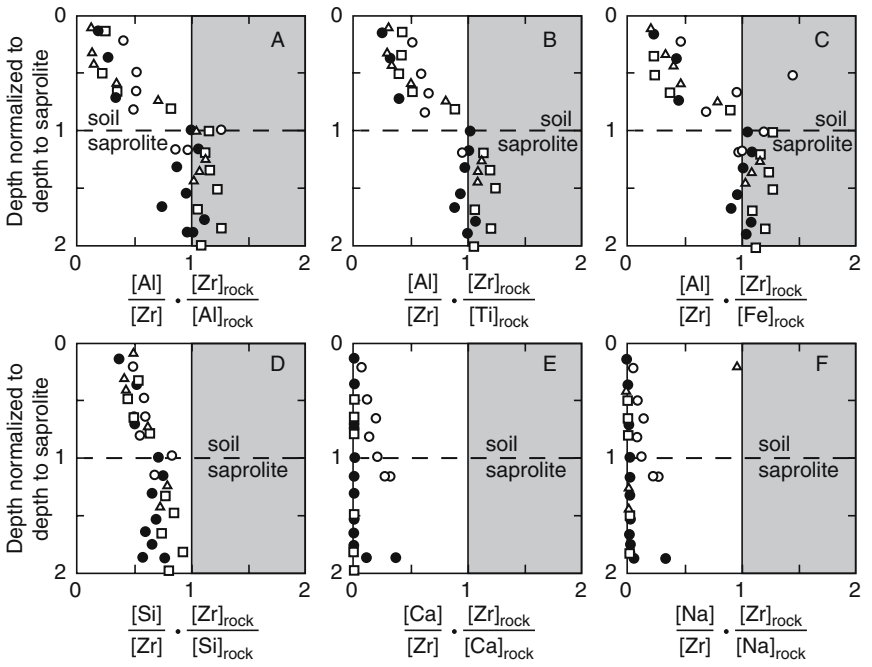

Fig. 10.26 Chemical depletion factors (CDF values from Eq. (10.36)) versus depth normalized to the soil/saprolites boundary in the Rio Icacos regolith. Values for immobile Al, Ti and Fe are near unity in the saprolites. Si is progressively enriched with depth and Ca and Na are nearly absent in the saprolites (After Ribbe et al., 2003)

Eq. (10.34) into Eq. (10.33) such that

$$Q_i = D\left(C_{j,p} - C_{j,w}\frac{C_{i,p}}{C_{iw}}\right) \tag{10.35}$$

If the weathering flux Q_j is expressed in a non-dimensional form by normalizing to the total denudation rate for component j such that

$$\frac{Q_j}{D \cdot C_{j,p}} = \left(1 - \frac{C_{j,w}}{C_{j,p}}\frac{C_{i,p}}{C_{i,w}}\right)_j \tag{10.36}$$

Riebe et al. (2003) defined the parameters in parenthesis as the chemical depletion factor or CDF which is the negative value for τ_j defined in Eq. (10.6) (Brimhall et al., 1991).

Average Rio Icacos soil, shallow saprolite and bedrock compositions are presented in Table 10.18 (Riebe et al., 2003). The change in major element losses in the soils normalized to the depth of the soil-saprolite boundary is shown in Fig. 10.26. Values are defined in terms of CDFs (Eq. (10.36)) assuming that Zr was chemically inert during weathering (Eq. (10.35)). Essentially all of the Ca and Na and moderate

amounts of Si are depleted in the soil and shallow saprolite relative to the bedrock with additional losses of Fe, Ti and Al in the shallow soils. These elemental trends correlate closely with the weathering sequence for plagioclase, biotite and kaolinite previously found by White et al. (1998) (see Fig. 10.5).

The total denudation rate which was based on ^{10}Be analyses of amalgamated soil samples was $D = 90\,t\,km^{-1}\,year^{-1}$ (Riebe et al., 2003), a value in good agreement with a previously reported rate of $68\,t\,km\,year^{-1}$ (Brown et al., 1995). Based on the CDF values and this denudation rate, Riebe et al. (2003) calculated chemical fluxes of individual elements Q_j (Eq. (10.36)) in addition to the total chemical denudation rate W (Eq. (10.31)) that are in close agreement with the previously calculated rates of White et al. (1998) who used cosmogenic denudation rates of Brown et al. (1995) and summed the elemental losses based over the entire regolith thickness based on calculated τ_j values and Eq. (10.7). These results also compare favorably to chemical denudation rates reported in Table 10.8 based on pore water compositions and infiltration rates (White et al., 1998) and on stream water solute discharge (McDowell and Asbury, 1994). As expected, in all cases, the elemental denudation rates are dominated by losses of Ca, Na and SiO_2.

10.7.6 Influence of Erosion, Topography and Tectonics

Dynamic equilibrium conditions such as in the Rio Icacos watershed imply that there is feedback between the chemical weathering rates and rates of physical erosion (see also Chaps. 12 and 13). Thickening regoliths decrease the rates of chemical weathering and thinning regoliths accelerate the rates of chemical weathering. These correlations are demonstrated in hillslope studies in which the rate of soil production or weathering decreases in profiles of progressively greater thickness (Fig. 10.27a; Heimsath et al., 2000). The role of regolith thickness and rates of chemical weathering rates is also supported in watershed studies. For the compilation of granite watersheds, Oliva et al. (2003) found a temperature correlation with weathering only when runoff is $> 1000\,mm\,year^{-1}$ (Fig. 10.23a). High runoffs are often associated with mountainous areas with relatively thin soil thicknesses. In lowland areas, the formation of thick soils produces low chemical weathering that masks any climate correlation.

As expected from the above discussion, a number of studies have found a strong correlation between rates of chemical weathering and physical erosion, i.e., W and E in Eq. (10.31). Examples included in Fig. 10.28 show a power law (log–log) relationship between physical erosion and chemical weathering for both small catchments (Riebe et al., 2003) and larger scales river systems (Millot et al., 2002). In the later study, a factor of 10 increase in physical erosion propagated a 4.5 increase in solute fluxes in the rivers.

Correlations also exist between chemical weathering and processes that govern physical erosion, including topography. Heimsath et al. (2000) found a relationship

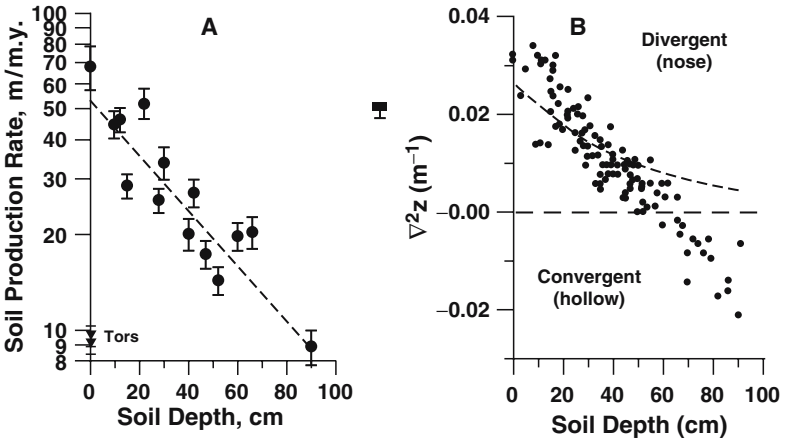

Fig. 10.27 Relationships between hillslope soil depth and (A) soil production rates from weathering and (B) hillslope curative (Heimsath et al., 2000)

between hillslope curvature and soil thickness. Divergent or concave portions of the hillslopes had thinner soils (Fig. 10.27b) and consequently faster soil production and weathering rates than did the convergent slopes or hollows with deeper soils. On time spans associated with long term regolith weathering, topography and physical erosion become dependent on tectonics. Discussions of the potential roles of active faulting, as well as regional tectonic uplift on physical erosion and weathering are found in Ruddiman (1997), Riebe et al. (2001), and von Blanckenburg (2006).

Chemical weathering of regoliths and watersheds possessing very different topography and physical erosion rates are expected to exhibit very different chemical weathering rates regardless of climatic effects. For example, the Rio Icacos has a similar precipitation and temperature as watersheds on the Guyana shield in South America, However, due to topographic effects; the rates of both physical and chemical denudations in the Rio Icacos are 5–10 times faster than those of Guyana (Millot et al., 2002). In contrast, climatic effects on weathering are discernable in comparisons of watersheds with similar topography and physical erosion rates (White and Blum, 1995; Desert et al., 2001; Oliva et al., 2003). In terms of understanding long term weathering on the earth's surface both the roles of climate and physical must be understood.

10.7.7 Role of Biology

Plants are both the beneficiaries and instigators of chemical weathering. Biological interaction can be classified in terms of approximate scale, ranging from bacteria

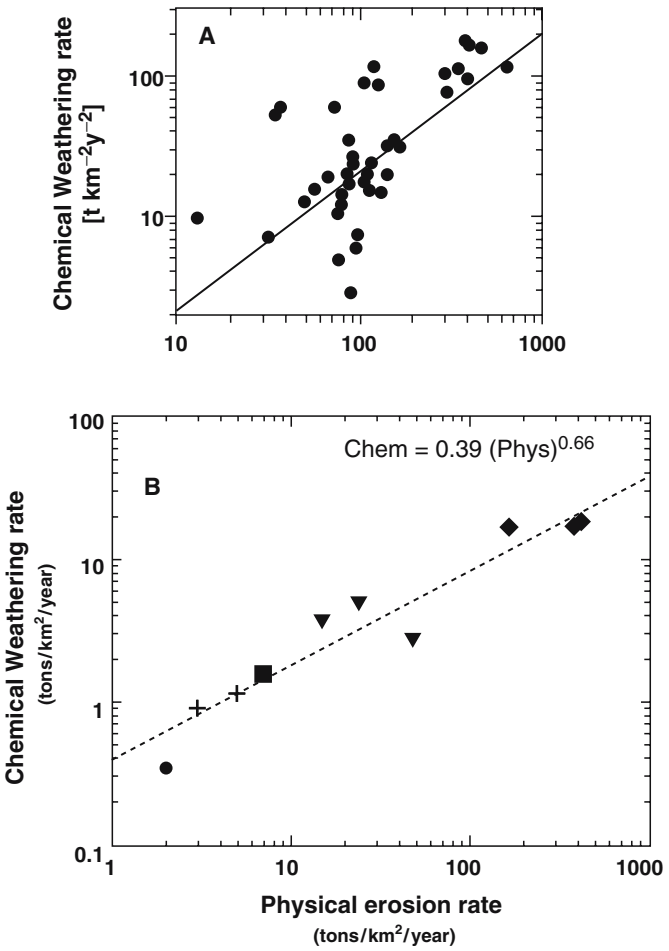

Fig. 10.28 Relationships between chemical weathering rates and rates of physical erosion for (A) small granitic catchments (Riebe et al., 2003) and (B) larger scales river systems (Millot et al., 2002)

to fungi, lichens and vascular plants. Recently, significant research has centered on geomicrobiology (see Chaps. 8–8.4.5.5). Numerous experimental studies have documented that bacteria produce organic acids and chelating agents that accelerate silicate dissolution (see review by Banfield and Nealson, 1997). However, evidence for the role of microbes in accelerating natural weathering is much more limited. Perhaps the best field evidence is for organic-rich environments such as peat bogs and shallow aquifers contaminated by oil spill. Both environments promote extensive microbial populations which colonize mineral surfaces (Bennett, 1991; Bennett et al., 1996). Many etch pits on the mineral surface approximated the size and shape of the colonizing bacteria implying they create a micro-reaction zone where organic

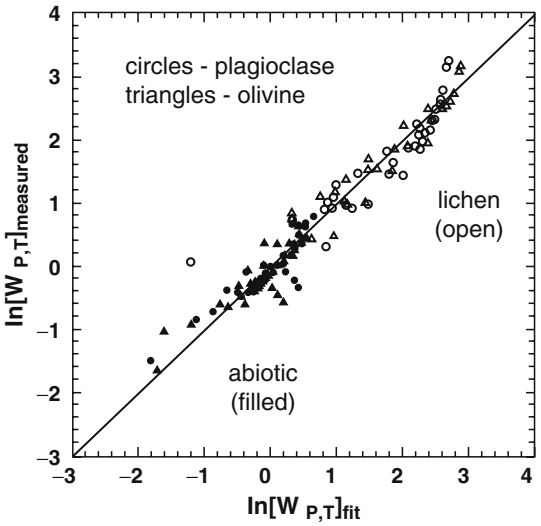

Fig. 10.29 Measured and predicted weathering rates based on etch pits for a basalt surface in which lichens are present or absent (Brady et al., 1999)

acids and other metabolites were concentrated. Alkali feldspars were selectively weathered, suggesting the bacteria were K-limited in their nutrient supply.

The role of fungi and lichens in accelerating chemical weathering is more extensively documented under field conditions. Mycorrhizal fungi associated with plant roots secrete organic acids and chelates which attack primary minerals that release nutrient cations needed by the roots (Griffiths et al., 1994). Organic acids (such as oxalic acid) increase the availability of PO_4^{3-}, an important soil nutrient. Oxalic acid also forms soluble complexes with Al and Fe, which are less toxic to higher plants than the free metal ions. This process also enhances the dissolution of minerals containing these elements. Van Breemen et al. (2000) and Jongmans et al. (1997) showed that ectomycorrhizal mycelia from fungi create micropores by the production of aluminum-complexing organic acids at their hyphal tips. These hyphae penetrate directly into silicate minerals in granitic rock to remove Ca and P from apatite inclusions in silicate minerals

Lichens are symbiotic associations of algae and fungi characterized by low growth rates and nutrient requirements that enable them to play the role of pioneer vegetation in the colonization of fresh rocks. A number of studies show that lichens physically and chemically attack rock surfaces and promote chemical weathering (Fry, 1927). Brady et al. (1999) studied the effect of abiotic versus lichen weathering across a transect in Hawaii where variation in rainfall and temperature is systematic. They compared the porosity developed in plagioclase and olivine crystals by weathering under lichens versus that developed on totally bare rocks. Using a model that considers climate, they found that lichen weathering was more sensitive to rainfall than abiotic weathering and that the weathering rate under lichens was 2–18 times as great as under abiotic conditions (Fig. 10.29). Other studies have

documented the role of lichens in the biophysical disaggregation, extraction of K and the transformations of biotite to vermiculite and smectite (Barker and Banfield, 1995).

Literature related to the direct impact of plants on chemical weathering was reviewed by Kelly (1998) and Berner et al. (2004). Plant roots actively mine selective mineral nutrients via symbiotic relationships with mycorrhizal fungi as discussed above. Studies of young Hawaiian basalts showed that even 150-year-old rocks show evidence of selective plagioclase dissolution by invading fungal hyphae and root hairs of plants (Berner and Cochran, 1998). After 3,000 years of weathering, basalt beneath higher plants showed removal of plagioclase from surface rocks down to a depth of several centimeters, concentrated along fractures.

Plants also take up soluble silica and deposit it inside the cell, in cell walls, and near evaporating surfaces, principally in the form of microscopic opaline silica phytoliths. When a plant dies and decays, these phytoliths are returned to the soil and slowly dissolve, contributing additional silica to the soil water. Alexandre et al. (1997) found that the biogenic silica input into the silica cycle from the dissolution of phytoliths was twice as large as silica input from primary silicate mineral weathering in the tropical Congo rainforest. In a study of Hawaiian streams, Kurtz et al. (2002) also concluded that a significant amount of dissolved silica had been recycled as biogenic silica.

A plant-controlled weathering system was proposed for areas of the central Amazon Basin by Lucas (2001). Laterites and bauxites in the humid tropical Central Amazonian rainforest commonly consist of an upper kaolinitic clay underlain by a thick aluminous, gibbsite-rich lower layer before a transition into the underlying saprolite. This soil sequence of kaolinite overlying gibbsite is the opposite of what most geochemical soil models predict. The Amazonian forest litter fall contains large quantities of silicon and aluminum, which are removed by leaching and carried downward by soil water percolating through the upper soil. Lucas (2001) proposed that kaolinite is stabilized against dissolution and conversion to gibbsite by high dissolved silica concentrations in the shallow soil solutions due to silica recycling by trees.

Plants also physically impact the environment, thus indirectly influencing chemical weathering. Transpiration, the release of water through stomata in plant leaves, is commonly the dominant component of evapotranspiration which significantly increases solute concentrations in pore waters and reduces deep drainage. The decay of plant roots also produce macropores which create preferential flow paths with soils and roots which also influence solute concentrations (Flury and Fluhler, 1994). Also, roots fracture mineral grains and increase soil porosity and permeability, which allows greater contact between soil solutions and minerals (April and Keller, 1993). By binding fine particles in the soil, plant roots also cause retention of water between rain events. This retained water results in continued chemical weathering (Drever, 1994). Also plants can bioturbate and homogenize soils by producing roots throws (Borman et al., 1998). Finally, the presence of forest trees tends to lower soil surface temperatures by shading the soil surface and reducing surface albedo (Kelly et al., 1998).

10.8 Summary

This chapter reviews approaches to quantifying chemical weathering rates under field conditions. Such rates are important in understanding weathering mechanisms and in addressing a number of economic and environment issues. Silicate weathering rates, defined as mass fluxes across an interface over a given time interval, can be described in terms of changes in either solid state or solute element, isotope or mineral abundances. Solid state mass changes in a bulk regolith must be corrected for the mobility of all components as well as volume and density changes due to compaction and bioturbation. This correction is commonly done by normalizing reactive concentrations against an element or mineral considered to be resistant to chemical weathering.

The calculation of rates based on changes in solute species concentrations in soils, aquifers and watersheds requires partitioning the reactant between sources produced by primary mineral dissolution and sinks created by secondary mineral precipitation. Calculation of weathering rates based on solute transport requires knowledge of the rate of fluid flow through soils, aquifers and watersheds.

Solid-state mass differences reflect weathering over geologic time scales while solute compositions reflect the residence time of the water. These mass losses or gains are normalized to surface area. Studies of natural weathering commonly define physical surface areas on a geographic, volumetric or mineral-specific basis. Specific surface areas of minerals are either geometric estimates, based on particle size dimensions, or else based on BET gas sorption isotherms which include surface areas associated with microscopic roughness and internal porosity. The difference in the scales of these measurements produces major differences in surface-normalized mineral weathering rates.

Factors affecting weathering rates can be categorized as either intrinsic or extrinsic to a specific mineral. The primary intrinsic factors are mineral composition and structure. Reaction rates are also affected by compositional differences within single mineral grains, such as zonations and exsolution features and by secondary surface coatings and leached layers.

Of the extrinsic factors influencing natural weathering rates, solute composition has the most direct impact. Solutions provide reactants that complex with and detach the oxygen-bonded metal species in the silicate structure. In addition, reaction rates depend on the thermodynamic saturation state of the dissolving phase. Unlike most experimental studies, natural weathering commonly involves long times and small solute/solid ratios, producing solutes close to thermodynamic saturation. This difference in saturation states explains, in part, why natural weathering rates are commonly orders magnitude slower than experimental rates and why the relative weatherability of minerals in the natural environment is often different from that predicted by experimental dissolution rates.

Studies comparing weathering rates in soils and small catchments often find a significant climate effect while solute concentrations and fluxes originating from large river systems do not. This discrepancy is related to the inability to isolate the effects of climate from other parameters, whose variability increases as the scale of

the weathering processes increases. An exponential relationship between reaction rate and temperature is observed in some weathering environments. Several studies have also documented linear increases in weathering with precipitation due to increases in wetted surface areas and thermodynamic reaction affinities.

As expected, the ratio of physical to chemical weathering is strongly scaled to differences in topography. An important relationship between physical weathering and chemical weathering is summarized in terms of weathering-limited and transport-limited weathering regimes. In addition to controlling the relative proportions of minerals available for weathering, physical erosion also has a profound effect on the physical development of weathering environments. Regoliths can be viewed as aggrading, steady state or degrading systems depending on whether their thickness increases, remains constant or decreases with time due to physical erosion.

The impact of biota on the rates of chemical weathering is variable and dependent on the scale and nature of the interactions. A significant amount of research is currently directed at microbial interaction with silicate mineral surfaces under laboratory conditions. However, except for environments with high organic carbon inputs, the overall impact microbes have on natural weathering is still uncertain. Mesoscale biota, including fungi and lichens are vehicles that physical break-down minerals and cause chemical mobilization of plant mineral nutrients. Chemical cycling by plants themselves significantly impacts soil and watershed chemical compositions by mobilizing mineral nutrients by aggradation and degradation processes. Plants also physically impact weathering environments through water loss by transpiration, temperature effects and bioturbation.

Acknowledgements

The author expresses his gratitude to his colleagues at the U.S. Geological Survey who collaborated on many of the studies described in this chapter, including Tom Bullen, Alex Blum, Dave Stonestrom and Davison Vivit. The author would also like to thank the researchers who provided original figures and tables from the cited contributions and to the staff at Penn State, in particular Denise Kowalski, who where instrumental in making this volume a reality. Funding during this work was provided through the National Research Program of the U.S. Geological Survey.

References

Alexandre A., Meunier J. D., Colin F., and Koud J. M. (1997) Plant impact on the biogeochemical cycle of silcon and related weathering processes. *Geochim. Cosmochim. Acta* **61**, 677–682.

Allegre C. J., Hart S. R., and Minster J. F. (1983) Chemical structure and evolution of the mantle continents determined by inversion of Nd and Sr isotopes 1. Theoretical methods. *Earth Planet. Sci. Lett.* **66**, 177–190.

Anderson S. P., Drever J. I., and Humphrey N. F. (1997) Chemical weathering in glacial enviroments. *Geology* **25**, 399–402.

April R., Newton R., and Coles L. T. (1986) Chemical weathering in two Adirondack watersheds: past and present-day rates. *Geol. Soc. Amer. Bult.* **97**, 1232–1238.

April R. and Keller D. (1993) Mineralogy of the rhizosphere in forest soils of the eastern United States. *Biogeochemistry* **9**, 1–18.

Bandstra J., Buss H., Moore J., Hausrath E., Liermann L., Navarre A., Jang J., and Brantley S. (2007) Fitting kinetic data for geochemical reactions. In *Kinetics of Geochemical Systems* (ed. S. F. Brantley, J. Kubiciki, and A. F. White). Springer Publishing, New York.

Banfield J. F. and Barker W. W. (1994) Direct observation of reactant-product interfaces formed in natural weathering of exsolved, defective amphibole to smectite: evidence for episodic, isovolumetric reactions involving structural inheritance. *Geochim. Cosmochim. Acta* **58**, 1419–1429.

Banfield J. F. and Nealson K. H. (1997) Geomicrobiology: interactions between microbes and minerals. In *Reviews in Mineralogy*, Vol. 35. Mineralogical Society of America, Washington, DC.

Barker W. W. and Banfield J. F. (1995) Biologically versus inorganically mediated weathering reactions: relationships between minerals and extracellular microbial polymers in litho-biontic communities. *Chem. Geol.* **132**, 55–69.

Barth T. F. (1961) Abundance of the elements, aerial averages and geochemical cycles. *Geochim. Cosmochim. Acta* **23**, 1–8.

Beauvais A. (1999) Geochemical balance of lateritization processes and climatic signatures in weathering profiles overlain by ferricretes in Central Africa. *Geochim. Cosmochim. Acta* **63**, 3939–3957.

Bennett P. C. (1991) Fate of silicate minerals in a peat bog. *Geology* **19**, 328–331.

Bennett P. C., Hiebert F. K., and Choi W. J. (1996) Microbial colonization and weathering of silicates in a petroleum-contaminated groundwater. *Chem. Geol.* **132**, 45–53.

Berner E. K. and Berner R. A. (1996) *Global Environment: Water, Air and Geochemical Cycles*. Prentice-Hall, New York.

Berner R. A. and Cochran M. F. (1998) Plant-induced weathering of Hawaiian basalts. *J. Sediment. Res.* **68**, 723–726.

Berner E. K., Berner R. A., and Molton K. L. (2004) Plants and mineral weathering: past and present. In *Surface and Groundwater, Weathering, Erosion and Soils* (ed. J. I. Drever) Elsevier, Amsterdam, pp. 69–188.

Blum A. E. and Lasaga A. C. (1987) Monte Carlo simulations of surface reaction rate laws (ed. W. Stumm), Wiley & Sons, New York, pp. 255–291.

Blum A. E. and Stillings L. L. (1995) Feldspar dissolution kinetics. In *Chemical Weathering Rates of Silicate Minerals* (ed. A. F. White and S. L. Brantley) Reviews in Mineralogy, Vol. 31, Mineralogical Society of America, Washington, DC, pp. 291–346.

Blum J. D. and Erel Y. (1997) Rb-Sr isotope systematics of a granitic soil chronosequence: the importance of biotite weathering. *Geochim. Cosmochim. Acta* **61**, 3193–3204.

Bluth G. S. and Kump L. R. (1994) Lithologic and climatic controls of river chemistry. *Geochim. Cosmochim. Acta* **58**, 2341–2359.

Borman F. H., Wang D., Bormann F. H., Benoit G., April R., and Snyder M. C. (1998) Rapid plant-induced weathering in an aggrading experimental ecosystem. *Biogeochemistry* **43**, 129–155.

Bowser C. J. and Jones B. J. (2002) Mineralogical controls on the composition of natural waters dominated by silicate hydrolysis. *Am. J. Sci.* **302**, 582–662.

Brady P. V. (1991) The effect of silicate weathering on global temperature and atmospheric CO_2. *J. Geophys. Res.* **96**, 18101–18106.

Brady P. V. and Carroll S. A. (1994) Direct effects of CO_2 and temperature on silicate weathering: possible implications for climate control. *Geochim. Cosmochim. Acta* **58**, 1853–1863.

Brady P. V., Dorn R. I., Brazel A. J., Clark J., Moore R. B., and Glidewell T. (1999) Direct measurement of the combined effects of lichen, rainfall and temperature on silicate weathering. *Geochim. Cosmochim. Acta* **63**, 3293–3305.

Brantley S. L., Crane S. R., Creear D., Hellmann R., and Stallard R. (1986) Dissolution at dislocation etch pits in quartz. *Geochim. Cosmochim. Acta* **50**, 2349–2361.

Brantley S. L., Blai A. C., Cremens D. L., MacInnis I., and Darmody R. G. (1993) Natural etching rates of feldspar and hornblende. *Aquat. Sci.* **55**, 262–272.

Brantley S. L., White A. F., and Hodson M. E. (1999) Surface area of primary silicate minerals. In *Growth, Dissolution and Pattern Formation in Geosystems* (ed. B. Jamtveit and P. Meakin), Kluwer Academic Publishers, Amsterdam, pp. 291–326.

Brantley S. L., Bau M., Yau, S., and Alexander B. (2001) Interpreting kinetics of groundwater-mineral interaction using major element, trace element and isotopic tracers. In *Water-Rock Interaction* 10 (ed. R. Cidu), Balkema, Rotterdam, pp. 13–18.

Brantley S. L. and Conrad C. F. (2007) Analysis of rates of chemical reactions. In *Kinetics of Geochemical Systems* (ed. S. L. Brantley, J. Kubiciki, and A. F. White). Springer Publications, New York.

Brenner D. L., Amundson R., Baisden W. T., Kendall C., and Harden J. (2001) Soil N and ^{15}N variations with time in a California grassland ecosystem. *Geochim. Cosmochim. Acta* **65,** 4171–4186.

Brimhall G. H., Lewis C. J., Ford C., Bratt J., Taylor G., and Warin O. (1991) Quantitative geochemical approach to pedogenesis: importance of parent material reduction, volumetric expansion, and eolian influx in lateritization. *Geoderma* **51**, 51–91.

Brown D. J., Helme P. A., and Clayton M. K. (2003) Robust geochemical indices for redox and weathering on a granitic laterite landscape in Central Uganda. *Geochim. Cosmochim. Acta* **67**, 2711–2723.

Brown E. T., Stallard R. F., Larsen M. C., Raisbeck G. M., and Yiou F. (1995) Denudation rates determined from the accumulation of in situ produced ^{10}Be in

the Luquillo Experimental Forest, Puerto Rico. *Earth Planet. Sci. Lett.* **129**, 193–202.

Bullen T. D. (1997) Chemical weathering of a soil chronosequence on granitic alluvium: II Mineralogic and isotopic constraints on the behavior of strontium. *Geochim. Cosmochim. Acta* **61**, 291–306.

Bullen T. D., Krabbenhoft D. P., and Kendal, C. (1996) Kinetic and mineralogic controls on the evolution of groundwater chemistry and $^{87}Sr/^{86}Sr$ in a sandy silicate aquifer, northern Wisconsin, USA. *Geochim. Cosmochim. Acta* **60**, 1807–1821.

Burch T. E., Nagy K. L., and Lasaga A. C. (1993) Free energy dependence of albite dissolution kinetics at 80° C, and pH 8.8. *Chem. Geol.* **105**, 137–162.

Burns D. A., Plummer L. N., McDonnell J. J., Busenberg E., Casile G. C., Kendall C., Hooper R. P., Freer J. E., Peters N. E., Beven K. J., and Schlosser P. (2003) The geochemical evolution of riparian groundwater in a forested Piedmont catchment. *Groundwater* **41**, 913–925.

Carson M. A. and Kirby K. T. (1972) *Hillslope, Form and Processes*. Cambridge University Press, New York.

Casey W. H. and Sposito G. (1992) On the temperature dependence of mineral dissolution rates. *Geochim. Cosmochim. Acta* **56**, 3825–3830.

Casey W. H. and Westrich H. R. (1992) Control of dissolution rates of orthosilicate minerals by divalent metal-oxygen bonds. *Nature* **355**, 157–159.

Chadwick O. A., Brimhall G. H., and Hendricks D. M. (1990) From black box to a grey box: a mass balance interpretation of pedogenesis. *Geomorphology* **3**, 369–390.

Chadwick O. A., Gavenda R. T., Kelly E. F., Ziegler K., Olson C. G., Elliot W. C., and Hendricks D. M. (2003) The impact of climate on the biogeochemical functioning of volcanic soils. *Chem. Geol.* **202**, 195–223.

Clayton J. L. (1986) An estimate of plagioclase weathering rate in the Idaho batholith based upon geochemical transport rates. In *Rates of Chemical Weathering of Rocks and Minerals* (S. Colman and D. Dethier eds.) Academic Press, Orlando, pp. 453–466.

Cleaves E. T. (1993) Climatic impact on isovolumetric weathering of a coarse-grained schist in the northern Piedmont Province of the central Atlantic states. *Geomorphology* **8**, 191–198.

Clow D. W. and Drever J. I. (1996) Weathering rates as a function of flow through an alpine soil. *Chem. Geol.* **132**, 131–141.

Delvaux B., Herbillion A. J., and Vielvoye L. (1989) Characterization of a weathering sequence of soils derived from volcanic ash in Cameroon, taxonomic, mineralogical and agronomic implications. *Geoderma* **45**, 375–388.

Desert C., Dupre B., Francois L., Schott J., Gaillard J., Chakrapani G., and Bajpai S. (2001) Erosion of Deccan Traps determined by river geochemistry: impact on global climate and the $^{87}Sr/^{86}Sr$ ratio of seawater. *Earth and Planetary Science Letters* **188**, 459–474.

Dethier D. P. (1986) Weathering rates and the chemical flux from catchment in the Pacific Northwest, U.S.A. In *Rates of Chemical Weathering of Rocks and Minerals* (eds. S. Colman and D. Dethier) Academic Press, Orlando, pp. 503–530.

Dorn R. I. and Brady P. V. (1995) Rock-based measurement of temperature-dependent plagioclase weathering. *Geochim. Cosmochim. Acta* **59**, 2847–2852.

Drever J. I. (1994) The effect of land plants on weathering rates of silicate minerals. *Geochim. Cosmochim. Acta* **58**, 2325–2332.

Drever J. I. and Clow D. W. (1995) Weathering rates in catchments. In *Chemical Weathering Rates of Silicate Minerals* (ed. A. F. White and S. L. Brantley), Reviews in Mineralogy **31** Mineral. Soc. Amer., Washington, DC, pp 463–481.

Driscoll C. T., Likens G. E., Hedlin L. O., Eaton J. S., and Bormann F. H. (1989) Changes in the chemistry of surface waters. *Environmental Sci. Technol*. **23**, 137–142.

Driscoll C. T., van Breemen N., and Mulder J. (1985) Aluminum chemistry in a forested spodosol. *Soil Sci. Soc. Am. J.* **49**, 437–444.

Dunne T. (1978) Rates of chemical denudation of silicate rocks in tropical catchments. *Nature* **274**, 244–246.

Dupre B., Gaillardet J., Rousseau J., and Allegre C. J. (1996) Major and trace elements of river-borne material: the Congo basin. *Geochim. Cosmochim. Acta* **60**, 1301–1321.

Duzgoren-Aydin N. S., Aydin A., and Malpas J. (2002) Re-assessment of chemical weathering indices: case study on pyroclastic rocks of Hong Kong. *Eng. Geol.* **63**, 99–109.

Edmond J. M., Palmer M. R., Measures C. I., Grant B., and Stallard R. F. (1995) The fluvial geochemistry and denudation rate of the Guyana Shield in Venezuela, Colombia, and Brazil. *Geochim. Cosmochim. Acta* **59**, 3301–3325.

Farley D. A. and Werritty A. (1989) Hydrochemical budgets for the Loch Dee experimental catchments, southwest Scotland (1981–1985). *J. Hydrol.* **109**, 351–368.

Fedo C. M., Nesbitt H., W., and Yong G. M. (1995) Unraveling the effects of potassium metasomatism in sedimentary rocks and paleosols, implications for paleoweatherng conditions and provenance. *Geology* **23**, 921–924.

Flury M. and Fluhler H. (1994) Susceptibility of soils to preferential flow of water: a field study. *Water Resour. Res.* **30**, 1945–1954.

Frankenberger W. T. and Benson S. (1994) Selenium in the Environment, Marcel Dekker, New York.

Fry E. J. (1927) The mechanical action of crustaceous lichens on substrata of shale, schist, gneiss and obsidian. *Ann. Botany* **41**, 437–460.

Gaillardet J., Dupre E. B., and Allegre C. J. (1995) A global geochemical mass budget applied to the Congo basin rivers: erosion rates and continental crust composition. *Geochimica Cosmochimica. Acta* **59**, 3469–3485.

Gaillardet J., Dupre E. B., and Allegre C. J. (1999) Geochemistry of large river sediments: silicate weathering or recycling tracer? *Geochimica. Cosmochimica. Acta* **63**, 4035–4051.

Gaillardet J. (2007) Isotope geochemistry as a tool for deciphering kinetics of water-rock interaction. In *Kinetics of Geochemical Systems* (ed. S. L. Brantley, J. Kubiciki, and A. F. White). Springer Publications, New York.

Gardner L. R. (1980) Mobilization of Al and Ti during weathering-isovolumetric geochemical evidence. *Chem. Geol.* **30**, 151–165.

Garrels R. M. and Mackenzie F. T. (1967) Origin of the chemical composition of some springs and lakes. In *Equilibrium concepts in natural water systems, Adv. Chem Ser*, Vol. 67 (ed. W. Stumm), Amer. Chem. Soc., Washington, DC, pp. 222–242

Gislason R. S. and Eugster H. P. (1987) Meteoric water-basalt interactions. I: A laboratory study. *Geochim. Cosmochim. Acta* **51**, 2827–2840.

Goldlich S. S. (1938) A study of Rock Weathering. *J. Geol.* **46**, 17–58.

Griffiths R. P., Baham J. E., and Caldwell B. A. (1994) Soil solution chemistry of ectomycorrhizal mats in forest soil. *Soil Biology and Biochemistry* **26**, 331–337.

Harden, J. W. (1987) Soils developed in granitic alluvium near Merced California. *U. S. Geologic Survey Bult.* **1590A** 104p.

Harrois L. and Moore J. M. (1988) The C. I. W. indices: a new chemical index of weathering. *Sediment. Geol.* **55**, 319–322.

Heimsath A. M., Chappell, J. Dietrich W. E., Nishiizumi K., and Finkel R. C. (2000) Soil production on a retreating escarpment in southeastern Australia. *Geology* **28**, 787–790.

Helgeson H. C. (1971) Kinetics of mass transfer among silicates and aqueous solutions. *Geochim. Cosmochim. Acta* **35**, 421–469.

Hillel D. (1982) *Introduction to Soil Physics*. Academic Press, Orlando.

Hodson M. E. (2002) Experimental evidence for the mobility of Zr and other trace elements in soils. *Geochim. Cosmochim. Acta* **66**, 819–828.

Hooper R. P., Christophersen N., and Peters N. E. (1990) Modeling stream water chemistry as a mixture of soil water end-members: an application to the Panola Mountain Catchment, Georgia, U.S.A. *J. of Hydrol.* **116**, 321–343.

Huh Y., Panteleyev G., Babich D., Zaitsev A., and Edmond J. (1998) The fluvial geochemistry of the rivers of Eastern Siberia: II. Tributaries of the Lena, Omloy, Yana, Indigirka, Kolyma, and Anadyr draining the collisional/accretionary zone of the Verkhoyansk and Cherskiy ranges. *Geochim. Cosmochim. Acta* **62**, 2053–2075.

Huntington T. G. (1995) Carbon sequestration in an aggrading forest ecosystem in the southern USA. *Soil Sci. Soc. Amer. J.* **59**, 1459–1467.

Jenny H. (1941) *Factors of soil formation*. McGraw-Hill, New York.

Johnsson M. J., Ellen S. D., and McKittrick M. A. (1993) Intensity and duration of chemical weathering: an example from soil clays of the southeastern Koolau Mountains, Oahu, Hawaii. *Geol. Soc. Am. Spec. Pub.* **284**, 147–170.

Jongmans A. G., Van Breeman N., Lundstrom U., van Hess P. A. W., Srinivason M., Unestam T., Giesle R., Melkerud P. A., and Olsson M. (1997) Rock-eating fungi. *Nature* **389**, 682–683.

Katz B. G., Bricker O. P., and Kennedy M. M. (1985) Geochemical mass-balance relationships for selected ions in precipitation and stream water, Catoctin Mountains, Maryland. *Am. J. Sci.* **285**, 931–962.

Katz B. G. (1989) Influence of mineral weathering reactions on the chemical composition of soil water, springs, and groundwater, Catoctin Mountains, Maryland. *Hydrol. Process.* **3**, 185–202.

Keating, E. H. and Bahr, J. M. (1998) Using reactive solutes to constrain groundwater flow models at a site in northern Wisconsin. *Water Resour. Res.* **34**, 3561–3571.

Kelly E. F., Chadwick O. A., and Hilinski T. E. (1998) The effect of plants on mineral weathering. *Biogeochemistry* **42**, 21–53.

Kenoyer G. J. and Bowser C. J. (1992a) Groundwater evolution in a sandy silicate aquifer in Northern Wisconsin 1. Patterns and rates of change. *Water Resour. Res.* **28**, 579–589.

Kenoyer G. J. and Bowser C. J. (1992b) Groundwater chemical evolution in a sandy silicate aquifer in Northern Wisconsin 2. Reaction modeling. *Water Resour. Res.* **28**, 591–600.

Kieffer B., Jove C. F., Oelkers E. H. and Schott J. (1999) An experimental study for the reactive surface area of the Fontainebleau sandstone as a function of porosity, permeability, and fluid flow rate. *Geochim. Cosmochim. Acta* **63**, 3525–3534.

Kim K. (2002) Plagioclase weathering in the groundwater system of a sandy silicate aquifer. *Hydro. Process* **16**, 1793–1806.

Kirkwood S. E. and Nesbitt H. W. (1991) Formation and evolution of soils from an acidified watershed: Plastic Lake, Ontario, Canada. *Geochim. Cosmochim. Acta* **55**, 1295–1308.

Kubicki J. (2007) Transiiton state theory and molecular orbital calculations applied to rates and reaction mechanisms in geochemical kineitics. In *Kinetics of Geochemical Systems* (ed. S. F. Brantley, J. Kubiciki, and A. F. White).Springer Publishing, New York.

Kurtz A. C., Derry L. A., and Chadwick O. A. (2002) Germanium-silicon fractionation in the weathering environment. *Geochim. Cosmochim. Acta* **66**, 1525–1537.

Lasaga A. C. (1984) Chemical kinetics of water-rock interaction. *J. Geophys. Res.* **89**, 4009–4025.

Land M., Ingri J., and Ohlander B. (1999) Past and present weathering rates in northern Sweden. *Appl. Geochem.* **14**, 761–774.

Lee M. R., Hodson M. E., and Parsons I. (1998) The role of intragranular microtextures and microstructures in chemical and mechanical weathering: direct comparisons of experimentally and naturally weathered alkali feldspars. *Geochim. Cosmochim. Acta*, **62**, 2771–2788.

Lerman A. and Wu L. (2007) Kinetics of global geochemical cycles. In *Kinetics of Geochemical Systems* (ed. S. L. Brantley, J. Kubicki, and A. F. White), Springer Publications, New York.

Likens G. E., Bormann F. H., Pierce R. S., Eaton J. S., and Johnson N. M. (1977) *Biogeochemistry of a Forested Ecosystem*. Springer-Verlag, Heidelberg.

Louvat P. and Allegre C. J. (1998) Factors controlling present weathering rates: new contributions from basalt erosion studies. *Mineral. Magazine* **62A**, 907–908.

Lucas Y. (2001) The role of plants in weathering. *Ann. Rev. Earth Planet. Sci.* **29**, 135–163.

Luttge A. B. and Lasaga, A.C. (1999) An interferometric study of the dissolution kinetics of anorthite: the role of reactive surface area. *Am. J. Sci.* **299**, 652–678.

Luttge A. and Arvidson R. S. (2007) The mineral-water interface. In *Kinetics of Geochemical Systems* (ed. S. L. Brantley, J. Kubicki, and A. F. White), Springer Publications, New York.

Maher K., DePaolo D. J. and Lin J. C. (2004) Rates of silicate dissolution in deep sea sediment: in situ measurment using $^{234}U/^{238}U$ of pore fluids. *Geochim. Cosmochim. Acta* **68**, 4629–4648.

Mast M. A., Drever J. I., and Barron J. (1990) Chemical weathering in the Loch Vale watershed, Rocky Mountain National Park, Colorado. *Water Resour. Res.* **26**, 2971–2978.

Maurice P., Forsythe J., Hersman L., and Sposito G. (1996) Application of atomic-force microscopy to studies of microbial interactions with hydrous Fe(III)-oxides. *Chem. Geol.* **132**, 33–43.

McDowell W. H. and Asbury C. E. (1994) Export of carbon, nitrogen, and major ions from three tropical montane watersheds. *Limnol. Oceanogr.* **39**, 111–125.

Merrill G. P. (1906) *A Treatise on Rocks, Rock Weathering and Soils*. MacMillian, New York.

Meyback M. (1994) *Material Fluxes on the Surface of the Earth*. National Academy of Sciences, Academy Press, New York.

Millot R., Gaillardet J., Dupre B., and Allegre C. J. (2002) The global control of silicate weathering rates and the coupling of physical erosion: new insights from rivers of the Canadian Shield. *Earth Planet. Lett*. **196**, 83–98.

Misra K. C. (2000) *Understanding Mineral Deposits*. Kluwer Academic Publishers, New York.

Mogk D. W. and Locke W. W. I. (1988) Application of auger electron spectroscopy (AES) to naturally weathered hornblende. *Geochim. Cosmochim. Acta* **52**, 2537–2542.

Murphy S. F., Brantley S. L., Blum A. E., White A. F., and Dong H. (1998) Chemical weathering in a tropical watershed, Luquillo Mountains, Puerto Rico. II Rate and mechanism of biotite weathering. *Geochim. Cosmochim. Acta* **62**, 227–243.

Nagy K. L., Blum A. E., and Lasaga A. C. (1991) Dissolution and precipitation kinetics of kaolinite at 80° C and pH 3. The dependence on the saturation state. *Am. J. Sci.* **291**, 649–686.

Negrel P., Allegre C. J., Dupre B., and Lewin E. (1993) Erosion sources determined by inversion of major and trace element ratios and strontium isotopic ratios in river water: the Congo basin case. *Earth Planet. Sci. Lett.* **120**, 59–76.

Nesbitt H. W., Young G. M., McLennan S. M., and Keys R. R. (1996) Effects of chemical weathering and sorting on the petrogenesis of siliciclastic sediments, with implications for provenance studies. *J. Geol.* **104**, 525–542.

Nesbitt H. W., Fedo C. M., and Young G. M. (1997) Quartz and feldspar stability, steady and non-steady state weathering and petrogenesis of siliciclastic sands and muds. *J. Geol.* **105**, 173–191.

Nugent M. A., Brantley S. L., Pantano C. G., and Maurice P. A. (1998) The influence of natural mineral coatings on feldspar weathering. *Nature* **396**, 527–622.

O'Brien A. K., Rice K. C., Bricker O. P., Kennedy M. M., and Anderson R. T. (1997) Use of geochemical mass balance modeling to evaluate the role of weathering in

determining stream chemistry in five mid-Atlantic watersheds of different lithologies. *Hydrol. Process.* **11**, 719–744.

Oelkers E. H. and Schott J. (1995) Experimental study of anorthite dissolution and the relative mechanism of feldspar hydrolysis. *Geochim. Cosmochim. Acta* **59**, 5039–5053.

Oelkers E. H. (2001) General kinetic description of multioxide silicate mineral and glass dissolution. *Geochim. Cosmochim. Acta* **65**, 3703–3719.

Oliva P., Viers J., and Dupre B. (2003) Chemical weathering in a granitic environment. *Chem. Geol.* **202**, 225–256.

Paces T. (1973) Steady-state kinetics and equilibrium between groundwater and granitic rock. *Geochim. Cosmochim. Acta* **37**, 2641–2663.

Paces T. (1986) Rates of weathering and erosion derived from mass balance in small drainage basins. In *Rates of Chemical Weathering of Rocks and Minerals* (ed. D. Dethier and S. Coleman) Academic Press, Orlando, pp. 531–550.

Parker A. (1970) An index of weathering for silicate rocks. *Geol. Magazine* **107**, 501–505.

Parkhurst D. L. and Plummer L. N. (1993) Geochemical models. In *Regional Ground-Water Quality* (ed. W. M. Alley), Van Nostrand Reinhold, New York, pp. 199–225.

Pavich M. J. (1986) Processes and rates of saprolite production and erosion on a foliated granitic rock of the Virginia Piedmont. In *Rates of Chemical Weathering of Rocks and Minerals* (ed. S. M. Dethier and D. P. Coleman), Academic Press. Orlando, pp. 551–590.

Perg L. A., Anderson R. S., and Finkel R. C. (2001) Use of a new ^{10}Be and ^{26}Al inventory method to date marine terraces, Santa Cruz, California, USA. *Geology* **29**, 879–882.

Plummer L., Prestemon E. C., and Parkhurst D. L. (1991) An interactive code (NETPATH) for modeling NET geochemical reactions along a flow path. Water Resoures Investigation Report 91–4078, 227p.

Plummer L. N., Prestemom E. C., and Parkhurst D. L. (1994) An interactive code (NETPATH) for modeling NET geochemical reactions along a flow path. U. S. Geological Survey Open File Report 94–4169, 191p.

Plummer L. N., Michel R. L., Turman, M. and Gyynn P. D. (1996) Environmental traces for age dating young ground water. In *Regional Ground-Water Quality* (ed. W. M. Alley), Van Nostrand Reinhold, New York, pp. 255–296.

Price J. and Velbel M. A. (2003) Chemical weathering indices applied to weathering profiles developed on heterogeneous felsic metamorphic parent rocks. *Chem. Geol.* **196**, 397–416.

Rademacher L. K., Clark J. F., Hudson G. B., Erman D. C., and Erman N. A. (2001) Chemical evolution of shallow groundwater as recorded by springs, Sagehen basin, Nevada County, California. *Chem. Geol.* **179**, 37–51.

Rice K. C. and Bricker O. P. (1995) Seasonal cycles of dissolved constituents in the streamwater in two forested catchments in the mid-Atlantic region of the eastern USA. *J. Hydrol.* **170**, 137–158.

Rice K. C. and Hornberger G. M. (1998) Comparison of hydrochemical tracers to estimate source contributions to peak flow in a small forested headwater catchment. *Water Resour. Res.* **34**, 1755–1766.

Riebe C. S., Kirchner J. K., Granger D. E., and Finkel R. C. (2001) Strong tectonic and weak climate control of long-term weathering rates. *Geology* **29**, 511–514.

Riebe C. S., Kirchner J. K., and Finkel R. C. (2003) Long-term rates of chemical weathering and physical erosion from cosmogenic nuclides and geochemical mass balance. *Geochim. Cosmochim. Acta* **67**, 441–4427.

Ruddiman W. F. (1997) *Tectonic Uplift and Climate Change*. Plenum Press, New York.

Rodden E. (2007) Microbial controls of geokinetics. In *Kinetics of Geochemical Systems* (ed. S. F. Brantley, J. Kubiciki, and A. F. White).Springer Publishing, New York.

Ruxton B. P. (1968) Measures of the degree of chemical weathering of rocks. *J. Geol.* **76**, 518–527.

Samma J. C. (1986) *Ore Fields and Continental Weathering*. Van Nostrand, New York.

Schnoor J. L. (1990) Kinetics of chemical weathering: a comparsion of laboratory and field rates. In *Aquatic Chemical Kinetics* (ed. W. Stumm), John Wiley & Sons, New York, pp. 475–504.

Schulz M. S. and White A. F. (1999) Chemical weathering in a tropical watershed, Luquillo Mountains, Puerto Rico III: quartz dissolution rates. *Geochim. Cosmochim. Acta* **63**, 337–350.

Siegal D. and Pfannkuch H. O. (1984) Silicate dissolution influence on Filson Creek chemistry, northeastern Minnesota. *Geol. Soc Am. Bult.* **95**, 1444–1453.

Stallard R. F. (1995) Tectonic, environmental, and human aspects of weathering and erosion: a global review using a steady-state perspective. *Ann. Rev. Earth Planet. Sci.* **23**, 11–39.

Stallard R. F. and Edmond J. M. (1983) Geochemistry of the Amazon,: 2. The influence of geology and weathering environment on dissolved load. *J. Geophys. Res.* **88**, 9671–9688.

Stewart B. W., Capo R. C., and Chadwick O. A. (2001) Effects of rainfall on weathering rate, base cation provenance, and Sr isotope composition of Hawaiian soils. *Geochim. Cosmochim. Acta* **65**, 1087–1099.

Steefel C. (2007) Geochemical kinetics and transport. In *Kinetics of Geochemical Systems* (ed. S. F. Brantley, J. Kubiciki, and A. F. White). Springer Publishing, New York.

Stillings S. L., Drever J. I., Brantley S., Sun Y., and Oxburgh R. (1996) Rates of feldspar dissolution at pH 3–7 with 0–8 M oxalic acid. *Chem. Geol.* **132**, 79–89.

Stonestrom D. A., White A. F., and Akstin K. C. (1998) Determining rates of chemical weathering in soils-solute transport versus profile evolution. *J. Hydrol.* **209**, 331–345.

Sverdrup H. and Warfvinge P. (1995) Estimating field weathering rates using laboratory kinetics. In *Chemical Weathering Rates of Silicate Minerals* (ed. A. F.

White and S. L. Brantley) Reviews in Mineralogy, Vol. 31, Mineralogical Society of. America, Washington, DC, pp. 485–539.

Swoboda-Colberg N. G. and Drever J. I. (1992) Mineral dissolution rates: a comparison of laboratory and field studies. In *Proceedings of the 7th International Symposium. Water-Rock Interaction* (ed. Y. K. Kharaka and A. S. Maest). Balkema, Leiden, pp. 115–117.

Taylor A. S., Blum J. D., and Lasaga A. C. (2000) The dependence of labradorite dissolution and Sr isotope release rates on solution saturation state. *Geochim. Cosmochim. Acta* **64**, 2389–2400.

Tisdall J. M. (1982) Organic matter and water-stable aggregates in soils. *J. Soil Sci.* **33**, 141–163.

Trudgill S. T. (1995) *Solute Modelling in Catchment Systems*. John Wiley & Sons, New York.

Turner B. F., Stallard R. F., and Brantley S. L. (2003) Investigation of in situ weathering of quartz diorite in the Rio Icacos basin, Luquillo Experimental Forest, Puerto Rico. *Chem. Geol.* **202**, 313–341.

Van Breemen N., Lundstrom U., Jongmans A. G., Gieler R., and Olsson M. (2000) Mycorrrhizal weathering: a true case of mineral plant nutrition? *Biogeochemistry* **49**, 53–67.

Velbel M. A. (1985) Geochemical mass balances and weathering rates in forested watersheds of the southern Blue Ridge. *Am. J. Sci.* **285**, 904–930.

Velbel M. A. (1986) The mathematical basis for determining rates of geochemical and geomorphic processes in small forested watersheds by mass balance: examples and impilications. In *Rates of Chemical Weathering of Rocks and Minerals* (ed. S. M. Colman and D. P. Dethier), Academic Press, Orlando, pp. 439–449.

Velbel M. C. (1993) Temperature dependence of silicate weathering in nature: how strong a feedback on long-term accumulation of atmospheric CO2 and global greenhouse warming. *Geology* **21**, 1059–1062.

Velbel M. C. (1996) Interaction of ecosystem processes and weathering processes. In *Solute Modeling in Catchment Systems* (ed. S. T. Trudgill) John Wiley & Sons, New York, pp. 193–209.

Von Blanckenburg, F. (2006) The control mechanisms of erosion and weathering at basin scale from cosmogenic nuclides in river sediment. *Earth Planet. Sci.* **242**, 224–239.

Walker J. F., Hunt R. L., Bullen T. D., Krabbenhoft D. P., and Kendall C. (2003) Variability of isotope and major ion chemistry in the Allequash Basin, Wisconsin. *Groundwater* **41**, 883–894.

White A. F. (1995) Chemical weathering rates in soils. In *Chemical Weathering Rates of Silicate Minerals*, Vol. 31 (ed. A. F. White and S. L. Brantley), Reviews in Mineralogy, Vol. 31, Mineralogical Society of America, Washington, DC, pp. 407–458.

White A. F. and Peterson M. L. (1990) Role of reactive surface area characterization in geochemical models. In *Chemical Modeling of Aqueous Systems II*, Vol. 416 (ed. R. D. Basset and R. L. Melchior). American Chemical Society. Advances in Chemistry Series **213**, pp. 461–475.

White A. F. and Blum A. E. (1995) Effects of climate on chemical weathering rates in watersheds. *Geochim. Cosmochim. Acta* **59**, 1729–1747.

White A. F. and Brantley S. L. (2003) The effect of time on the weathering of silicate minerals: why to weathering rates differ in the laboratory and field? *Chem. Geol.* **190**, 69–89.

White A. F., Blum A. E., Schulz M. S., Bullen T. D., Harden J. W., and Peterson M. L. (1996) Chemical weathering of a soil chronosequence on granitic alluvium 1. Reaction rates based on changes in soil mineralogy. *Geochim. Cosmochim. Acta* **60**, 2533–2550.

White A. F., Blum A. E., Schulz M. S., Vivit D. V., Larsen M., and Murphy S. F. (1998) Chemical weathering in a tropical watershed, Luquillo Mountains, Puerto Rico: I. Long-term versus short-term chemical fluxes. *Geochem. Cosmochim. Acta* **62**, 209–226.

White A. F., Blum A. E., Bullen T. D., Vivit D. V., Schulz M., and Fitzpatrick J. (1999a) The effect of temperature on experimental and natural weathering rates of granitoid rocks. *Geochim. Cosmochim. Acta* **63**, 3277–3291.

White A. F., Bullen T. D., Vivit D. V., and Schulz M. S. (1999b) The role of disseminated calcite in the chemical weathering of granitoid rocks. *Geochim. Cosmochim. Acta* **63**, 1939–1953.

White A. F., Blum A. E., Stonestrom D. A., Bullen T. D., Schulz M. S., Huntington T. G., and Peters N. E. (2001) Differential rates of feldspar weathering in granitic regoliths. *Geochim. Cosmochim. Acta* **65**, 847–869.

White A. F., Blum A. E., Schulz M. S., Huntington T. G., Peters N. E., and Stonestrom D. A. (2002) Chemical weathering of the Panola Granite: solute and regolith elemental fluxes and the dissolution rate of biotite. In *Water-rock Interaction, Ore Deposits, and Environmental Geochemistry: A tribute to David A. Crerar* (ed. R. Hellmann and S. A. Wood) The Geochemical Society. Special Publ. no. 7, pp. 37–59.

White A. F, Schulz M. S., Lowenstern J. B., Vivit D. V., and Bullen T. D. (2005) The ubiquitous nature of accessory calcite in granitoid rocks: implications for weathering, solute evolution and petrogensis. *Geochim. Cosmochim. Acta* **69**, 1455–1471

White A. F., Schulz M. S., Vivit D. V., Blum A. E., Stonestrom D. A., and Anderson S. P. (2007) Chemical weathering of a marine terrace chronosequence, Santa Cruz, California: what does element and mineral soil profiles tell us about weathering environments and reaction rates? *Geochim. Cosmochim. Acta* (in press).

Zeman L. J. and Slaymaker O. (1978) Mass balance model for calculation of ionic input loads in atmospheric fallout and discharge from a mountainous basin. *Hydrol. Sci.* **23**, 103–117.

Zhu C. (2005) In situ feldspar dissolution in an aquifer. *Geochim. Cosmochim. Acta* **69**, 847–869.

Chapter 11
Geochemical Kinetics and Transport

Carl I. Steefel

11.1 Introduction

The kinetics of geochemical and biogeochemical processes can be studied in isolation in the laboratory, but only rarely is it possible to separate these processes from those of transport when considering their importance in natural systems at the field scale. This is because the driving force for most reactions of interest in water–rock interaction is transport. The most intense geochemical and biogeochemical activity occurs at the interface between global compartments like the oceans, the atmosphere, and the Earth's crust where elemental and nutrient fluxes provide the maximum driving force for reactions to take place. The important role of transport in these settings makes it critical to consider these time-dependent processes in conjunction with those processes we think of as more purely biogeochemical. In other words, these global interfaces are *open systems*, where both mass and energy transfers must be accounted for.

For the sake of convenience, geochemical and biogeochemical kinetics are often studied in closed systems in the laboratory, but it is important to keep in mind how different the closed systems can be from open systems. In a closed system, the best analogue of which is the batch reactor in the laboratory (in its simplest form, just a laboratory beaker, Fig. 11.1a), the solution begins out of equilibrium initially and evolves over time towards either thermodynamic equilibrium, or to some other end point beyond which the reaction cannot proceed. Either equilibrium is achieved (where net reaction rates are, by definition, $= 0$), or rates become so slow that the system effectively no longer changes. In an open system, a good laboratory analogue of which is the continuously stirred tank reactor (CSTR) or well-mixed flowthrough reactor (Fig. 11.1b), the continuous injection of solution that is out of equilibrium (either with itself, or with a solid phase inside the reactor) causes the solution composition coming out of the reactor to reach a

Lawrence Berkeley National Laboratory, Earth Sciences Division, CISteefel@lbl.gov Aug 7, 2007

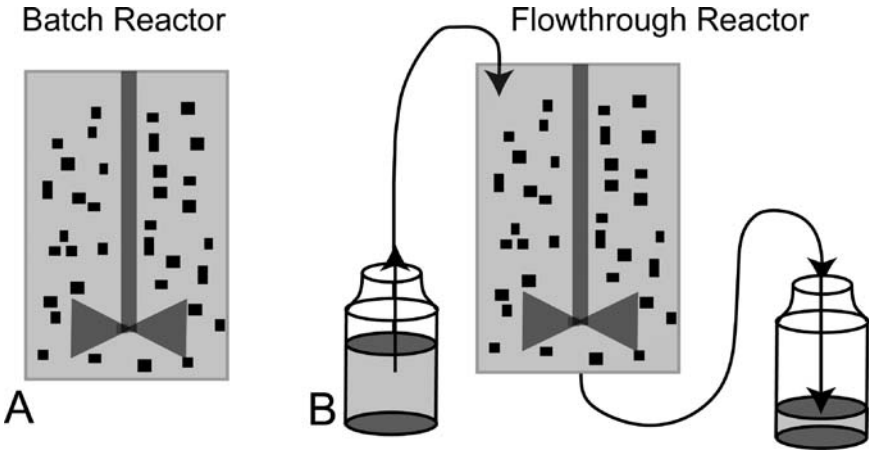

Fig. 11.1 Contrast between closed and open system behavior: **a**. In a laboratory batch reactor, the solution evolves from some initial state to a final equilibrium state, or one where the driving force for reaction disappears. **b**. In a continuously stirred tank reactor, the continuous injection of solution out of equilibrium with respect to the solid phases in the reactor results in steady-state conditions where solution and solids may remain out of equilibrium

steady state (Fig. 11.1b). If the residence time in the CSTR is long enough, equilibrium between the solution and solid phase may be achieved—otherwise, the solution and solid phase may remain some distance from equilibrium at steady state.

The characteristic residence and reaction times can be more formally compared in the case of a CSTR with a set of simple equations. Considering a dissolved species, we can define:

t = time (s)
M = mass of solute (g)
Q = volumetric flow rate (cm^3/s)
V = volume of reactor (cm^3)
C = concentration of solute (g/cm^3)
R = reaction rate (g/s),

where the concentration, volumetric flow rate, and reaction rate are defined respectively by

$$C = \frac{M}{V}, Q = \frac{V}{t}, \quad \text{and} \quad R = \frac{M}{t}. \tag{11.1}$$

The volumetric flow rate Q, therefore, can be thought of simply as the volume of fluid flowing through the reactor for a given time t. A mass balance equation for this system must account for the accumulation or loss of mass of the solute inside the reactor, the flux of the solute into and out of the reactor, and the loss or gain of the solute in the aqueous phase as a result of reaction (e.g., precipitation or dissolution).

The flux (mass per unit time) into the reactor is given by

$$J_{in} = \left[\frac{M}{V}\right]_{in}\left[\frac{V}{t}\right]_{in} = C_{in}Q_{in}, \tag{11.2}$$

while the flux out is given similarly by

$$J_{out} = \left[\frac{M}{V}\right]_{out}\left[\frac{V}{t}\right]_{out} = C_{out}Q_{out}, \tag{11.3}$$

leading to an overall mass balance for the aqueous phase in the reactor of

$$\frac{\mathrm{d}M}{\mathrm{d}t} = J_{in} - J_{out} - R = C_{in}Q_{in} - C_{out}Q_{out} - R, \tag{11.4}$$

where by convention R is taken as positive for precipitation, negative for dissolution. If the reaction rate is written as a first-order reaction with a rate k in units of s^{-1}

$$R = kCV, \tag{11.5}$$

then at steady state $(\mathrm{d}M/\mathrm{d}t = 0)$ the reaction rate is equal to the difference between the flux in and the flux out of the reactor (i.e., the divergence of the flux)

$$R = kC_{out}V = C_{in}Q_{in} - C_{out}Q_{out}. \tag{11.6}$$

Assuming the flow in the reactor is steady (so $Q_{in} = Q_{out}$) and defining the residence time (or characteristic transport time) as

$$\tau_{res} = \frac{V}{Q}. \tag{11.7}$$

The characteristic time for reaction, τ_{react}, is given by

$$\tau_{react} = \frac{1}{k}. \tag{11.8}$$

The ratio of the characteristic residence and reaction times, then, is given by

$$\frac{\tau_{res}}{\tau_{react}} = \frac{kV}{Q} = \frac{(C_{in} - C_{out})}{C_{out}}. \tag{11.9}$$

In the case where the reactions drive the system towards some equilibrium state, it is clear that the approach to equilibrium has nothing to do with geologic time, but is controlled by the ratio of the characteristic residence (or transport) time and reaction time in the reactor.

11.2 Transport Processes

The continuously stirred tank reactor provides perhaps the simplest example where rates of transport can be compared to rates of reaction. But in porous and/or fractured media, reactions can be driven by a variety of transport processes. The most important of these transport processes are advection, molecular diffusion, and mechanical dispersion. Although widely neglected, electrochemical migration is a flux created by the diffusion of charged species at differing rates which may be important in some cases. Below, these transport processes are defined mathematically in terms of fluxes, that is, the amount of solute passing through a unit area per unit time.

11.2.1 Advection

Advection is the most straightforward of the transport processes, since it involves the translation in space of dissolved or suspended material at the rate of movement of the bulk fluid phase. No modification of the shape of a front and no dilution occurs when transport is purely via advection—a sharp front remains so when undergoing purely advective transport. The advective flux of a dissolved species in porous media can be described mathematically as

$$J_{adv} = \phi v C_i, \tag{11.10}$$

where ϕ is the porosity, v is the average linear velocity in the media, and C_i is the concentration of the ith species. In most (but not all) examples of water–rock interaction, flow is through a porous medium and is described with Darcy's Law.

11.2.1.1 Darcy's Law

The fluid velocity in porous and fractured media is usually calculated from Darcy's Law, which states that the volumetric flux of water ($\mathrm{m}^3_{\mathrm{fluid}}/\mathrm{m}^2_{\mathrm{medium}}/\mathrm{s}$), $\mathbf{q}$, is a vector proportional to the gradient in the hydraulic head, h

$$\mathbf{q} = \phi \mathbf{v} = -\mathbf{K}\nabla h = -K_x \frac{\partial h}{\partial x} - K_y \frac{\partial h}{\partial y} - K_z \frac{\partial h}{\partial z}, \tag{11.11}$$

where $\mathbf{K}$ is the hydraulic conductivity (here a second-order tensor) in units of m/s (Darcy, 1856). One can also write Darcy's Law in terms of fluid pressure by defining the hydraulic head as

$$h = z + \frac{P}{\rho g}, \tag{11.12}$$

Table 11.1 Range of values of hydraulic conductivity and permeability (Modified from Bear, 1972. Additional information from Wikipedia, 2006)

K (cm/s)	10^{2}	10^{1}	10^{0}	10^{-1}	10^{-2}	10^{-3}	10^{-4}	10^{-5}	10^{-6}	10^{-7}	10^{-8}	10^{-9}	10^{-10}
K (cm^2)	10^{-3}	10^{-4}	10^{-5}	10^{-6}	10^{-7}	10^{-8}	10^{-9}	10^{-10}	10^{-11}	10^{-12}	10^{-13}	10^{-14}	10^{-15}
Unconsolidated sand gravel	Clean gravel		Clean sand or sand and gravel			Very fine sand, silt, loess, loam							
Unconsolidated clay and organic					Peat		Stratified clay			Unweathered clay			
Consolidated rocks	Highly fractured rocks				Oil reservoir rocks			Sandstone		Limestone		Granite	

where z is the depth, P is the fluid pressure, ρ is the fluid density, and g is the acceleration due to gravity. The hydraulic conductivity is defined as

$$\mathbf{K} = \frac{\kappa \rho g}{\mu}, \tag{11.13}$$

where κ is the permeability and μ is the dynamic viscosity. One can also write Darcy's law explicitly in terms of the fluid pressure, permeability, and the viscosity

$$\mathbf{q} = \phi \mathbf{v} = -\frac{\kappa_{\mathrm{r}} \kappa}{\mu} \left[\nabla P - \rho \mathbf{g}\right]. \tag{11.14}$$

In this case, we have also added the relative permeability, κ_{r}, which is equal to 1 under fully saturated conditions and is less than 1 under partially saturated conditions. Darcy's Law is applied where the porous medium can be treated as a continuum in which a representative elementary volume (REV) is significantly larger than the average grain size. In the case of flow at the pore-scale, the averaging does not apply and Darcy's Law cannot be used. Representative values of the hydraulic conductivity (or permeability) are given in Table 11.1 for various subsurface materials.

11.2.2 Molecular Diffusion

Molecular diffusion as a transport process in water–rock interaction has been relatively neglected. This may be partly due to the fact that much of the transport theory has been brought over from hydrogeology, where the medium of interest is often relatively permeable aquifers in which advection is much more important than diffusion. In water–rock interaction, however, we are often concerned with transport through low porosity and permeability material, in which case molecular diffusion needs to be considered carefully. The treatment of molecular diffusion has also suffered to some extent from the assumption that Fick's First Law (described below) is sufficient, but as shown below, this is *true only in the case of diffusion of uncharged species in dilute solutions*. A more general formulation relates the diffusive flux linearly to gradients in the *chemical potential rather than concentration*, but we

begin with the simpler Fickian description of diffusion so as to follow its historical presentation.

11.2.2.1 Fick's First Law

Molecular diffusion is usually described in terms of Fick's First Law, which states that the diffusive flux (here shown for only a single coordinate direction x) is proportional to the concentration gradient

$$J_i = -D_i \frac{\partial C_i}{\partial x}. \tag{11.15}$$

D_i is referred to as the diffusion coefficient and is specific to the chemical component considered as indicated by the subscript i. Fick's First Law is a phenomenological theory for diffusion that relates diffusion to the "driving force" provided by the concentration gradient, although it can also be derived atomistically (Lasaga, 1998). In the case of diffusion in porous media, it is normally necessary to include a tortuosity correction as well (see Sect. 9.2.2.5). Values of diffusion coefficients for selected ion at infinite dilution in water at 25° C are given in Table 11.2.

Table 11.2 Tracer diffusion coefficients of ions at infinite dilution in water at 25° C. (Modified from Lasaga, 1998)

Cation	$D_i \times 10^5$ cm^2/s	Anion	$D_i \times 10^5$ cm^2/s
H^+	9.31	OH^-	5.27
Li^+	1.03	F^-	1.46
Na^+	1.33	Cl^-	2.03
K^+	1.96	Br^-	2.01
Rb^+	2.06	I^-	2.00
Cs^+	2.07	IO_3^-	1.06
NH_4^+	1.98	HS^-	1.73
Ag^+	1.66	HSO_4^-	1.33
Mg^{2+}	0.705	NO_2^-	1.91
Ca^{2+}	0.793	NO_3^-	1.90
Sr^{2+}	0.794	HCO_3^-	1.18
Ba^{2+}	0.848	$H_2PO_4^-$	0.846
Mn^{2+}	0.688	$H_2AsO_4^-$	0.905
Fe^{2+}	0.719	$H_2SbO_4^-$	0.825
Co^{2+}	0.699	SO_4^{2-}	1.07
Ni^{2+}	0.679	SeO_4^{2-}	0.946
Cu^{2+}	0.733	CO_3^{2-}	0.955
Zn^{2+}	0.715	HPO_4^{2-}	0.734
Cd^{2+}	0.717	CrO_4^{2-}	1.12
Pb^{2+}	0.945	MoO_4^{2-}	0.991
UO_2^{2+}	0.426	PO_4^{3-}	0.612
Cr^{3+}	0.594		
Fe^{3+}	0.607		
Al^{3+}	0.559		

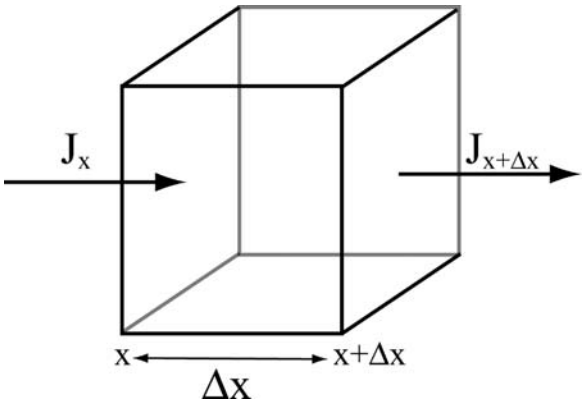

Fig. 11.2 Derivation of a continuity equation (Fick's Second Law)

11.2.2.2 Fick's Second Law

Integrating the diffusive fluxes over a control volume leads to Fick's Second Law, which is just one of many continuity equations in use (Bear, 1972; Lasaga, 1998). By defining the fluxes at the faces of an elemental volume as in Fig. 11.2 (here shown for only a single coordinate direction x) a general form of the continuity equation can be derived by considering the change in concentration inside an elemental volume for a given time increment (analogous to the flowthrough reactor described in Eq. (11.4)):

$$\frac{\mathrm{d}C}{\Delta t} = \frac{1}{\Delta x}\left[J_x - J_{x+\Delta x}\right] = -\frac{1}{\Delta x}\left[J_{x+\Delta x} - J_x\right]. \tag{11.16}$$

Written as a partial derivative as Δx and $\Delta t \rightarrow 0$, and substituting Fick's First Law (Eq. (11.15)), Eq. (11.16) becomes

$$\frac{\partial C_i}{\partial t} = -\frac{\partial}{\partial x}\left[J_i\right] = \frac{\partial}{\partial x}\left[D_i \frac{\partial C_i}{\partial x}\right], \tag{11.17}$$

which provides an expression for the change in concentration in terms of the divergence of the diffusive flux.

Integration of Eq. (11.17) provides a solution for the time and space evolution of the concentration field. This equation is quite straightforward to integrate numerically, but analytical solutions are also available, with the general form

$$C(x,t) = A + B\mathrm{erf}\left[\frac{x}{2\sqrt{Dt}}\right], \tag{11.18}$$

where A and B are constants that depend on the initial and boundary conditions. For the case where the initial mass is located between $-h$ and h, with concentrations

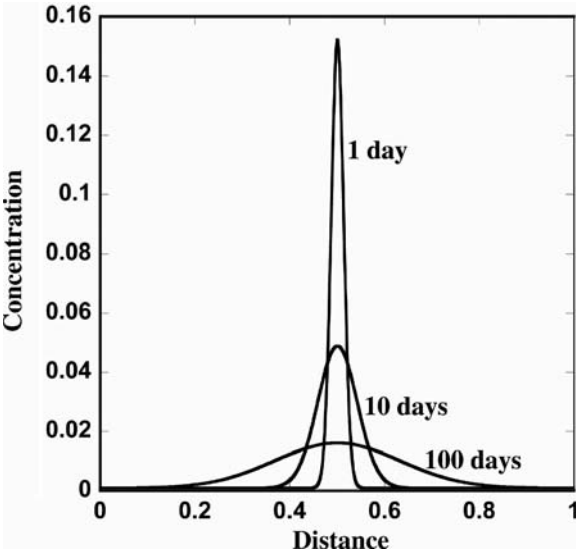

Fig. 11.3 Spreading of an initially sharp solute plume as a result of molecular diffusion

equal to zero elsewhere, the analytical solution is given by

$$C(x,t) = \frac{1}{2} C_0 \left[\text{erf}\left(\frac{x+h}{2\sqrt{Dt}} \right) - \text{erf}\left(\frac{x-h}{2\sqrt{Dt}} \right) \right], \tag{11.19}$$

where erf is the error function and C_0 is the initial concentration between -h and h (Lasaga, 1998). Figure 11.3 shows the evolution of such an initially narrow and sharp zone with time as a result of molecular diffusion.

11.2.2.3 Electrochemical Migration

Fick's First Law is strictly applicable only in the case of an infinitely dilute solution with uncharged chemical species. In electrochemical systems or systems containing charged species, it is also necessary to consider the process of electrochemical migration. Strictly speaking, this should be considered as a separate flux on the same level as advection and diffusion, but in most systems of interest in the Earth sciences, this effect is related to diffusion of charged species. The full expression for the migration of a charged species in an electric field (written again in terms of a single coordinate direction, x, for the sake of simplicity) is given by (Newman, 1991)

$$J_i^{migr} = -z_i u_i F C_i \frac{\partial \Phi}{\partial x}, \tag{11.20}$$

where z_i is the charge of the species, u_i is its mobility, F is Faraday's constant (= 96,487 C/equivalent), and Φ is the electrical potential. The mobility refers to the

average velocity of a species in solution acted upon by a unit force, independent of the origin of the force. The flux of charged species in an electric field gives rise to a current, which can be expressed as

$$i = F\sum_i z_i J_i, \tag{11.21}$$

where i is the current density in units of amperes per m^2. Expanding Eq. (11.21) in terms of the migration term (Eq. (11.20)) and the diffusive flux (Eq. (11.15)), the current density can be written as

$$i = -F^2\frac{\partial\Phi}{\partial x}\sum_i z_i^2 u_i C_i - F\sum_i z_i D_i\frac{\partial C_i}{\partial x}. \tag{11.22}$$

Where no concentration gradients are present, the current is given by the first term on the right hand side

$$i = -\kappa_e\frac{\partial\Phi}{\partial x} \tag{11.23}$$

where

$$\kappa_e = F^2\sum_i z_i^2 u_i C_i \tag{11.24}$$

is the conductivity of the solution. Note that using Eq. (11.24), it is possible to determine the mobility of an ion by measuring the conductivity of a solution. The mobility in turn can be used to determine the diffusion coefficient for an ion from the Nernst-Einstein equation (Lasaga, 1998; Newman, 1991)

$$D_i = RTu_i, \tag{11.25}$$

where R is the gas constant and T is the temperature on the Kelvin scale. Rearranging Eq. (11.22) to obtain an expression for the gradient in the electrical potential

$$\frac{\partial\Phi}{\partial x} = -\frac{i}{\kappa_e} - \frac{F}{\kappa_e}\sum_i z_i D_i\frac{\partial C_i}{\partial x}, \tag{11.26}$$

it is apparent that even in the absence of an electrical current, i, it is possible to have a gradient in the electrical potential as a result of concentration gradients of charged species. The second term on the right hand side of Eq. (11.26) is known as the diffusion potential, which vanishes when all of the diffusion coefficients for the charged species are the same. To proceed further, it is useful to define the fraction of the current carried by a species j (or the transference number)

$$t_j = \frac{z_j^2 u_j C_j}{\sum_i z_i^2 u_i C_i}, \tag{11.27}$$

which can be used along with the substitution of Eqs. (11.26) and (11.24) into Eq. (11.20) to obtain an expression for the migration flux

$$J_j^{migr} = \frac{t_j i}{z_j F} + \frac{t_j}{z_j} \sum z_i D_i \frac{\partial C_i}{\partial x}. \tag{11.28}$$

This equation (still only strictly applicable to relatively dilute solutions) can be used to describe the case where an electrical current is present (e.g., an electrochemical cell), although more commonly in water–rock interaction one encounters only the second term. It should be noted that even in the absence of a current, the diffusion of charged species are coupled through the diffusion potential in the case where diffusion coefficients differ (Newman, 1991).

In the absence of a current and advection, the total flux (combining Fickian diffusion and electrochemical migration) is then given by

$$J_i = -D_i \frac{\partial C_i}{\partial x} + \frac{t_j}{z_j} \sum z_i D_i \frac{\partial C_i}{\partial x}. \tag{11.29}$$

As noted above, the second term vanishes when all of the diffusion coefficients for the charged species are the same, but since this is in general not the case, this term should normally be retained along with the first term. Note also that the effect of electrochemical migration may be important (and perhaps even more important, as discussed below) in dilute systems.

Although widely neglected in quantitative studies of water–rock interaction, electrochemical migration has several important consequences. Inclusion of electrochemical migration prevents the unrealistic build up of charge in calculations using differing diffusivities for charged species. The typical way to avoid this problem in transport calculations is to use the same diffusion coefficient for all of the charged species, in which case the diffusion potential driving electrochemical migration disappears. However, this approach does not provide the same results as would a full treatment of electrochemical migration. An example illustrating some of the potential effects is shown in Fig. 11.4, where a fixed boundary condition on the left side is separated by 20 mm of 10% porosity material from a reacting feldspar (albite) grain. At 25° C, the dissolution rate of feldspar is sufficiently slow that concentration gradients will not develop (Murphy et al., 1989). At higher temperatures where the rate of surface reaction is more rapid, however, it is possible to develop diffusion-limited dissolution (the rate of surface reactions is significantly faster than the rate at which ions can diffuse across the 20 mm distance, and thus a gradient develops). Comparison of the full multicomponent diffusion and electrochemical migration calculation with one based on identical diffusion coefficients (no electrochemical migration) for all species indicates that conservative quantities like alkalinity need not have linear profiles where electrochemical migration is important. Comparing the two cases with identical albite dissolution rates, the concentrations of dissolved species next to the albite grain are not even the same. This is primarily due to the rapid diffusion of hydrogen ion, which results in a more nearly linear profile for pH

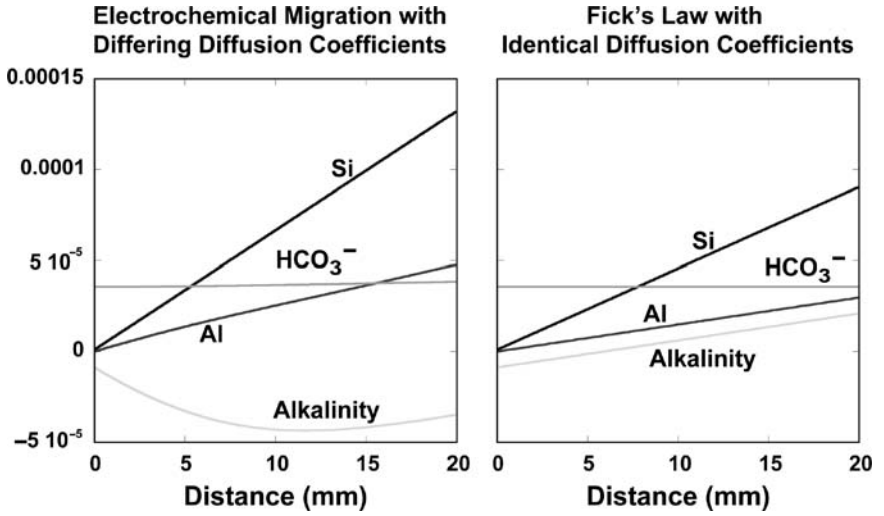

Fig. 11.4 Comparison of diffusion profiles in the case of a dilute, mildly acidic solution (pH 4) on the left reacting with an albite grain located 2 cm to the right. The left panel shows a calculation using differing diffusion coefficients for the ions (see Table 11.2) and includes electrochemical migration. The right panel shows a calculation in which identical diffusion coefficients for all species are used – in this case, electrochemical migration vanishes and diffusion occurs according to Fick's Law. Note the curvature of the alkalinity profile in the case where electrochemical migration and differing diffusion coefficients are used and the difference in concentrations of the various species immediately adjacent to the albite grain in the two cases

in the multicomponent diffusion/electrochemical migration case as compared to the identical diffusion coefficient case.

11.2.2.4 Diffusion in Concentrated Solutions

Ficks's First Law runs into additional difficulties in concentrated aqueous solutions. A more rigorous and general expression is given by

$$J_j^{diff} = -L_{ji}\frac{\partial \mu_j}{\partial x}, \tag{11.30}$$

where the L_{ij} are the phenomenological coefficients introduced in the theory of irreversible thermodynamics (Lasaga, 1998; Onsager, 1931; Prigogine, 1967) and μ_j is the chemical potential of the jth species. Here, the fluxes are linearly related to gradients in the chemical potentials of the solutes rather than to their concentrations as in Fick's Law. The phenomenological coefficients, L_{ij}, can be linked back to measurable quantities by making use of the mobility again as the "velocity" of a particle acted upon by a force, with the force in this case provided by the chemical

potential rather than the concentration

$$J_j^{diff} = -u_j C_j \frac{\partial \mu_j}{\partial x}. \tag{11.31}$$

In the case where a gradient in chemical potential rather than concentration is used, the migration flux (compare to Eq. (11.28) in the absence of a current) becomes

$$J_j^{migr} = \frac{t_j}{z_j} \sum_i z_i D_i \frac{\partial \mu_i}{\partial x}. \tag{11.32}$$

By writing the chemical potential as (Denbigh, 1981)

$$\mu_j = \mu_j^0 + RT \ln(\gamma_j C_j), \tag{11.33}$$

where γ_j is the activity coefficient for the species, and differentiating with respect to x, we obtain the following combined expression for the pure diffusive flux and electrochemical migration by making use again of the definition of the ion mobility (Eq. (11.25))

$$J_j = -D_j \frac{\partial C_j}{\partial x} - D_j C_j \frac{\partial \ln \gamma_j}{\partial x} + \frac{t_j}{z_j} \sum_i z_i D_i \frac{\partial C_i}{\partial x} + \frac{t_j}{z_j} \sum_i z_i D_i \frac{\partial \gamma_i}{\partial x}. \tag{11.34}$$

This more general expression, which reduces to Eq. (11.29) where gradients in activity coefficients are negligible (for example, for diffusion of a trace species in a strong electrolyte), makes clear that both the diffusive and electrochemical migration fluxes can depend on the activity coefficients for the species. If gradients in one or more activity coefficients are negative, it is possible for "uphill diffusion", in which a species diffuses up its own concentration gradient, to occur (Lasaga, 1998).

11.2.2.5 Tortuosity

Since water–rock interaction commonly takes place in porous materials, it is important to account for the effect of tortuosity (Fig. 11.5), which is defined as the ratio of the path length the solute would follow in water alone, L, relative to the tortuous path length it would follow in porous media, L_e (Bear, 1972)

$$T_L = (L/L_e)^2. \tag{11.35}$$

In this definition of tortuosity (sometimes the inverse of Eq. (11.35) is used), its value is always < 1 and the effective diffusion coefficient in porous media is obtained by multiplying the tortuosity by the diffusion coefficient for the solute in pure water. With this formulation, the diffusion coefficient in porous media is given by

$$D_i^* = T_L D_i. \tag{11.36}$$

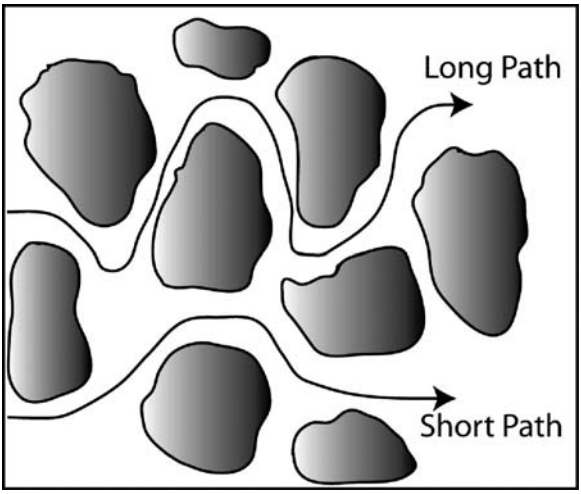

Fig. 11.5 Tortuous diffusion paths in porous material

The diffusive flux, then, is given by

$$J_i^{diff} = -\phi D_i T_L \frac{\partial C_i}{\partial x} = -\phi D_i^* \frac{\partial C_i}{\partial x}. \tag{11.37}$$

An alternative formulation for the coefficient for molecular diffusion in porous media is given by the formation factor, F, defined as (Bear, 1972)

$$F = (L_e/L)^2/\phi = 1/\phi T_L, \tag{11.38}$$

in which case the diffusive flux in porous media becomes

$$J_i^{diff} = -\frac{D_i}{F}\frac{\partial C_i}{\partial x}. \tag{11.39}$$

Various approaches for calculating formation factors (and thus, the diffusion coefficient in porous medium) are in use, with a formulation based on Archie's Law being the most common

$$F = \frac{1}{a\phi^m}, \tag{11.40}$$

where a is a fitted constant and m is the cementation exponent. Values of a $= 0.71$ and m $= 1.57$ have been suggested for unfractured granite (Pharmamenko, 1967), although values of m $= 2$ have been reported for many more porous and permeable subsurface materials (Oelkers, 1996). Values for the formation factor in igneous intrusive rock in Sweden range from 10^3 to 10^7 (Skagius and Neretnieks, 1986). In the case of low porosity materials, especially those with poor pore connectivity, the formation factor may be quite large (and thus, the diffusion coefficient in porous

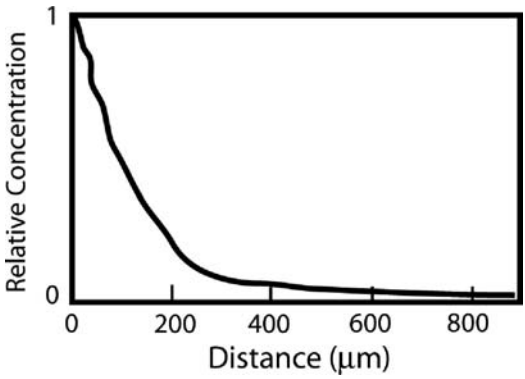

Fig. 11.6 Profile of bromide front in low porosity (3%–5%) basalt after 35 days as imaged with μ-X-ray fluorescence at the Advanced Light Source at the Lawrence Berkeley National Laboratory. Numerical modeling to match the diffusion profile indicated a formation factor of approximately 2×10^6. Sample courtesy of Alexis Navarre-Sitchler

media quite small). Values as high as 2×10^6 were determined using μ-X-ray fluorescence mapping of bromide tracer fronts in low porosity (3%–5%) basalt from Costa Rica at the Advanced Light Source at the Lawrence Berkeley National Laboratory (Fig. 11.6). Such an extremely low formation factor, combined with an only moderately low porosity, suggests the use of a percolation/diffusion threshold model in place of Archie's Law.

11.2.3 Hydrodynamic Dispersion

The phenomenon of hydrodynamic dispersion was noted as early as 1905 when Slichter reported that the concentration of an electrolyte monitored in an aquifer downstream of an injection point increased only gradually, with the plume shape becoming longer and wider as it advanced (Slichter, 1905). The spreading of the solute mass as a result of dispersion is a diffusion-like process that has led to the use of Fick's First Law to describe the process in one dimension as

$$J_i^{disp} = -D_h \frac{\partial C_i}{\partial x}, \tag{11.41}$$

where D_h is the hydrodynamic dispersion coefficient. The coefficient of hydrodynamic dispersion is defined as the sum of molecular diffusion and mechanical dispersion, since these effects are not separable where flow is involved (Bear, 1972)

$$D_h = D^* + D. \tag{11.42}$$

11.2.3.1 Mechanical Dispersion

Mechanical dispersion is a result of the fact that variations in the flow velocities exist, even where an average flow rate (as in Darcy's Law) can be defined for a particular representative elementary volume (REV). If all the detailed flow paths could

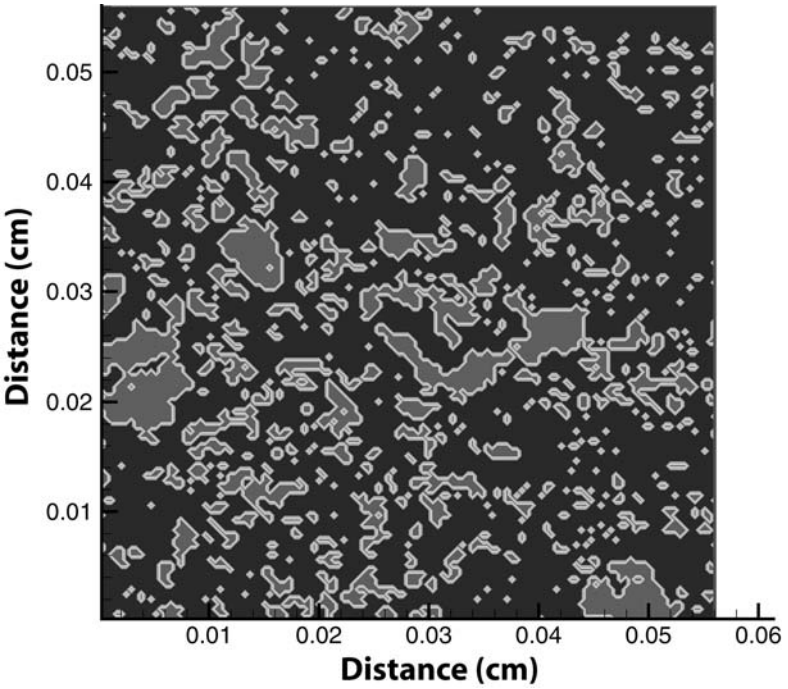

Fig. 11.7 Microtomographic image of micron-scale pores (red in color, gray in grayscale) and basaltic rock matrix (blue in color, dark gray in grayscale) based on X-ray synchrotron imaging at the Advanced Light Source

be captured (implying a resolution of microns or less), then there would be no need for inclusion of a dispersion coefficient. Even if such high resolution calculations were possible, however, a detailed knowledge of the actual pore structure (and thus the flow paths) is typically lacking. Although microscopic information on the pore structure of subsurface materials may never be routine, the increasing availability of X-ray synchrotron mapping has now made it possible to image the microscopic pore structure down to the micron scale. Figure 11.7 shows a 2D section through a 3D X-ray microtomographic image of a basalt specimen subjected to chemical weathering over tens of thousands of years. The mineral dissolution resulting from the weathering process has created new porosity or "micro-wormholes" that are clearly visible as red zones (in color) or gray (in grayscale image) in the skeletonized sections of the weathered rock (blue in color or dark gray in grayscale is the relatively unweathered rock matrix with pore sizes below the resolution of the synchrotron microtomography). Such heterogeneities will give rise to variations in flow velocity at the micron to centimeter scale, and thus to mechanical dispersion.

Mechanical dispersion was first clearly discussed for the case of laminar flow and transport within a cylindrical tube (Taylor, 1953). In the case where a non-reactive tracer is instantaneously released at the inlet of the tube and complete mixing does not occur, the tracer pulse will arrive first where the flow is fastest, later where the flow is slower. At any one time, the bulk concentration of the fluid leaving the

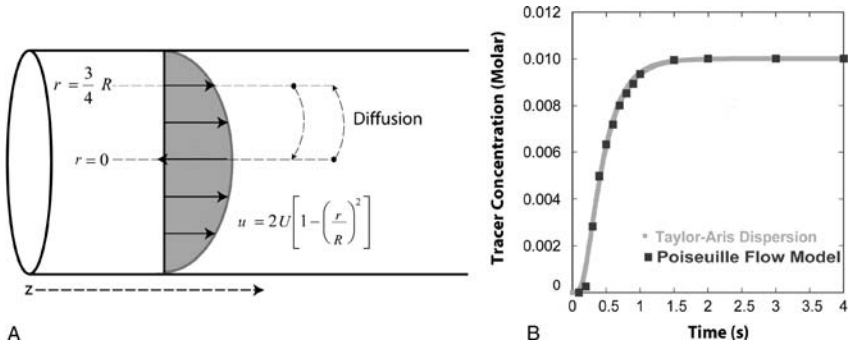

Fig. 11.8 **a**. Schematic representation of the parabolic velocity distribution that develops in the case of Poiseuille flow. **b**. Comparison of non-reactive tracer breakthrough profile using a Taylor-Aris dispersion coefficient (Taylor, 1953) and a full two-dimensional calculation of transport in a cylindrical tube using the analytical solution for Poiseuille flow (Eq. (11.43))

tube represents a flux-weighted average of the concentration in the fast and slow moving flow paths, so the breakthrough of the tracer will appear as disperse or gradual rather than sharp. This effect is referred to as Taylor dispersion (Aris, 1956; Taylor, 1953). Assuming Poiseuille's equation for flow in a cylinder holds, the steady-state parabolic velocity distribution as a function of radius r can be calculated from (Daugherty and Franzini, 1965)

$$u(r) = \frac{2Q}{\pi R^2}\left[1-\left(\frac{r}{R}\right)^2\right] = 2U\left[1-\left(\frac{r}{R}\right)^2\right], \tag{11.43}$$

where $u(r)$ is the local fluid velocity within the cylinder, Q is the volumetric flow rate, R is the radius of the cylinder, and U is the average velocity (Fig. 11.8a). Using Eq. (11.43), Taylor derived an analytical expression for the dispersion in the case of Poiseuille flow

$$D_h = D + \frac{UR^2}{D}, \tag{11.44}$$

where D_h is the dispersion coefficient, and D is the molecular diffusion coefficient. Note that the dispersion coefficient depends on the molecular diffusion coefficient for its contribution to longitudinal spreading (the first term on the right hand side of Eq. (11.44)), but also inversely on the molecular diffusion coefficient in the second term on the right hand side because radial diffusion acts to eliminate the gradients in concentration developed by the non-uniform velocity profile (Fig. 11.8a). A comparison of the breakthrough curve for a non-reactive tracer calculated with the Taylor-Aris dispersion coefficient given in Eq. (11.44) and a full two-dimensional axisymmetric cylindrical Poiseuille flow calculation in which dispersion is represented only through the variation in flow velocities and through molecular diffusion (i.e., no explicit dispersion coefficient is included) is given in Fig. 11.8b.

A similar effect occurs within porous media (which are often conceptualized as bundles of capillary tubes), since the velocity adjacent to a solid grain is slower than

the velocities in the center of the pore. Even in the case of a perfectly homogeneous porous medium (e.g., glass beads all of the same size), therefore, spreading of a solute plume will occur. Additional effects in porous media are related to the tortuosity of flow paths (Fig. 11.5) and to differences in pore size, since velocities will be higher in those pores with wider apertures (Bear, 1972).

Dispersion needs to be quantified at much larger scales in porous media, however, so some averaging of these dispersion mechanisms is usually required. Dispersion in porous media is typically defined as the product of the fluid velocity and a dispersivity, α, with longitudinal and transverse components

$$\begin{aligned} D_L &= \alpha_L V_i \\ D_T &= \alpha_T V_i \end{aligned}, \tag{11.45}$$

where V_i refers to the average velocity in the principal direction of flow, and the subscripts L (longitudinal) and T (transverse) refer to the dispersion coefficient parallel and perpendicular to the principal direction of flow respectively (Bear, 1972).

11.2.3.2 Macrodispersion

The treatment of hydrodynamic dispersion as a Fickian process (that is, one in which the flux is linearly proportional to the concentration gradient) has been widely criticized (Dagan, 1988; Gelhar, 1986; Gelhar and Axness, 1983; Gelhar et al., 1992). As pointed out by a number of investigators, dispersion is scale-dependent, with larger dispersivities observed for larger observation scales. At the column scale, a typical dispersivity may be on the order of a centimeter, but at the field scale, apparent dispersivities from 10 to 100 m or more are common. Gelhar (1986) showed that the dispersivity increased with scale of observation, although even at a single observation scale, dispersivities could range over 2–3 orders of magnitude due to differing degrees of aquifer heterogeneity at the different sites (Gelhar, 1986; Gelhar et al., 1992). The increase with dispersivity as a function of the scale of measurement is related to the hierarchical nature of natural porous medium and is often referred to as macrodispersion. At the pore-scale, variations in flow velocity and direction are related to pore-scale heterogeneities like the variation in grain size and pore apertures, but at the field scale, additional heterogeneity features (sedimentary features, fractures, faults) are encountered which add to the spreading of the solute plume. As in the case of Taylor dispersion, the spreading of a solute plume is fundamentally related to the variations in flow velocity, with fast-flowing pathways leading to earlier breakthrough than slow flow pathways. In the case of Poiseuille flow in a tube, the effect is predictable and rigorously quantifiable because of the well-defined physics of the system, but in natural porous media where multi-scale heterogeneities typically occur, the problem of determining dispersivities is much more difficult and usually requires a stochastic treatment.

The effect of macrodispersion can be illustrated with a simple example. Consider a permeability field with approximately 8 orders of magnitude variability in permeability (Fig. 11.9a). The heterogeneous distribution of and strong contrast in

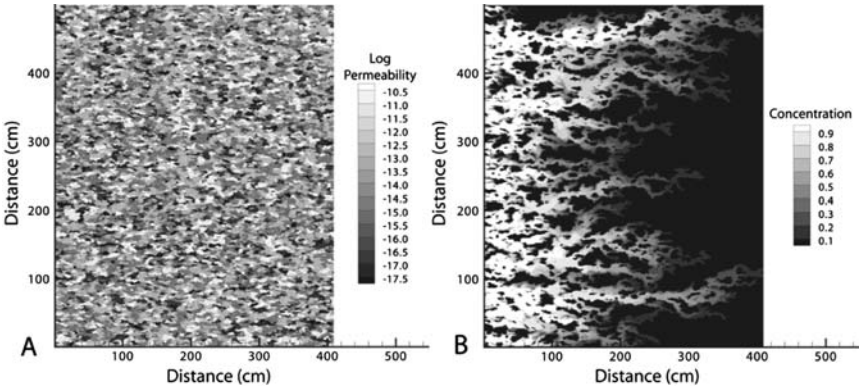

Fig. 11.9 **a**. Heterogeneous permeability (m^2) field for 2D problem. **b**. Concentration field at 0.5 years as a result of flow from left to right across the heterogeneous domain (see also color insert)

permeability results in preferred flow paths that lead to fingering of a non-reactive tracer plume as it moves with the flow from left to right (Fig. 11.9b). The two-dimensional numerical simulation was conducted without including a Fickian treatment of hydrodynamic dispersion and using an accurate Total Variation Diminishing (TVD) scheme that minimizes numerical dispersion (Steefel and MacQuarrie, 1996). When a flux-weighted average of the solute concentration is calculated over the entire length of the capture plane on the right hand side, perpendicular to the flow direction (similar conceptually to what occurs where flow converges into a pumping well), one observes a gradual, disperse breakthrough as a result of the mixing of the early and late arriving fluid packets (Fig. 11.10). To match the disperse breakthrough curve in the heterogeneous flow field with a one-dimensional simulation of flow in a homogeneous permeability field, it is necessary to use a dispersivity, α, of about 50 cm (Fig. 11.10).

11.2.3.3 Stochastic Descriptions of Dispersion

There is much interest now in more rigorous descriptions of macrodispersion in particular. One approach has been to treat the parameters controlling transport (primarily the hydraulic conductivity or permeability, but also potentially such parameters as mineral volume fractions and/or reactive surface area) as stochastic rather than deterministic parameters, since the exact distribution of these parameters in the subsurface is typically poorly known (Dagan, 1989; Gelhar, 1986, 1993). This is a particularly useful approach when the primary data available are breakthrough curves for tracers at an observation point. The shape of the curve can be used to deconvolve a stochastic distribution of hydraulic conductivities in the aquifer, implying that while we do not know the exact path a particular solute particle followed, we do have a statistical representation of the ensemble of solute travel times that could have produced the observed tracer concentrations at the observation point.

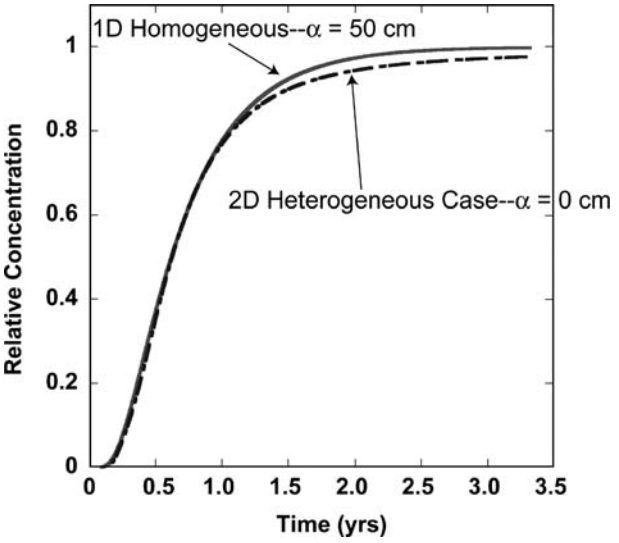

Fig. 11.10 Comparison of solute breakthrough curves for the case of the heterogeneous permeability field shown in Fig. 11.9a, calculated with a dispersivity, $\alpha, = 0$, and a 1D homogeneous permeability field calculated with $\alpha = 50\,\text{cm}$.

Tracer breakthrough data, therefore, is often used to generate probability density functions for hydraulic conductivities and travel times, although this concept need not be strictly stochastic.

11.3 Advection-Dispersion-Reaction Equation

We are now ready to combine the transport processes outlined above with expressions for kinetically controlled geochemical and biogeochemical reaction. A comprehensive and modern treatment would require the use of a sophisticated numerical simulator capable of handling variations in system properties (hydraulic conductivity, porosity, tortuosity, etc.) in both space and time, along with rigorous treatments of multicomponent diffusion and advection. Our interest here, however, is in exploring the first-order dynamics when reaction and transport are coupled, and for this purpose a simplified version of the advection-dispersion-reaction equation is adequate. For a system with transport of a non-reactive tracer, an expression for the conservation of solute mass can be derived by accounting for the flux of solute across the faces of a volume element. For a one-dimensional system (fluxes in the Y and Z directions = 0), the net flux is obtained from

$$\frac{\partial J_i}{\partial x} = \lim_{\Delta x \to 0} \frac{J_i|_{x+\Delta x} - J_i|_x}{\Delta x}. \tag{11.46}$$

In a multidimensional system involving porous media, the accumulation of solute mass is given by the difference (that is, the divergence) of the fluxes summed over all of the faces of the element

$$\frac{\partial(\phi C_i)}{\partial t} = -\nabla \cdot \mathbf{J}_i = -\left(\frac{\partial J_i}{\partial x} + \frac{\partial J_i}{\partial y} + \frac{\partial J_i}{\partial z}\right), \tag{11.47}$$

where $\boldsymbol{J_i}$ is the flux vector. Substitution of Eqs. (11.10) and (11.15) into Eq. (11.47) (neglecting electrochemical migration for simplicity) yields

$$\frac{\partial(\phi C_i)}{\partial t} = -\nabla \bullet (\phi \mathbf{v} C_i) + \nabla \bullet (\phi D_i^* \nabla C_i). \tag{11.48}$$

To include reactions, however, it is more instructive to use the one-dimensional version of the advection-dispersion equation, particularly since non-dimensionalization of the equation is more straightforward in this case. For a constant porosity, tortuosity, and flow system characterized by a first-order precipitation and dissolution reaction that can be described in terms of a single chemical component (e.g., $SiO2_{[aq]}$ reacting with the single mineral quartz), the advection-dispersion-reaction equation becomes

$$\phi \frac{\partial C}{\partial t} = -\phi v \frac{\partial C}{\partial x} + \phi D^* \frac{\partial^2 C}{\partial x^2} + Ak\left(1 - \frac{C}{C_{eq}}\right), \tag{11.49}$$

where k is the rate constant in units of moles $m^{-2}\,s^{-1}$, A is the reactive surface area of the mineral in units of $m^2\,m^{-3}$, and C_{eq} is the solubility of the mineral in moles m^{-3}.

11.3.1 Non-Dimensional Form of the Advection-Dispersion-Reaction Equation

The advantage of converting a partial differential equation to its non-dimensional form is that the relative importance of dynamic processes like chemical reaction, advection, and hydrodynamic dispersion are readily apparent. The first step is to define a length scale, l, which may be a characteristic length scale defined by the geology or hydrology (e.g., the flow length through an aquifer or weathering profile), or more commonly a length scale which reflects the spatial distribution of observations. Using this length scale, a non-dimensional or fractional distance can be defined as

$$x' = \frac{x}{l}. \tag{11.50}$$

In addition, this allows us to define a characteristic time for dispersive transport

$$t_D = \frac{l^2}{D^*}, \tag{11.51}$$

and advective transport

$$t_A = \frac{l}{v}. \tag{11.52}$$

When combined with a characteristic time for reaction

$$t_R = \frac{\phi C_{eq}}{Ak}, \tag{11.53}$$

it is possible to define a series of non-dimensional parameters that control the behavior of a water–rock interaction system involving transport: the Damköhler number for advective, Da_I, and diffusive (or dispersive), Da_{II}, systems respectively

$$Da_I = \frac{t_A}{t_R} = \frac{Akl}{\phi v C_{eq}} \tag{11.54}$$

$$Da_{II} = \frac{t_D}{t_R} = \frac{Akl^2}{\phi D^* C_{eq}}. \tag{11.55}$$

In addition, the relative importance of advective versus diffusive (or dispersive) transport is compared in the Péclet number

$$Pe = \frac{t_D}{t_A} = \frac{vl}{D^*}. \tag{11.56}$$

Note that each of these numbers depends on the characteristic length scale considered.

To develop a fully non-dimensional form of the advection-dispersion-reaction equation, it is convenient to introduce a non-dimensional form of the concentration

$$C' = \frac{C - C_{eq}}{C_0 - C_{eq}}, \tag{11.57}$$

where C_0 is the concentration of the fluid injected into the system (Lichtner,1998). Introducing a dimensionless time

$$t'_D = \frac{D^* t}{l^2}, \tag{11.58}$$

Eq. (11.49) becomes

$$\frac{\partial C'}{\partial t'_D} = \frac{\partial^2 C'}{\partial x'^2} - Pe\frac{\partial C'}{\partial x'} - Da_{II}C', \tag{11.59}$$

which makes clear how the Péclet and Damköhler numbers control the behavior of the advection-dispersion-reaction equation.

At high Péclet numbers ($Pe \gg 1$), advective transport dominates and dispersive and diffusive transport are negligible, with the result that the concentration front is relatively sharp (Fig. 11.11). Similarly, for Damköhler numbers $\gg 1$, reaction times are much faster than transport times for a given length scale. Where this is the case,

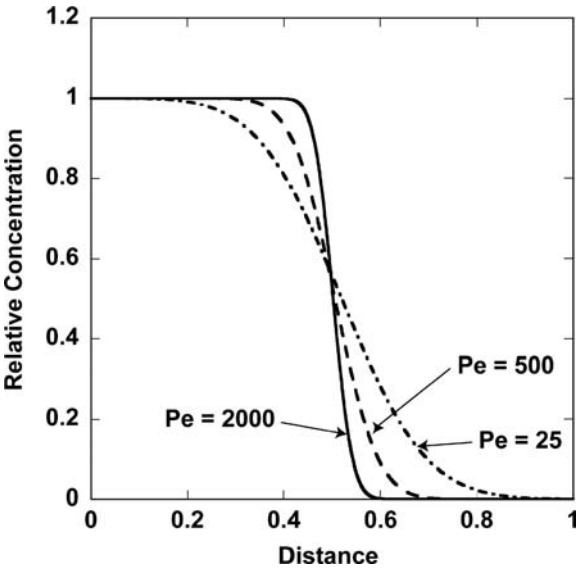

Fig. 11.11 Effect of the non-dimensional Péclet number on the shape of a concentration profile. The length scale is given by the flow distance, with flow from left to right

local equilibrium is achieved for a reaction of the form given in Eq. (11.49) over a length scale, l (Bahr and Rubin, 1987). In addition, reaction fronts are relatively sharp where the Damköhler number is large, since the approach to equilibrium requires a small amount of time relative to the time needed for a solute to traverse a distance l (Fig. 11.12). This has been shown more formally by Lichtner (Lichtner, 1988, 1998), who presented a pedagogically valuable solution to the stationary-state advection-dispersion-reaction equation

$$\frac{\mathrm{d}^2 C_i'}{\mathrm{d}x'^2} - Pe\frac{\mathrm{d}C_i'}{\mathrm{d}x'} - Da_{II}C_i' = 0. \tag{11.60}$$

or

$$\frac{1}{Pe}\frac{\mathrm{d}^2 C_i'}{\mathrm{d}x'^2} - \frac{\mathrm{d}C_i'}{\mathrm{d}x'} - Da_I C_i' = 0, \tag{11.61}$$

by noting that

$$Da_{II} = Da_I Pe. \tag{11.62}$$

Earlier solutions were presented by Ogata and Banks and by Bear (Bear, 1972; Ogata and Banks, 1961). To fully specify the system, boundary conditions are needed

$$C(0) = C_0, \tag{11.63}$$
$$C(\infty) = C_{eq}, \tag{11.64}$$

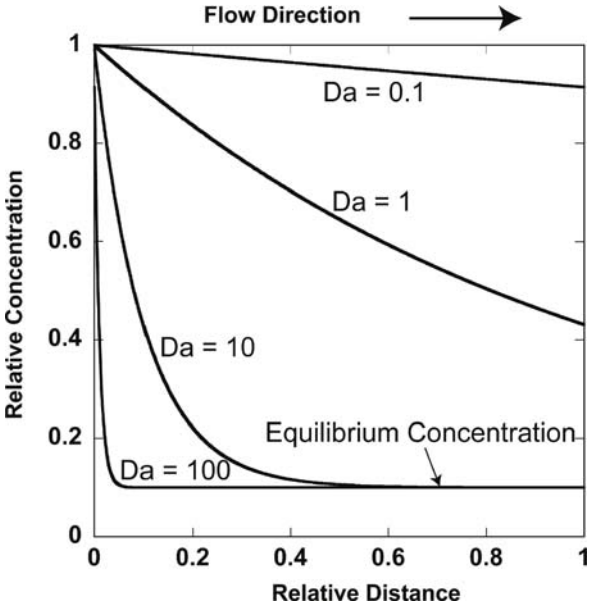

Fig. 11.12 Effect of the non-dimensional Damköhler number on the shape of a concentration profile at steady state. A large Damköhler number indicates that the reaction kinetics are rapid compared to transport rates over the length scale considered, or equivalently, that the characteristic time for transport is significantly more than the characteristic time for reaction. The local equilibrium approximation is justified in such cases

which in the non-dimensional system become

$$C'(0) = 1 \tag{11.65}$$

$$C'(\infty) = 0. \tag{11.66}$$

For the case of pure advective flow (infinite Péclet number) and the boundary condition in Eq. (11.65), the solution to Eq. (11.61) is given by an exponential function (Boyce and DiPrima, 1986; Lichtner, 1998)

$$C' = \mathrm{e}^{-\beta' x'}, \tag{11.67}$$

where

$$\beta' = Da_I = \frac{Akl}{C_{eq}\phi v}. \tag{11.68}$$

For the case of pure diffusive transport $(v = 0)$ and mixed dispersive-advective transport, the solution of the second-order differential equation in 11.60 can also be written in the form of Eq. (11.67), with the characteristic equation for β' given by (Boyce and DiPrima, 1986; Lichtner, 1998)

$$\beta'^2 - Pe \cdot \beta' - Pe \cdot Da_I = \beta'^2 - Pe \cdot \beta' - Da_{II} = 0. \tag{11.69}$$

The solution in the case of pure diffusive transport ($Pe = 0$) is

$$\beta' = Da_{II} = \frac{Akl^2}{\phi D^* C_{eq}}, \tag{11.70}$$

while for mixed dispersive (diffusive) and advective transport, the solution is given by

$$\beta' = \frac{1}{2}\left[-Pe + \sqrt{Pe^2 + 4Da_I \cdot Pe}\right] = \frac{1}{2}\left[-Pe + \sqrt{Pe^2 + 4Da_{II}}\right]. \tag{11.71}$$

11.3.2 Equilibration Length Scales

As pointed out by Lichtner, these solutions can be used to determine the length scale over which equilibration between the fluid and solid phase occurs. To express the stationary state Eq. (11.67) in terms of actual distance and the boundary conditions given in Eqs. (11.63) and (11.64), we define

$$\beta = \frac{\beta'}{l}, \tag{11.72}$$

which yields

$$C(x) = (C_0 - C_{eq})\mathrm{e}^{-\beta(Pe,Da)x} + C_{eq}. \tag{11.73}$$

The fractional distance required to approach equilibrium (referred to as the *equilibration length scale*) is given by the inverse of the parameter β (Lichtner, 1998)

$$\lambda' = \frac{\lambda}{l} = \frac{1}{\beta'}, \tag{11.74}$$

where λ is the equilibration length scale and λ' is the fractional length scale (Fig. 11.13). Where $\beta' > 1$ (implying $\lambda' < 1$), local equilibrium is attained for a given length scale l, while values of $\beta' < 1 (\lambda' > 1)$ correspond to dominantly surface reaction or kinetic control. Note that it is quite possible that the system is characterized by a mixed equilibrium (solubility) and kinetic control where $\beta' \sim 1 (\lambda \sim l)$. The overlap between a strict surface reaction and thermodynamic control can become larger when nonlinear rate laws are considered. The equilibration length scale corresponds to the width of the reaction front in a natural (real) system. In general, the width of the reaction front can depend on advection, dispersion, and the rates of surface reactions.

The theory outlined above provides an approach to estimating natural, *in situ* reaction rates if transport rates are independently known. Lacking an independent determination of transport rates, it is evident from Eqs. (11.68) through (11.71) that the width of a reaction front constrains only the *ratio of the transport to reaction rates*. In general, wide reaction fronts are characteristic of low Damköhler number systems. Sharp reaction fronts, which result from equilibration of the fluid phase

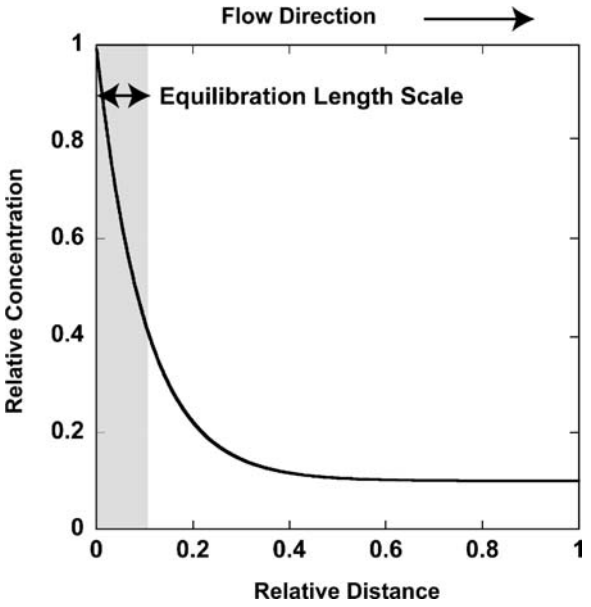

Fig. 11.13 Equilibration length scale given by $1/\lambda$

with the rock over a relatively short distance, indicate a local equilibrium system. Diffusion-reaction systems are particularly useful for assessing natural *in situ* reaction rates, since the range in values of the effective diffusion coefficient is generally less than the range of flow velocities in more permeable media. However, since relatively few determinations of tortuosities (or formation factors) have been carried out in low permeability materials, even the diffusion-reaction problem may be unconstrained.

11.3.3 Reaction Fronts in Natural Systems

While the non-dimensional analysis presented above has a real pedagogical value, the rather stringent assumptions used to derive it should be noted clearly. Perhaps most importantly, it assumes constant transport coefficients over the spatial domain considered. Significant changes in flow velocity over the flow path would have the effect of changing the local Péclet and Damköhler numbers, thus changing the width of the reaction front. Similarly, large changes in porosity can change the local effective diffusivity through the tortuosity effect, making the interpretation of reaction front widths considerably more difficult. A good example is provided by weathering rinds developed in basaltic clasts as reported by (Sak et al., 2004). In the highly weathered material, which is dominated by gibbsite and Fe-hydroxide, the porosity averages about 30%–50%, while in the unaltered basaltic rock, the average porosity

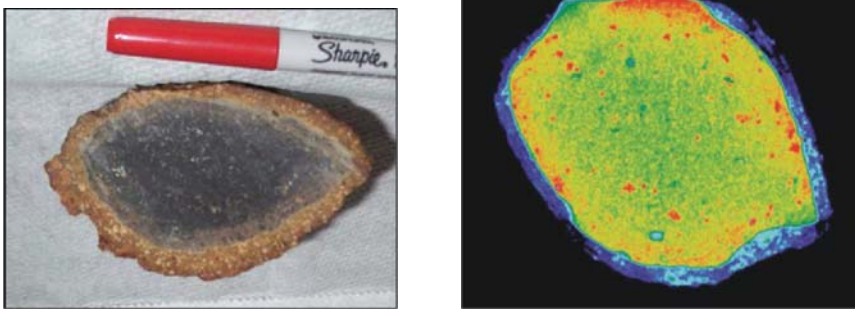

Fig. 11.14 **a**. Photograph of a weathering rind developed in basaltic rock from Costa Rica. **b.** CAT scan of a similar sample showing the sharp density contrast between unaltered (yellow and orange in color, light gray in grayscale) and weathered material (blue in color, mottled gray in grayscale). The interface between unweathered and weathered rock is associated with a large change in such physical properties as the porosity and tortuosity. Samples courtesy of Alexis Navarre-Sitchler (see also color insert)

is on the order of 3%–5% (Fig. 11.14). This discontinuity in porosity, and thus in transport parameters, can cause a sharpening of the reaction front that might be misinterpreted as a strict Damköhler number effect. In such a system characterized by transport rates that vary spatially, the principal control on rates may change depending on the portion of the system considered.

Another point that needs to be considered carefully is whether the width of a reaction front is not due in part to heterogeneous flow paths through the reacting material. The analysis presented above strictly applies only to a homogeneous system. If flow is not uniform through a reactive rock, then the extent of reaction will depend on the local flux. Integrated over long times, the extent of reaction will vary, with the result that a sampling transect carried out perpendicular to the principal flow direction (parallel to the reaction front in the homogeneous case) will result in a gradual or disperse reaction front if the results are averaged. This is another example of macrodispersion, in this case integrated over long periods of time to produce a disperse reaction front. Again, a simple Damköhler number analysis could underestimate the rates of reaction in this case by interpreting the broadness of the front has due solely to slow reaction kinetics. These cases, however, can be analyzed with numerical reactive transport software.

A third point to keep in mind is that the reaction kinetics presented above involved linear kinetics. In the case of important Earth-forming minerals like the feldspars, the rate laws may be considerably more complicated, with catalysis of the dissolution reaction (e.g., by H^+) and inhibition of the dissolution reaction (e.g., by Al^{3+}) contributing to a much more complicated behavior. In addition, a nonlinear dependence of the dissolution rate on the extent of undersaturation (or the reaction affinity) can also result in more complex behavior, with a much wider range of transport and kinetic parameters within which a mixed transport and surface reaction

control could be observed. Fortunately, these more complicated behaviors can be analyzed with modern reactive transport numerical software, even it is not possible with a relatively simple analytical solution.

A fourth point is that gradual reaction fronts may be due to other factors such as a temperature gradient or local sources of reactive constituents. "Gradient reactions," where reactions are driven by transport across a temperature gradient, are contrasted with isothermal "reaction front" case discussed above (Phillips, 1991; Steefel and Lasaga, 1994). When a temperature gradient is present, it is likely that a gradient in reaction products will develop even in the absence of any kinetic effects. Similarly, where local sources of reactive constituents are present along a flow path, as in the case of decaying organic matter producing the weak acid CO_2, then gradients in reaction products are likely to develop that can be unrelated to the equilibration length scale of the primary mineral of interest (e.g., feldspar dissolution). Care must be taken not to interpret either of these as a simple Damköhler number effect. In addition, it stresses the importance of including all relevant physical, chemical, and microbiological processes into the analysis of reaction rates (Maher et al., 2006).

11.3.4 Transport versus Surface Reaction Control

Under the steady-state conditions considered here, there is always some theoretical length scale over which local equilibrium could be attained (assuming such an equilibrium state exists), although this length scale may not be realized in a particular geological environment. Where the concentration in the aqueous phase increases or decreases to the point where equilibrium or near-equilibrium is achieved, the overall rate of reaction within the spatial domain defined by the length scale l becomes *transport-controlled*. This implies that the rate-limiting process in the overall reaction evaluated over the length scale l is transport, rather than the rate of attachment and detachment of ions from the mineral. Transport control has often been discussed in the geochemical literature, but usually with regard to experimental studies where transport involved diffusion across a boundary layer next to a reacting mineral (Berner, 1980). For example, numerous studies have shown that the dissolution of calcite is diffusion rather than surface reaction-controlled at pH values < 4. This can be verified in rotating disk reactors by increasing the speed of rotation—in the case of a diffusion control on the rate of dissolution, the faster rate of spinning reduces the size of the diffusion boundary layer adjacent to the crystal, thus increasing the overall rate of dissolution (Pokrovsky et al., 2005).

While the rotating disk experiment involving calcite is a particularly good example of a transport-controlled system, the concept is much more general and may be applied at any scale. Consider a flow path through a granite undergoing weathering. If a fluid percolating through the granite approaches equilibrium over a flow distance of about 25 m, but we collect water samples issuing from the profile 50 m from the start of flow path, then we are collecting waters close to or at equilibrium

that will express a transport control on the overall rate. Operationally, this means that the flow rate through the weathering profile (due, for example, to an increase in rainfall) controls the weathering flux, $J_{weather}$, in the advection-dominant case over the 50 m according to

$$J_{weather} = qC_{eq}, \tag{11.75}$$

where q is the flow rate and C_{eq} is the equilibrium concentration. If the scale of observation, l, is $\gg$ than the equilibration length scale λ, then the weathering rate will not depend on the reaction kinetics. This is a general result that applies to all water–rock interaction systems (Lichtner, 1993). A comparison of laboratory-determined rates of reaction, which are carried out in most cases under far from equilibrium conditions and thus under surface reaction control, and natural weathering rates evaluated at length scales greater than the equilibration length scale, will be meaningless in this case, since the rate control is not the same. By definition, the field rate when transport controlled will be slower than the surface reaction-controlled rate. But, as stressed above, the control on rates is scale-dependent, so data collected at a length scale $\ll$ than the equilibration length scale may show evidence for a surface reaction control on rates and far from equilibrium conditions. Thus, observations of etch pitting in primary minerals, generally taken as good evidence of far from equilibrium conditions (White and Brantley, 2003), may be fully compatible with an overall transport control on weathering rates, depending on how the scales of observations compare to the equilibration length scale.

11.3.5 Propagation of Reaction Fronts

The expressions presented above assume a reaction front present at x = 0, but the equations can be generalized easily to consider the case of a reaction front that propagates through space over time. For example, it is possible to define a new spatial coordinate in terms of distance from the reaction front, x_f, according to

$$x_f = x - l_f, \tag{11.76}$$

where l_f is the position of the reaction front, and to use this in the expressions discussed above.

The velocity at which fronts propagate as a function of transport and kinetic rates can also be determined. Lichtner has shown that the velocity of the reaction front, v_l, can be calculated from the expression (Lichtner, 1988)

$$v_l = \frac{\mathrm{d}l_f}{\mathrm{d}t} = \frac{1}{\tau_0 \beta}\left(\frac{C_{eq} - C_l}{C_{eq} - C_0}\right), \tag{11.77}$$

where C_l is the concentration at the reaction front, β is defined in Eqs. (11.68) through (11.72) and τ_0, the time required for a mineral to dissolve completely at the

inlet of a porous column, is given by

$$\tau_0 = \frac{\phi_m}{\bar{V}_m A k (C_{eq} - C_o)}, \tag{11.78}$$

where ϕ_m is the initial volume fraction of the mineral and $\bar{V}_m$ is its molar volume. In Eq. (11.77), the last term represents the jump in concentration across the reaction front and is given by

$$\frac{C_{eq} - C_l}{C_{eq} - C_0} = 1; \text{Pure Advection} \tag{11.79}$$

$$\frac{C_{eq} - C_l}{C_{eq} - C_0} = \frac{1}{\beta l + 1}; \text{Pure Diffusion} \tag{11.80}$$

$$\frac{C_{eq} - C_l}{C_{eq} - C_0} = \frac{\frac{v}{\beta D^*} \frac{1}{1 - e^{-vl/D^*}}}{\left(\frac{v}{\beta D^*} \frac{1}{1 - e^{-vl/D^*}} + 1\right)}; \text{General Case.} \tag{11.81}$$

The pure advective case can also be derived through the use of the traveling wave approximation (Ortoleva et al., 1986).

According to Lichtner, the formation of a reaction front can be divided into three periods: (1) a transient, surface reaction-controlled regime where the mineral in question is dissolved at the inlet to the system, (2) a transitional regime, and (3) an asymptotic regime which is at local equilibrium except within the reaction front (Lichtner, 1996). In the asymptotic regime, the rate of front propagation is independent of the kinetic rate constants. This was shown more formally in 1993 via a scaling analysis of the reactive transport equations in the case where boundary and initial conditions are scale-invariant and no inherent length scale exists for the system (Lichtner, 1993). In this case, the field variables of interest, F, obey the scaling relationship

$$\lim_{\sigma \to \infty} F(\sigma x, \sigma t; v, D_h, Ak) = \lim_{\sigma \to \infty} F(x, t; v, \sigma^{-1} D_h, \sigma Ak), \tag{11.82}$$

where σ is the scale factor. Eq. (11.82) states that in the limit of infinite space and time, the reactive transport equations approach the pure advective local equilibrium limit as diffusion and dispersion vanish and the reaction rate constant and surface area become infinitely large.

11.4 Rates of Water–Rock Interaction in Heterogeneous Systems

Most studies of the kinetics of water–rock interaction carried out to date have assumed flow and reaction through a homogeneous, well-mixed system, as would be the case with a single continuously stirred flowthrough reactor (Haggerty et al., 1998; Snodgrass and Kitanidis, 1998; White and Brantley, 2003; Zhu, 2005). This

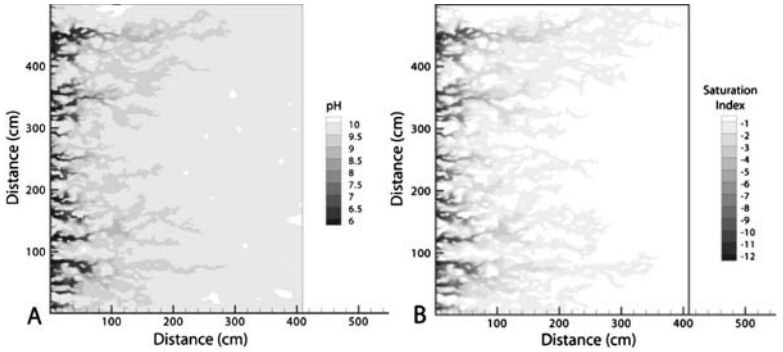

Fig. 11.15 **a**. pH distribution for the 2D heterogeneous flow field shown in Fig. 11.9. pH at the left side of the flow domain is fixed at 5. The principal reaction is the dissolution of plagioclase with a rate law that includes dissolved aluminum inhibition (from Oelkers et al., 1994). **b**. The saturation state of the pore fluid with respect to plagioclase $(\log Q/K_{eq})$ varies spatially, resulting in a heterogeneous distribution of surface reaction versus transport control of the rate (see also color insert)

is perhaps somewhat strange given the enormous number of studies on macrodispersion in the hydrologic literature indicating that travel times, and thus residence times, in the subsurface are not all the same. Fortunately, the effects of both physical and chemical heterogeneities and their role in water–rock interaction are now beginning to be discussed (Li et al., 2006; Malmström et al., 2000; Meile and Tuncay, 2006). The role of physical heterogeneties can be clarified by returning to the heterogeneous permeability field shown in Fig. 11.9. If we now include reactions along with the flow and transport, in this case the dissolution of plagioclase according to the kinetic scheme proposed by Oelkers and co-workers (Oelkers et al., 1994), we see that the numerical modeling of the reactive transport predicts a steady-state fingering of the pore water pH that follows the high permeability zones (Fig. 11.15a). Similarly, a contour plot of the logarithm of the mineral saturation states (the distance the pore water is from equilibrium with respect to plagioclase) shows a similar strong spatial variability—a transect in the Y direction at $X = 10\,cm$ would encounter up to 10 orders of magnitude variability, ranging from far from equilibrium to relatively close to equilibrium pore waters (Fig. 11.15b). Therefore, a single transect could encounter both surface reaction and at least partly transport-controlled rates. While this is a model result, it should be broadly representative of what would be expected for any reactive system with 7 orders of magnitude variation in the local permeability.

11.4.1 Residence Time Distributions

The concept of macrodispersion has important implications for the kinetics of water–rock interaction. One can also think of these variations in flow velocity and/or

flow length as leading to a distribution of residence times for aqueous species migrating through reactive material. A sample collected from a stream draining a catchment, for example, typically includes waters that have moved through a myriad of flow paths and distances. Some water may have moved through relatively shallow portions of the soil profile—these flow paths would typically involve relatively short residence times, with less exposure to primary reactive phases forming the bedrock. In contrast, other water may have moved along deeper, slower flow paths, encountering a greater abundance of reactive primary minerals along the way. The residence time of reactive water in contact with rock, therefore, can vary substantially in a natural system. Locally, the system may be far from equilibrium, elsewhere close to equilibrium. Conceptually, one might think of the overall system as an ensemble of flowthrough reactors, some with short residence times and/or small amounts of reactive material, others with much longer residence times. In some cases, the residence time will have been long enough that the fluid actually equilibrates within the reactor, leading to a rate that is transport rather than surface reaction-controlled. If the effluent of this ensemble of flowthrough reactors were to converge into a single sampling tube (the experimental analogue of a stream gauging station at the catchment scale or a pumping well drawing water from a heterogeneous aquifer), then the total extent of reaction (i.e., the upscaled, volume-averaged reaction rate) would reflect the full distribution of residence times and reactive mineral mass.

Many examples of reactive flow through permeable rocks or sediment exist where strong contrasts in porosity and permeability result in regions characterized by very different transport regimes. This is often referred to as multi-region transport (Harvey and Gorelick, 2000). The most common example is a dual permeability (or porosity) system, where a portion of the system is sufficiently permeable that macroscopic flow occurs within it, another portion is so impermeable that flow is negligible and transport is by molecular diffusion. Perhaps the best example of a dual permeability system is provided by fractured rock, where the permeability of the fractures is typically many orders of magnitude higher than the permeability of the rock matrix (Steefel and Lichtner, 1998).

Much of the evidence that multi-region transport systems exist in the subsurface comes from measurements of hydraulic conductivities on small laboratory-scale samples. Another source of evidence is provided by groundwater ages determined with various methods (Plummer et al., 2001). Although these groundwater ages are often interpreted as the result of mixing between two end members (old and young water), what we have learned about the distribution of hydraulic conductivities, and thus residence times, in heterogeneous 3D subsurface media argues against this (Bethke and Johnson, 2002; Tompson et al., 1999; Varni and Carrera, 1998; Weissmann et al., 2002). For example, Fig. 11.16 shows groundwater ages determined using the chlorofluorocarbon (CFC) technique compared to simulated CFC ages based on high resolution groundwater flow simulation of a heterogeneous alluvial fan aquifer in California (Weissmann et al., 2002). The high resolution flow modeling argues that the individual CFC ages are real, and not simply the result of mixing of old and young waters.

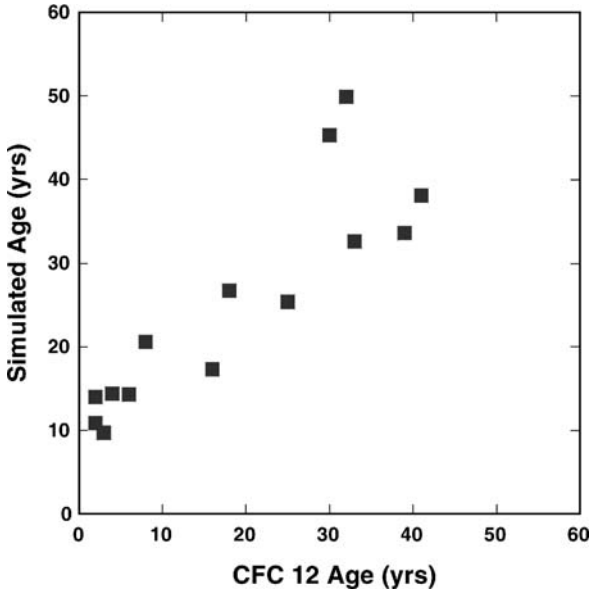

Fig. 11.16 Chlorofluorocarbon (CFC) ages compared to simulated CFC ages based on high resolution groundwater flow modeling from a heterogeneous alluvial fan aquifer in California (From Weissmann et al., 2002)

Evidence also comes from non-reactive tracer concentration profiles (or "breakthrough curves") determined in subsurface wells. Tracer concentration profiles at an observation well (or at the end of a laboratory column) characterized by multi-region effects typically show an early, usually sharp breakthrough, followed by a long gradual approach to a maximum value in the case of a constant injection. In the case of a transient pulse of a tracer followed by another fluid (a common case in contaminant hydrology), the tracer is eluted only very slowly from the column or aquifer. This behavior occurs because it requires some time for the tracer to be transported into the low permeability material, and once elution begins, then to be flushed from this zone.

Tracer breakthrough curves can be used to estimate a residence time distribution. With release of a non-reactive tracer pulse, fast pathways will deliver tracer first. Lower permeability regions within the flow domain will flush the tracer more slowly, providing information on the longer residence times. Using the first derivative of the concentration in the breakthrough curve in Fig. 11.10, the formal probability density function for residence times can be determined (Fig. 11.17).

11.4.2 Upscaling Reaction Rates in Heterogeneous Media

Mineral reaction rates are typically measured in well-stirred laboratory systems where the intent is to eliminate gradients in concentration within the solution.

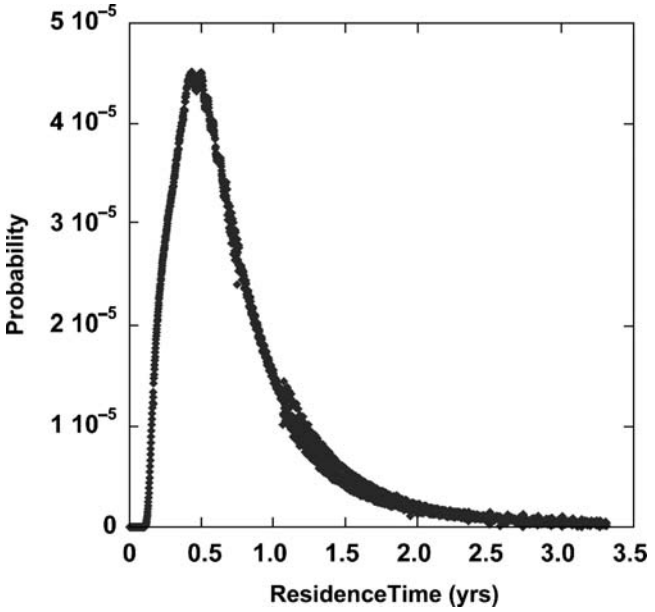

Fig. 11.17 Residence time distribution for the two-dimensional flow case presented in Fig. 11.9. Residence times are presented in terms of probabilities and are calculated recursively based on the breakthrough curve shown in Fig. 11.10

An individual crystal is expected experience the same chemical environment as its neighbor. To the extent that a diffusion boundary layer can be eliminated via stirring, potentially a problem with a rapidly reacting mineral like calcite at low pH (Pokrovsky et al., 2005), the rate of the mineral reaction is surface reaction-controlled. In porous media where water–rock interaction takes place, however, physical, chemical, and microbiological heterogeneities can lead to the development of gradients in concentration, and thus to a spatially variable reaction rates. Perhaps the clearest example is provided by the case where a reacting phase is distributed heterogeneously—obviously, in this case the reaction rate in the microenvironment next to the mineral is greater than what is determined over a larger volume average. If the system is well-mixed via either molecular diffusion or dispersion, however, then the rate should be scale-independent if correction is made for the distribution of reactive surface area. In the case where incomplete mixing at the individual pore or pore network scale occurs, however, significant spatial variations in concentration, mineral saturation state, and reaction rates can occur and lead to a scale dependence to the rate (Li et al., 2006). As shown by Li and co-workers in their study of plagioclase dissolution and kaolinite precipitation at the pore network scale, it is even possible for both precipitation and dissolution of kaolinite to occur simultaneously within the same pore network. A similar effect may occur at larger scale where slow transfer between low permeability zones (often referred to as "immobile") and higher permeability ("mobile") zones occurs—large scale

non-equilibrium between these zones may occur, creating gradients in concentration and thus a spatial variability in reaction rates (Harvey and Gorelick, 2000). From the preceding discussion, it should be clear that upscaling reaction rates is not as simple as normalizing the rates to the total reactive surface area in the water–rock system. Rates in natural heterogeneous porous media will always be scale-dependent where incomplete mixing occurs. Future research in water–rock interaction will doubtless focus on methods for upscaling reaction rates in such heterogeneous systems.

11.5 Determining Rates of Water–Rock Interaction Affected by Transport

Rates of reaction can be determined in water–rock interaction systems affected by transport using several approaches. In general, however, intrinsic rates of reaction (e.g., moles $m^{-2} s^{-1}$) cannot be determined uniquely without independently determining transport rates. An exception is the case where one process or the other (surface reaction or transport) is clearly the slowest and therefore rate-limiting step in the overall process. Unfortunately, a surface reaction or transport control is often assumed to apply in advance of a rigorous analysis that demonstrates this control. So, for example, it has been common to compare rates of weathering at the field scale to rates of reaction determined in laboratory experiments conducted under far from equilibrium conditions. Such a direct comparison, without the use of an appropriate process model for weathering based on reactive transport, assumes *a priori* that surface reactions control the overall rate (Steefel et al., 2005). Whether this is in fact true, or whether rates are transport or mixed transport–surface reaction-controlled, needs to be established on a case by case basis (Maher et al., 2006).

11.5.1 Rates from Aqueous Concentration Profiles

From Eq. (11.49), it is clear that rates of reaction can be determined from a concentration profile if the rates of transport are known. One can determine rates of water–rock interaction even where non-steady state conditions prevail, but the steady state case is much simpler to deal with. In the case of a steady state system, the rates of reaction in a pure diffusion system will be given by the curvature or second derivative of the concentration

$$R = \phi D^* \frac{\partial^2 C}{\partial X^2}, \tag{11.83}$$

while in a pure advective system, the rate is given by the first derivative or slope of the concentration

$$R = -\phi v \frac{\partial C}{\partial X}. \tag{11.84}$$

Eqs. (11.83) and (11.84) can be used with finite differencing of discrete data to determine local reaction rates, respectively

$$R_j = \left[\left(\phi D^*\right)_{j+1/2} \frac{C_{j+1} - C_j}{x_{j+1} - x_j} - \left(\phi D^*\right)_{j-1/2} \frac{C_j - C_{j-1}}{x_j - x_{j-1}} \right] \tag{11.85}$$

$$R_{j-1/2} = -\left(\phi v\right)_{j-1/2} \left[\frac{C_j - C_{j-1}}{x_j - x_{j-1}} \right], \tag{11.86}$$

where j refers to the discrete data points and x_j is the location of the data in space. In this form, the finite difference equations are written without assuming equally spaced data (implicitly assumed in Eqs. (11.83) and (11.84)). Alternatively, the rates can be fit using the analytical or numerical solution to the governing reactive transport equation, taking into account the appropriate boundary and initial conditions as necessary. If a species is affected by more than one reaction, then all of the relevant reactions need to be factored into the analysis and this is generally best accomplished with modern numerical reactive transport software.

An example of matching a single reaction rate to a concentration profile is shown in Fig. 11.18a. In this example from Site 984 in the north Atlantic (Maher et al., 2006), sulfate reduction under conditions of diffusive transport in unlithified sediments (the only advection term is from burial) results in a decrease in sulfate concentrations and a stoichiometric increase in ammonia. The sulfate reduction rate can be determined to the accuracy of the species diffusivities. Since diffusion coefficients and formation factors for marine sediments are reasonably well known (Boudreau, 1997), the rate determined in this fashion is quite reliable. More difficult is to make use of concentration profiles affected by more than a single reaction. The calcium profile at the same site is affected by the dissolution of plagioclase and by the precipitation of calcite. Fortunately, the alkalinity profile can be used to constrain the rates of both the plagioclase and calcite. Additional support for the reaction rates determined in this fashion are provided by the uranium isotope profiles from the site (Maher et al., 2006). In natural systems, reaction networks composed of multiple sequential or parallel reactions are more common than not and extracting rates from these systems requires fitting multiple concentration profiles simultaneously. Modern numerical reactive transport software is again essential here.

An additional advantage of using modern reactive transport software is that various rate law formulations can be tested relatively easily, including Michaelis-Menten kinetics in the case of microbially mediated systems, or mineral dissolution and precipitation laws based on linear or nonlinear dependences on solution saturation state.

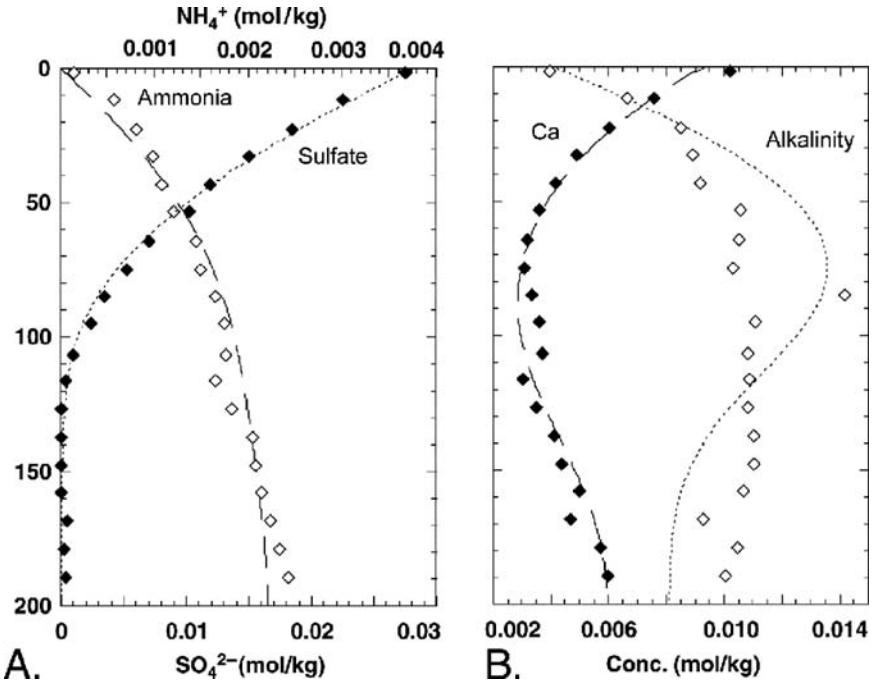

Fig. 11.18 **a**. Fit of the sulfate and ammonia profiles at Site 984 in the North Atlantic with the reactive transport code CrunchFlow allows the determination of the rate of microbially mediated sulfate reduction. **b**. Fit of the calcium and alkalinity profiles provides the rates of both plagioclase dissolution and calcite precipitation

11.5.2 Rates from Mineral Profiles

Determining rates from mineral profiles is generally more difficult, both because the mineral profiles reflect integrated rates, but also because the movement of the reaction fronts can introduce additional difficulties of interpretation. From the discussion of equilibration length scales in Sect. 11.3.2, it is clear that rates can be determined from the width of a reaction front in the case where transport rates are independently known. Determining intrinsic rates (per unit surface area mineral), however, is more difficult because the spatial variation of reactive surface area across the reaction front needs to be factored in. The simplest case involves a one-dimensional flow system with constant transport rates over time, an example of which is the chronosequence developed on granitic sand near Santa Cruz, California (White et al., 2006). Downward flow rates through the profile have been determined through tracer studies and the penetration distance of isotopes like ^{36}Cl. Potassium feldspar and plagioclase fronts show distinct penetration depths after 226,000 years of weathering, presumably reflecting the different solubilities and/or rates of the two minerals (Fig. 11.19). Interestingly, the plagioclase profile can be fit reasonably well

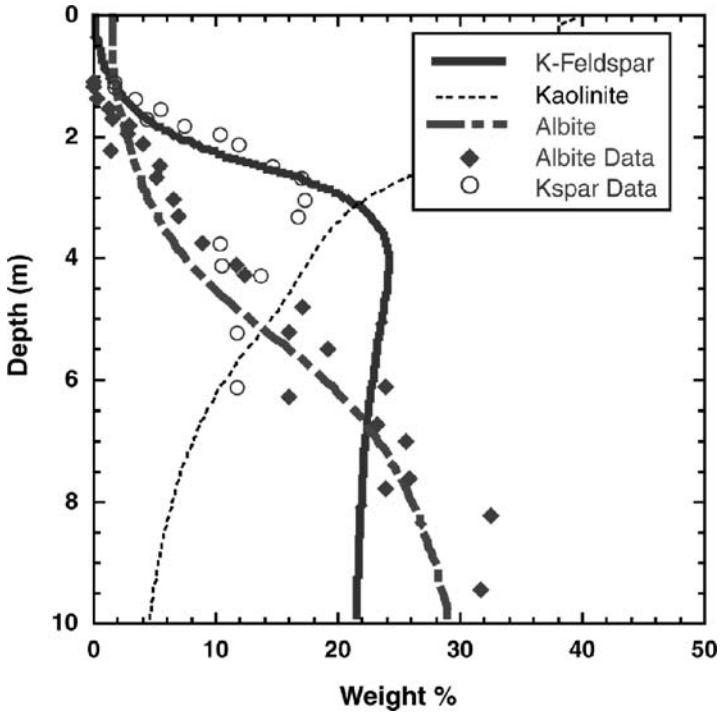

Fig. 11.19 Fitting of the profiles of plagioclase and potassium feldspar from Terrace 5 (226,000 years) at the Santa Cruz chronosequence (White et al., 2006) using the reactive transport code CrunchFlow. Simulations provided by Kate Maher

by allowing its reactive surface area to evolve with a 2/3 dependence on its volume fraction.

11.6 Feedback between Transport and Kinetics

Feedback between flow, transport, and biogeochemical kinetics can lead to an extraordinarily rich set of behaviors in water–rock systems, but the full range of phenomena associated with these effects is largely beyond the scope of this chapter. Positive feedbacks between these processes can lead to highly complex nonlinear behavior, and in some cases, to pattern formation or self-organization. Interested readers are referred to recent volumes on the topic (Jamtveit and Meakin, 1999; Ortoleva, 1994), but two important and widely discussed examples are treated briefly here. The field promises to be extremely fruitful in the future, with progress made as investigations of a mathematical nature are linked to experimentally and/or field-determined kinetic and transport parameters.

11.6.1 Reactive-Infiltration Instability

Mineral dissolution and precipitation, as well as biomass growth and decay, can modify the permeability and tortuosity of porous media, thus providing a nonlinear feedback between the biogeochemical and flow/transport processes. Perhaps the best known example involves the enhancement of the porosity and permeability via mineral dissolution, a positive feedback that can lead to unstable growth of "reaction fingers" or "wormholes", or in the extreme case, to karstification. This process is referred to as the "reactive-infiltration instability" (Ortoleva et al., 1987). It is important in the oil-field process of matrix acidizing, where the injection of acid is intended to reverse the damage to permeability caused by drilling. In carbonate rocks, the injected acid results in a dissolution front that propagates as "wormholes" rather than as a planar front. The instability develops as a result of even very minor variability in the permeability (at the macroscopic scale, the material may appear homogeneous). Regions with slightly higher permeability capture more reactive flow than adjacent regions with lower permeability, thus enhancing the propagation rate of the reaction front in the higher permeability regions. As more and more reactive flow is captured due to the enhancement of the local permeability, the reaction fingers accelerate their growth up to the point where diffusion homogenizes the concentration gradients within the reaction finger, or the flow rates outrun the rates of reaction. In fact, the reactive-infiltration instability requires a transport control within the growing fingers, with flow at low Damköhler number (surface reaction control) resulting in slower channel growth and more highly ramified dissolution patterns (Steefel and Lasaga, 1990).

Figure 11.20 shows a simulation illustrating the effect of reaction kinetics on reaction fingering. The simulation uses the heterogeneous permeability field shown in Fig. 11.9a, but in this case with a total initial permeability range of 4 orders of magnitude (10^{-16}–$10^{-12}\,\mathrm{m}^2$, with an average of $10^{-14}\,\mathrm{m}^2$) and with 10% reactive calcite in a rock with an initially uniform porosity of 2%. The complete dissolution of the calcite leads to an increase in porosity up to 12% and to an increase in permeability by a factor of about 300 according to

$$\kappa = \kappa_0 \left(\frac{\phi}{\phi_0} \right)^3 , \tag{11.87}$$

where κ_0 and ϕ_0 are the initial permeability and porosity, respectively. Figure 11.20a shows the results of a simulation in which the rate constant for the calcite is taken as $10^{-6.5}\,\mathrm{mol\,m^{-2}\,s^{-1}}$ and an initial reactive surface area of $100\,\mathrm{m}^2/\mathrm{m}^3$—in this case, the pore fluid at the tip of the propagating "wormholes" is close to equilibrium, with the result that the rate of advance of the fingers is transport controlled. Very fine, tortuous wormholes form as a gradual shift to a smaller number of more rapidly propagating fingers occurs at the expense of nearby, more slowly propagating fingers. In contrast, when the rate constant is taken as $10^{-10.5}\,\mathrm{mol\,m^{-2}\,s^{-1}}$ (or 4 orders of magnitude slower), the contrast between the rate of growth of individual

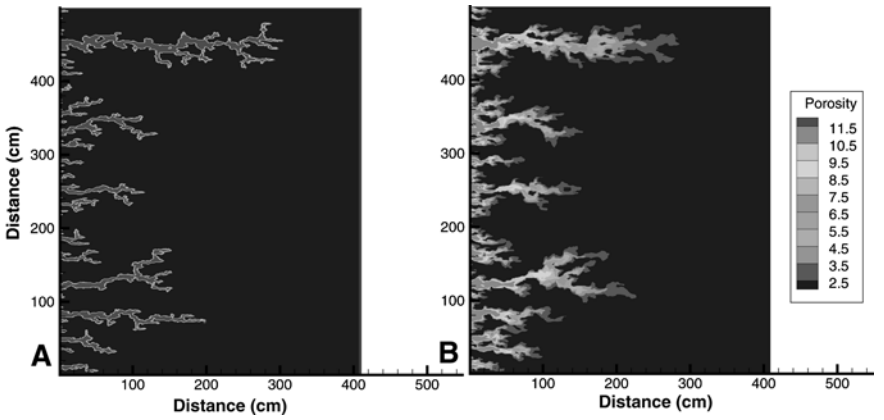

Fig. 11.20 The reactive-infiltration instability results in "wormholing", as regions experiencing an increase in porosity and permeability as a result of mineral dissolution accelerate their growth at the expense of adjacent regions. The wormholing rate is at a maximum under transport-controlled conditions (Panel A) – at lower Damköhler numbers (Panel B), fingers are more diffuse and the difference between the growth rates of individual fingers is less (see also color insert)

reaction fingers is less, and the pattern of dissolution is more highly ramified and diffuse.

11.6.2 Liesegang Banding

Liesegang banding or rings are often noted in subsurface materials, although the phenomenon has received more discussion in the chemical literature (Liesegang, 1896). In the classic theory, the phenomenon occurs in the absence of convection and involves the interdiffusion of reacting species (e.g., O_2 and ferrous iron) that precipitate in discrete bands separated in many cases by geometrically increasing spacing. The earliest explanation for the phenomenon was provided apparently by Ostwald, who suggested that the process involved local nucleation of crystal seeds where the necessary level of supersaturation was achieved. Once nucleation of crystal seeds occurs, crystal growth is assumed to become the dominant form of mass transfer, thus lowering the supersaturation of the local pore fluid (and adjacent regions influenced by molecular diffusion) below the nucleation threshold. The result is that secondary mineralization only develops in discrete zones or bands. This theory has been disputed based on experimental studies in which colloidal seed material was initially dispersed uniformly in the reacting material and yet banding still developed. Other models in which nucleation is coupled to Ostwald ripening have been suggested (Ortoleva et al., 1986). The nucleation/crystal growth hypothesis may be reasonable for water–rock systems, however, as in the case of discrete bands of iron hydroxide developed in sandstone (Fig. 11.21). Similar patterns may develop in

Fig. 11.21 Liesegang bands of ferric hydroxide in sandstone from Mount Diablo, California (see also color insert)

advection-dominant systems as a result of a nucleation/crystal growth mechanism, as shown by (Steefel and Van Cappellen, 1990).

11.7 Concluding Remarks

A good understanding of the coupling between transport and biogeochemical kinetics is essential in the study of water–rock interaction. In this chapter, we have shown that in open systems characterized by transport, the characteristic time scales of reaction need to be compared with the characteristic time scales for transport—geologic time is often irrelevant. The transport processes that are relevant for the study of water–rock interaction include advection, due in most cases to Darcy flow through porous media, molecular diffusion modified by electrochemical migration where charged species are present, and hydrodynamic dispersion. An idealized version of the reactive transport (or advection-dispersion-reaction) equation was presented and the important non-dimensional quantities were derived and discussed in terms of their control of water–rock interaction. Most significant of these for the discussion of the kinetics of water–rock interaction is the Damköhler number, which provides a measure of the importance of reaction kinetics relative to the transport rates in a particular system. The same quantity can be used to determine

approximately the length scale over which equilibrium can be reached and thus provides a useful metric for the validity of the local equilibrium assumption.

The treatment of water–rock interaction systems as well-mixed reactors is challenged and it was shown how an analysis of macrodispersion, which has been widely discussed in the hydrologic literature, can be used to produce a residence time probability density function that predicts the ensemble of reaction times for flow paths through heterogeneous media. Real water–rock systems are typically characterized by physical, chemical, and microbiological heterogeneities that can give rise to concentration gradients, and thus to spatially variable reaction rates. Upscaling reaction rates in water–rock systems that are not perfectly mixed is a new research challenge and will require a careful consideration of the interplay between transport and reactions at multiple scales. Methods for determining *in situ* reaction rates using concentration profiles and mineral volume profiles combined with reactive transport modeling were briefly presented. It was shown that it is necessary to independently determine transport rates in a particular water–rock system in order to uniquely determine *in situ* reaction rates. Finally, two examples of water–rock interaction were given where the feedback between transport and reaction results in pattern formation.

Acknowledgements

I am indebted to Alexis Navarre-Sitchler and Kate Maher for providing some of the unpublished material that has made its way into this contribution. I am also grateful to John Apps, Glen Hammond, Alexis Navarre-Sitchler, and Li Li for their careful reviews of this chapter at various stages of its preparation. I wish to acknowledge funding from the Office of Science at the U.S. Department of Energy through (1) the Geoscience Program in the Office of Basic Energy Sciences (Contract No. DeAC03-76SF00098), and (2) the joint NSF-DOE Environmental Molecular Science Institute at Pennsylvania State University supported by the Department of Energy Office of Biological and Environmental Research.

References

Aris R. (1956) On the dispersion of a solute in a fluid flowing through a tube. *Proceedings of the Royal Society London Series A* **235**, 67–77.

Bahr J. M. and Rubin J. (1987) Direct comparison of kinetic and local equilibrium formulations for solute transport affected by surface reactions. *Water Resources Research* **23**(3), 438–452.

Bear J. (1972) *Dynamics of Fluids in Porous Media*. Dover Publications, Inc., NY.

Berner R. A. (1980) *Early Diagenesis*: *A Theoretical Approach*. Princeton University Press, NJ.

Bethke C. M. and Johnson T. M. (2002) Paradox of groundwater age. *Geology* **30**(2), 107–110.

Boudreau B. P. (1997) *Diagenetic Models and Their Implementation*. Springer-Verlag, Heidelberg NY.

Boyce W. E. and DiPrima R. C. (1986) *Elementary Differential Equations and Boundary Value Problems*. John Wiley & Sons, NY.

Dagan G. (1988) Time-dependent macrodispersion for solute transport in anisotropic heterogeneous aquifers. *Water Resources Research* **24**, 1491–1500.

Dagan G. (1989) *Flow and transport in porous formations*. Springer-Verlag, Heidelberg NY.

Darcy H. (1856) *Les fontaines publiques de la ville de Dijon*. Dalmont, Paris.

Daugherty R. L. and Franzini J. B. (1965) *Fluid Mechanics with Engineering Applications*. McGraw-Hill, NY.

Denbigh K. (1981) *The Principles of Chemical Equilibrium*. Cambridge University Press, Cambridge.

Gelhar L. W. (1986) Stochastic subsurface hydrology from theory to applications. *Water Resources Research* **22**, 135S–145S.

Gelhar L. W. (1993) *Stochastic Subsurface Hydrology*. Prentice-Hall, Englewood Cliffs, NJ.

Gelhar L. W. and Axness C. L. (1983) Three-dimensional stochastic analysis of macrodispersion in aquifers. *Water Resources Research* **19**(1), 161–180.

Gelhar L. W., Welty C., and Rehfeldt K. R. (1992) A critical-review of data on field-scale dispersion in aquifers. *Water Resources Research* **28**(7), 1955–1974.

Haggerty R., Schroth M. H., and Istok J. D. (1998) Simplified method of "Push-Pull" test data analysis for determining in situ reaction rate coefficients. *Ground Water* **36**(2), 314–324.

Harvey C. and Gorelick S. M. (2000) Rate-limited mass transfer or macrodispersion: Which dominates plume evolution at the macrodispersion experiment (MADE) site? *Water Resources Research* **36**(3), 637–650.

Jamtveit B. and Meakin P. (1999) *Growth, Dissolution and Pattern Formation in Geosystems*, pp. 428. Springer, Berlin.

Lasaga A. C. (1998) *Kinetic Theory in the Earth Sciences*. Princeton University Press, NJ.

Li L., Peters C. A., and Celia M. A. (2006) Upscaling geochemical reaction rates using pore-scale network modeling. *Advances in Water Resources* **29**(9), 1351–1370.

Lichtner P. C. (1988) The quasi-stationary state approximation to coupled mass transport and fluid-rock interaction in a porous medium. *Geochimica Cosmochimica Acta* **52**(1), 143–165.

Lichtner P. C. (1993) Scaling properties of time-space kinetic mass transport equations and the local equilibrium limit. *American Journal of Science* **293**(4), 257–296.

Lichtner P. C. (1996) Continuum formulation of multicomponent-multiphase reactive transport. In *Reactive transport in porous media*, Vol. 34 (eds. P. C. Lichtner,

C. I. Steefel, and E. H. Oelkers), pp. 1–81. Mineralogical society of America, Washington DC.

Lichtner P. C. (1998) Modeling reactive flow and transport in natural systems. *Proceedings of the Rome Seminar on Environmental Geochemistry*, 5–72.

Liesegang R. E. (1896) *Naturwiss. Wonchenschr.* **11**, 353.

Maher K., Steefel C. I., DePaolo D. J., and Viani B. E. (2006) The mineral dissolution rate conundrum: Insights from reactive transport modeling of U isotopes and pore fluid chemistry in marine sediments. *Geochimica et Cosmochimica Acta* **70**(2), 337–363.

Malmström M. E., Destouni G., Banwart S. A., and Strömberg B. H. E. (2000) Resolving the scale-dependence of mineral weathering rates. *Environmental Science Technology* **34**(7), 1375–1378.

Meile C. and Tuncay K. (2006) Scale dependence of reaction rates in porous media. *Advances in Water Resources* **29**(1), 62–71.

Murphy W. M., Oelkers E. H., and Lichtner P. C. (1989) Surface reaction versus diffusion control of mineral dissolution and growth rates in geochemical processes. *Chemical Geology* **78**, 357–380.

Newman J. S. (1991) *Electrochemical Systems*. Prentice-Hall, Englewood Cliffs, NJ.

Oelkers E. A. (1996) Physical and chemical properties of rocks and fluids for chemical mass transport calculations. In *Reactive Transport in Porous Media*, Vol. 34 (eds. P. C. Lichtner, C. I. Steefel, and E. H. Oelkers), pp. 131–191. Mineralogical Society of America, Washington DC.

Oelkers E. H., Schott J., and Devidal J.-L. (1994) The effect of aluminum, pH, and chemical affinity on the rates of aluminosilicate dissolution reactions. *Geochimica et Cosmochimica Acta* **58**(9), 2011–2024.

Ogata A. and Banks R. B. (1961) A solution of the differential equation of logitudinal dispersion in porous media. In U.S. Geological Survey Professional Paper, 411-A.

Onsager L. (1931) Reciprocal relations in irreversible processes II. *Physical Review* **38**, 2265–2279.

Ortoleva P. (1994) *Geochemical Self-Organization*. Oxford University Press, NY.

Ortoleva P., Auchmuth G., Chadam J., Hettmer H., Merino E., Moore C. H., and Ripley E. (1986) Redox front propagation and banding modalities. *Physica* **19D**, 334–354.

Ortoleva P., Chadam J., Merino E., and Sen A. (1987) Geochemical self-organization II: The reactive-infiltration instability. *American Journal of Science* **287**, 1008–1040.

Pharmamenko E. I. (1967) *Electrical Properties of Rock*. Plenum Press, NY.

Phillips O. M. (1991) *Flow and Reactions in Permeable Rocks*. Cambridge University Press, Cambridge.

Plummer L. N., Busenberg E., Bohlke J. K., Nelms D. L., Michel R. L., and Schlosser P. (2001) Groundwater residence times in Shenandoah National Park, Blue Ridge Mountains, VA: A multi-tracer approach. *Chemical Geology* **179**, 93–111.

Pokrovsky O. S., Golubev S. V., and Schott J. (2005) Dissolution kinetics of calcite, dolomite and magnesite at 25 °C and 0 to 50 atm $_pCO_2$. *Chemical Geology* **217**(3–4), 239–255.

Prigogine I. (1967) *Introduction to the thermodynamics of irreversible processes.* Interscience.

Sak P. B., Fischer, D. M., Gardner T. W., Gardener, T., Murphy, K., M., and Brantley, S. L. (2004) Rates of weathering rind formation on Costa Rican basalt. *Geochimica et Cosmochimica Acta* **68**(7), 1453–1472.

Skagius K. and Neretnieks I. (1986) Diffusivity measurements and electrical-resistivity measurements in rock samples under mechanical stress. *Water Resources Research* **22**(4), 570–580.

Slichter C. S. (1905) Field measurement of the rate of movement of underground waters. In U.S. Geological Survey, Water Supply Paper.

Snodgrass M. F. and Kitanidis P. K. (1998) A method to infer in-situ reaction rates from push-pull experiments. *Ground Water* **36**, 645–650.

Steefel C. I., DePaolo D. J., and Lichtner P. C. (2005) Reactive transport modeling: An essential tool and a new research approach for the Earth Sciences. *Earth and Planetary Science Letters* **240**, 539–558.

Steefel C. I. and Lasaga A. C. (1990) The evolution of dissolution patterns: Permeability change due to coupled flow and reaction. In *Chemical Modeling of Aqueous Systems II*, Vol. 416 (eds. D. Melchior and R. L. Bassett), pp. 212–225. American Chemical Society, Washington.

Steefel C. I. and Lasaga A. C. (1994) A coupled model for transport of multiple chemical species and kinetic precipitation/dissolution reactions with application to reactive flow in single phase hydrothermal systems. *American Journal of Science* **294**, 529–592.

Steefel C. I. and Lichtner P. C. (1998) Multicomponent reactive transport in discrete fractures: II. Infiltration of hyperalkaline groundwater at Maqarin, Jordan, a natural analogue site. *Journal of Hydrology* **209**(1–4), 200–224.

Steefel C. I. and MacQuarrie K. T. B. (1996) Approaches to modeling of reactive transport in porous media. In *Reactive Transport in Porous Media*, Vol. 34 (eds. P. C. Lichtner, C. I. Steefel, and E. H. Oelkers), pp. 83–130. Mineralogical Society of America, Washington DC.

Steefel C. I. and Van Cappellen P. (1990) A new kinetic approach to modeling water-rock interaction: The role of nucleation, precursors, and Ostwald ripening. *Geochimica et Cosmochimica Acta* **54**(10), 2657–2677.

Taylor G. I. (1953) The dispersion of soluble matter in a solvent flowing through a tube. *Proceedings of the Royal Society London Series A* **219**, 196–203.

Tompson A. F. B., Carle S. F., Rosenberg N. D., and Maxwell R. M. (1999) Analysis of groundwater migration from artificial recharge in a large urban aquifer: A simulation perspective. *Water Resources Research* **35**(10), 2981–2998.

Varni M. and Carrera J. (1998) Simulation of groundwater age distributions. *Water Resources Research* **34**, 3271–3281.

Weissmann G. S., Zhang Y., LaBolle E. M., and Fogg G. E. (2002) Dispersion of groundwater age in an alluvial aquifer system. *Water Resources Research* **38**(10), 1198.

White A. F. and Brantley S. L. (2003) The effect of time on the weathering of silicate minerals: Why do weathering rates differ in the laboratory and field? *Chem. Geol.* **202**(3–4), 479–506.

White A. F., Schulz M. S., Vivit D. V., Blum A. E., and Stonestrom D. A. (2006) Controls on soil pore water solutes: An approach for distinguishing between biogenic and lithogenic processes. *Journal of Geochemical Exploration* **88**(1–3), 363–366.

Zhu C. (2005) In situ feldspar dissolution rates in an aquifer. *Geochimica et Cosmochimica Acta* **69**(6), 1435–1453.

Chapter 12
Isotope Geochemistry as a Tool for Deciphering Kinetics of Water-Rock Interaction

Jérôme Gaillardet

12.1 Introduction

What have isotopes added to our understanding of the kinetics of water-rock interaction processes at the surface of the Earth? Since the development of routine techniques of mass spectrometry, an impressive number of studies have used isotopes to constrain water-rock interaction processes. A number of these initial studies were not purposefully designed to determine the kinetics of water-rock interaction, but they demonstrated that isotopic kinetic effects were both sufficiently large and specific so that they could be used to constrain the kinetics of water-rock interactions. Here we provide a brief synthesis of the different approaches where isotopes have been applied to constrain the rates and timescales of water-rock interaction. We have adopted a very broad definition of the word "kinetics" for this review and have not limited the studies to reaction rates of particular reactions. Because most of the reactions occurring at the Earth's surface are occurring at low temperatures, they do not proceed rapidly enough to reach thermodynamic equilibrium; therefore, we face the problem of determining the rates at which they proceed. Physical processes, such as climate variability, glacier dynamics, landsliding and tectonic processes often proceed more rapidly than chemical weathering reactions. For example, mineral weathering and the subsequent formation of secondary minerals in soils occurs over timescales on the order of tens to hundreds of thousands of years, while the characteristic timescales of climate variability are much shorter. Isotopic approaches have proven to be very powerful in constraining rates of water-rock interaction in natural systems, where physical and chemical processes are inevitably coupled.

Isotopic ratios are measured using mass spectrometers, the most sophisticated being the multi-collector inductively coupled plasma mass spectrometer (MC-ICP-MS). Isotopic ratios can be determined much more precisely than concentrations and their fine variations in nature provide important information about natural processes.

Institut de Physique du Globe de Paris, Université Paris-Diderot – CNRS, gaillardet@ipgp.jussieu.fr

Isotopic variations are caused either by radioactive decay or by physical and chemical processes in which the different isotopes of a given element behave differently. Radioactive and radiogenic isotopes tend to have high atomic numbers and the number of stable isotopes tends to increase with increasing atomic number as well. Light isotopes are isotopes of elements with low atomic numbers. They are usually strongly fractionated by physical and chemical processes (the relative mass difference $\Delta M/M$ is high), while the stable isotopes of elements of higher atomic numbers display low or imperceptible fractionations. The classical delta notation (in per mil, ‰) will be used throughout the chapter. Using this notation, the isotopic ratio R of element E in the material x can be defined as

$$\delta^i E_x = \left(\frac{R_x^{i/j} - R_{STD}^{i/j}}{R_{STD}^{i/j}} \right) 10^3 \tag{12.1}$$

where i and j are the measured isotopes and STD refers to an international standard. In this chapter we have classified the isotopic studies that constrain the kinetics of water-rock interaction into three different sections. In the first section, we will discuss how the specific isotopic signatures of minerals can be used to track mineral dissolution and establish relative water-rock interaction sequences. This approach is valid in the laboratory and in the field, and also includes isotopic doping techniques where isotopes are artificially added to the solution to emphasize isotopic contrasts. The second section discusses the use of isotopes as a chronometer. The main property used here is the radioactivity of certain nuclides that allows for quantification of the time elapsed since water-rock interaction and thus reconstruction of the time evolution of a geological system. Finally, the last section concerns those isotopes that are fractionated by chemical reactions and physical processes. Their behavior is rate-dependent and we will show how their observed fractionation in nature relates to the kinetics of water-rock interaction.

12.2 Isotopes as a Fingerprint of Water-Rock Interaction Pathways

The Earth is a complex assemblage of minerals, rocks and global reservoirs, each of these entities displaying characteristic rates of interaction with water. Reaction rates vary from the mineral surface scale, where elements in the different crystallographic sites have different affinities (Chap. 3), to the global scale, where the different geochemical reservoirs of the Earth (the continental crust, for example) have greatly different reaction kinetics (Chap. 13). The chemistry of both the oceans and sedimentary rocks and their evolution over time are the best records of the diversity and the relative rates of water-rock interaction processes.

We report here a series of studies where isotopes have been successfully used to unravel this complexity. The property of isotopes used here is that each mineral or each crystal site has a specific isotopic signature, either inherited from

time-integrated chemical fractionation during their formation (radiogenic isotopes) or initially acquired when they formed. Both laboratory and field studies allow for reaction rates to be calculated or sequences of reactions to be established (relative rates).

12.2.1 Isotopic Doping Techniques

Isotopic doping techniques consist of adding a solution generally enriched in a rare isotope of a given element to the solution interacting with a mineral or a suite of minerals. The main advantage of this technique is that the amount of an element of interest liberated into solution by mineral dissolution can be calculated independently of its incorporation into secondary phases. The method is particularly useful at steady state. At steady state, the concentration of an element in solution is not changing. However, this does not mean the element is not involved in any reactions, but rather that dissolution and precipitation reactions involving the element are in equilibrium.

Isotopic doping techniques have been successfully used in a series of papers by a group in Paris (Houssein et al., 1993; Zuddas et al., 1994; Seimbille et al., 1998) to determine the rates of dissolution of K-feldspar, biotite and plagioclase during the hydrothermal alteration of a granite in conditions close to equilibrium. A solution corresponding to the equilibrium conditions with the secondary phases adularia + prehnite + low-temperature albite + kaolinite and calcite were spiked with strontium nitrate and potassium chloride artificially enriched in ^{84}Sr and ^{39}K respectively, and then reacted with a powdered granite. Concentrations and isotopic compositions ($^{39}K/^{41}K$ and $^{84}Sr/^{86}Sr$) were measured in solution over a period of six months. Strong decreases of both $^{39}K/^{41}K$ and $^{84}Sr/^{86}Sr$ isotopic ratios in solution were observed in the early stages of water-rock interaction, indicating the contribution of natural Sr and K from mineral dissolution. Secondary phases formed rapidly as indicated by the early depletion in Sr, Ca, Si and Al in solution. These secondary minerals have the Sr and K isotopic composition of the solution from which they precipitate. While Sr and K concentrations reached steady state after a month, their isotopic ratios changed with time as a result of primary and neoformed mineral dissolution. During these experiments, the dissolution of primary minerals contributed ^{41}K and ^{86}Sr to the solution, while the dissolution of secondary phases formed at the beginning of the experiment did not fractionate K and Sr isotopes. In the course of the experiment, a linear correlation was observed between $^{87}Sr/^{86}Sr$ and $^{84}Sr/^{86}Sr$ in solution (Fig. 12.1).

The radioactive decay of ^{87}Rb to ^{87}Sr creates $^{87}Sr/^{86}Sr$ anomalies from one mineral to another as a function of their Rb content, while ^{86}Sr and ^{84}Sr isotopes are essentially stable, with a ratio in terrestrial material of 0.0566. The linear correlation reported in Fig. 12.1 indicates that the dissolved Sr is a result of mixing between Sr from the spike and Sr from the granite, and that the source of Sr from the minerals did not change with time. The invariance in the isotopic composition of Sr released

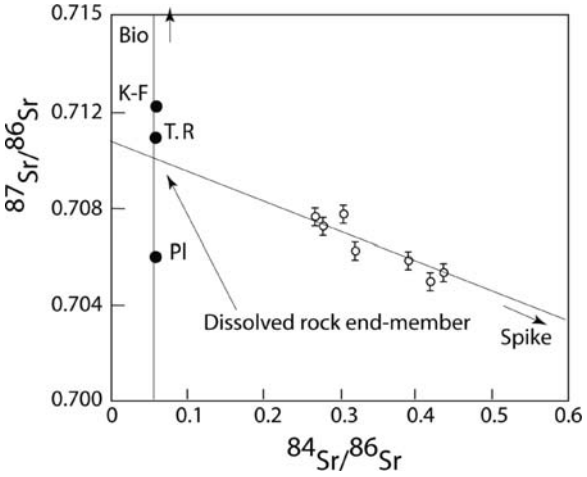

Fig. 12.1 Evolution of the Sr isotopic composition of a solution doped with ^{84}Sr interacting with a granite under near equilibrium conditions at 10 bars and 453 K. Isotopic compositions (^{84}Sr/^{86}Sr and ^{87}Sr/^{86}Sr) of the spike are approximately 18 and 0.5, respectively, while Earth materials have constant ^{84}Sr/^{86}Sr of 0.566. The intercept of the mixing line gives the origin of Sr from the rock and its concentration. Pl, T.R, K-F and Bio denote plagioclase, total rocks, K-feldspar and biotite respectively

from the minerals is one of the most interesting results from the study of Seimbille et al. (1998). The ^{87}Sr/^{86}Sr ratio of 0.711 for the mineral dissolution component is deduced from the mixing line of Fig. 12.1. Assuming that Sr is only released from biotite (^{87}Sr/^{86}Sr = 2.665) and plagioclase (^{87}Sr/^{86}Sr = 0.7074), the following mass budget equation

$$\left(\frac{^{87}Sr}{^{86}Sr}\right)_{fluid} = \left(\frac{^{87}Sr}{^{86}Sr}\right)_{bio} X + \left(\frac{^{87}Sr}{^{86}Sr}\right)_{plag} (1-X) \tag{12.2}$$

(where X is defined as the proportion of Sr derived from botite) shows that only X = 0.2% of Sr is derived from biotite weathering. The number $(1-\mathrm{X})/\mathrm{X}$ corresponds to the ratio of Sr in solution derived from plagioclase divided by the amount of Sr in solution derived from biotite weathering. If $\mathrm{Sr_{plag}}$ and $\mathrm{Sr_{bio}}$ denote the concentration (ppm) of Sr in plagioclase and biotite minerals, and $\mathrm{A_{bio}}$ and $\mathrm{A_{plag}}$ are the mass proportions of biotite and plagioclase minerals in the granite, the relative rate R of plagioclase alteration with respect to biotite is

$$\mathrm{R} = \frac{1 - X/X}{A_{plag}Sr_{plag}/A_{bio}Sr_{bio}} \tag{12.3}$$

The calculated ratio of plagioclase over biotite abundance in the granite is 2 and the concentrations of Sr in the plagioclase and biotite phases are 854 ppm and 7 ppm respectively. We then calculate that R = 2, which means that plagioclase dissolved

two times faster than biotite. Only the results from the first month of the experiment show a higher weathering rate of biotite (R = 1).

A similar reasoning can be applied to the K system. Rock minerals have different $Rb/^{39}K$ ratios but similar $^{41}K/^{39}K$. A plot of $Rb/^{39}K$ versus $^{41}K/^{39}K$ shows a mixing line between the spike and the biotite-derived K. The main advantage of the isotopic doping technique is that the amount of Sr and K derived from mineral dissolution can be calculated, despite the incorporation of these elements into secondary phases. The working hypothesis made by the authors is that no fractionation of Sr and K isotopes occurs during their incorporation into the secondary phases (e.g., secondary minerals precipitate with the isotopic composition of the fluid). Consequently, Seimbille et al. (1998), using mass budget equations and neglecting the contribution of minor phases hornblende, apatite and sphene, were able to calculate the mass of plagioclase, biotite and K feldspar dissolved during the experiment. They concluded that under the experimental conditions, the rate of plagioclase dissolution is 5 times higher than biotite and 10 times higher than K-feldspar. Normalized to the mineral specific surface area, the rate of plagioclase dissolution was observed to be $3 \pm 1 \times 10^{-12}\,mol/m^2/s$.

Using a similar approach, Beck et al. (1991) applied the isotopic doping technique to the recrystallization of calcite under hydrothermal conditions in a system close to equilibrium where chemical affinity (the driving force of reaction) was near zero. Beck et al. (1991) evaluated the kinetics of calcite recrystallization with flexible cell hydrothermal equipment by spiking the solution with ^{44}Ca and ^{84}Sr. The advantage of using isotopes is that even if the amount of material exchanged between the mineral and the fluid is small, major variations in the isotopic composition of the fluid are detected because the Sr isotopic compositions between the spiked solution and the mineral are sufficiently distinct. At a constant temperature (250° C), the $^{84}Sr/^{86}Sr$ of the fluid changed from 0.4127 to 0.3612, with the analytical precision of 0.0001, whereas Ca concentrations changed from 1010 ppm to 1031 ppm, with an analytical precision of 20 ppm. Because the Sr isotopic ratio of the fluid is not affected by calcite precipitation, it is an excellent index of the amount of primary mineral that dissolved, unlike the aqueous Ca concentration that depends both on dissolution and precipitation. Changes in the fluid isotopic composition with time can be used to determine the rates of reactions. At any time, the Sr isotopic composition of the fluid ($R_f = {}^{84}Sr/^{86}Sr)_f$ is a mixture between Sr from the mineral $R_m = (^{84}Sr/^{86}Sr)_m$ and Sr from the initial spiked solution $R_f{}^0 = (^{84}Sr/^{86}Sr)_f^0$:

$$R_f = R_f^0 X + R_m(1 - X) \tag{12.4}$$

Here, X is the proportion of Sr in the fluid derived from mineral dissolution:

$$X = \frac{C_f}{C_f^0} \tag{12.5}$$

where C_f is the concentration of an element in the fluid and $C_f{}^0$ the initial concentration. The evolution of the elemental and isotopic composition of the fluid can be described by an infinite number of infinitesimally small dissolution and precipitation

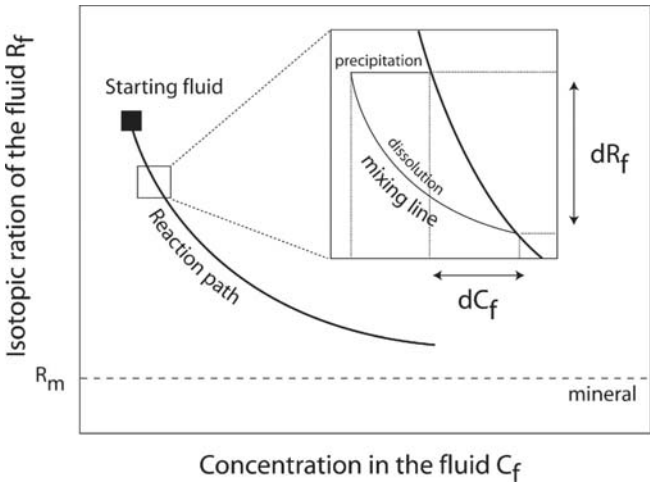

Fig. 12.2 Isotopic ratio-concentration space for a mineral exchanging with a fluid near equilibrium. The isotopic ratios of the starting solution and of the mineral are very distinct due to the doping technique. The reaction path of the solution can be represented as an infinite number of infinitesimally small dissolution and precipitation steps. The isotopic ratio of the fluid is only influenced by dissolution while the elemental concentrations change with both precipitation and dissolution. (From Beck et al. 1991, with permission from Elsevier)

steps. During a precipitation step, the fluid concentration of an element decreases but the isotopic composition of the fluid is constant. During the dissolution step, the concentration increases but the isotopic composition of the fluid moves on a mixing line between the mineral composition to the previous fluid composition (Fig. 12.2).

If dM and C_m are the incremental mass of mineral dissolved and the concentration of the element in the mineral, then a mass budget implies that

$dMC_m = M_f dC_f$ and C_f and R_f are related through the isotopic mixing equation written above. The differential form of the isotopic mixing equation is

$$dC_f = \frac{C_f}{R_f - R_m} dR_f \tag{12.6}$$

The integrated mass of mineral dissolved can then be written

$$M = \frac{M_f}{C_m} \int \frac{C_f}{R_f - R_m} dR_f \tag{12.7}$$

and calculated by specifying the dependence of C_f with R_f (reaction path). Beck et al. (1991) postulated a hyperbolic path through (C,R) space (Fig. 12.2). The above equation can then be integrated and an equation relating the mass of dissolved mineral to the isotopic and concentration data at any time of the experiment can be derived. The evolution of M with time gives rates of reactions. The results of this experimental study have been applied to seafloor carbonate dissolution (close to equilibrium conditions) by Beck et al. (1991). The time required to approach 99%

of isotopic equilibrium between seafloor carbonates and pore fluids varies between several months and 100 Myr depending on temperature, fluid flow rate and relative concentrations in the mineral and the fluid.

Isotopic doping techniques have also been employed in a number of cases to trace the kinetics of adsorption-desorption onto surfaces. The use of radioactive and stable isotopic tracers is a convenient method for monitoring the release or removal of elements. In a recent study, Gee and Bruland (2002) traced the adsorption kinetics of Ni, Cu and Zn onto suspended sediments from South San Francisco bay. ^{61}Ni, ^{65}Cu, and ^{68}Zn spiked solutions were added to bottles containing natural suspended sediments so that the total concentration in solution was consistent with possible natural concentrations. The use of high-resolution ICPMS allowed the authors to detect slight variations in dissolved metal isotopic composition and to propose kinetic rate constants for Ni, Cu and Zn adsorption onto a natural material. This isotopic doping study predicted that the equilibration times with respect to sorption were on the order of 2, 3 and 4 weeks for Zn, Cu and Ni respectively. This study clearly shows the potential of sensitive isotopic measurements to detect the mechanisms and rates of water-rock interactions and the importance of these rates to predict the seasonal cycling of metals in estuaries, in particular.

12.2.2 Experimental Mineral Dissolution Sequences

Several authors have attempted to use variations in the isotopic ratios of minerals from igneous rocks that result from radioactive decay to investigate mineral reaction rates. For example, Sr, Pb and more recently Os isotopes (Gannoun et al., 2006) have been tested. Due to the radioactive decay of Rb to Sr and U to Pb, the Rb/Sr and U/Pb ratios of minerals determine their isotopic compositions (^{87}Sr/^{86}Sr, ^{206}Pb/^{204}Pb, ^{207}Pb/^{204}Pb, ^{208}Pb/^{204}Pb). For example, of the more common rock-forming minerals, biotite and apatite are the most enriched in Rb and U (Faure and Mensing, 2005), respectively, and exhibit the highest ^{87}Sr/^{86}Sr, ^{206}Pb/^{204}Pb and ^{207}Pb/^{204}Pb ratios.

Brantley et al. (1998) were the first to attempt to derive Sr release rates from dissolving feldspars in a continuously stirred, flow-through reactor, at pH 3–4 in distilled water. This study demonstrated that the early release of Sr from feldspar is neither stoichiometric nor isotopically identical to the starting material. For example, for microcline dissolution, the isotopic value of the mineral before dissolution (^{87}Sr/^{86}Sr = 1) is reached after 2,500 hours, while the value obtained at the beginning of the experiment is very low (0.7). The authors interpreted the nonstoichiometric release of Sr and the evolution of Sr isotopic ratios in the early stages of dissolution as indicating the contribution of rare secondary phases (zeolites, fluorite) present within the primary minerals and/or to the preferential leaching of cations from defect sites of the newly abraded surfaces.

The same kind of approach was extended to Pb isotopes by Harlavan and Erel (2002). They showed that Pb with a radiogenic Pb isotopic composition is

preferentially released from accessory minerals (allanite, sphene, apatite) when minerals of a crushed granite are in contact with dilute acids. Granite dissolution was studied under far from equilibrium and low pH conditions by Erel et al. (2004). The release of Sr and Pb from a bulk crushed granite as well as three separate mineral separates (plagioclase-rich, perthite-rich and biotite- + chlorite-rich fractions) clearly showed that the release of Sr and Pb isotopes is not isotopically stoichiometric and reflects the preferential early dissolution of accessory minerals included in major minerals. The evolution of the $^{206}Pb/^{207}Pb$ and $^{87}Sr/^{86}Sr$ ratios in solution as function of time is shown in Fig. 12.3.

Based on this evolution, four stages of rock dissolution can be defined. Using major elements combined with Sr and Pb isotopes, the authors were able to propose the following reaction path. First, the initial stage of weathering (<200 h) is characterized by disseminated calcite dissolution and the release of Pb and Sr from the interlayer sites in biotites. In the second stage, the contribution of interlayer sites controls the chemical and isotopic composition of the solution. The third stage of dissolution (400–1,000 h) shows the major contribution of biotite and the minor effect of plagioclase, while in the last weathering stage plagioclase dissolution is dominant over that of biotite.

The kinetics of dissolution and Sr release during biotite and phlogopite weathering has been documented by Taylor et al. (2000) using flow-through column reactors at pH 3 under far from equilibrium conditions. With time, the Sr isotopic ratio from biotite and phlogopite experiments increases significantly. After 700 hours for biotite and 1,500 hours for phlogopite, a value similar to or above that of the bulk mineral is observed. The authors show in this study that the early release of Sr is due to the dissolution of disseminated calcite inclusions. After correction for the calcite dissolution, it appears that the Sr isotopic ratio of the solution increases to values above those of the biotite and phlogopite. The non-stoichiometric release of Sr from sheet silicates is attributed by the authors to a difference in weathering rates between the octahedral, tetrahedral and interlayer sites. Because interlayer sites are more reactive and concentrate Rb (which has decayed to ^{87}Sr), the preferential release of interlayer Sr causes the elevated Sr isotopic signal in the solution interacting with the minerals. These results allowed the authors to calculate release rates for Sr isotopes. For example, for biotite, the release rate of ^{87}Sr is $10^{-16}\,mol/m^2/s$, higher than that of ^{86}Sr $(10^{-16.2}\,mol/m^2/s)$. This small difference has important implications for the evolution of Sr isotopic ratio in a soil profile with time and the authors proposed a theoretical time evolution for the Sr isotopic ratio of a biotite during chemical weathering. The Sr isotopic ratio decreases slowly because ^{87}Sr from interlayer sites continues leaching. Then a more pronounced decrease occurs until the Sr isotopic ratio reaches the initial $^{87}Sr/^{86}Sr$ $(^{87}Rb/^{86}Sr = 0)$ of the mineral. Dissolution is then congruent and the Sr isotopic composition in solution becomes constant. In this scenario, 3,000 years are necessary for biotite to reach a steady value with respect to the release of Sr isotopes.

In conclusion, isotopic evolution during mineral dissolution is more complicated than originally thought, and it will be necessary to understand such evolution to interpret the sedimentary record at different time resolutions. The exposure of fresh

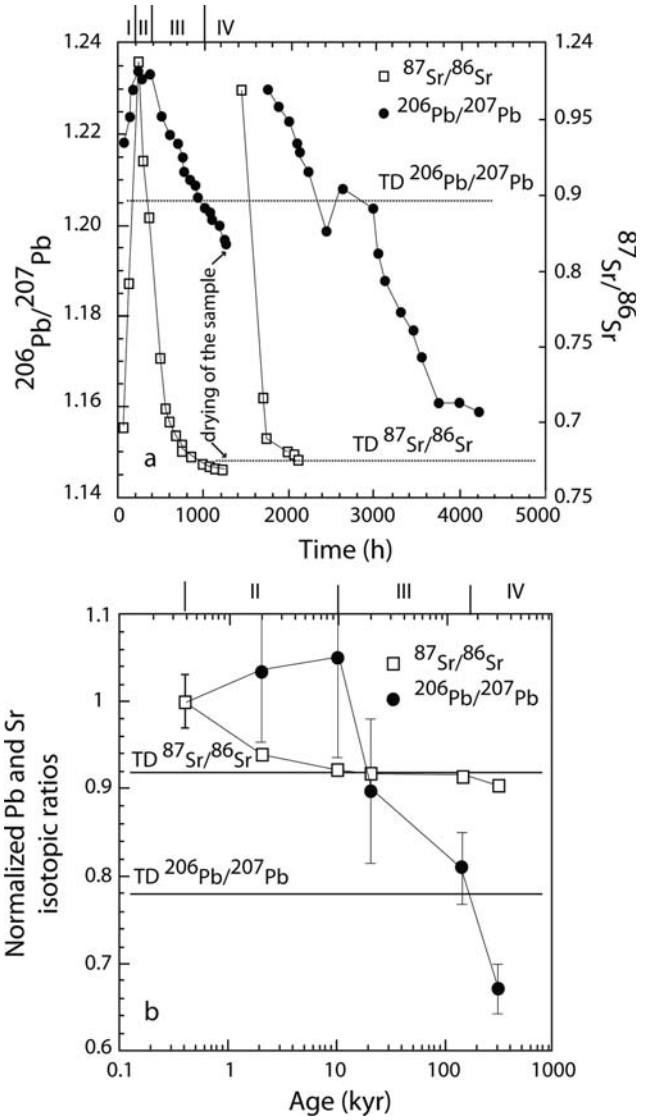

Fig. 12.3 **a**. Evolution of Pb and Sr isotopes during the experimental dissolution of a crushed granite at pH = 1 (Erel et al., 2004). Horizontal lines show the isotope value of a total digest (TD) of the rock. Stage I is marked by a sharp increase in isotopic ratios, stage II is marked by a decrease in Sr isotopes but not for Pb, stage III is marked by a decrease in Sr and Pb isotopic ratios where both are still above the total digest value, and stage IV is marked by a decrease of Sr and Pb isotopic ratios below the total digest value. **b**. Natural data from labile fraction of soils from the Wind River Mountains shown for comparison (Erel et al., 2004). Horizontal axis is the age of soils. Stage I is missing but a good agreement is observed with experimental results. Data are normalized to the values for the youngest soil. (From Erel et al., 2004, with permission from Elsevier)

rocks to a weathering environment where physical erosion is actively generating new mineral surfaces (glaciers, mass wasting) will lead to a specific isotopic signature in water and will influence the isotopic ratio delivered to the ocean by rivers. The isotopic ratio of radiogenic isotopes is therefore a powerful tool for constraining kinetics of water-rock interaction, but a better understanding of isotopic release mechanisms is necessary. This will be possible by developing more experimental studies that more closely mimic natural conditions. To date, most experimental studies are usually performed far from equilibrium and at low pH conditions (pH = 1), a condition rarely encountered in nature (see Chap. 5).

12.2.3 Natural Weathering Sequences of Granitic Rocks

The studies presented above were motivated by a need to understand the kinetics of weathering reactions. The studies that are presented below were initially conducted in order to interpret oceanic proxies such as the Sr and Os isotopic evolution of marine carbonates or the Pb isotopic composition of ferro-manganese crusts during the Tertiary. Geochemical records of such heavy isotopes contain information about the weathering sources on land because they are mostly derived from continental weathering or their hydrothermal input can be independently constrained. As a result, the evolution through time of Sr, Os or Pb isotopes in oceanic sediment may be useful to understand the weathering history of the continents and thus the climate or tectonics-weathering feedbacks.

When dated, terminal moraines, marine terraces, or lava flows are useful geological features that are classically studied to understand how chemical weathering reactions proceed as a function of time. In many cases, soils developed on these terranes define a chronosequence, which provides a setting to determine the order of weatherability of minerals and to calibrate the kinetics of isotopic release.

The use of Sr isotopes in natural systems to derive mineral weathering rates has received the most attention. Because each weathering mineral has its own distinct Sr isotopic ratio that depends on the Rb/Sr ratio and age of the mineral, it is possible, by analyzing the Sr isotopic composition of a stream or of a soil solution, to deduce the amount of Sr released by the weathering of each mineral and therefore to calculate relative weathering rates. Knowledge of the time elapsed since the beginning of chemical weathering can be used to turn relative weathering rates into absolute weathering rates. Pioneering studies in this field have focused on soil material (Blum and Erel, 1995; Bullen et al., 1997) and the chemistry of streams draining these soil chronosequences (Blum et al., 1994). These studies have shown that the Sr isotopic composition of streams and of the exchangeable pool of Sr in soils decreases with age, even though the soil parent material and the isotopic composition of atmospheric deposition are constant.

Blum and Erel (1997) reported analyses of soil parent material, soil digest and cation exchange fractions from a granitic glacial soil chronosequence (0.4–300 kyr) in the Wind River Mountains, Wyoming. Six soil profiles (horizon A, B and C)

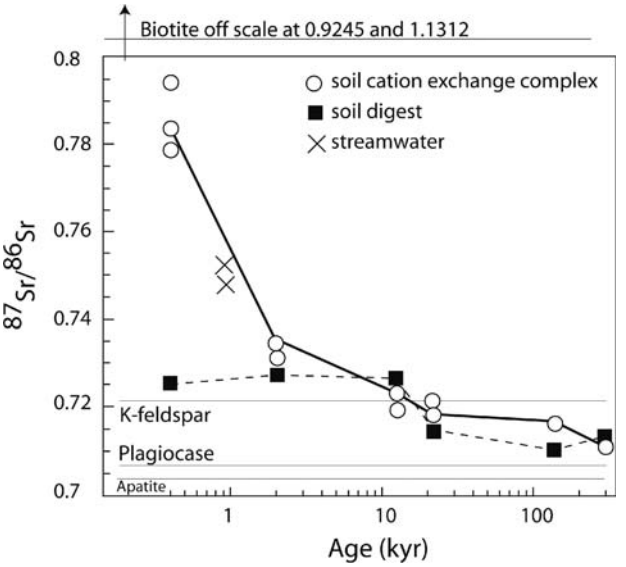

Fig. 12.4 Soil analyses of bedrock, soil digest and cation exchange fractions from a granitic glacial soil chronosequence (0.4–300 kyr) in the Wind River Mountains, Wyoming. Stream water data are added for comparison. All samples are from the B-horizon of soils. Sr isotopic values from the separate minerals are given (horizontal lines). (Data from Blum and Erel, 1997, with permission from Elsevier)

were analyzed for Sr isotopes. The depth of the soil profiles increases with age from 50 cm to 110 cm. Results are reported on Fig. 12.3 with more details in Fig. 12.4.

Exchangeable Sr (leached with ammonium acetate) is derived from chemical weathering and from atmospheric deposition, especially for soil surface samples. A remarkably continuous decrease of the Sr isotopic composition of the exchangeable pool from 0.79 to 0.711 is observed from the most recent profile to the oldest one. The total soil $^{87}Sr/^{86}Sr$ ratios show less change with soil age. Assuming that no isotopic fractionation of Sr occurs during its adsorption onto soil mineral surfaces and that the soil cation exchange pool is essentially controlled by chemical weathering of the dominant Sr-bearing phases (40% Plagioclase, 20% K-feldspar and 10% biotite) below 10 cm in depth, the authors determined the relative weathering rates necessary to explain the observed Sr isotopic ratios of the exchangeable pool. The results clearly show that biotite weathering has a dominant influence on the Rb-Sr isotopic systematics of soils and that the rate of biotite weathering is enhanced by a factor of 50 in the youngest soils compared to the oldest, and that the rate of biotite weathering strongly decreases with age. The results from Blum and Erel (1997) are different than those of White et al. (1992) and Bullen et al. (1997) who analyzed Sr isotopes in soil chronosequences developed on granitic alluvium in the eastern Central Valley of California. They showed that the soil exchange was dominated by the weathering of plagioclase and K-feldspar. The absence of fresh biotite in the soils studied by White et al. (1996) and Bullen et al. (1997) explains the significant differences in the Sr isotopes between the two field sites and shows that biotite

weathering plays a major role in the early stages of chemical weathering, particularly when freshly exposed mineral surfaces are exposed to chemical weathering reactions. These results led Blum and Erel (1995) to propose that the generation of weathering surfaces by continental glaciations and rapid physical erosion rates in regions of rapid uplift may thus have a major input on the Sr isotopic composition of rivers and the ocean for weathering periods less than 20 kyr.

The evolution of lead isotopes in soil chronosequences has been investigated by Erel et al. (1994) and Harlavan et al. (1998), in particular, on the same soil chronosequence of the Wind River Mountains. As can be seen in Fig. 12.3, a good agreement is observed between the evolution patterns of Sr and Pb isotopes in dissolution experiments (see above) and in the soil chronosequences. This suggests that the dissolution kinetics inferred from dissolution experiments (see stage I to IV) are operating in natural systems; therefore Sr and Pb isotopic compositions of soil leachates provide a "time-dependent mineral dissolution scheme" (Erel et al., 2004). Only the very early stage of weathering is not seen in the Sr data from the chronosequence, probably because calcite dissolves quickly and has already been removed from the most recent soil profile (400 years). Additional data will be necessary to refine this picture. In particular, the sensitivity of the above conclusions to lithology and climate remains to be established. However, the clear evolution of radiogenic isotopic ratios with time in soil chronosequences and the good correlation between the laboratory and the field patterns provides a good example of the use of radiogenic isotopes to constrain the kinetics of mineral dissolution in crystalline rocks. Of course, in order for these methods to be effective, the minerals must have different isotopic compositions.

12.2.4 Evolution of Isotopes Along Flowpaths

12.2.4.1 Diagenesis

One of the most interesting applications of isotopes to deduce rates of water-rock interaction comes from isotopic profiles in oceanic sediment pore water. Uncompacted oceanic sediments are a natural chemical reactor in which pore fluids, due to slight changes in pH, rapidly dissolve sedimentary carbonates and precipitate a new carbonate phase. When the sediment is homogenous and dominated by carbonates, a simple model of diagenetic exchange between the sediment and the pore fluid can be developed in order to predict the evolution with time and depth of the composition of the fluid and that of the solid. The mass conservation equation applies to a dispersive and advective system influenced by dissolution-precipitation reactions. An adaptation of the general diffusion-advection equation for diagenetic changes (Berner, 1980) is given by Richter and DePaolo (1987) for any chemical element or isotope in the form

$$\frac{\partial}{\partial t}(C_f) = D\frac{\partial^2 C_f}{\partial z^2} - v\frac{\partial C_f}{\partial z} + R\frac{\rho_s}{\rho_f}\frac{(1-\phi)}{\phi}(C_s - kC_f) \qquad (12.8)$$

Where ρ, C, ϕ, D, v, R represent the density (f for the fluid and s for the solid), concentration of chemical species in the fluid, porosity, diffusivity, the fluid velocity due to compaction, and the rate of carbonate dissolution-reprecipitation respectively. Parameter k is an effective partition coefficient between the solid and the fluid. The first two terms on the right-hand side represent diffusion and advection respectively and depend on physical characteristics of the system. In most diagenetic systems, transport is primarily diffusive, which makes the transport term much easier to constrain because diffusion coefficients are well known. The last term on the right side of the above equation is the reaction term. This model was applied to Sr isotopes (non-fractionating during the isotopic exchange between the fluid and the solid) by Richter and DePaolo (1987, 1988). Once the physical parameters are constrained, the rate of Sr exchange between pore water and solid carbonate is calculated such that the model matches the Sr concentration and Sr isotope profiles of both pore water and solid carbonate. For the oceanic corehole DSDP 590, for example, this method implies that the dissolution-reprecipitation rate (R) decreases rapidly with depth, from a near surface value of 10% of the solid per Myr to 1% of the solid per Myr below 200 m.

Carbon isotopic profiles in deep-sea sediments were also reproduced by Gehlen et al. (1999) using a reactive transport model to calculate the rates of production of metabolic CO_2 by organic matter decay and rates of $CaCO_3$ dissolution. The incorporation of biogenic processes into reaction kinetics is discussed further in Chaps. 8 and 8.4.5.5.

12.2.4.2 Groundwaters

Isotopic measurements in groundwater systems have been used in order to understand flow paths, mixing relationships and the kinetics of water-rock interaction (Bullen et al., 1996; Luo et al., 2000; Singleton et al., 2005; De Paolo et al., 2006). The simple idea that motivated these studies is that the evolution of isotopic ratios along a fluid flow path is controlled by the physical processes that govern the groundwater flow coupled to the chemical interaction of water and rocks. General models of isotopic reactive transport in groundwater systems have been proposed by Johnson and DePaolo (1994, 1997a, 1997b) and more recently by DePaolo (2006) for fracture-dominated fluid-rock systems. The basic equation that expresses isotopic ratios in a water body moving in a porous medium as a function of time (t) and position (x) is derived from the general equation of transport-reaction (see also Chap. 11). When applied to a system with two isotopes of a chemical element, with the approximation that the isotopic abundances of the denominator isotope approximates the elemental concentration, we have

$$\frac{\partial R_f}{\partial t} = D\left(\frac{\partial^2 R_f}{\partial x^2} + 2\frac{1}{C_f}\frac{\partial C_f}{\partial x}\frac{\partial R_f}{\partial x}\right) - v\frac{\partial R_f}{\partial x} + \sum_{i=1}^{n}\frac{J_i}{C_f}[R_i - R_f] \qquad (12.9)$$

with R_f and R_i are the isotopic ratios of the element of interest in the fluid and the reaction products, respectively, and C_f is the concentration of the normalizing isotope (or of the element). J_i are the reaction fluxes produced by dissolution, precipitation,

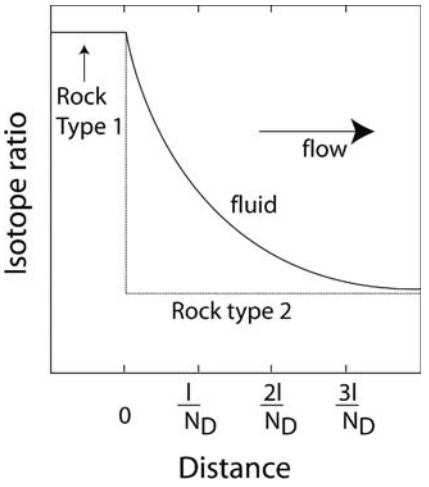

Fig. 12.5 Theoretical evolution of the isotopic ratio of the fluid in a simple water-rock system as a function of distance. Peclet and Damköhler numbers are fixed. Initially a strong isotopic contrast exists between rock type 1 and rock type 2. L is the characteristic length of the system and N_D is a critical parameter (the Damköhler number) that determines the response of the fluid isotopic ratio along the flowpath. The Damkölher number is the ratio of the total reaction fluxes to the advection rate. High N_D means that reaction is fast between the fluid and the rock. Steep curves are obtained for high N_D numbers while low numbers (low reaction rates or rapid fluid transport) correspond to flat curves

ion-exchange or sorption. D is the longitudinal dispersion coefficient and v is the mean groundwater velocity. The J_i terms are functions of the rates of dissolution/precipitation reactions and the solid to fluid ratio (mass of solid per unit volume of fluid). The isotopic composition of the fluid is therefore a balance between flow and the dissolution/reaction rates (Maher et al., 2006a). The fact that isotopic ratios can be measured very precisely and that substantial differences (in concentrations and isotopic ratio) may exist between the solution and the solids makes the above equation particularly useful. This equation holds for non-fractionating isotopes (e.g., Sr, Nd, Pb) and fractionating isotopes (e.g., O, B, S). In the former case, the precipitation term does not appear in the equation because precipitation does not change the isotopic composition of the fluid. Mathematically, the precipitation term drops out of the equation if no fractionation occurs between the fluid and the solid formed. This equation provides a theoretical framework by which isotopic data during fluid transport, aqueous dispersion, and interaction with rocks can be interpreted (Johnson and DePaolo, 1997). For advective systems, the above equation can be scaled and dimensionless parameters can be introduced. The evolution of the isotopic ratio in a simple water-rock system as a function of distance depends on two dimensionless numbers of importance (see also Chap. 11). The Peclet Number (Pe) compares the importance of advection relative to dispersion in the system ($Pe = v.l/D$ where l is the characteristic length of the system) and the Damköhler number compares the ratio of the reaction flux to the advection rate ($N_D = l.J_{tot}/v.C_{f\,f}$, with J_{tot} the total reaction flux) (Fig. 12.5). These two parameters describe the evolution of isotopic ratios along flowpaths.

Different elements have different N_D which allows their isotopes to be used as conservative tracers (low N_D, e.g., O) or tracers of water-rock interactions (high N_D, for highly reaction-dominated isotopes like Sr). When reactions with different kinetics take place in a water-rock system, rapid reactions (such as surface exchange reactions) lead to high Damköhler numbers and sharp isotopic fronts that propagate in the system after a perturbation. This formulation has been applied to Sr isotopes from the Yucca Mountains (Johnson and DePaolo, 1994) and in the clay-rich aquifer close to the Berkeley National Laboratory (Johnson and DePaolo, 1997). This study showed that the $^{87}Sr/^{86}Sr$ measured in the Berkeley groundwater changes greatly over short distances as a result of fast exchange reactions and slower silicate dissolution reactions. Inversion of Sr isotopic data according to two extreme scenarios shows that flow velocities necessary to explain the Sr isotopic patterns must be between 0.2 and 0.02 m/year. The first scenario assumes no dissolution and corresponds to the propagation of an isotopic exchange front while the second assumes that exchange fronts have completely passed through and only slow dissolution reactions are taken into account.

A more recent example is given by Maher et al. (2003) for a site in the Hanford/DOE complex in eastern Washington State. Lithology consists of detrital sediments comprised of quartz, plagioclase, K feldspar and trace biotite. Sr isotopes were measured in pore waters, nitric acid leachates and bulk sediments of a 72 m borehole. Sr isotopic ratios decrease sharply from the top to the bottom of the core (Fig. 12.6). A model considering that the Sr isotope profile results from the evolution of a downward percolating fluid interacting with local sediments (either by addition of Sr through chemical weathering or exchange) can be written. The equation describing the evolution of the Sr isotopic ratio is similar to that written above (Johnson and DePaolo, 1997b), and shows that the Sr isotopic signal is a balance between flow characteristics (hydrodynamic dispersion coefficient, flow velocity) and weathering/exchange rates. The retardation factor K_{ret} for the isotopic ratio is defined as

$$K_{ret} = 1 + \frac{m_e}{m_f} \tag{12.10}$$

where m_e and m_f are the masses of exchangeable Sr in the solid phase per unit volume and of dissolved Sr per unit volume of sediment respectively. Retardation factor in the Hanford formation ranges between 80 and 240, showing the importance of exchange reactions. The steady state solution of this model is shown in Fig. 12.6. Dissolution rates of bulk silicates are calculated for various values of infiltration rate. If the dissolution rates are constrained by results from a study of weathering rates in soils developed on similar granitic sediments in California (White et al., 1996), then infiltration rates of about 7 mm/year are deduced. Changing infiltration rates and/or weathering rates with time will result in different Sr isotopic profiles.

Although, in these examples, the weathering rates of minerals are fixed and the flow velocity calculated, the potential of the method for constraining rates of chemical weathering is probably greater in situations where the physical properties of the moving fluid can be constrained. Additional examples using coupled isotopic systems (using radioactive properties of elements) will be shown below.

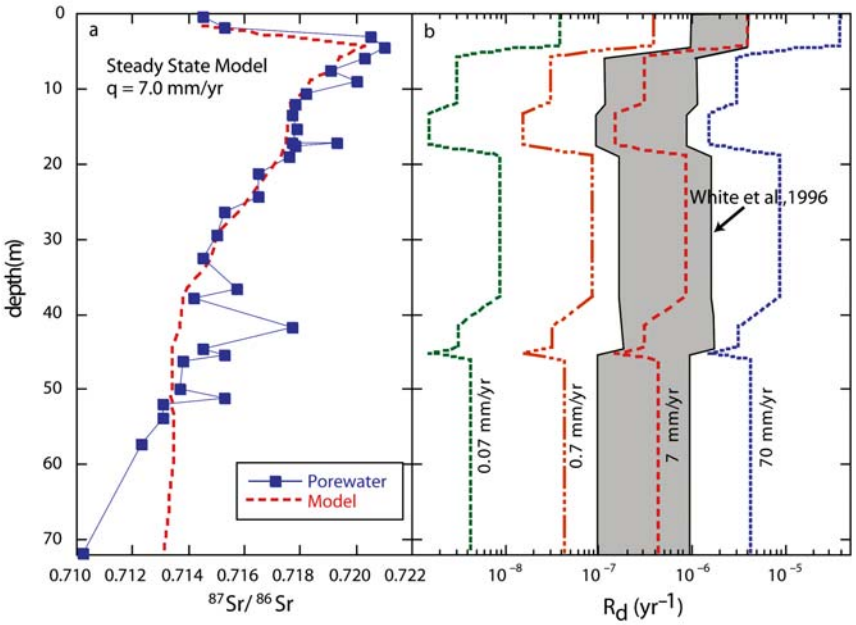

Fig. 12.6 Pore water Sr isotopic ratio profiles in the Hanford groundwater. Values from the upper part of the profiles are derived from biotite weathering, while lower values found in lower parts of the profiles are influenced by plagioclase weathering. The bold curve represents a steady state model of reactive transport assuming different values for infiltration rates. The range of weathering rates found in soils developed on granitic sediments in California (White et al., 1996) are used to deduce infiltration rates under steady state conditions

A recent example of using light isotopes to decipher the rates of water-rock interactions has been published by Lemarchand and Gaillardet (2006). B is a light element with two isotopes. The isotopic variations of B isotopes are important ranging from $-50‰$ to $+50‰$ in the classical delta notation ($\delta^{11}B = ([(^{11}B/^{10}B)/(^{11}B/^{10}B)_{standard}] - 1)10^3$. One of the main processes that fractionates B isotopes is B exchange between water and surfaces (Palmer et al., 1987, Lemarchand et al., 2005). Typical fractionations of 20‰ (light B is preferentially adsorbed) have been determined when B in solution is adsorbed onto clay minerals. Researchers believe that part of the ^{11}B enrichment of seawater is due to the preferential scavenging of the light isotope (^{10}B) when seawater B is adsorbed onto the clay mineral surfaces discharged by rivers to the ocean. Lemarchand and Gaillardet (2006) have reported B isotopic ratios in the dissolved load of the main rivers of the Mackenzie river basin. Although there is no big variation in the isotopic composition of bedrock, a large range of B isotopic variation is measured in the rivers throughout the drainage basin, from values close to the bedrock values in the Rocky and Mackenzie Mountains (0‰) to ^{11}B-enriched values in the lowlands (up to 15–20‰). Only mechanisms that fractionate B during water-rock interaction are able to explain such an enrichment in the heavy isotope. A discrete model of transport

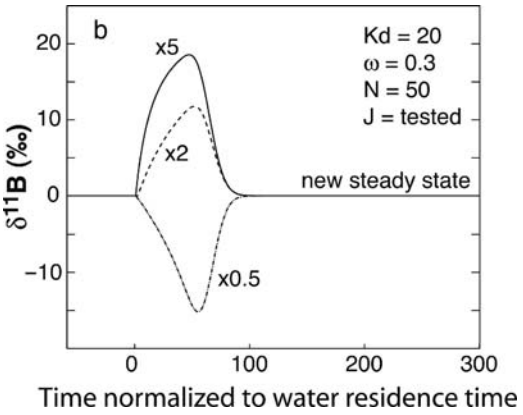

Fig. 12.7 Response of the B isotopic ratio of a system characterized by a water-rock ratio ω (mass of water/mass of solids in g/g) to modifications of the weathering rate. The numbers give the factor by which the weathering rate has changed. This curve has been calculated using a model of 50 connected elementary volumes in which B is supplied by slow weathering reactions and affected by rapid exchange reactions (compared to water advection). The parameters Kd, N, J denote the partition coefficient of B onto mineral surfaces, the number of connected volumes and the flux of B from chemical weathering, respectively. The B isotopic composition of the hosting rocks is fixed at 0‰. The X-axis is the characteristic time (i.e., the time normalized to residence time or water in the system). The maximum change in the isotope ratio is obtained for 50 times the residence time of water (Lemarchand and Gaillardet, 2006). (From Lemarchand and Gaillardet, 2006, with permission from Elsevier)

and reaction in soils or shallow aquifers (made of 50 connected volumes through which water flows) was developed by the authors. In each volume, two water-rock mechanisms act competitively. The first mechanism is the chemical weathering of the host rocks (shales) at a relatively low rate. The second mechanism is the exchange of B onto clay minerals, which is a rapid process and preferentially adsorbs ^{10}B onto surfaces. Ion-exchange equilibrium is thus reached rapidly, characterized by the partition coefficient of B ($\mathrm{Kd} = [\mathrm{B}]_{\mathrm{ads}}/[\mathrm{B}]_{\mathrm{solution}}$ with $[\mathrm{B}]_{\mathrm{ads}}$ and $[\mathrm{B}]_{\mathrm{solution}}$) indicating the concentrations of B adsorbed on surfaces and in solution respectively) and an isotopic fractionation coefficient of $\alpha = 0.975$ (25‰ between the solid and the solution). Figure 12.7 shows the calculated response of the B isotopic ratio in solution to changes of the weathering rate of hosting minerals in a model groundwater constituted of N connected volumes. In each volume ion-exchange equilibrium is assumed. When an increased weathering flux of B from the hosting minerals (0‰) is imposed, a net flux of B is added to the solution. As a result of adsorption onto surfaces in soils or shallow groundwaters, the B isotopic composition of the solution increases (^{10}B is scavenged). Advection of freshwater causes the exchange front to propagate through the system with a retardation factor of $1 + \mathrm{Kd}/\omega_{\mathrm{r}}$, where ω_{r} is the water-rock ratio. If the input flux decreases, desorption of the exchangeable pool decreases the B isotopic value of the solution. This ion-exchange front propagates and the system then slowly evolves back to a steady state that only depends on the isotopic ratio of the bulk B input. The contrasted values of B isotopes measured in

the rivers of the Mackenzie basin are consistent with a recent perturbation of the weathering regime, probably induced by the recent deglaciation of the basin. In the Rocky Mountains, where the residence time of water is short (high runoff conditions and steep slopes), groundwaters or soil solutions have reached a steady state characterized by a fluid isotopic value close to that of bedrock, while in the lowlands or plains, where the residence time of water is high, high B isotopic ratios show that the system is still dominated by ion-exchange reactions that retard the attainment of steady state. For a Kd value of 20, water-rock ratio $\omega = 0.3$ (mass of water/mass of solids) and initial adsorbed B concentration of 0.3 ppm, a system where the residence time of water is 500 year will be dominated by ion exchange reactions over 10–25 kyr, a scenario found in the lowlands. This example shows that B isotopes in groundwaters or rivers fed by groundwaters can be a useful proxy for constraining the time response of a system submitted to climatic or anthropogenic forcing.

The few examples of advection-transport models applied to physically well-characterized soils, catchments, and aquifers described above demonstrate the great potential of isotopic systems in characterizing and quantifying the kinetics of water-rock interaction and the history of chemical weathering.

12.2.4.3 Oceanic Crust Profiles

The last significant use of isotopic tracers to deduce rates of water-rock interaction along flow paths is exemplified by the Sr isotopic systematics of the oceanic crust. The isotopic contrast between seawater and minerals of the oceanic crust creates a change in the bulk isotopic composition of water during its downwelling circulation through the oceanic crust. Isotopic profiles have been used to deduce the fluid fluxes (Bickle and Teagle, 1992; Teagle et al., 2003). Large Sr isotopic variations occur in the upper part of the oceanic crust (pillow lavas), with values lower than seawater values (1.5 km depth). By contrast, the Sr isotopic composition of the sheeted dike zone (from 1.5 to 2.5 km depth) is more uniform, but with values still higher than the bedrock value. In the upper part, if a kinetically limited exchange regime is assumed, a simple linear kinetics exchange can be postulated:

$$\frac{\partial C_s}{\partial t} = \kappa(C_f - C_s) \tag{12.11}$$

where C_s and C_f are the Sr isotopic ratios of solid and fluid, respectively, and κ the solid-fluid exchange rate. Coupled with a differential equation describing transport of Sr isotopic ratio in the porous oceanic crust, the following governing equations can be deduced (Lassey and Blattner, 1988; Blattner and Lassey, 1989; Bickle, 1992; Bickle and Teagle, 1992; Teagle et al., 2003):

$$\frac{\partial(\Phi' C_f + C_s)}{\partial t'} + \Phi' \frac{\partial C_f}{\partial z'} = 0 \tag{12.12}$$

$$\frac{\partial C'_s}{\partial t'} = N_D(C'_f - C'_s) \tag{12.13}$$

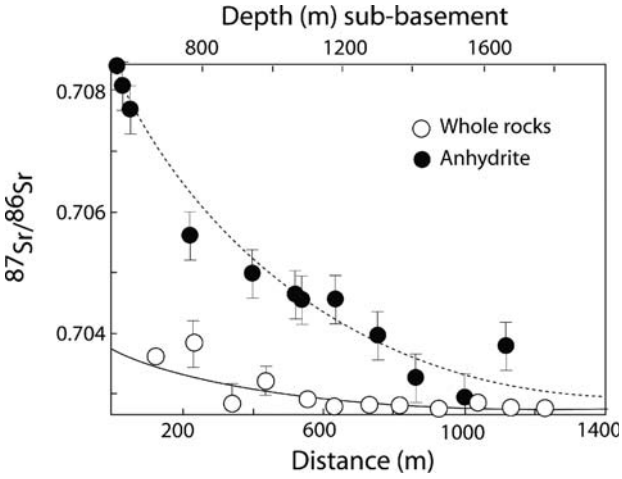

Fig. 12.8 Sr isotopes for whole rocks and anhydrite samples from the oceanic crust (hole 504B). Anhydrite is thought to represent the fluid composition, as a function of depth. Variations are modeled by assuming first-order kinetics for fluid-solid exchange between water and the crust. Damköhler number is adjusted to make the modeled curves fit the data. The good agreement between model and data validates the first-order kinetic rate law and shows that low Damköhler number (0.2) characterizes the system. The Damköhler number allows a determination of a time-integrated fluid flux between oceanic crust and seawater

In this equation, Φ' is the ratio of Sr between the fluid and the solid per unit volume ($\Phi' = \rho_f \mathrm{Sr_f} \phi / \rho_s \mathrm{Sr_s}$, ρ_f = density of fluid, ρ_s = density of solid, $\mathrm{Sr_f}$ = concentration in the fluid, $\mathrm{Sr_s}$ = concentration in the solid, and ϕ = porosity). In addition, $t'(t = t'l/v)$ and $z'(z = z'l)$ are nondimensional time and space parameters and v and l are the fluid velocity and a characteristic length scale respectively. Like in the previous reactive transport models, the Damköhler parameter plays a critical role ($N_D = \frac{\kappa l}{v}$) and determines the isotopic front shape due to limited exchange rates (Blattner and Lassey, 1989). An application is the exchange of Sr between the oceanic crust and the downwelling recharge fluids by using Sr isotopic ratios in secondary phases such as anhydrite and calcite as monitors of the isotopic composition of the fluid (Bickle, 1992; Teagle et al., 2003). As in the examples of the previous section, the kinetic dispersion of a geochemical front (for example here the seawater-crust boundary) increases as the Damköhler number decreases. Modeling of Sr isotopic profiles in the oceanic crust allowed Teagle et al. (2003), to deduce time integrated fluid fluxes ($\phi l t'$) of 1.7×10^6 kg/m for the high temperature hydrothermal circulation at ODP hole 504B (Fig. 12.8).

This example highlights the importance of isotopic measurements to constrain the rates of seawater interaction with the oceanic crust. The geochemical exchanges between seawater and the oceanic crust have crucial implications on the global cycling of elements and seawater geochemical budgets. In addition, the circulation of water at mid-ocean ridges is responsible for transport of the Earth's internal heat. The same kind of approach has been applied to O isotopes (Bickle and Teagle,

1992). As recently shown by Bach and Humphris (1999), a correlation between the Sr or O isotopic composition and spreading rates at oceanic spreading centers exist, indicating that the slowest ridge has experienced a greater extent of Sr and O exchange between the fluid and the crust.

More generally, the above examples show that the shape of a given isotopic tracer from an advective fluid is a function of the water-rock ratios and the kinetics of water-rock interaction. Numerous other examples could be found in metamorphic rocks (e.g., Bickle, 1992; Baxter and DePaolo, 2002a, b). In Baxter and DePaolo (2002a, b) the authors show that it is possible to use Sr and Nd isotopes as passive tracers along transects normal to lithologic contacts where a sharp isotopic contrast was present before high-temperature processes. The smoothing of the isotopic discontinuity gives information on the rates of exchange between the fluid from which new minerals precipitated and the minerals of the rock. Fine Sr isotope analyses on both sides of the contact can be interpreted by a diffusive transport model of Sr and exchange rates can be calculated. At Simplon Pass (Switzerland), the reaction rates inferred from detailed Sr isotope analyses at the contact between pelites and amphibolites are in the range of 1.4×10^{-7} year^{-1}, suggesting that equilibrium requires locally 10's of millions of years.

12.2.5 Isotopic Tracing of Global Kinetics

The chemical and isotopic composition of the ocean is a result of time-integrated interaction between the global water cycle and the oceanic and continental crusts. The isotopic signatures preserved in sedimentary rocks, such as carbonates, evaporites or fluid inclusions are records of the release or removal history of elements, and therefore of the evolution of the Earth's global reservoirs (see also Chap. 13). Global reservoirs are large scale geological entities (mantle, continental crust, oceanic crust, atmosphere, ocean). For example, carbonate rocks and sedimentary organic matter are the key reservoirs for the global carbon cycle. Depending on their residence time in the ocean, elements provide local (short residence time with regards to ocean mixing) or global information (long residence time). A few isotopic proxies (O, C, Sr, Os, S, U) have received attention so far, and among them the most studied is the isotopic evolution of Sr in limestones. The response of seawater isotopic composition to variations to climatic and tectonic forcing has been formalized by Richter and Turekian (1993). The conservation equation for an element in the ocean is

$$\frac{dN}{dt} = J_i - J_o \tag{12.14}$$

where N is the amount of the element in the ocean reservoir (for example in mol), and J is the total flux of the element into (J_i) or out of the ocean (J_o).

Assuming that Sr isotopes are not fractionated by the processes that remove Sr from the ocean and that the approximation of ^{86}Sr is a fixed proportion (k) of the

total concentration for the different input and output fluxes, then the conservation equation is

$$\frac{dR}{dt} = \frac{1}{\tau}\sum_i \frac{J_i}{J_{tot}}[R_i - R] \tag{12.15}$$

where J_i and R_i are the fluxes and isotopic ratios of Sr from the different sources (river 71%, hydrothermal alteration 22% and diagenetic 7%). Here, J_{tot} is the sum of the incoming fluxes, τ is the residence time of Sr in the ocean (assumed not to have changed with time), and R is the isotopic ratio of the ocean. It is possible to predict the response of the ocean to a periodic forcing of the input term. If $J_i = J_0(1 + \delta J(t))$ where J_0 is the flux at $t = 0$ and $\delta J(t)$ the time changing increment, the isotopic ratio of the ocean will change according to $R_i = R_0(1 + \delta R(t))$ where R_0 is the isotopic ratio at $t = 0$ and $\delta R(t)$ the incremental response of R. We assume that the output flux of Sr is proportional to N, the amount of Sr in the ocean: the constant of proportionality is the reciprocal of the residence time. By introducing the following new variables $\delta R' = \delta R/(R_i - R_0)$ and $\delta J' = \delta J_i/\sum J_i$, the following equation governing the normalized changes in the ocean can be derived:

$$\frac{d\delta R'}{dT} + \delta R' = \delta J' \tag{12.16}$$

where T is nondimensional time $T = t/\tau$.

The periodic forcing input term can be chosen as $\delta J'(T) = \sum a_n \sin(2\pi\tau T/P_n)$ with a_n the amplitude and P_n the forcing period. The corresponding solution for the oceanic response is then:

$$\delta R'(T) = \sum[a_n\alpha_n/(1+\alpha_n^2)]e^{-T} + \sum[a_n/(1+\alpha_n^2)^{1/2}]\sin(\alpha_n T - \theta) \tag{12.17}$$

with $\alpha_n = 2\pi\tau/P_n$ and $\theta = \tan^{-1}\alpha_n$. The oceanic response to periodic changing input fluxes is therefore attenuated at periods shorter than the residence time and phase-shifted. To illustrate simply this result, we have calculated the oceanic response for a simple input signal on Fig. 12.9a. Figure 12.9b shows the amplitude of the response of seawater Sr isotopic ratio as a function of the forcing period for a change of the riverine input up to 25% of the present day total input of Sr to the ocean.

For $^{87}Sr/^{86}Sr$ (Sr residence time close to 3 Myr) for example, the mathematical treatment indicates that, according to the analytical precision of Sr isotope analyses, the shortest resolvable periods are on the order of 0.1 Myr. This shows that Sr isotopes in seawater have little chance to record periodic climatic variations of periods less than 0.1 Myr.

A quantitative interpretation of the secular curve of Sr isotopes in the ocean has been attempted by Richter et al. (1992). The Sr budget is controlled by two main inputs: rivers and hydrothermal vents. By assuming a constant isotopic composition for riverine Sr, and a hydrothermal flux proportional to the oceanic crust accretion rate and of constant isotopic ratio (0.7035), Richter et al. (1992) deduced that the flux of Sr delivered by rivers must have increased three times after 40 Myr in order to make the predicted Sr isotopic curve match the observed one.

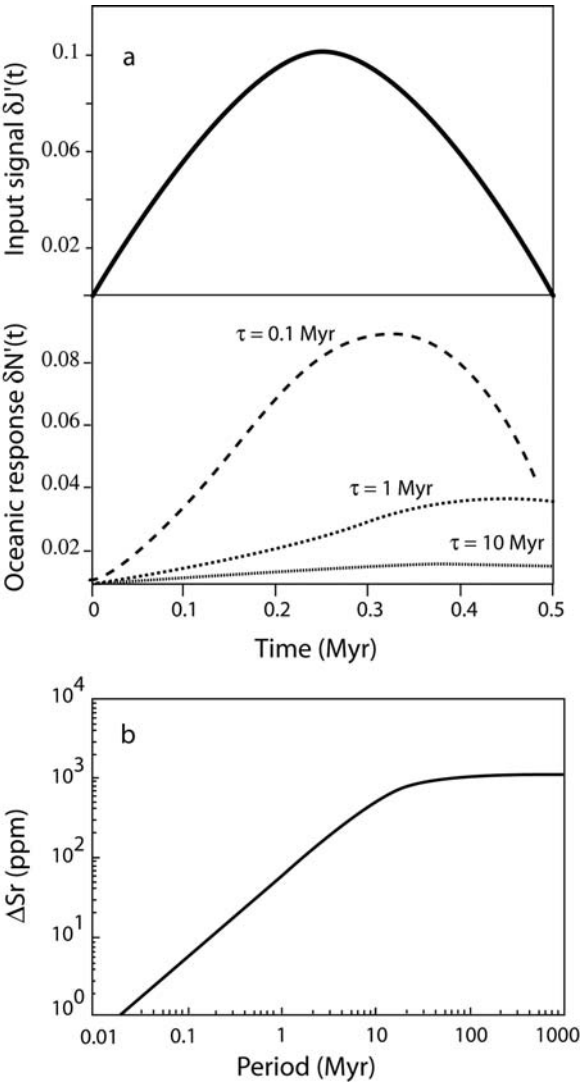

Fig. 12.9 **a**. Isotopic response of the ocean to a change in the input rate of the element. The input flux changes with time as $J_i = J_0(1 + \delta J(t))$. $\delta J'$ is δJ expressed in % of the total input fluxes assumed to be constant. The response of the ocean is $\delta R' = \delta R/(R_i - R_0)$ where R_i and R_o are the isotopic ratio of the input flux and of the ocean before its modification and δR is the incremental change in isotopic ratio. Different scenarios have been represented for varying residence time (τ). The higher the residence time, the higher the buffering capacity of the ocean. **b**. Amplitude of variations of $^{87}Sr/^{86}Sr$ of seawater as a function of the period of the input signal (amplitude of the input signal of 10^{10}mol/year, or 25% of the total input flux). ΔSr is $[(^{86}Sr/^{86}Sr) - (^{86}Sr/^{86}Sr)_{sw}/(^{86}Sr/^{86}Sr)_{sw}]10^6$ where sw denotes seawater. Routine analytical precision of mass spectrometers is between 1 and 10 ppm. This amplitude of the input signal shows periods higher than 0.01–0.1 Myr only (Richter and Turekian, 1993)

Derry and France-Lanord (1996) refined this analysis by separating the Himalayan rivers (GB) from the other rivers (r) and constraining the history of the Sr isotopic composition of the Ganga-Brahmaputra river using Sr isotope compositions measured in the clay minerals of the Bengal fan. Following the approach of Derry and France-Lanord (1996), the Sr isotopic curve is governed by

$$N\frac{dR}{dt} = J_{GB}(R_{GB} - R_{sw}) + J_r(R_r - R_{sw}) + J_h(R_h - R_{sw}) \tag{12.18}$$

where N is the amount of Sr in the ocean, R_{sw}, R_{GB}, R_r, and R_h, the isotopic ratio of seawater (0.70917), of the Ganges-Brahmaputra (variable with time), of the other rivers (0.711) and hydrothermal input (0.7035) respectively. The terms J_i denote the corresponding fluxes. The Sr isotopic ratio of the GB flux may have varied significantly, from 0.720 (20–8 Myr) to 0.740 (8–1 Myr). Based on the record of Sr isotopic ratio of the ocean preserved in carbonates, the authors calculated the rate (dR/dt) of change of Sr isotopic ratio with time and then calculated what should be the evolution of the Sr weathering flux $J_{GB}(t)$ from the Himalaya to fit the dR/dt curve. A significant decrease of the weathering flux is observed at 7 Myr and 3 Myr, in contrast to the view that increasing seawater Sr isotopic ratio results from increasing continental erosion. This study is a good example of the use of isotopic tracers in the ocean to deduce the kinetics of Himalayan weathering (Fig. 12.10).

The same kind of approach can be applied to isotopes fractionated by physical or chemical processes, such as O, H, C or B. The mathematical treatment is similar but complicated by fractionation factors affecting the output fluxes. Lemarchand et al. (2001) showed that the main flux of B to the oceans is due to rivers, and proposed a theoretical reconstruction of the B isotopic curve in the ocean, clearly showing the dominant influence of continental erosion (both sediments and solutes) on the B isotopic evolution of the ocean. They pointed out therefore that B isotopes in the ocean should be a good proxy for the time evolution of chemical weathering and global CO_2 consumption rates.

The isotopic evolution of oxygen (from the water molecule) in the ocean is regulated by the hydrothermal activity at oceanic ridges (Muehlenbachs and Clayton, 1976). A number of authors have measured O isotopic profiles in the oceanic crust and associated ophiolites. These profiles showed that the pillows and sheeted dikes in the upper crust are enriched in ^{18}O while gabbros below are depleted in ^{18}O relative to the fresh rock value. This pattern is attributed to the penetration and reaction of seawater in the highly permeable oceanic crust as it forms and ages. Although the high-temperature (at the ridge axis) and low-temperature (off ridge) interactions are complicated and highly variable, attempts have been made to model O isotope profiles as a function of physical parameters and hydraulic parameters (expansion rates, permeability, water rock ratio) and isotopic exchange coefficients to account for the mineral/water isotopic partitioning. For example, Lecuyer and Allemand (1998) created a model that was able to reproduce the observed O isotope profiles of the oceanic crust by using a dynamic model of seawater-crust. The model is divided into two parts: a thermal and hydraulic model of the oceanic crust

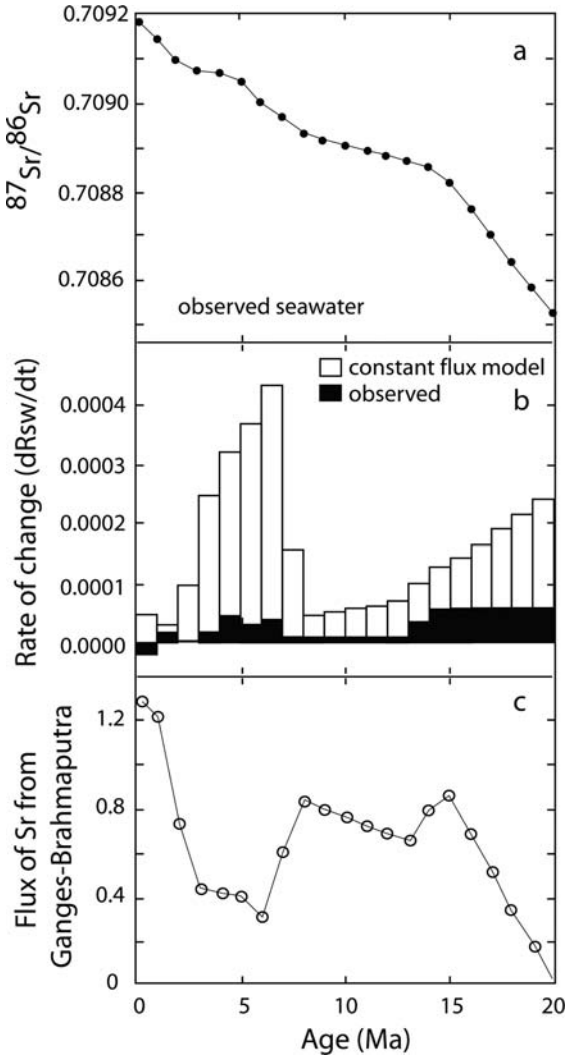

Fig. 12.10 **a**. Evolution of Sr isotopes in seawater during the Neogene (a) and deduced rate of change dRsw/dt (black bars). **b**. Bars are calculated by assuming that the flux of Sr from the Ganges-Brahmaputra rivers has been constant through time and equal to the modern value, and that the isotopic composition of Sr from the Ganges-Brahmaputra rivers followed the evolution of this ratio recorded in the Bengal fan sediments. The large contrast between calculated and observed values indicates that the flux of Sr was significantly lower in the past. **c**. The flux of Sr is calculated to fit the observed Sr isotopic curve and by assuming that the isotopic composition of Sr from the Ganges-Brahmaputra rivers followed the evolution of this ratio recorded in the Bengal fan sediments. This example shows the sensitivity of both fluxes of Sr and isotopic ratios for modeling the Sr isotopic curve. (From Derry and France-Lanord, 1996, with permission from Elsevier)

and a model incorporating the kinetics of oxygen isotope exchange between water and minerals (chlorite and plagioclase). After others (for example Gregory and Taylor, 1981; Stakes and Taylor, 1984), this model showed the sensitivity of the isotopic value of seawater to the ocean spreading rate and to the kinetics of oxygen isotopic exchange between rock forming minerals and seawater (i.e., temperature). The model indicates that the $\delta^{18}O$ of seawater may vary within 2‰ with a response time of 5–50 Myr for oceanic expansion rates of 1–10 cm/year. Because the oxygen isotopic composition of the ocean also depends on the amount of water frozen in ice, this model has important climatic consequences. These consequences are not within the scope of this chapter, but this example clearly shows how the oxygen isotopic evolution of seawater is also a record of the global water-oceanic crust interaction. Lécuyer et al. (1997) have attempted a similar kinetic treatment of the H global cycle.

12.3 The Use of Radioactive Decay to Constrain Timescales of Water-Rock Interactions

In this section, we show how adequate measurements of isotopic ratios in minerals and waters can provide rates and timescales of water-rock interactions. Radioactive decay is a set of processes by which unstable nuclides emit subatomic particles. The parent nuclide produces a daughter nuclide. The international unit for measuring radioactive decay is the Bequerel (Bq). One Bq corresponds to one decay per second. The rate at which a radioactive element decays is a first-order kinetic law, $dN/dt = -\lambda N$, where λ is called the decay constant (see Chap. 1). This fundamental law has allowed scientists to date geological material. Fortunately, some radioactive nuclides have half-lives on the same timescale as those of water-rock interactions at the surface of the Earth. However, the use of longer-lived nuclides is possible when the chemical fractionation between the parent and the daughter is important enough that only small periods of time are necessary to create measurable isotopic contrasts. This is exemplified in the case of crystal growth.

12.3.1 Crystal Growth

Radiogenic isotopes have been used to deduce rates of crystal growth based on a very simple principle. During crystal growth, radioactive isotopes that will decay with time are incorporated into the crystal. The radial variation of the isotopic ratios therefore gives information on the timing and rates of crystal growth, provided that a number of assumptions are checked. The source of the added isotopes should be homogeneous and only derive from a single source (matrix, fluid) whose composition did not change with time. Diffusion has to be low in order to not redistribute isotopes. These conditions are met for Rb and Sr isotopes in garnet as exemplified

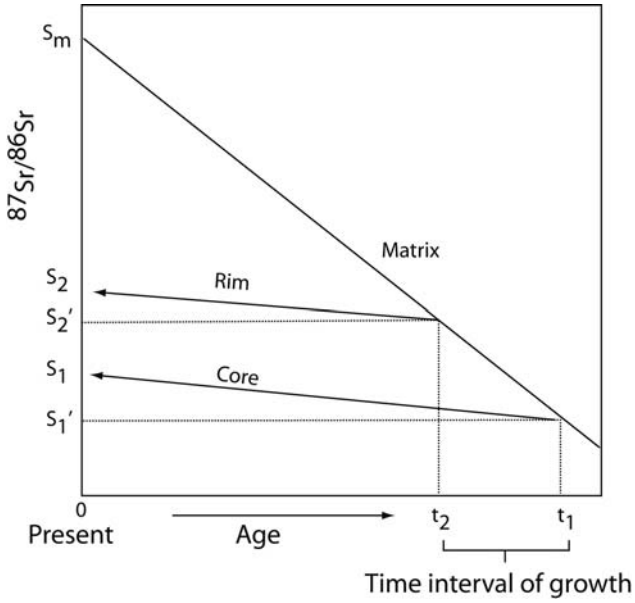

Fig. 12.11 Theoretical sketch diagram illustrating the use of Sr isotopes in garnet to calculate rate of crystal growth. The mineral is growing continuously between time t_1 and t_2 from a matrix with a much higher Rb/Sr ratio than the mineral. The time interval of growth is determined by measuring the Rb/Sr (the slope of the straight lines) in the matrix, rim and core as well as Sr isotopic ratios (see text)

by Christensen et al. (1989). The authors measured the variations of $^{87}Sr/^{86}Sr$ ratio in a single crystal from a metamorphic rock and deduced the crystal's growth rates. The method is illustrated in Fig. 12.11. At time t_1, the core of the garnet incorporates Sr from a matrix with isotopic composition of S_1'. With time, the crystal grows and preferentially incorporates Sr from the matrix. Because of the decay of Rb in the matrix, the isotopic composition of the matrix as well as of the growing minerals changes with time although defining a lower slope. The measurement of Rb/Sr and $^{87}Sr/^{86}Sr$ through the mineral gives the evolution of the time-corrected Sr isotopic ratio that reflects the evolution of the matrix, allowing rates to be deduced. Using garnet from rocks within the base of a Cambrian section in southeast Vermont, USA, that were metamorphosed 380 Myr ago, Christensen et al. (1989) calculated crystal growth rates of 1.4 mm/Myr. The use of long-lived isotopes is therefore crucial to the study of the kinetics of mineral growth and determining the timing and duration of orogenic processes. This technique has been applied in many other cases. In particular, the Sm/Nd system in zoned prograde garnet from the metamorphic zone of Newfoundland has been used by Vance and O'Nions (1989) to deduce growth rates in the range of 1.3–19 mm/Myr. A comparison between the Rb/Sr and Sm/Nd ages led the authors to conclude that Sr ages are close to those of Nd, but revealed that the Rb/Sr system may have experienced post-growth changes at temperatures of 800 K.

12.3.2 Uranium and Thorium Series Nuclides

Short-lived nuclides are naturally derived from radioactive decay chains of ^{238}U, ^{235}U and ^{232}Th. Half-lives of U and Th series nuclides range from seconds to hundreds of thousands of years, making them potentially interesting for determining timescales of water-rock interactions (Fig. 12.12).

At secular equilibrium, in an undisturbed system, activity ratios (where activity is defined as the product of the half-life and the number of atoms) of two nuclides from the same chain is equal to 1, or

$$\lambda_{\text{parent}} N_{\text{parent}} = \lambda_{\text{daughter}} N_{\text{daughter}} \tag{12.19}$$

This is true in particular for the $(^{234}U/^{238}U)$ activity ratio of any parent material at secular equilibrium.

Water-rock reactions result in variations between the different members within a decay chain disrupting secular equilibrium. The return to steady state conditions is a function of time and of the behavior of the parent and daughter elements, which can provide insight into the kinetics of natural processes. An extensive review of the use of U-series disequilibrium in Earth's processes can be found in Bourdon et al. (2004). Briefly, two types of mechanisms produce variations in the U-series nuclides. The first is when chemical or physical processes disturb parent and daughter element pairs (e.g., dissolution, adsorption, precipitation). The second is known as the α-recoil effect. During the ejection of an α particle, the daughter nuclide recoils in the opposite direction and moves within the host mineral. Because it may be ejected from the host mineral or because its crystallographic site is damaged, the parent daughter is more easily mobilized.

12.3.2.1 Determining Scavenging, Sedimentation and Precipitation Rates Using U and Th Isotopes

The application of U-series to oceanic processes has been extremely powerful. The very-short-lives nuclides like ^{234}Th(half life = 24.1 days), ^{227}Th (half life = 18.6 days), ^{228}Th (half life = 1.9 year) and ^{210}Po (half life = 138 days), have been used to quantify the rate of scavenging from solution onto particles and to predict the fate of particle-reactive pollutants. Th and Po nuclides are strongly sorbed onto organic matter and particles. However, these nuclides are derived from much more soluble parent elements (U, Ra). Once produced, Th and Po isotopes tend to hydrolyze and adsorb onto the available surfaces of particles. Bhat et al. (1969) first observed a depletion of the $^{234}Th/^{238}U$ isotopic ratio in the upper 200 m of the water column in the Indian Ocean followed by an increase at depths between 100 and 200 m, thus reflecting the dynamics of oceanic particles (sorption on biogenic material, sinking and remineralization). Initial models, which assumed vertical advective transport and postulated that atomic production rate of ^{234}Th (from ^{238}U) equals

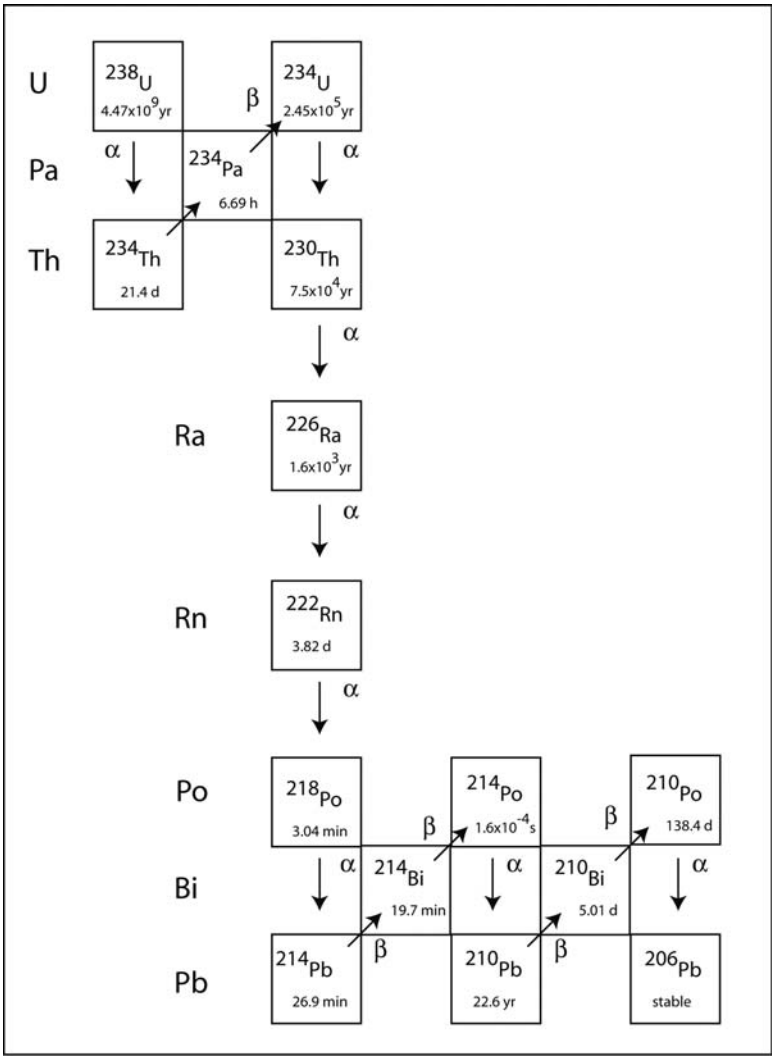

Fig. 12.12 ^{238}U is the main isotope of natural uranium (99.7% abundance). Between ^{238}U and the stable daughter product ^{206}Pb, a number of intermediate nuclides have variable radioactive decay constants from microseconds to hundreds of thousands of years. Some of these constants are on the order of characteristic timescales of water-rock interaction processes. In closed and undisturbed rocks and minerals older than 1 Myr, the activity ratio between different members is equal to 1 (secular equilibrium). Water-rock interaction may cause fractionation between parent and daughter of the chain, disrupting the steady state. The return to steady state condition is a function of time

scavenging and radioactive decay, used the following equation:

$$P = (\lambda + k)N \tag{12.20}$$

where k is a first-order kinetic constant for the rate of scavenging and λ is the radioactive decay constant of ^{234}Th. The inverse of k is the mean residence time of ^{234}Th in the water column. This approach lead Matsumoto et al. (1975) to determine a 0.4 years residence time for Th in the ocean, similar to estimates by Broecker et al. (1973) based on ^{228}Ra/^{228}Th disequilibrium.

Since these pioneering studies, scavenging models based on Th have been improved by taking into account both dissolved and particulate phases, aggregation and disaggregation of particles and more refined kinetic laws (see Cochran and Masqué, 2003, for an extensive review). An important application of ^{210}Po and ^{234}Th isotopes in the ocean is for constraining the dynamics of organic carbon, which is a critical issue in light of the global changes induced by human activities. Because Po and Th isotopes are preferentially scavenged onto organic particles in the ocean they track the carbon export between the shallow and deep ocean. Because of their short half-lives, these isotopes are sensitive to seasonal changes. International programs have been developed to better understand the oceanic carbon cycle and have placed a special emphasis on ^{234}Th measurements in the ocean (Buesseler et al., 1995; Cochran and Masqué, 2003). Associated with ^{234}Th, the short-lived ^{210}Pb isotope (with a half-life of 22.6 year) is produced by the decay of ^{226}Ra and atmospheric ^{222}Rn supply to the water column. Like ^{234}Th, ^{210}Pb is removed by sorption onto particles and used to estimate bioturbation in the uppermost layers of the sedimentary column. In the absence of bioturbation in the sediment, these isotopes would only be found in the uppermost layers down to a depth dependent upon the rate of sedimentation. The effect of bioturbation is to increase the depth and pattern of penetration of Th and Pb isotopes into the sediment, and several authors have used ^{210}Pb depth profiles to deduce mixing rates of sediments (see Henderson and Anderson, 2003, for a review). Determining mixing rates of sediment is extremely important in estimating the time resolution of the sediment record. For typical marine sediments with mixing depths of 10 cm and sedimentation rates on the order of the cm/kyr, it is clear that any signal from timescales less than 1000 year will not be recorded.

Longer-lived nuclides have been used to determine the rates of processes with longer time scales. In particular, like ^{234}Th, ^{230}Th (half life = 75400 year) is extremely insoluble and sorbs to particle surfaces soon after it forms from the decay of ^{234}U. As shown by Henderson and Anderson (2003), the coupled use of ^{230}Th and ^{231}Pa (Pa has the same chemistry as Th in the ocean) has permitted calculation of accurate sedimentation rates in the ocean by measuring their activity in the upper 1 cm of seafloor.

^{230}Th accumulation has also been used to calculate the growth rate of Mn crust and nodules growing on the seafloor (Chabaux et al., 1995). The time dependence of Th isotopes is given by the following equation:

$$\left(\frac{^{230}Th}{^{232}Th}\right) = \left(\frac{^{230}Th}{^{232}Th}\right)_0 \exp(-\lambda_{230} t) \tag{12.21}$$

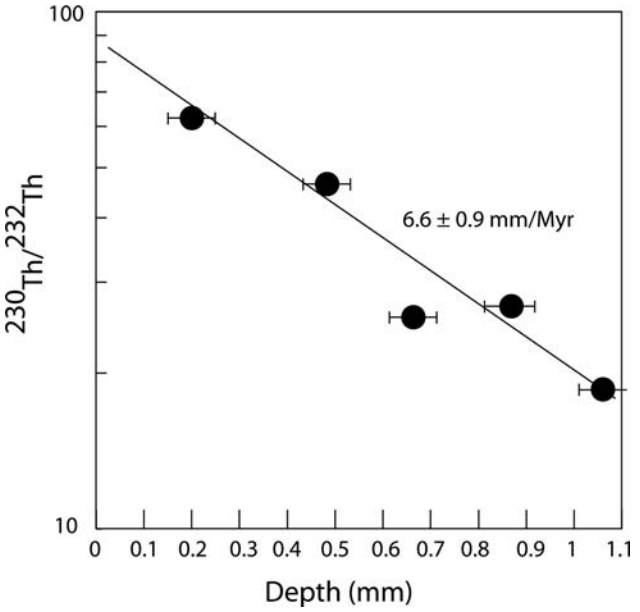

Fig. 12.13 Variations of activity ratio ($^{230}Th/^{232}Th$) as a function of depth in the D18–1 Fe-Mn crust (Lotab seamount, west equatorial Pacific). The growth rate is deduced from the slope. Error is 2σ (Chabaux et al., 1995). (From Chabaux et al., 1995, with permission from Elsevier)

where λ_{230} is the decay constant of ^{230}Th and t, the time since the closing of the system. An application of this calculation to a Fe-Mn crust from Lotab seamount, equatorial Pacific, is shown in Fig. 12.13. The two depth profiles analyzed are consistent with a growth rate of 6.6 ± 1 mm/Myr. The simultaneous analysis of $^{234}U/^{238}U$ isotopic ratios confirmed that the system remained closed after the precipitation of Fe-Mn crusts.

12.3.2.2 Dissolution Rates During the Diagenesis of Deep Sea Sediments

Although ^{234}U and ^{238}U have similar chemical behavior and should therefore not be fractionated by chemical weathering of minerals, several authors have shown that this assumption is not verified in nature. The reason why $^{234}U/^{238}U$ activity ratios of weathered solids are lower than unity is known as the α-recoil effect and is explained by the preferential leaching of ^{234}U from α-recoil-damaged lattice sites in minerals. Conversely, the solid phase is enriched in ^{238}U. These characteristics of U geochemistry have been used to calculate dissolution rates of silicates in a deep-sea sediment column from the North Atlantic (southwest of Iceland). The sediment is younger than 500 kyr and is composed of mixed biogenic carbonates, plagioclase, debris of basaltic material derived from Iceland and biogenic silica. Based on a simplified model of the advection-dispersion-exchange model of Johnson and DePaolo

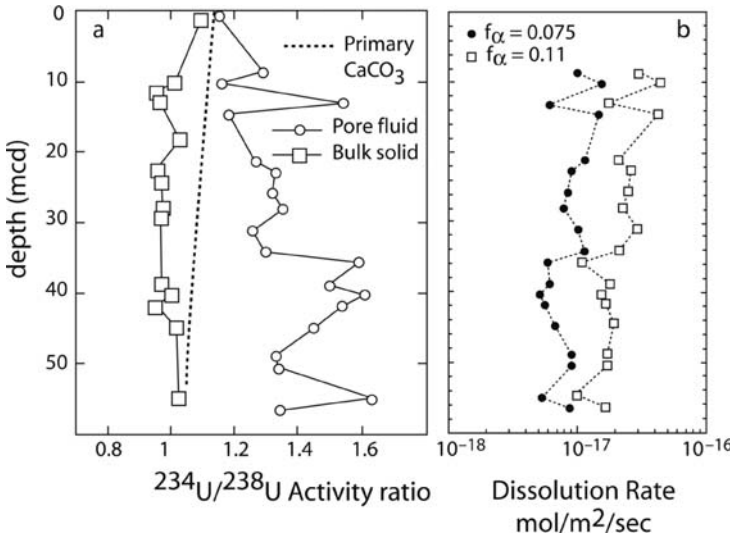

Fig. 12.14 **a**. Uranium activity ratios measured in the pore fluid and bulk sediments of site ODP 984A. The dashed line shows the evolution of primary calcite formed with the initial seawater activity ratio. These data are converted into dissolution rates on (**b**) with two different assumptions about the recoil loss factor of U. It is assumed that dissolution is dominated by plagioclase and that 50% of the sediment is plagioclase (Maher et al., 2004). (From Maher et al., 2004, with permission from Elsevier)

(1997a) for the coupled transport and chemical reactivity of U and ^{234}U and ^{238}U isotopes, Maher et al. (2004) have shown that at steady state of U activity ratio (R) in the pore fluid $(\partial R/\partial t = 0)$, the dissolution rate constant of the bulk solid phase (R_d) can be expressed in terms of the measured activity ratios in the pore fluid and in the solid phase (A_f and A_s respectively) and the "α–recoil factor" f_α:

$$R_d = \frac{f_\alpha \lambda}{A_f - A_s} \tag{12.22}$$

where λ denotes the decay constant for ^{234}U. This equation represents the balance between the preferential release of ^{234}U in the pore fluid due to α–recoil, the injection of U by solid-phase dissolution and the radioactive decay of this ^{234}U in the pore fluid and the adsorbed components. The factor f_α is the fraction of ^{238}U radioactive decay that results in the injection of ^{234}U into the pore fluid due to the α-recoil of ^{234}Th, and can be constrained geometrically. The dissolution rates calculated by this method are in the range of 4×10^{-7} to 2×10^{-6} g/g/year and decrease from top to bottom in the sediment, according to the increase in sediment age. These rates are converted into mol/m^2/s in Fig. 12.14. These results were later confirmed using a reactive transport model that considered transport, the major element geochemistry and U isotopes (Maher et al., 2006b). The results of the model based on major elements and that based on U isotopes are only compatible if calcite recrystallization is taken into account. Scavenging lowered U concentration in the pore

fluid, causing isotopic exchange of U between pore fluid and marine calcite. The rate of calcite recrystallization needed to reconcile major elements and U isotope data is about $10^{-10.6}\,\mathrm{mol/m^2/s}$. U series indicate that 10–20 wt. % of calcite is recrystallized at 70 m depth in the core. The weathering rates of silicates deduced from this study confirm that rates in natural systems are 10^2–10^5 times lower than laboratory-measured values. The "mineral dissolution rate conundrum" may be due to the aging (the loss of reactive sites) of silicate surfaces with time according to the authors (see discussion in Chap. 10).

12.3.2.3 Using U-Series Disequilibrium in Groundwaters

The use of U- and Th-series has been shown to provide estimates of weathering rates of particles in aquifers by Tricca et al. (2000, 2001) or Maher et al. (2006a). Tricca et al. (2000, 2001) undertook a comprehensive evaluation of U-and Th-series radionuclide transport (^{238}U, ^{235}U, ^{232}Th, ^{234}Th, ^{226}Ra, ^{222}Rn, ^{228}Ra, ^{228}Th, ^{224}Ra) in the unconfined aquifer of Long Island, N.Y. Based on a one-dimensional advective transport model considering weathering, recoil and interaction with a surface layer, the authors were able to calculate nuclide-specific dissolution rate constants. The presence of a given nuclide in the fluid is a balance between the inputs and the outputs. Inputs comprise weathering, recoil ejection (the preferential weathering of ^{234}U), production by the surface coatings and ejection into the water, desorption from the surface coatings and decay of the parent nuclide in the water. Outputs are the decay of the nuclide within the groundwater and adsorption onto the surface coatings. Applying this model to U, the authors demonstrated that the isotopic composition of U is directly related to the recoil/weathering rate ratios. In the vadose zone, calculated rates of U weathering can be as high as $10^{-13}\mathrm{s}^{-1}$, whereas in the aquifer, values close to $2.10^{-16}\,\mathrm{s}^{-1}$ are necessary to explain the measured U activities. Reported data for the long-lived (^{232}Th) and short-lived isotopes (^{234}Th and ^{238}Th) in groundwater show that desorption kinetics of Th is slow. The mean residence time of Th in the surface coatings is estimated to be about 3000 year, while it is found to be about 1 year in the water. U-and Th-series nuclides in aquifers not only provide information on the kinetics of bulk mineral dissolution, they also strongly constrain the transport properties of pollutant nuclides because they are analogues to naturally occurring radionuclides. The study from Tricca et al. (2001) clearly demonstrated that Th incorporation into coatings is highly variable, depending upon the oxidation state of the aquifer, which in turn depends upon its organic matter content or the dominant microbiological metabolisms.

Maher et al. (2006a) measured $^{234}\mathrm{U}/^{238}\mathrm{U}$ activity ratios in the Hanford site, a site previously investigated for Sr isotopes in order to couple the information of both systems and determine flow characteristics and rates of water-rock interaction (see Sect. 12.3.2). The U system differs from the Sr system because of the time-dependence of the U activity ratio because of ^{234}U and ^{238}U decay and the α-recoil term, which in turn depends on the specific surface area of the material. As the rate of the α-recoil process is a key parameter for using U isotopes in groundwaters, the

authors proposed different approaches to estimate the α-recoil loss fraction based on geometric methods, surface area investigations and chemical methods. U isotopic ratios increase with depth from values close to 1 to values higher than 1.2 at 70 m depth. A clear gradient of $^{234}U/^{238}U$ isotopes with depth is observed in pore waters. The two reactive transport equations (for U and Sr) allow for the determination of both infiltration rates and reaction rates. Because the reaction rates calculated using U isotope constraints and Sr isotope constraints respond oppositely to infiltration rate (because of the α–recoil process that only characterizes U), it is possible to find a compromise between reaction rates and infiltration rates. The fluid velocity deduced is on the order of $5 \pm 2\,mm/year$ and the bulk silicate weathering rates (between $10^{-15.7}$ and $10^{-16.5}\,mol/m^2/s$) are consistent with those deduced from the study of chemical weathering in soils of California having similar lithology. Clearly, the application of several coupled isotopic systems, through the use of realistic models of transport and reaction (e.g., Chap. 11), is a promising tool to deduce the natural rates of water-rock interactions as well as fluid flow characteristics.

12.3.2.4 Timescales of Erosion

The last example that we want to report is the application of U-series to erosion processes. ^{234}U (2.45×10^5 year), ^{230}Th (7.5×10^4 year), ^{226}Ra (1600 year) have been used because their decay periods have similar timescales to that of weathering processes. During chemical weathering, U and Th behave oppositely. While U is soluble and partitioned between waters and residual solids, Th and to a lesser extent Ra are immobile and concentrated in solids. Only organic-rich water can potentially mobilize Th. Therefore, when a mineral is in contact with water, U isotopes are preferentially dissolved and disequilibrium in the radioactive chain is initiated. In a plot of $^{234}U/^{238}U$ versus $^{230}Th/^{238}U$ (Fig. 12.15), the pathways of return to equilibrium for solid phases are shown for two cases: accumulation of U ($^{230}Th/^{238}U$ decrease) and leaching of U ($^{230}Th/^{238}U$ increase).

A first approach has been to analyze U series in soil profiles. As reviewed recently by Chabaux et al. (2003), 40 years of data have now shown that the idea that U is mobilized by soil water while Th is immobile is an over-simplification. Closed system behavior can not be assumed, as shown by evidence of U remobilization and reprecipitation (e.g., onto iron oxides) and Th mobilization by organic matter in soils. This is confirmed when U series disequilibrium data on soil materials are plotted (Fig. 12.15). The data plot in all of the quadrants indicating no simple behavior. The interpretation of U-Th-Ra disequilibrium variations with depth in terms of timescales requires the use of U chemical mobility models. A series of models of U mobility postulating instantaneous and/or continuous first order U gain and loss kinetic laws (Thiel et al., 1983; Scott et al., 1992; Hilaire-Marcel et al., 1990) have been applied to interpret U-Th-Ra disequilibrium. For example, Dequincey et al. (2002) showed that, for the Kaya laterite soil profile, a model including two continuous and contrasting U mobilization processes can explain the presence of data points in the forbidden regions of Fig. 12.15 and proposed that the U leaching and

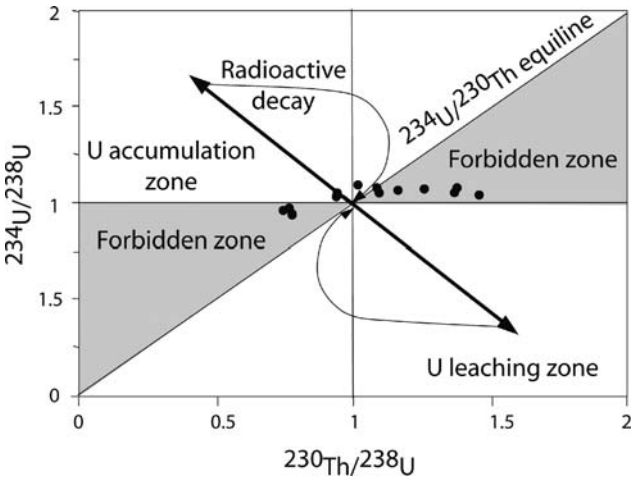

Fig. 12.15 Theoretical evolution of U/Th disequilibria in a $^{234}U/^{238}U$ versus $^{230}Th/^{238}U$ activity ratio plot. In this diagram, U gains and losses are represented by vectors and the return to secular equilibrium by radioactive decay by curved lines. Due to the relative decay constants of the nuclides, it is impossible for a sample to cross the ($^{234}U/^{238}U$) and ($^{234}U/^{230}Th$) equilines. This defines forbidden zones where natural samples should not plot. The α-recoil properties and the contrast between U and Th solubilities imply that portions of this plot should not contain any data point if instantaneous gains or losses of U are considered. As indicated by the data points from Dequincey et al. (2002), this is often not true and the presence of data points in the forbidden zones may be explained as a result of continuous and contrasting U mobilization processes (Chabaux et al., 2003). Depending on the relative rates of U gains and losses and on the intensity of the U fractionation, it is possible to explain the data points present in the forbidden zone

U gain coefficients vary with time (according to climate) and depth. These different examples show that the interpretation of U series disequilibrium in terms of weathering timescales needs further refinements.

U series disequilibrium in river-borne materials has been studied by a number of groups (see Chabaux et al., 2003). Compared with soil profiles, rivers have the advantage that they integrate weathering processes over large portions of the Earth's surface. U-Th-Ra systematics of the Mackenzie river (Vigier et al., 2001) confirm the higher mobility of U compared to Ra and Th and show a clear complementarity of the dissolved and suspended phases for ($^{234}U/^{238}U$) and ($^{230}Th/^{238}U$) (both higher than 1 in the dissolved load and lower than 1 in the suspended load). $^{226}Ra/^{230}Th$ shows the same kind of complementarity, with activity ratios higher than 1 in the dissolved load. Vigier et al. (2001) have proposed a model (Fig. 12.16, from Chabaux et al., 2003) that assumes that the bedrock is initially in secular equilibrium (activity ratios = 1) and that postulates a continuous leaching of U-Th and Ra from solids in the river basin. In order to interpret the behavior of U, Th and Ra isotopes, they assumed that the dissolved load and suspended load are complementary phases. The dissolved load of the river is supposed to result from the present day weathering reactions occurring within the soil profiles and the suspended load integrates the continuous leaching of U-Th-Ra over the residence of particles in the soils or in sediment

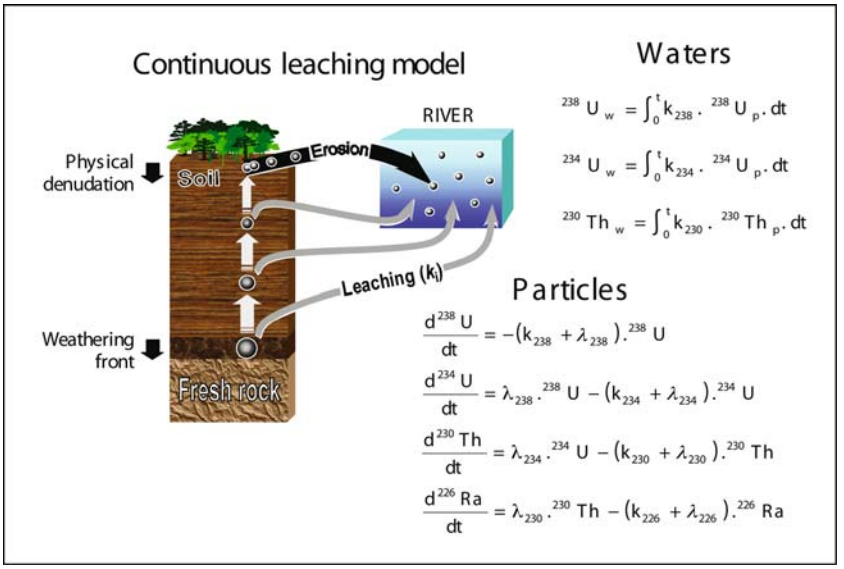

Fig. 12.16 Continuous leaching model from Vigier et al. (2001) for the interpretation of U-series disequilibrium data in rivers. This model assumes that most of the chemical weathering occurs in soils. Particles are continuously leached before reaching the river. The dissolved load integrates leaching of the whole profile. The k_i parameters are the leaching parameters for the different isotopes of U and Th. Leaching coefficients are $1.1 \times 10^{-5}, 1.6 \times 10^{-5}, 7 \times 10^{-8}$ and 4×10^{-4} for $^{238}U, ^{234}U, ^{230}Th$ and ^{226}Ra. λ are the radioactive decay constants. Both leaching coefficients and λ are in per year. In this model, dissolved and suspended loads are complementary phases and the resolution of equations leads to a calculation of the duration of chemical weathering

reservoirs within the drainage basin. Model equations are given in Fig. 12.16. The key parameters of the model are the leaching coefficients (according to first-order kinetic laws) of the different nuclides (^{226}Ra, ^{230}Th, ^{234}U, ^{238}U) and the duration of chemical erosion (i.e., the time elapsed between the fractionation of nuclides and today). This model was applied to the Mackenzie basin by Vigier et al. (2001), to Indian rivers by Vigier et al. (2005) and to the Amazon river by Dosseto et al. (2005, 2006). In the Mackenzie river, results show that the duration of chemical weathering is between 9 and 28 kyr, despite large uncertainties. The results imply significant recent changes of chemical erosion rates during the last deglaciation. In the Amazon basin, Dosseto et al. (2005) have shown that the sediments delivered to the sea by the Amazon have resided at Obidos for 6.1 ± 1 kyr, a relatively low duration given the high sediment storage capacity of the Amazon drainage basin (Andean foreland basin, Amazon floodplain and varzeas). Illustration of these results in Fig. 12.17 uses an isochron ^{230}Th-^{238}U diagram. The 1:1 line corresponds to secular equilibrium within the radioactive chain. Dashed curves are produced by the continuous leaching model and provide an estimate of the time required to explain the data from each large tributary. Model parameters are leaching coefficients and the activity ratios of the bedrock ($^{230}Th/^{232}Th$, $^{238}U/^{232}Th$).

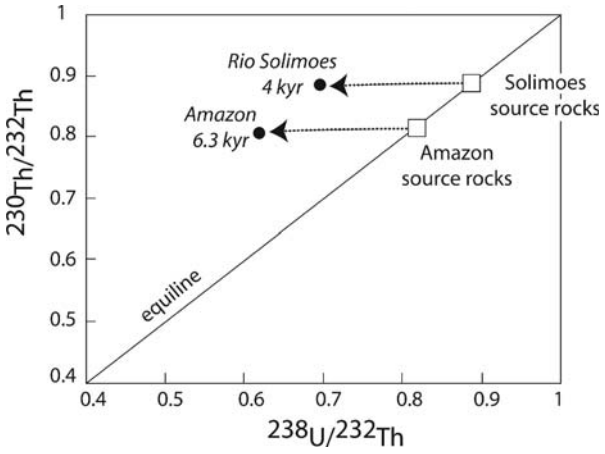

Fig. 12.17 Isochron ^{230}Th-^{238}U diagram showing the data measured in the suspended sediments of the Amazon, Solimoes and Madeira rivers. Dashed curves show continuous weathering scenarios calculated with the model of Vigier et al. (2001). Numbers indicate the duration of weathering (i.e., residence time of particles within the drainage basins). Bedrock, assumed to be at secular equilibrium, lies on the equiline. The position of the bedrock on the equiline is deduced from the isotopic composition of Pb isotopes (Dosseto et al., 2005). The Solimoes river is the main Andean tributary of the Amazon river. Results indicate that the characteristic timescales of erosion in the Amazon basin are on the order of 6000 years. (From Dosseto et al., 2005, with permission from Elsevier)

These studies generally show the promising tool offered by U-series disequilibrium in rivers and erosion products. However, they also show that timescales can only be calculated using a model of U, Th and Ra mobility during water-rock interactions. The first-order results of these models seem to be robust but they probably need improvement. Improvements will be made by taking the exchange between dissolved and suspended phases into account and postulating more realistic kinetic laws of chemical weathering. These studies remain very good examples of the potential use of radioactive nuclides to constrain weathering rates, weathering time constant and the recent history of chemical weathering. Except in tropical areas, large climatic variations during the last tens to hundred thousands of years need to be taken into account when modern soil or weathering products transported in rivers are analyzed.

12.3.3 Cosmogenic Isotopes and the Determination of Denudation Rates

Like U-series nuclides, cosmogenic isotopes have proven to be very useful in Earth sciences to constrain timescales of surface processes, mainly sedimentation and

erosion rates and surface exposure ages. Cosmogenic isotopes are produced *in situ* by particles of cosmic radiation. Because the *in situ* production rates decrease exponentially with soil depth, their concentrations are a function of the history of the surface (erosion or deposition). A number of cosmogenic isotopes, most of them radioactive, have been used to constrain erosion rates and weathering history (Lal, 1990). Like U-series nuclides, cosmogenic radionuclides (e.g., ^{10}Be, ^{26}Al, ^{14}C, ^{36}Cl) have half-lives between 35 days and 1.5 Myr, suitable for constraining the kinetics of Earth's surface processes. The literature on cosmogenic isotopes and their use in determining rates and timescales in surface processes is abundant and we will only give examples where they have been used to constrain erosion rates.

Theoretical support for using cosmogenic nuclides to deduce erosion rates was first reported by Lal (1990). The number of cosmogenic atoms produced in situ, at depth x, is

$$P(x) = P(0)e^{-\mu x}$$

where P is the production term (atom g^{-1} $year^{-1}$), P(0) the pre-exponential term at $x = 0$ and μ the absorption coefficient of the penetrating cosmic rays (1/L, with L the attenuation length (in g cm^{-2}) of the penetrating cosmic rays. If the erosion rate of the soil is ε yr, the change of cosmogenic nuclide concentration is

$$\frac{\partial N}{\partial t} = -\lambda N + P(0)e^{-\mu x(t)} \tag{12.23}$$

with $x(t) = x(0) - \varepsilon.t$ (the soil is moving upward).

The general solution of this equation is

$$N(x,t) = \frac{P(0)}{\lambda + \mu\varepsilon} e^{-\mu x}(1 - e^{-(\lambda+\mu\varepsilon)t}) \tag{12.24}$$

and in particular, at the soil surface:

$$N(0,t) = \frac{P(0)}{\lambda + \mu\varepsilon}(1 - e^{-(\lambda+\mu\varepsilon)t}) \tag{12.25}$$

At steady state, when $t > 1/(\varepsilon\mu + \lambda)$, cosmogenic nuclide concentrations reach a steady state (erosion loss balances radioactive decay) and then:

$$N = \frac{P(0)}{\lambda + \mu\varepsilon} = P(0)T_{eff} \tag{12.26}$$

where T_{eff} is the effective surface exposure time. It is, of course, very important to check the steady state condition. It can be done using two radionuclides of different half-lives (Lal, 1991). The accumulation of ^{10}Be in soils as a function of time is shown in Fig. 12.18a for different erosion rates. Figure 12.18b shows the suitability of each cosmogenic isotope to determine erosion rates.

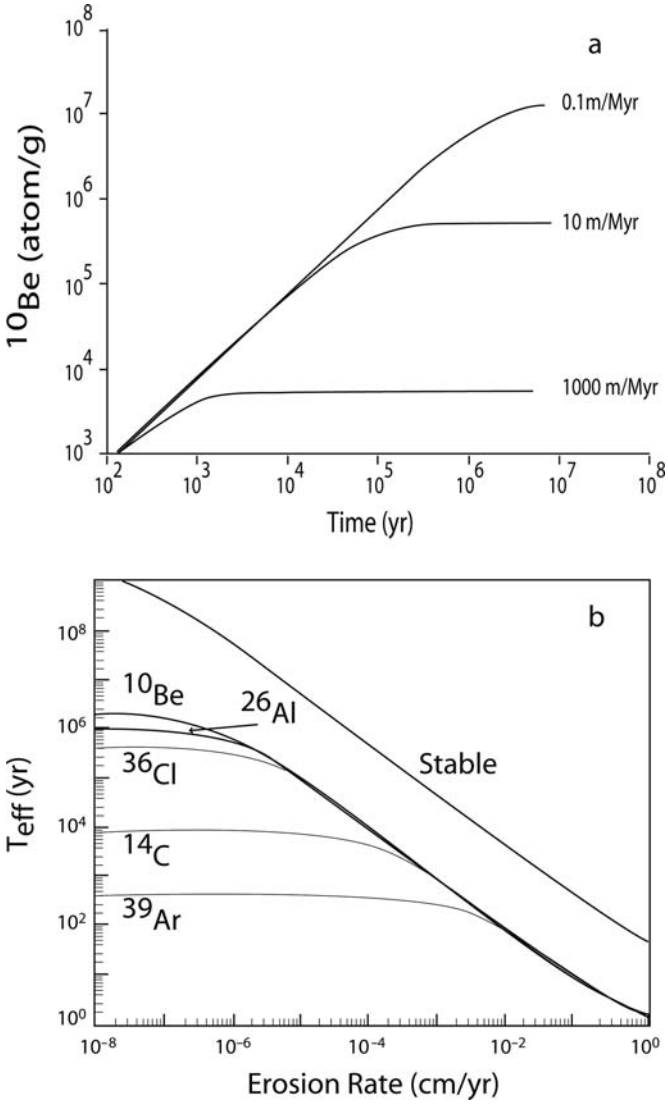

Fig. 12.18 **a**. Accumulation of ^{10}Be in a soil surface as a function of time and different erosion rates. A steady state of ^{10}Be concentration is obtained when production of the cosmogenic isotope is balanced by erosional loss and radioactive decay. **b**. Effective surface exposure ages, T_{eff}, as a function of erosion rate for different cosmogenic isotopes and a stable nuclide. T_{eff} is defined as the number of ^{10}Be atom/g divided by the production rate at the surface. Suitability of a cosmogenic nuclide to determine the rate of erosion is determined by the condition that its half life λ is of the same order as the product $\mu\varepsilon$ (Lal, 1991). (From Lal, 1991, with permission from Elsevier)

Application of cosmogenic isotopes to determine rates of soil processes (erosion, burial, creep, bioturbation) is based on the comparison between theoretical and measured profiles of cosmogenic nuclides (Brown et al., 2003; Gosse and Phillips, 2001 for reviews). Denudation rates have been determined using in situ-produced ^{10}Be in the Luquillo Experimental Forest, Puerto Rico by Brown et al. (1995). The ^{10}Be concentration of the A horizon of a soil profile gave 209×10^3 at/g while a sample of a bedrock exfoliation slab on a ridge gave 175×10^3 at/g. Assuming steady state conditions, $\mu = 0.5\,\mathrm{m}^{-1}$, using a production rate of 3.1 at/g/an, and the radioactive constant of ^{10}Be of $4.62 \times 10^{-7}\,\mathrm{year}^{-1}$, the calculated denudation rates are 29 m/Myr and 34 m/Myr for the A horizon and ridge respectively. These rates, typical of Puerto Rico watershed, are among the highest denudation rates globally, and are consistent with more conventional estimates based on sediment and solute yields.

Cosmogenic isotopes have also proven to be useful for basin-scale approaches by measuring their content in stream and river sediments (Sarda et al., 1993; Brown et al., 1995; Bierman and Staig, 1995; Granger et al., 1996; Riebe et al., 2000, 2001; Schaller et al., 2001; Von Blanckenburg et al., 2005). This method assumes that sediments are derived from the different regions of the catchment and that the whole basin is in steady state (production equals total erosion and radioactive decay). Recent measurement of erosion rates using cosmogenic isotopes has provided strong constraints to the climatic versus tectonic controls of chemical erosion rates (and associated atmospheric CO_2 consumption rates). The emerging picture from cosmogenic nuclide results is that the climatic control over chemical weathering is negligible and that rejuvenation of mineral surfaces by physical erosion exerts a dominant control (Riebe et al., 2001, Von Blanckenburg et al., 2005).

12.4 Fractionation of Isotopes as a Kinetic Process

This section focuses on the fractionation of stable isotopes during water-rock interactions. Kinetic effects of isotopic exchange reaction were initially considered in experimental studies aimed at determining equilibrium fractionation factors between gases, aqueous species or aqueous and solid phases. It appeared that, provided some knowledge of the equilibrium fractionation factors, isotopic disequilibrium could provide information on the kinetics of water-rock interactions, whatever the operating mechanisms.

In the following section, we give a couple of examples where natural or experimental isotopic data have been used to constrain the kinetics of geological reactions. The most commonly used stable isotopes are those of H, C, O and S. Due to the recent analytical development using MC-ICPMS (multi-collector inductively coupled plasma mass spectrometry), "non traditional" stable isotopes (e.g., Si, Ca, Mg, Fe, Zn, Li, Cr, Se, Mo, Ge) that were difficult to measure with precision a couple of years ago today are now measured routinely.

12.4.1 Equilibrium and Kinetic Fractionation of Isotopes

In 1947, Harold Urey published a paper on the thermodynamic properties of isotopic substances. He demonstrated that the isotopic composition of cogenetic phases in thermodynamic equilibrium depends on the temperature of equilibrium. For example, the fractionation of ^{18}O and ^{16}O between calcium carbonate and water can be used as a paleothermometer. Urey's work and Nier's development of the mass spectrometer led to the development of stable isotope geochemistry. In order to explain equilibrium fractionation, Urey (1947) considered the isotopic exchange (between A and B compounds) reaction:

$$aA_1 + bB_2 \Leftrightarrow aA_2 + bB_1 \tag{12.27}$$

where A_1, A_2, B_1 and B_2 are two isotopes of A and B compounds respectively, where a and b are the stoichiometric coefficients. The equilibrium constant can be defined as the isotopic ratio of A over the isotopic ratio of B and is called the isotopic fractionation factor (Bottinga, 1968; Richet et al., 1977; O'Neil, 1986 and Chacko et al., 2001).

Experimental verification of calculated isotopic fractionation factors has faced kinetic issues. Kinetic fractionation of isotopes is an important process in both nature and experimental studies and is associated with unidirectional, fast or incomplete reactions. One of the most classic examples is the reaction between water and water vapor. Evaporation far from equilibrium fractionates O isotopes kinetically, while evaporation (or condensation) at a water vapor pressure close to that of equilibrium induces an equilibrium fractionation. The magnitude of kinetic fractionation can be as large as or larger than equilibrium effects in the opposite direction. During kinetic processes the light isotope is preferentially mobilized. In the case of evaporation, the isotopic shift in $\delta^{18}\mathrm{O}(\delta^{18}O = ([(^{18}O/^{16}O)/(^{18}O/^{16}O)_{standard}] - 1)1000)$ between solution and vapor is $13‰$ due to kinetic fractionation and $9‰$ in case of an equilibrium process. The magnitude of the fractionation reduces to the equilibrium value as the vapor phase approaches saturation. Kinetic theory simply shows that the isotopic fractionation factor should be $\sqrt{M_2/M_1}$ where M_2 and M_1 are the masses of the heavy and light molecules, respectively, involved in the reaction. A classic example is the determination of equilibrium fractionation factors using the "two-direction approach" (O'Neil, 1986). For example, to determine the equilibrium fractionation factor of quartz and water, two solutions of different isotopic composition (one above the equilibrium value, one below) are placed in contact with the mineral and their isotopic compositions are measured as a function of time. The isotopic composition of water depends on time and on the rate of the exchange reaction. Equilibrium is reached after 1 week at 500° C. This can be expanded to the "three isotope method". The reacting solid is mixed with a water whose isotopic composition is not lying on the mass dependent fractionation line of the solid (see O'Neil, 1986; Johnson et al., 2004). Movement toward isotopic equilibrium moves the phases along a new mass dependent fractionation line. Equilibrium is attained when the slope of the new line is the same as that of the two other solutions. Since

the early work of Urey (1947), many geochemists have worked to determine equilibrium fractionation factors. Historically, scientists designed laboratory experiments to determine equilibrium fractionation factors, and in a number of cases found that kinetic effects were perturbing the results. Departures from the theoretical fractionation factors are known as "kinetic effects," even if a great variety of processes are responsible. Some examples will be given below.

12.4.2 Kinetics of Isotopic Exchange

The determination of C, H, O and S isotopes, and more recently non-traditional isotopes (Cu, Zn, Fe, Ca, Mo…) in fluids and minerals has become a very useful approach in determining the timescales of fluid-rock interaction in the Earth's crust. Isotopic disequilibrium for these major components exists at low and high temperatures, showing that the exchange of isotopes between coexisting phases is kinetically limited. Slow kinetics precludes the homogenization of mineral and global reservoirs. An excellent review on the kinetics of isotopic exchange can be found in Cole and Chakraborty (2001).

The kinetics of isotope exchange between gases has received considerable attention. Isotopic exchange reactions between gases are rapid. Isotopic data have shown, for example, that equilibrium between CO and CO_2 is attained within minutes at high temperatures. Examples can be found in Cole and Ohmoto (1986) where kinetic rate laws were established based on isotopic data. A classic example of the kinetics of isotopic exchange reactions in solution is the sulfate-sulfide system. Ohmoto and Lasaga (1982) determined the rates of sulfur isotope exchange between sulfate and sulfide in solution and showed that the isotopic fractionation factors at $t = 0$ and at equilibrium are a simple function of the overall rate of chemical reaction:

$$\ln\left(\frac{\alpha_{eq} - \alpha_t}{\alpha_{eq} - \alpha_0}\right) = -kt([\Sigma SO_4^{2-}] + [\Sigma S^{2-}]) \tag{12.28}$$

where $\alpha_O, \alpha_t, \alpha_{eq}$ are the fractionation factors at $t = 0$, at t and at equilibrium, respectively, and k is the rate constant of reaction. They found in particular that the rates of reactions are controlled by pH, which allowed them to propose a model for the reaction mechanism. This model involves thiosulfate as a reaction intermediate where the intermolecular exchange reaction of sulfur atoms in the thiosulfate is the rate-limiting step for exchange between sulfate and sulfide. Recent refinement of the rates of sulfur exchange can be found in Chu and Ohmoto (1991) and Chu et al. (2004).

The kinetics of isotopic exchange have been studied using both natural isotopic compositions and enriched isotope tracers. The use of enriched tracers results in large isotopic effects which make it possible to trace the isotopic composition through time with a high sensitivity (Johnson et al., 2004). A recent example is given using Fe isotopes. Welch et al. (2003) used enriched ^{57}Fe to trace the kinetics

of isotopic exchange between aqueous ferric and ferrous Fe. Shifts in isotopic composition were expressed as

$$\delta^{57/56}\mathrm{Fe} = ({}^{57}\mathrm{Fe}/{}^{56}\mathrm{Fe}_{\mathrm{sample}}/{}^{57}\mathrm{Fe}/{}^{56}\mathrm{Fe}_{\mathrm{igneous\ rocks}} - 1)10^3$$

The ferric species were separated rapidly from the solution where ferric and ferrous species were equilibrating. The large isotopic differences (initial solution was $\delta^{57/56}\mathrm{Fe} = 0$ for Fe[II] and $\delta^{57/56}\mathrm{Fe} = 330‰$ for Fe[III]) were used to minimize the importance of isotopic re-equilibration during species separation. Separation of Fe(II) and Fe(III) were accomplished in this experiment by coprecipitation with $\mathrm{Ba}(\mathrm{CO}_3)$. The fact that initial isotopic compositions were much higher than intrinsic equilibrium or kinetic isotope fractionations of Fe made it easier to determine the kinetics of Fe isotope exchanges. This elegant method allowed the authors to show that the kinetics of Fe isotope exchange follows a second-order rate law. They showed in particular that isotopic equilibrium between hexaquo Fe(II) and Fe(III) is attained within 60 seconds at 22° C, which is quite rapid.

The kinetics of isotope exchange between a fluid and a mineral is much slower. The isotopic exchange between a mineral and a solution can be achieved either by chemical reaction (dissolution-precipitation) or diffusion. Diffusion is operating at or near equilibrium conditions, while isotopic exchange by reaction is the dominant process when conditions are far from equilibrium. The latter rates have been shown to be several orders of magnitude higher than the former at temperatures below 500° C.

12.4.2.1 Reaction-Controlled Mineral-Fluid Exchange

The isotopic compositions of O (the most abundant atom in the Earth's crust) and H of rocks and fluids from hydrothermal systems have been used to decipher fluid-rock interactions. As quoted by Gregory and Criss (1986), "oxygen and hydrogen isotopes are particularly useful in elucidating water-rock interactions and their measurement in thousands of rock and water samples over the last three decades has radically changed the way geologists view the role of surface fluids in the evolution of crust." At equilibrium, isotopic shifts between minerals and fluids are a function of the origin of water and water/rock ratios (Taylor, 1977; Criss et al., 1987). However, in many hydrothermal systems, equilibrium is not attained and kinetic processes are responsible for the observed isotopic variations. Models have been developed and isotope exchange experiments have been conducted (Cole et al., 1983, 1987, 1991; Doremus, 1998). In particular Cole et al. (1983) derived the following simple law for the isotopic exchange rate, r, of O and H isotopes as a function of W and S, the numbers of moles of oxygen in the fluid and solid, respectively. Here A is the surface area, t is time and F is the fraction of oxygen isotope exchange:

$$r = \frac{-\ln(1-F)(WS)}{(W+S)tA} \tag{12.29}$$

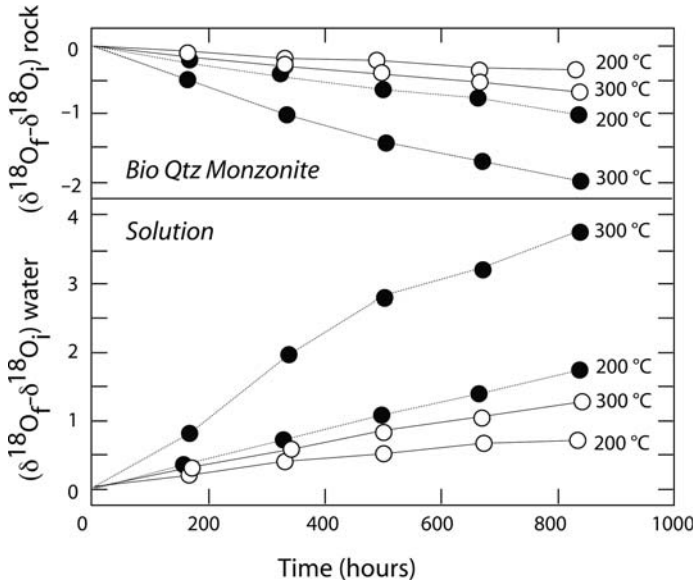

Fig. 12.19 Changes in the oxygen isotopic composition of biotite quartz monzonite and interacting with solution as a function of reaction time and temperature. Indexes i and f refer to initial and final conditions respectively. Black circles designate experiments run in 0.1 M NaCl solution and open circles in pure water. The isotopic change in the solution is greater than the solids for mass balance reasons. The major result is the enrichment of the heavy isotope in the solution. This experiment is designed to simulate oxygen exchange between fluid and granite under hydrothermal conditions. From these curves, rates can be calculated (Cole et al., 1991). (From Cole et al., 1991, with permission from Elsevier)

The equation is a first-order rate law based on a surface reaction model. Measurements of oxygen and hydrogen compositions in experimental conditions led to the determination of rates and activation energy for the interaction of basalt with seawater or in the granite-H_2O system at high temperature (Cole et al., 1987, 1991). Examples of isotopic exchange evolution with time are shown in Fig. 12.19 for the hydrothermal reaction of K-feldspar, plagioclase and biotite at different temperatures.

Light O is enriched in the altered phases while enrichment of deuterium is reported during a basalt-seawater interaction experiment, consistent with equilibrium fractionation factors. The rates that can be deduced from the oxygen data are in agreement with the expected first-order rates and are orders of magnitude higher than the rates predicted solely by the diffusion of O. This shows that most of the isotopic exchange occurs through dissolution-precipitation reactions. The evolution of $\delta^{18}O$ in fluid and solids is in good agreement with the evolution of the mineralogical assemblage, which is an additional argument that O isotopic exchange is controlled by surface dissolution-precipitation reactions. Deduced rates for the isotopic exchange of oxygen between Mid Oceanic Ridge basalts and seawater reach typical values of $10^{-9.5}$–10^{-8} mol $O/m^2/s$. Rate constants for O isotope exchange between altered granite and pure water range between 10^{-9} and 10^{-8} mol $O/m^2/s$

for temperatures of 170–300° C. Biotite to chlorite reaction rates are the highest, ranging between $10^{-7.4}$ and $10^{-6.5}$ mol O/m^2/s. O isotopes show that fluid-rock isotopic equilibration is achieved for the interaction of basalt with seawater in a few hundred to a few thousand years at 350° C, depending on the water/rock ratio. At 300° C, O isotopic equilibration between granite and fluid is achieved between a couple of hundred years and 10^5 years, depending on water/rock ratio and the mineral or rock grain radius (1 mm to 1 m). Isotopic exchange experiments have shown that the isotopic exchange fraction is a function of the classical parameters controlling rates of reactions: solution composition, temperature, pressure, surface area and mineral chemistry (see Cole and Chakraborty, 2001).

Dubinina and Lakshtanov (1997) developed a kinetic model of isotopic exchange between a mineral and fluid for three types of dissolution-precipitation processes that involved the transformation of an unstable mineral into a stable one, and mineral-fluid mass transfer with partial or complete dissolution of the starting mineral. As an application, the authors calculated the predicted isotopic exchange fraction for a silica gel-quartz-water system at 500° C. This model remains theoretical but clearly shows that isotopic evolution during water-rock interaction can be used to determine the history and mechanism of natural crystal growth. Geological applications are missing in the literature, because numerous other parameters can cause isotopic variations that complicate the study of kinetics and because the inspection of microscale isotopic variations requires microanalytical methods that are still in development.

12.4.2.2 Diffusion-Controlled Mineral Fluid Exchange

Diffusion plays a major role in Earth Sciences, especially at high temperature. Knowledge of the timescales of mineral-fluid, mineral-mineral, or mineral-melts diffusion is crucial to understanding the history and setting of metamorphism and hydrothermal reactions. The interpretation of isotopic diffusion patterns requires a complete understanding of the laws of diffusion mechanisms. A considerable amount of literature exists on the subject, recently reviewed by Cole and Chakraborty (2001). Most of the studies have focused on O and H isotopes at high temperature. The basic equation governing diffusion is Fick's second law relating the variation of concentration (C) with time to the chemical (or isotopic) gradient ∇ (∂C/∂x for a one dimensional problem):

$$\frac{\partial C}{\partial t} = D[\nabla^2 + (2/r)\nabla]$$

for radial diffusion in a sphere, where D is the diffusion coefficient and r the radius. Figure 12.20 is one example of an oxygen isotope profile determined by SIMS (secondary ion mass spectrometry) in calcite reacted for 22 hours at 700° C and 800 bars with a fluid containing CO_2 (Labotka et al., 1999) for 22 hours.

This curve can be modeled using the diffusion equation for transport normal to the surface of a semi-infinite volume with a planar surface and the value for the

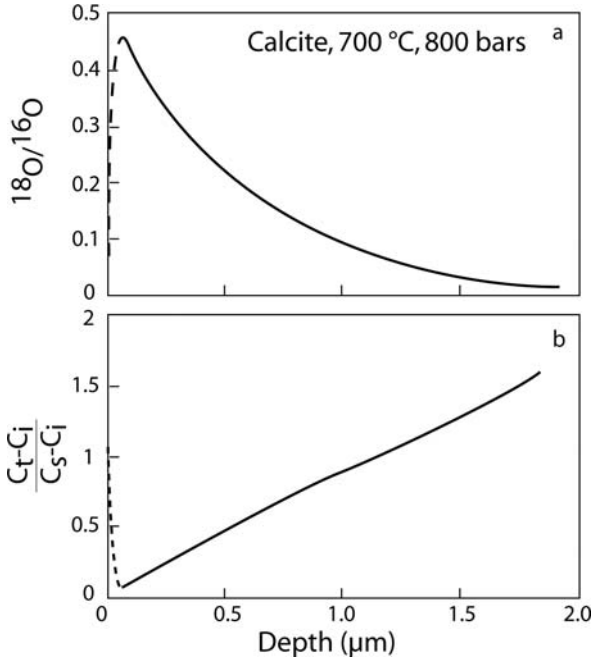

Fig. 12.20 **a**. Example of a diffusion profile of oxygen isotopes in calcite at 700° C, 800 bars, with a fluid containing a 50–50% mixture of CO_2 and H_2O for 22 hours. The data of the beginning of the profile are aberrant. **b**. Data are reduced using the solution to the diffusion equation. The diffusion coefficient of O in calcite can be calculated from the slope of the graph. Ci, Cs and Ct denote the ^{18}O concentration at the crystal surface, crystal interior and at depth x respectively (Labotka et al., 1999)

diffusion coefficient can be calculated. O and H isotope profiles in minerals have been determined in order to address the relationships among diffusivity, temperature, pressure, presence of water, oxidation state, defects and impurities, in particular, for quartz and feldspar minerals. Studies show that ^{18}O transport is dominated by diffusion of molecular water, as indicated by the positive correlations between the diffusion rate of O and H and H_2O fugacity. In many silicates, O profiles have shown that diffusion is strongly anisotropic, with preferential transport along the c crystallographic axis. In quartz for example, O diffusion is 100 times faster along the c axis. As pointed out by Cole and Chakraborty (2001), isotopic studies have shown that diffusion is not only facilitated by the channel structure, but also by the presence of point defects, which provide some kind of molecular "porosity."

12.4.3 Rate-Dependent Isotopic Effects

Kinetic effects on isotopes are particularly visible during the precipitation of a solid phase from a solution. The determination of equilibrium fractionation factors has

been problematic due to kinetic effects, but isotopic ratios are also an indirect way of deciphering reaction mechanisms. The following examples show that stable isotope fractionation depends on the way the element is incorporated into the crystal. Different degrees of fractionation are observed depending on whether crystal incorporation is controlled by the transport of the element to the mineral surface or by the rate of precipitation.

12.4.3.1 Carbon and Oxygen Isotopes

Kinetic effects on C and O have been reported for both abiotic and biotic systems. In the case of biotic systems, these are often referred to as "vital effects."

Turner (1982) precipitated abiotic carbonates under open system conditions (using a CO_2/N_2 mixture) and showed that the enrichment of ^{12}C in $CaCO_3$ with respect to HCO_3^- ion in solution varies from 0.4 to 3.4‰ as a function of precipitation rate, where enrichment of ^{12}C in the solid phase increases with increasing precipitation rate. These results can be interpreted by a surface diffusion crystal growth model. The surface of the crystal, where the ions precipitate, is separated from the solution by an adsorbed layer. During rapid crystal growth, diffusion of adsorbed species through the diffusion layer is the limiting step (see Chaps. 1 and 7). The light isotope is then favored during diffusion. The more rapid the precipitation, the more important are the kinetic effects. These experimental results are consistent with observations made on natural carbonates. Usdowski et al. (1978) and Dandurand et al. (1981) observed that during the precipitation of carbonates from oversaturated spring waters, the isotopic composition of the precipitated carbonate is similar to that of the dissolved carbonate and is not isotopically heavier as expected by an equilibrium control of the isotopic fractionation. This suggests that precipitation rates are faster than the time it takes to reach isotopic equilibrium.

More recently, Mickler et al. (2004) compared O and C isotopic compositions of modern speleothem samples from Harrison's cave (Barbados) with that of their corresponding drip waters. Nonequilibrium fractionation between aqueous HCO_3^- and solid carbonates occurs when ambient conditions favor a high rate of calcite growth. During rapid mineral precipitation, carbonate species are incorporated into calcite without isotopic effects. Theoretical developments can be found in Michaelis et al. (1985). It is important to note that the rate-controlled precipitation of carbonates is subject to debate. The experiments of Turner (1982) have been criticized and reinterpreted by Romanek et al. (1991) to show that the C isotopic shift between calcium carbonate and solution was not controlled by the rate of precipitation but rather by different reaction mechanisms associated with homogeneous (spontaneous) and heterogeneous (seeded-growth) nucleation. Experiments conducted by Romanek et al. (1991) using a "chemostat" (an experimental system designed to maintain a constant supersaturation to precipitate $CaCO_3$ at a constant rate) reported no rate control on the C isotopic composition of precipitated calcite. Kim and O'Neil (1997) reported that the isotopic composition of synthetic carbonates is a function of the initial concentration of Ca^{2+} and HCO_3^- in solution, and thus of the precipitation

rate. Fractionations increase with increasing initial concentration and decrease with increasing temperature. The effect of the precipitation rate of calcite was tested on isotope fractionation with different N_2 bubbling techniques (bubbling releases CO_2 and facilitates calcite precipitation) and it was found that the isotopic composition of calcite was not dependent upon precipitation rate. Part of the debate on C and O isotopic fractionation during crystal growth is due to different behavior of isotopes between a solution and a crystal depending upon a precipitation which is interface- or diffusion-limited.

C and O isotopes in biogenic carbonates may not necessarily be in equilibrium with precipitating solutions. Different reasons can explain the departure from isotopic equilibrium, usually classified into metabolic and kinetic isotope effects. While metabolic effects are caused by local changes of the isotopic composition of the precipitating fluids (e.g., by respiration and photosynthesis), kinetic effects are the results of the different behavior of light and heavy isotopes during the hydration ($CO_2 + H_2O = HCO_3^- + H^+$) and hydroxylation ($CO_2 + OH^- = HCO_3^-$) of CO_2 in aqueous solution (McConnaughey, 1988a, b). Kinetic effects favor the light isotopes. Rapid skeletogenesis in corals is associated with strong isotopic effects leading to a correlation between $\delta^{18}O$ and $\delta^{13}C$. Erez (1978) showed that $\delta^{13}C$ and $\delta^{18}O$ in Acropora are lower when calcification rate is high. The associated isotopic variations are in the range of 4‰ for O isotopes and more than 10‰ for C isotopes in corals (Fig. 12.21). As shown in Fig. 12.21, a correlation is observed in the skeleton of various organisms, reflecting the rate-dependent isotopic fractionation of C and O. McConnaughey (1988b) was able to simulate such large isotopic effects *in vitro* using an apparatus that reproduces rapid precipitation thought to occur during carbonate formation. In this experiment, CO_2 (derived from the cells in organisms) entering into the thin calcifying solution (the extracytoplasmic fluids in calcifying organisms) diffuses out without reacting, but the small fraction of CO_2 that forms HCO_3^- ion precipitates rapidly and does not undergo back reaction to CO_2. The experiment therefore simulates *in vitro* kinetic isotope effects. Under such a kinetic environment, the precipitated carbonate shows depletion in the heavy isotope for O and C (-6‰ and -11‰ for the isotopic shift between calcite and CO_2 for O and C respectively). Incomplete isotopic equilibration between HCO_3^- and CO_2 causes the linear trend observed in biological carbonates between $\delta^{18}O$ and $\delta^{13}C$. If this interpretation is correct, then a pH effect on O and C isotopic composition is expected because pH determines the balance between hydration and hydroxylation of CO_2. Given that the kinetics of these reactions are different, different kinetic isotope effects are expected.

Such kinetic effects were demonstrated recently by Rollion-Bard et al. (2003). These authors measured O, C and B isotopic composition (as an indirect pH tracer) with an ion microprobe at a millimeter scale in the coral *Porites lutea* in order to understand the discrepancy frequently observed in biogenic carbonates between the measured O isotopic composition and that predicted for inorganic aragonite precipitation at equilibrium. B isotopic compositions showed that the variability in $\delta^{18}O$ observed at the millimeter scale is associated with variations in pH at the calcification site (between 7 and 9). The authors attributed the isotopic data to both a pH

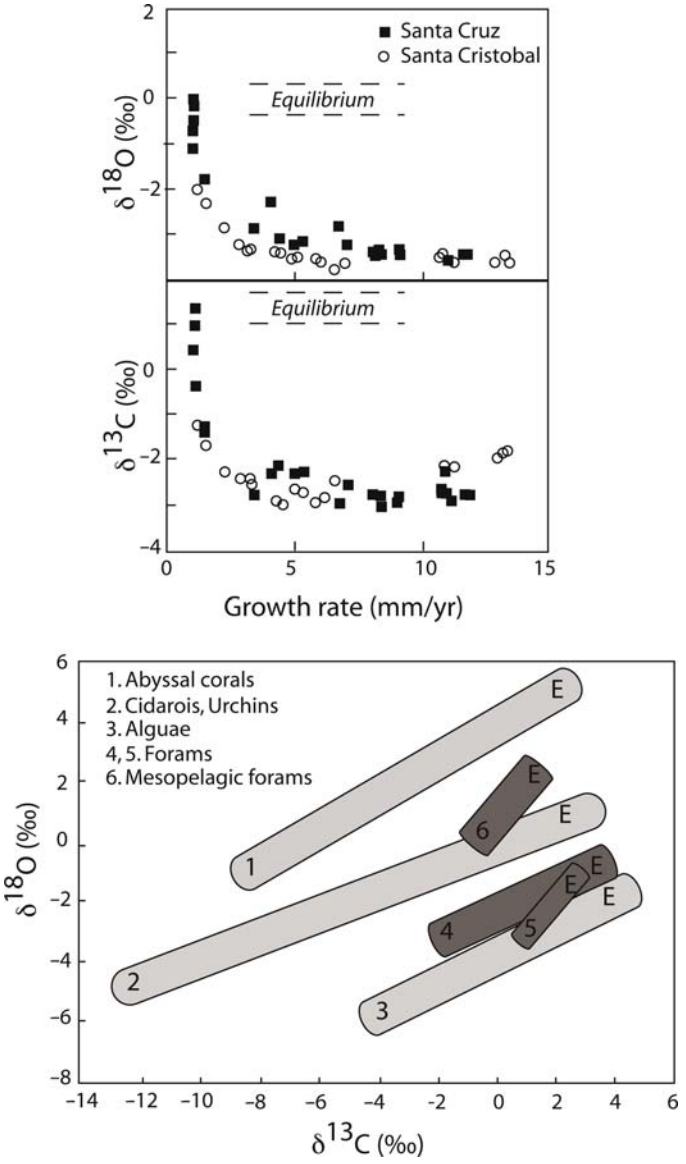

Fig. 12.21 **a**. Dependence of C and O isotope composition as a function of growth rate in a photosynthetic coral species (Pavona calves). Rapid skeletogenesis favors strong kinetic effects. **b**. In various biogenic carbonates a linear correlation is observed between C and O isotopes showing departure from equilibrium fractionation due to kinetic effects and enrichment in the light isotopes (McConnaughey, 1988a). Equilibrium conditions are calculated using the best estimates of calcite and aragonite equilibrium fractionation factors and seawater temperature. In addition to kinetic effects, "metabolic" effects are responsible for additional C isotope fractionation reflecting the change in $\delta^{13}C$ of dissolved organic carbon caused by the metabolic processes of photosynthesis and respiration. (From McConnaughey et al., 1989, with permission from Elsevier)

effect and to the difference in residence time of dissolved carbonate in the precipitating fluid. Depending upon pH, dissolved bicarbonate is produced by either hydration ($CO_2 + H_2O = HCO_3^- + H^+$) or hydroxylation ($CO_2 + OH^- = HCO_3^-$). These two reactions occur at different rates and the rate of O equilibration of HCO_3^- with seawater is therefore lower at high pH. The authors showed that their data can be modeled using a combined effect of pH and residence time of water in the calcifying fluid before being precipitated as aragonite. At high pH, the time necessary to reach isotopic equilibrium between HCO_3^- and water is more than 12 h, while this number decreases to 1 h at pH 7. Oxygen isotopic variations therefore occur because $CaCO_3$ precipitation occurs faster than O isotopic equilibration in the carbonate-water species system. Variations between day and night reflect the photosynthetic activity of the symbiotic zooxanthellae.

In forams, Spero and Lea (1996) reported that C and O isotopic ratios in calcite decrease as the pH of the culture media increases and CO_3^{2-} concentration increases.

12.4.3.2 Other Stable Isotopes

The above observations reported with C, O, S and H isotopes are now shown to be valid on other stable isotope systems, recently named "non traditional" isotopes (Johnson et al., 2004). Here we take the example of Ca and Fe isotopes.

Lemarchand et al. (2004) analyzed Ca isotopes and reported their behavior during carbonate precipitation. Calcite crystals were obtained experimentally from stirred and unstirred solutions with different calcium concentrations satisfying $[Ca^{2+}] > [CO_3^{2-}]$. Ca isotopes ($^{44}Ca/^{40}Ca$) were determined in the solids. The isotopic shift between the solution and the calcite crystals was shown to be a linear function of the saturation state of the solution with respect to calcite. The isotopic shift between the solution and calcite appeared to increase as a function of the rate of crystal growth for the unstirred solution, while for a stirred solution the isotopic shift was smaller (Fig. 12.22).

The largest Ca isotopic shift is found for the slowest precipitation rate with no stirring. These results were interpreted to reflect isotopic equilibrium exchange of Ca isotopes moderated by kinetic effects (depending on how fast the crystals grow). The precipitation rate of calcite is limited by the rate at which the transfer of CO_3^{2-} occurs from the solution to the growing crystals. The value of $-1.5‰$ between the crystal and the solution for a solution close to saturation state is assumed to be an equilibrium fractionation factor between the crystal and the solution. A surface layer where chemical and isotopic equilibrium between solution and solid is achieved develops. At higher saturation states of the solution, i.e., when the rate of CO_3^{2-} ion supply to the crystal surface is high, growth proceeds with an increased amount of precipitation of Ca with the isotopic composition of the fluid because the rate of isotopic exchange in the equilibrium surface layer is too slow compared to the rate of supply of carbonate ions to the surface of the growing crystals.

At low precipitation rates, the effect of stirring is to decrease the crystal-liquid boundary layer and increase the amount of Ca precipitating from outside of the

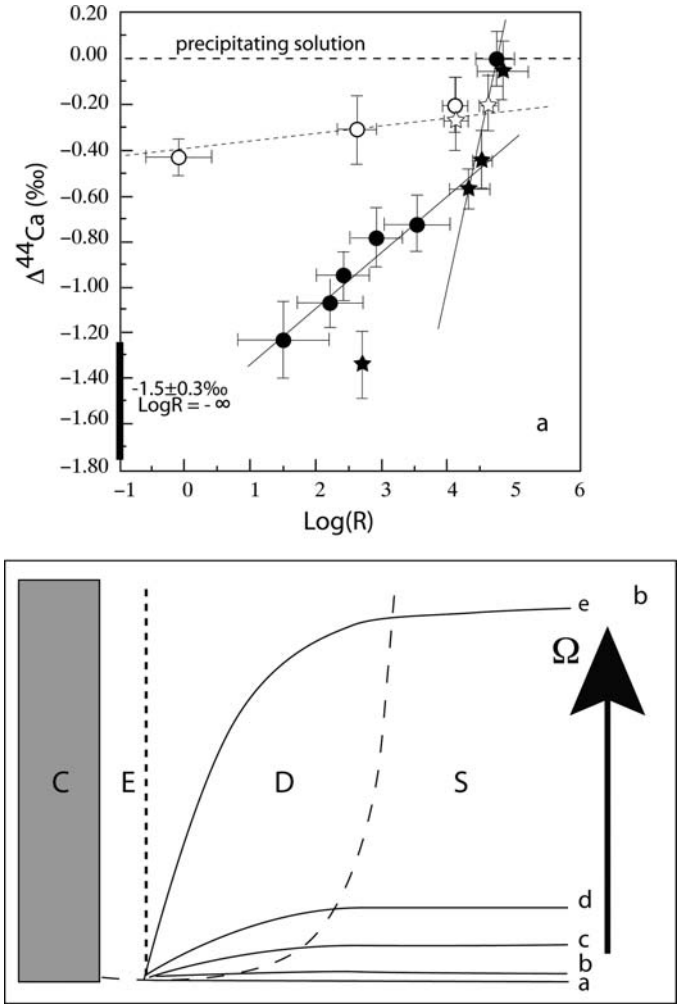

Fig. 12.22 **a**. Abiotic precipitation of synthetic calcite (Lemarchand et al., 2004). Experiment (**a**) shows that the isotopic variation of Ca depends on the rate of precipitation R ($\mu mol/m^2/h$). Filled circles and stars represent data from unstirred solution but differ in Ca concentration. Open symbols are for stirred solution. Below (**b**) is a conceptual diagram showing the crystal (C)-solution (S) interface. E is the narrow zone where crystal and surface boundary layer are in chemical and isotopic equilibrium through exchange reactions. D is the $HCO_3^- + CO_3^{2-}$ diffusive zone. Curves show the values of supersaturation as a function of distance to the crystal. Ω is the saturation factor, and curve *a* corresponds to saturation. At high Ω values, the amount of precipitated Ca is high and the diffusive inflow rate of carbonate species is high. The Ca isotopic composition of the crystal precipitated is then close to the solution value. When the solution is at saturation, the slow inflow flux of carbonate species lead to a low rate of carbonate precipitation and an equilibrium fractionation of Ca isotopes. Stirring decreases the thickness of the D region and thus the contribution of Ca with isotopic composition from the bulk solution

equilibration zone. These results clearly show that equilibrium isotopic effects can be limited by the rate of supply of carbonate ions, and thus, the precipitation rate of crystals. The rate-dependent fractionations of Ca isotopes are thus not related to complex kinetic fractionation effects of Ca, but rather to the diffusive inflow of carbonate species to the crystal surface (and thus supersaturation state). The results of this study must have some implications for natural crystals of calcite. It is interesting to note that the range of Ca isotopic composition found here covers the whole range of isotopic composition found in natural carbonates. Clearly, in the experiments of Lemarchand et al. (2004), the limiting step is the calcite precipitation, and very different results would have been observed if CO_3^{2-} ions had been in excess. In this case, transport of Ca would then have been the limiting step.

The isotope geochemistry of iron has received considerable attention over the last decade because of the potential use of Fe isotopes as a proxy for the origin and evolution of life on Earth and other planets. In addition, iron is the fourth most abundant element at the Earth's surface and understanding the behavior of its isotopes during water-rock interactions is of great interest for constraining both mechanisms and rates. In order to determine an equilibrium coefficient between a solution and a precipitating phase, Skulan et al. (2002) measured the isotopic (^{54}Fe, ^{56}Fe, ^{57}Fe) effects between $[Fe^{III}(H_2O)_6]^{3+}$ and hematite at 98° C. Long-term and short-term experiments clearly showed that kinetic effects dominate during the precipitation of ferric oxides. The equilibrium fractionation factor is estimated to be $-0.1 \pm 0.2‰$, whereas a kinetic fractionation of $1.3‰ \pm 0.1‰$ controls the isotopic shift between the solution and the precipitating phase. The isotopic shift $\Delta^{56}Fe(\delta^{56}Fe_H - \delta^{56}Fe_S)$ between solution (S) and hematite (H) increased with the rate of hematite precipitation, showing that kinetic effects dominate at high precipitation rates. The equilibrium fractionation factor is estimated by interpolation to a zero precipitation rate. In addition, complex time effects are also reported and explained by a kinetic model of hematite dissolution/precipitation. This example shows that it may not be straightforward to deduce reaction rates from isotopic measurements of fractionating isotopes, even with well-constrained experimental conditions. This is due to our poor understanding of the precipitation/dissolution mechanisms at the molecular scale. In addition, as outlined by Beard et al. (2003), the attainment of the steady state conditions for elemental concentrations may not be related to the attainment of isotopic equilibrium, depending on the relative reaction rates and rates of isotopic exchange. This complicates the use of isotopes to trace the kinetics of water-rock reactions.

Another example of the potential use of ^{54}Fe and ^{56}Fe isotopes to understand water-rock interaction, more precisely mineral dissolution, is given by the experimental work of Brantley et al. (2001, 2004). The authors determined the Fe isotope fractionation during hornblende dissolution in the presence and absence of organic ligands and bacteria (see also Chap. 5). The results show that an isotopic shift exists between Fe in solution and Fe in hornblende. The apparent fractionation of Fe isotopes depends on the affinity of organic molecules for Fe and is at most $\pm 0.4‰$ when hornblende is in contact with bacteria. Interestingly, experiments where solutions were constantly agitated showed higher fractionation of Fe isotopes between

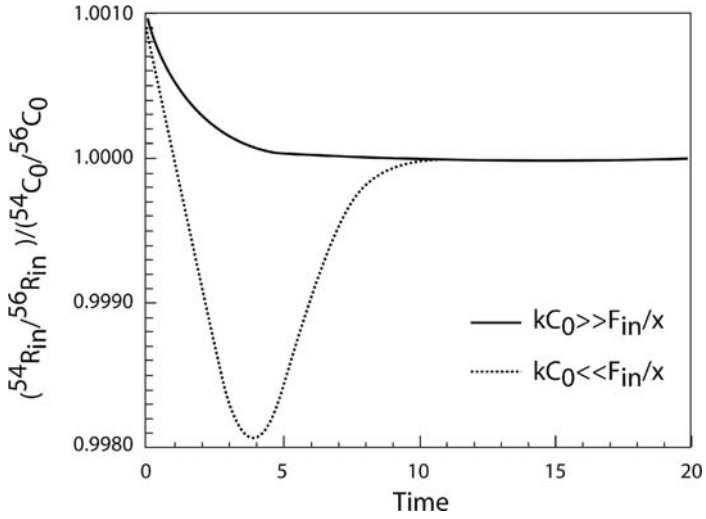

Fig. 12.23 This diagram is an illustration of a simple model of hornblende dissolution for iron isotopes assuming the presence of a leached layer between the mineral and the solution (Brantley et al., 2004). The Y-axis gives the instantaneous fractionation of Fe leaving the leached layer to solution. $^{i}R_{in}$ is the rate at which the isotope i enters the solution. $^{54}C_0/^{56}C_0$ is the isotopic ratio of the bulk mineral. At time zero, initial Fe leaving the leached layer is 1‰ lighter relative to the bulk mineral. At steady state, there is no difference between Fe leaving the leached layer and mineral isotopic composition. In between, the isotopic trajectories depend on the relative magnitude of kC_0 (rate of supply of Fe from the leached layer to the solution) and F_{in}/x (rate of Fe release from the mineral to the leached layer). (From Brantley et al., 2004, with permission from Elsevier)

solution and starting material (1.2‰). This demonstrates the high sensitivity of Fe isotope fractionation to experimental conditions. Results are interpreted by the authors as resulting from the preferential leaching of Fe from a leached surface layer. Hornblende dissolution, like dissolution of other silicates, does not occur stoichiometrically in the sense that a leached layer is developed without reaching steady state dissolution, even after a very long time (see Chap. 5). This transient state makes kinetic isotope effects possible. A simple kinetic model was proposed by Brantley et al. (2004) to understand the effect of the leached layer on isotopes. The rate of change of Fe concentration in the leached layer (dC/dt) can be expressed as

$$\frac{dC}{dt} = \frac{F_{in}}{X} - kC \tag{12.30}$$

where F_{in} is the input flux of Fe (per unit area) to the leached layer, X is the thickness of the leached layer and k is a first-order kinetic constant of Fe released from the layer. The equation can be written for isotopes and another equation can be derived for predicting the isotopic evolution of Fe entering solution. If the rate constant, k, of ^{54}Fe and ^{57}Fe are different, then the isotopic composition of Fe released from the leached layer is different from the Fe isotopic composition of hornblende, provided that the surface layer did not reach a steady state. The predicted offset between solution and the bulk mineral is illustrated in Fig. 12.23 for two cases: high input of

Fe to the leached layer with low release by leaching and low input rate of Fe to the leached layer, but easy leaching from the surface layer. The agitation of the solution may change the thickness of the leached layer and hence produce the isotopic effects. In Fig. 12.23, the preferential leaching of ^{54}Fe (1% enriched compared to ^{56}Fe) is assumed to be the result of a kinetic isotope fractionation. This diagram is a theoretical exercise but it shows that it is possible, under transient conditions, to produce significant isotopic variations of Fe that change with time in a mineral dissolution system.

Although a lot of progress in our understanding of equilibrium versus kinetic fractionation mechanisms remains to be made, this simple example shows that the application of Fe isotopes to natural dissolution and precipitation systems, like other fractionating isotopes, has great potential to trace non-steady state behaviors and to constrain the rates of the processes operating. In this regard, we clearly need experimental studies and data from natural systems. For Fe, a first step was made by Brantley et al. (2004): in agreement with experiments, isotopically light Fe was found on exchangeable sites on soil surfaces from New York, USA.

12.5 Conclusion and Perspectives

From the molecular reaction to the Earth's global reservoirs, isotopes are of great help to constrain the time evolution of geological systems. Examples discussed above show that isotopes are useful in different ways. They are tracers of minerals, rocks, reservoirs, and their isotopic evolution with time is a record of the history of water-rock interaction. Radioactivity is a major feature of certain isotopes whose abundance directly indicates the timescales of water-rock interaction. Finally, isotopic exchange reactions may be slow and the time evolution of isotopic compositions can therefore be a guide for constraining the mechanisms and rates of abiotic and biological reactions. From the above examples, several general statements and perspectives emerge.

- Because most of the isotopes belong to trace elements and because trace elements have abundances that vary more than major rock components, isotopic data have great potential to trace the interaction of water with particular phases (such as calcite in granite). They emphasize the behavior of discrete phases that are not necessarily visible when analyzing major cations. This is less true for isotopes of major elements such as O or Fe.
- Except for some simple cases where isotopes are used to date and deduce rates of mineral precipitation, the interpretation of isotopic data in terms of kinetics requires a model of elemental mobility. This is particularly apparent in the interpretation of oceanic isotopic proxies. The interpretation of a given isotopic record not only depends upon the sources and mechanisms of isotope fractionation, but also on the fluxes involved for each of these mechanisms. The interpretation of

U series data in soil or in groundwater is also a good example, where a model of U mobility is needed prior to the interpretation of isotopic data.
– Isotopic data should be regarded as an additional constraint when analyzing water-rock interaction in natural systems, and well-chosen isotopes should be more widely used in kinetic studies. The incorporation of several isotopic systems into more powerful numerical reactive-transport models should be coupled with major element geochemistry. These approaches are uniquely able to track multiple reaction pathways and essentially allow us to interpret kinetic data in terms of thermodynamic properties and rate laws, so that experimental and natural system data can be more rigorously compared.
– The isotopic disequilibrium observed for several decades for the conventional stable isotopes during gas, liquid and solid interactions has given rise to an impressive body of work, of which many studies were motivated by the determination of equilibrium fractionation factors. This approach is still an active area of research and is now renewed by the analysis of the "non traditional" isotopes and the development of MC-ICPMS. But a lot of research must be done in this direction to understand the fractionation of these "new" isotopes. As shown by the recent literature on Fe isotopes, results are very sensitive to experimental conditions and the interpretation of results clearly needs to be constrained by realistic chemical models.
– The so-called vital effects are isotopic effects that are due to biological processes. More work is needed to understand their origin more fully and to determine if vital effects can be recognized in geochemical systems where abiotic effects are also important. The identification of vital effects during physiological processes is obvious but the identification of vital effects in complex geochemical systems is not.
– Much work is being done using short-lived and cosmogenic nuclides to determine the rate constants for water-rock interaction processes. Analysis of these isotopes is a powerful approach that is adding new constraints on geomorphologic processes (rate constant of landscape evolution) and tectonics (crust deformation rates).
– Finally, although not emphasized here, a promising field is the use of *in situ* measurement of isotopes. The considerable progress in the analysis of small and localized amounts of isotopes in solid phases should improve our knowledge of kinetically controlled isotopic fractionation.

Acknowledgments

I thank Sue Brantley for her encouragements and fruitful discussions. Discussions with J. Schott, D. Lemarchand, F. Chabaux, C. France-Lanord, E. Lajeunesse, L. Meynadier, B. Bourdon, and D. Anbar and K. Maher were greatly appreciated. Reviews and English editing from A. Lerman, L. Carpenter, B. Kimball, and K. Maher were greatly appreciated. This is IPGP contribution number IPGP 2212.

References

Bach W. and Humphris S. E. (1999) Relationships between Sr and O isotope composition of hydrothermal fluids and the spreading and magma-supply rates of oceanic spreading centers. *Geology* **27**(12), 1067–1070.

Bath S. G., Khrishnaswami S., Lal D., Rama, and More W. S. (1969) 234^{Th}/238U ratios in the ocean. *Earth and Planetary Science Letters* **5**, 483–491.

Baxter E. F. and DePaolo D. J. (2002a) Field measurement of high temperature bulk reaction rates I: Theory and technique. *American Journal of Science* **302**, 442–464.

Baxter E. F. and DePaolo D. J. (2002b) Field measurement of high temperature bulk reaction rates II: Interpretation of results from a field site near Simplon Pass, Switzerland. *American Journal of Science* **302**, 465–516.

Beard B. L., Johnson, C. M., Skulan, J. L., Nealson, K. H., Cox L., and Sun H. (2003) Application of Fe isotopes to tracing the geochemical and biological cycling of Fe. *Chemical Geology* **195**, 87–117.

Beck J. W., Berndt M. E., and Seyfried J. W. E. (1992) Application of isotopic doping techniques to evaluation of reaction kinetics and fluid/mineral distribution coefficients: An experimental study of calcite at elevated temperatures and pressures. *Chemical Geology* **97**(1–2), 125.

Berner R. A. (1980) *Early Diagenesis: A Theoretical Approach*. Princeton University Press, Princeton, NJ.

Bickle M. J. (1992) Transport mechanisms by fluid-flow in metamorphic rocks: Oxygen and strontium decoupling in the Trois Seigneurs Massif – a consequence of kinetic dispersion? *American Journal of Science* **292**(5), 289.

Bickle M. J. and Teagle D. A. H. (1992) Strontium alteration in the Troodos ophiolite: Implications for fluid fluxes and geochemical transport in mid-ocean ridge hydrothermal systems. *Earth and Planetary Science Letters* **113**, 219–237.

Bierman P. R. and Steig E. J. (1996) Estimating rates of denudation using cosmogenic isotopes abundances in sediment. *Earth Surface Processes and Landforms* **21**, 121–139.

Blattner P. and Lassey K. R. (1989) Stable-isotope exchange fronts, Damköhler numbers, and fluid to rock ratios. *Chemical Geology* **78**, 381–392.

Blum J. D. and Erel Y. (1995) A silicate weathering mechanism linking increases in marine Sr/Sr with global glaciation. *Nature* **373**(6513), 415.

Blum J. D. and Erel Y. (1997) Rb-Sr isotope systematics of a granitic soil chronosequence: The importance of biotite weathering. *Geochimica et Cosmochimica Acta* **61**(15), 3193.

Blum J. D., Erel Y., and Brown K. (1993) 87Sr/86Sr ratios of Sierra Nevada stream waters: Implications for relative mineral weathering rates. *Geochimica et Cosmochimica Acta* **57**(21–22), 5019.

Bottinga Y. (1968) Calculation of fractionation factor for C and O isotope exchange in the system caclite-carbon dioxide-water. *Journal of Physical Chemistry* 72(3), 800–808.

Bourdon B., Henderson G. M., Lundstrom C. C., and Turner S. P. (2003) Uranium-series geochemistry. *Reviews in Mineralogy and Geochemistry* **52**.

Brantley S. L., Chesley J. T., and Stillings L. L. (1998) Isotopic ratios and release rates of strontium measured from weathering feldspars. *Geochimica et Cosmochimica Acta* **62**(9), 1493.

Brantley S. L., Liermann L., and Bullen T. D. (2001) Fractionation of Fe isotopes by soil microbes and organic acids. *Geology* **29**(6), 535.

Brantley S. L., Liermann L. J., Guynn R. L., Anbar A., Icopini G. A., and Barling J. (2004) Fe isotopic fractionation during mineral dissolution with and without bacteria. *Geochimica et Cosmochimica Acta* **68**(15), 3189.

Broecker W. S., Kaufman A., and Trier R. M. (1973) The residence time of thorium in surface seawater and its implications regarding the fate of reactive pollutants. *Earth and Planetary Science Letters* **20**, 35–44.

Brown E. T., Colin F., and Bourles D. L. (2003) Quantitative evaluation of soil processes using in situ-produced cosmogenic nuclides. *Comptes Rendus Geosciences* **335**(16), 1161.

Brown E. T., Stallard R. F., Larsen M. C., Raisbeck G. M., and Yiou F. (1995) Denudation rates determined from the accumulation of in situ-produced 10Be in the Luquillo experimental forest, Puerto Rico. *Earth and Planetary Science Letters* **129**(1–4), 193.

Buesseler K. O., Andrews J. A., Hartman M. C., Belastock R., and Chai F. (1995) Regional estimates of the export flux of particulate organic carbon derived from thorium-234 during the JGOFS EqPac program. *Deep Sea Research Part II: Topical Studies in Oceanography* **42**(2–3), 777.

Bullen T., White A., Blum A., Harden J., and Schulz M. (1997) Chemical weathering of a soil chronosequence on granitoid alluvium: II. Mineralogic and isotopic constraints on the behavior of strontium. *Geochimica et Cosmochimica Acta* **61**(2), 291.

Bullen T. D., Krabbentoft D. P., and Kendall C. (1996) Kinetic and mineralogic controls on the evolution of groundwater chemistry and $^{87}Sr/^{86}Sr$ in a sandy silicate aquifer, Northern Wisconsin, USA. *Geochilica et Cosmochimica Acta* 60, 1807–1821.

Chabaux F., Cohen A. S., Onions R. K., and Hein J. R. (1995) 238U–234U–230Th chronometry of Fe–Mn crusts: Growth processes and recovery of thorium isotopic ratios of seawater. *Geochimica et Cosmochimica Acta* **59**(3), 633.

Chabaux F., Riotte J., and Dequincey O. (2003) Uranium-series geochemistry: U-Th-Ra fractionation during weathering and river transport. *Reviews in Mineralogy and geochemistry* **52**, 533–576.

Chacko T, Cole D. R., and Horita J. (2001) Equilibrium oxygen, hydrogen and carbon isotope fractionation factors applicable to geological systems. *Reviews in Mineralogy and Geochemistry* **43**, 1–82.

Christensen J. N., Rosenfeld J. L., and DePaolo D. J. (1989) Rates of tectonometamorphism processes from Rubidium and Strontium isotopes in Garnet. *Science* **244**, 1465–1469.

Chu X. and Ohmoto H. (1991) Kinetic of isotope exchange reactions involving intra- and intermolecular reactions: I. Rate law for a system with two chemical compounds and three exchangeable atoms. *Geochimica et Cosmochimica Acta* **55**, 1953–1961.

Chu X., Ohmoto H., and Cole D. R. (2004) Kinetics of sulfur isotope exchange between aqueous sulfide and thiosulfate involving intra- and intermolecular reactions at hydrothermal conditions. *Chemical Geology* **211**(3–4), 217.

Cochran J. K. and Masqué P. (2003) U-series geochemistry: Short-lives U/Th series radionuclides in the ocean: Tracers for scavenging rates, export fluxes and particles dynamics. *Reviews in Mineralogy and geochemistry* **52**, 461–492.

Cole D. R. and Chakraborty S. (2001) Rates and mechanisms of isotopic exchange. *Stable Isotope Geochemistry, Reviews in Mineralogy and geochemistry* **43**, 83–223.

Cole D. R., Mottl M. J., and Ohmoto H. (1987) Isotopic exchange in mineral-fluid systems. II. Oxygen and hydrogen isotopic investigation of the experimental basalt-seawater system. *Geochimica et Cosmochimica Acta* **51**(6), 1523.

Cole D. R. and Ohmoto H. (1986) Kinetics of isotopic exchange at elevated temperatures. *Stable Isotope in High Temperature Geological Processes, Reviews in Mineralogy* **16**, 40–90.

Cole D. R., Ohmoto H., and Jacobs G. K. (1992) Isotopic exchange in mineral-fluid systems: Rates and mechanisms of oxygen isotope exchange in the system granite $\pm$H2O $\pm$ NaCl $\pm$ KCl at hydrothermal conditions. *Geochimica et Cosmochimica Acta* **56**, 445–466.

Cole D. R., Ohmoto H., and Lasaga A. C. (1983) Isotopic exchange in mineral-fluid systems. I. Theoretical evaluation of oxygen isotopic exchange accompanying surface reactions and diffusion. *Geochimica et Cosmochimica Acta* **47**(10), 1681.

Criss R. E., Gregory R. T., and Taylor J. H. P. (1987) Kinetic theory of oxygen isotopic exchange between minerals and water. *Geochimica et Cosmochimica Acta* **51**(5), 1099.

Dandurand J. L., Gout R., Hoefs J., Menschel G., Schott J., and Usdowski E. (1982) Kinetically controlled variations of major components and carbon and oxygen isotopes in a calcite-precipitating spring. *Chemical Geology* **36**(3–4), 299.

DePaolo D. J. (2006) Isotopic effects in fracture-dominated reactive fluid-rock systems. *Geochimica et Cosmochimica Acta* 70, 1077–1096.

Dequincey O., Chabaux F., Clauer N., Sigmarsson O., Liewig N., and Leprun J. C. (2002) Chemical mobilizations in laterites: Evidence from trace elements and 238U-234U-230Th disequilibria. *Geochimica et Cosmochimica Acta* **66**(7), 1197.

Derry L. A. and France-Lanord C. (1996) Neogene Himalayan weathering history and river 87Sr/86Sr: Impact on the marine Sr record. *Earth and Planetary Science Letters* **142**(1–2), 59.

Doremus R. H. (1998) Diffusion of water and oxygen in quartz: Reaction-diffusion model. *Earth and Planetary Science Letters* **163**(1–4), 43.

Dosseto A., Bourdon B., Gaillardet J., Allegre C. J., and Filizola N. (2005) Time scale and conditions of weathering under tropical climate: Study of the Amazon basin with U-series. *Geochimica et Cosmochimica Acta*, **69**(14), 3519–3533.

Dosseto A., Bourdon B., Gaillardet J., Maurice-Bourgoin L. and Allegre C. J. (2006) Weathering and transport of sediments in the Bolivian Andes: Time constraints from U-series isotopes. *Earth and Planetary Science Letters* **248**(3–4), 759–771.

Dubinina E. O. and Lakshtanov L. Z. (1997) A kinetic model of isotopic exchange in dissolution-precipitation processes. *Geochimica et Cosmochimica Acta* **61**(11), 2265.

Erel Y., Blum J. D., Roueff E., and Ganor J. (2004) Lead and strontium isotopes as monitors of experimental granitoid mineral dissolution. *Geochimica et Cosmochimica Acta* **68**(22), 4649–4663.

Erel Y., Harlavan Y., and Blum J. D. (1994) Lead isotope systematics of granitoid weathering. *Geochimica et Cosmochimica Acta* **58**(23), 5299.

Erez J. (1978) Vital effect on stable-isotope composition seen in foraminifera and coral skeletons. *Nature* **273**(5659), 199.

Faure G. and Mensing T. M. (2005) Isotope principles and applications. Third Edition. John Wiley & Sons, NJ.

Gannoun A., Burton, K. W., Vigier N., Gislason S. R., Rogers N., Mokadem F., and Sigfusson B. (2006) The influence of weathering process on riverine osmium isotopes in a basaltic terrain. *Earth and Planetary Science Letters* **243**, 732–748.

Gee A. K. and Bruland K. W. (2002) Tracing Ni, Cu, and Zn kinetics and equilibrium partitioning between dissolved and particulate phases in South San Francisco Bay, California, using stable isotopes and high-resolution inductively coupled plasma mass spectrometry. *Geochimica et Cosmochimica Acta* **66**(17), 3063.

Gehlen M., Mucci A., and Boudreau B. (1999) Modelling the distribution of stable carbon isotopes in porewaters of deep-sea sediments. *Geochimica et Cosmochimica Acta* **63**, 2763–2773.

Gosse J. C. and Phillips F. M. (2001) Terrestrial in situ cosmogenic nuclides: Theory and application. *Quaternary Science Reviews* **20**(14), 1475.

Granger D. E., Kirchner J. W., and Finkel R. (1996) Spatially averaged long-term erosion rates measured from in situ-produced cosmogenic nuclides in alluvial sediment. *Journal of Geology* **104**(3), 249.

Gregory R. T. and Criss R. E. (1986) Stable isotopes in high temperature geolical processes: Isotopic exchange in open and closed systems. *Reviews in Mineralogy* **16**, 91–126.

Gregory R. T. and Taylor H. P. (1981) An oxygen isotope profile in a section of Cretaceous oceanic crust, Samail ophiolite, Oman: Evidence for [delta] O buffering of the oceans by deep (>5 km) seawater-hydrothermal circulation at mid-ocean ridges. *Journal of Geophysical Research* **86**(B4), 2737.

Harlavan Y. and Erel Y. (2002) The release of Pb and REE from granitoids by the dissolution of accessory phases. *Geochimica et Cosmochimica Acta* **61**, 291–306.

Harlavan Y., Erel Y., and Blum J. D. (1998) Systematic changes in lead isotopic composition with soil age in glacial granitic terrains. *Geochimica et Cosmochimica Acta* **62**(1), 33.

Henderson G. M. and Anderson R. F. (2003) Uranium-series geochemistry: The U-series toolbox for paleoceanography. *Reviews in Mineralogy and Geochemistry* **52**, 493–531.

Hilaire-Marcel C., Vallières S., Ghaleb B., and Mareschal J. C. (1990) Déséquilibres Th-U dans les sols carbonatés en climat subaride: Estimation des flux d'uranium et vitesse d'érosion. Le cas du Bassin de Palmyre, Syrie. *C. R. Acad. Sci. Paris, série IIa* **311**, 233–238.

Houssein I., Michard G., and Dupre B. (1993) Interaction eau-roche au voisinage de l'équilibre: Utilisation simultanée des éléments majeursn des éléments traces et des isotopes. *C. R. Acad. Sci. Paris, série II* **t. 316**, 77–83.

Johnson C. M., Beard B. L., and Albarède F. (2004) Geochemistry of non-traditional stable isotopes: Overview and general concepts. *Reviews in Mineralogy and geochemistry* **55**, 1–24.

Johnson T. M. and DePaolo D. J. (1994) Interpretation of isotopic data in groundwater-rock systems: Model development and application to Sr isotope data from Yucca Mountain. *Water Resources Research* **30**(5), 1571–1587.

Johnson T. M. and DePaolo D. J. (1997a) Rapid exchange effects on isotope ratios in groundwater systems 1. Development of a transport-dissolution-exchange model. *Water Resources Research* **33**(1), 187–195.

Johnson T. M. and DePaolo D. J. (1997b) Rapid exchange effects on isotope ratios in groundwater systems 2. Flow investigation using Sr isotopes. *Water Resources Research* **33**, N°1, 197–2009.

Kim S.-T. and O'Neil J. R. (1997) Equilibrium and nonequilibrium oxygen isotope effects in synthetic carbonates. *Geochimica et Cosmochimica Acta* **61**(16), 3461.

Labotka T. C., Cole D. R., and Riciputi L. R. (2000) Diffusion of C and O in calcite at 100 MPa. *American Mineralogist* **85**, 488–494.

Lal D. (1991) Cosmic ray labelling of erosion surfaces: In situ production rates and erosion models. *Earth and Planetary Science Letters* **104**, 424–439.

Lassey K. R. and Blattner P. (1988) Kinetically controlled oxygen isotope exchange between fluid and rock in one-dimensional advective flow. *Geochimica et Cosmochimica Acta* **52**(8), 2169.

Lecuyer C. and Allemand P. (1999) Modelling of the oxygen isotope evolution of seawater: Implications for the climate interpretation of the [delta]18O of marine sediments. *Geochimica et Cosmochimica Acta* **63**(3–4), 351.

Lecuyer C., Gillet P., and Robert F. (1998) The hydrogen isotope composition of seawater and the global water cycle. *Chemical Geology* **145**(3–4), 249.

Lemarchand D., Gaillardet J., Lewin E., and Allegre C. J. (2001) The influence of rivers on marine B isotopes and implications for reconstructing past ocean pH. *Nature* **408**(6815), 951.

Lemarchand D., Wasserburg G. J., and Papanastassiou D. A. (2004) Rate-controlled calcium isotope fractionation in synthetic calcite. *Geochimica et Cosmochimica Acta* **68**(22), 4665.

Lemarchand E., Schott J., and Gaillardet J. (2005) Boron isotopic fractionation related to boron sorption on humic acids and the structure of the surface complexes formed. *Geochimica et Cosmochimica Acta* **69**(14), 3519.

Lemarchand D. and Gaillardet J. (2006) Transient features of the erosion of shales in the Mackenzie basin (Canada), evidences from B isotopes. *Earth and Planetary Science Letters* **245**, 174–189.

Luo S., Ku T.-L., Roback R., Murrell M., and McLing T. L. (2000) In-situ radionuclide transport and preferential groundwater flows at INEEL (Idaho): Decay-series disequilibrium studies. *Geochimica et Cosmochimica Acta* **64**(5), 867–881.

Maher K., DePaolo D. J., Conrad M. E., and Sterne R. J. (2003) Vadose infiltration rate at Hanford, Washington, inferred from Sr isotope measurements. *Water Resources Research*, **39**, 1204.

Maher K., DePaolo D. J., and Lin J. C.-F. (2004) Rates of silicate dissolution in deep-sea sediment: In situ measurement using 234U/238U of pore fluids. *Geochimica et Cosmochimica Acta* **68**(22), 4629.

Maher K., DePaolo D. J., and Christensen J. N. (2006a) U-Sr isotopic speedometer: Fluid flow and chemical weathering rates in aquifers. *Geochimica et Cosmochimica Acta* **70**(17), 4417–4435.

Maher K., Steefel C. I., DePaolo D. J., and Viani B. E. (2006b) The mineral dissolution rate conundrum: Insights from reactive transport modeling of U isotopes and pore fluid chemistry in marine sediments. *Geochimica et Cosmochimica Acta* **70**(2), 337–363.

Matsumoto E. (1975) 234Th-238U radioactive disequilibrium in the surface layer of the oceans. *Geochimica et Cosmochimica Acta* **39**, 205–212.

McConnaughey T. (1989a) 13C and 18O isotopic disequilibrium in biological carbonates: I. Patterns. *Geochimica et Cosmochimica Acta* **53**(1), 151.

McConnaughey T. (1989b) 13C and 18O isotopic disequilibrium in biological carbonates: II. In vitro simulation of kinetic isotope effects. *Geochimica et Cosmochimica Acta* **53**(1), 163.

Michaelis J., Usdowski E., and Menschel G. (1985) Partitioning of C and C on the degassing of CO2 and the precipitation of calcite – Rayleigh-type fractionation and a kinetic model. *American Journal of Science* **285**(4), 318.

Mickler P. J., Banner J. L., Stern L., Asmerom Y., Edwards R. L., and Ito E. (2004) Stable isotope variations in modern tropical speleothems: Evaluating equilibrium vs. kinetic isotope effects. *Geochimica et Cosmochimica Acta* **68**(21), 4381.

Muehlenbachs K. and Clayton R. N. (1976) Oxygen isotope composition of the oceanic crust and its bearing on seawater. *Journal of Geophysical Research* **81**(23), 4365.

O'Neil J. R. (1986) Theoretical and experimental aspects of isotopic fractionation. *Stable Isotopes in High Temperature Geological Processes, Published by Mineralogical Society of America; Reviews in Mineralogy*, Editor Valley J. W. **16**, 1–40.

Ohmoto H. and Lasaga A. C. (1982) Kinetics of reactions between aqueous sulfates and sulfides in hydrothermal systems. *Geochimica et Cosmochimica Acta* **46**(10), 1727.

Palmer M. R., Spivack A. J., and Edmond J. M. (1987) Temperature and pH controls over isotopic fractionation during adsorption of B on marine clay. *Geochimica et Cosmochimica Acta* **51,** 2319–2323.

Richet P., Bottinga Y., and Javoy M. (1977) A review of hydrogen, carbon, nitrogen, oxygen, sulfur and chlorine stable isotope fractionation among gaseous molecules. *Annual Review of Earth and Planetary Sciences* **5**, 65–110.

Richter F. M. and DePaolo D. J. (1987) Numerical models for diagenesis and the Neogene Sr isotopic evolution of seawater from DSDP Site 590B. *Earth and Planetary Science Letters* **83**(1–4), 27.

Richter F. M. and DePaolo D. J. (1988) Diagenesis and Sr isotopic evolution of seawater using data from DSDP 590B and 575. *Earth and Planetary Science Letters* **90**(4), 382.

Richter F. M., Rowley D. B., and DePaolo D. J. (1992) Sr isotope evolution of seawater: The role of tectonics. *Earth and Planetary Science Letters* **109**, 11–23.

Richter F. M. and Turekian K. K. (1993) Simple models for the geochemical response of the ocean to climatic and tectonic forcing. *Earth and Planetary Science Letters* **119**(1–2), 121.

Riebe C. S., Kirchner J. W., Granger D. E., and Finkel R. (2001) Strong tectonic and weak climatic control of long-term chemical weathering. *Geology* **29**(6), 511–514.

Riebe C. S., Kirchner J. W., Granger D. E., and Finkel R. C. (2000) Erosional equilibrium and disequilibrium in the Sierra Nevada, inferred from cosmogenic Al and Be in alluvial sediment. *Geology* **28**(9), 803.

Rollion-Bard C., Chaussidon M., and France-Lanord C. (2003) pH control on oxygen isotopic composition of symbiotic corals. *Earth and Planetary Science Letters* **215**(1–2), 275.

Romanek C. S., Grossman E. L., and Morse J. W. (1992) Carbon isotopic fractionation in synthetic aragonite and calcite: Effects of temperature and precipitation rate. *Geochimica et Cosmochimica Acta* **56**(1), 419.

Sarda P., Staudacher T., Allegre C. J., and Lecomte A. (1993) Cosmogenic neon and helium at Reunion: Measurement of erosion rate. *Earth and Planetary Science Letters* **119**(3), 405.

Schaller M., von Blanckenburg F., Hovius N., and Kubik P. W. (2001) Large-scale erosion rates from in situ-produced cosmogenic nuclides in European river sediments. *Earth and Planetary Science Letters* **188**(3–4), 441.

Scott R. D., MacKenzie A. B., and Alexander W. R. (1992) The interpretation of 238U-234U-230Th-226Ra disequilibria produced by rock-water interactions. *Journal of Geochemical Exploration* **45**(1–3), 323.

Seimbille F., Zuddas P., and Michard G. (1998) Granite-hydrothermal interaction: A simultaneous estimation of the mineral dissolution rate based on the isotopic doping technique. *Earth and Planetary Science Letters* **157**(3–4), 183.

Singleton M. J., Maher K., DePaolo D. J., Conrad M. E., and Evan Dresel P. (2006) Dissolution rates and vadose zone drainage from strontium isotope measurements of groundwater in the Pasco Basin, WA unconfined aquifer. *Journal of Hydrology* **321**(1–4), 39–58.

Skulan J. L., Beard B. L., and Johnson C. M. (2002) Kinetic and equilibrium Fe isotope fractionation between aqueous Fe(III) and hematite. *Geochimica et Cosmochimica Acta* **66**(17), 2995.

Spero H. J. and Lea D. W. (1996) Experimental determination of stable isotope variability in Globigerina bulloides: Implications for paleoceanographic reconstructions. *Marine Micropaleontology* **28**(3–4), 231.

Stakes D. S. and Taylor Jr H. P. (1992) The northern Samail Ophiolite: An oxygen isotope, microprobe, and field study. *Journal of Geophysical Research* **97**(B5), 7043.

Taylor A. S., Blum J. D., Lasaga A. C., and MacInnis I. N. (2000) Kinetics of dissolution and Sr release during biotite and phlogopite weathering. *Geochimica et Cosmochimica Acta* **64**(7), 1191.

Taylor H. P. J. (1977) Water/rock interaction and the origin of H2O in granitic batholiths. *Journal of the Geological Society of London* **133**, 509–558.

Teagle D. A. H., Bickle M. J., and Alt J. C. (2003) Recharge flux to ocean-ridge black smoker systems: A geochemical estimate from ODP Hole 504B. *Earth and Planetary Science Letters* **210**(1–2), 81.

Thiel K., Vorwerk R., Saager R., and Stupp H. D. (1983) 235U fission tracks and 238U-series disequilibria as a means to study recent mobilization of uranium in Archaean pyritic conglomerates. *Earth and Planetary Science Letters* **65**(2), 249.

Tricca A., Porcelli D., and Wasserburg G. J. (2000) Factors controlling the groundwater transport of U, Th, Ra and Rn. *In Gopalan Festschrift Volume* (ed. Rao Y. J. B. et al.), **109** (Proceedings of the Indian Academy of Science).

Tricca A., Wasserburg G. J., Porcelli D., and Baskaran M. (2001) The transport of U- and Th-series nuclides in a sandy unconfined aquifer. *Geochimica et Cosmochimica Acta* **65**(8), 1187.

Turner J. V. (1982) Kinetic fractionation of carbon-13 during calcium carbonate precipitation. *Geochimica et Cosmochimica Acta* **46**(7), 1183.

Urey H. C. (1947) The thermodynamics properties of isotopic substances. *Journal of Chemical Society (London)*, 562–581.

Usdowski E., Hoefs J., and Menschel G. (1979) Relationship between 13C and 18O fractionation and changes in major element composition in a recent calcite-depositing spring — A model of chemical variations with inorganic CaCO3 precipitation. *Earth and Planetary Science Letters* **42**(2), 267.

Vance D. and O'Nions R. K. (1990) Isotopic chronometry of zoned garnets: Growth kinetics and metamorphic histories. *Earth and Planetary Science Letters* **97**(3–4), 227.

Vigier N., Bourdon B., Lewin E., Dupre B., Turner S., Chakrapani G. J., van Calsteren P., and Allegre C. J. (2005) Mobility of U-series nuclides during basalt weathering: An example from the Deccan Traps (India). *Chemical Geology* **219**(1–4), 69.

Vigier N., Bourdon B., Turner S., and Allegre C. J. (2001) Erosion timescales derived from U-decay series measurements in rivers. *Earth and Planetary Science Letters* **193**(3–4), 549.

von Blanckenburg F. (2005) The control mechanisms of erosion and weathering at basin scale from cosmogenic nuclides in river sediment. *Earth and Planetary Science Letters* **237**(3–4), 462.

Welch S. A., Beard B. L., Johnson C. M., and Braterman P. S. (2003) Kinetic and equilibrium Fe isotope fractionation between aqueous Fe(II) and Fe(III). *Geochimica et Cosmochimica Acta* **67**(22), 4231.

White A. F., Blum A. E., and Bullen T. D. (1992) A three million year weathering record for a soil chronosequence developed in granitic alluvium, Merced, California, USA. In: Kharaka Y.K. and Maest A. S., Editors, *Proceedings of the 7th International Symposium of Water-Rock Interaction*, Balkema (1992), pp. 607–610.

White A. F., Blum A. E., Schulz M. S., Bullen T. D., Harden J. W., and Peterson M. L. (1996) Chemical weathering rates of a soil chronosequence on granitic alluvium: I. Quantification of mineralogical and surface area changes and calculation of primary silicate reaction rates. *Geochimica et Cosmochimica Acta* **60**(14), 2533.

Zuddas P., Seimbille F., and Michard G. (1995) Granite-fluid interaction at near-equilibrium conditions: Experimental and theoretical constraints from Sr contents and isotopic ratios. *Chemical Geology* **121**(1–4), 145.

Chapter 13
Kinetics of Global Geochemical Cycles

Abraham Lerman and Lingling Wu

13.1 Introduction

Geochemical systems of the Earth's surface and interior are often studied by means of conceptual models that represent them as geochemical or biogeochemical cycles of chemical elements. Such models usually address the various geological, geochemical, geophysical, and biological processes within the cycle or system, and they focus on the model's ability to evaluate the system changes at different time scales, often extending from the remote past into the future. The time dimension of changes taking place in the different parts of the Earth System makes it necessary to understand the mechanisms and rates of the numerous processes that control the element interactions in geochemical systems of different physical structures and degrees of complexity.

In this chapter, we present first a brief overview of the history of development of geochemical cycles and the concept of the rock cycle that encompasses the system of the Earth's surface and upper lithosphere. Further, we discuss the essentials of geochemical cycle models and some simple mathematical relationships that can be used in their analysis, such as the rate parameters of the fluxes, residence time, and the time of approach to steady state. After this theoretical section, we address the global phosphorus cycle as an example of a biogeochemical cycle of an element of indispensable importance to life. We focus on the structure and dynamics of the cycle, as well as the uncertainties inherent in some of the cycle data and parameters that can affect the conclusions of even a simple cycle analysis. Mineral-water reactions in the continental environment are an extensively studied subject that is fundamental to the understanding of the material fluxes between the atmosphere, sedimentary and crystalline lithosphere, and the world ocean, and their effects on global climate. In this field, we estimate global average denudation rates of the land surface by physical and chemical processes. Drawing on the published, very

Northwestern University, Department of Earth and Planetary Sciences, alerman@northwestern.edu

extensive data-base, we discuss both the rates obtainable from field-observational data as well as from experimental studies of mineral dissolution of silicate minerals.

Participation of carbon dioxide in mineral weathering reactions is of major importance in the controls of the global carbon cycle at different geologic time scales and dissolution of rock-forming minerals in the sedimentary and crystalline crust that releases mineral components to ground and river waters. We estimate the proportions of the common rock-forming minerals in the weathering sources that were responsible through dissolution for the composition of average river waters. The results indicate that the mineral abundances in such sources differ significantly from those in an average sediment. These discrepancies can be explained by the differences in the dissolution rates of the minerals occurring in the sedimentary and crystalline crust, such as the carbonates, sulfates, chlorides, sulfide in pyrite, and divalent and monovalent-cation silicates. Different evaluation methods of CO_2 uptake in weathering lead to consistently similar results.

Sulfuric acid, produced by oxidation of pyrite, is a reactive component in the weathering cycle that releases metal and carbonate ions and, possibly, carbon dioxide to natural waters. Because sulfur emissions from fossil fuel burning represent an additional acid forcing on the environment, we evaluate the possible effects of H_2SO_4 addition from human industrial activities to the weathering cycle. We also address the reverse of the pyrite oxidation and acid formation – namely, the reduction of sulfate and formation of pyrite in the marine environment and its possible effects on the calcium carbonate marine cycle.

In the last section of the chapter, we discuss some major imbalances in the global carbon cycle at a time scale from the Last Glacial Maximum, about 18,000 year before present, to the end of pre-industrial time, about 300 years ago. Attributing part of the estimated imbalances to an inadequate data-base for the fluxes between the atmosphere, land organic reservoir, and the ocean that include weathering of the sedimentary and crustal rocks, sediment storage in the ocean, and CO_2 emission from the surface ocean to the atmosphere, we outline a pathway for CO_2 in weathering that reduces the carbon imbalances in the atmosphere and land organic reservoir.

13.2 Historical Development of Geochemical Cycles

The material in this section is based in part on its presentation in Mackenzie et al. (2004).

Perceptions of many natural processes as cycles are undoubtedly rooted in the changes of day and night, seasons of the year, and astronomical observations in the times of antiquity, from which the concept of cycles and epicycles of planetary motions emerged. Another cyclical phenomenon of great importance is the cycle of water on Earth that is also responsible for the circulation and transport of many materials near and at the Earth surface. An early description of the water cycle is sometimes attributed to a verse in the book of *Ecclesiastes* (i, 7), believed to have been written in the third century BC, that speaks of the rivers running into the sea

and returning from there to their place of origin (but there is no mention of the salt nor of water evaporation and precipitation). The modern concept of the global water cycle is the result of observations of atmospheric precipitation, its infiltration into the ground, river runoff, and experiments on water evaporation conducted in the 1600s in France and England (Linsey, 1964). These concepts were well accepted by the time of the first edition of Charles Lyell's *Principles of Geology* (Lyell, 1830, p. 168). By 1872, Lyell referred to a cycle – "the whole cycle of changes returns into itself" – in his description of alternating generations of asexual and sexual reproduction among certain classes of marine invertebrates, which he likened to insect metamorphosis (Lyell, 1872, p. 329; 1875, p. 329).

The earlier discoveries that plants use carbon dioxide for growth in sunlight and return it to the atmosphere in darkness must have been the first scientific observation of the carbon cycle. Living plants use carbon dioxide to make their tissues, and when they die they become organic matter in soil and water that later decomposes to carbon dioxide. The discovery of carbon dioxide as a gas that forms by fermentation and burning of charcoal, under the name of *spiritus silvestris*, is attributed to Jan Baptista (or Baptist) van Helmont, a man of medicine, alchemy, and early chemistry in the then Spanish Netherlands, in the first half of the 1600s (e.g., Graham, 1974). The formation of organic matter from carbon dioxide and water under the action of light, the process known as photosynthesis, has been studied since the later part of the 1700s, when molecular oxygen was discovered in the process and carbon dioxide identified as a component of air. Short histories of successive discoveries in photosynthesis, since the late 1700s to the twentieth century, have been given by several authors (Gaffron, 1964; Meyer, 1964, p. 21; Bassham, 1974; Whitmarsh and Govindjee, 1995). Presentation of the first general scheme of the carbon and nitrogen cycles was attributed to the French chemist, Jean Baptiste André Dumas, in 1841 (Rankama and Sahama, 1950, p. 535). Dumas (1842) described the cycle of CO_2 consumption and production by respiration, pointing to the sources of "carbonic acid" in the air and soil where it forms from decomposition of manure or organic fertilizers. He made estimates of the residence time of atmospheric oxygen with respect to animal respiration and pointed out that animal respiration consuming oxygen and producing carbon dioxide would cause very small changes in the oxygen content of the atmosphere at a centurial time scale. Significantly, he also pointed out (p. 5) that the Earth's primordial atmosphere must have contained all the carbon dioxide and nitrogen that have been taken up by living organisms.

As to geochemical cycles, an early treatment of the subject appeared in 1875, where several chapters on the cycles of chemical elements were included in a book on Earth's history by Friedrich Mohr, a professor at the University of Bonn, with short chapters on the silicon and carbon cycles among them (Mohr, 1875, pp. 397–398). Since then and to the early part of the twentieth century, the cyclical nature of the major geological processes, that involve shaping of the Earth surface by tectonic forces and running water, and transfer of molten rock material from depth to the surface, must have developed to a well accepted concept.

In the later part of the 19th and early twentieth centuries, the concept of cycles of the biologically important elements expanded to include the various physical,

chemical, geological, and biological processes on Earth, and the material flows between the living organisms and their surroundings, as well as between different environmental reservoirs. By the 1920s, the cycles of the chemical elements that are involved in biological processes – carbon, nitrogen, and phosphorus – and are also transported between soil, crustal rocks, atmosphere, land and ocean waters, and the Earth's interior were well recognized by modern standards. Alfred Lotka's book, *Elements of Physical Biology*, published in 1925, has chapters on the cycles of carbon dioxide, nitrogen, and phosphorus that present a modern treatment of what we call today the biogeochemical cycles (Lotka, 1925). Furthermore, he wrote that his ideas of the nutrient element cycles and mathematical treatment of biogeochemical problems were developed as far back as 1902 and in his publications starting in 1907. The term biogeochemical reflects the fact that biological, physical, and chemical processes play important roles and interact with each other in the element cycles that are mediated by photosynthetic primary production and respiration or mineralization of organic matter.

By 1950, the geochemical cycles of elements in the Earth interior and on its surface became textbook material (Rankama and Sahama, 1950), with the variable degree of detail in each cycle that reflected knowledge of the igneous and sedimentary reservoir contents and some of the inter-reservoir fluxes at the time. This early, if not first, systematic textbook treatment of the geochemical cycles presented diagrams of the geochemical reservoirs as boxes and fluxes between them, and tabulations of the elemental concentrations or masses in some of the individual reservoirs. Subsequent decades produced the knowledge we have today of the chemical speciation of the elements in the different compartments of the Earth, their abundances, and mechanisms responsible for their flows. While the earlier models of the global biogeochemical cycles of individual elements were static, describing the cycles without their evolution in time, developments in the mathematical treatment of time-dependent multireservoir systems (e.g., Meadows et al., 1972) found their application in the analysis of geochemical cycles (e.g., Lerman et al., 1975). Since then, there has been a great proliferation of cycle models, and in particular of carbon cycle models, at very different physical and time scales, aimed at interpretation of cycle evolution in the past and its projection into the future for the world as a whole, as well as for such global reservoirs as the atmosphere, land, coastal oceanic zone, and the open ocean.

Considerable attention became focused on the global sedimentary cycle and the cycling of salts in the ocean as a result of Kelvin's (William Thomson, later Lord Kelvin) estimates of the age of the Earth between 24 and 94 Ma, made between 1864 and 1899 (Carslaw and Jaeger, 1959, pp. 85–87), and the estimates of the age of the ocean from the rate of accumulation of sodium brought in by rivers, as was done, for example, by Joly (1899) whose age of the ocean was about 90 Ma. Gregor (1988, 1992) summarized and discussed in detail the geological arguments in the second half of the 1800s and the early 1900s for the recycling of oceanic sediments after their deposition (Croll, 1871) and for the existing sinks of dissolved salts in ocean water, such as their removal by adsorption on clays, entrapment in sediment pore water, and formation of evaporites that were contrary to the earlier

idea of the ocean continuously filling up with dissolved salts (Fisher, 1900; Becker, 1910). The chemical composition of the ocean was analyzed as a balance between inputs of dissolved materials from land and mineral formation in oceanic sediments by Mackenzie and Garrels (1966). Garrels and Mackenzie (1971) presented the concepts of the sedimentary cycling of materials, that had laid dormant for some years, in book form, and in 1972 these authors developed a quantitative model of the complete sedimentary rock cycle. Quantitative estimates of sediment recycling rates, based on mass-age sediment distributions, were made by Gregor (1970, 1980) and Garrels and Mackenzie (1971, 1972): the total sedimentary mass has a mass half-age of 600 Ma. The differential weathering rates of different rock types gave the half-age of shales and sandstones of about 600 Ma, longer than the ages of more easily weathered rocks, such as carbonates of half-age 300 Ma and evaporites of about 200 Ma. Later work (Veizer, 1988) showed that the recycling rates of the sedimentary lithosphere and the various rock types within it are mainly a function of the recycling rates of the tectonic realms, such as active margin basins, oceanic crust, and continental basement, in which the sediments were accumulated.

13.3 The Rock Cycle

The rock cycle is a conceptual model of material transfers between the Earth interior and its surface or, more specifically, between the mantle, crystalline crust, sedimentary rocks, and younger unconsolidated sediments. A model of the rock cycle that shows the essentials of sediment formation and recycling is given in Fig. 13.1.

Sediments are formed mainly by erosion of crustal rocks (flux S_c) and they are recycled by erosion, redeposition and continental accretion (flux S_s). Unconsolidated sediments and sedimentary rocks are returned to the crystalline crust by metamorphism (flux C_s) and to the upper mantle by subduction of the ocean floor. The more recent estimates of the masses of sediments, continental and oceanic crust, and upper mantle differ somewhat from those used by Gregor (1988), as shown in italics for the reservoirs in Fig. 13.1, but they do not affect the conceptual nature of the rock cycle and its fluxes. Although neither the water reservoirs nor water flows are shown in the rock cycle of Fig. 13.1, they are implicit in the diagram as the main chemical reactive and physical pathways that are responsible for the material flows between the deep and surface reservoirs.

The sediment recycling rate $S_s = 7 \times 10^9$ ton/year and the sediment mass of 3×10^{18} ton give the sediment mean age of $3 \times 10^{18}/7 \times 10^9 \approx 430 \times 10^6$ year. Because old recycled sediments are redeposited as new sediments, a total global sedimentation rate is $S_s + S_c = 9 \times 10^9$ ton/year from the data in Fig. 13.1 (other estimates are given in Sect. 13.6.1). As far as the recycling of the ocean floor is concerned, the rate of new ocean floor formation at the spreading zones is $6.0 \pm 0.8 \times 10^{16}$ g/year or an area of $3.3 \pm 0.2\,\mathrm{km}^2$/year (Mottl, 2003). The mass of the upper mantle down to the depth 700 km, representing 18.5% of the Earth's mass, is $1,110 \times 10^{24}$ g (Li, 2000). In a balanced system, the mass of oceanic crust

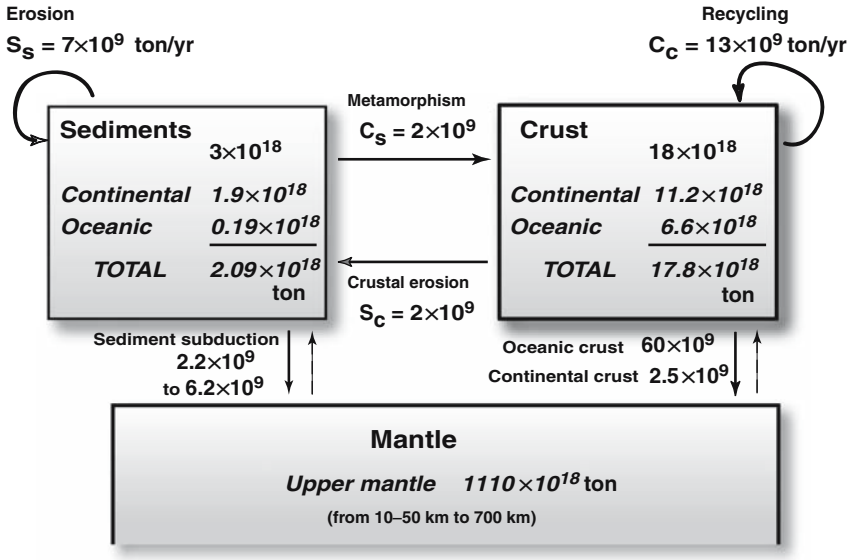

Fig. 13.1 The rock cycle (Gregor, 1988). Reservoir masses shown in italics from Li (2000); continental crust is upper part of 22 km thickness. Oceanic crust subduction rate from Mottl (2003), and continental crust subduction from Scholl and von Huene (2004), further details in the text. Reservoir masses are in units of ton and fluxes in units of ton/year, 1 ton $= 10^3$ kg $= 10^6$ g

subducted is the same as the newly formed crust, 6.0×10^{16} g/year. The rate of recycling of the ocean floor, 60×10^9 ton/year as shown in Fig. 13.1, is the rate of oceanic crust subduction only.

Total mass of oceanic sediments, 1.9×10^{23} g (Li, 2000), is about 50 times greater than the sediment mass in oceanic trenches that are the active subduction zones containing $4 \pm 2 \times 10^{21}$ g solid material, as estimated from the data of von Huene and Scholl (1991). Sediment subducted at the active tectonic plate margins that consists of ocean floor sediment, primarily of continental origin, amounts to 1 km^3/year or about 2.5×10^9 ton/year. Additional material eroded from the lower part of the continental crust is subducted at the rate of about 1.5 km^3/year (Scholl and von Huene, 2004), making the total subduction of 2.5 km^3/year, equivalent to about 6.2×10^9 ton/year:

$$\begin{aligned}\text{Sediment subduction rate} &\approx (1+1.5)\,\text{km}^3/\text{year} \times 2.5 \times 10^9\,\text{ton/km}^3 \\ &\approx 6.2 \times 10^9\,\text{ton/year}\end{aligned}$$

The deep ocean is characterized by slower sedimentation rates of biogenic materials produced in ocean water and the finer particle-size detrital components from land, of an order of magnitude of millimeters per 1,000 years. One estimate of an upper

bound of the deep-ocean sediment mass that may be subducted with the ocean floor can be based on a mean unweighted sedimentation rate for different sections of the deep ocean in the range $3 \pm 1.5 \times 10^{-4}$ cm/year (Chester, 2000, p. 346). For the deep-ocean sediment, of bulk density $2\,\mathrm{g/cm^3}$ and mean age of $110 \pm 5 \times 10^6$ year (Veizer, 1988) that enters the subduction zone with the underlying oceanic crustal plate, where $3.3\,\mathrm{km^2/year}$ of oceanic crust is subducted, the sediment subduction rate is:

$$\begin{aligned}\text{Sediment subduction rate} \approx\ & (3 \times 10^{-4}\,\mathrm{cm/year}) \times 2\,\mathrm{g/cm^3} \times 110 \times 10^6 \text{ year} \\ & \times 3.3 \times 10^{10}\mathrm{cm^2/year} \approx 2.2 \times 10^9\,\mathrm{ton/year}\end{aligned}$$

Both the higher and lower estimates of sediment subduction are shown in Fig. 13.1. For the sediment cycle to be balanced, the other fluxes, as shown in Fig. 13.1, should have values assigned to them, but these are not well known at present.

13.4 Essentials of Cycle Modeling

13.4.1 Calcium Carbonate and Silicate Cycle

An example of the global cycle of calcium carbonate and silicate involves the Earth surface and upper mantle. The chemical reaction between calcium silicate and CO_2 is a shorthand notation for the weathering of calcium in silicate rocks:

$$CaSiO_3 + CO_2 \rightarrow CaCO_3 + SiO_2 \tag{13.1a}$$

The reaction is generally known as the Urey reaction, following Urey (1952, pp. 148 and ff.). According to Berner and Maasch (1996), the reaction and interpretation of its role in the global carbon cycle were introduced by J. J. Ebelmen much earlier, in 1845. In Eq. (13.1a), $CaSiO_3$ stands for calcium silicate minerals of different stoichiometric proportions of CaO and SiO_2 that occur in igneous and metamorphic crustal rocks reacting with CO_2 and ultimately producing $CaCO_3$ by such a reaction as

$$Ca^{2+} + 2HCO_3{}^- \rightarrow CaCO_3 + CO_2 + H_2O \tag{13.1b}$$

Subduction of $CaCO_3$ accumulating on the ocean floor into the upper mantle can break down $CaCO_3$ and release CO_2 and/or allow $CaCO_3$ to react with SiO_2 that represents silica in the melt or igneous rock:

$$CaCO_3 \rightarrow CaO + CO_2 \tag{13.1c}$$

$$CaCO_3 + SiO_2 \rightarrow CaSiO_3 + CO_2 \tag{13.1d}$$

Equation (13.1d) is the Urey–Ebelmen Equation (13.1a) going from the right to the left that closes the mantle–Earth-surface cycle of carbonate and silicate. Geochemical cycles involving the interior of the Earth are known as the *endogenic* cycles and

they are generally characterized by long time scales of the order of 10^8–10^9 years. The sediments, hydrosphere, biosphere, and atmosphere are grouped in the *exogenic* cycle, although some authors relegate the sediments to the endogenic cycle.

13.4.2 A Simple Cycle Model

A conceptual model of a geochemical cycle is a system of reservoirs, represented by boxes, and flows or fluxes between them, represented by arrows, as in schematic two-reservoir models with first-order kinetics of the fluxes shown in Fig. 13.2.

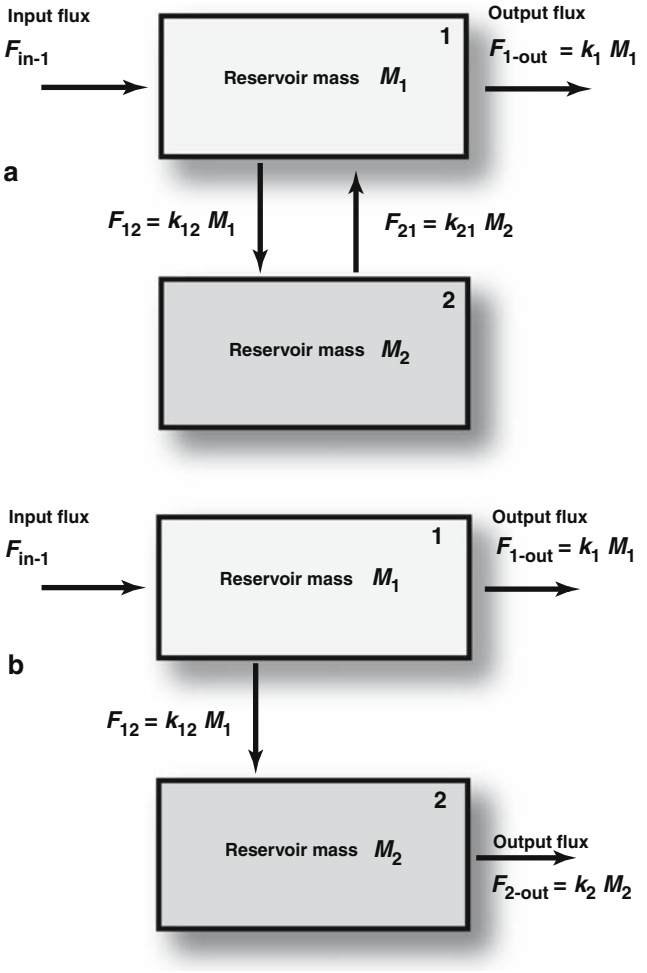

Fig. 13.2 Models of two-reservoir systems with inputs and outputs

A cycle with external inputs and/or outputs is an *open* cycle. In a *closed* cycle material may be produced and consumed within the reservoirs or redistributed between them. The latter case of redistribution of a chemically conservative substance in a two-reservoir system is frequently discussed in the geochemical literature (e.g., Albarède, 2003, p. 88). The various natural analogues of such open two-reservoir systems include, for example, a reservoir of ground water interacting with host rocks, a column of water interacting with sediment, the ocean and sediments or oceanic crust, or land phytomass and soil or soil water. There are significant differences between the two cycle models. In Fig. 13.2a, external input flux, $F_{\text{in}-1}$, enters reservoir 1 where it is redistributed between the two reservoirs by fluxes F_{12} and F_{21}, and the material leaves the system from reservoir 1 by means of flux $F_{1-\text{out}}$. When the system is at a steady state, the input flux is equal to the output flux from reservoir 1 and the fluxes between reservoirs 1 and 2 are also equal.

In such a system, the residence time in reservoir 1, $\tau_1 = 1/k_1$, where parameter k is a first-order rate constant, is not affected by other reservoirs exchanging material with it. In Fig. 13.1b, input to reservoir 1 is removed by external output and by the flux to reservoir 2. Thus at a steady state, input flux to the system, $F_{\text{in}-1}$, is equal to the sum of the two outgoing fluxes, $F_{1-\text{out}} + F_{2-\text{out}}$. A cycle must be defined in terms of the reservoir masses or volumes and the flows in units of mass/time or volume/time. The nature and sizes of the reservoirs correspond to the cycle being studied, as mentioned above. Mass balance of each reservoir in a geochemical cycle is the algebraic sum of all the inputs and outputs from that reservoir:

$$\frac{dM_i}{dt} = \sum_j F_{ji} - \sum_i F_{ij} \pm \sum_n R_{i,n} \text{ (mass/time)} \tag{13.2}$$

The preceding equation defines the rate of change in the mass of the i reservoir, M_i, as the difference between the sum of all the input fluxes from other reservoirs j to $i (j \neq i)$, F_{ji}, and the sum of all the outgoing fluxes from i to other reservoirs j, F_{ij}, and addition or subtraction of biogeochemically produced or consumed material within reservoir i by reactions R_n. Depending on the magnitudes of the input and output fluxes, the reservoir may either increase in size, be at a steady state $(dM_i/dt = 0)$ or decrease in size:

$$\frac{dM_i}{dt} \begin{matrix} \geq \\ = \\ < \end{matrix} 0 \tag{13.3}$$

With reference to the simple cycle model shown in Fig. 13.2a, a steady state is maintained when the fluxes into reservoir 1 are balanced by the fluxes out of it:

$$F_{\text{in}-1} + F_{21} = F_{12} + F_{1-\text{out}} \text{ (mass/time)} \tag{13.4}$$

Fluxes may be either constant quantities (such fluxes are called zero order fluxes) or they may depend on a variety of environmental conditions and the reservoir mass. In the latter case, the flux is a function of the reservoir mass (M) and a rate parameter (k) that may be either a constant or a variable dependent on environmental

conditions. Such a first order flux is:

$$F_{ij} = k_{ij} M_i \ (\text{mass/time}) \tag{13.5}$$

where the rate parameter k_{ij} has the units of time^{-1}. Higher order fluxes may be represented by terms that depend on more than the mass of one chemical species or on some power of the mass that is either smaller or greater than 1. The appeal of using first order fluxes in geochemical cycle models is that equations of the type of Eq. (13.2) are easier to solve numerically than more complex equations with nonlinear terms. Substitution from Eq. (13.5) in Eq. (13.4) gives:

$$F_{\text{in}-1} + k_{21} M_{2,\text{ss}} = (k_{12} + k_1) M_{1,\text{ss}} \tag{13.6a}$$

$$k_{12} M_{1,\text{ss}} = k_{21} M_{2,\text{ss}} \tag{13.6b}$$

from which the steady state reservoir masses, $M_{1,\text{ss}}$ and $M_{2,\text{ss}}$, can be obtained if the input flux and rate parameters are known:

$$M_{1,\text{ss}} = \frac{F_{\text{in}-1}}{k_1} \tag{13.7a}$$

$$M_{2,\text{ss}} = \frac{F_{\text{in}-1} k_{12}}{k_1 k_{21}} \tag{13.7b}$$

The steady state mass in reservoir 2, $M_{2,\text{ss}}$, is either greater or smaller than $M_{1,\text{ss}}$ depending on whether rate parameter k_{12} is greater or smaller than k_{21}, respectively.

In the cycle model shown in Fig. 13.2b, material balance at a steady state is analogous to that shown in Fig. 13.2a and the preceding discussion:

$$F_{\text{in}-1} = (k_1 + k_{12}) M_{1,\text{ss}} \tag{13.8a}$$

$$k_{12} M_{1,\text{ss}} = k_2 M_{2,\text{ss}} \tag{13.8b}$$

from which the steady state masses are:

$$M_{1,\text{ss}} = \frac{F_{\text{in}-1}}{k_1 + k_{12}} \tag{13.9a}$$

$$M_{2,\text{ss}} = \frac{F_{\text{in}-1} k_{12}}{(k_1 + k_{12}) k_2} \tag{13.9b}$$

In the latter case, the steady state mass in reservoir 1, Eq. (13.9a), is smaller than in the preceding model, Eq. (13.7a), if k_1 is the same in both.

For a two-reservoir system, simultaneous algebraic linear equations, such as Eqs. (13.6a, b), can be easily solved by hand, by such methods as substitution or determinants. For multireservoir systems, the unknown steady-state masses, M_i, can be computed if all the rate and other parameters are known, using computer programs for solution of systems of simultaneous algebraic linear equations.

In a transient state, mass changes in the two reservoirs shown in Fig. 13.2a are defined by two ordinary differential equations:

$$\frac{dM_1}{dt} = F_{\text{in}-1} + k_{21}M_2 - (k_1 + k_{12})M_1 \tag{13.10a}$$

$$\frac{dM_2}{dt} = k_{12}M_1 - k_{21}M_2 \tag{13.10b}$$

If the input term $(F_{\text{in}-1})$ and all the rate parameters k_{ij} are known, systems of simultaneous differential equations, such as Eqs. (13.10a,b), for a multi-reservoir cycle model can be solved by a variety of numerical techniques, suitable for a small or large number of equations, that are available either commercially or in the public domain (e.g., Lerman et al., 1975; Walker, 1991; Albarède, 1995; Chameides and Perdue, 1997; Lasaga, 1998).

13.4.3 Residence and Mixing Times

The residence time of a substance (τ) in a reservoir at a steady state is defined as the ratio of the reservoir mass to the sum of either all input or all output fluxes:

$$\tau_i = \frac{M_i}{\sum\limits_j F_{ij}} = \frac{1}{\sum\limits_j k_{ij}}(\text{time}) \tag{13.11}$$

For experimental and natural systems with flow, residence time is also defined in Chaps. 1 and 10. An alternative definition of residence time, τ_i, in terms of the residence times with respect to the individual removal processes is from Eq. (13.11):

$$\frac{1}{\tau_i} = \sum_j \frac{1}{\tau_{ij}} = \frac{1}{\tau_{i1}} + \frac{1}{\tau_{i2}} + \frac{1}{\tau_{i3}} + \cdots \tag{13.12}$$

Residence time in a reservoir with respect to one of the outgoing fluxes (for example, residence time with respect to outflow in Fig. 13.2a, $\tau_1 = 1/k_1$) usually differs from the residence time with respect to another flux $(\tau_{12} = 1/k_{12})$. Total residence time with respect to all the fluxes, as shown in Eq. (13.11), is the reciprocal of the sum of the rate parameters.

The reservoirs of a geochemical cycle, such as those shown in Fig. 13.2 and treated by means of Eqs. (13.2) or (13.10), are assumed to be well mixed, if they are fluid, or have outputs averaged over their contents. As mixing of a reservoir takes some length of time, computation of a changing reservoir mass for time periods much shorter than the mixing time gives only approximate results. The mixing time of the global ocean is usually taken as of an order of magnitude 10^3 years, and 1,600 year is an often cited value derived from oceanographic models and, later, the measurements of ^{14}C activity (half-life 5,715 year) in the surface and deep ocean water layers (Munk, 1966; Broecker, 1974; Stumm and Morgan, 1981; Albarède, 1995);

typical residence or renewal times of water in freshwater lakes are $10^0 - 10^2$ year, with the modal value of 5.5 year (Lerman, 1994); for groundwater, estimated runoff to the ocean at 6% per year (Berner and Berner, 1996) translates into residence or renewal time of about 17 year; soil water reservoir, representing soil moisture and upper 10 m of shallow ground waters, was estimated to have water residence time with respect to outflow of 5 year (Ver, 1998); and residence times of water in the major rivers are probably measurable in months.

In cycle models with first order fluxes, the time needed to attain a steady state is mathematically infinitely long. A practical measure of attainment of a steady state may be taken as 95% of the steady state value, considered to be sufficiently close to the steady state. Perhaps one of the simplest demonstrations of this relationship is Fig. 13.2a, reservoir 1 alone with its constant input flux and output, not interacting with reservoir 2. Then mass balance in the reservoir 1, omitting subscript 1, is:

$$\frac{dM}{dt} = F_{\text{in}} - kM \tag{13.13}$$

where constant input flux F_{in} is in units of mass/time and rate parameter k is 1/time. At a steady state $(dM/dt = 0)$, the reservoir mass is

$$M_{\text{ss}} = \frac{F_{\text{in}}}{k} \tag{13.14}$$

and the solution of Eq. (13.13) with the initial condition $M = M_0$ at $t = 0$ and $M = M_{ss}$ at $t \to \infty$ is:

$$M = M_{\text{ss}}\,(1 - e^{-kt}) + M_0 e^{-kt} \tag{13.15}$$

In (13.15), kt is a dimensionless product of a constant rate parameter k and time t. As kt increases with time, reservoir mass M changes from an initial value M_0 ($\geq$0) to the steady-state value M_{ss}. Subtracting M_0 from both sides of (13.15) and rearranging the terms, we have:

$$\frac{M - M_0}{M_{ss} - M_0} = 1 - e^{-kt} \tag{13.16}$$

Time to steady state corresponds in (13.16) to the quotient of masses equal to 0.95 and it is determined by the dimensionless parameter kt (e.g., Lerman, 1979):

$$\frac{M - M_0}{M_{ss} - M_0} = 1 - e^{-kt} = 0.95 \text{ to } 0.98 \tag{13.17}$$

In Fig. 13.3 is shown the change in the mass ratio as a function of kt, where the 95% level of the steady state value is attained at $kt \approx 3$. This corresponds to the time to steady state equal to approximately 3 residence times of the reservoir: $t_{\text{ss}} \approx 3\tau$. After 4 residence times $(kt = 4)$, the reservoir mass attains 98% of the steady state value. The above relationship for the time to steady state also holds, in principle, for multi-reservoir systems, where the computation of M as a function of time is done numerically.

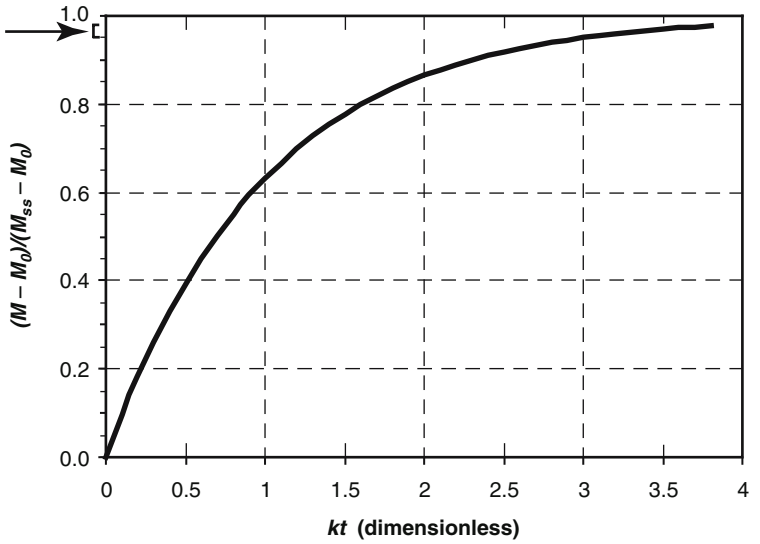

Fig. 13.3 Approach to steady state of reservoir mass M, Eq. (13.17). Arrow points to the values close to a steady state, 0.95 at $kt = 3$ and 0.98 and $kt = 4$

13.4.4 Connections to Geochemical Cycles

The discussion in the preceding sections of simple one- and two-reservoir systems is only an introduction to the much more detailed, multi-reservoir models of biogeochemical cycles at different space and time scales, ranging from local to global and from short-term to geologically long-term. The main kinetic characteristics of a biogeochemical cycle are represented by the rate parameters k that define the fluxes within and between the reservoirs. Although the simplest flux relationships are those of a zero-order or constant flux and a first-order flux that depends on the reservoir mass, as was shown in the preceding sections, some chemical reactions and biologically mediated processes may be of a different order, such as the rates of calcite and aragonite dissolution and precipitation that can be of order > 1 (e.g., Morse and Arvidson, 2002) or bacterial decomposition of organic matter that follows the Michaelis-Menten or Monod kinetics (e.g., Van Cappellen et al., 1993). Geochemical cycles can be in a non-steady state over variable periods of time, such as the increase in the atmospheric CO_2 concentration during the Industrial Age or longer-term changes in the chemical composition of ocean water during Phanerozoic time. A residence time in a reservoir at a steady state is given by such relationships as (13.5) and (13.11), but in a non-steady state the picture is different. The difference between the input and output fluxes of a reservoir is its mass imbalance, $F_{\text{in}} - F_{\text{out}}$, that can be either negative or positive. If an imbalance does not change for some time, the ratio of the reservoir mass to its imbalance, $M/(F_{\text{in}} - F_{\text{out}})$, is an "instantaneous residence time". For a negative imbalance, the preceding ratio gives a

measure of time to complete depletion, irrespective of whether such a situation is or is not geologically possible. For a positive imbalance, an instantaneous residence time gives a length of time to some specified increase in the reservoir mass, such as its doubling.

A number of estimates of the reservoir masses and fluxes, from which the first-order flux rate parameters k and residence times can be computed using Eq. (13.11), are given for the global phosphorus cycle in Sect. 13.5 and for the carbon cycle in Sect. 13.10.

13.5 Global Phosphorus Cycle

13.5.1 Phosphorus Cycle Structure

The global biogeochemical importance of the element phosphorus lies in its role as one of the most important nutrient elements that support life on Earth. Because of the relatively low abundance of phosphorus in the crystalline crust, sediments, and continental and oceanic waters, it is generally considered as an element limiting biological production in many natural environments and ecosystems. The structure of the global phosphorus cycle is shown in Fig. 13.4 and the data sources for the reservoirs and fluxes are given in Table 13.1.

In natural waters, P occurs mostly as aqueous ions $H_2PO_4^-$ and HPO_4^{2-} and as phosphate attached to organic molecules. In the Earth's crust, phosphorus is the tenth most abundant element occurring in a wide variety of phosphate minerals, mainly apatite, with the total mass in the rock reservoir of 645×10^{12} moles (Richey, 1983). In sediments, the main mineral forms of phosphorus include apatite and phosphate adsorbed on clays and iron oxyhydroxide. In soils, aluminum and ferric phosphates and other calcium phosphate minerals may occur as a result of reactions with soluble inorganic phosphate fertilizers. Among the reservoir masses and fluxes listed in Table 13.1, P in the sedimentary organic matter is based on the range of atomic ratios C_{org}:P_{org} = 250:1–2,500:1 (Ingall and Van Cappellen, 1990; Anderson et al., 2001) and the mass of organic carbon in continental and oceanic sediments (Li, 2000). The weathering flux of organic phosphorus from sediments to soils (F_{12}) by land uplift and erosion corresponds to the ratio C_{org}:P_{org} =250:1 in sediments and organic carbon flux of 5×10^{12} mol/year (Ver et al., 1999).

There are various estimates of the fractions of particulate inorganic phosphorus (PIP) transported by rivers that are reactive and refractory (e.g., Ruttenberg and Canfield, 1994; Berner and Rao, 1994; Colman and Holland, 2000). Here we use 25–45% as the reactive PIP fraction of the total PIP riverine transport of 0.387 to 0.812×10^{12} mol/year (Ver et al., 1999).

In the ocean, the fluxes between the surface and deep ocean are driven by the water upwelling and downwelling at the rate of 20 sverdrups $(6.32\,\mathrm{km^3/year}; 1\,\mathrm{sverdrup} = 1 \times 10^6\,\mathrm{m^3/s})$ or about 2 m/year averaged over 90%

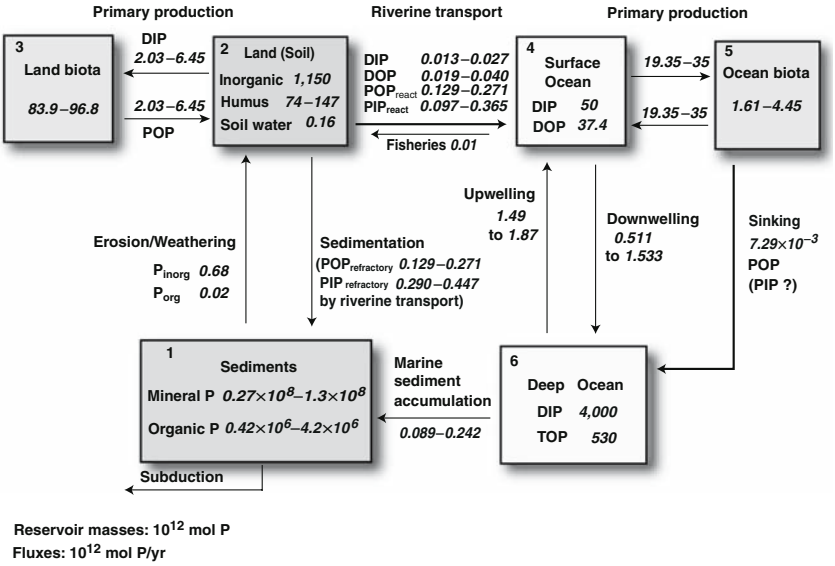

Fig. 13.4 Global phosphorus cycle in the land and ocean domains. Data and reservoir numbers in Table 13.1. DIP: dissolved inorganic phosphorus. DOP: dissolved organic phosphorus. PIP: particulate inorganic phosphorus. POP: particulate organic phosphorus. TOP: total organic phosphorus. Subscripts: inorg is inorganic, org is organic, and react is reactive

of the ocean surface area. The P flux of ocean biota particles settling to the deep ocean was estimated as follows (sedimentation rate from Chester, 2000):

$$\begin{aligned} F_{56} &= (P_{org} \text{ in young ocean sediments}) \times (\text{sedimentation rate}) \\ &\quad \times (\text{deep ocean area}) \times (\text{bulk sediment density}) \\ &= 100 \text{ ppm} \times 3 \times 10^{-4} \,\text{cm/year} \times 90\% \times 3.61 \times 10^{18} \,\text{cm}^2 \times [(1\text{–}50\%) \times 2.6 \\ &\quad + 50\% \times 1.03] \text{g/cm}^3 \\ &= 7.29 \times 10^9 \,\text{mol P/year} \end{aligned}$$

Although the global P cycle in Fig. 13.4 does not include the shallow-water domain of the continental shelf, it should be borne in mind that the phosphorus sediment storage rate in the coastal zone is high because of the high primary production (Ruttenberg, 2004).

13.5.2 Dynamics of Mineral and Organic P Weathering

Soil is a mixture of minerals, partly inherited from the crustal source, partly weathered, and partly formed *in situ*: this is the *inorganic* soil. The other soil component is *organic* matter or humus and, finally, there is *soil water*. (Additional discussion

Table 13.1 Reservoirs and fluxes of the global phosphorus cycle (Fig. 13.4)

Reservoirs (1–6) and Fluxes (F_{ij})		Units: 10^{12} mol P for reservoirs; 10^{12} mol P/year for fluxes	References
1 Sediments	Marine	$0.27 \times 10^8 - 1.3 \times 10^8$	Lerman et al., 1975; Richey, 1983; Jahnke, 1992; Mackenzie et al., 1993; Ruttenberg, 2004
	Organic	$0.42 \times 10^6 - 4.2 \times 10^6$	See text
2 Land (soil)	Inorganic	1,150	
	Humus	74–147	Ver et al., 1999
	Soil water	0.16	
3 Land biota		83.9–96.8	Lerman et al., 1975; Richey, 1983; Jahnke, 1992; Mackenzie et al., 1993; Ruttenberg, 2004
4 Surface ocean	DIP	50	Ver, 1998
	DOP	37.4	Lerman et al., 1975; Jahnke, 1992
5 Ocean biota		1.61–4.45	Lerman et al., 1975; Richey, 1983; Jahnke, 1992; Mackenzie et al., 1993; Ruttenberg, 2004
6 Deep ocean	DIP	4,000	Ver et al., 1999
	TOP	530	
F_{12} (erosion, weathering)	P_{inorg}	0.68	Ver et al., 1999
	P_{org}	0.02	See text
F_{21} (PIP sedimentation and POP refractory by rivers)	$POP_{refractory}$	0.129–0.271	Ver et al., 1999
	$PIP_{refractory}$	0.290–0.447	See text
$F_{23} = F_{32}$ (primary production and return to soil)		2.03–6.45	Lerman et al., 1975; Richey, 1983; Jahnke, 1992; Mackenzie et al., 1993; Ruttenberg, 2004
F_{24} (riverine transport)	DIP	0.013–0.027	Ver et al., 1999
	DOP	0.019–0.040	
	$POP_{reactive}$	0.129–0.271	
	$PIP_{reactive}$	0.097–0.365	See text
F_{42} (fisheries)		0.01	Mackenzie et al., 1993
$F_{45} = F_{54}$ (primary productioand decay)		19.35–35	Lerman et al., 1975; Richey, 1983; Jahnke, 1992; Mackenzie et al., 1993; Ruttenberg, 2004
F_{46} (downwelling)		0.581	Lerman et al., 1975; Jahnke, 1992
F_{64} (upwelling)		1.87	Lerman et al., 1975; Jahnke, 1992
F_{56} (sinking)		7.29×10^{-3}	See text
F_{61} (marine sedimentation)		0.089–0.242	Ver et al., 1999; Ruttenberg, 2004

of the different soils is given in Chap. 10). The inorganic mineral components react with soil water and release P among their chemical constituents; the organic components undergo remineralization or decomposition that also results in release of phosphorus to soil water. In addition, both the inorganic and organic solid fractions are eroded and transported by surface runoff and rivers. Riverine fluxes of the inorganic and organic, dissolved and particulate P species (F_{24} and F_{21}, Table 13.1) are based on estimates of their mean concentrations in river water and global discharge to the oceans (3.74×10^{16} kg/year; Sect. 13.6.1). Thus the riverine fluxes are computed from measured concentrations in river waters rather than from the dissolution rates of individual mineral components of soils and crustal rocks. Some part of the humus P_{org} is converted to phosphate in soil water; plants take up dissolved phosphate (DIP) from the remineralized humus and from the leaching and dissolution of mineral phases; and plants return P_{org} as POP to humus when they die. If the land phytomass maintains a constant size then there is a continuous input of POP to the soil humus that is greater than its remineralized fraction taken up as DIP by plants. However, in a non-steady state of the land biomass and soil organic matter, there could be increases and/or depletion of the reservoir masses.

The rate of phosphorus loss by soil erosion, from the mean values of the flux ranges in Table 13.1 (F_{21} and particulate P fluxes F_{24}), is 1×10^{12} mol P/year. Taking the transport fluxes of P from the soil as first order fluxes, as given in the simple cycle model of Eqs. (13.13–(13.17), then the rate parameter for physical denudation is from Eq. (13.5):

$$k_{\text{erosion}} = (1 \times 10^{12}\,\text{mol P/year})/(1{,}260 \times 10^{12}\,\text{mol P}) = 7.9 \times 10^{-4}\ \text{year}^{-1}$$

and residence time of P in soil with respect to erosion is about 1,300 year.

The dissolved forms of P in riverine flow, DIP and DOP, and DIP taken by land plants from soil water where it forms by dissolution of mineral phases and remineralization of humus, represent chemical weathering of soil. From the mean values of the DIP and DOP outgoing fluxes, the first-order rate parameter of soil chemical denudation is:

$$k_{\text{chem}} = (4.29 \times 10^{12}\,\text{mol P/year})/(1{,}260 \times 10^{12}\,\text{mol P}) = 3.4 \times 10^{-3}\ \text{year}^{-1}$$

that gives a residence time of P in soil with respect to chemical denudation as about 300 year. The short residence time is accounted for by a large DIP uptake by plants from soil, a mean of 4.24×10^{12} mol P/year (Fig. 13.4). Without the vegetation uptake of phosphorus, the dissolved load in rivers is only about 100 times smaller, 0.05×10^{12} mol P/year, and the P residence time with respect to chemical denudation would be 25,000 year, longer than the residence time with respect to physical erosion.

The ranges of the input and output fluxes in soil and other reservoirs show that the global P cycle may be out of balance. A new steady-state P mass in soil would

be somewhat smaller than the present mass of $1,260 \times 10^{12}$ mol P (Fig. 13.4):

$$M_{ss} = \frac{F_{12} + F_{32}}{k_{\text{erosion}} + k_{\text{chem}}} = \frac{4.93 \times 10^{12} \text{ mol P/year}}{(3.4 + 0.79) \times 10^{-3} \text{ year}^{-1}} = 1175 \times 10^{12} \text{ mol P}$$

and a theoretical time to attainment of this new steady state is from Eq. (13.17):

$$t_{ss} = 4/(4.19 \times 10^{-3} \text{ year}^{-1}) \approx 950 \text{ year}$$

The soil reservoir, as given in Fig. 13.4 where the P uptake and return by the land vegetation is in a steady state, has an excess of output over input of $(1.03 - 0.70) \times 10^{12} = 0.33 \times 10^{12}$ mol P/year. If this imbalance remained constant, then the phosphorus soil reservoir would be exhausted in:

$$(1,260 \times 10^{12} \text{ mol P})/[(1.03 - 0.70) \times 10^{12} \text{ mol P/year}] \approx 3,800 \text{ year}$$

Imbalances of such nature are fairly common in geochemical cycles and they reflect, in general, our insufficient knowledge of the fluxes and/or reservoir magnitudes. These results demonstrate the uncertainties that are associated with the analysis of time-dependent changes in geochemical cycles when the cycle structure and dynamics are incompletely known, as is almost always the case in studies of either relatively simple cycle models, such as the P cycle in Fig. 13.4, or much more complex multi-reservoir and multi-component models of interacting cycles.

13.5.3 Experimental and Observational Evidence

The geologically long-term source of phosphorus in the biosphere is the weathering of igneous and sedimentary rocks where different forms of apatite are the main phosphate-bearing minerals (Delaney, 1998; Filippelli and Delaney, 1994; Meybeck, 1993). A number of experimental studies of the dissolution behavior of different types of apatite show dissolution rates varying up to four orders of magnitude in the pH range from 5 to 6.5 (Table 13.2). Synthetic hydroxyapatites are considered as proxies of skeletal and dental material, while fluorapatite and carbonate apatites occur in igneous and sedimentary rocks. Apatite dissolution and the resultant phosphorus flux in the geologic record are functions of the mineral composition, temperature, and mineral surface area (Guidry and Mackenzie, 2003). Soil studies have shown that phosphorus pools in soils may be strongly affected by such climatic factors as the rainfall, and they also vary with the stability of organic matter and secondary iron and aluminum oxyhydroxides and non-crystalline aluminosilicates in soils (Miller et al., 2001). However, a study of riverine transport of dissolved reactive phosphorus in large rivers in Eastern Asia (Russia, China, and Vietnam) suggests that such climate factors as atmospheric precipitation together with human population density primarily control phosphorus flux from continental weathering (Wu and Huh, 2007).

Table 13.2 Experimental dissolution rates of apatites at 25° C

Mineral	Rate R_P (10^{-12} mol P m^{-2} s^{-1})	Method and Experimental Data	Reference
Fluorapatite $(Ca_{10}(PO_4)_6F_2$			
Igneous fluorapatite	1,830	Batch reactor (pH = 5.2)	Valsami-Jones et al. (1998)
Fluorapatite (natural)	380	Fluidized bed reactor (pH = 5.2)	Guidry and Mackenzie (2003)
Hydroxyapatite $(Ca_{10}(PO_4)_6(OH)_2)$			
Sedimentary carbonate fluorapatite	5.01	Fluidized bed reactor (pH = 5.0)	Guidry and Mackenzie (2003)
Pure hydroxyapatite	53.3	Batch reactor (pH = 6.5)	Valsami-Jones et al. (1998)
Carbonated hydroxyapatite	52,000	Constant composition (pH = 5.5, undersaturation = 0.60)	Tang et al. (2003)

It should be reiterated that the DIP transport in rivers (Fig. 13.4) does not represent the weathering rate of phosphorus from phosphate minerals in sediments and the continental crust, because some of the phosphate released in mineral dissolution is taken up by plants and some unknown fraction of DIP in soil water and rivers may be a product of decomposition of organic phosphorus compounds.

13.6 Water Cycle and Physical Denudation

13.6.1 Geographic Variation of Transport from Land to the Oceans

A fraction of 59–67% of the global land surface $(149 \times 10^6$ km$^2)$ is drained to the oceans. The land surface areas that drain to the oceans, also called the external, exorheic or peripheral areas, have been variably estimated at 76.1×10^6 km^2 (Meybeck, 2003), 88.6×10^6 km^2 (Milliman and Meade, 1983, with references to earlier estimates; Berner and Berner, 1996) to 99.9×10^6 km^2 (Meybeck, 1984, p. v–2), excluding Greenland and Antarctica. Annual water flow from the external drainage area is 3.74×10^{16} kg/year; and with the contribution of melting ice from Greenland and Antarctica, it is 3.97×10^{16} kg/year (Baumgartner and Reichel, 1975; Meybeck, 1979, 1984). A considerably higher estimate of the global runoff to the oceans, 4.7×10^{16} kg/year, was given by Shiklomanov (1993). Global sedimentation in the oceans includes contributions from the following sources:

(1) Transport of dissolved materials by rivers and surface runoff to the oceans
(2) Riverine transport of particulate materials from land

Table 13.3 Land drainage areas, river discharge, and particulate (TPS) and dissolved (TDS) solids transport in 30° latitudinal zones

Latitude (degrees) N and S(–)	Drainage Area $10^3\,km^2$	Discharge $km^3/year$	Drainage Area[a] $10^3\,km^2$	Discharge[a] $km^3/year$	Drainage Area $10^3\,km^2$	Discharge $km^3/year$	Particulate load $10^6 ton/year$	Dissolved load (TDS) 10^6 ton/year
Baumgartner and Reichel (1975)			**Meybeck (1984)**		**Meybeck and Ragu (1995)**			
90 – 60	17,152	3,551	15,422	3,238	15,846	3,532	306	381
60 – 30	32,855	8,252	32,855	8,252	20,758	5,173	3,208	841
30 – 0	23,984	12,597	23,984	12,597	23,209	13,461	4,708	1,086
0 to −30	23,359	11,746	23,359	11,746	11,144	3,358	639	159
−30 to −60	4,282	1,567	4,282	1,567	4,765	1,009	152	76
−60 to −90	14,062	1,987						
Total	115,694	39,700	99,902	37,400	75,722	26,533	9,015	2,543

[a] Excluding Greenland and Antarctica.

(3) Sedimentation and burial of biogenic (mostly $CaCO_3$ and SiO_2 and organic carbon taken as CH_2O) and inorganic mineral phases forming in ocean water and in ocean-floor sediments
(4) Eolian (wind-transported) dust
(5) Glacial ice-derived debris

Rivers transport to the oceans between 2.78 and 4.43×10^9 ton/year of dissolved materials derived from the chemical weathering of crystalline and sedimentary rocks (Meybeck, 1979, 1984; also in Drever, 1988; Berner and Berner, 1996). An estimated amount of particulate matter transported from land at present is much larger: 15 to 20×10^9 ton/year (Garrels and Mackenzie, 1971; Holland, 1978; Milliman and Syvitski, 1992; Berner and Berner, 1996). Global wind-blown load has been variably estimated as $1.1 \pm 0.5 \times 10^9$ ton year^{-1} (Goldberg, 1971), 0.06×10^9 ton year^{-1} (Garrels and Mackenzie, 1971, p. 111), and global dust deposition of 0.53 to 0.85×10^9 ton year^{-1} (Prospero, 1981; Rea et al., 1994). Additionally, about 2×10^9 ton year^{-1} enter the ocean as glacial ice debris (Garrels and Mackenzie, 1971). Thus the three input fluxes of dissolved, suspended, and eolian materials to the oceans deliver about 24×10^9 ton/year. The suspended-particle inflow is distributed unevenly over the ocean floor, where a major part of the input settles in the continental margins.

The greater land surface area of the Northern Hemisphere accounts for a greater portion of runoff to the global ocean than the Southern Hemisphere. Distribution of the land drainage areas and runoff in latitudinal belts of 30° (Table 13.3, Fig. 13.5) show that climate and amount of atmospheric precipitation are globally controlling factors of the discharge. The size of the drainage area is also unquestionably an important factor, as can be seen from the smaller areas and runoff volumes in the high latitudes of the North and South. Products of chemical reactions between water and minerals in soils, weathered regolith, and crustal rocks are transported primarily by riverine flow to the oceans. Transport of dissolved material or total dissolved solids

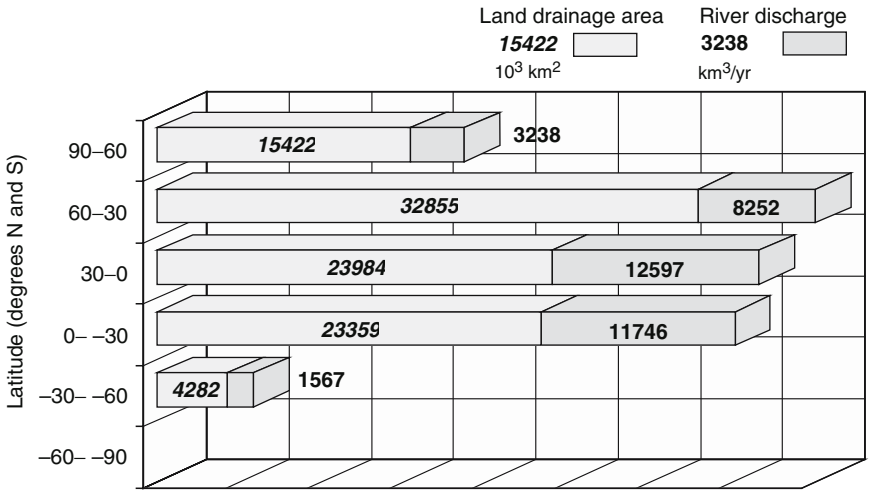

Fig. 13.5 Land drainage areas (e.g., ***4282*** $\times$ ***10³*** km^2) and riverine flow to the oceans (e.g., **1567** km^3/year) by 30° latitudinal belts, excluding Greenland and Antarctica (Table 13.3; Baumgartner and Reichel, 1975; Meybeck, 1984)

(TDS) is a function of climate, topography, and rock lithology of the drainage areas. Studies of transport of erosional products (total particulate solids or TPS), as measured by the TPS loads of rivers, however, have demonstrated that physical denudation of land is also a function of human land-use practices that include deforestation, conversion of vegetated land to cropland, overgrazing, poor soil conservation, and other agricultural and construction activities, in particular the damming of the rivers.

Dissolved or TDS load of rivers is between 2.78 and 4.43×10^9 ton/year from the chemical weathering of crystalline and sedimentary rocks, and particulate or TPS load is at present much larger, about 20×10^9 ton/year. There is a considerable variation of water flow and particulate fluxes with geographic latitude (Fig. 13.6). It should be noted from the data in Table 13.3 that Meybeck and Ragu's (1995) estimated runoff is about 71% of the Baumgartner and Reichel's (1975) value (26,533/37,400) and total drainage area is 76% of the latter's estimate. River discharge data correspond to the geographical coordinates of river mouths.

The particulate and dissolved solids fluxes that are shown in Fig. 13.6 vary from TPS/TDS of about 1:1 in the far northern latitudes to 4:1 in the temperate and tropical zones. At these rates of physical denudation, the continental drainage area of about 800 m mean elevation at present would be reduced to sea level in 10–20 million years. The rise of the continental lithosphere counteracts physical denudation and, as has been stated by a number of investigators, the present-day physical denudation rates may be considerably higher than in the periods of the geologic past due to the mountain-building in Early Cenozoic time.

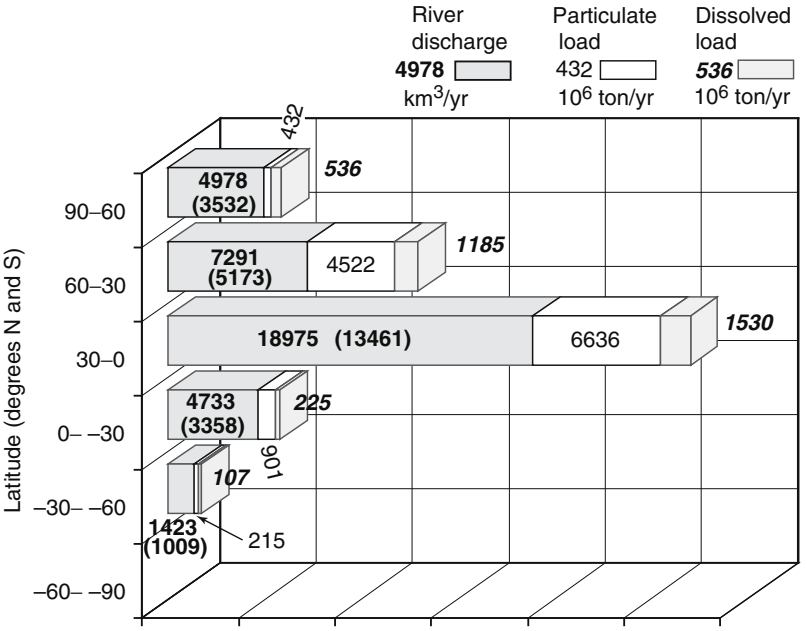

Fig. 13.6 Riverine flow to the oceans (e.g., **4978** km^3/year), particulate or TPS load (e.g., 432×10^6 ton/year), and dissolved or TDS load (e.g., ***536*** $\times$ ***10^6*** ton/year) by 30° latitudinal zones (Table 13.3). Meybeck and Ragu (1995) data for discharge and particulate and dissolved load adjusted by a factor of 3.74/2.65. Discharge values in parentheses are those given in Table 13.3

13.6.2 Land and Soil Erosion Rates

Sediment transport by rivers to the oceans is computed from the measured concentrations of suspended materials or total particulate solids (TPS) and annual river water discharge. Land surface erosion rates computed from the riverine transport of suspended solids to the oceans are usually considerably smaller than the soil erosion rates, estimated by different methods (Table 13.4).

Wind and water are the main agents of soil erosion. Wind erosion is common in arid and semiarid areas with rare precipitation, sparse vegetation, strong, frequent wind and flat terrain (Hagen, 1991), while water erosion is a more common process all over the world, especially in humid regions with a sloping terrain. Wind erosion can remove the nutrient-rich topsoil particles from the soil's entire surface and is the main factor responsible for organic carbon losses in certain areas (Woodruff et al., 1965; de Jong and Kachanoski, 1988). The estimated wind erosion rates in the arid and semiarid parts of China range from 600 to 8,000 ton km^{-2} $year^{-1}$ that is 0.4–5.3 mm/year (Dong et al., 2000).

In the practice of soil science, soil erosion rate caused by water is estimated from the RUSLE model (Revised Universal Soil Loss Equation), originally derived

Table 13.4 Estimates of soil erosion rates and riverine transport of solids

Erosion Rates (W_E ton km^{-2} year^{-1})	GIS-Based RUSLE[a]	Riverine Suspended Load[b,c]
River Basins		
Amazon	400	190
Huanghe	766	1400
Yangtze	2960	250
Mekong	839	200
Ganges	4040	530
Indus	2070	260
Mississippi	451	120
Nile	452	40
Amur	264	28
Continents		
Africa	410	35
Asia	1140	380
Australia	270	28
Europe	1120	50
North America	790	84
South America	710	97
Global average	1020	174–226

[a] The Revised Universal Soil Loss Equation (RUSLE) model estimates soil erosion rate caused by water. Cited are average values for the period of 1900s to 1980s (After Yang et al., 2003).
[b] Data for river basins from Milliman and Syvitski (1992).
[c] Data for the continents from Milliman and Meade (1983).

empirically by Wischmeier and Smith (1978):

$$\mathrm{A} = \mathrm{R} \times \mathrm{K} \times \mathrm{LS} \times \mathrm{C} \times \mathrm{P}\ (\text{ton km}^{-2}\ \text{year}^{-1}) \tag{13.18}$$

where the individual parameters are: R is rain erosivity, K is soil erodibility factor, LS is slope length and steepness topographic factor, C is cropping system properties, and P is erosion protection measures. Some of the individual parameters (R, K) depend on such factors as the energy and quantity of rainfall, whereas others are scaled and topography-dependent quantities (dimensionless parameter LS) that are characteristic of the specific soil and topographic area. Examples of application of these parameters to estimation of soil erosion rates can be found in Nill (1997), Gertner et al. (2002), and Yang et al. (2003).

The cropping system properties, topographic characteristics, and other soil properties affect soil loss rate to a much greater extent than rainfall and erosion conservation techniques, as demonstrated by investigations of soil loss in tropical Africa (Nill, 1997). Other soil properties include parent rock type, soil texture, and organic carbon content, all affecting the soil erodibility (K factor). If soil organic matter declines during cropping, associated soil properties will degrade as well, which will enhance soil erosion rate (Nill, 1997). Estimates of the global soil organic carbon pool, such as those of Post et al. (1982), were used to estimate various soil erodibilities in different ecosystems.

The vegetative cover that protects soil from erosion consists of the living phytomass (shrubs, trees, and grasses) and dead and decaying organic litter. The root systems of plants hold the soil together. Plants slow down water flow over the land, allowing rain water to penetrate into the ground. Plants can also break the impact of raindrops before they hit the soil thereby also reducing erosion to some extent. When the vegetation cover is stripped away through deforestation, over-grazing, ploughing or fire, soil erosion rate is greatly enhanced. Over-cultivation and compaction can also cause the soil to lose its structure and cohesion so that it becomes more easily eroded. Soils with high clay content are more cohesive, although less permeable to water, and in clayey soils particles adhere to each other, making the soil less vulnerable to erosion than soil with high sand or silt content.

13.6.3 Physical Denudation Rate and Residence Time

The relationship between the mass erosion rates, W_E or W_m (ton km^{-2} year^{-1}), and physical denudation rates, W_H or W_h (cm/year), is discussed in Sect. 13.7.1. The denudation rate, measured as a loss of soil thickness, is:

$$W_H = \frac{10^{-4} W_E}{\rho} (\text{cm year}^{-1}) \tag{13.19}$$

where ρ is the bulk density of the eroded material, in g/cm^3. The porosity of up to 50 vol % of soils and partly weathered regolith reduces the mineral density of 2.6–2.7 g cm^{-3} by 1/2, to bulk density of about 1.3 g cm^{-3} for dry material. On a global scale, the bulk densities of several thousand samples of different soils fall mostly in a range from 1.2 to 1.7 g/cm^3 (Batjes, 1996). Thus the physical denudation rates, based on the two estimates of W_E in Table 13.4, from soil erosion rate and riverine particulate load (TPS) are:

From soil erosion:

$$W_H = \frac{10^{-4} \times 1020}{(1.3 \text{ to } 2.6)} = 0.08 \text{ to } 0.04 \,\text{cm year}^{-1} \approx 80 \text{ to } 40 \,\text{cm}/1000 \text{year}$$

From riverine TPS:

$$W_H = \frac{10^{-4} \times (174 \text{ to } 226)}{(1.3 \text{ to } 2.6)} = 0.013 \text{ to } 0.009 \,\text{cm year}^{-1} \approx 13 \text{ to } 9 \,\text{cm}/1000 \,\text{year}$$

Land erosion rate, based on the TPS riverine load of 15 to 20×10^9 ton/year, is lower by a factor of about 5 than the rate based on soil erosion. The much higher global mean soil erosion rate, as given by the values based on the model RUSLE (Table 13.4), suggests that eroded soils are at least temporarily redeposited and stored on land rather than directly transported to the ocean (e.g., Walling, 1983; Smith et al., 2001). Land erosion rates on a regional scale of several square

kilometers in Puerto Rico, estimated from cosmogenic ^{10}Be and mass balance of river-transported solids (Brown et al., 1995), were reported as $4.3 \pm 1.5\,\mathrm{cm}/1{,}000\,\mathrm{year}$ by the ^{10}Be method and $7.5 \pm 3.7\,\mathrm{cm}/1{,}000\,\mathrm{year}$ from the mass balance.

The residence time of solids in a layer that is being eroded depends on its thickness. For a 1 m-thick layer of soil or partly weathered regolith that is being eroded at a rate of about 10 cm/1,000 year, the residence time is about 10^4 year. Ages of many near-surface soils are in the range from 10,000 to 15,000 years, although occurrences of much older Pleistocene and Pliocene soils, $>1 \times 10^6$ year, are well known (White, 1995; Vidic, 1998). In a model analysis of soil erosion under different climatic and rainfall conditions, Amundson (2003) treated soil erosion as a diffusion-like process and arrived at a positive relationship between soil thickness and soil residence time: the residence time increases from about 10^3 year for a 10-cm-thick soil to 10^4 year for a 70-cm-thick layer.

13.7 Chemical Denudation

This section discusses the processes of chemical denudation on a global scale, whereas extensive results from regional case studies of the weathering in lithologically different terrains and under different climatic conditions are given in Chap. 10.

13.7.1 Sedimentary and Crystalline Lithosphere

Chemical weathering of soils, sediments, and continental crustal rocks is effected by mineral reactions with water from atmospheric precipitation that contains, in general, such acidic species as CO_2, sulfate, nitrate, and organic acids from decomposition of organic matter in soils. Chemical weathering reactions between the source minerals and water result in dissolution and formation of new minerals. The sediments occurring on the continents have to a large extent been deposited or formed in the oceans of the geologic past and their composition is usually classified by *lithology* or *sedimentary rock type*, such as carbonates, shales, sandstones, and evaporites. Each of these sedimentary rock types contains varying proportions of *minerals* that in their chemical composition are primarily carbonates, silicates, sulfates, sulfides, chlorides, oxides, and hydroxides. The mineral sources and abundances of the major dissolved constituents of continental waters in different sedimentary rock types and the upper continental crust are given in Table 13.5.

The carbonate mineral components, $CaCO_3$ and $MgCO_3$, metal-cation silicates, pyrite, and calcium sulfate occur in all the sediment types. NaCl occurs in all the sediments as well as in the igneous crust. Relative abundances of the sedimentary rock types and main mineral groups in the continental sediments are shown in Fig. 13.7. The most abundant sedimentary rocks are shales and sandstones, which

Table 13.5 Major cations (Ca^{2+}, Mg^{2+}, Na^{+}, and K^{+}) and pyrite-sulfur (S_{pyr}) in four main sediment classes and upper continental crust. Note that carbonate, silicate (Ca-, Mg-, Na-, and K-silicates), and evaporite minerals ($CaSO_4$ and NaCl) occur in all sediment classes. The weathering potential, ratio ψ, is described in Sect. 13.8.2

	Carbonates	**Shales**	**Sandstones**	**Evaporites[b]**	**Average Sediment**	**Upper Crust[c]**	**Average Sediment 63 wt% and Crust 37 wt%**
Mass (10^{24} g) and	0.48	0.96	0.44	0.02	1.90	1.12	3.02
sediment fraction (%)	25.3%	50.5%	23.2%	1.0%	100%		
Mineral components				10^{-3} mol cation/g rock[a]			
Calcite and component of dolomite	6.510	0.6782	0.6782	0.2215	2.147	—	1.352
Dolomite component	1.102	0.1148	0.1148	0.0375	0.3635	—	0.2290
In albite-anorthite series and other Ca-Mg silicates	0.5091	0.0153	0.1387	—	0.1685	0.7989	0.4017
Chlorite in sediments; other Mg and Ca-Mg silicates	0.1059	0.5178	0.3516	—	0.3698	0.6575	0.4763
Na-feldspar (albite)	0.1272	0.3181	0.4639	0.0445	0.3007	1.099	0.5962
K-feldspar (orthoclase)	0.1274	0.6412	0.4162	0.0004	0.4525	0.6646	0.5310
Sulfur in pyrite (FeS_2)	0.0374	0.0873	0.0624	—	0.06802	—	0.0429
Gypsum or anhydrite	0.1162	0.0412	0.0212	3.140	0.08814	—	0.0555
Halite NaCl	0.0116	0.0240	0.0169	7.116	0.09386	0.0042	0.0607
Sylvite KCl				0.0675	0.0007107	—	0.0004
$MgCl_2$				0.1114	0.001172	—	0.0007
$MgSO_4$				0.0799	0.0008407	—	0.0005
$\psi = (CO_2$ consumable)/(HCO_3^- producible)	**0.53**	**0.75**	**0.74**	**0.54**	**0.61**	**1.00**	**0.73**

[a] Concentrations of cationic components from weight percent of their oxides (except for S_{pyr}) and masses of the sediment classes as given by Li (2000, p. 269).
[b] Mineral composition of evaporites was balanced by addition of 3.0% Cl (2.23×10^{-4} mol/g rock) and 2.6% S (7.99×10^{-5} mol/g) to make KCl, $MgCl_2$, and $CaSO_4$.
[c] Upper crust of composition 2/3 granite and 1/3 basalt (Li, 2000, p. 222). Mass of 1.12×10^{24} g is based on density 2.8 g/cm^3, thickness 2.3 km, occurring over the area of continents and shelves, 177×10^6 km^2. Other compositional variants given by Rudnick and Gao (2003). Upper crust thickness from seismic evidence is 19 km (Wedepohl, 1995).

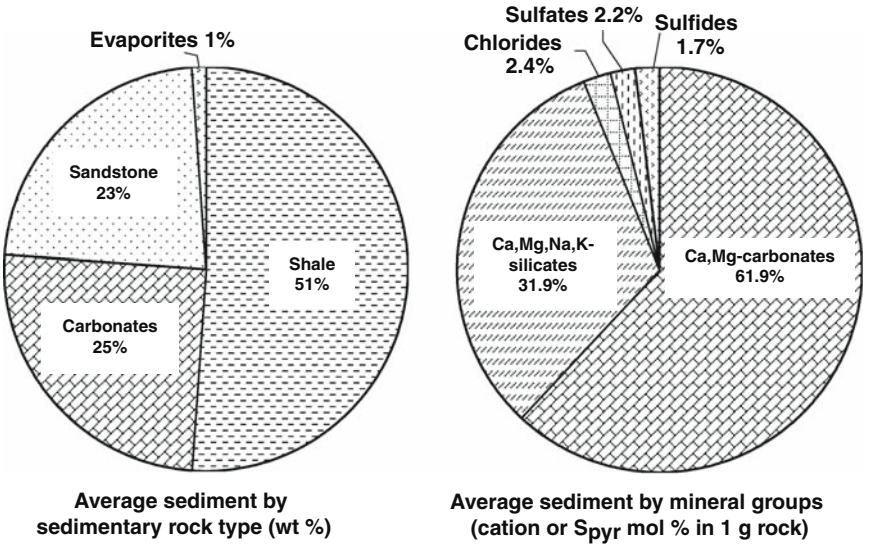

Fig. 13.7 Composition of an average sediment by sedimentary rock types and by mineral groups based on chemical composition: carbonates, $(Ca,Mg)CO_3$; silicates of Ca, Mg, Na, and K; sulfates, mostly $CaSO_4$; chlorides, mainly NaCl with minor additions of $MgCl_2$ and KCl; sulfides taken here as pyrite, FeS_2. (From data in Li (2000))

are mainly silicates in their mineral composition. However, because carbonate rocks (limestones and dolomites) contain silicate minerals in the form of clays and sands, and shales and sandstones contain carbonate minerals calcite and dolomite, the picture of the mineral abundances is different: the most abundant mineral group in sediments is the carbonates, $(Ca,Mg)CO_3$, followed by the silicates containing Ca, Mg, Na, and K. Ca in sulfates, Na in chlorides, and reduced sulfur in pyrite each accounts for about 2 mol % per 1 gram of sediment.

Five sets of data on the global mean composition of rivers, variably corrected for industrial-age pollution and recycling of oceanic salts brought onto the land by seawater spray are given in Table 13.6. The bicarbonate-ion is the most abundant anion in river water that is mostly derived from the reactions of metal-silicates and metal-carbonates with atmospheric and(or) soil CO_2, and additionally from the carbonate minerals reacting with sulfuric acid that forms in the oxidation of mineral pyrite, as discussed in more detail in Sect. 13.8.

Chemical weathering acts on sedimentary rocks (shales, sandstones, limestones, dolomites, evaporites) and igneous and metamorphic minerals (mostly silicates), such that a world average river represents a pooled average of water-mineral reactions within a layer of sediments and crustal rocks of some thickness, extending over a part of the continental surface that drains into the oceans. The chemical denudation rate is a measure of either mass (W_m) or thickness (W_h) loss of the continental surface:

$$W_m = \frac{C_{\text{flow}} V_{\text{flow}}}{S_{\text{land}}} (\text{g m}^{-2}\ \text{year}^{-1}) \tag{13.20}$$

Table 13.6 Dissolved constituents of five world average rivers. Concentrations in mg/kg or mg/L reported by Holland (1978), Meybeck (1979), Drever (1988), and Berner and Berner (1996). Concentrations in mol/kg in *italics* adjusted to reduce the ionic charge imbalance to <0.1%

Chemical Species	Global Mean (Livingstone, 1963; Holland, 1978)	Holland (1978), Corrected for Atmospheric Input	Natural (Unpolluted) (Meybeck, 1979; Drever, 1988)		Natural, Corrected for Pollution and Recycling Salts (Mackenzie, 1992)		Natural, Corrected for Pollution and Recycling Salts (Berner and Berner, 1996; Tables 5.6, 5.10, 5.11)	
	mg/kg	mg/kg	mg/kg	10^{-3} mol/kg	mg/kg	10^{-3} mol/kg	mg/kg	10^{-3} mol/kg
Na^+	6.3	4.8	5.15	0.2240	3.66	0.1590	4.47	0.1944
K^+	2.3	2.4	1.3	0.03325	1.25	0.03200	1.29	0.03299
Ca^{2+}	15	14.8	13.4	0.3343	13.39	0.3340	13.39	0.3341
Mg^{2+}	4.1	4.0	3.35	0.1378	3.22	0.1325	3.33	0.1370
HCO_3^-	58.4	54.3	52	0.8522	52.90	0.8670	52.0	0.8522
		(18.9)[a]	(16.7–18.1)[a]		(18.3)[a]		(16.2–16.7)[a]	
Cl^-	7.8	5.7	5.75	0.1622	3.19	0.09000	4.76	0.1343
SO_4^{2-}	11.2	6.7	8.25	0.08588	8.02	0.08350	5.19	*0.09185*
SiO_2	13.1	12.6	10.4		10.4		10.4	
Total	118.2	105.3	99.6		96.0		94.8	
Total from source rock[b]		69.9	65.0		61.4		59.3	

[a] Lower HCO_3^- concentration in parentheses is the fraction of total HCO_3^- that is derived from dissolution of carbonates, $(Ca, Mg)CO_3$ (see also Table 13.10).
[b] Carbonate-derived HCO_3^-, all other ionic constituents, and SiO_2.

and

$$W_h = \frac{10^{-4} W_m}{\rho} (\text{cm year}^{-1}) \tag{13.21}$$

where C_{flow} is concentration of dissolved solids in riverine flow (g/kg), V_{flow} is the annual runoff to the oceans (kg/year or liter/year), S_{land} is the geographic surface area (m^2) of land that is drained to the oceans, and ρ is the mean bulk density (g/cm^3) of the source rocks undergoing weathering. From the dissolved solid concentrations in average rivers (Table 13.6) and other parameter values (Sect. 13.6.1), the mean chemical denudation rate is:

$$W_m = \frac{(59 \text{ to } 70) \times 10^{-3}\,\text{g/kg} \times 3.74 \times 10^{16}\,\text{kg/year}}{(76 \text{ to } 100) \times 10^{12}\,\text{m}^2} \approx 29 \text{ to } 26\,\text{g m}^{-2}\ \text{year}^{-1}$$

A smaller value of $22\,\text{g m}^{-2}\ \text{year}^{-1}$ was given by Holland (1978). In granitoid watersheds on different continents, chemical weathering rates in the range from 0.35 to $20\,\text{g m}^{-2}\ \text{year}^{-1}$ were reported by Millot et al. (2002). The chemical denudation rate of basaltic rocks in Iceland is higher than the mean, $55\,\text{g m}^{-2}\ \text{year}^{-1}$ (Gíslason et al., 1996). The differences between the denudation rate per unit of geographic land surface area and per unit of mineral reactive surface area are addressed in Sect. 13.7.6. The porosity of up to 50 vol % of soils and partly weathered regolith reduces the mineral density of $2.6–2.7\,\text{g cm}^{-3}$ by 1/2, to bulk density of about $1.3\,\text{g cm}^{-3}$ for dry material. On a global scale, the bulk densities of several thousand samples of different soils fall mostly in a range from $1.2–1.7\,\text{g/cm}^3$ (Batjes, 1996). The rate W_h, using mean bulk density $\rho \approx 1.3–2.5\,\text{g/cm}^3$, is:

$$W_h = \frac{10^{-4} \times 27\,\text{g m}^{-2}\ \text{yr}^{-1}}{(1.3 \text{ to } 2.5)\ \text{g cm}^{-3}} \approx 2.1 \text{ to } 1.1 \times 10^{-3\cdot}\,\text{cm/year}$$

or about 1–2 cm/1,000 year.

Propagation of the weathering front at the boundary between soil (saprolite) and parent rock of granite and schist has been estimated between 0.3 and 3.7 cm/1,000 year (White, 1995, with references), the range of rates bracketing the preceding estimate of chemical denudation rate. Other values of global and regional denudation rates, and relationships between the TPS and TDS concentrations in individual rivers can be found in many publications (e.g., Garrels and Mackenzie, 1971; Lerman, 1988; Drever, 1988; Berner and Berner, 1996; and references cited therein).

13.7.2 Mineral Dissolution Rates

Two main approaches to the study of chemical weathering are through the geochemistry of water catchments based on field studies (Chap. 10) and the determination of individual mineral dissolution rates in the laboratory (Chap. 5). As these two approaches rarely produce the same results, we summarize in this section some of the

experimental and field-based data on the dissolution rates of common rock-forming minerals and their interpretations. For a more detailed discussion of mineral dissolution mechanisms and additional data on mineral dissolution rates the reader is referred to Chaps. 1, 5, 6, and the Appendix.

It has been reported by many workers that the weathering rates of silicate minerals in the field are 1–3 or more orders of magnitude slower than would be predicted from dissolution rates of the same minerals in laboratory experiments (e.g., Schnoor, 1990). Various reasons have been proposed to explain these discrepancies, such as the differences in reactivity between freshly crushed and weathered minerals, errors in estimating the exposed surface areas of minerals in the field, differences in solution composition, and the degree of solution saturation under field and laboratory conditions (Drever et al., 1994). Dissolution rates of the common rock-forming minerals, taken both from primary sources and others' compilations, are summarized in Table 13.7, and additional data are given in Chs. 5 and 6 and the Appendix. Considerable variation within the laboratory rates as well as within the field-determined rates for some of the minerals should be noted.

A similar compilation of laboratory dissolution rates of clays and the three major carbonate minerals, calcite, aragonite, and dolomite, is also given in Table 13.7. The reported experimental dissolution rates of carbonate minerals at Earth's surface temperatures under conditions far from equilibrium (at a pH of $\sim$6) are much higher than those of silicate minerals regardless of the variation in the carbonate dissolution rate data. The variation in measured carbonate dissolution rates may be caused by factors such as back reactions involving dissolution products, grain-size (single crystal or mineral powder) and the distribution of reactive surface sites (Arvidson et al., 2003; Jeschke and Dreybrodt, 2002). It has been established that calcite dissolution is controlled by surface-reaction kinetics with increasing pH under alkaline conditions far from equilibrium (Sjöberg, 1976; Sjöberg and Rickard, 1984). A detailed review of the dissolution kinetics of carbonate minerals has been given by Morse and Arvidson (2002).

13.7.3 Chemical Denudation of Sediments

13.7.3.1 Silicates

Clastic sediments, shales and sandstones, account for 75% of the sedimentary mass, but the fraction of the cation-silicates (i.e., excluding quartz and other forms of pure SiO_2) is 32% of the sediment (Fig. 13.7). In this section we estimate synthetic dissolution rates of silicate minerals in shales and sandstones, without the carbonate minerals, which do not lend themselves to a comparison with the observational data because of their high experimental dissolution rates.

The mineral content of an average shale, computed from its chemical composition, is (Garrels and Mackenzie, 1971): quartz 22 wt % (SiO_2), K-feldspar 29% ($KAlSi_3O_8$), albite 9% ($NaAlSi_3O_8$), Mg-chlorite 5% ($Mg_5Al_2Si_3O_{10}(OH)_8$),

Table 13.7 Comparisons of laboratory (near 25° C) and field weathering rates of silicates and carbonates (see also White and Brantley, 1995 and Chaps. 5 and 6 and the Appendix of this volume). Mineral composition in the table is for pure minerals. Dissolution and weathering rates are in mol of whole mineral (if rate is only for Si, then it is specified as Si release). Mineral densities in g/cm^3 (Deer et al., 1975)

Mineral (Density in g/cm^3)	Laboratory Dissolution Rates (10^{-12} mol m^{-2} s^{-1})	Method or Experimental Data	Field Weathering Rates (10^{-12} mol m^{-2} s^{-1})	Method	Reference
Enstatite (3.21–3.96) $MgSiO_3$	158.5–10.0	pH = 4.8-7.0			Ferruzzi (1993)
Diopside (3.44–3.55) $CaMgSi_2O_6$	125.9–15.8	pH = 4.5-6.0			Schott et al. (1981)
Olivine (forsterite) (3.22–4.39) Mg_2SiO_4	316.2				Blum and Lasaga (1988)
Hornblende (3.02–3.45) $Ca_2(Mg,Fe,Al)_5(Si,Al)_8O_{22}(OH)_2$	1.4	Fluidized bed reactor (pH = 4.5)	0.003	Small-plot (silica flux)	Swoboda-Colberg and Drever (1993)
			3.16×10^{-6}	Soil	White et al. (1996)
K-feldspar (2.55–2.63) $KAlSi_3O_8$			0.0174	Mass balance	Clow and Drever (1996)
	16.7	Fluidized bed reactor (pH = 4.5)	0.052	Small-plot (silica flux)	Swoboda-Colberg and Drever (1993)
			1.58×10^{-5}	Saprolite	White et al. (2001)
			1.58×10^{-6}	Soil	White et al. (1996)
$Ab_{27}Or_{71}$	0.63–2.0	pH = 5.7			Blum and Stillings (1995)
Albite (2.63) $NaAlSi_3O_8$	0.55				Burch et al. (1993); Chou et al (1985)
($Ab_{98}An_{02}$)	5.01	pH = 5.19			Blum and Stillings (1995)
Oligoclase ($Ab_{73}An_{22}$–$Ab_{87}An_{12}$)	0.22	Column	0.167	Mass balance	Clow and Drever (1996)
	1.84	Fluidized bed reactor			Clow and Drever (1996)
			2.00×10^{-4}	Bedrock	White et al. (2001)
			3.98×10^{-6}	Soil	White et al. (1996)
	1.3×10^{-3}	Column			White et al. (2003)
	0.79–2.3	pH = 5.0–7.0			Blum and Stillings (1995)
Plagioclase ($Ab_{70}An_{30}$)	13.6	Fluidized bed reactor (pH = 4.5)	0.052	Small-plot (silica flux)	Swoboda-Colberg and Drever (1993)
Andesine ($Ab_{60}An_{40}$)	6.3	pH = 5			Oxburgh et al. (1994)

(*cont.*)

Table 13.7 (*Continued*)

$Ab_{47}An_{48}Or_5$	17–20	pH = 5.75–7.7			Blum and Stillings (1995)
Labradorite (2.705) $(Ab_{40}An_{60})$	5.01	Batch reactor			Siegal and Pfannkuch (1984)
Bytownite $(Ab_{20}An_{80})$	12.6	pH = 5			Oxburgh et al. (1994)
$Ab_{23}An_{76}Or_1$–$Ab_{25}An_{75}$	14–63	pH = 4.9–7.25			Blum and Stillings (1995)
Anorthite (2.76)	2.82×10^3				Fleer (1982)
$CaAl_2Si_2O_8$	1×10^4	pH = 5			Sverdrup (1990); Blum and Stillings (1995)
Biotite (2.7–3.3)			0.12	Mass balance	Velbel (1985)
$K(Mg,Fe)_3AlSi_3O_{10}(F,OH)_2$			0.0088		Clow and Drever (1996)
	3.8	Fluidized bed reactor (pH = 4.5)	0.009	Small-plot (silica flux)	Swoboda-Colberg and Drever (1993)
	10	pH = 4			Kalinowski and Schweda (1996)
Phlogopite (2.76–2.90)	9.0	pH = 4			Kalinowski and Schweda (1996)
$K_2Mg_6(Al_2Si_6O_{20})(OH,F)_4$	2.4 ± 1.2	AFM fluid cell (pH = 5.7)			Rufe and Hochella (1999)
Muscovite (2.77–2.88)	6.3	Fluidized bed reactor (pH = 4.5)	0.021	Small-plot (silica flux)	Swoboda-Colberg and Drever (1993)
$KAl_3Si_3O_{10}(F,OH)_2$	0.5970 (Si release)	Flow-through (pH = 4.1)			Knauss et al. (1989)
	0.7	pH = 4			Kalinowski and Schweda (1996)
Kaolinite (2.61–2.68)	0.0123 (Si release)	Batch reactor (pH = 5.7)			Huertas et al. (1999)
$Al_2Si_2O_5(OH)_4$	0.4	pH = 5			Wieland and Stumm (1992)
	0.32 ± 0.02	pH = 3			Sutheimer et al. (1999)
Hectorite	190	AFM observation (pH = 2)			Bosbach et al. (2000)
$Na_{0.7}(Mg_{5.3}Li_{0.7})Si_8O_{20}(OH)_4$					

Montmorillonite (2–3) $(Na, Ca)_{0.33}(Al, Mg)_2\ Si_4O_{10}(OH)_2$	9.8 (Si release)	pH = 12.56, T = 35° C			Bauer and Berger (1998)
Smectite (2–3) $K_{0.19}Na_{0.51}\ Ca_{0.195}Mg_{0.08}\ (Al_{2.56}\ Fe_{0.42}\ Mg_{1.02})(Si_{7.77}\ Al_{0.23})\ O_{20}(OH)_4$	8.1	pH = 8.8, T = 80° C			Cama et al. (2000)
$K_{0.02}Na_{0.05}\ Ca_{0.41}Mg_{0.18}\ (Mg_{1.11}\ Fe_{0.17}\ Al_{2.77})(Al_{0.30}\ Si_{7.70})\ O_{20}(OH)_4$	0.006–0.017[a] (Si release)	pH = 4.1, T = 25° C			Amram and Ganor (2004); Metz et al. (2004)
Illite (2.6–2.9) $(Si_{3.55}Al_{0.45})\ (Al_{1.27}Fe_{0.36}\ Mg_{0.44})\ O_{10}(OH)_2\ (Ca_{0.01}Na_{0.01}K_{0.53})$	0.0032	pH = 4.7			Köhler et al. (2003)
Chlorite (2.6–3.3) $Mg_5Al_2Si_3O_{10}(OH)_8$	3.3	Fluidized bed reactor (pH = 4.5)	0.010	Small-plot (silica flux)	Swoboda-Colberg and Drever (1993)
	1.10 ± 0.17	Flow experiment and AFM (pH = 5.3)			Brandt et al. (2003)
Talc (2.58–2.83) $Mg_3Si_4O_{10}(OH)_2$	1	pH = 5			Lin and Clemency (1981)
Gibbsite (2.4) $Al(OH)_3$	0.3	pH = 5			Mogollon et al. (1994)
Quartz (2.65)	15	Flow-through (pH = 6.2)			Knauss et al. (1988)
SiO_2	0.041				Rimstidt and Barnes (1980)
Calcite (2.72) $CaCO_3$	1.995×10^6	Fluidized bed reactor (pH = 6)			Chou et al. (1989)
	7.14×10^6	Rotating disk (pH = 8.4)			Sjöberg and Richard (1984)
	1.5×10^6	SFM and fluid cell ($pH = 5.6, pCO_2 = 10^{-3.5}$ atm)			Jordan and Rammensee (1998)
	7.53×10^7	Rotating disk (pH = 3)			Alkattan et al. (1998)

(*cont.*)

Table 13.7 (*Continued*)

	1.12×10^5	VSI (vertical scanning interferometry), pH = 8.8, $pCO_2 = 10^{-3.41}$ atm	Arvidson et al. (2003)
	$(0.29 - 2.69) \times 10^6$	Mixed-flow reactor (pH = 5.1 − 9.5)	Cubillas et al. (2005)
	$(0.89–1.58) \times 10^6$	(pH = 7.67 − 8.25)	Gutjahr et al. (1996)
Aragonite (2.94) $CaCO_3$	$(0.52 - 3.19) \times 10^6$	Mixed-flow reactor (pH = 6.2-9.5)	Cubillas et al. (2005)
	1.1×10^6	pH = 7.81	Gutjahr et al. (1996)
Dolomite (2.86) $CaMg(CO_3)_2$	3.98×10^5	Fluidized bed reactor (pH = 5.7)	Chou et al. (1989)
	1.5×10^7	pH = 3	
	1.20×10^6	pH = 4.4	Luttge et al. (2003)
	9.76×10^6	Rotating disk technique (pH = 3)	Gautelier et al. (1999)
	1.54×10^5	Crystal weight loss ($pH = 5.7, pCO_2 = 0$ atm)	Busenberg and Plummer (1982)

[a] The dissolution rate given by Amram and Ganor (2004) is in mol (Si) $g^{-1}\,s^{-1}$. We converted it into mol $m^{-2}\,s^{-1}$ using the BET surface area for the raw smectite sample used in the same experiment as 34–97 m^2/g from Metz et al. (2004).

kaolinite 22% ($Al_2Si_2O_5(OH)_4$), Fe_2O_3 8%, and 5% Ca-Mg-carbonates. From the mineral dissolution rates in Table 13.7, a synthetic dissolution rate of this average shale, excluding iron oxide and carbonates, can be calculated as:

$$\begin{aligned} R_{\text{shale}-1} &\approx [22\% \times 60.1 \times (0.041 \text{ to } 15) + 29\% \times 278 \times (0.63 \text{ to } 2.0) + 9\% \times 262 \\ &\quad \times 5.0 + 5\% \times 555.8 \times (1.1 \text{ to } 3.3) + 22\% \times 258 \times 0.4] \times 10^{-12} \\ &= 2.23 \text{ to } 5.92 \times 10^{-10}\,\text{g m}^{-2}\,\text{s}^{-1} = 0.70 \text{ to } 1.87 \times 10^{-2}\,\text{g m}^{-2}\,\text{year}^{-1} \end{aligned}$$

A different mineralogical composition of an average shale is given by Shaw and Weaver (1965): quartz 30.8%, feldspar 4.5%, clay minerals 60.9%, and carbonates 3.6%. In addition, the authors list 1% organic matter, and <2.5% iron oxides and other minerals. The chemical composition of the feldspar and clay minerals is not detailed in the analysis, beyond an indication that illite is an abundant component. The large fraction of clays in this shale (61%), in comparison to 27% in the preceding composition, can be taken as another example of an average shale containing quartz 31%, K-feldspar 4.5%, carbonates 3.5%, Mg-chlorite 5%, and 56% illite-smectite of a synthetic composition $K_{0.2}\ Na_{0.2}\ Ca_{0.1}\ Al_{2.19}\ Si_{3.71}\ O_{10}(OH)_2$. As in the preceding computation of the dissolution rate of the silicate components of the shale, the dissolution rates of illite and other minerals from Table 13.7 give the following result:

$$\begin{aligned} R_{\text{shale}-2} &\approx [31\% \times 60.1 \times (0.041 \text{ to } 15) + 4.5\% \times 278 \times (0.63 \text{ to } 2.0) + 5\% \\ &\quad \times 555.8 \times (1.1 \text{ to } 3.3) + 56\% \times 373.72 \times 0.0032] \times 10^{-12} \\ &= 0.40 \text{ to } 3.97 \times 10^{-10}\,\text{g m}^{-2}\,\text{s}^{-1} = 0.13 \text{ to } 1.25 \times 10^{-2}\,\text{g m}^{-2}\,\text{year}^{-1} \end{aligned}$$

It may be reiterated that there is a considerable variation in the values of the mineral dissolution rates among those listed in Table 13.7 where, in particular, there is a wide spread in the quartz dissolution rates, of which we prefer the lower value of $0.041 \times 10^{-12}\,\text{mol m}^{-2}\,\text{s}^{-1}$. From the two preceding results for shale, a mean dissolution rate of the silicate components can be taken as:

$$\begin{aligned} R_{\text{shale}} &= (0.70 + 0.13) \times 10^{-2}/2 \text{ to } (1.87 + 1.25) \times 10^{-2}/2 \\ &= 0.0042 \text{ to } 0.0156\,\text{g m}^{-2}\,\text{year}^{-1} \end{aligned}$$

The main mineral components of an average sandstone, calculated from the chemical composition, are (Garrels and Mackenzie, 1971): quartz 62 wt %, K-feldspar 8%, albite 10%, Mg-chlorite 3%, kaolinite 7%, Fe_2O_3 4%, and calcite 6%. Disregarding the potential contributions from ferric oxide and calcite, the synthetic dissolution rate of sandstone is:

$$\begin{aligned} R_{\text{sandstone}} &\approx [62\% \times 60.1 \times (0.041 \text{ to } 15) + 8\% \times 278 \times (0.63 \text{ to } 2.0) + 10\% \\ &\quad \times 262 \times 5.0 + 3\% \times 555.8 \times (1.1 \text{ to } 3.3) + 7\% \times 258 \times 0.4] \times 10^{-12} \\ &= 1.72 \text{ to } 7.97 \times 10^{-10}\,\text{g m}^{-2}\,\text{s}^{-1} = 0.54 \text{ to } 2.52 \times 10^{-2}\,\text{g m}^{-2}\,\text{year}^{-1} \end{aligned}$$

In the sedimentary lithosphere, shales account for 51 wt % and sandstones for 23% (Li, 2000) of the continental sediment mass. In the mineral composition of shale, as used above, silicate minerals make $92 \pm 5\%$ of total shale and 90% of sandstone. Thus the lower bound of the dissolution rate of an average sedimentary silicate rock, excluding carbonate and evaporite minerals in it, is from the preceding results:

$$\begin{aligned} R_{\text{sed. silicates}} &= 0.51 \times R_{\text{shale}} + 0.23 \times R_{\text{sandstone}} \\ &= 0.51 \times (0.0042 \text{ to } 0.0156) + 0.23 \times (0.0054 \text{ to } 0.0252) \\ &= 0.003 \text{ to } 0.014 \,\text{g m}^{-2} \text{ year}^{-1} \end{aligned}$$

The value of $R_{\text{sed. silicates}}$ based on the silicate mineral components but excluding the carbonates in the sedimentary mass is, as might be expected, smaller than the synthetic dissolution rate of the continental crust, R_{crust}, that is given in the Sect. 13.7.4.

Mineral dissolution rates $R(\text{mol m}^{-2}\,\text{s}^{-1})$, such as those listed in Table 13.7, have been used by Lasaga (1998) to compute the lifetime of a crystal or the length of time it would take to its complete dissolution (t_{life}) at a constant dissolution rate R. For a spherical crystal of initial radius r_0, the crystal lifetime is defined by the linear rate of decrease in the sphere radius from an initial value of r_0 to $r = 0$:

$$t_{\text{life}} = \frac{r_0 \rho}{RM} \text{ (year)} \tag{13.22a}$$

where M is gram-formula weight (g/mol) and ρ is density (g/cm^3); the quotient $M/\rho(\text{cm}^3/\text{mol})$ is the molar volume, V_{m}, of the mineral that is also available from such sources as Robie et al. (1978) and *Handbook of Chemistry and Physics*. For spherical crystals of initial radius 1 mm $(r_0 = 0.1\,\text{cm})$, lifetimes of the faster soluble silicates, such as olivine forsterite, is about 2,300 years; and for the plagioclase albite, with the range of dissolution rates as given in Table 13.7 from 0.55 to 5.01 picomol $\text{m}^{-2}\,\text{s}^{-1}$, lifetime of a 1-mm-radius crystal is 575,000–63,000 years. At another extreme, lifetime of kaolinite particles is 810,000 years, at the dissolution rate of 0.4 picomol $\text{m}^{-2}\,\text{s}^{-1}$ at pH = 5 (Table 13.7), and that of quartz crystals is 34 million years. Additional computed values of such mineral longevities are given in Chap. 5.

Equation (13.22a) for a spherical crystal is a particulate case of a general relationship for the decrease in the mineral volume $(-dV/dt)$ by a constant dissolution rate R operating over the crystal surface area S that also changes with time. This relationship can be written as:

$$-\frac{dV}{dt} = SRM/\rho \tag{13.22b}$$

Equation (13.22a) also applies to such model shapes as cubes or cylinders equidimensional to a sphere (i.e., the cube edge is equal to the sphere diameter, $2r_0$, and the cylinder base diameter and height each is also $2r_0$), if any crystal-edge effects on dissolution are disregarded. However, if only part of the mineral surface is reactive then the time to complete dissolution would be longer. For other crystal shapes, such as elongated or flattened cylinders, octahedra, and flakes or prisms (parallelepipeds,

disregarding the possibly faster dissolution rates at the edges and apices) that bear some linear relationships to a sphere of diameter $2r_0$, t_{life} is modified by a factor b that depends on the relative dimensions and aspect ratios of these crystal shapes:

$$t_{\text{life}} = \frac{br_0\rho}{RM} \tag{13.22c}$$

The factor $b = 1$ for a sphere, cube, and equidimentional circular cylinder, but it may differ from1 for other geometric shapes, making the time to dissolution either longer or shorter than for a spherical crystal.

13.7.3.2 Carbonates

Laboratory-determined dissolution rates of carbonate minerals, calcite, aragonite, and dolomite, are much faster that those of silicates (Table 13.7), although it has been demonstrated that the rates become smaller as the solution approaches saturation with respect to the mineral, by a general relationship of the form (Cubillas et al., 2005, with references to earlier work of others):

$$\begin{aligned} R &= R_{\Omega=0}(1-\Omega)^{\text{n}} \\ &\approx 2.2\times10^{-6}(1-\Omega)^{1.25}\,\text{mol m}^{-2}\,\text{s}^{-1} \end{aligned} \tag{13.22d}$$

where Ω is the degree of saturation of the solution with respect to a mineral and $R_{\Omega=0}$ is the mineral dissolution rate near infinite dilution. At saturation $\Omega = 1$, and at undersaturation $\Omega < 1$. Another measure of a degree of saturation that is used in the literature is the Calcite Saturation Index (CSI), defined as $\text{CSI} = \log\Omega$; for solutions from saturation to undersaturation, the index values are $\text{CSI} \leq 0$.

Most rivers and many big freshwater lakes are pronouncedly undersaturated with respect to calcite, as shown in Fig. 13.8. However, the degree of saturation (Ω) increases with increasing Ca^{2+} concentration and pH, both of which increase the alkalinity of river or lake water. The undersaturation of continental surface waters with respect to calcite is a consequence of higher internal CO_2 concentrations in water due to decomposition of organic matter in soils and the release of CO_2 to the flowing waters and atmosphere.

Calcite dissolution rates, in the pH range from 5.5 to 9.5, fall within a band of $(2.2 \pm 1.0)\times10^{-6}$ mol $\text{m}^{-2}\,\text{s}^{-1}$ or, at an annual time scale, $70 \pm 32\,\text{mol m}^{-2}$ $CaCO_3$ year^{-1} (Plummer et al., 1978; Shiraki et al., 2000; Cubillas et al., 2005). This rate corresponds to a lifetime of 5 months for a spherical particle of 1 mm in radius or 55 years in a solution that is within 2% of saturation at $\Omega = 0.98$. In view of the fact that many rivers are strongly undersaturated with respect to calcite, yet they transport detrital $CaCO_3$, the experimentally determined fast dissolution rates of pure mineral phases are difficult to apply uniformly to a natural weathering environment.

The rate of chemical denudation of carbonate rocks (limestone and dolomite) may be estimated from the Ca^{2+} and Mg^{2+} concentrations in an average river

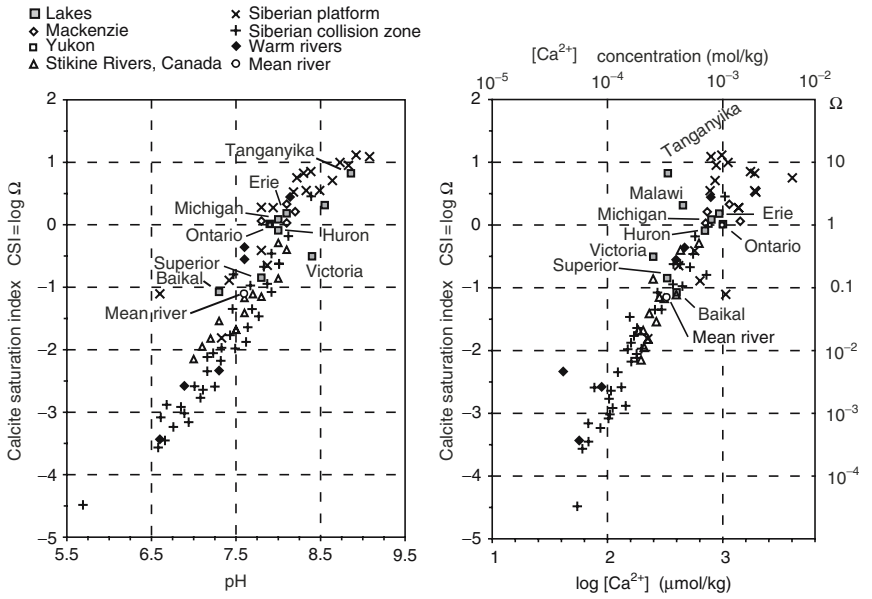

Fig. 13.8 Degree of saturation of rivers and lakes with respect to calcite as a function of the pH (**a**) and calcium concentration (**b**). Northern rivers from Millot et al. (2003), Gaillardet et al. (2003), Huh and Edmond (1999), and Huh et al. (1998a, b). Warm rivers: Amazon (Gaillardet et el., 1997), Orinoco (Edmond et al., 1996), Ganges and Brahmaputra (Galy and France-Lanord, 1999), Indus (Karim and Veizer, 2000), Niger (Tardy et al., 2004). Data for North American Great Lakes from Weiler and Chawla (1969), East African lakes from Oliver (2002), and Baikal from Votintsev (1993). Mean river values are for the data plotted in the figure

(Table 13.6), and their fractions derived from the dissolution of carbonates (given in Table 13.12 that is discussed in Sect. 13.8.4): 0.60 of Ca^{2+} and 0.24 of Mg^{2+} are derived from dissolution of carbonates. Outcrop area of the carbonate rocks (limestone and dolomite) is estimated as $14 \times 10^6\,km^2$, from 16% (Meybeck, 1987) of the land drainage area of $88 \pm 12 \times 10^6\,km^2$, indicated in Sect. 13.6.1. Other authors' estimates of the carbonate outcrop area range from 12 to $23 \times 10^6\,km^2$, as summarized by Lerman et al. (2007). Using the preceding numbers, the mass weathering rate of the carbonates, taken as $CaCO_3$ and $MgCO_3$, is:

$$W_{\text{carbonates}} = \frac{(0.334 \times 10^{-3}\,\text{mol/kg} \times 0.60 \times 100\,\text{g/mol} + 0.136 \times 10^{-3}\,\text{mol/kg} \times 0.24 \times 84\,\text{g/mol}) \times 3.74 \times 10^{16}\,\text{kg year}^{-1}}{0.159 \times 88 \times 10^{12}\,\text{m}^2}$$

$$\approx 61\,\text{g m}^{-2}\,\text{year}^{-1}$$

If the carbonate rocks are taken only as $CaCO_3$, the weathering rate would be slightly lower, about $54\,\text{g m}^{-2}\,\text{year}^{-1}$. The mass weathering rate of carbonates, 54–61 g m^{-2} $year^{-1}$, is fortuitously close to the $CaCO_3$ dissolution rate at the saturation value of the solution $\Omega = 0.98$ that is based on the experimental Eq. (13.22d):

52 g m^{-2} $year^{-1}$. As a whole, the weathering rate of carbonate rocks is about twice the global mean sediment weathering rate and it is close to the weathering rate of geologically young basalts, both as given in Sect. 13.7.1.

13.7.4 Chemical Denudation of Continental Crust

The composition of an average continental crust has been approximated as consisting of 2/3 granite and 1/3 basalt (Li, 2000), and a summary of other chemical and mineralogical variants is given by Rudnick and Gao (2003). The thickness of the upper crystalline crust was estimated at 19 km by Wedepohl (1995), based on seismic evidence. The three main mineral components of granite are 33 wt % K-feldspar ($KAlSi_3O_8$), 33% sodic plagioclase ($Na_{0.7}Ca_{0.3}Al_{1.3}Si_{2.7}O_8$), and 33% quartz ($SiO_2$) (Bowen, 1928; Mason and Moore, 1982, p. 96). Thus a synthetic dissolution rate of granite is a sum of each mineral's mass fraction, its gram formula mass, and its dissolution rate (Table 13.7):

$$\begin{aligned} R_{\text{granite}} \approx\ & [33.3\% \times 278 \times (0.63 \text{ to } 2.0) + 33.3\% \times 265 \times (0.79 \text{ to } 2.3) + 33.3\% \\ & \times 60.1 \times (0.041 \text{to } 15)] \times 10^{-12} = 1.29 \text{ to } 6.88 \times 10^{-10} \text{ g m}^{-2} \text{ s}^{-1} \\ =\ & 0.0041 \text{ to } 0.022 \text{ g m}^{-2} \text{ year}^{-1} \end{aligned}$$

An average basalt in the continental crust may consist of 60 wt % calcic plagioclase ($Na_{0.4}Ca_{0.6}Al_{1.6}Si_{2.4}O_8$), 30 wt % pyroxene (diopside, $CaMgSi_2O_6$), and 10 wt % olivine (forsterite, Mg_2SiO_4) (Mason and Moore, 1982). From the mineral dissolution rates in Table 13.7, the dissolution rate of an average basalt is:

$$\begin{aligned} R_{\text{basalt}} \approx\ & [60\% \times 271.9 \times 5.01 + 30\% \times 216.2 \times (15.8 \text{ to } 125.9) + 10\% \times 140.1 \\ & \times 316.2] \times 10^{-12} = 62.72 \text{ to } 134.1 \times 10^{-10} \text{ g m}^{-2} \text{ s}^{-1} \\ =\ & 0.20 \text{ to } 0.42 \text{ g m}^{-2} \text{ year}^{-1} \end{aligned}$$

This range includes the experimental basalt dissolution rate of 0.22 g m^{-2} $year^{-1}$ or 69.7×10^{-10} g m^{-2} s^{-1} (Gíslason and Eugster, 1987). The chemical weathering rate of basalt is up to 50–100 times greater than that of granite (from the estimates given above, 0.42/0.022 or 0.42/0.0041). A rate ratio of 110 for basalt/granite from laboratory dissolution rates at pH = 5 was reported by Drever and Clow (1995). The faster dissolution rate of basalt than that of granite agrees qualitatively with the order of mineral resilience in the weathering cycle, known as the Goldich series (Goldich, 1938), often cited in the geochemical literature (e.g., Pettijohn, 1957; Lerman, 1979; Stallard, 1988; Lasaga, 1998): Mg-Fe-rich silicates and Ca-rich feldspars forming at higher magmatic temperatures are less stable in weathering than the minerals crystallizing at lower temperatures. Thus the mean weighted dissolution rate of an

average continental crust is:

$$R_{\text{crust}} = \frac{2}{3}R_{\text{granite}} + \frac{1}{3}R_{\text{basalt}}$$
$$= \frac{2}{3} \times (0.004 \text{ to } 0.022) + \frac{1}{3} \times (0.2 \text{ to } 0.42) = 0.069 \text{ to } 0.155\,\text{g m}^{-2}\,\text{year}^{-1}$$

In comparison to the mean chemical denudation rate of sediments, about $27\,\text{g m}^{-2}$ year^{-1} (Sect. 13.7.1), computed from the geographic surface area, the mass weathering rates of the continental crust and silicate sediments suggest that, as expected, the mineral surface area in weathering is much greater than the geographic surface area. This relationship is discussed in the next section.

13.7.5 Weathering Layer Thickness

The mass of dissolved solids in water runoff from land per unit area of land surface corresponds to the mass dissolved from the surface area of minerals occurring within a layer of some thickness. The thickness of such a weathering layer depends on its texture and distribution within it of interconnected joints or pore spaces that are water conduits, the mineral surface area that is a function of the grain size, and rates of mineral dissolution under the weathering conditions. Following the common practice of considering model mineral particles as spheres, we present below estimates of a weathering layer thickness of different textures.

Dissolution rate per unit area of land surface, W_m in Eq. (13.20), is a product of mineral dissolution rate, R_{i} (grams per $1\,\text{m}^2$ of mineral surface per unit of time), and the geometric mineral surface area that is

$$S_{\text{i}} = 4\pi r^2 N \tag{13.23}$$

where r is the particle radius (cm) and N is the number of particles in a layer volume of $1\,\text{cm}^2$ base. The dissolution mass balance equation is therefore:

$$4\pi r^2 N R_{\text{i}} = W_m \tag{13.24}$$

N particles of radius r occupy a volume h cm high and $1\,\text{cm}^2$ base, of porosity φ (Fig. 13.9):

$$\frac{4}{3}\pi r^3 N = h \times 1 \times (1 - \varphi) \tag{13.25}$$

The layer thickness h is from (13.24) and (13.25):

$$h = \frac{W_m}{3(1-\varphi)R_{\text{i}}} \cdot r \tag{13.26}$$

The geometric surface area of the particles may be increased by the roughness factor $\lambda = S_{BET}/S_{GEO}$ that relates the surface area measured by a gas adsorption method

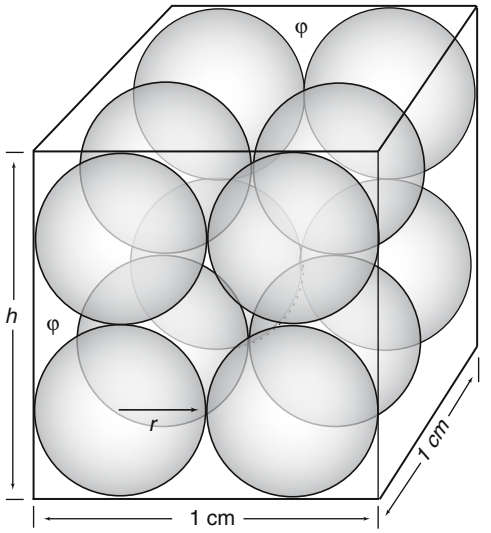

Fig. 13.9 Spherical particles of radius r and interstitial pore space (porosity volume fraction φ) in a sediment column h cm high and 1 cm^2 cross-section

(BET) to the geometric area (GEO) (White and Brantley, 2003). In general, $\lambda > 1$ and values from about 20 to 200 for silicates are given in Chap. 10. Conversely, the mineral surface area may be decreased due to the occurrence of unreactive sections of the surface, cementation or the packing texture, by some factor $\varepsilon < 1$. With these two possible corrections to the mineral reactive surface area, the weathering layer thickness becomes:

$$h = \frac{W_m}{3(1-\varphi)R_i\lambda\varepsilon} \cdot r \tag{13.27}$$

If the product $\lambda\varepsilon \approx 1$ then Eqs. (13.27) and (13.26) are identical and describe dissolution of a mineral geometric reactive surface area. It should be noted that the layer thickness is directly related to the particle size, radius r, and it increases with increasing porosity φ. Cubic or hexagonal close packing of spheres of the same size has a volume porosity fraction of 0.2595 or 26%. At the maximum possible packing, the porosity fraction is 0.2216 or 22%. Random close packing of spheres gives greater porosities of the aggregates, from 35% and higher (Weisstein, 2005).

In river waters, SiO_2 and variable fractions of the major ions Ca^{2+}, Mg^{2+}, Na^+, and K^+, are derived from dissolution of silicate minerals in sedimentary and crystalline rocks. These fractions are given in Table 13.12 that is discussed in Sect. 13.8.4. In sediments, shales and sandstones are the main sources of the four cations from silicate minerals. The sedimentary silicates contained in shales (51 weight % of sediment mass, Table 13.5) and sandstones (23 wt %) are characterized by dissolution rates in the range $R_i = 0.003$–$0.014\,g\,m^{-2}\ year^{-1}$, as estimated in Sect. 13.7.3, with the lower estimate probably more representative

of the sedimentary weathering environment. The silicate-derived ion concentrations in river water may be stoichiometrically equated to masses of such common rock-forming minerals as Ca-plagioclase, Mg-olivine and(or) Mg-chlorite, Na-plagioclase, and K-feldspar, giving a combined mass weathering rate of 16–20 g m^{-2} $year^{-1}$ of silicates, as compared to the total rate of chemical denudation of 26–29 g m^{-2} $year^{-1}$ that includes carbonates and evaporites. For an order of magnitude estimate of a thickness of the weathering layer, we assign the preceding silicate weathering rate to the shales and sandstones and use the mineral dissolution rate $R_i = 0.003$ g m^{-2} $year^{-1}$ for particle sizes from silt to fine sand, 60 microns to 1 mm in diameter ($r = 3 \times 10^{-3}$ to 0.05 cm), in Eq. (13.26):

$$h \geq \frac{16 \text{ to } 20 \text{ g m}^{-2} \text{ year}^{-1}}{3 \times (1 - 0.26) \times 0.003 \text{ g m}^{-2} \text{ year}^{-1}} \times (0.003 \text{ to } 0.05 \text{ cm}) = 7.2 \text{ to } 150 \text{ cm}$$

The latter result for the weathering layer thickness is based on the silicate dissolution rates only and an assumption that the reactive surface area is identical to the geometric surface area of the mineral particles. As mentioned earlier, cementation and aggregation of particles may make the effective area smaller and/or the particle size larger. Hypothetically, but perhaps not inconceivably, if only 10–1% of the geometric particle surface area were reactive ($\varepsilon = 0.1$–0.01), the weathering layer thickness with an effective particle size of 1 mm ($r = 0.05$ cm) would be 15–150 m. A conclusion that can be drawn from the preceding results is that the thickness of the weathering rock layer strongly depends on the reactive surface area of the mineral particles and the texture of the weathering source rock, as reflected in the roughness factor of the mineral surfaces, possible reduction of the reactive area, and increase in the particle size owing to compaction, cementation or aggregation.

13.8 Mineral-CO_2 Reactions in Weathering

13.8.1 CO_2 Reactions with Carbonates and Silicates

Consumption of CO_2 in mineral dissolution and, more generally, weathering reactions is one of the major fluxes in the global carbon cycle that drives the weathering process and transport of dissolved solids from the land by surface runoff to the ocean. The role of CO_2 as a natural acid that reacts with carbonate and silicate minerals in sediments and continental crystalline crust is supplemented by other acids, such as the sulfuric acid forming in oxidation of reduced sulfur minerals (mainly pyrite, FeS_2), inorganic acids occurring in the atmosphere from volcanic eruptions or biogeochemical reactions on the land or ocean surface (e.g., sulfuric, hydrochloric, and nitric acids), and organic acids forming by biological processes in soils. Reactions between dissolved CO_2 and minerals containing the common alkali and alkaline-earth metals Na, K, Mg, and Ca produce negatively charged bicarbonate and carbonate ions that neutralize the positive cation charges in solution and create

alkalinity. The most frequently used examples of this process are dissolution reactions of $CaCO_3$, as a generic proxy for carbonates, and $CaSiO_3$, as a generic notation for Ca and Mg in a silicate, where two bicarbonate ions, $2HCO_3^-$, are produced in each reaction, but the dissolution of $CaCO_3$ requires one CO_2 whereas dissolution of the calcium silicate requires $2CO_2$. Thus the dissolution of a divalent-metal carbonate consumes CO_2 and produces HCO_3^- in the molar ratio of $CO_2/HCO_3^- = 1:2$ and dissolution of a divalent-metal silicate consumes CO_2 and produces HCO_3^- in the ratio of $CO_2/HCO_3^- = 1{:}1$. If these two minerals occurred in equal proportions in a rock, their weathering would consume $3CO_2$ and produce $4HCO_3^-$, making the CO_2 consumption 75% of the bicarbonate or of the cation mol-equivalents produced (2 mol Ca^{2+} are 4 mol-equivalents):

$$\begin{aligned} CaCO_3 + CO_2 + H_2O &= Ca^{2+} + 2HCO_3^- \\ CaSiO_3 + 2CO_2 + H_2O &= Ca^{2+} + 2HCO_3^- + SiO_2 \\ \hline 3CO_2 \qquad\qquad & \qquad 4HCO_3^- \end{aligned}$$

In dissolution of common silicate minerals, the mass of CO_2 consumed depends both on the stoichiometric composition of the mineral and its abundance, as has been demonstrated by such reactions as given below that are often cited in many textbooks (e.g., Garrels and Mackenzie, 1971; Drever, 1988, 1997; Berner and Berner, 1996; Faure, 1998):

$$NaAlSi_3O_8 + CO_2 + 2H_2O = Na^+ + HCO_3^- + 3SiO_2 + Al(OH)_3$$

where Na-silicate albite reacts with one CO_2 producing one of each Na^+ and HCO_3^-, and SiO_2 and $Al(OH)_3$ that balance the reaction as dissolved and/or solid species. For monovalent-cation silicates, the ratio of CO_2 consumed to HCO_3^- formed is 1:1. Similarly, dissolution of Ca-feldspar anorthite and Mg-silicates olivine and chlorite shows the 1:1 relationship between the HCO_3^- formed and CO_2 consumed:

$$\begin{aligned} CaAl_2S_{i2}O_8 + 2CO_2 + 4H_2O &= Ca^{2+} + 2HCO_3^- + 2SiO_2 + 2Al(OH)_3 \\ Mg_2SiO_4 + 4CO_2 + 2H_2O &= 2Mg^{2+} + 4HCO_3^- + SiO_2 \\ Mg_5Al_2Si_3O_{10}(OH)_8 + 10CO_2 + 4H_2O &= 5Mg^{2+} + 10HCO_3^- + 3SiO_2 \\ &\quad + 2Al(OH)_3 \end{aligned}$$

The preceding reactions are congruent dissolution with respect to the cations: for example, if a K- or Mg-containing clay mineral forms as a weathering product of a K-feldspar or Mg-silicate and the clay also weathers, then the balance of the K^+ or Mg^{2+}-ion released congruently would be the same and there would be no net effect on CO_2 consumption. However, if clay minerals were forming by removal of such main cations as Mg^{2+}, K^+, and Na^+ from water (Faure, 1998) and without further dissolution, then the cation masses released would be smaller and the potential uptake of CO_2 in silicate weathering would also be smaller. In sediments, it is generally not known how much and what kind of clays form from parent silicate minerals

and it is therefore difficult to estimate any effects of the clay–water reactions on the CO_2 uptake in weathering.

Sediments contain reduced sulfur associated mostly with pyrite (FeS_2) that produces sulfuric acid when pyrite is oxidized (Stumm and Morgan, 1981):

$$FeS_2 + 3.75\ O_2 + 3.5\ H_2O = 2H_2SO_4 + Fe(OH)_3$$

Oxidation of pyrite involves transfer of 15 electrons in oxidation of Fe^{2+} to Fe^{3+} and S^{-1} to S^{+6} that are taken up by the 7.5 oxygen atoms. Sulfuric acid may react with carbonate and silicate minerals, releasing cations to solution and producing HCO_3^- or CO_2 from carbonates in different stoichiometric proportions (Mackenzie, 1992; Berner and Berner, 1996):

$$2CaCO_3 + H_2SO_4 = 2Ca^{2+} + 2HCO_3^- + SO_4^{2-} \quad (13.28a)$$

$$CaCO_3 + H_2SO_4 = Ca^{2+} + SO_4^{2-} + H_2O + CO_2 \quad (13.28b)$$

If all the pyrite-bound sulfur in sediments (S_{pyr}, Table 13.5) is oxidized to H_2SO_4 that reacts with carbonate and silicate minerals in the proportions of their abundance in an average sediment, Eqs. (13.28a) and (13.28b) would add SO_4^{2-} and cations to the water with a concomitant formation of HCO_3^- or CO_2 from the carbonate minerals. In this case, bicarbonate is produced by dissolution of carbonate minerals without CO_2 consumption.

Reactions of H_2SO_4 with divalent and monovalent-cation silicates produce cation/acid ratios of 1:1 and 2:1, without CO_2 consumption:

$$CaAl_2Si_2O_8 + H_2SO_4 = Ca^{2+} + SO_4^{2-} + 2SiO_2 + 2AlOOH$$

$$2NaAlSi_3O_8 + H_2SO_4 = 2Na^+ + SO_4^{2-} + 6SiO_2 + 2AlOOH$$

where SiO_2 and AlOOH are shorthand notation for conservation of silica and alumina in mineral oxides and hydroxides. More generally, other acids, such as hydrochloric acid, HCl, from hydrothermal circulation or monoprotic organic acids, RCOOH, from decomposition of organic matter may also react with carbonates and generate HCO_3^-:

$$2CaCO_3 \left| \begin{array}{l} +2HCl = 2Ca^{2+} + 2Cl^- + 2HCO_3^- \\ +2RCOOH = 2Ca^{2+} + 2RCOO^- + 2HCO_3^- \end{array} \right.$$

$$CaCO_3 \left| \begin{array}{l} +2HCl = Ca^{2+} + 2Cl^- + H_2O + CO_2 \\ +2RCOOH = Ca^{2+} + 2RCOO^- + H_2O + CO_2 \end{array} \right.$$

13.8.2 CO_2 Consumption and HCO_3^- Production

In one sediment type or a weight-averaged total sediment mass, the ratio of the CO_2 consumed to the HCO_3^- produced can be written in terms of the individual cation

concentrations or p_i, for those in the silicates (where $i = 4$, for Ca, Mg, Na, and K, in mol cation/g rock), and p_j, for those in the carbonates ($j = 2$, for Ca and Mg). The cation mol fraction of carbonates, y, in a rock containing both carbonates and silicates is:

$$y = \frac{\sum_{j=1}^{2} p_j}{\sum_{i=1}^{4} p_i + \sum_{j=1}^{2} p_j} \tag{13.29}$$

and the cation mol faction of silicates, with $i = 4$ for the four major cations, is:

$$1 - y = \frac{\sum_{i=1}^{4} p_i}{\sum_{i=1}^{4} p_i + \sum_{j=1}^{2} p_j} \tag{13.30}$$

For Ca- and Mg-carbonates reacting with CO_2 and sulfuric acid, the CO_2 consumption and HCO_3^- production depend on the mol fractions of $CO_2(x)$ and acid $(1-x)$ in a reacting mixture (Lerman and Wu, 2006):

$$\psi = \frac{CO_2 \text{ consumed}}{HCO_3^- \text{ produced}} = \frac{x}{2x + (1-x)} = \frac{x}{1+x} \tag{13.31}$$

In the absence of any sulfuric acid in weathering, the CO_2 fraction is $x = 1$ and the weathering potential for carbonates is $\psi = 0.5$.

When CO_2 (x) and $H_2SO_4(1-x)$ react with a mixture of carbonates (fraction y) and silicates $(1-y)$, the consumption/production ratio depends on whether HCO_3^- or CO_2 is produced in a reaction between carbonate and sulfuric acid, as discussed in Sect. 13.8.1. If the product is HCO_3^- then its fraction $(1-x)y$ is produced from H_2SO_4–$CaCO_3$ reaction, $2xy$ is produced from CO_2 and $CaCO_3$, and $x(1-y)$ from CO_2 and silicates. Thus the following ratio ψ_1 describes the CO_2 uptake in mineral weathering as a function of the CO_2 (x) and acid $(1-x)$ fractions reacting with the carbonates (y) and CO_2 reacting with the silicates (acid reactions with silicates consume no CO_2):

$$\begin{aligned} \psi_1 &= \frac{CO_2 \text{ consumed}}{HCO_3^- \text{ produced}} = \frac{xy + x(1-y)}{2xy + x(1-y) + (1-x)y} \\ &= \frac{x}{x+y} \end{aligned} \tag{13.32}$$

The effect of H_2SO_4 as part of a reactive mixture of acids (H_2SO_4 and CO_2) is shown in Fig. 13.10 on the CO_2 consumption/HCO_3^- production ratio for rocks varying in their mineral composition from pure carbonates to pure silicates. Equation (13.32) describes the case of $CaCO_3$ reaction with H_2SO_4 producing the bicarbonate ion HCO_3^-. In the absence of acid $(x = 1)$, pure carbonates $(y = 1)$ have a CO_2 consumption/HCO_3^- production ratio of 0.5, and pure silicates $(y = 0)$ have the same ratio of 1.0.

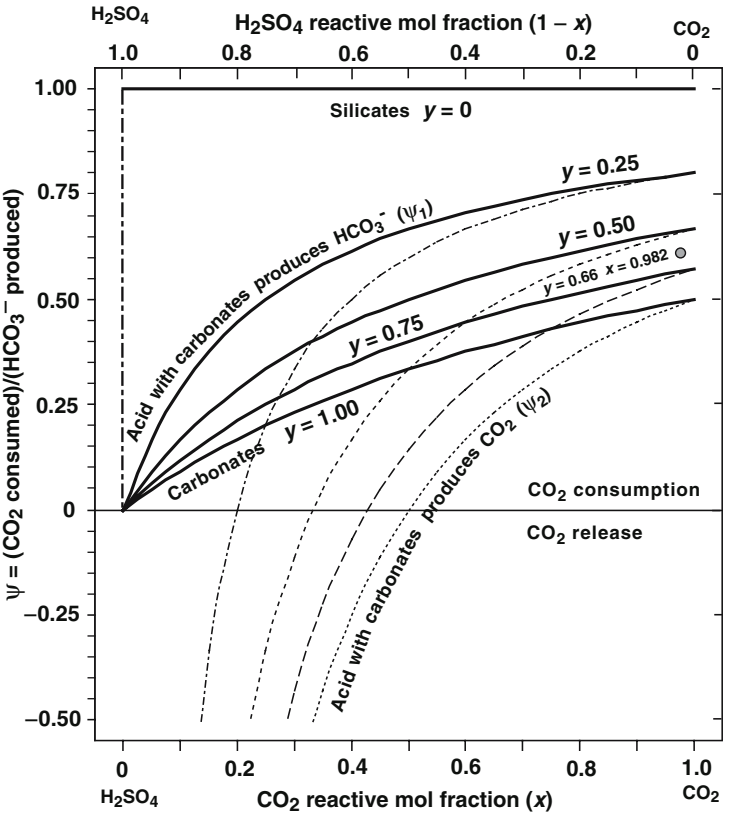

Fig. 13.10 Consumption of CO_2 and production of HCO_3^- in silicates and calcium carbonate reactions with water containing dissolved CO_2 and sulfuric acid, Eqs. (13.32) and (13.33). y is the cation mol fraction of carbonates in the source rock, x is the CO_2 fraction in CO_2–H_2SO_4 mix. The point at $x = 0.982$, $y = 0.66$ represents an average sediment (see also color insert)

If the carbonate reaction with sulfuric acid produces CO_2, its fraction produced is $(1-x)y$, and a possible return of this CO_2 to the atmosphere reduces the CO_2 consumed from x to $x-(1-x)y$. The fraction of HCO_3^- produced is $2xy$ from CO_2–carbonate reactions and $x(1-y)$ from CO_2–silicate reactions. In this case, the ratio of net CO_2 consumed to HCO_3^- produced is:

$$\psi_2 = \frac{\text{CO}_2 \text{ consumed}}{\text{HCO}_3^- \text{ produced}} = \frac{x-(1-x)y}{2xy+x(1-y)} = \frac{x-(1-x)y}{x(1+y)} \tag{13.33}$$

In the reaction path of Eq. (13.33), if the acid fraction is relatively large, then the CO_2 returned to the atmosphere significantly reduces or even exceeds the amount

consumed ($\psi_2 < 0$). However, in a normal weathering environment where CO_2 is the main reactant ($x > 0.90$), contribution of H_2SO_4 is small and the values of ψ_1 and ψ_2 shown in Fig. 13.10 are similar. The CO_2 consumption and HCO_3^- production potential, ψ_1 in Eq. (13.32), is smaller for carbonate sediments and evaporites that contain more carbonate minerals than for shales and sandstones (Table 13.5), because carbonate minerals produce some of the HCO_3^- in solution. For an average continental sediment, consisting of carbonate rocks, shales, sandstones, and evaporites in proportions that are given in Table 13.5 and Fig. 13.7, the ratio of potentially consumable CO_2 to producible HCO_3^- is 0.61: the weathering of an average sediment requires 61% of HCO_3^- to be taken from atmospheric or soil CO_2 and the remaining 39% supplied by carbonate minerals.

13.8.3 CO_2 Consumption from Mineral-Precipitation Model

The masses of minerals weathering in the global sedimentary cycle that produce the composition of a world average river have been studied along two main lines: the approach of a "backward precipitation" that withdraws minerals sequentially from the river water, thereby accounting for the mineral sources (Garrels and Mackenzie, 1967, 1971; Mackenzie, 1992; Berner and Berner, 1996), and "forward dissolution" that estimates the proportions of the different mineral components of the sedimentary and crystalline crust that account for the solution composition (Holland, 1978; Meybeck, 1987). More recent studies of river systems on large subcontinental scales (e.g., Gaillardet et al., 1999; Huh et al., 1998a; Dalai et al., 2002; Jacobson et al., 2002; Oliver et al., 2003; Millot et al., 2003; Mortatti and Probst, 2003) have estimated the crustal and sedimentary contributions on the basis of the ionic and $^{87}Sr/^{86}Sr$ ratios in river waters.

We apply the "backward precipitation" method of mineral removal uniformly to each of the three world average rivers (Table 13.6) that we call, in chronological order, the Meybeck (1979), the Mackenzie (1992), and the Berners (Berner and Berner, 1996). The sequence of minerals' withdrawal is explained below and shown for one average river in Table 13.8, where the computational steps are similar, but not identical, to those of the authors cited above.

Precipitation of individual minerals from an average river water is constrained by the following abundance ratios in the weathering source, taken as an average sediment (Tables 13.5, 13.9):

1. Sulfide (S_{pyr}) mol fraction of total sulfur (sulfate and sulfide): 0.244
2. Ca mol fraction of Ca-Mg-carbonates: 0.855

3a. Ca-carbonate mol fraction of Ca-carbonates and Ca-silicates: 0.927

First, in step 1 (Table 13.8), all Cl^- is removed from river water as NaCl. Next, in step 2, part of SO_4^{2-} is removed as S^- into pyrite (S_{pyr}) in the proportion of the occurrence of S_{pyr} in an average sediment, 0.244 (however, a smaller fraction of 0.11 for pyrite-derived sulfate in rivers was given by Berner and Berner, 1996).

Table 13.8 Removal of minerals from dissolved ionic components of a world average river of Mackenzie (1992) (Table 13.6)

Mineral Removal and Solution Balance	mol/kg river water								Minerals	Fraction of Total Precipitated (%)	Fraction of HCO_3^- Produced (%)
	Ca^{2+}	Mg^{2+}	Na^+	K^+	Cl^-	SO_4^{2-}	HCO_3^-	Precipitated			
Start concentration	3.34E–04	1.33E–04	1.59E–04	3.20E–05	9.00E–05	8.35E–05	8.67E–04				
1. Removal of NaCl			−9.00E–05		−9.00E–05			9.00E–05	NaCl	13.28	
Remaining	3.34E–04	1.33E–04	6.90E–05	3.20E–05	0	8.35E–05	8.67E–04				
2. Removal of S_{pyr} and carbonates and silicates dissolved by H_2SO_4 from pyrite											
a. Removal of S_{pyr} as SO_4^{2-} formed from pyrite						−2.03E–05		2.03E–05	S_{pyr}	3.00	
b. Removal of Ca & Mg carbonates dissolved by H_2SO_4	−2.30E–05	−3.89E–06				−1.34E–05	−2.69E–05	2.69E–05	$(Ca, Mg)CO_3$	3.96	3.10
c. Removal of cation silicates dissolved by H_2SO_4	−9.02E–07	−1.98E–06	−3.22E–06	−4.84E–06		−6.91E–06		1.09E–05	Ca, Mg, Na, K silicates	1.61	
Remaining	3.10E–04	1.27E–04	6.58E–05	2.72E–05		6.32E–05	8.40E–04				
3. Removal of Ca sulfates	−6.32E–05					−6.32E–05		6.32E–05	$CaSO_4$	9.32	
Remaining	2.47E–04	1.27E–04	6.58E–05	2.72E–05		0	8.40E–04				
4. Removal of Ca, Mg carbonates	−2.29E–04	−3.88E–05					−5.36E–04	2.68E–04	$(Ca, Mg)CO_3$	39.50	61.77
Remaining	1.80E–05	8.79E–05					3.04E–04				
5. Removal of Ca, Mg silicates	−1.80E–05	−8.79E–05					−2.12E–04	1.06E–04	Ca, Mg silicates	15.61	24.41
6. Removal of Na, K silicates			−6.58E–05	−2.72E–05			−9.29E–05	9.29E–05	Na, K silicates	13.71	10.72
Total removed	3.34E–04	1.33E–04	1.59E–04	3.20E–05	9.00E–05	8.35E–05	8.67E–04	6.778E–04		100	100
Remaining	0	0	0	0	0	0	0				

Table 13.9 Parameters and stoichiometric relationships for computation of S_{pyr} removed from river water and carbonate and silicate minerals dissolving by reactions with H_2SO_4. Reaction stoichiometry in Sect. 8.1. Data on sediment and river water composition in Tables 13.5 and 13.6

	Mineral Component			Cation Mol Fraction in Sediment (n_i)	Fraction of C_s in River Water Reacting with Cation		Cation Removed with Equivalent $S_{pyr}(C_s)$	
Sulfate and Sulfide S	**Sequential no.**	**Mineral**	**mol cation/g rock**			**mol/kg water**		**mol/kg water**
S_{pyr}/SO_3 in sediment (mol/mol) : =	1	$CaCO_3$	2.147E − 03	0.5646	n_1C_s	1.149×10^{-5}	$2n_1C_s$	2.298×10^{-5}
$(0.12/32.066)/\ (0.93/80.0642) = 0.322$	2	$MgCO_3$	3.635E − 04	0.09562	n_2C_s	1.946×10^{-6}	$2n_2C_s$	3.891×10^{-6}
S_{pyr} fraction of total S = 0.244	3	Ca-silicate	1.685E − 04	0.04432	n_3C_s	9.017×10^{-7}	n_3C_s	9.017×10^{-7}
	4	Mg-silicate	3.698E − 04	0.09728	n_4C_s	1.979×10^{-6}	n_4C_s	1.979×10^{-6}
S_{pyr} from average river (Mackenzie, 1992):	5	Na-silicate	3.007E − 04	0.07911	n_5C_s	1.610×10^{-6}	$2n_5C_s$	3.219×10^{-6}
$C_s = 0.244 \times [SO_4{}^{2-}] = 0.244 \times 8.350$	6	K-silicate	4.525E − 04	0.1190	n_6C_s	2.422×10^{-6}	$2n_6C_s$	4.844×10^{-6}
$\times 10^{-5} = 2.035 \times 10^{-5}$ mol/kg water	Sum		3.802E − 03	1.00		2.035×10^{-5}		

This is equivalent to concentration $C_s = 2.035 \times 10^{-5}$ mol SO_4^{2-}/kg (Table 13.9) that was produced by oxidation of pyrite and reacted with the carbonate and silicate minerals, releasing the metal cations to solution and forming some HCO_3^- from the carbonates. We take the amounts of cations dissolved from these minerals in the stoichiometric proportions of the reactions given in Sect. 13.8.1. For example, the mass of $CaCO_3$ that is dissolved by a reaction with H_2SO_4 is:

$$2CaCO_3 + H_2SO_4 = 2Ca^{2+} + 2HCO_3^- + SO_4^{2-}$$

where $2Ca^{2+}$ are produced for $1SO_4^{2-}$. Accordingly, removal of $1SO_4^{2-}$ from solution into pyrite sulfur S_{pyr} is accompanied by precipitation of $2CaCO_3$. Using the sediment abundances and river water sulfate concentration (Tables 13.5, 13.6, and 13.9), the mass of Ca^{2+} precipitated is

$$2 \times 0.5646 \times 2.035 \times 10^{-5} \text{ mol } SO_4^{2-}/\text{kg} = 2.298 \times 10^{-5} \text{ mol } Ca^{2+} \text{ as } CaCO_3/\text{kg}$$

This amount is shown in Table 13.8 as 2.30×10^{-5} mol Ca^{2+}/kg. The amount of HCO_3^- removed in this step is equal to the amount of Ca^{2+} and Mg^{2+} removed as carbonates from river water. Using a similar procedure, the amounts of silicates dissolved by reactions with H_2SO_4 are returned as divalent and monovalent-cation silicates to the weathering source.

Step 3 follows the removal of S_{pyr} and the carbonates and silicates dissolved by sulfuric acid: it is removal of the remaining SO_4^{2-} as $CaSO_4$. Because sulfates and chlorides dissolve without production of HCO_3^-, the preceding removal steps 1–3 determine the subsequent removal of the bicarbonate ion by the remaining divalent (Ca, Mg) and monovalent (Na, K) cations. In other words, the fractional abundances in the source rock of the cations not producing HCO_3^-, such as in the minerals NaCl and $CaSO_4$, affect the consumption of atmospheric CO_2 and production of HCO_3^- by other minerals. After the first three steps (1–3) of cation removal into chlorides and sulfates, as well as reconstitution of the silicates that reacted with H_2SO_4 producing no HCO_3^- and of carbonates that produce only little HCO_3^-, the remaining cations in river water determine the CO_2 consumption and HCO_3^- production with only little dependence on how these cations are partitioned between the carbonates and silicates. This is so in the precipitation model where SiO_2 and Al_2O_3 are stoichiometrically available for making cation-aluminosilicates by reaction of cations with dissolved or amorphous SiO_2, cation-free aluminosilicate minerals such as kaolinite, and/or Al-oxyhydroxides.

In the next step 4, Ca and Mg are removed as carbonates, in proportions of their occurrence in an average sediment. In Table 13.8, Ca^{2+} is removed from river water into $CaCO_3$ as its fraction of the Ca-carbonate and Ca-silicate in sediments: $0.927 \times 2.47 \times 10^{-4}$ mol/kg water $= 2.29 \times 10^{-4}$ mol Ca^{2+}/kg. Then Mg^{2+} is removed in the proportion of its occurrence with Ca^{2+} in sedimentary carbonates: $(2.29 \times 10^{-4} \text{ mol } Ca^{2+}/\text{kg}) \times 0.145/0.855 = 3.88 \times 10^{-5}$ molMg^{2+}/kg.

In step 5, the remaining Ca and Mg are removed as silicates into the weathering source, and the final step 6 is the removal Na and K silicates. The relative proportions of the precipitated minerals, grouped into carbonates (Ca, Mg), silicates

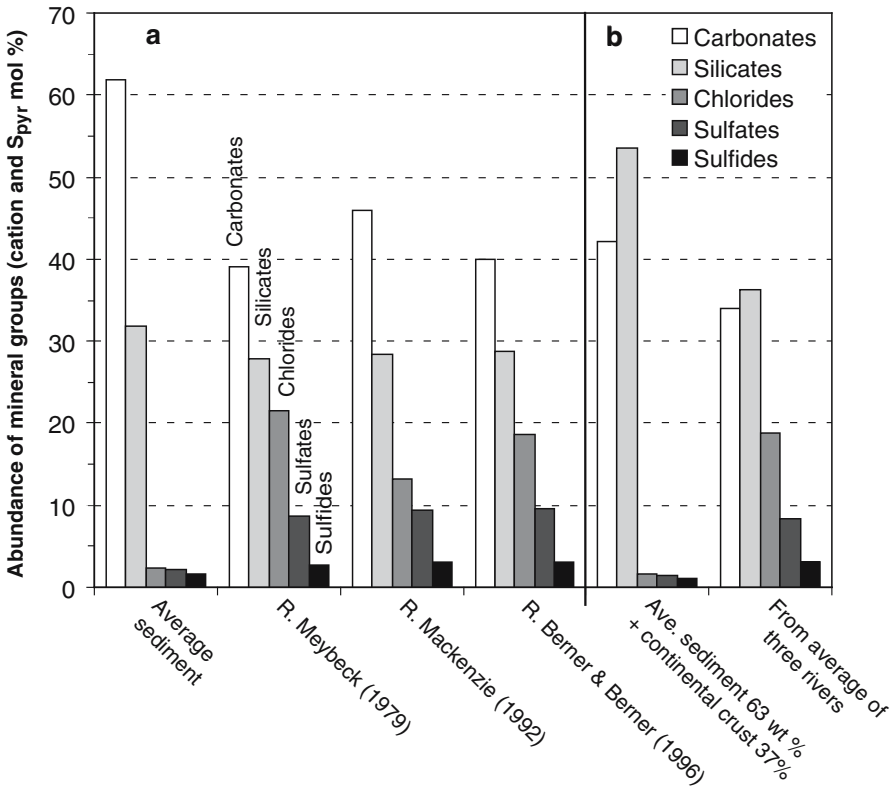

Fig. 13.11 **a**. Mineral composition of an average sediment and of the sediment "precipitated" from three average rivers (R.). Removal of elements from river water into minerals in the same proportions as in an average sediment (Tables 13.5, 13.6, and 13.8). **b**. mineral composition of a weathering source consisting of 63 wt % average sediment and 37% upper continental crust, and minerals "precipitated" from an average river. Removal of elements from river water into minerals in the same proportions as their occurrence in the weathering source

(Ca, Mg, Na, K), chlorides (NaCl), sulfates $(CaSO_4)$, and sulfides (S_{pyr}), are shown in Fig. 13.11a. Carbonates are the most abundant minerals in the average sediment source and in the calculated source of the three average rivers. However, inclusion of the continental crystalline crust in the weathering source rock, as 37 wt % crust and 63 wt % average sediment, increases the abundance of silicates, as shown in Fig. 13.11b. For this source, the fractions of S_{pyr} of total S (0.244) and of Ca in Ca-Mg carbonates (0.855) remain unchanged, but the mol fraction of Ca-carbonate in the combined Ca-carbonate and Ca-silicate minerals is smaller than in an average sediment source, as was given earlier in this section, 0.927:

3b. Ca-carbonate mol fraction of Ca-carbonates and Ca-silicates: 0.771

The larger proportions of the cations in silicates in the sediment + crust source are also reflected in a larger fraction of silicates in the precipitated minerals. From the "backward precipitation" method applied uniformly to three global average

Table 13.10 Cation, S_{pyr}, and HCO_3^- sources in three world average rivers (mol %). Percentages shown are for concentrations in mol/g rock contributing to river water

	Meybeck (1987)	This Study	Mackenzie (1992)	This Study	Berner and Berner (1996)	This Study
Cations (Ca^{2+}, Mg^{2+}, Na^+, K^+)						
Carbonates	46.7	39.1	45.2	43.5	39.7	39.9
from reaction with CO_2		35.4	41.5	39.5		35.9
from sulfuric acid dissolution		3.7	3.7	4.0		4.1
Silicates	37.4	27.9	29.6	30.9	30.7	28.7
from CO_2 and Ca-Mg-sil reactions	11.1	14.8	13.7	15.6		15.3
from CO_2 and Na-K-sil reactions	26.3	11.6	13.7	13.7		11.7
from sulfuric acid dissolution		1.5	2.1	1.6		1.7
Evaporites	15.9	30.3	22.2	22.6	29.6	28.3
NaCl	9.1	21.6	13.3	13.3		18.6
$CaSO_4$	6.8	8.7	8.9	9.3		9.6
Pyrite S^- (oxidized to SO_4^{2-})		2.8	3.0	3.0		3.1
HCO_3^- from carbonates	69.5	64.4	69.1	64.9	62.2	64.2
from Ca and Mg carbonates	65.6	61.2	66.3	61.8		60.7
from sulfuric acid dissolution	3.9	3.2	2.9	3.1		3.5
HCO_3^- from silicates	30.5	36.3	30.9	35.1	37.8	35.8
from Ca and Mg silicates		26.3	20.1	24.4		25.9
from Na and K silicates		10.0	10.7	10.7		9.9
HCO_3^- from atmosphere or soil CO_2	65.3	66.2	65.4	66.0	68.9	66.2
HCO_3^- from carbonates	34.8	33.8	34.6	34.0	31.1	33.8

rivers (the Meybeck, Mackenzie, and Berners), the CO_2 consumption in weathering that produces the given river composition is given in Table 13.10 where it is also compared to the estimates of the authors cited. Our calculated values agree closely with their results. The calculated CO_2 consumption to HCO_3^- production ratio is $\psi_1 = 0.66$, as explained in Sect. 13.8.2 and shown in Table 13.10; the three authors' estimates are $\psi_1 = 0.65$–0.69. Including the estimates of Holland (1978) and Gaillardet et al. (1999), the range is $\psi_1 = 0.63$–0.69.

It should be noted that the mineral reactions with H_2SO_4 from pyrite oxidation account for about 5% of the silicate-mineral dissolution and about 10% of the carbonate dissolution. The results of CO_2 consumption given in Table 13.10 may be compared with those in Table 13.5. The differences between the average sediment and the sediment source calculated from the river-water composition may be attributed to the differences between the dissolution rates of individual minerals, as will be discussed in the next section.

13.8.4 Mineral Dissolution Model

An average river water composition is a product of the weathering reactions between the continental sedimentary and crystalline lithosphere and atmospheric waters percolating through the soils and rocks. The water composition depends on the

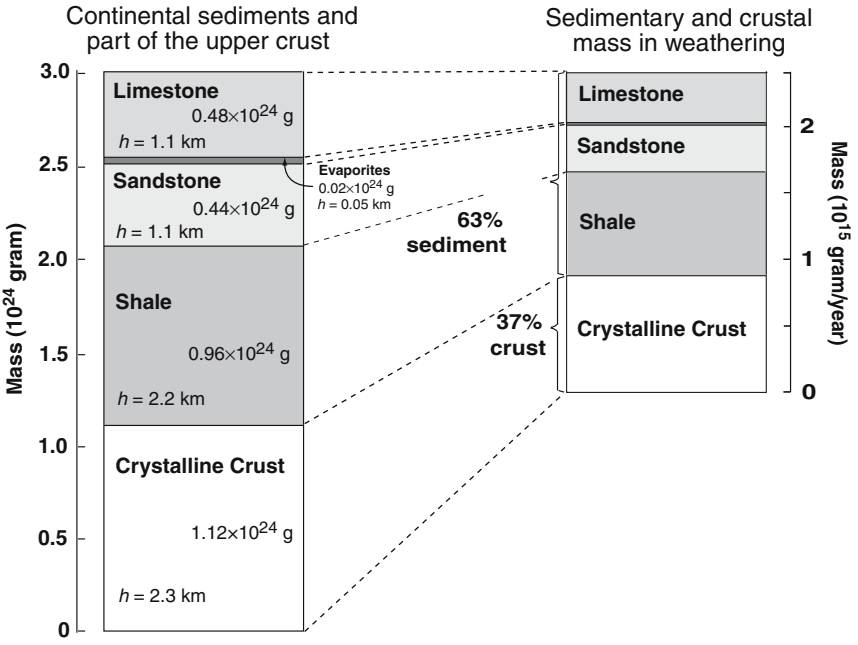

Fig. 13.12 The mass of the lithologic constituents of continental sediments and part of the continental upper crust that are the weathering source in a dissolution model (Table 13.5 and Fig. 7). On the right is shown the mass transported as dissolved solids by world rivers. Note the difference between the scales of the two parts of the figure and that the chemical denudation rate is much lower than the physical denudation and recycling of the sediments (Sects. 13.6.3 and 13.7.4)

mineral masses that react and dissolve, as well as the rates of the carbonate, silicate, and evaporite mineral dissolution that vary greatly in laboratory studies and field observations. The masses of the continental sediments and upper part of the continental crystalline crust that amount to 3×10^{24} g or about 6.5 km in thickness are schematically shown in Fig. 13.12, spread over the area of the continents and continental shelves, 177×10^6 km^2. Only a very small fraction of this mass is dissolved by waters discharging to the oceans. The figure shows that on a global scale chemical weathering or denudation of the continents is a much slower process than mechanical denudation and sediment recycling that are discussed in Sect. 13.7.4. An average sediment or a composite weathering source consisting of an average sediment and upper part of the continental crust has a chemical composition that differs significantly from that of an average river water. The compositional differences between the individual average rivers and an average sediment, and between the rivers and a source consisting of 63% average sediment and 37% continental crust, come to light in the molar concentration ratios ion/HCO_3^- that are shown in Fig. 13.13a.

Relative to an average sediment, river water is variably enriched in Ca^{2+}, Mg^{2+}, Na^+, Cl^-, and SO_4^{2-}. No single mix of an average sediment and continental crust

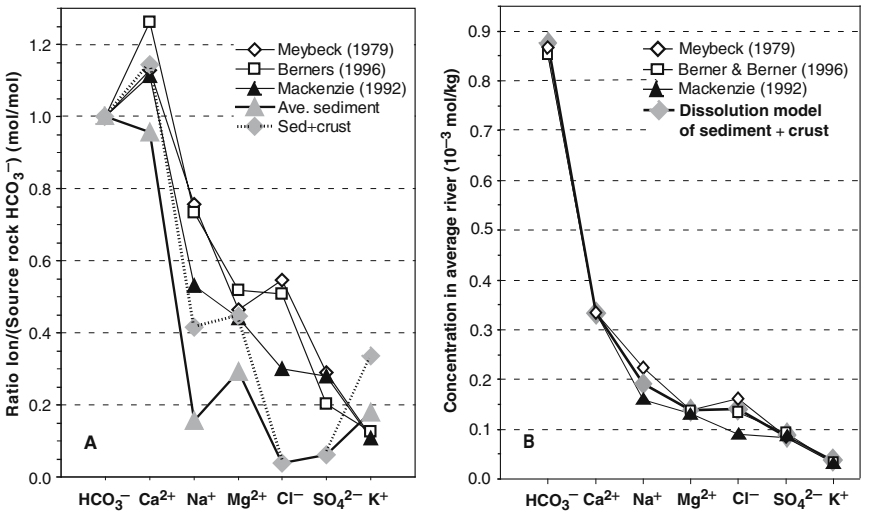

Fig. 13.13 **a**. Ratios of CO_2 to cationic and anionic mineral constituents in an average sediment, in a composite weathering source consisting of 63 weight % average sediment and 37% continental upper crust, and ratios of HCO_3^- derived from the CO_2 of sediment carbonates to other ions in three world average rivers (Table 13.5). **b**. Calculated concentrations of the major ions from the dissolution of a weathering source rock consisting of 63% average sediment and 37% continental crust. and those in the three average rivers

satisfies all the ion/HCO_3^- ratios of the average rivers, and this suggests that river-water constituents are derived from minerals dissolving at different rates. A mass balance relationship between the supply of Ca to river water and its removal by river flow may demonstrate the essential point of the dissolution model. In the weathering rock source, Ca occurs in $CaCO_3$, Ca-silicate, and $CaSO_4$, and dissolution of these minerals results in a Ca^{2+}-ion concentration in river water, C_{Ca}. A balance can be written as:

$$(X_{\text{Ca-carb}}k_{\text{Ca-carb}} + X_{\text{Ca-sil}}k_{\text{Ca-sil}} + X_{\text{Ca-sulf}}k_{\text{Ca-sulf}})M_{\text{rock}} = C_{\text{Ca}}F_{\text{river}} \qquad (13.34)$$

where $X_{\text{Ca-mineral}}$ is Ca concentration in the source rock (mol Ca/g rock), k_{mineral} is a dissolution rate parameter of a mineral (year^{-1}), M_{rock} is the rock mass undergoing weathering (g), and F_{river} is water discharge (kg/year or m^3/year)). From the known Ca-mineral concentrations that occur in different rock types and the Ca concentration in river water, the factors $k_{\text{mineral}} \times M_{\text{rock}}/F_{\text{river}}$ (g rock/kg river water) are determined empirically and the uptake of CO_2 in mineral dissolution and production of HCO_3^- are calculated simultaneously. The consumption of CO_2 in weathering reactions and production of the bicarbonate ion are the results of the mineral dissolution computation, and their values provide an additional check of the procedure. Furthermore, the calculated concentrations of the individual ions in river water, including HCO_3^- that is only in part derived from the weathered rock, shown in Fig. 13.13b, are within the range of values of the different average river

Table 13.11 Order of relative dissolution rates in the weathering of an average sediment and upper continental crust, the $CaCO_3$ dissolution rate taken as 1. ψ is the ratio of (CO_2 consumed)/(HCO_3^- produced), (Eq. (13.31) and Tables 13.10, 13.12. Details in the text)

	Na-,K-, Mg-chlorides	**Ca-sulfates**	**S_{pyr} to SO_4^{2-}**	**Mg-silicates**	**(Ca,Mg) CO_3**	**Ca-silicates**	**Na-silicates**	**K-silicates**	ψ
Dissolution of average sediment + crust[a]	×15.0	×7.8	×3.3	×1.4	×1	×1	×0.6	×0.4	0.72
Precipitation of average sediment + crust[b]	×13.7	×7.7	×3.2	×1.4	×1	×1	×0.7	×0.4	0.72

[a] From average sediment 63 wt % and crystalline crust 37 wt % (16% carbonate rocks, 32% shale, 15% sandstone, 1% evaporites, 37% upper crust; Table 13.5).
[b] Removal or precipitation from an average river water of dissolved solids as minerals in the proportions of their occurrence in a weathering source consisting of 63 wt % average sediment and 37 wt % crystalline crust (Fig. 13.11).

compositions. The calculated river concentrations are for the weathering of a source consisting of 63 wt % sediments and 37 wt % upper continental crust or, in rounded numbers, 16% carbonate rocks, 32% shale, 15% sandstone, 1% evaporites, and 37% silicate crust. The agreement between the model results and the reported average river concentrations is good in light of the differences between the individual average rivers and the uncertainties involved in the composition of an average sediment.

A relative dissolution rate of a mineral is represented by a factor, greater or smaller than 1 (Table 13.11), in the following general sequence from the less stable in weathering to the more stable, as is also shown in Fig. 13.14:

$$\text{Chlorides} \rightarrow \text{Sulfates} \rightarrow \text{Pyrite} \rightarrow \text{Mg-silicates} \rightarrow \text{Carbonates} \rightarrow \text{Ca-silicates} \rightarrow \text{Na-silicates} \rightarrow \text{K-silicates}$$

The relative dissolution rate factors are analogous to the Goldich stability series of minerals in the weathering cycle that was introduced by Goldich (1938; Pettijohn, 1957; Lerman, 1979; Lasaga, 1998) for the silicates from studies of the suspended load of rivers and further developed by Stallard (1988) from studies of weathering of different rock types in the tropical Amazon River basin. The results show that the evaporite mineral chlorides and sulfates dissolve faster than carbonates, and pyrite is also oxidized faster than the carbonate dissolution. For the silicate minerals, Mg-silicates weather somewhat faster than carbonates, but Ca-, Na- and K-silicates slower than carbonates. Among the latter three, the order of stability agrees with the observations of Ca-rich plagioclases dissolving faster than Na-plagioclases.

The mineral relative dissolution rates, within their value range given in Table 13.11, produce a mean river composition that is shown by the thick black line in Fig. 13.13b. These rates agree well with the relative mineral masses precipitated

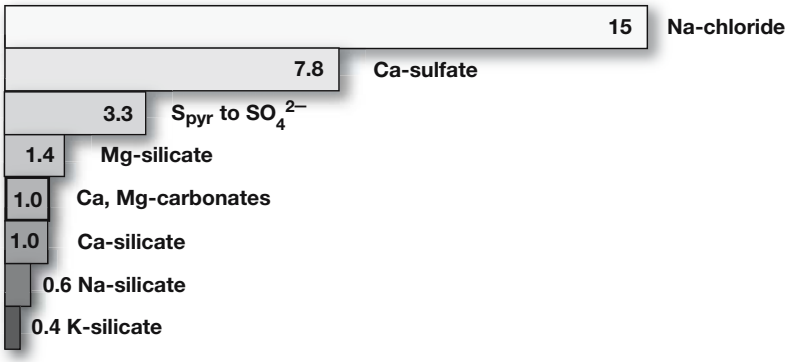

Fig. 13.14 Relative order of mineral stability in chemical weathering of a source consisting of 63% average sediment and 37% upper continental crust that corresponds to the ion concentrations in an average river (Fig. 13.13b)

from an average river water in the proportions of their occurrence in the sediment + crust weathering source (Table 13.11). The proportions of the main constituents in an average river water, derived from the dissolution model, are given in Table 13.12. The ratio of CO_2 consumed to HCO_3^- produced $\psi = 0.72$ is higher than 0.65–0.69 that was derived from the mineral precipitation model (Table 13.10). In the latter, an average sediment was taken as a weathering source rock, but for a source rock that is richer in metal silicates, more CO_2 is consumed, and this is reflected in the value of $\psi = 0.72$ both in the case of precipitation or dissolution from a mixed source (Figs. 13.11b, 13.13b).

On the basis of carbon isotopic data, Mook and Tan (1991) concluded that the main source of dissolved inorganic carbon in rivers (DIC) is "CO_2 derived from the decay of organic matter in continental soils and from the dissolution of carbonate, while in general the contribution of atmospheric CO_2 is negligibly small." From their data on the present-day $\delta^{13}C$ of soil CO_2 $(-26‰)$ and HCO_3^- in rivers $(-12‰)$, the Phanerozoic sedimentary carbonates $(+1.5‰)$, and fractionation

Table 13.12 Proportions of ionic constituents (mol %) in an average river water derived from a source consisting of 63 wt % average sediment and 37 wt % crystalline crust (Fig. 13.12, Table 13.5)

Balance	Ca^{2+}	Mg^{2+}	Na^+	K^+	Cl^-	SO_4^{2-}	HCO_3^-	
From atmosphere/soil CO_2								**72**
From silicate minerals and CO_2	18	71.3	27.6	83.0			46	
From carbonate minerals and CO_2	59.8	24.4					53	**28**
From evaporite minerals	19.4	1.6	70.7	2.7	100	75.6		
From H_2SO_4 reactions	2.9	2.7	1.7	14.3		24.4	1	
Total	100	100	100	100	100	100	100	100

factors between $HCO_{3(aq)}^-$ and $CO_{2(g)}$ it is possible to estimate the fraction of soil organic matter that contributes to the dissolved HCO_3^- in rivers and shallow groundwaters. The $\delta^{13}C$ of HCO_3^- in rivers can vary greatly (-17.3 to $+0.7‰$) (Cameron et al., 1995; Yang et al., 1996; Amiotte-Suchet et al., 1999; Probst and Brunet, 2005). It has been suggested by these authors that HCO_3^- in rivers is mainly from carbonate dissolution in soils mediated by bacteria- and plant-derived CO_2 and in-stream processes, and the isotopic exchange with the atmosphere plays an important role in controlling the heavier $\delta^{13}C_{DIC}$ in river waters. Modern soil carbonate $\delta^{13}C$ was reported as ranging from $-10.3‰$ to $1.1‰$ (Cerling, 1984). The soil-respired CO_2 deeper in the soil is characterized by $\delta^{13}C$ of about -21 to $-24‰$ (Dudziak and Halas, 1996; Hahn and Buchmann, 2003, 2005), whereas heavier $\delta^{13}C$ values may occur at shallower depths, of about 30 cm (Rightmire, 1978), where CO_2 in the soil pore space may exchange with atmospheric CO_2 of $\delta^{13}C \approx -7.5‰$. The fractionation of $^{13}C/^{12}C$ in a gas-solution system makes $HCO_{3(aq)}^-$ heavier than $CO_{2(g)}$ by $9.5‰$ at $10^\circ C$ and by $7.9‰$ at $25^\circ C$ (Mook et al., 1974; Friedman and O'Neil, 1977). With the preceding fractionation and $\delta^{13}C$ values of Mook and Tan (1991), cited above, the following balance equation gives fraction x of soil CO_2 in rivers:

$$\begin{aligned} &[-26‰ + (9.6 \text{ to } 7.9)‰]x + 1.5‰(1-x) = -12‰; \\ &x = 0.69 \text{ to } 0.75 \end{aligned} \tag{13.35}$$

Thus 69–75% of HCO_3^- is derived from soil CO_2 that reacts with the silicates and carbonates and the remaining 31–25% from the weathering and dissolution of carbonates. The soil source of CO_2 in weathering was also advocated by Berner and Berner (1996).

To summarize, estimates of ratio ψ range from 0.65 to 0.75, including the values computed from the precipitation and dissolution models (Tables 13.10 and 13.12). They correspond to a global CO_2 uptake in mineral weathering reactions of 20 to 24×10^{12} mol C/year, at the rate of HCO_3^- transport by rivers of 32×10^{12} mol C/year.

13.9 Environmental Acid Forcing

In addition to carbon dioxide, other acids in the environment may play variable roles in weathering, such as the organic acids in soils and nitric and sulfuric acids. The specific effects of such acids on a global scale are not well known, but their occurrence and behavior are often reported on local scales where pollution from industrial sources or sulfur emissions from volcanic eruptions is significant. During the Industrial Age of the last 200–300 years, fossil fuel burning has been the main source of nitrogen and sulfur oxide (NO_x and SO_2) emissions to the atmosphere. Some of the oxides become nitric and sulfuric acids, although not all the emitted nitrogen and sulfur return to the land surface and oceanic coastal zone, and the parts that return may not all be in the form of HNO_3 and H_2SO_4, and their involvement in the biological production and decomposition of organic matter leads

to the utilization of nitrate and sulfate, and their subsequent reduction or modification by bacteria in soils and water. In the year 2000, the emissions of N and S to the atmosphere were of a comparable magnitude: about 70×10^6 ton S/year (Mt S/year) or 2.2×10^{12} mol S/year, and about 30×10^6 ton N/year or 2.1×10^{12} mol N/year. One of the estimates of sulfur emission for the year 2015 projects a rise to as high as 100 Mt S/year or 3.1×10^{12} mol S/year (Brown et al., 1997; Dignon, 1992; Dignon and Hameed, 1989; Hameed and Dignon, 1992; Ver et al., 1999; Nakićenović et al., 2000). For the purpose of demonstrating the potential effect of H_2SO_4 on mineral weathering, the latter value may be considered an upper bound of anthropogenic addition of sulfuric acid to the environment. It should nevertheless be noted that even if only a fraction of sulfur emissions is converted to sulfuric acid, it is likely that at least some of this H_2SO_4 on the land surface is neutralized fast by reactions with minerals: addition of non-neutralized H_2SO_4 at a current rate of about 2×10^{12} mol S/year to the volume of freshwater lakes of 125×10^3 km^3 and(or) the volume of soil water to depth of 10 m, 121×10^3 km^3 (Lerman, 1994; Berner and Berner, 1996; Ver, 1998), would add 1.6 to 3.3×10^{-5} mol H^+/kg to the continental waters and, if not neutralized, make them much more acidic than the range of 3×10^{-7} to 3×10^{-8} mol H^+/kg (pH $\approx$ 6.5–7.5). In local environments and where freshwater lakes occur in crystalline-rock drainage basins, the observed water acidification is likely to be a combined effect of acid deposition and slow reaction rates of silicate minerals. Lakes in Scandinavia, Swiss Alps, parts of Canada, and Eastern United States include many acidic lakes among several thousand lakes of surface area < 20 km^2 (Overton et al., 1986; Lerman, 1979; Berner and Berner, 1996).

In comparison to the CO_2 consumption in weathering, the consumption of H_2SO_4 that forms from pyrite oxidation is much smaller, $0.64 \pm 0.15 \times 10^{12}$ mol S/year, based on the pyrite-derived fraction of 24.4% of total dissolved SO_4^{2-} in the Meybeck, Mackenzie, and Berners average rivers (Table 13.9). The projected flux of 3.1×10^{12} mol S/year is 5 times greater than the natural H_2SO_4 flux from oxidation of pyrite in sediments. An increasing input of anthropogenic H_2SO_4 to the weathering system would result in additional dissolution of metal carbonates and silicates in the sediments and crust, and increase the concentration of dissolved solids and the sulfate-ion in river water (Fig. 13.15). An estimated upper bound of the input of anthropogenic sulfuric acid to the weathering cycle would increase the H_2SO_4 fraction in the reactive CO_2–H_2SO_4 mix in an average sediment from the present value of 1.8 mol%, that is shown in Fig. 13.10, to 8.6%.

However, this addition would have only a very small effect on the CO_2 consumption to HCO_3^- production ratio. This is in agreement to the results from a model simulation by Amiotte-Suchet et al. (1995) that the global uptake of CO_2 would be decreased by no more than 10%. Thus the consequences of H_2SO_4 deposition on the continental surface seem to be mainly in its effects on local water systems and ecological communities of land plants, and on primary producers and higher animals in bodies of water, rather than on the global carbon dioxide consumption in weathering.

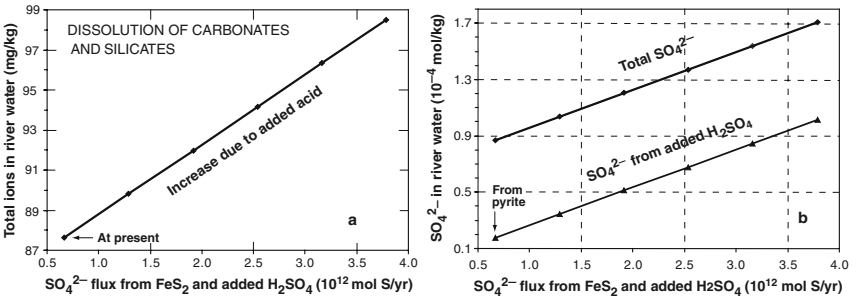

Fig. 13.15 Computed results of addition of anthropogenic H_2SO_4 to the weathering cycle. **a**. Increase in concentration of total dissolved ions in an average river due to anthropogenic acid addition. **b**. Increase in total and acid-derived SO_4^{2-} in an average river

13.10 CO_2 in the Global Carbon Cycle

13.10.1 Cycle Structure and Imbalances

The global carbon cycle, probably the most extensively studied biogeochemical cycle, can be represented by three major domains – atmosphere, land, and ocean – and interreservoir fluxes that are shown in Fig. 13.16 and their main values that are summarized in Table 13.13.

Secular changes in the carbon reservoir sizes over geologic time imply that the cycle is to a variable degree imbalanced. Net imbalance of a reservoir is the difference between the sum of the input fluxes and the sum of outflows. Although most of the estimated flux imbalances in the major reservoirs are small fractions of the total inputs or outputs, they provide important information on the cycle dynamics at geologically short time scales of 10^2–10^4 years. At the current state of knowledge of the reservoir sizes and fluxes, the carbon cycle is not balanced at the end of pre-industrial time, about 300 years ago, nor in Last Glacial Maximum time (LGM), about 18,000 years ago. In pre-industrial time, the imbalances of the atmosphere and land organic reservoir are small, but the surface ocean shows a loss of about -22×10^{12} mol C/year. At both periods, net storage of inorganic and organic carbon in oceanic sediments and its transfer to the atmosphere by the CO_2 flux at the ocean surface exceed the riverine input of carbon to the surface ocean layer. In this cycle representation, the CO_2 sea-to-air flux is driven by CO_2 production from $CaCO_3$ formation and oxidation of organic matter in the surface ocean layer, and the carbonate and organic carbon net storage in sediments (Lerman and Mackenzie, 2005). A better understanding of these imbalances would lead to a better understanding of the cycle kinetics at geologically different time scales. The atmospheric imbalance could be much greater if the net CO_2 consumption in rock weathering, about 22×10^{12} mol C/year, were by direct outflow from the atmosphere rather than from soil, as shown in Fig. 13.16. Although the atmospheric CO_2 concentration is believed to have varied greatly through the Phanerozoic, in response to changes in

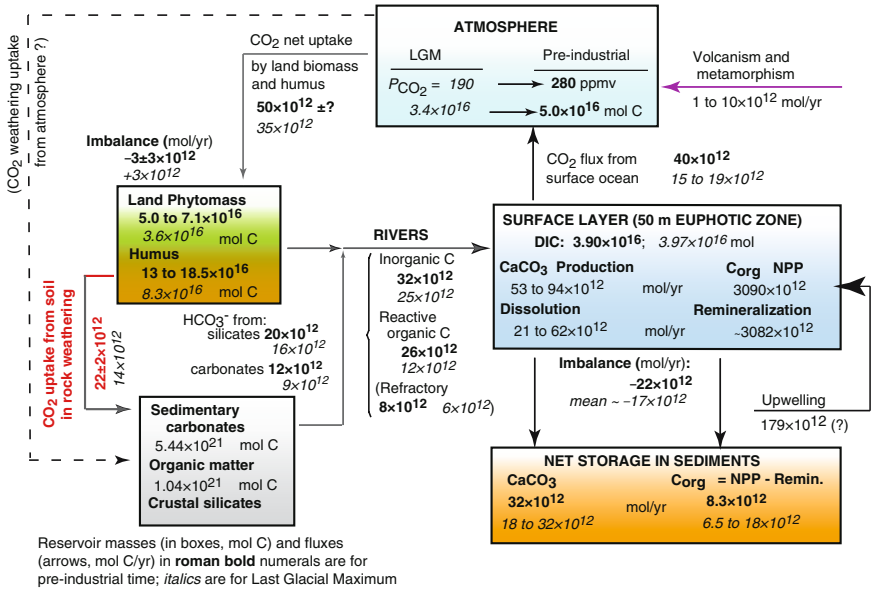

Fig. 13.16 Global carbon cycle at the end of pre-industrial time, taken as the year 1700, and at the last glacial maximum, about 18,000 year ago, showing the three main domains of the land, ocean, and atmosphere, interreservoir fluxes. The CO_2 weathering flux reacting with sedimentary and crystalline rocks is coming from the soil in the land organic reservoir. Data mostly from Lerman and Mackenzie (2005), recalculated for the LGM mean temperature of 11° C (see also color insert)

biological, tectonic, hydrological, and climatic factors (e.g., Berner and Kothavala, 2001), a complete depletion of one of the major carbon reservoirs is not a geological possibility. The land gains carbon from the atmosphere due to primary production of land plants that stores more organic carbon on land than is remineralized from the soil humus and exported by rivers to the ocean. Thus the current imbalances, taken at their face value, could not last a long time and the fluxes would have to change to maintain a secular balance within the cycle.

13.10.2 Changes in CO_2 Uptake in Weathering

Atmospheric CO_2 concentration near the Last Glacial Maximum was close to 190 ppmv (Petit et al., 1999; Wahlen, 2002) and it increased to 280 ppmv by the end of pre-industrial time near the year 1700 (Siegenthaler and Oeschger, 1987). The increase of 90 ppmv over a period of 18,000 years was neither smooth nor linear with time, but it translates into an average increase rate of 0.9×10^{12} mol C/year (0.01 Gt C/year). This is a small value in comparison to the fluxes between the major reservoirs of the pre-industrial and LGM carbon cycle that are in the range from about 15 to 50×10^{12} mol C/year (0.2–0.6 Gt C/year), such as the net storage of

Table 13.13 Reservoir sizes and fluxes of the pre-industrial carbon cycle (Fig. 13.16)

Reservoirs	**mol C**	**Reference**
Atmosphere	5×10^{16}	280 ppmv CO_2
Land	22×10^{16}	
Phytomass	$6 \pm 1 \times 10^{16}$	Lerman et al. (1989), Friedligstein et al. (1995), Ver et al. (1999)
Humus	$16 \pm 3 \times 10^{16}$	Ajtay et al. (1979) Friedligstein et al. (1995)
Sediments	6.48×10^{21}	
Carbonates	5.44×10^{21}	Li (2000)
Organic carbon	1.04×10^{21}	Li (2000)
Fluxes	$\mathbf{10^{12}}$ **mol C/year**	**Reference**
To atmosphere	5250	
From volcanism and metamorphism	6 ± 4	Mackenzie (1992) Mackenzie et al. (1993)
From surface ocean	40 ± 2	Lerman and Mackenzie (2005)
From humus	5200	Ver et al. (1999)
From atmosphere		
To land biota	$-5250 \pm ?$	Ver et al. (1999)
To land		
From atmosphere net	$50 \pm ?$	Ver et al. (1999)
From land (organic C)	-34	
To surface ocean	-26	Ver et al. (1999)
To ocean sediments	-8	Ver et al. (1999)
To surface ocean $(DIC + C_{org})$		
From land and rocks	56 ± 2	
From surface ocean	-80	
To atmosphere	-40 ± 2	Lerman and Mackenzie (2005)
To ocean sediments	-40	Milliman (1993) Mackenzie et al. (2004)

organic carbon on land, uptake of CO_2 in rock weathering, carbon transport to the ocean, and sea-to-air CO_2 flux. However, the present data base is not sufficiently detailed to allow flux estimates with an accuracy that would make 0.9×10^{12} mol/year a significant net imbalance of one of the major reservoirs, such as the atmosphere.

For the time near the Last Glacial Maximum (LGM) 18,000 years ago, estimates of the CO_2 consumption in weathering and riverine transport of HCO_3^- vary considerably. Gibbs and Kump (1994) estimated that the HCO_3^- flux at the LGM was 20% higher than at present. Ludwig et al. (1999) found that the overall CO_2 consumption at the LGM was about 20% greater than at present and attributed this to a greater carbonate outcrop area; in their estimate, the uptake by silicate weathering decreased by $\sim 10\%$ due to deceasing runoff at the LGM compared to the present. Munhoven (2002) reported from several Global Circulation Models that total CO_2 consumption in rock weathering at the LGM was higher by 2.7 to 5.3×10^{12} mol/year and the HCO_3^- flux was higher by 5.8 to 10.3×10^{12} mol/year than at present. Higher

dissolution rates in LGM time may conceivably be due to the grinding effects of ice on the size and surface area of mineral particles (Gíslason et al., 1996, with references to earlier work). Field and laboratory studies also suggested that glaciers can produce a significant amount of highly reactive mineral surface area which will then increase silicate weathering fluxes (Anderson et al., 2000; Anderson, 2005). Foster and Vance (2006) find that the weathering rates in the glaciated interior of the North Atlantic region were two to three times lower during glacial periods than during the interglacial phases. However, in their estimation, this decrease was balanced by an increased weathering of carbonates exposed on the continental shelves, such that the overall chemical weathering rate did not change much during the Pleistocene glaciations. They report for the Holocene, 1–11 ka ago, a weathering rate about 20% lower than that for the Slave Province of Canada, 0.35 g m^{-2} $year^{-1}$ (Millot et al., 2002), the latter being the lowest in the estimated range for granitoid terrains (Sect. 13.7.1). Lerman and Mackenzie (2005) estimated the CO_2 uptake in weathering at the LGM lower than at the end of pre-industrial time, based on smaller land surface area, lower temperature, and smaller river discharge. Possible effects of relatively small changes in the CO_2 atmospheric partial pressure from the Last Glacial Maximum to the end of pre-industrial time, such as an increase from 1.9×10^{-4} to 2.8×10^{-4} atm, on the mineral weathering rates are not well known.

We consider two main effects on the CO_2 consumption rate in weathering: the exposed land surface area and temperature. As the sea level at the LGM was lower by about 120 m, increasing the exposed area of the continental shelf, and the ice-covered land area greater than at present, the net non-glaciated continental area at the LGM was about 92% of the present-day area (fraction $f_L = 0.92$). The global mean Earth's surface temperature, as shown in Fig. 13.17c, curve 1, has increased from 11° to 15° C, with a dip of about 2° C in the Younger Dryas, mostly observed in the North Atlantic latitudes, and a rise of about 1° C in the Mid-Holocene maximum relative to the present. Some regional histories of temperature change since the LGM show different patterns. The temperature record in the Benguela upwelling region, Southwest Africa, based on the Mg/Ca abundance ratio in foraminifera and shown in Fig. 13.17c, curve 2, presents a pattern considerably different from the global average curve. A sediment record from a tropical lake, Lake Malawi (Nyassa), based on the organic analytical technique TEX_{86} (Fig. 13.17b), shows considerably higher temperatures since the LGM to the present, and a pronounced Mid-Holocene maximum. Pre-industrial CO_2 consumption rate in weathering, 22×10^{12} mol/year, is reduced by the surface area of non-glaciated land and the slower dissolution rates of the silicate and carbonate minerals at a mean LGM temperature that was about 4° C lower than at present. A representative value of the activation energy of silicate dissolution is $\Delta E = 15$ kcal/mol (Brady, 1991; Berner, 1994) and that of $CaCO_3$ near equilibrium is about 8.4 kcal/mol (Gutjahr et al., 1996; Morse and Arvidson, 2002). The activation energy term that controls the change in the dissolution rate with temperature is constrained for silicates by a range from 7.1 to 19.2 kcal/mol, and a mean value of $\Delta E = 18.4$ kcal/mol for feldspars near neutral pH (Velbel, 1993). Accordingly, for a temperature decrease from 15° to 10.7° C (Fig. 13.17c, curve 1), the reduction factors for the dissolution rate of the silicates (f_{Tsil}) and

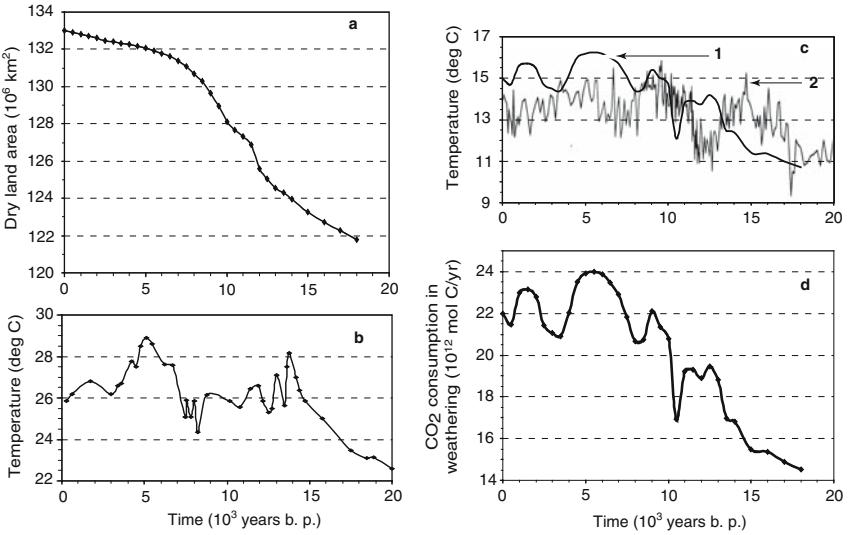

Fig. 13.17 Global and regional changes in dry land area and temperature since the last glacial maximum and calculated CO_2 weatherinig flux. **a**. Dry land area calculated from the sea-level curve and ice-covered area. **b**. Temperature record of sediments in lake Malawi (Nyassa), based on the organic anayltical method TEX_{86} (Powers et al., 2005). **c**. Curve 1, global mean temperature (UCAR/OIES, 1991); curve 2, temperature record from Mg/Ca abundance ratio in foraminifera, Bernguela upwelling region, Southwest Africa (Farmer et al., 2005). **d**. CO_2 weathering flux, calculated as explained in the text (modified from Lerman et al. 2006)

carbonates (f_{Tcarb}) are approximately:

$$\ln f_{\mathrm{Tsil}} = \frac{\Delta E}{R}\left(\frac{1}{T_0}-\frac{1}{T}\right) = \frac{15}{1.987\times 10^{-3}}\left(\frac{1}{288}-\frac{1}{284}\right) = -0.397; f_{\mathrm{Tsil}}=0.67; \tag{13.20}$$

$$\ln f_{\mathrm{Tcarb}} = \frac{\Delta E}{R}\left(\frac{1}{T_0}-\frac{1}{T}\right) = \frac{8.4}{1.987\times 10^{-3}}\left(\frac{1}{288}-\frac{1}{284}\right) = -0.222; f_{\mathrm{Tcarb}}=0.80 \tag{13.21}$$

where temperature T is in kelvin (K) and the gas constant $R = 1.987 \times 10^{-3}$ kcal mol^{-1} K^{-1}. Values of ΔE greater than those used in the preceding calculation would make the factors f_{Tsil} and f_{Tcarb} and the dissolution rates smaller. In pre-industrial time (Table 13.12), 63% or $46/(46+53/2)$ of the HCO_3^- in rivers was derived from the silicate mineral reactions with CO_2 and 37% from the reactions with carbonates. From the preceding parameters, the CO_2 consumption rate at the Last Glacial Maximum is:

$$\begin{aligned} CO_2 \text{ consumption} &= 22\times 10^{12}\times f_{\mathrm{L}}\times(0.63 f_{\mathrm{Tsil}}+0.37 f_{\mathrm{Tcarb}}) \\ &= 14.5\times 10^{12}\,\mathrm{mol/year} \end{aligned} \tag{13.22}$$

If the silicate and carbonate mineral fractions in the weathering of the lithosphere were in LGM time the same as later, then the estimate of 14.5×10^{12} mol/year of CO_2 consumption in weathering, given above, would represent a fraction 0.72 of HCO_3^- in rivers, making the total inorganic carbon flux from silicate and carbonate mineral weathering reactions 18×10^{12} mol/year. Thus, from the estimates cited above, the CO_2 consumption in weathering at the LGM might have been between our estimate of 14.5×10^{12} mol C/year and, from Munhoven (2002), 27×10^{12} mol C/year when the atmospheric CO_2 content was about 190 ppmv or 3.4×10^{16} mol C, which is 30% lower than at the end of pre-industrial time. The computed CO_2 consumption rate is shown in Fig. 13.17d. The rate is driven primarily by the global temperature change (Fig. 13.17c) that affects the dissolution rate factors f_T of the silicates and carbonates, and to a lesser extent by an increased land surface area (Fig. 13.17a) due to combined effects of the rising sea level and decrease in the continental ice cover (fraction of exposed land f_L increases from 0.92 to 1).

The organic carbon reservoir in soils has increased from about 2.5 times of the atmospheric CO_2 mass at the LGM to 3.5 times at the end of pre-industrial time (Fig. 13.16)) and, if the weathering flux of CO_2 is derived from the decomposition of soil organic matter rather than directly from the atmosphere, the bigger carbon reservoir of soils may provide a buffering effect against possibly faster changes in the consumption of atmospheric CO_2 in the weathering of sediments and upper continental crust. In the 18,000 years since the LGM to the beginning of industrial time, there has been a net increase in the mass of carbon stored in the atmosphere, land phytomass, and soil humus (Fig. 13.16), amounting to a total of about 11.5×10^{16} mol C or 1,380 Gt C. This amount is equivalent to a mean storage rate of 6×10^{12} mol C/year or 0.08 Gt C/year. In comparison to this flux, the CO_2 consumption rate in weathering, 14 to 22×10^{12} mol C/year, points to the importance of the CO_2 weathering flux as a regulator of atmospheric CO_2 and organic carbon storage on land even at geologically short time scales of 10^3–10^4 years.

13.10.3 CO_2 Weathering Pathways

The imbalances at pre-industrial time and LGM indicate potential depletion of the surface ocean layer at a time scale of 10^3 years or doubling of the carbon mass in the land organic carbon reservoir at a time scale of 10^4. These imbalances should be considered in light of the accuracy of some of the fluxes shown in Fig. 13.16. A major atmospheric imbalance of about -22×10^{12} mol C/year would arise if the CO_2 in weathering were taken directly from the atmosphere: input to the atmosphere of about 50×10^{12} mol C/year as compared to the output of $(50 + 22) \times 10^{12}$ mol C/year. One aspect of the atmospheric imbalance is the net CO_2 storage as organic carbon on land, 50×10^{12} mol C/year or 0.6 Gt C/year in pre-industrial time. Net carbon storage on land is a small difference, about 1%

of the much larger net primary production rate (NPP $= 5,250 \times 10^{12}$ mol C/year of 63 Gt C/year), that stores CO_2 in the land phytomass, and humus decomposition rate ($5,200 \times 10^{12}$ mol C/year) that remineralizes organic matter and returns CO_2 to the atmosphere (Mackenzie et al., 1993; Ver et al., 1999). However, as was pointed out earlier, the CO_2 in mineral weathering reactions is likely to be taken from soil than directly from the atmosphere, providing a buffering effect against possibly faster changes in the consumption of atmospheric CO_2 and delivery of dissolved solids to the ocean.

CO_2 drawdown in weathering, 20 to 24×10^{12} mol C/year (corresponding to a fraction of 0.65–0.75 of riverine HCO_3^-, Sect. 13.8.4) that comes from soil, has significant consequences to the global carbon balance. In fact, the occurrence of isotopically light dissolved inorganic carbon in rivers, the increase in the concentration of dissolved inorganic carbon since 1950 in the Mississippi River (Raymond and Cole, 2003), and the calculated global increase of both inorganic and organic carbon in rivers for the same time period (Mackenzie et al., 2002) are consistent with the carbon source that is the decomposition and oxidation of organic matter in soils and subsequent reactions of the CO_2 with minerals. Decomposition and erosion of humus remove to rivers 34×10^{12} mol C/year and rock weathering flux from soil CO_2 consumes $22 \pm 2 \times 10^{12}$ mol C/year, making a total removal of 54 to 58×10^{12} mol/year. Thus the land organic reservoir is close to being balanced, within about $\pm 3 \times 10^{12}$ mol C/year or between ± 0.03 to ± 0.04 Gt C/year. Between the LGM and the end of pre-industrial time, the organic carbon on land increased at a mean rate of 6×10^{12} mol C/year, as was pointed out in the preceding section. However, a nearly balanced atmosphere and land organic reservoir would leave the ocean in a negative balance, with nominal depletion times of only a few thousand years for the surface layer. A conclusion that can be drawn from the preceding discussion of the magnitudes of the inter-reservoir fluxes, the short turnover times, and imbalances rooted in the flux estimates is that the atmosphere and surface ocean are closely tied to the land and crustal reservoirs, yet the currently available observational evidence and analytical data-bases do not support a closer balanced cycle at time scales of 10^2–10^4 years.

13.10.4 Further Ties between Carbonate and Sulfate

As oxidation of the reduced sulfur in pyrite and subsequent reactions of H_2SO_4 with carbonate minerals produce HCO_3^- or CO_2 (Sects. 13.8.1 and 13.9), it is worth examining the possible consequences of a reverse process of SO_4^{2-} reduction on the carbonate balance. Most of the pyrite forms not on land but in marine sediments and its formation is commonly associated with occurrences of organic matter that reduces sulfate and an increase in the degree of supersaturation of sea water with respect to calcite (Morse and Mackenzie, 1990, p. 270; Canfield and Raiswell, 1991). An exception to the conditions that promote carbonate precipitation are the occurrences of pyrite replacing calcareous skeletons, which indicate that the carbonate

mineral dissolves before the pyrite precipitation (Canfield and Raiswell, 1991). A number of reactions between pyrite, calcium carbonate, and organic matter was discussed by Garrels and Perry (1974), and the association between these phases is represented here by the reactions listed below.

Sulfate reduction by organic matter (Berner, 1982):

$$2CH_2O + SO_4^{2-} = 2HCO_3^- + H_2S \tag{13.36a}$$

Calcite precipitation:

$$Ca^{2+} + 2HCO_3^- = CaCO_3 + CO_2 + 2H_2O \tag{13.36b}$$

Organic matter formation:

$$CO_2 + H_2O = CH_2O + O_2 \tag{13.36c}$$

Formation of pyrite (e.g., Sternbeck and Sohlenius, 1997):

$$Fe(OH)_3 + 2H_2S + 0.25CO_2 = FeS_2 + 0.25CH_2O + 3.25H_2O \tag{13.36d}$$

$$Fe(OH)_3 + H_2S = 0.5FeS_2 + 0.5Fe(OH)_2 + 2H_2O \tag{13.36e}$$

Sum of reactions (13.35a–d), with stoichiometric coefficients balanced:

$$Fe(OH)_3 + 3.75CH_2O + 2Ca^{2+} + 2SO_4^{2-} = FeS_2 + 2CaCO_3 + 1.75CO_2 + 5.25H_2O \tag{13.37}$$

The preceding reactions represent combined results of pyrite and $CaCO_3$ formation from the reduction of sulfate in water and ferric iron in sediments by organic matter. Equation (13.37) shows that formation of 1 mole pyrite or reduction of 2 moles SO_4^{2-} is accompanied by precipitation of 2 moles C in $CaCO_3$.

Global burial rate of pyrite in oceanic sediments was estimated as 1.22×10^{12} mol S/year (Berner, 1982), which is nearly twice the amount of S from the oxidation of pyrite in an average sediment that is transported by rivers, 0.64×10^{12} mol S/year, as was given in Sect. 13.9. In Eq. (13.37), the precipitated $CaCO_3$ is equal to the mass of the pyrite-sulfur stored in sediments that are relatively rich in organic carbon and form in anoxic environments where sulfate is reduced. This carbonate mass represents a fraction of 4–5% of the global $CaCO_3$ storage in sediments in pre-industrial time, estimated at between 26 and 32×10^{12} mol C/year (Fig. 13.16; Milliman, 1993; Berner and Berner, 1996; Mackenzie et al., 2004; Lerman and Mackenzie, 2005).

13.11 Summary and Overview

The concept of geochemical cycles, as they are recognized now, emerged in the 1920s on the multidisciplinary foundations that evolved since at least the late 1700s.

Simple one- or two-box cycle models, with zero order or first order fluxes, provide a background for the understanding of the more complex cycle models of global systems and geochemical processes within them. The rate parameters quantitatively characterize a cycle and connect the fluxes to reservoir masses (first-order rate constants k, of dimensions time^{-1}) or the residence times ($\tau = 1/k$). They provide the first information on rates of change in a reservoir that is perturbed by external forcings from a steady state, affecting its mass, inputs, and outflows. Under a steady perturbation, the rate constants or residence times give the length of time for the system to approach a new steady state, to a level of 95–98% of the difference between the initial and new steady-state values.

How basic kinetic relationships can be used in an analysis of a cycle is demonstrated for the phosphorus cycle that is an example of an element not only indispensable to life, but also limiting biological primary production because of the low abundance of phosphorus in natural waters.

In the global sedimentary cycle, land-surface erosion and mineral-water reactions supply the particulate and dissolved solids that are transported to the ocean. In the present-day world, the magnitudes of transport show a strong variation with geographic latitude that reflects the land surface area of the river drainage basins, amount of atmospheric precipitation, and possibly temperature dependence of bacterial activity and(or) chemical reaction rates in weathering. Physical denudation of the land surface, estimated from soil erosion rates, is considerably faster than the estimates based on the suspended solid concentrations in rivers. The difference may be attributed to a geologically short-term storage of soil-erosion products on land, such as in lower lying areas and river flood plains.

Chemical composition of river waters is the best evidence of the chemical denudation rate of the continental sedimentary and crystalline lithosphere due to mineral–water reactions occurring within some thickness of the sediments and crustal rocks. From an average river water composition, a global mean chemical denudation rate is about 27 g m^{-2} year^{-1} or about 1–2 cm/1,000 year. Of this total weathering rate, about 10–15 g m^{-2} year^{-1} is attributable to the dissolution of silicates, the remainder coming from the carbonates and evaporites.

The mineral sources of average river water, represented by three somewhat different compositions, were estimated by two methods: (1) "backward precipitation" or subtraction of the mineral components from solution and (2) "forward dissolution" of an average sediment and a mixed source, consisting of 63 wt % average sediment and 37 wt % crystalline crust. Because the proportions of the major cations and anions in an average sediment and upper continental crust are significantly different from their proportions in river water, this suggests that the individual minerals dissolve at different rates. The results give a computed river-water composition that is well within the variation range of the reported values, and they also give a relative order of increasing mineral resilience in weathering, from the least stable chlorides to monovalent-cation silicates, that agrees in part with the mineral stability sequences in weathering, as reported in the literature.

CO_2 and sulfuric acid (H_2SO_4), forming in the oxidation of pyrite (FeS_2), react with carbonate and silicate minerals, producing the bicarbonate ion, HCO_3^-.

The ratio of CO_2 consumed to HCO_3^- produced depends on the proportions of the carbonic and sulfuric acids in the solution and mineral composition of the weathering source. The weathering potential is the ratio $\psi = (CO_2 \text{ consumed})/(HCO_3^- \text{ produced})$ that is a function of both the mineral-cation carbonate and silicate mol fractions in the rock and the mol fractions of CO_2 and H_2SO_4 in the reacting solution. A global range of this ratio is 0.65–0.75.

In addition to the oxidation of pyrite in sediments, the burning of fossil fuels emits sulfur that at the projected emission limit in the year 2015 may be five times greater than the sulfuric acid flux from the oxidation of pyrite. For the emitted sulfur taken as sulfuric acid, this forcing scenario indicates a significant increase in the sulfate concentration in river waters and an increase of close to 3% in dissolved ionic solids. Sulfate reduction and pyrite formation in marine sediments may contribute to precipitation of $CaCO_3$ that amounts to 4–6% of the $CaCO_3$ sediment storage rate in the ocean.

The drawdown of CO_2 in mineral weathering and dissolution reactions is an important flux of about 22×10^{12} mol C/year in the global carbon cycle, of a magnitude comparable to the storage of carbon in the land organic reservoir, riverine transport of carbon from land to the ocean, emission of CO_2 from the surface ocean to the atmosphere, and the formation and storage of carbonate and organic carbon in sediments. A pathway of CO_2 consumption in mineral weathering reactions that takes CO_2 from soil where it forms by decomposition of organic matter, rather than directly from the atmosphere, is indicated by the carbon isotopic composition of the land and atmospheric reservoirs. The current state of knowledge of the fluxes in the carbon cycle at the Last Glacial Maximum, about 18,000 years ago, and at the end of pre-industrial time, about 300 years ago, indicates significant imbalances of the individual reservoirs. The land organic reservoir, consisting of the phytomass and soil humus, has been gaining carbon since the LGM. The surface ocean reservoir, however, has been losing carbon due to a greater removal of carbonate and organic carbon into sediments and CO_2 transfer to the atmosphere that exceed the input from land. Since the LGM, the computed CO_2 uptake rate in weathering was primarily driven by the global temperature change and an increase in the exposed land area. The CO_2 consumption rate increased from 14×10^{12} to 22×10^{12} mol C/year. The total mass of carbon stored on land during the same period, about 11.5×10^{16} mol C, corresponds to an average increase rate of 6×10^{12} mol C/year, which indicates the importance of the weathering flux as one of the regulators of atmospheric CO_2 and carbon accumulation on land at time scales of 10^3 to 10^4 years and longer.

Acknowledgements

This research was supported by NSF Grant EAR-0223509 and additionally by the Arthur L. Howland Fund of the Department of Geological Sciences, Northwestern University. We thank the following individuals, in alphabetical order, for helpful discussion of the various aspects of this paper and for providing us with information

and literature sources: Susan L. Brantley (Pennsylvania State University, University Park, Penn.), Oliver A. Chadwick (University of California, Santa Barbara), James I. Drever (University of Wyoming, Laramie) for also pointing to us a possible CO_2–generating pathway in one of the weathering reactions, Gabriel Filippelli (Indiana-Purdue University, Indianapolis), C. Bryan Gregor (Wright State University, Dayton, Ohio) for permission to use one of his figures, Volker Hahn (Max Planck Institut für Biochemie, Jena) and Nina Buchmann (Eidgenössische Technische Hochschule Zürich) for unpublished data kindly made available to us, Robert D. Larter (British Antarctic Survey, Cambridge), Fred T. Mackenzie (University of Hawaii, Honolulu), Romain Millot (Bureau de Recherches Géologiques et Minières, Orléans), Michael J. Mottl (University of Hawaii, Honolulu), David W. Scholl (U. S. Geological Survey, Menlo Park, and Stanford University, Stanford, California), Arthur F. White (U. S. Geological Survey, Menlo Park, California), and Richard E. Zeebe (University of Hawaii, Honolulu). We also thank James I. Drever and Fred T. Mackenzie for reviews of this chapter.

References

Albarède F. (1995) *Introduction to Geochemical Modeling*. Cambridge University Press, Cambridge, xx + 543 pp.

Albarède F. (2003) *Geochemistry: An Introduction*. Cambridge University Press, Cambridge, xiv + 248 pp.

Alkattan M., Oelkers E. H., Dandurand J.-L., and Schott J. (1998) An experimental study of calcite and limestone dissolution rates as a function of pH from -1 to 3 and temperature from 25 to 80° C. *Chem. Geol.* **151**, 199–214.

Amiotte-Suchet, P., Probst, A., and Probst, J.-L., 1995. Influence of acid rain on CO2 consumption by rock weathering: local and global scales. *Water Air Soil Pollut.* **85**, 1563–1568.

Amiotte-Suchet P., Aubert D., Probst J.-L., Gauthier-Lafaye F., Probst A., Andreux F., and Viville D. (1999) $\delta^{13}C$ pattern of dissolved inorganic carbon in a small granitic catchment; the Strengbach case study (Vosges Mountains, France). *Chem. Geol.* **159**(1–4), 129–145.

Amram K. and Ganor J. (2005) The combined effect of pH and temperature on smectite dissolution rate under acidic conditions. *Geochim. Cosmochim. Acta* **69**, 2535–2546.

Anderson L. D., Delaney M. L., and Faul K. L. (2001) Carbon to phosphorus ratios in sediments: Implications for nutrient cycling. *Global Biogeochem. Cycles* **15**(1), 65–79.

Anderson S. P. (2005) Glaciers show direct linkage between erosion rate and chemical weathering fluxes. *Geomorphology* **67**(1–2), 147–157.

Anderson S. P., Drever J. I., Frost C. D., and Holden P. (2000) Chemical weathering in the foreland of a retreating glacier. *Geochim. Cosmochim. Acta* **64**(7), 1173–1189.

Amundson R. (2003) Soil formation. In *Treatise on Geochemistry*, Vol. 3 (ed. J. I. Drever). Elsevier, Amsterdam, pp. 1–35.

Arvidson R. S., Ertan I. E., Amonette J. E., and Lüttge A. (2003) Variation in calcite dissolution rates: a fundamental problem? *Geochim. Cosmochim. Acta* **67**, 1623–1634.

Ajtay G. L., Ketner P., and Duvigneaud P. (1979) Terrestrial primary production and phytomass. In: *The Global Carbon Cycle* (eds. B. Bolin, E. T. Degens, S. Kempe and P. Ketner), SCOPE 13 (Scientific Committee On Problems of the Environment), Unwin Brothers, Gresham Press, Kingston-on-Thames, pp. 129–181.

Bassham J. A. (1974) Photosynthesis. *Encycl. Brit., Macropaedia*, 1974 edition, **14**, 365–373.

Batjes N. H. (1996) Total carbon and nitrogen in the soils of the world. *Eur. J. Soil. Sci*. **47**, 151–163.

Bauer A. and Berger G. (1998) Kaolinite and smectite dissolution rate in high molar KOH solutions at 35 degrees and 80 degrees C. *Appl. Geochem.* **13**(7), 905–916.

Baumgartner A. and Reichel E. (1975) *The World Water Balance*. R. Oldenburg Verlag, München, Germany, 181 pp.

Becker G. F. (1910) The age of the earth. *Smithsonian Misc. Collect.* **56**, 6–28.

Berner E. K. and Berner R. A. (1996) *The Global Environment: Water, Air and Geochemical Cycles*. Prentice-Hall, Upper Saddle River, NJ, 376 pp.

Berner R. A. (1982) Burial of organic carbon and pyrite sulfur in the modern ocean: its geochemical and environmental significance. *Am. J. Sci.* **282**, 451–473.

Berner R. A. and Kothavala Z. (2001) Geocarb III: A revised model of atmospheric CO_2 over Phanerozoic time. *Am. J. Sci.* **301**, 182–204.

Berner R. A. and Maasch K. A. (1996) Chemical weathering and controls on atmospheric O_2 and CO_2: fundamental principles were enunciated by J. J. Ebelmen in 1845. *Geochim. Cosmochim. Acta* **60**, 1633–1637.

Berner R. A. and Rao J.-L. (1994) Phosphorus in sediments of the Amazon river and estuary: implications for the global flux of phosphorus to the sea. *Geochim. Cosmochim. Acta* **58**, 2333–2339.

Blum A. E. and Lasaga A. C. (1988) Role of surface speciation in the low-temperature dissolution of minerals. *Nature* **331**(6155), 431–433.

Blum A. E. and Stillings L. L. (1995) Feldspar dissolution kinetics. In *Chemical Weathering Rates of Silicate Minerals* (eds. A. F. White and S. L. Brantley). *Rev. Mineral.* **31**, 291–351. Mineralogical Society of America, Washington, DC.

Bosbach D., Charlet L., Bickmore B., and Hochella Jr. M. F. (2000) The dissolution of hectorite; in-situ, real-time observations using atomic force microscopy. *Am. Mineral*. **85**(9), 1209–1216.

Bowen N. L. (1928) *The Evolution of Igneous Rocks*. Princeton University Press, Princeton, NJ, x + 332 pp.

Brandt F., Bosbach D., Krawczyk-Baersch E., Arnold T., and Bernhard G. (2003) Chlorite dissolution in the acid pH-range; a combined microscopic and macroscopic approach. *Geochim. Cosmochim. Acta* **67**, 1451–1461.

Broecker W. S. (1974) *Chemical Oceanography*. Harcourt Brace Jovanovich, New York, x + 214 pp.

Brown E. T., Stallard R. F., Larsen M. C., Raisbeck G. M., and Yiou, F. (1995) Denudation rates determined from the accumulation of in situ-produced ^{10}Be in Luquillo experimental forest, Puerto Rico. *Earth Planet. Sci. Lett.* **129**, 193–202.

Brown L. R., Renner M., and Flavin C. (1997) *The Environmental Trends that are Shaping Our Future: Vital Signs 1997*. W.W. Norton, New York, 165 pp.

Burch T. E., Nagy K. L., and Lasaga A. C. (1993) Free energy dependence of albite dissolution kinetics at 80° C and pH 8.8. *Chem. Geol.* **105**, 137–162.

Busenberg E. and Plummer L. N. (1982) The kinetics of dissolution of dolomite in CO_2–H_2O systems at 1.5 to 65° C and 0 to 1 atm Pco_2. *Am. J. Sci.* **282**, 45–78.

Cama J., Ganor J., Ayora C., and Lasaga A. C. (2000) Smectite dissolution kinetics at 80° C and pH 8.8. *Geochim. Cosmochim. Acta* **64**, 2701–2717.

Cameron E. M., Hall G. E. M., Veizer J., and Krouse H. R. (1995) Isotopic and elemental hydrogeochemistry of a major river system: Fraser river, British Columbia, Canada. *Chem. Geol.* **122**(1–4), 149–169.

Canfield D. E. and Raiswell R. (1991) Pyrite formation and fossil preservation. In *Taphonomy: Releasing the Data Locked in the Fossil Record* (eds. P. A. Allison and D. E. G. Briggs). Plenum Press, New York, pp. 337–387.

Carslaw H. S. and Jaeger J. C. (1959) *Conduction of Heat in Solids*, 2nd edition. Oxford University Press, Oxford, x + 510 pp.

Cerling T. E. (1984) The stable isotopic composition of modern soil carbonate and its relationship to climate. *Earth Planet. Sci. Lett.* **71**(2), 229–240.

Chameides W. L. and Perdue E. M. (1997) *Biogeochemical Cycles*. Oxford University Press, New York, x + 224 pp.

Chester R. (2000) *Marine Geochemistry*, 2nd edition. Blackwell, Oxford, xiv + 506 pp.

Chou L., Garrels R. M., and Wollast R. (1989) Comparative study of the kinetics and mechanisms of dissolution of carbonate minerals. *Chem. Geol.* **78**, 269–282.

Clow D.W. and Drever J. I. (1996) Weathering rates as a function of flow through an alpine soil. *Chem. Geol.* **132**, 131–141.

Colman A. S. and Holland H. D. (2000) The global diagenetic flux of phosphorus from marine sediments to the oceans; redox sensitivity and the control of atmospheric oxygen levels. *Soc. Sediment. Geol. Spec. Pub.* **66**, 53–75.

Croll J. (1871) On a method of determining the mean thickness of the sedimentary rocks of the globe. *Geol. Mag.* **8**(97–102), 285–287.

Cubillas P., Köhler S., Prieto M., Chaïrat C., and Oelkers E. H. (2005) Experimental determination of dissolution rates of calcite, aragonite, and bivalves. *Chem. Geol.* **216**, 59–77.

Dalai T. K., Krishnaswami S., and Sarin M. M. (2002) Major ion chemistry in the headwaters of the Yamuna river system: chemical weathering, its temperature dependence and CO_2 consumption in the Himalaya. *Geochim. Cosmochim. Acta* **19**, 3397–3416.

Deer W. A., Howie R. A., and Zussman J. (1975) *An Introduction to the Rock-Forming Minerals*. Longman, London, x + 528 pp.

de Jong E. and Kachanoski R. G. (1988) The importance of erosion in the carbon balance of prairie soils. *Can. J. Soil Sci.* **68**, 111–119.

Delaney M. L. (1998) Phosphorus accumulation in marine sediments and the oceanic phosphorus cycle. *Global Biogeochem. Cycles* **12**, 563–572.

Dignon J. (1992) NO_x and SO_x emissions from fossil fuels: a global distribution. *Atmospheric Environ.* **26**, 1157–1163.

Dignon J. and Hameed S. (1989) Global emissions of nitrogen and sulfur oxides from 1860 to 1980. *J. Air Poll. Control Assoc.* **39**, 180–186.

Dong Z. B., Wang X. M., and Liu L. Y. (2000) Wind erosion in arid and semiarid China: an overview. *J. Soil Water Conserv.* **55**, 439–444.

Drever J. I. (1988) *The Geochemistry of Natural Waters*, 2nd edition. Prentice-Hall, Englewood Cliffs, NJ, xii + 388 pp.

Drever J. I. (1997) *The Geochemistry of Natural Waters*, 3rd edition. Prentice-Hall, Upper Saddle River, NJ, xii + 388 pp.

Drever J. I. and Clow D. W. (1995) Weathering rates in catchments. In *Chemical Weathering Rates of Silicate Minerals* (eds. A. F. White and S. L. Brantley). Mineralogical Society of America., Washington, DC. *Rev. Mineralogy* **31**, 463–483.

Drever J. I., Murphy K. M., and Clow D.W. (1994) Field weathering rates versus laboratory dissolution rates: an update. *Mineral. Mag.* **58A**, 239–240.

Dudziak A. and Halas S. (1996) Influence of freezing and thawing on the carbon isotope composition in soil CO_2. *Geoderma* **69**(3–4), 209–216.

Dumas J. (1842) *Essai de Statique Chimique des Êtres Organisés*, 2ème édit. Fortin, Masson, Paris, 4 + 88 pp.

Edmond J. M., Palmer M. R., Measures C. I., Brown E. T., and Huh Y. (1996) Fluvial geochemistry of the eastern slope of the northeastern Andes and its foredeep in the drainage of the Orinoco in Colombia and Venezuela. *Geochim. Cosmochim. Acta* **60**, 2949–2974.

Farmer C. E., deMenocal P. B., and Marchitto T. M. (2005) Holocene and deglacial temperature variability in the Benguela upwelling region: implications for low-latitude atmospheric circulation. *Paleoceangr.* **20**, PA2018, doi:10.1029/2004PA001049.

Faure G. (1998) *Principles and Applications of Geochemistry*, 2nd edition. Prentice-Hall, Upper Saddle River, NJ, xv + 600 pp.

Ferruzzi G. G. (1993) The character and rates of dissolution of pyroxenes and pyroxenoids. MS Thesis, University California, Davis, CA, 105 pp.

Filippelli G. M. and Delaney M. L. (1994) The oceanic phosphorus cycle and continental weathering during the Neogene. *Paleoceanography* **9**, 643–652.

Fisher O. (1900) An estimate of the geological age of the earth, by J. Joly, M.A., etc. *Geol. Mag.*, *Decade* **4** (*New Series*) **7**, 124–132.

Fleer V. N. (1982) The dissolution kinetics of anorthite $(Ca_2Al_2Si_2O_8)$ and synthetic strontium feldspar $(SrAl_2Si_2O_8)$ in aqueous solutions at temperatures below 100° C with applications to the geological disposal of radioactive nuclear wastes. Monograph, Pennsylvania State University, University Park, University Park, PA.

Foster G. L. and Vance D. (2006) Negligible glacial–interglacial variation in continental chemical weathering rates. *Nature* **444**, 918–921.

Friedlingstein P., Fung I. Y., Holland E., John J. G., Brasseur G. P., Erickson D., and Schimel D. (1995) On the contribution of CO_2 fertilization to the missing biospheric sink. *Global Biogeochem. Cycles* **9**, 541–556.

Friedman I. and O'Neil J. R. (1977) Compilation of stable isotope fractionation factors of geochemical interest, in *Data of Geochemistry*, 6th edition (ed. M. Fleischer). *U.S. Geol. Survey Prof. Pap.*, **440-KK**.

Gaffron H. (1964) Photosynthesis. *Encycl. Brit.*, 1964 edition, **17**, 855–856B.

Gaillardet J., Dupré B., Allègre C. J., and Negrel P. (1997) Chemical and physical denudation in the Amazon river basin. *Chem. Geol.* **142**, 141–173.

Gaillardet J., Dupré B., Louovat P., and Allègre C. J. (1999) Global silicate weathering and CO_2 consumption rates deduced from the chemistry of large rivers. *Chem. Geol.* **159**, 3–30.

Gaillardet J., Millot R., and Dupré B. (2003) Chemical denudation rates of the western Canadian orogenic belt: the Stikine terrane. *Chem. Geol.* **201**, 257–279.

Galy A. and France-Lanord C. (1999) Weathering processes in the Ganges-Brahmaputra basin and the riverine alkalinity budget. *Chem. Geol.* **159**, 31–60.

Garrels R. M. and Mackenzie F. T. (1967) Origin of the chemical compositions of some springs and lakes. In *Equilibrium Concepts in Natural Water Systems* (ed. W. Stumm). *Adv. Chem. Ser.* **67**, 222–242.

Garrels R. M. and Mackenzie F. T. (1971) *Evolution of Sedimentary Rocks*. W. W. Norton, New York, xvi + 397 pp.

Garrels R. M. and Mackenzie F. T. (1972) A quantitative model for the sedimentary rock cycle. *Mar. Chem.* **1**, 27–41.

Garrels R. M. and Perry Jr. E. A. (1974) Cycling of carbon, sulfur and oxygen through geologic time. In *The Sea*, Vol. 5 (ed. E. D. Godlberg). Wiley, New York, pp. 303–336.

Gautelier M., Oelkers E. H., and Schott J. (1999) An experimental study of dolomite dissolution rates as a function of pH from -0.5 to 5 and temperature from 25 to 80° C. *Chem. Geol.* **157**, 13–26.

Gertner G., Wang G., Fang S., and Anderson A. B. (2002) Effect and uncertainty of digital elevation model spatial resolutions on predicting the topographical factor for soil loss estimation. *J. Soil Water Conserv.* **57**, 164–175.

Gibbs M. T. and Kump L. R. (1994). Global chemical erosion during the last glacial maximum and the present; sensitivity to changes in lithology and hydrology. *Paleoceanography* **9**, 529–543.

Gíslason S. R. and Eugster H. P. (1987) Meteoric water-basalt interactions. I: A laboratory study. *Geochim. Cosmochim. Acta* **51**, 2827–2840.

Gíslason S. R., Arnórsson S., and Ármannsson H. (1996) Chemical weathering of basalt in Southwest iceland: effects of runoff, age of rocks and vegetative/glacial cover. *Am. J. Sci.* **296**, 837–907.

Goldberg E. D. (1971) Atmospheric dust, the sedimentary cycle and man. *Geophysics* **1**, 117–132.

Goldich S. (1938) A study in rock-weathering. *J. Geol.* **46**, 17–58.

Graham, L. (1974) Heat. *Encycl. Brit.*, *Macropaedia*, 1974 edition., Vol. 8, pp. 700–706; *Micropaedia*, 1974 edition., Vol. 4, 1007.

Gregor C. B. (1970) Denudation of the continents. *Nature* **228**, 273–275.

Gregor C. B. (1980) Weathering rates of sedimentary and crystalline rocks. *Proc. Kon. Ned. Akad. Wet. Ser. B Phys. Sci.* **83**, 173–181.

Gregor C. B. (1988) Prologue: cyclic processes in geology, a historical sketch. In *Chemical Cycles in the Evolution of the Earth* (eds. C. B. Gregor, R. M. Garrels, F. T. Mackenzie and J. B. Maynard). Wiley, New York, pp. 5–16.

Gregor C. B. (1992) Some ideas on the rock cycle: 1788–1988. *Geochim. Cosmochim. Acta* **56**, 2993–3000.

Guidry M. W. and Mackenzie F. T. (2003) Experimental study of igneous and sedimentary apatite dissolution: control of pH, distance from equilibrium, and temperature on dissolution rates. *Geochim. Cosmochim. Acta* **67**, 2949–2963.

Gutjahr A., Dabringhaus H., and Lacmann R. (1996) Studies of the growth and dissolution kinetics of $CaCO_3$ polymorphs calcite and aragonite. I. Growth and dissolution rates in water. *J. Crystal Growth* **158**, 296–309.

Hagen L. J. (1991) A wind erosion prediction system to meet the users' need. *J. Soil Water Conserv.* **46**, 106–111.

Hahn V. and Buchmann N. (2003) $\delta^{13}C, \delta^{18}O, \delta^{14}C$ of soil CO_2 and soil respired CO_2. Abstracts of CarboEurope Conference, "The Continental Carbon Cycle", Paper no. 72, Lisbon, Portugal, 19–21 March 2003. http://www.bgc.mpg.de/public/carboeur/workshop/Poster2/hahn1.htm.

Hahn V. and Buchmann N. (2005) Measurements of CO_2 in soils at six sites in northern and southern Europe in 2001. *Personal communication*.

Hameed S. and Dignon J. (1992) Global emissions of nitrogen and sulfur oxides in fossil fuel combustion 1970–1986. *J. Air Waste Manag. Assoc.* **42**, 159–163.

Holland H. D. (1978) *The Chemistry of the Atmosphere and Oceans*. Wiley, New York, xiv + 351 pp.

Huertas F. J., Chou L., and Wollast R. (1999) Mechanism of kaolinite dissolution at room temperature and pressure; Part II, Kinetic study. *Geochim. Cosmochim. Acta* **63**, 3261–3275.

Huh Y. and Edmond J. M. (1999) The fluvial geochemistry of the rivers of eastern Siberia; III, Tributaries of the Lena and Anabar draining the basement terrain of the Siberian Craton and the Trans-Baikal highlands. *Geochim. Cosmochim. Acta* **63**, 967–987.

Huh Y., Tsoi M.-Y., Zaitsev A., and Edmond J. M. (1998a) The fluvial geochemistry of the rivers of Eastern Siberia: I. Tributaries of the Lena river draining the sedimentary platform of the Siberian Craton. *Geochim. Cosmochim. Acta* **62**, 1657–1676.

Huh Y., Panteleyev G., Babich D., Zaitsev A., and Edmond J. M (1998b) The fluvial geochemistry of the rivers of Eastern Siberia: II. Tributaries of the Lena, Omoloy, Yana, Indigirka, Kolyma, and Anadyr draining the collisional/accretionary zone of the Verkhoyansk and Cherskiy ranges. *Geochim. Cosmochim. Acta* **62**, 2053–2075.

Ingall E. D. and Van Cappellen P. (1990) Relation between sedimentation rate and burial of organic phosphorus and organic carbon in marine sediments. *Geochim. Cosmochim. Acta* **54**, 373–386.

Jacobson A. D., Blum J. D., and Walter L. M. (2002) Reconciling the elemental and Sr isotope composition of Himalayan weathering fluxes: insights from the carbonate geochemistry of stream waters. *Geochim. Cosmochim. Acta* **66**, 3417–3429.

Jahnke R. A. (1992) The phosphorus cycle. In *Global Biogeochemical Cycles* (eds. S. S. Butcher, R. J. Charlson, G. H. Orians, and G. V. Wolfe). Academic Press, New York, pp. 301–315.

Jeschke A. A. and Dreybrodt W. (2002) Dissolution rates of minerals and their relation to surface morphology. *Geochim. Cosmochim. Acta* **66**, 3055–3062.

Joly J. (1899) An estimate of the geological age of the earth. *Royal Dublin Soc., Sci. Trans* [2], **7**, 23–66.

Jordan G. and Rammensee W. (1998) Dissolution rates of calcite (1014) obtained by scanning force microscopy; microtopography-based dissolution kinetics on surfaces with anisotropic step velocities. *Geochim. Cosmochim. Acta* **62**, 941–947.

Kalinowski B. E. and Schweda P. (1996) Kinetics of muscovite, phlogopite, and biotite dissolution and alteration at pH 1–4, room temperature. *Geochim. Cosmochim. Acta* **60**, 367–385.

Karim A. and Veizer J. (2000) Weathering processes in the Indus river basin: implications from riverine carbon, sulfur, oxygen, and strontium isotopes. *Chem. Geol.* **170**, 153–177.

Knauss K. G. and Wolery T. J. (1988) The dissolution kinetics of quartz as a function of pH and time at 70° C. *Geochim. Cosmochim. Acta* **52**, 43–53.

Knauss K. G. and Wolery T. J. (1989) Muscovite dissolution kinetics as a function of pH and time at 70° C. *Geochim. Cosmochim. Acta* **53**, 1493–1501.

Köhler S. J., Dufaud F., and Oelkers E. H. (2003) An experimental study of illite dissolution kinetics as a function of pH from 1.4 to 12.4 and temperature from 5 to 50[deg]C. *Geochim. Cosmochim. Acta* **67**, 3583–3594.

Lasaga A. C. (1998) *Kinetic Theory in the Earth Sciences*. Princeton University Press, Princeton, NJ, x + 811 pp.

Lerman A. (1979) *Geochemical Processes – Water and Sediment Environments*. Wiley, New York, viii + 481 pp.

Lerman A. (1988) Weathering rates and major transport processes – an introduction. In *Physical and Chemical Weathering in Geochemical Cycles* (eds. A. Lerman and M. Meybeck). Kluwer, Dordrecht and Boston, pp. 1–10.

Lerman A. (1994) Surficial weathering fluxes and their geochemical controls. In *Material Fluxes on the Surface of the Earth* (eds. W. W. Hay and others). Studies in Geophysics, National Research Council, National Academic Press, Washington, DC, pp. 28–45.

Lerman A. and Mackenzie F. T. (2005) CO_2 air-sea exchange due to calcium carbonate and organic matter storage, and its implications for the global carbon cycle. *Aquatic Geochem.* **11**, 345–390. Erratum, ibid. **12**, 389–390.

Lerman A. and Wu L. (2006) CO_2 and sulfuric acid controls of weathering and river water composition. *J. Geochem. Exploration* **88**, 427–430.

Lerman A., Mackenzie F. T., and Garrels R. M. (1975) Modeling of geochemical cycles: phosphorus as an example. *Geol. Soc. Am. Mem.* **142**, 205–218.

Lerman A., Wu L., and Mackenzie F. T. (2006) Carbon dioxide weathering flux since the last glacial maximum to the present, its control of river water composition, and its role in the global carbon cycle. *Eos Trans. Am. Geophys. Un.* **87**(52), Fall Meet. Suppl., Abs. B43B-0266.

Lerman A., Wu L., and Mackenzie F. T. (2007) CO_2 and H_2SO_4 consumption in weathering and material transport to the ocean, and their role in the global carbon balance. *Mar. Chem.* **106**, 326–350.

Li Y.-H. (2000) *A Compendium of Geochemistry*. Princeton University Press, Princeton, NJ, xiv + 475 pp.

Lin F.-C. and Clemency C. V. (1981) The dissolution kinetics of brucite, antigorite, talc and phlogopite at room temperature and pressure. *Am. Mineral.* **66**, 801–806.

Linsey R. K. (1964) Hydrology. *Encycl. Brit.*, 1964 edition, **11**, 959–961.

Livingstone D. A. (1963) Chemical composition of rivers and lakes. *U. S. Geol. Surv. Prof. Pap.* **440G**, 64 pp.

Lotka A. J. (1925) *Elements of Physical Biology*. Williams & Wilkins, Baltimore, MD, published as Lotka A. J. (1956) *Elements of Mathematical Biology*. Dover, New York, xxx + 465 pp.

Ludwig W., Amiotte-Suchet P., and Probst J.-L. (1999) Enhanced chemical weathering of rocks during the last glacial maximum; a sink for atmospheric CO_2? *Chem. Geol.* **159**(1–4), 147–161.

Lüttge A., Winkler U., and Lasaga A. C. (2003) Interferometric study of the dolomite dissolution; a new conceptual model for mineral dissolution. *Geochim. Cosmochim. Acta* **67**, 1099–1116.

Lyell C. (1830) *Principles of Geology*, Vol. 1. John Murray, London, xvi + 511 pp. Facsimile of 1st edition. University Chicago Press, Chicago, IL, 1990.

Lyell C. (1872) *Principles of Geology*, 11th edition, Vol. 2. D. Appleton & Co., New York, xx + 652 pp.

Lyell C. (1875) *Principles of Geology*, 12th edition, Vol. 2. John Murray, London, xx + 652 pp.

Mackenzie F. T. (1992) Chemical mass balance between rivers and oceans. *Encycl. Earth Sys. Science*. Academic Press, New York, **1**, 431–445.

Mackenzie F. T. and Garrels R. M. (1966) Chemical mass balance between rivers and oceans. *Am. J. Sci.* **264**, 507–525.

Mackenzie F. T., Ver L. M., Sabine C., Lane M., and Lerman A. (1993) C, N, P, S global biogeochemical cycles and modeling of global change. In *Interactions of C, N, P and S Biogeochemical Cycles and Global Change* (eds. R. Wollast, F. T. Mackenzie and L. Chou). *NATO ASI Series. Series I: Global Environmental Change*, Vol. 4. Springer-Verlag, Berlin, pp. 1–61.

Mackenzie F. T., Ver L. M., and Lerman A. (2002) Century-scale nitrogen and phosphorus controls of the carbon cycle. *Chem. Geol.* **190**, 13–32.

Mackenzie F. T., Lerman A., and Andersson A. J. (2004) Past and present of sediment and carbon biogeochemical cycling models. *Biogeosciences* **1**, 11–32.

Mason B. H. and Moore C. B. (1982) *Principles of Geochemistry*, 4th edition. Wiley, New York, vi + 344 pp.

Meadows D. H., Meadows D. L., Randers J., and Behrens III, W. W. (1972) *The Limits to Growth*. Universe Books, New York.

Metz V., Amram K., and Ganor J. (2005) Stoichiometry of smectite dissolution reaction. *Geochim. Cosmochim. Acta* **69**, 1755–1772.

Meybeck M. (1979) Concentrations des eaux fluviales en éléments majeurs et apports en solution aux océans. *Rev. Géol. Dyn. Géogr. Phys.* **21**(3), 215–246.

Meybeck M. (1984) Les fleuves et le cycle géochimique des éléments. Thèse de Doctorat d'Etat ès Sciences Naturelles, N° 84–35. Université Pierre et Marie Curie, Paris.

Meybeck M. (1987) Global chemical weathering of surficial rocks estimated from river dissolved loads. *Am. J. Sci.* **287**, 401–428.

Meybeck M. (2003) Global occurrence of major elements in rivers. In *Treatise on Geochemistry*, Vol. 5 (ed. J. I. Drever), Elsevier, Amsterdam, pp. 207–223.

Meybeck M. and Ragu A. (1995) Water quality of world river basins. UNEP GEMS Collaborating Centre for Fresh Water Quality Monitoring and Assessment, United Nations Environment Programme, Nairobi, Kenya, 40 pp.

Meyer B. S. (1964) Plant physiology. *Encycl. Brit.*, 1964 edition, **18**, 16–31.

Miller A. J., Schuur E. A. G., and Chadwick O. A. (2001) Redox control of phosphorus pools in Hawaiian montane forest soils. *Geoderma* **102**, 219–237.

Milliman J. D. (1993) Production and accumulation of calcium carbonate in the ocean: budget of a nonsteady state. *Global Biogeochem. Cycles* **7**, 927–957.

Milliman J. D. and Meade R. H. (1983) World-wide delivery of river sediment to the oceans. *J. Geol.* **91**, 1–21.

Milliman J. D. and Syvitski J. P. M. (1992) Geomorphic/tectonic control of sediment discharge to the ocean; the importance of small mountainous rivers. *J. Geol.* **100**, 525–544.

Millot R., Gaillardet J., Dupré B., and Allègre C. J. (2002) The global control of silicate weathering rates and the coupling with physical erosion: new insights from rivers of the Canadian Shield. *Earth Planet Sci. Lett.* **196**, 83–98.

Millot R., Gaillardet J., Dupré B., and Allègre C. J. (2003) Northern latitude chemical weathering rates: clues from the Mackenzie river basin, Canada. *Geochim. Cosmochim. Acta* **67**, 1305–1329.

Mogollon J. L., Perez D. A., Lo Monaco S., Ganor J., and Lasaga A. C. (1994) The effect of pH, $HClO_4$, HNO_3 and ΔG_r on the dissolution rate of natural gibbsite using column experiments. *Mineral. Mag.* **58A**, 619–620.

Mohr F., 1875. *Geschichte der Erde*, 2. Aufl. Verlag Max Cohen & Sohn, Bonn, xx + 544 pp.

Mook W. G. and Tan F. C. (1991) Stable carbon isotopes in rivers and estuaries. In *Biogeochemistry of Major World Rivers* (eds. E. T. Degens, S. Kempe and J. E. Richey). SCOPE 42 (Scientific Committee On Problems of the Environment), Wiley, Chichester, Chapter 11.

Mook W. G., Bommerson J. C., and Staverman W. H. (1974) Carbon isotope fractionation between dissolved bicarbonate and gaseous carbon dioxide. *Earth Planet. Sci. Lett.* **22**, 169–176.

Morse J. W. and Arvidson R. S. (2002) The dissolution kinetics of major sedimentary carbonate minerals. *Earth Sci. Rev.* **58**, 51–84.

Morse J. W. and Mackenzie F. T. (1990) *Geochemistry of Sedimentary Carbonates*. Elsevier, New York, xvi + 707 pp.

Mortatti J. and Probst J.-L. (2003) Silicate rock weathering and atmospheric/soil CO2 uptake in the Amazon basin estimated from river water geochemistry: seasonal and spatial variations. *Chem. Geol.* **197**, 177–196.

Mottl M. J. (2003) Partitioning of energy and mass fluxes between mid-ocean ridge axes and flanks at high and low temperature. In *Energy and Mass Transfer in Marine Hydrothermal Systems* (eds. P. E. Halbach, V. Tunnicliffe and J. R. Hein). Dahlem University Press, Berlin, pp. 271–286.

Munhoven G. (2002) Glacial-interglacial changes of continental weathering; estimates of the related CO_2 and HCO_3^- flux variations and their uncertainties. *Global Planet. Change* **33**, 155–176.

Munk W. H. (1966) Abyssal recipes. *Deep Sea Res.* **13**, 707–730.

Nakićenović N. and others (2000) *Emissions Scenarios, a Special Report of Working Group III of the Intergovernmental Panel on Climate Change (IPCC)*, Cambridge University Press, Cambridge, 599 pp.

Nill D. (1997) Valuation of erosion-determining-factors and their quantitative influence on soil loss in tropical Africa. In Soils and environment: soil processes from mineral to landscape scale (eds. K. Auerswald, H. Stanjek and J. M. Bigham). *Adv. Geoecol.* **30**, 23–38.

Oliver L., Harris N., Bickle M., Chapman H., Dise N., and Horstwood M. (2003) Silicate weathering rates decoupled from the $^{87}Sr/^{86}Sr$ ratio of the dissolved load during Himalayan erosion. *Chem. Geol.* **201**, 119–139.

Oliver M. K. (2002) What is the chemical composition of lake Malawi water? How does it compare with lakes Victoria and Tanganyika? http://malawicichlids.com/mw01011.htm.

Overton W. S., Kanciruk P., Hook L. A., Eilers J. M., Landers D. H., Brakke D. F., Blick Jr. D. J., Linthurst R. A., DeHaan M. D., and Omernik J. M. (1986) *Characteristics of Lakes in the Eastern United States, Vol. II: Lakes Sampled and Descriptive Statistics for Physical and Chemical Variables*. U. S. Environmental Protection Agency, Washington, DC, EPA/600/4–86/007b.

Oxburgh R., Drever J. I., and Sun Y.-T. (1994) Mechanism of plagioclase dissolution in acid solution at 25° C. *Geochim. Cosmochim. Acta* **58**, 661–669.

Petit J.-R., Jouzel J., Raynaud D., Barkov N. I., Barnola J.-M., Basile I., Bender M., Chappellaz J., Devis M., Delaygue G., Delmotte G. M., Kotlyakov V. M., Legrand M., Lipenkov V. Y., Lorius C., Pepin L., Ritz C., Saltzman E., and Stievenard M. (1999) Climate and atmospheric history of the past 420,000 years from the Vostok ice core, Antarctica. *Nature* **399**, 429–436.

Pettijohn F. J. (1957) *Sedimentary Rocks*, 2nd edition. Harper, New York, xvi + 718 pp.

Plummer L. N., Wigley T. M. L., and Parkhurst D. L. (1978) The kinetics of calcite dissolution in CO_2–water systems at 5° and 60° C and 0.0 to 1.0 atm CO_2. *Am. J. Sci.* **278**, 179–216.

Post W., Emmanuel W., Zinke P., and Stangenberger A. (1982) Soil carbon pools and world life zones. *Nature* **298**, 156–159.

Powers L. A., Johnson T. C., Werne J. P., Castañeda I. S., Ellen C. Hopmans E. C., Sinninghe Damsté J. S., and Schouten S. (2005) Large temperature variability in the southern African tropics since the last glacial maximum. *Geophys. Res. Lett.* **32**, L08706, doi:10.1029/2004GL022014.

Probst J.-L. and Brunet F. (2005) $\delta^{13}C$ tracing of dissolved inorganic carbon sources in major world rivers. Abs. 15th Ann. Goldschmidt Conf. *Geochim. Cosmochim. Acta* **69** (Suppl. 1), A726.

Prospero J. M. (1981) Eolian transport to the world ocean. In *The Sea: The Oceanic Lithosphere*, Vol. 7 (ed. C. Emiliani). Wiley, New York, pp. 801–874.

Rankama K. and Sahama Th. G. (1950) *Geochemistry*. University Chicago Press, Chicago, IL, xvi + 912 pp.

Raymond P. A. and Cole J. J. (2003) Increase in the export of alkalinity from North America's largest river. *Science* **301**, 88–91.

Rea D. K., Hovan S. A., and Janecek T. R. (1994) Late quaternary flux of eolian dust to the pelagic ocean. In *Geomaterial Fluxes on the Surface of the Earth* (eds. W. W. Hay and others). Studies in Geophysics, National Research Council, National Academy Press, Washington, DC, pp. 116–123.

Richey J. E. (1983) The phosphorus cycle. In *The Major Biogeochemical Cycles and their Interactions* (eds. B. Bolin and R. B. Cook). Wiley, Chichester, pp. 51–56.

Rightmire C. T. (1978) Seasonal variation in pCO_2 and ^{13}C content of soil atmosphere. *Water Resour. Res.* **14**, 691–692.

Rimstidt J. D. and Barnes H. L. (1980) The kinetics of silica-water reactions. *Geochim. Cosmochim. Acta* **44**, 1683–1700.

Robie R. A., Hemingway B. S., and Fisher J. R. (1978) Thermodynamic properties of minerals and related substances at 298.15 K and 1 bar (10^5 pascals) pressure and at higher temperatures. *U.S. Geol. Surv. Bull.* **1452**, 1–456.

Rufe E. and Hochella Jr. M. F. (1999) Quantitative assessment of reactive surface area of phlogopite during acid dissolution. *Science* **285**, 874–876.

Rudnick R. L. and Gao S. (2003) Composition of the continental crust. In *Treatise on Geochemistry*, Vol. 3 (ed. J. I. Drever). Elsevier, Amsterdam, pp. 1–64.

Ruttenberg K. C. (2004) The global phosphorus cycle. In *Treatise on Geochemistry*, Vol. 8 (ed. W. Schlesinger). Elsevier, Amsterdam, pp. 585–643.

Ruttenberg K. C. and Canfield D. E. (1994) Chemical distribution of phosphorus in suspended particulate matter from twelve North American rivers: evidence for bioavailability of particulate-P. *EOS, Trans. Am. Geophys. Un.* **69**, 1235.

Schnoor J. L. (1990) Kinetics of chemical weathering; a comparison of laboratory and field weathering rates. In *Aquatic Chemical Kinetics* (ed. W. Stumm), Wiley, New York, pp. 475–504.

Scholl D. W. and von Huene R. (2004) Exploring the implications for continental basement tectonics if estimated rates of crustal removal (recycling)

at Cenozoic subduction zones are applied to Phanerozoic and Precambrian convergent ocean margins. *Abs. 17th International Basement Tectonics Association Conference 2004: 4-D Framework of the Continental Crust – Integrating Crustal Processes Through Time*. Oak Ridge, Tennessee, pp. 33–36. http://geoweb.gg.utk.edu/ibta04crust/meeting.html.

Schott J., Berner R. A., and Sjöberg E. L. (1981) Mechanism of pyroxene and amphibole weathering: I, Experimental studies of iron-free minerals. *Geochim. Cosmochim. Acta* **45**, 2123–2135.

Shaw D. B. and Weaver C. E. (1965) The mineralogical composition of shales. *J. Sed. Petrology* **35**(1), 213–222.

Shiklomanov I. A. (1993) World fresh water resources. In *Water in Crisis; A Guide to the World's Fresh Water Resources* (ed. P. H. Gleick). Oxford University Press, New York, pp. 13–24.

Shiraki R., Rock P. A., and Casey W. H. (2000) Dissolution kinetics of calcite in 0.1M NaCl solution at room temperature: an atomic force microscopic (AFM) study. *Aquatic Geochem.* **6**, 87–108.

Siegel D. I. and Pfannkuch H. O. (1984) Silicate mineral dissolution at pH 4 and near standard temperature and pressure. *Geochim. Cosmochim. Acta* **48**, 197–201.

Siegenthaler U. and Oeschger H. (1987) Biospheric CO_2 emissions during the past 200 years reconstructed by deconvolution of ice core data. *Tellus* **39B**, 140–154.

Sjöberg E. L. (1976) A fundamental equation for calcite dissolution kinetics. *Geochim. Cosmochim. Acta* **40**, 441–447.

Sjöberg E. L. and Rickard D. T. (1984) Temperature-dependence of calcite dissolution kinetics between 1° C and 62° C at pH 2.7 to 8.4 in aqueous solutions. *Geochim. Cosmochim. Acta* **48**, 485–493.

Smith, S. V., Renwick, W. H., Buddemeier, R. W., and Crossland C. J. (2001) Budgets of soil erosion and deposition for sediments and sedimentary organic carbon across the conterminous United States. *Global Biogeochem. Cycles* **15**(3), 697–707.

Stallard R. F. (1988) Weathering and erosion in the humid tropics. In *Physical and Chemical Weathering in Geochemical Cycles* (eds. A. Lerman and M. Meybeck). Kluwer, Dordrecht, pp. 225–246.

Sternbeck J. and Sohlenius G. (1997) Authigenic sulfide and carbonate mineral formation in Holocene sediments of the Baltic sea. *Chem. Geol.* **135**, 55–73.

Stumm W. and Morgan J. J. (1981) *Aquatic Chemistry: An Introduction Emphasizing Chemical Equilibria in Natural Waters*, 2nd edition. Wiley, New York, xvi + 780 pp.

Sutheimer S. H., Maurice P. A., and Zhou Q. (1999) Dissolution of well and poorly crystallized kaolinites; Al speciation and effects of surface characteristics. *Am. Mineral.* **84**, 620–628.

Sverdrup H. U. (1990) *The Kinetics of Base Cation Release Due to Chemical Weathering*. Lund University Press, Lund, Sweden, 245 pp.

Swoboda-Colberg N. G. and Drever J. I. (1993) Mineral dissolution rates in plot-scale field and laboratory experiments. *Chem. Geol.* **105**, 51–69.

Tang R., Henneman Z. J., and Nancollas G. H. (2003) Constant composition kinetics study of carbonated apatite dissolution. *J. Crystal Growth* **249**, 614–624.

Tardy Y., Bustillo V., and Boeglin J.-L. (2004) Geochemistry applied to the watershed survey: hydrograph separation, erosion and soil dynamics. A case study: the basin of the Niger river, Africa. *Appl. Geochem.* **19**, 469–518.

UCAR/OIES (1991) Changes in time in the temperature of the Earth. University Center for Atmospheric Research, Office for Interdisciplinary Earth Studies, Boulder, Colo. *EarthQuest* **5**(1). http://gcrio.org/CONSEQUENCES/winter96/article1-fig2.html.

Urey H. C. (1952) *The Planets: Their Origin and Development*. Yale University Press, New Haven, CT, xvii + 245 pp.

Valsami-Jones E., Ragnarsdottír K. V., Putnis A., Bosbach D., Kemp A. J., and Cressey G. (1998) The dissolution of apatite in the presence of aqueous metal cations at pH 2–7. *Chem. Geol.* **151**, 215–233.

Van Cappellen P., Gaillardet, J., and Rabouille C. (1993) Biogeochemical transformations in sediments: kinetic models of early diagenesis. In *Interactions of C, N, P and S Biogeochemical Cycles and Global Change* (eds. R. Wollast, F. T. Mackenzie and L. Chou). *NATO ASI Series. Series I: Global Environmental Change* **4**, 401–445, Springer-Verlag, Berlin.

Veizer J. (1988) The evolving exogenic cycle. In *Chemical Cycles in the Evolution of the Earth* (eds. C. B. Gregor, R. M. Garrels, F. T. Mackenzie, and J. B. Maynard). Wiley, New York, pp. 175–261.

Velbel M. A. (1985) Geochemical mass balances and weathering rates in forested watersheds of the southern Blue Ridge. *Am. J. Sci.* **285**, 904–930.

Ver L. M. (1998) Global kinetic models of the coupled C, N, P, and S biogeochemical cycles: implications for global environmental change. Ph. D. Thesis, University Hawaii, Honolulu, HI, xxi + 681 pp.

Ver L. M., Mackenzie F. T., and Lerman A. (1999) Biogeochemical responses of the carbon cycle to natural and human perturbations: past, present and future. *Am. J. Sci.* **299**, 762–801.

Vidic N. (1998) Soil-age relationships and correlations: comparison of chronosequences in the Ljubljana basin, Slovenia and USA. *Catena* **34**, 113–129.

von Huene R. and Scholl D. W. (1991) Observations at convergent margins concerning sediment subduction, subduction erosion, and the growth of continental crust. *Rev. Geophys.* **29**, 279–316.

Votintsev K. K. (1993) On the natural conditions of lake Baikal in connection with the development of its water quality standard. *Water Resour.* **20**, 595–604.

Walker J. C. G. (1991) *Numerical Adventures with Geochemical Cycles*. Oxford University Press, New York.

Walling E. (1983) The sediment delivery problem. *J. Hydrol.* **65**, 209–237.

Wedepohl H. K. (1995) The composition of the continental crust. *Geochim. Cosmochim. Acta* **59**, 1217–1232.

Weiler R. R. and Chawla V. K. (1969) Dissolved mineral quality of great lakes waters. *Proc. 12th Conf. Great Lakes Res.*, pp. 801–818, International Association of Great Lakes Research, Ann Arbor, MI.

Weisstein E. W. (2005) Sphere Packing. From *MathWorld* – A Wolfram Web Resource. http://mathworld.wolfram.com/SpherePacking.html.

Wahlen M. (2002) *Carbon-Isotopic Composition of Atmospheric CO_2 Since the Last Glacial Maximum*. National Snow and Ice Data Center, digital media, Boulder, CO, http://nsidc.org/data/docs/agdc/nsidc0108_wahlen/index.html.

White A. F. (1995) Chemical weathering rates in soils. In *Chemical Weathering Rates of Silicate Minerals* (eds. A. F. White and S. L. Brantley). Mineralogical Society of America, Washington, DC, *Rev. Mineralogy* **31**, 407–458.

White A. F. and Brantley S. L. (eds.) (1995) *Chemical Weathering Rates of Silicate Minerals*. Mineralogical Society of America., Washington, DC, *Rev. Mineralogy* **31**, 1–584.

White A. F. and Brantley S. L. (2003) The effect of time on the weathering of silicate minerals: why do weathering rates differ in the laboratory and field? *Chem. Geol.* **202**, 479–506.

White A. F., Blum A. E., Schulz M. S., Bullen T. D., Harden J. W., and Peterson M. L. (1996) Chemical weathering of a soil chronosequence on granitic alluvium: 1. Reaction rates based on changes in soil mineralogy. *Geochim. Cosmochim. Acta* **60**, 2533–2550.

White A. F., Bullen T. D., Schulz M. S., Blum A. E., Huntington T. G., and Peters N. E. (2001) Differential rates of feldspar weathering in granitic regoliths. *Geochim. Cosmochim. Acta* **65**, 847–869.

Whitmarsh J. and Govindjee (1995) The photosynthetic process. In *Concepts in Photobiology: Photosynthesis and Photomorphogenesis* (eds. G. S. Singhal, G. Renger, S. K. Soppory, K.-D. Irrgang and Govindjee). Kluwer, Dordrecht, pp. 11–51.

Wieland E. and Stumm W. (1992) Dissolution kinetics of kaolinite in acidic aqueous solutions at 25° C. *Geochim. Cosmochim. Acta* **56**, 3357–3363.

Wischmeier W. H. and Smith D. D. (1978) Predicting rainfall erosion losses – a guide to conservation planning. U. S. Department of Agriculture, Agriculture Handbook no. 537, 58 pp.

Woodruff N. P. and Siddoway F. H. (1965) A wind erosion equation. *Soil Sci. Soc. Am. Proc.* **29**, 602–608.

Wu L. and Huh Y. (2007) Dissolved reactive phosphorus in large rivers of East Asia. *Biogeochemistry* **85**, 263–288.

Yang C., Telmer K., and Veizer J. (1996) Chemical dynamics of the "St. Lawrence" riverine system; δD_{H_2O}, $\delta^{18}O_{H_2O}$, $\delta^{13}C_{DIC}$, $\delta^{34}S_{sulfate}$, and dissolved $^{87}Sr/^{86}Sr$. *Geochim. Cosmochim. Acta* **60**(5), 851–866.

Yang D. W., Kanae S., Oki T., Koike T., and Musiake K. (2003) Global potential soil erosion with reference to land use and climate changes. *Hydrol. Process.* **17**(4), 2913–2928.

Appendix: Compilation of Mineral Dissolution Rates

Joel Z. Bandstra[1], Heather L. Buss[2], Richard K. Campen[1,2], Laura J. Liermann[2], Joel Moore[1,2], Elisabeth M. Hausrath[2], Alexis K. Navarre-Sitchler[1,2], Je-Hun Jang[2], Susan L. Brantley[1,2]

This appendix contains mineral dissolution rate data collected in laboratory experiments and compiled primarily from the peer-reviewed literature. The focus of the compilation is on experiments conducted at (or near) 25° C and far from equilibrium. Minerals included in the compilation are: apatite, basalt, biotite, hornblende, kaolinite, olivine, plagioclase, potassium feldspar, pyroxene, and quartz. Many of these data sets have been analyzed using standard rate equations such as those found in Chap. 5. The fitted parameters and uncertainty estimates may be found in Chap. 6, Table 6.3. The fitted curves are displayed graphically in this appendix. The data may also be accessed via the internet at czen.org or cyber-chem.ist.psu.edu.

The tables are organized by mineral and are in alphabetical order. Plagioclase has been broken up into several sub-tables corresponding to albite, andesine/labradorite, anorthite, bytownite, and oligoclase. Each table contains information on pH, initial fluid composition, specific surface area, grain size, temperature, the experimental duration, element (usually Si) release rate, and surface area normalized dissolution rate. The surface area normalized dissolution rate is based on moles of mineral formula unit dissolved per unit time per unit surface area and, except for apatite, is based on the Si relearse rate. Basalt rates are cited as mol of Si m^{-2} s^{-1}. "ng" stands for not given.

Below each table we have included a plot of the surface area normalized dissolution rate vs. pH and an annotated bibliography that provides additional information about the reference from which the data were obtained and the experimental design used in each study. If the data were fit, the fitted curve is plotted on the rate vs. pH figures. Data that were excluded from the fits are plotted as line-art symbols (+, ×, etc.) and the reason(s) for excluding these data are given in the annotated bibliography. Data that were included in the fits are plotted as open symbols (○, □, etc.).

[1] Center for Environmental Kinetics Analysis, Pennsylvania State University
[2] Department of Geosciences, The Pennsylvania State University

Albite

References	Initial (Final) pH	Initial Fluid Composition	Initial (Final) Specific Surface Area [m^2/g]	Grain Size (min, max) [m]	Temperature [K]	Duration of Dissolution [s]	Si Release Rate [$mol/m^2/s$]	Mineral Dissolution Rate [$mol/m^2/s$]
Chou and Wollast (1984)	5.1 (3.5)	HCl and $Ba(OH)_2$	0.075 (ng)	5E-05, 1E-04	298	9.47E05	7.64E-12	3.40E-11
Chou and Wollast (1984)	3.5 (2.5)	HCl and Ba(OH)2	0.075 (ng)	5E-05, 1E-04	298	2.00E06	7.75E-12	3.44E-11
Chou and Wollast (1984)	2.5 (1.2)	HCl and Ba(OH)2	0.075 (ng)	5E-05, 1E-04	298	3.04E06	1.78E-11	7.90E-11
Chou and Wollast (1984)	1.2 (7.11)	HCl and Ba(OH)2	0.075 (ng)	5E-05, 1E-04	298	4.60E06	5.94E-11	2.64E-10
Chou and Wollast (1985)	ng (1.1)	HCl	0.075 (ng)	5E-05, 1E-04	298	ng	1.68E-10	5.62E-11
Chou and Wollast (1985)	ng (2.05)	HCl	0.075 (ng)	5E-05, 1E-04	298	ng	8.40E-11	2.82E-11
Chou and Wollast (1985)	ng (ng)	HCl	0.075 (ng)	5E-05, 1E-04	298	ng	4.51E-11	1.51E-11
Chou and Wollast (1985)	ng (2.9)	HCl	0.075 (ng)	5E-05, 1E-04	298	ng	1.68E-11	5.62E-12
Chou and Wollast (1985)	ng (3)	HCl	0.075 (ng)	5E-05, 1E-04	298	ng	2.37E-11	7.94E-12
Chou and Wollast (1985)	ng (3.5)	HCl	0.075 (ng)	5E-05, 1E-04	298	ng	1.19E-11	3.98E-12
Chou and Wollast (1985)	ng (4.1)	HCl	0.075 (ng)	5E-05, 1E-04	298	ng	1.01E-11	3.39E-12
Chou and Wollast (1985)	ng (5.1)	HCl	0.075 (ng)	5E-05, 1E-04	298	ng	4.51E-12	1.51E-12
Chou and Wollast (1985)	ng (5.35)	HCl	0.075 (ng)	5E-05, 1E-04	298	ng	5.30E-12	1.78E-12
Chou and Wollast (1985)	ng (5.47)	HCl	0.075 (ng)	5E-05, 1E-04	298	ng	6.67E-12	2.24E-12
Chou and Wollast (1985)	ng (5.63)	HCl	0.075 (ng)	5E-05, 1E-04	298	ng	4.41E-12	1.48E-12
Chou and Wollast (1985)	ng (5.63)	HCl	0.075 (ng)	5E-05, 1E-04	298	ng	3.58E-12	1.20E-12
Chou and Wollast (1985)	ng (5.73)	HCl	0.075 (ng)	5E-05, 1E-04	298	ng	3.58E-12	1.20E-12
Chou and Wollast (1985)	ng (7.73)	HCl	0.075 (ng)	5E-05, 1E-04	298	ng	4.41E-12	1.48E-12
Chou and Wollast (1985)	ng (7.95)	Ba(OH)2, LiOH, NaOH	0.075 (ng)	5E-05, 1E-04	298	ng	6.37E-12	2.14E-12
Chou and Wollast (1985)	ng (9.95)	Ba(OH)2, LiOH, NaOH	0.075 (ng)	5E-05, 1E-04	298	ng	3.19E-11	1.07E-11
Chou and Wollast (1985)	ng (9.95)	Ba(OH)2, LiOH, NaOH	0.075 (ng)	5E-05, 1E-04	298	ng	2.66E-11	8.91E-12
Chou and Wollast (1985)	ng (9.95)	Ba(OH)2, LiOH, NaOH	0.075 (ng)	5E-05, 1E-04	298	ng	2.21E-11	7.41E-12
Chou and Wollast (1985)	ng (10.6)	Ba(OH)2, LiOH, NaOH	0.075 (ng)	5E-05, 1E-04	298	ng	3.34E-11	1.12E-11
Chou and Wollast (1985)	ng (11.2)	Ba(OH)2, LiOH, NaOH	0.075 (ng)	5E-05, 1E-04	298	ng	8.40E-11	2.82E-11
Chou and Wollast (1985)	ng (11.55)	Ba(OH)2, LiOH, NaOH	0.075 (ng)	5E-05, 1E-04	298	ng	7.49E-11	2.51E-11
Chou and Wollast (1985)	ng (12.3)	Ba(OH)2, LiOH, NaOH	0.075 (ng)	5E-05, 1E-04	298	ng	1.24E-10	4.17E-11
Casey et al. (1991a)	2 (ng)	0.010 N HCl	0.49 (ng)	2.5E-05, 7.5E-05	298	2.00E06	3.6E-12	1.08E-11
Casey et al. (1991b)	2 (ng)	0.010 N HCl	0.405 (ng)	2.5E-05, 7.5E-05	298	2.00E06	7.32E-12	2.05E-11

Knauss and Wolery (1986)	4 (ng)	0.05 m KHPhth + 0.001 m HCl	0.086 (ng)	7.5E-05, 1.3E-04	298	4.32E06	1.41E-12	4.70E-13
Knauss and Wolery (1986)	5.04 (ng)	0.05 m KHPhth + 0.024 m NaOH	0.086 (ng)	7.5E-05, 1.3E-04	298	4.32E06	1.29E-12	4.30E-13
Knauss and Wolery (1986)	5.98 (ng)	0.05 m KHPhth + 0.045 m NaOH	0.086 (ng)	7.5E-05, 1.3E-04	298	4.32E06	1.38E-12	4.60E-13
Knauss and Wolery (1986)	8.06 (ng)	0.05 m H3BO3 + 0.004 m NaOH	0.086 (ng)	7.5E-05, 1.3E-04	298	4.32E06	2.46E-12	8.20E-13
Knauss and Wolery (1986)	9.07 (ng)	0.05 m H3BO3 + 0.021 m NaOH	0.086 (ng)	7.5E-05, 1.3E-04	298	4.32E06	6.30E-12	2.10E-12
Knauss and Wolery (1986)	10.06 (ng)	0.05 m H3BO3 + 0.044 m NaOH	0.086 (ng)	7.5E-05, 1.3E-04	298	4.32E06	7.50E-12	2.50E-12
Rose (1991)	1.4 (ng)	0.05 m KCl + 0.05 m HCl	0.1063 (ng)	5.3E-05, 1E-04	297	1.68E06	5.29E-12	1.76E-12
Holdren and Speyer (1987)	3 (ng)	0.01 N HCl	0.066 (ng)	7.5E-05, 1.5E-04	ng	ng	1.22E-10	4.1E-11
Holdren and Speyer (1987)	3 (ng)	0.01 N HCl	0.034 (ng)	6E-04, ng	ng	ng	1.21E-10	4.0E-11
Holdren and Speyer (1987)	3 (ng)	0.01 N HCl	0.036 (ng)	3E-04, 6E-04	ng	ng	1.33E-10	4.4E-11
Holdren and Speyer (1987)	3 (ng)	0.01 N HCl	0.049 (ng)	1.5E-04, 3E-04	ng	ng	1.17E-10	3.9E-11
Holdren and Speyer (1987)	3 (ng)	0.01 N HCl	0.154 (ng)	3.7E-05, 7.5E-05	ng	ng	4.52E-11	1.5E-11
Holdren and Speyer (1987)	3 (ng)	0.01 N HCl	1.19 (ng)	ng, 3.7E-05	ng	ng	1.44E-11	4.8E-12
Stillings and Brantley (1995a)	3 (3)	1 mM HCl	0.0426 (0.0701)	7.5E-05, 1.5E-04	298	1.07E07	8.08E-12	2.71E-12
Stillings and Brantley (1995a)	3 (3)	1 mM HCl	0.0426 (0.0851)	7.5E-05, 1.5E-04	298	1.70E07	6.71E-12	2.25E-12
Stillings and Brantley (1995b)	3 (2.98)	1 mM HCl, 10 mM NaCl	0.0426 (0.1071)	7.5E-05, 1.5E-04	298	2.41E07	8.08E-13	2.71E-13
Stillings and Brantley (1995b)	3 (3.02)	1 mM HCl, 100 mM NaCl	0.0426 (0.126)	7.5E-05, 1.5E-04	298	3.00E07	4.17E-13	1.40E-13
Stillings and Brantley (1995c)	3 (3.06)	1 mM HCl, 1 mM (CH3)4NCl	0.0426 (0.0643)	7.5E-05, 1.5E-04	298	4.64E06	1.03E-11	3.46E-12
Stillings and Brantley (1995c)	3 (3.06)	1 mM HCl, 100 mM (CH3)4NCl	0.0426 (0.0587)	7.5E-05, 1.5E-04	298	8.91E06	1.42E-11	4.77E-12

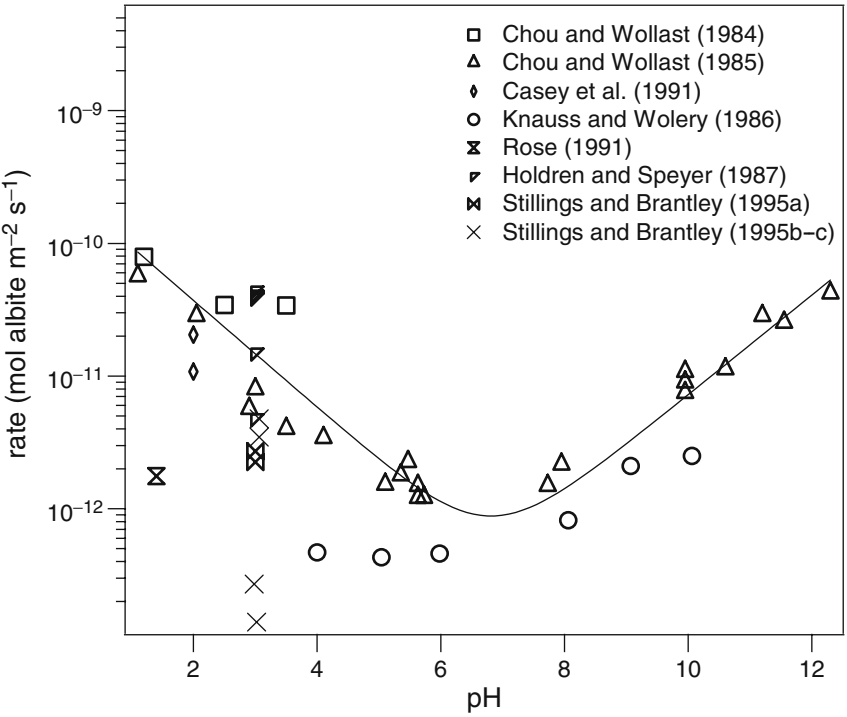

References

Chou and Wollast (1984) *Geochimica et Cosmochimica Acta* 48, 2205–2217. K0.01Na0.98Ca0.02Al1.01Si2.98O8, fluidized bed reactor, pO2 and pCO2 were atmospheric, surface area measured by N_2-BET, dissolution was stoichiometric. pH was manipulated over the course of these experiments.

Chou and Wollast (1985) *American Journal of Science* 285, 963–993. K0.01Na0.98Ca0.02Al1.01Si2.98O8, fluidized bed reactor, pO2 and pCO2 were atmospheric, surface area measured by N_2-BET, dissolution was not stoichiometric.

Casey (1991a) *American Mineralogist* 76, 211–217. K0.01Na0.97Ca0.02Al0.99Si3O8, batch reactor, pO2 and pCO2 were atmospheric, surface area measured by BET, dissolution was not stoichiometric.

Casey (1991b) *American Mineralogist* 76, 211–217. K0.08Na0.68Ca0.21Al1.20Si2.8O8, batch reactor, pO2 and pCO2 were atmospheric, surface area measured by BET, dissolution was stoichiometric.

Knauss and Wolery (1986) *Geochimica et Cosmochimica Acta* 50(11), 2481–2497. NaAlSi3O8, plug-flow reactor, pO2 and pCO2 were atmospheric, surface area measured by Ar-BET, dissolution was stoichiometric.

Rose N. M. (1991) *Geochimica et Cosmochimica Acta* 55, 3273–3286. Na0.99Ca0.002Al0.98Si3.01O8, batch reactor, pO2 and pCO2 were atmospheric, surface area measured by Kr-BET, dissolution was stoichiometric.

Holdren and Speyer (1987) *Geochimica et Cosmochimica Acta* 51, 2311–2318. NaAlSi3O8, batch reactor, pO2 and pCO2 were atmospheric, surface area measured by Ar-BET.

Stillings and Brantley (1995a) *Geochimica et Cosmochimica Acta* 59, 1483–1496. K0.1Na0.98Ca0.02Al1.01Si2.98O8, continuously stirred flow through reactor, pO2 and pCO2 were atmospheric, surface area measured by Kr-BET, final surface area used for normalization, dissolution was stoichiometric.

Stillings and Brantley (1995b) *Geochimica et Cosmochimica Acta* 59, 1483–1496. K0.1Na0.98Ca0.02Al1.01Si2.98O8, continuously stirred flow through reactor, pO2 and pCO2 were atmospheric, surface area measured by Kr-BET, final surface area used for normalization, NaCl was added to reactors, dissolution was stoichiometric.

Stillings and Brantley (1995c) *Geochimica et Cosmochimica Acta* 59, 1483–1496. K0.1Na0.98Ca0.02Al1.01Si2.98O8, continuously stirred flow through reactor, pO2 and pCO2 were atmospheric, surface area measured by Kr-BET, final surface area used for normalization, (CH3)4NCl was added to reactors, dissolution was not stoichiometric.

Andesine/Labradorite

References	Initial (Final) pH	Initial Fluid Composition	Initial (Final) Specific Surface Area [m^2/g]	Grain Size (min, max) [m]	Temperature [K]	Duration of Dissolution [s]	Si Release Rate [$mol/m^2/s$]	Mineral Dissolution Rate [$mol/m^2/s$]
Holdren and Speyer (1987)	3 (ng)	0.001 N HCl	0.21 (ng)	7.5E-05, 1.5E-04	298	ng	4.00E-11	1.62E-11
Holdren and Speyer (1987)	3 (ng)	0.01 N HCl	0.11 (ng)	6E-04, ng	298	ng	6.21E-11	2.51E-11
Holdren and Speyer (1987)	3 (ng)	0.01 N HCl	0.119 (ng)	3E-04, 6E-04	298	ng	7.00E-11	2.83E-11
Holdren and Speyer (1987)	3 (ng)	0.01 N HCl	0.134 (ng)	1.5E-04, 3E-04	298	ng	6.55E-11	2.65E-11
Holdren and Speyer (1987)	3 (ng)	0.01 N HCl	0.368 (ng)	3.7E-05, 7.5E-05	298	ng	2.95E-11	1.19E-11
Holdren and Speyer (1987)	3 (ng)	0.01 N HCl	1.088 (ng)	ng, 3.7E-05	298	ng	2.27E-11	9.19E-12
Stillings and Brantley (1995a)	3 (3.13)	1 mM HCl	0.0845 (0.5756)	7.5E-05, 1.5E-04	298	1.07E07	1.99E-11	8.06E-12
Stillings and Brantley (1995a)	3 (3.07)	1 mM HCl	0.0845 (0.8108)	7.5E-05, 1.5E-04	298	1.70E07	1.51E-11	6.11E-12
Stillings and Brantley (1995a)	3 (3)	1 mM HCl, 10 mM NaCl	0.0845 (1.2986)	7.5E-05, 1.5E-04	298	2.46E07	4.62E-12	1.87E-12
Stillings and Brantley (1995a)	3 (3.03)	1 mM HCl, 100 mM NaCl	0.0845 (1.5915)	7.5E-05, 1.5E-04	298	3.05E07	2.62E-12	1.06E-12
Stillings and Brantley (1995b)	3 (3.12)	1 mM HCl, 1 mM (CH3)4NCl	0.0845 (0.5957)	7.5E-05, 1.5E-04	298	6.38E06	1.25E-11	5.06E-12
Stillings and Brantley (1995b)	3 (3.05)	1 mM HCl, 100 mM (CH3)4NCl	0.0845 (0.9175)	7.5E-05, 1.5E-04	298	8.91E06	7.48E-12	3.03E-12
Stillings et al. (1996a)	3 (2.96)	1 mM oxalate, 3 mM HCl	0.084 (9.4)	7.5E-05, 1E-04	298	1.12E07	3.20E-10	1.27E-10
Stillings et al. (1996a)	5 (5.72)	1 mM oxalate	0.084 (2.5)	7.5E-05, 1E-04	298	9.86E06	1.22E-10	4.86E-11
Stillings et al. (1996a)	5.08 (5.61)	DI	0.084 (0.1)	7.5E-05, 1E-04	298	1.43E07	7.61E-12	3.02E-12
Stillings et al. (1996b)	3 (3.09)	1 mM oxalic acid, HCl	0.2 (ng)	7.5E-05, 1E-04	298	1.44E06	7.43E-11	2.95E-11
Stillings et al. (1996b)	3 (2.97)	2 mM oxalic acid, HCl	0.16 (ng)	7.5E-05, 1E-04	298	2.94E06	9.58E-11	3.80E-11

Stillings et al. (1996b)	3 (3.04)	4 mM oxalic acid, HCl	0.16 (ng)	7.5E-05, 1E-04	298	2.94E06	1.05E-10	4.17E-11
Stillings et al. (1996b)	3 (3.18)	8 mM oxalic acid, HCl	0.16 (ng)	7.5E-05, 1E-04	298	2.94E06	1.29E-10	5.13E-11
Stillings et al. (1996b)	4 (4.12)	1 mM oxalic acid, HCl	0.2 (ng)	7.5E-05, 1E-04	298	8.32E05	3.81E-11	1.51E-11
Stillings et al. (1996b)	4 (5.23)	2 mM oxalic acid, HCl	0.16 (ng)	7.5E-05, 1E-04	298	2.94E06	3.88E-11	1.54E-11
Stillings et al. (1996b)	4 (4.11)	4 mM oxalic acid, HCl	0.16 (ng)	7.5E-05, 1E-04	298	2.94E06	8.34E-11	3.31E-11
Stillings et al. (1996b)	4 (4.11)	8 mM oxalic acid, HCl	0.16 (ng)	7.5E-05, 1E-04	298	2.94E06	1.21E-10	4.79E-11
Stillings et al. (1996b)	5 (5.06)	1 mM oxalic acid, HCl	0.2 (ng)	7.5E-05, 1E-04	298	1.98E06	2.70E-11	1.07E-11
Stillings et al. (1996b)	5 (6.82)	2 mM oxalic acid, HCl	0.16 (ng)	7.5E-05, 1E-04	298	2.94E06	5.19E-12	2.06E-12
Stillings et al. (1996b)	5 (6.6)	4 mM oxalic acid, HCl	0.16 (ng)	7.5E-05, 1E-04	298	2.94E06	8.19E-12	3.25E-12
Stillings et al. (1996b)	5 (5.54)	8 mM oxalic acid, HCl	0.16 (ng)	7.5E-05, 1E-04	298	2.94E06	5.90E-11	2.34E-11
Stillings et al. (1996b)	7 (7.18)	1 mM oxalic acid, 2 mM KHCO3	0.2 (ng)	7.5E-05, 1E-04	298	3.13E06	2.48E-11	9.83E-12
Stillings et al. (1996b)	7 (7.65)	2 mM oxalic acid, 2 mM KHCO3	0.16 (ng)	7.5E-05, 1E-04	298	2.94E06	5.12E-12	2.03E-12
Stillings et al. (1996b)	7 (7.61)	4 mM oxalic acid, 2 mM KHCO3	0.16 (ng)	7.5E-05, 1E-04	298	2.94E06	9.58E-12	3.80E-12
Stillings et al. (1996b)	7 (7.48)	8 mM oxalic acid, 2 mM KHCO3	0.16 (ng)	7.5E-05, 1E-04	298	2.94E06	1.60E-11	6.36E-12
Oxburgh et al. (1994)	3 (3.1)		0.2 (ng)	7.5E-05, 1.5E-04	295	1.99E06	6.05E-11	2.40E-11

References	Initial (Final) pH	Initial Fluid Composition	Initial (Final) Specific Surface Area [m^2/g]	Grain Size (min, max) [m]	Temperature [K]	Duration of Dissolution [s]	Si Release Rate [$mol/m^2/s$]	Mineral Dissolution Rate [$mol/m^2/s$]
Oxburgh et al. (1994)	4 (4.1)	0.1 mM 2,4-dinitro-phenol buffer	0.2 (ng)	7.5E-05, 1.5E-04	295	1.37E06	1.78E-11	7.08E-12
Oxburgh et al. (1994)	5 (5.1)	0.5 mM ammonium acetate buffer	0.2 (ng)	7.5E-05, 1.5E-04	295	1.19E06	1.45E-11	5.75E-12
Oxburgh et al. (1994)	6.5 (7.3)	0.15 mM potassium bicarbonate buffer	0.2 (ng)	7.5E-05, 1.5E-04	295	3.13E06	1.55E-11	6.16E-12
Taylor et al. (2000)	3.08 (ng)	HCl	0.0203 (0.021)	4.3E-05, 1.1E-04	298	2.16E07	6.00E-11	2.51E-11
Casey et al. (1991)	2 (ng)	0.010 N HCl	0.405 (ng)	2.5E-05, 7.5E-05	298	2.00E06	2.74E-11	6.85E-11
Casey et al. (1991)	2 (ng)	0.010 N HCl	0.35 (ng)	2.5E-05, 7.5E-05	298	2.00E06	3.95E-11	9.88E-11

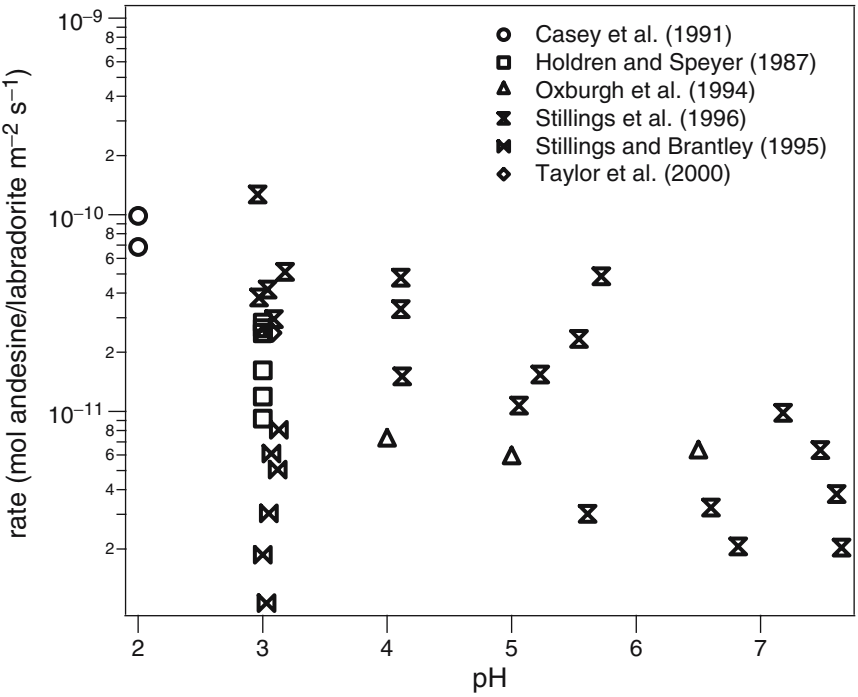

References

Holdren and Speyer (1987) *Geochimica et Cosmochimica Acta* 51, 2311–2318. Andesine, K0.05Na0.46Ca0.46Al1.5Si2.5O8, batch reactor, pO2 and pCO2 were atmospheric, surface area measured by Ar-BET.

Stillings and Brantley (1995a) *Geochimica et Cosmochimica Acta* 59, 1483–1496. Labradorite, K0.06Na0.43Ca0.37Al1.42Si2.47O8, continuously stirred flow through reactor, pO2 and pCO2 were atmospheric, surface area measured by Kr-BET, final surface area used for normalization, dissolution was not stoichiometric.

Stillings and Brantley (1995b) *Geochimica et Cosmochimica Acta* 59, 1483–1496. Labradorite, K0.06Na0.43Ca0.37Al1.42Si2.47O8, continuously stirred flow through reactor, pO2 and pCO2 were atmospheric, surface area measured by Kr-BET, final surface area used for normalization, (CH3)4NCl was added to reactors, dissolution was stoichiometric.

Stillings (1996a) *Chemical Geology* 132, 79–89. Andesine, K0.02Na0.51Ca0.46Al1.48Si2.52O8, continuously stirred flow through reactor, pO2 and pCO2 were atmospheric, surface area measured by Kr-BET, initial surface area used for normalization, dissolution was not stoichiometric. These experiments contained organics.

Stillings (1996b) *Chemical Geology* 132, 79–89. Andesine, K0.02Na0.51Ca0.46Al1.48Si2.52O8, fluidized bed reactor, pO2 and pCO2 were atmospheric, surface area measured by Kr-BET, initial surface area used for normalization, dissolution was not stoichiometric. These experiments contained organics.

Oxburgh (1994) *Geochimica et Cosmochimica Acta* 58, 661–669. Andesine, K0.02Na0.51Ca0.46Al1.48Si2.52O8, fluidized bed reactor, pO2 and pCO2 were atmospheric, surface area measured by N_2-BET.

Taylor (2000) *Geochimica et Cosmochimica Acta* 64, 2389–2400. Labradorite, Ca0.63Na0.39Al1.60Si2.39O8, flow through reactor,, pO2 and pCO2 were atmospheric, surface area measured by N_2-BET, initial and final surface areas were identical within measurement error, dissolution was stoichiometric.

Anorthite

References	Initial (Final) pH	Initial Fluid Composition	Initial (Final) Specific Surface Area [m^2/g]	Grain Size (min, max) [m]	Temperature [K]	Duration of Dissolution [s]	Si Release Rate [$mol/m^2/s$]	Mineral Dissolution Rate [$mol/m^2/s$]
Fleer (1982)	2 (ng)	Ng	3.42E-04 (ng)	ng, ng	298	1.21E06	9.89E-07	4.80E-07
Fleer (1982)	5.6 (ng)	Ng	3.95E-04 (ng)	ng, ng	299	1.21E06	1.15E-08	5.60E-09
Hodson (2003a)	2.6 (ng)	HCl	0.16 (1.65)	5.3E-05, 6.3E-05	298	2.16E07	5.00E-10	2.50E-10
Hodson (2003b)	2.6 (ng)	FeCl3	0.16 (3.89)	5.3E-05, 6.3E-05	298	2.16E07	6.40E-10	3.20E-10
Holdren and Speyer (1987)	3 (ng)	0.001 N HCl	0.757 (ng)	7.5E-05, 1.5E-04	298	ng	6.79E-10	3.25E-10
Holdren and Speyer (1987)	3 (ng)	0.01 N HCl	0.483 (ng)	6E-04, ng	298	ng	6.21E-10	2.98E-10
Holdren and Speyer (1987)	3 (ng)	0.01 N HCl	0.619 (ng)	3E-04, 6E-04	298	ng	6.16E-10	2.95E-10
Holdren and Speyer (1987)	3 (ng)	0.01 N HCl	0.7 (ng)	1.5E-04, 3E-04	298	ng	6.13E-10	2.94E-10
Holdren and Speyer (1987)	3 (ng)	0.01 N HCl	1.02 (ng)	3.7E-05, 7.5E-05	298	ng	5.85E-10	2.80E-10
Holdren and Speyer (1987)	3 (ng)	0.01 N HCl	4.475 (ng)	ng, 3.7E-05	298	ng	1.69E-10	8.12E-11
Casey et al. (1991)	2 (ng)	0.010 N HCl	0.52 (ng)	2.5E-05, 7.5E-05	298	2.00E06	3.08E-09	6.43E-09
Amrhein and Suarez (1992)	4.6 (5)	Ng	0.68 (ng)	2E-05, 5E-05	298	1.06E08	3.36E-12	1.61E-12
Amrhein and Suarez (1992)	4.4 (5)	Ng	0.68 (ng)	2E-05, 5E-05	298	1.06E08	5.39E-12	2.58E-12
Amrhein and Suarez (1992)	4.4 (4.9)	Ng	0.68 (ng)	2E-05, 5E-05	298	1.06E08	4.72E-12	2.26E-12
Amrhein and Suarez (1992)	7.6 (7.7)	Ng	0.68 (ng)	2E-05, 5E-05	298	1.06E08	4.25E-12	2.04E-12
Amrhein and Suarez (1992)	7.2 (7.5)	Ng	0.68 (ng)	2E-05, 5E-05	298	1.03E08	5.09E-15	2.44E-15
Amrhein and Suarez (1992)	7.1 (7.7)	Ng	0.68 (ng)	2E-05, 5E-05	298	1.03E08	1.40E-14	6.71E-15
Amrhein and Suarez (1992)	6.2 (6.6)	Ng	0.11 (ng)	5E-05, 1E-04	298	7.95E07	1.06E-13	5.08E-14
Amrhein and Suarez (1992)	3.6 (4.1)	20 mM NaCl	0.11 (ng)	5E-05, 1E-04	298	6.91E07	1.57E-12	7.52E-13
Amrhein and Suarez (1992)	5.9 (6)	20 mM NaCl	0.11 (ng)	5E-05, 1E-04	298	6.84E07	5.02E-13	2.41E-13
Amrhein and Suarez (1992)	6 (6.6)	5 mM NaCl	0.11 (ng)	5E-05, 1E-04	298	6.84E07	5.06E-13	2.42E-13

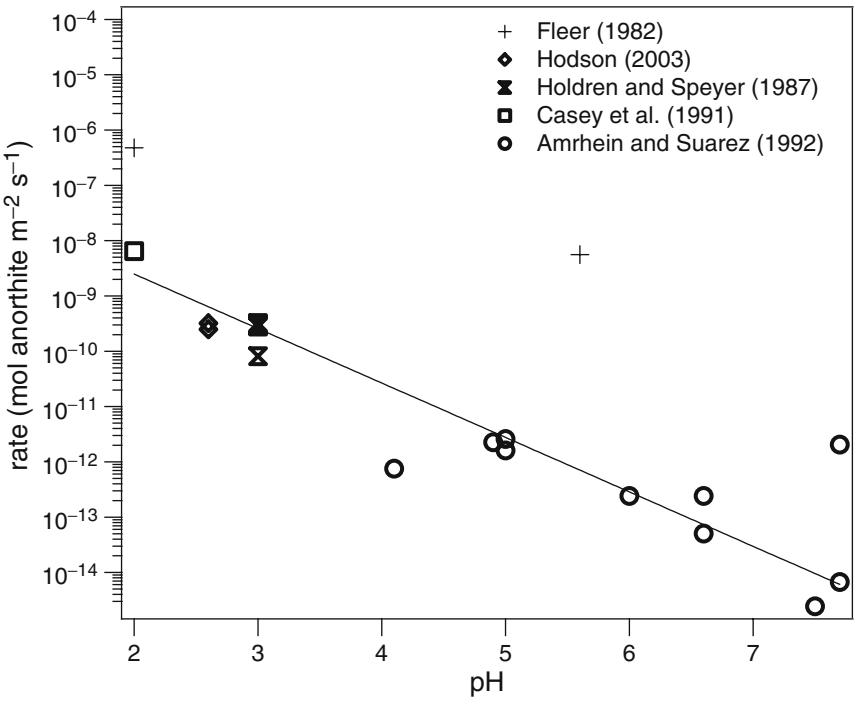

References

Fleer (1982) Ph.D. Dissertation, The Pennsylvania State University. Ca0.94Na0.06Al1.94Si2.06O8, Batch reactor, pO2 and pCO2 were atmospheric, surface area measured by BET, dissolution was nearly stoichiometric. These data were not included in the fit at the discretion of the data analyst.

Hodson (2003a) *Geochimica et Cosmochimica Acta* 67 3355–3363. Ca1.1Al1.9Si2O8, Flow through reactor, pO2 and pCO2 were atmospheric, surface area measured by N2-BET, initial surface area used for normalization, dissolution was stoichiometric.

Hodson (2003b) *Geochimica et Cosmochimica Acta* 67 3355–3363. Ca1.1Al1.9Si2O8, Flow through reactor, pO2 and pCO2 were atmospheric, surface area measured by N2-BET, initial surface area used for normalization, FeCl3 added to reactors resulted in an Fe-rich surface coating, dissolution was stoichiometric.

Holdren and Speyer (1987) *Geochimica et Cosmochimica Acta* 51, 2311–2318. Na0.071Ca0.957(Fe,Mg)0.038Al1.86Si2.087, Batch reactor, pO2 and pCO2 were atmospheric, surface area measured by Ar-BET.

Casey (1991) *American Mineralogist* 76, 211–217. Na0.08Ca0.92Al1.90Si2.09O8, Batch reactor, pO2 and pCO2 were atmospheric, surface area measured by BET, dissolution was not stoichiometric.

Amrhein and Suarez (1992) *Geochimica et Cosmochimica Acta* 56, 1815–1826. Na0.071Ca0.957(Fe,Mg)0.038Al1.86Si2.087, Batch reactor, pO2 and pCO2 were atmospheric, surface area measured by Kr-BET, dissolution was not stoichiometric.

Apatite

References	Initial (Final) pH	Initial Fluid Composition	Initial (Final) Specific Surface Area [m^2/g]	Grain Size (min, max) [m]	Temperature [K]	Duration of Dissolution [s]	Si Release Rate [$mol/m^2/s$]	Mineral Dissolution Rate [$mol/m^2/s$]
Guidry and Mackenzie (2003a)	2.02 (2.2)	NaCl, I = 0.1 M	0.026 (ng)	1.1E-04, 2.1E-04	298	2.6E05	na	1.2E-07
Guidry and Mackenzie (2003a)	3 (3.15)	NaCl, I = 0.1 M	0.026 (ng)	1.1E-04, 2.1E-04	298	2.6E05	na	1.3E-08
Guidry and Mackenzie (2003a)	3.88 (3.95)	NaCl, I = 0.1 M	0.026 (ng)	1.1E-04, 2.1E-04	298	2.6E05	na	2.7E-09
Guidry and Mackenzie (2003a)	4 (4.2)	NaCl, I = 0.1 M	0.026 (ng)	1.1E-04, 2.1E-04	298	2.6E05	na	1.7E-09
Guidry and Mackenzie (2003a)	4.1 (4.31)	NaCl, I = 0.1 M	0.026 (ng)	1.1E-04, 2.1E-04	298	2.6E05	na	1.6E-09
Guidry and Mackenzie (2003a)	4.56 (4.9)	NaCl, I = 0.1 M	0.026 (ng)	1.1E-04, 2.1E-04	298	2.6E05	na	5.0E-10
Guidry and Mackenzie (2003b)	5.22 (5.38)	NaCl, I = 0.1 M	0.026 (ng)	1.1E-04, 2.1E-04	298	2.6E05	na	3.8E-10
Guidry and Mackenzie (2003b)	3.51 (3.75)	NaCl, I = 0.1 M	0.026 (ng)	1.1E-04, 2.1E-04	298	2.6E05	na	7.1E-09
Guidry and Mackenzie (2003b)	4.16 (4.37)	NaCl, I = 0.1 M	0.026 (ng)	1.1E-04, 2.1E-04	298	2.6E05	na	2.1E-09
Guidry and Mackenzie (2003b)	4.5 (4.72)	NaCl, I = 0.1 M	0.026 (ng)	1.1E-04, 2.1E-04	298	2.6E05	na	9.5E-10
Guidry and Mackenzie (2003b)	7.86 (7.9)	NaCl, I = 0.1 M	0.026 (ng)	1.1E-04, 2.1E-04	298	2.6E05	na	7.9E-11
Guidry and Mackenzie (2003b)	6.5 (6.65)	NaCl, I = 0.1 M	0.026 (ng)	1.1E-04, 2.1E-04	298	2.6E05	na	4.0E-11
Guidry and Mackenzie (2003b)	8.45 (8.52)	NaCl, I = 0.1 M	0.026 (ng)	1.1E-04, 2.1E-04	298	2.6E05	na	4.0E-11
Guidry and Mackenzie (2003b)	7.3 (7.46)	NaCl, I = 0.1 M	0.026 (ng)	1.1E-04, 2.1E-04	298	2.6E05	na	5.0E-11
Guidry and Mackenzie (2003b)	5.9 (6.78)	NaCl, I = 0.1 M	0.026 (ng)	1.1E-04, 2.1E-04	298	2.6E05	na	6.3E-11
Guidry and Mackenzie (2003b)	4.97 (6.26)	NaCl, I = 0.1 M	0.026 (ng)	1.1E-04, 2.1E-04	298	2.6E05	na	6.3E-11
Guidry and Mackenzie (2003c)	3.01 (4.85)	NaCl, I = 0.002 M	9.1 (ng)	1.1E-04, 2.1E-04	298	1.7E05	na	2.6E-10
Guidry and Mackenzie (2003d)	2.98 (4.4)	NaCl, I = 0.002 M	6.8 (ng)	1.1E-04, 2.1E-04	298	1.7E05	na	1.2E-10
Guidry and Mackenzie (2003d)	5.02 (7.09)	NaCl, I = 0.002 M	6.8 (ng)	1.1E-04, 2.1E-04	298	1.7E05	na	5.0E-12
Guidry and Mackenzie (2003e)	3.03 (4.33)	NaCl, I = 0.002 M	16 (ng)	1.1E-04, 2.1E-04	298	1.7E05	na	1.3E-10
Guidry and Mackenzie (2003e)	3 (4.4)	NaCl, I = 0.002 M	16 (ng)	1.1E-04, 2.1E-04	298	1.7E05	na	1.1E-10

Guidry and Mackenzie (2003e)	4.8 (6.33)	NaCl, I = 0.002 M	16 (ng)	1.1E-04, 2.1E-04	298	1.7E05	na	4.0E-12
Guidry and Mackenzie (2003e)	3.56 (5.1)	NaCl, I = 0.002 M	16 (ng)	1.1E-04, 2.1E-04	298	1.7E05	na	2.0E-11
Guidry and Mackenzie (2003f)	3.02 (4.5)	NaCl, I = 0.002 M	8.1 (ng)	1.1E-04, 2.1E-04	298	1.7E05	na	1.2E-10
Guidry and Mackenzie (2003f)	5.02 (6.77)	NaCl, I = 0.002 M	8.1 (ng)	1.1E-04, 2.1E-04	298	1.7E05	na	2.5E-12
Valsami-Jones et al. (1998a)	4.7 (7)	0.1 M NaNO3	80 (ng)	9.0E-05, 5.0E-04	298	2.9E04	na	4.5E-11
Valsami-Jones et al. (1998a)	3.6 (6.8)	0.1 M NaNO3	80 (ng)	9.0E-05, 5.0E-04	298	2.9E04	na	5.3E-11
Valsami-Jones et al. (1998a)	2.2 (5.2)	0.1 M NaNO3	80 (ng)	9.0E-05, 5.0E-04	298	1.4E04	na	6.7E-10
Valsami-Jones et al. (1998a)	2.2 (5.1)	HCl/KCl	80 (ng)	9.0E-05, 5.0E-04	298	1.4E04	na	1.0E-09
Valsami-Jones et al. (1998a)	1.7 (4.2)	HCl/KCl	80 (ng)	9.0E-05, 5.0E-04	298	2.9E04	na	2.3E-09
Valsami-Jones et al. (1998b)	4.7 (6.2)	0.1 M NaNO3	0.17 (ng)	2.0E-05, 9.0E-05	298	2.9E04	na	1.8E-09
Valsami-Jones et al. (1998b)	3.6 (4.6)	0.1 M NaNO3	0.17 (ng)	2.0E-05, 9.0E-05	298	2.9E04	na	3.0E-09
Welch et al. (2002)	2 (2.4)	1 mM NaCl	0.027 (ng)	1.5E-04, 5.0E-04	295	2.6E05	na	4.8E-08
Welch et al. (2002)	3 (3.9)	1 mM NaCl	0.027 (ng)	1.5E-04, 5.0E-04	295	2.6E05	na	3.0E-09
Welch et al. (2002)	4 (6)	1 mM NaCl	0.027 (ng)	1.5E-04, 5.0E-04	295	2.6E05	na	3.7E-11
Welch et al. (2002)	5.5 (7)	1 mM NaCl	0.027 (ng)	1.5E-04, 5.0E-04	295	2.6E05	na	5.0E-12
Welch et al. (2002)	2 (2.4)	1 mM acetate	0.027 (ng)	1.5E-04, 5.0E-04	295	2.6E05	na	3.7E-08
Welch et al. (2002)	3 (3.9)	1 mM acetate	0.027 (ng)	1.5E-04, 5.0E-04	295	2.6E05	na	4.6E-09
Welch et al. (2002)	4 (6)	1 mM acetate	0.027 (ng)	1.5E-04, 5.0E-04	295	2.6E05	na	1.6E-10
Welch et al. (2002)	5.5 (6.5)	1 mM acetate	0.027 (ng)	1.5E-04, 5.0E-04	295	2.6E05	na	8.0E-11
Welch et al. (2002)	2 (2.4)	1 mM oxalate	0.027 (ng)	1.5E-04, 5.0E-04	295	2.6E05	na	5.4E-08
Welch et al. (2002)	3 (3.9)	1 mM oxalate	0.027 (ng)	1.5E-04, 5.0E-04	295	2.6E05	na	9.8E-09
Welch et al. (2002)	4 (6)	1 mM oxalate	0.027 (ng)	1.5E-04, 5.0E-04	295	2.6E05	na	7.0E-10
Welch et al. (2002)	5.5 (7.5)	1 mM oxalate	0.027 (ng)	1.5E-04, 5.0E-04	295	2.6E05	na	1.1E-10

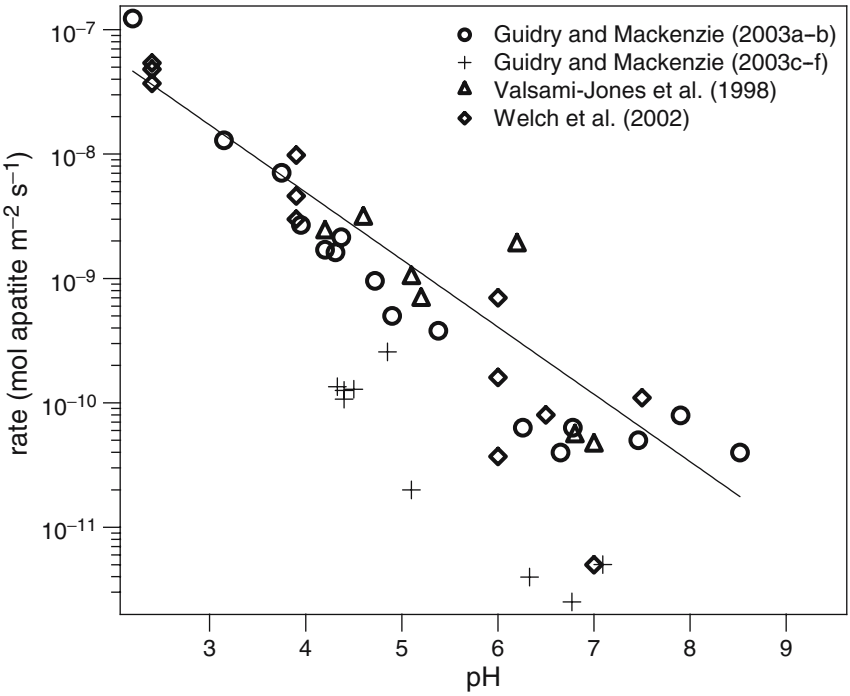

References

Guidry and Mackenzie (2003a) *Geochimica et Cosmochimica Acta*, 67, 2949–2963. Fluorapatite, Ca5(PO4)3F, Fluidized bed reactor, pO2 = 1 atm pCO2 = 0, surface area measured by Kr-BET, dissolution was stoichiometric. Element(s) monitored: Ca, P, F.

Guidry and Mackenzie (2003b) *Geochimica et Cosmochimica Acta*, 67, 2949–2963. Fluorapatite, Ca5(PO4)3F, Stirred tank reactor, pO2 = 1 atm pCO2 = 0, surface area measured by Kr-BET, dissolution was stoichiometric. Element(s) monitored: Ca, P, F.

Guidry and Mackenzie (2003c) *Geochimica et Cosmochimica Acta*, 67, 2949–2963. Carbonated Fluorapatite-1, Ca7.4(CO3)(PO4)3.7F2, Fluidized bed reactor, pO2 = 1 atm pCO2 = 0, surface area measured by Kr-BET, dissolution was stoichiometric. Carbonated apatites were excluded from the fit. Element(s) monitored: Ca, P, F.

Guidry and Mackenzie (2003d) *Geochimica et Cosmochimica Acta*, 67, 2949–2963. Carbonated Fluorapatite-3, Ca20(CO3)(PO4)11.5F4.6, Fluidized bed reactor, pO2 = 1 atm pCO2 = 0, surface area measured by Kr-BET, dissolution was stoichiometric. Carbonated apatites were excluded from the fit. Element(s) monitored: Ca, P, F.

Guidry and Mackenzie (2003e) *Geochimica et Cosmochimica Acta*, 67, 2949–2963. Carbonated Fluorapatite-9, Ca11.4(CO3)(PO4)6F2.8, Fluidized bed reactor, pO2 = 1 atm pCO2 = 0, surface area measured by Kr-BET, dissolution was stoichiometric. Carbonated apatites were excluded from the fit. Element(s) monitored: Ca, P, F.

Guidry and Mackenzie (2003f) *Geochimica et Cosmochimica Acta*, 67, 2949–2963. Carbonated Fluorapatite-10, Ca9.8(CO3)(PO4)5.2F2.5, Fluidized bed reactor, pO2 = 1 atm pCO2 = 0, surface area measured by Kr-BET, dissolution was stoichiometric. Carbonated apatites were excluded from the fit. Element(s) monitored: Ca, P, F.

Valsami-Jones et al. (1998a) *Chemical Geology*, 151, 215–233. Synthetic hydroxylapatite, Ca5(PO4)3(OH), Batch reactor, pO2 = 1 atm pCO2 = 1 atm, surface area measured by N2-BET, dissolution was assumed to be stoichiometric. Element(s) monitored: Ca.

Valsami-Jones et al. (1998b) *Chemical Geology*, 151, 215–233. Fluorapatite, Ca5(PO4)3F, Batch reactor, pO2 = 1 atm pCO2 = 1 atm, surface area measured by N2-BET, dissolution was assumed to be stoichiometric. Element(s) monitored: Ca.

Welch et al. (2002) *Geomicrobiology Journal*, 19, 343–367. Fluorapatite, Ca5(PO4)3F, Batch reactor, pO2 = 1 atm pCO2 = 1 atm, surface area measured by Kr-BET, dissolution was not stoichiometric. Element(s) monitored: P.

Basalt

References	Initial (Final) pH	Initial Fluid Composition	Initial (Final) Specific Surface Area [m^2/g]	Grain Size (min, max) [m]	Temperature [K]	Duration of Dissolution [s]	Si Release Rate [$mol/m^2/s$]	Mineral Dissolution Rate [$molSi/m^2/s$]
Gislason and Eugster (1987a)	5.6 (9.13)	Ng	0.16 (ng)	1.3E-04, 2.5E-04	297	1.0E07	ng	1.78E-11
Gislason and Eugster (1987b)	5.6 (9.36)	Ng	0.025 (0.03)	1.3E-04, 2.5E-04	298	1.0E07	ng	2.82E-10
Gislason and Eugster (1987b)	5.6 (9.55)	Ng	0.025 (0.03)	1.3E-04, 2.5E-04	298	1.0E07	ng	2.4E-10
Eick et al. (1996a)	3 (3)	I = 0.066 M	0.187 (ng)	3.8E-05, 8.5E-04	298	3.1E07	1.88E-12	1.88E-12
Eick et al. (1996a)	5 (5)	I = 0.107 M	0.187 (ng)	3.8E-05, 8.5E-04	298	3.1E07	8.88E-13	8.88E-13
Eick et al. (1996a)	7 (7)	I = 0.051 M	0.187 (ng)	3.8E-05, 8.5E-04	298	3.1E07	1.69E-13	1.69E-13
Eick et al. (1996a)	7 (7)	I = 0.011 M	0.187 (ng)	3.8E-05, 8.5E-04	298	3.1E07	1.67E-13	1.67E-13
Eick et al. (1996a)	7 (7)	I = 0.006 M	0.187 (ng)	3.8E-05, 8.5E-04	298	3.1E07	1.70E-13	1.70E-13
Eick et al. (1996b)	3 (3)	I = 0.066 M	0.683 (ng)	3.8E-05, 8.5E-04	298	3.1E07	4.60E-10	4.60E-10
Eick et al. (1996b)	5 (5)	I = 0.107 M	0.683 (ng)	3.8E-05, 8.5E-04	298	3.1E07	3.31E-11	3.31E-11
Eick et al. (1996b)	7 (7)	I = 0.051 M	0.683 (ng)	3.8E-05, 8.5E-04	298	3.1E07	6.91E-11	6.91E-11
Eick et al. (1996b)	7 (7)	I = 0.011 M	0.683 (ng)	3.8E-05, 8.5E-04	298	3.1E07	7.04E-11	7.04E-11
Eick et al. (1996b)	7 (7)	I = 0.006 M	0.683 (ng)	3.8E-05, 8.5E-04	298	3.1E07	7.12E-11	7.12E-11
Oelkers and Gislason (2001)	3 (3.08)	HCl	0.23, (ng)	4.0E-05, 1.2E-04	298	7.2E03 – 8.0E04	ng	1.22E-09
Oelkers and Gislason (2001)	3 (3)	HCl	0.23, (ng)	4.0E-05, 1.2E-04	298	7.2E03 – 8.0E04	ng	1.33E-09
Oelkers and Gislason (2001)	3 (3.03)	HCl	0.23, (ng)	4.0E-05, 1.2E-04	298	7.2E03 – 8.0E04	ng	1.23E-09
Oelkers and Gislason (2001)	3 (3.09)	HCl	0.23, (ng)	4.0E-05, 1.2E-04	298	7.2E03 – 8.0E04	ng	1.38E-09
Oelkers and Gislason (2001)	3 (3.08)	HCl	0.23, (ng)	4.0E-05, 1.2E-04	298	7.2E03 – 8.0E04	ng	1.65E-09
Oelkers and Gislason (2001)	3 (3.08)	HCl	0.23, (ng)	4.0E-05, 1.2E-04	298	7.2E03 – 8.0E04	ng	1.13E-09
Oelkers and Gislason (2001)	3 (3.18)	HCl	0.23, (ng)	4.0E-05, 1.2E-04	298	7.2E03 – 8.0E04	ng	2.19E-09
Oelkers and Gislason (2001)	3 (3.03)	HCl	0.23, (ng)	4.0E-05, 1.2E-04	298	7.2E03 – 8.0E04	ng	1.18E-09
Oelkers and Gislason (2001)	3 (3)	HCl	0.23, (ng)	4.0E-05, 1.2E-04	298	7.2E03 – 8.0E04	ng	1.22E-09
Oelkers and Gislason (2001)	3 (2.99)	HCl	0.23, (ng)	4.0E-05, 1.2E-04	298	7.2E03 – 8.0E04	ng	6.71E-10
Oelkers and Gislason (2001)	3 (3)	HCl	0.23, (ng)	4.0E-05, 1.2E-04	298	7.2E03 – 8.0E04	ng	4.27E-10
Oelkers and Gislason (2001)	3 (2.98)	HCl	0.23, (ng)	4.0E-05, 1.2E-04	298	7.2E03 – 8.0E04	ng	8.43E-10
Oelkers and Gislason (2001)	3 (3.11)	HCl	0.23, (ng)	4.0E-05, 1.2E-04	298	7.2E03 – 8.0E04	ng	5.09E-10

Oelkers and Gislason (2001)	3 (3.04)	HCl	0.23, (ng)	4.0E-05, 1.2E-04	298	7.2E03 – 8.0E04	ng	4.53E-10
Oelkers and Gislason (2001)	3 (3.05)	4.91E-05 mol Si/kg, HCl	0.23, (ng)	4.0E-05, 1.2E-04	298	7.2E03 – 8.0E04	ng	9.40E-10
Oelkers and Gislason (2001)	3 (3.05)	HCl	0.23, (ng)	4.0E-05, 1.2E-04	298	7.2E03 – 8.0E04	ng	9.96E-10
Oelkers and Gislason (2001)	3 (3.08)	7.9E-05 mol Si/kg, HCl	0.23, (ng)	4.0E-05, 1.2E-04	298	7.2E03 – 8.0E04	ng	7.15E-10
Oelkers and Gislason (2001)	3 (2.98)	7.9E-05 mol Si/kg, HCl	0.23, (ng)	4.0E-05, 1.2E-04	298	7.2E03 – 8.0E04	ng	1.00E-09
Oelkers and Gislason (2001)	3 (3.04)	17.5E-05 mol Si/kg, HCl	0.23, (ng)	4.0E-05, 1.2E-04	298	7.2E03 – 8.0E04	ng	5.36E-10
Oelkers and Gislason (2001)	3 (3)	17.5E-05 mol Si/kg, HCl	0.23, (ng)	4.0E-05, 1.2E-04	298	7.2E03 – 8.0E04	ng	5.55E-10
Oelkers and Gislason (2001)	3 (3.1)	HCl	0.23, (ng)	4.0E-05, 1.2E-04	298	7.2E03 – 8.0E04	ng	6.66E-10
Oelkers and Gislason (2001)	3 (2.91)	HCl	0.23, (ng)	4.0E-05, 1.2E-04	298	7.2E03 – 8.0E04	ng	1.73E-09
Oelkers and Gislason (2001)	3 (3.03)	HCl	0.23, (ng)	4.0E-05, 1.2E-04	298	7.2E03 – 8.0E04	ng	1.31E-09
Oelkers and Gislason (2001)	11 (10.97)	NaOH	0.23, (ng)	4.0E-05, 1.2E-04	298	7.2E03 – 8.0E04	ng	9.92E-11
Oelkers and Gislason (2001)	11 (10.97)	NaOH	0.23, (ng)	4.0E-05, 1.2E-04	298	7.2E03 – 8.0E04	ng	7.52E-11
Oelkers and Gislason (2001)	11 (10.96)	NaOH	0.23, (ng)	4.0E-05, 1.2E-04	298	7.2E03 – 8.0E04	ng	5.49E-11
Oelkers and Gislason (2001)	11 (10.98)	NaOH	0.23, (ng)	4.0E-05, 1.2E-04	298	7.2E03 – 8.0E04	ng	8.89E-11
Oelkers and Gislason (2001)	11 (11)	NaOH	0.23, (ng)	4.0E-05, 1.2E-04	298	7.2E03 – 8.0E04	ng	6.78E-11
Oelkers and Gislason (2001)	11 (10.97)	11.44E-05 mol Si/kg, NaOH	0.23, (ng)	4.0E-05, 1.2E-04	298	7.2E03 – 8.0E04	ng	6.17E-11
Oelkers and Gislason (2001)	11 (11)	NaOH	0.23, (ng)	4.0E-05, 1.2E-04	298	7.2E03 – 8.0E04	ng	6.40E-11
Oelkers and Gislason (2001)	11 (10.99)	NaOH	0.23, (ng)	4.0E-05, 1.2E-04	298	7.2E03 – 8.0E04	ng	6.16E-11
Oelkers and Gislason (2001)	11 (11)	NaOH	0.23, (ng)	4.0E-05, 1.2E-04	298	7.2E03 – 8.0E04	ng	5.35E-11

References	Initial (Final) pH	Initial Fluid Composition	Initial (Final) Specific Surface Area [m^2/g]	Grain Size (min, max) [m]	Temperature [K]	Duration of Dissolution [s]	Si Release Rate [$mol/m^2/s$]	Mineral Dissolution Rate [$molSi/m^2/s$]
Oelkers and Gislason (2001)	11 (11.02)	8.39E-05 mol Si/kg, NaOH	0.23, (ng)	4.0E-05, 1.2E-04	298	7.2E03 – 8.0E04	ng	5.11E-11
Oelkers and Gislason (2001)	11 (11)	NaOH	0.23, (ng)	4.0E-05, 1.2E-04	298	7.2E03 – 8.0E04	ng	5.87E-11
Oelkers and Gislason (2001)	11 (11.06)	NaOH	0.23, (ng)	4.0E-05, 1.2E-04	298	7.2E03 – 8.0E04	ng	4.87E-11
Oelkers and Gislason (2001)	11 (11.04)	NaOH	0.23, (ng)	4.0E-05, 1.2E-04	298	7.2E03 – 8.0E04	ng	5.07E-11
Gislason and Oelkers (2003)	ng (4.37)	I = 0.01 kg/mol	2.3 (29.1)	4.0E-05, 1.2E-04	279	ng	ng	9.15E-12
Gislason and Oelkers (2003)	ng (4.86)	I = 0.01 kg/mol	2.3 (29.1)	4.0E-05, 1.2E-04	279	ng	ng	5.07E-12
Gislason and Oelkers (2003)	ng (7.08)	I = 0.01 kg/mol	2.3 (29.1)	4.0E-05, 1.2E-04	280	ng	ng	3.64E-12
Gislason and Oelkers (2003)	ng (8.25)	I = 0.01 kg/mol	2.3 (29.1)	4.0E-05, 1.2E-04	280	ng	ng	4.47E-12
Gislason and Oelkers (2003)	ng (9.49)	I = 0.01 kg/mol	2.3 (29.1)	4.0E-05, 1.2E-04	280	ng	ng	1.17E-11
Gislason and Oelkers (2003)	ng (10.31)	I = 0.01 kg/mol	2.3 (29.1)	4.0E-05, 1.2E-04	280	ng	ng	9.85E-12
Gislason and Oelkers (2003)	ng (11.11)	I = 0.01 kg/mol	2.3 (29.1)	4.0E-05, 1.2E-04	280	ng	ng	1.44E-11
Gislason and Oelkers (2003)	ng (3.34)	I = 0.01 kg/mol	2.3 (29.1)	4.0E-05, 1.2E-04	283	ng	ng	3.17E-10
Gislason and Oelkers (2003)	ng (2.25)	I = 10 mM	2.3 (29.1)	4.0E-05, 1.2E-04	284	ng	ng	1.48E-09
Gislason and Oelkers (2003)	ng (4.17)	I = 10 mM	2.3 (29.7)	4.0E-05, 1.2E-04	303	ng	ng	4.74E-11
Gislason and Oelkers (2003)	ng (3.31)	I = 10 mM	2.3 (29.7)	4.0E-05, 1.2E-04	303	ng	ng	7.93E-10
Gislason and Oelkers (2003)	ng (2.4)	I = 10 mM	2.3 (29.7)	4.0E-05, 1.2E-04	303	ng	ng	8.79E-09
Gislason and Oelkers (2003)	ng (6.75)	I = 10 mM	2.3 (1.4)	4.0E-05, 1.2E-04	302	ng	ng	3.97E-11
Gislason and Oelkers (2003)	ng (7.94)	I = 10 mM	2.3 (1.4)	4.0E-05, 1.2E-04	303	ng	ng	7.39E-11
Gislason and Oelkers (2003)	ng (8.88)	I = 10 mM	2.3 (1.4)	4.0E-05, 1.2E-04	303	ng	ng	1.52E-10

Gislason and Oelkers (2003)	ng (9.95)	I = 10 mM	2.3 (1.4)	4.0E-05, 1.2E-04	303	ng	ng	1.66E-10
Gislason and Oelkers (2003)	ng (10.55)	I = 10 mM	2.3 (1.4)	4.0E-05, 1.2E-04	303	ng	ng	2.52E-10
Gislason and Oelkers (2003)	ng (3.94)	I = 10 mM	2.3 (ng)	4.0E-05, 1.2E-04	323	ng	ng	1.83E-10
Gislason and Oelkers (2003)	ng (6.23)	I = 10 mM	2.3 (ng)	4.0E-05, 1.2E-04	323	ng	ng	7.83E-11
Gislason and Oelkers (2003)	ng (6.99)	I = 10 mM	2.3 (ng)	4.0E-05, 1.2E-04	323	ng	ng	2.10E-10
Gislason and Oelkers (2003)	ng (8.13)	Ng	2.3 (ng)	4.0E-05, 1.2E-04	323	ng	ng	2.04E-10
Gislason and Oelkers (2003)	ng (8.99)	Ng	2.3 (ng)	4.0E-05, 1.2E-04	323	ng	ng	2.28E-10
Gislason and Oelkers (2003)	ng (9.52)	Ng	2.3 (ng)	4.0E-05, 1.2E-04	323	ng	ng	4.73E-10
Gislason and Oelkers (2003)	ng (3.1)	I = 0.066 M	2.3 (ng)	4.0E-05, 1.2E-04	323	ng	ng	3.17E-09
Gislason and Oelkers (2003)	ng (2.14)	I = 0.107 M	2.3 (ng)	4.0E-05, 1.2E-04	322	ng	ng	1.43E-08
Gislason and Oelkers (2003)	ng (5.31)	I = 0.051 M	2.3 (28.2)	4.0E-05, 1.2E-04	303	ng	ng	2.78E-11
Gislason and Oelkers (2003)	ng (5.03)	I = 0.011 M	2.3 (28.2)	4.0E-05, 1.2E-04	333	ng	ng	2.10E-10
Gislason and Oelkers (2003)	ng (4.8)	I = 0.006 M	2.3 (28.2)	4.0E-05, 1.2E-04	373	ng	ng	6.92E-10
Gislason and Oelkers (2003)	ng (4.58)	I = 0.066 M	2.3 (28.2)	4.0E-05, 1.2E-04	422	ng	ng	3.09E-09
Wolff-Boenisch et al. (2004a)	4.07 (ng)	I = 0.107 M, HCl	0.11 (ng)	4.5E-05, 1.25E-04	298	ng	ng	4.17E-10
Wolff-Boenisch et al. (2004b)	4.08 (ng)	I = 0.051 M, HCl	0.14 (ng)	4.5E-05, 1.25E-04	298	ng	ng	1.38E-10
Wolff-Boenisch et al. (2004b)	10.69 (ng)	I = 0.011 M, NH4OH	0.14 (ng)	4.5E-05, 1.25E-04	298	ng	ng	1.38E-09
Wolff-Boenisch et al. (2004c)	4.12 (ng)	I = 0.006 M, HCl	0.14 (ng)	4.5E-05, 1.25E-04	298	ng	ng	1.70E-10
Wolff-Boenisch et al. (2004c)	10.78 (ng)	NH4OH	0.14 (ng)	4.5E-05, 1.25E-04	298	ng	ng	1.07E-09
Wolff-Boenisch et al. (2004d)	4.17 (ng)	HCl	0.94 (ng)	4.5E-05, 1.25E-04	298	ng	ng	4.27E-11
Wolff-Boenisch et al. (2004d)	10.5 (ng)	NH4OH	0.94 (ng)	4.5E-05, 1.25E-04	298	ng	ng	6.17E-10
Wolff-Boenisch et al. (2004e)	4.17 (ng)	HCl	0.19 (ng)	4.5E-05, 1.25E-04	298	ng	ng	1.48E-10
Wolff-Boenisch et al. (2004e)	10.65 (ng)	NH4OH	0.19 (ng)	4.5E-05, 1.25E-04	298	ng	ng	1.82E-09
Wolff-Boenisch et al. (2004e)	10.49 (ng)	NH4OH	0.19 (ng)	4.5E-05, 1.25E-04	298	ng	ng	1.91E-09
Wolff-Boenisch et al. (2004f)	4 (ng)	HCl	5.22 (ng)	4.5E-05, 1.25E-04	298	ng	ng	6.03E-12
Wolff-Boenisch et al. (2004f)	10.77 (ng)	NH4OH	5.22 (ng)	4.5E-05, 1.25E-04	298	ng	ng	7.41E-11

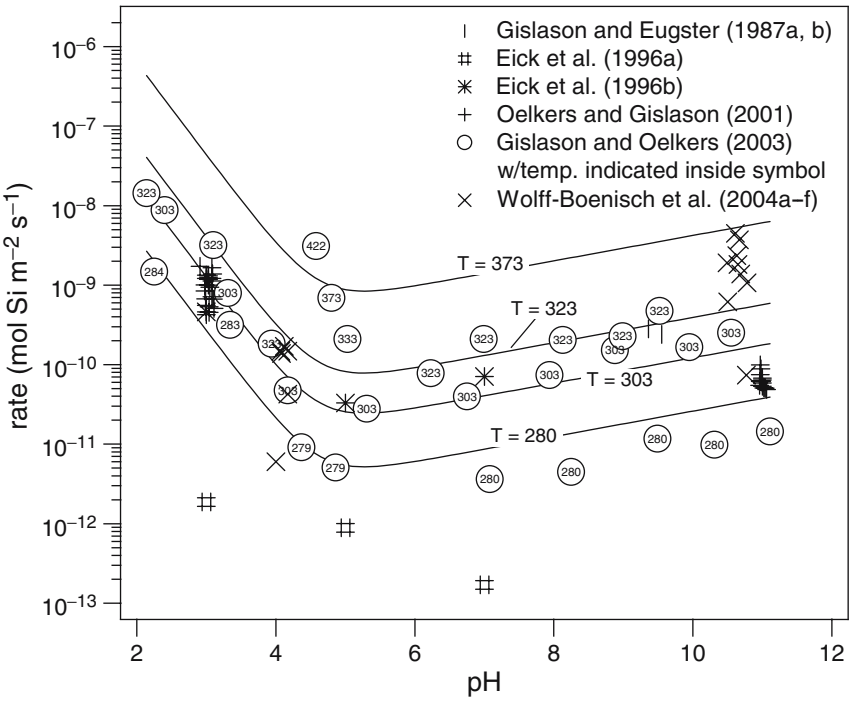

References

Gislason and Eugster (1987a) *Geochimica et Cosmochimica Acta* 51, 2827–2840. Crystalline Basalt, Na0.76Ca0.323K0.01P0.004Mg0.15Fe0.502Mn0.009Ti0.053Al0.296SiO1.846, batch reactor, initially ambient pO_2 and pCO_2, surface area measured by BET, dissolution was not stoichiometric. These data were not included in the fit because they did not reach steady-state.

Gislason and Eugster (1987b) *Geochimica et Cosmochimica Acta* 51, 2827–2840. Basaltic Glass, Na0.792Ca0.326K0.008P0.005Mg0.144Fe0.502Mn0.009Ti0.058Al0.285SiO1.838, batch reactor, initially ambient pO_2 and pCO_2, surface area measured by BET, dissolution was stoichiometric. These data were not included in the fit because they did not reach steady-state.

Eick (1996a) *Geochimica et Cosmochimica Acta* 60, 157–170. Basaltic Glass (Lunar), Na0.07Ca0.326K0.013P0.009Mg0.160Fe0.525Ti0.148Al0.385SiO2.024, batch reactor, ambient pO_2 and pCO_2, surface area measured by BET N_2, dissolution was stoichiometric. These data were not included in the fit because the high Ti content significantly slowed the dissolution rate.

Eick (1996b) *Geoderma* 74, 139–160. Basaltic Glass (Lunar), Na0.07Ca0.326K0.013P0.009Mg0.160Fe0.525Ti0.148Al0.385SiO2.024, batch reactor, ambient pO_2 and pCO_2, surface area measured by N_2 BET, dissolution was not

stoichiometric. These data were not included in the fit because the high Ti content significantly slowed the dissolution rate.

Oelkers and Gislason (2001) *Geochimica et Cosmochimica Acta* 65, 3671–3681. Basaltic Glass, Na0.08Ca0.263Mg0.281Fe0.188Ti0.02Al0.358SiO3.45, mixed flow reactor, pO_2 and pCO_2 not given, surface area measured by N_2 and krypton BET, dissolution was nearly stoichiometric, paper examines effect of $\{Al^{3+}\}$ by varying flow rate and reactor input solution. These data were not included in the fit because $\{Al^{3+}\}$ was varried.

Gislason and Oelkers (2003) *Geochimica et Cosmochimica Acta* 67, 3817–3832. Basaltic Glass, Na0.08Ca0.263Mg0.281Fe0.188Al0.358SiO3.32, mixed flow reactor, surface area measured by N_2 and krypton BET, dissolution was not stoichiometric.

Wolff-Boenisch et al. (2004a) *Geochimica et Cosmochimica Acta* 68, 4843–4858. Basaltic Glass, Na0.08Ca0.3K0.02P0.005Mg0.14Fe(II)0.33Fe(III)0.07Ti0.06Al0.32SiO1.83, mixed flow reactor, surface area measured by N_2 and krypton BET, dissolution was not stoichiometric. These data were not included in the fit because basalt composition was treated as the primary independent variable.

Wolff-Boenisch et al. (2004b) *Geochimica et Cosmochimica Acta* 68, 4843–4858. Basaltic Glass, Na0.08Ca0.27K0.02P0.005Mg0.12Fe(II)0.36Fe(III)0.15Ti0.07Al0.29SiO1.84, mixed flow reactor, surface area measured by N_2 and krypton BET, dissolution was not stoichiometric. These data were not included in the fit because basalt composition was treated as the primary independent variable.

Wolff-Boenisch et al. (2004c) *Geochimica et Cosmochimica Acta* 68, 4843–4858. Basaltic Glass, Na0.07Ca0.31K0.01P0.004Mg0.15Fe(II)0.39Fe(III)0.09Ti0.05Al0.3SiO1.85, mixed flow reactor, surface area measured by N_2 and krypton BET, dissolution was not stoichiometric. These data were not included in the fit because basalt composition was treated as the primary independent variable.

Wolff-Boenisch et al. (2004d) *Geochimica et Cosmochimica Acta* 68, 4843–4858. Basaltic Glass, Na0.09Ca0.30K0.03P0.01Mg0.13Fe(II)0.39Fe(III)0.008Ti0.12Al0.3SiO1.92, mixed flow reactor, surface area measured by N_2 and krypton BET, dissolution was not stoichiometric. These data were not included in the fit because basalt composition was treated as the primary independent variable.

Wolff-Boenisch et al. (2004e) *Geochimica et Cosmochimica Acta* 68, 4843–4858. Basaltic Glass, Na0.12Ca0.32K0.02P0.007Mg0.16Fe(II)0.34Fe(III)0.007Ti0.07Al0.4SiO1.97, mixed flow reactor, surface area measured by N_2 and krypton BET, dissolution was not stoichiometric. These data were not included in the fit because basalt composition was treated as the primary independent variable.

Wolff-Boenisch et al. (2004f) *Geochimica et Cosmochimica Acta* 68, 4843–4858. Basaltic Glass, Na0.09Ca0.34K0.02P0.009Mg0.15Fe(II)0.35Fe(III)0.20Ti0.12Al0.32SiO1.97, mixed flow reactor, surface area measured by N_2 and krypton BET, dissolution was not stoichiometric. These data were not included in the fit because basalt composition was treated as the primary independent variable.

Biotite

References	Initial (Final) pH	Initial Fluid Composition	Initial (Final) Specific Surface Area [m^2/g]	Grain Size (min, max) [m]	Temperature [K]	Duration of Dissolution [s]	Si Release Rate [$mol/m^2/s$]	Mineral Dissolution Rate [$mol/m^2/s$]
Kalinowski and Schweda (1996)	1.1 (1.1)	HCl	5.59 (273)	1E-05, 2E-05	295	3.96E06	7.42E-10	1.23E-10
Kalinowski and Schweda (1996)	1.1 (1.1)	HCl	5.59 (226)	1E-05, 2E-05	295	2.41E06	3.37E-10	5.81E-11
Kalinowski and Schweda (1996)	2 (2)	HCl	5.59 (33.8)	1E-05, 2E-05	295	1.01E07	7.08E-11	1.22E-11
Kalinowski and Schweda (1996)	3 (3)	HCl	5.59 (7.61)	1E-05, 2E-05	295	1.01E07	2.76E-11	4.76E-12
Kalinowski and Schweda (1996)	3 (3.2)	H2SO4	5.59 (7.54)	1E-05, 2E-05	295	7.27E06	1.79E-11	3.09E-12
Kalinowski and Schweda (1996)	4 (4.3)	HCl	5.59 (12.2)	1E-05, 2E-05	295	3.96E06	6.79E-11	1.17E-12
Acker and Bricker (1992)	3 (3.07)	H2SO4	0.51 (ng)	4.2E-04, ng	295	6.48E05	3.79E-11	6.31E-12
Acker and Bricker (1992)	4 (4.28)	H2SO4	0.51 (ng)	4.2E-04, ng	295	6.48E05	1.58E-11	2.63E-12
Acker and Bricker (1992)	5 (5.73)	H2SO4	0.51 (ng)	4.2E-04, ng	295	6.48E05	7.05E-12	1.17E-12
Acker and Bricker (1992)	5.5 (5.96)	H2SO4	0.51 (ng)	4.2E-04, ng	295	6.48E05	4.55E-12	7.59E-13
Acker and Bricker (1992)	3 (3.03)	H2SO4	0.84 (ng)	1.49E-04, 4.2E-04	295	4.32E05	1.90E-11	3.16E-12
Acker and Bricker (1992)	4 (4.78)	H2SO4	0.84 (ng)	1.49E-04, 4.2E-04	295	4.32E05	1.65E-11	2.75E-12
Acker and Bricker (1992)	5 (5.91)	H2SO4	0.84 (ng)	1.49E-04, 4.2E-04	295	4.32E05	5.35E-12	8.91E-13
Acker and Bricker (1992)	5.5 (6.3)	H2SO4	0.84 (ng)	1.49E-04, 4.2E-04	295	4.32E05	7.55E-12	1.26E-12
Acker and Bricker (1992)	3 (3.11)	H2SO4	2.04 (ng)	ng, 1.49E-04	295	4.68E05	1.73E-11	2.88E-12
Acker and Bricker (1992)	4 (5.28)	H2SO4	2.04 (ng)	ng, 1.49E-04	295	4.68E05	6.89E-12	1.15E-12
Acker and Bricker (1992)	4 (5.13)	H2SO4	0.84 (ng)	1.49E-04, 4.2E-04	295	4.43E05	3.30E-12	5.50E-13
Acker and Bricker (1992)	3 (3.19)	H2SO4	0.84 (ng)	1.49E-04, 4.2E-04	295	3.92E05	1.94E-11	3.24E-12
Acker and Bricker (1992)	4 (4.78)	H2SO4	0.84 (ng)	1.49E-04, 4.2E-04	295	4.43E05	4.15E-12	6.92E-13
Acker and Bricker (1992)	3 (3.14)	H2SO4	0.84 (ng)	1.49E-04, 4.2E-04	295	3.92E05	1.85E-11	3.09E-12
Acker and Bricker (1992)	3 (3.16)	H2SO4	0.84 (ng)	1.49E-04, 4.2E-04	295	6.04E05	5.86E-11	9.77E-12
Acker and Bricker (1992)	4 (4.08)	H2SO4	0.84 (ng)	1.49E-04, 4.2E-04	295	6.01E05	1.90E-11	3.16E-12
Acker and Bricker (1992)	5 (5.074)	H2SO4	0.84 (ng)	1.49E-04, 4.2E-04	295	6.12E05	1.07E-11	1.78E-12
Acker and Bricker (1992)	5.5 (5.62)	H2SO4	0.84 (ng)	1.49E-04, 4.2E-04	295	4.50E05	7.91E-12	1.32E-12
Acker and Bricker (1992)	3 (3.06)	H2SO4	0.84 (ng)	1.49E-04, 4.2E-04	295	1.19E06	5.73E-11	9.55E-12
Acker and Bricker (1992)	4 (4.92)	H2SO4	0.84 (ng)	1.49E-04, 4.2E-04	295	1.19E06	8.67E-12	1.45E-12
Acker and Bricker (1992)	5 (6.67)	H2SO4	0.84 (ng)	1.49E-04, 4.2E-04	295	1.19E06	3.45E-12	5.75E-13

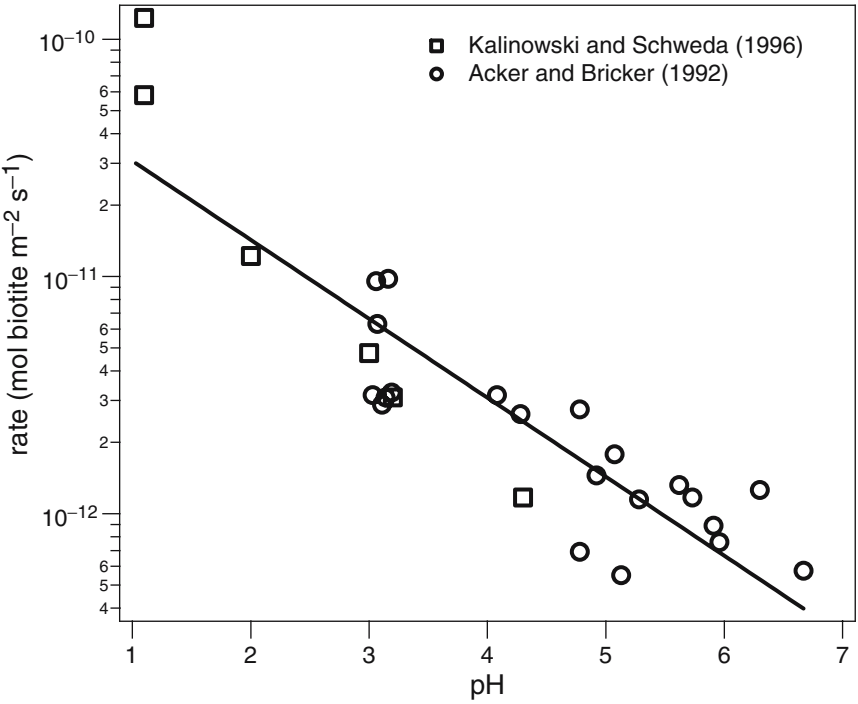

References

Kalinowski and Schweda (1996) *Geochimica et Cosmochimica Acta* 60, 367–385. $(Ca_{0.02}Na_{0.04}K_{1.82})(Al_{0.33}Fe^{III}_{0.82}Fe^{II}_{1.71}Mn_{0.01}Mg_{2.70})(Si_{5.80}Al_{2.20})O_{20}(OH)_{3.97}F_{0.03}$, dialysis cell reactor, pO_2 and pCO_2 not given, surface area measured by 3:7 N2:He mixture BET.

Acker and Bricker (1992) *Geochimica et Cosmochimica Acta* 56, 3073–3092. $Ca_{.008}Na_{.14}K_{1.83}(Mg_{3.17}Fe^{II}_{2.19}Fe^{III}_{0.05}Al_{0.38})(Si_6Al_2O_{20}(OH)_4)$, fluidized bed reactor, $pO_2 = 0, pCO_2$ not given, surface area measured by N2-BET.

Bytownite

References	Initial (Final) pH	Initial Fluid Composition	Initial (Final) Specific Surface Area [m^2/g]	Grain Size (min, max) [m]	Temperature [K]	Duration of Dissolution [s]	Si Release Rate [$mol/m^2/s$]	Mineral Dissolution Rate [$mol/m^2/s$]
Stillings and Brantley (1995a)	3 (3.51)	1 mM HCl	0.0952 (0.4768)	7.5E-05, 1.5E-04	298	1.07E07	4.95E-11	2.28E-11
Stillings and Brantley (1995a)	3 (3.34)	1 mM HCl	0.0952 (0.7608)	7.5E-05, 1.5E-04	298	1.61E07	6.86E-11	3.16E-11
Stillings and Brantley (1995a)	3 (3.19)	1 mM HCl, 10 mM NaCl	0.0952 (1.1198)	7.5E-05, 1.5E-04	298	2.37E07	1.98E-11	9.12E-12
Stillings and Brantley (1995a)	3 (3.15)	1 mM HCl, 100 mM NaCl	0.0952 (1.3749)	7.5E-05, 1.5E-04	298	2.97E07	8.68E-12	4.00E-12
Stillings and Brantley (1995b)	3 (3.47)	1 mM HCl, 1 mM (CH3)4NCl	0.0952 (0.4364)	7.5E-05, 1.5E-04	298	8.18E06	5.21E-11	2.40E-11
Stillings and Brantley (1995b)	3 (3.61)	1 mM HCl, 100 mM (CH3)4NCl	0.0952 (1.0607)	7.5E-05, 1.5E-04	298	7.17E06	1.83E-11	8.43E-12
Stillings et al. (1996)	3 (3.7)	1 mM oxalate + 1 mM HCl	0.095 (9.4)	7.5E-05, 1E-04	298	1.48E07	7.75E-10	3.57E-10
Stillings et al. (1996)	5 (4.43)	1 mM oxalate	0.095 (1.9)	7.5E-05, 1E-04	298	9.86E06	4.71E-10	2.17E-10
Stillings et al. (1996)	5 (4.75)	DI water	0.095 (0.098)	7.5E-05, 1E-04	298	1.80E07	3.80E-11	1.75E-11
Holdren and Speyer (1987)	3 (ng)	DI	0.214 (ng)	7.5E-05, 1.5E-04	298	ng	2.14E-10	9.86E-11
Holdren and Speyer (1987)	3 (ng)	1 mM KNO3	0.099 (ng)	6E-04, ng	298	ng	8.00E-10	3.69E-10
Holdren and Speyer (1987)	3 (ng)	1 mM Na acetate	0.13 (ng)	3E-04, 6E-04	298	ng	2.14E-10	9.85E-11
Holdren and Speyer (1987)	3 (ng)	1 mM Na oxalate	0.127 (ng)	1.5E-04, 3E-04	298	ng	2.19E-10	1.01E-10
Holdren and Speyer (1987)	3 (ng)	1 mM Na gluconate	0.473 (ng)	3.7E-05, 7.5E-05	298	ng	1.67E-10	7.71E-11
Holdren and Speyer (1987)	3 (ng)	DI	1.62 (ng)	ng, 3.7E-05	298	ng	1.24E-10	5.69E-11
Casey et al. (1991)	2 (ng)	1 mM KNO3	0.2 (ng)	2.5E-05, 7.5E-05	298	2.00E06	5.83E-11	1.40E-10
Casey et al. (1991)	2 (ng)	1 mM Na acetate	0.27 (ng)	2.5E-05, 7.5E-05	298	2.00E06	9.26E-10	2.12E-09

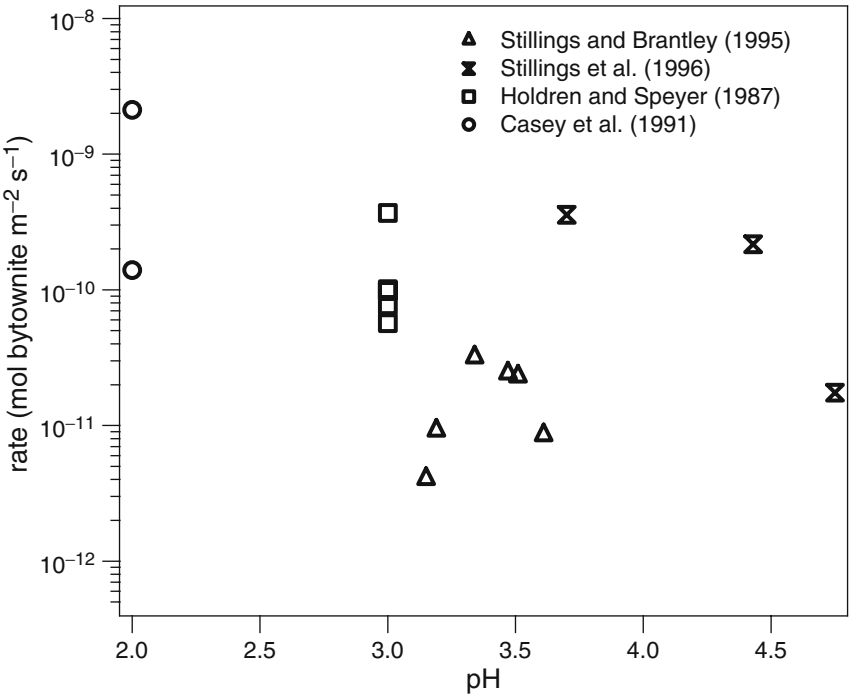

References

Stillings and Brantley (1995a) *Geochimica et Cosmochimica Acta* 59, 1483–1496. Na0.24Ca0.73Al1.67Si2.17O8, continuously stirred tank reactor, pO2 and pCO2 were atmospheric, surface area measured by Kr-BET, final surface area used for normalization, dissolution was stoichiometric.

Stillings and Brantley (1995b) *Geochimica et Cosmochimica Acta* 59, 1483–1496. Na0.24Ca0.73Al1.67Si2.17O8, continuously stirred tank reactor, pO2 and pCO2 were atmospheric, surface area measured by Kr-BET, final surface area used for normalization, (CH3)4NCl was added to reactors, dissolution was stoichiometric.

Stillings et al. (1996) *Chemical Geology* 132, 79–89. Na0.24Ca0.73Al1.67Si2.17O8, continuously stirred flow through reactor, pO2 and pCO2 were atmospheric, surface area measured by Kr-BET, initial surface area used for normalization, dissolution was not stoichiometric. Some of these experiments contained organics.

Holdren and Speyer (1987) *Geochimica et Cosmochimica Acta* 51, 2311–2318. Na0.24Ca0.73Al1.67Si2.17O8, batch reactor, pO2 and pCO2 were atmospheric, surface area measured by Ar-BET.

Casey et al. (1991) 76, 211–217. K0.02Na0.38Ca0.6Al1.58Si2.4O8, batch reactor, pO2 and pCO2 were atmospheric, surface area measured by BET, dissolution was not stoichiometric.

Hornblende

References	Initial (Final) pH	Initial Fluid Composition	Initial (Final) Specific Surface Area [m^2/g]	Grain Size (min, max) [m]	Temperature [K]	Duration of Dissolution [s]	Si Release Rate [$mol/m^2/s$]	Mineral Dissolution Rate [$mol/m^2/s$]
Frogner and Schweda (1998a)	1 (ng)	Ng	0.28 (ng)	1.3E-04, 2.5E-04	298	2.16E07	1.37E-11	1.86E-12
Frogner and Schweda (1998a)	2 (ng)	Ng	0.28 (ng)	1.3E-04, 2.5E-04	298	2.16E07	9.8E-12	1.33E-12
Frogner and Schweda (1998b)	3 (ng)	Ng	0.28 (ng)	1.3E-04, 2.5E-04	298	2.16E07	7.9E-12	1.06E-12
Frogner and Schweda (1998b)	4 (ng)	Ng	0.28 (ng)	1.3E-04, 2.5E-04	298	2.16E07	2.3E-12	3.10E-13
Frogner and Schweda (1998b)	5 (ng)	Ng	0.28 (ng)	1.3E-04, 2.5E-04	298	2.16E07	7E-13	9.47E-14
Frogner and Schweda (1998a)	1 (ng)	0.01 M KCl	0.28 (ng)	1.3E-04, 2.5E-04	298	1.08E07	1.6E-11	2.17E-12
Frogner and Schweda (1998c)	2 (ng)	0.01 M KCl	0.28 (ng)	1.3E-04, 2.5E-04	298	1.08E07	1.42E-11	1.92E-12
Swoboda-Colberg and Drever (1993)	4 (ng)	Ng	0.08 (ng)	7.5E-05, 1.5E-04	298	9.07E06	ng	1.80E-12
Swoboda-Colberg and Drever (1993)	4.5 (ng)	Ng	0.08 (ng)	1.5E-04, 1.5E-04	298	9.07E06	ng	1.40E-12
Zhang et al. (1996)	3.6 (ng)	0.01 M lithium acetate, LiOH buffer	0.098 (ng)	1.1E-04, 2.5E-04	298	9.94E06	1.7E-11	2.73E-12
Zhang et al. (1996)	3.8 (ng)	0.01 M lithium acetate, LiOH buffer	0.098 (ng)	1.1E-04, 2.5E-04	298	9.94E06	1.2E-11	1.93E-12
Zhang et al. (1996)	4 (ng)	0.01 M lithium acetate, LiOH buffer	0.098 (ng)	1.1E-04, 2.5E-04	298	9.94E06	7.4E-12	1.16E-12
Zhang et al. (1996)	3.6 (ng)	0.01 M lithium acetate, LiOH buffer	0.086 (ng)	2.5E-04, 5.0E-04	298	9.94E06	1.7E-11	2.74E-12
Zhang et al. (1996)	3.8 (ng)	0.01 M lithium acetate, LiOH buffer	0.086 (ng)	2.5E-04, 5.0E-04	298	9.94E06	1.2E-11	1.83E-12
Zhang et al. (1996)	4 (ng)	0.01 M lithium acetate, LiOH buffer	0.086 (ng)	2.5E-04, 5.0E-04	298	9.94E06	1.0E-11	1.59E-12

Zhang et al. (1993)	4 (ng)	0.01 M lithium acetate	ng (0.68)	4.5E-05, 7.5E-05	298	5.10E06	6.1E-14	3.88E-13
Zhang et al. (1993)	4 (ng)	0.01 M lithium acetate	0.166 (0.37)	7.5E-05, 1.1E-04	298	5.10E06	1.8E-13	1.14E-12
Zhang et al. (1993)	4 (ng)	0.01 M lithium acetate	0.098 (0.27)	1.1E-04, 2.5E-04	298	5.10E06	2.1E-13	1.31E-12
Zhang et al. (1993)	4 (ng)	0.01 M lithium acetate	0.077 (0.14)	5.0E-04, 1.0E-03	298	5.10E06	1.9E-13	1.21E-12
Zhang (1990)	3.6 (ng)	0.01 M lithium acetate	0.102 (ng)	1.1E-04, 2.5E-04	298	9.94E06	ng	2.59E-12
Zhang (1990)	3.8 (ng)	0.01 M lithium acetate	0.102 (ng)	1.1E-04, 2.5E-04	298	9.94E06	ng	1.80E-12
Zhang (1990)	4 (ng)	0.01 M lithium acetate	0.102 (ng)	1.1E-04, 2.5E-04	298	9.94E06	ng	1.11E-12
Zhang (1990)	3.6 (ng)	0.01 M lithium acetate	0.086 (ng)	2.5E-04, 5.0E-04	298	9.94E06	ng	2.78E-12
Zhang (1990)	3.8 (ng)	0.01 M lithium acetate	0.086 (ng)	2.5E-04, 5.0E-04	298	9.94E06	ng	1.85E-12
Zhang (1990)	4 (ng)	0.01 M lithium acetate	0.086 (ng)	2.5E-04, 5.0E-04	298	9.94E06	ng	1.59E-12
Zhang (1990)	3.4 (ng)	0.01 M lithium acetate	0.24 (ng)	2.5E-04, 5.0E-04	298	2.85E06	ng	2.50E-12
Zhang (1990)	3.59 (ng)	0.01 M lithium acetate	0.24 (ng)	2.5E-04, 5.0E-04	298	2.85E06	ng	1.97E-12
Zhang (1990)	3.86 (ng)	0.01 M lithium acetate	0.24 (ng)	2.5E-04, 5.0E-04	298	2.85E06	ng	1.57E-12
Zhang (1990)	3.96 (ng)	0.01 M lithium acetate	0.24 (ng)	2.5E-04, 5.0E-04	298	2.85E06	ng	1.47E-12
Zhang (1990)	4.2 (ng)	0.01 M lithium acetate	0.24 (ng)	2.5E-04, 5.0E-04	298	2.85E06	ng	1.06E-12
Zhang (1990)	4.43 (ng)	0.01 M lithium acetate	0.24 (ng)	2.5E-04, 5.0E-04	298	2.85E06	ng	6.32E-13

References	Initial (Final) pH	Initial Fluid Composition	Initial (Final) Specific Surface Area [m^2/g]	Grain Size (min, max) [m]	Temperature [K]	Duration of Dissolution [s]	Si Release Rate [$mol/m^2/s$]	Mineral Dissolution Rate [$mol/m^2/s$]
Zhang (1990)	4.62 (ng)	0.01 M lithium acetate	0.24 (ng)	2.5E-04, 5.0E-04	298	2.85E06	ng	4.80E-13
Sverdrup (1990a)	1.6 (ng)	Ng	0.24 (ng)	ng, ng	298	ng	ng	5.01E-11
Sverdrup (1990a)	2.4 (ng)	Ng	0.24 (ng)	ng, ng	298	ng	ng	2.51E-11
Sverdrup (1990a)	2.5 (ng)	Ng	0.24 (ng)	ng, ng	298	ng	ng	3.98E-11
Sverdrup (1990a)	3.1 (ng)	Ng	0.24 (ng)	ng, ng	298	ng	ng	2.51E-11
Sverdrup (1990a)	3.5 (ng)	Ng	0.24 (ng)	ng, ng	298	ng	ng	7.94E-12
Sverdrup (1990a)	4.4 (ng)	Ng	0.24 (ng)	ng, ng	298	ng	ng	1.58E-12
Sverdrup (1990a)	5 (ng)	Ng	0.24 (ng)	ng, ng	298	ng	ng	5.01E-13
Sverdrup (1990a)	5.5 (ng)	Ng	0.24 (ng)	ng, ng	298	ng	ng	2.00E-13
Sverdrup (1990a)	6.5 (ng)	Ng	0.24 (ng)	ng, ng	298	ng	ng	2.00E-13
Sverdrup (1990a)	7 (ng)	Ng	0.24 (ng)	ng, ng	298	ng	ng	1.00E-13
Sverdrup (1990b)	6.7 (ng)	Ng	0.24 (ng)	ng, ng	298	ng	ng	2.51E-13
Nickel (1973)	0.2 (ng)	Ng	0.237 (ng)	2E-05, 3.5E-05	298	1.30E06	6.46E-11	9.36E-12
Nickel (1973)	3.6 (ng)	Ng	0.237 (ng)	2E-05, 3.5E-05	298	2.59E06	1.81E-11	2.63E-12
Nickel (1973)	5.6 (ng)	Ng	0.237 (ng)	2E-05, 3.5E-05	298	2.59E06	1.29E-11	1.87E-12
Nickel (1973)	10.6 (ng)	Ammonia	0.237 (ng)	2E-05, 3.5E-05	298	2.59E06	1.66E-11	2.40E-12
Cygan et al. (1989)	4.05 (ng)	0.01 N potassium hydrogen phtalate	4.93 (ng)	3.7E-05, 1.49E-04	298	1.81E06	1.2E-12	1.6E-13
Cygan et al. (1989)	4.05 (ng)	0.01 N potassium hydrogen phtalate pH	6.72 (ng)	3.7E-05, 1.49E-04	298	1.81E06	2.6E-12	3.5E-13
Cygan et al. (1989)	4.05 (ng)	0.01 N potassium hydrogen phtalate pH	6.44 (ng)	3.7E-05, 1.49E-04	298	1.81E06	4.0E-12	5.3E-13
Cygan et al. (1989)	4.05 (ng)	0.01 N potassium hydrogen phtalate	4.86 (ng)	3.7E-05, 1.49E-04	298	1.81E06	4.5E-12	6.0E-13
Givens and Brantley (unpublished)	1.12 (ng)	Ng	0.33 (0.21)	7.5E-05, 1.5E-04	298	3.17E07	ng	1.04E-11

Givens and Brantley (unpublished)	2.09 (ng)	Ng	0.33 (0.56)	7.5E-05, 1.5E-04	298	4.17E07	ng	6.55E-12
Givens and Brantley (unpublished)	3.07 (ng)	Ng	0.33 (0.35)	7.5E-05, 1.5E-04	298	3.31E07	ng	4.37E-12
Givens and Brantley (unpublished)	5.67 (ng)	Ng	0.33 (0.51)	7.5E-05, 1.5E-04	298	3.57E07	ng	2.82E-13
Golubev et al. (2005a)	4 (ng)	I = 0.01 M	0.39 (ng)	0.00005, 0.0001	298	3.60E + 05	ng	3.29E-12
Golubev et al. (2005b)	2.1 (ng)	I = 0.01 M	0.39 (ng)	0.00005, 0.0001	298	3.60E + 05	ng	9.72E-12
Golubev et al. (2005b)	3.05 (ng)	I = 0.01 M	0.39 (ng)	0.00005, 0.0001	298	3.60E + 05	ng	7.04E-12
Golubev et al. (2005b)	4.06 (ng)	I = 0.01 M	0.39 (ng)	0.00005, 0.0001	298	3.60E + 05	ng	3.78E-12
Golubev et al. (2005b)	4.72 (ng)	I = 0.01 M	0.39 (ng)	0.00005, 0.0001	298	3.60E + 05	ng	3.87E-12
Golubev et al. (2005b)	5.66 (ng)	I = 0.01 M	0.39 (ng)	0.00005, 0.0001	298	3.60E + 05	ng	3.45E-12
Golubev et al. (2005b)	6.74 (ng)	I = 0.01 M	0.39 (ng)	0.00005, 0.0001	298	3.60E + 05	ng	1.85E-12
Golubev et al. (2005b)	8.82 (ng)	I = 0.01 M	0.39 (ng)	0.00005, 0.0001	298	3.60E + 05	ng	3.15E-12
Golubev et al. (2005b)	9.9 (ng)	I = 0.01 M	0.39 (ng)	0.00005, 0.0001	298	3.60E + 05	ng	4.65E-12
Golubev et al. (2005b)	10.1 (ng)	I = 0.01 M	0.39 (ng)	0.00005, 0.0001	298	3.60E + 05	ng	4.24E-12
Golubev et al. (2005b)	11.13 (ng)	I = 0.01 M	0.39 (ng)	0.00005, 0.0001	298	3.60E + 05	ng	7.55E-12
Golubev et al. (2005c)	8.15 (ng)	I = 0.01 M	0.39 (ng)	0.00005, 0.0001	298	3.60E + 05	ng	3.45E-12
Golubev et al. (2005c)	10.9 (ng)	I = 0.02 M	0.39 (ng)	0.00005, 0.0001	298	3.60E + 05	ng	5.72E-12
Golubev et al. (2005d)	11.2 (ng)	I = 0.10 M	0.39 (ng)	0.00005, 0.0001	298	3.60E + 05	ng	5.86E-12
Golubev et al. (2005b)	9.05 (ng)	I = 0.01 M	0.39 (ng)	0.00005, 0.0001	298	3.60E + 06	ng	1.98E-13
Golubev et al. (2005b)	6.85 (ng)	I = 0.01 M	0.39 (ng)	0.00005, 0.0001	298	3.60E + 06	ng	4.99E-13

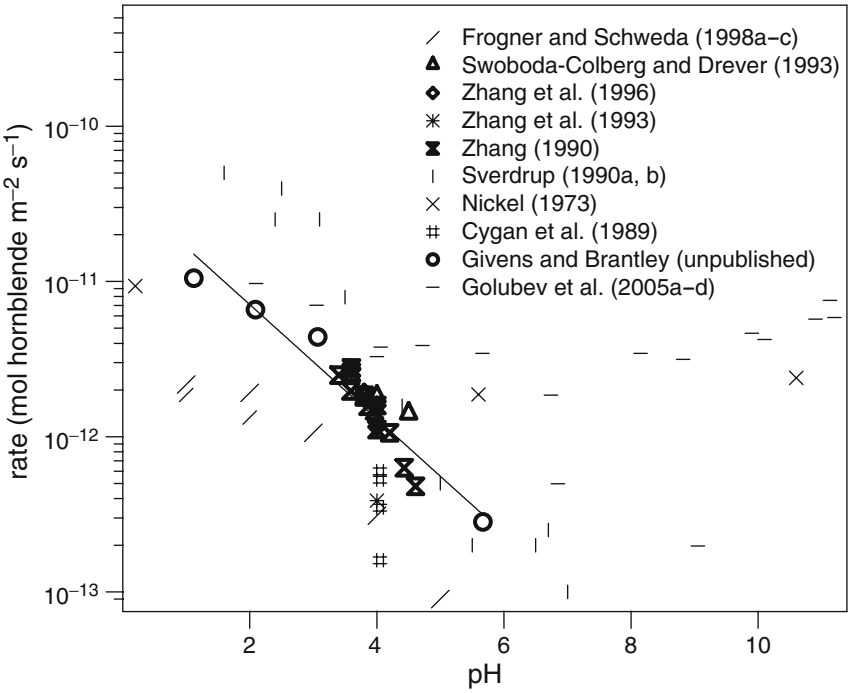

References

Frogner and Schweda (1998a) *Chemical Geology* 151, 169–179. K0.02Na0.11 Ca1.7Mg3.68Fe2 + 1.02Fe3 + 0.14(Al0.37Si7.39)O22(OH)2, Plug flow reactor, pO2 and pCO2 were atmospheric, surface area measured by Kr-BET, dissolution was stoichiometric only with respect to Fe Mg, Ca. These data were excluded from the fit due to reactor design.

Frogner and Schweda (1998b) *Chemical Geology* 151, 169–179. K0.02 Na0.11 Ca1.7Mg3.68Fe2+1.02 Fe3+0.14(Al0.37Si7.39)O22(OH)2, Plug flow reactor, pO2 and pCO2 were atmospheric, surface area measured by Kr-BET, dissolution was stoichiometric only with respect to Ca. These data were excluded from the fit due to reactor design.

Frogner and Schweda (1998c) *Chemical Geology* 151, 169–179. K0.02Na0.11 Ca1.7Mg3.68Fe2+1.02Fe3+0.14(Al0.37Si7.39)O22(OH)2, Plug flow reactor, pO2 and pCO2 were atmospheric, surface area measured by Kr-BET, stoichiometry of dissolution was not discussed. These data were excluded from the fit due to reactor design.

Swoboda-Colberg and Drever (1993) *Chemical Geology* 105, 51–69. K0.09Na0. 14Ca2Mg2Fe1.78Al2Si7O22(OH)2, Fluidized bed reactor, pO2 and pCO2 were

atmospheric, Geometric surface area, dissolution was assumed to be stoichiometric.

Zhang et al. (1996) *Geochimica et Cosmochimica Acta* 60, 941–950. K0.11Na 0.66Ca1.66(Mg3.11Fe2+1.02Al0.79Fe3+0.32)(Al1.64Si6.36)O22(OH)2, batch reactor, pO2 and pCO2 were atmospheric, surface area measured by N2-BET, dissolution was not stoichiometric.

Zhang et al. (1993) *Geochimica et Cosmochimica Acta* 57, 1681–1689. K0.11Na 0.66Ca1.66(Mg3.11Fe2+1.02Al0.79Fe3+0.32)(Al1.64Si6.36)O22(OH)2, batch reactor, pO2 and pCO2 were atmospheric, surface area measured by N2-BET, initial surface area used for normalization, dissolution was not stoichiometric. These data were excluded from the fit due to a simple oversight by the data analyst.

Zhang (1990) PhD thesis, University of Minnesota. K0.11Na0.66Ca1.66(Mg3.11 Fe2+1.02Al0.79Fe3+0.32)(Al1.64Si6.36)O22(OH)2, batch reactor, pO2 and pCO2 were atmospheric, surface area measured by N2-BET, dissolution was not stoichiometric.

Sverdrup (1990a) The kinetics of base cation release due to chemical weathering. Lund University Press, Sweden. 246 pp. Na0.08Ca2.1Mg4.5Al2.1Si7O22(OH)2, Continuously stirred tank reactor, pO2 and pCO2 were atmospheric, Geometric surface area, BET-N2. These data were excluded from the fit because too little is known about the experimental setup.

Sverdrup (1990b) The kinetics of base cation release due to chemical weathering. Lund University Press, Sweden. 246 pp. Na0.16Ca2Mg4Al0.4Si8.3O22(OH)2, Continuously stirred tank reactor, pO2 and pCO2 were atmospheric, Geometric surface area, BET-N2. These data were excluded from the fit because too little is known about the experimental setup.

Nickel (1973) *Contributions in Sedimentology* 1, 1–68. Ca1.7Mg3.5Fe1.3Al1.4 Si6.9O22(OH)2, Continuously stirred tank reactor, pO2 and pCO2 were atmospheric, surface area measured by N2-BET, dissolution was not stoichiometric. These data were excluded from the fit.

Cygan et al. (1989) *Chemical Geology* 78, 229–244. Ca2(Mg3.3Fe1.7)(Si7.5 Al0.5)O22(OH)2, batch reactor, pO2 and pCO2 were atmospheric, surface area measured by N2-BET, dissolution was not stoichiometric. These data were excluded from the fit because the mineral grains were shocked.

Givens and Brantley (unpublished). (K0.1Na0.7)(Ca1.4,Mg0.4)Al1.0Fe1.4Mg2.6 Ti0.1Si6.5Al1.5O22(OH)2 Trace Mn (0.01), flow through reactor, pO2 and pCO2 were atmospheric, surface area measured by Kr-BET, dissolution may have been stoichiometric.

Golubev et al. (2005a) *Chemical Geology* 217, 227–238. K0.08Na0.63Ca1.87 (Mg2.90Fe1.15Al0.71)(Al2.08Si5.92)O22(OH)11, mixed flow through reactor, $pO2 = 0 pCO2 = 1$ atm, surface area measured by Kr-BET.

Golubev et al. (2005b) *Chemical Geology* 217, 227–238. K0.08Na0.63Ca1.87 (Mg2.90Fe1.15Al0.71)(Al2.08Si5.92)O22(OH)11, mixed flow through reactor, $pO2 = 0 pCO2 = 0$ atm, surface area measured by Kr-BET.

Golubev et al. (2005c) *Chemical Geology* 217, 227–238. K0.08Na0.63Ca1.87 (Mg2.90Fe1.15Al0.71)(Al2.08Si5.92)O22(OH)11, mixed flow through reactor, pO2 = 0pCO2 = 0.01 atm, surface area measured by Kr-BET.

Golubev et al. (2005d) *Chemical Geology* 217, 227–238. K0.08Na0.63Ca1.87 (Mg2.90Fe1.15Al0.71)(Al2.08Si5.92)O22(OH)11, mixed flow through reactor, pO2 = 0pCO2 = 0.05 atm, surface area measured by Kr-BET.

Kaolinite

References	Initial (Final) pH	Initial Fluid Composition	Initial (Final) Specific Surface Area [m^2/g]	Grain Size (min, max) [m]	Temperature [K]	Duration of Dissolution [s]	Si Release Rate [mol/s]	Mineral Dissolution Rate [$mol/m^2/s$]
Carroll-Webb and Walther (1988)	0.99 (ng)	KCl, HCl, I = 0.05	11.2 (11.2)	ng, ng	298	7.20E5 – 3.60E6	6.47E-13	3.24E-13
Carroll-Webb and Walther (1988)	1.27 (ng)	KCl, HCl, I = 0.025	11.2 (11.2)	ng, ng	298	7.20E5 – 3.60E6	5.90E-13	2.95E-13
Carroll-Webb and Walther (1988)	1.98 (ng)	KCl, HCl, I = 0.005	11.2 (11.2)	ng, ng	298	7.20E5 – 3.60E6	4.91E-13	2.45E-13
Carroll-Webb and Walther (1988)	2.03 (ng)	KCl, HCl, I = 0.05	11.2 (11.2)	ng, ng	298	7.20E5 – 3.60E6	3.32E-13	1.66E-13
Carroll-Webb and Walther (1988)	2.23 (ng)	KCl, HCl, I = 0.025	11.2 (11.2)	ng, ng	298	7.20E5 – 3.60E6	2.83E-13	1.41E-13
Carroll-Webb and Walther (1988)	2.93 (ng)	KCl, HCl, I = 0.005	11.2 (11.2)	ng, ng	298	7.20E5 – 3.60E6	2.64E-13	1.32E-13
Carroll-Webb and Walther (1988)	2.99 (ng)	KHPthalate, HCl, I = 0.05	11.2 (11.2)	ng, ng	298	7.20E5 – 3.60E6	2.70E-13	1.35E-13
Carroll-Webb and Walther (1988)	3.06 (ng)	KHPthalate, HCl, I = 0.025	11.2 (11.2)	ng, ng	298	7.20E5 – 3.60E6	4.48E-13	2.24E-13
Carroll-Webb and Walther (1988)	3.29 (ng)	KHPthalate, HCl, I = 0.005	11.2 (11.2)	ng, ng	298	7.20E5 – 3.60E6	3.40E-13	1.70E-13
Carroll-Webb and Walther (1988)	3.54 (ng)	Tris, HCl, 0.001 M malonic acid, I = 0.005	11.2 (11.2)	ng, ng	298	7.20E5 – 3.60E6	3.24E-13	1.62E-13
Carroll-Webb and Walther (1988)	4 (ng)	KHPthalate, HCl, I = 0.05	11.2 (11.2)	ng, ng	298	7.20E5 – 3.60E6	2.83E-13	1.41E-13
Carroll-Webb and Walther (1988)	4.01 (ng)	Succinic Acid, NaOH, I = 0.05	11.2 (11.2)	ng, ng	298	7.20E5 – 3.60E6	5.64E-13	2.82E-13
Carroll-Webb and Walther (1988)	4.01 (ng)	Succinic Acid, NaOH, 0.0001 M malonic acid, I = 0.05	11.2 (11.2)	ng, ng	298	7.20E5 – 3.60E6	2.24E-13	1.12E-13

References	Initial (Final) pH	Initial Fluid Composition	Initial (Final) Specific Surface Area $[m^2/g]$	Grain Size (min, max) [m]	Temperature [K]	Duration of Dissolution [s]	Si Release Rate $[mol/s]$	Mineral Dissolution Rate $[mol/m^2/s]$
Carroll-Webb and Walther (1988)	4.04 (ng)	KHPthalate, HCl, I = 0.025	11.2 (11.2)	ng, ng	298	7.20E5 – 3.60E6	2.70E-13	1.35E-13
Carroll-Webb and Walther (1988)	4.21 (ng)	KHPthalate, HCl, I = 0.005	11.2 (11.2)	ng, ng	298	7.20E5 – 3.60E6	2.46E-13	1.23E-13
Carroll-Webb and Walther (1988)	4.73 (ng)	Succinic Acid, NaOH, 0.001 M malonic acid, I = 0.05	11.2 (11.2)	ng, ng	298	7.20E5 – 3.60E6	2.52E-13	1.26E-13
Carroll-Webb and Walther (1988)	4.75 (ng)	Succinic Acid, NaOH, 0.001 M malonic acid, I = 0.005	11.2 (11.2)	ng, ng	298	7.20E5 – 3.60E6	2.14E-13	1.07E-13
Carroll-Webb and Walther (1988)	4.83 (ng)	Succinic Acid, NaOH, 0.001 M malonic acid, I = 0.025	11.2 (11.2)	ng, ng	298	7.20E5 – 3.60E6	1.59E-13	7.94E-14
Carroll-Webb and Walther (1988)	4.85 (ng)	Succinic Acid, NaOH, 0.01 M 2,4pentane-dione, I = 0.05	11.2 (11.2)	ng, ng	298	7.20E5 – 3.60E6	2.09E-13	1.05E-13
Carroll-Webb and Walther (1988)	5.54 (ng)	Succinic Acid, NaOH, 0.001 M malonic acid, I = 0.05	11.2 (11.2)	ng, ng	298	7.20E5 – 3.60E6	1.59E-13	7.94E-14
Carroll-Webb and Walther (1988)	5.54 (ng)	Succinic Acid, NaOH, 0.001 M malonic acid, I = 0.005	11.2 (11.2)	ng, ng	298	7.20E5 – 3.60E6	1.87E-13	9.33E-14

Carroll-Webb and Walther (1988)	5.65 (ng)	Tris, HCl, 0.001 M malonic acid, I = 0.025	11.2 (11.2)	ng, ng	298	7.20E5 – 3.60E6	2.09E-13	1.05E-13
Carroll-Webb and Walther (1988)	5.71 (ng)	Succinic Acid, NaOH, 0.001 M malonic acid, I = 0.025	11.2 (11.2)	ng, ng	298	7.20E5 – 3.60E6	1.95E-13	9.77E-14
Carroll-Webb and Walther (1988)	5.78 (ng)	Succinic Acid, NaOH, 0.01 M 2,4 pentane-dione, I = 0.05	11.2 (11.2)	ng, ng	298	7.20E5 – 3.60E6	2.09E-13	1.05E-13
Carroll-Webb and Walther (1988)	6.56 (ng)	Tris, HCl, 0.001 M malonic acid, I = 0.05	11.2 (11.2)	ng, ng	298	7.20E5 – 3.60E6	1.45E-13	7.24E-14
Carroll-Webb and Walther (1988)	6.73 (ng)	Tris, HCl, 0.001 M malonic acid, I = 0.005	11.2 (11.2)	ng, ng	298	7.20E5 – 3.60E6	1.66E-13	8.32E-14
Carroll-Webb and Walther (1988)	6.93 (ng)	Tris, HCl, 0.01 M 2,4 pentane-dione, I = 0.05	11.2 (11.2)	ng, ng	298	7.20E5 – 3.60E6	1.95E-13	9.77E-14
Carroll-Webb and Walther (1988)	7.87 (ng)	Tris, HCl, 0.001 M malonic acid, I = 0.025	11.2 (11.2)	ng, ng	298	7.20E5 – 3.60E6	8.73E-14	4.37E-14
Carroll-Webb and Walther (1988)	7.89 (ng)	Tris, HCl, 0.001 M malonic acid, I = 0.05	11.2 (11.2)	ng, ng	298	7.20E5 – 3.60E6	1.35E-13	6.76E-14
Carroll-Webb and Walther (1988)	7.89 (ng)	Tris, HCl, 0.01 M 2,4 pentane-dione, I = 0.05	11.2 (11.2)	ng, ng	298	7.20E5 – 3.60E6	2.52E-13	1.26E-13
Carroll-Webb and Walther (1988)	8.18 (ng)	Tris, HCl, I = 0.05	11.2 (11.2)	ng, ng	298	7.20E5 – 3.60E6	1.48E-13	7.41E-14
Carroll-Webb and Walther (1988)	8.18 (ng)	Tris, HCl, 0.0001 M malonic acid, I = 0.05	11.2 (11.2)	ng, ng	298	7.20E5 – 3.60E6	1.05E-13	5.25E-14

References	Initial (Final) pH	Initial Fluid Composition	Initial (Final) Specific Surface Area [m^2/g]	Grain Size (min, max) [m]	Temperature [K]	Duration of Dissolution [s]	Si Release Rate [mol/s]	Mineral Dissolution Rate [$mol/m^2/s$]
Carroll-Webb and Walther (1988)	8.51 (ng)	Tris, HCl, I = 0.05	11.2 (11.2)	ng, ng	298	7.20E5 – 3.60E6	5.90E-14	2.95E-14
Carroll-Webb and Walther (1988)	8.53 (ng)	Tris, HCl, 0.0001 M malonic acid, I = 0.05	11.2 (11.2)	ng, ng	298	7.20E5 – 3.60E6	1.12E-13	5.62E-14
Carroll-Webb and Walther (1988)	8.63 (ng)	Tris, HCl, 0.01 M 2,4 pentane-dione, I = 0.05	11.2 (11.2)	ng, ng	298	7.20E5 – 3.60E6	1.03E-13	5.13E-14
Carroll-Webb and Walther (1988)	9.33 (ng)	Tris, HCl, 0.0001 M malonic acid, I = 0.05	11.2 (11.2)	ng, ng	298	7.20E5 – 3.60E6	7.43E-14	3.72E-14
Carroll-Webb and Walther (1988)	9.35 (ng)	Tris, HCl, I = 0.05	11.2 (11.2)	ng, ng	298	7.20E5 – 3.60E6	1.21E-13	6.03E-14
Carroll-Webb and Walther (1988)	9.36 (ng)	Tris, HCl, 0.001 M 2,4 pentane-dione, I = 0.025	11.2 (11.2)	ng, ng	298	7.20E5 – 3.60E6	8.15E-14	4.07E-14
Carroll-Webb and Walther (1988)	9.37 (ng)	Tris, HCl, 0.001 M 2,4 pentane-dione, I = 0.05	11.2 (11.2)	ng, ng	298	7.20E5 – 3.60E6	7.96E-14	3.98E-14
Carroll-Webb and Walther (1988)	9.4 (ng)	Tris, HCl, I = 0.025	11.2 (11.2)	ng, ng	298	7.20E5 – 3.60E6	9.80E-14	4.90E-14
Carroll-Webb and Walther (1988)	9.48 (ng)	NaHCO3, NaOH, I = 0.05	11.2 (11.2)	ng, ng	298	7.20E5 – 3.60E6	1.32E-13	6.61E-14
Carroll-Webb and Walther (1988)	10.12 (ng)	NaBorate, NaOH, I = 0.005	11.2 (11.2)	ng, ng	298	7.20E5 – 3.60E6	3.24E-14	1.62E-14
Carroll-Webb and Walther (1988)	10.15 (ng)	NaBorate, NaOH, 0.001 M 2,4 pentane-dione, I = 0.025	11.2 (11.2)	ng, ng	298	7.20E5 – 3.60E6	3.24E-14	1.62E-14

Carroll-Webb and Walther (1988)	10.26 (ng)	NaBorate, NaOH, 0.001 M 2,4 pentane-dione, I = 0.05	11.2 (11.2)	ng, ng	298	7.20E5 – 3.60E6	3.24E-14	1.62E-14
Carroll-Webb and Walther (1988)	10.27 (ng)	NaBorate, NaOH, I = 0.025	11.2 (11.2)	ng, ng	298	7.20E5 – 3.60E6	8.73E-14	4.37E-14
Carroll-Webb and Walther (1988)	10.27 (ng)	Tris, HCl, I = 0.005	11.2 (11.2)	ng, ng	298	7.20E5 – 3.60E6	9.80E-14	4.90E-14
Carroll-Webb and Walther (1988)	11.74 (ng)	KCl, NaOH, I = 0.025	11.2 (11.2)	ng, ng	298	7.20E5 – 3.60E6	1.21E-12	6.03E-13
Carroll-Webb and Walther (1988)	12.17 (ng)	KCl, NaOH, I = 0.05	11.2 (11.2)	ng, ng	298	7.20E5 – 3.60E6	2.83E-12	1.41E-12
Wieland and Stumm (1992)	2 (ng)	HNO3, I = 0.1 M NaNO3	13.2 (ng)	ng, ng	298	8.64E5 – 1.30E6	1.95E-12	9.75E-13
Wieland and Stumm (1992)	2 (ng)	HNO3, I = 0.1 M NaNO3	13.2 (ng)	ng, ng	298	8.64E5 – 1.30E6	1.54E-12	7.69E-13
Wieland and Stumm (1992)	2.25 (ng)	HNO3, I = 0.1 M NaNO3	13.2 (ng)	ng, ng	298	8.64E5 – 1.30E6	1.54E-12	7.69E-13
Wieland and Stumm (1992)	2.5 (ng)	HNO3, I = 0.1 M NaNO3	13.2 (ng)	ng, ng	298	8.64E5 – 1.30E6	2.01E-12	1.01E-12
Wieland and Stumm (1992)	2.75 (ng)	HNO3, I = 0.1 M NaNO3	13.2 (ng)	ng, ng	298	8.64E5 – 1.30E6	1.64E-12	8.19E-13
Wieland and Stumm (1992)	2.75 (ng)	HNO3, I = 0.1 M NaNO3	13.2 (ng)	ng, ng	298	8.64E5 – 1.30E6	1.59E-12	7.94E-13
Wieland and Stumm (1992)	3 (ng)	HNO3, I = 0.1 M NaNO3	13.2 (ng)	ng, ng	298	8.64E5 – 1.30E6	1.46E-12	7.31E-13
Wieland and Stumm (1992)	3 (ng)	HNO3, I = 0.1 M NaNO3	13.2 (ng)	ng, ng	298	8.64E5 – 1.30E6	1.86E-12	9.28E-13
Wieland and Stumm (1992)	3.25 (ng)	HNO3, I = 0.1 M NaNO3	13.2 (ng)	ng, ng	298	8.64E5 – 1.30E6	1.61E-12	8.06E-13
Wieland and Stumm (1992)	3.25 (ng)	HNO3, I = 0.1 M NaNO3	13.2 (ng)	ng, ng	298	8.64E5 – 1.30E6	1.45E-12	7.25E-13
Wieland and Stumm (1992)	3.5 (ng)	HNO3, I = 0.1 M NaNO3	13.2 (ng)	ng, ng	298	8.64E5 – 1.30E6	1.18E-12	5.92E-13

References	Initial (Final) pH	Initial Fluid Composition	Initial (Final) Specific Surface Area [m^2/g]	Grain Size (min, max) [m]	Temperature [K]	Duration of Dissolution [s]	Si Release Rate [mol/s]	Mineral Dissolution Rate [$mol/m^2/s$]
Wieland and Stumm (1992)	3.75 (ng)	HNO3, I = 0.1 M NaNO3	13.2 (ng)	ng, ng	298	8.64E5 – 1.30E6	8.89E-13	4.44E-13
Wieland and Stumm (1992)	4 (ng)	HNO3, I = 0.1 M NaNO3	13.2 (ng)	ng, ng	298	8.64E5 – 1.30E6	8.28E-13	4.14E-13
Wieland and Stumm (1992)	4 (ng)	HNO3, I = 0.1 M NaNO3	13.2 (ng)	ng, ng	298	8.64E5 – 1.30E6	7.61E-13	3.81E-13
Wieland and Stumm (1992)	4.25 (ng)	HNO3, I = 0.1 M NaNO3	13.2 (ng)	ng, ng	298	8.64E5 – 1.30E6	7.67E-13	3.83E-13
Wieland and Stumm (1992)	4.5 (ng)	HNO3, I = 0.1 M NaNO3	13.2 (ng)	ng, ng	298	8.64E5 – 1.30E6	8.44E-13	4.22E-13
Wieland and Stumm (1992)	4.5 (ng)	HNO3, I = 0.1 M NaNO3	13.2 (ng)	ng, ng	298	8.64E5 – 1.30E6	8.11E-13	4.06E-13
Wieland and Stumm (1992)	4.75 (ng)	HNO3, I = 0.1 M NaNO3	13.2 (ng)	ng, ng	298	8.64E5 – 1.30E6	6.89E-13	3.44E-13
Wieland and Stumm (1992)	5 (ng)	HNO3, I = 0.1 M NaNO3	13.2 (ng)	ng, ng	298	8.64E5 – 1.30E6	7.00E-13	3.50E-13
Wieland and Stumm (1992)	5.5 (ng)	HNO3, I = 0.1 M NaNO3	13.2 (ng)	ng, ng	298	8.64E5–1.30E6	6.94E-13	3.47E-13
Wieland and Stumm (1992)	6 (ng)	HNO3, I = 0.1 M NaNO3	13.2 (ng)	ng, ng	298	8.64E5–1.30E6	5.00E-13	2.50E-13
Wieland and Stumm (1992)	6.5 (ng)	HNO3, I = 0.1 M NaNO3	13.2 (ng)	ng, ng	298	8.64E5–1.30E6	4.83E-13	2.42E-13
Ganor et al. (1995)	3.02 (3.15)	HClO4	7.5 (10)	ng, ng	298	9.00E5	1.36E-12	6.80E-13
Ganor et al. (1995)	3.06 (3.16)	HClO4	7.5 (10)	ng, ng	298	7.20E5	1.32E-12	6.60E-13
Ganor et al. (1995)	3.22 (3.42)	HClO4	7.5 (10)	ng, ng	298	3.60E5	1.44E-12	7.20E-13
Ganor et al. (1995)	3.31 (3.32)	HClO4	7.5 (10)	ng, ng	298	5.22E5	1.48E-12	7.40E-13

Ganor et al. (1995)	3.49 (3.68)	HClO4	7.5 (10)	ng, ng	298	9.90E5	6.40E-13	3.20E-13
Ganor et al. (1995)	4.02 (4.23)	HClO4	7.5 (10.2)	ng, ng	298	1.80E6	4.80E-13	2.40E-13
Huertas et al. (1999)	0.95 (ng)	0.1 M HCl, I = 1 M (NaCl + acid or base)	8.16 (ng)	ng, ng	298	3.64E7	3.72E-13	1.86E-13
Huertas et al. (1999)	1.94 (ng)	0.01 M HCl, I = 1 M (NaCl + acid or base)	8.16 (ng)	ng, ng	298	3.64E7	9.80E-14	4.90E-14
Huertas et al. (1999)	2.94 (ng)	0.001 M HCl, I = 1 M (NaCl + acid or base)	8.16 (ng)	ng, ng	298	3.64E7	3.81E-14	1.91E-14
Huertas et al. (1999)	3.76 (ng)	8.5 mM HAcO/1.5 mM NaAcO, I = 1 M (NaCl + acid or base)	8.16 (ng)	ng, ng	298	3.64E7	3.03E-14	1.51E-14
Huertas et al. (1999)	4.71 (ng)	3.6 mM HAcO/6.4 mM NaAcO, I = 1 M (NaCl + acid or base)	8.16 (ng)	ng, ng	298	3.64E7	3.10E-14	1.55E-14
Huertas et al. (1999)	5.7 (ng)	0.5 mM HAcO/9.5 mM NaAcO, I = 1 M (NaCl + acid or base)	8.16 (ng)	ng, ng	298	3.64E7	2.46E-14	1.23E-14
Huertas et al. (1999)	6.05 (ng)	0.1 mM NaHCO3, I = 1 M (NaCl + acid or base)	8.16 (ng)	ng, ng	298	3.64E7	1.82E-14	9.12E-15
Huertas et al. (1999)	7.79 (ng)	1 mM NaHCO3, I = 1 M (NaCl + acid or base)	8.16 (ng)	ng, ng	298	3.64E7	1.32E-14	6.61E-15
Huertas et al. (1999)	8.92 (ng)	8.5 mM NaHCO3/1.5 mM Na2CO3, I = 1 M (NaCl + acid or base)	8.16 (ng)	ng, ng	298	3.64E7	7.43E-15	3.72E-15

References	Initial (Final) pH	Initial Fluid Composition	Initial (Final) Specific Surface Area [m^2/g]	Grain Size (min, max) [m]	Temperature [K]	Duration of Dissolution [s]	Si Release Rate [mol/s]	Mineral Dissolution Rate [$mol/m^2/s$]
Huertas et al. (1999)	9.73 (ng)	3.9 mM NaHCO3/6.1 mM Na2CO3, I = 1 M (NaCl + acid or base)	8.16 (ng)	ng, ng	298	3.64E7	2.30E-14	1.15E-14
Huertas et al. (1999)	10.72 (ng)	0.001 NaOH, I = 1 M (NaCl + acid or base)	8.16 (ng)	ng, ng	298	1.04E7	1.18E-13	5.89E-14
Huertas et al. (1999)	11.96 (ng)	0.01 NaOH, I = 1 M (NaCl + acid or base)	8.16 (ng)	ng, ng	298	1.28E7	1.21E-12	6.03E-13
Huertas et al. (1999)	12.99 (ng)	0.1 NaOH, I = 1 M (NaCl + acid or base)	8.16 (ng)	ng, ng	298	1.04E7	6.62E-12	3.31E-12
Cama et al. (2002)	0.45 (0.52)	HClO4, I = 0.41 (in M)	18.4 (18.4)	ng, ng	298	8.81E6	2.32E-13	1.16E-13
Cama et al. (2002)	1.04 (1.00)	HClO4, I = 0.1224 (in M)	18.4 (18.4)	ng, ng	298	8.81E6	2.52E-13	1.26E-13
Cama et al. (2002)	1.51 (1.51)	HClO4, I = 0.0365 (in M)	19.1 (19.1)	ng, ng	298	2.89E7	9.74E-14	4.87E-14
Cama et al. (2002)	2.04 (2.02)	HClO4, I = 0.011 (in M)	17.9 (17.9)	ng, ng	298	5.48E6	7.22E-14	3.61E-14
Cama et al. (2002)	2.5 (2.47)	HClO4, I = 0.0034 (in M)	18.3 (18.3)	ng, ng	298	1.67E6	6.00E-14	3.00E-14
Cama et al. (2002)	2.5 (2.46)	HClO4, I = 0.0034 (in M)	18.3 (18.3)	ng, ng	298	5.89E6	5.52E-14	2.76E-14

Cama et al. (2002)	2.99 (3.00)	HClO4, I = 0.0011 (in M)	19.1 (19.1)	ng, ng	298	4.24E6	5.06E-14	2.53E-14
Cama et al. (2002)	3 (2.92)	HClO4, I = 0.001 (in M)	17.3 (17.3)	ng, ng	298	6.99E6	5.18E-14	2.59E-14
Cama et al. (2002)	3 (2.96)	HClO4, I = 0.0011 (in M)	19.2 (19.2)	ng, ng	298	1.17E7	5.20E-14	2.60E-14
Cama et al. (2002)	3.57 (3.46)	HClO4, I = 0.0004 (in M)	18.2 (18.2)	ng, ng	298	4.03E7	5.00E-14	2.50E-14
Cama et al. (2002)	4 (4.03)	HClO4, I = 0.0001 (in M)	17.9 (17.9)	ng, ng	298	4.03E7	3.56E-14	1.78E-14
Cama et al. (2002)	4.02 (4.07)	HClO4, I = 0.0001 (in M)	17.9 (17.9)	ng, ng	298	8.80E6	4.38E-14	2.19E-14
Cama et al. (2002)	4.49 (4.52)	HClO4, I = 0.0001 (in M)	18.2 (18.2)	ng, ng	298	2.49E7	2.28E-14	1.14E-14
Cama et al. (2002)	4.49 (4.51)	HClO4, I = 0 (in M)	17.9 (17.9)	ng, ng	298	2.49E7	1.75E-14	8.73E-15

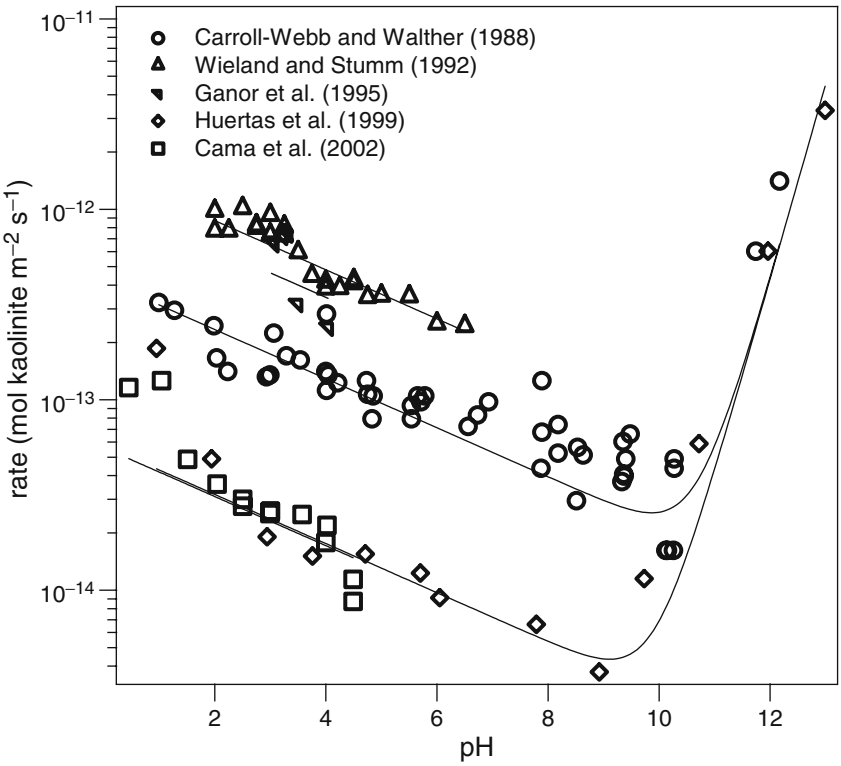

References

Carroll-Webb and Walther (1988) *Geochimica et Cosmochimica Acta* 52, 2609–2623. Al2Si2O5(OH)4, batch reactor, pO2 and pCO2 were atmospheric, surface area measured by BET-Kr, dissolution was nearly stoichiometric with aluminum release consistently lower than silica release from pH 2–9.

Wieland and Stumm (1992) *Geochimica et Cosmochimica Acta* 56, 3339–3355. Al2Si2O5(OH)4, batch reactor, pO2 and pCO2 were atmospheric, surface area measured by BET-N2, dissolution was not stoichiometric with silica preferentially released over aluminum from pH 2–5.

Ganor et al. (1995) *Geochimica et Cosmochimica Acta* 59, 1037–1052. Al2Si2O5(OH)4, continuously stirred tank reactor, pO2 and pCO2 were atmospheric, surface area measured by BET-N2, dissolution was stoichiometric within margin of error.

Huertas et al. (1999) *Geochimica et Cosmochimica Acta* 63, 3261–3275. Al2Si2O5(OH)4, batch reactor, pO2 and pCO2 were atmospheric, surface area

measured by BET, dissolution was not stoichiometric between pH 5 and 10 and stoichiometric from pH 1–4 and 11–13.

Cama et al. (2002) *Geochimica et Cosmochimica Acta* 66, 3919–3926. Al2Si2O5(OH)4, non-stirred tank reactor reactor, pO2 and pCO2 were atmospheric, surface area measured by BET-N2, dissolution was nearly stoichiometric (aluminum to silicon ratio is 0.9–1.2 for most experiments).

K-feldspar

References	Initial (Final) pH	Initial Fluid Composition	Initial (Final) Specific Surface Area [m^2/g]	Grain Size (min, max) [m]	Temperature [K]	Duration of Dissolution [s]	Si Release Rate [$mol/m^2/s$]	Mineral Dissolution Rate [$mol/m^2/s$]
Manley and Evans (1986)	4 (ng)	Ng	0.0214 (ng)	0.000106, 0.0005	288.15	6.05E + 06	1.18E-11	3.92E-12
Manley and Evans (1986)	3.82 (ng)	Ng	0.0214 (ng)	0.000106, 0.0005	288.15	6.05E + 06	9.64E-12	3.21E-12
Manley and Evans (1986)	3.92 (ng)	Ng	0.0214 (ng)	0.000106, 0.0005	288.15	6.05E + 06	9.83E-12	3.28E-12
Manley and Evans (1986)	4.03 (ng)	Ng	0.0214 (ng)	0.000106, 0.0005	288.15	6.05E + 06	1.12E-11	3.73E-12
Manley and Evans (1986)	4.25 (ng)	Ng	0.0214 (ng)	0.000106, 0.0005	288.15	6.05E + 06	9.25E-12	3.08E-12
Manley and Evans (1986)	4.25 (ng)	Ng	0.0214 (ng)	0.000106, 0.0005	288.15	6.05E + 06	9.25E-12	3.08E-12
Manley and Evans (1986)	4.32 (ng)	Ng	0.0214 (ng)	0.000106, 0.0005	288.15	6.05E + 06	7.71E-12	2.57E-12
Manley and Evans (1986)	4.37 (ng)	Ng	0.0214 (ng)	0.000106, 0.0005	288.15	6.05E + 06	7.71E-12	2.57E-12
Manley and Evans (1986)	4.37 (ng)	Ng	0.0214 (ng)	0.000106, 0.0005	288.15	6.05E + 06	6.75E-12	2.25E-12
Manley and Evans (1986)	5.65 (ng)	Ng	0.0214 (ng)	0.000106, 0.0005	288.15	6.05E + 06	5.78E-12	1.93E-12
Tan (1980)	7 (ng)	Ng	11.3 (ng)	ng, 5e − 05	297.15	3.19E + 06	9.69E-12	3.23E-12
Tan (1980)	7 (ng)	Ng	11.3 (ng)	ng, 5e − 05	297.15	3.19E + 06	3.88E-12	1.29E-12
Schweda (1989a)	3 (ng)	Ng	ng (ng)	0.000125, 0.00025	298.15	7.20E + 06	7.45E-12	2.48E-12
Schweda (1989a)	3 (ng)	Ng	ng (ng)	0.000125, 0.00025	298.15	7.20E + 06	3.09E-12	1.03E-12
Schweda (1989a)	4 (ng)	Ng	ng (ng)	0.000125, 0.00025	298.15	7.20E + 06	2.41E-12	8.02E-13
Schweda (1989a)	5.7 (ng)	Ng	ng (ng)	0.000125, 0.00025	298.15	7.20E + 06	5.62E-13	1.87E-13
Schweda (1989a)	11 (ng)	Ng	ng (ng)	0.000125, 0.00025	298.15	7.20E + 06	1.30E-12	4.32E-13
Schweda (1989a)	11 (ng)	Ng	ng (ng)	0.000125, 0.00025	298.15	7.20E + 06	8.79E-13	2.93E-13

Schweda (1989b)	1.1 (ng)	Ng	ng (ng)	0.000125, 0.00025	298.15	7.20E+06	2.60E-11	8.65E-12
Schweda (1989b)	2.04 (ng)	Ng	ng (ng)	0.000125, 0.00025	298.15	7.20E+06	1.13E-11	3.78E-12
Schweda (1989b)	3.06 (ng)	Ng	ng (ng)	0.000125, 0.00025	298.15	7.20E+06	2.57E-12	8.56E-13
Schweda (1989b)	2.99 (ng)	Ng	ng (ng)	0.000125, 0.00025	298.15	7.20E+06	3.60E-12	1.20E-12
Schweda (1989b)	4.03 (ng)	Ng	ng (ng)	0.000125, 0.00025	298.15	7.20E+06	8.43E-13	2.81E-13
Schweda (1989b)	5.62 (ng)	Ng	ng (ng)	0.000125, 0.00025	298.15	7.20E+06	1.42E-13	4.74E-14
Schweda (1989b)	5.79 (ng)	Ng	ng (ng)	0.000125, 0.00025	298.15	7.20E+06	1.97E-13	6.57E-14
Schweda (1989b)	11 (ng)	Ng	ng (ng)	0.000125, 0.00025	298.15	7.20E+06	7.54E-13	2.51E-13
Schweda (1989b)	10.98 (ng)	Ng	ng (ng)	0.000125, 0.00025	298.15	7.20E+06	1.02E-12	3.41E-13
Schweda (1989b)	12.01 (ng)	Ng	ng (ng)	0.000125, 0.00025	298.15	7.20E+06	4.26E-12	1.42E-12
Schweda (1989b)	12.72 (ng)	Ng	ng (ng)	0.000125, 0.00025	298.15	7.20E+06	1.54E-11	5.13E-12
van Hess et al. (2002a)	3.5 (ng)	Ng	0.113 (ng)	0.000125, 0.00025	298.15	7.20E+06	4.03E-12	1.34E-12
van Hess et al. (2002b)	3.5 (ng)	Ng	0.113 (ng)	0.000125, 0.00025	298.15	7.20E+06	4.61E-12	1.53E-12
van Hess et al. (2002a)	5 (ng)	Ng	0.113 (ng)	0.000125, 0.00025	298.15	7.20E+06	1.91E-12	6.33E-13
van Hess et al. (2002b)	5 (ng)	Ng	0.113 (ng)	0.000125, 0.00025	298.15	7.20E+06	6.62E-12	2.20E-12
van Hess et al. (2002a)	3.5 (ng)	Ng	0.113 (ng)	0.000125, 0.00025	298.15	7.20E+06	1.26E-11	4.18E-12
van Hess et al. (2002b)	3.5 (ng)	Ng	0.113 (ng)	0.000125, 0.00025	298.15	7.20E+06	8.79E-12	2.92E-12
van Hess et al. (2002a)	5 (ng)	Ng	0.113 (ng)	0.000125, 0.00025	298.15	7.20E+06	7.65E-12	2.54E-12
van Hess et al. (2002b)	5 (ng)	Ng	0.113 (ng)	0.000125, 0.00025	298.15	7.20E+06	1.82E-11	6.06E-12
Stillings and Brantley (1995)	3 (3.02)	Ng	0.157 (0.31)	7.5e − 05, 0.00015	298.15	1.07E+07	4.86E-12	1.63E-12
Stillings and Brantley (1995)	3 (3.02)	Ng	0.157 (0.31)	7.5e − 05, 0.00015	298.15	1.07E+07	4.86E-12	1.63E-12
Stillings and Brantley (1995)	3 (3.01)	Ng	0.157 (0.39)	7.5e − 05, 0.00015	298.15	6.27E+06	4.56E-12	1.53E-12

References	Initial (Final) pH	Initial Fluid Composition	Initial (Final) Specific Surface Area [m^2/g]	Grain Size (min, max) [m]	Temperature [K]	Duration of Dissolution [s]	Si Release Rate [$mol/m^2/s$]	Mineral Dissolution Rate [$mol/m^2/s$]
Stillings and Brantley (1995)	3 (3.02)	Ng	0.157 (0.31)	7.5e − 05, 0.00015	298.15	1.07E + 07	4.86E-12	1.63E-12
Stillings and Brantley (1995)	3 (3.01)	Ng	0.157 (0.39)	7.5e − 05, 0.00015	298.15	6.27E + 06	4.56E-12	1.53E-12
Stillings and Brantley (1995)	3 (2.98)	I = 0.005 M	0.157 (0.515)	7.5e − 05, 0.00015	298.15	7.60E + 06	2.13E-12	7.15E-13
Stillings and Brantley (1995)	3 (3.03)	I = 0.05 M	0.157 (0.608)	7.5e − 05, 0.00015	298.15	5.97E + 06	7.72E-13	2.59E-13
Stillings and Brantley (1995)	3 (3.06)	I = 0.005 M	0.157 (0.216)	7.5e − 05, 0.00015	298.15	6.38E + 06	4.26E-12	1.43E-12
Busenberg and Clemency (1976)	5 (ng)	Ng	1.07 (ng)	ng, 3.7e − 05	298.65	1.81E + 06	1.52E-12	5.07E-13
Busenberg and Clemency (1976)	5 (ng)	Ng	1.52 (ng)	ng, 3.7e − 05	298.65	1.81E + 06	1.67E-12	5.58E-13

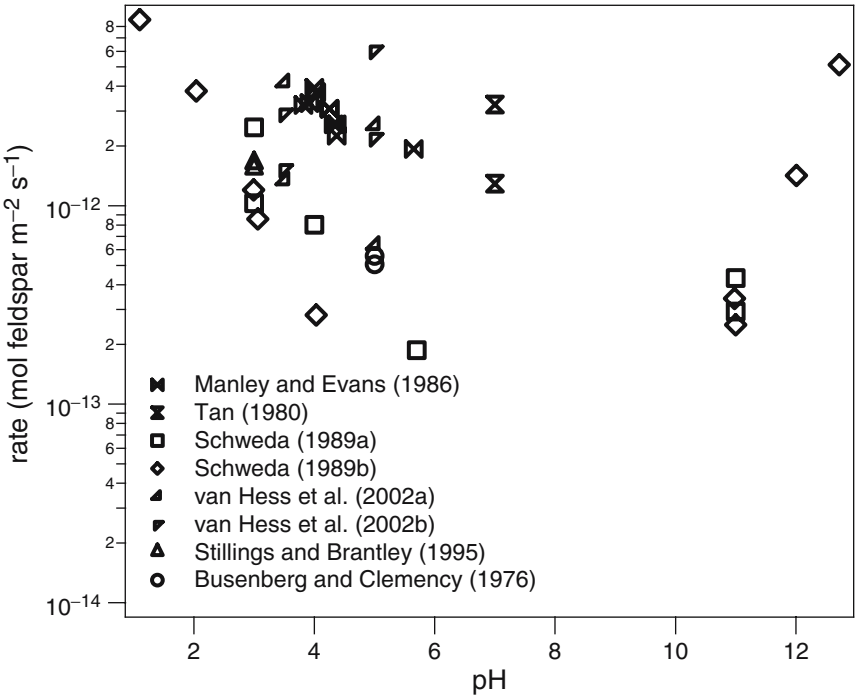

References

Manley and Evans (1986) *Soil Science* 141, 106–112. Microcline, KAlSi3O8, Batch reactor, pO2 and pCO2 were not given, Geometric surface area, dissolution was not stoichiometric. These data were excluded from the fit because of uncertainty in the surface area.

Tan (1980) *Soil Science* 129, 5–11. Microcline, KAlSi3O8, Batch reactor, pO2 and pCO2 were not given, Geometric surface area, dissolution was not stoichiometric. These data were excluded from the fit because of uncertainty in the surface area.

Schweda (1989a) Proceedings of the Sixth International Symposium on Water/Rock Interaction (ed. D. L. Miles) A. A. Balkema, Rotterdam, 609–612. Sanidine, (K,Na)AlSi3O8 (Ab027Or071Cn002), Flow through reactor, pO2 and pCO2 were not given, surface area measurement method not given, dissolution was stoichiometric.

Schweda (1989b) Proceedings of the Sixth International Symposium on Water/Rock Interaction (ed. D. L. Miles) A. A. Balkema, Rotterdam, 609–612. Microcline, KAlSi3O8 (Ab020Or080), Flow through reactor, pO2 and pCO2 were not given, surface area measurement method not given, dissolution was stoichiometric.

Van Hess et al. (2002a) *Chemical Geology* 189, 199–211. Microcline, K0.69Na0.24Ca0.02Al1.00Si3.01O8, Flow through reactor, pO2 and pCO2 were not given, surface area measured by N2 BET, dissolution was not stoichiometric.

Van Hess et al. (2002b) *Chemical Geology* 189, 199–211. Microcline, K0.69Na0.24Ca0.02Al1.00Si3.01O8, Flow through reactor, pO2 and pCO2 were not given, surface area measured by N2 BET, dissolution was not stoichiometric. These data were excluded from the fit because the experiments contained dissolved organic matter.

Stillings and Brantley (1995) *Geochimica et Cosmochimica Acta* 59, 1483–1496. Microcline, K0.77Na0.22Al1.02Si2.98O8, Continuously stirred flow through reactor, pO2 and pCO2 were not given, surface area measured by Kr BET, dissolution was stoichiometric.

Busenberg and Clemency (1976) *Geochimica et Cosmochimica Acta* 40, 41–49. Microcline, KAlSi3O8 (Or75.15Al24.81An0.04), batch reactor, pO2 = 0.963 pCO2 was not given, surface area measured by BET, dissolution was not stoichiometric.

Oligoclase

References	Initial (Final) pH	Initial Fluid Composition	Initial (Final) Specific Surface Area [m^2/g]	Grain Size (min, max) [m]	Temperature [K]	Duration of Dissolution [s]	Si Release Rate [$mol/m^2/s$]	Mineral Dissolution Rate [$mol/m^2/s$]
Stillings and Brantley (1995a)	3 (3.03)	1 mM HCl	0.0877 (0.1851)	7.5E-05, 1.5E-04	298	1.07E07	1.76E-11	6.20E-12
Stillings and Brantley (1995a)	3 (3.01)	1 mM HCl	0.0877 (0.2222)	7.5E-05, 1.5E-04	298	1.70E07	1.79E-11	6.30E-12
Stillings and Brantley (1995a)	3 (2.98)	1 mM HCl + 10 mM NaCl	0.0877 (0.3094)	7.5E-05, 1.5E-04	298	2.46E07	6.79E-12	2.39E-12
Stillings and Brantley (1995a)	3 (3.04)	1 mM HCl + 100 mM NaCl	0.0877 (0.3466)	7.5E-05, 1.5E-04	298	3.05E07	5.06E-12	1.78E-12
Stillings and Brantley (1995b)	3 (3.03)	1 mM HCl + 1 mM (CH3)4NCl	0.0877 (0.2471)	7.5E-05, 1.5E-04	298	6.38E06	4.74E-12	1.67E-12
Stillings and Brantley (1995b)	3 (3.07)	1 mM HCl + 100 mM (CH3)4NCl	0.0877 (0.1637)	7.5E-05, 1.5E-04	298	8.91E06	3.27E-12	1.15E-12
Stillings et al. (1996)	3 (2.85)	4 mM HCl + 1 mM oxalate	0.088 (1.4)	7.5E-05, 1E-04	298	1.33E07	9.94E-11	3.50E-11
Stillings et al. (1996)	5 (5.68)	1 mM oxalate	0.088 (0.51)	7.5E-05, 1E-04	298	9.86E06	6.33E-11	2.23E-11
Stillings et al. (1996)	5 (5.4)	DI water	0.088 (0.094)	7.5E-05, 1E-04	298	1.59E07	6.59E-12	2.32E-12
Holdren and Speyer (1987)	3 (ng)	0.001 N HCl	0.128 (ng)	7.5E-05, 1.5E-04	298	ng	4.21E-11	1.48E-11
Holdren and Speyer (1987)	3 (ng)	0.01 N HCl	0.065 (ng)	6E-04, ng	298	ng	5.59E-11	1.97E-11
Holdren and Speyer (1987)	3 (ng)	0.01 N HCl	0.079 (ng)	3E-04, 6E-04	298	ng	6.49E-11	2.29E-11
Holdren and Speyer (1987)	3 (ng)	0.01 N HCl	0.09 (ng)	1.5E-04, 3E-04	298	ng	6.82E-11	2.40E-11
Holdren and Speyer (1987)	3 (ng)	0.01 N HCl	0.334 (ng)	3.7E-05, 7.5E-05	298	ng	8.10E-12	2.85E-12
Holdren and Speyer (1987)	3 (ng)	0.01 N HCl	0.889 (ng)	ng, 3.7E-05	298	ng	1.14E-11	4.01E-12
Casey et al. (1991)	2 (ng)	0.010 N HCl	0.18 (ng)	2.5E-05, 7.5E-05	298	2.00E06	4.95E-12	1.41E-11
Casey et al. (1991)	2 (ng)	0.010 N HCl	0.645 (ng)	2.5E-05, 7.5E-05	298	2.00E06	1.27E-11	3.62E-11

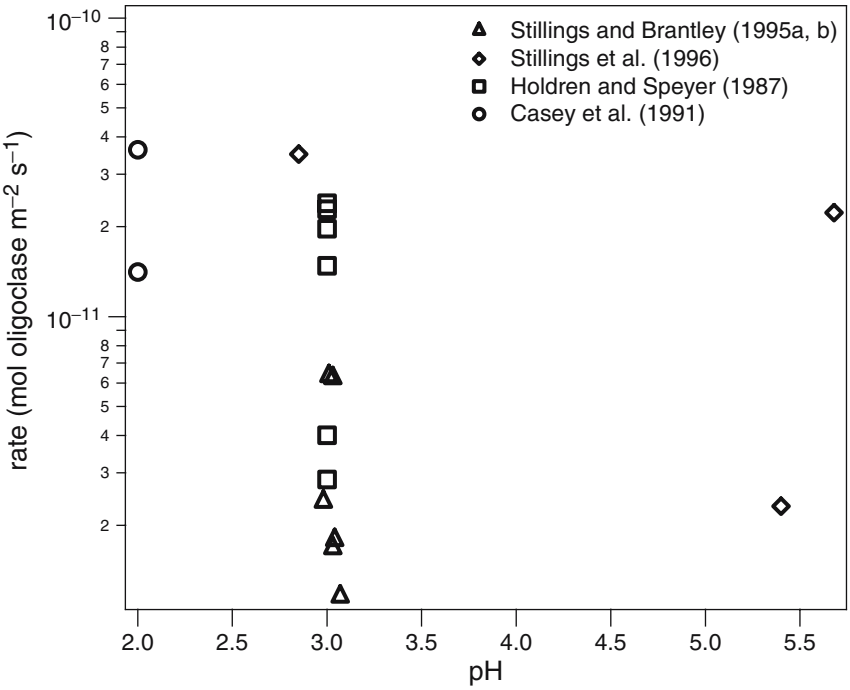

References

Stillings and Brantley (1995a) *Geochimica et Cosmochimica Acta* 59, 1483–1496. K0.05Na0.68Ca0.20Al1.13Si2.84O8, continuously stirred flow through reactor, pO2 and pCO2 were atmospheric, surface area measured by Kr-BET, final surface area used for normalization, dissolution was not stoichiometric.

Stillings and Brantley (1995b) *Geochimica et Cosmochimica Acta* 59, 1483–1496. K0.05Na0.68Ca0.20Al1.13Si2.84O8, continuously stirred flow through reactor, pO2 and pCO2 were atmospheric, surface area measured by Kr-BET, final surface area used for normalization, (CH3)4NCl was added to reactors, dissolution was not stoichiometric.

Stillings et al. (1996) *Chemical Geology* 132, 79–89. K0.05Na0.68Ca0.20Al1.13Si2.84O8, continuously stirred flow through reactor, pO2 and pCO2 were atmospheric, surface area measured by Kr-BET, initial surface area used for normalization, dissolution was not stoichiometric. Some of these experiments contained organics.

Holdren and Speyer (1987) *Geochimica et Cosmochimica Acta* 51, 2311–2318. K0.05Na0.68Ca0.20Al1.13Si2.84O8, Batch reactor, pO2 and pCO2 were atmospheric, surface area measured by Ar-BET.

Casey et al. (1991) *American Mineralogist* 76, 211–217. K0.02Na0.78Ca0.2Al1.15Si2.85O8, Batch reactor, pO2 and pCO2 were atmospheric, surface area measured by BET, dissolution was not stoichiometric.

Olivine

References	Initial (Final) pH	Initial Fluid Composition	Initial (Final) Specific Surface Area [m^2/g]	Grain Size (min, max) [m]	Temperature [K]	Duration of Dissolution [s]	Si (Mg) Release Rate [$mol/m^2/s$]	Mineral Dissolution Rate base on Si (Mg) [$mol/m^2/s$]
Pokrovsky and Schott (2000a)	1.03 (ng)	0.1 M NaCl	0.08 (ng)	5E-05, 1.E-4	298	2.88E4	5.89E-08(6.17E-08)	5.89E-08(3.39E-08)
Pokrovsky and Schott (2000a)	1.12 (ng)	0.1 M NaCl	0.08 (ng)	5E-05, 1.E-4	298	7.22E4	5.25E-08(5.25E-08)	5.25E-08(2.88E-08)
Pokrovsky and Schott (2000a)	1.11 (ng)	0.1 M NaCl	0.08 (ng)	5E-05, 1.E-4	298	9.36E4	4.68E-08(5.02E-08)	4.68E-08(2.75E-08)
Pokrovsky and Schott (2000a)	2.13 (ng)	0.1 M NaCl	0.08 (ng)	5E-05, 1.E-4	298	2.88E4	2.00E-08(2.24E-08)	2.00E-08(1.23E-08)
Pokrovsky and Schott (2000a)	2.18 (ng)	0.1 M NaCl	0.08 (ng)	5E-05, 1.E-4	298	5.76E4	1.95E-08(2.09E-08)	1.95E-08(1.15E-08)
Pokrovsky and Schott (2000a)	2.21 (ng)	0.1 M NaCl	0.08 (ng)	5E-05, 1.E-4	298	1.008E5	1.91E-08(2.00E-08)	1.91E-08(1.10E-08)
Pokrovsky and Schott (2000a)	2.7 (ng)	0.1 M NaCl	0.08 (ng)	5E-05, 1.E-4	298	1.404E5	1.86E-08 (ng)	1.86E-08 (ng)
Pokrovsky and Schott (2000a)	2.81 (ng)	0.1 M NaCl	0.08 (ng)	5E-05, 1.E-4	298	1.512E5	1.51E-08	1.51E-08 (ng)
Pokrovsky and Schott (2000a)	2.82 (ng)	0.1 M NaCl	0.08 (ng)	5E-05, 1.E-4	298	2.52E5	1.29E-08 (ng)	1.29E-08 (ng)
Pokrovsky and Schott (2000a)	2.74 (ng)	0.1 M NaCl	0.08 (ng)	5E-05, 1.E-4	298	1.08E5	1.48E-08 (ng)	1.48E-08 (ng)
Pokrovsky and Schott (2000a)	2.88 (ng)	0.1 M NaCl	0.08 (ng)	5E-05, 1.E-4	298	9.36E4	1.26E-08 (ng)	1.26E-08 (ng)
Pokrovsky and Schott (2000a)	2.89 (ng)	0.1 M NaCl	0.08 (ng)	5E-05, 1.E-4	298	1.728E5	1.10E-08 (ng)	1.10E-08 (ng)
Pokrovsky and Schott (2000a)	2.99 (ng)	0.1 M NaCl	0.08 (ng)	5E-05, 1.E-4	298	1.116E5	1.17E-08 (ng)	1.17E-08 (ng)
Pokrovsky and Schott (2000a)	3.03 (ng)	0.1 M NaCl	0.08 (ng)	5E-05, 1.E-4	298	1.296E5	1.07E-08 (ng)	1.07E-08 (ng)

Pokrovsky and Schott (2000a)	3.08 (ng)	0.1 M NaCl	0.08 (ng)	5E-05, 1.E-4	298	9.0E4	7.24E-09 (ng)	7.24E-09 (ng)
Pokrovsky and Schott (2000a)	3.05 (ng)	0.1 M NaCl	0.08 (ng)	5E-051.E-4	298	1.728E5	6.61E-09 (ng)	6.61E-09 (ng)
Pokrovsky and Schott (2000a)	3.16 (ng)	0.1 M NaCl	0.08 (ng)	5E-05, 1.E-4	298	2.376E5	5.62E-09 (ng)	5.62E-09 (ng)
Pokrovsky and Schott (2000a)	3.26 (ng)	0.1 M NaCl	0.08 (ng)	5E-05, 1.E-4	298	2.7E5	4.57E-09 (ng)	4.57E-09 (ng)
Pokrovsky and Schott (2000a)	3.05 (ng)	0.1 M NaCl	0.08 (ng)	5E-05, 1.E-4	298	1.836E5	5.25E-09 (ng)	5.25E-09 (ng)
Pokrovsky and Schott (2000a)	4.15 (ng)	0.001 M NaCl	0.08 (ng)	5E-05, 1.E-4	298	9.36E4	9.33E-10(8.91E-10)	9.33E-10(4.90E-10)
Pokrovsky and Schott (2000a)	3.6 (ng)	0.001 M NaCl	0.08 (ng)	5E-05, 1.E-4	298	1.116E5	1.58E-09(1.58E-09)	1.58E-09(8.71E-10)
Pokrovsky and Schott (2000a)	3.34 (ng)	0.001 M NaCl	0.08 (ng)	5E-05, 1.E-4	298	9.36E4	2.82E-09(2.88E-09)	2.82E-09(1.58E-09)
Pokrovsky and Schott (2000a)	2.85 (ng)	0.001 M NaCl	0.08 (ng)	5E-05, 1.E-4	298	1.008E5	5.01E-09(5.13E-09)	5.01E-09(2.82E-09)
Pokrovsky and Schott (2000a)	4.2 (ng)	0.1 M NaCl	0.08 (ng)	5E-05, 1.E-4	298	1.26E5	2.04E-09 (ng)	2.04E-09 (ng)
Pokrovsky and Schott (2000a)	4.41 (ng)	0.1 M NaCl	0.08 (ng)	5E-05, 1.E-4	298	1.512E5	1.58E-09 (ng)	1.58E-09 (ng)
Pokrovsky and Schott (2000a)	4.49 (ng)	0.1 M NaCl	0.08 (ng)	5E-05, 1.E-4	298	2.52E5	1.05E-09 (ng)	1.05E-09 (ng)
Pokrovsky and Schott (2000a)	4.22 (ng)	0.1 M NaCl	0.08 (ng)	5E-05, 1.E-4	298	1.08E5	1.70E-09 (ng)	1.66E-09 (ng)
Pokrovsky and Schott (2000a)	4.77 (ng)	0.1 M NaCl	0.08 (ng)	5E-05, 1.E-4	298	1.512E5	1.05E-09 (ng)	1.05E-09 (ng)
Pokrovsky and Schott (2000a)	4.85 (ng)	0.1 M NaCl	0.08 (ng)	5E-05, 1.E-4	298	1.512E5	9.55E-10 (ng)	9.55E-10 (ng)
Pokrovsky and Schott (2000a)	4.95 (ng)	0.1 M NaCl	0.08 (ng)	5E-05, 1.E-4	298	2.52E5	7.08E-10 (ng)	7.08E-10 (ng)

References	Initial (Final) pH	Initial Fluid Composition	Initial (Final) Specific Surface Area [m^2/g]	Grain Size (min, max) [m]	Temperature [K]	Duration of Dissolution [s]	Si (Mg) Release Rate [$mol/m^2/s$]	Mineral Dissolution Rate base on Si (Mg) [$mol/m^2/s$]
Pokrovsky and Schott (2000a)	4.55 (ng)	0.1 M NaCl	0.08 (ng)	5E-05, 1.E-4	298	9.36E4	9.33E-10 (ng)	9.33E-10 (ng)
Pokrovsky and Schott (2000a)	5.7 (ng)	0.1 M NaCl	0.08 (ng)	5E-05, 1.E-4	298	9.0E4	3.24E-10(3.63E-10)	3.24E-10(1.99E-10)
Pokrovsky and Schott (2000a)	6.18 (ng)	0.1 M NaCl	0.08 (ng)	5E-05, 1.E-4	298	1.728E5	2.51E-10(2.51E-10)	2.51E-10(1.38E-10)
Pokrovsky and Schott (2000a)	6.28 (ng)	0.1 M NaCl	0.08 (ng)	5E-05, 1.E-4	298	2.376E5	1.91E-10(1.86E-10)	1.91E-10(1.02E-10)
Pokrovsky and Schott (2000a)	6.13 (ng)	0.1 M NaCl	0.08 (ng)	5E-05, 1.E-4	298	2.7E5	1.20E-10(1.38E-10)	1.20E-10(7.58E-11)
Pokrovsky and Schott (2000a)	5.61 (ng)	0.1 M NaCl	0.08 (ng)	5E-05, 1.E-4	298	1.836E5	1.62E-10(1.70E-10)	1.62E-10(9.33E-11)
Pokrovsky and Schott (2000a)	7.33 (ng)	0.1 M NaCl	0.08 (ng)	5E-05, 1.E-4	298	4.968E5	1.17E-10(1.26E-10)	1.17E-10(6.92E-11)
Pokrovsky and Schott (2000a)	7.19 (ng)	0.1 M NaCl	0.08 (ng)	5E-05, 1.E-4	298	9.72E5	7.76E-11(7.94E-11)	7.76E-11(4.36E-11)
Pokrovsky and Schott (2000a)	7.21 (ng)	0.1 M NaCl	0.08 (ng)	5E-05, 1.E-4	298	3.996E5	9.12E-11(8.91E-11)	9.12E-11(4.90E-11)
Pokrovsky and Schott (2000a)	7.25 (ng)	0.1 M NaCl	0.08 (ng)	5E-05, 1.E-4	298	3.456E5	1.32E-10(1.26E-10)	1.32E-10(6.92E-11)
Pokrovsky and Schott (2000a)	6.6 (ng)	0.1 M NaCl	0.08 (ng)	5E-05, 1.E-4	298	1.08E5	1.07E-10 (ng)	1.07E-10 (ng)
Pokrovsky and Schott (2000a)	6.39 (ng)	0.1 M NaCl	0.08 (ng)	5E-05, 1.E-4	298	2.016E5	9.12E-11(1.02E-10)	9.12E-11(5.62E-11)
Pokrovsky and Schott (2000a)	6.37 (ng)	0.1 M NaCl	0.08 (ng)	5E-05, 1.E-4	298	1.728E5	9.77E-11 (ng)	9.77E-11 (ng)

Pokrovsky and Schott (2000a)	6.3 (ng)	0.1 M NaCl	0.08 (ng)	5E-05, 1.E-4	298	1.728E5	9.12E-11 (ng)	9.12E-11 (ng)
Pokrovsky and Schott (2000a)	6.29 (ng)	0.1 M NaCl	0.08 (ng)	5E-05, 1.E-4	298	1.692E5	8.91E-11 (ng)	8.91E-11 (ng)
Pokrovsky and Schott (2000a)	6.29 (ng)	0.1 M NaCl	0.08 (ng)	5E-05, 1.E-4	298	1.62E5	9.12E-11 (ng)	9.12E-11 (ng)
Pokrovsky and Schott (2000a)	6.28 (ng)	0.1 M NaCl	0.08 (ng)	5E-05, 1.E-4	298	1.656E5	8.32E-11 (ng)	8.32E-11 (ng)
Pokrovsky and Schott (2000a)	6.32 (ng)	0.1 M NaCl	0.08 (ng)	5E-05, 1.E-4	298	1.728E5	8.51E-11 (ng)	8.51E-11 (ng)
Pokrovsky and Schott (2000a)	9.3 (ng)	0.1 M NaCl	0.08 (ng)	5E-05, 1.E-4	298	4.968E5	3.24E-11(2.34E-11)	3.24E-11(1.29E-11)
Pokrovsky and Schott (2000a)	7.9 (ng)	0.1 M NaCl	0.08 (ng)	5E-05, 1.E-4	298	1.044E6	2.69E-11(2.57E-11)	2.69E-11(1.41E-11)
Pokrovsky and Schott (2000a)	7.6 (ng)	0.1 M NaCl	0.08 (ng)	5E-05, 1.E-4	298	4.032E5	3.39E-11(3.55E-11)	3.39E-11(1.95E-11)
Pokrovsky and Schott (2000a)	7.98 (ng)	0.1 M NaCl	0.08 (ng)	5E-05, 1.E-4	298	1.62E5	4.07E-11(3.63E-11)	4.07E-11(1.99E-11)
Pokrovsky and Schott (2000a)	10.24 (ng)	0.02 M NaCl	0.08 (ng)	5E-05, 1.E-4	298	3.276E5	ng (1.91E-11)	ng (1.04E-11)
Pokrovsky and Schott (2000a)	10.08 (ng)	0.02 M NaCl	0.08 (ng)	5E-05, 1.E-4	298	3.168E5	1.62E-11(1.29E-11)	1.62E-11(7.08E-12)
Pokrovsky and Schott (2000a)	9.58 (ng)	0.02 M NaCl	0.08 (ng)	5E-05, 1.E-4	298	4.536E5	2.88E-11(9.33E-12)	2.88E-11(5.13E-12)
Pokrovsky and Schott (2000a)	10.76 (ng)	0.1 M NaCl	0.08 (ng)	5E-05, 1.E-4	298	1.08E6	4.17E-11(2.40E-11)	4.17E-11(1.31E-11)
Pokrovsky and Schott (2000a)	10.9 (ng)	0.1 M NaCl	0.08 (ng)	5E-05, 1.E-4	298	4.032E5	3.63E-11(2.63E-11)	3.63E-11(1.45E-11)
Pokrovsky and Schott (2000a)	12.06 (ng)	0.02 M NaCl	0.08 (ng)	5E-05, 1.E-4	298	8.28E5	1.41E-11(1.41E-11)	1.41E-11(7.76E-12)
Pokrovsky and Schott (2000a)	10.9 (ng)	0.1 M NaCl	0.08 (ng)	5E-05, 1.E-4	298	5.04E5	2.04E-11(2.09E-11)	2.04E-11(1.15E-11)

References	Initial (Final) pH	Initial Fluid Composition	Initial (Final) Specific Surface Area [m^2/g]	Grain Size (min, max) [m]	Temperature [K]	Duration of Dissolution [s]	Si (Mg) Release Rate [$mol/m^2/s$]	Mineral Dissolution Rate base on Si (Mg) [$mol/m^2/s$]
Pokrovsky and Schott (2000a)	10.78 (ng)	0.1 M NaCl	0.08 (ng)	5E-05, 1.E-4	298	6.48E5	1.12E-11(1.15E-11)	1.12E-11(6.31E-12)
Pokrovsky and Schott (2000a)	11.45 (ng)	0.1 M NaCl	0.08 (ng)	5E-05, 1.E-4	298	4.32E5	6.46E-12(9.77E-12)	6.46E-12(5.37E-12)
Pokrovsky and Schott (2000a)	11.42 (ng)	0.1 M NaCl	0.08 (ng)	5E-05, 1.E-4	298	5.832E5	6.61E-12(6.31E-12)	6.61E-12(3.47E-12)
Pokrovsky and Schott (2000a)	11.46 (ng)	0.1 M NaCl	0.08 (ng)	5E-05, 1.E-4	298	1.044E6	5.62E-12(6.76E-12)	5.62E-12(3.71E-12)
Pokrovsky and Schott (2000a)	11.5 (ng)	0.1 M NaCl	0.08 (ng)	5E-05, 1.E-4	298	9.0E5	9.55E-12(1.05E-11)	9.55E-12(5.75E-12)
Pokrovsky and Schott (2000a)	10.95 (ng)	0.1 M NaCl	0.08 (ng)	5E-05, 1.E-4	298	3.816E5	2.51E-11(1.02E-11)	2.51E-11(5.62E-12)
Pokrovsky and Schott (2000a)	10.85 (ng)	0.1 M NaCl	0.08 (ng)	5E-05, 1.E-4	298	4.86E5	4.90E-11(9.55E-12)	4.90E-11(5.25E-12)
Pokrovsky and Schott (2000a)	11.14 (ng)	0.1 M NaCl	0.08 (ng)	5E-05, 1.E-4	298	4.428E5	ng (4.27E-12)	ng (2.34E-12)
Pokrovsky and Schott (2000a)	11.01 (ng)	0.0015 M NaCl	0.08 (ng)	5E-05, 1.E-4	298	3.816E5	2.69E-11(2.88E-11)	2.69E-11(1.58E-11)
Pokrovsky and Schott (2000a)	11.13 (ng)	0.0015 M NaCl	0.08 (ng)	5E-05, 1.E-4	298	4.86E5	1.95E-11(1.78E-11)	1.95E-11(9.77E-12)
Pokrovsky and Schott (2000a)	11.26 (ng)	0.0015 M NaCl	0.08 (ng)	5E-05, 1.E-4	298	4.428E5	ng (3.16E-12)	ng (1.74E-12)
Pokrovsky and Schott (2000a)	8.02 (ng)	0.001 M NaCl	0.08 (ng)	5E-05, 1.E-4	298	3.816E5	7.41E-11(7.41E-11)	7.41E-11(4.07E-11)
Pokrovsky and Schott (2000a)	8.13 (ng)	0.001 M NaCl	0.08 (ng)	5E-05, 1.E-4	298	4.86E5	4.68E-11(5.37E-11)	4.68E-11(2.95E-11)

Pokrovsky and Schott (2000a)	11.02 (ng)	0.001 M NaCl	0.08 (ng)	5E-05, 1.E-4	298	4.428E5	ng (2.29E-12)	ng (1.26E-12)
Pokrovsky and Schott (2000a)	11.21 (ng)	0.01 M NaCl	0.08 (ng)	5E-05, 1.E-4	298	6.48E5	ng (1.82E-11)	ng (1.00E-11)
Pokrovsky and Schott (2000a)	11.16 (ng)	0.01 M NaCl	0.08 (ng)	5E-05, 1.E-4	298	5.976E5	ng (1.45E-11)	ng (7.94E-12)
Pokrovsky and Schott (2000a)	9.45 (ng)	0.01 M NaCl	0.08 (ng)	5E-05, 1.E-4	298	2.088E5	ng (3.39E-11)	ng (1.86E-11)
Pokrovsky and Schott (2000a)	8.65 (ng)	0.01 M NaCl	0.08 (ng)	5E-05, 1.E-4	298	2.736E5	ng (3.80E-11)	ng (2.09E-11)
Pokrovsky and Schott (2000a)	8.89 (ng)	0.01 M NaCl	0.08 (ng)	5E-05, 1.E-4	298	2.88E5	ng (2.82E-11)	ng (1.55E-11)
Pokrovsky and Schott (2000a)	8.69 (ng)	0.01 M NaCl	0.08 (ng)	5E-05, 1.E-4	298	2.592E5	ng (2.40E-11)	ng (1.32E-11)
Pokrovsky and Schott (2000a)	8.74 (ng)	0.01 M NaCl	0.08 (ng)	5E-05, 1.E-4	298	4.392E5	ng (1.66E-11)	ng (9.12E-12)
Pokrovsky and Schott (2000b)	5.4 (ng)	I = 0.012 M	0.08 (ng)	5E-05, 1.E-4	298	1.548E5	4.90E-10(5.50E-10)	4.90E-10(3.02E-10)
Pokrovsky and Schott (2000b)	5.44 (ng)	I = 0.012 M	0.08 (ng)	5E-05, 1.E-4	298	1.62E5	3.39E-10(3.98E-10)	3.39E-10(2.19E-10)
Pokrovsky and Schott (2000b)	5.47 (ng)	I = 0.012 M	0.08 (ng)	5E-05, 1.E-4	298	1.08E5	2.69E-10(3.80E-10)	2.69E-10(2.09E-10)
Pokrovsky and Schott (2000b)	5.44 (ng)	I = 0.012 M	0.08 (ng)	5E-05, 1.E-4	298	5.76E4	3.39E-10(3.80E-10)	3.39E-10(2.09E-10)
Pokrovsky and Schott (2000b)	8.38 (ng)	I = 0.1 M	0.08 (ng)	5E-05, 1.E-4	298	4.968E5	6.61E-11(6.76E-11)	6.61E-11(3.71E-11)
Pokrovsky and Schott (2000b)	8.55 (ng)	I = 0.1 M	0.08 (ng)	5E-05, 1.E-4	298	9.504E5	3.80E-11(3.72E-11)	3.80E-11(2.04E-11)
Pokrovsky and Schott (2000b)	8.5 (ng)	I = 0.1 M	0.08 (ng)	5E-05, 1.E-4	298	3.996E5	4.68E-11(4.68E-11)	4.68E-11(2.57E-11)
Pokrovsky and Schott (2000b)	8.53 (ng)	I = 0.1 M	0.08 (ng)	5E-05, 1.E-4	298	3.456E5	6.76E-11(6.61E-11)	6.76E-11(3.63E-11)

References	Initial (Final) pH	Initial Fluid Composition	Initial (Final) Specific Surface Area [m^2/g]	Grain Size (min, max) [m]	Temperature [K]	Duration of Dissolution [s]	Si (Mg) Release Rate [$mol/m^2/s$]	Mineral Dissolution Rate base on Si (Mg) [$mol/m^2/s$]
Pokrovsky and Schott (2000b)	10.39 (ng)	I = 0.02 M	0.08 (ng)	5E-05, 1.E-4	298	6.408E5	ng (9.12E-12)	ng (5.01E-12)
Pokrovsky and Schott (2000b)	8.68 (ng)	I = 0.1 M	0.08 (ng)	5E-05, 1.E-4	298	1.584E6	3.47E-11(3.89E-11)	3.47E-11(2.14E-11)
Pokrovsky and Schott (2000b)	8.55 (ng)	I = 0.1 M	0.08 (ng)	5E-05, 1.E-4	298	3.24E5	3.98E-11(3.98E-11)	3.98E-11(2.19E-11)
Pokrovsky and Schott (2000b)	8.63 (ng)	I = 0.1 M	0.08 (ng)	5E-05, 1.E-4	298	7.2E5	3.63E-11(3.39E-11)	3.63E-11(1.86E-11)
Pokrovsky and Schott (2000b)	8.46 (ng)	I = 0.1 M	0.08 (ng)	5E-05, 1.E-4	298	1.872E5	ng (1.78E-11)	ng (9.77E-12)
Pokrovsky and Schott (2000b)	8.65 (ng)	I = 0.1 M	0.08 (ng)	5E-05, 1.E-4	298	2.484E5	ng (2.00E-11)	ng (1.10E-11)
Pokrovsky and Schott (2000b)	8.71 (ng)	I = 0.1 M	0.08 (ng)	5E-05, 1.E-4	298	5.904E5	2.51E-11(1.74E-11)	2.51E-11(9.55E-12)
Pokrovsky and Schott (2000b)	8.92 (ng)	I = 0.1 M	0.08 (ng)	5E-05, 1.E-4	298	1.0368E6	1.58E-11(1.55E-11)	1.58E-11(8.51E-12)
Pokrovsky and Schott (2000b)	8.8 (ng)	I = 0.1 M	0.08 (ng)	5E-05, 1.E-4	298	8.64E5	9.55E-12(1.23E-11)	9.55E-12(6.76E-12)
Pokrovsky and Schott (2000b)	11.15 (ng)	I = 0.1 M	0.08 (ng)	5E-05, 1.E-4	298	6.12E5	2.69E-11(7.94E-12)	2.69E-11(4.36E-12)
Pokrovsky and Schott (2000b)	11.11 (ng)	I = 0.1 M	0.08 (ng)	5E-05, 1.E-4	298	5.184E5	2.75E-11(5.37E-12)	2.75E-11(2.95E-12)
Pokrovsky and Schott (2000b)	11.1 (ng)	I = 0.1 M	0.08 (ng)	5E-05, 1.E-4	298	4.32E5	2.24E-11(7.41E-12)	2.24E-11(4.07E-12)
Pokrovsky and Schott (2000b)	11.12 (ng)	I = 0.1 M	0.08 (ng)	5E-05, 1.E-4	298	2.052E5	3.02E-11(9.77E-12)	3.02E-11(5.37E-12)

Pokrovsky and Schott (2000b)	11.23 (ng)	I = 0.1 M	0.08 (ng)	5E-05, 1.E-4	298	1.872E5	ng (4.47E-12)	ng (2.45E-12)
Pokrovsky and Schott (2000b)	11.25 (ng)	I = 0.1 M	0.08 (ng)	5E-05, 1.E-4	298	2.484E5	ng (4.57E-12)	ng (2.51E-12)
Pokrovsky and Schott (2000b)	11.22 (ng)	I = 0.1 M	0.08 (ng)	5E-05, 1.E-4	298	5.904E5	ng (2.57E-12)	ng (1.41E-12)
Pokrovsky and Schott (2000b)	11.22 (ng)	I = 0.1 M	0.08 (ng)	5E-05, 1.E-4	298	1.044E6	ng (2.09E-12)	ng (1.15E-12)
Pokrovsky and Schott (2000b)	11.23 (ng)	I = 0.1 M	0.08 (ng)	5E-05, 1.E-4	298	8.64E5	ng (1.91E-12)	ng (1.05E-12)
Oelkers (2001)	2 (ng)	I = 0	0.0808 (ng)	5E-05, 1.E-4	298	7.2E3–8.64E4	ng (1.57E-08)	ng (8.82E-09)
Oelkers (2001)	2 (ng)	I = 0	0.0808 (ng)	5E-05, 1.E-4	298	7.2E3–8.64E4	ng (1.76E-08)	ng (9.89E-09)
Oelkers (2001)	2 (ng)	I = 0	0.0808 (ng)	5E-05, 1.E-4	298	7.2E3–8.64E4	ng (1.21E-08)	ng (6.80E-09)
Oelkers (2001)	2 (ng)	I = 0	0.0808 (ng)	5E-05, 1.E-4	298	7.2E3–8.64E4	ng (1.23E-08)	ng (6.91E-09)
Oelkers (2001)	2 (ng)	I = 0	0.0808 (ng)	5E-05, 1.E-4	298	7.2E3–8.64E4	ng (1.41E-08)	ng (7.92E-09)
Oelkers (2001)	2 (ng)	I = 0	0.0808 (ng)	5E-05, 1.E-4	298	7.2E3–8.64E4	ng (1.55E-08)	ng (8.71E-09)
Oelkers (2001)	2 (ng)	I = 0	0.0808 (ng)	5E-05, 1.E-4	298	7.2E3–8.64E4	ng (1.05E-08)	ng (5.90E-09)
Oelkers (2001)	2 (ng)	0.001 M Mg	0.0808 (ng)	5E-05, 1.E-4	298	7.2E3–8.64E4	ng (1.33E-08)	ng (7.47E-09)
Oelkers (2001)	2 (ng)	0.001 M Mg	0.0808 (ng)	5E-05, 1.E-4	298	7.2E3–8.64E4	ng (1.33E-08)	ng (7.47E-09)
Oelkers (2001)	2 (ng)	0.001 M Mg	0.0808 (ng)	5E-05, 1.E-4	298	7.2E3–8.64E4	ng (1.27E-08)	ng (7.13E-09)
Oelkers (2001)	2 (ng)	0.001 M Mg	0.0808 (ng)	5E-05, 1.E-4	298	7.2E3–8.64E4	ng (1.29E-08)	ng (7.25E-09)
Oelkers (2001)	2 (ng)	0.001 M Mg	0.0808 (ng)	5E-05, 1.E-4	298	7.2E3–8.64E4	ng (1.21E-08)	ng (6.80E-09)
Oelkers (2001)	2 (ng)	0.0004579 M Si	0.0808 (ng)	5E-05, 1.E-4	298	7.2E3–8.64E4	ng (1.25E-08)	ng (7.02E-09)
Oelkers (2001)	2 (ng)	0.0004579 M Si	0.0808 (ng)	5E-05, 1.E-4	298	7.2E3–8.64E4	ng (1.23E-08)	ng (6.91E-09)
Oelkers (2001)	2 (ng)	0.0004579 M Si	0.0808 (ng)	5E-05, 1.E-4	298	7.2E3–8.64E4	ng (1.34E-08)	ng (7.53E-09)
Oelkers (2001)	2 (ng)	0.0004579 M Si	0.0808 (ng)	5E-05, 1.E-4	298	7.2E3–8.64E4	ng (1.18E-08)	ng (6.63E-09)
Oelkers (2001)	2 (ng)	0.0005 M Mg	0.0808 (ng)	5E-05, 1.E-4	298	7.2E3–8.64E4	ng (1.22E-08)	ng (6.85E-09)

References	Initial (Final) pH	Initial Fluid Composition	Initial (Final) Specific Surface Area [m^2/g]	Grain Size (min, max) [m]	Temperature [K]	Duration of Dissolution [s]	Si (Mg) Release Rate [$mol/m^2/s$]	Mineral Dissolution Rate base on Si (Mg) [$mol/m^2/s$]
Oelkers (2001)	2 (ng)	0.0005 M Mg	0.0808 (ng)	5E-05, 1.E-4	298	7.2E3–8.64E4	ng (1.17E-08)	ng (6.57E-09)
Oelkers (2001)	2 (ng)	0.0005 M Mg	0.0808 (ng)	5E-05, 1.E-4	298	7.2E3–8.64E4	ng (1.3E-08)	ng (7.30E-09)
Oelkers (2001)	2 (ng)	0.0002272 M Si	0.0808 (ng)	5E-05, 1.E-4	298	7.2E3–8.64E4	ng (1.03E-08)	ng (5.79E-09)
Oelkers (2001)	2 (ng)	0.0002272 M Si	0.0808 (ng)	5E-05, 1.E-4	298	7.2E3–8.64E4	ng (1.29E-08)	ng (7.25E-09)
Oelkers (2001)	2 (ng)	0.0002272 M Si	0.0808 (ng)	5E-05, 1.E-4	298	7.2E3–8.64E4	ng (1.2E-08)	ng (6.74E-09)
Rosso and Rimstidt (2000)	1.8 (ng)	I = 0	0.654 (ng)	0.00025, 0.00035	298	ng	1.58E-08 (ng)	1.58E-08 (ng)
Rosso and Rimstidt (2000)	1.8 (ng)	0.00004 M Mg	0.654 (ng)	0.00025, 0.00035	298	ng	1.58E-08 (ng)	1.58E-08 (ng)
Rosso and Rimstidt (2000)	1.8 (ng)	0.0004 M Mg	0.654 (ng)	0.00025, 0.00035	298	ng	1.58E-08 (ng)	1.58E-08 (ng)
Rosso and Rimstidt (2000)	1.8 (ng)	0.004 M Mg	0.654 (ng)	0.00025, 0.00035	298	ng	1.63E-08 (ng)	1.63E-08 (ng)
Rosso and Rimstidt (2000)	3.8 (ng)	0	0.654 (ng)	0.00025, 0.00035	298	ng	1.49E-09 (ng)	1.49E-09 (ng)
Rosso and Rimstidt (2000)	3.8 (ng)	0.0006 M Mg	0.654 (ng)	0.00025, 0.00035	298	ng	1.54E-09 (ng)	1.54E-09 (ng)
Rosso and Rimstidt (2000)	1.81 (ng)	Ng	0.654 (ng)	0.00025, 0.00035	298	6.8268E5	1.5E-08(2.71E-08)	1.5E-08(1.47E-08)
Rosso and Rimstidt (2000)	1.86 (ng)	Ng	0.654 (ng)	0.00025, 0.00035	298	6.8268E5	1.39E-08(2.3E-08)	1.39E-08(1.25E-08)
Rosso and Rimstidt (2000)	1.77 (ng)	Ng	0.654 (ng)	0.00025, 0.00035	298	5.9652E5	1.32E-08(2.49E-08)	1.32E-08(1.35E-08)

Rosso and Rimstidt (2000)	2.77 (ng)	Ng	0.654 (ng)	0.00025, 0.00035	298	9.2214E5	5.49E-09(1.01E-08)	5.49E-09(5.49E-09)
Rosso and Rimstidt (2000)	2.74 (ng)	Ng	0.654 (ng)	0.00025, 0.00035	298	3.3384E5	5.53E-09(9.51E-09)	5.53E-09(5.17E-09)
Rosso and Rimstidt (2000)	2.9 (ng)	Ng	0.654 (ng)	0.00025, 0.00035	298	3.3384E5	5.49E-09(8.64E-09)	5.49E-09(4.7E-09)
Rosso and Rimstidt (2000)	3.75 (ng)	Ng	0.654 (ng)	0.00025, 0.00035	298	5.9598E5	1.49E-09(2.16E-09)	1.49E-09(1.17E-09)
Rosso and Rimstidt (2000)	3.73 (ng)	Ng	0.654 (ng)	0.00025, 0.00035	298	5.9598E5	2.17E-09(3.02E-09)	2.17E-09(1.64E-09)
Rosso and Rimstidt (2000)	3.73 (ng)	Ng	0.654 (ng)	0.00025, 0.00035	298	7.7988E5	ng (2.52E-09)	ng (1.37E-09)
Wogelius and Walther (1992b)	3 (ng)	unbuffered	ng (ng)	0.000149, 0.00042	298	ng	3.23E-09(5.13E-09)	3.23E-09(2.82E-09)
Wogelius and Walther (1992b)	4 (ng)	KCl-HCl buffer	ng (ng)	0.000149, 0.00042	298	ng	1.88E-09(3.78E-09)	1.88E-09(2.08E-09)
Wogelius and Walther (1992b)	5 (ng)	NaOH-Na-borate buffer	ng (ng)	0.000149, 0.00042	298	ng	1.93E-09(1.83E-09)	1.93E-09(1.01E-09)
Wogelius and Walther (1992b)	4.2 (ng)	Ng	ng (ng)	0.000149, 0.00042	298	ng	1.31E-09(1.74E-09)	1.31E-09(9.56E-10)
Wogelius and Walther (1991a)	4.1 (ng)	Ng	ng (ng)	0.000149, 0.00042	298	1.5444E6	ng (ng)	7.94E-10(8.51E-10)
Wogelius and Walther (1991a)	5.7 (ng)	Ng	ng (ng)	0.000149, 0.00042	298	2.0736E6	ng (ng)	ng (1.66E-10)
Wogelius and Walther (1991a)	12 (ng)	Ng	ng (ng)	0.000149, 0.00042	298	2.34E5	ng (ng)	ng (4.37E-11)

References	Initial (Final) pH	Initial Fluid Composition	Initial (Final) Specific Surface Area [m^2/g]	Grain Size (min, max) [m]	Temperature [K]	Duration of Dissolution [s]	Si (Mg) Release Rate [$mol/m^2/s$]	Mineral Dissolution Rate base on Si (Mg) [$mol/m^2/s$]
Wogelius and Walther (1991a)	10.4 (ng)	HCl	ng (ng)	0.000149, 0.00042	298	9.612E5	ng (ng)	7.24E-11(1.82E-11)
Wogelius and Walther (1991a)	7.4 (ng)	Ng	ng (ng)	0.000149, 0.00042	298	5.976E5	ng (ng)	1.7E-10(1.58E-10)
Wogelius and Walther (1991a)	9.9 (ng)	KOH	ng (ng)	0.000149, 0.00042	298	5.112E5	ng (ng)	ng (3.47E-11)
Wogelius and Walther (1991a)	9.9 (ng)	KOH	ng (ng)	0.000149, 0.00042	298	8.568E5	ng (ng)	3.39E-11(2.63E-11)
Wogelius and Walther (1991a)	9.9 (ng)	KOH	ng (ng)	0.000149, 0.00042	298	4.284E5	ng (ng)	7.94E-11(4.17E-11)
Wogelius and Walther (1991a)	3.7 (ng)	NaOH	ng (ng)	0.000149, 0.00042	298	1.2024E6	ng (ng)	5.62E-09(5.37E-09)
Wogelius and Walther (1991b)	10.8 (ng)	NaOH	ng (ng)	0.000149, 0.00042	298	5.94E5	ng (ng)	3.02E-11(5.37E-12)
Wogelius and Walther (1991b)	3 (ng)	NAOH	ng (ng)	0.000149, 0.00042	298	2.2932E6	ng (ng)	1.48E-09(1.62E-09)
Wogelius and Walther (1991a)	5 (ng)	0.001 M ASC	ng (ng)	0.000149, 0.00042	298	1.2096E6	ng (ng)	1.91E-09(1.86E-09)

Wogelius and Walther (1991a)	5.7 (ng)	NaOH	ng (ng)	0.000149, 0.00042	298	1.5516E6	ng (ng)	6.17E-11(4.57E-11)
Wogelius and Walther (1991a)	2 (ng)	HCl	ng (ng)	0.000149, 0.00042	298	8.46E5	ng (ng)	7.08E-09(1.02E-08)
Wogelius and Walther (1991a)	9.1 (ng)	10^ − 1.3M KHP+ NaOH	ng (ng)	0.000149, 0.00042	298	7.632E5	ng (ng)	9.33E-11(2.88E-11)
Wogelius and Walther (1991a)	3.7 (ng)		ng (ng)	0.000149, 0.00042	298	3.2544E6	ng (ng)	5.01E-09(4.9E-09)
Wogelius and Walther (1991a)	2.5 (ng)	HCl	ng (ng)	0.000149, 0.00042	298	1.8E6	ng (ng)	6.76E-09(6.17E-09)
Wogelius and Walther (1991a)	4.4 (ng)	NaOH	ng (ng)	0.000149, 0.00042	298	5.184E5	ng (ng)	6.03E-09(3.02E-09)
Wogelius and Walther (1991a)	3.7 (ng)		ng (ng)	0.000149, 0.00042	298	3.2544E6	ng (ng)	5.01E-09(4.9E-09)
Wogelius and Walther (1991a)	2.5 (ng)	HCl	ng (ng)	0.000149, 0.00042	298	1.8E6	ng (ng)	6.76E-09(6.17E-09)
Wogelius and Walther (1991a)	4.4 (ng)	NaOH	ng (ng)	0.000149, 0.00042	298	5.184E5	ng (ng)	6.03E-09(3.02E-09)
Wogelius and Walther (1991a)	3.1 (ng)	0.001 M ASC	ng (ng)	0.000149, 0.00042	298	1.0296E6	ng (ng)	6.61E-09(4.57E-09)
Wogelius and Walther (1991a)	4 (ng)	0.001 M ASC + HCl	ng (ng)	0.000149, 0.00042	298	1.8972E6	ng (ng)	1.91E-09(3.8E-09)

References	Initial (Final) pH	Initial Fluid Composition	Initial (Final) Specific Surface Area [m^2/g]	Grain Size (min, max) [m]	Temperature [K]	Duration of Dissolution [s]	Si (Mg) Release Rate [$mol/m^2/s$]	Mineral Dissolution Rate base on Si (Mg) [$mol/m^2/s$]
Wogelius and Walther (1991a)	3 (ng)	0.001 M ASC + NaOH	ng (ng)	0.000149, 0.00042	298	4.5468E6	ng (ng)	3.24E-09(5.13E-09)
Wogelius and Walther (1991b)	3.5 (ng)	0.01 M ASC	ng (ng)	0.000149, 0.00042	298	1.2132E6	ng (ng)	5.5E-09(5.01E-09)
Wogelius and Walther (1991b)	3.1 (ng)	10^ – 1.3 M KHP + HCl	ng (ng)	0.000149, 0.00042	298	1.7856E6	ng (ng)	4.07E-09(1.32E-08)
Wogelius and Walther (1991a)	5.3 (ng)	10^ – 1.3 M KHP + HCl	ng (ng)	0.000149, 0.00042	298	1.1124E6	ng (ng)	1.86E-09(1.7E-09)
Wogelius and Walther (1991a)	10.8 (ng)	0.001 M ASC	ng (ng)	0.000149, 0.00042	298	3.6972E6	ng (ng)	1.26E-10(5.37E-11)
Wogelius and Walther (1991b)	11.1 (ng)	0.01 M ASC	ng (ng)	0.000149, 0.00042	298	1.5768E6	ng (ng)	6.46E-10 (ng)
Wogelius and Walther (1991a)	12.4 (ng)	0.0001 M ASC	ng (ng)	0.000149, 0.00042	298	3.006E6	ng (ng)	3.16E-10 (ng)
Wogelius and Walther (1991a)	4.1 (ng)	NaBorate/ NaOH	ng (ng)	0.000149, 0.00042	298	1.2276E6	ng (ng)	8.91E-09(8.13E-09)
Wogelius and Walther (1991a)	8.1 (ng)	NaOH	ng (ng)	0.000149, 0.00042	298	1.206E6	ng (ng)	5.75E-11(1.05E-10)
Wogelius and Walther (1991a)	10.7 (ng)	NaOH	ng (ng)	0.000149, 0.00042	298	1.206E6	ng (ng)	ng (4.17E-10)
Wogelius and Walther (1991a)	10.3 (ng)	10^ – 1.3 M KHP + NaOH	ng (ng)	0.000149, 0.00042	298	1.1412E6	ng (ng)	2.40E-10(9.33E-10)

Wogelius and Walther (1991a)	9.3 (ng)	BaBorate/ HCL	ng (ng)	0.000149, 0.00042	298	1.1376E6	ng (ng)	ng (9.12E-10)
Wogelius and Walther (1991b)	12.2 (ng)	BaBorate/ NaOH	ng (ng)	0.000149, 0.00042	298	5.58E5	ng (ng)	9.12E-09(9.55E-10)
Wogelius and Walther (1991a)	10.1 (ng)	BaBorate/ NaOH	ng (ng)	0.000149, 0.00042	298	5.112E5	ng (ng)	ng (ng)
Siegel and Pfannkuch (1984)	4 (ng)	Ng	1.2 (ng)	3.8E-05, 4.2E-05	295	5.6052E6	ng (3.98E-11)	5.01E-12(2.54E-11)
Eriksson (1982)	3.55 (ng)	Ng	0.04 (ng)	0.0006, ng	278–280	3.5424E6	ng (9E-10)	ng (1.24E-08)
Eriksson (1982)	4.3 (ng)	Ng	0.04 (ng)	0.0006, ng	278–280	3.5424E6	ng (3.5E-10)	ng (4.81E-09)
Eriksson (1982)	5.2 (ng)	Ng	0.04 (ng)	0.0006, ng	278–280	3.5424E6	ng (9E-11)	ng (1.24E-09)
Eriksson (1982)	3.7 (ng)	Ng	0.054 (ng)	0.00025, ng	278–280	3.5424E6	ng (1.18E-09)	ng (1.2E-08)
Eriksson (1982)	4.5 (ng)	Ng	0.054 (ng)	0.00025, ng	278–280	3.5424E6	ng (4E-10)	ng (4.07E-09)
Eriksson (1982)	5.05 (ng)	Ng	0.054 (ng)	0.00025, ng	278–280	3.5424E6	ng (2.3E-10)	ng (2.34E-09)
Eriksson (1982)	3.55 (ng)	Ng	0.108 (ng)	0.00025, ng	278–280	3.2832E6	ng (1.35E-09)	ng (6.87E-09)
Eriksson (1982)	4.3 (ng)	Ng	0.108 (ng)	0.00025, ng	278–280	3.2832E6	ng (5E-10)	ng (2.54E-09)
Eriksson (1982)	4.9 (ng)	Ng	0.108 (ng)	0.00025, ng	278–280	3.2832E6	ng (4E-10)	ng (2.04E-09)

References	Initial (Final) pH	Initial Fluid Composition	Initial (Final) Specific Surface Area [m^2/g]	Grain Size (min, max) [m]	Temperature [K]	Duration of Dissolution [s]	Si (Mg) Release Rate [$mol/m^2/s$]	Mineral Dissolution Rate base on Si (Mg) [$mol/m^2/s$]
Eriksson (1982)	3.7 (ng)	Ng	0.04 (ng)	0.0006, ng	278–280	2.592E6	ng (2.2E-10)	ng (3.02E-09)
Eriksson (1982)	4.45 (ng)	Ng	0.04 (ng)	0.0006, ng	278–280	2.592E6	ng (6E-10)	ng (8.24E-09)
Eriksson (1982)	5.2 (ng)	Ng	0.04 (ng)	0.0006, ng	278–280	2.592E6	ng (0)	ng (0)
Eriksson (1982)	4 (ng)	Ng	0.054 (ng)	0.00025, ng	278–280	2.592E6	ng (4.7E-10)	ng (4.78E-09)
Eriksson (1982)	4.7 (ng)	Ng	0.054 (ng)	0.00025, ng	278–280	2.592E6	ng (0)	ng (0)
Eriksson (1982)	5.05 (ng)	Ng	0.054 (ng)	0.00025, ng	278–280	2.592E6	ng (0)	ng (0)
Eriksson (1982)	3.85 (ng)	Ng	0.108 (ng)	0.00025, ng	278–280	3.3696E6	ng (1.41E-09)	ng (7.17E-09)
Eriksson (1982)	4.45 (ng)	Ng	0.108 (ng)	0.00025, ng	278–280	3.3696E6	ng (5.3E-10)	ng (2.7E-09)
Eriksson (1982)	4.95 (ng)	Ng	0.108 (ng)	0.00025, ng	278–280	3.3696E6	ng (4.9E-10)	ng (2.49E-09)
Eriksson (1982)	3.8 (ng)	Ng	0.04 (ng)	0.0006, ng	278–280	3.2832E6	ng (5.2E-10)	ng (7.14E-09)
Eriksson (1982)	5.25 (ng)	Ng	0.04 (ng)	0.0006, ng	278–280	3.2832E6	ng (2E-10)	ng (2.75E-09)
Eriksson (1982)	5.25 (ng)	Ng	0.04 (ng)	0.0006, ng	278–280	3.2832E6	ng (0)	ng (0)
Eriksson (1982)	4.3 (ng)	Ng	0.054 (ng)	0.00025, ng	278–280	3.2832E6	ng (2.2E-10)	ng (2.24E-09)

Eriksson (1982)	4.8 (ng)	Ng	0.054 (ng)	0.00025, ng	278–280	3.2832E6	ng (0)	ng (0)
Eriksson (1982)	5.2 (ng)	Ng	0.054 (ng)	0.00025, ng	278–280	3.2832E6	ng (0)	ng (0)
Grandstaff (1980)	3.2 (ng)	Ng	0.93 (ng)	7.4E-05, 0.000149	298	>4.32E6	7.96E-11(1.34E-10)	7.96E-11(8.1E-11)
Grandstaff (1986)	3.48 (ng)	Ng	0.93 (0.93)	7.4E-05, 0.000149	299	>4.32E6	ng (9.33E-11)	5.25E-11(5.69E-11)
Grandstaff (1986)	3.6 (ng)	Ng	0.93 (0.93)	7.4E-05, 0.000149	299	>4.32E6	ng (5.37E-10)	1.12E-11(3.27E-10)
Grandstaff (1986)	4.5 (ng)	Ng	0.93 (0.93)	7.4E-05, 0.000149	299	>4.32E6	ng (1.23E-10)	2.63E-10(7.5E-11)
Grandstaff (1986)	4.5 (ng)	Ng	0.93 (0.93)	7.4E-05, 0.000149	299	>4.32E6	ng (2.04E-11)	6.91E-11(1.24E-11)
Grandstaff (1986)	4.5 (ng)	Ng	0.93 (0.93)	7.4E-05, 0.000149	299	>4.32E6	ng (6.17E-12)	1.23E-11(3.76E-12)
Grandstaff (1986)	4.5 (ng)	Ng	0.93 (0.93)	7.4E-05, 0.000149	299	>4.32E6	ng (9.55E-12)	ng (5.82E-12)
Grandstaff (1986)	4.5 (ng)	Ng	0.93 (0.93)	7.4E-05, 0.000149	299	>4.32E6	ng (1.12E-11)	5.24E-12(6.84E-12)
Grandstaff (1986)	4.5 (ng)	Ng	0.93 (0.93)	7.4E-05, 0.000149	299	>4.32E6	ng (4.07E-11)	6.17E-12(2.48E-11)
Grandstaff (1986)	4.5 (ng)	Ng	0.93 (0.93)	7.4E-05, 0.000149	299	>4.32E6	ng (7.76E-11)	2.63E-11(4.73E-11)
Grandstaff (1986)	4.5 (ng)	Ng	0.93 (0.93)	7.4E-05, 0.000149	299	>4.32E6	ng (1.91E-10)	ng (1.16E-10)
Grandstaff (1986)	4.5 (ng)	Ng	0.93 (0.93)	7.4E-05, 0.000149	299	>4.32E6	ng (7.76E-12)	1.2E-10(4.73E-12)
Grandstaff (1986)	4.5 (ng)	Ng	0.93 (0.93)	7.4E-05, 0.000149	299	>4.32E6	ng (5.37E-12)	ng (3.27E-12)
Grandstaff (1986)	4.5 (ng)	Ng	0.93 (0.93)	7.4E-05, 0.000149	299	>4.32E6	ng (6.61E-11)	3.39E-12(4.03E-11)

References	Initial (Final) pH	Initial Fluid Composition	Initial (Final) Specific Surface Area [m^2/g]	Grain Size (min, max) [m]	Temperature [K]	Duration of Dissolution [s]	Si (Mg) Release Rate [$mol/m^2/s$]	Mineral Dissolution Rate base on Si (Mg) [$mol/m^2/s$]
Grandstaff (1986)	4.5 (ng)	Ng	0.93 (0.93)	7.4E-05, 0.000149	299	>4.32E6	ng (2.51E-11)	ng (1.53E-11)
Grandstaff (1986)	4.5 (ng)	Ng	0.93 (0.93)	7.4E-05, 0.000149	299	>4.32E6	ng (1.58E-10)	ng (9.66E-11)
Grandstaff (1986)	4.5 (ng)	Ng	0.93 (0.93)	7.4E-05, 0.000149	299	>4.32E6	ng (1.26E-10)	9.5E-11(7.68E-11)
Grandstaff (1986)	2.9 (ng)	Ng	0.93 (0.93)	7.4E-05, 0.000149	299	>4.32E6	ng (1.91E-09)	ng (1.16E-09)
Grandstaff (1986)	4.5 (ng)	Ng	0.93 (0.93)	7.4E-05, 0.000149	299	>4.32E6	ng (3.24E-11)	1.12E-9(1.97E-11)
Grandstaff (1986)	4.5 (ng)	Ng	0.93 (0.93)	7.4E-05, 0.000149	299	>4.32E6	ng (6.17E-11)	1.51E-11(3.76E-11)
Grandstaff (1986)	4.5 (ng)	Ng	0.93 (0.93)	7.4E-05, 0.000149	299	>4.32E6	ng (1.95E-10)	3.89E-11(1.19E-10)
Grandstaff (1986)	4.5 (ng)	Ng	0.93 (0.93)	7.4E-05, 0.000149	299	>4.32E6	ng (5.75E-10)	1.02E-10(3.51E-10)
Grandstaff (1986)	3.5 (ng)	Ng	0.93 (0.93)	7.4E-05, 0.000149	299	>4.32E6	ng (5.13E-10)	3.31E-10(3.13E-10)
Grandstaff (1986)	3 (ng)	Ng	0.93 (0.93)	7.4E-05, 0.000149	299	>4.32E6	ng (1.91E-10)	3.16E-10(1.16E-10)
Grandstaff (1986)	3.2 (ng)	Ng	0.93 (0.93)	7.4E-05, 0.000149	299	>4.32E6	ng (1.35E-10)	1.35E-10(8.23E-11)
Grandstaff (1986)	4 (ng)	Ng	0.93 (0.93)	7.4E-05, 0.000149	299	>4.32E6	ng (2.19E-11)	7.94E-11(1.33E-11)
Grandstaff (1986)	4.5 (ng)	Ng	0.93 (0.93)	7.4E-05, 0.000149	299	>4.32E6	ng (5.13E-12)	1.23E-11(3.13E-12)

Grandstaff (1986)	5 (ng)	Ng	0.93 (0.93)	7.4E-05, 0.000149	299	>4.32E6	ng (1.41E-12)	2.91E-12(8.61E-13)
Brady and Walther (1989)	8 (ng)	Ng	ng (ng)	ng, ng	ng	ng	ng (ng)	ng (6.31E-11)
Blum and Lasaga (1988)	3.04 (ng)	Ng	ng (ng)	ng, ng	ng	ng	ng (ng)	ng (7.38E-09)
Blum and Lasaga (1988)	4.38 (ng)	Ng	ng (ng)	ng, ng	ng	ng	ng (ng)	ng (1.91E-09)
Blum and Lasaga (1988)	4.08 (ng)	Ng	ng (ng)	ng, ng	ng	ng	ng (ng)	ng (1.08E-09)
Blum and Lasaga (1988)	4.73 (ng)	Ng	ng (ng)	ng, ng	ng	ng	ng (ng)	ng (3.65E-10)
Blum and Lasaga (1988)	8.78 (ng)	Ng	ng (ng)	ng, ng	ng	ng	ng (ng)	ng (8.46E-11)
Blum and Lasaga (1988)	8.93 (ng)	Ng	ng (ng)	ng, ng	ng	ng	ng (ng)	ng (8.11E-11)
Blum and Lasaga (1988)	4.41 (ng)	Ng	ng (ng)	ng, ng	ng	ng	ng (ng)	ng (1.76E-09)
Blum and Lasaga (1988)	2.89 (ng)	Ng	ng (ng)	ng, ng	ng	ng	ng (ng)	ng (6.81E-09)
Blum and Lasaga (1988)	1.8 (ng)	Ng	ng (ng)	ng, ng	ng	ng	ng (ng)	ng (1.62E-08)
Blum and Lasaga (1988)	2.35 (ng)	Ng	ng (ng)	ng, ng	ng	ng	ng (ng)	ng (8.81E-09)
Blum and Lasaga (1988)	3.38 (ng)	Ng	ng (ng)	ng, ng	ng	ng	ng (ng)	ng (3.19E-09)
Blum and Lasaga (1988)	3.7 (ng)	Ng	ng (ng)	ng, ng	ng	ng	ng (ng)	ng (2.46E-09)
Blum and Lasaga (1988)	8.97 (ng)	Ng	ng (ng)	ng, ng	ng	ng	ng (ng)	ng (9.57E-11)

References	Initial (Final) pH	Initial Fluid Composition	Initial (Final) Specific Surface Area [m^2/g]	Grain Size (min, max) [m]	Temperature [K]	Duration of Dissolution [s]	Si (Mg) Release Rate [$mol/m^2/s$]	Mineral Dissolution Rate base on Si (Mg) [$mol/m^2/s$]
Blum and Lasaga (1988)	5.53 (ng)	Ng	ng (ng)	ng, ng	ng	ng	ng (ng)	ng (2.25E-12)
Blum and Lasaga (1988)	7.24 (ng)	Ng	ng (ng)	ng, ng	ng	ng	ng (ng)	ng (1.29E-12)
Blum and Lasaga (1988)	9.46 (ng)	Ng	ng (ng)	ng, ng	ng	ng	ng (ng)	ng (2.89E-11)
Blum and Lasaga (1988)	11.02 (ng)	Ng	ng (ng)	ng, ng	ng	ng	ng (ng)	ng (1.23E-10)
Blum and Lasaga (1988)	11.35 (ng)	Ng	ng (ng)	ng, ng	ng	ng	ng (ng)	ng (5.62E-11)

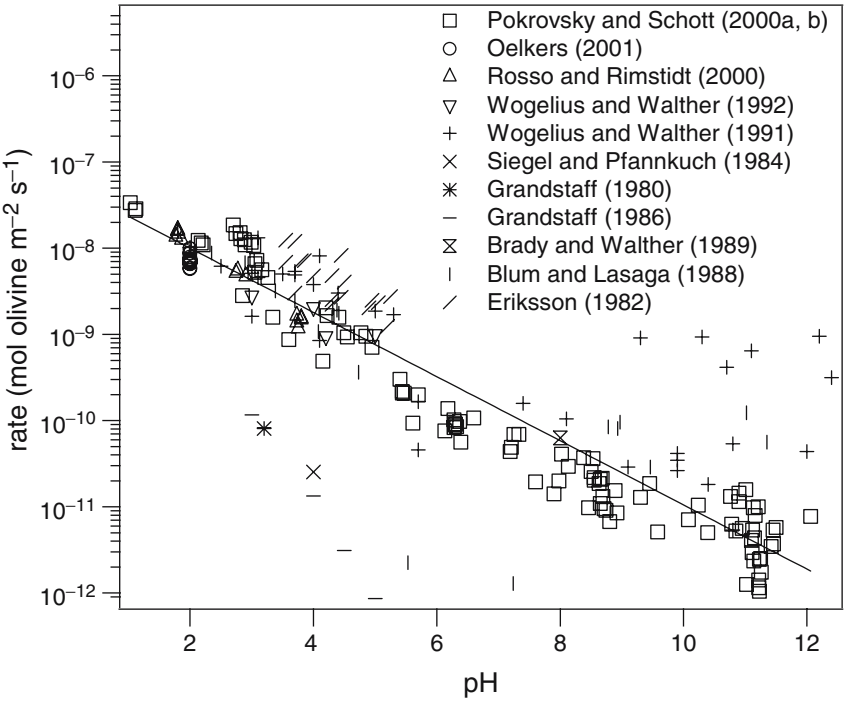

References

Pokrovsky and Schott (2000a) *Geochimica et Cosmochimica Acta* 64, 3313–3325. Forsterite, (Mg1.82Fe0.18)SiO4, Open-system mixed-flow reactor, pO2 not given pCO2 = 0, surface area measured by BET, dissolution was stoichiometric.

Pokrovsky and Schott (2000b) *Geochimica et Cosmochimica Acta* 64, 3313–3325. Forsterite, (Mg1.82Fe0.18)SiO4, Open-system mixed-flow reactor, pO2 not given pCO2 = 0.5 atm, surface area measured by BET, dissolution was stoichiometric.

Oelkers (2001) *Chemical Geology* 175, 485–494. Forsterite, (Mg1.78Fe0.17)SiO4, mixed flow reactor, pO2 and pCO2 not given, surface area measured by BET, dissolution was stoichiometric.

Rosso and Rimstidt (2000) *Geochimica et Cosmochimica Acta* 64, 797–811. Forsterite, (Mg1.84Fe0.14)SiO4, internally stirred mixed flow reactor, pO2 = ambient pCO2 = ambient, surface area measured by BET, dissolution was stoichiometric.

Wogelius and Walther (1992a) *Chemical Geology* 97, 101–112. Forsterite, (Mg1.82Fe0.18)SiO4, batch reactor, pO2 and pCO2 not given, surface area measured by BET, dissolution was stoichiometric.

Wogelius and Walther (1992b) *Chemical Geology* 97, 101–112. Forsterite, (Mg1.82Fe0.18)SiO4, fluidized bed reactor, pO2 and pCO2 not given, surface area measured by BET, dissolution was stoichiometric.

Wogelius and Walther (1991a) *Geochimica et Cosmochimica Acta* 55, 943–954. Forsterite, (Mg1.82Fe0.18)SiO4, fluidized bed reactor, pO2 not given pCO2 = ambient, surface area measured by BET (Kr), dissolution was stoichiometric. These data were excluded from the fit because of differences in the reactor type.

Wogelius and Walther (1991b) *Geochimica et Cosmochimica Acta* 55, 943–954. Forsterite, Mg2SiO4, batch reactor, pO2 not given pCO2 = ambient, surface area measured by BET, dissolution was stoichiometric. These data were excluded from the fit because of differences in the reactor type.

Siegel and Pfannkuch (1984) *Geochimica et Cosmochimica Acta* 48, 197–201. Olivine, (Mg1.57Fe0.26)SiO4, batch reactor, pO2 and pCO2 = ambient, surface area measured by BET, dissolution was stoichiometric. These data were excluded from the fit because of differences in the reactor type.

Eriksson (1982) *Vatten* 38, 409–415. Olivine, batch reactor, pO2 = 90% air pCO2 = 10% CO2, surface area measured by instrument from Micrometrics Instrument Corp, dissolution was stoichiometric.

Grandstaff (1980) Third International Symposium on Water-Rock Interaction, WRI-3, 72–74. Forsterite, (Mg1.66Fe0.34)SiO4, batch reactor, pO2 and pCO2 not given, surface area measured by BET, dissolution was stoichiometric. These data were excluded from the fit because of differences in the reactor type.

Grandstaff (1986) In *Rates of Chemical Weathering of Rocks and Minerals* (ed. S. M. Colman and D. P. Dethier), pp. 41–59. Academic Press, Inc. Forsterite, (Mg1.64Fe0.36)SiO4, pH-stat reactor, pO2 = ambient pCO2 = ambient, surface area measured by BET, dissolution was stoichiometric. These data were excluded from the fit because of differences in the reactor type.

Brady and Walther (1989) *Geochimica et Cosmochimica Acta* 53, 2823–2830. From Blum and Lasaga (1988) *Nature* 331, 431–433. Forsterite, (Mg1.86Fe0.14)SiO4, flow-through fluidized bed reactor, pO2 and pCO2 not given, surface area measured by BET (N2 Kr), dissolution was stoichiometric.

Blum and Lasaga (1988) *Nature* 331, 431–433. Forsterite, (Mg1.86Fe0.14)SiO4, flow-through fluidized bed reactor, pO2 and pCO2 not given, surface area measured by BET (N2 Kr), dissolution was stoichiometric. These data were excluded from the fit because of differences in the reactor type.

Pyroxene

References	Initial (Final) pH	Initial (Final) Ionic Strength [mol/L]	Initial (Final) Specific Surface Area [m^2/g]	Grain Size (min, max) [m]	Temperature [K]	Duration of Dissolution [s]	Si Release Rate [mol/s]	Mineral Dissolution Rate [$mol/m^2/s$]
Hoch et al. (1996a)	5.8 (ng)	ng (ng)	0.39 (ng)	7.5e-05,0.00015	298	5616000	5.55E-12	2.78E-12
Hoch et al. (1996a)	5.8 (ng)	ng (ng)	0.39 (ng)	7.5e-05,0.00015	298	15811200	8.95E-12	4.48E-12
Hoch et al. (1996a)	5.8 (ng)	ng (ng)	0.39 (ng)	7.5e-05,0.00015	298	7084800	2.58E-11	1.29E-11
Hoch et al. (1996a)	5.8 (ng)	ng (ng)	0.39 (ng)	7.5e-05,0.00015	298	5270400	2.31E-11	1.15E-11
Schott and Berner (1985)	6 (ng)	ng (ng)	ng (ng)	ng, ng	293	ng	ng	1.26E-11
Siegel and Pfannkuch (1984a)	4.1 (ng)	ng (ng)	ng (ng)	ng, ng	295	ng	ng	7.94E-13
Sverdrup (1990a)	2.5 (ng)	ng (ng)	ng (ng)	ng, ng	298	ng	ng	1.26E-10
Sverdrup (1990a)	3.1 (ng)	ng (ng)	ng (ng)	ng, ng	298	ng	ng	6.31E-11
Sverdrup (1990a)	3.1 (ng)	ng (ng)	ng (ng)	ng, ng	298	ng	ng	3.98E-11
Sverdrup (1990a)	3.4 (ng)	ng (ng)	ng (ng)	ng, ng	298	ng	ng	3.16E-11
Sverdrup (1990a)	5.6 (ng)	ng (ng)	ng (ng)	ng, ng	298	ng	ng	1.58E-13
Sverdrup (1990a)	6.8 (ng)	ng (ng)	ng (ng)	ng, ng	298	ng	ng	3.98E-13
Sverdrup (1990b)	3.1 (ng)	ng (ng)	ng (ng)	ng, ng	296.5	ng	ng	5.01E-11
Sverdrup (1990b)	4.8 (ng)	ng (ng)	ng (ng)	ng, ng	296.5	ng	ng	2.51E-12
Sverdrup (1990b)	6.5 (ng)	ng (ng)	ng (ng)	ng, ng	296.5	ng	ng	2.51E-12
Grandstaff (1977)	1.19 (ng)	ng (ng)	ng (ng)	ng, ng	Ng	ng	ng	1.00E-10
Grandstaff (1977)	2.12 (ng)	ng (ng)	ng (ng)	ng, ng	Ng	ng	ng	1.58E-11
Grandstaff (1977)	2.33 (ng)	ng (ng)	ng (ng)	ng, ng	Ng	ng	ng	2.51E-11
Grandstaff (1977)	2.39 (ng)	ng (ng)	ng (ng)	ng, ng	Ng	ng	ng	2.00E-11
Grandstaff (1977)	3.3 (ng)	ng (ng)	ng (ng)	ng, ng	Ng	ng	ng	2.51E-12
Grandstaff (1977)	3.96 (ng)	ng (ng)	ng (ng)	ng, ng	Ng	ng	ng	1.58E-12
Schott and Berner (1983)	1 (ng)	ng (ng)	ng (ng)	ng, ng	Ng	ng	ng	1.58E-11
Schott and Berner (1983)	6 (ng)	ng (ng)	ng (ng)	ng, ng	Ng	ng	ng	1.00E-11
Schott and Berner (1983)	6 (ng)	ng (ng)	ng (ng)	ng, ng	Ng	ng	ng	1.00E-12

References	Initial (Final) pH	Initial (Final) Ionic Strength [mol/L]	Initial (Final) Specific Surface Area [m^2/g]	Grain Size (min, max) [m]	Temperature [K]	Duration of Dissolution [s]	Si Release Rate [mol/s]	Mineral Dissolution Rate [$mol/m^2/s$]
Ferruzzi et al. (1993)	2 (ng)	ng (ng)	ng (ng)	ng, ng	298	ng	ng	2.00E-10
Ferruzzi et al. (1993)	4.8 (ng)	ng (ng)	ng (ng)	ng, ng	298	ng	ng	1.58E-10
Ferruzzi et al. (1993)	7 (ng)	ng (ng)	ng (ng)	ng, ng	298	ng	ng	1.00E-11
Luce et al. (1972)	1.6 (ng)	ng (ng)	ng (ng)	ng, ng	298	ng	ng	7.94E-10
Schott et al. (1981c)	1 (ng)	ng (ng)	ng (ng)	ng, ng	295	ng	ng	3.16E-10
Schott et al. (1981c)	2 (ng)	ng (ng)	ng (ng)	ng, ng	295	ng	ng	6.31E-11
Schott et al. (1981c)	6 (ng)	ng (ng)	ng (ng)	ng, ng	295	ng	ng	3.16E-13
Siegel and Pfannkuch (1984b)	4.1 (ng)	ng (ng)	ng (ng)	ng, ng	295	ng	ng	3.98E-13
Oelkers and Schott	2 (ng)	ng (ng)	0.08 (0.17)	5e-05, 0.0001	301	ng	ng	2.7E-10
Chen and Brantley (1998)	1 (1.23)	HCl-H2O	0.086 (0.139)	7.5e-05, 0.00015	298	1.22E+07	5.20E-12	3.02E-11
Chen and Brantley (1998)	2 (2.05)	HCl-H2O	0.086 (ng)	7.5e-05, 0.00015	298	1.22E+07	4.27E-12	2.48E-11
Chen and Brantley (1998)	3 (3.16)	HCl-H2O	0.086 (ng)	7.5e-05, 0.00015	298	1.22E+07	3.14E-12	1.83E-11
Chen and Brantley (1998)	3.5 (3.55)	HCl-H2O	0.086 (ng)	7.5e-05, 0.00015	298	1.22E+07	1.58E-12	9.21E-12
Eggleston et al. (1989)	1 (1)	HCl-H2O	ng (ng)	ng, 7.5e-05	293	9.00E+04	ng	5.01E-11
Hoch et al. (1996b)	5.8 (5.8)	KHCO3	0.2 (ng)	7.5e-05, 0.00015	298	2.07E+06	ng	1.36E-12
Hoch et al. (1996b)	5.8 (5.8)	KHCO3	0.2 (ng)	7.5e-05, 0.00015	298	2.07E+06	ng	5.67E-13
Knaus et al. (1993)	2 (2.03)	HCL-KHPhth	0.055 (ng)	7.5e-05, 0.000125	298	4.5E+06	ng	1.12E-10
Knaus et al. (1993)	4 (4.08)	KOH-KHPhth	0.055 (ng)	7.5e-05, 0.000125	298	4.5E+06	ng	8.51E-11
Knaus et al. (1993)	6 (5.95)	KOH-KHPhth	0.055 (ng)	7.5e-05, 0.000125	298	4.5E+06	ng	1.48E-11
Knaus et al. (1993)	8 (7.57)	KOH-H3BO3	0.055 (ng)	7.5e-05, 0.000125	298	4.5E+06	ng	1.07E-11
Knaus et al. (1993)	10 (9.41)	KOH-H3BO3	0.055 (ng)	7.5e-05, 0.000125	298	4.5E+06	ng	6.92E-12
Knaus et al. (1993)	12 (12.07)	KOH-H3BO3	0.055 (ng)	7.5e-05, 0.000125	298	4.5E+06	ng	6.92E-12

Knaus et al. (1993)	7 (7.64)	KOH-H3BO3	0.055 (ng)	7.5e-05, 0.000125	298	3.5E+06	ng	1.15E-11
Knaus et al. (1993)	10 (9.82)	KOH-H3BO3	0.055 (ng)	7.5e-05, 0.000125	298	4.4E+06	ng	7.59E-12
Knaus et al. (1993)	12 (12.2)	KOH-H3BO3	0.055 (ng)	7.5e-05, 0.000125	298	2.4E+06	ng	4.68E-12
Schott et al. (1981a)	1 (1)	HCl-KHPth-KCl-NaOH	ng (ng)	8.3e-05, 0.000125	295	6.7E+06	ng	6.31E-09
Schott et al. (1981a)	1.5 (1.5)	HCl-KHPth-KCl-NaOH	ng (ng)	8.3e-05, 0.000125	295	6.7E+06	ng	7.94E-09
Schott et al. (1981a)	2 (2)	HCl-KHPth-KCl-NaOH	ng (ng)	8.3e-05, 0.000125	295	6.7E+06	ng	6.31E-09
Schott et al. (1981a)	2.4 (2.4)	HCl-KHPth-KCl-NaOH	ng (ng)	8.3e-05, 0.000125	295	6.7E+06	ng	5.01E-09
Schott et al. (1981a)	3 (3)	HCl-KHPth-KCl-NaOH	ng (ng)	8.3e-05, 0.000125	295	6.7E+06	ng	2.51E-09
Schott et al. (1981a)	4 (4)	HCl-KHPth-KCl-NaOH	ng (ng)	8.3e-05, 0.000125	295	6.7E+06	ng	5.01E-10
Schott et al. (1981a)	4.5 (4.5)	HCl-KHPth-KCl-NaOH	ng (ng)	8.3e-05, 0.000125	295	6.7E+06	ng	1.26E-10
Schott et al. (1981a)	5 (5)	HCl-KHPth-KCl-NaOH	ng (ng)	8.3e-05, 0.000125	295	6.7E+06	ng	7.94E-11
Schott et al. (1981a)	5.6 (5.6)	HCl-KHPth-KCl-NaOH	ng (ng)	8.3e-05, 0.000125	295	6.7E+06	ng	3.16E-11
Schott et al. (1981a)	6 (6)	HCl-KHPth-KCl-NaOH	ng (ng)	8.3e-05, 0.000125	295	6.7E+06	ng	1.58E-11
Schott et al. (1981b)	1 (1)	HCl-KHPth-KCl-NaOH	0.06 (ng)	8.3e-05, 0.000125	293	6.7E+06	ng	3.16E-10
Schott et al. (1981b)	6 (6)	HCl-KHPth-KCl-NaOH	0.06 (ng)	8.3e-05, 0.000125	293	6.7E+06	ng	1.26E-11
Golubev et al. (2005)	ng (1.08)	NaCl-NaHCO3-Na2CO3	0.125 (ng)	5e-05, 0.0001	298	7.20E+05	ng	4.90E-11
Golubev et al. (2005)	ng (2.1)	NaCl-NaHCO3-Na2CO4	0.125 (ng)	5e-05, 0.0001	298	7.20E+05	ng	5.13E-11
Golubev et al. (2005)	ng (3.08)	NaCl-NaHCO3-Na2CO5	0.125 (ng)	5e-05, 0.0001	298	7.20E+05	ng	5.89E-11
Golubev et al. (2005)	ng (4.05)	NaCl-NaHCO3-Na2CO6	0.125 (ng)	5e-05, 0.0001	298	1.08E+06	ng	3.98E-11
Golubev et al. (2005)	ng (5.5)	NaCl-NaHCO3-Na2CO7	0.125 (ng)	5e-05, 0.0001	298	1.08E+06	ng	1.38E-11
Golubev et al. (2005)	ng (6.5)	NaCl-NaHCO3-Na2CO8	0.125 (ng)	5e-05, 0.0001	298	1.08E+06	ng	1.02E-11
Golubev et al. (2005)	ng (8.6)	NaCl-NaHCO3-Na2CO9	0.125 (ng)	5e-05, 0.0001	298	1.08E+06	ng	7.94E-12
Golubev et al. (2005)	ng (10.5)	NaCl-NaHCO3-Na2CO10	0.125 (ng)	5e-05, 0.0001	298	1.08E+06	ng	8.91E-12
Golubev et al. (2005)	ng (11.75)	NaCl-NaHCO3-Na2CO11	0.125 (ng)	5e-05, 0.0001	298	1.08E+06	ng	8.91E-12
Golubev et al. (2005)	ng (4.25)	NaCl-NaHCO3-Na2CO12	0.125 (ng)	5e-05, 0.0001	298	1.08E+06	ng	2.40E-11
Golubev et al. (2005)	ng (3)	NaCl-NaHCO3-Na2CO13	0.125 (ng)	5e-05, 0.0001	298	1.08E+06	ng	6.03E-11
Golubev et al. (2005)	ng (5.26)	NaCl-NaHCO3-Na2CO14	0.125 (ng)	5e-05, 0.0001	298	1.08E+06	ng	9.33E-12
Golubev et al. (2005)	ng (10.6)	NaCl-NaHCO3-Na2CO15	0.125 (ng)	5e-05, 0.0001	298	1.08E+06	ng	4.79E-12
Golubev et al. (2005)	ng (1)	NaCl-NaHCO3-Na2CO16	0.125 (ng)	5e-05, 0.0001	298	7.20E+05	ng	6.46E-11
Golubev et al. (2005)	ng (2)	NaCl-NaHCO3-Na2CO17	0.125 (ng)	5e-05, 0.0001	298	7.20E+05	ng	7.59E-11
Golubev et al. (2005)	ng (3.03)	NaCl-NaHCO3-Na2CO18	0.125 (ng)	5e-05, 0.0001	298	7.20E+05	ng	5.37E-11
Golubev et al. (2005)	ng (3.97)	NaCl-NaHCO3-Na2CO19	0.125 (ng)	5e-05, 0.0001	298	1.08E+06	ng	3.16E-11
Golubev et al. (2005)	ng (7.7)	NaCl-NaHCO3-Na2CO20	0.125 (ng)	5e-05, 0.0001	298	1.08E+06	ng	9.33E-12

References	Initial (Final) pH	Initial (Final) Ionic Strength [mol/L]	Initial (Final) Specific Surface Area [m^2/g]	Grain Size (min, max) [m]	Temperature [K]	Duration of Dissolution [s]	Si Release Rate [mol/s]	Mineral Dissolution Rate [$mol/m^2/s$]
Golubev et al. (2005)	ng (8)	NaCl-NaHCO3-Na2CO21	0.125 (ng)	5e-05, 0.0001	298	1.08E + 06	ng	1.00E-11
Golubev et al. (2005)	ng (8.3)	NaCl-NaHCO3-Na2CO22	0.125 (ng)	5e-05, 0.0001	298	1.08E + 06	ng	9.55E-12
Golubev et al. (2005)	ng (8.5)	NaCl-NaHCO3-Na2CO23	0.125 (ng)	5e-05, 0.0001	298	1.08E + 06	ng	9.33E-12
Golubev et al. (2005)	ng (8)	NaCl-NaHCO3-Na2CO24	0.125 (ng)	5e-05, 0.0001	298	1.08E + 06	ng	8.13E-12
Golubev et al. (2005)	ng (10)	NaCl-NaHCO3-Na2CO25	0.125 (ng)	5e-05, 0.0001	298	1.08E + 06	ng	1.05E-11
Golubev et al. (2005)	ng (10.6)	NaCl-NaHCO3-Na2CO26	0.125 (ng)	5e-05, 0.0001	298	1.08E + 06	ng	5.75E-12
Golubev et al. (2005)	ng (11)	NaCl-NaHCO3-Na2CO27	0.125 (ng)	5e-05, 0.0001	298	1.08E + 06	ng	6.03E-12
Golubev et al. (2005)	ng (11.05)	NaCl-NaHCO3-Na2CO28	0.125 (ng)	5e-05, 0.0001	298	1.08E + 06	ng	7.08E-12
Golubev et al. (2005)	ng (11.15)	NaCl-NaHCO3-Na2CO29	0.125 (ng)	5e-05, 0.0001	298	1.08E + 06	ng	9.12E-12
Golubev et al. (2005)	ng (11.4)	NaCl-NaHCO3-Na2CO30	0.125 (ng)	5e-05, 0.0001	298	1.08E + 06	ng	1.10E-11

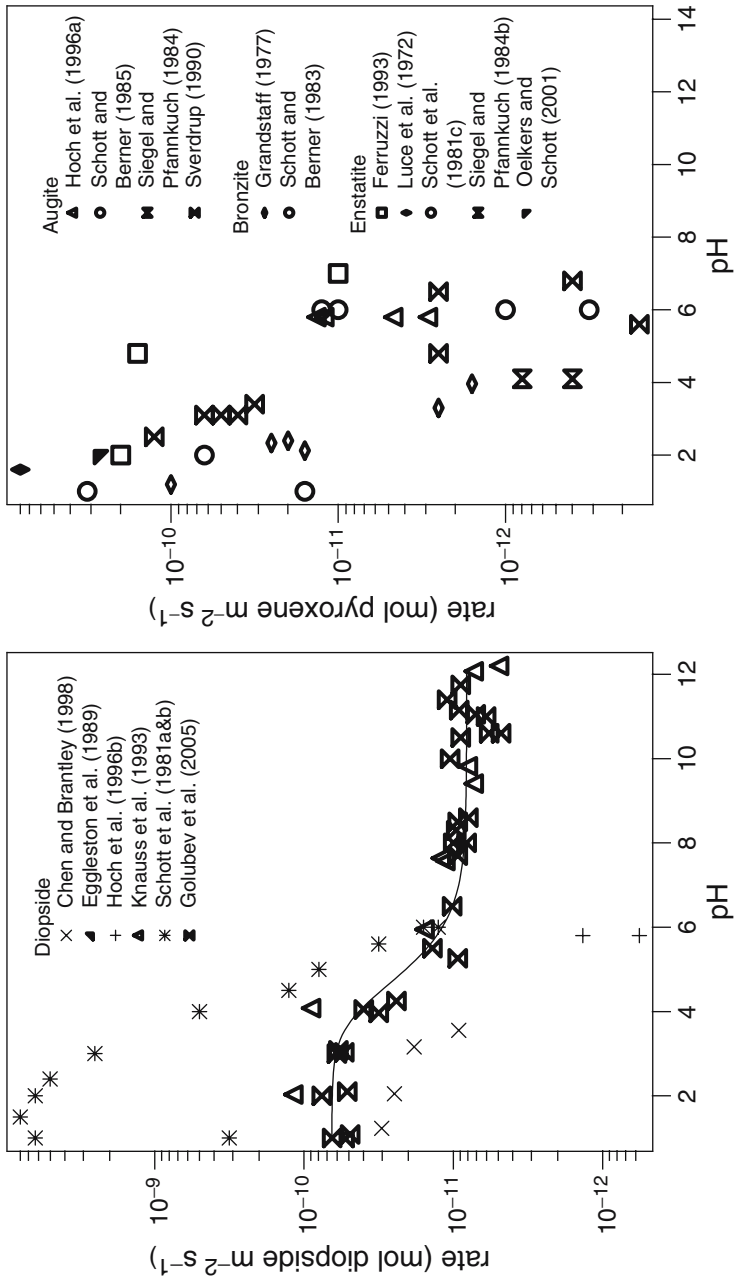
Diopside
Chen and Brantley (1998)
Eggleston et al. (1989)
Hoch et al. (1996b)
Knauss et al. (1993)
Schott et al. (1981a&b)
Golubev et al. (2005)
rate (mol diopside m⁻² s⁻¹)
pH
Augite
Hoch et al. (1996a)
Schott and Berner (1985)
Siegel and Pfannkuch (1984)
Sverdrup (1990)
Bronzite
Grandstaff (1977)
Schott and Berner (1983)
Enstatite
Ferruzzi (1993)
Luce et al. (1972)
Schott et al. (1981c)
Siegel and Pfannkuch (1984b)
Oelkers and Schott (2001)
rate (mol pyroxene m⁻² s⁻¹)
pH

References

Hoch, et al. (1996a) *Chemical Geology*, 132, 151–156. augite, Mg0.87Ca0. 85Fe0.19Na0.09Al0.03Si2O6, Flow through reactor, pO2 and pCO2 not given, surface area measured by BET.

Schott and Berber (1985) Dissolution mechanisms of pyroxenes and olivines during weathering. In *The Chemistry of Weathering* (ed. J. I. Drever). Reidel, vol. 149. Augite, pO2 and pCO2 not given.

Siegel and Pfannkuch (1984a) Silicate *Geochimica et Cosmochimica Acta*, 48, 197–201. augite, Na0.1Ca0.6Mg0.4Fe0.77Al0.05Si1.8O6, pO2 and pCO2 not given.

Sverdrup (1990a) The Kinetics of Base Cation Release due to Chemical Weathering. Lund University Press. augite, Ca0.55Fe0.55Mg0.9Si2O6, pO2 and pCO2 not given.

Sverdrup (1990b) The Kinetics of Base Cation Release due to Chemical Weathering. Lund University Press. augite, Mg1.02Ca0.88Fe0.10Si2O6, pO2 and pCO2 not given.

Grandstaff (1977) *Geochimica et Cosmochimica Acta*, 41, 1097–1103. bronzite, Mg1.54Fe0.42Ca0.04Si2O6, pO2 and pCO2 not given.

Schott and Berner (1983) *Geochimica et Cosmochimica Acta* 47, 2233–2240 bronzite, Mg1.77Fe0.23Si2O6, pO2 and pCO2 not given.

Ferruzzi et al. (1993) M.S. Thesis, University of California, Davis. enstatite, MgSiO3, pO2 and pCO2 not given.

Luce et al. (1972) *Geochimica et Cosmochimica Acta* 36, 35–50. enstatite, Mg1.85Fe0.1Si2O6, pO2 and pCO2 not given.

Schott et al. (1981c) *Geochimica et Cosmochimica Acta* 45, 2123–2135. enstatite, Mg2Fe0.08Ti0.002Al0.004Si1.97O6, pO2 and pCO2 not given.

Siegel and Pfannkuch (1984b) *Geochimica et Cosmochimica Acta* 48, 197–201. enstatite, Na0.1Ca0.03Mg1.6Fe0.6Al0.2Si1.6O6, pO2 and pCO2 not given.

Oelkers and Schott (2001) *Geochimica et Cosmochimica Acta*, 65, 1219–1231. enstatite, Mg0.849Fe0.136Ca0.004Si1.002O3, mixed flow reactor, pO2 and pCO2 not given, surface area measured by BET-Kr.

Chen and Brantley (1998) *Chemical Geology*, 147, 233–248. diopside, Ca0.8Mg0.8Fe0.2Al0.1Si2O6, pO2 and pCO2 not given. These data not included in the fit due to judgment by the data analyst.

Eggleston et al. (1989) *Geochimica et Cosmochimica Acta* 53, 797–804. diopside, CaMgSi2O6, pO2 and pCO2 not given.

Hoch et al. (1996b) *Chemical Geology*, 132, 151–156. diopside, Ca0.93Fe0. 07Mg0.91Mn0.05 Na0.03Al0.02Si2.01O6, Flow through reactor, pO2 and pCO2 not given, surface area measured by BET. These data not included in the fit due to judgment by the data analyst.

Knauss et al. (1993) *Geochimica et Cosmochimica Acta* 57, 285–294. diopside, Ca0.97Mg0.89Fe0.08Al0.04Si1.99O6, pO2 and pCO2 not given.

Schott et al. (1981a) *Geochimica et Cosmochimica Acta* 45, 2123–2135. diopside, Ca1.04Mg1.01Fe0.01Al0.015Si1.96O6, pO2 and pCO2 not given. These data not included in the fit due to judgment by the data analyst.

Schott et al. (1981b) *Geochimica et Cosmochimica Acta* 45, 2123–2135. diopside, Ca1.04Mg0.98Fe0.02Ti0.004Al0.01Si1.95O6, pO2 and pCO2 not given. These data not included in the fit due to judgment by the data analyst.

Golubev et al. (2005) *Chemical Geology* 217, 227–238 diopside, Ca0.99Mg0.98Fe0.02Cr0.01Si2O6, mixed flow reactor, pO2 = 1 pCO2 not given, surface area measured by BET-Kr, dissolution was stoichiometric below pH 10.

Quartz

References	Initial (Final) pH	Initial (Fluid) Composition	Initial (Final) Specific Surface Area [m^2/g]	Grain Size (min, max) [m]	Temperature [K]	Duration of Dissolution [s]	Si Release Rate [mol/s]	Mineral Dissolution Rate [$mol/m^2/s$]
Bennett et al. (1988)	3 (ng)	HCl, NaOH, NaHCO3, 0.02 mmol/kg HgCl2, I = 2.40 mmol/kg	0.17 (ng)	1.5E-05, 5E-05	298	6.30E6	ng	6.31E-14
Bennett et al. (1988)	5 (ng)	HCl, NaOH, NaHCO3, 0.02 mmol/kg HgCl2, I = 2.17 mmol/kg	0.17 (ng)	1.5E-05, 5E-05	298	6.30E6	ng	7.94E-14
Bennett et al. (1988)	6.6 (ng)	HCl, NaOH, NaHCO3, 0.02 mmol/kg HgCl2, I = 1.60 mmol/kg	0.17 (ng)	1.5E-05, 5E-05	298	6.30E6	ng	2.00E-13
Bennett et al. (1988)	7 (ng)	HCl, NaOH, NaHCO3, 0.02 mmol/kg HgCl2, I = 0.53 mmol/kg	0.17 (ng)	1.5E-05, 5E-05	298	6.30E6	ng	1.91E-13
Wollast and Chou (1988)	1.2 (ng)	0.2 M NaCl	0.03 (ng)	5E-05, 0.0001	298	ng	ng	2.24E-12
Wollast and Chou (1988)	2.2 (ng)	0.2 M NaCl	0.03 (ng)	5E-05, 0.0001	298	ng	ng	1.26E-12
Wollast and Chou (1988)	3 (ng)	0.2 M NaCl	0.03 (ng)	5E-05, 0.0001	298	ng	ng	5.62E-13
Wollast and Chou (1988)	4 (ng)	0.2 M NaCl	0.03 (ng)	5E-05, 0.0001	298	ng	ng	7.94E-13
Wollast and Chou (1988)	7.3 (ng)	0.2 M NaCl	0.03 (ng)	5E-05, 0.0001	298	ng	ng	5.01E-12
Wollast and Chou (1988)	8.9 (ng)	0.2 M NaCl	0.03 (ng)	5E-05, 0.0001	298	ng	ng	1.58E-11
Wollast and Chou (1988)	9.7 (ng)	0.2 M NaCl	0.03 (ng)	5E-05, 0.0001	298	ng	ng	2.82E-11
Wollast and Chou (1988)	11.1 (ng)	0.2 M NaCl	0.03 (ng)	5E-05, 0.0001	298	ng	ng	7.08E-11
Wollast and Chou (1988)	12.2 (ng)	0.2 M NaCl	0.03 (ng)	5E-05, 0.0001	298	ng	ng	1.12E-10

Brady and Walther (1990)	2.15 (ng)	KCl-HCl	0.00111 (0.00111)	7.9E-05, 0.000149	298	7.20E5–2.79E6	ng	8.91E-13
Brady and Walther (1990)	4.03 (ng)	NaCl-HCl	0.00111 (0.00111)	7.9E-05, 0.000149	298	7.20E5–2.79E6	ng	5.89E-13
Brady and Walther (1990)	4.09 (ng)	NaCl-HCl	0.00111 (0.00111)	7.9E-05, 0.000149	298	7.20E5–2.79E6	ng	7.94E-13
Brady and Walther (1990)	5.5 (ng)	Distilled H2O	0.00111 (0.00111)	7.9E-05, 0.000149	298	7.20E5–2.79E6	ng	3.63E-13
Brady and Walther (1990)	6.9 (ng)	Distilled H2O	0.00111 (0.00111)	7.9E-05, 0.000149	298	7.20E5-2.79E6	ng	1.26E-12
Brady and Walther (1990)	8.33 (ng)	TRIS-HCl	0.00111 (0.00111)	7.9E-05, 0.000149	298	7.20E5–2.79E6	ng	2.82E-12
Brady and Walther (1990)	9.02 (ng)	NaOH-NaCl	0.00111 (0.00111)	7.9E-05, 0.000149	298	7.20E5–2.79E6	ng	5.62E-12
Brady and Walther (1990)	10.27 (ng)	Na-borate-NaOH	0.00111 (0.00111)	7.9E-05, 0.000149	298	7.20E5–2.79E6	ng	7.94E-12
Brady and Walther (1990)	10.3 (ng)	KCl	0.00111 (0.00111)	7.9E-05, 0.000149	298	7.20E5–2.79E6	ng	1.26E-11
Brady and Walther (1990)	10.3 (ng)	KCl	0.00111 (0.00111)	7.9E-05, 0.000149	298	7.20E5–2.79E6	ng	4.90E-12
Brady and Walther (1990)	10.9 (ng)	NaOH-KCl	0.00111 (0.00111)	7.9E-05, 0.000149	298	7.20E5–2.79E6	ng	2.14E-11
Brady and Walther (1990)	11 (ng)	NaOH-NaCl	0.00111 (0.00111)	7.9E-05, 0.000149	298	7.20E5–2.79E6	ng	8.32E-12
Brady and Walther (1990)	11.04 (ng)	NaOH-NaCl	0.00111 (0.00111)	7.9E-05, 0.000149	298	7.20E5–2.79E6	ng	1.17E-11
Brady and Walther (1990)	12.3 (ng)	NaOH-KCl	0.00111 (0.00111)	7.9E-05, 0.000149	298	7.20E5–2.79E6	ng	3.98E-11
Brady and Walther (1990)	12.3 (ng)	NaOH-KCl	0.00111 (0.00111)	7.9E-05, 0.000149	298	7.20E5–2.79E6	ng	5.37E-11
Casey et al. (1990)	3 (ng)	0.001 M HCl	0.0492 (ng)	7.5E-05, 0.00015	298	2.59E5–2.59E6	ng	7.0E-13
Bennett (1991)	1.1 (ng)	HCl, HgCl2 (40 mg/L Hg)	0.17 (ng)	3E-05, 7.5E-05	298	1.44E6–5.4E6	ng	1.58E-13
Bennett (1991)	5.7 (ng)	< 0.001 HCO3 molal	0.17 (ng)	3E-05, 7.5E-05	298	1.44E6–5.4E6	ng	1.00E-13
Bennett (1991)	6 (ng)	< 0.001 HCO3 molal, < 0.000 Na molal	0.17 (ng)	3E-05, 7.5E-05	298	1.44E6–5.4E6	ng	2.00E-13
House and Orr (1992)	4.42 (ng)	0.01 M KHCO3, K2CO3, KCl-HCl	2.09 (ng)	2E-06, 2.6E-06	298	ng	ng	1.5E-13

References	Initial (Final) pH	Initial (Fluid) Composition	Initial (Final) Specific Surface Area [m^2/g]	Grain Size (min, max) [m]	Temperature [K]	Duration of Dissolution [s]	Si Release Rate [mol/s]	Mineral Dissolution Rate [$mol/m^2/s$]
House and Orr (1992)	4.43 (ng)	0.01 M KHCO3, K2CO3, KCl-HCl	2.09 (ng)	2E-06, 2.2E-06	298	ng	ng	1.90E-13
House and Orr (1992)	4.45 (ng)	0.01 M KHCO3, K2CO3, KCl-HCl	2.09 (ng)	2E-06, 2.6E-06	298	ng	ng	1.6E-13
House and Orr (1992)	4.46 (ng)	0.01 M KHCO3, K2CO3, KCl-HCl	2.3 (ng)	2E-06, 2.2E-06	298	ng	ng	1.8E-13
House and Orr (1992)	4.46 (ng)	0.01 M KHCO3, K2CO3, KCl-HCl	2.3 (ng)	2E-06, 2.2E-06	298	ng	ng	1.8E-13
House and Orr (1992)	4.48 (ng)	0.01 M KHCO3, K2CO3, KCl-HCl	2.09 (ng)	2E-06, 2.6E-06	298	ng	ng	1.90E-13
House and Orr (1992)	4.53 (ng)	0.01 M KHCO3, K2CO3, KCl-HCl	2.3 (ng)	2E-06, 2.2E-06	298	ng	ng	1.40E-13
House and Orr (1992)	4.54 (ng)	0.01 M KHCO3, K2CO3, KCl-HCl	2.3 (ng)	2E-06, 2.2E-06	298	ng	ng	1.40E-13
House and Orr (1992)	6.25 (ng)	0.01 M KHCO3, K2CO3, KCl-HCl	2.3 (ng)	2E-06, 2.2E-06	298	ng	ng	1.70E-13
House and Orr (1992)	6.41 (ng)	0.01 M KHCO3, K2CO3, KCl-HCl	2.3 (ng)	2E-06, 2.2E-06	298	ng	ng	1.70E-13
House and Orr (1992)	6.48 (ng)	0.01 M KHCO3, K2CO3, KCl-HCl	2.09 (ng)	2E-06, 2.6E-06	298	ng	ng	2.30E-13
House and Orr (1992)	6.5 (ng)	0.01 M KHCO3, K2CO3, KCl-HCl	2.09 (ng)	2E-06, 2.6E-06	298	ng	ng	2.30E-13
House and Orr (1992)	8.25 (ng)	0.01 M KHCO3, K2CO3, KCl-HCl	2.12 (ng)	2E-06, 2.6E-06	298	ng	ng	3.22E-12
House and Orr (1992)	8.35 (ng)	0.01 M KHCO3, K2CO3, KCl-HCl	2.12 (ng)	2E-06, 2.6E-06	298	ng	ng	2.56E-12
House and Orr (1992)	8.46 (ng)	0.01 M KHCO3, K2CO3, KCl-HCl	2.3 (ng)	2E-06, 2.2E-06	298	ng	ng	4.27E-12
House and Orr (1992)	8.47 (ng)	0.0 1 M KHCO3, K2CO3, KCl-HCl	2.12 (ng)	2E-06, 2.6E-06	298	ng	ng	4.52E-12
House and Orr (1992)	8.48 (ng)	0.01 M KHCO3, K2CO3, KCl-HCl	2.12 (ng)	2E-06, 2.6E-06	298	ng	ng	4.25E-12

House and Orr (1992)	8.55 (ng)	0.01 M KHCO3, K2CO3, KCl-HCl	2.09 (ng)	2E-06, 2.6E-06	298	ng	ng	3.41E-12
House and Orr (1992)	8.7 (ng)	0.01 M KHCO3, K2CO3, KCl-HCl	2.3 (ng)	2E-06, 2.2E-06	298	ng	ng	3.07E-12
House and Orr (1992)	8.72 (ng)	0.01 M KHCO3, K2CO3, KCl-HCl	2.09 (ng)	2E-06, 2.6E-06	298	ng	ng	4.40E-12
House and Orr (1992)	8.72 (ng)	0.01 M KHCO3, K2CO3, KCl-HCl	2.3 (ng)	2E-06, 2.2E-06	298	ng	ng	2.95E-12
House and Orr (1992)	10.46 (ng)	0.01 M KHCO3, K2CO3, KCl-HCl	2.3 (ng)	2E-06, 2.2E-06	298	ng	ng	2.72E-11
House and Orr (1992)	10.46 (ng)	0.01 M KHCO3, K2CO3, KCl-HCl	2.3 (ng)	2E-06, 2.2E-06	298	ng	ng	2.87E-11
House and Orr (1992)	10.49 (ng)	0.01 M KHCO3, K2CO3, KCl-HCl	2.12 (ng)	2E-06, 2.6E-06	298	ng	ng	1.92E-11
House and Orr (1992)	10.49 (ng)	0.01 M KHCO3, K2CO3, KCl-HCl	2.12 (ng)	2E-06, 2.6E-06	298	ng	ng	1.82E-11
Berger et al. (1994)	5.5 (ng)	DW	0.31 (ng)	ng, 5E-05	298	5.40E6	ng	2.00E-13
Berger et al. (1994)	6.5 (ng)	DW	0.31 (ng)	ng, 5E-05	298	5.40E6	ng	2.00E-13
Tester et al. (1994a)	7 (ng)	DW	0.0225 (ng)	0.00059, 0.00085	296	7.64E7	ng	3.16E-14
Tester et al. (1994a)	7 (ng)	DW	0.0225 (ng)	0.00059, 0.00085	296	7.64E7	ng	3.47E-14
Tester et al. (1994a)	7 (ng)	DW	0.0225 (ng)	0.00059, 0.00085	296	7.64E7	ng	3.55E-14
Tester et al. (1994a)	7 (ng)	DW	0.0225 (ng)	0.00059, 0.00085	296	7.64E7	ng	3.39E-14
Tester et al. (1994a)	7 (ng)	DW	0.0225 (ng)	0.00059, 0.00085	296	7.01E7	ng	5.75E-15
Tester et al. (1994a)	7 (ng)	DW	0.0225 (ng)	0.00059, 0.00085	295	7.01E7	ng	6.17E-15
Tester et al. (1994b)	7 (ng)	DW	0.0225 (ng)	0.00059, 0.00085	298	8.64E4	ng	1.41E-12
Tester et al. (1994b)	7 (ng)	DW	0.0225 (ng)	0.00059, 0.00085	298	8.64E4	ng	3.31E-13

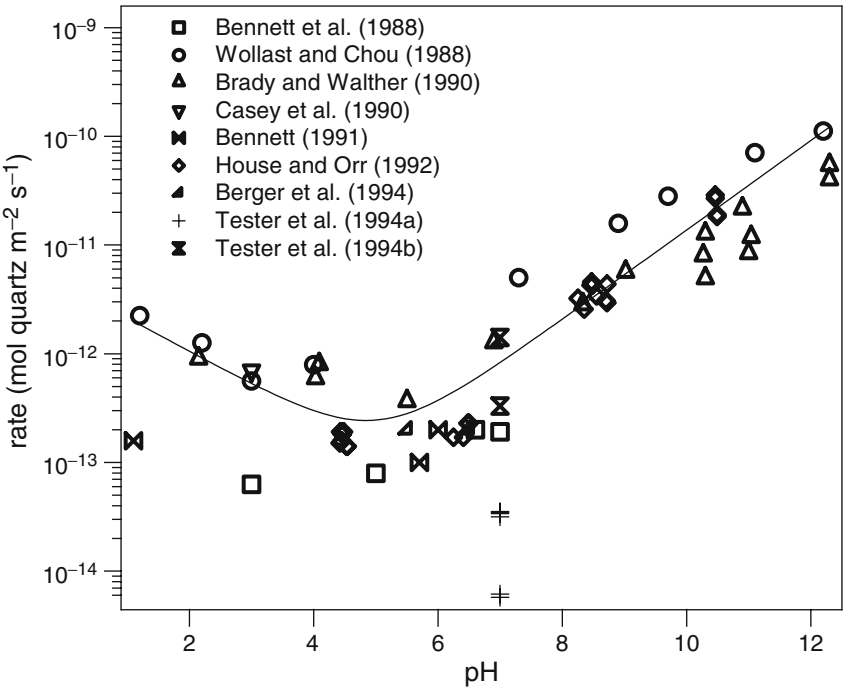

References

Bennett et al. (1988) *Geochimica et Cosmochimica Acta* 52, 1521–1530. SiO2, batch reactor, pO2 and pCO2 were atmospheric, surface area measured by BET-4 pt, dissolution was stoichiometric.

Wollast and Chou (1988) In *Physical and Chemical Weathering in Geochemical Cycles* (ed. A. Lerman and M. Maybeck), pp. 11–32. Kluwer Academic Publishers – as cited in Dove and Elston (1992) *Geochimica et Cosmochimica Acta* 56, 4147–4156. SiO2, fluidized bed reactor, pO2 and pCO2 were atmospheric, Geometric surface area, dissolution was stoichiometric.

Brady and Walther (1990) *Chemical Geology* 82, 253–64. SiO2, batch reactor, pO2 and pCO2 were atmospheric, surface area measured by BET-Kr, dissolution was stoichiometric.

Casey et al. (1990) *Geochimica et Cosmochimica Acta* 54, 3369–3378 – as cited in Dove and Elston (1992) *Geochimica et Cosmochimica Acta* 56, 4147–4156. SiO2, batch reactor, pO2 and pCO2 were atmospheric, surface area measured by BET-Kr,He, dissolution was stoichiometric.

Bennett (1991) *Geochimica et Cosmochimica Acta* 55, 1781–1797. SiO2, batch reactor, pO2 and pCO2 were atmospheric, surface area measured by BET-4 pt, dissolution was stoichiometric.

House and Orr (1992) *Journal of Chemical Society Faraday Transactions* 88, 233–241. SiO2, batch reactor, pO2 and pCO2 were atmospheric, surface area measured by BET-N2, dissolution was stoichiometric.

Berger et al. (1994) *Geochimica et Cosmochimica Acta* 58, 541–551. SiO2, batch reactor, pO2 and pCO2 were atmospheric, surface area measured by BET-Kr, dissolution was stoichiometric.

Tester et al. (1994a) *Geochimica et Cosmochimica Acta* 58, 2407–2420. SiO2, batch reactor, pO2 and pCO2 were atmospheric, surface area measured by BET-Kr, dissolution was stoichiometric. These data were excluded from the fit because of discrepancies with the Tester et al. (1994b) data, which more closely conformed to other measured quartz dissolution rates.

Tester et al. (1994b) *Geochimica et Cosmochimica Acta* 58, 2407–2420. SiO2, plug flow reactor, pO2 and pCO2 were atmospheric, surface area measured by BET-Kr, dissolution was stoichiometric.

Index

E

R

S

T